ISSN 1949-8470 (online)

World Journal of *Radiology*

World J Radiol 2023 January 28; 15(1): 1-31



Published by Baishideng Publishing Group Inc

World Journal of Radiology

Contents

Monthly Volume 15 Number 1 January 28, 2023

MINIREVIEWS

1 Clinical anatomy of hepatic vessels by computed tomography angiography: A minireview

Firat A, Abbasoglu TT, Karcaaltincaba M, Balaban YH

10 Advancements of molecular imaging and radiomics in pancreatic carcinoma

Pang XX, Xie L, Yao WJ, Liu XX, Pan B, Chen N

ORIGINAL ARTICLE

Retrospective Study

20 Diagnostic efficacy of diffusion-weighted imaging and semiquantitative and quantitative dynamic contrast-enhanced magnetic resonance imaging in salivary gland tumors

Gökçe E, Beyhan M

World Journal of Radiology

Monthly Volume 15 Number 1 January 28, 2023

Contents

ABOUT COVER

Editorial Board Member of *World Journal of Radiology*, Fernando Santiago, PhD, Doctor, Professor, Teacher, Department of Radiology, Santiago, FR (reprint author), Hosp Traumatol Ciudad Sanitaria Virgen de las Nie, Dept Radiol, Carretera Jaen SN, Granada 18013, Spain. ferusan12@gmail.com

AIMS AND SCOPE

The primary aim of *World Journal of Radiology* (*WJR*, *World J Radiol*) is to provide scholars and readers from various fields of radiology with a platform to publish high-quality basic and clinical research articles and communicate their research findings online.

WJR mainly publishes articles reporting research results and findings obtained in the field of radiology and covering a wide range of topics including state of the art information on cardiopulmonary imaging, gastrointestinal imaging, genitourinary imaging, musculoskeletal imaging, neuroradiology/head and neck imaging, nuclear medicine and molecular imaging, pediatric imaging, vascular and interventional radiology, and women's imaging.

INDEXING/ABSTRACTING

The *WJR* is now abstracted and indexed in PubMed, PubMed Central, Emerging Sources Citation Index (Web of Science), Reference Citation Analysis, China National Knowledge Infrastructure, China Science and Technology Journal Database, and Superstar Journals Database. The 2022 edition of Journal Citation Reports ® cites the 2021 Journal Citation Indicator (JCI) for *WJR* as 0.48.

RESPONSIBLE EDITORS FOR THIS ISSUE

Production Editor: *Si Zhao*; **Production Department Director:** *Xu Guo*; **Editorial Office Director:** *Jia-Ru Fan*.

NAME OF JOURNAL
World Journal of Radiology

ISSN
ISSN 1949-8470 (online)

LAUNCH DATE
January 31, 2009

FREQUENCY
Monthly

EDITORS-IN-CHIEF
Thomas J Vogl

EDITORIAL BOARD MEMBERS
https://www.wjgnet.com/1949-8470/editorialboard.htm

PUBLICATION DATE
January 28, 2023

COPYRIGHT
© 2023 Baishideng Publishing Group Inc

INSTRUCTIONS TO AUTHORS
https://www.wjgnet.com/bpg/gerinfo/204

GUIDELINES FOR ETHICS DOCUMENTS
https://www.wjgnet.com/bpg/GerInfo/287

GUIDELINES FOR NON-NATIVE SPEAKERS OF ENGLISH
https://www.wjgnet.com/bpg/gerinfo/240

PUBLICATION ETHICS
https://www.wjgnet.com/bpg/GerInfo/288

PUBLICATION MISCONDUCT
https://www.wjgnet.com/bpg/gerinfo/208

ARTICLE PROCESSING CHARGE
https://www.wjgnet.com/bpg/gerinfo/242

STEPS FOR SUBMITTING MANUSCRIPTS
https://www.wjgnet.com/bpg/GerInfo/239

ONLINE SUBMISSION
https://www.f6publishing.com

© 2023 Baishideng Publishing Group Inc. All rights reserved. 7041 Koll Center Parkway, Suite 160, Pleasanton, CA 94566, USA
E-mail: bpgoffice@wjgnet.com https://www.wjgnet.com

World Journal of Radiology

Submit a Manuscript: https://www.f6publishing.com

World J Radiol 2023 January 28; 15(1): 1-9

DOI: 10.4329/wjr.v15.i1.1

ISSN 1949-8470 (online)

MINIREVIEWS

Clinical anatomy of hepatic vessels by computed tomography angiography: A minireview

Aysegul Firat, Tugce Taskindere Abbasoglu, Musturay Karcaaltincaba, Yasemin H Balaban

Specialty type: Anatomy and morphology

Provenance and peer review: Invited article; Externally peer reviewed.

Peer-review model: Single blind

Peer-review report's scientific quality classification
Grade A (Excellent): 0
Grade B (Very good): 0
Grade C (Good): C, C
Grade D (Fair): D
Grade E (Poor): 0

P-Reviewer: Rasti S, Iran; Wu SZ, China

Received: September 19, 2022
Peer-review started: September 19, 2022
First decision: October 19, 2022
Revised: November 2, 2022
Accepted: December 27, 2022
Article in press: December 27, 2022
Published online: January 28, 2023

Aysegul Firat, Tugce Taskindere Abbasoglu, Department of Anatomy, Hacettepe University Faculty of Medicine, Ankara 06100, Turkey

Musturay Karcaaltincaba, Department of Radiology, Hacettepe University Faculty of Medicine, Ankara 06100, Turkey

Yasemin H Balaban, Department of Gastroenterology, Hacettepe University Faculty of Medicine, Ankara 06100, Turkey

Corresponding author: Yasemin H Balaban, MD, Professor, Department of Gastroenterology, Hacettepe University Faculty of Medicine, Gevher Nesibe caddesi, Ankara 06100, Turkey. ybalaban@hacettepe.edu.tr

Abstract

The liver has a complex vascular anatomy with a unique dual blood supply. Clinical conditions of the liver vary widely and include disorders originating in the vascular and biliary systems as well as the parenchyma. In most vascular disorders, the effects on the liver are generally subclinical because of its abundant blood supply. However, early diagnosis of such vascular diseases can significantly reduce patient morbidity and mortality. Because imaging findings of vascular disease are not always readily apparent, diagnosis can be difficult. Computed tomography angiography is an excellent imaging modality for visualizing the vascular anatomy of patients for treatment planning. In this review article, we focus on the vascular anatomy of the liver and the imaging findings in some acute hepatic vascular diseases.

Key Words: Computed tomography angiography; Hepatic artery; Portal vein; Sinusoid; Portal triad; Periportal region

©The Author(s) 2023. Published by Baishideng Publishing Group Inc. All rights reserved.

Core Tip: The liver has a complex vascular anatomy. Imaging findings may not be readily apparent in vascular disorders of the liver. Computed tomography angiography is an excellent imaging modality for visualizing the vascular anatomy of patients for treatment planning. This review article focuses on the vascular anatomy of the liver and imaging findings in some acute hepatic vascular diseases.

Citation: Firat A, Abbasoglu TT, Karcaaltincaba M, Balaban YH. Clinical anatomy of hepatic vessels by computed tomography angiography: A minireview. *World J Radiol* 2023; 15(1): 1-9
URL: https://www.wjgnet.com/1949-8470/full/v15/i1/1.htm
DOI: https://dx.doi.org/10.4329/wjr.v15.i1.1

INTRODUCTION

The liver performs a variety of metabolic processes for homeostasis, nutrition, and immune defence. For example, it is important for the removal and breakdown of toxic or potentially toxic substances from the blood; the regulation of blood glucose and lipids; the storage of certain vitamins, iron, and other micronutrients; the synthesis of proteins and clotting factors; the metabolism of amino acids; and the production of bile. It is involved in a variety of other biochemical reactions. Since most of these processes are exothermic, a significant portion of the body's thermal energy production, especially at rest, is provided by the liver. Acute clinical conditions of the liver vary widely and include disorders originating in the vascular and biliary systems as well as the parenchyma. The liver has a complex vascular anatomy with a unique dual blood perfusion. The portal vein provides 70% of the hepatic blood flow, while the hepatic artery provides the remaining 30%[1]. In most vascular disorders, the effects on the liver are generally subclinical due to this rich blood supply. However, some acute diseases of these vessels may be accompanied by abdominal pain. Early diagnosis of such vascular disease can significantly reduce patient morbidity and mortality. Computed tomography angiography (CTA) is now the standard procedure for surgical planning of living liver donors in whom most of the right lobe of liver with associated vessels and ducts, is removed for transplantation to the recipient. CTA visualises both the vascular and parenchymal anatomy of the liver. In this technique, the contrast agent is administered directly into the splanchnic bed by injection into the superior mesenteric artery. CT images acquired after an appropriate delay provide hepatic and portal phase images of the liver. Rapid image acquisition of vessels with thin sections is a critical feature of an optimal CTA protocol that prevents artefacts due to motion and respiration. Two-phase liver protocols include both an arterial and portal venous phase. CTA is an excellent imaging modality for visualising the patient's vascular anatomy for surgical planning of liver transplantation. Because imaging findings of vascular disorders may not be readily recognized, diagnosis can be difficult. In this review article, we focus on the vascular anatomy of the liver and the imaging findings in common acute diseases of the hepatic vasculature[2].

EMBRYOLOGY OF THE LIVER

The liver begins to develop from the anterior bulge of the endoderm of the foregut. From the cephalic part of this diverticular structure, splanchnic mesodermal cells migrate into the septum transversum. These cells, which concentrate around the vitelline veins, differentiate into hepatic cells as single-layered plaques. Kupffer cells also differentiate from the endothelial cells of the vitelline plexus. Biliary capillaries and cholangioles also develop from the mesenchyme between the hepatocellular plates. The vitelline veins form a plexus in the liver, which then unites with the umbilical veins and opens into the sinus venosus of the heart. Later, some portions of the vitelline veins undergo atresia and become the portal vein, which unites with the splenic vein and the superior mesenteric veins. The proximal portions of the vitelline vein join the right and left hepatic veins (RHV and LHV, respectively) between the sinus venosus and the hepatic plexus. The entire right umbilical vein and the proximal portion of the left umbilical vein, which is connected to the hepatic sinusoids, atrophy. Over time, venous blood from the placenta flows into the right vitelline vein in the liver and then directly to the heart *via* the ductus venosus, a large venous trunk that separates from the hepatic sinusoids. Meanwhile, half of the blood from the umbilical vein flows through the liver and the other half through the ductus venosus. The umbilical vein settles in the falciform ligament as the ligamentum teres, and as the liver continues to grow in the abdomen, it maintains contact with the septum transversum under the diaphragm[3].

HEPATIC ORGANIZATION

The liver has a spongy structure consisting of irregular single-row cell strands and spaces called lacunae between them. The diameter of the lacunae is larger than that of the hepatocytes. The capillaries within these lacunae are called sinusoids, which are lined with a basement membrane and are permeable to macromolecules. Kupffer cells, which are part of the reticuloendothelial system, are located around the endothelium of the sinusoids. The hexagonal cells of the cell strands are called hepatocytes. They form the critical cell layer between the sinusoids and the bile canaliculi. They have a unique polarity, with the basement membrane facing the sinusoidal endothelium, while one or more apical poles may contribute

to multiple bile canaliculi[2]. Between the endothelium of the sinusoids and the hepatocytes is a potential gap called the space of Disse. The fluid accumulated in this space is drained by the lymphatic vessels and blood capillaries. Since hepatocytes are polygonal in shape and have many facets, two or three facets are in contact with the space of Disse, while the remaining facets are in contact with the neighbouring liver cells. Bile canaliculi run between adjacent hepatocytes. Hepatocyte polarity is essential in explaining many functions of the liver. Hepatocyte strands and sinusoids run past each other in a branched and interlocking fashion, which increases metabolic exchange between the blood and biliary systems. The combination of the bile duct, hepatic artery, and hepatic portal vein is termed a portal triad. As they enter the liver, each divides into segmental branches surrounded by a perivascular fibrous capsule. The hepatic lobule is a hexagonal unit consisting of a concentric arrangement of a central vein in the middle and surrounding portal triads located at the vertices of each hexagon and hepatocyte strands, although the boundaries are not very sharp. Each portal triad is surrounded by a hepatocyte plate, which is traversed by the bile canaliculi and blood vessels. Between the portal triad and the hepatocyte strand is a gap called the space of Mall (periportal area). The hepatic lobule is perfused by the branches of the hepatic artery and portal vein at the periphery and drained by the central vein in the middle of the lobule. Blood flows centrifugally from the portal triad. Bile produced by the hepatocytes also flows centrifugally to the periphery. There is blood flow from the portal vein and hepatic artery to the hepatic vein depending on the blood pressure gradient. Each central vein opens through a sublobular vein, which eventually forms the right and LHVs, and opens into the inferior vena cava. Since there is no such blood pressure gradient in the embryo, the lobular cell arrangement is not observed, and this arrangement develops after birth. In this case, the lobule structure may change with blood pressure and blood flow[3].

Another functional concept is the liver acinus: A diamond-shaped area supplied by the terminal branches of the hepatic artery and portal vein. This small unit is important in describing functional and pathologic changes in many clinical conditions. Its short axis runs along the borders of the hepatic lobules and its imaginary long axis is located between the two central veins. The hepatocytes are located in three elliptical zones around the short axis[3-5]. The areas near the center of the acini receive more oxygenated blood because they are near the afferent vessels and are referred to as zone 1 (periportal zone). Zone 2 (intermediate zone) is the intermediate region that is more peripheral to the acini, and zone 3 is the region closest to the central vein at the end of the acini. Zone 3 is most affected by ischemic damage. The lobule and acinus formation systems, which complement each other, can be related to the gross anatomy that integrates functional modulation[6,7].

In the right and left lobes of the liver, arteries, portal veins, and bile ducts run parallel to each other. These vessels and ducts branch to disperse into segments and show many individual variations, and no anastomosis was observed between the intraparenchymal branches.

The bile duct, hepatic artery, portal vein, lymphatics, and nerves open horizontally into the porta hepatis, which is located in the middle part of the visceral surface of the liver.

CT protocol

CT examinations were performed with a 16-MDCT scanner (Somatom Sensation 16, Siemens, Germany). All patients received 100 mL of iodinated contrast material (Ultravist 300/100 mg/mL; Bayer Schering Pharma, Berlin, Germany) at a flow rate of 4 mL/s using a power injector. CT images were obtained 70 s after the injection of contrast for the portal venous phase, 15-20 s for the early arterial phase, and 30-40 s for the late arterial phase. Technical parameters were detector collimation, 1.5 mm; pitch, 1.5; gantry rotation time: 0.5 s. Axial images were reconstructed at a thickness of 2 mm and 5 mm and transferred to Picture Archiving and Communication System.

Portal vein

The portal vein is formed by the union of the superior mesenteric and splenic veins. It begins at the level of the second lumbar vertebra, where it lies behind the neck of the pancreas. It has an average length of 6.50 cm and a diameter of 1.09 cm and rises behind the first part of the duodenum. After entering the right margin of the lesser omentum anterior to the epiploic foramen, it reaches the right end of the porta hepatis and divides into right and left hepatic branches that accompany the corresponding branches of the hepatic artery, lymphatic vessels, and hepatic nerve plexus. It is located behind the common bile duct and hepatic artery in the lesser omentum. The superior gastroduodenal vein empties into the portal vein from the lower right, into the left gastric vein from the lower right, and into the right gastric vein from the right. The cholecystic vein drains into the right hepatic branch of the portal vein. The left portal vein receives only the obliterated umbilical vein. The right branch supplies segments V, VI, VII, and VIII. Segments I, II, III, and IV receives the left obliterated umbilical vein *via* the ligamentum teres. It eventually opens into intraparenchymal venules that arise at right angles from a distributive vein and are less than 0.3 mm in diameter. Blood in the branches of the portal vein and hepatic artery flows into the sinusoidal microcirculation. Blood within the sinusoids flows through the radially arranged plates and empties into the central vein[3,6,7].

Some anatomic variations in the portal venous system lead to contraindications for certain surgeries such as transplantation or increase the risk of postoperative complications. Shunt operations for portal hypertension have increased interest in portal vein anatomy and studies have shown that the portal

vein has fewer variations than the hepatic artery. Portal venous variants are frequent and account approximately 20%-35% of the population[8]: (1) The most common variant is the so-called ''portal vein trifurcation'' in which the main portal vein divides into three branches: The left portal vein, the right anterior portal vein, and the right posterior portal vein; (2) the second most common variant is a right posterior portal vein arising as the first branch of the portal vein; (3) in 10% of cases, no vein opens into the main trunk of the portal vein; (4) the left gastric vein joins the main trunk of the portal vein to the left side of the junction of the superior mesenteric vein and the splenic vein; (5) in 24% of cases, the left gastric vein joins the splenic vein; (6) the inferior mesenteric vein may drain from the junction of the splenic vein and the superior mesenteric vein into the portal vein; and (7) the inferior mesenteric vein may join with the superior mesenteric vein.

Imaging findings of disorders of the portal vein

The anatomy of the portal vein is best visualised in the coronal plane of CT angiography. Acute portal vein thrombosis is sudden blood clot formation in the portal vein lumen[9]. It can occur in cirrhosis, pylephlebitis, hematologic disorders, pancreatitis, diverticulitis of the colon, appendicitis, malignancies, and surgical procedures[10]. CT is commonly used for diagnosis and usually shows the absence/presence of enhancement within the thrombus, which is critical for characterising the thrombus (Figure 1A). Acute thrombosis is usually hyperdense on pre-contrast CT images, whereas chronic thrombosis can lead to calcifications in the portal vein and abnormal liver perfusion areas can be detected in the liver parenchyma, especially in the arterial phase[11,12]. A decrease in portal vein flow may be caused by portal vein or hepatic vein thrombosis, compression by focal masses such as abscesses, long-standing biliary obstruction, or parenchymal trauma. Pylephlebitis is defined as infectious thrombosis of either the portal vein or its intrahepatic branches or both and may lead to abscess formation in the parenchyma[13]. Diverticulitis of the colon is the most common cause of septic thrombophlebitis of the mesenteric and portal venous systems[14]. The standard treatment for acute portal vein thrombosis is anticoagulation. Portal vein aneurysms are rare and account for 3% of all venous aneuryms[15]. Most of these aneurysms are acquired, as a significant number of portal vein aneurysms are discovered in patients with underlying hepatocellular disease and portal hypertension.

Hepatic artery

The proper hepatic artery supplies the liver. It is a branch of the common hepatic artery separated from the coeliac trunk. The coeliac trunk is an anterior branch of the abdominal aorta and passes through the hiatus aorticus. It runs anteriorly and transversely over the pancreas and after a short course divides into the left gastric, splenic, and common hepatic branches. The common hepatic artery runs anteriorly and enters the lesser omentum from the right margin. Here it is located to the left of the common bile duct and anterior to the portal vein. On its way up, it branches into the gastroduodenal artery, the supraduodenal artery, and the right gastric artery. Simultaneously, it continues to ascend as the proper hepatic artery. When it reaches the porta hepatis of the liver, it branches into the right (RHA) and left (LHA) hepatic arteries. Normally, the RHA passes behind the common hepatic duct and branches into the cholecystic artery. In the portal triad, the branches of the hepatic artery run parallel to the portal vein. The arterioles distribute in the lobular parenchyma and they form a peribiliary plexus around the biliary capillaries.

The Michels' classification of the hepatic arterial anatomy with the approximate frequency of occurrence of each type of variant in the general population is shown in Table 1[16].

Classical branching of the hepatic artery is observed in around 76% of people[17]. Thus, a significant proportion of patients have a variant arterial anatomy (Figure 1B and C). Hepatic artery variations do not cause absolute contraindications for transplantation. However, being informed about these variations prior to the transplantation is a factor that would simplify the surgery, decrease the rate of contraindications, and improve the chance of technical success[16,17]: (1) The common hepatic artery, as a branch of the superior mesenteric artery, passes through or behind the pancreas and courses upward; (2) the common hepatic artery branches more proximal to the right and left hepatic artery before reaching the porta hepatis; (3) the right hepatic artery arises from the superior mesenteric artery, and the left hepatic artery arises from the coeliac trunk; (4) presence of accessory right hepatic artery originating from the superior mesenteric artery; (5) presence of accessory left hepatic artery originating from the left gastric artery; (6) presence of accessory left gastric artery coming out of the right gastric artery; and (7) the right hepatic artery crosses the common bile duct anteriorly.

These variations are also important in terms of collaterals that may occur after the ligation or occlusion of an artery. In transplantation, the mapping and perfect knowledge of hepatic vascularisation is essential for the surgeon.

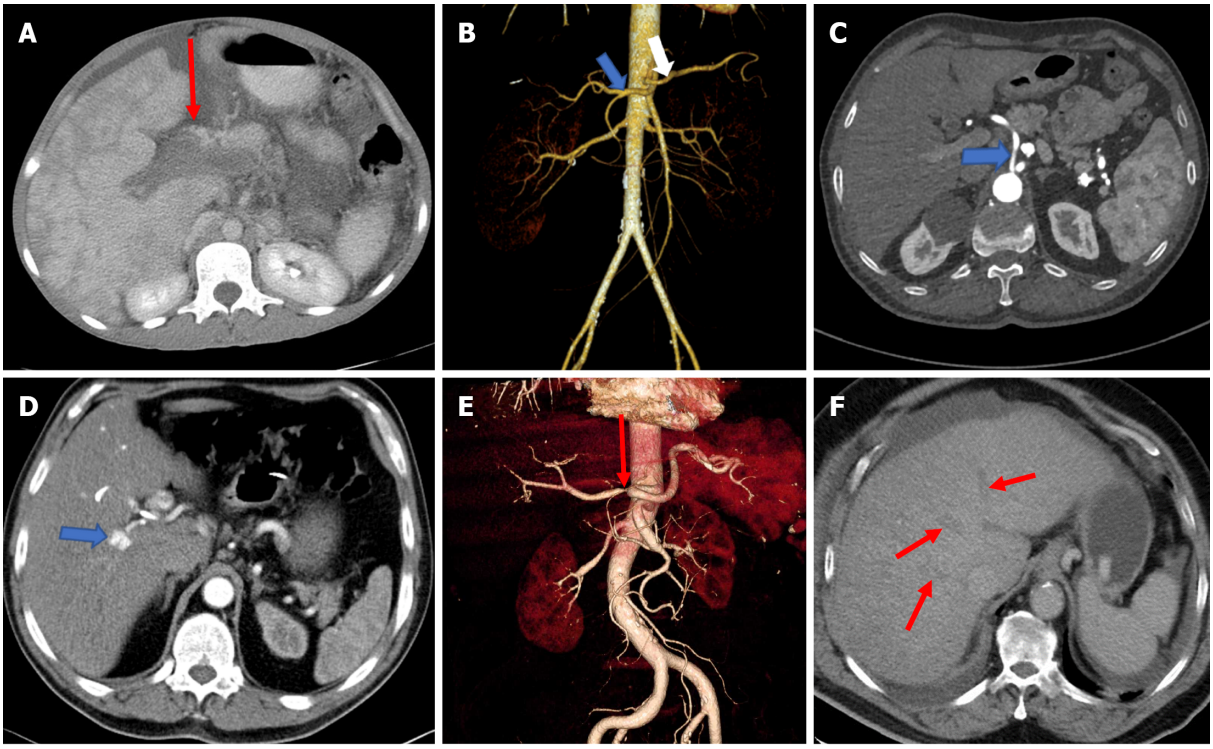
Imaging findings of disorders of the hepatic artery

The vascular anatomy of the liver influences surgical interventions to minimize surgical morbidity. It is possible to diagnose hepatic arterial disorders (thrombosis, aneurysm, and dissection and pseudoaneurysm formation) preoperatively and after liver transplantation by CTA. Coronal oblique slices are ideal for evaluating hepatic arterial anatomy. If the portal venous supply of the liver is intact, occlusion

Table 1 Michels' classification of the hepatic arterial anatomy[16]

Type	Frequency (%)	Description
I	55.0	RHA, MHA, and LHA arise from common hepatic artery
II	10.0	RHA, MHA, and LHA arise from common hepatic artery; replaced LHA arises from left gastric artery
IV	1.0	Replaced RHA and LHA
V	8.0	RHA, MHA, and LHA arise from common hepatic artery; accessory LHA arises from left gastric artery
VI	7.0	RHA, MHA, and LHA arise from common hepatic artery; accessory RHA
VII	1.0	Accessory RHA and LHA
VIII	4.0	Replaced RHA and accessory LHA or replaced LHA and accessory RHA
IX	4.5	Entire hepatic trunk arises from superior mesenteric artery
X	0.5	Entire hepatic trunk arises from left gastric artery

RHA: Right hepatic artery; MHA: Middle hepatic artery; LHA: Left hepatic artery.



DOI: 10.4329/wjr.v15.i1.1 **Copyright** ©The Author(s) 2023.

Figure 1 Image examination. A: Axial computed tomography (CT) shows portal vein thrombosis; B: Separate origins of the common hepatic artery and the splenic artery. Coronal volume rendered image of a 44-year-old female presenting with right lumber pain demonstrates a hepatic arterial variation as the common hepatic artery (blue arrow) and the splenic artery (white arrow) originating directly from the abdominal aorta separately; C: The common hepatic artery directly originating from the abdominal aorta. Axial contrast-enhanced CT of a 55-year-old male patient with known peripheral vascular disease presenting direct origin of the common hepatic artery (arrow) from the abdominal aorta; D: Hepatic artery pseudoaneurysm. Axial contrast-enhanced arterial phase CT image of a 42-year-old man, suffering from epigastric pain and presenting with hemobilia and elevated liver enzymes, shows an 8 mm diameter pseudoaneurysm (arrow); E: High grade stenosis of the common hepatic artery. Coronal volume rendered CT image of a 76-year-old male with the diagnosis of vasculitis demonstrates severe stenosis (arrow); F: Occlusion of all hepatic veins consistent with Budd-Chiari syndrome. Venous phase axial CT scan shows thrombosed hepatic veins (arrows).

or stenosis of hepatic arterial flow does not generally result in parenchymal infarction (Figure 1E). CTA is the most commonly utilized modality to demonstrate localization and severity of the abrupt vessel. A wedge-shaped low-attenuation area in the liver periphery can be observed when hepatic infarctions are caused by hepatic artery flow disturbances. Central liver infarcts are characterized by a round-shaped lesion instead of wedge-shaped[18]. Vascular complications following liver transplantation include hepatic artery thrombosis occurring in 2%-5% of cases and stenosis occurring in 5%-11%, which may lead to irreversible infarctions and loss of the liver graft[19,20]. Hepatic artery dissection may occur

spontaneously and/or following liver transplants. Hypertension and preexisting vascular disease prior to surgery may be related with spontaneous dissection[21]. Hepatic artery aneurysms represent 20% of all visceral aneurysms. They usually have an extrahepatic location at the level of common hepatic or right hepatic arteries and common etiologies are trauma, tumors, infection, and iatrogenic reasons[22]. CT is an excellent diagnostic tool in which aneurysm appears as a fusiform dilatation of the vessel lumen, as well-defined focal enhancing lesions that may simulate hypervascular tumours[18]. Hepatic artery pseudoaneurysms (Figure 1D) differ from true aneurysms with the appearance of more irregular peripheral margins[22]. Hepatic arterio-portal shunts (HAPS) occur due to fistulization of blood flow from the hepatic artery to the portal vein. HAPS are frequently asymptomatic. However, systemic complications may arise including the development of portal hypertension, as well as accelerated metastasis in patients with malignant tumors. HAPS is divided into three types according to the anatomic location of the shunt within the liver: (1) Central HAPS: When the shunt is located in the porta hepatis, such central HAPS is manifested as earlier enhancement and arterial-phase opacification of the central portal veins during CT scanning; (2) Peripheral HAPS: When the shunt is located in peripheral liver parenchyma. Given the smaller hepatic vascular size in this region, early contrast into the portal veins generally does not occur. Shunts in this region of the liver usually manifest as transient hepatic enhancement differences; and (3) mixed HAPS: Alternatively, HAPS may demonstrate both central and peripheral findings[22]. Abnormal vessels that arise from the hepatic arteries promptly opacify the liver, thereby giving rise to the characteristic blush of an arteriovenous shunt.

Lymphatics of the liver

The liver is the largest lymph-producing organ, accounting for 25%-50% of lymph passing through the thoracic duct[23]. The hepatic lymphatic system transport lymph through lymphatic vessels to draining lymph nodes to remove waste products and immune cells. Sinusoids are covered by fenestrated liver sinusoidal endothelial cells (LSECs). Hepatic lymphatic fluid originates mainly from plasma components filtered through the fenestrae of LSECs and flows into the space of Disse. In this tight space between the hepatocytes and the sinusoid, fluid and solid materials pass through. The space of Disse cannot be observed by biopsy and is mainly occupied by reticular arcuate fibers. Especially during passive hepatic congestion, anoxia, or in some toxic conditions resulting from hepatic edema, we observe a dilatation of this perisinusoidal space filled with protein-rich fluid. These spaces have contact with the periportal spaces (space of Mall) between the stroma of the portal tract and the outermost hepatocytes. The lymphatic fluid inside the perisinusoidal and periportal spaces drains into the lymphatics in the portal triad. A rich lymphatic network is also shown around the bile ducts, reaching under the epithelium. There may also be very thin lymphatic vessels accompanying arterioles in the parenchyma. In addition, under the Glisson capsule, there is a subperitoneal lymph drainage communicating with both the lymphatics in the gallbladder bed and the parenchymal lymph vessels. The lymphatic vessels in the portal triad take different routes: Most of them first travel to the hepatic lymph nodes and drain into the coeliac lymph nodes and the lymph nodes around the cisterna chyli; some reach the thoracic duct directly from the porta hepatis; some drain into the lymph nodes around the inferior vena cava. The subcapsular lymphatics drain to the lymph nodes around the inferior vena cava and the diaphragmatic hiatus and then reach the thoracic duct directly. Lymphatics coming from the left side of the posterior surface of the liver drain into the paracardial group of the left gastric lymph nodes, and those coming from the right side directly into the coeliac lymph nodes. Although the lymph from the gallbladder and extrahepatic bile ducts mostly drains into the hepatic lymph nodes, a few vessels from the common hepatic duct go to the pyloric lymph nodes. Normally, hepatic lymph vessels do not anastomose with duodenal and pancreatic lymph vessels. A significant increase in the number of lymphatic vessels (lymphangiogenesis) has been reported in various pathological conditions of the liver, including cirrhosis, viral hepatitis, lymphedema, cholestasis, portal hypertension, biliary cholangitis, and hepatocellular carcinoma[23-29].

Hepatic vein

Most of the venous blood of the liver is drained by the three main hepatic veins (RHV, LHV, and intermediate hepatic vein), which open into the suprahepatic part of the superior vena cava. Numerous small hepatic veins open into the intrahepatic portion (at the sulcus for the inferior vena cava) of the inferior vena cava. The RHV drains liver segments V-VII, the middle hepatic vein (MHV) drains segments IV, V, VIII, and the LHV drains segments II and III[3]. Impairment of the hepatic venous outflow can be catastrophic. Patients may experience rapid onset jaundice and severe ascites. The increased intrahepatic pressure, caused by the inability of the massive blood flow into the liver, causes severe centrilobular congestion and subsequent parenchymal necrosis. This clinical condition of hepatic venous outflow obstruction is called the Budd-Chiari syndrome (BCS) (Figure 1F)[18]. This definition excludes the outflow impairment that results from heart failure or pericardial diseases. The definition also excludes sinusoidal obstruction syndrome. The compromised hepatic venous flow results in dramatically increased sinusoidal pressure that reverses hepatic drainage into the portal venous system. In approximately 75% of the cases, a hematologic abnormality or an underlying thrombotic diathesis can be identified[30,31]. CT clearly shows the obstructed hepatic veins and associating parenchymal changes[32]. The absence of contrast enhancement in the hepatic vein is the pathognomonic imaging

findings on CT[12]. In the acute phase, the liver becomes enlarged with smooth contours and appears heterogeneously edematous with parenchymal perfusion abnormalities with the decreased flow in the liver periphery and enhanced flow in the central liver parenchyma in the hepatic arterial phase. Patchy and decreased contrast enhancement in the liver periphery, in the arterial phase, results from edema and congestion in the peripheral regions due to flow stasis in portal vein branches and the liver sinusoids[12,19,33]. This finding is related to elevated post-sinusoidal pressure[33]. A heterogeneous and mottled mosaic pattern of parenchymal enhancement can also be encountered in congestive hepatopathy. Congestion is due to passive stasis of blood within the liver parenchyma secondary to impaired hepatic venous outflow due to decompensated cardiac disease[18,31]. Visualization of patency of hepatic veins and inferior vena cava differentiates congestive hepatopathy from BCS. A mosaic pattern of enhancement with linear and curvilinear areas of poor enhancement is seen in the portal venous phase images, described as nutmeg liver. A "flip-flop" pattern may occur in the portal venous phase as the central part of the liver demonstrates low attenuation due to contrast wash-out and gradual increase of the peripheral attenuation. The caudate lobe may demonstrate better venous enhancement due to its unique venous drainage pattern[32]. Associated features of cardiac dysfunction aid diagnosis [18].

The vascular variants that are of surgical importance include variants of the hepatic vein also: (1) An accessory RHV occurs in 52.5% of patients; (2) two accessory hepatic veins in 12%; (3) an accessory vein draining the caudate lobe in 12%; (4) an accessory inferior RHV; and (5) early branching of the vein that drains the right superoanterior segment (segment VIII) into the MHV.

Significant hepatic venous variants affecting both donors and recipients are seen in approximately 30% of patients, thus presenting a problem for the surgeon, and may result in a modification of the hepatectomy plane[34].

CONCLUSION

CTA may slightly be favourable in hepatic vascular disorders due to being time saving in critically ill patients with distended abdomen and pain. For a complete mapping of the hepatic vasculature, CT scan is preferable to other imaging modalities. Correct diagnosis and proper intervention are crucial for appropriate clinical management. CTA is an effective, high-resolution, noninvasive imaging technique that demonstrates the presence of vascular pathology, with a direct impact on treatment decisions including patient selection for surgical management. Also, the objective of vascular imaging in patients with liver neoplasms is to provide a vascular map for understanding the relationship of the tumor to adjacent vessels, which is needed for tumor resection that includes a peripheral tumor-free margin. Multiplanar reformation and 3D reconstruction are very helpful in demonstrating the relationship of liver tumors to the hepatic veins and inferior vena cava. Awareness of the imaging findings of hepatic vascularization is crucial for the correct diagnosis and optimization of the treatment to avoid complications.

FOOTNOTES

Author contributions: Firat A and Balaban YH designed, wrote, and finally edited the paper; Firat A and Abbasoglu TT analyzed and interpreted the data; Karcaaltincaba M and Balaban YH performed the clinical interventions and made critical revisions to the manuscript.

Conflict-of-interest statement: The authors declare that they have no conflict of interest to disclose.

Open-Access: This article is an open-access article that was selected by an in-house editor and fully peer-reviewed by external reviewers. It is distributed in accordance with the Creative Commons Attribution NonCommercial (CC BY-NC 4.0) license, which permits others to distribute, remix, adapt, build upon this work non-commercially, and license their derivative works on different terms, provided the original work is properly cited and the use is non-commercial. See: https://creativecommons.org/Licenses/by-nc/4.0/

Country/Territory of origin: Turkey

ORCID number: Aysegul Firat 0000-0001-5105-0057; Tugce Taskindere Abbasoglu 0000-0003-2747-417X; Musturay Karcaaltincaba 0000-0002-3384-0909; Yasemin H Balaban 0000-0002-0901-9192.

S-Editor: Chen YL
L-Editor: Wang TQ
P-Editor: Chen YL

REFERENCES

1 **Colagrande S**, Centi N, La Villa G, Villari N. Transient hepatic attenuation differences. *AJR Am J Roentgenol* 2004; **183**: 459-464 [PMID: 15269041 DOI: 10.2214/ajr.183.2.1830459]
2 **Price M**, Patino M, Sahani D. Computed Tomography Angiography of the Hepatic, Pancreatic, and Splenic Circulation. *Radiol Clin North Am* 2016; **54**: 55-70 [PMID: 26654391 DOI: 10.1016/j.rcl.2015.08.009]
3 **Standring S**. Gray's Anatomy The Anatomical Basis of Clinical Practice. 42nd ed. London: Churchill Livingstone Elsevier, 2021: 327-329, 1205-1217
4 **Gissen P**, Arias IM. Structural and functional hepatocyte polarity and liver disease. *J Hepatol* 2015; **63**: 1023-1037 [PMID: 26116792 DOI: 10.1016/j.jhep.2015.06.015]
5 **Sun P**, Zhang G, Su X, Jin C, Yu B, Yu X, Lv Z, Ma H, Zhang M, Wei W, Li W. Maintenance of Primary Hepatocyte Functions In Vitro by Inhibiting Mechanical Tension-Induced YAP Activation. *Cell Rep* 2019; **29**: 3212-3222.e4 [PMID: 31801084 DOI: 10.1016/j.celrep.2019.10.128]
6 **Erwin K**, Hans-Dieter K. Hepatology: Textbook and Atlas. 3rd ed. Heidelberg: Springer Medizin Verlag, 2008: 26-28
7 **William KO**, Patrick CN. Netter's Essential Histology. 2nd ed. Philadelphia: Elsevier Sauders, 2013: 314-316
8 **Schmidt S**, Demartines N, Soler L, Schnyder P, Denys A. Portal vein normal anatomy and variants: implication for liver surgery and portal vein embolization. *Semin Intervent Radiol* 2008; **25**: 86-91 [PMID: 21326549 DOI: 10.1055/s-2008-1076688]
9 **DeLeve LD**, Valla DC, Garcia-Tsao G; American Association for the Study Liver Diseases. Vascular disorders of the liver. *Hepatology* 2009; **49**: 1729-1764 [PMID: 19399912 DOI: 10.1002/hep.22772]
10 **Chawla Y**, Duseja A, Dhiman RK. Review article: the modern management of portal vein thrombosis. *Aliment Pharmacol Ther* 2009; **30**: 881-894 [PMID: 19678814 DOI: 10.1111/j.1365-2036.2009.04116.x]
11 **Onur MR**, Karaosmanoglu AD, Akca O, Ocal O, Akpinar E, Karcaaltincaba M. Imaging features of non-traumatic vascular liver emergencies. *Jpn J Radiol* 2017; **35**: 215-224 [PMID: 28243837 DOI: 10.1007/s11604-017-0624-0]
12 **Gallego C**, Velasco M, Marcuello P, Tejedor D, De Campo L, Friera A. Congenital and acquired anomalies of the portal venous system. *Radiographics* 2002; **22**: 141-159 [PMID: 11796904 DOI: 10.1148/radiographics.22.1.g02ja08141]
13 **Bazan F**, Busto M. IMAGES IN CLINICAL MEDICINE. Pylephlebitis as a Complication of Diverticulitis. *N Engl J Med* 2015; **373**: 2270 [PMID: 26630145 DOI: 10.1056/NEJMicm1501584]
14 **Kanellopoulou T**, Alexopoulou A, Theodossiades G, Koskinas J, Archimandritis AJ. Pylephlebitis: an overview of non-cirrhotic cases and factors related to outcome. *Scand J Infect Dis* 2010; **42**: 804-811 [PMID: 20735334 DOI: 10.3109/00365548.2010.508464]
15 **Turner KC**, Bohannon WT, Atkins MD. Portal vein aneurysm: a rare occurrence. *J Vasc Nurs* 2011; **29**: 135-138 [PMID: 22062791 DOI: 10.1016/j.jvn.2011.08.001]
16 **Michels NA**. Blood supply and anatomy of the upper abdominal organs with a descriptive atlas. Philadelphia: Lippincott, 1955: 64-69
17 **Favelier S**, Germain T, Genson PY, Cercueil JP, Denys A, Krausé D, Guiu B. Anatomy of liver arteries for interventional radiology. *Diagn Interv Imaging* 2015; **96**: 537-546 [PMID: 24534562 DOI: 10.1016/j.diii.2013.12.001]
18 **Virmani V**, Ramanathan S, Virmani VS, Kielar A, Sheikh A, Ryan J. Non-neoplastic hepatic vascular diseases: spectrum of CT and MRI appearances. *Clin Radiol* 2014; **69**: 538-548 [PMID: 24581966 DOI: 10.1016/j.crad.2013.12.017]
19 **Khalaf H**. Vascular complications after deceased and living donor liver transplantation: a single-center experience. *Transplant Proc* 2010; **42**: 865-870 [PMID: 20430192 DOI: 10.1016/j.transproceed.2010.02.037]
20 **Hwang JY**, Kim KW, Lee SJ, Kim SY, Lee JS, Kim HJ, Lee J, Song GW, Lee SG. The computed tomographic angiography finding of hepatic artery dissection after living donor liver transplantation; what is the clinical significance? *Clin Imaging* 2016; **40**: 130-136 [PMID: 26271148 DOI: 10.1016/j.clinimag.2015.06.007]
21 **Müller MF**, Kim D. Spontaneous dissection of the hepatic artery. *Abdom Imaging* 1995; **20**: 462-465 [PMID: 7580786 DOI: 10.1007/BF01213273]
22 **O'Driscoll D**, Olliff SP, Olliff JF. Hepatic artery aneurysm. *Br J Radiol* 1999; **72**: 1018-1025 [PMID: 10673957 DOI: 10.1259/bjr.72.862.10673957]
23 **Tanaka M**, Iwakiri Y. The Hepatic Lymphatic Vascular System: Structure, Function, Markers, and Lymphangiogenesis. *Cell Mol Gastroenterol Hepatol* 2016; **2**: 733-749 [PMID: 28105461 DOI: 10.1016/j.jcmgh.2016.09.002]
24 **Wang Q**, Koniaris LG, Milgrom DP, Patel A, Hu M, Cui E, Deng Y, Akisik F. CT and MRI imaging and interpretation of hepatic arterioportal shunts. *Transl Gastroenterol Hepatol* 2019; **4**: 34 [PMID: 31231701 DOI: 10.21037/tgh.2019.05.05]
25 **Chung C**, Iwakiri Y. The lymphatic vascular system in liver diseases: its role in ascites formation. *Clin Mol Hepatol* 2013; **19**: 99-104 [PMID: 23837133 DOI: 10.3350/cmh.2013.19.2.99]
26 **Thelen A**, Jonas S, Benckert C, Weichert W, Schott E, Bötcher C, Dietz E, Wiedenmann B, Neuhaus P, Scholz A. Tumor-associated lymphangiogenesis correlates with prognosis after resection of human hepatocellular carcinoma. *Ann Surg Oncol* 2009; **16**: 1222-1230 [PMID: 19224279 DOI: 10.1245/s10434-009-0380-1]
27 **Oikawa H**, Masuda T, Sato S, Yashima A, Suzuki K, Satodate R. Changes in lymph vessels and portal veins in the portal tract of patients with idiopathic portal hypertension: a morphometric study. *Hepatology* 1998; **27**: 1607-1610 [PMID: 9620334 DOI: 10.1002/hep.510270621]
28 **Yamauchi Y**, Michitaka K, Onji M. Morphometric analysis of lymphatic and blood vessels in human chronic viral liver diseases. *Am J Pathol* 1998; **153**: 1131-1137 [PMID: 9777944 DOI: 10.1016/s0002-9440(10)65657-x]
29 **Soyer P**, Heath D, Bluemke DA, Choti MA, Kuhlman JE, Reichle R, Fishman EK. Three-dimensional helical CT of intrahepatic venous structures: comparison of three rendering techniques. *J Comput Assist Tomogr* 1996; **20**: 122-127 [PMID: 8576462 DOI: 10.1097/00004728-199601000-00023]
30 **Cura M**, Haskal Z, Lopera J. Diagnostic and interventional radiology for Budd-Chiari syndrome. *Radiographics* 2009; **29**: 669-681 [PMID: 19448109 DOI: 10.1148/rg.293085056]
31 **Valla DC**, Cazals-Hatem D. Vascular liver diseases on the clinical side: definitions and diagnosis, new concepts. *Virchows*

Arch 2018; **473**: 3-13 [PMID: 29572606 DOI: 10.1007/s00428-018-2331-3]

32 **Karaosmanoglu AD**, Uysal A, Akata D, Ozmen MN, Karcaaltincaba M. Role of imaging in visceral vascular emergencies. *Insights Imaging* 2020; **11**: 112 [PMID: 33057847 DOI: 10.1186/s13244-020-00913-3]

33 **Torabi M**, Hosseinzadeh K, Federle MP. CT of nonneoplastic hepatic vascular and perfusion disorders. *Radiographics* 2008; **28**: 1967-1982 [PMID: 19001652 DOI: 10.1148/rg.287085067]

34 **Sahani D**, Mehta A, Blake M, Prasad S, Harris G, Saini S. Preoperative hepatic vascular evaluation with CT and MR angiography: implications for surgery. *Radiographics* 2004; **24**: 1367-1380 [PMID: 15371614 DOI: 10.1148/rg.245035224]

World Journal of Radiology

Submit a Manuscript: https://www.f6publishing.com

World J Radiol 2023 January 28; 15(1): 10-19

DOI: 10.4329/wjr.v15.i1.10

ISSN 1949-8470 (online)

MINIREVIEWS

Advancements of molecular imaging and radiomics in pancreatic carcinoma

Xiao-Xi Pang, Liang Xie, Wen-Jun Yao, Xiu-Xia Liu, Bo Pan, Ni Chen

Specialty type: Oncology

Provenance and peer review: Invited article; Externally peer reviewed.

Peer-review model: Single blind

Peer-review report's scientific quality classification
Grade A (Excellent): 0
Grade B (Very good): B
Grade C (Good): C
Grade D (Fair): 0
Grade E (Poor): 0

P-Reviewer: Chisthi MM, India; Wu CQ, China

Received: September 30, 2022
Peer-review started: September 30, 2022
First decision: October 29, 2022
Revised: November 12, 2022
Accepted: January 9, 2023
Article in press: January 9, 2023
Published online: January 28, 2023

Xiao-Xi Pang, Liang Xie, Xiu-Xia Liu, Department of Nuclear Medicine, The Second Hospital of Anhui Medical University, Hefei 230601, Anhui Province, China

Wen-Jun Yao, Department of Radiology, The Second affiliated hospital of Anhui Medical University, Hefei 230601, Anhui Province, China

Bo Pan, PET/CT Center, The First Affiliated Hospital of USTC, Division of Life Sciences and Medicine, University of Science and Technology of China, Hefei 230001, Anhui Province, China

Ni Chen, Department of Nuclear Medicine, School of Basic Medicine Anhui Medical University, Hefei 230032, Anhui Province, China

Corresponding author: Ni Chen, Department of Nuclear Medicine, School of Basic Medicine Anhui Medical University, No. 81 Meishan Road, Hefei 230032, Anhui Province, China. icefei@mail.ustc.edu.cn

Abstract

Despite the recent progress of medical technology in the diagnosis and treatment of tumors, pancreatic carcinoma remains one of the most malignant tumors, with extremely poor prognosis partly due to the difficulty in early and accurate imaging evaluation. This paper focuses on the research progress of magnetic resonance imaging, nuclear medicine molecular imaging and radiomics in the diagnosis of pancreatic carcinoma. We also briefly described the achievements of our team in this field, to facilitate future research and explore new technologies to optimize diagnosis of pancreatic carcinoma.

Key Words: Pancreatic carcinoma; Magnetic resonance imaging; Molecular imaging; Positron emission tomography-computed tomography; Positron emission tomography-magnetic resonance; Artificial intelligence

©The Author(s) 2023. Published by Baishideng Publishing Group Inc. All rights reserved.

Core Tip: Pancreatic carcinoma remains high incidence and poor prognosis. Molecular imaging enables early and precise diagnosis, efficient assessment, non-invasive pathological classification. This paper aims to review the recent research progress of nuclear medicine, magnetic resonance imaging and radiomics in the diagnosis of pancreatic carcinoma, and also briefly describe our team's work in this field.

Citation: Pang XX, Xie L, Yao WJ, Liu XX, Pan B, Chen N. Advancements of molecular imaging and radiomics in pancreatic carcinoma. *World J Radiol* 2023; 15(1): 10-19
URL: https://www.wjgnet.com/1949-8470/full/v15/i1/10.htm
DOI: https://dx.doi.org/10.4329/wjr.v15.i1.10

INTRODUCTION

In the past decade, significant progress has been made in the medical technology for the treatment of cancers. However, the prognosis of pancreatic carcinoma remains extremely poor due to its insidious location, high malignancy, easy metastasis and rapid progression, which increases the difficulty of early and accurate assessment. Radical surgical resection rate of pancreatic cancer patients is less than 20%. Pancreatic carcinoma is also resistant to radiotherapy and chemotherapy. Moreover, targeted drug therapy, and cytotoxic T-lymphocyte-associated protein 4 and programmed death-1/programmed death-ligand 1 antibody immunotherapy are ineffective. The five-year survival rate of patients remains below 5%-9%, and the number of deaths is the fourth highest among malignant tumors[1]. Early and accurate diagnosis as well as efficacious assessment of pancreatic carcinoma have important clinical significance.

Conventional imaging techniques makes important significance in theranostic of pancreatic cancer; however, these technologies are still deficiencies yet. First of all, magnetic resonance (MR) and computed tomography (CT) only detects limited range with regional scan in clinical routine diagnosis of pancreatic carcinoma, therefore, many patients with distant metastasis are misdiagnosed or never diagnosed. Secondly, the rate of misdiagnosis was high in lymphatic metastasis by MR and CT scan. By reason of no static image provided, ultrasound examination is very unfavorable for reading in clinical work, even this method has the double advantage of real time imaging and radiation lessness. What's more, ultrasound is affected greatly by operators. Finally, some patients who cannot have a proper assessment in regional lymphatic metastasis, especially patients after chemotherapy, even whole body ^{18}F-FDG positron emission tomography (PET)/CT scan.

Molecular imaging has advanced rapidly in recent years. It enables early and precise diagnosis, efficacy assessment, non-invasive pathological classification, and acts as an important "bridge" to achieve precise diagnosis and treatment[2]. It can meet clinical demands and better protect patient privacy compared to genetic testing. This paper aimed to review the recent research progress of nuclear medicine, magnetic resonance imaging, molecular imaging and radiomics in the diagnosis and treatment of pancreatic carcinoma, and also briefly describe our team's work in this field.

NUCLEAR MEDICINE MOLECULAR IMAGING

Nuclear medicine molecular imaging is based on the principle of injecting microscopic molecular probes into the body and selectively targeting them to appropriate sites based on different properties, in order to qualify or quantify organs, tissues or lesions for assessing diseases at the molecular level. Molecular imaging in nuclear medicine has made significant advances in the treatment of pancreatic carcinoma in recent years.

Glucose metabolism imaging

^{18}F-FDG is a glucose analogue, which is rapidly taken up by the glucose-transporter on the cell surface after intravenous injection. Various tumor cells, including pancreatic carcinoma, and inflammatory cells in the tumor microenvironment absorb a large amount of ^{18}F-FDG, but the uptake is influenced by various conditions and the underlying mechanisms are complex[3].

^{18}F-FDG PET/CT has high specificity, accuracy and sensitivity in the diagnosis of pancreatic carcinoma, and has important clinical value in the diagnosis, staging, surgical indication and evaluation efficacy of pancreatic carcinoma[4]. ^{18}F-FDG PET/CT is more sensitive and accurate than CT in detecting tumor metastasis, and its whole-body scan is beneficial for tumor staging[5]. This technique detected distant metastases in about one-third of pancreatic carcinoma patients and changed the staging of approximately 26.8% of patients[6]. Its standardized uptake value (SUV) quantification and the rate of change were significantly correlated with tumor size[7], malignancy[8], vascular invasion[9], and lymph node metastasis. In addition, ^{18}F-FDG PET has significant value in efficacy assessment[10] and survival

prediction[11]. For example, the patients with baseline SUV < 3.5 (and/or) SUV decrease ≥ 60% had better overall survival (OS) and progression-free survival (PFS)[12]. In locally advanced or metastatic pancreatic carcinoma, the PFS of patients with SUV_{max} < 6.8 was significantly longer than that of patients with SUV_{max} ≥ 6.8[13]. ^{18}F-FDG PET/CT-guided radiotherapy with metabolic tumor volume and total lesion glycolysis (TLG) can be used as independent factors affecting prognosis[14]. Yamamoto *et al*[15] found that the early postoperative recurrence rate of pancreatic carcinoma in patients with SUV_{max} ≥ 6.0 was higher than that of patients with SUV_{max} < 6.0, and median OS of the former was lower than the latter (Table 1)[16].

With the increasing application of ^{18}F-FDG PET/CT in recent years, several shortcomings have been gradually revealed. First, as a non-tumor-specific imaging agent, ^{18}F-FDG PET reflects glucose metabolism and is not directly related to the biological properties of the tumor. So non-neoplastic lesions such as inflammation, tuberculosis, or even non-specific uptake with increased glucose metabolism can lead to false positive results. Second, if the patient has high blood glucose levels, uses short-acting insulin or exercises, ^{18}F-FDG can also lead to reduced sensitivity due to increased background uptake. In order to address these problems, nuclear medicine researchers have developed a series of more specific imaging agents for different targets.

Non-glucose metabolism imaging

The highly specific non-FDG molecular probes with different targets achieve accurate diagnosis of pancreatic carcinoma, and also enable non-invasive visualization of the expression of different receptors in tumors, facilitating individualized precision medicine. These imaging agents have been particularly successful in imaging of integrin receptor, somatostatin receptor, tumor-associated fibroblasts, *etc*. Our team has also conducted in-depth research on PD-L1-targeted imaging, non-radioactive molecular imaging and highly specific targeted radiotherapy.

Somatostatin receptor imaging

Somatostatin receptor imaging is mainly used in pancreatic neuroendocrine tumors, with sensitivity of 86%-100% and specificity of 79%-100%[17]. The precursors of somatostatin receptor (SSTR) imaging agents are mainly Tyr(3)-octreotate, 1-Nal(3)-octreotide and D-Phe1-Tyr(3)-octreotide, which have different affinities for different somatostatin receptor subtypes[17]. The neuroendocrine tumors with high differentiation (G1-G2, Ki-67 < 10%) generally showed high expression of SSTR and positive SSTR imaging. Moreover, the degree of malignancy was low, the level of glycolysis was decreased, and the metabolism of FGD was only slightly increased or defective, which led to low sensitivity of ^{18}F-FDG PET [18,19]. In contrast, due to the loss of SSTR and negative SSTR imaging, the increase of malignant degree led to increased glycolysis[20], high metabolism of FGD and increased sensitivity of ^{18}F-FDG PET/CT. In addition to the above three SSTR agonists, SSTR inhibitors have other advantages such as several binding sites, low degradation rate and longer retention in tumors[21] (Table 2)[17].

Fibroblast activation protein imaging

Cancer-associated fibroblasts (CAFs) are a major component of the mesenchyme surrounding epithelial cancer cells. Fibroblast activating protein (FAP) is a marker of CAFs. It is highly expressed in tumor stromal fibroblasts of most common human epithelial carcinomas, and has lower expression in normal tissues[22]. CAFs can form physical and metabolic barriers, which is partly responsible for the resistance of pancreatic carcinoma to chemotherapy and radiotherapy, by reducing the therapeutic effect of combined chemotherapy on pancreatic carcinoma[23]. High expression of CAFs in pancreatic carcinoma is associated with shorter OS and disease-free survival[24,25].

At present, the commonly used FAP-targeted imaging agents are various radionuclide-labeled small molecular FAP inhibitors (FAPIs), mainly FAPI-04, FAPI-21 and FAPI-46. The commonly used imaging agent ^{68}Ga/^{18}F-labeled FAPI-04 shows a significantly high uptake in pancreatic carcinoma, which has a good diagnostic efficacy for the primary focus of pancreatic carcinoma. In a comparative study of pancreatic carcinoma and pancreatitis, ^{68}Ga-FAPI-04 PET/MR and ^{18}F-FDG PET/CT positive rates were both 100%, but the former SUV_{max} was significantly higher than the latter SUV_{max} (P < 0.05). In addition, ^{68}Ga-FAPI-04 could detect more lymph node metastases, but ^{18}F-FDG was able to detect more liver metastases than ^{68}Ga-FAPI-04[26]. ^{68}Ga-FAPI-04 may be superior to ^{18}F-FDG and CT in the diagnosis of lymph node, bone, liver, lung, peritoneal and pleural metastases of pancreatic carcinoma[27,28]. Deng *et al*[29] reported a 65-year-old male patient with pancreatic head cancer and liver metastasis. ^{18}F-FDG showed slight uptake in the pancreatic lesions and the tenth rib on the right, but not in many low-density or isodensity nodules in the liver, while ^{68}Ga-FAPI PET/CT showed strong FAPI uptake in the pancreatic lesions and the tenth rib on the right, as well as multiple liver lesions.

Our team conducted a comparative study of FAPI and FDG imaging of pancreatic cancer (Figure 1), and redesigned FAPI based on new ideas, which is expected to exceed the existing FAPI-04, FAPI-21 and FAPI-46 in imaging and therapeutic effects. At present, chemical synthesis has been completed and radionuclides such as iodine and technetium have been labeled, and further cellular and animal experiments will be conducted soon.

Table 1 Summary of sensitivity and specificity of different imaging modalities for the diagnosis of pancreatic cancer[16]

Year	Study type	Pancreatic cancer–all (*n*)	^{18}F-FDG PET-CT		CT		MRI		EUS	
			Sens	Spec	Sens	Spec	Sens	Spec	Sens	Spec
2016	Retrospective study	139-139	0.78	–	0.76	–	–	–	–	–
2014	Retrospective study	33–52	1	0.9	0.92	0.5	0.89	0.75	1	0.88
2009	Meta-analysis	3857[1]	0.9	0.8	–	–	–	–	0.81	0.93
2017	Meta-analysis	3567–5399	0.89	0.7	0.9	0.87	0.93	0.89	0.91	0.86
2014	Retrospective study	80–91	0.68	0.73	–	–	–	–	–	–
2018	Prospective study	278–583	0.93	0.76	0.89	0.71	–	–	–	–
2015	Retrospective study	50–70	0.92	0.65	0.82	0.65	–	–	–	–

[1]The study included a total of 3857 patients, but we were unable to obtain the specific number of pancreatic cancer.
This table is adopted from[16]. Sens: Sensitivity, Spec: Specificity. PET: Positron emission tomography; CT: Computed tomography; MRI: Magnetic resonance imaging; EUS: Endoscopic ultrasound.

Table 2 Summary of the main clinical key points of the two EANM/ENETS recommended radiopharmaceuticals[17]

Clinical key points			
Radiopharmaceuticals	**Main indication**	**Diagnostic accuracy**	**False positive findings**
^{68}Ga-TATE, TOC, NOC	Staging and restaging any non-insulinoma panNET case; detection of the unknown primary tumour site or early relapse; evaluation in-vivo SRE; selection for PRRT and/or cold SSA	Sensitivity: 86% to 100%; specificity: from 79% to 100%	Pancreatic uncinate process, accessory spleens (including intra-pancreatic, splenules, infectious/inflammatory findings, non-neuroendocrine tumours)
^{18}F-FDG	High grade G2, G3 and NEC; prognosis; rapid tumour progression in earlier diagnosed G1–G2 tumours	Sensitivity: 40% in G1, 60% in G2; 95% in G3 patients	Infectious/inflammatory findings, non-neuroendocrine tumours

This table is adopted from[17]. TATE: Tyr(3)-octreotate; NOC: 1-Nal(3)-octreotide; TOC: D-Phe1-Tyr(3)-octreotide; NEC: Neuroendocrine carcinomas.

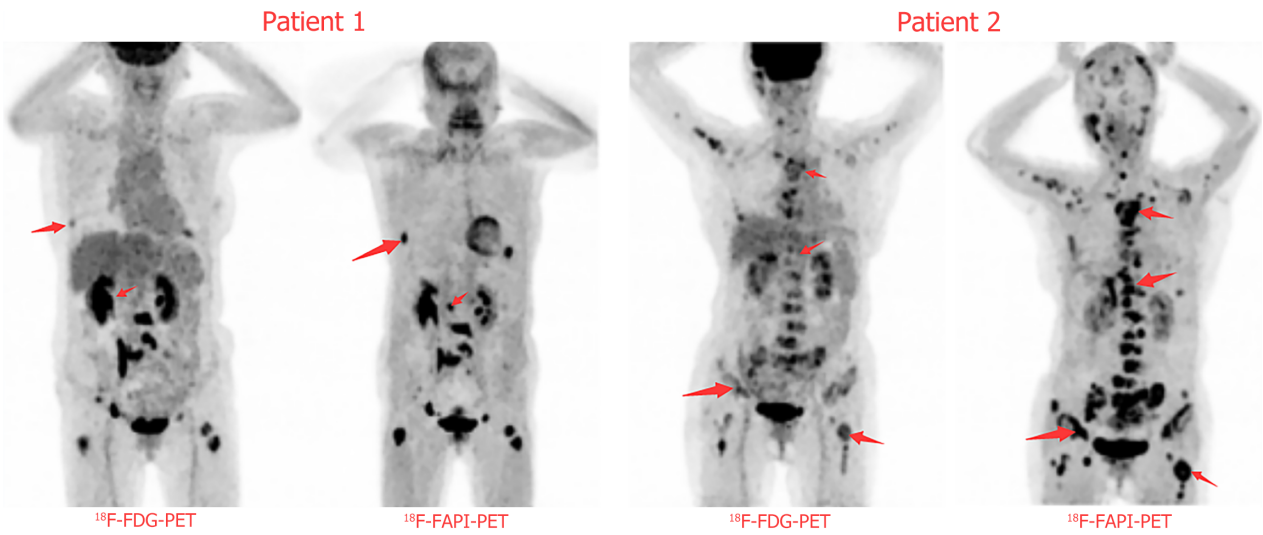
Integrin receptor imaging

Tumor neovascularization (angiogenesis) is necessary for maintaining the growth of malignant tumors, which plays a key role in tumor growth, invasion and metastasis, it is an important target for tumor diagnosis and treatment.

Integrin $\alpha v\beta_3$ receptor is an important component of the 24 integrins, which is highly expressed on the cell surface of tumor neovascular endothelial cells and many solid tumors. However, it has low or no expression in mature vascular endothelial cells and most normal tissues and organs in healthy people, and plays an important role in angiogenesis, metastasis and tumor invasion[30,31]. The integrin $\alpha v\beta_3$ receptor is highly expressed in about 60% of invasive pancreatic carcinomas, and the small polypeptide arginine glycine aspartic acid sequence (RGD) can be targeted to bind to $\alpha v\beta_3$ receptor. Using radionuclide-labeled RGD peptides, such as ^{111}In, ^{18}F, ^{68}Ga-labeled RGD, can be used to visualize and treat pancreatic carcinoma. Our research team has also studied RII and RIT based on molecular probes constructed by different radionuclide-labeled RGD and RRL peptides[32].

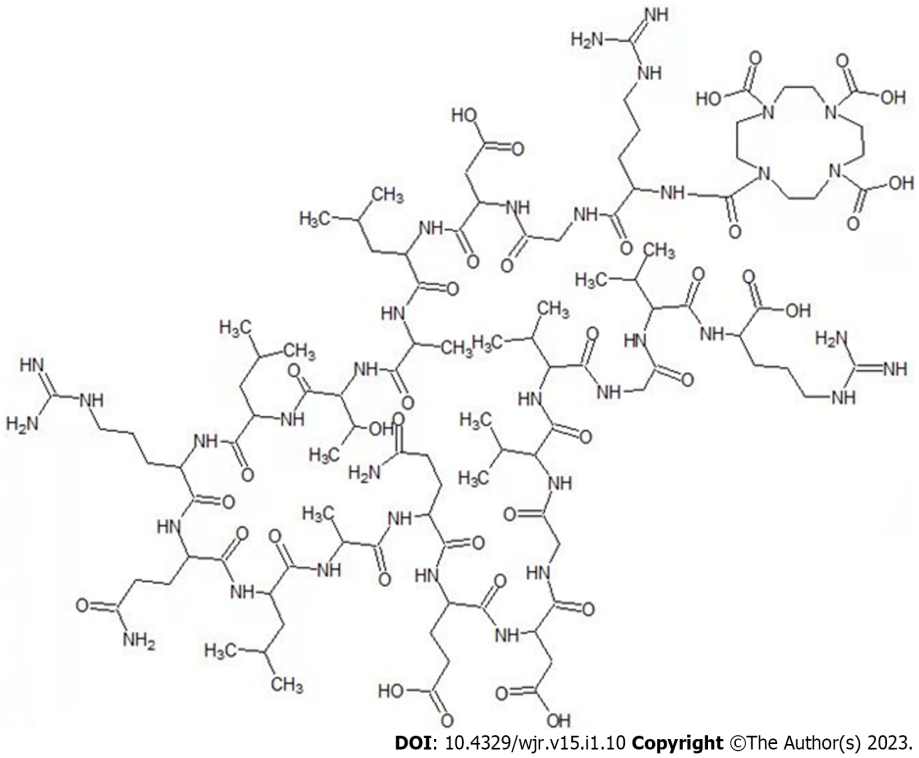
In addition to the integrin $\alpha v\beta_3$ receptor, integrin $\alpha V\beta_6$ is also highly expressed in pancreatic carcinoma[33]. Radiation molecular pancreatic probes constructed from the radionuclide ^{99m}Tc and ^{111}In-labeled HHK can target $\alpha v\beta_6$ with high specificity to achieve early diagnosis of pancreatic carcinoma and its metastases[34,35]. Based on previous studies, our research team redesigned the HHK peptide (Figure 2). The Gd-DOTA-HHK compound was obtained by chelating Gd^{3+}, which can achieve high specific enhancement of tumor $\alpha v\beta_6$ receptor during MRI T1WI scanning. Single photon emission CT imaging with high sensitivity and MRI with high soft tissue resolution combine perfectly to achieve high sensitivity and non-invasive visualization of $\alpha v\beta_6$ targets at high resolution.

In addition, some researchers have explored the application of radionuclide labeling dopa, Exendin-4, CXCR4, and PSMA in pancreatic carcinoma.



DOI: 10.4329/wjr.v15.i1.10 **Copyright** ©The Author(s) 2023.

Figure 1 Two patients with pancreatic cancer imaged with ^{18}F-FDG-positron emission tomography compared with ^{18}F-FAPI-positron emission tomography. Patient 1 was a 69-year-old female. Patient 2 was a 70-year-old female. ^{18}F-FAPI-positron emission tomography (PET) detected more lesions than ^{18}F-FDG-PET, and also had better contrast. PET: Positron emission tomography.



DOI: 10.4329/wjr.v15.i1.10 **Copyright** ©The Author(s) 2023.

Figure 2 Structure of the redesigned HHK peptide.

MAGNETIC RESONANCE MOLECULAR IMAGING

MRI utilizes magnetic resonance to obtain electromagnetic signals from the human body, which can be reconstructed by computer to show the different chemical components in the same tissue. Because MRI has the advantages of high soft tissue resolution, non-radiation, unrestricted imaging depth and multi-sequence imaging, and with the development of MRI-specific imaging agents, it is possible to evaluate lesions from multiple dimensions of functional and molecular images by MRI.

Diffusion-weighted imaging

Diffusion-weighted imaging (DWI) is the most widely used conventional MRI technique in addition to

T1WI and T2WI. The diffusion movement of water molecules reflects the microstructure of the tumor, such as internal cell density, extracellular space and heterogeneity. When the cell density increases, edema, fibrosis, *etc*., affect the cell membrane function, which can be detected due to enhanced signal.

Increased b-value (>1000 s/mm^2) DWI can increase lesion detection, but high b-value DWI images often exhibit low signal noise ratio, large diffusion-sensitive gradients that tend to distort images and longer scan times. The emergence of computed DWI has partially solved the above problem[36]. Liang *et al*[37] explored the value of computed DWI (cDWI) technique in the diagnosis of pancreatic carcinoma, and the results initially showed that a b-value of c1000-c1500 s/mm^2 at cDWI technique could effectively display pancreatic carcinoma as well as maintain the image quality. Compared to DWI, intravoxel incoherent motion imaging is based on a biexponential model, which can quantify the diffusion and perfusion motions of water molecules separately. It can reflect the diffusion and perfusion characteristics of tissue cells, respectively, and has the advantages of fast-imaging, low-noise, and multi-parameters[38].

MR dynamic enhancement/Perfusion imaging

MR enhanced or perfusion imaging facilitates T-staging of pancreatic carcinoma by observing the relationship between the lesion, its surrounding tissue and vascular invasion. Both dynamic contrast-enhanced MRI (DCE-MRI) and perfusion MRI can provide quantitative information on blood flow perfusion of lesions (such as tumor tissue)[39]. The most common forms include T2*-weighted dynamic susceptibility contrast (DSC) perfusion and T1-weighted DCE perfusion[40]. However, there are significant differences between the two imaging methods, PWI (DCE and DSC) can reflect the tumor microenvironment such as blood vessel density and blood flow state by quantitative and functional parameters, such as first transit time, mean transit time, time to peak, *etc*. while dynamic enhancement can only obtain time perfusion curves through multi-phase dynamic enhancement, but they are not molecular imaging *per se*.

MR targeted molecular imaging

The basic principle of MR targeted molecular imaging is similar to nuclear medicine molecular imaging. The first step is to construct a specific molecular probe, and then introduce it into the body. After the probe actively and specifically binds to the imaging target, the lesions containing specific molecular targets in the body will be imaged by MRI[41]. Due to the high specificity of the molecular probe, delayed scan time, continuous enhancement within the tumor and relatively high signal on T1WI during the delayed scan, the specificity of the diagnosis is greatly improved[42,43], which helps to improve the detection rate of early microscopic pancreatic carcinoma lesions.

MR molecular probes meet the requirements of high specificity, affinity and signal elements that can be detected by MRI, such as T1 contrast agent represented by gadolinium (Gd), manganese, zinc chelates (Positive) and T2 contrast agent represented by MNP (Negative). Gd is used as a signal component to synthesize paramagnetic molecular imaging probes, mainly to shorten the longitudinal relaxation time of hydrogen protons, increase the T1 relaxation rate and produce positive T1WI contrast [43]. The traditional Gd agent enhanced MRI is diagnosed by the hemodynamic characteristics of lack of blood supply in pancreatic carcinoma, with low relaxation rate and lack of tissue specificity[44]. In recent years, MNP, as represented by SPION, has been applied in MR molecular imaging studies, mainly to shorten the transverse relaxation time, improve the T2 relaxation rate and produce negative T2WI contrast. Compared with Gd and SPION, it has better magnetization and biocompatibility, and no risk of nephrogenic systemic fibrosis[45,46].

In recent years, MR molecular imaging of pancreatic carcinoma is mainly based on basic scientific research. At present, the main targets involved are SSTR[47], urokinase-type plasminogen activator receptor[48], insulin-like growth factor-1 receptor, $\alpha V\beta_6$, epidermal growth factor receptor, vascular endothelial growth factor receptor-2[49], *etc*., but their prospect of clinical application requires further study. In addition, targets such as reticulin-1 (plectin-1)[50], mucin-1[51], MUC4, carcinoembryonic antigen-related cell adhesion molecule 6[52], γ-glutamyltransferase 5[53], P32 protein[54], mesothelin [55], thymus fine cell differentiation antigen-1, cathepsin E, neutrophil gelatinase-associated lipid transport protein[56] were also examined, which could lead to a new imaging target for pancreatic carcinoma.

The slow progress of MR targeted molecular imaging compared to nuclear medicine molecular imaging is mainly due to its own limitations. First, the specificity of the above-mentioned types of targets is poor, which affects the specificity of MR molecular imaging[56]. Second, high concentrations of Gd molecular probes are required for imaging, which is difficult to achieve when some molecular targets are expressed at low levels. Finally, factors such as low blood supply, low perfusion in pancreatic carcinoma, denser stromal components in the tumor, and excessive uptake of the molecular probe by the reticuloendothelial system such as liver and spleen *in vivo* decrease the aggregation dose in the tumor, thus affecting the effect of MR molecular imaging[57]. It can be optimized from the following aspects: (1) Improve the biocompatibility of molecular probes and appropriately prolong their blood circulation time to promote more molecular probes to bind to the tumor; (2) The molecular probe simultaneously combines more Gd ions to obtain higher relaxation rate[43]; (3) Multi-target molecular imaging facilitates specific imaging of lesions[42]; and (4) Reduce the volume and molecular weight of

molecular probe to achieve better penetration efficiency, paramagnetic resonance effect, reduce immunity and reticuloendothelial system uptake *in vivo*[42].

Different imaging techniques have their advantages and disadvantages, and their combined application can achieve complementary advantages and improve the value of clinical applications[58]. In addition, the management of radiopharmaceuticals is extremely strict in some countries, and very few radiopharmaceuticals are clinically approved. Therefore, in addition to the research and development of various imaging agents with high specificity and high sensitivity mentioned above, AI technology to improve diagnostic performance or complement existing technologies may be worth exploring.

ARTIFICIAL INTELLIGENCE AND RADIOMICS

AI, artificial intelligence, can be used to mine various medical images for biometric information and imaging features that are not easily perceived by physicians. In recent years, the application of AI-based radiomics has been used for lesion detection, pathological diagnosis, radiotherapy target delineation and curative effect prediction, so as to improve effective treatment decision-making for cancer patients. Based on radiomics, the cross-validated support vector machine classification diagnostic model can automatically extract quantitative features from MDCT[59]. Liu *et al*[60] used the AI system of R-CNN depth neural network to verify the diagnosis of CT images of pancreatic carcinoma in 100 cases, and established an AI diagnosis system of pancreatic carcinoma based on enhanced CT images. The system can assist doctors to identify pancreatic carcinoma, normal pancreatic tissue, chronic pancreatitis or benign pancreatic tumors. Mori *et al*[61] constructed ^{18}F-FDG-PET/CT radiomic model to predict the recurrence survival value of patients with LAPC after radiotherapy for locally advanced pancreatic cancer, which could significantly improve treatment outcome while avoiding over-treatment of patients with poorer expected outcomes.

Radiomics based on AI has the potential to supplement information for clinical diagnosis and treatment and help solve certain clinical problems, but there are some limitations, such as incorrect tumor screening, insufficient design of database, case number and sensitive feature algorithm.

CONCLUSION

Nuclear medicine molecular imaging is based on the principle of injecting microscopic molecular probes into the body and selectively targeting them to appropriate sites based on different properties, in order to qualify or quantify organs, tissues or lesions for assessing diseases at the molecular level. Molecular imaging in nuclear medicine has made significant advances in the assessment of pancreatic carcinoma in recent years.

FOOTNOTES

Author contributions: Pang XX and Xie L wrote the paper; Pan B provided cases of 18F-FDG *vs* 18F-FAPI PET/CT scan and advice on 18F-FDG *vs* 18F-FAPI of pancreatic carcinoma; Yao WJ and Liu XX provided advice on MRI scan of pancreatic carcinoma; Chen N and Pang XX cooperated on scientific research in Gd-DOTA-HHK and 99mTc-DOTA-HHK compounds.

Supported by The Basic and Clinical Cooperative Research Promotion Plan of Anhui Medical University, No. 2019xkjT011; Anhui Provincial Natural Science Foundation, No. 2008085QH406; and Anhui Medical University Joint Project of Nuclear Medicine and Radiation Medicine, No. 2021 Lcxk035.

Conflict-of-interest statement: The authors have declared that no conflicts of interest exist.

Open-Access: This article is an open-access article that was selected by an in-house editor and fully peer-reviewed by external reviewers. It is distributed in accordance with the Creative Commons Attribution NonCommercial (CC BY-NC 4.0) license, which permits others to distribute, remix, adapt, build upon this work non-commercially, and license their derivative works on different terms, provided the original work is properly cited and the use is non-commercial. See: https://creativecommons.org/Licenses/by-nc/4.0/

Country/Territory of origin: China

ORCID number: Xiao-Xi Pang 0000-0002-1303-5224; Liang Xie 0000-0002-3748-0648; Wen-Jun Yao 0000-0002-6504-7673; Bo Pan 0000-0002-9167-6983; Ni Chen 0000-0001-7533-7546.

S-Editor: Wang JL

L-Editor: A
P-Editor: Chen YX

REFERENCES

1 **Siegel RL**, Miller KD, Jemal A. Cancer statistics, 2020. *CA Cancer J Clin* 2020; **70**: 7-30 [PMID: 31912902 DOI: 10.3322/caac.21590]
2 **Sellmyer MA**, Lee IK, Mankoff DA. Building the Bridge: Molecular Imaging Biomarkers for 21(st) Century Cancer Therapies. *J Nucl Med* 2021; **62**: 1672-1676 [PMID: 34446450 DOI: 10.2967/jnumed.121.262484]
3 **Peppicelli S**, Andreucci E, Ruzzolini J, Bianchini F, Calorini L. FDG uptake in cancer: a continuing debate. *Theranostics* 2020; **10**: 2944-2948 [PMID: 32194847 DOI: 10.7150/thno.40599]
4 **Ghaneh P**, Hanson R, Titman A, Lancaster G, Plumpton C, Lloyd-Williams H, Yeo ST, Edwards RT, Johnson C, Abu Hilal M, Higginson AP, Armstrong T, Smith A, Scarsbrook A, McKay C, Carter R, Sutcliffe RP, Bramhall S, Kocher HM, Cunningham D, Pereira SP, Davidson B, Chang D, Khan S, Zealley I, Sarker D, Al Sarireh B, Charnley R, Lobo D, Nicolson M, Halloran C, Raraty M, Sutton R, Vinjamuri S, Evans J, Campbell F, Deeks J, Sanghera B, Wong WL, Neoptolemos JP. PET-PANC: multicentre prospective diagnostic accuracy and health economic analysis study of the impact of combined modality 18fluorine-2-fluoro-2-deoxy-d-glucose positron emission tomography with computed tomography scanning in the diagnosis and management of pancreatic cancer. *Health Technol Assess* 2018; **22**: 1-114 [PMID: 29402376 DOI: 10.3310/hta22070]
5 **Daamen LA**, Groot VP, Goense L, Wessels FJ, Borel Rinkes IH, Intven MPW, van Santvoort HC, Molenaar IQ. The diagnostic performance of CT versus FDG PET-CT for the detection of recurrent pancreatic cancer: a systematic review and meta-analysis. *Eur J Radiol* 2018; **106**: 128-136 [PMID: 30150034 DOI: 10.1016/j.ejrad.2018.07.010]
6 **Topkan E**, Parlak C, Yapar AF. FDG-PET/CT-based restaging may alter initial management decisions and clinical outcomes in patients with locally advanced pancreatic carcinoma planned to undergo chemoradiotherapy. *Cancer Imaging* 2013; **13**: 423-428 [PMID: 24240137 DOI: 10.1102/1470-7330.2013.0035]
7 **Xi Y**, Guo R, Hu J, Zhang M, Zhang X, Li B. ^{18}F-fluoro-2-deoxy-D-glucose retention index as a prognostic parameter in patients with pancreatic cancer. *Nucl Med Commun* 2014; **35**: 1112-1118 [PMID: 25098308 DOI: 10.1097/MNM.0000000000000178]
8 **Ahn SJ**, Park MS, Lee JD, Kang WJ. Correlation between ^{18}F-fluorodeoxyglucose positron emission tomography and pathologic differentiation in pancreatic cancer. *Ann Nucl Med* 2014; **28**: 430-435 [PMID: 24623151 DOI: 10.1007/s12149-014-0833-x]
9 **Myssayev A**, Myssayev A, Ideguchi R, Eguchi S, Adachi T, Sumida Y, Tobinaga S, Uetani M, Kudo T. Usefulness of FDG PET/CT derived parameters in prediction of histopathological finding during the surgery in patients with pancreatic adenocarcinoma. *PLoS One* 2019; **14**: e0210178 [PMID: 30629646 DOI: 10.1371/journal.pone.0210178]
10 **Barreto SG**, Loveday B, Windsor JA, Pandanaboyana S. Detecting tumour response and predicting resectability after neoadjuvant therapy for borderline resectable and locally advanced pancreatic cancer. *ANZ J Surg* 2019; **89**: 481-487 [PMID: 30117669 DOI: 10.1111/ans.14764]
11 **Hyun SH**, Kim HS, Choi SH, Choi DW, Lee JK, Lee KH, Park JO, Kim BT, Choi JY. Intratumoral heterogeneity of (18)F-FDG uptake predicts survival in patients with pancreatic ductal adenocarcinoma. *Eur J Nucl Med Mol Imaging* 2016; **43**: 1461-1468 [PMID: 26872788 DOI: 10.1007/s00259-016-3316-6]
12 **Chang JS**, Choi SH, Lee Y, Kim KH, Park JY, Song SY, Cho A, Yun M, Lee JD, Seong J. Clinical usefulness of ^{18}F-fluorodeoxyglucose-positron emission tomography in patients with locally advanced pancreatic cancer planned to undergo concurrent chemoradiation therapy. *Int J Radiat Oncol Biol Phys* 2014; **90**: 126-133 [PMID: 25015206 DOI: 10.1016/j.ijrobp.2014.05.030]
13 **Moon SY**, Joo KR, So YR, Lim JU, Cha JM, Shin HP, Yang YJ. Predictive value of maximum standardized uptake value (SUVmax) on ^{18}F-FDG PET/CT in patients with locally advanced or metastatic pancreatic cancer. *Clin Nucl Med* 2013; **38**: 778-783 [PMID: 24107806 DOI: 10.1097/RLU.0b013e31829f8c90]
14 **Zhang A**, Ren S, Yuan Y, Li X, Zhu X, Jiang L, Li D, Zuo C. Prognostic values of ^{18}F-FDG PET/CT metabolic parameters and clinical figures in locally advanced pancreatic cancer underwent chemotherapy combined with stereotactic body radiation therapy. *Medicine (Baltimore)* 2019; **98**: e15064 [PMID: 30921238 DOI: 10.1097/MD.0000000000015064]
15 **Yamamoto T**, Sugiura T, Mizuno T, Okamura Y, Aramaki T, Endo M, Uesaka K. Preoperative FDG-PET predicts early recurrence and a poor prognosis after resection of pancreatic adenocarcinoma. *Ann Surg Oncol* 2015; **22**: 677-684 [PMID: 25190125 DOI: 10.1245/s10434-014-4046-2]
16 **Pu Y**, Wang C, Zhao S, Xie R, Zhao L, Li K, Yang C, Zhang R, Tian Y, Tan L, Li J, Li S, Chen L, Sun H. The clinical application of (18)F-FDG PET/CT in pancreatic cancer: a narrative review. *Transl Cancer Res* 2021; **10**: 3560-3575 [PMID: 35116659 DOI: 10.21037/tcr-21-169]
17 **Calabrò D**, Argalia G, Ambrosini V. Role of PET/CT and Therapy Management of Pancreatic Neuroendocrine Tumors. *Diagnostics (Basel)* 2020; **10** [PMID: 33297381 DOI: 10.3390/diagnostics10121059]
18 **Carideo L**, Prosperi D, Panzuto F, Magi L, Pratesi MS, Rinzivillo M, Annibale B, Signore A. Role of Combined [(68)Ga]Ga-DOTA-SST Analogues and [(18)F]FDG PET/CT in the Management of GEP-NENs: A Systematic Review. *J Clin Med* 2019; **8** [PMID: 31337043 DOI: 10.3390/jcm8071032]
19 **Zhang P**, Yu J, Li J, Shen L, Li N, Zhu H, Zhai S, Zhang Y, Yang Z, Lu M. Clinical and Prognostic Value of PET/CT Imaging with Combination of (68)Ga-DOTATATE and (18)F-FDG in Gastroenteropancreatic Neuroendocrine Neoplasms. *Contrast Media Mol Imaging* 2018; **2018**: 2340389 [PMID: 29681780 DOI: 10.1155/2018/2340389]
20 **Evangelista L**, Ravelli I, Bignotto A, Cecchin D, Zucchetta P. Ga-68 DOTA-peptides and F-18 FDG PET/CT in patients with neuroendocrine tumor: A review. *Clin Imaging* 2020; **67**: 113-116 [PMID: 32559681 DOI:

10.1016/j.clinimag.2020.05.035]
21 **Fani M**, Nicolas GP, Wild D. Somatostatin Receptor Antagonists for Imaging and Therapy. *J Nucl Med* 2017; **58**: 61S-66S [PMID: 28864614 DOI: 10.2967/jnumed.116.186783]
22 **Liu Y**, Watabe T, Kaneda-Nakashima K, Shirakami Y, Naka S, Ooe K, Toyoshima A, Nagata K, Haberkorn U, Kratochwil C, Shinohara A, Hatazawa J, Giesel F. Fibroblast activation protein targeted therapy using [(177)Lu]FAPI-46 compared with [(225)Ac]FAPI-46 in a pancreatic cancer model. *Eur J Nucl Med Mol Imaging* 2022; **49**: 871-880 [PMID: 34537893 DOI: 10.1007/s00259-021-05554-2]
23 **Sunami Y**, Häußler J, Kleeff J. Cellular Heterogeneity of Pancreatic Stellate Cells, Mesenchymal Stem Cells, and Cancer-Associated Fibroblasts in Pancreatic Cancer. *Cancers (Basel)* 2020; **12** [PMID: 33333727 DOI: 10.3390/cancers12123770]
24 **Ji X**, Qian J, Rahman SMJ, Siska PJ, Zou Y, Harris BK, Hoeksema MD, Trenary IA, Heidi C, Eisenberg R, Rathmell JC, Young JD, Massion PP. xCT (SLC7A11)-mediated metabolic reprogramming promotes non-small cell lung cancer progression. *Oncogene* 2018; **37**: 5007-5019 [PMID: 29789716 DOI: 10.1038/s41388-018-0307-z]
25 **Zhang L**, Huang Y, Ling J, Zhuo W, Yu Z, Luo Y, Zhu Y. Overexpression of SLC7A11: a novel oncogene and an indicator of unfavorable prognosis for liver carcinoma. *Future Oncol* 2018; **14**: 927-936 [PMID: 29528250 DOI: 10.2217/fon-2017-0540]
26 **Zhang Z**, Jia G, Pan G, Cao K, Yang Q, Meng H, Yang J, Zhang L, Wang T, Cheng C, Zuo C. Comparison of the diagnostic efficacy of (68) Ga-FAPI-04 PET/MR and (18)F-FDG PET/CT in patients with pancreatic cancer. *Eur J Nucl Med Mol Imaging* 2022; **49**: 2877-2888 [PMID: 35243518 DOI: 10.1007/s00259-022-05729-5]
27 **Röhrich M**, Naumann P, Giesel FL, Choyke PL, Staudinger F, Wefers A, Liew DP, Kratochwil C, Rathke H, Liermann J, Herfarth K, Jäger D, Debus J, Haberkorn U, Lang M, Koerber SA. Impact of (68)Ga-FAPI PET/CT Imaging on the Therapeutic Management of Primary and Recurrent Pancreatic Ductal Adenocarcinomas. *J Nucl Med* 2021; **62**: 779-786 [PMID: 33097632 DOI: 10.2967/jnumed.120.253062]
28 **Gallo A**, Dedionigi C, Civitelli C, Panzeri A, Corradi C, Squizzato A. Optimal Management of Cirrhotic Ascites: A Review for Internal Medicine Physicians. *J Transl Int Med* 2020; **8**: 220-236 [PMID: 33511049 DOI: 10.2478/jtim-2020-0035]
29 **Deng M**, Chen Y, Cai L. Comparison of 68Ga-FAPI and ^{18}F-FDG PET/CT in the Imaging of Pancreatic Cancer With Liver Metastases. *Clin Nucl Med* 2021; **46**: 589-591 [PMID: 33630809 DOI: 10.1097/RLU.0000000000003561]
30 **Xiong J**, Balcioglu HE, Danen EH. Integrin signaling in control of tumor growth and progression. *Int J Biochem Cell Biol* 2013; **45**: 1012-1015 [PMID: 23428797 DOI: 10.1016/j.biocel.2013.02.005]
31 **Herter J**, Zarbock A. Integrin Regulation during Leukocyte Recruitment. *J Immunol* 2013; **190**: 4451-4457 [PMID: 23606722 DOI: 10.4049/jimmunol.1203179]
32 **Huo Y**, Kang L, Pang X, Shen H, Yan P, Zhang C, Liao X, Chen X, Wang R. Noninvasive PET Imaging of a Ga-68-Radiolabeled RRL-Derived Peptide in Hepatocarcinoma Murine Models. *Mol Imaging Biol* 2019; **21**: 286-296 [PMID: 29916116 DOI: 10.1007/s11307-018-1234-7]
33 **Reader CS**, Vallath S, Steele CW, Haider S, Brentnall A, Desai A, Moore KM, Jamieson NB, Chang D, Bailey P, Scarpa A, Lawlor R, Chelala C, Keyse SM, Biankin A, Morton JP, Evans TJ, Barry ST, Sansom OJ, Kocher HM, Marshall JF. The integrin αvβ6 drives pancreatic cancer through diverse mechanisms and represents an effective target for therapy. *J Pathol* 2019; **249**: 332-342 [PMID: 31259422 DOI: 10.1002/path.5320]
34 **Liu Z**, Liu H, Ma T, Sun X, Shi J, Jia B, Sun Y, Zhan J, Zhang H, Zhu Z, Wang F. Integrin αvβ$_6$-Targeted SPECT Imaging for Pancreatic Cancer Detection. *J Nucl Med* 2014; **55**: 989-994 [PMID: 24711651 DOI: 10.2967/jnumed.113.132969]
35 **Koay EJ**, Hall W, Park PC, Erickson B, Herman JM. The role of imaging in the clinical practice of radiation oncology for pancreatic cancer. *Abdom Radiol (NY)* 2018; **43**: 393-403 [PMID: 29110053 DOI: 10.1007/s00261-017-1373-3]
36 **Higaki T**, Nakamura Y, Tatsugami F, Kaichi Y, Akagi M, Akiyama Y, Baba Y, Iida M, Awai K. Introduction to the Technical Aspects of Computed Diffusion-weighted Imaging for Radiologists. *Radiographics* 2018; **38**: 1131-1144 [PMID: 29995614 DOI: 10.1148/rg.2018170115]
37 **Liang L**, Gu JY, Liu K, Fu CX, Rao SX, Zeng MS. [Application of cDWI in diagnosis of pancreatic cancer: a preliminary study]. *Fangshexue Shijian* 2019; **34**: 1081-1087 [DOI: 10.13609/j.cnki.1000-0313.2019.10.006]
38 **Kaandorp MPT**, Barbieri S, Klaassen R, van Laarhoven HWM, Crezee H, While PT, Nederveen AJ, Gurney-Champion OJ. Improved unsupervised physics-informed deep learning for intravoxel incoherent motion modeling and evaluation in pancreatic cancer patients. *Magn Reson Med* 2021; **86**: 2250-2265 [PMID: 34105184 DOI: 10.1002/mrm.28852]
39 **Ottens T**, Barbieri S, Orton MR, Klaassen R, van Laarhoven HWM, Crezee H, Nederveen AJ, Zhen X, Gurney-Champion OJ. Deep learning DCE-MRI parameter estimation: Application in pancreatic cancer. *Med Image Anal* 2022; **80**: 102512 [PMID: 35709559 DOI: 10.1016/j.media.2022.102512]
40 **Valenzuela RF**, Kundra V, Madewell JE, Costelloe CM. Advanced Imaging in Musculoskeletal Oncology: Moving Away From RECIST and Embracing Advanced Bone and Soft Tissue Tumor Imaging (ABASTI) - Part I - Tumor Response Criteria and Established Functional Imaging Techniques. *Semin Ultrasound CT MR* 2021; **42**: 201-214 [PMID: 33814106 DOI: 10.1053/j.sult.2020.08.012]
41 **Chen X**, Zhou H, Li X, Duan N, Hu S, Liu Y, Yue Y, Song L, Zhang Y, Li D, Wang Z. Plectin-1 Targeted Dual-modality Nanoparticles for Pancreatic Cancer Imaging. *EBioMedicine* 2018; **30**: 129-137 [PMID: 29574092 DOI: 10.1016/j.ebiom.2018.03.008]
42 **Wang Q**, Yan H, Jin Y, Wang Z, Huang W, Qiu J, Kang F, Wang K, Zhao X, Tian J. A novel plectin/integrin-targeted bispecific molecular probe for magnetic resonance/near-infrared imaging of pancreatic cancer. *Biomaterials* 2018; **183**: 173-184 [PMID: 30172243 DOI: 10.1016/j.biomaterials.2018.08.048]
43 **Huang X**, Fan C, Zhu H, Le W, Cui S, Chen X, Li W, Zhang F, Huang Y, Sh D, Cui Z, Shao C, Chen B. Glypican-1-antibody-conjugated Gd-Au nanoclusters for FI/MRI dual-modal targeted detection of pancreatic cancer. *Int J Nanomedicine* 2018; **13**: 2585-2599 [PMID: 29750031 DOI: 10.2147/IJN.S158559]
44 **Lee S**, Kim SH, Park HK, Jang KT, Hwang JA, Kim S. Pancreatic Ductal Adenocarcinoma: Rim Enhancement at MR Imaging Predicts Prognosis after Curative Resection. *Radiology* 2018; **288**: 456-466 [PMID: 29664340 DOI: 10.1148/radiol.2018172331]
45 **Zhang C**, Yan Y, Zou Q, Chen J, Li C. Superparamagnetic iron oxide nanoparticles for MR imaging of pancreatic cancer:

Potential for early diagnosis through targeted strategies. *Asia Pac J Clin Oncol* 2016; **12**: 13-21 [PMID: 26663873 DOI: 10.1111/ajco.12437]

46 **Ze X**, Zou W, Li Z. Translational research in anti-pancreatic fibrosis drug discovery and development. *J Transl Int Med* 2021; **9**: 225-227 [PMID: 35136719 DOI: 10.2478/jtim-2021-0036]

47 **Ahmadi Y**, Kostenich G, Oron-Herman M, Wadsak W, Mitterhauser M, Orenstein A, Mirzaei S, Knoll P. In vivo magnetic resonance imaging of pancreatic tumors using iron oxide nanoworms targeted with PTR86 peptide. *Colloids Surf B Biointerfaces* 2017; **158**: 423-430 [PMID: 28719864 DOI: 10.1016/j.colsurfb.2017.06.051]

48 **Li H**, Wang P, Gong W, Wang Q, Zhou J, Zhu WH, Cheng Y. Dendron-Grafted Polylysine-Based Dual-Modal Nanoprobe for Ultra-Early Diagnosis of Pancreatic Precancerosis *via* Targeting a Urokinase-Type Plasminogen Activator Receptor. *Adv Healthc Mater* 2018; **7** [PMID: 29195018 DOI: 10.1002/adhm.201700912]

49 **Morin E**, Sjöberg E, Tjomsland V, Testini C, Lindskog C, Franklin O, Sund M, Öhlund D, Kiflemariam S, Sjöblom T, Claesson-Welsh L. VEGF receptor-2/neuropilin 1 trans-complex formation between endothelial and tumor cells is an independent predictor of pancreatic cancer survival. *J Pathol* 2018; **246**: 311-322 [PMID: 30027561 DOI: 10.1002/path.5141]

50 **Zhang W**, Liang X, Zhu L, Zhang X, Jin Z, Du Y, Tian J, Xue H. Optical magnetic multimodality imaging of plectin-1-targeted imaging agent for the precise detection of orthotopic pancreatic ductal adenocarcinoma in mice. *EBioMedicine* 2022; **80**: 104040 [PMID: 35525203 DOI: 10.1016/j.ebiom.2022.104040]

51 **Zou Q**, Zhang CJ, Yan YZ, Min ZJ, Li CS. MUC-1 aptamer targeted superparamagnetic iron oxide nanoparticles for magnetic resonance imaging of pancreatic cancer in vivo and in vitro experiment. *J Cell Biochem* 2019; **120**: 18650-18658 [PMID: 31338877 DOI: 10.1002/jcb.28950]

52 **Zou J**, Chen S, Li Y, Zeng L, Lian G, Li J, Huang K, Chen Y. Nanoparticles modified by triple single chain antibodies for MRI examination and targeted therapy in pancreatic cancer. *Nanoscale* 2020; **12**: 4473-4490 [PMID: 32031201 DOI: 10.1039/c9nr04976b]

53 **Ramsay EE**, Decollogne S, Joshi S, Corti A, Apte M, Pompella A, Hogg PJ, Dilda PJ. Employing pancreatic tumor γ-glutamyltransferase for therapeutic delivery. *Mol Pharm* 2014; **11**: 1500-1511 [PMID: 24654974 DOI: 10.1021/mp400664t]

54 **Jiang Y**, Liu S, Zhang Y, Li H, He H, Dai J, Jiang T, Ji W, Geng D, Elzatahry AA, Alghamdi A, Fu D, Deng Y, Zhao D. Magnetic mesoporous nanospheres anchored with LyP-1 as an efficient pancreatic cancer probe. *Biomaterials* 2017; **115**: 9-18 [PMID: 27871003 DOI: 10.1016/j.biomaterials.2016.11.006]

55 **Nahm CB**, Turchini J, Jamieson N, Moon E, Sioson L, Itchins M, Arena J, Colvin E, Howell VM, Pavlakis N, Clarke S, Samra JS, Gill AJ, Mittal A. Biomarker panel predicts survival after resection in pancreatic ductal adenocarcinoma: A multi-institutional cohort study. *Eur J Surg Oncol* 2019; **45**: 218-224 [PMID: 30348604 DOI: 10.1016/j.ejso.2018.10.050]

56 **Tummers WS**, Willmann JK, Bonsing BA, Vahrmeijer AL, Gambhir SS, Swijnenburg RJ. Advances in Diagnostic and Intraoperative Molecular Imaging of Pancreatic Cancer. *Pancreas* 2018; **47**: 675-689 [PMID: 29894417 DOI: 10.1097/MPA.0000000000001075]

57 **Dadfar SM**, Roemhild K, Drude NI, von Stillfried S, Knüchel R, Kiessling F, Lammers T. Iron oxide nanoparticles: Diagnostic, therapeutic and theranostic applications. *Adv Drug Deliv Rev* 2019; **138**: 302-325 [PMID: 30639256 DOI: 10.1016/j.addr.2019.01.005]

58 **Feng L**, Guo J, Wang S, Liu X, Ge N, Wang G, Sun S. Endoscopic Transmural Drainage and Necrosectomy in Acute Necrotizing Pancreatitis: A Review. *J Transl Int Med* 2021; **9**: 168-176 [PMID: 34900627 DOI: 10.2478/jtim-2021-0031]

59 **Wei R**, Lin K, Yan W, Guo Y, Wang Y, Li J, Zhu J. Computer-Aided Diagnosis of Pancreas Serous Cystic Neoplasms: A Radiomics Method on Preoperative MDCT Images. *Technol Cancer Res Treat* 2019; **18**: 1533033818824339 [PMID: 30803366 DOI: 10.1177/1533033818824339]

60 **Liu SL**, Li S, Guo YT, Zhou YP, Zhang ZD, Lu Y. Establishment and application of an artificial intelligence diagnosis system for pancreatic cancer with a faster region-based convolutional neural network. *Chin Med J (Engl)* 2019; **132**: 2795-2803 [PMID: 31856050 DOI: 10.1097/CM9.0000000000000544]

61 **Mori M**, Passoni P, Incerti E, Bettinardi V, Broggi S, Reni M, Whybra P, Spezi E, Vanoli EG, Gianolli L, Picchio M, Di Muzio NG, Fiorino C. Training and validation of a robust PET radiomic-based index to predict distant-relapse-free-survival after radio-chemotherapy for locally advanced pancreatic cancer. *Radiother Oncol* 2020; **153**: 258-264 [PMID: 32681930 DOI: 10.1016/j.radonc.2020.07.003]

World Journal of Radiology

Submit a Manuscript: https://www.f6publishing.com

World J Radiol 2023 January 28; 15(1): 20-31

DOI: 10.4329/wjr.v15.i1.20

ISSN 1949-8470 (online)

ORIGINAL ARTICLE

Retrospective Study

Diagnostic efficacy of diffusion-weighted imaging and semiquantitative and quantitative dynamic contrast-enhanced magnetic resonance imaging in salivary gland tumors

Erkan Gökçe, Murat Beyhan

Specialty type: Radiology, nuclear medicine and medical imaging

Provenance and peer review: Invited article; Externally peer reviewed.

Peer-review model: Single blind

Peer-review report's scientific quality classification

Grade A (Excellent): 0
Grade B (Very good): B
Grade C (Good): C
Grade D (Fair): 0
Grade E (Poor): 0

P-Reviewer: Li T, China; Ma C, China

Received: July 5, 2022
Peer-review started: July 5, 2022
First decision: September 5, 2022
Revised: September 15, 2022
Accepted: December 13, 2022
Article in press: December 13, 2022
Published online: January 28, 2023

Erkan Gökçe, Murat Beyhan, Department of Radiology, Tokat Gaziosmanpasa University, Faculty of Medicine, Tokat 60100, Turkey

Corresponding author: Erkan Gökçe, MD, Professor, Department of Radiology, Tokat Gaziosmanpasa University, Faculty of Medicine, Kaleardı Neighborhood, Muhittin Fisunoglu Street, Tokat 60100, Turkey. drerkangokce@gmail.com

Abstract

BACKGROUND

Increased use of functional magnetic resonance imaging (MRI) methods such as diffusion-weighted imaging (DWI) and dynamic contrast-enhanced (DCE) MRI consisting of sequential contrast series, allows us to obtain more information on the microstructure, cellularity, interstitial distance, and vascularity of tumors, which has increased the discrimination power for benign and malignant salivary gland tumors (SGTs). In the last few years, quantitative DCE MRI data containing T1 perfusion parameters (K_{trans}, K_{ep} and V_e), were reported to contribute to the differentiation of benign or malignant subtypes in SGTs.

AIM

To evaluate the diagnostic efficacy of DWI and semiquantitative and quantitative perfusion MRI parameters in SGTs.

METHODS

Diffusion MRI [apparent diffusion coefficient (ADC) value] with a 1.5 T MR machine, semiquantitative perfusion MRI [time intensity curve (TIC) pattern], and quantitative perfusion MRI examinations (K_{trans}, K_{ep} and V_e) of 73 tumors in 67 patients with histopathological diagnosis performed from 2017 to 2021 were retrospectively evaluated. In the ADC value and semiquantitative perfusion MRI measurements, cystic components of the tumors were not considered, and the region of interest (ROI) was manually placed through the widest axial section of the tumor. TIC patterns were divided into four groups: Type A = T_{peak} > 120 s; type B = T_{peak} ≤ 120 s, washout ratio (WR) ≥ 30%; type C = T_{peak} ≤ 120 s, WR < 30%; and type D = flat TIC. For the quantitative perfusion MRI analysis, a 3D ROI was placed in the largest solid component of the tumor, and the K_{trans}, K_{ep} and V_e values were automatically generated.

RESULTS

The majority of SGTs were located in the parotid glands (86.3%). Of all the SGTs, 68.5% were benign and 31.5% were malignant. Significant differences were found for ADC values among pleomorphic adenomas (PMAs), Warthin's tumors (WTs), and malignant tumors (MTs) ($P < 0.001$). PMAs had type A and WTs had type B TIC pattern while the vast majority of MTs and other benign tumors (OBTs) (54.5% and 45.5%, respectively) displayed type C TIC pattern. PMAs showed no washout, while the highest mean WR was observed in WTs (59% ± 11%). K_{trans} values of PMAs, WTs, OBTs, and MTs were not significantly different. K_{ep} values of PMAs and WTs were significantly different from those of OBTs and MTs. Mean V_e value of WTs was significantly different from those of PMAs, OBTs, and MTs ($P < 0.001$).

CONCLUSION

The use of quantitative DCE parameters along with diffusion MRI and semiquantitative contrast-enhanced MRI in SGTs could improve the diagnostic accuracy.

Key Words: Diffusion-weighted imaging; Dynamic contrast-enhanced imaging; Magnetic resonance imaging; Perfusion imaging; Salivary gland tumor; Tumor

©The Author(s) 2023. Published by Baishideng Publishing Group Inc. All rights reserved.

Core Tip: In this study, the diagnostic features of diffusion-weighted imaging and semiquantitative and quantitative perfusion magnetic resonance imaging (MRI) parameters were evaluated in salivary gland tumors. The apparent diffusion coefficient (ADC) values of pleomorphic adenomas (PMAs) were significantly higher than those of Warthin's tumors (WTs), other benign tumors (OBTs), and malignant tumors (MTs). On semiquantitative MRI, PMAs were distinguished from all other tumors by their long T_{peak} times and lack of washout. WTs had the shortest T_{peak} and highest washout ratio values. For quantitative perfusion MRI parameters, the K_{ep} value of WTs was significantly higher than those of other tumors. The V_e values of WTs and OBTs differed significantly from those of PMAs and MTs.

Citation: Gökçe E, Beyhan M. Diagnostic efficacy of diffusion-weighted imaging and semiquantitative and quantitative dynamic contrast-enhanced magnetic resonance imaging in salivary gland tumors. *World J Radiol* 2023; 15(1): 20-31

URL: https://www.wjgnet.com/1949-8470/full/v15/i1/20.htm

DOI: https://dx.doi.org/10.4329/wjr.v15.i1.20

INTRODUCTION

Salivary gland tumors (SGTs) account for about 2.0%-6.5% of all head and neck tumors. Approximately 70% of them originate from the parotid glands, and a small number have submandibular, sublingual, and minor salivary gland origins. While the majority of tumors from the parotid glands are benign, malignancies are more common in those located in other glands. Preoperative characterization of SGTs is important for treatment planning. The choice of surgery method for SGTs is closely associated with the histology of the tumor. Diagnosis is mostly based on combined evaluation of clinical features and findings from physical examinations, imaging and cytological observations. Fine-needle aspiration biopsy (FNAB) is the most commonly used method for cytological examinations but complex pathologies can result in false positives and false negatives in malignant tumors (MTs)[1,2]. Conventional magnetic resonance imaging (MRI) is very useful for identifying the tumor location, morphology, extension, and its association with the nerves and inner structure[1-3]. However, diagnosing MTs and benign tumors (BTs) by conventional MRI can be difficult due to overlapping findings[1,2,4]. In recent years, an increase has been reported in diagnostic accuracy in SGTs for distinguishing between MTs and BTs with the use of diffusion-weighted imaging (DWI) and dynamic contrast-enhanced (DCE) MRI techniques[1,5-9]. DCE MRI is used to track an exogenous, paramagnetic contrast agent in tissues and has been a powerful tool in the characterization of tumor hemodynamics[1,3,10,11]. As a semiquantitative method in DCE MRI, patterns have been established by measuring time to peak (T_{peak}) and washout ratio (WR) on the time intensity curve (TIC)[1,3]. T_{peak} is closely related to microvessel count while WR reflects the stromal cellularity grade. On quantitative DCE MRI, on the other hand, perfusion parameters such as K_{trans} [volume transfer constant between blood plasma and the extracellular extravascular space (EES)], K_{ep} (flux rate constant between the EES and plasma), and V_e (EES fractional volume) are used[1,3]. Although there are many studies dealing with diffusion and semiquantitative

DCE MRIs in SGTs, the number of quantitative MRI studies is limited[12-15]. In the present study, the diagnostic value of diffusion MRI and semiquantitative and quantitative perfusion MRI parameters was evaluated in SGTs.

MATERIALS AND METHODS

Patients

The study was conducted retrospectively following approval by the local ethics committee (20-KAEK-105). A total of 67 patients with tumors originating from or involving the salivary glands were included. The study included patients who had swelling of the face or in the salivary glands, who were subjected to MRI, diffusion MRI, and perfusion MRI examinations at our hospital between April 2017 and February 2021 and who were diagnosed histopathologically after FNAB, Tru-cut biopsy, or surgical removal. For this study, patients whose neck and maxillofacial MRI examination reports included the description of a mass in the salivary glands were surveyed in picture archiving and communication systems. A total of 33 patients were excluded: 2 patients with intra-lesion hemorrhage due to FNAB before the MRI examination, 16 patients who had contrast-enhanced MRI but did not have perfusion MRI series, and 15 patients whose diagnosis was not confirmed histopathologically. Thus, a total of 73 MTs and BTs, which originated from major and minor salivary glands in 67 patients, were included in the study (Figure 1).

MRI scanning and measurements

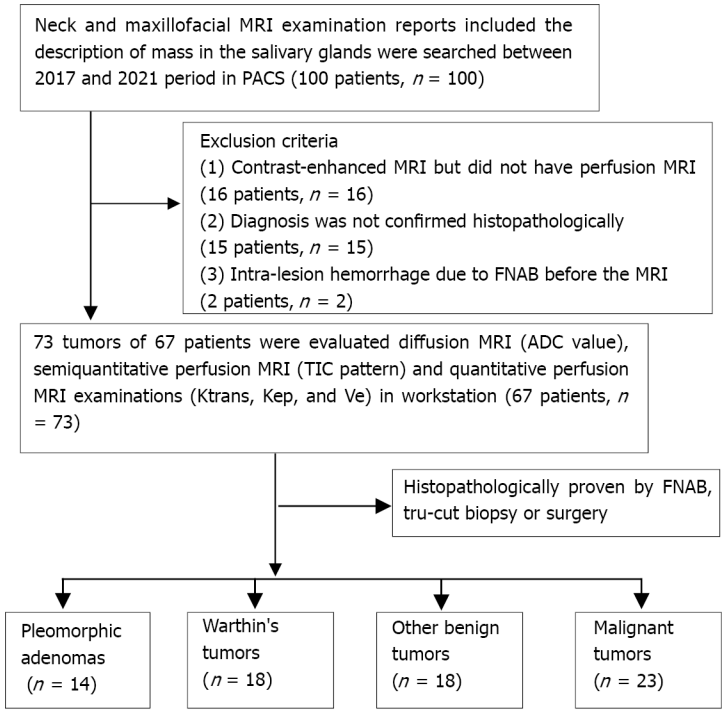
MRI was performed on a 1.5 T superconducting MRI system [General Electric (GE) Signa Explorer Software Version 25; GE Healthcare, Milwaukee, WI, United States, 2016] with head and neck array coils. Routine MRI sequences included axial T1-weighted [time to repetition/time to echo (TR/TE), 456 ms/8.1 ms], in phase axial T2-weighted (TR/TE, 3711 ms/82.8 ms), sagittal T2-weighted (TR/TE, 4499 ms/88.2 ms), and coronal T2-weighted (TR/TE, 4380 ms/84.6 ms). DCE MRI was performed with a T1-weighted 3D fast spoiled gradient echo sequence [TR/TE/time to inversion, 3.8 ms/1.3 ms/15 ms; flip angle, 20°]. The contrast agent Gd-DTPA (Dotarem, Guerbet, France) was injected after the fourth dynamic sequence acquisition at a rate of 2.0 mL/s *via* the right antecubital vein. The contrast agent was administered at a dose of 0.2 mmoL/kg body weight. Immediately after the injection of the contrast agent, a 20 mL saline flush was carried out at the same injection rate. In total, 18-21 dynamic sequence acquisitions with 30 dynamic images per sequence were performed with total scanning time ranging from 3 min and 11 s to 5 min and 24 s. The location, morphology, and internal structure of the tumor were evaluated by conventional MRI (Figures 2A and B, 3A and B, 4A and B, 5A and B).

DWI was performed using a multislice echo-planar single-shot spin-echo sequence, on the axial plane (TR/TE = 5476 ms/95.4 ms, field of view = 26 cm, matrix = 96 × 128, section thickness = 4-5 mm, and interslice gap = 4 mm). Three diffusion gradients were applied sequentially in the x, y, and z directions with *b* values of 0 and 1000 s/mm^2 (Figure 2B). The acquisition time varied from 60 s to 120 s. The apparent diffusion coefficient (ADC) maps were generated automatically.

"GE Advantage Windows Workstation 4.7" was used to determine ADC values on diffusion MRI and to perform measurements in semiquantitative and quantitative perfusion MRI. Image analysis and region of interest (ROI) measurements were carried out on a consensus basis by two neuroradiologists (Erkan Gökçe and Murat Beyhan with more than 12 and 7 years of work experience, respectively) who were not aware of the clinical status of the patients. On ADC value measurements, cystic components of the tumors were not considered, the ROI was manually placed through the widest axial section of the tumor, and the ADC value was determined as mm^2/s (Figures 2C, 3C, 4C and 5C). Semiquantitative analysis of DCE MRI was based on TIC (Figures 2D and E, 3D and E, 4D and E, 5D and E). T_{peak} was measured as the time from the point where the lesion began to show contrast enhancement to the point with the highest level of contrast enhancement. TICs were evaluated in four different categories based on Yabuuchi *et al*[10]: Type A = T_{peak} > 120 s; type B = T_{peak} ≤ 120 s, WR ≥ 30%; type C = T_{peak} ≤ 120 s, WR < 30%; and type D = flat TIC. To confirm the accuracy of TIC and perfusion biomarker analyses, ROIs were drawn in a way to avoid the vascular and cystic parts of the tumors. Quantitative perfusion DCE MRI parameters were measured using the Tofts kinetic model[16]. For quantitative perfusion MRI analysis, a 3D ROI was placed in the largest solid component of the tumor, and the K_{trans}, K_{ep} and V_e values were generated automatically(Figures 2F-H, 3F-H, 4F-H, 5F-H).

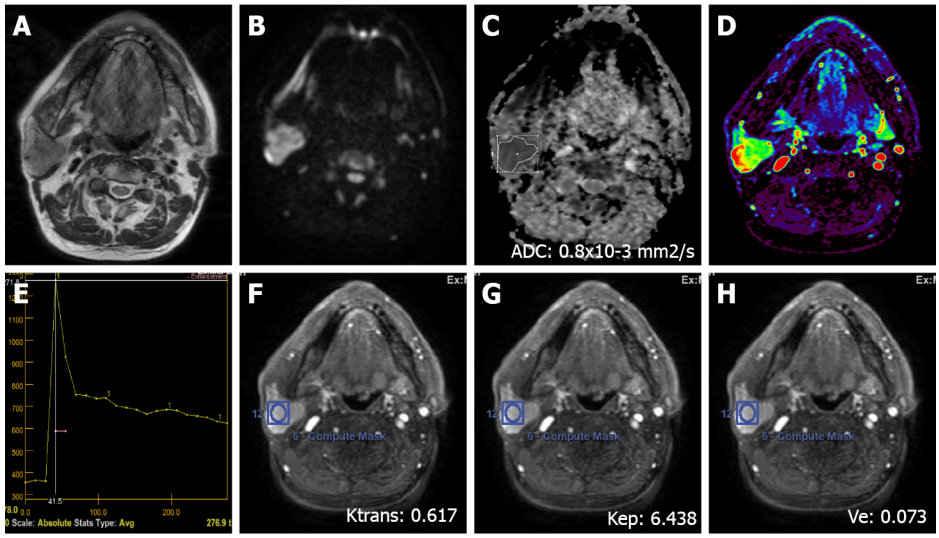
Statistical analysis

Statistical analyses were performed using SPSS 18.0 software (IBM, Chicago, IL, United States) and MedCalc statistical software version 20.009 (MedCalc software bvba, Ostend, Belgium). For each parameter, the conformity of the groups to the normal distribution was evaluated by the Shapiro-Wilk test, and the Levene test was used to evaluate the homogeneity of variances. Data are expressed as the mean ± SD or frequency and percent. One-way ANOVA was used for the groups with a normal distribution for comparison of the groups, and Bonferroni correction was applied in multiple comparisons. The Kruskal-Wallis test was used to compare the groups that did not fit the normal distribution, and



DOI: 10.4329/wjr.v15.i1.20 **Copyright** ©The Author(s) 2023.

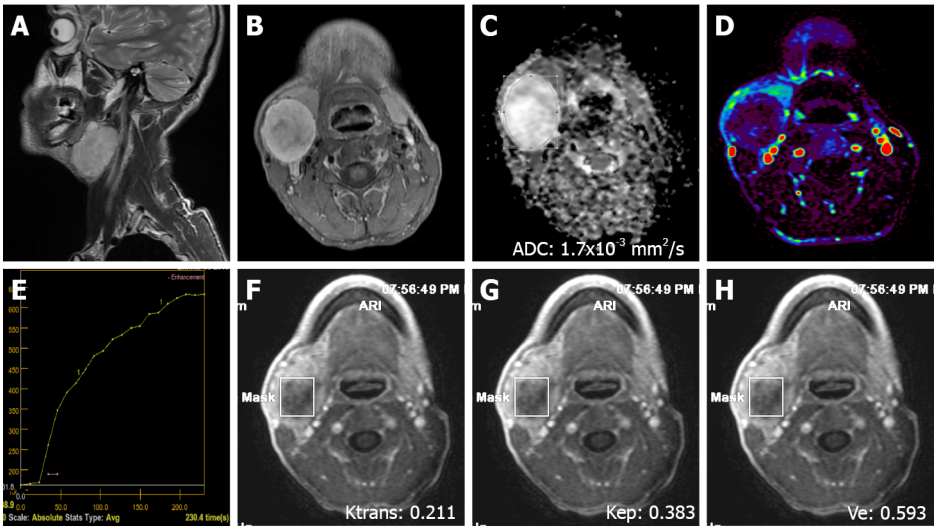
Figure 1 Patient inclusion and exclusion flowchart.



DOI: 10.4329/wjr.v15.i1.20 **Copyright** ©The Author(s) 2023.

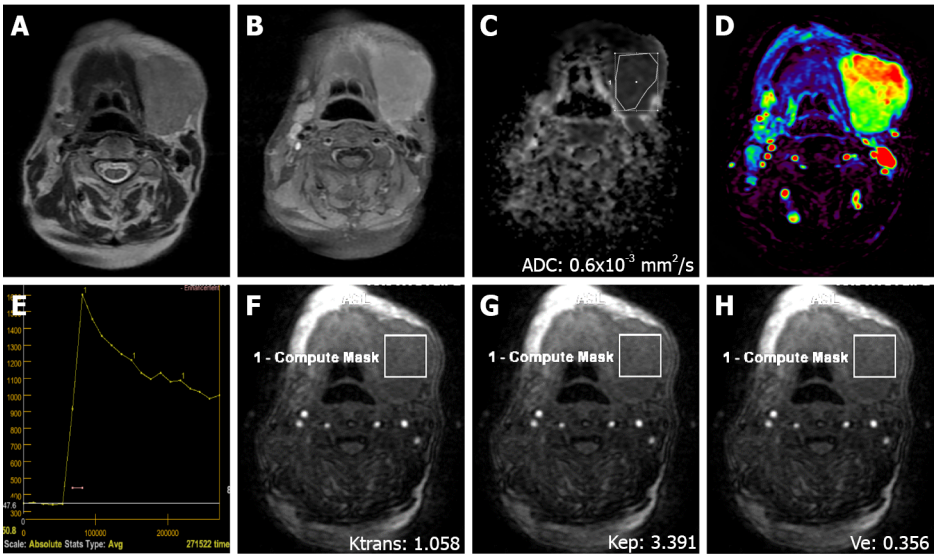
Figure 2 A 72-year-old male patient with a Warthin's tumor in the right parotid gland. A: On axial plane T2-weighted image, a mildly hypointense (compared to the gland), smooth-contoured mass localized in the center of the parotid gland is observed; B: On the diffusion-weighted image, the mass appears to be hyperintense; C: ADC value was 0.8 × 10^{-3} mm^2/s on the apparent diffusion coefficient map; D: The mass is hyperperfused on color-coded perfusion image; E: Type B time intensity curve shows a washout ratio of 75%; F, G, and H: K_{trans}, K_{ep}, and V_e values on quantitative perfusion images were 0.617 min^{-1}, 6.438 min^{-1}, and 0.073, respectively. ADC: Apparent diffusion coefficient.

Bonferroni correction was applied in multiple comparisons. The area under curve (AUC), sensitivity, specificity, positive predictive value (PPV), negative predictive value (NPV), and cut-off values of diagnostic parameters were calculated for each tumor group by performing receiver operating characteristic curve (ROC) analysis.



DOI: 10.4329/wjr.v15.i1.20 **Copyright** ©The Author(s) 2023.

Figure 3 A 38-year-old male patient with a pleomorphic adenoma in the right submandibular gland. A: On sagittal plane T2-weighted image, a hyperintense (compared to the gland), smooth, slightly lobule-contoured mass is observed; B: On contrast-enhanced axial plane T1-weighted image, intense contrast-enhancement is observed in the mass; C: The mass is hyperintense on the apparent diffusion coefficient map due to facilitated diffusion (ADC value: 1.7 × 10^{-3} mm^2/s); D: The mass is hypoperfused on color coded perfusion image; E: The tumor has type A time intensity curve; F, G, and H: K_{trans}, K_{ep}, and V_e values on quantitative perfusion images were 0.211 min^{-1}, 0.383 min^{-1}, and 0.593, respectively. ADC: Apparent diffusion coefficient.



DOI: 10.4329/wjr.v15.i1.20 **Copyright** ©The Author(s) 2023.

Figure 4 A 76-year-old female patient with diffuse large B cell lymphoma and a mass in the left submandibular gland region. A: On axial T2-weighted image, a smooth-contoured mass with homogeneous internal structure and an intensity similar to that of the submandibular gland is observed; B: Axial contrast-enhanced image shows the intense homogeneous contrast enhancement of the mass; C: On the apparent coefficient mapping image, the mass features prominent diffusion restriction (ADC value: 0.6 × 10^{-3} mm^2/s); D: The mass is hyperperfused on color coded perfusion image; E: Type B time intensity curve shows a 48% washout ratio; F, G, and H: K_{trans}, K_{ep}, and V_e values on quantitative perfusion images were 1.058 min^{-1}, 3.391 min^{-1}, and 0.356, respectively. ADC: Apparent diffusion coefficient.

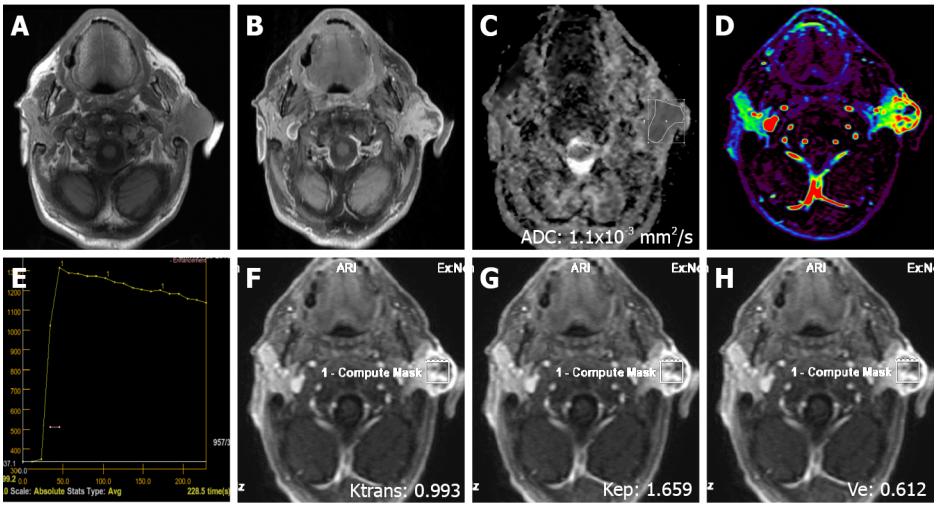
RESULTS

The age range of the 67 patients (40 male and 27 female) included in the study was 12-93 years (mean age = 56.9 ± 15.8 years). One patient had three lesions in the salivary glands, while four patients had two and the remaining 62 had one lesion. Thus, 73 lesions in 67 patients were evaluated. The majority of the lesions (86.3%) were located in the parotid glands, while a small number (4.1%) originated from minor salivary glands. The locations, numbers, and frequencies of SGTs are shown in Table 1. Approximately two-thirds of the lesions (68.5%) were benign (Figures 2 and 3), and one-third (31.5%) was malignant (Figures 4 and 5). Warthin's tumors (WTs) (36.0%) were the most common BTs, followed by pleomorphic adenomas (PMAs) (28.0%). Of the MTs, squamous cell cancer (47.8%), adenoid cystic

Table 1 Locations, numbers, and frequencies of salivary gland tumors

Location	*n* (%)
Unilateral parotid gland	61 (83.6)
Submandibular gland	6 (8.2)
Minor salivary gland	3 (4.1)
Bilateral parotid gland	2 (2.7)
Sublingual gland	1 (1.4)

n: Number of salivary gland tumors



DOI: 10.4329/wjr.v15.i1.20 **Copyright** ©The Author(s) 2023.

Figure 5 A 79-year-old male patient with squamous cell cancer in the left parotid gland. A: On axial plane T1-weighted image, an irregularly contoured, hypointense mass involving skin and subcutaneous tissues is observed; B: On axial contrast-enhanced T1-weighted image, the mass shows an intense heterogeneous contrast enhancement; C: ADC value on the apparent diffusion coefficient map was 1.1 × 10^{-3} mm^2/s; D: The mass is heterogeneously hyperperfused on color coded perfusion image; E: Type C time intensity curve shows a 10% washout ratio; F, G, and H: K_{trans}, K_{ep}, and V_e values on quantitative perfusion images were 0.993 min^{-1}, 1.659 min^{-1}, and 0.612, respectively. ADC: Apparent diffusion coefficient.

cancers (13.0%), and malignant lymphomas (13.0%) were the most common. The numbers of benign and malignant SGTs are provided in Table 2. The ADC values of PMAs were significantly higher than those of WTs, other benign tumors (OBTs), and MTs ($P < 0.001$). However, there was no significant difference in ADC values for OBTs, WTs, and MTs. Significant differences were not found for ADC values of all BTs and MTs. The mean ADC values of SGTs are shown in Table 3.

An evaluation of T_{peak} values of semiquantitative perfusion MRI parameters revealed that PMAs reached T_{peak} significantly later (mean T_{peak} = 202.74 ± 21.48 s) than WTs, OBTs, and MTs while the difference between OBTs and MTs for T_{peak} values was not significant. WTs reached T_{peak} significantly earlier than other tumors. With regard to WR, no washout was observed in PMAs. WTs had the highest mean WR value (59% ± 11%), which was significantly different from the mean WR values of MTs and OBTs. PMAs had type A and WTs had type B TIC pattern, while the majority of MTs and OBTs (54.5% and 45.5%, respectively) exhibited type C TIC pattern. Semiquantitative DCE MRI parameters of SGTs are provided in Table 4.

For quantitative perfusion MRI parameters, K_{trans} values of PMAs, WTs, OBTs, and MTs were not significantly different. The K_{ep} value of WTs, on the other hand, was significantly higher than those of other tumors ($P < 0.001$). For V_e value, WTs and OBTs differed significantly from PMAs and MTs ($P < 0.001$). An evaluation of all BTs and MTs showed significant differences for K_{ep} and V_e values ($P < 0.05$) but not for K_{trans} values. Quantitative DCE MRI parameters of SGTs are shown in Table 3.

The results of ROC analysis and cut-off values used for the parameters of DWI, semiquantitative and quantitative MRI of PMAs, WTs, and malignant SGTs are given in Table 5.

Table 2 Numbers of benign and malignant salivary gland tumors

Benign SGTs	*n* (%)	Malignant SGTs	*n* (%)
Warthin's tumor	18 (24.7)	Squamous cell carcinoma	11 (15.1)
Pleomorphic adenoma	14 (19.2)	Adenoid cystic carcinoma	3 (4.1)
Inflammatory process	12 (16.4)	Malignant lymphoma	3 (4.1)
Lipoma	4 (5.5)	Adenocarcinoma	1 (1.4)
Benign cystic lesions	1 (1.4)	Mucoepidermoid carcinoma	1 (1.4)
		Carcinoma ex pleomorphic adenoma	1 (1.4)
Other benign lesions	1 (1.4)	Acinic cell carcinoma	1 (1.4)
		Follicular dendritic cell sarcoma	1 (1.4)
		Salivary duct carcinoma	1 (1.4)
Total	50 (68.5)		23 (31.5)

SGTs: Salivary gland tumors; *n*: Number of salivary gland tumors

Table 3 Mean ADC values and quantitative dynamic contrast-enhanced magnetic resonance imaging parameters of different histopathologic salivary gland tumors

	Pleomorphic adenoma	Warthin's tumor	Other benign tumors	Malignant tumors	*P* value
ADC ($\times 10^{-3}$ mm^2/s)	1.61 ± 0.26 (a)	0.72 ± 0.09 (b)	0.77 ± 0.19 (b)	0.96 ± 0.33 (b)	< 0.001
K_{trans} (min^{-1})	0.42 ± 0.35	0.75 ± 0.55	0.57 ± 0.37	0.77 ± 0.56	0.131
K_{ep} (min^{-1})	0.69 ± 0.33 (a)	6.2 ± 3.13 (b)	1.95 ± 0.94 (c)	1.72 ± 0.92 (c)	< 0.001
V_e	0.65 ± 0.25 (a)	0.11 ± 0.04 (b)	0.3 ± 0.12 (c)	0.48 ± 0.24 (ac)	< 0.001

Data are shown as the mean ± SD. One-way ANOVA was used. abc: Indicates that means with the same letters in the same column are not significantly different; $P < 0.05$ indicates a statistically significant difference among the groups. ADC: Apparent diffusion coefficient; K_{trans}: Volume transfer constant between blood plasma and the extracellular extravascular space; K_{ep}: Flux rate constant between the EES and plasma; V_e: EES fractional volume; EES: Extracellular extravascular space.

Table 4 Semiquantitative dynamic contrast-enhanced magnetic resonance imaging parameters of different histopathologic salivary gland tumors

	TIC Pattern, *n*(%)				T_{peak} (s)	WR (%)
	A	B	C	D		
Pleomorphic adenomas	14 (70.0)	0 (0)	0 (0)	0 (0)	202.74 ± 21.48 (a)	-
Warthin's tumors	0 (0)	18 (66.7)	0 (0)	0 (0)	20.26 ± 11.72 (b)	59.33 ± 10.99 (a)
Other benign tumors	4 (20.0)	4 (14.8)	10 (45.5)	0 (0)	74.94 ± 75.47 (c)	17.89 ± 14.99 (b)
Malignant tumors	2 (10.0)	5 (18.5)	12 (54.5)	4 (100)	60.60 ± 55.78 (c)	18.48 ± 18.38 (b)
P value	< 0.001				< 0.001	< 0.001

Data are shown as the mean ± SD. One-way ANOVA was used. abc: Indicates that the means with the same letters in the same column are not significantly different. TIC: Time intensity curve; T_{peak}: Time to peak; WR: Washout ratio; *n*: Number of salivary gland tumors.

DISCUSSION

In recent years, diffusion MRI has been an essential complement to conventional sequences in the radiological evaluation of SGTs[1,3,6-10,13-15,17,18]. Diffusion MRI allows us to evaluate the cellularity in tissues and the changes that physiological processes create on microstructural features. As malignant or benign SGTs include a highly heterogeneous group, their ADC values could also be highly variable. In cell-rich tumors such as WT and lymphoma, ADC values are low, but tumors containing hetero-

Table 5 Comparison of pleomorphic adenomas, Warthin's tumors, and malignant salivary gland tumors by ROC analysis using ADC, T_{peak}, K_{trans}, K_{ep}, and V_e values

Variable	Cut-off	AUC (95% CI)	Sensitivity	Specificity	PPV	NPV	*P* value
Pleomorphic adenomas							
ADC value	> 1.1	0.977 (0.911-0.998)	1.000	0.898	0.700	1.000	< 0.001
T_{peak}	> 120	0.947 (0.868-0.986)	1.000	0.898	0.700	1.000	< 0.001
K_{trans}	≤ 0.46	0.702 (0.584-0.804)	0.857	0.627	0.353	0.949	0.005
K_{ep}	≤ 1.14	0.926 (0.840-0.974)	0.929	0.831	0.565	0.980	< 0.001
V_e	≥ 0.4	0.849 (0.746-0.922)	0.929	0.729	0.448	0.977	< 0.001
Warthin's tumors							
ADC value	≤ 0.8	0.742 (0.626-0.837)	0.944	0.582	0.425	0.970	< 0.001
T_{peak}	≤ 19.1	0.869 (0.769-0.936)	0.667	0.909	0.706	0.893	< 0.001
WR	> 43	0.981 (0.917-0.999)	0.944	0.909	0.773	0.980	< 0.001
K_{trans}	> 0.3	0.577 (0.455-0.692)	0.889	0.346	0.308	0.905	0.291
K_{ep}	> 2.44	0.973 (0.905-0.997)	1.000	0.855	0.692	1.000	< 0.001
V_e	≤ 0.17	0.958 (0.883-0.991)	1.000	0.909	0.783	1.000	< 0.001
Malignant tumors							
ADC value	> 0.7	0.541 (0.420-0.658)	0.783	0.440	0.391	0.815	0.569
T_{peak}	≤ 120	0.531 (0.410-0.649)	0.913	0.360	0.396	0.900	0.648
WR	≤ 49	0.562 (0.441-0.678)	1.000	0.300	0.397	1.000	0.351
K_{trans}	> 0.53	0.599 (0.477-0.712)	0.652	0.600	0.429	0.789	0.194
K_{ep}	≤ 3.7	0.592 (0.471-0.706)	1.000	0.300	0.397	1.000	0.160
V_e	> 0.35	0.702 (0.584-0.804)	0.696	0.660	0.485	0.825	0.001

ADC ($\times 10^{-3}$ mm^2/s): Apparent diffusion coefficient; T_{peak} (s): Time to peak; K_{trans} (min^{-1}): Volume transfer constant between blood plasma and the extracellular extravascular space; K_{ep} (min^{-1}): Flux rate constant between the EES and plasma; V_e: EES fractional volume; AUC: Area under the ROC curve; CI: Confidence interval; PPV: Positive predictive value; NPV: Negative predictive value; WR (%): Washout ratio; EES: Extracellular extravascular space.

geneous components such as PMA have higher ADC values[1,13]. In many DWI studies involving SGTs, ADC values were reported to be useful in distinguishing BTs and MTs[6-8,17,19-21]. However, there are also studies reporting that DWI was not sufficient to make this distinction but ADC values could be useful in distinguishing some subtypes of MTs or BTs[10,22-24]. An evaluation of mean ADC values of all BTs and MTs in the present study showed that ADC values of BTs ($0.98 \times 10^{-3} \pm 0.43$ mm^2/s) and MTs ($0.95 \times 10^{-3} \pm 0.31$ mm^2/s) were similar and did not differ significantly. However, when specific tumoral subgroups were evaluated, significant differences were found in the mean ADC values among PMAs, WTs, and MTs ($P < 0.001$). In a ROC analysis using an ADC cut-off value of $> 1.1 \times 10^{-3}$ mm^2/s for PMAs, the AUC, sensitivity, and specificity were 97.7%, 100%, and 89.8%, respectively. A ROC analysis of WTs using an ADC cut-off value of $\leq 0.8 \times 10^{-3}$ mm^2/s, on the other hand, resulted in AUC, sensitivity, and specificity values of 74.2%, 94.4%, and 58.2%, respectively. These values were 54.1%, 78.3%, and 44.0%, respectively, for MTs with an ADC cut-off value of $> 0.7 \times 10^{-3}$ mm^2/s. In the present study, the mean ADC value of malignant lymphomas was $0.56 \times 10^{-3} \pm 0.05$ mm^2/s, which was well below the average ADC value of all MTs. This finding indicated that diffusion MRI could be more useful in distinguishing the subgroups within both BTs and MTs than contributing to a more general distinction between MTs and BTs.

In addition to diffusion MRI, the parameters of semiquantitative DCE MRI (TIC patterns) have also been frequently used in recent years for the differential diagnosis of SGTs[9,12,20,25,26]. On DCE MRI, TIC is obtained from signal intensity changes before the contrast agent administration, during the transition of contrast agent from the capillary bed to extravascular-intercellular distance, and during the washing of contrast agent from the tissue[1,18]. TIC patterns are correlated with tumor cellularity and vascularity[1,5,18,27]. PMAs have progressive contrast-enhancement due to low microvessel count and cellularity-stromal grade, and their washout patterns are mostly negative and, to a lesser degree, in the form of a plateau[1,27]. In the present study, type A TIC pattern (curve pattern with progression towards the late phases) was observed in all PMAs. T_{peak} values ranged from 161.80 s to 251.70 s. The

average T_{peak} value of PMAs (202.74 ± 21.48 s) was significantly longer compared to the T_{peak} values of all other SGTs. In ROC analysis of PMAs using a cut-off value of T_{peak} > 120 s, AUC, sensitivity, specificity, PPV, and NPV were 94.7%, 100%, 89.8%, 70.0%, and 100%, respectively. WTs feature rapid contrast enhancement and washout due to their high microvessel count and cellularity-stromal grade. In the present study, type B TIC pattern (T_{peak} ≤ 120 s, WR ≥ 30%) was observed in all WTs. T_{peak} values ranged from 10.80 s to 46.40 s, while WR varied from 31% to 75%. The mean T_{peak} of WTs (20.26 ± 11.72 s) was significantly shorter than that of other parotid lesions. The average WR value of WTs (59.33% ± 10.99%) was significantly higher than that of any other tumors. In ROC analysis of WTs using a cut-off value of WR > 43%, AUC, specificity, and PPV were quite high (98.1%, 94.4%, and 90.9%, respectively). Due to their high microvessel count and lower cellularity-stromal grade, MTs have rapid enhancement but their washouts tend to be slower than those of WTs[1,27]. In the present study, the mean T_{peak} value of MTs (60.60 ± 55.78 s) was significantly shorter than the T_{peak} value of PMAs. The mean WR value of MTs (18.48 ± 18.38%) was significantly lower than that of WTs, but was not different from the mean WR value of OBTs. In ROC analysis of MTs with cut-off values of T_{peak} ≤ 120 s and WR ≤ 49%, sensitivities were quite high (91.3% and 100%, respectively) but specificities were quite low (36.0% and 30.0%, respectively). A survey of semiquantitative DCE MRI studies in the literature showed that PMAs generally had type A pattern, while WTs had type B and MTs had type C TIC patterns[4,5,26]. TIC patterns are considered to have a higher diagnostic accuracy in distinguishing subgroups in SGTs compared to their power to distinguish all BTs from MTs. However, it was mentioned that TIC patterns had higher specificity especially in PMAs and WTs while their specificity in MTs was lower[4,18,25,26]. In their study with all SGTs, Lam *et al*[26] showed that all MTs except lymphomas showed type C TIC pattern (T_{peak} < 150 s and WR < 30%), while 70% of lymphomas had type B TIC pattern (T_{peak} < 150 s and WR ≥ 30%). Similar to the findings of Lam *et al*[26], 66.7% of lymphomas in the present study showed type B TIC pattern. However, unlike their findings, some other MTs showed types A, B, and D TIC patterns. There are also studies in the literature reporting that all WTs had type B TIC pattern[4,10,12]. In accordance with their findings, 100% of WTs in the present study featured type B TIC pattern. Subtypes of SGTs in the present study generally had similar TIC patterns to those reported in the literature.

The literature contains several studies on quantitative DCE perfusion MRI parameters (K_{trans}, K_{ep}, and V_e) in SGTs[3,14,15,28]. In these studies, mean K_{trans} values for PMAs ranged from 0.101 ± 0.069 min^{-1} to 0.217 ± 0.036 min^{-1}, mean K_{ep} values from 0.245 ± 0.160 min^{-1} to 0.567 ± 0.048 min^{-1}, and mean V_e values from 0.360 to 0.590 ± 0.478, while mean K_{trans} values for WTs varied between 0.105 min^{-1} ± 0.064 min^{-1} and 0.464 ± 0.036 min^{-1}, mean K_{ep} values between 0.729 ± 0.112 min^{-1} and 2.299 ± 1.312 min^{-1}, and mean V_e values between 0.1439 ± 0.093 and 0.272 ± 0.013. For MTs, mean K_{trans} values varied from 0.130± 0.035 min^{-1} to 0.327 ± 0.030 min^{-1}; mean K_{ep} values from 0.463 ± 0.103 min^{-1} to 0.784 ± 0.064 min^{-1}; and mean V_e values from 0.264 ± 0.119 to 0.445 ± 0.025. In all of these studies in the literature, the K_{trans} values of PMAs were lower than those of other SGTs[3,14,15,28]. Xu *et al*[3] found that the mean K_{trans} value of PMAs was slightly different from that of WTs (P = 0.05). Yabuuchi *et al*[14] found no significant differences among K_{trans} values of other SGTs. Huang *et al*[15] found that the K_{trans} values of PMAs were significantly lower than those of other SGTs. Similar to the results of Yabuuchi *et al*[14], in our study, mean K_{trans} value of PMAs was the lowest among all SGTs, but it was not significantly different from those of other tumors. In the studies by Xu *et al*[3], Yabuuchi *et al*[14], and Huang *et al*[15], the mean K_{ep} value was the lowest in PMAs and highest in WTs. K_{ep} values of PMAs, WTs, and MTs in the studies of both Xu *et al*[3] and Yabuuchi *et al*[14] were significantly different. However, in the study by Huang *et al* [15], the K_{ep} value of only WTs was significantly different from those of other tumors. In another study by Huang *et al*[28], significant differences were found in K_{ep} values between WTs and PMAs, and between WTs and OBTs. Similar to the results of those studies in the literature, the mean K_{ep} value in the present study was the lowest in PMAs and highest in WTs, and K_{ep} values of PMAs and WTs were significantly different from those of other tumors[3,13,14,28]. Xu *et al*[3], Yabuuchi *et al*[14], and Huang *et al*[15] found that mean V_e values of WTs were significantly lower than those of other tumors. Similar to the results of their studies, the mean V_e value of WTs in the present study was significantly lower than those of other tumors[3,14]. In another study by Huang *et al*[28], unlike other studies, the V_e value of WTs and the V_e values of PMAs and OBTs were found to be significantly lower. In ROC analysis using a cut-off value of K_{ep} ≥ 2.44 min^{-1} for WTs, the AUC, sensitivity, and specificity were 97.3%, 100%, and 85.5%, respectively. On the other hand, in ROC analysis using a cut-off value of V_e ≤ 0.17, quite high AUC, sensitivity, and specificity values (95.8%, 100%, and 90.9%, respectively) were obtained. High K_{ep} and low V_e values in WTs are explained by the limited extravascular and extracellular space in these tumors. As many studies in the literature and the present study revealed, ADC and TIC patterns of WTs could overlap with those of MTs[11]. However, similar to the findings of the studies in the literature, the present study showed that quantitative perfusion MRI parameters K_{ep} and V_e could contribute greatly to distinguishing WTs from MTs[3,14,15]. Nevertheless, our findings need to be verified by future quantitative perfusion MRI studies performed with larger series.

There are some limitations in this study. First, the parameters (number of dynamic series, acquisition time, *etc.*) varied on perfusion MRI series due to the retrospective nature of the study. Second, most of the tumors in our study were benign SGTs, and the number of MTs in the primary salivary gland was relatively low, which may have resulted in an overestimation of the diagnostic accuracy. Third, the

manual definition of ROI might have increased the variability in quantitative measurements. Although the cystic-necrotic components of the lesions were excluded from the ROI in our study, contamination of these areas can lead to significant changes in quantitative values, even if it is small in manual measurements. Fourth, for the measurements of ADC values and semiquantitative and quantitative DCE perfusion MRI parameters, interobserver agreement could not be evaluated in the study as the measurements were made by two observers with consensus.

CONCLUSION

Combined use of quantitative DCE MRI along with diffusion MRI and semiquantitative DCE MRI could help radiologists in the differential diagnosis of different subtypes of SGTs by providing higher diagnostic accuracy.

ARTICLE HIGHLIGHTS

Research background

Conventional magnetic resonance imaging (MRI) provides more data than other radiological modalities in determining the extent of tumor spread in salivary gland tumors (SGTs) and assessing its relationship to vascular and neural structures, but falls short of distinguishing subtypes of SGTs. As the malignant or benign nature of SGTs affects the treatment protocol, it is important to differentiate between malignant (MTs) and benign tumors (BTs) noninvasively with high diagnostic accuracy.

Research motivation

In recent years, advanced MRI techniques such as diffusion-weighted imaging (DWI) and semi-quantitative MRI have been increasingly used in the radiological evaluation of SGTs. However, various studies on quantitative dynamic contrast-enhanced (DCE) perfusion MRI parameters (K_{trans}, K_{ep}, and V_e) in SGTs are limited. Therefore, in this study, the effectiveness of advanced MRI applications, including all three methods, in the diagnosis of SGTs was evaluated in light of the literature.

Research objectives

To determine the diagnostic efficiency of DWI and DCE (semiquantitative perfusion) MRI and quantitative perfusion MRI parameters in SGTs.

Research methods

Apparent diffusion coefficient (ADC) values of SGTs on DWI were measured with manually inserted regions of interest, excluding the cystic components of the tumors. Time intensity curve (TIC) patterns were created for semiquantitative perfusion MRI based on T_{peak} and washout ratios (WRs) of tumors. On quantitative DCE MRI, perfusion parameters such as K_{trans} [volume transfer constant between blood plasma and extracellular extravascular space (EES)], K_{ep} (flux rate constant between the EES and plasma), and V_e (EES fractional volume) were used.

Research results

The ADC values of pleomorphic adenomas (PMAs) were significantly higher than those of Warthin's tumors (WTs), other benign tumors (OBTs), and MTs ($P < 0.001$). However, there was no significant difference in ADC values for OBTs, WTs, and MTs. PMAs had type A and WTs had type B TIC pattern while the vast majority of MTs and OBTs (54.5% and 45.5%, respectively) displayed type C TIC pattern. PMAs showed no washout, while the highest mean WR was observed in WTs. For quantitative perfusion MRI parameters, the K_{ep} value of WTs was significantly higher than those of other tumors ($P < 0.001$). For the V_e value, WTs and OBTs differed significantly from PMAs and MTs ($P < 0.001$). K_{trans} values of PMAs, WTs, OBTs, and MTs were not significantly different.

Research conclusions

DWI and semiquantitative and quantitative perfusion MRI, which provide more information on the microstructure, cellularity, interstitial distance, and vascularity of tumors, have increased the discrimination power for subtypes of SGTs.

Research perspectives

Although there is some overlap in the findings of the subtypes of SGTs obtained by advanced MRI methods, the combined use of DWI and semiquantitative and quantitative perfusion MRI will increase the power for distinguishing subtypes of SGTs.

ACKNOWLEDGEMENTS

We thank Demir O and Gürpınar AB for their help with the statistical analyses.

FOOTNOTES

Author contributions: Gökçe E designed the study; Beyhan M supervised the study; Gökçe E and Beyhan M participated in literature research and manuscript preparation, and read and approved the final version.

Institutional review board statement: This study was reviewed and approved by the Ethics Committee of the Tokat Gaziosmanpasa University Faculty of Medicine (20-KAEK-105).

Informed consent statement: Patients were not required to give informed consent for the study as figures from picture archiving and communication systems were studied retrospectively.

Conflict-of-interest statement: All the authors report no relevant conflicts of interest for this article.

Data sharing statement: No additional data are available.

Open-Access: This article is an open-access article that was selected by an in-house editor and fully peer-reviewed by external reviewers. It is distributed in accordance with the Creative Commons Attribution NonCommercial (CC BY-NC 4.0) license, which permits others to distribute, remix, adapt, build upon this work non-commercially, and license their derivative works on different terms, provided the original work is properly cited and the use is non-commercial. See: https://creativecommons.org/Licenses/by-nc/4.0/

Country/Territory of origin: Turkey

ORCID number: Erkan Gökçe 0000-0003-3947-2972; Murat Beyhan 0000-0002-8630-4632.

S-Editor: Liu XF
L-Editor: Wang TQ
P-Editor: Liu XF

REFERENCES

1 **Gökçe E**. Multiparametric Magnetic Resonance Imaging for the Diagnosis and Differential Diagnosis of Parotid Gland Tumors. *J Magn Reson Imaging* 2020; **52**: 11-32 [PMID: 32065489 DOI: 10.1002/jmri.27061]
2 **Lobo R**, Hawk J, Srinivasan A. A Review of Salivary Gland Malignancies: Common Histologic Types, Anatomic Considerations, and Imaging Strategies. *Neuroimaging Clin N Am* 2018; **28**: 171-182 [PMID: 29622112 DOI: 10.1016/j.nic.2018.01.011]
3 **Xu Z**, Zheng S, Pan A, Cheng X, Gao M. A multiparametric analysis based on DCE-MRI to improve the accuracy of parotid tumor discrimination. *Eur J Nucl Med Mol Imaging* 2019; **46**: 2228-2234 [PMID: 31372671 DOI: 10.1007/s00259-019-04447-9]
4 **Zheng N**, Li R, Liu W, Shao S, Jiang S. The diagnostic value of combining conventional, diffusion-weighted imaging and dynamic contrast-enhanced MRI for salivary gland tumors. *Br J Radiol* 2018; **91**: 20170707 [PMID: 29902075 DOI: 10.1259/bjr.20170707]
5 **Yabuuchi H**, Fukuya T, Tajima T, Hachitanda Y, Tomita K, Koga M. Salivary gland tumors: Diagnostic value of gadolinium-enhanced dynamic MR imaging with histopathologic correlation. *Radiology* 2003; **226**: 345-354 [PMID: 12563124 DOI: 10.1148/radiol.2262011486]
6 **Lechner Goyault J**, Riehm S, Neuville A, Gentine A, Veillon F. Interest of diffusion-weighted and gadolinium-enhanced dynamic MR sequences for the diagnosis of parotid gland tumors. *J Neuroradiol* 2011; **38**: 77-89 [PMID: 20542568 DOI: 10.1016/j.neurad.2009.10.005]
7 **Abdel Razek AA**, Samir S, Ashmalla GA. Characterization of Parotid Tumors With Dynamic Susceptibility Contrast Perfusion-Weighted Magnetic Resonance Imaging and Diffusion-Weighted MR Imaging. *J Comput Assist Tomogr* 2017; **41**: 131-136 [PMID: 27636248 DOI: 10.1097/RCT.0000000000000486]
8 **Yuan Y**, Tang W, Tao X. Parotid gland lesions: Separate and combined diagnostic value of conventional MRI, diffusion-weighted imaging and dynamic contrast-enhanced MRI. *Br J Radiol* 2016; **89**: 20150912 [PMID: 26892378 DOI: 10.1259/bjr.20150912]
9 **Mikaszewski B**, Markiet K, Smugała A, Stodulski D, Szurowska E, Stankiewicz C. Diffusion- and Perfusion-Weighted Magnetic Resonance Imaging-An Alternative to Fine Needle Biopsy or Only an Adjunct Test in Preoperative Differential Diagnostics of Malignant and Benign Parotid Tumors? *J Oral Maxillofac Surg* 2017; **75**: 2248-2253 [PMID: 28412261 DOI: 10.1016/j.joms.2017.03.018]
10 **Yabuuchi H**, Matsuo Y, Kamitani T, Setoguchi T, Okafuji T, Soeda H, Sakai S, Hatakenaka M, Nakashima T, Oda Y, Honda H. Parotid gland tumors: Can addition of diffusion-weighted MR imaging to dynamic contrast-enhanced MR imaging improve diagnostic accuracy in characterization? *Radiology* 2008; **249**: 909-916 [PMID: 18941162 DOI:

10.1148/radiol.2493072045]
11 **Gökçe E**, Beyhan M. Advanced magnetic resonance imaging findings in salivary gland tumors. *World J Radiol* 2022; **14**: 256-271 [PMID: 36160835 DOI: 10.4329/wjr.v14.i8.256]
12 **Eida S**, Sumi M, Nakamura T. Multiparametric magnetic resonance imaging for the differentiation between benign and malignant salivary gland tumors. *J Magn Reson Imaging* 2010; **31**: 673-679 [PMID: 20187211 DOI: 10.1002/jmri.22091]
13 **Munhoz L**, Ramos EADA, Im DC, Hisatomi M, Yanagi Y, Asaumi J, Arita ES. Application of diffusion-weighted magnetic resonance imaging in the diagnosis of salivary gland diseases: A systematic review. *Oral Surg Oral Med Oral Pathol Oral Radiol* 2019; **128**: 280-310 [PMID: 31029591 DOI: 10.1016/j.oooo.2019.02.020]
14 **Yabuuchi H**, Kamitani T, Sagiyama K, Yamasaki Y, Hida T, Matsuura Y, Hino T, Murayama Y, Yasumatsu R, Yamamoto H. Characterization of parotid gland tumors: Added value of permeability MR imaging to DWI and DCE-MRI. *Eur Radiol* 2020; **30**: 6402-6412 [PMID: 32613285 DOI: 10.1007/s00330-020-07004-3]
15 **Huang N**, Xiao Z, Chen Y, She D, Guo W, Yang X, Chen Q, Cao D, Chen T. Quantitative dynamic contrast-enhanced MRI and readout segmentation of long variable echo-trains diffusion-weighted imaging in differentiating parotid gland tumors. *Neuroradiology* 2021; **63**: 1709-1719 [PMID: 34241661 DOI: 10.1007/s00234-021-02758-z]
16 **Tofts PS**, Brix G, Buckley DL, Evelhoch JL, Henderson E, Knopp MV, Larsson HB, Lee TY, Mayr NA, Parker GJ, Port RE, Taylor J, Weisskoff RM. Estimating kinetic parameters from dynamic contrast-enhanced T(1)-weighted MRI of a diffusable tracer: Standardized quantities and symbols. *J Magn Reson Imaging* 1999; **10**: 223-232 [PMID: 10508281 DOI: 10.1002/(sici)1522-2586(199909)10:3<223::aid-jmri2>3.0.co;2-s]
17 **Celebi I**, Mahmutoglu AS, Ucgul A, Ulusay SM, Basak T, Basak M. Quantitative diffusion-weighted magnetic resonance imaging in the evaluation of parotid gland masses: A study with histopathological correlation. *Clin Imaging* 2013; **37**: 232-238 [PMID: 23465973 DOI: 10.1016/j.clinimag.2012.04.025]
18 **Assili S**, Fathi Kazerooni A, Aghaghazvini L, Saligheh Rad HR, Pirayesh Islamian J. Dynamic Contrast Magnetic Resonance Imaging (DCE-MRI) and Diffusion Weighted MR Imaging (DWI) for Differentiation between Benign and Malignant Salivary Gland Tumors. *J Biomed Phys Eng* 2015; **5**: 157-168 [PMID: 26688794]
19 **Milad P**, Elbegiermy M, Shokry T, Mahmoud H, Kamal I, Taha MS, Keriakos N. The added value of pretreatment DW MRI in characterization of salivary glands pathologies. *Am J Otolaryngol* 2017; **38**: 13-20 [PMID: 27806890 DOI: 10.1016/j.amjoto.2016.09.002]
20 **Tao X**, Yang G, Wang P, Wu Y, Zhu W, Shi H, Gong X, Gao W, Yu Q. The value of combining conventional, diffusion-weighted and dynamic contrast-enhanced MR imaging for the diagnosis of parotid gland tumours. *Dentomaxillofac Radiol* 2017; **46**: 20160434 [PMID: 28299943 DOI: 10.1259/dmfr.20160434]
21 **Eida S**, Sumi M, Sakihama N, Takahashi H, Nakamura T. Apparent diffusion coefficient mapping of salivary gland tumors: Prediction of the benignancy and malignancy. *AJNR Am J Neuroradiol* 2007; **28**: 116-121 [PMID: 17213436]
22 **Elmokadem AH**, Abdel Khalek AM, Abdel Wahab RM, Tharwat N, Gaballa GM, Elata MA, Amer T. Diagnostic Accuracy of Multiparametric Magnetic Resonance Imaging for Differentiation Between Parotid Neoplasms. *Can Assoc Radiol J* 2019; **70**: 264-272 [PMID: 30922790 DOI: 10.1016/j.carj.2018.10.010]
23 **Habermann CR**, Arndt C, Graessner J, Diestel L, Petersen KU, Reitmeier F, Ussmueller JO, Adam G, Jaehne M. Diffusion-weighted echo-planar MR imaging of primary parotid gland tumors: Is a prediction of different histologic subtypes possible? *AJNR Am J Neuroradiol* 2009; **30**: 591-596 [PMID: 19131405 DOI: 10.3174/ajnr.A1412]
24 **Faheem MH**, Shady S, Refaat MM. Role of magnetic resonance imaging (MRI) including diffusion weighted images (DWIs) in assessment of parotid gland masses with histopathological correlation. *Egypt J Radiol Nucl Med* 2018; **49**: 368-373 [DOI: 10.1016/j.ejrnm.2018.03.001]
25 **Ogawa T**, Kojima I, Ishii R, Sakamoto M, Murata T, Suzuki T, Kato K, Nakanome A, Ohkoshi A, Ishida E, Kakehata S, Shiga K, Katori Y. Clinical utility of dynamic-enhanced MRI in salivary gland tumors: Retrospective study and literature review. *Eur Arch Otorhinolaryngol* 2018; **275**: 1613-1621 [PMID: 29623392 DOI: 10.1007/s00405-018-4965-9]
26 **Lam PD**, Kuribayashi A, Imaizumi A, Sakamoto J, Sumi Y, Yoshino N, Kurabayashi T. Differentiating benign and malignant salivary gland tumours: Diagnostic criteria and the accuracy of dynamic contrast-enhanced MRI with high temporal resolution. *Br J Radiol* 2015; **88**: 20140685 [PMID: 25791568 DOI: 10.1259/bjr.20140685]
27 **Abdel Razek AAK**, Mukherji SK. State-of-the-Art Imaging of Salivary Gland Tumors. *Neuroimaging Clin N Am* 2018; **28**: 303-317 [PMID: 29622121 DOI: 10.1016/j.nic.2018.01.009]
28 **Huang N**, Chen Y, She D, Xing Z, Chen T, Cao D. Diffusion kurtosis imaging and dynamic contrast-enhanced MRI for the differentiation of parotid gland tumors. *Eur Radiol* 2022; **32**: 2748-2759 [PMID: 34642805 DOI: 10.1007/s00330-021-08312-y]



Published by **Baishideng Publishing Group Inc**
7041 Koll Center Parkway, Suite 160, Pleasanton, CA 94566, USA
Telephone: +1-925-3991568
E-mail: bpgoffice@wjgnet.com
Help Desk: https://www.f6publishing.com/helpdesk
https://www.wjgnet.com



© 2023 Baishideng Publishing Group Inc. All rights reserved.

ISSN 1949-8470 (online)

World Journal of *Radiology*

*World J Radiol*2023 February 28; 15(2): 32-55



Published byBaishideng Publishing Group Inc

World Journal of Radiology

Contents

Monthly Volume 15 Number 2 February 28, 2023

ORIGINAL ARTICLE

Prospective Study

32 Effects of combining multiple dose reduction techniques on coronary computed tomography angiography

Hu XL, Huang PK, Zhang M, Chen J, Xiao MQ

SYSTEMATIC REVIEWS

42 Imaging of paraduodenal pancreatitis: A systematic review

Bonatti M, De Pretis N, Zamboni GA, Brillo A, Crinò SF, Valletta R, Lombardo F, Mansueto G, Frulloni L

World Journal of Radiology

Monthly Volume 15 Number 2 February 28, 2023

Contents

ABOUT COVER

Editorial Board Member of *World Journal of Radiology*, Mustafa Z Mahmoud, PhD, Adjunct Professor, Full Professor, Radiology and Medical Imaging Department, Prince Sattam bin Abdulaziz University, Al-Kharj 11942, Saudi Arabia. zuhairmustafa4@hotmail.com

AIMS AND SCOPE

The primary aim of *World Journal of Radiology* (*WJR*, *World J Radiol*) is to provide scholars and readers from various fields of radiology with a platform to publish high-quality basic and clinical research articles and communicate their research findings online.

WJR mainly publishes articles reporting research results and findings obtained in the field of radiology and covering a wide range of topics including state of the art information on cardiopulmonary imaging, gastrointestinal imaging, genitourinary imaging, musculoskeletal imaging, neuroradiology/head and neck imaging, nuclear medicine and molecular imaging, pediatric imaging, vascular and interventional radiology, and women's imaging.

INDEXING/ABSTRACTING

The *WJR* is now abstracted and indexed in PubMed, PubMed Central, Emerging Sources Citation Index (Web of Science), Reference Citation Analysis, China National Knowledge Infrastructure, China Science and Technology Journal Database, and Superstar Journals Database. The 2022 edition of Journal Citation Reports ® cites the 2021 Journal Citation Indicator (JCI) for *WJR* as 0.48.

RESPONSIBLE EDITORS FOR THIS ISSUE

Production Editor:*Si Zhao*; **Production Department Director:***Xu Guo*; **Editorial Office Director:***Jia-Ru Fan*.

NAME OF JOURNAL
World Journal of Radiology

ISSN
ISSN 1949-8470 (online)

LAUNCH DATE
January 31, 2009

FREQUENCY
Monthly

EDITORS-IN-CHIEF
Thomas J Vogl

EDITORIAL BOARD MEMBERS
https://www.wjgnet.com/1949-8470/editorialboard.htm

PUBLICATION DATE
February 28, 2023

COPYRIGHT
© 2023 Baishideng Publishing Group Inc

INSTRUCTIONS TO AUTHORS
https://www.wjgnet.com/bpg/gerinfo/204

GUIDELINES FOR ETHICS DOCUMENTS
https://www.wjgnet.com/bpg/GerInfo/287

GUIDELINES FOR NON-NATIVE SPEAKERS OF ENGLISH
https://www.wjgnet.com/bpg/gerinfo/240

PUBLICATION ETHICS
https://www.wjgnet.com/bpg/GerInfo/288

PUBLICATION MISCONDUCT
https://www.wjgnet.com/bpg/gerinfo/208

ARTICLE PROCESSING CHARGE
https://www.wjgnet.com/bpg/gerinfo/242

STEPS FOR SUBMITTING MANUSCRIPTS
https://www.wjgnet.com/bpg/GerInfo/239

ONLINE SUBMISSION
https://www.f6publishing.com

© 2023 Baishideng Publishing Group Inc. All rights reserved. 7041 Koll Center Parkway, Suite 160, Pleasanton, CA 94566, USA
E-mail: bpgoffice@wjgnet.com https://www.wjgnet.com

World Journal of Radiology

Submit a Manuscript: https://www.f6publishing.com

World J Radiol 2023 February 28; 15(2): 32-41

DOI: 10.4329/wjr.v15.i2.32

ISSN 1949-8470 (online)

ORIGINAL ARTICLE

Prospective Study

Effects of combining multiple dose reduction techniques on coronary computed tomography angiography

Xiao-Lu Hu, Pei-Kai Huang, Meng Zhang, Jun Chen, Meng-Qiang Xiao

Specialty type: Radiology, nuclear medicine and medical imaging

Provenance and peer review: Unsolicited article; Externally peer reviewed.

Peer-review model: Single blind

Peer-review report's scientific quality classification

Grade A (Excellent): 0
Grade B (Very good): B
Grade C (Good): C
Grade D (Fair): D
Grade E (Poor): 0

P-Reviewer: Crocé LS, Italy; El-Serafy AS, Egypt; Shariati MBH, Iran

Received: May 29, 2022
Peer-review started: May 29, 2022
First decision: August 22, 2022
Revised: September 23, 2022
Accepted: February 13, 2023
Article in press: February 13, 2023
Published online: February 28, 2023

Xiao-Lu Hu, Pei-Kai Huang, Meng Zhang, Jun Chen, Meng-Qiang Xiao, Department of Imaging, Zhuhai Hospital, Guangdong Provincial Hospital of Traditional Chinese Medicine, Zhuhai 650031, Guangdong Province, China

Corresponding author: Meng-Qiang Xiao, Doctor, Deputy Doctor, Department of Imaging, Zhuhai Hospital, Guangdong Provincial Hospital of Traditional Chinese Medicine, No. 53 Jingle Road, Zhuhai 650031, Guangdong Province, China. xmqzhuhai@163.com

Abstract

BACKGROUND

Coronary computed tomography angiography (CCTA) is the preferred non-invasive examination method for coronary heart disease. However, the radiation from computed tomography has become a concern since public awareness of radiation hazards continue to increase.

AIM

To explore the value of multiple dose reduction techniques for CCTA.

METHODS

Consecutive normal and overweight patients were prospectively divided into two groups: Group A_1, patients who received multiple dose reduction scans (n = 82); and group A_2, patients who received conventional scans (n = 39). The scan parameters for group A_1 were as follows: Isocentric scan, tube voltage = 80 kV, and tube current control using 80% smart milliampere. The scan parameters for group A_2 were as follows: Normal position, tube voltage = 100 kV, and smart milliampere.

RESULTS

The average effective doses (EDs) for groups A_1 and A_2 were 1.13 ± 0.35 and 3.36 ± 1.30 mSv, respectively. There was a statistically significant difference in ED between the two groups (P < 0.01). Furthermore, noise was significantly lower, and both signal-to-noise ratio and contrast signal-to-noise ratio were higher in group A_2 when compared to group A_1 (P < 0.01). Moreover, the subjective image quality (IQ) scores were excellent in both groups, in which there was no significant difference in subjective IQ score between the two groups (P = 0.12).

CONCLUSION

Multiple dose reduction scan techniques can significantly decrease the ED of

patients receiving CCTA examinations for clinical diagnosis.

Key Words: Isocentric scanning; Coronary heart disease; Dose reduction techniques; Coronary computed tomography angiography; Radiation

©The Author(s) 2023. Published by Baishideng Publishing Group Inc. All rights reserved.

Core Tip: Coronary computed tomography angiography (CCTA) is the preferred non-invasive examination method for coronary heart disease (CHD). The present study was the first to combine multiple dose reduction techniques, including narrow acquisition window, low tube voltage, lower tube current, and isocentric scanning, to decrease CCTA radiation exposure of patients with suspected CHD. The radiation dose for the group with multiple dose reduction was approximately 33.63% (1.13 ± 0.35/3.36 ± 1.30) of the dose associated with the conventional method.

Citation: Hu XL, Huang PK, Zhang M, Chen J, Xiao MQ. Effects of combining multiple dose reduction techniques on coronary computed tomography angiography. *World J Radiol* 2023; 15(2): 32-41
URL: https://www.wjgnet.com/1949-8470/full/v15/i2/32.htm
DOI: https://dx.doi.org/10.4329/wjr.v15.i2.32

INTRODUCTION

Coronary computed tomography angiography (CCTA) is the preferable non-invasive method to check for coronary heart disease (CHD)[1,2]. In terms of technology, CCTA has advanced significantly during the last 20 years. For those who suspect they may have CHD, CCTA has largely taken the role of conventional invasive coronary angiography since it is so effective at detecting moderate to severe coronary artery stenosis[2]. But as individuals become increasingly conscious of the risks associated with radiation, computed tomography (CT) radiation has risen to the forefront of discussion[3].

Numerous dose-reduction techniques have been developed as a result of the advancement of computer technology, including prospective electrocardiography gating, iterative reconstruction, personalized scanning, as well as "smart milliampere" (the CT can automatically calculate the tube current based on the position scan) have been developed[3,4]. Furthermore, with the emergence of high-end CT machines, adjusting the tube voltage and tube current has become a useful approach for dose reduction in CCTA scanning[1,5,6]. Some organizations have reported the application of dual-source CT (Siemens Healthcare, Malvern, PA, United States) and GE gem energy spectrum CT (Medical Systems, Milwaukee, WI, United States) to reduce the tube voltage to 80 kV and manage the tube current with smart milliamperes, thereby decreasing the effective dose (ED) to a significant degree[7,8]. Furthermore, previous researchers have employed single dose reduction techniques to minimize the CCTA radiation dose. However, there are limitations in reducing the overall ED. Therefore, more advanced methods are warranted to further decrease the radiation exposure during CCTA.

Isocentric scanning has been proven as an effective approach to reduce radiation exposure in patients receiving CCTA examinations[9,10]. The direction of the beam in the CT is fixed in the middle of the CT frame. The beam in multislice spiral CT has a cone-like form. More light would reach the system through a spherical tube and frame-hole-center-scanning detector, which would enhance the quality of the objective picture [image quality (IQ)]. When an object is being scanned isocentrically, it aligns with the gantry's empty center. This technology has been heavily utilized by all varieties of CT. Additionally, it has been shown that using this technique in CT may lower the ED of scans for organs that are not in the middle[11,12].

To our knowledge, the present study was the first to combine multiple dose reduction techniques, including narrow acquisition window, low tube voltage, lower tube current, and isocentric scanning, in order to decrease the CCTA radiation exposure of patients with suspected CHD. The present study aimed to determine whether multiple dose reduction approaches can efficiently reduce the radiation exposure while maintaining the IQ in CCTA examinations.

MATERIALS AND METHODS

Study population

The present prospective research was approved by the institutional review board of Guangdong Provincial Hospital of Traditional Chinese Medicine Medical Ethics Committee (BF2020-229-01), and all

patients provided written informed consent. Between November 2020 and August 2021, consecutive patients with clinically suspected CHD were screened for inclusion in the present study. The inclusion criteria were as follows: Age ≥ 18-years-old; heart rate < 70 bpm; and body mass index (BMI): 18.0-29.9 kg/m^2. Patients with pacemakers, severe respiratory artifacts, metal implants within the scan range, allergies to contrast media or Betaloc, or a history of cardiac tumors or cardiac surgery were excluded.

The study population comprised 118 patients with CHD. These patients were classified according to their BMI, as described above, and divided into two groups [the groups were classified as normal or overweight (BMI: 18.0-29.9 kg/m^2)[13], BMI = weight (kg)/height (m)^2]: Multi-modality normal group (group A_1, n = 82) and conventional normal group (group A_2, n = 39). Coronary artery segmentation was performed according to the 15-segment coronary artery segmentation method developed by the American Heart Association[1].

CCTA examination

The CCTA examination was performed using the Canon 320-row dynamic CT system (Aquilion ONE Genesis, Canon Medical Systems). Prospective electrocardiography gating was used to reduce the radiation dose[6]. The scanning range was extended 140 mm upwards, starting from the lower edge of the heart. For group A_1, the isocentric scan was performed with the patient supine and their body shifted to the right (Figure 1). Before the CCTA scan, an ultrasound examination was performed to mark the leftmost and rightmost edges of the heart on the body surface, and perpendicular lines were placed along the leftmost and rightmost edges of the heart. The centerline of the two vertical lines was used as the vertical positioning line, and the horizontal axillary centerline was used as the horizontal positioning line.

Patients in group A_2 were scanned using the conventional method, with the patient placed in the natural supine position. Similarly, the horizontal axillary centerline was used for the horizontal positioning, and the median line was used as the vertical positioning line. The scan parameters were as follows: Group A_1, tube voltage = 80 kV, 80% tube current, smart milliampere setting; group A_2, tube voltage = 100 kV, tube current control using milliampere (Table 1).

Preparations before scanning

All patients provided a written informed consent before participating in the study. Heart rate and blood pressure were measured at rest before the examination. Patients with a heart rate of > 70 bpm were given metoprolol (Betaloc, 25-100 mg). These patients were randomly assigned into two groups (groups A_1 and A_2) at a ratio of 2:1. Before the examination, these patients were administered with 0.5 mg nitroglycerine tablets.

Radiation dose

The CT dose index volume (mGy) and dose length product (mGy × cm) were automatically calculated by the scanner software for all CT protocols. Then, the dose length product was multiplied by a conversion coefficient (k) to determine the ED (ED = dose length product × k, k = 0.014)[13] for each patient (Table 2).

Image processing

All images were reconstructed using Adaptive Iterative Dose Reduction Using Three Dimensional Processing. The scanning parameters were as follows: Scan length, 140 mm; slice thickness, 0.5 mm; reconstruction field of view, 220 mm; kernel, EU10 (Table 2).

Subjective and objective evaluation of IQ

The objective IQ was evaluated by two experienced cardiovascular radiologists (MQ Xiao, 17 years of experience; PK Huang, 13 years of experience), who were blinded to the scan and reconstruction parameters. A circular region of interest (ROI), with a diameter of 1 cm, was placed within the cortical part of the main bronchus. The coronary artery attenuation values for the proximal ROIs of the left main coronary artery and right coronary artery were measured. The ROI was selected as large as possible, and the vascular wall, vascular calcifications, and non-calcified plaques and artifacts were excluded. The average coronary artery attenuation was equal to the average value of the left main coronary artery and proximal right coronary artery. The ROI measurement was performed on the adjacent myocardial fat. This was repeated three times at each location, and averaged to ensure data consistency. The CT value standard deviation for the main bronchus, and average attenuation values for the coronary artery and pericardial fat were calculated by averaging the values obtained by the two observers. Noise was calculated as the standard deviation of the CT value of the main bronchus[14]. The signal-to-noise ratio and contrast signal-to-noise ratio (CNR) were calculated as follows: Signal-to-noise ratio = average main bronchus CT value/image noise; CNR = (average attenuation of coronary artery - perivascular fat attenuation)/image noise[15].

Coronary artery segmentation was performed according to the 15-segment coronary artery segmentation method developed by the American Heart Association[1]. Two radiologists with 18 years (MQ Xiao) and 13 years (PK Huang) of experience in cardiovascular medicine conducted independent

Table 1 Computed tomography parameters for the conventional and multi-modality treatment groups

Dose group	Conventional group	Multi-modality group
Tube voltage, kV	100	80
Tube current, mA	Smart milliampere	80% smart milliampere
D-FOV, mm	220	220
Rotation time, s	0.275	0.275
Thickness, mm	0.5	0.5
Interval, mm	0.5	0.5
AIDR3D	Standard EU10	Standard EU10
Scanning method	ECG gating	ECG gating
Cardiac cycle	30%-80%	60%-80%
Scan position	Conventional	Isocentric
Scan length	140 mm	140 mm

AIDR3D: Adaptive Iterative Dose Reduction Using Three Dimensional Processing; ECG: Electrocardiography.

Table 2 Characteristics of the two groups

Group, *n*	Sex, F/M	Age, yr	BMI, kg/m^2	CTD_{vol}, mGy	DLP, mGy × cm	ED, mSv
A_1, *n* = 82	31/51	59.59 ± 9.66	23.06 ± 1.95	5.89 ± 1.85	80.58 ± 24.80	1.13 ± 0.36
A_2, *n* = 36	19/20	64.15 ± 13.28	22.58 ± 1.96	17.92 ± 8.02	250.90 ± 112.25	3.36 ± 1.30
P value	0.43	0.17	0.89	0.00	0.00	0.00

BMI: Body mass index; CTD_{vol}: Computed tomography dose index volume; DLP: Dose length product; ED: Effective dose; F: Female; M: Male.

evaluations for coronary arteries with a diameter of ≥ 1.5 mm. For inter-rater disagreements, a consensus was reached through consultation. Furthermore, a 5-point Likert scale was used[13] as follows: 5 = excellent (sharp, smooth contours of the vascular wall and no streaking or radiating artifacts); 4 = good (slight irregularities on the contours and few streaks or radiating artifacts); 3 = fair (blurred and irregular contour of the vascular wall and numerous streaks or radiating artifacts); 2 = poor (deformation of the vascular wall and various artifacts); 1 = very poor (obvious deformation of the vascular wall and extensive artifacts). Images with IQ scores of 3-5 satisfied the requirements for the diagnostic assessment (Figure 2).

RESULTS

The study population comprised 118 patients (71 male and 47 female patients), who were within 37-87-years-old (mean ± SD: 61.06 ± 9.10 years).

These normal and overweight patients were divided into two groups: Group A_1, patients who underwent multiple dose reduction scan techniques (*n* = 82); and group A_2, patients who underwent the conventional scan technique (*n* = 39). Sex, age, and BMI did not significantly vary across the groups (*P* is between 0.06 and 0.43; Table 2).

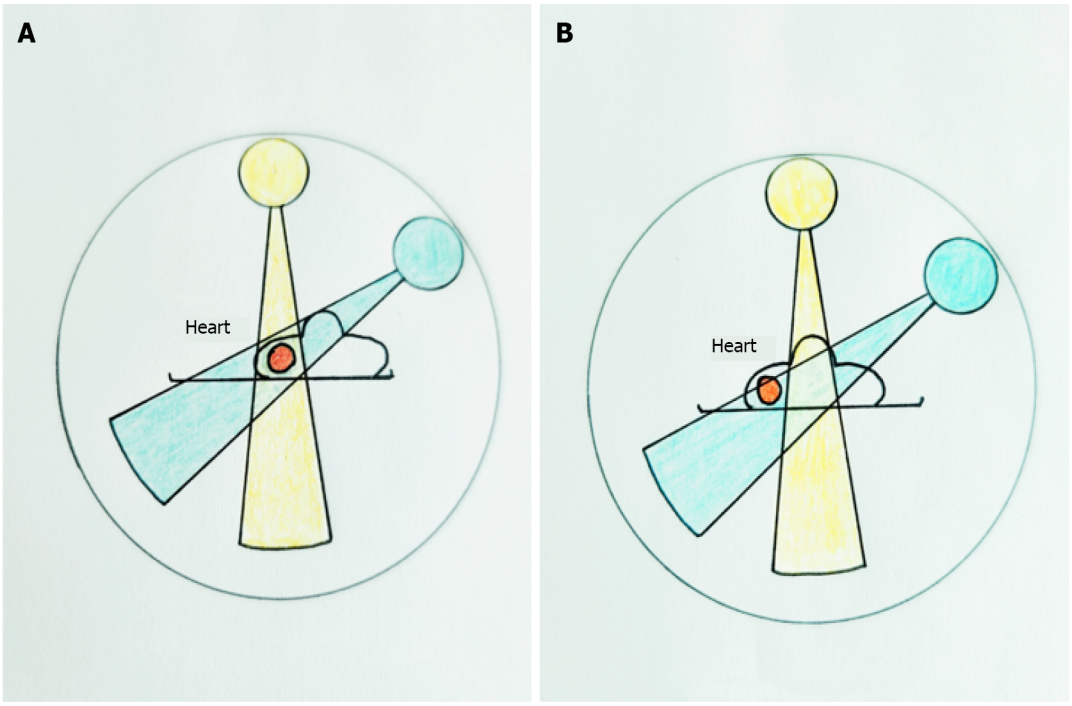
The average ED of group A_1 was 1.13 ± 0.35 mSv, whereas the average ED of group A_2 was 3.36 ± 1.30 mSv. The difference between the ED of these two groups was statistically significant (all *P* less than 0.01). Additionally, the average noise in group A_2 was much lower than group A_1 (all *P* more than 0.05; Table 3), and the signal-to-noise ratio and CNR in group A_2 were significantly higher than group A_1. Additionally, group A_1 had considerably higher CT values than group A_2 for the right coronary artery root, left main coronary artery, and ascending aortic root (*P* less than 0.05).

There was a total of 1603 potentially evaluable segments. Among these, in the 100 kV group, 40 segments were deemed unevaluable, and in the 80 kV group, 49 segments were deemed unevaluable due to having a diameter of < 1.5 mm or occlusion. The statistics for the coronary artery segments in groups A_1 and A_2 were presented in Table 2. The average IQ score for groups A_1 and A_2 was 4.46 ± 0.59 and 4.45 ± 0.62, respectively (Figures 3-5). There were no significant differences in IQ scores among the

Table 3 Computed tomography values and objective image quality scores for the aortic roots and proximal coronary vessels

Group, *n*	Aortic root, HU			Noise		
A_1, *n* = 82	512.18 ± 108.22	477.20 ± 117.93	485.88 ± 4100.40	15.52 ± 4.73	66.00 ± 25.30	41.32 ± 16.13
A_2, *n* = 39	601.92 ± 125.34	534.67 ± 117.33	546.99 ± 109.30	19.29 ± 6.26	54.28 ± 17.72	38.45 ± 12.06
P value	0.07	0.32	0.37	0.00	0.00	0.00

HU: Hounsfield unit.



DOI: 10.4329/wjr.v15.i2.32 **Copyright** ©The Author(s) 2023.

Figure 1 For group A_1, the isocentric scan was performed with the patient in supine position and their body shifted to the right. A: Conventional position; B: Isocentric scanning.

two groups (*P* equal to 0.08-0.31). According to the observers, the subjective IQ values of the two groups were very high (intraclass correlation coefficients equal to 0.71-0.90; Tables 3 and 4).

DISCUSSION

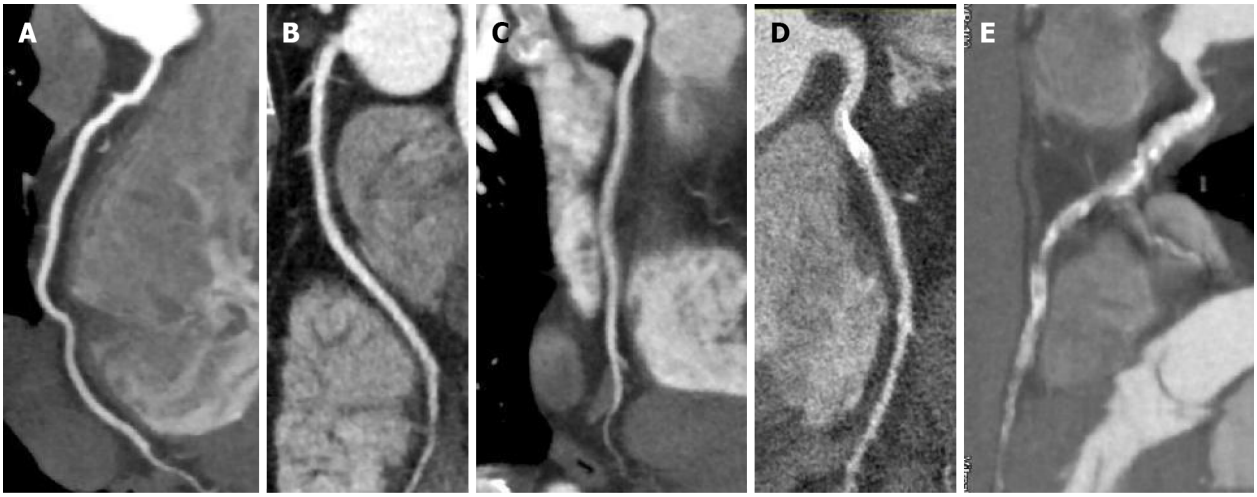
In the present study, the multiple dose reduction scan techniques significantly decreased the ED during the CCTA of patients under clinical diagnosis situations. The radiation dose for the group with multiple dose reduction was approximately 33.63% (1.13 ± 0.35/3.36 ± 1.30) of the dose associated with the conventional method, and the proportion of IQ that met the needs for the clinical diagnosis was > 99% (images with IQ scores of ≥ 3). There was no difference in subjective IQ when compared to conventional coronary CT scans.

Previous studies have only employed lower tube voltages, smart milliampere[1,7,14], or merely a narrow acquisition window for dose reduction techniques in CCTA[16,17]. To our knowledge, the present study was the first in the English literature to combine multiple technologies (narrow acquisition window, tube voltage of 80 kV, smart milliampere, and isocentric scanning) to reduce the CCTA radiation dose. The ED was significantly higher in the conventional group when compared to the multi-modality group ($P < 0.05$). A previous study performed a low-dose CCTA with the a CT scanner by Canon with 640 slices on patients whose heart rate was less than 70 beats/min and reported the mean ED as 2.67 ± 0.5 mSv[14]. Similar to this, using the same signal equipment (Aquilion ONE Genesis, Canon Medical Systems), Di Cesare *et al*[18] and Li *et al*[7] determined that ED medians were 2.80 ± 0.57 and 3.36 ± 2.35 mSv, respectively. During the present study, the value of the latter was the same as that of the conventional group. Although multi-modality technology was used to reduce the radiation dose

Table 4 Subjective image quality scores and the number of score segments in the two groups

Group	All segments	5	4	3	2	1	Average IQ score
A_1	1085	420 (38.71%)	611 (56.48%)	45 (4.15%)	6 (0.55%)	1 (0.09%)	4.46 ± 0.59
A_2	518	258 (49.81%)	232 (44.79%)	19 (3.67%)	8 (1.54%)	1 (0.19%)	4.45 ± 0.62
P value							0.12

IQ: Image quality.



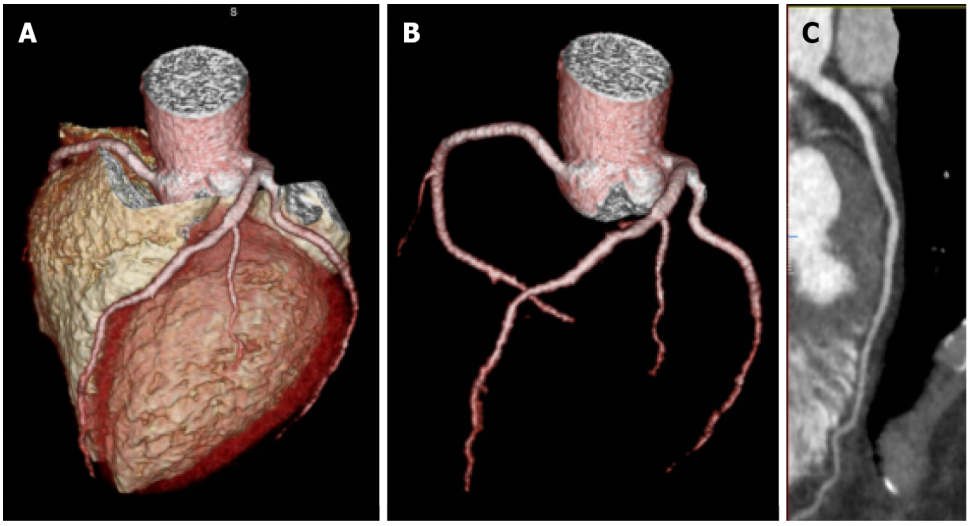
DOI: 10.4329/wjr.v15.i2.32 **Copyright** ©The Author(s) 2023.

Figure 2 Subjective imaging quality scores. A: Excellent imaging quality (IQ) (score = 5) with sharp, smooth contours of the vascular wall and no streaking or radiating artifacts; B: Good IQ (score = 4) with slight irregularities on the contour and few streaks or radiating artifacts; C: Fair IQ (score = 3) with blurred and irregular contours of the vascular wall and numerous streaks or radiating artifacts; D: Poor IQ (score = 2) with deformation of the vascular wall and various artifacts; E: Very poor IQ (score = 1) with obvious deformation of the vascular wall and extensive artifacts. Images with IQ scores within 3-5 satisfy the requirements for the diagnostic assessment.

of CCTA, there were no significant differences in subjective IQ scores (P = 0.12).

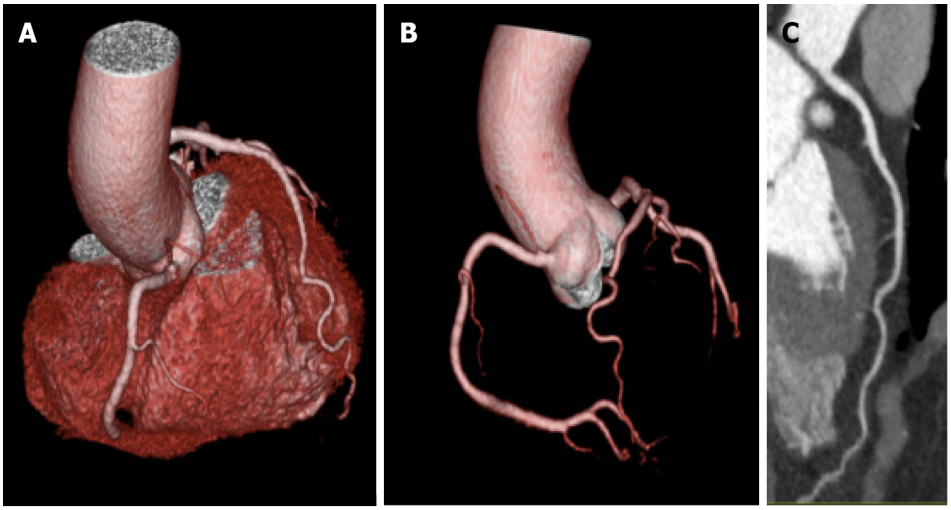
The present study revealed that the radiation dose of CCTA significantly decreased after the application of multiple dose reduction scan techniques. The radiation dose in group A_1 was approximately 33.63% (1.13 ± 0.35/3.36 ± 1.30) in comparison with the traditional method. Low-dose CCTA has been shown to significantly reduce ED in some studies using dual source CTs (Siemens Healthcare)[7,14], GE gem energy spectrum CTs (GE Medical Systems)[8], as well as Philips Brilliance 256-slice iCTs (Philips Medical Systems)[4], with a tube voltage of 80 kV. The current research was the first to report the use of a low-dose CCTA at an 80 kV tube voltage utilizing a Canon CT system. A craniocaudal coverage of 16 cm was achieved, exceeding the length of the median scan employed in clinical practice. Furthermore, the tube generally rotates 360°, allowing it to be sufficient for cardiac scanning. Li *et al*[7] and Khosa *et al*[17] performed CCTA using the Canon 320-row dynamic CT system (Aquilion ONE, Toshiba Medical Systems; the present study used the same signal equipment), with a tube voltage of 120 kV. Both studies used the following parameters: RR interval, 66%-80%; BMI, 28 kg/m^2; and heart rate, < 70 bpm. Furthermore, the present study employed 1.54 mSv, while the study conducted by Khosa *et al*[17] employed 633 mSv. According to some studies, radiation doses can reach 1.76 ± 0.43-2.72 ± 0.50 mSv when CCTA is used with an 80 kV tube voltage[7,13] when compared to the doses in the present study, and the ED was high.

A positive correlation exists between the intensity of X-rays and the square of tube voltage and current. In contrast to lowering tube current, reducing tube voltage substantially reduces radiation dose. In previous research, low tube voltage was found to reduce radiation dosage. However, this has the disadvantage of increasing picture noise and lowering CNR, which limits the reduction of the radiation dose[17-19]. Adaptive Iterative Dose Reduction Using Three Dimensional Processing was used in those studies to reconstruct the image, and the results were compared using conventional methods. This approach effectively improved the IQ and reduced the radiation dose in scans for different areas[17-19]. In another study, the use of Adaptive Iterative Dose Reduction Using Three Dimensional Processing and ultra-low-dose CT has been shown to significantly increase IQ[20].



DOI: 10.4329/wjr.v15.i2.32 **Copyright** ©The Author(s) 2023.

Figure 3 A 69-year-old female patient in group A_1. For the multislice computed tomographic angiography, the image quality score was 5 (excellent) for left anterior descending artery segments 5-8. A and B: Volume rendering; C: Curved planar reformation. Body mass index: 26.40; Effective dose: 1.18 mSv; Noise: 18.80; Signal-to-noise ratio: 52.68; Contrast signal-to-noise ratio: 42.89.

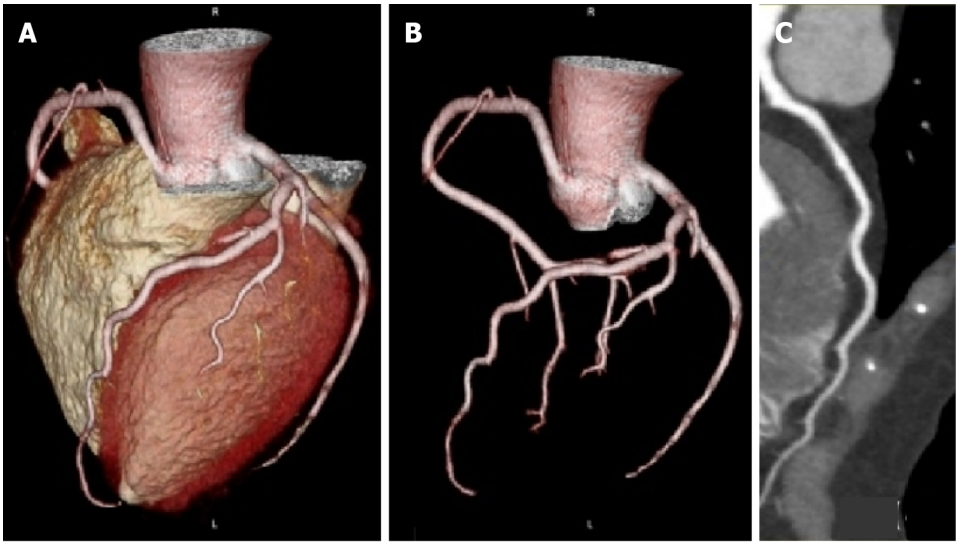


DOI: 10.4329/wjr.v15.i2.32 **Copyright** ©The Author(s) 2023.

Figure 4 A 64-year-old female patient in group A_1. For the multislice computed tomographic angiography, the image quality score was 5 (excellent) for left anterior descending artery segments 5-8. A and B: Volume rendering; C: Curved planar reformation. Body mass index: 26.40; Effective dose: 1.83 mSv; Noise: 22.50; Signal-to-noise ratio: 43.90; Contrast signal-to-noise ratio: 30.40.

Computed tomography angiography (CTA) is a non-invasive examination method and has the advantages of convenience, speed, safety, and reliability. This technique can clearly display the stenosis of the coronary lumen and plaque on the wall and determine whether the coronary artery has stenosis. Furthermore, its accuracy for CHD diagnosis is very high[17-19,21]. Digital subtraction angiography (DSA) is an invasive examination and is poorly accepted by patients. Coronary DSA can only determine vascular stenosis. Although coronary DSA is the gold standard for accurately determining vascular stenosis, it is an invasive examination with high radiation dose, high cost, and poor patient acceptance. A dose reduction on CTA examinations, such as the reduction of radiation exposure, could benefit patients with suspected CHD, who could not endure a DSA examination[22]. Our research group is performing further explorations on the effects of dose reduction techniques for patients who could not endure DSA examinations in order to increase its clinical practicability.

There are a few limitations to the current research. A minimum heart rate less than 70 beats/min was required for all patients, including those with low BMIs. A second drawback is that there was no correlation between the CCTA and DSA for the coronary artery, and the IQ was only rated subjectively for the coronary artery. A more in-depth investigation is required for individuals who are classified as obese according to their obesity grade (grade 1, BMI = 30-37.5 kg/m^2 and grade 3, BMI ≥ 37.5 kg/m^2).



DOI: 10.4329/wjr.v15.i2.32 **Copyright** ©The Author(s) 2023.

Figure 5 A 68-year-old female patient in group A_2. For the multislice computed tomographic angiography, the image quality score was 5 (excellent) for left anterior descending artery segments 5-8. A and B: Volume rendering; C: Curved planar reformation. Body mass index: 22.38; Effective dose: 3.33 mSv; Noise: 13.10; Signal-to-noise ratio: 74.69; Contrast signal-to-noise ratio: 58.85.

CONCLUSION

Multiple dose reduction scan techniques can significantly reduce the radiation dose under conditions that meet the requirements for clinical diagnosis.

ARTICLE HIGHLIGHTS

Research background

Coronary computed tomography angiography (CCTA) is considered to be an ideal non-invasive test for coronary heart disease (CHD). Nevertheless, as more people become aware of the dangers associated with radiation, the issue of computed tomography radiation has emerged as a major concern.

Research motivation

The present study aimed to explore the value of multiple dose reduction techniques on CCTA.

Research objectives

A consecutive sample of individuals with clinically suspected CHD was screened for inclusion in the current research. The inclusion criteria were: ≥ 18-years-old; heart rate less than 70 beats/min; and body mass index of 18.0 to 29.9 kg/m^2. Patients having pacemakers, significant respiratory artifacts, metallic implants located within the scanning range, an allergy to contrast agents or Betaloc, or patients who had undergone cardiac surgery or had a history of cardiac tumors were not eligible for treatment.

Research methods

Consecutive normal and overweight patients were prospectively divided into two groups: Group A_1, patients who received multiple dose reduction scans (n = 82); and group A_2, patients who received conventional scans (n = 39). The scan parameters for group A_1 consisted of the following: An isocentric scan, a tube voltage of 80 kV, and an 80% smart milliampere for tube current control. The scan parameters for group A_2 were as follows: Normal position, tube voltage = 100 kV, and smart milliampere.

Research results

The average effective doses (EDs) for groups A_1 and A_2 were 1.13 ± 0.35 and 3.36 ± 1.30 mSv, respectively. A statistically significant difference was found between the two groups in terms of ED (P < 0.01). The signal-to-noise ratio as well as contrast signal-to-noise ratio of group A2 were significantly higher than those of group A1, in addition to having less noise. Moreover, the subjective image quality (IQ) scores were excellent in both groups, and the subjective IQ scores of the two groups did not differ significantly (P = 0.12).

Research conclusions

Multiple dose reduction scan techniques can significantly decrease the ED of patients receiving CCTA examinations for clinical diagnosis.

Research perspectives

This study supports the application of the multiple dose reduction scan techniques in patients receiving CCTA.

FOOTNOTES

Author contributions: Hu XL and Huang PK were involved in drafting the manuscript; Zhang M and Huang PK were involved in acquisition of data; Chen J prepared the figures; Xiao MQ reviewed and revised the manuscript; All authors have read and approved the final manuscript.

Supported by Zhuhai Medical Research Fund, No. ZH3310200001PJL.

Institutional review board statement: This study was approved by the institutional review board of Guangdong Provincial Hospital of Traditional Chinese Medicine, No. BF2020-229-01.

Informed consent statement: All patients provided written consent, and written informed consent was obtained from each patient or the patient's family before performing the computed tomography scan. This study was conducted in accordance with the Declaration of Helsinki.

Conflict-of-interest statement: All the authors report no relevant conflicts of interest for this article.

Data sharing statement: The datasets used or analyzed during the current study are available from the corresponding author on reasonable request.

CONSORT 2010 statement: The authors have read the CONSORT 2010 Statement, and the manuscript was prepared and revised according to the CONSORT 2010 Statement.

Open-Access: This article is an open-access article that was selected by an in-house editor and fully peer-reviewed by external reviewers. It is distributed in accordance with the Creative Commons Attribution NonCommercial (CC BY-NC 4.0) license, which permits others to distribute, remix, adapt, build upon this work non-commercially, and license their derivative works on different terms, provided the original work is properly cited and the use is non-commercial. See: https://creativecommons.org/Licenses/by-nc/4.0/

Country/Territory of origin: China

ORCID number: Xiao-Lu Hu 0000-0003-4638-0646; Pei-Kai Huang 0000-0003-3463-5154; Jun Chen 0000-0002-1936-9954; Meng-Qiang Xiao 0000-0001-6970-6405.

S-Editor: Fan JR
L-Editor: Filipodia
P-Editor: Fan JR

REFERENCES

1 **Jia CF**, Zhong J, Meng XY, Sun XX, Yang ZQ, Zou YJ, Wang XY, Pan S, Yin D, Wang ZQ. Image quality and diagnostic value of ultra low-voltage, ultra low-contrast coronary CT angiography. *Eur Radiol* 2019; **29**: 3678-3685 [PMID: 30888481 DOI: 10.1007/s00330-019-06111-0]

2 **Serruys PW**, Hara H, Garg S, Kawashima H, Nørgaard BL, Dweck MR, Bax JJ, Knuuti J, Nieman K, Leipsic JA, Mushtaq S, Andreini D, Onuma Y. Coronary Computed Tomographic Angiography for Complete Assessment of Coronary Artery Disease: JACC State-of-the-Art Review. *J Am Coll Cardiol* 2021; **78**: 713-736 [PMID: 34384554 DOI: 10.1016/j.jacc.2021.06.019]

3 **Aghayev A**, Murphy DJ, Keraliya AR, Steigner ML. Recent developments in the use of computed tomography scanners in coronary artery imaging. *Expert Rev Med Devices* 2016; **13**: 545-553 [PMID: 27140944 DOI: 10.1080/17434440.2016.1184968]

4 **Tang S**, Zhang G, Chen Z, Liu X, He L. Application of prospective ECG-gated multiphase scanning for coronary CT in children with different heart rates. *Jpn J Radiol* 2021; **39**: 946-955 [PMID: 34046853 DOI: 10.1007/s11604-021-01133-5]

5 **Apfaltrer G**, Albrecht MH, Schoepf UJ, Duguay TM, De Cecco CN, Nance JW, De Santis D, Apfaltrer P, Eid MH, Eason CD, Thompson ZM, Bauer MJ, Varga-Szemes A, Jacobs BE, Sorantin E, Tesche C. High-pitch low-voltage CT coronary artery calcium scoring with tin filtration: accuracy and radiation dose reduction. *Eur Radiol* 2018; **28**: 3097-3104 [PMID: 29404770 DOI: 10.1007/s00330-017-5249-2]

6 **Zhang W**, Ba Z, Wang Z, Lv H, Zhao J, Zhang Y, Zhang F, Song L. Diagnostic performance of low-radiation-dose and low-contrast-dose (double low-dose) coronary CT angiography for coronary artery stenosis. *Medicine (Baltimore)* 2018; **97**: e11798 [PMID: 30142766 DOI: 10.1097/MD.0000000000011798]

7 **Li RF**, Hou CL, Zhou H, Dai YS, Jin LQ, Xi Q, Zhang JH. Comparison on radiation effective dose and image quality of right coronary artery on prospective ECG-gated method between 320 row CT and 2nd generation (128-slice) dual source CT. *J Appl Clin Med Phys* 2020; **21**: 256-262 [PMID: 32510768 DOI: 10.1002/acm2.12911]

8 **Liu K**, Diao K, Hu S, Xu X, Zhang J, Peng W, Xia C, Zhang K, Li Y, Guo Y, He S, He Y, Li Z. Achieving Low Radiation Dose in "One-Stop" Myocardial Computed Tomography Perfusion Imaging in Coronary Artery Disease Using 16-cm Wide Detector CT. *Acad Radiol* 2020; **27**: 1531-1539 [PMID: 31859211 DOI: 10.1016/j.acra.2019.11.018]

9 **Ali I**, Ahmad S. Evaluation of the effects of sagging shifts on isocenter accuracy and image quality of cone-beam CT from kV on-board imagers. *J Appl Clin Med Phys* 2009; **10**: 180-194 [PMID: 19692976 DOI: 10.1120/jacmp.v10i3.2930]

10 **Chow JC**. Cone-beam CT dosimetry for the positional variation in isocenter: a Monte Carlo study. *Med Phys* 2009; **36**: 3512-3520 [PMID: 19746785 DOI: 10.1118/1.3166934]

11 **Dane B**, O'Donnell T, Liu S, Vega E, Mohammed S, Singh V, Kapoor A, Megibow A. Radiation dose reduction, improved isocenter accuracy and CT scan time savings with automatic patient positioning by a 3D camera. *Eur J Radiol* 2021; **136**: 109537 [PMID: 33454459 DOI: 10.1016/j.ejrad.2021.109537]

12 **Olden KL**, Kavanagh RG, James K, Twomey M, Moloney F, Moore N, Carey K, Murphy KP, Grey TM, Nicholson P, Chopra R, Maher MM, O'Connor OJ. Assessment of isocenter alignment during CT colonography: Implications for clinical practice. *Radiography (Lond)* 2018; **24**: 334-339 [PMID: 30292502 DOI: 10.1016/j.radi.2018.04.003]

13 **Khan AR**, Awan FR, Najam SS, Islam M, Siddique T, Zain M. Elevated serum level of human alkaline phosphatase in obesity. *J Pak Med Assoc* 2015; **65**: 1182-1185 [PMID: 26564289]

14 **Cao JX**, Wang YM, Lu JG, Zhang Y, Wang P, Yang C. Radiation and contrast agent doses reductions by using 80-kV tube voltage in coronary computed tomographic angiography: a comparative study. *Eur J Radiol* 2014; **83**: 309-314 [PMID: 24315475 DOI: 10.1016/j.ejrad.2013.06.032]

15 **Nakanishi R**, Sankaran S, Grady L, Malpeso J, Yousfi R, Osawa K, Ceponiene I, Nazarat N, Rahmani S, Kissel K, Jayawardena E, Dailing C, Zarins C, Koo BK, Min JK, Taylor CA, Budoff MJ. Automated estimation of image quality for coronary computed tomographic angiography using machine learning. *Eur Radiol* 2018; **28**: 4018-4026 [PMID: 29572635 DOI: 10.1007/s00330-018-5348-8]

16 **Smit EB**, Bouwstra H, Roorda LD, van der Wouden JHC, Wattel ELM, Hertogh CMPM, Terwee CB. A Patient-Reported Outcomes Measurement Information System Short Form for Measuring Physical Function During Geriatric Rehabilitation: Test-Retest Reliability, Construct Validity, Responsiveness, and Interpretability. *J Am Med Dir Assoc* 2021; **22**: 1627-1632.e1 [PMID: 33640312 DOI: 10.1016/j.jamda.2021.01.079]

17 **Khosa F**, Khan A, Nasir K, Shuaib W, Budoff M, Blankstein R, Clouse ME. Influence of image acquisition on radiation dose and image quality: full *vs* narrow phase window acquisition using 320 MDCT. *ScientificWorldJournal* 2013; **2013**: 731590 [PMID: 24453899 DOI: 10.1155/2013/731590]

18 **Di Cesare E**, Gennarelli A, Di Sibio A, Felli V, Splendiani A, Gravina GL, Masciocchi C. Image quality and radiation dose of single heartbeat 640-slice coronary CT angiography: a comparison between patients with chronic atrial fibrillation and subjects in normal sinus rhythm by propensity analysis. *Eur J Radiol* 2015; **84**: 631-636 [PMID: 25617080 DOI: 10.1016/j.ejrad.2014.11.035]

19 **Liu S**, Fu Q, Yu H, Zhang C, Yang Q, Hu Y, Xu W. Evaluate of the effect of low tube voltage on the radiation dosage using 640-slice coronary CT angiography. *J Xray Sci Technol* 2018; **26**: 463-471 [PMID: 29562576 DOI: 10.3233/XST-17332]

20 **Xiao M**, Zhang M, Lei M, Hu X, Wang Q, Chen Y, Ye J, Xu R, Chen J. Application of ultra-low-dose CT in 3D printing of distal radial fractures. *Eur J Radiol* 2021; **135**: 109488 [PMID: 33385624 DOI: 10.1016/j.ejrad.2020.109488]

21 **Di Cesare E**, Gennarelli A, Di Sibio A, Felli V, Perri M, Splendiani A, Gravina GL, Barile A, Masciocchi C. 320-row coronary computed tomography angiography (CCTA) with automatic exposure control (AEC): effect of 100 kV *vs* 120 kV on image quality and dose exposure. *Radiol Med* 2016; **121**: 618-625 [PMID: 27169907 DOI: 10.1007/s11547-016-0643-4]

22 **Guo W**, Liu X, Gao Z, Pirbhulal S, Huang W, Lin WH, Zhang H, Tan N, Zhang YT. Quantification of three-dimensional computed tomography angiography for evaluating coronary luminal stenosis using digital subtraction angiography as the standard of reference. *Biomed Eng Online* 2015; **14**: 50 [PMID: 26024658 DOI: 10.1186/s12938-015-0048-y]

World Journal of Radiology

Submit a Manuscript: https://www.f6publishing.com

World J Radiol 2023 February 28; 15(2): 42-55

DOI: 10.4329/wjr.v15.i2.42

ISSN 1949-8470 (online)

SYSTEMATIC REVIEWS

Imaging of paraduodenal pancreatitis: A systematic review

Matteo Bonatti, Nicolò De Pretis, Giulia A Zamboni, Alessandro Brillo, Stefano Francesco Crinò, Riccardo Valletta, Fabio Lombardo, Giancarlo Mansueto, Luca Frulloni

Specialty type: Radiology, nuclear medicine and medical imaging

Provenance and peer review: Invited article; Externally peer reviewed.

Peer-review model: Single blind

Peer-review report's scientific quality classification
Grade A (Excellent): 0
Grade B (Very good): 0
Grade C (Good): C
Grade D (Fair): D, D
Grade E (Poor): 0

P-Reviewer: Kaneko J, Japan; Tellez-Avila F, United States

Received: September 28, 2022
Peer-review started: September 28, 2022
First decision: October 17, 2022
Revised: October 24, 2022
Accepted: December 6, 2022
Article in press: December 6, 2022
Published online: February 28, 2023

Matteo Bonatti, Riccardo Valletta, Department of Radiology, Ospedale Centrale di Bolzano, Bolzano 39100, Italy

Nicolò De Pretis, Alessandro Brillo, Luca Frulloni, Gastroenterology and Digestive Endoscopy Unit, The Pancreas Institute, G.B. Rossi University Hospital of Verona, Verona 37134, Italy

Giulia A Zamboni, Giancarlo Mansueto, Department of Diagnostics and Public Health, Radiology Section, Policlinico GB Rossi, University of Verona, Verona 37134, Verona, Italy

Stefano Francesco Crinò, Department of Medicine, University of Verona, Verona 37134, Italy

Fabio Lombardo, Department of Radiology, IRCCS Sacro Cuore Don Calabria Hospital, Negrar 37024, Italy

Corresponding author: Matteo Bonatti, MD, Adjunct Professor, Doctor, Department of Radiology, Ospedale Centrale di Bolzano, Via Boehler 5, 39100 Bolzano, Italy.
matteo.bonatti@sabes.it

Abstract

BACKGROUND

Paraduodenal pancreatitis (PP) represents a diagnostic challenge, especially in non-referral centers, given its potential imaging overlap with pancreatic cancer. There are two main histological variants of PP, the cystic and the solid, with slightly different imaging appearances. Moreover, imaging findings in PP may change over time because of disease progression and/or as an effect of its risk factors exposition, namely alcohol intake and smoking.

AIM

To describe multimodality imaging findings in patients affected by PP to help clinicians in the differential diagnosis with pancreatic cancer.

METHODS

The systematic review was conducted according to the Preferred Reporting Items for Systematic reviews and Meta-analyses 2009 guidelines. A Literature search was performed on PubMed, Embase and Cochrane Library using (groove pancreatitis [Title/Abstract]) OR (PP [Title/Abstract]) as key words. A total of 593 articles were considered for inclusion. After eliminating duplicates, and title and abstract screening, 53 full-text articles were assessed for eligibility. Eligibility criteria were: Original studies including 8 or more patients, fully written in English, describing imaging findings in PP, with pathological confirmation or

clinical-radiological follow-up as the gold standard. Finally, 14 studies were included in our systematic review.

RESULTS

Computed tomography (CT) findings were described in 292 patients, magnetic resonance imaging (MRI) findings in 231 and endoscopic ultrasound (EUS) findings in 115. Duodenal wall thickening was observed in 88.8% of the cases: Detection rate was 96.5% at EUS, 91.0% at MRI and 84.1% at CT. Second duodenal portion increased enhancement was recognizable in 76.3% of the cases: Detection rate was 84.4% at MRI and 72.1% at CT. Cysts within the duodenal wall were detected in 82.6% of the cases: Detection rate was 94.4% at EUS, 81.9% at MRI and 75.7% at CT. A solid mass in the groove region was described in 40.9% of the cases; in 78.3% of the cases, it showed patchy enhancement in the portal venous phase, and in 100% appeared iso/hyperintense during delayed phase imaging. Only 3.6% of the lesions showed restricted diffusion. The prevalence of radiological signs of chronic obstructive pancreatitis, namely main pancreatic duct dilatation, pancreatic calcifications, and pancreatic cysts, was extremely variable in the different articles.

CONCLUSION

PP has peculiar imaging findings. MRI is the best radiological imaging modality for diagnosing PP, but EUS is more accurate than MRI in depicting duodenal wall alterations.

Key Words: Pancreatitis; Paraduodenal pancreatitis; Diagnostic imaging; Computed tomography; Magnetic resonance imaging; Endoscopic ultrasound

©The Author(s) 2023. Published by Baishideng Publishing Group Inc. All rights reserved.

Core Tip: Paraduodenal pancreatitis (PP) represents a diagnostic challenge, especially in non-referral centers, given its potential imaging overlap with neoplastic processes, namely pancreatic and duodenal carcinoma. Numerous articles show imaging features of PP, but most of them are represented by case reports or reviews with poor scientific background. This systematic review describes the multimodality imaging features (computed tomography, magnetic resonance imaging and endoscopic ultrasound) of PP according to original research articles with pathologic samples and or clinical-radiological follow-up as the gold standard.

Citation: Bonatti M, De Pretis N, Zamboni GA, Brillo A, Crinò SF, Valletta R, Lombardo F, Mansueto G, Frulloni L. Imaging of paraduodenal pancreatitis: A systematic review. *World J Radiol* 2023; 15(2): 42-55
URL: https://www.wjgnet.com/1949-8470/full/v15/i2/42.htm
DOI: https://dx.doi.org/10.4329/wjr.v15.i2.42

INTRODUCTION

Paraduodenal pancreatitis (PP), also known as groove pancreatitis, is a peculiar form of chronic pancreatitis characterized by an inflammatory mass-forming involvement of the duodenal wall in the so-called groove area, located between the head of the pancreas, the duodenum, and the common bile duct[1]. The inflammatory process may lead to a solid thickening of the duodenal wall and/or to the development of cystic changes centered in the groove area. PP has been subdivided into cystic or solid type, based on the presence or absence of cysts in the groove area at imaging or pathology. According to a large Italian study, two thirds of patients present the cystic type of PP and one third the solid one[2]; similar data were reported on a more limited series from India[3]. The inflammatory process, arising from the groove area, might also extend to the whole pancreas secondary to the compression and obstruction of the main pancreatic duct by the inflamed and thickened groove area, leading to obstructive chronic pancreatitis. No definitive epidemiological data have been published, but PP is a rare disease considering that in an observational study including 893 patients with chronic pancreatitis, PP prevalence was 6%[4]. On the other hand, a German study published in 2014 reported 3.5% of PP on 373 consecutive pancreatic resections in a single center[5].

Adsay *et al*[1] described the typical histological features of PP, namely dilated ducts in the duodenal wall with pseudocystic changes and granulation tissue, Brunner's gland hyperplasia, dense myoid stromal proliferation and fibrosis of the pancreas and of the surrounding soft tissue of the groove area [1].

As reported by many previously published papers, patients suffering from PP are typically middle-aged men, heavy smokers, and drinkers[2-4,6-14]. Acute pancreatitis and abdominal pain have been described as the most frequent presenting symptoms, followed by symptoms related to duodenal obstruction (vomiting and weight loss) and to common bile duct obstruction (jaundice)[2,9-11]. Symptoms related to pancreatic insufficiency (diabetes and steatorrhea) are less frequent and generally reported in patients with advanced disease.

PP diagnosis may be challenging since patients often present with symptoms mimicking pancreatic cancer, such as abdominal pain, vomiting, weight loss or jaundice, and, especially in the solid type, also at imaging the differential diagnosis with pancreatic cancer can be extremely difficult. Therefore, a significant proportion of patients (reported between 5% and 21%, even in referral centers) undergo demolitive pancreatic surgery because of misdiagnosis or malignancy suspicion[2,6,15,16].

Many different therapeutic strategies have been proposed for symptoms' management in PP and, nowadays, no definitive data have been published about the best choice between medical treatment and endoscopic or surgical interventions. A step-up approach should probably be considered, starting with medical treatment based on pain control, alcohol consumption cessation, and smoke cessation. Endoscopic treatment might be considered in the case of bile duct stenosis and surgery should be reserved for patients with intractable pain, duodenal obstruction, or recurrent bile duct obstruction and cholangitis.

Despite the rarity of the disease, a precise radiological and clinical diagnosis is crucial for patients' management and a multidisciplinary approach is needed to reduce the risk of misdiagnosis and of inappropriate surgical resections. Therefore, the aim of our study was to conduct a systematic literature review to show the multimodality imaging appearance of PP and to assess imaging performance in the differential diagnosis between PP and pancreatic cancer.

MATERIALS AND METHODS

Studies selection

The study was conducted according to the Preferred Reporting Items for Systematic reviews and Meta-analyses (PRISMA) guidelines. We performed a database search on PubMed, Embase and Cochrane Library, looking for articles published from January 1990 to July 2022. The following string was used: (Groove pancreatitis [Title/Abstract]) OR (PP [Title/Abstract]). A total of 593 papers were identified and considered for inclusion. After eliminating duplicates, and title and abstract screening, 53 full-text articles were assessed for eligibility by two radiologists independently. Discrepancies were solved by consensus, which was necessary in 2 cases. Eligibility criteria were original studies including 8 or more patients, written in English, describing imaging findings in PP, with pathological confirmation or clinical-radiological follow-up as the gold standard (Figure 1). Finally, 14 studies were included in our systematic review[2,3,7,9,11,12,15-22].

Data extraction

Study characteristics, including publication date, journal type, inclusion period, aim of the study, study design, characteristics of the patients considered for inclusion, number of patients with PP included, and study limitations were extracted from the included studies (Table 1). The presence of potential bias was evaluated by two Authors in consensus using the Newcastle-Ottawa Quality Assessment Scale for Cohort Studies (https://www.ohri.ca/programs/clinical_epidemiology/oxford.asp) (Table 2). The maximum number of points given to each item was 4, 2 and 3, with a total maximum number of 9 points.

The following data were extracted from the included studies: Number of patients examined with the different imaging modalities [computed tomography (CT), magnetic resonance imaging (MRI), ultrasound (US), and endoscopic ultrasound (EUS)], PP variant (cystic/solid), lesions' size (mean maximum and minimum diameter), presence of duodenal wall thickening (yes/no), duodenal wall thickening distribution (eccentric/circumferential), presence of second duodenal portion increased wall enhancement (yes/no), presence (yes/no) number (single/multiple) and size (mm) of duodenal wall cysts, presence of a discrete pancreatic mass (yes/no), lesion's signal intensity on T2-weighted images, on T1-weighted images, on high b value diffusion-weighted images and on apparent diffusion coefficient (ADC) map (hypo-/iso-/hyper-intense in comparison to "normal" pancreas), enhancement on arterial, portal venous and delayed phase images (hypo-/iso-/hyper-intense/dense in comparison to "normal" pancreas), enhancement pattern in portal venous phase (hypo/patchy/rim), presence of pancreatic cysts (yes/no), presence of main pancreatic duct dilatation (yes/no), presence of pancreatic calcifications (yes/no), presence of biliary duct dilatation (yes/no), presence of portal vein stenosis (yes/no), presence of gastroduodenal artery displacement (yes/no), presence of peripancreatic fat stranding (yes/no), presence of peripancreatic enlarged lymph nodes (yes/no). The above-mentioned variables were not considered in every study (Tables 3 and 4). The absolute number of patients for which the variable was evaluated is reported in the text as (n = #).

Table 1 Characteristics of the included studies

Ref.	Year	Journal type	Aim	Inclusion period	Study design	Patients considered for inclusion	Paraduodenal pancreatitis patients included	Limitations
Ishigami *et al* [17]	2010	Radiological	Differential diagnosis cancer *vs* paraduodenal pancreatitis	2001-2008	Retrospective, single center	Institutional database search using "groove pancreatitis or groove pancreatic carcinoma" (n = 22)	15	Small population, no clear distinction between computed tomography and magnetic resonance imaging findings
Kalb *et al*[18]	2013	Radiological	Differential diagnosis cancer *vs* paraduodenal pancreatitis	2007-2010	Retrospective, single center	Institutional database search using "Whipple and/or pancreatectomy" and diagnosis of cancer or paraduodenal pancreatitis (n = 47)	17	Surgically resected patients only, small population
Zaheer *et al* [19]	2014	Radiological	Findings description	2002-2013	Retrospective, single center	Patients undergoing pancreaticoduodenectomy and histological paraduodenal pancreatitis diagnosis (n = 12)	12	Surgically resected patients only, small population
Arvanitakis *et al*[11]	2014	Gastroenterological	Endoscopic and medical management	1995-2010	Retrospective, single center	Institutional database search using "paraduodenal pancreatitis" (n = 51)	51	Poor imaging findings description based on radiological reports
Wagner *et al* [20]	2015	Radiological	Findings description	"14 yr"	Retrospective, single center	Patients with cystic dystrophy in heterotopic pancreas diagnosis at endoscopic ultrasound (n = 138)	76	Only cystic variant of paraduodenal pancreatitis included
Arora *et al*[3]	2015	Radiological	Findings description	2010-2014	Retrospective, single center	Patients treated for paraduodenal pancreatitis at gastroenterology or surgical units (n = 33)	33	Poor imaging findings description based on radiological reports, no clear distinction between computed tomography and magnetic resonance imaging findings
Shin *et al*[21]	2016	Radiological	Differential diagnosis cancer *vs* paraduodenal pancreatitis	2005-2011	Retrospective, 2 centers	Multidetector computed tomography for pancreas protocols (n = 2561) with groove mass	8	Surgically resected patients only, small population
Boninsegna *et al*[22]	2017	Radiological	Differential diagnosis cancer *vs* paraduodenal pancreatitis	2012-2015	Retrospective, single center	Abdominal Magnetic Resonance Imaging with groove mass	28	None
de Pretis *et al* [2]	2017	Multidisciplinary	Clinical and morphological features	1994-2012	Retrospective, single center	Patients with diagnosis of paraduodenal pancreatitis (n = 120)	120	Poor imaging findings description based on radiological reports, no clear distinction between computed tomography and magnetic resonance imaging findings
Muraki *et al* [9]	2017	Surgical	Imaging and pathologic correlation	2004-2015	Retrospective, single center	All pancreatic resections	47	Surgically resected patients only, poor imaging findings description, no clear distinction between computed tomography and magnetic resonance imaging findings
Tarvainen *et al*[16]	2021	Multidisciplinary	Diagnosis, natural course and treatment	2005-2015	Retrospective, multicentric	Institutional database search using "groove and/or paraduodenal" (n = 192)	33	Poor imaging findings description, no clear distinction between computed tomography and magnetic resonance imaging findings
Ooka *et al*[7]	2021	Gastroenterological	Clinical management	2000-2014	Retrospective,	Institutional database search using "groove pancre-	48	No clear distinction between computed

					single center	atitis and/or paraduodenal pancreatitis" (*n* = 211)		tomography and magnetic resonance imaging findings
Değer *et al* [15]	2022	Surgical	Clinical features and outcome	2013-2019	Retrospective, single center	Institutional database search using "groove and/or paraduodenal" (*n* = 28)	25	Poor imaging findings description based on radiological reports, no clear distinction between computed tomography and magnetic resonance imaging findings
Kulkarni *et al* [12]	2022	Radiological	Findings description	2007-2020	Retrospective, single center	Patients with pancreatitis (*n* = 2120)	30	None

Diagnostic performance of imaging studies in the differential diagnosis between PP and pancreatic cancer was also assessed.

Statistical analysis

Absolute numbers and percentages were used to describe quantitative variables. For continuous data, mean values were calculated. Sensitivity, specificity, negative predictive value and positive predictive value in differentiating between PP and pancreatic cancer were reported, when available. P values <0.05 were considered statistically significant.

RESULTS

Included studies characteristics

All the included studies had a retrospective design and encompassed a total of 543 patients, 489 (90%) males and 54 (10%) females, with a mean age of 48 years. History of chronic alcohol abuse was reported in 87% of the cases (*n* = 524) and 78% of the patients were heavy smokers (*n* = 334). The included studies were published on radiological journals in 8/14 cases (*n* = 219), on multidisciplinary journals in 2/14 (*n* = 153), on gastroenterological journals in 2/14 (*n* = 99), and on surgical journals in 2/14 (*n* = 72).

Pathology was the gold standard in 9/14 studies (*n* = 261), pathology or clinical-radiological follow up in 3/14 (*n* = 183), follow-up alone in 2/14 (*n* = 99). Cross-sectional images were reviewed by one or two Radiologists in 10/14 studies (*n* = 314), whereas in 4/14 studies (*n* = 229) the described CT and MRI imaging findings were based on the original radiological reports.

Nine out of the 14 evaluated studies included imaging findings obtained from 2 or more imaging modalities, whereas 4 studies were based on CT images only and 3 on MRI only. In 7 of the included studies, it was not always possible to clearly understand if the described findings were derived from CT or MRI images. Therefore, CT findings were described for 292 patients, MRI findings for 231 and EUS findings for 115; US findings were not described in any of the included studies.

Duodenal findings

Duodenal wall thickening was described in 88.8% of the cases (*n* = 420); at EUS, duodenal thickening was recognizable in 96.5% of the cases (*n* = 115), at MRI in 91.0% (*n* = 78) and at CT in 84.1% (*n* = 227). The cutoff value for the duodenal wall thickening definition was reported in three studies[18,21,22] (*n* =

Table 2 Risk of bias assessment

Ref.	Representativeness of the exposed cohort	Selection of the non-exposed cohort	Ascertainment of exposure	Outcome of interest was not present at start of study	Comparability of cohorts	Assessment of outcome	Follow-up long enough	Adequacy of follow up	Total
Ishigami *et al*[17]	±	-	-	-	-	-	NA	NA	6
Kalb *et al* [18]	±	-	-	-	-	-	NA	NA	6
Zaheer *et al* [19]	±	NA	-	+	NA	-	NA	NA	2
Arvanitakis *et al*[11]	±	NA	±	+	NA	-	-	-	3
Wagner *et al*[20]	+	NA	±	-	NA	+	NA	NA	1
Arora *et al* [3]	±	NA	±	+	NA	-	-	-	3
Shin *et al* [21]	±	-	-	-	±	-	NA	NA	4
Boninsegna *et al*[22]	-	±	-	-	±	-	NA	NA	4
de Pretis *et al*[2]	-	NA	-	-	NA	-	-	-	6
Muraki *et al* [9]	-	-	-	-	-	-	NA	NA	7
Tarvainen *et al*[16]	±	±	-	-	-	-	-	-	6
Ooka *et al* [7]	-	-	-	-	-	-	-	-	9
Değer *et al* [15]	-	NA	-	-	NA	-	-	-	6
Kulkarni *et al*[12]	-	NA	-	-	NA	-	NA	NA	4

-: Low risk of bias; ±: Unknown risk of bias; +: High risk of bias; NA: Not appliable.

53) and was 3 mm in all of them. Mean maximum duodenal wall thickness was assessed in two studies [19,20] and was 19 mm (n = 88). Wall thickening distribution was evaluated in one study only[19] and was eccentric, involving the second duodenal portion medial wall, in 81.8% of the cases and concentric in 18.2% (n = 11). The second duodenal portion showed an increased enhancement in comparison to the adjacent intestinal walls in 76.3% of the cases (n = 93); second duodenal portion increased enhancement was recognizable in 84.4% of the cases at MRI (n = 32) and in 72.1% at CT (n = 61).

Cysts within the duodenal wall were detected in 82.6% of the cases (n = 419); duodenal wall cysts were recognizable in 94.4% of the cases at EUS (n = 108), in 81.9% of the cases at MRI (n = 138) and in 75.7% of the cases at CT (n = 173). Duodenal wall cysts were single in 65.8% of the cases and multiple in 34.2% (n = 149). Cyst size was evaluated in three studies[9,18,20]. Muraki *et al*[9] and Wagner *et al*[20] reported a mean maximum size of the cystic component of 13 mm (n = 123), whereas Kalb *et al*[18] reported cystic components diameters ranging from 6 to 27 mm (n = 17).

The cystic variant of PP was depicted in 72.0% of the cases and the solid variant in 28.0% (n = 543).

Groove region findings

A solid mass in the groove region was described in 40.9% of the cases (n = 88). Mean maximum diameter of the lesion was 38 mm (n = 75), whereas mean minimum diameter was 16 mm (n = 27). Lesions' signal intensity on T2-weighted images was evaluated in two articles[17,22] (n = 43): The solid lesion was iso-intense to "normal" pancreatic parenchyma in 48.8% of the cases, hyperintense in 30.2% and hypointense in 21.0%. Lesions' signal intensity on other imaging sequences was assessed only by Boninsegna *et al*[22] (n = 28): On T1-weighted images the lesion was hypointense in 64.3% of the cases

Table 3 Variables evaluated in the included studies

Ref.	Duodenal wall thickening	Thickening distribution	Duodenal wall enhancement	Duodenal wall cysts	Cysts number	Cysts size	Pancreatic mass	Signal intensity on T2-weighted images	Signal intensity on T1-weighted images, diffusion-weighted images, apparent diffusion coefficient map	Arterial phase enhancement	Portal venous phase enhancement
Ishigami *et al* [17]				+				+			
Kalb *et al*[18]	+		+	+		1					
Zaheer *et al* [19]	1, 2	1		1			1, 2			1	1
Arvanitakis *et al*[11]	2			+, 2	+, 2						
Wagner *et al* [20]	1, 2			+, 1, 2	1	1					
Arora *et al*[3]	+, 1		+, 1	+, 1							
Shin *et al*[21]	1										1
Boninsegna *et al*[22]	+							+	+	+	+
de Pretis *et al* [2]											
Muraki *et al* [9]						+					
Tarvainen *et al*[16]											
Ooka *et al*[7]	1						1				
Değer *et al* [15]	+, 1			+, 1			1				
Kulkarni *et al* [12]	1		1	1							

+: Described at MRI; 1: Described at CT; 2: Described at EUS; MRI: Magnetic resonance imaging; EUS: Endoscopic ultrasound; CT: Computed tomography.

and isointense in 35.7%, on high b-value diffusion-weighted images it was isointense in 71.4% of the cases and hypointense in 28.6%, whereas on ADC maps it was isointense in 71.4% of the cases, hyperintense in 25.0% and hypointense in 3.6%. During the arterial phase of the dynamic study, the lesion appeared hypovascular in 82.4% of the cases and isovascular in 17.6% (n = 34). During the portal

Table 4 Variables evaluated in the included studies

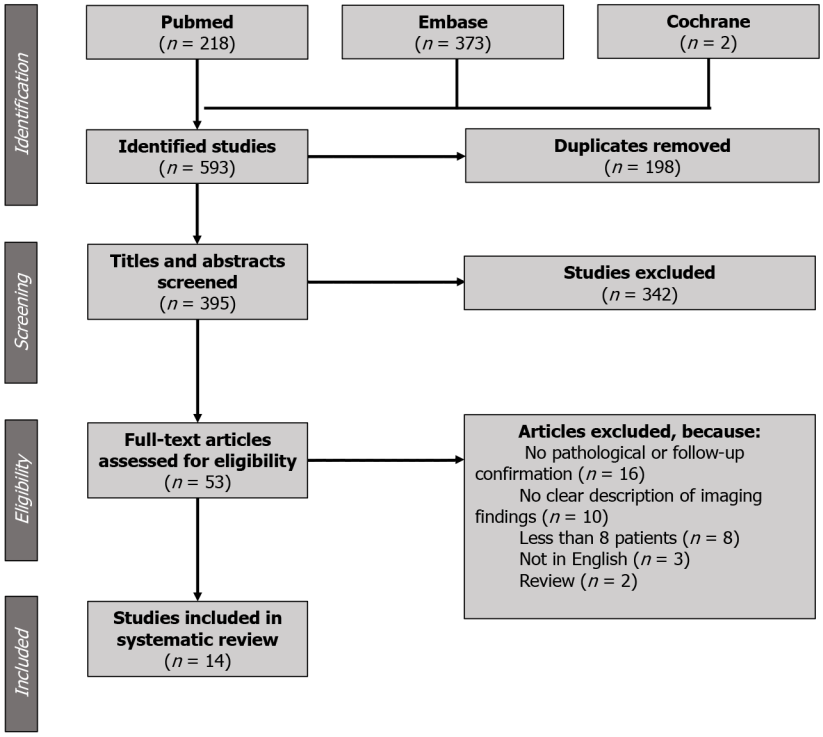
Ref.	Delayed enhancement	Enhancement pattern	Pancreatic cysts	Main pancreatic duct dilatation	Pancreatic calcifications	Biliary duct dilatation	Portal vein stenosis	Gastroduodenal artery displacement	Peripancreatic fat stranding	Peripancreatic lymph nodes
Ishigami *et al* [17]		+		+	1	+				
Kalb *et al*[18]			+	+		+	+			
Zaheer *et al* [19]			2	1	1	1			1	1
Arvanitakis *et al*[11]				+, 1	1	+, 1				
Wagner *et al* **[20]**				+, 1	1	+, 1			1	
Arora *et al*[3]			+, 1	+, 1	1	+, 1		+, 1		
Shin *et al*[21]		1	1	1	1	1		1		1
Boninsegna *et al*[22]	+		+	+		+				
de Pretis *et al* [2]					1					
Muraki *et al*[9]			+	+		+, 1				
Tarvainen *et al* [16]			+, 1	+, 1	1	+, 1				
Ooka *et al*[7]			1	1	1				1	
Değer *et al*[15]				+, 1						
Kulkarni *et al* [12]			1	1	1	1		1		

+: Described at MRI; 1: Described at CT; 2: Described at EUS; MRI: Magnetic resonance imaging; EUS: Endoscopic ultrasound; CT: Computed tomography.

venous phase, the lesion appeared isovascular in 47.6% of the cases, hypovascular in 42.9% and hypervascular in 9.5% (n = 42). Enhancement pattern during the portal venous phase was described as "patchy" in 78.3% of the cases, whereas no cases of ring enhancement were detected (n = 23). During the delayed phase, the lesion appeared hyperintense in 53.6% of the cases and isointense in 46.4% (n = 28).

Pancreatic findings

Main pancreatic duct dilatation was present in 56.5% of the cases (n = 499); in the single included studies, prevalence of main pancreatic duct dilatation ranged from 28.9%[16] to 95.5%[20]. Pancreatic



DOI: 10.4329/wjr.v15.i2.42 **Copyright** ©The Author(s) 2023.

Figure 1 PRISMA flowchart showing studies inclusion and exclusion criteria.

cysts were detected in 64.5% of the cases (n = 269); pancreatic cysts detection rate was 80.3% at MRI (n = 122), 52.4% at CT (n = 147) and 42.9% (n = 7) at EUS. Pancreatic calcifications were present in 48.3% of the cases (n = 383); in the single included studies, prevalence of pancreatic calcifications ranged from 20%[7] to 100%[11]. Calcifications in the region of the minor papilla were recognizable in 43.4% of the cases (n = 76).

Alterations in the adjacent structures

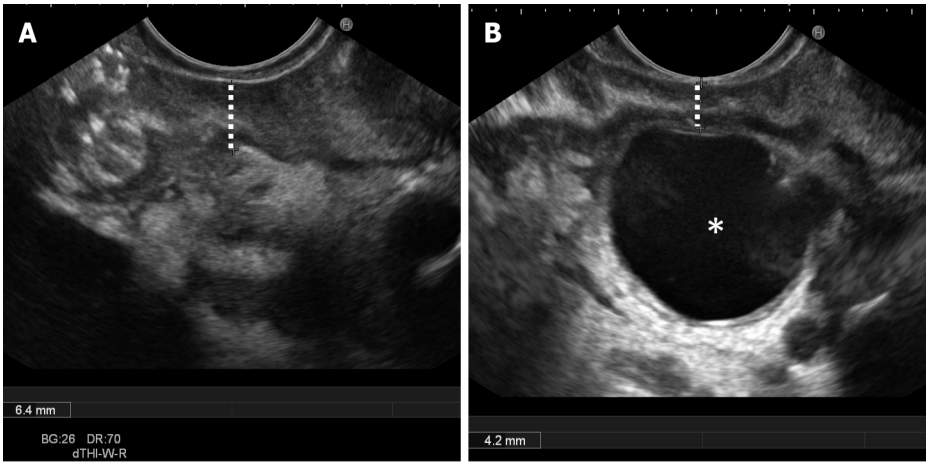
Biliary duct dilatation was observed in 41.2% of the cases (n = 417), portal vein stenosis in 47.1% (n = 17) and gastroduodenal artery displacement in 64.3% (n = 84). Peripancreatic fat stranding was described in 88.1% of the cases (n = 134) and enlarged peripancreatic lymph nodes were appreciable in 65.0% (n = 20).

Differential diagnosis PP vs cancer

Four articles[17,18,21,22] explored imaging accuracy in the differential diagnosis between PP and pancreatic cancer, including a total of 68 patients with PP and 73 with pancreatic adenocarcinoma. Shin *et al*[21] showed that, at CT, absence of the malignant appearance of biliary duct stenosis (*i.e.* abrupt duct cutoff or shouldering), presence of duodenal wall thickening and presence of cysts in the groove region are significantly associated with PP (P = 0.002, 0.026 and 0.001, respectively). Ishigami *et al*[17] found that a patchy enhancement pattern in the portal venous phase at CT and/or MRI is significantly associated with PP (P < 0.0001). Kalb *et al*[18] showed that poorly experienced radiologists can correctly diagnose PP at MRI with an accuracy of 87.2% (88.2% sensitivity, 86.7% specificity, 78.9% PPV, 92.9% NPV) by looking for the presence of 3 key imaging findings: Focal thickening (> 3 mm) of the second portion of the duodenum, increased enhancement of the second portion of the duodenum and cysts in the groove region. Boninsegna *et al*[22] observed that, at MRI, iso-/hypo-intensity on high b-value diffusion weighted imaging (DWI), iso-/hyper-intensity on ADC maps and delayed phase iso-/hyper-intensity are significantly associated with PP (P = 0.004, 0.005 and 0.003, respectively), as well as focal thickening of the second portion of the duodenum, presence of cysts in the groove area and absence of main pancreatic duct dilatation (P = 0.001, 0.001 and 0.005, respectively). Moreover, mean maximum diameter was significantly larger in PP than in adenocarcinoma (P = 0.0003).

DISCUSSION

Our systematic review included 14 original articles showing multimodality imaging findings in PP.



DOI: 10.4329/wjr.v15.i2.42 **Copyright** ©The Author(s) 2023.

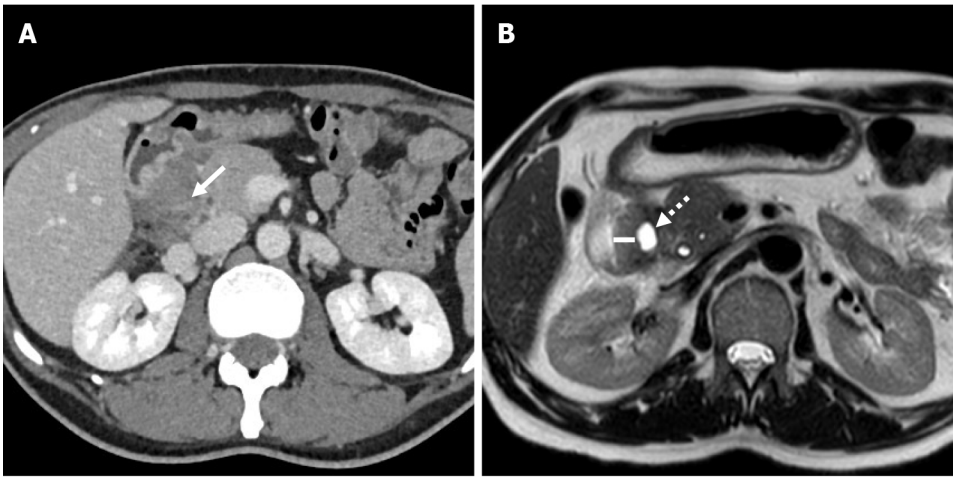
Figure 2 Endoscopic ultrasound. A: Endoscopic ultrasound (EUS) clearly shows second duodenal portion wall thickening in a patient with chronic alcohol abuse history and abdominal pain, findings suggestive of solid subtype of paraduodenal pancreatitis; B EUS shows mild second duodenal portion wall thickening and a large duodenal wall cyst (star), findings pathognomonic for paraduodenal pancreatitis.

Imaging was the main topic in eight of the included articles, whereas it was ancillary in six of them; in these latter articles, imaging findings were not always extensively and accurately described. A total of 22 different imaging features were considered by the Authors in the included articles, with a mean of 4,4 imaging features *per* article. Surprisingly, the most frequently described imaging features were not directly correlated with PP appearance and were in the presence of main pancreatic duct dilatation (reported in 13 studies), presence of biliary duct dilatation (11 studies) and presence of pancreatic calcifications (10 studies). Presence of duodenal wall thickening and of duodenal walls cysts were also frequently assessed in the included studies (10 and 8 studies, respectively).

Typical imaging findings in PP are second duodenal portion wall thickening (88.8% of the cases), which is usually eccentric (81.8%), associated with the presence of duodenal wall cysts (82.6%) and second duodenal portion increased wall enhancement (76.3%). Duodenal wall cysts were more frequently single (65.8%) and showed a mean maximum diameter of 13 mm. The above-described imaging findings detection rates varied largely according to the adopted imaging modality. For example, duodenal wall thickening prevalence was 96.5% at EUS (Figure 2A), 91.0% at MRI and 84.1% at CT, and, similarly, duodenal wall cysts prevalence was 94.4% at EUS, 81.9% at MRI and 75.7% at CT. These differences are probably the consequence of the increased tissue contrast resolution of EUS over MRI and of MRI over CT (Figures 2B and 3). Consequently, the prevalence of cystic and solid subtypes of PP can be extremely variable and depends on the patients' population characteristics (solid subtype prevalence increases in the surgical series, given to the difficulty in differential diagnosis with pancreatic cancer, and decreases in the gastroenterological series) and from the adopted imaging modality (cystic subtype prevalence is higher in MRI and EUS series in comparison to CT series).

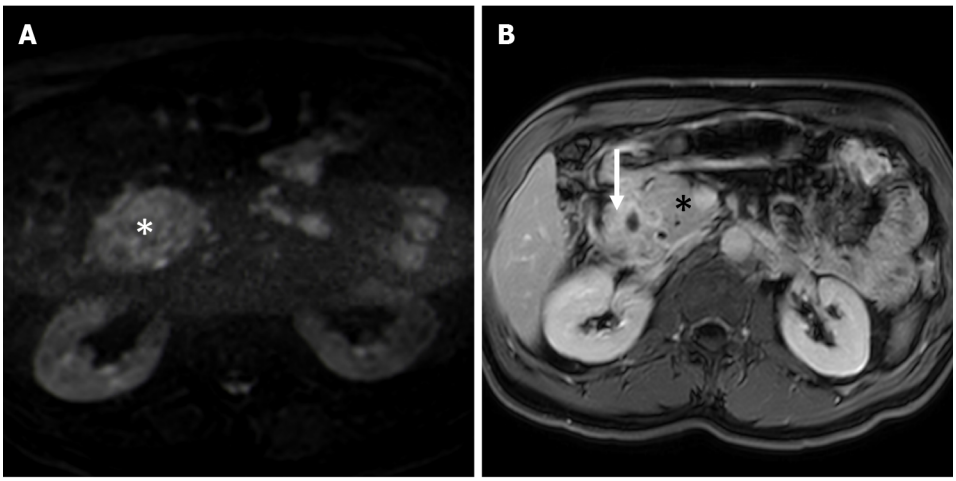
A solid mass in the groove region was described in less than a half (40.9%) of patients with PP. At MRI, lesion signal intensity was quite variable on T1- and T2-weighted images. On the other hand, the included lesions were hypo- to iso-intense in comparison to a normal pancreas on high b-value DWI in 100% of the cases (Figure 4A) and were iso- to hyper-intense on the ADC map in 96.4%. Therefore, the presence of increased diffusivity restriction (*i.e.* hyperintensity on high b-value DWI and hypointensity on the ADC map) has high negative predictive value for the diagnosis of PP. The solid components typically (82.4%) appeared hypovascular in the arterial phase of the dynamic study and showed a progressive enhancement during the portal venous (57.1% iso- to hyper-intense/attenuating) and the delayed (100% iso- to hyper-intense/attenuating) phases (Figure 4B). The enhancement pattern during the portal venous phase was mainly described as "patchy" (78.3% of the cases). Both patchy enhancement during portal venous phase, which is the consequence of the presence of normal pancreatic tissue between the areas of inflammatory changes[9], and delayed phase enhancement, which is the direct consequence of the presence of fibro-inflammatory tissue, are useful in the differential diagnosis between PP and pancreatic cancer.

Presence of radiological signs of obstructive chronic pancreatitis were reported with extremely variable prevalence in the included studies. For example, prevalence of main pancreatic duct dilatation ranged from 28.9% to 95.5%, prevalence of pancreatic calcifications from 20.0% to 100%, and prevalence of pancreatic cysts from 35.1% to 94.1%. The rationale of these wide differences is clearly explained in the work of de Pretis *et al*[2], which demonstrated that the prevalence of both pancreatic calcifications and main pancreatic duct dilatation significantly increases during the course of the disease. Therefore, despite the results reported by Boninsegna *et al*[22], signs of obstructive chronic pancreatitis should not be used for a differential diagnosis between PP and pancreatic cancer.



DOI: 10.4329/wjr.v15.i2.42 **Copyright** ©The Author(s) 2023.

Figure 3 A 49-year-old male patient with weight loss and abdominal pain. A: Axial 3 mm thick multiplanar reconstruction of portal venous phase computed tomography acquisition shows a hypodense mass in the groove region with patchy enhancement (arrow); B: Axial T2-weighted magnetic resonance imaging image acquired 2 mo later clearly shows eccentric second duodenal portion wall thickening (line) with cystic component (dotted arrow).



DOI: 10.4329/wjr.v15.i2.42 **Copyright** ©The Author(s) 2023.

Figure 4 Magnetic resonance imaging. A: Axial high b value (b = 800 s/mm^2) diffusion weighted imaging image shows absence of increased diffusivity restriction in the thickened groove area (star) in comparison to adjacent "normal" pancreas, finding associated with paraduodenal pancreatitis and uncommon in pancreatic cancer; B: Axial delayed phase T1-weighted magnetic resonance imaging acquisition shows increased enhancement of the duodenal walls and of the groove region (arrow) in comparison to "normal" pancreas (star), finding often associated with paraduodenal pancreatitis.

Given its expansile inflammatory nature, PP determines reactive alterations in the adjacent structures. The most frequently encountered finding was peripancreatic fat stranding, which was appreciable in 88.1% of the cases, often associated with enlarged reactive peripancreatic lymph nodes (65%). Gastroduodenal artery displacement, without infiltration or occlusion, must also be considered a common finding in PP (64.3%).

Given the central role of duodenal wall changes depiction in the differential diagnosis between PP and pancreatic cancer[21,22], MRI is mandatory if CT is inconclusive, and EUS must be performed if doubts remain even after MRI[23]. Moreover, EUS-guided fine needle aspiration/biopsy should be performed in inconclusive cases, warranting diagnostic sensitivity, specificity, positive predictive value, negative predictive value, and accuracy in differentiating PP from pancreatic cancer of 90%, 100%, 100%, 93%, and 96%, respectively[13].

The main strength of our study is that it is the first systematic literature review of imaging findings in PP. By systematically reviewing 14 different original articles dealing with imaging findings in PP, we have been able to bring together a total of 543 patients affected by PP. The article has also some weaknesses, mainly due to selection bias in the included articles and to the extreme variability of the evaluated and described imaging findings. Moreover, the differential diagnosis between PP and pancreatic cancer, which represents the main criticality, was only addressed in 4 Papers.

CONCLUSION

PP has peculiar imaging findings that enable differential diagnosis with pancreatic cancer, namely second duodenal portion eccentric wall thickening, increased enhancement, and cystic changes. Absence of increased diffusivity restriction in the groove area, patchy enhancement during the portal venous phase and delayed phase enhancement are also imaging features strongly correlated with PP. Signs of obstructive chronic pancreatitis and biliary obstruction are often present in advanced disease and must not be considered worrisome features.

CT can be considered the first line imaging modality in pancreatic pathologies and enables clinicians to perform a differential diagnosis between PP and pancreatic cancer in most of the cases. Given its higher tissue contrast resolution, MRI represents the second level imaging modality of choice in the case of inconclusive CT findings. EUS has higher accuracy than CT and MRI in depicting duodenal wall changes, offers the possibility of obtaining cyto-histologic samples, but is more invasive and less tolerated; therefore, EUS must be considered a problem-solving technique in difficult cases.

ARTICLE HIGHLIGHTS

Research background

Paraduodenal pancreatitis (PP) is a relatively rare benign inflammatory pathology that can create differential diagnosis dilemmas with pancreatic cancer. Many articles deal with imaging findings in PP, but most of them are represented by case reports, short series, or reviews.

Research motivation

The aim of our work was to perform a systematic literature review of imaging findings in PP considering only original research articles with pathology and/or clinical-radiological follow-up as the reference standard.

Research objectives

To critically describe multimodality imaging findings in PP to help clinicians in the differential diagnosis with pancreatic cancer.

Research methods

Systematic review of original articles describing imaging findings in 8 or more patients affected by PP with pathological confirmation or clinical-radiological follow-up as the gold standard.

Research results

14 articles including 543 patients were included. Computed tomography, magnetic resonance imaging (MRI) and Endoscopic ultrasound (EUS) findings were described.

Research conclusions

PP has typical findings at imaging. MRI is the most accurate radiological imaging modality, but EUS has higher sensitivity in depicting duodenal wall alterations.

Research perspectives

Radiomics features extraction may be an option in order to further increase imaging accuracy in the differential diagnosis between PP and pancreatic cancer.

FOOTNOTES

Author contributions: Bonatti M, De Pretis N and Valletta R designed the research; Bonatti M, De Pretis N, Crinò SF and Brillo A performed the research; Bonatti M, De Pretis N and Lombardo F analyzed the data; Bonatti M, Zamboni GA, Lombardo F, Mansueto G and Frulloni L wrote the paper; All authors approved the final version of the article.

Conflict-of-interest statement: All the authors report no relevant conflicts of interest for this article.

PRISMA 2009 Checklist statement: The authors have read the PRISMA 2009 Checklist, and the manuscript was prepared according to the PRISMA 2009 Checklist.

Open-Access: This article is an open-access article that was selected by an in-house editor and fully peer-reviewed by external reviewers. It is distributed in accordance with the Creative Commons Attribution NonCommercial (CC BY-NC 4.0) license, which permits others to distribute, remix, adapt, build upon this work non-commercially, and license

their derivative works on different terms, provided the original work is properly cited and the use is non-commercial. See: https://creativecommons.org/Licenses/by-nc/4.0/

Country/Territory of origin: Italy

ORCID number: Matteo Bonatti 0000-0002-4477-8944; Nicolò De Pretis 0000-0002-3558-681X; Giulia A Zamboni 0000-0002-5059-3305; Stefano Francesco Crinò 0000-0003-4560-8741; Giancarlo Mansueto 0000-0002-1857-0613; Luca Frulloni 0000-0001-7417-2655.

S-Editor: Liu GL
L-Editor: Filipodia
P-Editor: Liu GL

REFERENCES

1 **Adsay NV**, Zamboni G. Paraduodenal pancreatitis: a clinico-pathologically distinct entity unifying "cystic dystrophy of heterotopic pancreas", "para-duodenal wall cyst", and "groove pancreatitis". *Semin Diagn Pathol* 2004; **21**: 247-254 [PMID: 16273943 DOI: 10.1053/j.semdp.2005.07.005]
2 **de Pretis N**, Capuano F, Amodio A, Pellicciari M, Casetti L, Manfredi R, Zamboni G, Capelli P, Negrelli R, Campagnola P, Fuini A, Gabbrielli A, Bassi C, Frulloni L. Clinical and Morphological Features of Paraduodenal Pancreatitis: An Italian Experience With 120 Patients. *Pancreas* 2017; **46**: 489-495 [PMID: 28196024 DOI: 10.1097/MPA.0000000000000781]
3 **Arora A**, Rajesh S, Mukund A, Patidar Y, Thapar S, Arora A, Bhatia V. Clinicoradiological appraisal of 'paraduodenal pancreatitis': Pancreatitis outside the pancreas! *Indian J Radiol Imaging* 2015; **25**: 303-314 [PMID: 26288527 DOI: 10.4103/0971-3026.161467]
4 **Frulloni L**, Gabbrielli A, Pezzilli R, Zerbi A, Cavestro GM, Marotta F, Falconi M, Gaia E, Uomo G, Maringhini A, Mutignani M, Maisonneuve P, Di Carlo V, Cavallini G; PanCroInfAISP Study Group. Chronic pancreatitis: report from a multicenter Italian survey (PanCroInfAISP) on 893 patients. *Dig Liver Dis* 2009; **41**: 311-317 [PMID: 19097829 DOI: 10.1016/j.dld.2008.07.316]
5 **Vitali F**, Hansen T, Kiesslich R, Heinrich S, Kumar A, Mildenberger P, Amodio A, Benini L, Vantini I, Frulloni L. Frequency and characterization of benign lesions in patients undergoing surgery for the suspicion of solid pancreatic neoplasm. *Pancreas* 2014; **43**: 1329-1333 [PMID: 25058888 DOI: 10.1097/MPA.0000000000000193]
6 **Balduzzi A**, Marchegiani G, Andrianello S, Romeo F, Amodio A, De Pretis N, Zamboni G, Malleo G, Frulloni L, Salvia R, Bassi C. Pancreaticoduodenectomy for paraduodenal pancreatitis is associated with a higher incidence of diabetes but a similar quality of life and pain control when compared to medical treatment. *Pancreatology* 2020; **20**: 193-198 [PMID: 31952917 DOI: 10.1016/j.pan.2019.12.014]
7 **Ooka K**, Singh H, Warndorf MG, Saul M, Althouse AD, Dasyam AK, Paragomi P, Phillips AE, Zureikat AH, Lee KK, Slivka A, Papachristou GI, Yadav D. Groove pancreatitis has a spectrum of severity and can be managed conservatively. *Pancreatology* 2021; **21**: 81-88 [PMID: 33309222 DOI: 10.1016/j.pan.2020.11.018]
8 **Casetti L**, Bassi C, Salvia R, Butturini G, Graziani R, Falconi M, Frulloni L, Crippa S, Zamboni G, Pederzoli P. "Paraduodenal" pancreatitis: results of surgery on 58 consecutives patients from a single institution. *World J Surg* 2009; **33**: 2664-2669 [PMID: 19809849 DOI: 10.1007/s00268-009-0238-5]
9 **Muraki T**, Kim GE, Reid MD, Mittal P, Bedolla G, Memis B, Pehlivanoglu B, Freedman A, Erbarut Seven I, Choi H, Kooby D, Maithel SK, Sarmiento JM, Krasinskas A, Adsay V. Paraduodenal Pancreatitis: Imaging and Pathologic Correlation of 47 Cases Elucidates Distinct Subtypes and the Factors Involved in its Etiopathogenesis. *Am J Surg Pathol* 2017; **41**: 1347-1363 [PMID: 28795998 DOI: 10.1097/PAS.0000000000000919]
10 **Vujasinovic M**, Pozzi Mucelli R, Grigoriadis A, Palmér I, Asplund E, Rutkowski W, Baldaque-Silva F, Waldthaler A, Ghorbani P, Verbeke CS, Löhr JM. Paraduodenal pancreatitis - problem in the groove. *Scand J Gastroenterol* 2022; 1-8 [PMID: 35138983 DOI: 10.1080/00365521.2022.2036806]
11 **Arvanitakis M**, Rigaux J, Toussaint E, Eisendrath P, Bali MA, Matos C, Demetter P, Loi P, Closset J, Deviere J, Delhaye M. Endotherapy for paraduodenal pancreatitis: a large retrospective case series. *Endoscopy* 2014; **46**: 580-587 [PMID: 24839187 DOI: 10.1055/s-0034-1365719]
12 **Kulkarni CB**, Moorthy S, Pullara SK, Prabhu NK. CT imaging patterns of paraduodenal pancreatitis: a unique clinicoradiological entity. *Clin Radiol* 2022; **77**: e613-e619 [PMID: 35589430 DOI: 10.1016/j.crad.2022.04.008]
13 **Jun JH**, Lee SK, Kim SY, Cho DH, Song TJ, Park DH, Lee SS, Seo DW, Kim MH. Comparison between groove carcinoma and groove pancreatitis. *Pancreatology* 2018; **18**: 805-811 [PMID: 30224296 DOI: 10.1016/j.pan.2018.08.013]
14 **Egorov VI**, Vankovich AN, Petrov RV, Starostina NS, Butkevich ATs, Sazhin AV, Stepanova EA. Pancreas-preserving approach to "paraduodenal pancreatitis" treatment: why, when, and how? *Biomed Res Int* 2014; **2014**: 185265 [PMID: 24995273 DOI: 10.1155/2014/185265]
15 **Değer KC**, Köker İH, Destek S, Toprak H, Yapalak Y, Gönültaş C, Şentürk H. The clinical feature and outcome of groove pancreatitis in a cohort: A single center experience with review of the literature. *Ulus Travma Acil Cerrahi Derg* 2022; **28**: 1186-1192 [PMID: 35920434 DOI: 10.14744/tjtes.2022.12893]
16 **Tarvainen T**, Nykänen T, Parviainen H, Kuronen J, Kylänpää L, Sirén J, Kokkola A, Sallinen V. Diagnosis, natural course and treatment outcomes of groove pancreatitis. *HPB (Oxford)* 2021; **23**: 1244-1252 [PMID: 33483260 DOI: 10.1016/j.hpb.2020.12.004]
17 **Ishigami K**, Tajima T, Nishie A, Kakihara D, Fujita N, Asayama Y, Ushijima Y, Irie H, Nakamura M, Takahata S, Ito T, Honda H. Differential diagnosis of groove pancreatic carcinomas vs. groove pancreatitis: usefulness of the portal venous

phase. *Eur J Radiol* 2010; **74**: e95-e100 [PMID: 19450943 DOI: 10.1016/j.ejrad.2009.04.026]

18 **Kalb B**, Martin DR, Sarmiento JM, Erickson SH, Gober D, Tapper EB, Chen Z, Adsay NV. Paraduodenal pancreatitis: clinical performance of MR imaging in distinguishing from carcinoma. *Radiology* 2013; **269**: 475-481 [PMID: 23847255 DOI: 10.1148/radiology.13112056]

19 **Zaheer A**, Haider M, Kawamoto S, Hruban RH, Fishman EK. Dual-phase CT findings of groove pancreatitis. *Eur J Radiol* 2014; **83**: 1337-1343 [PMID: 24935140 DOI: 10.1016/j.ejrad.2014.05.019]

20 **Wagner M**, Vullierme MP, Rebours V, Ronot M, Ruszniewski P, Vilgrain V. Cystic form of paraduodenal pancreatitis (cystic dystrophy in heterotopic pancreas (CDHP)): a potential link with minor papilla abnormalities? *Eur Radiol* 2016; **26**: 199-205 [PMID: 25991480 DOI: 10.1007/s00330-015-3799-8]

21 **Shin LK**, Jeffrey RB, Pai RK, Raman SP, Fishman EK, Olcott EW. Multidetector CT imaging of the pancreatic groove: differentiating carcinomas from paraduodenal pancreatitis. *Clin Imaging* 2016; **40**: 1246-1252 [PMID: 27636383 DOI: 10.1016/j.clinimag.2016.08.004]

22 **Boninsegna E**, Negrelli R, Zamboni GA, Tedesco G, Manfredi R, Pozzi Mucelli R. Paraduodenal pancreatitis as a mimicker of pancreatic adenocarcinoma: MRI evaluation. *Eur J Radiol* 2017; **95**: 236-241 [PMID: 28987673 DOI: 10.1016/j.ejrad.2017.08.031]

23 **Oza VM**, Skeans JM, Muscarella P, Walker JP, Sklaw BC, Cronley KM, El-Dika S, Swanson B, Hinton A, Conwell DL, Krishna SG. Groove Pancreatitis, a Masquerading Yet Distinct Clinicopathological Entity: Analysis of Risk Factors and Differentiation. *Pancreas* 2015; **44**: 901-908 [PMID: 25899649 DOI: 10.1097/MPA.0000000000000351]



Published by **Baishideng Publishing Group Inc**
7041 Koll Center Parkway, Suite 160, Pleasanton, CA 94566, USA
Telephone: +1-925-3991568
E-mail: bpgoffice@wjgnet.com
Help Desk: https://www.f6publishing.com/helpdesk
https://www.wjgnet.com



© 2023 Baishideng Publishing Group Inc. All rights reserved.

ISSN 1949-8470 (online)

World Journal of *Radiology*

World J Radiol 2023 March 28; 15(3): 56-88



Published by Baishideng Publishing Group Inc

World Journal of Radiology

Contents

Monthly Volume 15 Number 3 March 28, 2023

REVIEW

56 Hepatocellular carcinoma: State of the art diagnostic imaging

Criss C, Nagar AM, Makary MS

MINIREVIEWS

69 Multi-modality parathyroid imaging: A shifting paradigm

Gulati S, Chumber S, Puri G, Spalkit S, Damle NA, Das CJ

CASE REPORT

83 Magnetic resonance imaging findings of spontaneous pyomyoma in a premenopausal woman managed with myomectomy: A case report

Martínez D, Sanchez GE, Gómez J, Sonda LJ, Suárez LD, López CS, Vega JJ, Cepeda DA

World Journal of Radiology

Monthly Volume 15 Number 3 March 28, 2023

Contents

ABOUT COVER

Editorial Board Member of *World Journal of Radiology*, Wing-Chi E Kwok, PhD, Associate Professor, Department of Imaging Sciences, University of Rochester, Rochester, NY 14642, United States.
edmund_kwok@urmc.rochester.edu

AIMS AND SCOPE

The primary aim of *World Journal of Radiology* (*WJR*, *World J Radiol*) is to provide scholars and readers from various fields of radiology with a platform to publish high-quality basic and clinical research articles and communicate their research findings online.

WJR mainly publishes articles reporting research results and findings obtained in the field of radiology and covering a wide range of topics including state of the art information on cardiopulmonary imaging, gastrointestinal imaging, genitourinary imaging, musculoskeletal imaging, neuroradiology/head and neck imaging, nuclear medicine and molecular imaging, pediatric imaging, vascular and interventional radiology, and women's imaging.

INDEXING/ABSTRACTING

The *WJR* is now abstracted and indexed in PubMed, PubMed Central, Emerging Sources Citation Index (Web of Science), Reference Citation Analysis, China National Knowledge Infrastructure, China Science and Technology Journal Database, and Superstar Journals Database. The 2022 edition of Journal Citation Reports ® cites the 2021 Journal Citation Indicator (JCI) for *WJR* as 0.48.

RESPONSIBLE EDITORS FOR THIS ISSUE

Production Editor: *Xiang-Di Zhang*; **Production Department Director:** *Xu Guo*; **Editorial Office Director:** *Jia-Ru Fan*.

NAME OF JOURNAL
World Journal of Radiology

ISSN
ISSN 1949-8470 (online)

LAUNCH DATE
January 31, 2009

FREQUENCY
Monthly

EDITORS-IN-CHIEF
Thomas J Vogl

EDITORIAL BOARD MEMBERS
https://www.wjgnet.com/1949-8470/editorialboard.htm

PUBLICATION DATE
March 28, 2023

COPYRIGHT
© 2023 Baishideng Publishing Group Inc

INSTRUCTIONS TO AUTHORS
https://www.wjgnet.com/bpg/gerinfo/204

GUIDELINES FOR ETHICS DOCUMENTS
https://www.wjgnet.com/bpg/GerInfo/287

GUIDELINES FOR NON-NATIVE SPEAKERS OF ENGLISH
https://www.wjgnet.com/bpg/gerinfo/240

PUBLICATION ETHICS
https://www.wjgnet.com/bpg/GerInfo/288

PUBLICATION MISCONDUCT
https://www.wjgnet.com/bpg/gerinfo/208

ARTICLE PROCESSING CHARGE
https://www.wjgnet.com/bpg/gerinfo/242

STEPS FOR SUBMITTING MANUSCRIPTS
https://www.wjgnet.com/bpg/GerInfo/239

ONLINE SUBMISSION
https://www.f6publishing.com

© 2023 Baishideng Publishing Group Inc. All rights reserved. 7041 Koll Center Parkway, Suite 160, Pleasanton, CA 94566, USA
E-mail: bpgoffice@wjgnet.com https://www.wjgnet.com

World Journal of Radiology

Submit a Manuscript: https://www.f6publishing.com

World J Radiol 2023 March 28; 15(3): 56-68

DOI: 10.4329/wjr.v15.i3.56

ISSN 1949-8470 (online)

REVIEW

Hepatocellular carcinoma: State of the art diagnostic imaging

Cody Criss, Arpit M Nagar, Mina S Makary

Specialty type: Radiology, nuclear medicine and medical imaging

Provenance and peer review: Invited article; Externally peer reviewed.

Peer-review model: Single blind

Peer-review report's scientific quality classification

Grade A (Excellent): A
Grade B (Very good): B
Grade C (Good): 0
Grade D (Fair): 0
Grade E (Poor): 0

P-Reviewer: Kumar SKY, India; Papadopoulos N, Greece

Received: December 18, 2022
Peer-review started: December 18, 2022
First decision: January 31, 2023
Revised: February 12, 2023
Accepted: March 22, 2023
Article in press: March 22, 2023
Published online: March 28, 2023

Cody Criss, Heritage College of Osteopathic Medicine, Ohio University, Athens, OH 45701, United States

Arpit M Nagar, Mina S Makary, Department of Radiology, The Ohio State University Medical Center, Columbus, OH 43210, United States

Corresponding author: Mina S Makary, MD, Assistant Professor, Attending Doctor, Director, Department of Radiology, The Ohio State University Medical Center, 395 W. 12th Ave., Columbus, OH 43210, United States. mina.makary@osumc.edu

Abstract

Primary liver cancer is the fourth most common malignancy worldwide, with hepatocellular carcinoma (HCC) comprising up to 90% of cases. Imaging is a staple for surveillance and diagnostic criteria for HCC in current guidelines. Because early diagnosis can impact treatment approaches, utilizing new imaging methods and protocols to aid in differentiation and tumor grading provides a unique opportunity to drastically impact patient prognosis. Within this review manuscript, we provide an overview of imaging modalities used to screen and evaluate HCC. We also briefly discuss emerging uses of new imaging techniques that offer the potential for improving current paradigms for HCC characterization, management, and treatment monitoring.

Key Words: Hepatocellular carcinoma; Imaging; Diagnostic; Magnetic resonance imaging; Computed tomography; Ultrasound; Radiogenomics

©The Author(s) 2023. Published by Baishideng Publishing Group Inc. All rights reserved.

Core Tip: Successful tumor assessment can be a critical component to patient management and prognosis. The expansion of imaging techniques beyond conventional modalities (*e.g.* ultrasound, computed tomography, magnetic resonance imaging) provides an opportunity to improve the identification of small or well-differentiated hepatocellular carcinoma tumors, along with the capability to monitor treatment responses to surgery or locoregional therapy.

Citation: Criss C, Nagar AM, Makary MS. Hepatocellular carcinoma: State of the art diagnostic imaging. *World J Radiol* 2023; 15(3): 56-68
URL: https://www.wjgnet.com/1949-8470/full/v15/i3/56.htm
DOI: https://dx.doi.org/10.4329/wjr.v15.i3.56

INTRODUCTION

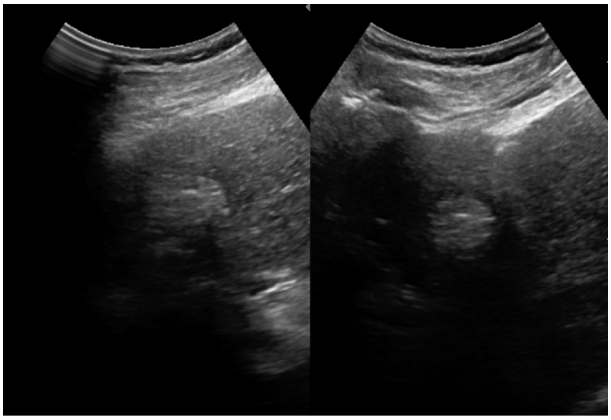
Hepatocellular carcinoma (HCC) is the most common liver malignancy, accounting for 90% of liver tumors, and a leading cause of mortality worldwide[1,2]. Global risk factors for HCC include cirrhosis, existing in up to 90% of new cases[3], or patients with long-standing liver infections such as viral hepatitis B and C[4]. East Asia and sub-Saharan Africa account for greater than 80% of cases, and incidence within the United States continues to rise[3,4]. Unfortunately, many patients are diagnosed in the advanced stages of the disease, which emphasizes the importance of early detection and surveillance [5]. Surveillance and early tumor detection using ultrasonography is recommended by the American Association for the study of Liver Diseases (AASLD) for high-risk populations driven by ultrasound-guided imaging. Unlike other malignancies, HCC expresses distinctive characteristics that can be diagnosed based on imaging features alone, without the need for confirmation from tissue sampling[6]. In this review, we provide a summary of diagnostic criteria and imaging modalities used to detect and stage HCC, as well as emerging methods to further assist in the surveillance and characterization of the disease.

SURVEILLANCE AND SCREENING

Conventional ultrasound

Tumor burden can significantly impact management, where patients with small, localized tumors can receive curative methods such as liver transplantation, resection, or locoregional therapies. On the other hand, treatment options are limited in patients with HCC displaying more aggressive features (*e.g.*, extrahepatic metastases, multifocal tumors, and vascular invasion). As a result, early detection may offer a significant benefit in select patients. Patient populations recommended for HCC surveillance differs between AASLD[7], the European Association for the Study of the Liver (EASL)[8] and the Asian Pacific Association for the Study of the Liver (APASL)[9], but largely consist of adults with cirrhosis or patients with hepatitis B virus (HBV)[10]. Across surveillance recommendations, biannual abdominal ultrasonography (Figure 1) is the standard modality for HCC detection with major advantages including accessibility, cost-effectiveness, and safety[10].

Surveillance programs typically consist of ultrasound examination performed at either 6- or 12-mo intervals. Across all stages of HCC, ultrasound detection carries 84% sensitivity. A number of investigations have found a mortality and cost-benefit of biannual ultrasonography for imaging surveillance of HCC[10-12]. For example, a study in HBV-infected patients in China found a 37% reduction in mortality in those receiving biannual ultrasonography examinations compared to the control group[12]. Suboptimal visualization poses a major limitation for ultrasound screening. Poor visualization and sonographic sensitivity to HCC lesions can be caused by a number of different extrinsic factors such as morbid obesity, patient inability to suspend respiration, obscured portions of the liver by bowel gas or rib shadowing, and intrinsic factors such as hepatic steatosis or fibrosis causing parenchymal heterogenicity[13]. A recent investigation reported approximately 20% of scans were inadequate to exclude liver lesions[14]. Detecting smaller nodules (< 2 cm) appears to be a major limitation of ultrasound, with studies reporting detection rates as low as approximately 28%[15]. In response, the American College of Radiology (ACR) screening guidelines have recommended the use of systematic documentation and scoring for visualization (A: No or minimal limitations; B: Moderate limitations; C: Severe limitations). The use of tumor biomarkers, such as alpha-fetoprotein (AFP), in concert with ultrasound examination appears to have an additive effect on detection rate[16]. For example, a recent meta-analysis of prospective studies found the sensitivity for ultrasound alone to detect any stage of HCC was 78% compared to 97% when adding AFP[17]. Interestingly, the synergistic impact of combining ultrasound with AFP also exists for detection of earlier, smaller nodules (45% *vs* 63% sensitivity, respectively)[17] which is particularly salient given the limitations of ultrasound and earlier stages of HCC. This is not without controversy, however. The 2018 AASLD guidelines do not designate any preferences between adjunctive use of AFP while the 2017 APASL guidelines recommend the combination of ultrasound and AFP[18]. In contrast, the 2018 EASL guidelines discourage the use of ultrasound with AFP for 6-mo HCC surveillance, citing concerns of false-positives in the setting of active liver inflammation with infection[18].



DOI: 10.4329/wjr.v15.i3.56 **Copyright** ©The Author(s) 2023.

Figure 1 Screening ultrasound. Hyperechoic segment IV liver lesion compatible and later characterized as hepatocellular carcinoma.

While the objective of this review is to elucidate the latest advancements in technological imaging for the screening and diagnosis of HCC, it is important to note the efficacy of detection can be limited due to multifactorial screening challenges. In fact, less than 1 in 5 patients with cirrhosis receive surveillance screening for HCC[19]. Previous reviews have extensively examined the numerous challenges encountered during the screening process, including the inability to properly stratify high-risk patients, the presence of socio-economic and logistical impediments to accessing healthcare, as well as training and detection limitations using conventional imaging techniques, as previously discussed. One of the most common attributable factors to surveillance underuse includes lack of surveillance orders or unrecognized cirrhosis[5]. Therefore, strategies to improve education and integrating primary care providers in surveillance efforts can have a drastic and meaningful effect on rates of patients undergoing HCC screening[20]. The implementation of patient-centered outreach programs such as reminder protocols or embedding best-practice advisories within the electronic health record may be solutions to improve barriers of patients undergoing surveillance[5,20]. The decision to select which patients to screen also been discussed and studies have developed scoring systems across different risk factors (*e.g.* hepatitis or cirrhosis) to refine and improve risk stratification have been proposed[21]. Other methods have also focused on improving surveillance outcomes and detection rates, such as utilizing serological biomarkers (*e.g.* AFP) either as a single screening modality or in concert with imaging to improve sensitivity, at the potential cost of increased rates of false positivity. The use of biomarkers may also be especially helpful for smaller HCCs, not easily visible with ultrasound[21].

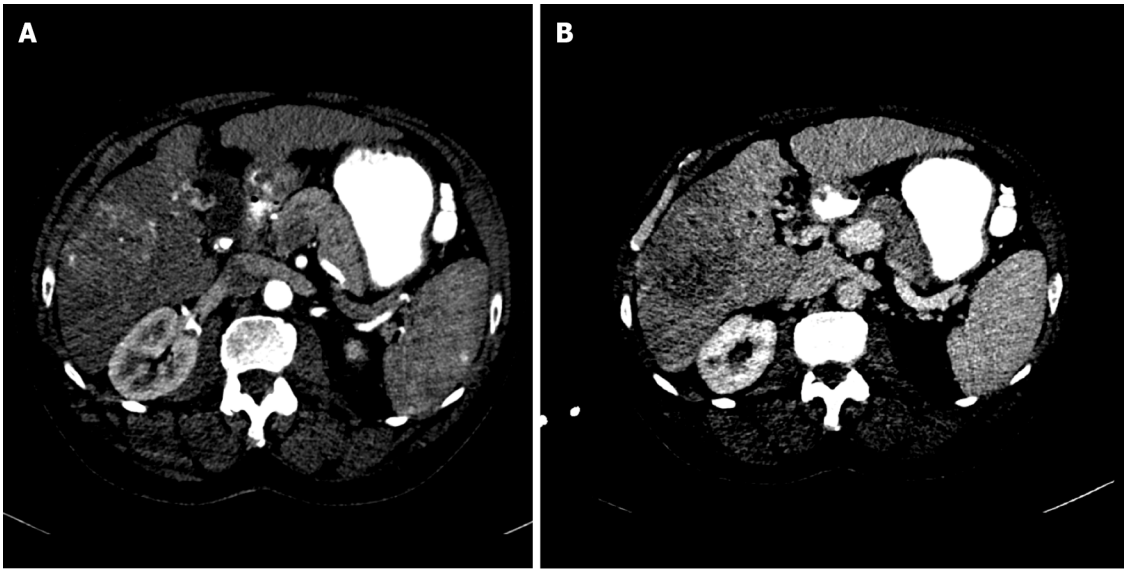
HCC DIAGNOSTIC MODALITIES

Liver imaging reporting and data systems diagnostic reporting system

Established by the ACR, standardized methods for imaging interpretation and reporting are defined using the liver imaging reporting and data systems (LI-RADS). The application of the LI-RADS diagnostic algorithm was initially developed for computed tomography (CT)/magnetic resonance imaging (MRI). LI-RADS is subdivided into 8 categories and ranges in greater probability of malignancy from LR-1 to LR-5 with additional categories including LI-RADS M (LR-M) (probably or definitely malignant but not HCC specific), LR-definite tumor in vein, and LR-cannot be categorized (NC)[13,22]. Observation of lesions categorized in LR-5 is designated as almost certainly HCC, with a systematic review of 454 studies reporting 94% of LR-5 lesions confirmed to be HCC and 97% malignant[23]. The Organ Procurement and Transplantation Network (OPTN) is another diagnostic criterion established by National Organ Transplant Act, with subcategories ranging from class 0-5. Specificities are similar between LI-RADSv2018 LR-5 and OPTN class 5[24]. However, inter-reader agreement and sensitivity of LI-RADS (sensitivity: 63.9%) is higher than that of OPTN (sensitivity: 53.6%)[24].

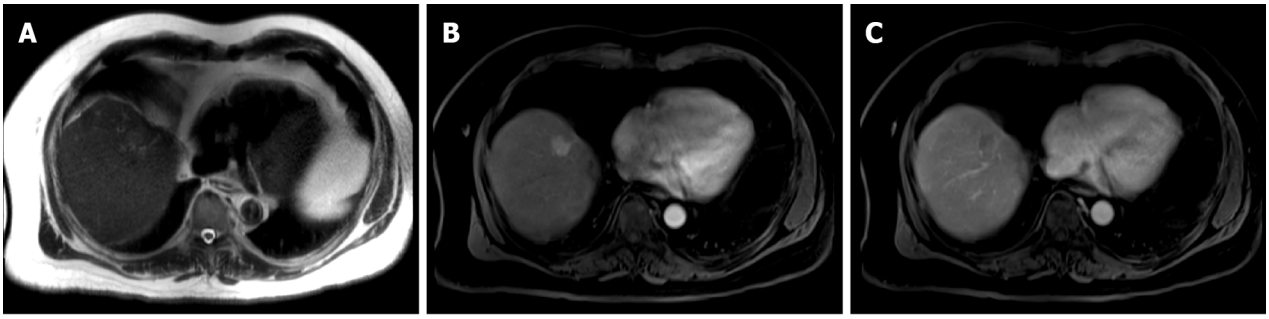
Cross-sectional imaging: Multiphase CT and MRI

Standard recommendations for HCC diagnosis include multiphase CT or MRI which are beneficial modalities for highlighting unique features of HCC (Figures 2 and 3). Physiological differences in blood perfusion between hepatocarcinogenic lesions and non-neoplastic tissue display distinguishing differences in imaging characteristics using multiphasic contrast examinations[25]. Phases consist of late hepatic arterial (20-40 s), portal venous (60-90 s), and delayed (3-5 min). Late arterial phase is useful for detecting hypervascular lesions with HCC lesions characteristically enhancing relative to surrounding liver parenchyma. Arterial lesion enhancement can be appreciated within lesions as small as 1 cm.



DOI: 10.4329/wjr.v15.i3.56 **Copyright** ©The Author(s) 2023.

Figure 2 Axial multiphasic computed tomography imaging 75-year-old male with suspected hepatocellular carcinoma. A: Hyperenhancing liver lesion in segment VIII during the arterial phase; B: Corresponding washout within the delayed venous phase.



DOI: 10.4329/wjr.v15.i3.56 **Copyright** ©The Author(s) 2023.

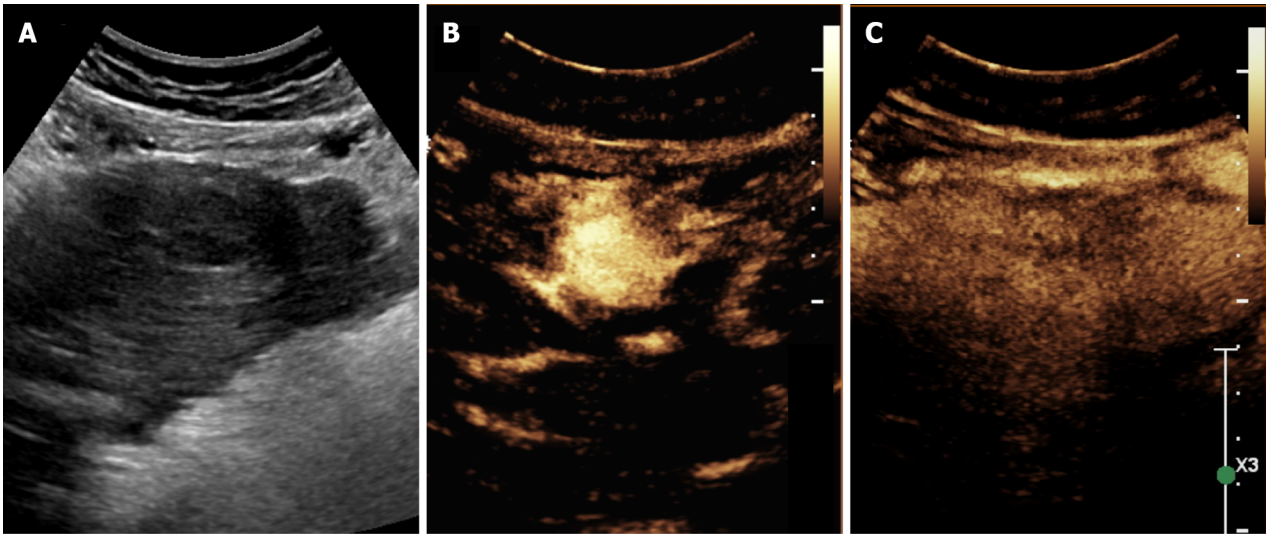
Figure 3 Axial multiphasic magnetic resonance imaging. A: T2-weighted axial sequence imaging of the abdomen; B: T1-weighted fat saturation post-contrast axial sequence image of the abdomen with arterial enhancement of segment VIII lesion; C: Delayed venous phase washout.

Within the portal venous and delayed phases, washout or hypointensity is commonly observed for HCC lesions[26]. During the delayed or equilibrium phase, other characteristics of HCC such as capsule features (*e.g.* lesion washout with pseudocapsule enhancement) and mosaic architecture can be visualized[26]. The introduction of gadolinium-based contrast agents (Gadobenate dimeglumine and gadoxetate acid) may aid LI-RADS categorization. These agents are taken up by hepatocytes of normal liver parenchyma and there is little uptake in non-functioning or dysfunctional hepatocytes, such as the case for HCC. Gadolinium-based agents function similarly to extracellular agents, but can aid in the diagnosis of lesions with atypical features (*e.g.* without washout, arterial hyperenhancement) or distinguish HCC from pseudolesions[27,28]. For example, these agents permit an additional post-contrast hepatobiliary phase, which will display a majority of HCC lesions (90%-95%) as hypointense relative to surrounding hyperintense liver parenchyma[27,29].

MRI is recommended for staging of HCC disease given that some reports have estimated CT to underestimate 52% of cases[1,2]. MRI also has superior diagnostic efficiency to CT in the detection of small (≤ 3cm) lesions[30]. However, CT is more readily available than MRI, and limitations to using MRI including greater costs and technical complexity make CT a complementary diagnostic alternative[31,32]. A report showed that the combined use of CT/MRI provides better diagnostic accuracy in characterizing liver lesions using LI-RADS (91.29%) than MRI (85.37%) or CT (67.6%) alone, but combined protocols should be limited to difficult or uncertain cases in order to warrant use[32].

Contrast-enhanced ultrasound

In recent years, there has been an emerging use of contrast-enhanced ultrasound (CEUS) for the evaluation of focal liver lesions (Figure 4). CEUS combines the benefit of accessible, non-invasive assessment without ionizing radiation as well as improvements in temporal resolution. Given some of



DOI: 10.4329/wjr.v15.i3.56 **Copyright** ©The Author(s) 2023.

Figure 4 Contrast-enhanced ultrasound. A: 62-year-old female with lesion in segment III with hepatocellular carcinoma; B: Gray-scale conventional ultrasound; C: Contrast-enhanced ultrasound revealing hyperechoic lesion in arterial phase with corresponding washout in venous phase.

the limitations in ultrasound sensitivity, CEUS may offer a useful solution. CEUS utilizes highly echogenic microbubble contrast agents (such as SonoVue®, Definity®) which are rapidly injected *via* the antecubital vein. These agents circulate freely among capillary beds, and the use of dynamic phases of contrast enhancement [*e.g.* arterial (start 10-20 s), portal (start 30-45 s), late (start > 120 s) phases] can help differentiate liver lesions[33].

The reporting system was initially developed for CT and MRI; however, in 2016, CEUS-LIRADS was released to improve standardization in reporting and interpretation specific to CEUS for nodule evaluation[33]. CEUS LI-RADS consists of 8 categories and ranges in greater levels of severity from LR-1 to LR-5, with additional categories such as LR-M (probably or definitely malignant but not HCC specific), LR-TIV, and LR-NC[33]. Diagnostic features of CEUS LI-RADS are based on arterial phase hyperenhancement and washout, or reductions in enhancement relative to the liver[33]. Features specific to HCC include arterial phase hypervascularity and late or low washout[34,35]. HCC displays earlier levels of enhancement compared to native liver tissue, and detection rates are greater for larger lesions (2-3 cm) compared to smaller ones (≤ 1 cm)[36]. Within nodules approximately 2 cm or greater, detection rates for ultrasound approach that of CT or MRI. For example, Gaiani *et al*[37] reported a detection rate of 91%-97.3% for evaluating hypervascularity in 103 cirrhotic nodules > 2 cm using CEUS [37]. Limitations of CEUS are like that of conventional ultrasound. Disadvantages of CEUS include user-dependent accuracy, the requirement for multiple contrast injections to survey or investigate separate liver lesions, and restricted ability to distinguish HCC from cholangiocarcinoma and stage disease[34, 38].

EMERGING ADVANCED IMAGING PROTOCOLS

CT and MR perfusion

The acquisition of sequential imaging combined with IV contrast administration by multidetector can permit the assessment of tissue perfusion. The distribution of contrast media between the intravascular and interstitial compartments depends on the extent of blood flow and capillary permeability. Using kinetic modules, perfusion parameters across liver tissue can be calculated (blood flow, volume, permeability, hepatic arterial perfusion, portal venous perfusion, perfusion index, slope of increase/decrease). Quantitative color-graded perfusion maps can be used to localize lesions with abnormal tissue perfusion with a high degree of spatial resolution[39-42]. Tumor angiogenesis mediates differences in blood supply between normal liver parenchyma and HCC[42]. Quantitative parameters from CT perfusion, such as hepatic perfusion index, carries high sensitivity and specificity (≥ 99%) for HCC detection in patients with cirrhosis[43]. Early HCC lesions or hepatocellular nodules will demonstrate increased arterial supply as hepatocarcinogenesis progresses, reflected in increased hepatic arterial perfusion and perfusion indices[40]. Other common focal liver lesions can exhibit unique CT perfusion behavior and therefore be used to identify HCC from hemangiomas, liver metastases, and arterioportal shunts[44]. Bai *et al*[45] reported histopathological features such as microvascular density, a poor prognostic factor for HCC, is correlated with multiple perfusion parameters[45]. A major prognostic factor for HCC, microvascular density has been shown to be correlated with multiple CT

perfusion parameters.

Similar to CT perfusion, dynamic contrast-enhanced MRI (DCE-MRI) permits the quantification of perfusion characteristics of liver lesions[46]. This approach is accomplished using gadolinium IV contrast administration followed by image acquisition with high temporal resolution and kinetic modules to quantify contrast distribution perfusion to reflect focal perfusion differences[47]. DCE-MRI perfusion parameters have highlighted unique physiological characteristics in HCC lesions, including increased arterial hepatic blood flow, arterial fraction, and lower portal hepatic blood flow, compared to normal liver parenchyma[46]. Pahwa *et al*[48] reported, arterial fraction and distribution volume are high in HCC and metastatic lesions compared to normal liver parenchyma[48]. Metastatic lesions may also be distinguished from HCC and normal liver parenchyma by the perfusion parameter mean transit time[48]. By evaluating tumor vascularity pre- and post-treatment, DCE-MRI has shown efficacy for treatment monitoring (*e.g.* following administration of anti-angiogenic agents, transarterial chemoembolization or radiotherapy) and predicting survival outcomes for HCC patients[49].

Elastography

Elastography is an imaging method to quantify mechanical properties, notably stiffness, to evaluate focal fibrotic cirrhotic changes (Figure 5). Either MRI or ultrasound, coupled with a device that generates low frequency vibrations (*i.e.* shear waves) and wave propagation, can be quantified in order to calculate levels of stiffness in a focal area of interest[50]. First introduced with ultrasound, there are multiple elastography methods which include transient elastography, point shear wave, two-dimensional sheer wave, and quasi-static elastography. Ultrasound elastography has shown to provide satisfactory sensitivity and specificity for identifying histological stages of severe fibrosis (sensitivity: 81.9%, specificity: 84.7%) and cirrhosis (sensitivity: 84.8%, specificity 87.5%)[51]. MRI elastography may also aid to differentiate focal liver lesions. For example, malignant tumors have been reported to have greater levels of stiffness relative to benign lesions, focal fibrotic regions, and normal liver parenchyma [52].

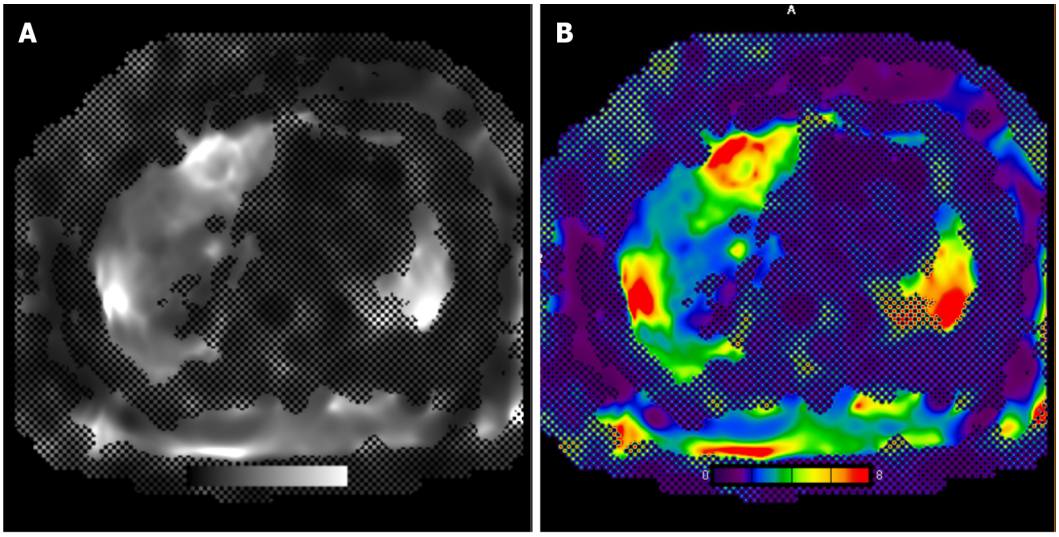
Evaluation of liver stiffness may also offer a prognostic biomarker for determining risk of HCC development and survival. A meta-analysis of 9 studies by Singh *et al*[53] reported increased liver stiffness is associated with an elevated risk of HCC[53]. A more recent metanalysis of 1735 patients reported a varied sensitivity (31%-100%) and high specificity (81%-94%) for predicting HCC development. The use of MR elastography can also be used as a biomarker to predict treatment response and tumor recurrence[54-56]. A prospective investigation assessed 192 patients undergoing HCC treatment (*e.g.* transarterial chemboembolization, ablation, or resection) found liver parenchymal stiffness to be an independent predictor of early recurrence[54]. A recent investigation also reported efficacy for predicting both early and late recurrence in 180 patients with HBV-related HCC prior to undergoing hepatectomy[56]. Qayyum *et al*[57] reported the use of MR elastography to evaluate stiffness changes in patients treated with immunotherapy (*i.e.* Pembrolizumab). HCC tumor stiffness significantly correlated with survival outcomes, including overall survival and time to disease progression, as well as intratumoral T-lymphocyte abundance[57].

T1 mapping

Similarly, T1 mapping is an MR method by which T1 relaxation time is measured and can be useful for identifying liver fibrosis. In the setting of inflammation and fibrosis, T1 relaxation time will be increased and has been used extensively to evaluate myocardial edema and scarring[58]. In fact, there is a moderate correlation between T1 relaxation time and elastography-measured stiffness[59]. T1 relaxation time can also be measured before and after administering hepatobiliary contrast agents such as GD-EOB-DTPA (Eovist®) to provide a more reliable, quantitative evaluation of contrast media uptake within the liver parenchyma[60]. Given that T1 relaxation is influenced by intrinsic properties of tissue, T1 mapping can overcome some of the traditional limitations of conventional MR signal intensity, which can be influenced by technical factors and imaging parameters. Combining T1 mapping and GD-EOB-DTPA has shown to be useful for identifying and classifying differentiated lesions (*e.g.* reduced uptake associated with increased HCC grade), and can be used to distinguish HCC from other focal liver lesions, including hepatic cysts, focal nodular hyperplasia, and hemangiomas[61-63]. HCCs with microvascular invasion have also shown reductions in T1 relaxation relative to lesions without evidence of microvascular invasion[64], showing promise of another imaging method for predicting prognosis.

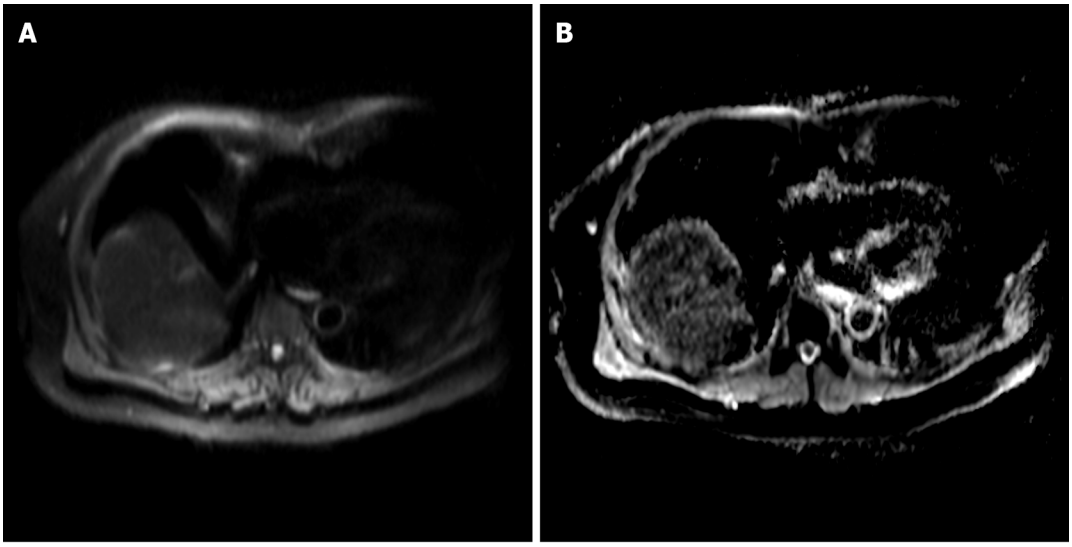
Diffusion weighted imaging

Diffusion weighted imaging (DWI) is a non-invasive MR sequence which can characterize focal liver lesions without the need for contrast media by measuring diffusion properties of water molecules within tissues (Figure 6). Gradations of diffusion are measured using b-values, with greater values denoting more sensitivity to diffusion and higher signal intensity. These values are used to calculate and generate apparent diffusion coefficient (ADC) maps, used clinically to assess local changes in liver tissue diffusion[65]. Changes in cellularity, cell architecture and extracellular space, combined with necrosis and vascularization, can restrict diffusion and thus, HCC will appear hyperintense on DWI[65,66]. DWI has exhibited exceptionally high sensitivity and specificity for a single HCC lesion (100%) and moderate sensitivity and high specificity for multiple lesions (75% and 100%, respectively)[67]. The detection of



DOI: 10.4329/wjr.v15.i3.56 **Copyright** ©The Author(s) 2023.

Figure 5 Magnetic resonance imaging elastography of the liver. Resoundant driver system was used to induce acoustic vibrations in the liver, which were then tracked using magnetic resonance imaging (MRI) scanner to estimate hepatic stiffness. Gray scale and color-scale MRI elastography stiffness sequence. The mean liver stiffness is 4.0 kPa (range: 3.8-4.2 kPa). < 2.5 kPa = Normal; 0.5 to 2.93 kPa = Normal or inflammation; 2.93-3.5 kPa = Stage 1-2 fibrosis; 3.5-4 kPa = Stage 2-3 fibrosis; 4-5 kPa = Stage 3-4 fibrosis; > 5 kPa = Stage 4 or cirrhosis. A: Gray scale; B: Color-scale.



DOI: 10.4329/wjr.v15.i3.56 **Copyright** ©The Author(s) 2023.

Figure 6 Diffusion-weighted imaging. A: Diffusion-weighted imaging sequence; B: Apparent diffusion coefficient (ADC) map. Increased signal can be observed within the segment VIII lesion with corresponding hypointensity on ADC map, compatible with diffusion restriction.

early, smaller HCC (≤ 2 cm) is a clinically useful feature of DWI, especially when combined with contrast use. Generally, poorly differentiated lesions will exhibit lower ADC compared to well-differentiated lesions[66]. A meta-analysis of 21 studies (1799 HCC lesions) by Surov *et al*[68] reported that DWI can provide grading and prognostic utility by demonstrating use of ADC values can predict tumor grade and microvascular invasiveness (specifically, minimum ADC values)[68]. A recent study in 81 patients with HCC also reported microvascular invasiveness to be associated with ADC with a receiver operating characteristic curve AUC values ranging from 0.860-0.909[69]. DWI has been used as a biomarker for monitoring and predicting tumor response following locoregional therapy[70,71]. ADC correlates with tumor response, according to mRECIST, 6 mo after TACE[70]. ADC values of 1.84 × 10−3 $mm^2/s10$ have been reported to have high sensitivity (92.3%) and specificity values (100%) for identifying evidence of necrosis following TACE[71]. For Y90-radioembolization, increases in ADC value (> 30%) can predict objective mRECIST response with 90% sensitivity and 100% specificity. Further, a > 30% change in ADC following TACE is associated with prolonged overall survival[72]. A prospective investigation of 40 patients treated with radiofrequency ablation found an ADC value of

1.01×10^{-3} mm²/s yields the highest sensitivity (80%) and specificity (100%) for detecting residual HCCs 3 mo following treatment[73]. However, differentiation between benign and malignant lesions are difficult in the setting of cirrhosis, as the ADC between both lesion types exhibit considerable overlap [65]. Further, standardization for DWI sequences may be needed since different study protocols can alter ADC calculation[74].

MR spectroscopy

MR spectroscopy is an analytical technique that permits the characterization and quantification of tissue metabolite composition in vivo. For each given voxel, a plot of signal intensity and metabolites/chemicals are expressed by their frequencies[75]. Malignant hepatic lesions have been found to have elevated choline levels relative to normal liver parenchyma. Changes in metabolite frequencies exist between healthy and cirrhotic livers, namely choline and lipid levels[76]. Choline is a component of phospholipid membranes, which increases in states of cell proliferation and carcinogenesis. Zhang *et al* [77] reported the diagnostic efficacy of measuring choline-containing compounds using MR spectroscopy is high for discriminating malignant and benign tumors (sensitivity: 94.3% and specificity: 93.3%)[77]. Determining ratios of choline and lipids within a given lesion has also been used to monitor treatment responses after locoregional therapy[78]. For example, prospective investigations have found choline levels to decline following TACE therapy[79,80].

Radiogenomics/radiomics

The integration of artificial intelligence and diagnostic imaging modalities has led to an exponential rise in radiogenomics or radiomics, which collectively refers to processes that aim to bridge quantitative radiologic data with immunobiological or clinical characteristics to inform prognosis or predict treatment outcomes[81]. The computing process consists of extracting quantitative features from medical images (CT, MRI or positron emission tomography) into large analyzable databases[82]. This process is carried out in multiple steps, including: (1) Defining volumes or regions of interest; (2) image segmentation (performed manually, semi-automatic or automatic tools); (3) image processing used to normalize grey-level intensities, denoise and improve data quality (*e.g.* signal intensity normalization, motion correction, filtering, image interpolation, and bias field correction); (4) feature extraction; and (5) statistical model building[83,84]. The final process, specific to oncology, includes generating association maps to correlate radiomic-based models with clinical outcome data, microvascular invasion, histological grade, or genomic/molecular data (*e.g.* immune marker expression).

Multiple studies have utilized either radiogenomic or radiomic models to diagnose and differentiate liver tumors or predict treatment efficacy for HCC[85-87]. For example, Lewis *et al*[88] reported greater prediction accuracy when combining LI-RADS and DWI-derived radiomics models using the ADC values than LI-RADS alone for distinguishing HCC from other primary liver cancers[88]. Banerjee *et al* [89] evaluated radiomic-models using contrast-enhanced CT to predict prognostic factors, such as microvascular invasion[89]. Radiogenomic venous invasion, an imaging biomarker, can predict microvascular invasion and correlates with lower overall and recurrence-free survival[89]. A recent meta-analysis/systematic review including 4947 patients showed promising predictive potential of radiomic models for microvascular invasion, reporting a pooled area under the curve (AUC) of 0.85, 0.87, and 0.74 across studies using CT, MR, and ultrasound-based models, respectively[90].

Given the link between gene expression and immunotherapy response, the ability to predict HCC immunoprofiles can be critical for delineating appropriate treatment. Hectors *et al*[91] retrospectively evaluated the relationship between MRI radiomic features (*e.g.* models using tumor size, enhancement ratios, fat content, ADC, texture features) and HCC immunhistochemical and genomic makers[91]. In particular, multiple relationships were found to exist between radiomic features and immunotherapy targets, cytotoxic T-lymphocyte-associated antigen 4 and programmed death 1[91]. Radiomic models have also shown promise for predicting treatment response and potential adverse outcomes after locoregional therapy use[92-96]. For example, MRI-based radiomics models have a reported AUC of 0.861 and 0.884 for predicting tumor response at 3-mo post TACE, evaluated using the mRECIST criterion. While larger, multi-center cohort models should be investigated in the future, the use of radiogenomics or radiomic models provide a novel method that can improve tumor grading, predicting prognosis and clinical decision-making strategies.

CONCLUSION

In summary, the use of imaging is an essential component to the diagnosis and management of HCC. Ultrasound is cost-effective modality for the screening. The utility of diagnostic modalities such as MR or CT for differentiation and grading of HCC continues to expand, especially with the advancement of new techniques and image analyses. The implementation of techniques, including elastography, T1 mapping, perfusion imaging and CEUS provide multiple unique benefits to further aid in the characterization of HCC. Other methods, such as radiomics/radiogenomics, which seek to integrate imaging data to predict prognostic risk factors and determine treatment response probability, will be a new frontier

for informing clinical decision-making with the ultimate goal to generate more precise and personalized treatment management strategies for patients with HCC.

FOOTNOTES

Author contributions: Cody C designed and wrote the review; Nagar AM reviewed and critically advised the paper; Makary MS supervised and critically revised the paper.

Conflict-of-interest statement: All the authors report no relevant conflicts of interest for this article.

Open-Access: This article is an open-access article that was selected by an in-house editor and fully peer-reviewed by external reviewers. It is distributed in accordance with the Creative Commons Attribution NonCommercial (CC BY-NC 4.0) license, which permits others to distribute, remix, adapt, build upon this work non-commercially, and license their derivative works on different terms, provided the original work is properly cited and the use is non-commercial. See: https://creativecommons.org/Licenses/by-nc/4.0/

Country/Territory of origin: United States

ORCID number: Mina S Makary 0000-0002-2498-7132.

S-Editor: Fan JR
L-Editor: A
P-Editor: Fan JR

REFERENCES

1 **Villanueva A**. Hepatocellular Carcinoma. *N Engl J Med* 2019; **380**: 1450-1462 [PMID: 30970190 DOI: 10.1056/NEJMra1713263]
2 **Chakraborty E**, Sarkar D. Emerging Therapies for Hepatocellular Carcinoma (HCC). *Cancers (Basel)* 2022; **14** [PMID: 35681776 DOI: 10.3390/cancers14112798]
3 **Harris PS**, Hansen RM, Gray ME, Massoud OI, McGuire BM, Shoreibah MG. Hepatocellular carcinoma surveillance: An evidence-based approach. *World J Gastroenterol* 2019; **25**: 1550-1559 [PMID: 30983815 DOI: 10.3748/wjg.v25.i13.1550]
4 **McGlynn KA**, Petrick JL, El-Serag HB. Epidemiology of Hepatocellular Carcinoma. *Hepatology* 2021; **73** Suppl 1: 4-13 [PMID: 32319693 DOI: 10.1002/hep.31288]
5 **Parikh ND**, Tayob N, Al-Jarrah T, Kramer J, Melcher J, Smith D, Marquardt P, Liu PH, Tang R, Kanwal F, Singal AG. Barriers to Surveillance for Hepatocellular Carcinoma in a Multicenter Cohort. *JAMA Netw Open* 2022; **5**: e2223504 [PMID: 35867057 DOI: 10.1001/jamanetworkopen.2022.23504]
6 **Willatt J**, Ruma JA, Azar SF, Dasika NL, Syed F. Imaging of hepatocellular carcinoma and image guided therapies - how we do it. *Cancer Imaging* 2017; **17**: 9 [PMID: 28259177 DOI: 10.1186/s40644-017-0110-z]
7 **Marrero JA**, Kulik LM, Sirlin CB, Zhu AX, Finn RS, Abecassis MM, Roberts LR, Heimbach JK. Diagnosis, Staging, and Management of Hepatocellular Carcinoma: 2018 Practice Guidance by the American Association for the Study of Liver Diseases. *Hepatology* 2018; **68**: 723-750 [PMID: 29624699 DOI: 10.1002/hep.29913]
8 **European Association for the Study of the Liver**. EASL Clinical Practice Guidelines: Management of hepatocellular carcinoma. *J Hepatol* 2018; **69**: 182-236 [PMID: 29628281 DOI: 10.1016/j.jhep.2018.03.019]
9 **Omata M**, Cheng AL, Kokudo N, Kudo M, Lee JM, Jia J, Tateishi R, Han KH, Chawla YK, Shiina S, Jafri W, Payawal DA, Ohki T, Ogasawara S, Chen PJ, Lesmana CRA, Lesmana LA, Gani RA, Obi S, Dokmeci AK, Sarin SK. Asia-Pacific clinical practice guidelines on the management of hepatocellular carcinoma: a 2017 update. *Hepatol Int* 2017; **11**: 317-370 [PMID: 28620797 DOI: 10.1007/s12072-017-9799-9]
10 **Ahn JC**, Lee YT, Agopian VG, Zhu Y, You S, Tseng HR, Yang JD. Hepatocellular carcinoma surveillance: current practice and future directions. *Hepatoma Res* 2022; **8** [PMID: 36161213 DOI: 10.20517/2394-5079.2021.131]
11 **Pocha C**, Dieperink E, McMaken KA, Knott A, Thuras P, Ho SB. Surveillance for hepatocellular cancer with ultrasonography vs. computed tomography -- a randomised study. *Aliment Pharmacol Ther* 2013; **38**: 303-312 [PMID: 23750991 DOI: 10.1111/apt.12370]
12 **Zhang BH**, Yang BH, Tang ZY. Randomized controlled trial of screening for hepatocellular carcinoma. *J Cancer Res Clin Oncol* 2004; **130**: 417-422 [PMID: 15042359 DOI: 10.1007/s00432-004-0552-0]
13 **Morgan TA**, Maturen KE, Dahiya N, Sun MRM, Kamaya A; American College of Radiology Ultrasound Liver Imaging and Reporting Data System (US LI-RADS) Working Group. US LI-RADS: ultrasound liver imaging reporting and data system for screening and surveillance of hepatocellular carcinoma. *Abdom Radiol (NY)* 2018; **43**: 41-55 [PMID: 28936543 DOI: 10.1007/s00261-017-1317-y]
14 **Schoenberger H**, Chong N, Fetzer DT, Rich NE, Yokoo T, Khatri G, Olivares J, Parikh ND, Yopp AC, Marrero JA, Singal AG. Dynamic Changes in Ultrasound Quality for Hepatocellular Carcinoma Screening in Patients With Cirrhosis. *Clin Gastroenterol Hepatol* 2022; **20**: 1561-1569.e4 [PMID: 34119640 DOI: 10.1016/j.cgh.2021.06.012]
15 **Kim SY**, An J, Lim YS, Han S, Lee JY, Byun JH, Won HJ, Lee SJ, Lee HC, Lee YS. MRI With Liver-Specific Contrast for Surveillance of Patients With Cirrhosis at High Risk of Hepatocellular Carcinoma. *JAMA Oncol* 2017; **3**: 456-463 [PMID:

27657493 DOI: 10.1001/jamaoncol.2016.3147]
16 **Tzartzeva K**, Singal AG. Testing for AFP in combination with ultrasound improves early liver cancer detection. *Expert Rev Gastroenterol Hepatol* 2018; **12**: 947-949 [PMID: 30118333 DOI: 10.1080/17474124.2018.1512855]
17 **Tzartzeva K**, Obi J, Rich NE, Parikh ND, Marrero JA, Yopp A, Waljee AK, Singal AG. Surveillance Imaging and Alpha Fetoprotein for Early Detection of Hepatocellular Carcinoma in Patients With Cirrhosis: A Meta-analysis. *Gastroenterology* 2018; **154**: 1706-1718.e1 [PMID: 29425931 DOI: 10.1053/j.gastro.2018.01.064]
18 **Yilmaz N**, Yilmaz UE, Suer K, Goral V, Cakir N. Screening for hepatocellular carcinoma: summary of current guidelines up to 2018. Hepatoma Research. 2018;4:46. DOI:10.20517/2394-5079.2018.49 [DOI: 10.20517/2394-5079.2018.49]
19 **Choi DT**, Kum HC, Park S, Ohsfeldt RL, Shen Y, Parikh ND, Singal AG. Hepatocellular Carcinoma Screening Is Associated With Increased Survival of Patients With Cirrhosis. *Clin Gastroenterol Hepatol* 2019; **17**: 976-987.e4 [PMID: 30616961 DOI: 10.1016/j.cgh.2018.10.031]
20 **Beste LA**, Ioannou GN, Yang Y, Chang MF, Ross D, Dominitz JA. Improved surveillance for hepatocellular carcinoma with a primary care-oriented clinical reminder. *Clin Gastroenterol Hepatol* 2015; **13**: 172-179 [PMID: 24813175 DOI: 10.1016/j.cgh.2014.04.033]
21 **Sherman M**. How to improve HCC surveillance outcomes. *JHEP Rep* 2019; **1**: 460-467 [PMID: 32039398 DOI: 10.1016/j.jhepr.2019.10.007]
22 **Kanmaniraja D**, Dellacerra G, Holder J, Erlichman D, Chernyak V. Liver Imaging Reporting and Data System (LI-RADS) v2018: Review of the CT/MRI Diagnostic Categories. *Can Assoc Radiol J* 2021; **72**: 142-149 [PMID: 32063008 DOI: 10.1177/0846537119888393]
23 **van der Pol CB**, Lim CS, Sirlin CB, McGrath TA, Salameh JP, Bashir MR, Tang A, Singal AG, Costa AF, Fowler K, McInnes MDF. Accuracy of the Liver Imaging Reporting and Data System in Computed Tomography and Magnetic Resonance Image Analysis of Hepatocellular Carcinoma or Overall Malignancy-A Systematic Review. *Gastroenterology* 2019; **156**: 976-986 [PMID: 30445016 DOI: 10.1053/j.gastro.2018.11.020]
24 **Kierans AS**, Song C, Gavlin A, Roudenko A, Lu L, Askin G, Hecht EM. Diagnostic Performance of LI-RADS Version 2018, LI-RADS Version 2017, and OPTN Criteria for Hepatocellular Carcinoma. *AJR Am J Roentgenol* 2020; **215**: 1085-1092 [PMID: 32877248 DOI: 10.2214/AJR.20.22772]
25 **Choi JY**, Lee JM, Sirlin CB. CT and MR imaging diagnosis and staging of hepatocellular carcinoma: part I. Development, growth, and spread: key pathologic and imaging aspects. *Radiology* 2014; **272**: 635-654 [PMID: 25153274 DOI: 10.1148/radiol.14132361]
26 **Kulkarni NM**, Fung A, Kambadakone AR, Yeh BM. Computed Tomography Techniques, Protocols, Advancements, and Future Directions in Liver Diseases. *Magn Reson Imaging Clin N Am* 2021; **29**: 305-320 [PMID: 34243919 DOI: 10.1016/j.mric.2021.05.002]
27 **Hope TA**, Fowler KJ, Sirlin CB, Costa EA, Yee J, Yeh BM, Heiken JP. Hepatobiliary agents and their role in LI-RADS. *Abdom Imaging* 2015; **40**: 613-625 [PMID: 25287679 DOI: 10.1007/s00261-014-0227-5]
28 **Niendorf E**, Spilseth B, Wang X, Taylor A. Contrast Enhanced MRI in the Diagnosis of HCC. *Diagnostics (Basel)* 2015; **5**: 383-398 [PMID: 26854161 DOI: 10.3390/diagnostics5030383]
29 **Schima W**, Heiken J. LI-RADS v2017 for liver nodules: how we read and report. *Cancer Imaging* 2018; **18**: 14 [PMID: 29690933 DOI: 10.1186/s40644-018-0149-5]
30 **Wang G**, Zhu S, Li X. Comparison of values of CT and MRI imaging in the diagnosis of hepatocellular carcinoma and analysis of prognostic factors. *Oncol Lett* 2019; **17**: 1184-1188 [PMID: 30655882 DOI: 10.3892/ol.2018.9690]
31 **Roberts LR**, Sirlin CB, Zaiem F, Almasri J, Prokop LJ, Heimbach JK, Murad MH, Mohammed K. Imaging for the diagnosis of hepatocellular carcinoma: A systematic review and meta-analysis. *Hepatology* 2018; **67**: 401-421 [PMID: 28859233 DOI: 10.1002/hep.29487]
32 **Basha MAA**, AlAzzazy MZ, Ahmed AF, Yousef HY, Shehata SM, El Sammak DAEA, Fathy T, Obaya AA, Abdelbary EH. Does a combined CT and MRI protocol enhance the diagnostic efficacy of LI-RADS in the categorization of hepatic observations? *Eur Radiol* 2018; **28**: 2592-2603 [PMID: 29368164 DOI: 10.1007/s00330-017-5232-y]
33 **Bartolotta TV**, Terranova MC, Gagliardo C, Taibbi A. CEUS LI-RADS: a pictorial review. *Insights Imaging* 2020; **11**: 9 [PMID: 32020352 DOI: 10.1186/s13244-019-0819-2]
34 **Bartolotta TV**, Taibbi A, Midiri M, Lagalla R. Contrast-enhanced ultrasound of hepatocellular carcinoma: where do we stand? *Ultrasonography* 2019; **38**: 200-214 [PMID: 31006227 DOI: 10.14366/usg.18060]
35 **D'Onofrio M**, Crosara S, De Robertis R, Canestrini S, Mucelli RP. Contrast-Enhanced Ultrasound of Focal Liver Lesions. *AJR Am J Roentgenol* 2015; **205**: W56-W66 [PMID: 26102419 DOI: 10.2214/AJR.14.14203]
36 **Zheng SG**, Xu HX, Liu LN. Management of hepatocellular carcinoma: The role of contrast-enhanced ultrasound. *World J Radiol* 2014; **6**: 7-14 [PMID: 24578787 DOI: 10.4329/wjr.v6.i1.7]
37 **Gaiani S**, Celli N, Piscaglia F, Cecilioni L, Losinno F, Giangregorio F, Mancini M, Pini P, Fornari F, Bolondi L. Usefulness of contrast-enhanced perfusional sonography in the assessment of hepatocellular carcinoma hypervascular at spiral computed tomography. *J Hepatol* 2004; **41**: 421-426 [PMID: 15336445 DOI: 10.1016/j.jhep.2004.04.022]
38 **Schwarze V**, Marschner C, Völckers W, Grosu S, Negrão de Figueiredo G, Rübenthaler J, Clevert DA. Diagnostic value of contrast-enhanced ultrasound versus computed tomography for hepatocellular carcinoma: a retrospective, single-center evaluation of 234 patients. *J Int Med Res* 2020; **48**: 300060520930151 [PMID: 32529869 DOI: 10.1177/0300060520930151]
39 **Navin PJ**, Venkatesh SK. Hepatocellular Carcinoma: State of the Art Imaging and Recent Advances. *J Clin Transl Hepatol* 2019; **7**: 72-85 [PMID: 30944823 DOI: 10.14218/JCTH.2018.00032]
40 **Kim SH**, Kamaya A, Willmann JK. CT perfusion of the liver: principles and applications in oncology. *Radiology* 2014; **272**: 322-344 [PMID: 25058132 DOI: 10.1148/radiol.14130091]
41 **Oğul H**, Kantarcı M, Genç B, Pirimoğlu B, Cullu N, Kızrak Y, Yılmaz O, Karabulut N. Perfusion CT imaging of the liver: review of clinical applications. *Diagn Interv Radiol* 2014; **20**: 379-389 [PMID: 24834487 DOI: 10.5152/dir.2014.13396]
42 **Nakamura Y**, Higaki T, Honda Y, Tatsugami F, Tani C, Fukumoto W, Narita K, Kondo S, Akagi M, Awai K. Advanced CT techniques for assessing hepatocellular carcinoma. *Radiol Med* 2021; **126**: 925-935 [PMID: 33954894 DOI:

10.1007/s11547-021-01366-4]
43 **Fischer MA**, Kartalis N, Grigoriadis A, Loizou L, Stål P, Leidner B, Aspelin P, Brismar TB. Perfusion computed tomography for detection of hepatocellular carcinoma in patients with liver cirrhosis. *Eur Radiol* 2015; **25**: 3123-3132 [PMID: 25903707 DOI: 10.1007/s00330-015-3732-1]
44 **Chartampilas E**, Rafailidis V, Georgopoulou V, Kalarakis G, Hatzidakis A, Prassopoulos P. Current Imaging Diagnosis of Hepatocellular Carcinoma. *Cancers (Basel)* 2022; **14** [PMID: 36010991 DOI: 10.3390/cancers14163997]
45 **Bai RJ**, Li JP, Ren SH, Jiang HJ, Liu XD, Ling ZS, Huang Q, Feng GL. A correlation of computed tomography perfusion and histopathology in tumor edges of hepatocellular carcinoma. *Hepatobiliary Pancreat Dis Int* 2014; **13**: 612-617 [PMID: 25475863 DOI: 10.1016/s1499-3872(14)60298-8]
46 **Taouli B**, Johnson RS, Hajdu CH, Oei MT, Merad M, Yee H, Rusinek H. Hepatocellular carcinoma: perfusion quantification with dynamic contrast-enhanced MRI. *AJR Am J Roentgenol* 2013; **201**: 795-800 [PMID: 24059368 DOI: 10.2214/AJR.12.9798]
47 **Aronhime S**, Calcagno C, Jajamovich GH, Dyvorne HA, Robson P, Dieterich D, Fiel MI, Martel-Laferriere V, Chatterji M, Rusinek H, Taouli B. DCE-MRI of the liver: effect of linear and nonlinear conversions on hepatic perfusion quantification and reproducibility. *J Magn Reson Imaging* 2014; **40**: 90-98 [PMID: 24923476 DOI: 10.1002/jmri.24341]
48 **Pahwa S**, Liu H, Chen Y, Dastmalchian S, O'Connor G, Lu Z, Badve C, Yu A, Wright K, Chalian H, Rao S, Fu C, Vallines I, Griswold M, Seiberlich N, Zeng M, Gulani V. Quantitative perfusion imaging of neoplastic liver lesions: A multi-institution study. *Sci Rep* 2018; **8**: 4990 [PMID: 29563601 DOI: 10.1038/s41598-018-20726-1]
49 **Chen BB**, Shih TT. DCE-MRI in hepatocellular carcinoma-clinical and therapeutic image biomarker. *World J Gastroenterol* 2014; **20**: 3125-3134 [PMID: 24695624 DOI: 10.3748/wjg.v20.i12.3125]
50 **Guglielmo FF**, Venkatesh SK, Mitchell DG. Liver MR Elastography Technique and Image Interpretation: Pearls and Pitfalls. *Radiographics* 2019; **39**: 1983-2002 [PMID: 31626569 DOI: 10.1148/rg.2019190034]
51 **Malik P**, Pillai S, Agarwal K, Abdelwahed S, Bhandari R, Singh A, Chidharla A, Patel K, Singh P, Manaktala P, Rabbani R, Koritala T, Gupta S. Diagnostic Accuracy of Elastography and Liver Disease: A Meta-Analysis. *Gastroenterology Res* 2022; **15**: 232-239 [PMID: 36407808 DOI: 10.14740/gr1557]
52 **Venkatesh SK**, Yin M, Glockner JF, Takahashi N, Araoz PA, Talwalkar JA, Ehman RL. MR elastography of liver tumors: preliminary results. *AJR Am J Roentgenol* 2008; **190**: 1534-1540 [PMID: 18492904 DOI: 10.2214/AJR.07.3123]
53 **Singh S**, Fujii LL, Murad MH, Wang Z, Asrani SK, Ehman RL, Kamath PS, Talwalkar JA. Liver stiffness is associated with risk of decompensation, liver cancer, and death in patients with chronic liver diseases: a systematic review and meta-analysis. *Clin Gastroenterol Hepatol* 2013; **11**: 1573-84.e1 [PMID: 23954643 DOI: 10.1016/j.cgh.2013.07.034]
54 **Cho HJ**, Kim B, Kim HJ, Huh J, Kim JK, Lee JH, Seo CW, Ahn HR, Eun JW, Kim SS, Cho SW, Cheong JY. Liver stiffness measured by MR elastography is a predictor of early HCC recurrence after treatment. *Eur Radiol* 2020; **30**: 4182-4192 [PMID: 32189053 DOI: 10.1007/s00330-020-06792-y]
55 **Gordic S**, Ayache JB, Kennedy P, Besa C, Wagner M, Bane O, Ehman RL, Kim E, Taouli B. Value of tumor stiffness measured with MR elastography for assessment of response of hepatocellular carcinoma to locoregional therapy. *Abdom Radiol (NY)* 2017; **42**: 1685-1694 [PMID: 28154910 DOI: 10.1007/s00261-017-1066-y]
56 **Zhang L**, Chen J, Jiang H, Rong D, Guo N, Yang H, Zhu J, Hu B, He B, Yin M, Venkatesh SK, Ehman RL, Wang J. MR elastography as a biomarker for prediction of early and late recurrence in HBV-related hepatocellular carcinoma patients before hepatectomy. *Eur J Radiol* 2022; **152**: 110340 [PMID: 35580445 DOI: 10.1016/j.ejrad.2022.110340]
57 **Qayyum A**, Hwang KP, Stafford J, Verma A, Maru DM, Sandesh S, Sun J, Pestana RC, Avritscher R, Hassan MM, Amin H, Rashid A, Wistuba II, Ehman RL, Ma J, Kaseb AO. Immunotherapy response evaluation with magnetic resonance elastography (MRE) in advanced HCC. *J Immunother Cancer* 2019; **7**: 329 [PMID: 31779702 DOI: 10.1186/s40425-019-0766-y]
58 **Taylor AJ**, Salerno M, Dharmakumar R, Jerosch-Herold M. T1 Mapping: Basic Techniques and Clinical Applications. *JACC Cardiovasc Imaging* 2016; **9**: 67-81 [PMID: 26762877 DOI: 10.1016/j.jcmg.2015.11.005]
59 **Hoffman DH**, Ayoola A, Nickel D, Han F, Chandarana H, Shanbhogue KP. T1 mapping, T2 mapping and MR elastography of the liver for detection and staging of liver fibrosis. *Abdom Radiol (NY)* 2020; **45**: 692-700 [PMID: 31875241 DOI: 10.1007/s00261-019-02382-9]
60 **Katsube T**, Okada M, Kumano S, Hori M, Imaoka I, Ishii K, Kudo M, Kitagaki H, Murakami T. Estimation of liver function using T1 mapping on Gd-EOB-DTPA-enhanced magnetic resonance imaging. *Invest Radiol* 2011; **46**: 277-283 [PMID: 21343827 DOI: 10.1097/RLI.0b013e318200f67d]
61 **Peng Z**, Jiang M, Cai H, Chan T, Dong Z, Luo Y, Li ZP, Feng ST. Gd-EOB-DTPA-enhanced magnetic resonance imaging combined with T1 mapping predicts the degree of differentiation in hepatocellular carcinoma. *BMC Cancer* 2016; **16**: 625 [PMID: 27520833 DOI: 10.1186/s12885-016-2607-4]
62 **Peng Z**, Li C, Chan T, Cai H, Luo Y, Dong Z, Li ZP, Feng ST. Quantitative evaluation of Gd-EOB-DTPA uptake in focal liver lesions by using T1 mapping: differences between hepatocellular carcinoma, hepatic focal nodular hyperplasia and cavernous hemangioma. *Oncotarget* 2017; **8**: 65435-65444 [PMID: 29029443 DOI: 10.18632/oncotarget.18918]
63 **Mio M**, Fujiwara Y, Tani K, Toyofuku T, Maeda T, Inoue T. Quantitative evaluation of focal liver lesions with T1 mapping using a phase-sensitive inversion recovery sequence on gadoxetic acid-enhanced MRI. *Eur J Radiol Open* 2021; **8**: 100312 [PMID: 33392362 DOI: 10.1016/j.ejro.2020.100312]
64 **Rao C**, Wang X, Li M, Zhou G, Gu H. Value of T1 mapping on gadoxetic acid-enhanced MRI for microvascular invasion of hepatocellular carcinoma: a retrospective study. *BMC Med Imaging* 2020; **20**: 43 [PMID: 32345247 DOI: 10.1186/s12880-020-00433-y]
65 **Kele PG**, van der Jagt EJ. Diffusion weighted imaging in the liver. *World J Gastroenterol* 2010; **16**: 1567-1576 [PMID: 20355235 DOI: 10.3748/wjg.v16.i13.1567]
66 **Saito K**, Tajima Y, Harada TL. Diffusion-weighted imaging of the liver: Current applications. *World J Radiol* 2016; **8**: 857-867 [PMID: 27928467 DOI: 10.4329/wjr.v8.i11.857]
67 **Shankar S**, Kalra N, Bhatia A, Srinivasan R, Singh P, Dhiman RK, Khandelwal N, Chawla Y. Role of Diffusion Weighted Imaging (DWI) for Hepatocellular Carcinoma (HCC) Detection and its Grading on 3T MRI: A Prospective Study. *J Clin*

Exp Hepatol 2016; **6**: 303-310 [PMID: 28003720 DOI: 10.1016/j.jceh.2016.08.012]

68 **Surov A**, Pech M, Omari J, Fischbach F, Damm R, Fischbach K, Powerski M, Relja B, Wienke A. Diffusion-Weighted Imaging Reflects Tumor Grading and Microvascular Invasion in Hepatocellular Carcinoma. *Liver Cancer* 2021; **10**: 10-24 [PMID: 33708636 DOI: 10.1159/000511384]

69 **Jing M**, Cao Y, Zhang P, Zhang B, Lin X, Deng L, Han T, Zhou J. The Benefit of Apparent Diffusion Coefficient in Evaluating the Invasiveness of Hepatocellular Carcinoma. *Front Oncol* 2021; **11**: 719480 [PMID: 34504795 DOI: 10.3389/fonc.2021.719480]

70 **Ludwig JM**, Camacho JC, Kokabi N, Xing M, Kim HS. The Role of Diffusion-Weighted Imaging (DWI) in Locoregional Therapy Outcome Prediction and Response Assessment for Hepatocellular Carcinoma (HCC): The New Era of Functional Imaging Biomarkers. *Diagnostics (Basel)* 2015; **5**: 546-563 [PMID: 26854170 DOI: 10.3390/diagnostics5040546]

71 **Yuan Z**, Zhang J, Yang H, Ye XD, Xu LC, Li WT. Diffusion-Weighted MR Imaging of Hepatocellular Carcinoma: Current Value in Clinical Evaluation of Tumor Response to Locoregional Treatment. *J Vasc Interv Radiol* 2016; **27**: 20-30; quiz 31 [PMID: 26621785 DOI: 10.1016/j.jvir.2015.10.003]

72 **Kokabi N**, Camacho JC, Xing M, Qiu D, Kitajima H, Mittal PK, Kim HS. Apparent diffusion coefficient quantification as an early imaging biomarker of response and predictor of survival following yttrium-90 radioembolization for unresectable infiltrative hepatocellular carcinoma with portal vein thrombosis. *Abdom Imaging* 2014; **39**: 969-978 [PMID: 24740759 DOI: 10.1007/s00261-014-0127-8]

73 **Elrefaey Hasan BM**, Abd ElHamid HAE, Khater NH, ElGendy W, Abdelrahman AS. Role of DWI in evaluation of HCC after radiofrequency ablation compared to dynamic MRI using MRI (3 T). *Egyptian J Radiol Nucl Med* 2021; **52**: 267 [DOI: 10.1186/s43055-021-00647-2]

74 **Granata V**, Fusco R, Filice S, Incollingo P, Belli A, Izzo F, Petrillo A. Comment on "State of the art in magnetic resonance imaging of hepatocellular carcinoma": the role of DWI. *Radiol Oncol* 2019; **53**: 369-370 [PMID: 31318697 DOI: 10.2478/raon-2019-0031]

75 **Qayyum A**. MR spectroscopy of the liver: principles and clinical applications. *Radiographics* 2009; **29**: 1653-1664 [PMID: 19959513 DOI: 10.1148/rg.296095520]

76 **Wang D**, Li Y. 1H Magnetic Resonance Spectroscopy Predicts Hepatocellular Carcinoma in a Subset of Patients With Liver Cirrhosis: A Randomized Trial. *Medicine (Baltimore)* 2015; **94**: e1066 [PMID: 26166077 DOI: 10.1097/MD.0000000000001066]

77 **Zhang L**, Zhao X, Ouyang H, Wang S, Zhou C. Diagnostic value of 3.0T (1)H MRS with choline-containing compounds ratio (ΔCCC) in primary malignant hepatic tumors. *Cancer Imaging* 2016; **16**: 25 [PMID: 27549094 DOI: 10.1186/s40644-016-0082-4]

78 **Yang K**, Zhang XM, Yang L, Xu H, Peng J. Advanced imaging techniques in the therapeutic response of transarterial chemoembolization for hepatocellular carcinoma. *World J Gastroenterol* 2016; **22**: 4835-4847 [PMID: 27239110 DOI: 10.3748/wjg.v22.i20.4835]

79 **Kuo YT**, Li CW, Chen CY, Jao J, Wu DK, Liu GC. In vivo proton magnetic resonance spectroscopy of large focal hepatic lesions and metabolite change of hepatocellular carcinoma before and after transcatheter arterial chemoembolization using 3.0-T MR scanner. *J Magn Reson Imaging* 2004; **19**: 598-604 [PMID: 15112309 DOI: 10.1002/jmri.20046]

80 **Chen CY**, Li CW, Kuo YT, Jaw TS, Wu DK, Jao JC, Hsu JS, Liu GC. Early response of hepatocellular carcinoma to transcatheter arterial chemoembolization: choline levels and MR diffusion constants--initial experience. *Radiology* 2006; **239**: 448-456 [PMID: 16569781 DOI: 10.1148/radiol.2392042202]

81 **Jeong WK**, Jamshidi N, Felker ER, Raman SS, Lu DS. Radiomics and radiogenomics of primary liver cancers. *Clin Mol Hepatol* 2019; **25**: 21-29 [PMID: 30441889 DOI: 10.3350/cmh.2018.1007]

82 **Gillies RJ**, Kinahan PE, Hricak H. Radiomics: Images Are More than Pictures, They Are Data. *Radiology* 2016; **278**: 563-577 [PMID: 26579733 DOI: 10.1148/radiol.2015151169]

83 **Shur JD**, Doran SJ, Kumar S, Ap Dafydd D, Downey K, O'Connor JPB, Papanikolaou N, Messiou C, Koh DM, Orton MR. Radiomics in Oncology: A Practical Guide. *Radiographics* 2021; **41**: 1717-1732 [PMID: 34597235 DOI: 10.1148/rg.2021210037]

84 **van Timmeren JE**, Cester D, Tanadini-Lang S, Alkadhi H, Baessler B. Radiomics in medical imaging-"how-to" guide and critical reflection. *Insights Imaging* 2020; **11**: 91 [PMID: 32785796 DOI: 10.1186/s13244-020-00887-2]

85 **Gong XQ**, Tao YY, Wu YK, Liu N, Yu X, Wang R, Zheng J, Huang XH, Li JD, Yang G, Wei XQ, Yang L, Zhang XM. Progress of MRI Radiomics in Hepatocellular Carcinoma. *Front Oncol* 2021; **11**: 698373 [PMID: 34616673 DOI: 10.3389/fonc.2021.698373]

86 **Fu J**, Cao SJ, Song L, Tong XQ, Wang J, Yang M, Zou YH. Radiomics/Radiogenomics in hepatocellular carcinoma: Applications and challenges in interventional management. *iLIVER* 2022; **1**: 96-100 [DOI: 10.1016/j.iliver.2022.07.001]

87 **Yao S**, Ye Z, Wei Y, Jiang HY, Song B. Radiomics in hepatocellular carcinoma: A state-of-the-art review. *World J Gastrointest Oncol* 2021; **13**: 1599-1615 [PMID: 34853638 DOI: 10.4251/wjgo.v13.i11.1599]

88 **Lewis S**, Peti S, Hectors SJ, King M, Rosen A, Kamath A, Putra J, Thung S, Taouli B. Volumetric quantitative histogram analysis using diffusion-weighted magnetic resonance imaging to differentiate HCC from other primary liver cancers. *Abdom Radiol (NY)* 2019; **44**: 912-922 [PMID: 30712136 DOI: 10.1007/s00261-019-01906-7]

89 **Banerjee S**, Wang DS, Kim HJ, Sirlin CB, Chan MG, Korn RL, Rutman AM, Siripongsakun S, Lu D, Imanbayev G, Kuo MD. A computed tomography radiogenomic biomarker predicts microvascular invasion and clinical outcomes in hepatocellular carcinoma. *Hepatology* 2015; **62**: 792-800 [PMID: 25930992 DOI: 10.1002/hep.27877]

90 **Zhong X**, Long H, Su L, Zheng R, Wang W, Duan Y, Hu H, Lin M, Xie X. Radiomics models for preoperative prediction of microvascular invasion in hepatocellular carcinoma: a systematic review and meta-analysis. *Abdom Radiol (NY)* 2022; **47**: 2071-2088 [PMID: 35364684 DOI: 10.1007/s00261-022-03496-3]

91 **Hectors SJ**, Lewis S, Besa C, King MJ, Said D, Putra J, Ward S, Higashi T, Thung S, Yao S, Laface I, Schwartz M, Gnjatic S, Merad M, Hoshida Y, Taouli B. MRI radiomics features predict immuno-oncological characteristics of hepatocellular carcinoma. *Eur Radiol* 2020; **30**: 3759-3769 [PMID: 32086577 DOI: 10.1007/s00330-020-06675-2]

92 **Niu XK**, He XF. Development of a computed tomography-based radiomics nomogram for prediction of transarterial

chemoembolization refractoriness in hepatocellular carcinoma. *World J Gastroenterol* 2021; **27**: 189-207 [PMID: 33510559 DOI: 10.3748/wjg.v27.i2.189]

93 **Kong C**, Zhao Z, Chen W, Lv X, Shu G, Ye M, Song J, Ying X, Weng Q, Weng W, Fang S, Chen M, Tu J, Ji J. Prediction of tumor response *via* a pretreatment MRI radiomics-based nomogram in HCC treated with TACE. *Eur Radiol* 2021; **31**: 7500-7511 [PMID: 33860832 DOI: 10.1007/s00330-021-07910-0]

94 **Sheen H**, Kim JS, Lee JK, Choi SY, Baek SY, Kim JY. A radiomics nomogram for predicting transcatheter arterial chemoembolization refractoriness of hepatocellular carcinoma without extrahepatic metastasis or macrovascular invasion. *Abdom Radiol (NY)* 2021; **46**: 2839-2849 [PMID: 33388805 DOI: 10.1007/s00261-020-02884-x]

95 **Bai H**, Meng S, Xiong C, Liu Z, Shi W, Ren Q, Xia W, Zhao X, Jian J, Song Y, Ni C, Gao X, Li Z. Preoperative CECT-based Radiomic Signature for Predicting the Response of Transarterial Chemoembolization (TACE) Therapy in Hepatocellular Carcinoma. *Cardiovasc Intervent Radiol* 2022; **45**: 1524-1533 [PMID: 35896687 DOI: 10.1007/s00270-022-03221-z]

96 **Zhao Y**, Wang N, Wu J, Zhang Q, Lin T, Yao Y, Chen Z, Wang M, Sheng L, Liu J, Song Q, Wang F, An X, Guo Y, Li X, Wu T, Liu AL. Radiomics Analysis Based on Contrast-Enhanced MRI for Prediction of Therapeutic Response to Transarterial Chemoembolization in Hepatocellular Carcinoma. *Front Oncol* 2021; **11**: 582788 [PMID: 33868988 DOI: 10.3389/fonc.2021.582788]

World Journal of Radiology

Submit a Manuscript: https://www.f6publishing.com

World J Radiol 2023 March 28; 15(3): 69-82

DOI: 10.4329/wjr.v15.i3.69

ISSN 1949-8470 (online)

MINIREVIEWS

Multi-modality parathyroid imaging: A shifting paradigm

Shrea Gulati, Sunil Chumber, Gopal Puri, Stanzin Spalkit, N A Damle, CJ Das

Specialty type: Radiology, nuclear medicine and medical imaging

Provenance and peer review: Invited article; Externally peer reviewed.

Peer-review model: Single blind

Peer-review report's scientific quality classification

Grade A (Excellent): 0
Grade B (Very good): 0
Grade C (Good): C, C
Grade D (Fair): 0
Grade E (Poor): 0

P-Reviewer: Nambi G, Saudi Arabia; Wu SZ, China

Received: December 24, 2022
Peer-review started: December 24, 2022
First decision: January 3, 2023
Revised: January 20, 2023
Accepted: March 1, 2023
Article in press: March 1, 2023
Published online: March 28, 2023

Shrea Gulati, Stanzin Spalkit, CJ Das, Department of Radiodiagnosis and Interventional Radiology, All India Institute of Medical Sciences, New Delhi 110029, Delhi, India

Sunil Chumber, Gopal Puri, Department of Surgical Disciplines, All India Institute of Medical Sciences, New Delhi 110029, Delhi, India

N A Damle, Department of Nuclear Medicine, All India Institute of Medical Sciences, New Delhi 110029, Delhi, India

Corresponding author: CJ Das, FRCP, MBBS, MD, Professor, Department of Radiodiagnosis and Interventional Radiology, All India Institute of Medical Sciences, Aurobindo Marg Ansari Nagar, New Delhi 110029, Delhi, India. docchandan17@gmail.com

Abstract

The goal of parathyroid imaging in hyperparathyroidism is not diagnosis, rather it is the localization of the cause of hyperparathyroidism for planning the best therapeutic approach. Hence, the role of imaging to accurately and precisely localize the abnormal parathyroid tissue is more important than ever to facilitate minimally invasive parathyroidectomy over bilateral neck exploration. The common causes include solitary parathyroid adenoma, multiple parathyroid adenomas, parathyroid hyperplasia and parathyroid carcinoma. It is highly imperative for the radiologist to be cautious of the mimics of parathyroid lesions like thyroid nodules and lymph nodes and be able to differentiate them on imaging. The various imaging modalities available include high resolution ultrasound of the neck, nuclear imaging studies, four-dimensional computed tomography (4D CT) and magnetic resonance imaging. Contrast enhanced ultrasound is a novel technique which has been recently added to the armamentarium to differentiate between parathyroid adenomas and its mimics. Through this review article we wish to review the imaging features of parathyroid lesions on various imaging modalities and present an algorithm to guide their radiological differentiation from mimics.

Key Words: Parathyroid adenoma; Ultrasound; Four-dimensional computed tomography; Magnetic resonance imaging; Nuclear Imaging; Contrast enhanced ultrasound

©The Author(s) 2023. Published by Baishideng Publishing Group Inc. All rights reserved.

Core Tip: Parathyroid adenoma is the commonest cause of primary hyperparathyroidism, the management of which lies in definitive surgery. Accurate preoperative imaging is of prime importance to facilitate surgery. Imaging modalities include radiological investigations like ultrasound, four-dimensional computed tomography and magnetic resonance imaging which provide anatomical localization and nuclear scans like MIBI, single photon emission computed tomography and Fluoro-choline positron emission tomography which provide functional imaging details. Contrast-enhanced ultrasound is a novel modality which is being explored in the evaluation of parathyroid adenomas.

Citation: Gulati S, Chumber S, Puri G, Spalkit S, Damle NA, Das CJ. Multi-modality parathyroid imaging: A shifting paradigm. *World J Radiol* 2023; 15(3): 69-82
URL: https://www.wjgnet.com/1949-8470/full/v15/i3/69.htm
DOI: https://dx.doi.org/10.4329/wjr.v15.i3.69

INTRODUCTION

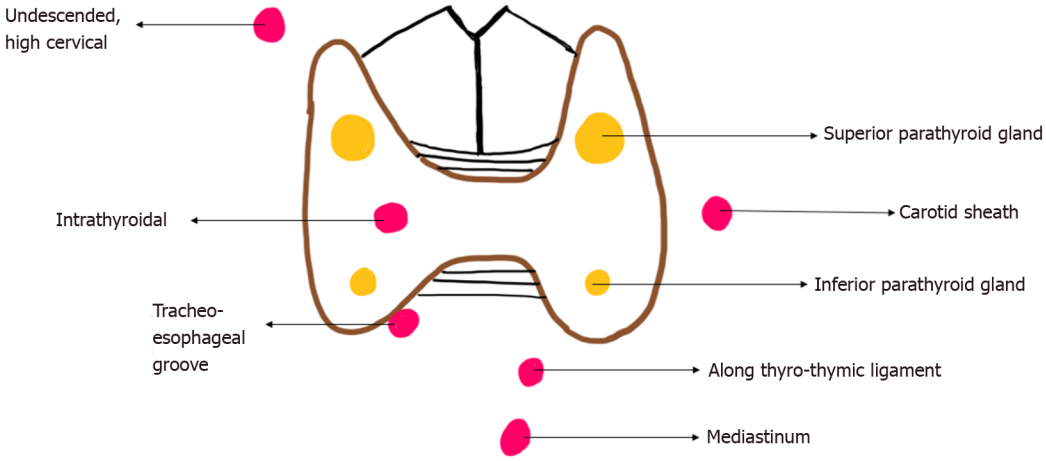
Primary hyperparathyroidism is the commonest cause of hypercalcemia resulting from pathologies intrinsic to the parathyroid glands[1]. It manifests biochemically as raised parathyroid hormone and calcium levels[2]. Primary hyperparathyroidism is most commonly due to a single benign parathyroid adenoma (approximately 80% of the patients), with multiglandular disease seen in approximately 15%-20% of patients[3]. Primary hyperparathyroidism is due to multiglandular involvement consisting of either multiple adenomas or hyperplasia of all 4 glands (5%-10%) and very rarely by parathyroid carcinoma (< 1%)[4]. The definitive management is achieved by surgical excision of the abnormal parathyroid tissue. Preoperative imaging is mandatory in deciding the surgical approach and improves localisation of the abnormal gland. The commonly accepted modalities to guide imaging include ultrasound, 4-dimensional computed tomography (4D CT), magnetic resonance imaging (MRI) and nuclear medicine studies whereas contrast-enhanced ultrasound (CEUS) is the new kid on the block. In this review, we would like to revisit the characteristic imaging findings on various modalities and will present an algorithm of differentiating parathyroid adenomas from their mimics.

ANATOMY

The usual number of parathyroid glands is four, but this can vary. Some persons have more than four parathyroid glands. The normal shape of the parathyroid gland is ovoid or bean shaped and it measures 4-6 mm in length, 2-4 mm in width and 1-2 mm in thickness. The plane of the recurrent laryngeal nerve (RLN), identified by the trachea-oesophageal groove helps identify the superior and inferior parathyroid glands, the superior is posterior to the RLN while the inferior is anterior to the RLN[5]. In 16 % of the individuals the parathyroid glands are ectopically located[6]. The embryological origin of the inferior parathyroid glands is from the third pharyngeal pouch while the origin of the superior parathyroid gland is from the fourth pharyngeal pouch. The longer course of embryological migration of the superior parathyroid glands makes it more prone for ectopic location. Ectopic superior parathyroid glands are found in the retropharyngeal or retroesophageal locations, while ectopic inferior parathyroid glands may be seen within the carotid sheath or mediastinum (Figure 1)[7]. Uncommonly, there may be failure of descent of the inferior parathyroid glands, which may be finally located cephalad to the superior parathyroid glands[8].

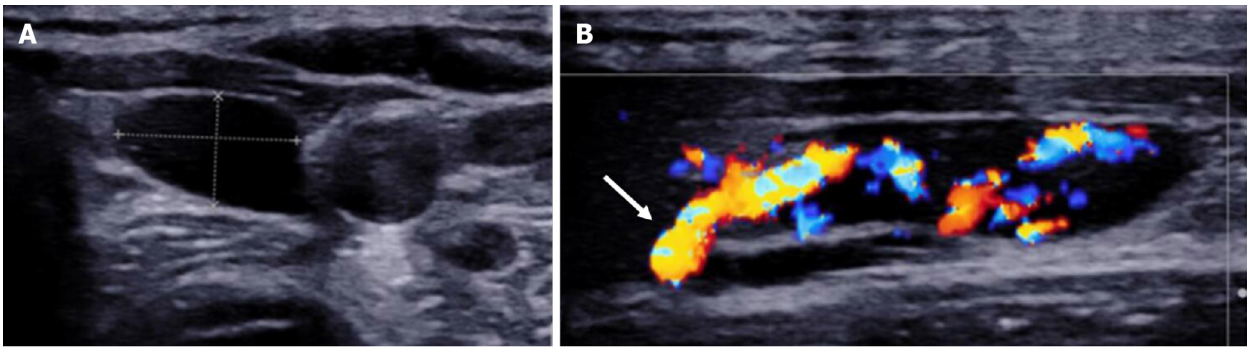
ROLE OF IMAGING

The diagnosis of primary hyperparathyroidism is made biochemically with demonstration of raised parathormone (PTH) levels. The role of radiology in hyperparathyroidism is not diagnosis, rather it is accurate localisation and surgical planning[5]. There are two approaches to surgical management of hyperparathyroidism - bilateral neck exploration (BNE) and minimally invasive parathyroidectomy (MIP). BNE is the conventional surgical approach which involves a large midline surgical incision, exploration and examination of all four parathyroid glands and excision of the abnormal tissue. Due to the large incision involved and meticulous exploration, it is associated with excellent long term cure rates[9]. The downside of this meticulousness is the associated higher risk of recurrent laryngeal nerve damage and poor cosmesis. MIP involves a unilateral small incision on the affected side and surgical removal of only the pathological gland identified precisely and accurately by preoperative imaging studies[5]. As per the European Society of Endocrine Surgeons, in experienced hands, keeping in view



DOI: 10.4329/wjr.v15.i3.69 **Copyright** ©The Author(s) 2023.

Figure 1 Diagrammatic representation of location of eutopic (yellow) and ectopic (red) parathyroid glands.



DOI: 10.4329/wjr.v15.i3.69 **Copyright** ©The Author(s) 2023.

Figure 2 Left inferior parathyroid adenoma. A: High resolution ultrasound image of the neck in the transverse plane demonstrates a well-circumscribed homogenously hypoechoic ovoid lesion located at the lower pole of the left lobe of thyroid gland; B: Colour Doppler shows a big feeding vessel, likely from the inferior thyroid artery (arrow) supplying the lesion.

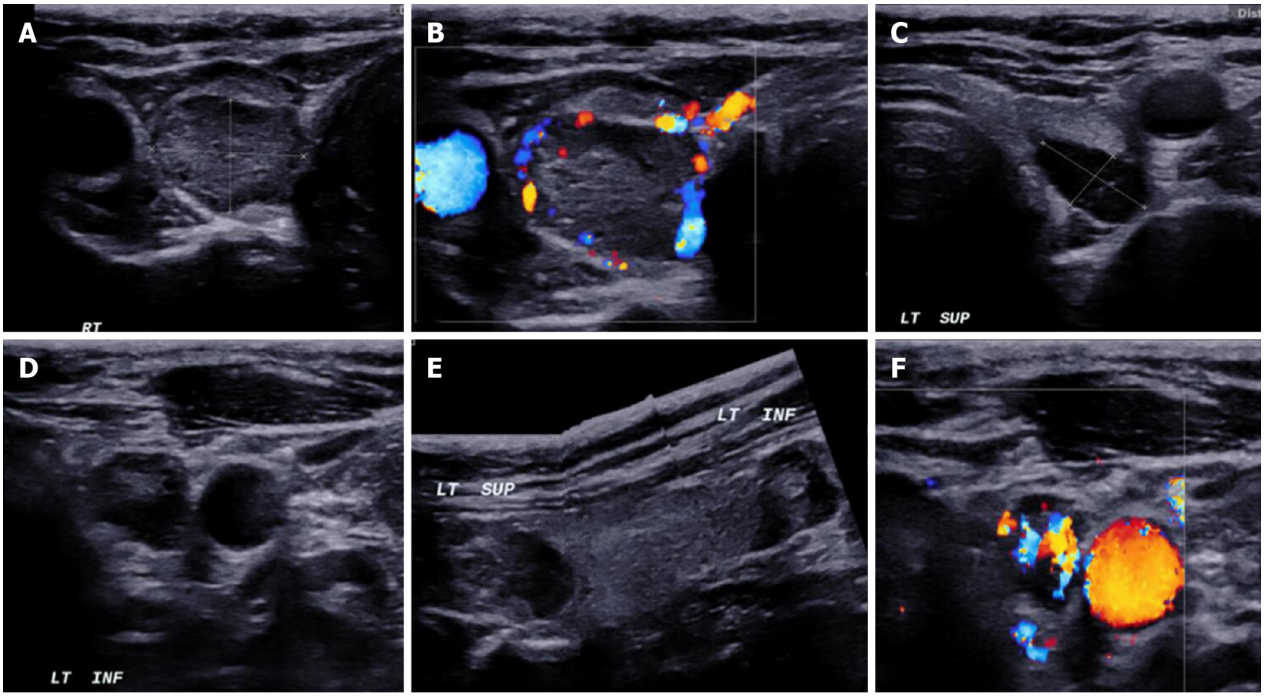
the indications and contraindications of the surgery, MIP is a reliable and safe procedure with equivalent cure rates[9]. As compared to BNE, MIP is associated with shorter operative times, better cosmesis, shorter hospital stays and therefore lower costs[10].

IMAGING

The imaging techniques available for parathyroid imaging include high resolution ultrasound of the neck, Tc99m sestamibi scan, 4D CT and MRI.

HIGH RESOLUTION ULTRASONOGRAPHY

Duplex ultrasound with a linear array transducer with 10 MHz or higher frequency is used for imaging of the parathyroid glands. With the patient in supine position and mild neck extension (using a pillow under the upper back), the neck is scanned in both transverse and longitudinal planes focusing on the region behind the thyroid gland. The normal location of parathyroid glands lesions is lateral to the trachea and oesophagus and medial to the carotid artery and the jugular vein. This knowledge helps to closely inspect the expected locations meanwhile differentiating it from close mimics. The small size and deep location of the normal parathyroid gland makes it non-identifiable on ultrasound. Parathyroid adenomas which are larger than 1 cm in size are readily visible on ultrasound. The sonographic detection of small parathyroid adenomas, especially those < 1 cm in size can be enhanced by using graded compression technique[11]. Parathyroid adenomas are oval/bean shaped, well circumscribed lesions which are homogenously hypoechoic as compared to the neighbouring thyroid gland (Figure 2). Color Doppler provides associate information of the origin and course of the feeding artery of the



DOI: 10.4329/wjr.v15.i3.69 **Copyright** ©The Author(s) 2023.

Figure 3 In a patient with MEN-1 syndrome. A-F: Ultrasound neck images show multiple (3) parathyroid adenoma in the right superior and left superior and inferior parathyroid glands respectively.

parathyroid adenoma[12,13]. This is attributed to the high vascularity of the parathyroid adenomas which are supplied by an enlarged feeding inferior thyroidal artery (Feeding vessel sign). Spectral Doppler can determine the blood flow velocity of the feeding artery and get information of a low resistive index. This polar vascularity sign helps in differentiation from a lymph node which typically shows central hilar vascularity on Doppler[14]. Along with hypervascularity of the affected parathyroid, the ipsilateral thyroid gland can also show hyperaemia in 85% of the cases and this may serve as a surrogate marker of underlying parathyroid adenoma[11,14]. In patients with known syndromes like MEN-1 (Figure 3), multiple adenomas can be seen and identification of a single adenoma should not lead to a false sense of satisfaction of search. Uncommonly, parathyroid adenomas can show atypical features such as ectopic location, completely intrathyroidal location, internal areas of cystic degeneration, heterogenous internal echotexture rather than the homogenous hypoechoic echotexture which make prospective sonographic diagnosis difficult[15-18].

High resolution ultrasound has the advantage of non-involvement of radiation, low cost and easy availability. Although ultrasound is highly operator dependant in the detection of parathyroid adenomas, it has a sensitivity of 84% in the hands of an experienced sonologist[19]. The two most important differentials of parathyroid adenomas are thyroid nodules and lymph nodes, and ultrasound is a useful modality for their differentiation (Table 1). The oesophagus and the longus colli muscle can sometimes mimic parathyroid adenomas[14].

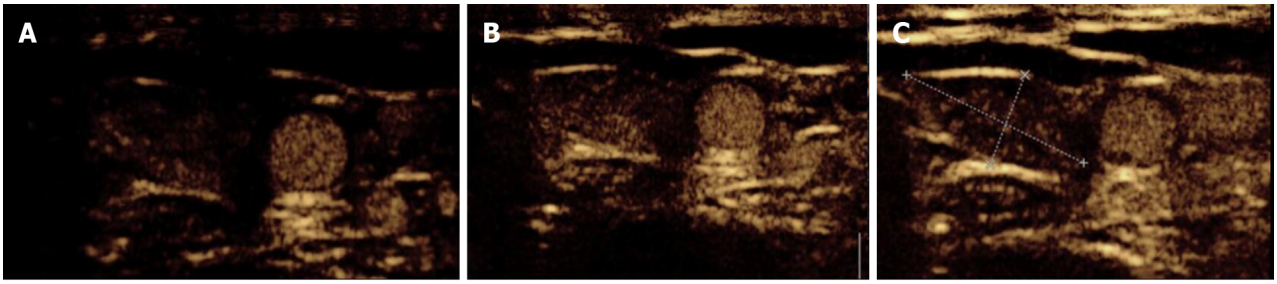
CEUS

CEUS is the new armamentarium added in the evaluation of parathyroid adenomas. The differentiation of parathyroid adenomas from parathyroid hyperplasia as well as non-parathyroid lesions like lymph nodes and thyroid nodules is difficult on conventional ultrasound[7,20]. Studies have demonstrated the use of contrast enhanced ultrasound as a novel technique in the differentiation of these entities[21-23]. On CEUS, parathyroid adenomas show early peripheral hyperenhancement with central washout in the later phases (Figure 4)[21]. Parathyroid hyperplasia on the other hand shows more homogenous contrast uptake[21]. Physiological lymph nodes show homogenous and centrifugal pattern of enhancement[24-26]. Thyroid nodules tend to show homogenous hyperenhancement with a fast wash-in and slow washout pattern[21].

Table 1 Differentiating features of parathyroid adenoma from lymph nodes and thyroid nodules on imaging

Modality	Features	Parathyroid adenoma	Thyroid nodule	Lymph node
USG	Echogenicity	Homogenously markedly hypoechoic	Homo/Heterogenously hypo/isoechoic	Central echogenic hilum
	Vascularity	Peripheral polar vessel sign present	Not seen	Central/hilar vascularity
	Calcification	Less common	Common	+/-
	Cystic changes	Less common	More common	+/-
CT	Non contrast	Hypodense	Hyperdense	Hypodense
	Arterial	Intense arterial enhancement	Enhancement in arterial phase but less than parathyroid adenomas	No enhancement in the arterial phase
	Venous	Washout	Persistent enhancement	Progressive enhancement in venous phase
MRI	Morphology	Cleavage plane with thyroid gland	No cleavage plane	Cleavage plane present
	Diffusion weighted Image	High SI		High SI
PET Choline	Uptake	Present	Variable	Uptake may be present, however is delayed and of lesser intensity

USG: Ultrasound; CT: Computed tomography; MRI: Magnetic resonance imaging; SI: Signal intensity; PET: Positron emission tomography.



DOI: 10.4329/wjr.v15.i3.69 **Copyright** ©The Author(s) 2023.

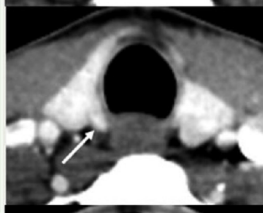
Figure 4 Contrast-enhanced ultrasound in parathyroid adenoma. A-C: A 33-year-old female with raised parathormone levels (87 IU) was assessed using contrast enhanced ultrasound. A circumscribed lesion at the lower pole of the left lobe of thyroid gland was found consistent with parathyroid adenoma, demonstrating early peripheral enhancement with central washout.

SHEAR WAVE ELASTOGRAPHY

This is a newer modality which has been explored for distinguishing parathyroid adenoma from the neighbouring thyroid tissue. Parathyroid adenomas show a significantly lower tissue elasticity than thyroid tissue. This may serve as an additional differentiating feature between the two entities[27].

PARATHYROID SCINTIGRAPHY

The most common radiotracer used for imaging parathyroid glands is sestamibi with ^{99m}Tc. Both thyroid and parathyroid glands take up sestamibi, however the differentiating point is that the uptake by hyperplastic or adenomatous parathyroid tissue is more intense, and also shows a delayed wash-out as compared to thyroid tissue which shows faster wash-out[28]. Therefore, foci of increased radiotracer uptake persisting on a delayed scan (variably acquired at 60-180 min after radio-tracer administration) represents parathyroid tissue. Subtracting images acquired by using two radio-tracer agents, the first one which is taken up by both thyroid and parathyroid tissue (like sestamibi) and a second which is taken up by only thyroid tissue (^{99m}Tc pertechnetate or ^{123}I) can help image the parathyroid. This was the basis of the famous Thallium- Technetium subtraction scan. However, this technique is less used these days due to the availability of more effective radiotracer, sestamibi.

S no.	Phase of CT	Region scanned	Time delay after start of contrast injection	Imaging features	Representative image
1	Non-contrast	Hyoid bone to clavicle	-	Hypodense (as compared to the thyroid gland which is hyperdense)	
2	Arterial phase	Angle of mandible to carina	25 s	Hyperenhancement on the arterial phase	
3	Delayed (venous phase)	Angle of mandible to carina	80 s	Washout on the venous phase	

DOI: 10.4329/wjr.v15.i3.69 **Copyright** ©The Author(s) 2023.

Figure 5 Imaging features of parathyroid adenomas on four-dimensional computed tomography. CT: Computed tomography.

4D CT

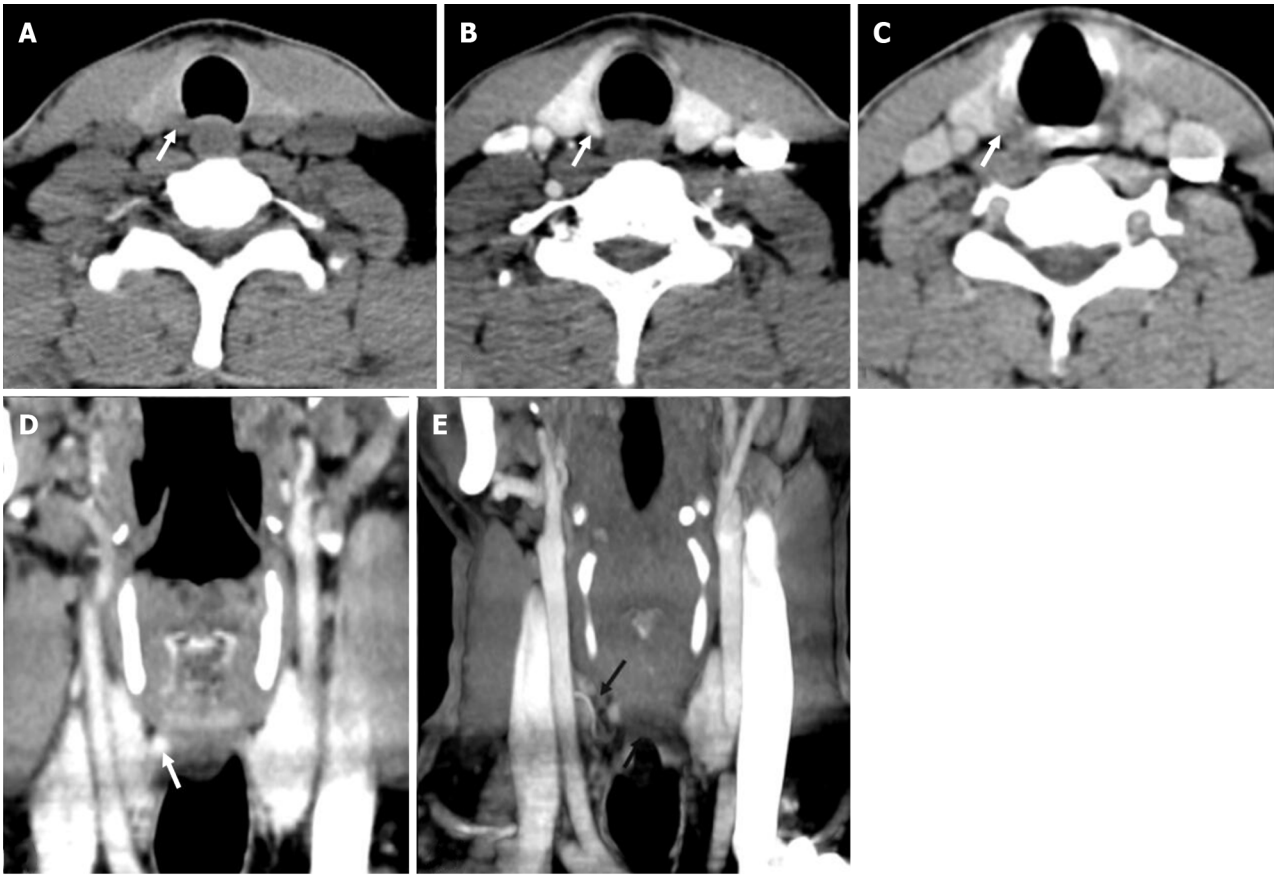
4D CT is advantageous over both ultrasonography and nuclear imaging studies in the precise localisation of both orthotopic and ectopic glands and better differentiation of parathyroid adenomas from mimics like lymph nodes and thyroid nodules (Table 1)[29]. 4D-CT demonstrates an accuracy of 93%. 4D-CT has a suboptimal 44% sensitivity, but 100% specificity, for multigland disease[30].

The first three dimensions in 4D CT are the three planes of image interpretation - axial, sagittal and coronal, while the fourth dimension refers to the change in enhancement pattern with time in the non-contrast, arterial and delayed (venous) phases (Figure 5).

Streak artifacts from hyperattenuating materials like high density contrast in neck vessels and surgical clips can hamper evaluation. The streak artifact caused by venous pooling may be prevented by using a saline chase after contrast injection[29]. The beam hardening artifact caused by clavicles and the shoulder girdle can interfere with interpretation of imaging findings which may be reduced by neck elevation achieved by putting a rolled towel under the shoulders[29]. In addition, patients are advised to avoid speaking, swallowing or coughing during image acquisition to avoid motion artifacts.

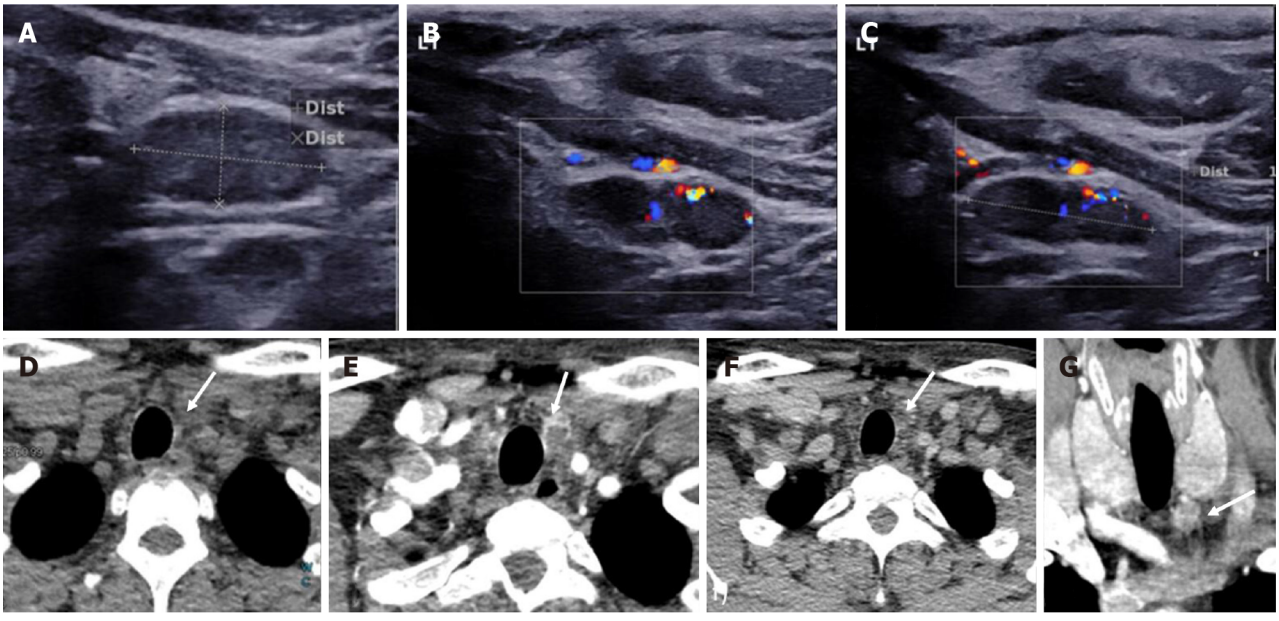
In order to facilitate the precise detection of parathyroid adenomas, Hoang *et al*[29] described a systematic five step approach: (1) Search for potential eutopic lesions in the arterial phase (2) Search for potential ectopic lesions in the arterial phase (3) Review the pattern of enhancement on other phases (4) Evaluate the morphological appearance; and (5) Correlate the computed tomography (CT) findings with other imaging modalities and clinical history. The characteristic imaging findings of a parathyroid adenoma are low attenuation on the non-contrast image, intense arterial enhancement (138-180 HU) and wash-out in the venous phase (Figures 6 and 7)[31,32]. The low attenuation on non-contrast images is important to differentiate from thyroid lesions, which are hyperdense on non-contrast CT owing to the iodine content. The typical search should start from the most common location of parathyroid adenoma *i.e.*, around the thyroid gland. This should be followed by a keen search along the expected path of migration of parathyroid glands *i.e.*, superiorly extending from the level of carotid bifurcation to the carina inferiorly. Rarer sites of ectopic parathyroid adenomas like the retropharyngeal space and intrathyroidal locations should also be screened (Figures 8-11).

Since the ultimate goal of imaging is to facilitate precise operative planning, it is important to provide the surgeon with relevant information while reporting parathyroid adenomas preferably using a predefined cartoon (Figure 1). This includes number of candidate lesions, size of the lesions, location of the lesion with respect to standard surgical landmarks (superior and inferior thyroid poles, suprasternal notch and trachea-oesophageal groove), ectopic or supernumerary parathyroid glands, underlying thyroid pathology and arterial anomalies associated with non-recurrent laryngeal nerve (aberrant right subclavian artery) which may increase risk of operative injury to the nerve[5].



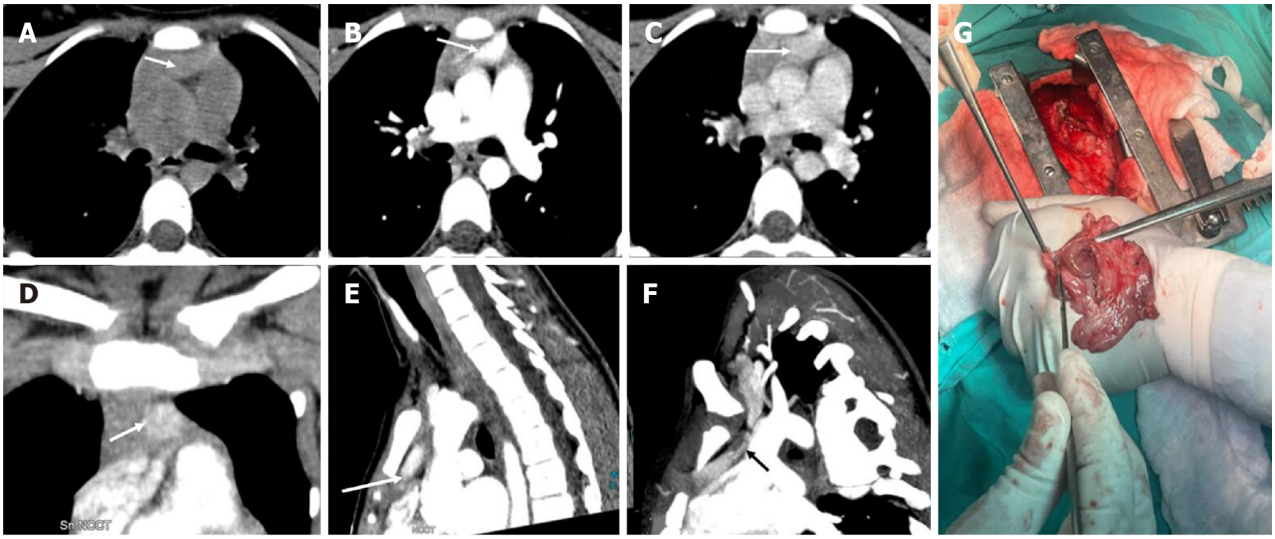
DOI: 10.4329/wjr.v15.i3.69 **Copyright** ©The Author(s) 2023.

Figure 6 Right superior adenoma: Four-dimensional computed tomography. A: Non-contrast computed tomography shows a small oval hypodense lesion which shows B: Intense enhancement on the arterial phase; C: Washout on the venous phase consistent with right superior parathyroid adenoma; D: Coronal image and E: Coronal maximum intensity projection image in the arterial phase better demonstrate the lesion with the feeding vessel (black arrow).



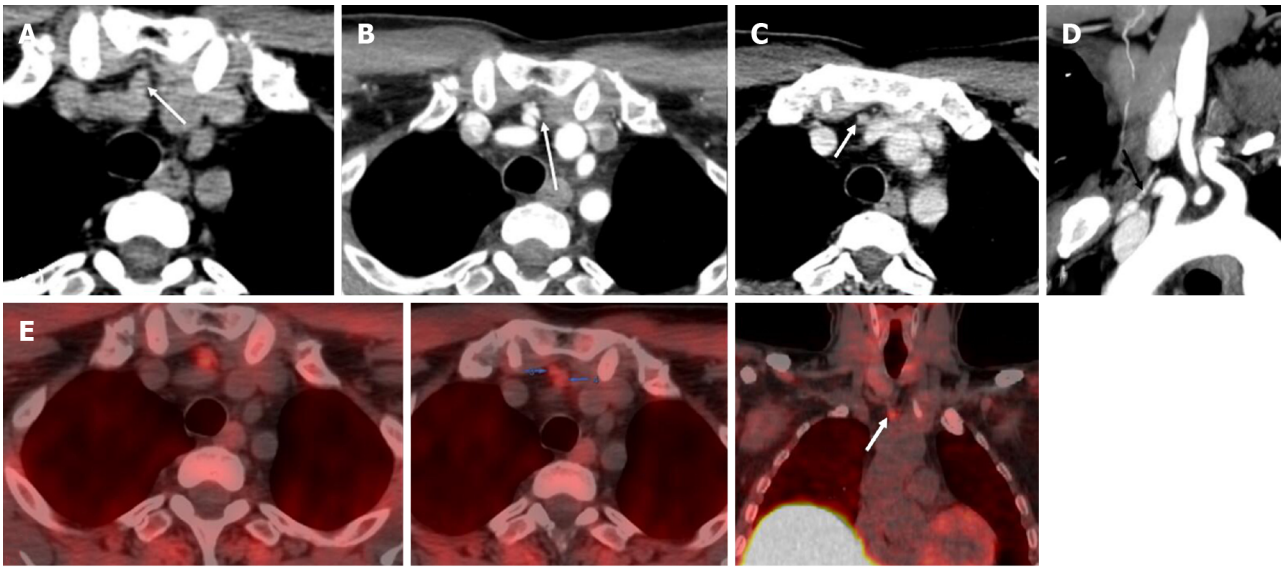
DOI: 10.4329/wjr.v15.i3.69 **Copyright** ©The Author(s) 2023.

Figure 7 Left inferior parathyroid adenoma. In a patient with raised parathormone levels (290 IU), grey scale ultrasound A: and colour doppler flow imaging; B and C: Showed a hypoechoic lesion with vascularity just below the left lobe of the; D: 4-dimensional computed tomography showed the lesion to be hypodense on noncontrast computer tomography; E: Hyperenhancing with central necrosis on arterial phase; F: Washout on the venous phase; G: Coronal image better demonstrates the lesion.



DOI: 10.4329/wjr.v15.i3.69 **Copyright** ©The Author(s) 2023.

Figure 8 Ectopic parathyroid adenoma in the anterior mediastinum. A: 4-dimensional computed tomography done in the 12-year-old female with hyperparathyroidism showed a well-defined lesion in the anterior mediastinum just behind the sternum which was hypodense on non-contrast computed tomography; B: intense arterial enhancement; C: washout on the venous phase; D: Multiplanar reformatted coronal; E: sagittal images in the arterial phase show the lesion better; F: Oblique sagittal maximum intensity projection image shows the feeding vessel (black arrow); G: Sternotomy followed by thymectomy was done and the thymus opened - the adenoma can be seen within the thymic parenchyma as pointed by the forceps.

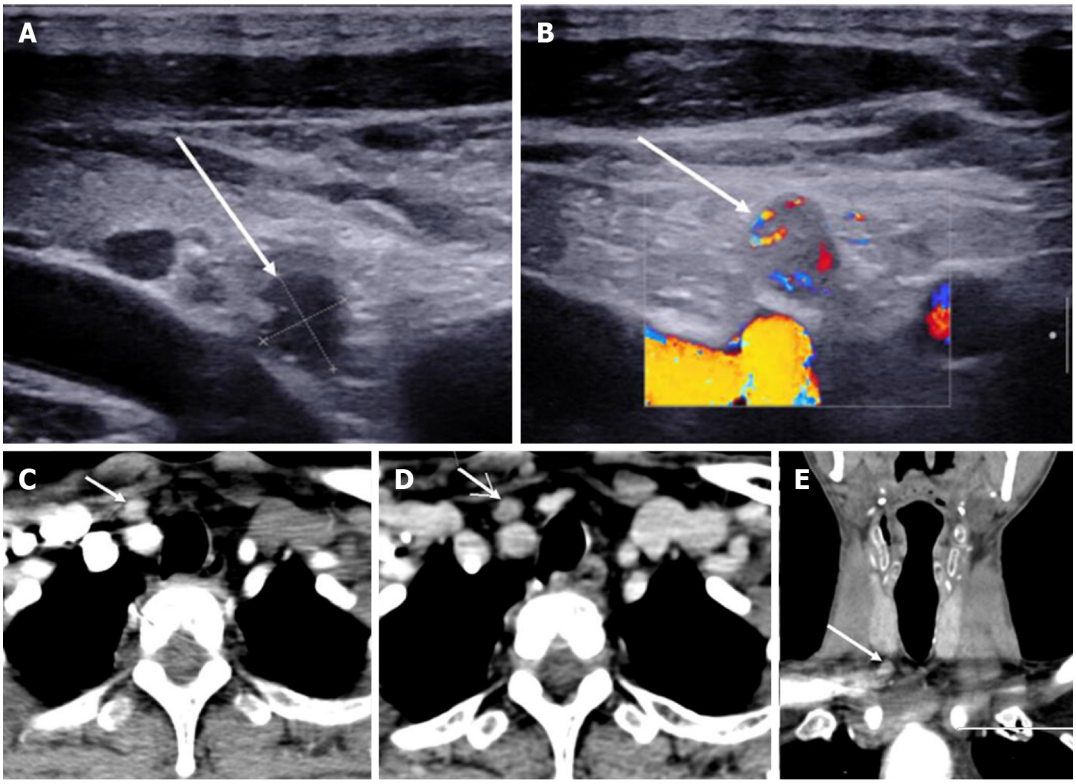


DOI: 10.4329/wjr.v15.i3.69 **Copyright** ©The Author(s) 2023.

Figure 9 Ectopic parathyroid adenoma in the anterior mediastinum. A: Computed tomography in a 45-year-old male patient showed a well-defined ovoid lesion in the prevascular space just posterior to the sternal notch and anterior to the inferior thyroid vessels appearing hypodense on the non-contrast phase; B: Showing intense enhancement on the arterial phase; C: washout in the venous phase; D: Coronal maximum intensity projection image demonstrates the inferior thyroid artery supplying the lesion (feeding vessel - black arrows); E: Fluoro-choline positron emission tomography shows a small tracer avid lesion in ectopic location which correlates with the computed tomography images.

Exophytic thyroid nodules and level VI cervical lymph nodes can mimic parathyroid adenomas as they have similar shape and locations. The differentiation may be done on the basis of contrast enhancement patterns. Thyroid nodules show high attenuation on the non-contrast image owing to their high iodine content and show delayed enhancement as compared to parathyroid adenoma. Lymph nodes although similar in shape to parathyroid adenomas can be differentiated from the latter based on contrast kinetics. Lymph nodes show progressive enhancement on the delayed phase as compared to parathyroid adenomas which show washout of contrast.

The detection of one lesion should not give a false sense of satisfaction to the radiologist since multiglandular disease can occur in 10% of the cases[33]. Hence, a relook is always suggested.



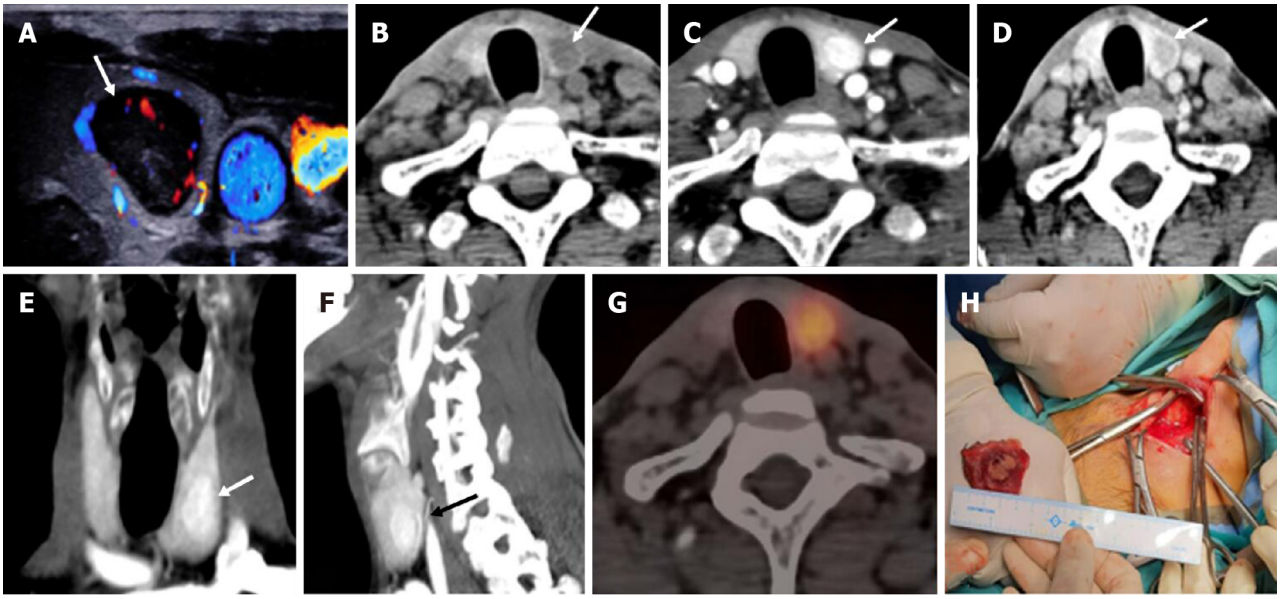
DOI: 10.4329/wjr.v15.i3.69 **Copyright** ©The Author(s) 2023.

Figure 10 Ectopic Parathyroid Adenoma in the Supraclavicular fossa. A: Grey scale ultrasound of the neck on a 49-year-old male patient, with history of bilateral renal stones and elevated parathormone reveals a hypoechoic lesion in the right supraclavicular location; B: On color doppler, internal vascularity was detected; C: 4-dimensional computed tomography showed a lesion with arterial enhancement; D: Washout seen on the venous phase; E: Coronal reformatted image better depicts the ectopic parathyroid adenoma in the right supraclavicular fossa.

While 4D CT is an excellent modality for detection of parathyroid adenomas, it does involve considerable radiation exposure. The effective dose is 10.4 mSv for 4D CT as compared to 7.8 mSv for nuclear scintigraphy, however 4D CT is associated with 50 times higher organ dose to the thyroid gland which becomes a cause of concern in young females since it increases the life time risk of development of thyroid cancer[34].

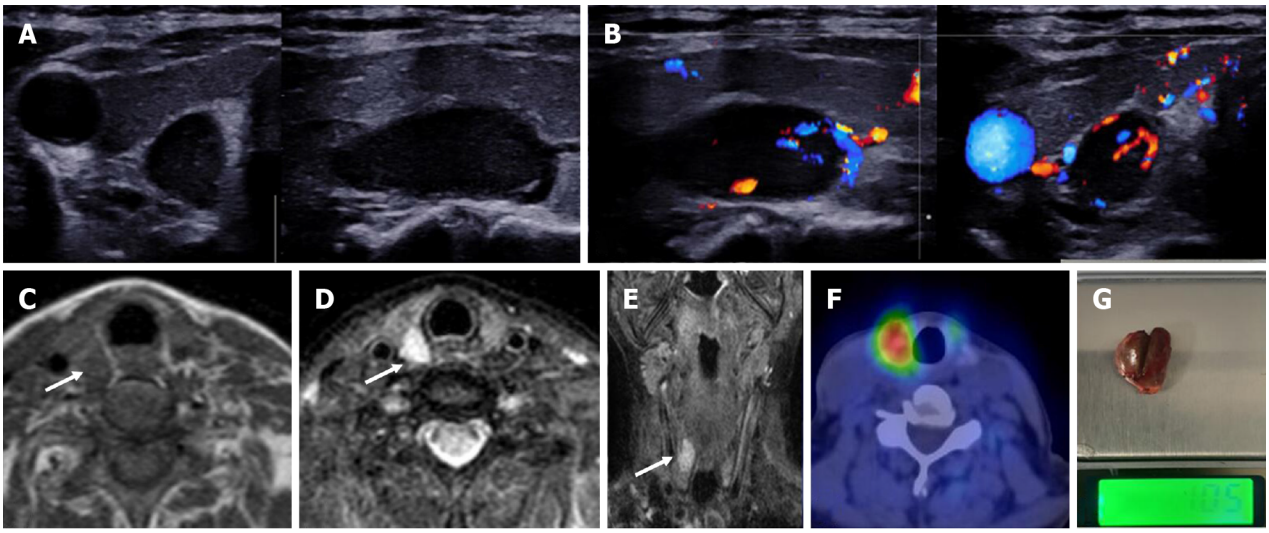
MRI

MRI is often not used as a first line modality. It is more commonly used as problem solving modality in patients with recurrent or residual disease. The non-involvement of ionizing radiation makes it a safer modality as compared to 4D CT and nuclear imaging studies; however, the modality is time consuming and isn't readily available. On a 1.5 T MRI machine, the sensitivity is 80%[35-37]. Benign parathyroid lesions are seen as well-circumscribed ovoid lesions with a cleavage plane with the thyroid tissue which is best seen on out of phase images[37]. The signal characteristics of parathyroid adenomas vary on MRI, but most commonly they tend to show homogenously hyperintense signal on T2 weighted images (Figure 12)[37]. Post gadolinium injection, they show rapid enhancement in the arterial phase. Solid parathyroid lesions show higher signal on diffusion weighted images as compared to the other anatomically neighbouring structures in the neck thus helping in differentiation from the former[38]. 4D MRI is a novel method which has been explored in the imaging of parathyroid adenomas. The sensitivity of 4D MRI was 90% and after optimisation, 100% and the specificity was 90%[39]. 4D MRI has similar accuracy to 4D CT for the detection of parathyroid lesions. However, 4D MRI has the advantage of lack of exposure to ionizing radiation, which can be beneficial in younger patients[40]. The protocol used is the acquisition of fast T1 VIBE sequences in the axial plane prior to and after administration of gadolinium acquiring the images every 13 s for 10 sequential scans[39]. Parathyroid adenomas showed fast enhancement after 26-30 s similar to their pattern on 4D CT[39].



DOI: 10.4329/wjr.v15.i3.69 **Copyright** ©The Author(s) 2023.

Figure 11 Intrathyroidal parathyroid adenoma. In a patient with raised parathormone (208 IU), A: Color doppler ultrasound of the neck showed a circumscribed solid hypoechoic lesion within the left lobe of thyroid gland; B: 4-dimensional computed tomography revealed the lesion to be hypodense as compared to thyroid tissue on non-contrast; C: showed intense arterial hyperenhancement; D: Washout on the venous phase, consistent with the diagnosis of intra-thyroid parathyroid adenoma; E and F: Coronal (E) and Sagittal maximum intensity projection images better depict the lesions with vascular pedicle (black arrow) seen supplying the lesion (F); G: Single photon emission computed tomography image showing a thyroid nodule which is mildly tracer avid; H: Left hemithyroidectomy was done and the cut open section confirmed the presence of the tumor.



DOI: 10.4329/wjr.v15.i3.69 **Copyright** ©The Author(s) 2023.

Figure 12 Right superior parathyroid adenoma. A 50-year-old female with raised parathormone levels (96 IU) was examined using duplex ultrasound for parathyroid glands. A: Grey scale sonography in the transverse and longitudinal plane showed a well circumscribed lesion posterior to the right lobe of thyroid gland and separated from it by a clear fat plane; B: Colour doppler image shows a feeding vessel. Corroborative magnetic resonance imaging axial images show a subcentimetric lesion (arrows) posterior to the middle third of the right lobe of thyroid gland which is C: T1 hypointense; D: T2 hyperintense; E: Coronal T2w image better demonstrates the lesion; F: Correlative single photon emission computed tomography component of MIBI scan showing tracer avid lesion at the superior pole of the right lobe of thyroid; G: Image of the resected adenoma weighing 1.05 g.

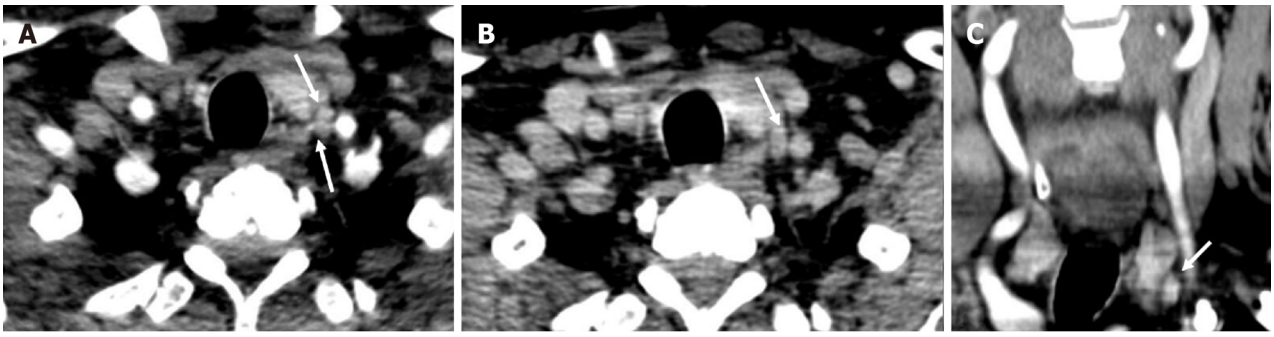
CHOLINE POSITRON EMISSION TOMOGRAPHY

Positron emission tomography (PET) is a non-invasive nuclear imaging study which provides both anatomical and functional information post intravenous injection of a radio-tracer agent. Choline labelled with positron emitters like carbon-11 or fluorine-18 is used for parathyroid imaging[41]. Increased choline uptake can be seen in parathyroid adenomas owing to the parathormone induced upregulation of choline kinase[42]. The image acquisition is done with the patient in a supine position

Table 2 Differentiating features of various parathyroid lesions

	Parathyroid hyperplasia	Parathyroid adenoma	Parathyroid carcinoma
USG	Small; Ovoid; Well-circumscribed; Homogenously hypoechoic; Calcifications uncommon; No local invasion; CEUS - Homogeneous enhancement	Small; Ovoid; Well-circumscribed; Homogenously hypoechoic; Calcifications uncommon; No local invasion; CEUS - Peripheral enhancement with central washout on delayed image	Large; Irregular shape; Non circumscribed margins; Heterogenous echotexture; Intra-nodular calcifications; Local invasion
CT	Small hypodense lesion (as compared to thyroid gland); Intense arterial enhancement; Washout on the venous phase; May not be identifiable on CT	Small hypodense lesion (as compared to thyroid gland); Intense arterial enhancement; Washout on the venous phase	Lesions may show infiltration into the surrounding structures
MRI	Small sized; Well defined; Homogenous;Low on T1; High on T2; Avid enhancement	Small sized; Well defined; Homogenous;Low on T1; High on T2; Avid enhancement	Large; Ill-defined; Heterogenous

USG: Ultrasound; CT: Computed tomography; MRI: Magnetic resonance imaging; CEUS: Contrast enhanced ultrasound.



DOI: 10.4329/wjr.v15.i3.69 **Copyright** ©The Author(s) 2023.

Figure 13 Parathyroid carcinoma. A 62-year-old male patient with recurrent hyperparathyroidism (previously operated parathyroid carcinoma), 4-dimensional computed tomography done showed few hypodense lesions with ill-defined margins near the lower pole of the left lobe of thyroid gland which showed, A: arterial enhancement however; B: No washout on the venous phase - atypical contrast kinetics for parathyroid adenoma; C: Coronal image better demonstrates the lesion. Surgical exploration and histopathological examination revealed parathyroid carcinoma recurrence.

about 45 to 60 min post intravenous injection of 18-fluoro choline[43]. Eyeballing is used to detect lesions in the eutopic or ectopic locations with parathyroid tissue being identified as maximum standardized uptake value (SUV max) four times greater than thyroid tissue[44]. Fluoro-choline PET can identify abnormal parathyroid gland in 92% patients in whom ultrasound and other nuclear imaging studies are negative[45]. It has excellent ability to detect small adenomas. The radiation dose is around 6 mSv which is lesser than that involved in MIBI scan and 4D CT. The scan involves a single acquisition as compared to the MIBI scan which involves imaging at two time points[46]. Choline is highly sensitive in the detection of parathyroid adenomas especially in multi-glandular disease. The high lesion to thyroid ratio improves the ability to detect smaller lesions. There are however several limitations with choline PET which include limited availability, high cost and the absence of a standardized protocol for imaging.

CONCLUSION

The primary goal of imaging in a clinically diagnosed case of hyperparathyroidism is precise localisation of the presence of parathyroid lesions which permits accurate surgical planning. The first line imaging modalities are ultrasound of the neck and scintigraphy. The inability to localise on these modalities or disconcordant findings on these modalities necessitates the use of 4D CT, MRI or F-Choline PET. Novel modalities such as contrast enhanced ultrasound and shear wave elastography of the neck should be coming up in a big way as it is free of radiation as well as safe for the kidneys. The various imaging modalities may also be used to differentiate parathyroid hyperplasia, parathyroid adenoma and parathyroid carcinoma (Table 2, Figure 13), though this may not always be possible and histopathological examination is the gold standard.

FOOTNOTES

Author contributions: Gulati S, Das JC, Spalkit S wrote the paper; Chumber S and Puri G provided the surgical expertise; Damle N provided the nuclear medicine expertise. All authors were involved in careful editing of the final manuscript.

Conflict-of-interest statement: All the authors declare that they have no conflict of interest.

Open-Access: This article is an open-access article that was selected by an in-house editor and fully peer-reviewed by external reviewers. It is distributed in accordance with the Creative Commons Attribution NonCommercial (CC BY-NC 4.0) license, which permits others to distribute, remix, adapt, build upon this work non-commercially, and license their derivative works on different terms, provided the original work is properly cited and the use is non-commercial. See: https://creativecommons.org/Licenses/by-nc/4.0/

Country/Territory of origin: India

ORCID number: CJ Das 0000-0001-6505-5940.

S-Editor: Liu JH
L-Editor: A
P-Editor: Liu JH

REFERENCES

1 **Fraser WD**. Hyperparathyroidism. *Lancet* 2009; **374**: 145-158 [PMID: 19595349 DOI: 10.1016/S0140-6736(09)60507-9]
2 **Bunch PM**, Kelly HR. Preoperative Imaging Techniques in Primary Hyperparathyroidism: A Review. *JAMA Otolaryngol Head Neck Surg* 2018; **144**: 929-937 [PMID: 30193297 DOI: 10.1001/jamaoto.2018.1671]
3 **Bilezikian JP**, Bandeira L, Khan A, Cusano NE. Hyperparathyroidism. *Lancet* 2018; **391**: 168-178 [PMID: 28923463 DOI: 10.1016/S0140-6736(17)31430-7]
4 **Bilezikian JP**, Cusano NE, Khan AA, Liu JM, Marcocci C, Bandeira F. Primary hyperparathyroidism. *Nat Rev Dis Primers* 2016; **2**: 16033 [PMID: 27194212 DOI: 10.1038/nrdp.2016.33]
5 **Bunch PM**, Randolph GW, Brooks JA, George V, Cannon J, Kelly HR. Parathyroid 4D CT: What the Surgeon Wants to Know. *Radiographics* 2020; **40**: 1383-1394 [PMID: 32678698 DOI: 10.1148/rg.2020190190]
6 **Phitayakorn R**, McHenry CR. Incidence and location of ectopic abnormal parathyroid glands. *Am J Surg* 2006; **191**: 418-423 [PMID: 16490559 DOI: 10.1016/j.amjsurg.2005.10.049]
7 **Kuzminski SJ**, Sosa JA, Hoang JK. Update in Parathyroid Imaging. *Magn Reson Imaging Clin N Am* 2018; **26**: 151-166 [PMID: 29128002 DOI: 10.1016/j.mric.2017.08.009]
8 **Akerström G**, Malmaeus J, Bergström R. Surgical anatomy of human parathyroid glands. *Surgery* 1984; **95**: 14-21 [PMID: 6691181]
9 **Wilhelm SM**, Wang TS, Ruan DT, Lee JA, Asa SL, Duh QY, Doherty GM, Herrera MF, Pasieka JL, Perrier ND, Silverberg SJ, Solórzano CC, Sturgeon C, Tublin ME, Udelsman R, Carty SE. The American Association of Endocrine Surgeons Guidelines for Definitive Management of Primary Hyperparathyroidism. *JAMA Surg* 2016; **151**: 959-968 [PMID: 27532368 DOI: 10.1001/jamasurg.2016.2310]
10 **Minisola S**, Cipriani C, Diacinti D, Tartaglia F, Scillitani A, Pepe J, Scott-Coombes D. Imaging of the parathyroid glands in primary hyperparathyroidism. *Eur J Endocrinol* 2016; **174**: D1-D8 [PMID: 26340967 DOI: 10.1530/EJE-15-0565]
11 **Reeder SB**, Desser TS, Weigel RJ, Jeffrey RB. Sonography in primary hyperparathyroidism: review with emphasis on scanning technique. *J Ultrasound Med* 2002; **21**: 539-52; quiz 553 [PMID: 12008817 DOI: 10.7863/jum.2002.21.5.539]
12 **Wolf RJ**, Cronan JJ, Monchik JM. Color Doppler sonography: an adjunctive technique in assessment of parathyroid adenomas. *J Ultrasound Med* 1994; **13**: 303-308 [PMID: 7932996 DOI: 10.7863/jum.1994.13.4.303]
13 **Lane MJ**, Desser TS, Weigel RJ, Jeffrey RB Jr. Use of color and power Doppler sonography to identify feeding arteries associated with parathyroid adenomas. *AJR Am J Roentgenol* 1998; **171**: 819-823 [PMID: 9725323 DOI: 10.2214/ajr.171.3.9725323]
14 **Kamaya A**, Quon A, Jeffrey RB. Sonography of the abnormal parathyroid gland. *Ultrasound Q* 2006; **22**: 253-262 [PMID: 17146333 DOI: 10.1097/01.ruq.0000237260.33509.4f]
15 **Johnson NA**, Yip L, Tublin ME. Cystic parathyroid adenoma: sonographic features and correlation with 99mTc-sestamibi SPECT findings. *AJR Am J Roentgenol* 2010; **195**: 1385-1390 [PMID: 21098199 DOI: 10.2214/AJR.10.4472]
16 **Chandramohan A**, Sathyakumar K, John RA, Manipadam MT, Abraham D, Paul TV, Thomas N, Paul MJ. Atypical ultrasound features of parathyroid tumours may bear a relationship to their clinical and biochemical presentation. *Insights Imaging* 2014; **5**: 103-111 [PMID: 24293304 DOI: 10.1007/s13244-013-0297-x]
17 **Polga JP**, Balikian JP. Partially calcified functioning parathyroid adenoma. Casedemonstrated roentgenographically. *Radiology* 1971; **99**: 55-56 [PMID: 5548688 DOI: 10.1148/99.1.55]
18 **Randel SB**, Gooding GA, Clark OH, Stein RM, Winkler B. Parathyroid variants: US evaluation. *Radiology* 1987; **165**: 191-194 [PMID: 3306784 DOI: 10.1148/radiology.165.1.3306784]
19 **Vitetta GM**, Neri P, Chiecchio A, Carriero A, Cirillo S, Mussetto AB, Codegone A. Role of ultrasonography in the management of patients with primary hyperparathyroidism: retrospective comparison with technetium-99m sestamibi scintigraphy. *J Ultrasound* 2014; **17**: 1-12 [PMID: 24616746 DOI: 10.1007/s40477-014-0067-8]

20 **Tsai K**, Liang TZ, Grant EG, Swanson MS, Barnett B. Optimal imaging modality for diagnosis of parathyroid adenoma: Case report and review of the literature. *J Clin Transl Endocrinol Case Rep* 2020; **17**: 100065. [DOI: 10.1016/j.jecr.2020.100065]

21 **Pavlovics S**, Radzina M, Niciporuka R, Ratniece M, Mikelsone M, Tauvena E, Liepa M, Prieditis P, Ozolins A, Gardovskis J, Narbuts Z. Contrast-Enhanced Ultrasound Qualitative and Quantitative Characteristics of Parathyroid Gland Lesions. *Medicina (Kaunas)* 2021; **58** [PMID: 35056309 DOI: 10.3390/medicina58010002]

22 **Platz Batista da Silva N**, Jung EM, Jung F, Schlitt HJ, Hornung M. VueBox® perfusion analysis of contrast-enhanced ultrasound (CEUS) examinations in patients with primary hyperparathyroidism for preoperative detection of parathyroid gland adenoma. *Clin Hemorheol Microcirc* 2018; **70**: 423-431 [PMID: 30347604 DOI: 10.3233/CH-189307]

23 **Parra Ramírez P**, Santiago Hernando A, Barquiel Alcalá B, Martín Rojas-Marcos P, Lisbona Catalán A, Álvarez Escolá C. Potential Utility of Contrast-Enhanced Ultrasound in the Preoperative Evaluation of Primary Hyperparathyroidism. *J Ultrasound Med* 2019; **38**: 2565-2571 [PMID: 30693978 DOI: 10.1002/jum.14949]

24 **Ling W**, Nie J, Zhang D, Yang Q, Jin H, Ou X, Ma X, Luo Y. Role of Contrast-Enhanced Ultrasound (CEUS) in the Diagnosis of Cervical Lymph Node Metastasis in Nasopharyngeal Carcinoma (NPC) Patients. *Front Oncol* 2020; **10**: 972 [PMID: 32766127 DOI: 10.3389/fonc.2020.00972]

25 **Chen L**, Chen L, Liu J, Wang B, Zhang H. Value of Qualitative and Quantitative Contrast-Enhanced Ultrasound Analysis in Preoperative Diagnosis of Cervical Lymph Node Metastasis From Papillary Thyroid Carcinoma. *J Ultrasound Med* 2020; **39**: 73-81 [PMID: 31222782 DOI: 10.1002/jum.15074]

26 **Cui XW**, Jenssen C, Saftoiu A, Ignee A, Dietrich CF. New ultrasound techniques for lymph node evaluation. *World J Gastroenterol* 2013; **19**: 4850-4860 [PMID: 23946589 DOI: 10.3748/wjg.v19.i30.4850]

27 **Azizi G**, Piper K, Keller JM, Mayo ML, Puett D, Earp KM, Malchoff CD. Shear wave elastography and parathyroid adenoma: A new tool for diagnosing parathyroid adenomas. *Eur J Radiol* 2016; **85**: 1586-1593 [PMID: 27501893 DOI: 10.1016/j.ejrad.2016.06.009]

28 **Johnson NA**, Tublin ME, Ogilvie JB. Parathyroid imaging: technique and role in the preoperative evaluation of primary hyperparathyroidism. *AJR Am J Roentgenol* 2007; **188**: 1706-1715 [PMID: 17515397 DOI: 10.2214/AJR.06.0938]

29 **Hoang JK**, Sung WK, Bahl M, Phillips CD. How to perform parathyroid 4D CT: tips and traps for technique and interpretation. *Radiology* 2014; **270**: 15-24 [PMID: 24354373 DOI: 10.1148/radiol.13122661]

30 **Chazen JL**, Gupta A, Dunning A, Phillips CD. Diagnostic accuracy of 4D-CT for parathyroid adenomas and hyperplasia. *AJNR Am J Neuroradiol* 2012; **33**: 429-433 [PMID: 22135127 DOI: 10.3174/ajnr.A2805]

31 **Gafton AR**, Glastonbury CM, Eastwood JD, Hoang JK. Parathyroid lesions: characterization with dual-phase arterial and venous enhanced CT of the neck. *AJNR Am J Neuroradiol* 2012; **33**: 949-952 [PMID: 22241395 DOI: 10.3174/ajnr.A2885]

32 **Beland MD**, Mayo-Smith WW, Grand DJ, Machan JT, Monchik JM. Dynamic MDCT for localization of occult parathyroid adenomas in 26 patients with primary hyperparathyroidism. *AJR Am J Roentgenol* 2011; **196**: 61-65 [PMID: 21178047 DOI: 10.2214/AJR.10.4459]

33 **Ruda JM**, Hollenbeak CS, Stack BC Jr. A systematic review of the diagnosis and treatment of primary hyperparathyroidism from 1995 to 2003. *Otolaryngol Head Neck Surg* 2005; **132**: 359-372 [PMID: 15746845 DOI: 10.1016/j.otohns.2004.10.005]

34 **Mahajan A**, Starker LF, Ghita M, Udelsman R, Brink JA, Carling T. Parathyroid four-dimensional computed tomography: evaluation of radiation dose exposure during preoperative localization of parathyroid tumors in primary hyperparathyroidism. *World J Surg* 2012; **36**: 1335-1339 [PMID: 22146947 DOI: 10.1007/s00268-011-1365-3]

35 **Grayev AM**, Gentry LR, Hartman MJ, Chen H, Perlman SB, Reeder SB. Presurgical localization of parathyroid adenomas with magnetic resonance imaging at 3.0 T: an adjunct method to supplement traditional imaging. *Ann Surg Oncol* 2012; **19**: 981-989 [PMID: 21879264 DOI: 10.1245/s10434-011-2046-z]

36 **Lopez Hänninen E**, Vogl TJ, Steinmüller T, Ricke J, Neuhaus P, Felix R. Preoperative contrast-enhanced MRI of the parathyroid glands in hyperparathyroidism. *Invest Radiol* 2000; **35**: 426-430 [PMID: 10901104 DOI: 10.1097/00004424-200007000-00005]

37 **Sacconi B**, Argirò R, Diacinti D, Iannarelli A, Bezzi M, Cipriani C, Pisani D, Cipolla V, De Felice C, Minisola S, Catalano C. MR appearance of parathyroid adenomas at 3 T in patients with primary hyperparathyroidism: what radiologists need to know for pre-operative localization. *Eur Radiol* 2016; **26**: 664-673 [PMID: 26024849 DOI: 10.1007/s00330-015-3854-5]

38 **Yildiz S**, Aralasmak A, Yetis H, Kilicarslan R, Sharifov R, Alkan A, Toprak H. MRI findings and utility of DWI in the evaluation of solid parathyroid lesions. *Radiol Med* 2019; **124**: 360-367 [PMID: 30607865 DOI: 10.1007/s11547-018-0970-8]

39 **Merchavy S**, Luckman J, Guindy M, Segev Y, Khafif A. 4D MRI for the Localization of Parathyroid Adenoma: A Novel Method in Evolution. *Otolaryngol Head Neck Surg* 2016; **154**: 446-448 [PMID: 26598499 DOI: 10.1177/0194599815618199]

40 **Murugan N**, Kandasamy D, Sharma R, Goyal A, Gupta AK, Tandon N, Gupta N, Goswami R, Vurthaluru S, Damle N, Agrawal S. Comparison of 4DMRI and 4DCT for the preoperative evaluation of patients with primary hyperparathyroidism. *Eur J Radiol* 2021; **138**: 109625 [PMID: 33714845 DOI: 10.1016/j.ejrad.2021.109625]

41 **Vallabhajosula S**. (18)F-labeled positron emission tomographic radiopharmaceuticals in oncology: an overview of radiochemistry and mechanisms of tumor localization. *Semin Nucl Med* 2007; **37**: 400-419 [PMID: 17920348 DOI: 10.1053/j.semnuclmed.2007.08.004]

42 **Ishizuka T**, Kajita K, Kamikubo K, Komaki T, Miura K, Nagao S, Nozawa Y. Phospholipid/Ca2+-dependent protein kinase activity in human parathyroid adenoma. *Endocrinol Jpn* 1987; **34**: 965-968 [PMID: 3450512 DOI: 10.1507/endocrj1954.34.965]

43 **Tay D**, Das JP, Yeh R. Preoperative Localization for Primary Hyperparathyroidism: A Clinical Review. *Biomedicines* 2021; **9** [PMID: 33917470 DOI: 10.3390/biomedicines9040390]

44 **Parvinian A**, Martin-Macintosh EL, Goenka AH, Durski JM, Mullan BP, Kemp BJ, Johnson GB. (11)C-Choline PET/CT for Detection and Localization of Parathyroid Adenomas. *AJR Am J Roentgenol* 2018; **210**: 418-422 [PMID: 29140118 DOI: 10.2214/AJR.17.18312]

45 **Michaud L**, Burgess A, Huchet V, Lefèvre M, Tassart M, Ohnona J, Kerrou K, Balogova S, Talbot JN, Périé S. Is 18F-fluorocholine-positron emission tomography/computerized tomography a new imaging tool for detecting hyperfunctioning parathyroid glands in primary or secondary hyperparathyroidism? *J Clin Endocrinol Metab* 2014; **99**: 4531-4536 [PMID: 25215560 DOI: 10.1210/jc.2014-2821]

46 **Kluijfhout WP**, Vorselaars WM, Vriens MR, Borel Rinkes IH, Valk GD, de Keizer B. Enabling minimal invasive parathyroidectomy for patients with primary hyperparathyroidism using Tc-99m-sestamibi SPECT-CT, ultrasound and first results of (18)F-fluorocholine PET-CT. *Eur J Radiol* 2015; **84**: 1745-1751 [PMID: 26047823 DOI: 10.1016/j.ejrad.2015.05.024]

World Journal of Radiology

Submit a Manuscript: https://www.f6publishing.com

World J Radiol 2023 March 28; 15(3): 83-88

DOI: 10.4329/wjr.v15.i3.83

ISSN 1949-8470 (online)

CASE REPORT

Magnetic resonance imaging findings of spontaneous pyomyoma in a premenopausal woman managed with myomectomy: A case report

David Martínez, Gustavo E Sanchez, Jhonatan Gómez, Luis J Sonda, Luis D Suárez, Carlos S López, Juan J Vega, Daniel A Cepeda

Specialty type: Radiology, nuclear medicine and medical imaging

Provenance and peer review: Unsolicited article; Externally peer reviewed.

Peer-review model: Single blind

Peer-review report's scientific quality classification

Grade A (Excellent): 0
Grade B (Very good): 0
Grade C (Good): C, C
Grade D (Fair): 0
Grade E (Poor): E

P-Reviewer: Aydin S, Turkey; Cheng YS, China; Hegazy AA, Egypt

Received: September 1, 2022
Peer-review started: September 1, 2022
First decision: November 25, 2022
Revised: January 24, 2023
Accepted: March 9, 2023
Article in press: March 9, 2023
Published online: March 28, 2023

David Martínez, Gustavo E Sanchez, Department of Radiology, Hospital Christus Muguerza, Puebla 72501, Puebla, Mexico

Jhonatan Gómez, Department of Radiology, Hospital Regional Dr. Juan Graham Casasùs, Villahermosa 86126, Tabasco, Mexico

Luis J Sonda, Luis D Suárez, Carlos S López, Juan J Vega, Daniel A Cepeda, Department of Radiology, Hospital de Especialidades 5 de Mayo, Puebla 72550, Puebla, Mexico

Corresponding author: David Martinez, MD, Doctor, Department of Radiology, Hospital Christus Muguerza, Av. 11 Ote. 1826, Azcarate, 72501 Puebla, Puebla, Mexico.
www_david_@msn.com

Abstract

BACKGROUND

Acute fibroid complications are rare. However, failure to recognize and treat acute complications expeditiously when they occur can lead to catastrophic, even deadly, complications. Pyomyoma is a rare but potentially fatal condition resulting from infarction and infection of a fibroid through bacterial seeding and direct, hematogenous, or lymphatic dissemination. Even though the diagnosis is established through clinical and laboratory findings, imaging is an important complementary method to support the suspected diagnosis.

CASE SUMMARY

Herein, we report a case of a pyomyoma in a nulliparous woman previously diagnosed with uterine leiomyomatosis according to ultrasound findings. The patient had previously attended the emergency room due to hypogastric pain unresponsive to analgesics. After a week of persistent pain, she developed sepsis without any identifiable foci. Magnetic resonance imaging revealed findings compatible with uterine myomatosis with red degeneration, and a possible diagnosis of a pyomyoma was made according to the imaging findings along with the patient's clinical features. We decided to perform myomectomy (which is an infrequently performed surgical treatment due to the procedure's intrinsic implications) due to the patient's desire to preserve fertility. Histopathologic results revealed a uterine leiomyoma with coagulative and liquefactive necrosis, while the tissue culture showed gram-negative cocci bacteria, which were successfully treated using antibiotic therapy. The patient's health status improved after several

days.

CONCLUSION
The main diagnostic tools to evaluate pyomyomas are the clinical and laboratory findings as well as tissue cultures. Nonetheless, magnetic resonance imaging can help to corroborate these findings as well as to better characterize myomas with its different complications.

Key Words: Diffusion-weighted images; Apparent diffusion coefficient; Leiomyoma; Sepsis; Magnetic resonance imaging; Case report

©The Author(s) 2023. Published by Baishideng Publishing Group Inc. All rights reserved.

Core Tip: Pyomyoma is a rare but potentially fatal condition resulting from infarction and infection of a fibroid through bacterial seeding and direct, hematogenous, or lymphatic dissemination. Diffusion-weighted images, apparent diffusion coefficient quantification and the addition of T1- and T2-weighted sequences with fat suppression can improve the characterization of the components of a myoma during degeneration.

Citation: Martínez D, Sanchez GE, Gómez J, Sonda LJ, Suárez LD, López CS, Vega JJ, Cepeda DA. Magnetic resonance imaging findings of spontaneous pyomyoma in a premenopausal woman managed with myomectomy: A case report. *World J Radiol* 2023; 15(3): 83-88
URL: https://www.wjgnet.com/1949-8470/full/v15/i3/83.htm
DOI: https://dx.doi.org/10.4329/wjr.v15.i3.83

INTRODUCTION

A pyomyoma is a rare but potentially fatal condition resulting from infarction and infection of a leiomyoma[1] through bacterial seeding and direct, hematogenous, or lymphatic dissemination. Because of the rarity of pyomyomas, low clinical suspicion delays its diagnosis and predisposes patients to possible complications, such as purulent peritonitis or sepsis.

The definitive treatment of a pyomyoma is hysterectomy[2]. An alternative consists of intravenous administration of broad-spectrum antibiotics and myomectomy. Surgery can be adjusted according to the size and number of pyomyomas while considering the future reproductive wishes of the patient[3]. Surgery can also be performed to make a definitive diagnosis[1] while decreasing associated morbidity and mortality[4].

While ultrasound and computed tomography are often the first tools used for the detection of pyomyomas[5], magnetic resonance imaging (MRI) is the most precise imaging technique that can be used to characterize myomas with different types of degeneration (including the identification of purulent collections in the pyomyoma), which makes it potentially useful for diagnosis. However, the emergency use of MRI is still controversial[5].

Differential diagnoses of pyomyoma include gynecological tumors (benign or malignant ovarian tumors, tubo-ovarian abscess, uterine sarcoma, or pyometra), endometritis, gastrointestinal stromal tumors, and appendiceal mucocele[3,5]. However, red degeneration should be considered as an important entity due to its similarities to a pyomyoma on MRI. Red degeneration can exhibit peripheral or diffused hyperintensities in T1-weighted images and variable signal intensity, with or without a hypointense rim in T2-weighted images[5]. As an additional complementary sequence, diffusion-weighted imaging can be obtained. Generally, tissues with high cellularity have lower diffusion coefficients, which can be clinically related to purulent materials.

The ethics committee of hospital Christus Muguerza Hospital Betania approved this study. A signed informed consent by the patient was obtained for the publication of this case report.

CASE PRESENTATION

Chief complaints

A 26-year-old premenopausal nulliparous woman was evaluated for severe hypogastric pain in the prior 24 h with no response to analgesics.

History of present illness

The patient had a history of uterine myomatosis, which was confirmed by a pelvic ultrasound. She was prescribed with analgesics and sent home; however, she returned to the emergency department of our hospital a week later with abnormal uterine bleeding and abdominal pain.

History of past illness

The patient had no prior chronic or systemic disease. The patient had no prior surgeries.

Personal and family history

The patient did not have prior pregnancies or deliveries. Her menstrual cycle was reported as regular. There was no family history of chronic diseases or cancer.

Physical examination

A depressible and tender abdomen with a slight increase in volume in the hypogastrium was observed during the physical examination.

Laboratory examinations

On admission, there were no abnormal laboratory findings. A reverse transcription PCR for severe acute respiratory syndrome coronavirus 2 was obtained, with a negative result.

Imaging examinations

Requested MRI showed a mass located in the posterior wall of the uterus, with a T1- and T2-weighted hyperintense component, a T1-weighted hyperintense halo as well as some materials with high T1-weighted fat-saturation signal (suggesting a hematic content) and content with high T2-weighted fat-saturation signal indicating liquid content (Figure 1). In the diffusion-weighted images, an apparent diffusion coefficient map was obtained by measuring the region of interest with a low apparent diffusion coefficient (ADC) value (1.5 x 10^{-3} mm^2/s) (Figure 2). The results obtained suggested the presence of a leiomyoma with red degeneration; however, pyomyoma was considered as a differential diagnosis due to the low ADC value.

FINAL DIAGNOSIS

The final given diagnosis was uterine myomatosis with red degeneration complicated with pyomyoma.

TREATMENT

After evaluating the case and considering that the patient was a nulliparous woman, a laparoscopic myomectomy was performed to preserve the patient's fertility wishes (Figure 3). This also resulted in the discovery of an intraoperative large myoma that was peripherally hypovascularized with friable tissue in its center.

OUTCOME AND FOLLOW-UP

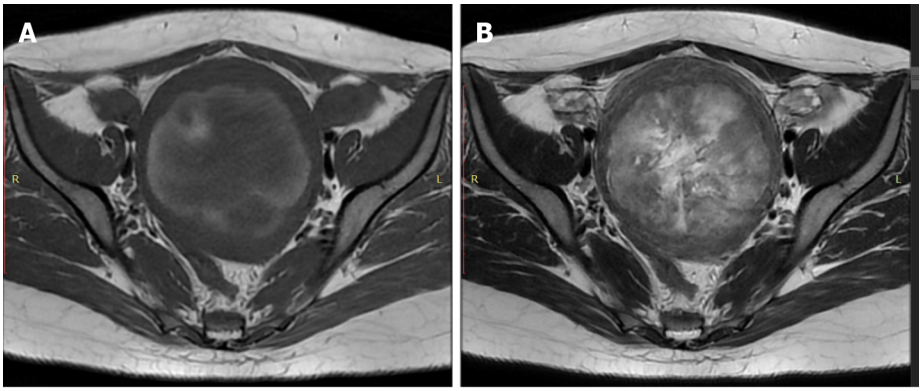
At 12 h postoperatively, the patient experienced sepsis symptoms, consisting of hypotension (70/40 mmHg), tachycardia (150 bpm), fever (39.8 °C), respiratory distress (30 rpm; SPO_2 80%), and drowsiness. Therefore, she was admitted to the intensive care unit for management with oxygen therapy, fluid resuscitation, and empiric antibiotic therapy.

After performing myomectomy, laboratory results were obtained, showing anemia (10.4 g/dL), leukocytosis with bandemia (18.32 K/uL; 10.0%), high C-reactive protein levels (123.94 mg/L), procalcitonin (5.55 ng/mL), pCO2 (31.0 mmHg), HCO3 (20.6), BEb (-2.5), and lactate (1.3).

The histopathologic report showed a uterine leiomyoma with coagulative and liquefactive necrosis, while a tissue culture showed gram-negative cocci bacteria, which confirmed the diagnosis of a pyomyoma. Antibiotic treatment was adjusted towards gram-negative cocci, resulting in normalization of inflammatory markers and clinical improvement after 3 d.

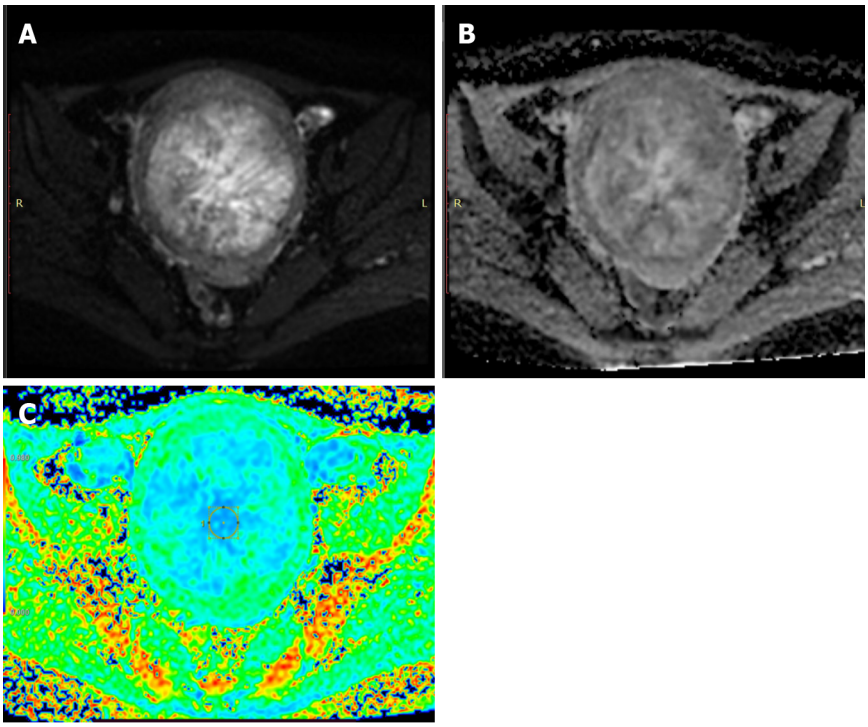
DISCUSSION

Myomas are the most common solid pelvic tumor in women during reproductive years, occurring in



DOI: 10.4329/wjr.v15.i3.83 **Copyright** ©The Author(s) 2023.

Figure 1 Magnetic resonance imaging findings. An axial view T1 and T2-weighted showed a large intramural lesion in the myometrium with materials. A: High-signal intensity in T1-weighted view indicated the presence of a hemorrhagic component; B: High-signal intensity material in T2-weighted view indicated the presence of a liquid component.



DOI: 10.4329/wjr.v15.i3.83 **Copyright** ©The Author(s) 2023.

Figure 2 Magnetic resonance imaging findings by diffusion-weighted images. A: An axial diffusion-weighted view showed areas with restrictions; B: Apparent diffusion coefficient map; C: Apparent diffusion coefficient color map.

approximately 20%-40% of this population[6]. It is estimated that 50% of women bearing myomas will remain asymptomatic through their lives. Also known as fibroids or leiomyomas, these tumors are benign and originate from smooth muscle cells of the uterus, but cases have been reported in which smooth muscle from uterine blood vessels may become their source[6]. The remaining 50% of women will develop symptoms related to their size, location, or degenerative changes, if present. Some of these symptoms may include polymenorrhea, hypermenorrhea, or even menometrorrhagia[6].

Associated pain in myomatosis is relatively infrequent, and it usually presents upon certain criteria: (1) Fibroids above 5 cm; (2) Posterior wall fibroids; and (3) Fibroids with a sudden increase in size (often related to pregnancy) as the blood supply may become insufficient, producing tissue anoxia, necrotic infarction, and the subsequent release of prostaglandins[7]. Cases of severe pain are often associated with torsion of pedunculated myomas, cervical dilation by submucosal myomas, and fibroid red degeneration of the pregnancy[7]. All of these conditions usually call for immediate action.

In this reviewed case, the patient had a previous history of myomatosis and presented with acute persistent pain, which prompted an ultrasound evaluation. The study did not show relevant changes within myomas. On ultrasound, a painful myoma above 200 cm^3 with changes in the echogenicity



DOI: 10.4329/wjr.v15.i3.83 **Copyright** ©The Author(s) 2023.

Figure 3 Follow–up magnetic resonance imaging. A: Sagittal T2-weighted image showed an intramural lesion before surgery; B: Sagittal T2-weighted imaged showed an intramural lesion after myomectomy.

suggesting internal cystic lesions can suggest red degeneration and infarction[7]. Even so, according to clinical suspicion, an MRI was ordered to exclude complications from the myomas, considering that red degeneration is an important complication of leiomyomas.

Myomas with red degeneration are characterized by acute onset abdominal pain, mild fever, localized tenderness over the myoma (as in this case), and leukocytosis. As mentioned before, they can become infected and turn to pyomyomas. Extensive necrotic areas can become infected with anaerobic bacteria. MRI should be considered in such situations to confirm the diagnosis and facilitate fibroid mapping before surgery. Pyomyomas usually lead to inflammatory changes and tissue necrosis, compatible with those present at the moment of presentation in this case, arising suspicion due to the low ADC on MRI[7].

Patients with a history of myomatosis who develop sepsis with unidentifiable foci should be suspected for pyomyoma. In our case, sepsis occurred after the surgical procedure. However, according to available literature, the clinical picture can be very unspecific, and the clinical presentation of pyomyomas can be insidious. Therefore, the diagnosis could be complicated.

CONCLUSION

The main diagnostic tools to evaluate pyomyomas are the clinical and laboratory findings as well as tissue cultures. Nonetheless, MRI can help to corroborate these findings as well as to better characterize myomas along with its complications.

FOOTNOTES

Author contributions: Martínez D designed the study and wrote the manuscript; Sánchez GE wrote the manuscript; G ómez J reviewed the manuscript; Sonda LJ wrote the introduction; Suárez LD wrote the manuscript; López CS wrote the discussion; Vega JJ wrote the abstract; Cepeda DA reviewed the manuscript.

Informed consent statement: The patient provided informed written consent about personal and medical data collection prior to study enrollment.

Conflict-of-interest statement: The authors report no relevant conflicts of interest for this article.

CARE Checklist (2016) statement: The authors have read the CARE Checklist (2016), and the manuscript was prepared and revised according to the CARE Checklist (2016).

Open-Access: This article is an open-access article that was selected by an in-house editor and fully peer-reviewed by

external reviewers. It is distributed in accordance with the Creative Commons Attribution NonCommercial (CC BY-NC 4.0) license, which permits others to distribute, remix, adapt, build upon this work non-commercially, and license their derivative works on different terms, provided the original work is properly cited and the use is non-commercial. See: https://creativecommons.org/Licenses/by-nc/4.0/

Country/Territory of origin: Mexico

ORCID number: David Martinez 0000-0003-1417-4784; Gustavo E Sanchez 0000-0003-3579-8027; Jhonatan Gomez 0000-0002-8710-8684; Luis J Sonda 0000-0002-9638-9094; Luis D Suarez 0000-0003-3463-5111; Carlos S Lopez 0000-0002-0590-7766; Juan J Vega 0000-0003-3877-3431.

S-Editor: Liu GL
L-Editor: Filipodia
P-Editor: Liu GL

REFERENCES

1 **Iwahashi N**, Mabuchi Y, Shiro M, Yagi S, Minami S, Ino K. Large uterine pyomyoma in a perimenopausal female: A case report and review of 50 reported cases in the literature. *Mol Clin Oncol* 2016; **5**: 527-531 [PMID: 27882238 DOI: 10.3892/mco.2016.1005]
2 **Kitamura Y**, Ascher SM, Cooper C, Allison SJ, Jha RC, Flick PA, Spies JB. Imaging manifestations of complications associated with uterine artery embolization. *Radiographics* 2005; **25** Suppl 1: S119-S132 [PMID: 16227486 DOI: 10.1148/rg.25si055518]
3 **Karcaaltincaba M**, Sudakoff GS. CT of a ruptured pyomyoma. *AJR Am J Roentgenol* 2003; **181**: 1375-1377 [PMID: 14573437 DOI: 10.2214/ajr.181.5.1811375]
4 **Ono H**, Kanematsu M, Kato H, Toyoki H, Hayasaki Y, Furui T, Morishige K, Hatano Y. MR imaging findings of uterine pyomyoma: radiologic-pathologic correlation. *Abdom Imaging* 2014; **39**: 797-801 [PMID: 24615512 DOI: 10.1007/s00261-014-0112-2]
5 **Peris H**, Del Riego J, Criado E, García-Chamón RB, Vall E, Mayoral M, Martín A. Value of diffusion-weighted magnetic resonance imaging in the diagnosis of pyomyoma. *Radiol Case Rep* 2022; **17**: 137-141 [PMID: 34820037 DOI: 10.1016/j.radcr.2021.10.018]
6 **Wallach EE**, Vlahos NF. Uterine myomas: an overview of development, clinical features, and management. *Obstet Gynecol* 2004; **104**: 393-406 [PMID: 15292018 DOI: 10.1097/01.aog.0000136079.62513.39]
7 **Milazzo GN**, Catalano A, Badia V, Mallozzi M, Caserta D. Myoma and myomectomy: Poor evidence concern in pregnancy. *J Obstet Gynaecol Res* 2017; **43**: 1789-1804 [PMID: 28892210 DOI: 10.1111/jog.13437]



Published by **Baishideng Publishing Group Inc**
7041 Koll Center Parkway, Suite 160, Pleasanton, CA 94566, USA
Telephone: +1-925-3991568
E-mail: bpgoffice@wjgnet.com
Help Desk: https://www.f6publishing.com/helpdesk
https://www.wjgnet.com

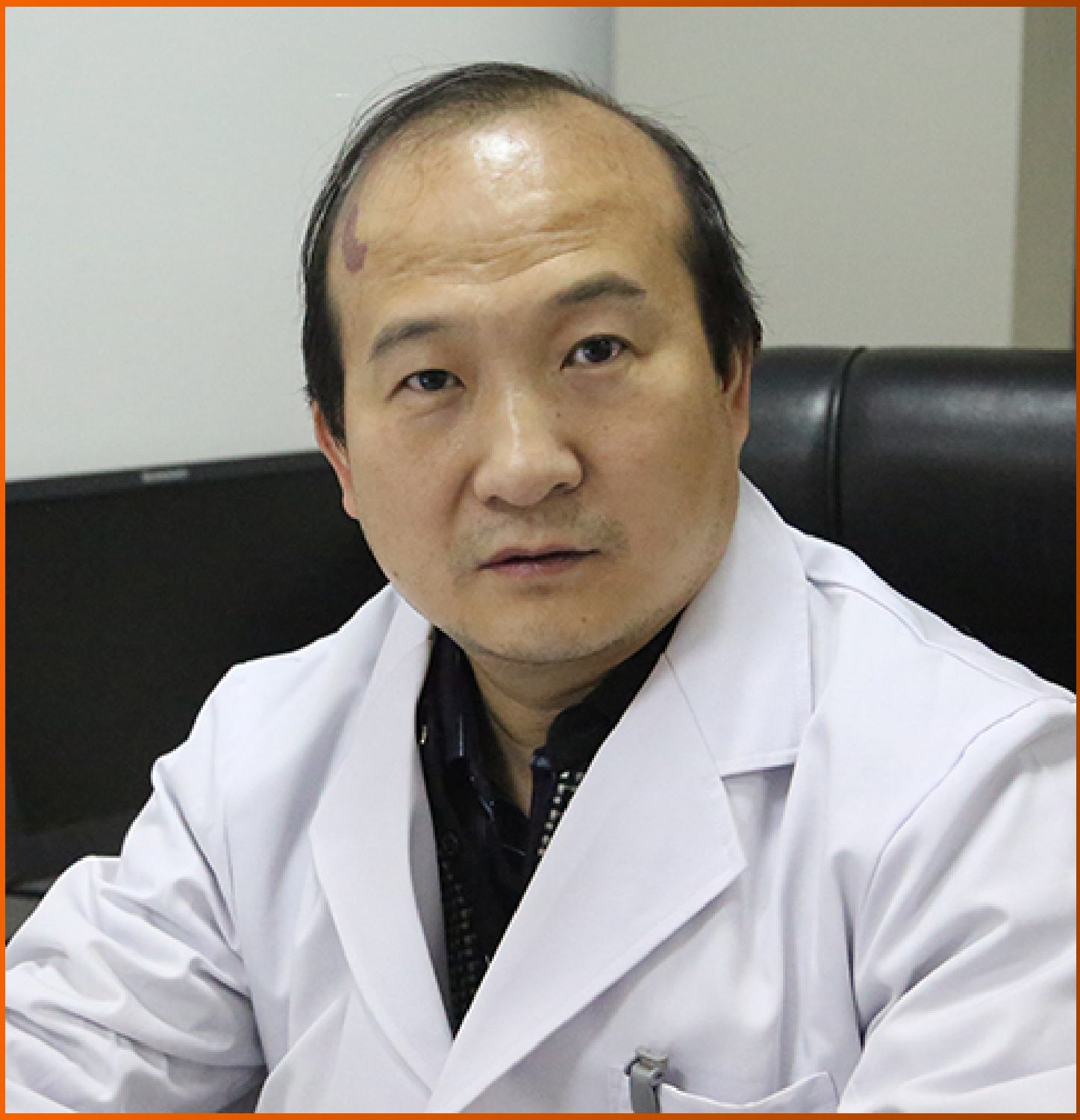


© 2023 Baishideng Publishing Group Inc. All rights reserved.

ISSN 1949-8470 (online)

World Journal of *Radiology*

World J Radiol 2023 April 28; 15(4): 89-135



Published by Baishideng Publishing Group Inc

World Journal of Radiology

Contents

Monthly Volume 15 Number 4 April 28, 2023

MINIREVIEWS

89 Radiomic advances in the transarterial chemoembolization related therapy for hepatocellular carcinoma

Chen TY, Yang ZG, Li Y, Li MQ

98 Evaluation of causal heart diseases in cardioembolic stroke by cardiac computed tomography

Yoshihara S

ORIGINAL ARTICLE

Retrospective Study

118 Detection of tracheal branching with computerized tomography: The relationship between the angles and age-gender

Kahraman Ş, Yazar MF, Aydemir H, Kantarci M, Aydin S

127 Does sevoflurane sedation in pediatric patients lead to "pseudo" leptomeningeal enhancement in the brain on 3 Tesla magnetic resonance imaging?

Hilal K, Khandwala K, Rashid S, Khan F, Anwar SSM

World Journal of Radiology

Monthly Volume 15 Number 4 April 28, 2023

Contents

ABOUT COVER

Editorial Board Member of *Word Journal of Radiology*, Bu-Lang Gao, MD, PhD, Professor, CT/MRI ROOM, Affiliated Hospital of Hebei University, Baoding 070000, Hebei Province, China. browngao@163.com

AIMS AND SCOPE

The primary aim of *World Journal of Radiology* (*WJR*, *World J Radiol*) is to provide scholars and readers from various fields of radiology with a platform to publish high-quality basic and clinical research articles and communicate their research findings online.

WJR mainly publishes articles reporting research results and findings obtained in the field of radiology and covering a wide range of topics including state of the art information on cardiopulmonary imaging, gastrointestinal imaging, genitourinary imaging, musculoskeletal imaging, neuroradiology/head and neck imaging, nuclear medicine and molecular imaging, pediatric imaging, vascular and interventional radiology, and women's imaging.

INDEXING/ABSTRACTING

The *WJR* is now abstracted and indexed in PubMed, PubMed Central, Emerging Sources Citation Index (Web of Science), Reference Citation Analysis, China National Knowledge Infrastructure, China Science and Technology Journal Database, and Superstar Journals Database. The 2022 edition of Journal Citation Reports ® cites the 2021 Journal Citation Indicator (JCI) for *WJR* as 0.48.

RESPONSIBLE EDITORS FOR THIS ISSUE

Production Editor: *Si Zhao*; **Production Department Director:** *Xu Guo*; **Editorial Office Director:** *Jia-Ru Fan*.

NAME OF JOURNAL
World Journal of Radiology

ISSN
ISSN 1949-8470 (online)

LAUNCH DATE
January 31, 2009

FREQUENCY
Monthly

EDITORS-IN-CHIEF
Thomas J Vogl

EDITORIAL BOARD MEMBERS
https://www.wjgnet.com/1949-8470/editorialboard.htm

PUBLICATION DATE
April 28, 2023

COPYRIGHT
© 2023 Baishideng Publishing Group Inc

INSTRUCTIONS TO AUTHORS
https://www.wjgnet.com/bpg/gerinfo/204

GUIDELINES FOR ETHICS DOCUMENTS
https://www.wjgnet.com/bpg/GerInfo/287

GUIDELINES FOR NON-NATIVE SPEAKERS OF ENGLISH
https://www.wjgnet.com/bpg/gerinfo/240

PUBLICATION ETHICS
https://www.wjgnet.com/bpg/GerInfo/288

PUBLICATION MISCONDUCT
https://www.wjgnet.com/bpg/gerinfo/208

ARTICLE PROCESSING CHARGE
https://www.wjgnet.com/bpg/gerinfo/242

STEPS FOR SUBMITTING MANUSCRIPTS
https://www.wjgnet.com/bpg/GerInfo/239

ONLINE SUBMISSION
https://www.f6publishing.com

© 2023 Baishideng Publishing Group Inc. All rights reserved. 7041 Koll Center Parkway, Suite 160, Pleasanton, CA 94566, USA
E-mail: bpgoffice@wjgnet.com https://www.wjgnet.com

World Journal of Radiology

Submit a Manuscript: https://www.f6publishing.com

World J Radiol 2023 April 28; 15(4): 89-97

DOI: 10.4329/wjr.v15.i4.89

ISSN 1949-8470 (online)

MINIREVIEWS

Radiomic advances in the transarterial chemoembolization related therapy for hepatocellular carcinoma

Tian-You Chen, Zong-Guo Yang, Ying Li, Mao-Quan Li

Specialty type: Gastroenterology and hepatology

Provenance and peer review: Invited article; Externally peer reviewed.

Peer-review model: Single blind

Peer-review report's scientific quality classification
Grade A (Excellent): 0
Grade B (Very good): 0
Grade C (Good): C, C
Grade D (Fair): 0
Grade E (Poor): 0

P-Reviewer: Elsayed MOK, United Kingdom; Nakano H, Japan

Received: November 18, 2022
Peer-review started: November 18, 2022
First decision: February 15, 2023
Revised: March 3, 2023
Accepted: March 30, 2023
Article in press: March 30, 2023
Published online: April 28, 2023

Tian-You Chen, Department of Interventional Medicine, Shanghai Public Health Clinical Center, Fudan University, Shanghai 201508, China

Zong-Guo Yang, Department of Integrative Medicine, Shanghai Public Health Clinical Center, Fudan University, Shanghai 201508, China

Ying Li, Department of Radiology, Jinshan Hospital, Fudan University, Shanghai 201508, China

Mao-Quan Li, Department of Interventional & Vascular Surgery, Tenth People's Hospital of Tongji University, Tongji University, Shanghai 200433, China

Corresponding author: Mao-Quan Li, MD, PhD, Director, Professor, Department of Interventional & Vascular Surgery, Tenth People's Hospital of Tongji University, Institute of Interventional & Vascular Surgery, Tongji University, No. 301 Middle Yan Chang Road, Shanghai 200072, China. cjr.limaoquan@vip.163.com

Abstract

Radiomics is a hot topic in the research on customized oncology treatment, efficacy evaluation, and tumor prognosis prediction. To achieve the goal of mining the heterogeneity information within the tumor tissue, the image features concealed within the tumoral images are turned into quantifiable data features. This article primarily describes the research progress of radiomics and clinical-radiomics combined model in the prediction of efficacy, the choice of treatment modality, and survival in transarterial chemoembolization (TACE) and TACE combination therapy for hepatocellular carcinoma.

Key Words: Transarterial chemoembolization; Hepatocellular carcinoma; Radiomics; Magnetic resonance imaging; Computed tomography

©The Author(s) 2023. Published by Baishideng Publishing Group Inc. All rights reserved.

Core Tip: Hepatic cancer is a highly varied primary liver malignancy, and distinct tumor stages necessitate different techniques to guarantee appropriate therapeutic efficacy. Radiomics is a potential method, which can predict the benefits of patients with different treatment methods and different tumor stages through the obtained potential information of clinical medical imaging that is difficult to identify with the naked eye, and predict the outcome of patients, thereby assisting precision medical decision-making. In this paper, we propose and discuss the possible use of radiomics in the selection of treatment modalities and efficacy prediction for liver cancer.

Citation: Chen TY, Yang ZG, Li Y, Li MQ. Radiomic advances in the transarterial chemoembolization related therapy for hepatocellular carcinoma. *World J Radiol* 2023; 15(4): 89-97
URL: https://www.wjgnet.com/1949-8470/full/v15/i4/89.htm
DOI: https://dx.doi.org/10.4329/wjr.v15.i4.89

INTRODUCTION

Approximately 90% of all liver tumors are primary hepatocellular carcinomas (HCC), which are the most frequent primary liver tumors[1]. Among the most prevalent malignant tumors worldwide, HCC is the sixth most prevalent. HCC ranks third in the mortality rate of malignant tumors, which has a significant impact on people's quality of life and physical well-being[2]. According to statistics from the World Health Organization 2018, there are 840000 new instances of HCC each year, of which 780000 cases die[3].

The occurrence and progression of HCC is a complex process with multi-factor participation and multi-step interconnection. The majority of patients would lose their opportunity for radical treatment, such as surgical resection and liver transplantation, due to its insidious onset, atypical symptoms and signs, low early diagnosis rate, rapid disease progression, tumor multicentric origin, abundant blood supply, easy to form cancer thrombus, cause metastasis, highly heterogeneous tumor, and other malignant biological behaviors. The selection of HCC treatments is also constrained by characteristics other than the tumor itself, including the degree of cirrhosis, liver function reserve, and portal hypertension. The effectiveness of a single surgical procedure has demonstrated a "ceiling impact" in light of the HCC's biological nature, which is very aggressive.

With the continuous development of interventional oncology therapeutics, interventional therapy for HCC has developed from straightforward transhepatic arterial therapy to a diversified, combined treatment mode, covering early-, intermediate- and advanced-stage HCC. In the field of minimally invasive treatment of HCC, transarterial chemoembolization (TACE) is the most commonly used technique, which uses lipiodol and/or drug-eluting beads. In process of TACE, cytotoxic drugs like doxorubicin or cisplatin are injected while being emulsified in the radiopaque oil compound lipiodol. After that, the embolic agents, like a gelatin sponge, are given. Lipiodol promotes embolization of the tumor microcirculation and delivers cytotoxic drugs directly to the tumor[4]. Nevertheless, there is no acceptable approach to accurately assess the efficiency of interventional therapy due to the significant individual discrepancies presently.

Radiomics is a technique that combines high-throughput extraction of advanced quantitative features to objectively and quantitatively define tumor behaviors. It was first proposed in 2012 by Dutch researcher Lambin[5]. Radiomics extract a huge number of features from medical pictures in high throughput and turn imaging data into a high-resolution mining data space by automatic or semi-automatic analysis methods[5,6]. It is possible to comprehensively, non-invasively, and quantitatively monitor the spatial and temporal heterogeneity of tumors. Radiomics can be divided into below parts: (1) Image acquisition; (2) Region of interest (ROI) segmentation; (3) Feature Extraction; (4) Feature Selection; (5) Model establishment and evaluation; and (6) Clinical application[5,6]. Radiomics has no restrictions on the sorts of medical pictures used for sample collection, and the objects of analysis can include ultrasound, X-ray, CT, magnetic resonance imaging (MRI), positron emission tomography, and other medical images. The ROI can be altered depending on the clinical situation, whether it is normal tissue, the full tumor area, or a metastatic lesion. Generally, both manual and automatic segmentation of the ROI is used in radiomics. However, the segmentation effect of these automatic segmentation techniques is unstable. Currently, manual ROI segmentation by skilled imaging specialists is the approach most frequently used in medical imaging toolkits (such as ITK-SNAP segmentation software). Nevertheless, manual segmentation takes a lot of time, costs a lot of money, and is susceptible to subjective factors despite having a high accuracy rate. Extraction of high-throughput features for quantitative analysis of the important ROI attributes is the first stage in radiomics. The following three categories generally correspond to the extracted features: (1) Shape feature: Reflecting the information of tumor morphology, size, and regularity; (2) Histogram features: The most basic statistical descriptor is based on a global histogram of grayscale values, which includes the grayscale mean, maximum,

minimum, variance, and percentile. These features are also known as first-order features because they are based on single-pixel or monomer element analysis; and (3) Texture feature: characteristics can measure details that are hard for the eye to easily see, such as tissue distribution inside the tumor or textural patterns. Such high-dimensional abstract features like the Baud sign may play varied roles to capture clinical information that is not readily perceptible by the vision for clinical problems that are difficult to convey by simple visual features of tumor images. Many hundred to tens of thousands of features may be obtained by feature extraction for feature screening, but not all of them are connected to the clinical issues that need to be resolved. On the other hand, because there are so few samples and so many characteristics in practice, it is simple to cause the overfitting phenomena in later models. Hence, choosing the extracted features is a crucial step in the study of radiomics. The commonly used feature selection methods include filtering, packaging, and embedding. The last step is model construction and model evaluation. To establish the key features of the above feature screening based on clinical research questions, or to further combine features other than imaging omics (such as clinical signs, pathology, and genetic test data) to establish predictive models (Figure 1). According to previous studies[5-8], radiomics properties are directly associated with tumor aggressiveness and heterogeneity indices at the cellular level. Radiomics is believed to be able to forecast clinical endpoints including survival and therapeutic response. Second, radiomics data are mineable, which means that, in sufficiently big data groups, they may be utilized to find previously unidentified indicators and patterns of illness evolution, progression, and treatment response.

The aim of this review was to summarize the predictive value of radiomics in TACE alone and combination therapy for HCC and its guiding significance for the formulation of treatment regimens.

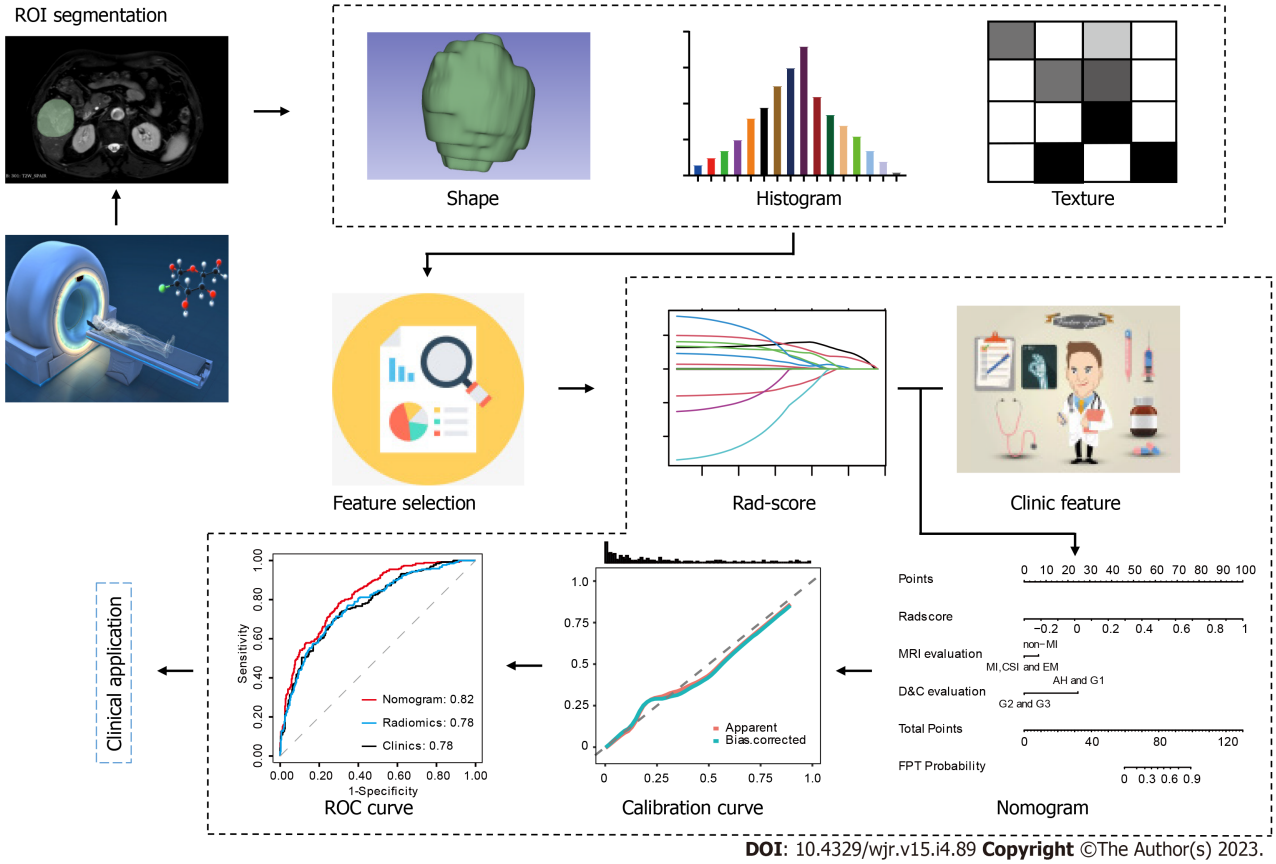
PREDICTION OF EFFICACY

Tumors less than 5 cm

Kuang *et al*[9] retrospectively collected MRI images and clinical data of 153 patients from 3 hospitals, and divided the subjects into 1 internal training group (n = 113) and 1 external validation group (n = 40) to establish MRI radiomics nomograms that can forecast a patient's short-term response to TACE for an HCC with a diameter under 5 cm. By examining pictures [enhanced computed tomography (CT)/magnetic resonance (MR) scans] of all patients 3/4 mo after their initial TACE treatment, the response of HCC patients to TACE was assessed using the modified Response Evaluation Criteria in Solid Tumors (mRECIST). All cases were split into two groups based on the evaluation results: those who responded well (complete response, CR, and partial response, PR), and those who did not (stable disease, SD, and progressive disease, PD). Images from dynamic enhanced MRI (DCE-MRI) arterial phase and T2-weighted imaging (T2WI) were used to establish radiomics model, clinical model, and radiomics nomogram (by combining the radiomics and clinical model). Radiomics selected the image features using the minimum absolute contraction and selection operator (LASSO) regression and the maximum correlation-minimum redundancy (mRMR) algorithm and then selected 11 of the best subsets of features based on the arterial phase to calculate the radscore. The clinical model based on T2WI was ultimately developed by combining platelet count (PLT), pseudocapsule, boundary, and peritumoral augmentation, and well-response was suggested by a normal PLT value (> 100 × 10^9/L), pseudocapsule, and obvious border on the T2WI sequence. Another clinical model based on DCE-MRI arterial phase (AP) was developed by combining Child-Pugh class, border, and peritumoral augmentation. Low ChildPugh class (class A), clear border, and no peritumoral enhancement on AP all point to well-response. In contrast with radiomics and clinical models alone, the results showed that the nomogram had superior predictive potential for postoperative response to TACE. Clinics models and Radiomics were obtained which could predict the postoperative response of TACE, and the maximum area under the curve (AUC) value was 0.76, and 0.78 respectively. When combing Clinics models with Radiomics models, predictive power peaked at 0.84. The T2WI-Nomogram and AP-Nomogram were the models with the highest clinical decision effectiveness, according to a comparison of each model's clinical decision effectiveness. Furthermore, T2WI-based and DCE-MRI-based nomograms had approximately comparable predictive abilities. It is demonstrated that the T2WI sequence may effectively represent the heterogeneity of lesions and that adopting a T2WI sequence can result in the formulation of a stable prediction model, eliminate the need for enhanced scanning, lower the side effects of unnecessary contrast injections and medical costs. Patients included in this study were under MRI scanning from different manufacturers (GE and Siemens) with various field strengths (1.5T and 3.0T) and with various sequence parameters. It was discovered through analyzing and processing data that various machines and magnetic field strengths had a mild influence on the radiomics findings. This result indicated that the radiomics has a high degree of repeatability and stability.

Barcelona clinical liver cancer B

TACE offers a considerable survival advantage over supportive therapy for patients with stage B HCC who are initially diagnosed with Barcelona clinical liver cancer (BCLC). These patients had significant survival heterogeneity following TACE despite getting comparable therapies. Some pre-existing



DOI: 10.4329/wjr.v15.i4.89 **Copyright** ©The Author(s) 2023.

Figure 1 Radiomics flowchart. Based on the imaging data obtained through scanning, the region of interest is delineated on the image, corresponding imaging features are extracted, features are filtered and dimensioned, and imageomics labels are constructed to obtain the rad-score of the image. Then, combined with clinical features, a joint prediction model is established, and a series of clinical applications are conducted by constructing nomogram, calibration curve, and receiver operating characteristic curve. ROI: Region of interest; ROC: Receiver operating characteristic; FPT: Ferroptosis; MRI: Magnetic resonance imaging.

prognostic models have been put forth to forecast clinical outcomes following TACE, including Six-and-twelve score[10], Four-and-seven score[11], Hepatoma arterial-embolization prognostic (HAP score)[12], modified hepatoma arterial embolization prognostic (mHAP score)[13], modified hepatoma arterial embolization II (mHAP-II score)[14], modified hepatoma arterial embolization III (mHAP-III score)[15] and albumin-bilirubin(ALBI) grade[16] for arterial embolization of liver cancer. Using minimum absolute contraction and selection operator approaches, the author of this study creates radiomic signatures for survival (rad signatures). The most predictive 6 radiomic features were ultimately chosen. The remaining 4 features were generated from tumor variants of interest (VOI) imaging in the portal vein phase, leaving 2 of the 6 features based on tumor VOI and peritumoral VOI imaging in the arterial phase. Univariate Cox regression analyses were used to ascertain prognostic clinical factors. With multivariate Cox regression analyses, a combined radiomics-clinic (CRC) model was developed using the Rad-signature and clinical factors with a potential association with overall survival (OS). And then contrasted with a prognostic model that had previously been published. Researchers[17] conducted a retrospective multicenter analysis, and the outcomes revealed that the CRC model which was finally established with tumor number (< 4 *vs* ≥ 4) and the Rad-signature performed better than the other previously mentioned seven established prognostic models, with Harrell's concordance-index (C-index) of 0.73 (95%CI: 0.68–0.79) and 0.70 (95%CI: 0.62–0.82) in the training and testing cohort, respectively. Among the seven models tested, the six-and-12 score and four-and-seven criteria performed better than the other models, with C-indices of 0.64 (95%CI: 0.58–0.70) and 0.65 (95%CI: 0.55–0.75) in the testing cohort, respectively. The authors created customized risk scores by linearly combining the radscore and the number of tumors (< 4 *vs* ≥ 4), weighted by their respective coefficients in the multivariate Cox regression model, in order to aid clinical practice. Patients were separated into two groups based on their median risk scores for the training cohort (0.0214): stratum 1, with a risk score of < -0.0214, and stratum 2, with a risk score of > -0.0214. In the training cohort, stratum 1 patients had a considerably longer median survival (31.3 mo) than stratum 2 patients (12.5 mo), with a hazard ratio of 3.63 (95%CI: 2.36-5.60, log-rank test $P < 0.0001$). Applying the same cutoff to the testing cohort the hazard ratio was 2.43 (95%CI: 1.91-4.98, $P = 0.0014$), and the median survival for the two groups was 30.9 and 17.0 mo, respectively. The CRC model showed improved survival predictive performance, and researchers believe that the CT radiomics signature represents an independent biomarker of survival in patients with HCC undergoing TACE.

Sun *et al*[18] used five distinct MR machines with various field strengths for traditional T1WI, T2WI, and T2 grease pressing as well as diffusion-weighted imaging (DWI) (b = 0 and b = 500) scanning. A total of 84 BCLC B HCC patients were enrolled, of whom 67 were enrolled in the training group and 17 in the test group. The mRECIST was used to assign patients into the disease progression (PD) group and nonprogressive disease (N-PD) group if they progressed 6 mo following TACE treatment. In the test group, the calculated AUC of the DWI feature-based model for TACE efficacy prediction is 0.79 (b = 0) and 0.73 (b = 500), followed by T2WI (0.729) and ADC (0.71). In comparison to any single MRI-based radiomics feature, the multiparametric MRI-based radiomics features' AUC rises to 0.80. While clinical data including age, α-fetoprotein (AFP), and tumor size were not statistically significant, a multivariate logistic analysis could identify the independent prognostic indicators of the radiomics signature of PD.

According to mRECIST 1.1, Bai *et al*[19] aim to evaluate the effectiveness of radiomics features based on preoperative contrast-enhanced computed tomography (CECT) in predicting response to transarterial chemotherapy (TACE), categorized 111 patients with intermediate HCC who received CE-CT in the arterial phase and venous phase before and following TACE into objective response group (n = 38) and non-response group (n = 73) groups. Radiomic feature extraction from CECT pictures. The best monophasic radiomic features of AP and VP in the training set were discovered using two feature ranking methods and three classifiers. In parallel, decision level fusion and feature level fusion were used to combine the pictures of the two CECT phases and establish the multiphase radiomic properties. For the AP signature, the combination of minimum redundancy maximum relevance (MRMR), and support vector machine (SVM) showed the best performance (AUC = 0.814). For VP signatures, the best performance was obtained by MRMR and LASSO (AUC = 0.861). For the performance of multiphase radiomic signatures, DLF signatures had the highest AUC value of 0.883 among all radiomic signatures by using the features selected by MRMR and SVM classifiers. Eventually, a nomogram was constructed by combining two common features (tumor size and tumor number) and radiomics signature, using multivariate logistic regression, and its prediction ability was assessed by AUC on the test data. To determine the accuracy, sensitivity, and specificity values, the cut-off point closest to the upper left corner of the training receiver operating characteristic (ROC) was used. Scores below or above the cutoff were considered to be either objective-response or non-response. It was discovered that multiphase radiomics features (AUC = 0.883) outperformed the best single-phase radiomics signature (AUC = 0.861) in predicting response to TACE treatment. The nomogram in the test dataset and training dataset showed better performance than any radiomics signatures. The authors conclude that the radiomic model will be helpful in assessing the therapeutic advantages of TACE treatment.

Barcelona clinical liver cancer B+C

Kong *et al*[20] enrolled 99 patients with intermediate and advanced HCC (BCLC B and C) treated with TACE. Among them, 69 cases were enrolled in the training group and 30 cases in the test group. MRI was performed before TACE, and efficacy was evaluated according to mRECIST criteria 3 mo after TACE. The patients were divided into response groups (CR and PR) and non-response groups (PD and SD). There were significant differences in AFP values, Child-Pugh scores, and BCLC staging between the two groups. Before TACE, 396 radiomics characteristics were extracted from T2WI, and 6 features were chosen using minimal absolute contraction and selection operator (LASSO) regression. These features are variance, inverse difference moment angle90 offset7, long run emphasis angle90 offset7, short run emphasis all direction offset 4 SD, short run emphasis angle 135 offset1, and high intensity large area emphasis. They are combined to provide radscore to create response prediction models. In the training and validation cohorts, the AUCs of the ROC curve based on Radscore were 0.812 and 0.866, respectively. While the prediction performance of the radiomics model was greatly enhanced when the Child-Pugh class, BCLC stage, and AFP level were added. The AUC of the training group was 0.861 (95%CI: 0.774–0.949) with specificity and sensitivity as high as 0.811 and 0.844, respectively. The AUC of the validation group was 0.884 (95%CI: 0.764–1.000), and the specificity and sensitivity were 0.75 and 1.00, respectively. Based on the above conclusion, the authors believe that the quantitative nomogram model based on radscore and clinical predictors can accurately predict the response to TACE in intermediate and advanced HCC and can also be used as an auxiliary diagnosis for clinical prognosis.

Barcelona clinical liver cancer A+B

Retrospectively, 122 HCC (BCLC A and B) patients who had MRI scanning prior to initial TACE (response = 63; non-response = 59) were recruited by Ying Zhao *et al*[21] and randomly divided into training group (n = 85) and validation group (n = 37). The manual segmentation of arteries, veins, and delayed periods on CE-MRI yielded a total of 2367 radiomics characteristics. Of all radiomics features, the three-phase radiomics model performed better in the training group, with an AUC of 0.838. The AUC of radiomics nomogram combining three-phase radiomics score and clinical-radiological risk factors (total bilirubin, tumor shape, and tumor encapsulation) were 0.878 and 0.833, respectively, which showed good calibration and prediction with better predictive power. However, other studies[22,23] have demonstrated that while total bilirubin can predict survival in HCC patients treated with TACE, it cannot be utilized as a clinical risk factor to evaluate the effectiveness of treatment.

CHOICE OF TREATMENT MODALITY

Almost all the guidelines advocate transitioning to systemic medication or combination therapy when a patient's response to TACE is poor. To tackle this problem, the concept of "TACE refractoriness" is put forth[24,25]. According to the Japanese Liver Association[26], vascular invasion, distant metastases, persistently increased tumor markers or an ongoing partial response to at least two TACEs are indicative of intractable resolution of TACE. New vascular invasion or distant metastases can operate as stand-in markers for refractory TACE during TACE therapy, according to a Korean study[27]. It's critical to anticipate TACE refractoriness while considering a potentially better treatment. The ability to predict TACE refractoriness before surgery has been demonstrated by some researchers utilizing the radiomics nomogram approach on arterial CT scans of 80 HCC patients who did not have extrahepatic metastases or macrovascular involvement[28]. The authors believe that the radscore, which consists of the Gray-Level Zone Length Matrix (GLZLM)-Long-Zone Low Gray-Level Emphasis and GLZLM-Gray-Level Non-Uniformity, T-stage, log AFP, and bilobar distribution is significantly related to TACE refractoriness. Multivariate logistic regression model reveals that these factors, such as radscore+T-stage (AUC = 0.95); radscore+bilobar distribution (AUC = 0.91); and radscore+logAFP (AUC = 0.91), perform well in predicting TACE refractoriness. Additionally, according to Niu *et al*[29], the radiomics nomogram of CT can be used to forecast the pretreatment prediction of TACE refractoriness and offer better guidance for choosing the next course of TACE treatment.

SURVIVAL ANALYSIS

A multicenter retrospective analysis included 140 patients with TACE HCC (BCLC A+B+C)[30]. In order to predict tumor response, response-related radscores were created using T2WI and DCE-MRI, respectively. The T2WI outperformed 4 MRI sequences with an AUC of 0.75. The T2WI radscore, BCLC stage, and albumin-bilirubin grade were combined to generate a nomogram using the logistic regression model. The nomogram yielded AUCs of 0.81 and 0.78 for the train and test groups for predicting tumor response. Progression-free survival (PFS) and OS in survival analyses showed substantial differences between responders and non-responders of TACE treatment. Albumin bilirubin grading, satellite nodes, and BCLC staging are independent predictors of OS. PFS and OS were independently predicted by albumin bilirubin grading and BCLC staging. According to the Cox model, PFS and OS's consistency indices were 0.70 and 0.73, respectively.

Another study extracted radiomics features from intratumoral and perineoplastic dilatation (1, 3, and 5 mm, respectively) from 184 patients with HCC treated with TACE. The radiomics model was constructed using LASSO[31], which was used to investigate the relationship between preoperatively CE-MRI and recurrence-free survival (RFS) in HCC patients regarding the RFS of HCC patients after TACE. Seven models of radiomics (APETV, PVPETV, PVPB1, PVPB3, and PVPB5, in which the TV stands for the total tumor volume and B represents millimeters beyond the tumor boundary), clinical-radiology parameters, and a combination model (nomogram) were generated. The results showed that sex, AFP, BCLC stage, IM (defined as a tumor with a budding portion at its periphery in both the AP and PVP), and APE (which was interpreted as the contrast enhanced shadow around the tumor in the AP, and isointensity compared with the background liver parenchyma in the PVP and delayed phase) were independent risk factors related to RFS after TACE. The performance of the PVPB3 model was 0.714 (C-index), which was equivalent to that of the portal stage intratumor model (C-index, 0.727, P = 0.409). The nomogram, which had a C-index of 0.802 with the best performance, incorporated five independent risk factors from PVPETV characteristics and clinical-radiological parameters. It was more useful for assessing RFS in HCC patients following TACE treatment. The combined model's cutoff relative to the median (1.74) allowed for a precise division of these individuals into high- and low-risk groupings, according to the Kaplan-Meier analysis. A study[29] based on radiomics features by CE-CT in the arterial phase had also revealed that radscore, BCLC stage, irregular tumor margin, largest tumor size, and tumor number were independent influencing factors for OS. CT-based radiomics nomogram could classify patients into high-risk (> 3.5) and low-risk (≤ 3.5) groups with significantly different prognoses between the two groups (OS: 12.3 mo *vs* 23.6 mo, P < 0.001). Another study came to the same conclusion that the combined model (nomogram) included five radiomics features (surface area-to-volume ratio, kurtosis, median, gray-level co-occurrence matrix contrast, and size zone variability) and three clinical factors (Child-Pugh score, α-fetoprotein level, and tumor size) was better in predicting survival than either the clinical scoring model or the radscore model (hazard ratio 19.88; P < 0.001).

COMBINATION THERAPY

TACE + radio frequency ablation (RFA)

TACE and RFA combination therapy have synergistic cytotoxic effects for intermediate and advanced

HCC, compared to TACE alone, which can better control local tumor recurrence and lengthen survival [4]. TACE lessens the "heat sink" that blood flow creates during radiofrequency ablation. It aggravates the edema of tissues, and clearly displays the outlines of lesions induced by iodine oil deposition on CT, making it easier to determine the RFA range. These elements may increase the severity of coagulation necrosis and, as a result, improve OS prominently[32]. However, there are also significant differences in the efficacy of TACE combined with RFA. Some scholars[33] combined radiomics and clinical factors to construct a predictive nomogram model, which can be used as a new strategy for predicting advanced HCC PFS in the treatment of TACE+RFA.

TACE+lenvatinib

Lenvatinib is just as efficient as sorafenib as a multikinase inhibitor with antiangiogenic effects in the first-line treatment of advanced HCC[34]. Combination therapy with TACE and lenvatinib has been shown to be effective in recent studies[35,36]. According to the findings, combination therapy outperformed lenvatinib monotherapy and TACE by a wide margin. Luo *et al*[37] studied 61 HCC patients and extracted radiomics characteristics from T1WI, T1WI arterial phase, T1WI portal phase, T1WI delay phase, T2WI, DWI (b = 800), and ADC maps. The results showed that the number of tumors [risk ratio, HR = 4.64, 95%CI: 1.03-20.88, P = 0.045] and arterial phase intensity HR = 0.24, (95%CI: 0.09-0.64) with a sensitivity of 0.99, specificity of 0.95, and accuracy of 0.71. The combined model significantly increased the clinical model's performance in predicting disease progression.

CURRENT LIMITATIONS

We discussed the use of radiomics in predicting TACE treatment in HCC, which quantifies the heterogeneity of HCC on medical images. These radiomics features can be further used as predictors of clinical outcomes to determine the efficacy of TACE, as well as provide individualized guidance for patient treatment options. However, there are also some difficulties need to be further resolved. First, it might be challenging by using a computer to pinpoint the tumor boundary automatically, and hand outlining may vulnerable to significant subjective variation. Second, considering radiomics is still in its infancy and different researchers employ different imaging tools and image algorithms, it is impossible for other researchers to evaluate and put the results to clinical use[38]. Last but not the least, it is challenging to create a worldwide uniform paradigm for radiomics in HCC research because the underlying etiology of the disease varies between different regions[39].

CONCLUSION

Radiomics can forecast the efficacy of TACE and TACE combined therapy regimens before the treatment conducting. Tailored counsel for patient treatment based on radiomics and increased comprehensive prediction abilities would be achieved when combined with clinical data.

FOOTNOTES

Author contributions: Chen TY, Yang ZG, Li Y, Li MQ equally contributed to this paper with conception and design of the study, literature review and analysis, drafting and critical revision and editing, and final approval of the final version.

Conflict-of-interest statement: All the authors declare that they have no conflicting interests.

Open-Access: This article is an open-access article that was selected by an in-house editor and fully peer-reviewed by external reviewers. It is distributed in accordance with the Creative Commons Attribution NonCommercial (CC BY-NC 4.0) license, which permits others to distribute, remix, adapt, build upon this work non-commercially, and license their derivative works on different terms, provided the original work is properly cited and the use is non-commercial. See: https://creativecommons.org/Licenses/by-nc/4.0/

Country/Territory of origin: China

ORCID number: Tian-You Chen 0000-0002-8668-6650; Zong-Guo Yang 0000-0002-6623-4841; Ying Li 0000-0001-5062-0230; Mao-Quan Li 0000-0001-7849-7350.

S-Editor: Liu JH
L-Editor: A
P-Editor: Zhao S

REFERENCES

1 **Dy GW**, Gore JL, Forouzanfar MH, Naghavi M, Fitzmaurice C. Global Burden of Urologic Cancers, 1990-2013. *Eur Urol* 2017; **71**: 437-446 [PMID: 28029399 DOI: 10.1016/j.eururo.2016.10.008]

2 **Yang JD**, Hainaut P, Gores GJ, Amadou A, Plymoth A, Roberts LR. A global view of hepatocellular carcinoma: trends, risk, prevention and management. *Nat Rev Gastroenterol Hepatol* 2019; **16**: 589-604 [PMID: 31439937 DOI: 10.1038/s41575-019-0186-y]

3 **Bray F**, Ferlay J, Soerjomataram I, Siegel RL, Torre LA, Jemal A. Global cancer statistics 2018: GLOBOCAN estimates of incidence and mortality worldwide for 36 cancers in 185 countries. *CA Cancer J Clin* 2018; **68**: 394-424 [PMID: 30207593 DOI: 10.3322/caac.21492]

4 **Chang Y**, Jeong SW, Young Jang J, Jae Kim Y. Recent Updates of Transarterial Chemoembolilzation in Hepatocellular Carcinoma. *Int J Mol Sci* 2020; **21** [PMID: 33142892 DOI: 10.3390/ijms21218165]

5 **Lambin P**, Rios-Velazquez E, Leijenaar R, Carvalho S, van Stiphout RG, Granton P, Zegers CM, Gillies R, Boellard R, Dekker A, Aerts HJ. Radiomics: extracting more information from medical images using advanced feature analysis. *Eur J Cancer* 2012; **48**: 441-446 [PMID: 22257792 DOI: 10.1016/j.ejca.2011.11.036]

6 **Kumar V**, Gu Y, Basu S, Berglund A, Eschrich SA, Schabath MB, Forster K, Aerts HJ, Dekker A, Fenstermacher D, Goldgof DB, Hall LO, Lambin P, Balagurunathan Y, Gatenby RA, Gillies RJ. Radiomics: the process and the challenges. *Magn Reson Imaging* 2012; **30**: 1234-1248 [PMID: 22898692 DOI: 10.1016/j.mri.2012.06.010]

7 **Choi ER**, Lee HY, Jeong JY, Choi YL, Kim J, Bae J, Lee KS, Shim YM. Quantitative image variables reflect the intratumoral pathologic heterogeneity of lung adenocarcinoma. *Oncotarget* 2016; **7**: 67302-67313 [PMID: 27589833 DOI: 10.18632/oncotarget.11693]

8 **Sala E**, Mema E, Himoto Y, Veeraraghavan H, Brenton JD, Snyder A, Weigelt B, Vargas HA. Unravelling tumour heterogeneity using next-generation imaging: radiomics, radiogenomics, and habitat imaging. *Clin Radiol* 2017; **72**: 3-10 [PMID: 27742105 DOI: 10.1016/j.crad.2016.09.013]

9 **Kuang Y**, Li R, Jia P, Ye W, Zhou R, Zhu R, Wang J, Lin S, Pang P, Ji W. MRI-Based Radiomics: Nomograms predicting the short-term response after transcatheter arterial chemoembolization (TACE) in hepatocellular carcinoma patients with diameter less than 5 cm. *Abdom Radiol (NY)* 2021; **46**: 3772-3789 [PMID: 33713159 DOI: 10.1007/s00261-021-02992-2]

10 **Wang Q**, Xia D, Bai W, Wang E, Sun J, Huang M, Mu W, Yin G, Li H, Zhao H, Li J, Zhang C, Zhu X, Wu J, Gong W, Li Z, Lin Z, Pan X, Shi H, Shao G, Liu J, Yang S, Zheng Y, Xu J, Song J, Wang W, Wang Z, Zhang Y, Ding R, Zhang H, Yu H, Zheng L, Gu W, You N, Wang G, Zhang S, Feng L, Liu L, Zhang P, Li X, Chen J, Xu T, Zhou W, Zeng H, Huang W, Jiang W, Zhang W, Shao W, Li L, Niu J, Yuan J, Lv Y, Li K, Yin Z, Xia J, Fan D, Han G; China HCC-TACE Study Group. Development of a prognostic score for recommended TACE candidates with hepatocellular carcinoma: A multicentre observational study. *J Hepatol* 2019; **70**: 893-903 [PMID: 30660709 DOI: 10.1016/j.jhep.2019.01.013]

11 **Yamakado K**, Miyayama S, Hirota S, Mizunuma K, Nakamura K, Inaba Y, Maeda H, Matsuo K, Nishida N, Aramaki T, Anai H, Koura S, Oikawa S, Watanabe K, Yasumoto T, Furuichi K, Yamaguchi M. Subgrouping of intermediate-stage (BCLC stage B) hepatocellular carcinoma based on tumor number and size and Child-Pugh grade correlated with prognosis after transarterial chemoembolization. *Jpn J Radiol* 2014; **32**: 260-265 [PMID: 24615165 DOI: 10.1007/s11604-014-0298-9]

12 **Kadalayil L**, Benini R, Pallan L, O'Beirne J, Marelli L, Yu D, Hackshaw A, Fox R, Johnson P, Burroughs AK, Palmer DH, Meyer T. A simple prognostic scoring system for patients receiving transarterial embolisation for hepatocellular cancer. *Ann Oncol* 2013; **24**: 2565-2570 [PMID: 23857958 DOI: 10.1093/annonc/mdt247]

13 **Pinato DJ**, Arizumi T, Allara E, Jang JW, Smirne C, Kim YW, Kudo M, Pirisi M, Sharma R. Validation of the hepatoma arterial embolization prognostic score in European and Asian populations and proposed modification. *Clin Gastroenterol Hepatol* 2015; **13**: 1204-8.e2 [PMID: 25528009 DOI: 10.1016/j.cgh.2014.11.037]

14 **Park Y**, Kim SU, Kim BK, Park JY, Kim DY, Ahn SH, Park YE, Park JH, Lee YI, Yun HR, Han KH. Addition of tumor multiplicity improves the prognostic performance of the hepatoma arterial-embolization prognostic score. *Liver Int* 2016; **36**: 100-107 [PMID: 26013186 DOI: 10.1111/liv.12878]

15 **Campani C**, Vitale A, Dragoni G, Arena U, Laffi G, Cillo U, Giannini EG, Tovoli F, Rapaccini GL, Di Marco M, Caturelli E, Zoli M, Sacco R, Cabibbo G, Mega A, Guarino M, Gasbarrini A, Svegliati-Baroni G, Foschi FG, Biasini E, Masotto A, Nardone G, Raimondo G, Azzaroli F, Vidili G, Brunetto MR, Farinati F, Trevisani F, Marra F. Time-Varying mHAP-III Is the Most Accurate Predictor of Survival in Patients with Hepatocellular Carcinoma Undergoing Transarterial Chemoembolization. *Liver Cancer* 2021; **10**: 126-136 [PMID: 33977089 DOI: 10.1159/000513404]

16 **Hiraoka A**, Kumada T, Kudo M, Hirooka M, Tsuji K, Itobayashi E, Kariyama K, Ishikawa T, Tajiri K, Ochi H, Tada T, Toyoda H, Nouso K, Joko K, Kawasaki H, Hiasa Y, Michitaka K; Real-Life Practice Experts for HCC (RELPEC) Study Group and HCC 48 Group (hepatocellular carcinoma experts from 48 clinics). Albumin-Bilirubin (ALBI) Grade as Part of the Evidence-Based Clinical Practice Guideline for HCC of the Japan Society of Hepatology: A Comparison with the Liver Damage and Child-Pugh Classifications. *Liver Cancer* 2017; **6**: 204-215 [PMID: 28626732 DOI: 10.1159/000452846]

17 **Meng XP**, Wang YC, Ju S, Lu CQ, Zhong BY, Ni CF, Zhang Q, Yu Q, Xu J, Ji J, Zhang XM, Tang TY, Yang G, Zhao Z. Radiomics Analysis on Multiphase Contrast-Enhanced CT: A Survival Prediction Tool in Patients With Hepatocellular Carcinoma Undergoing Transarterial Chemoembolization. *Front Oncol* 2020; **10**: 1196 [PMID: 32850345 DOI: 10.3389/fonc.2020.01196]

18 **Sun Y**, Bai H, Xia W, Wang D, Zhou B, Zhao X, Yang G, Xu L, Zhang W, Liu P, Xu J, Meng S, Liu R, Gao X. Predicting the Outcome of Transcatheter Arterial Embolization Therapy for Unresectable Hepatocellular Carcinoma Based on Radiomics of Preoperative Multiparameter MRI. *J Magn Reson Imaging* 2020; **52**: 1083-1090 [PMID: 32233054 DOI: 10.1002/jmri.27143]

19 **Bai H**, Meng S, Xiong C, Liu Z, Shi W, Ren Q, Xia W, Zhao X, Jian J, Song Y, Ni C, Gao X, Li Z. Preoperative CECT-based Radiomic Signature for Predicting the Response of Transarterial Chemoembolization (TACE) Therapy in Hepatocellular Carcinoma. *Cardiovasc Intervent Radiol* 2022; **45**: 1524-1533 [PMID: 35896687 DOI:

10.1007/s00270-022-03221-z]

20 **Kong C**, Zhao Z, Chen W, Lv X, Shu G, Ye M, Song J, Ying X, Weng Q, Weng W, Fang S, Chen M, Tu J, Ji J. Prediction of tumor response *via* a pretreatment MRI radiomics-based nomogram in HCC treated with TACE. *Eur Radiol* 2021; **31**: 7500-7511 [PMID: 33860832 DOI: 10.1007/s00330-021-07910-0]

21 **Zhao Y**, Wang N, Wu J, Zhang Q, Lin T, Yao Y, Chen Z, Wang M, Sheng L, Liu J, Song Q, Wang F, An X, Guo Y, Li X, Wu T, Liu AL. Radiomics Analysis Based on Contrast-Enhanced MRI for Prediction of Therapeutic Response to Transarterial Chemoembolization in Hepatocellular Carcinoma. *Front Oncol* 2021; **11**: 582788 [PMID: 33868988 DOI: 10.3389/fonc.2021.582788]

22 **Abajian A**, Murali N, Savic LJ, Laage-Gaupp FM, Nezami N, Duncan JS, Schlachter T, Lin M, Geschwind JF, Chapiro J. Predicting Treatment Response to Intra-arterial Therapies for Hepatocellular Carcinoma with the Use of Supervised Machine Learning-An Artificial Intelligence Concept. *J Vasc Interv Radiol* 2018; **29**: 850-857.e1 [PMID: 29548875 DOI: 10.1016/j.jvir.2018.01.769]

23 **Zhang H**, He X, Yu J, Song W, Liu X, Liu Y, Zhou J, Guo D. Preoperative MRI features and clinical laboratory indicators for predicting the early therapeutic response of hepatocellular carcinoma to transcatheter arterial chemoembolization combined with High-intensity focused ultrasound treatment. *Br J Radiol* 2019; **92**: 20190073 [PMID: 31166700 DOI: 10.1259/bjr.20190073]

24 **Raoul JL**, Sangro B, Forner A, Mazzaferro V, Piscaglia F, Bolondi L, Lencioni R. Evolving strategies for the management of intermediate-stage hepatocellular carcinoma: available evidence and expert opinion on the use of transarterial chemoembolization. *Cancer Treat Rev* 2011; **37**: 212-220 [PMID: 20724077 DOI: 10.1016/j.ctrv.2010.07.006]

25 **Yamashita T**, Kaneko S. Treatment strategies for hepatocellular carcinoma in Japan. *Hepatol Res* 2013; **43**: 44-50 [PMID: 22583802 DOI: 10.1111/j.1872-034X.2012.01029.x]

26 **Kudo M**, Izumi N, Kokudo N, Matsui O, Sakamoto M, Nakashima O, Kojiro M, Makuuchi M; HCC Expert Panel of Japan Society of Hepatology. Management of hepatocellular carcinoma in Japan: Consensus-Based Clinical Practice Guidelines proposed by the Japan Society of Hepatology (JSH) 2010 updated version. *Dig Dis* 2011; **29**: 339-364 [PMID: 21829027 DOI: 10.1159/000327577]

27 **Kim HY**, Park JW, Joo J, Jung SJ, An S, Woo SM, Kim HB, Koh YH, Lee WJ, Kim CM. Severity and timing of progression predict refractoriness to transarterial chemoembolization in hepatocellular carcinoma. *J Gastroenterol Hepatol* 2012; **27**: 1051-1056 [PMID: 22098152 DOI: 10.1111/j.1440-1746.2011.06963.x]

28 **Sheen H**, Kim JS, Lee JK, Choi SY, Baek SY, Kim JY. A radiomics nomogram for predicting transcatheter arterial chemoembolization refractoriness of hepatocellular carcinoma without extrahepatic metastasis or macrovascular invasion. *Abdom Radiol (NY)* 2021; **46**: 2839-2849 [PMID: 33388805 DOI: 10.1007/s00261-020-02884-x]

29 **Niu XK**, He XF. Development of a computed tomography-based radiomics nomogram for prediction of transarterial chemoembolization refractoriness in hepatocellular carcinoma. *World J Gastroenterol* 2021; **27**: 189-207 [PMID: 33510559 DOI: 10.3748/wjg.v27.i2.189]

30 **Liu QP**, Yang KL, Xu X, Liu XS, Qu JR, Zhang YD. Radiomics analysis of pretreatment MRI in predicting tumor response and outcome in hepatocellular carcinoma with transarterial chemoembolization: a two-center collaborative study. *Abdom Radiol (NY)* 2022; **47**: 651-663 [PMID: 34918174 DOI: 10.1007/s00261-021-03375-3]

31 **Song W**, Yu X, Guo D, Liu H, Tang Z, Liu X, Zhou J, Zhang H, Liu Y. MRI-Based Radiomics: Associations With the Recurrence-Free Survival of Patients With Hepatocellular Carcinoma Treated With Conventional Transcatheter Arterial Chemoembolization. *J Magn Reson Imaging* 2020; **52**: 461-473 [PMID: 31675174 DOI: 10.1002/jmri.26977]

32 **Iezzi R**, Pompili M, Posa A, Coppola G, Gasbarrini A, Bonomo L. Combined locoregional treatment of patients with hepatocellular carcinoma: State of the art. *World J Gastroenterol* 2016; **22**: 1935-1942 [PMID: 26877601 DOI: 10.3748/wjg.v22.i6.1935]

33 **Fang S**, Lai L, Zhu J, Zheng L, Xu Y, Chen W, Wu F, Wu X, Chen M, Weng Q, Ji J, Zhao Z, Tu J. A Radiomics Signature-Based Nomogram to Predict the Progression-Free Survival of Patients With Hepatocellular Carcinoma After Transcatheter Arterial Chemoembolization Plus Radiofrequency Ablation. *Front Mol Biosci* 2021; **8**: 662366 [PMID: 34532340 DOI: 10.3389/fmolb.2021.662366]

34 **Kudo M**, Finn RS, Qin S, Han KH, Ikeda K, Piscaglia F, Baron A, Park JW, Han G, Jassem J, Blanc JF, Vogel A, Komov D, Evans TRJ, Lopez C, Dutcus C, Guo M, Saito K, Kraljevic S, Tamai T, Ren M, Cheng AL. Lenvatinib *vs* sorafenib in first-line treatment of patients with unresectable hepatocellular carcinoma: a randomised phase 3 non-inferiority trial. *Lancet* 2018; **391**: 1163-1173 [PMID: 29433850 DOI: 10.1016/S0140-6736(18)30207-1]

35 **Ando Y**, Kawaoka T, Amioka K, Naruto K, Ogawa Y, Yoshikawa Y, Kikukawa C, Kosaka Y, Uchikawa S, Morio K, Fujino H, Nakahara T, Murakami E, Yamauchi M, Tsuge M, Hiramatsu A, Fukuhara T, Mori N, Takaki S, Tsuji K, Nonaka M, Hyogo H, Aisaka Y, Masaki K, Honda Y, Moriya T, Naeshiro N, Takahashi S, Imamura M, Chayama K, Aikata H. Efficacy and Safety of Lenvatinib-Transcatheter Arterial Chemoembolization Sequential Therapy for Patients with Intermediate-Stage Hepatocellular Carcinoma. *Oncology* 2021; **99**: 507-517 [PMID: 33946070 DOI: 10.1159/000515865]

36 **Fu Z**, Li X, Zhong J, Chen X, Cao K, Ding N, Liu L, Zhang X, Zhai J, Qu Z. Lenvatinib in combination with transarterial chemoembolization for treatment of unresectable hepatocellular carcinoma (uHCC): a retrospective controlled study. *Hepatol Int* 2021; **15**: 663-675 [PMID: 33877527 DOI: 10.1007/s12072-021-10184-9]

37 **Luo J**, Huang Z, Wang M, Li T, Huang J. Prognostic role of multiparameter MRI and radiomics in progression of advanced unresectable hepatocellular carcinoma following combined transcatheter arterial chemoembolization and lenvatinib therapy. *BMC Gastroenterol* 2022; **22**: 108 [PMID: 35260095 DOI: 10.1186/s12876-022-02129-9]

38 **Orlhac F**, Frouin F, Nioche C, Ayache N, Buvat I. Validation of A Method to Compensate Multicenter Effects Affecting CT Radiomics. *Radiology* 2019; **291**: 53-59 [PMID: 30694160 DOI: 10.1148/radiol.2019182023]

39 **Kim DY**, Ryu HJ, Choi JY, Park JY, Lee DY, Kim BK, Kim SU, Ahn SH, Chon CY, Han KH. Radiological response predicts survival following transarterial chemoembolisation in patients with unresectable hepatocellular carcinoma. *Aliment Pharmacol Ther* 2012; **35**: 1343-1350 [PMID: 22486716 DOI: 10.1111/j.1365-2036.2012.05089.x]

World Journal of Radiology

Submit a Manuscript: https://www.f6publishing.com

World J Radiol 2023 April 28; 15(4): 98-117

DOI: 10.4329/wjr.v15.i4.98

ISSN 1949-8470 (online)

MINIREVIEWS

Evaluation of causal heart diseases in cardioembolic stroke by cardiac computed tomography

Shu Yoshihara

Specialty type: Cardiac and cardiovascular systems

Provenance and peer review: Invited article; Externally peer reviewed.

Peer-review model: Single blind

Peer-review report's scientific quality classification

Grade A (Excellent): 0
Grade B (Very good): B, B, B
Grade C (Good): 0
Grade D (Fair): 0
Grade E (Poor): 0

P-Reviewer: Gupta P, United States; Liao X, China; Ong H, Malaysia

Received: December 6, 2022
Peer-review started: December 6, 2022
First decision: March 1, 2023
Revised: March 8, 2023
Accepted: March 30, 2023
Article in press: March 30, 2023
Published online: April 28, 2023

Shu Yoshihara, Department of Diagnostic Radiology, Iwata City Hospital, Iwata 438-8550, Shizuoka, Japan

Corresponding author: Shu Yoshihara, MD, PhD, Doctor, Department of Diagnostic Radiology, Iwata City Hospital, 512-3 Ookubo, Iwata 438-8550, Shizuoka, Japan.
shuy@hospital.iwata.shizuoka.jp

Abstract

Cardioembolic stroke is a potentially devastating condition and tends to have a poor prognosis compared with other ischemic stroke subtypes. Therefore, it is important for proper therapeutic management to identify a cardiac source of embolism in stroke patients. Cardiac computed tomography (CCT) can detect the detailed visualization of various cardiac pathologies in the cardiac chambers, interatrial and interventricular septum, valves, and myocardium with few motion artifacts and few dead angles. Multiphase reconstruction images of the entire cardiac cycle make it possible to demonstrate cardiac structures in a dynamic manner. Consequently, CCT has the ability to provide high-quality information about causal heart disease in cardioembolic stroke. In addition, CCT can simultaneously evaluate obstructive coronary artery disease, which may be helpful in surgical planning in patients who need urgent surgery, such as cardiac tumors or infective endocarditis. This review will introduce the potential clinical applications of CCT in an ischemic stroke population, with a focus on diagnosing cardioembolic sources using CCT.

Key Words: Acute ischemic stroke; Cardioembolic stroke; Cardiac computed tomography

©The Author(s) 2023. Published by Baishideng Publishing Group Inc. All rights reserved.

Core Tip: Cardiac computed tomography (CCT) can detect the detailed visualization of causal heart disease in cardioembolic stroke. This review introduces the potential clinical applications of CCT in an ischemic stroke population, with a focus on diagnosing cardioembolic sources using CCT. Specifically, left atrial thrombus and associated pathologies, left ventricular thrombus and associated pathologies, intracardiac tumors, valvular abnormalities, and causal pathologies of paradoxical embolism are discussed.

Citation: Yoshihara S. Evaluation of causal heart diseases in cardioembolic stroke by cardiac computed tomography. *World J Radiol* 2023; 15(4): 98-117
URL: https://www.wjgnet.com/1949-8470/full/v15/i4/98.htm
DOI: https://dx.doi.org/10.4329/wjr.v15.i4.98

INTRODUCTION

Ischemic stroke is a sudden onset of a focal neurologic deficit attributed to cerebral ischemia that results in neuron death. Ischemic stroke is etiologically sub-classified into four categories: Large artery atherosclerosis, cardiac embolism, small vessel occlusion, and other uncommon causes[1,2]. Ischemic stroke due to cardiac embolism commonly has a sudden onset, is more prone to hemorrhagic transformation, and generally carries a worse prognosis with respect to disability, mortality, and early and long-term recurrence of stroke compared with other etiologies. Therefore, in the diagnostic work-up of ischemic stroke patients with suspected embolism, identification of a cardioembolic source is essential in determining appropriate secondary prevention. The diagnosis of cardioembolic stroke is usually performed based on medical history information, physical examination, laboratory testing, 12-lead electrocardiogram (ECG), heart rhythm monitoring (in-hospital telemetry, ambulant 24-h Holter), and transthoracic echocardiography (TTE)[3]. Transesophageal echocardiography (TEE) is highly accurate in the detection of abnormalities in the left atrium and left atrial appendage (LAA), atrial septum, mitral valve, and aortic arch. In fact, TEE has been shown to be superior to TTE for detecting potential sources of cardiac embolism in patients with ischemic stroke[4,5]. However, TEE has inherent associated risks, including esophageal injury, aspiration, and hypertension or hypotension during the procedure. Although TEE complication rates are very low, TEE may be difficult to perform in stroke patients with neurologic deficits that make it impossible to cooperate with instructions given during the procedure. Progress in the technical development of cardiac computed tomography (CCT) enables rapid, accurate imaging of the cardiovascular system. With CCT, it is necessary to use either prospective or retrospective ECG gating to synchronize the CT image with the ECG. In both methods, the ECG waveform is used to coordinate image reconstruction with the heart's position in the chest. The diagnostic accuracy of CCT compared with invasive coronary angiography has been evaluated in multiple trials. A meta-analysis across nine studies identified 97% sensitivity with 78% specificity for detecting > 50% stenosis[6]. In addition to stenosis location and severity, CCT can simultaneously evaluate the plaque characteristics and plaque burden of the coronary artery (Table 1). With its high spatial resolution and multiplanar reconstruction capabilities, CCT can detect the detailed visualization of various cardiac pathologies in the cardiac chambers, interatrial and interventricular septum, valves, and myocardium with few motion artifacts and few dead angles. In addition, multiphase reconstruction images of the entire cardiac cycle detected by retrospective ECG gating can provide a functional assessment of cardiac structure in a dynamic manner (Cine-CT)[7]. Therefore, CCT has the ability to provide high-quality information about causal heart disease in cardioembolic stroke. Indeed, current guidelines indicate that CCT should be performed as a second step if echocardiography is non-diagnostic in evaluating cardiac mass, valvular heart disease, and congenital heart disease[8].

This review will introduce the potential clinical applications of CCT in an ischemic stroke population, with a focus on diagnosing cardioembolic sources using CCT.

CARDIOEMBOLIC SOURCES OF ISCHEMIC STROKE

Numerous cardiac conditions have been proposed as potential sources of embolism. Based on the evidence of their relative propensities for embolism, cardiac sources are divided into two categories: High risk and medium risk (Table 2). Compared to standard stroke management, patients at high risk for cardioembolic stroke require a different therapeutic strategy, such as the prescription of anticoagulants. Patients at medium risk for cardioembolic stroke exhibit a strong association with increased risk of stroke, but currently there are no clear and appropriate management guidelines for the prevention of stroke occurrence. Cardiac sources of embolism are classified into arrhythmias and structural cardiac diseases. Atrial fibrillation (Af) is the most common arrhythmia related to embolic stroke. Atrial flutter and sick sinus syndrome (tachycardia-bradycardia syndrome) are also associated with a higher risk of stroke. The diagnosis of atrial dysrhythmias is performed by 12-lead ECG and heart rhythm monitoring (in-hospital telemetry, 24-h Holter ECG, prolonged rhythm monitoring). Structural cardiac diseases are usually diagnosed by echocardiography. CCT can provide complementary information to echocardiography in the diagnosis of structural cardiac sources of embolism.

Table 1 Information suitable for detection by cardiac computed tomography

Condition	Location	Information
Coronary artery disease	Coronary artery	Stenosis location and severity
		Plaque characteristics
		Plaque burden: CAC score, plaque volume
		Other: Pericoronary FAI, FFR_{CT}
	Myocardium	Enhancement pattern: Perfusion defect, LIE
		Degeneration: Fat, calcification, wall thinning
	Wall motion	Regional wall motion abnormality: LV, RV
		Global function: LV, RV
Valvular heart disease	Native heart valve	Aortic stenosis: BAV or TAV, AVA, pre and post evaluation of TAVR
		Chronic secondary mitral regurgitation: Etiology assessment
		Calcium score: AV, MAC
	Prosthetic heart valve	Mechanical valve dysfunction
	Infective endocarditis	Periannular complication
Congenital heart disease		Anomaly of coronary artery
		Anomaly of thoracic arteriovenous vessels
		Complex and repaired adult congenital heart disease
		Unusual anatomy of atrial and ventricular septal defect
		Quantitative evaluation of right ventricular function

CAC: Coronary artery calcium; FAI: Fat attenuation index; FFR_{CT}: CT-derived fractional flow reserve; LIE: Late iodine enhancement; LV: Left ventricle; RV: Right ventricle; BAV: Bicuspid aortic valve; TAV: Tricuspid aortic valve; AVA: Aortic valve area; TAVR: Transcatheter aortic valve replacement; AV: Aortic valve; MAC: Mitral annular calcification.

CARDIAC CT FOR DIAGNOSIS OF SPECIFIC CARDIOEMBOLIC SOURCES

Left atrial thrombus and associated pathologies

Stroke associated with Af is attributed to embolism of thrombus from the left atrium (LA). The LAA is an anterolateral muscular extension of the LA arising adjacent to the left superior pulmonary vein and lying in the left atrioventricular sulcus close to the left circumflex coronary artery. The LAA is an embryological remnant that functions as a reservoir during conditions of fluid overload. Because of its hooked morphology, blood stasis tends to occur in the LAA. As a result, more than 90% of thrombi in patients with Af originate from the LAA[9]. Structural and functional aspects of the LAA are linked to stroke risk in patients with Af. For example, stasis resulting from decreased emptying of the LAA due to loss of organized mechanical contraction during the cardiac cycle, as evidenced by reduced LAA flow velocities on TEE, is associated with thrombus formation and stroke risk.

In CCT examination under sinus rhythm, the LAA is opacified with a contrast medium in the early phase, which evaluates the coronary artery. By contrast, in CCT examination under atrial fibrillation, a contrast medium filling defect is usually observed in the LAA, which reflects the stasis of blood flow within the LAA. A contrast medium filling defect in the LAA is an important finding by itself. In patients with Af, increased contrast heterogeneity within the LAA on contrast-enhanced CT correlates with an increased degree of spontaneous echo contrast and decreased LAA emptying velocity on TEE [10-12]. Furthermore, in a study of 1019 patients who underwent CCT before first-time radiofrequency catheter ablation for Af, Kawaji *et al*[13] reported that patients with severe contrast medium filling defects in the LAA are associated with higher incidence of ischemic stroke compared to patients with mild or no filling defects in the LAA during a mean follow-up of 4.4 years. However, the assessment of thrombi in the LAA is confounded by such filling defects. Therefore, a second scan should be performed several minutes after the initial first-pass scan. The addition of delayed imaging enables a better distinction of both thrombus and blood stasis. An apparent filling defect in the LAA observed in early phase resolves in delayed phase if no thrombus is present (Figure 1). On the other hand, true thrombi in the LAA can be recognized as a filling defect in both early and delayed phases (Figure 2). In a meta-analysis of seven studies with a total of 753 patients for whom delayed images were obtained, CCT

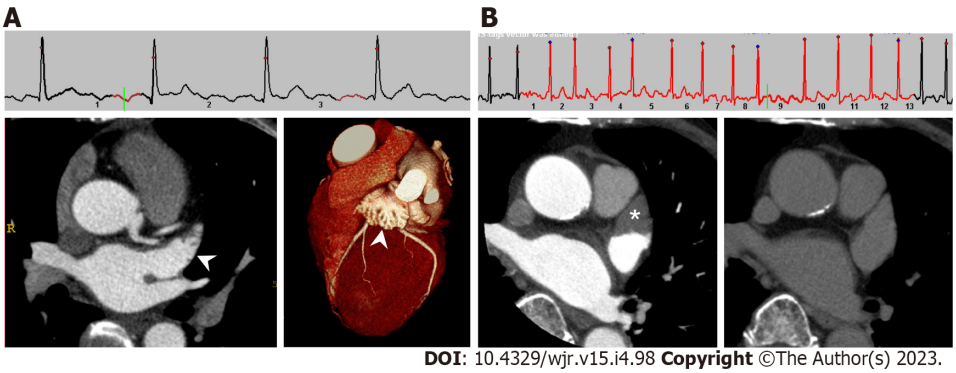
Table 2 Sources of cardioembolism

Risk level	Source	Condition
High-risk sources	Left atrial thrombus	Atrial fibrillation (Af)
		Mitral valve stenosis
	Left ventricular thrombus	Acute myocardial infarction
		Cardiomyopathy (ischemic, nonischemic)
		Congestive heart failure with low ejection fraction
	Cardiac tumor	Primary cardiac tumor
		Secondary cardiac tumor
	Vegetation	Infective endocarditis
		Nonbacterial thrombotic endocarditis
	Mechanical prosthetic heart valve	
Medium-risk sources	Interatrial septal abnormalities	Patent foramen ovale
		Atrial septal aneurysm
		Atrial septal defect
	Interventricular septal abnormalities	Interventricular membranous septal aneurysm
		Ventricular septal defect
	Pulmonary arteriovenous malformation	
	Bioprosthetic heart valve	
	Valvular abnormalities other than tumor and vegetation	Aortic valve sclerosis/stenosis
		Mitral annular calcification
		Lambl's excrescences
		Calcified amorphous tumor
		Mitral valve prolapse
	Atrial cardiomyopathy	
	Atrial arrhythmias other than Af	Atrial flutter
		Sick sinus syndrome

showed equivalent diagnostic accuracy as TEE for detecting LA/LAA thrombus in patients with Af. Specifically, two-phase CCT yielded sensitivity, specificity, positive predictive value, and negative predictive value of 100%, 99%, 92%, and 100%, respectively, compared with TEE as a reference standard [14]. Although the LAA is the most frequent site of atrial thrombi, they can occur in the right atrial appendage or in the atrial chambers themselves, especially in the context of Af and/or significant valvular heart disease such as mitral and tricuspid stenoses (Figure 3).

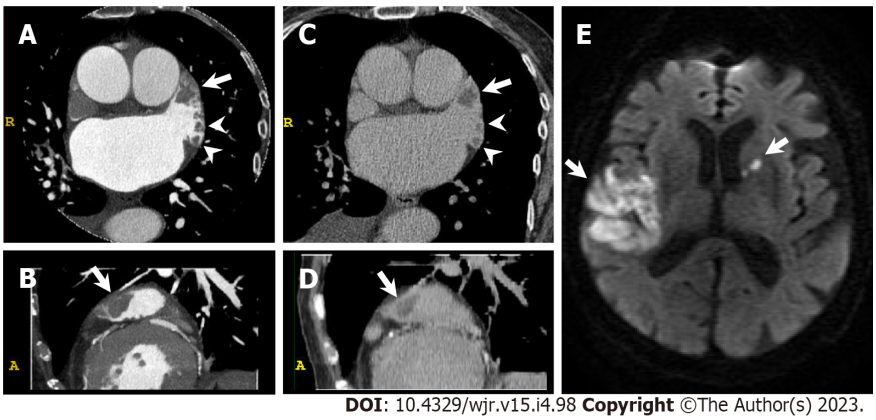
Among all native valvular heart disease, the risk of systemic emboli is highest for rheumatic mitral valve disease. Compared to normal controls, Af with rheumatic heart disease is associated with a 17-fold increase in stroke incidence, whereas it is five-fold for Af in the absence of RHD[15]. The risk of embolization is higher for mitral stenosis than mitral regurgitation, and the risk of embolism increases approximately seven-fold in the presence of Af compared to those with sinus rhythm in patients with rheumatic mitral valve disease[16]. In addition to delineating the morphological abnormalities of the mitral valve apparatus, CCT can comprehensively evaluate LA function and the presence or absence of LAA thrombus in a single examination (Figure 4).

LAA size is associated with increased thromboembolic risk[17,18]. Veinot *et al*[19] studied 500 normal autopsy hearts, and reported the size of normal LAAs differentiated by age group and sex. Mean LAA orifice diameter, body width, and length in subjects aged 20 or older were, respectively, 1.16, 1.83, and 2.59 cm for men and 1.07, 1.66, and 2.53 cm for women. Figure 5 shows a case of LAA aneurysm. Although a clear consensus on a definition of LAA aneurysm does not exist, Aryal *et al*[20] proposed defining it as a LAA with dimensions larger than 2.7 cm in orifice diameter, 4.8 cm in body width, and 6.75 cm in length. Whether congenital or acquired, LAA aneurysms grow in size over several years, and they tend to become symptomatic with an increasing risk of thromboembolism. Thus, surgical treatment for LAA aneurysm is often recommended, even in asymptomatic patients. By reconstructing images of



DOI: 10.4329/wjr.v15.i4.98 Copyright ©The Author(s) 2023.

Figure 1 Cardiac computed tomography images of left atrial appendage in patients with sinus rhythm and atrial fibrillation. A: Under normal sinus rhythm, left atrial appendage (LAA) is filled with contrast medium in early phase, which evaluates the coronary artery. Left: axial image; right: three-dimensional volume-rendered image; B: Under atrial fibrillation, axial early phase image shows triangular filling defect in LAA (left, asterisk). On delayed phase (right), LAA filling defect completely disappeared, which means the filling defect reflected blood stasis in LAA rather than thrombus.



DOI: 10.4329/wjr.v15.i4.98 Copyright ©The Author(s) 2023.

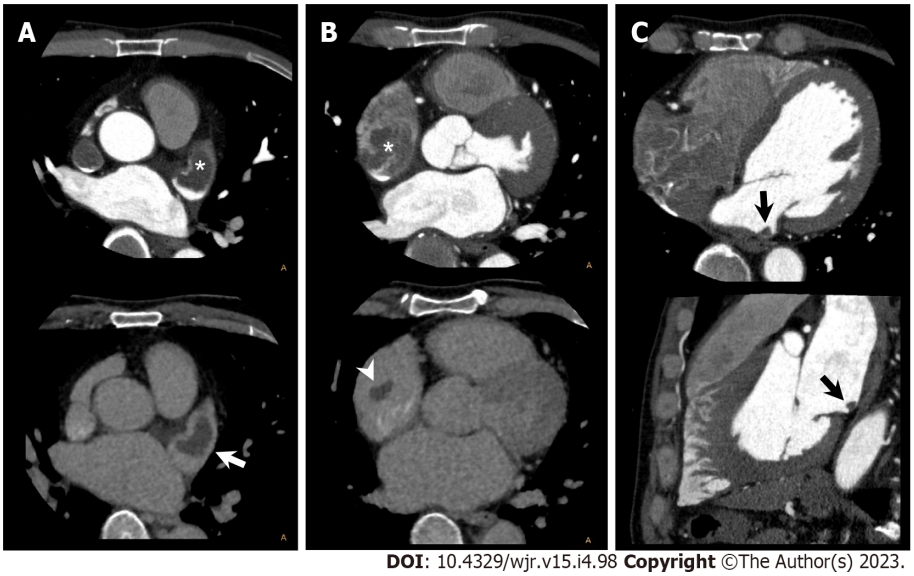
Figure 2 Left atrial appendage thrombus. An 85-year-old woman with congestive heart failure and atrial fibrillation underwent cardiac computed tomography (CCT) in search of underlying heart disease. She suffered from acute ischemic stroke three months after CCT. A and B: Early phase CCT images (A: Axial; B: Sagittal) show multiple filling defects in left atrial appendage (LAA, arrow and arrowheads); C and D: Delayed phase CCT images (C: Axial; D: Sagittal) also show multiple filling defects in LAA (arrow and arrowheads) confirming multiple LAA thrombus; E: Diffusion-weighted brain magnetic resonance imaging shows hyperintense lesions in right temporoparietal lobe and left anterior limb of internal capsule (arrows).

multiple phases throughout the cardiac cycle acquired by retrospective ECG gating, CCT can accurately quantify the volumes of cardiac chambers and calculate ventricular and atrial ejection fraction. The average maximum volume of the LAA on CCT in subjects with sinus rhythm and no history of cardiac disease was reported to be 12.54 mL for men and 11.74 mL for women[21]. In the presented case of LAA aneurysm, the CCT-derived maximum LAA volume was 56 mL (Figure 5).

Based on the imaging characteristics, the shapes of the LAA are classified into four different categories: chicken-wing, cactus, windsock, and cauliflower[22]. There is growing evidence that the morphology of the LAA delineated by CCT can assist with risk stratification in patients with nonvalvular Af. Specifically, patients with non-chicken-wing LAA morphology are significantly more likely to experience thromboembolic events than patients with chicken-wing LAA morphology[9]. Moreover, with regard to the cauliflower LAA morphology, defined as a main lobe less than 4 cm long and without forked lobes, Kimura *et al*[23] demonstrated that it was significantly more common in patients with stroke.

Left ventricular thrombus and associated pathologies

Left ventricular (LV) thrombus is complicated with various cardiac diseases that impair LV wall motion and can induce thromboembolic complications such as stroke. Causal pathologies that generate LV thrombus are classified into acute disorders and chronic disorders. Acute myocardial infarction (AMI) is a representative acute disorder. Prolonged myocardial ischemia results in subendocardial and endothelial injury and increased concentration of procoagulant factors, whereas akinetic areas of necrotic myocardium lead to blood stasis, especially at the LV apex. In data from the era without early coronary reperfusion therapy for AMI, LV thrombus was present in 46% of patients, usually in the first two weeks after onset, and most frequently in acute anterior or apical MI[24]. Although the frequency of LV thrombus in AMI has been significantly lowered since the advent of primary percutaneous coronary



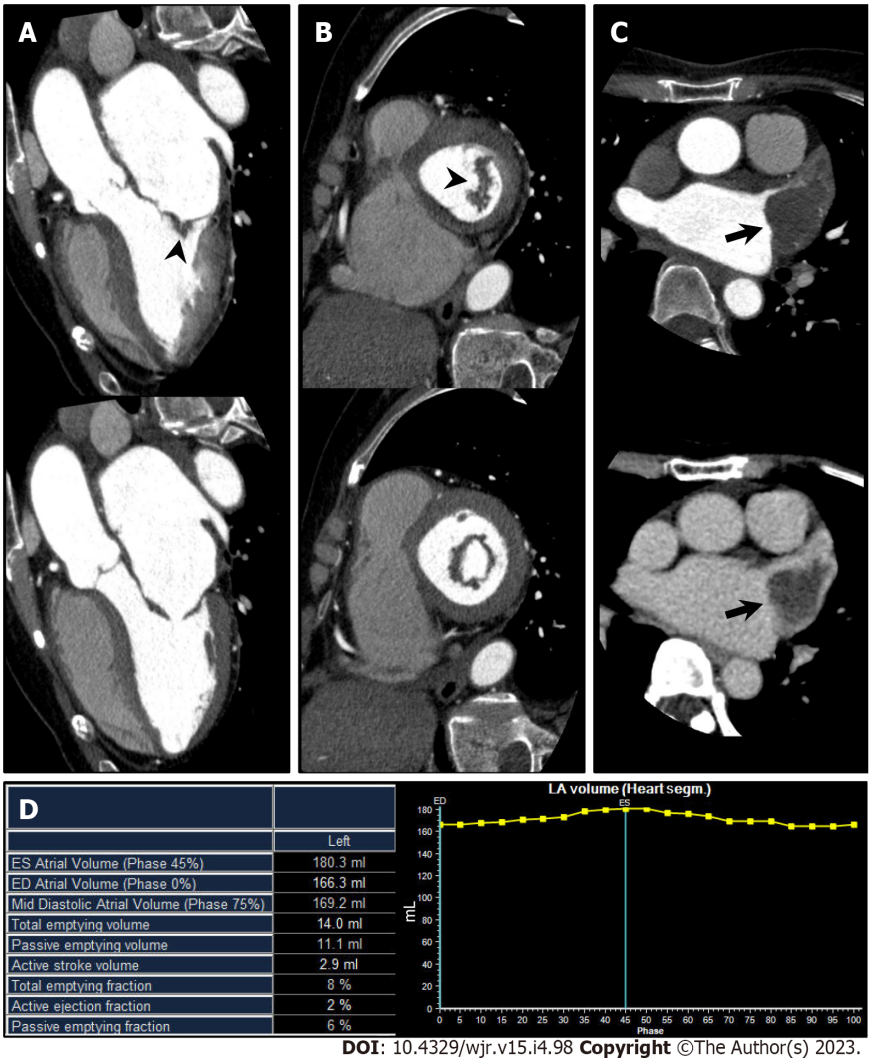
DOI: 10.4329/wjr.v15.i4.98 **Copyright** ©The Author(s) 2023.

Figure 3 Bilateral atrial thrombus. A 53-year-old man with atrial fibrillation and right renal infarction underwent cardiac computed tomography (CCT) in search of causal heart pathology of cardioembolism. A: Axial early phase CCT image shows filling defect in left atrial appendage (LAA, upper, asterisk). Axial delayed phase CCT image also shows filling defect in LAA confirming LAA thrombus (lower, arrow); B: Axial early phase CCT image shows filling defect in right atrial appendage (RAA, upper, asterisk). Axial delayed phase CCT image also shows filling defect in RAA confirming RAA thrombus (lower, arrowhead); C: Early phase CCT images (upper: Axial; lower: Sagittal) show filling defect in LA posterior wall, which suggests LA thrombus (black arrow).

intervention and dual antiplatelet therapy, the predilection site of LV thrombus has not changed and most frequently occurs in patients with acute anterior or apical MI[25]. Patients with MI also have a long-term risk of stroke after the acute phase. In the Survival and Ventricular Enlargement study, the cumulative rate of stroke risk was 8.1% during the five years after MI, and a lower LV ejection fraction (EF) was the independent predictor of stroke[26]. Specifically, patients with LVEF values of 35% or more and 28% or less had a cumulative stroke rate of 4.1% and 8.9%, respectively. Weinsaft *et al*[27] used cardiac magnetic resonance imaging (MRI) in 784 patients with LV systolic dysfunction (LVEF values of 50% or less), predominantly of chronic MI, and found the prevalence of thrombus to be 7% in this population. Patients with thrombus were more likely to have LV aneurysms, lower LVEF, and more extensive myocardial scarring by delayed enhanced MRI. Figure 6 shows a case of acute ischemic stroke due to LV apical thrombus complicated with chronic anteroseptal MI. In CCT, because the LV endocardial border is clearly depicted, LV thrombus is easily detected as a hypodense mass within the contrast-enhanced LV cavity. When blood stasis within the left ventricle disturbs the visibility of LV thrombus in the early phase image, a second scan should be performed several minutes after the initial first-pass scan. The addition of delayed imaging enables a better distinction of both thrombus and blood stasis. The LV apex is one of the anatomical blind spots at TTE[28]. Especially, when the LV apex becomes aneurysmal, the finding tends to be missed at TTE because the true apex often extends beyond its usual visualized location. Indeed, the diagnostic performance of TTE for detecting LV thrombus is inferior compared with cardiac MRI[29]. Takotsubo syndrome is also an acute disorder that generates LV thrombus. Takotsubo syndrome, caused in part by sympathetic activation and excess catecholamines, leads to LV apical ballooning, global or focal LV and/or right ventricular wall motion abnormalities, and increased risk of stroke and TIA[30].

A representative chronic disorder that generates LV thrombus is cardiomyopathy. In patients with cardiomyopathy, annual stroke rates are reported to be in the range of 1.3% to 3.5%[31]. The risk of stroke is inversely related to LVEF in patients with cardiomyopathy, whether its etiology is ischemic or nonischemic[31]. Risk factors that predispose patients with cardiomyopathies to thromboembolic events include extensive LV wall motion abnormalities, very dilated left ventricles, low cardiac output with the stagnation of blood within the ventricle, significant slow swirling streaks of blood within the left ventricle, and the presence of Af. Figure 7 shows a case of LV noncompaction. LV noncompaction is a rare congenital cardiomyopathy caused by an arrest of myocardial morphogenesis that results in prominent endomyocardial trabeculations in the LV myocardium. Deep myocardial recesses are thought to aggravate the risk of ventricular thrombus formation. Because thromboembolic risk is recognized to be high, anticoagulation should be considered in patients with LV noncompaction[32].

Figure 8 shows a case of mid-ventricular obstructive hypertrophic cardiomyopathy (HCM) with LV apical aneurysm and LV apical thrombus. In HCM, the location and degree of hypertrophy are variable. Although asymmetric septal hypertrophy is the classic and most common morphologic subtype of HCM, hypertrophy can involve various LV segments and may be focal or concentric. Mid-ventricular obstructive HCM is an uncommon type of HCM and is complicated with LV apical aneurysms in more



DOI: 10.4329/wjr.v15.i4.98 Copyright ©The Author(s) 2023.

Figure 4 Mitral stenosis. A 70-year-old man with mitral stenosis and atrial fibrillation underwent cardiac computed tomography (CCT) to rule out obstructive coronary artery disease. A and B: Left ventricular outflow tract long axis (A) and short axis (B) reformatted CCT images (upper: Mid systole at 20% of the R-R interval; lower: Mid diastole at 80% of the R-R interval) show thickened anterior and posterior mitral valve leaflets (arrowhead) and restricted mitral valve opening, representing mitral stenosis. Associated severe enlargement of left atrium is also found; C: Axial early phase CCT image shows triangular filling defect in left atrial appendage (LAA, upper, arrow). Axial delayed phase CCT image also shows filling defect in LAA confirming LAA thrombus (lower, arrow); D: Atrial functional analysis shows severely impaired LA function. LA end-systolic volume, end-diastolic volume, and ejection fraction were 180.3 mL, 166.3 mL, and 8%, respectively.

than 20% of cases of this phenotype[33]. In patients with HCM, the presence of LV apical aneurysm increases the risk for thromboembolic events six-fold compared with HCM patients without LV apical aneurysm[34].

Figure 9 shows a case of interventricular membranous septal aneurysm (IVMSA). Because the membranous portion of the interventricular septum notably lacks myocardium, this structure predisposes to the development of IVMSA upon exposure to a high-pressure gradient. The blood stasis in this abnormal structure predisposes to thrombus formation within the IVSMA. Although IVMSA is a rare condition, it can be one of the causal pathologies of LV thrombus and a potential source of cardioembolic stroke[35].

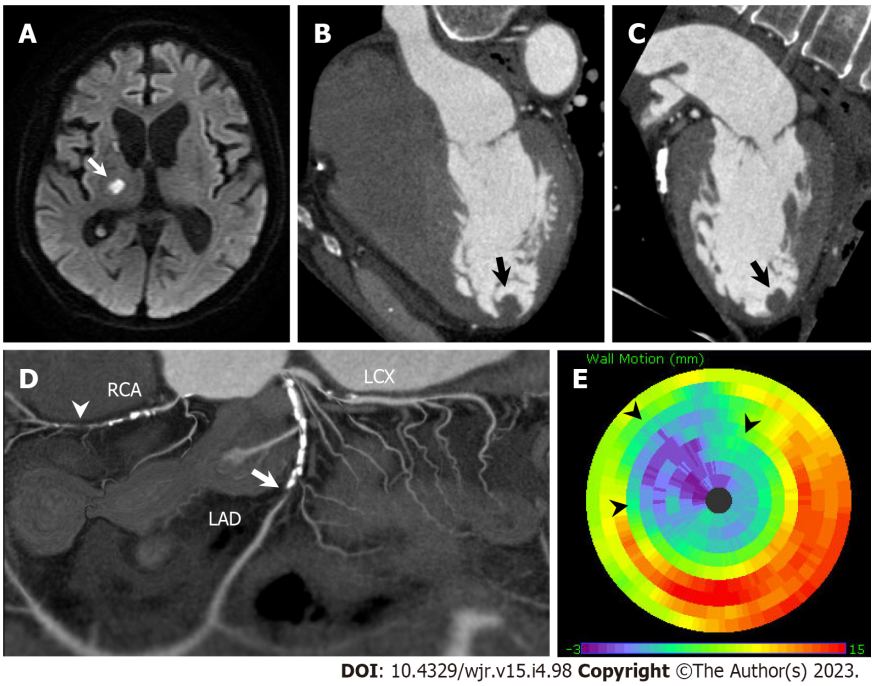
Intracardiac tumors

Cardiac tumors are classified into primary and secondary tumors. Primary cardiac tumors are very rare, and secondary or metastatic cardiac tumors are 30 times more common[36]. The affected cardiac chamber of predilection is different among cardiac tumor subtypes. Cardiac tumors that affect left heart chambers and valves provoke systemic thromboembolic phenomena. Tumor fragment detachment or superimposed thrombi underlie embolic risk. A representative cardiac tumor that induces embolic stroke is cardiac myxoma (Figure 10 and 11), which is the most frequent primary cardiac neoplasm in adults. Cardiac myxomas are most commonly found within the left atrium but may arise from other cardiac chambers and rarely from the valves. Although they are histologically benign, they can provoke potentially life-threatening conditions like thromboembolic phenomena or intracardiac obstructive complications. Neurologic complications can be the first manifestation of cardiac myxoma[37,38]. For



DOI: 10.4329/wjr.v15.i4.98 **Copyright** ©The Author(s) 2023.

Figure 5 Left atrial appendage aneurysm. A 56-year-old man with atrial fibrillation (Af) underwent cardiac computed tomography (CCT) to rule out obstructive coronary artery disease before catheter ablation for Af. A and B: Axial (A) and sagittal (B) reformatted CCT images show enlarged left atrial appendage (LAA, arrow) with triangular filling defect inside. LAA orifice diameter, body width, and length were 3.4 cm, 5.2 cm, and 6.8 cm, respectively; C: Three-dimensional volume-rendered image of CCT shows LAA aneurysm. CCT-derived maximum LAA volume was 56 mL.



DOI: 10.4329/wjr.v15.i4.98 **Copyright** ©The Author(s) 2023.

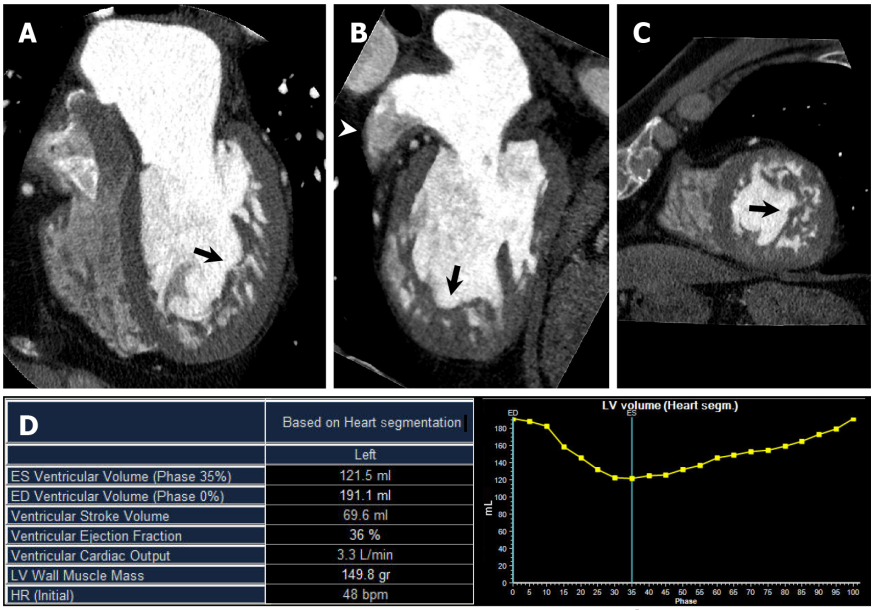
Figure 6 Left ventricular thrombus complicated with anteroseptal myocardial infarction. An 80-year-old man hospitalized with acute ischemic stroke underwent cardiac computed tomography (CCT) to rule out obstructive coronary artery disease. A: Diffusion-weighted brain magnetic resonance imaging shows hyperintense lesions in right thalamus and right posterior limb of internal capsule (arrow); B and C: Horizontal long axis (B) and vertical long axis (C) reformatted CCT images show round-shaped thrombus in left ventricular apex (arrow); D: Soap-bubble maximum intensity projection reconstruction image of whole coronary artery shows total occlusion of left anterior descending coronary artery (LAD, arrow) and right coronary artery (RCA, arrowhead); E: Polar map of left ventricular wall motion shows severely reduced anterior to anteroseptal wall motion perfused by LAD (arrowheads). LCX: left circumflex coronary artery.

those with serious clinical manifestations, immediate surgical tumor resection should be performed to prevent devastating embolic complications or sudden cardiac death. While echocardiography remains the first-line imaging modality, CCT has come to be increasingly utilized as a modality for assessing cardiac tumors, particularly when other imaging modalities are non-diagnostic (Figure 11)[8].

Valvular abnormalities

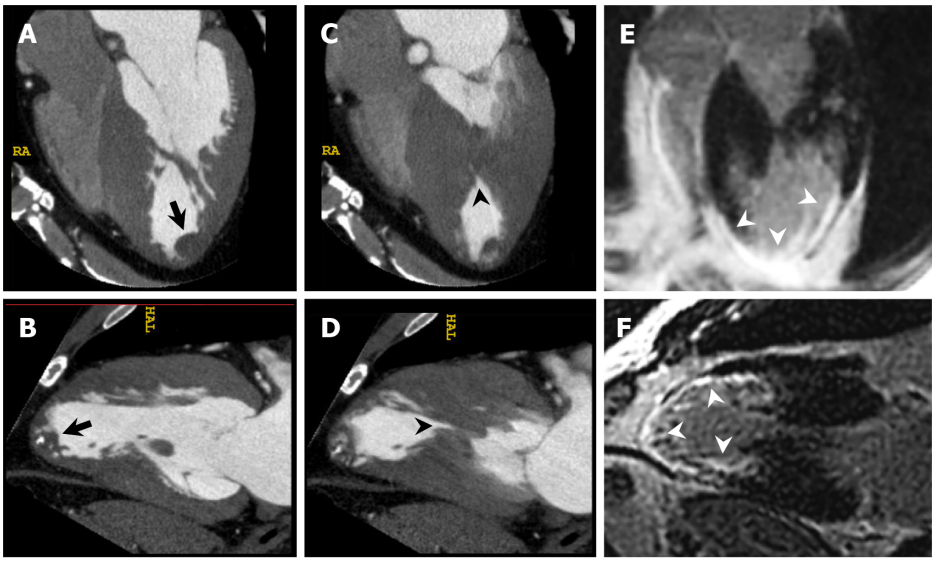
Various valvular abnormalities can lead to thromboembolism, such as infective or noninfective vegetations, and valvular thrombi with or without pannus formation and calcific debris. Several specific valvular abnormalities have been associated with cardioembolic stroke, including infective endocarditis (IE), nonbacterial thrombotic endocarditis, valvular papillary fibroelastoma, biologic or prosthetic valve thrombosis, and valvular calcifications.

Figure 12 shows a case of IE complicated with ischemic stroke. IE is a systemic septic disease that accompanies generation of vegetation containing aggregations of bacteria occurring on the valve, endocardium, and intima of large vessels. Various clinical symptoms are demonstrated in IE, including



DOI: 10.4329/wjr.v15.i4.98 **Copyright** ©The Author(s) 2023.

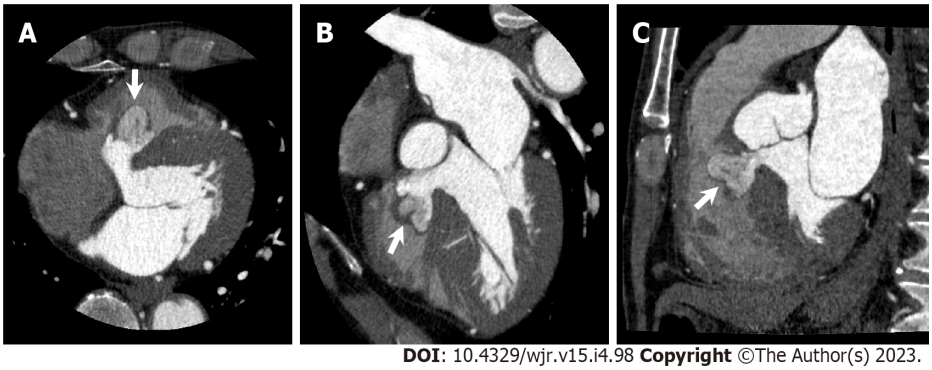
Figure 7 Left ventricular noncompaction. A 60-year-old man with congestive heart failure underwent cardiac computed tomography (CCT) in search of underlying heart disease. A–C Horizontal long axis (A), vertical long axis (B), and short axis (C) reformatted CCT images show increased trabeculations from mid to apical portion of left ventricle (arrows). Noncompacted-to-compacted layer ratio at end-diastolic was 2.6. Note contrast heterogeneity within left atrial appendage (LAA), which reflects blood stasis in LAA (arrowhead); D: Left ventricular (LV) functional analysis shows impaired LV function. LV end-diastolic volume, end-systolic volume, and ejection fraction were 191.1 mL, 121.5 mL, and 36%, respectively.



DOI: 10.4329/wjr.v15.i4.98 **Copyright** ©The Author(s) 2023.

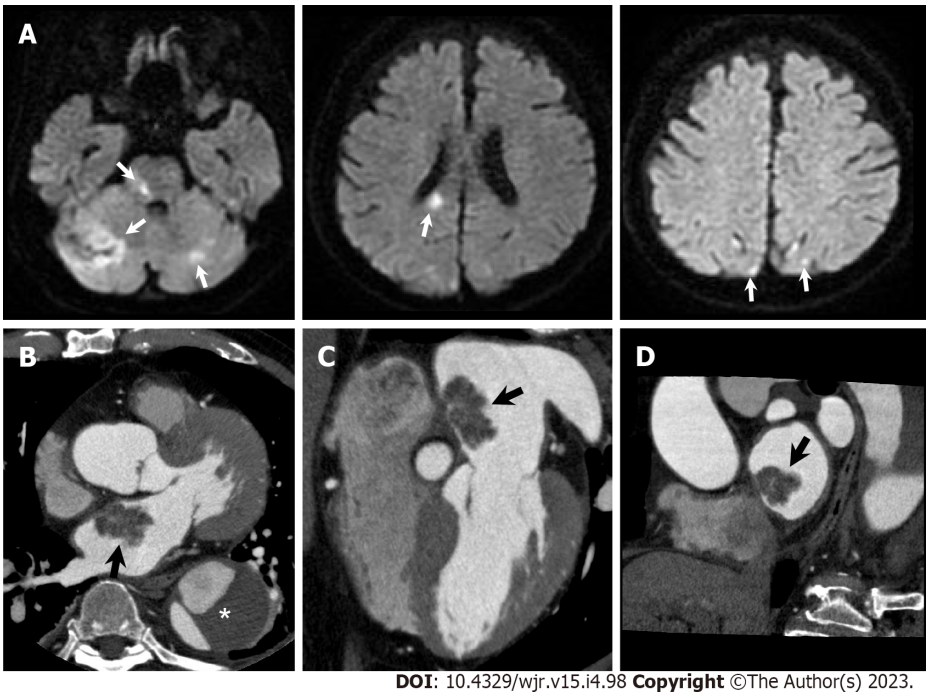
Figure 8 Left ventricular apical thrombus complicated with mid-ventricular obstructive hypertrophic cardiomyopathy. A 56-year-old man with unsustained ventricular tachycardia underwent cardiac computed tomography (CCT) in search of underlying heart disease. A and B: Horizontal long axis (A) and vertical long axis (B) reformatted CCT images at end diastole show partially calcified round-shaped thrombus in left ventricular apex (arrow). C and D: Horizontal long axis (C) and vertical long axis (D) reformatted CCT images at end systole show mid-ventricular hypertrophy and mid-cavitary obliteration of left ventricle (arrowhead) with thin-walled left ventricular apical aneurysm; E and F: Horizontal long axis (E) and vertical long axis (F) reformatted images of delayed enhanced cardiac magnetic resonance imaging show transmural late gadolinium enhancement in mid to apical portion of left ventricle (arrowheads).

bacteremia, vascular embolization, and cardiac disorders. Symptomatic neurological complications are seen in 10% to 35% of IE patients, and 65% to 80% of patients show one or more neurological complications when asymptomatic cases are included[39]. Echocardiography is the first-line imaging modality for the diagnosis of IE. TEE is more sensitive than TTE for the detection of both vegetation and periannular complications. However, the sensitivity of echocardiography is lower in IE patients with a prosthetic valve or an intracardiac device, even with the use of TTE. A recent meta-analysis showed that the addition of CCT to TEE can improve diagnostic accuracy for vegetations and periannular complic-



DOI: 10.4329/wjr.v15.i4.98 Copyright ©The Author(s) 2023.

Figure 9 Interventricular membranous septal aneurysm. A 78-year-old man underwent cardiac computed tomography (CCT) to further evaluate pathologic outpouching from the left ventricular outflow tract (LVOT) observed on transthoracic echocardiography. A–C: Axial (A), horizontal long axis (B), and sagittal (C) reformatted CCT images show multi-lobular outpouching projecting into right ventricle from LVOT (arrows) consistent with interventricular membranous septal aneurysm (IVMSA), with no evidence of a shunt. Note contrast heterogeneity within IVMSA, which reflects blood stasis in IVMSA.

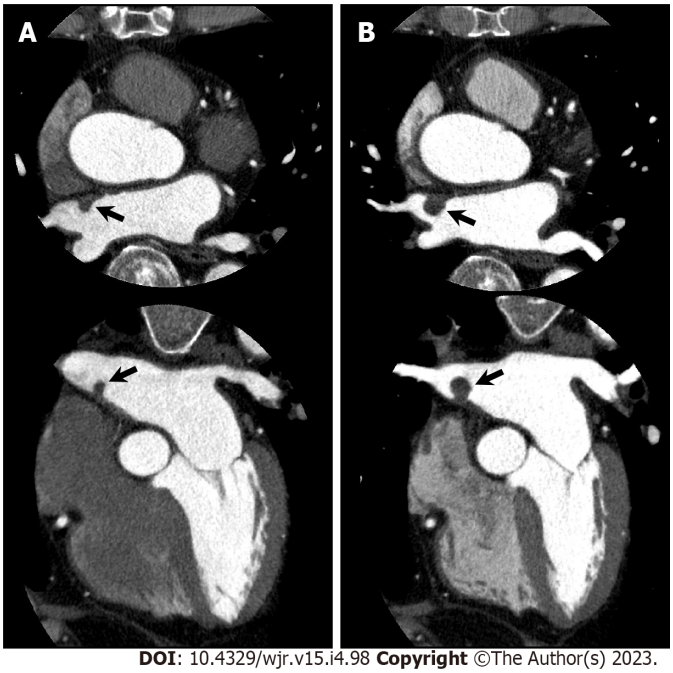


DOI: 10.4329/wjr.v15.i4.98 Copyright ©The Author(s) 2023.

Figure 10 Atrial myxoma. A 76-year-old man hospitalized with acute ischemic stroke underwent cardiac computed tomography (CCT) to further evaluate a left atrial mass observed on transthoracic echocardiography. A: Diffusion-weighted brain magnetic resonance imaging shows hyperintense lesions in bilateral cerebellar hemisphere, pons, splenium of corpus callosum, and bilateral occipital lobe (arrows); B–D: Axial (B), horizontal long axis (C), and short axis (D) reformatted CCT images show a 31-mm-sized lobulated left atrial mass attached to the interatrial septum (arrows). He had a previous history of chronic aortic dissection (asterisk). Urgent surgical mass resection was performed. Histological examination confirmed cardiac myxoma.

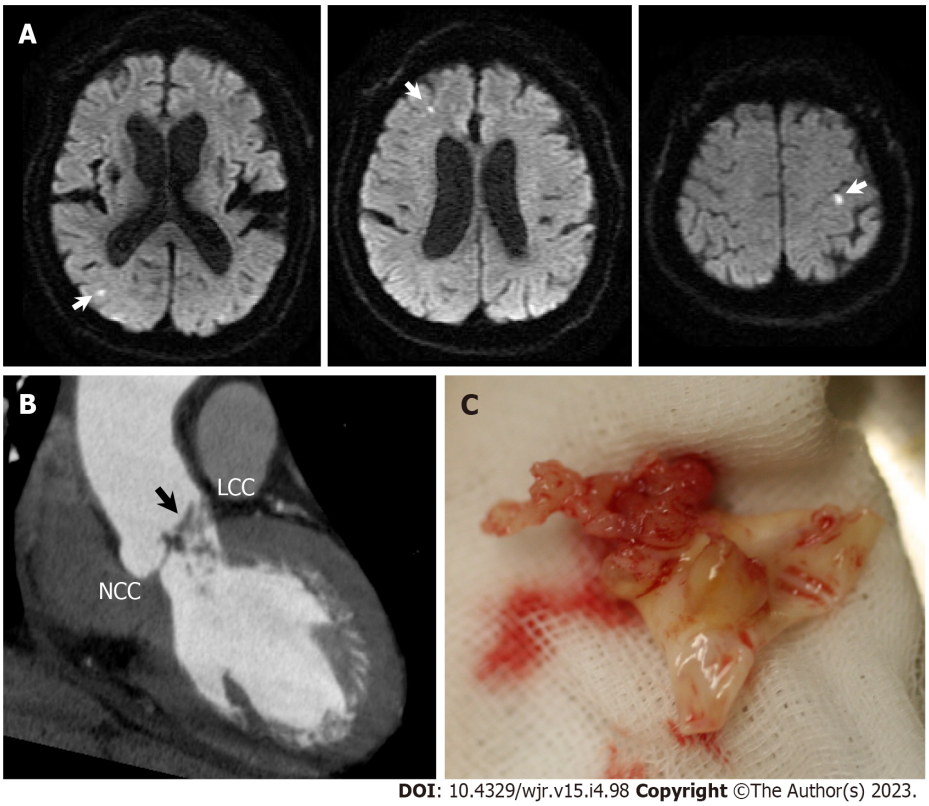
ations in patients with prosthetic heart valve endocarditis[40].

In patients with prosthetic heart valves, the incidence of thromboembolism ranges from 0.6% to 2.3% per patient-year[41]. The absolute risk of thromboembolism is higher for prosthetic valves in the mitral position than the aortic position. Figure 13 shows a case of mechanical mitral valve dysfunction. The most common causes of prosthetic valve dysfunction are thrombus formation and pannus overgrowth. One particular advantage of CCT is the ability to evaluate patients with mechanical valves, because mechanical valves often have significant artifacts on echocardiography. In the absence of contrast medium administration, CCT can demonstrate abnormal leaflet or disc motion of a mechanical prosthetic valve. Indeed, the opening and closing angles measured by non-contrast CCT strongly correlate with those measured by cinefluoroscopy[42]. In daily clinical practice, doppler-echocardiography is the method of choice to evaluate prosthetic valve function. To identify thrombus or pannus by CCT, contrast enhancement of the blood pool is necessary. Because contrast-enhanced CCT can visualize details of soft-tissue anatomy surrounding the prosthesis, it can provide reliable information for the diagnosis and differentiation of valvular thrombosis and pannus overgrowth when there is suspicion of prosthetic valve dysfunction[43,44].



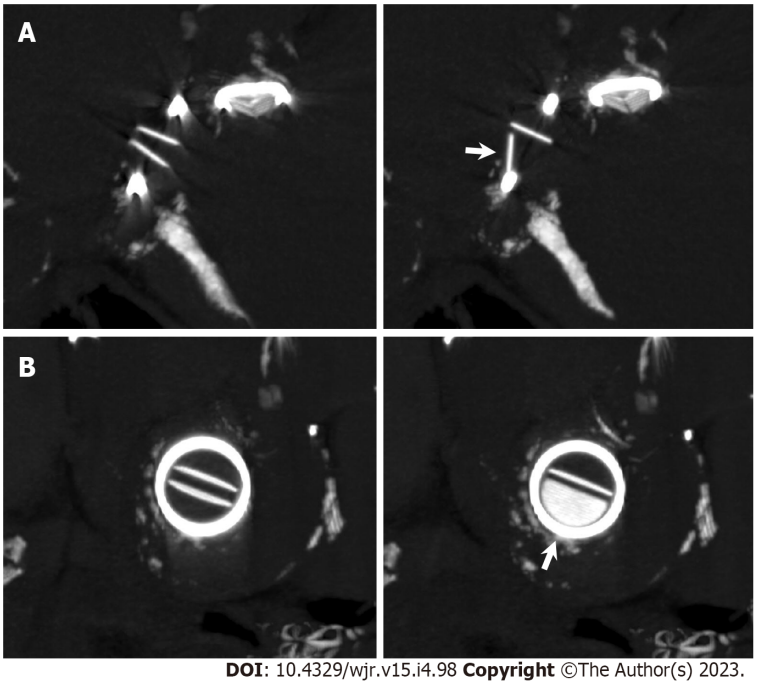
DOI: 10.4329/wjr.v15.i4.98 **Copyright** ©The Author(s) 2023.

Figure 11 Gradually increased atrial myxoma. An 80-year-old man with chest pain underwent cardiac computed tomography (CCT) to evaluate obstructive coronary artery disease. CCT showed severe stenosis in the left anterior descending coronary artery, and percutaneous coronary intervention was performed. Simultaneously, CCT incidentally demonstrated a left atrial mass that could not be visualized on transthoracic echocardiography. A: Axial (upper) and horizontal long axis (lower) reformatted CCT images show left atrial mass of 7 mm by 5 mm in diameter attached to interatrial septum (arrows); B: Axial (upper) and horizontal long axis (lower) reformatted CCT images performed one year later show increased mass size of 11 mm by 11 mm in diameter. Subsequently, elective surgical mass resection was performed. Histological examination confirmed cardiac myxoma.



DOI: 10.4329/wjr.v15.i4.98 **Copyright** ©The Author(s) 2023.

Figure 12 Infective endocarditis. A 73-year-old man hospitalized with infective endocarditis and acute ischemic stroke underwent cardiac computed tomography (CCT) to rule out obstructive coronary artery disease before urgent surgical aortic valve replacement. A: Diffusion-weighted brain magnetic resonance imaging shows hyperintense lesions in bilateral cerebral hemisphere (arrows). B: Left ventricular outflow tract long axis reformatted CCT image shows irregularly shaped aortic valve vegetations adherent to left coronary cusp (LCC); C: Surgically resected LCC of aortic valve with fragile vegetations. NCC: Noncoronary cusp.



DOI: 10.4329/wjr.v15.i4.98 **Copyright** ©The Author(s) 2023.

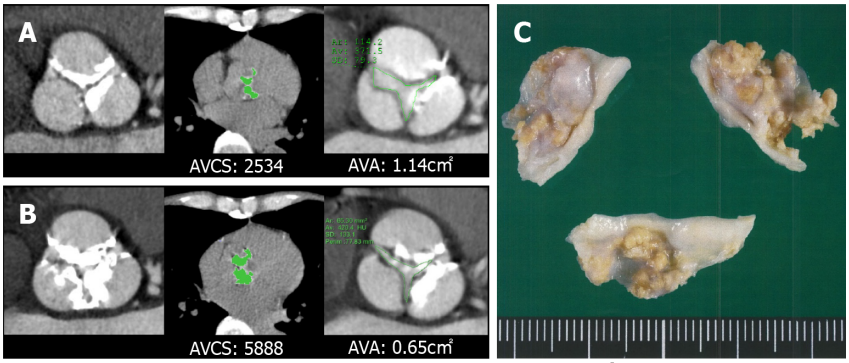
Figure 13 Mechanical mitral valve dysfunction. An 86-year-old woman who had undergone St. Jude Medical 29 mm-sized mitral valve replacement 17 years earlier and now presented with congestive heart failure underwent non-contrast cardiac computed tomography (CCT) to evaluate the etiology of mitral regurgitation observed on transthoracic echocardiography. A and B: Multiplanar reformatted images perpendicular to valve leaflet (A) and short axis images (B) of non-contrast CCT show incomplete opening of bileaflet mechanical mitral valve (arrows).

Aortic valve sclerosis and mitral annular calcification are associated with atherosclerotic vascular disease. While their association with stroke reflects their status as a marker for atherosclerotic disease, several reports show their potential as a direct source of calcific or thrombotic debris. Aortic valve sclerosis is irregular thickening and/or calcification of the aortic valve leaflets without significant flow obstruction. The prevalence of aortic valve sclerosis without stenosis increases with age and ranges from 9% in populations with a mean age of 54 to 42% in populations with a mean age of 81. The rate of progression from aortic sclerosis to stenosis is 1.8% to 1.9% per year[45]. Figure 14 shows a case of aortic stenosis (AS) for which evaluation by CCT over time was possible. The coronary artery calcium score is usually calculated by the Agatston method and is a marker of coronary atherosclerotic plaque burden [46]. The severity of aortic sclerosis can also be determined by calculating the Agatston calcium score of the aortic valve. The aortic valve calcium score (AVCS) can help in the classification of AS severity. Reported mean AVCSs were 3219 for severe AS, 1808 for moderate AS, and 584 for mild AS[47]. AVCS is reported to be a useful prognostic imaging marker in AS and is associated with higher rates of mortality during follow-up, with a hazard ratio of 2.11 as a binary threshold[47]. In addition, a higher AVCS is reported to be an independent risk factor for acute stroke after transcatheter aortic valve replacement[48].

Mitral annular calcification (MAC) is defined as calcific deposition in the mitral annulus. Similar to AVCS, the severity of MAC can be determined by calculating the Agatston calcium score. It has been shown that a higher MAC calcium score is associated with increased risk of ischemic stroke[49]. Figure 15 shows a case of caseous MAC. Caseous MAC is a rare variant of MAC with a central liquefaction necrosis that typically affects the posterior annulus. It is sometimes misdiagnosed as a cardiac tumor or abscess. Macroscopically, the inner fluid of the caseous MAC appears as a toothpaste-like milky caseous material. Histological examination of the inner fluid reveals amorphous, eosinophilic acellular content surrounded by macrophages and lymphocytes[50]. A recent comprehensive review of the literature showed that the prevalence of cardioembolic events is significantly higher in patients with caseous MAC than in patients with non-caseous MAC[51]. The high incidence of cardioembolic events in caseous MAC is assumed to be due to spontaneous fistulization and embolization of caseous necrotic debris.

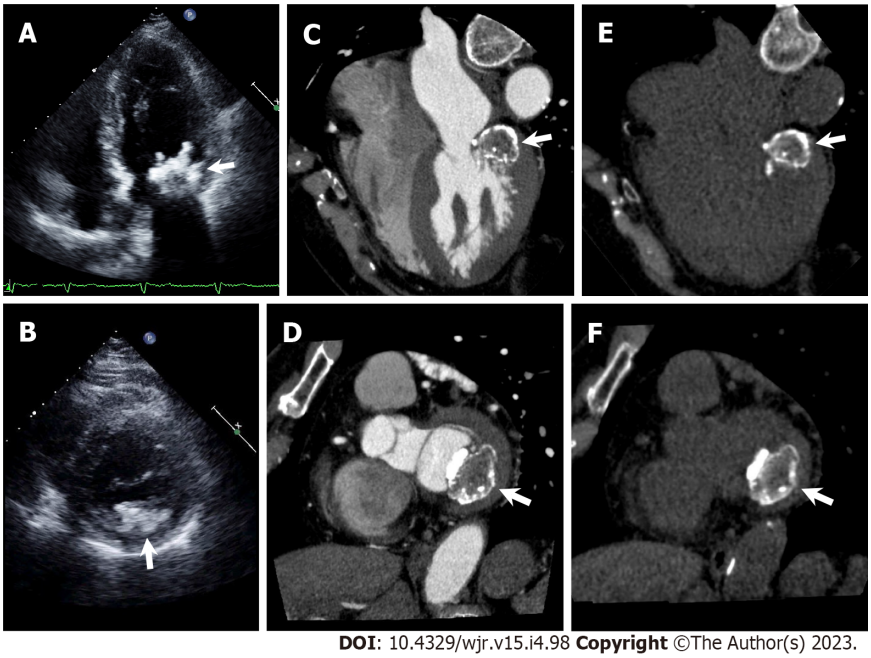
Paradoxical embolism

Paradoxical embolism is a type of stroke or arterial thrombosis caused by embolic sources of venous origin transiting from the right chambers of the heart to the left chambers without passing through the lung filters. Paradoxical embolism can occur *via* interatrial, interventricular, or pulmonary arteriovenous malformations.



DOI: 10.4329/wjr.v15.i4.98 **Copyright** ©The Author(s) 2023.

Figure 14 Aortic stenosis. A man in his seventies with chronic renal failure requiring hemodialysis and aortic stenosis underwent cardiac computed tomography (CCT) on two occasions to evaluate obstructive coronary artery disease. A: 19 years after initiation of hemodialysis. Left: Short axis reformatted CCT image in diastole shows tricuspid aortic valve with calcification. Middle: Aortic valve calcium score (AVCS) by Agatston method and aortic valve calcium volume were 2534 and 1988 mm^3, respectively. Right: Quantification of aortic valve area (AVA) by planimetry is 1.14 cm^2; B: 24 years after initiation of hemodialysis. Left: Extent of aortic valve calcification has increased. Middle: AVCS by Agatston method and aortic valve calcium volume were 5888 and 4447 mm^3, respectively. Right: Quantification of AVA by planimetry is 0.65 cm^2; C: Surgical aortic valve replacement was performed after second CCT examination. Gross specimen of surgically resected aortic valve is shown.

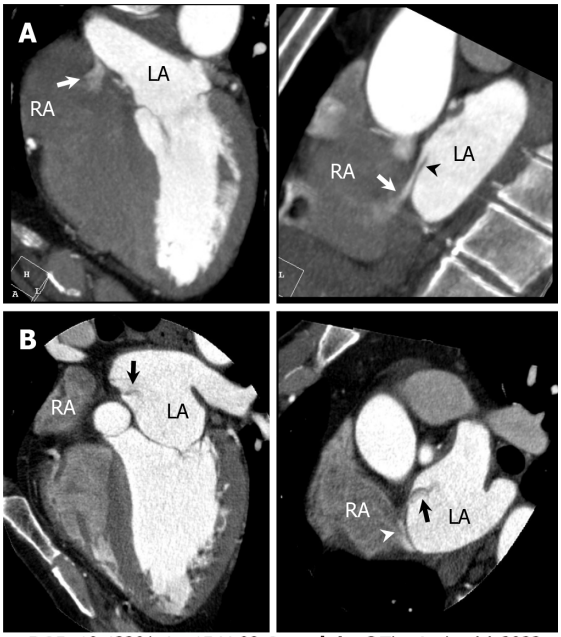


DOI: 10.4329/wjr.v15.i4.98 **Copyright** ©The Author(s) 2023.

Figure 15 Caseous mitral annular calcification. A and B: Apical four chamber view (A) and parasternal short axis view (B) of transthoracic echocardiography show irregularly shaped calcific mass attached to mitral annulus adjacent to posterior mitral valve leaflet (arrows); C–F: Cardiac computed tomography (CCT) images with (C, D) and without (E, F) contrast medium. Horizontal long axis (C, E) and short axis (D, F) reformatted CCT images show a centrally hypodense mass with irregular calcified borders attached to mitral annulus adjacent to posterior mitral valve leaflet (arrows).

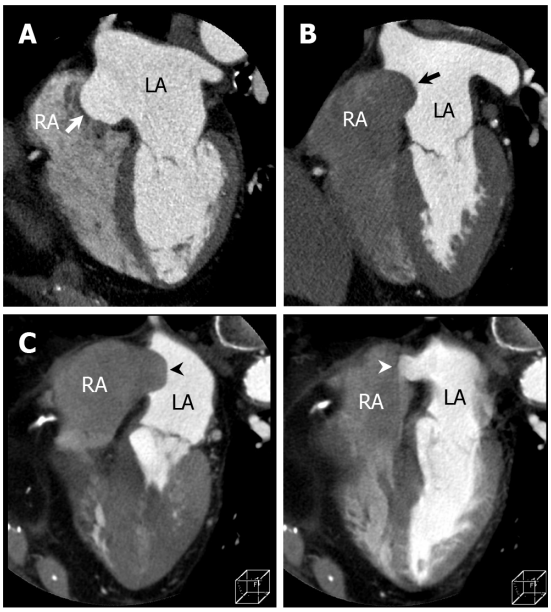
A patent foramen ovale (PFO) is an integral part of normal fetal circulation. Although PFOs typically close shortly after birth, they may still be open in approximately 25% to 30% of the general population [52]. Therefore, PFOs are considered to be a normal variant rather than a pathologic finding. By cardiac imaging, a PFO is demonstrated as a flap-like opening at the fossa ovalis, which allows intermittent bidirectional shunting between the atria. A left-to-right shunt is more frequent than a right-to-left shunt. In CCT, a contrast material jet with a flap-like appearance of the interatrial septum is a highly confirmative finding of PFO (Figure 16). In a study of 152 patients with ischemic stroke, both findings of interatrial septum (contrast material jet and flap-like appearance) on CCT yielded sensitivity, specificity, positive predictive value, and negative predictive value of 73.1%, 98.4%, 90.5%, and 94.7%, respectively, compared with TEE as a reference standard[53].

Atrial septal aneurysm (ASA) is a localized sacculation or deformity in the interatrial septum at the level of the fossa ovalis, and protrudes to the right or left atrium or both atria. ASAs are roughly classified into three types according to the direction and movement of protrusion during the cardiac



DOI: 10.4329/wjr.v15.i4.98 **Copyright** ©The Author(s) 2023.

Figure 16 Patent foramen ovale. A: Horizontal long axis (left) and short axis oblique (right) reformatted cardiac computed tomography (CCT) images show passage of higher-contrast jet (arrow) from left atrium (LA) *via* patent foramen ovale (PFO) with channel-like appearance (arrowhead) into adjacent right atrium (RA). B: Horizontal long axis (left) and short axis oblique (right) reformatted CCT images show passage of lower-contrast jet (arrow) from RA *via* PFO with channel-like appearance (arrowhead) into adjacent LA.

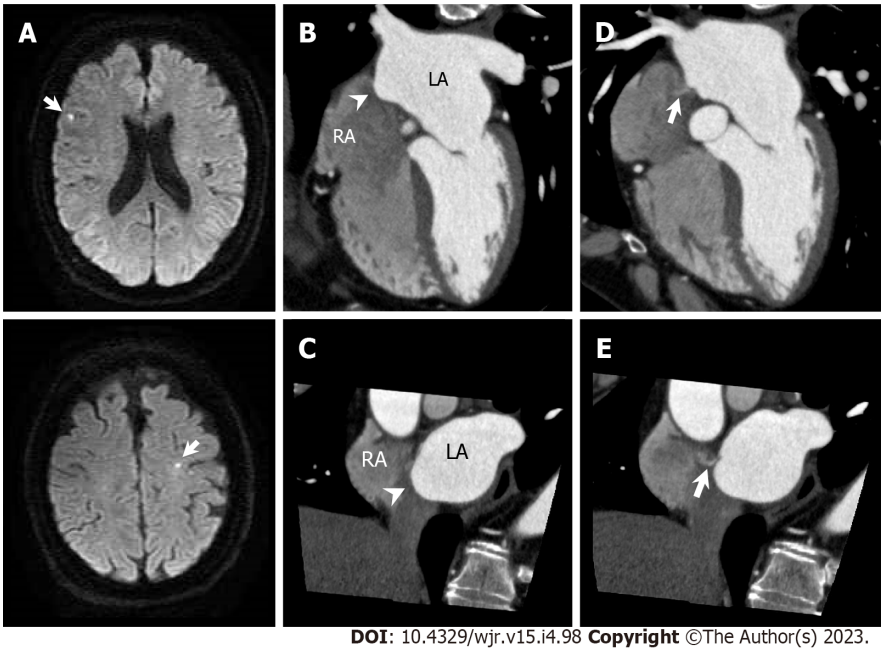


DOI: 10.4329/wjr.v15.i4.98 **Copyright** ©The Author(s) 2023.

Figure 17 Classification of atrial septal aneurysm. A: Cardiac computed tomography (CCT) image of right bulging atrial septal aneurysm [Atrial septal aneurysm (ASA), arrow] in which bulging during cardiac cycle is right atrium (RA) only; B: CCT image of left bulging ASA (arrow) in which bulging during cardiac cycle is left atrium (LA) only; C: CCT image of bidirectional ASA (arrowheads) in which ASA movement during cardiac cycle is bidirectional.

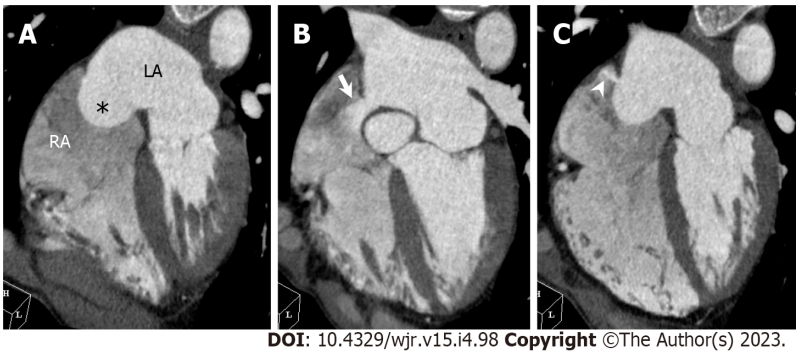
cycle: right-bulging ASA, left-bulging ASA, and bidirectional ASA (Figure 17)[54]. In a study of 103 autopsy hearts, Kuramoto *et al*[55] reported that PFO was more frequently found in subjects with ASA than in those without ASA. A prospective study of 581 patients with cryptogenic stroke showed that a PFO with concomitant ASA is associated with a significant risk of recurrent stroke (Figure 18)[56].

Atrial septal defect (ASD) is the most common congenital heart disease in adults. ASD can also appear in conjunction with ASA (Figure 19). In ASD, CCT shows different features compared with PFO, namely a contrast material jet passing through a sharply defined defect hole, not a channel, in the atrial septum, and perpendicular to the atrial septum. Patients with ASD and right-to-left shunt are at risk for stroke due to paradoxical embolism. ASD is classified in three main types: ostium secundum, ostium



DOI: 10.4329/wjr.v15.i4.98 **Copyright** ©The Author(s) 2023.

Figure 18 Atrial septal aneurysm with patent foramen ovale. A 53-year-old man with acute ischemic stroke underwent cardiac computed tomography (CCT) to rule out obstructive coronary artery disease. A: Diffusion-weighted brain magnetic resonance imaging shows hyperintense lesions in right frontal lobe and left precentral gyrus (arrows); B and C: Horizontal long axis (B) and short axis oblique (C) reformatted cardiac computed tomography (CCT) images show right bulging atrial septal aneurysm (arrowheads); D and E: Horizontal long axis (D) and short axis oblique (E) reformatted CCT images show small pinhole-like jet from LA *via* patent foramen ovale into RA (arrows). LA: Left atrium; RA: Right atrium.



DOI: 10.4329/wjr.v15.i4.98 **Copyright** ©The Author(s) 2023.

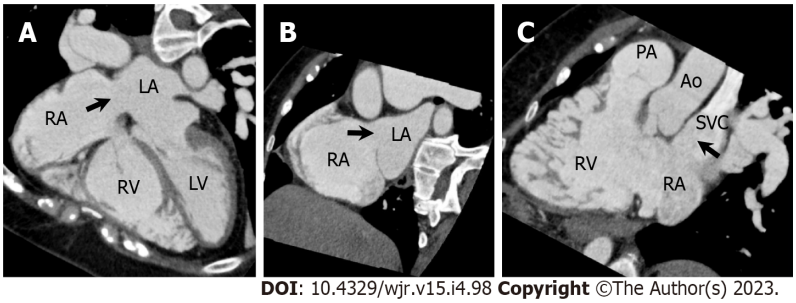
Figure 19 Atrial septal aneurysm with atrial septal defect. A 66-year-old man underwent cardiac computed tomography (CCT) to further evaluate outpouching of the interatrial septum observed on transthoracic echocardiography. Transthoracic echocardiography did not detect interatrial shunt flow. A: Horizontal long axis reformatted CCT image shows right bulging atrial septal aneurysm [Atrial septal aneurysm (ASA), asterisk]. B: Above ASA, in upper portion of interatrial septum just below aortic valve, atrial septal defect (ASD) with contrast shunt from LA into RA is found (arrow). Measured size of ASD is 14 mm by 10 mm; C: Below ASA, in lower portion of interatrial septum, another 5 mm-sized ASD with left to right shunt is found (arrowhead). LA: Left atrium; RA: Right atrium.

primum, and sinus venosus. Coronary sinus ASD is very rare. Echocardiography is generally an accurate means in the diagnosis of most secundum and primum ASDs, but sinus venosus ASDs are sometimes overlooked. CCT is a useful supplementary imaging modality for depicting sinus venosus ASDs and defining associated partial anomalous pulmonary venous return (Figure 20)[57].

Pulmonary arteriovenous malformations are structurally abnormal vessels that provide direct communication between a pulmonary artery and vein, and the absence of lung filtering capillary beds offers the potential for paradoxical embolism[58]. CT is recognized to be the gold standard investigation for diagnosis and also plays an important role in treatment planning. They are demonstrated as a nodule or serpiginous mass connected with blood vessels (Figure 21).

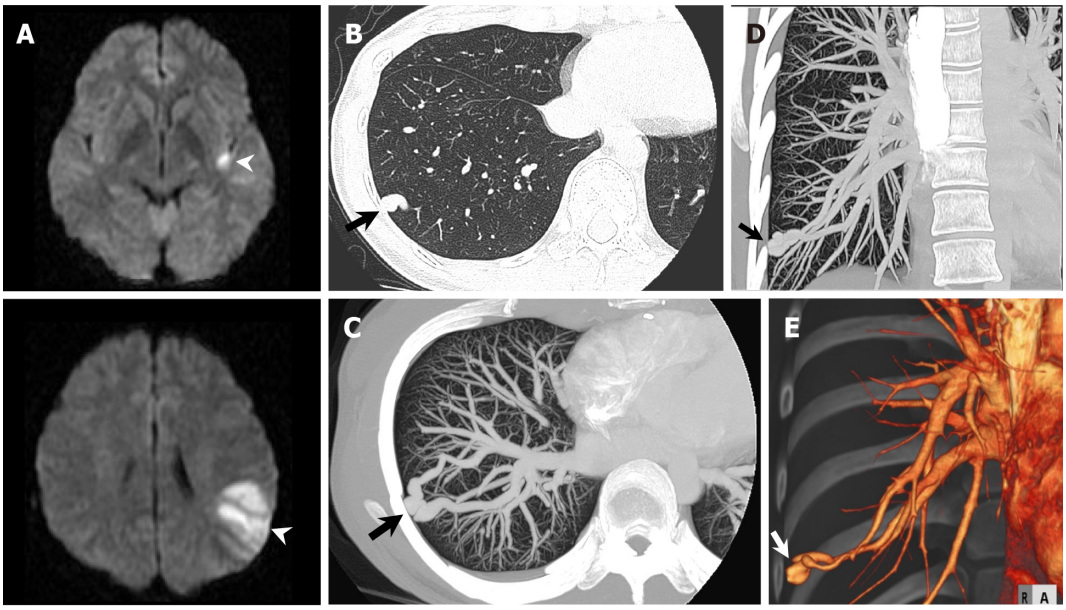
CONCLUSION

CCT can provide high-quality information about the causal heart disease in patients with cardioembolic stroke. In addition, CCT can simultaneously evaluate obstructive coronary artery disease, which may be



DOI: 10.4329/wjr.v15.i4.98 Copyright ©The Author(s) 2023.

Figure 20 Superior sinus venosus atrial septal defect. A 57-year-old woman underwent cardiac computed tomography (CCT) to evaluate right ventricular (RV) morphology and function because transthoracic echocardiography revealed gradual RV dilatation over time. She had a previous history of cryptogenic ischemic stroke when she was 3 years old. A–C: Horizontal long axis (A), short axis oblique (B), and RV long axis reformatted CCT images show atrial septal defect (ASD) in superior aspect of interatrial septum at level of entry of superior vena cava (SVC, arrows). Measured size of ASD is 26 mm by 25 mm. Partial anomalous pulmonary venous return is not complicated. Subsequently, she underwent right and left heart catheterization. The Qp/Qs ratio and mean pulmonary artery pressure measured using right heart catheterization were 4.8 and 23 mmHg, respectively. Surgical ASD closure was performed. LA: Left atrium; LV: Left ventricle; RA: Right atrium; PA: Pulmonary artery; Ao: Aorta.



DOI: 10.4329/wjr.v15.i4.98 Copyright ©The Author(s) 2023.

Figure 21 Pulmonary arteriovenous malformation. A 31-year-old woman hospitalized with acute ischemic stroke underwent chest computed tomography (CT) to further evaluate a nodular shadow in right lower lung field on chest radiography. A: Diffusion-weighted brain magnetic resonance imaging shows hyperintense lesions in left insula and left parietal lobe (arrowheads); B: Non-contrast chest CT shows nodular shadow in lateral basal segment of right inferior lobe (arrow); C–E: Maximum intensity projection reconstruction images (C: Axial; D: Coronal) and three-dimensional volume-rendered image (E) of contrast-enhanced CT show pulmonary arteriovenous malformation in lateral basal segment of right inferior lobe (arrow).

helpful in surgical planning in patients who need urgent surgery, such as for cardiac myxoma or infective endocarditis. However, clinicians should sift through the information derived from CCT and determine whether the clinical symptoms, physical findings, and results of neuroimaging are consistent with the causal relationship in individual patients with ischemic stroke.

FOOTNOTES

Author contributions: Yoshihara S made all of this manuscript and figures.

Conflict-of-interest statement: Shu Yoshihara does not have any conflict-of-interest.

Open-Access: This article is an open-access article that was selected by an in-house editor and fully peer-reviewed by external reviewers. It is distributed in accordance with the Creative Commons Attribution NonCommercial (CC BY-NC 4.0) license, which permits others to distribute, remix, adapt, build upon this work non-commercially, and license their derivative works on different terms, provided the original work is properly cited and the use is non-

commercial. See: https://creativecommons.org/Licenses/by-nc/4.0/

Country/Territory of origin: Japan

ORCID number: Shu Yoshihara 0000-0001-9294-3767.

S-Editor: Liu JH
L-Editor: A
P-Editor: Zhao S

REFERENCES

1 **Adams HP Jr**, Bendixen BH, Kappelle LJ, Biller J, Love BB, Gordon DL, Marsh EE 3rd. Classification of subtype of acute ischemic stroke. Definitions for use in a multicenter clinical trial. TOAST. Trial of Org 10172 in Acute Stroke Treatment. *Stroke* 1993; **24**: 35-41 [PMID: 7678184 DOI: 10.1161/01.str.24.1.35]

2 **Amarenco P**, Bogousslavsky J, Caplan LR, Donnan GA, Hennerici MG. New approach to stroke subtyping: the A-S-C-O (phenotypic) classification of stroke. *Cerebrovasc Dis* 2009; **27**: 502-508 [PMID: 19342826 DOI: 10.1159/000210433]

3 **Powers WJ**, Rabinstein AA, Ackerson T, Adeoye OM, Bambakidis NC, Becker K, Biller J, Brown M, Demaerschalk BM, Hoh B, Jauch EC, Kidwell CS, Leslie-Mazwi TM, Ovbiagele B, Scott PA, Sheth KN, Southerland AM, Summers DV, Tirschwell DL. Guidelines for the Early Management of Patients With Acute Ischemic Stroke: 2019 Update to the 2018 Guidelines for the Early Management of Acute Ischemic Stroke: A Guideline for Healthcare Professionals From the American Heart Association/American Stroke Association. *Stroke* 2019; **50**: e344-e418 [PMID: 31662037 DOI: 10.1161/STR.0000000000000211]

4 **de Bruijn SF**, Agema WR, Lammers GJ, van der Wall EE, Wolterbeek R, Holman ER, Bollen EL, Bax JJ. Transesophageal echocardiography is superior to transthoracic echocardiography in management of patients of any age with transient ischemic attack or stroke. *Stroke* 2006; **37**: 2531-2534 [PMID: 16946152 DOI: 10.1161/01.STR.0000241064.46659.69]

5 **Strandberg M**, Marttila RJ, Helenius H, Hartiala J. Transoesophageal echocardiography in selecting patients for anticoagulation after ischaemic stroke or transient ischaemic attack. *J Neurol Neurosurg Psychiatry* 2002; **73**: 29-33 [PMID: 12082041 DOI: 10.1136/jnnp.73.1.29]

6 **Knuuti J**, Ballo H, Juarez-Orozco LE, Saraste A, Kolh P, Rutjes AWS, Jüni P, Windecker S, Bax JJ, Wijns W. The performance of non-invasive tests to rule-in and rule-out significant coronary artery stenosis in patients with stable angina: a meta-analysis focused on post-test disease probability. *Eur Heart J* 2018; **39**: 3322-3330 [PMID: 29850808 DOI: 10.1093/eurheartj/ehy267]

7 **Leipsic J**, Abbara S, Achenbach S, Cury R, Earls JP, Mancini GJ, Nieman K, Pontone G, Raff GL. SCCT guidelines for the interpretation and reporting of coronary CT angiography: a report of the Society of Cardiovascular Computed Tomography Guidelines Committee. *J Cardiovasc Comput Tomogr* 2014; **8**: 342-358 [PMID: 25301040 DOI: 10.1016/j.jcct.2014.07.003]

8 **Taylor AJ**, Cerqueira M, Hodgson JM, Mark D, Min J, O'Gara P, Rubin GD; American College of Cardiology Foundation Appropriate Use Criteria Task Force; Society of Cardiovascular Computed Tomography; American College of Radiology; American Heart Association; American Society of Echocardiography; American Society of Nuclear Cardiology; North American Society for Cardiovascular Imaging; Society for Cardiovascular Angiography and Interventions; Society for Cardiovascular Magnetic Resonance. ACCF/SCCT/ACR/AHA/ASE/ASNC/NASCI/SCAI/SCMR 2010 Appropriate Use Criteria for Cardiac Computed Tomography. A Report of the American College of Cardiology Foundation Appropriate Use Criteria Task Force, the Society of Cardiovascular Computed Tomography, the American College of Radiology, the American Heart Association, the American Society of Echocardiography, the American Society of Nuclear Cardiology, the North American Society for Cardiovascular Imaging, the Society for Cardiovascular Angiography and Interventions, and the Society for Cardiovascular Magnetic Resonance. *J Cardiovasc Comput Tomogr* 2010; **4**: 407.e1-407.33 [PMID: 21232696 DOI: 10.1016/j.jcct.2010.11.001]

9 **Lupercio F**, Carlos Ruiz J, Briceno DF, Romero J, Villablanca PA, Berardi C, Faillace R, Krumerman A, Fisher JD, Ferrick K, Garcia M, Natale A, Di Biase L. Left atrial appendage morphology assessment for risk stratification of embolic stroke in patients with atrial fibrillation: A meta-analysis. *Heart Rhythm* 2016; **13**: 1402-1409 [PMID: 27016474 DOI: 10.1016/j.hrthm.2016.03.042]

10 **Kim YY**, Klein AL, Halliburton SS, Popovic ZB, Kuzmiak SA, Sola S, Garcia MJ, Schoenhagen P, Natale A, Desai MY. Left atrial appendage filling defects identified by multidetector computed tomography in patients undergoing radiofrequency pulmonary vein antral isolation: a comparison with transesophageal echocardiography. *Am Heart J* 2007; **154**: 1199-1205 [PMID: 18035095 DOI: 10.1016/j.ahj.2007.08.004]

11 **Kim SC**, Chun EJ, Choi SI, Lee SJ, Chang HJ, Han MK, Bae HJ, Park JH. Differentiation between spontaneous echocardiographic contrast and left atrial appendage thrombus in patients with suspected embolic stroke using two-phase multidetector computed tomography. *Am J Cardiol* 2010; **106**: 1174-1181 [PMID: 20920660 DOI: 10.1016/j.amjcard.2010.06.033]

12 **Hsieh BP**, Jha O, Chandra R, Garcia M, Boxt L, Taub C. Novel computed tomography indexes of left atrial appendage stasis. *Int J Cardiovasc Imaging* 2013; **29**: 237-244 [PMID: 22588712 DOI: 10.1007/s10554-012-0062-0]

13 **Kawaji T**, Yamgami S, Shizuta S, Aizawa T, Kato M, Yokomatsu T, Miki S, Ono K, Kimura T. Relation of a Filling Defect of Left Atrial Appendage by Contrast Computed Tomography Image With Subsequent Clinical Events in Patients With Atrial Fibrillation Receiving Catheter Ablation Procedures. *Am J Cardiol* 2022; **180**: 29-36 [PMID: 35863941 DOI: 10.1016/j.amjcard.2022.06.009]

14 **Romero J**, Husain SA, Kelesidis I, Sanz J, Medina HM, Garcia MJ. Detection of left atrial appendage thrombus by cardiac computed tomography in patients with atrial fibrillation: a meta-analysis. *Circ Cardiovasc Imaging* 2013; **6**: 185-194 [PMID: 23406625 DOI: 10.1161/CIRCIMAGING.112.000153]

15 **Wolf PA**, Dawber TR, Thomas HE Jr, Kannel WB. Epidemiologic assessment of chronic atrial fibrillation and risk of stroke: the Framingham study. *Neurology* 1978; **28**: 973-977 [PMID: 570666 DOI: 10.1212/wnl.28.10.973]

16 **Salem DN**, Daudelin HD, Levine HJ, Pauker SG, Eckman MH, Riff J. Antithrombotic therapy in valvular heart disease. *Chest* 2001; **119**: 207S-219S [PMID: 11157650 DOI: 10.1378/chest.119.1_suppl.207s]

17 **Somerville W**, Chambers RJ. Systemic embolism in mitral stenosis: relation to the size of the left atrial appendix. *Br Med J* 1964; **2**: 1167-1169 [PMID: 14190485 DOI: 10.1136/bmj.2.5418.1167]

18 **Taina M**, Vanninen R, Hedman M, Jäkälä P, Kärkkäinen S, Tapiola T, Sipola P. Left atrial appendage volume increased in more than half of patients with cryptogenic stroke. *PLoS One* 2013; **8**: e79519 [PMID: 24223960 DOI: 10.1371/journal.pone.0079519]

19 **Veinot JP**, Harrity PJ, Gentile F, Khandheria BK, Bailey KR, Eickholt JT, Seward JB, Tajik AJ, Edwards WD. Anatomy of the normal left atrial appendage: a quantitative study of age-related changes in 500 autopsy hearts: implications for echocardiographic examination. *Circulation* 1997; **96**: 3112-3115 [PMID: 9386182 DOI: 10.1161/01.cir.96.9.3112]

20 **Aryal MR**, Hakim FA, Ghimire S, Giri S, Pandit A, Bhandari Y, Bhandari N, Pathak R, Karmacharya P, Pradhan R. Left atrial appendage aneurysm: a systematic review of 82 cases. *Echocardiography* 2014; **31**: 1312-1318 [PMID: 24976376 DOI: 10.1111/echo.12667]

21 **Boucebci S**, Pambrun T, Velasco S, Duboe PO, Ingrand P, Tasu JP. Assessment of normal left atrial appendage anatomy and function over gender and ages by dynamic cardiac CT. *Eur Radiol* 2016; **26**: 1512-1520 [PMID: 26310584 DOI: 10.1007/s00330-015-3962-2]

22 **Maan A**, Heist EK. Left Atrial Appendage Anatomy: Implications for Endocardial Catheter-based Device Closure. *J Innov Card Rhythm Manag* 2020; **11**: 4179-4186 [PMID: 32724709 DOI: 10.19102/icrm.2020.110704]

23 **Kimura T**, Takatsuki S, Inagawa K, Katsumata Y, Nishiyama T, Nishiyama N, Fukumoto K, Aizawa Y, Tanimoto Y, Tanimoto K, Jinzaki M, Fukuda K. Anatomical characteristics of the left atrial appendage in cardiogenic stroke with low CHADS2 scores. *Heart Rhythm* 2013; **10**: 921-925 [PMID: 23384894 DOI: 10.1016/j.hrthm.2013.01.036]

24 **Asinger RW**, Mikell FL, Elsperger J, Hodges M. Incidence of left-ventricular thrombosis after acute transmural myocardial infarction. Serial evaluation by two-dimensional echocardiography. *N Engl J Med* 1981; **305**: 297-302 [PMID: 7242633 DOI: 10.1056/NEJM198108063050601]

25 **Gianstefani S**, Douiri A, Delithanasis I, Rogers T, Sen A, Kalra S, Charangwa L, Reiken J, Monaghan M, MacCarthy P. Incidence and predictors of early left ventricular thrombus after ST-elevation myocardial infarction in the contemporary era of primary percutaneous coronary intervention. *Am J Cardiol* 2014; **113**: 1111-1116 [PMID: 24485697 DOI: 10.1016/j.amjcard.2013.12.015]

26 **Loh E**, Sutton MS, Wun CC, Rouleau JL, Flaker GC, Gottlieb SS, Lamas GA, Moyé LA, Goldhaber SZ, Pfeffer MA. Ventricular dysfunction and the risk of stroke after myocardial infarction. *N Engl J Med* 1997; **336**: 251-257 [PMID: 8995087 DOI: 10.1056/NEJM199701233360403]

27 **Weinsaft JW**, Kim HW, Shah DJ, Klem I, Crowley AL, Brosnan R, James OG, Patel MR, Heitner J, Parker M, Velazquez EJ, Steenbergen C, Judd RM, Kim RJ. Detection of left ventricular thrombus by delayed-enhancement cardiovascular magnetic resonance prevalence and markers in patients with systolic dysfunction. *J Am Coll Cardiol* 2008; **52**: 148-157 [PMID: 18598895 DOI: 10.1016/j.jacc.2008.03.041]

28 **Grant MD**, Mann RD, Kristenson SD, Buck RM, Mendoza JD, Reese JM, Grant DW, Roberge EA. Transthoracic Echocardiography: Beginner's Guide with Emphasis on Blind Spots as Identified with CT and MRI. *Radiographics* 2021; **41**: 1022-1042 [PMID: 34115535 DOI: 10.1148/rg.2021200142]

29 **Weinsaft JW**, Kim HW, Crowley AL, Klem I, Shenoy C, Van Assche L, Brosnan R, Shah DJ, Velazquez EJ, Parker M, Judd RM, Kim RJ. LV thrombus detection by routine echocardiography: insights into performance characteristics using delayed enhancement CMR. *JACC Cardiovasc Imaging* 2011; **4**: 702-712 [PMID: 21757159 DOI: 10.1016/j.jcmg.2011.03.017]

30 **Ghadri JR**, Wittstein IS, Prasad A, Sharkey S, Dote K, Akashi YJ, Cammann VL, Crea F, Galiuto L, Desmet W, Yoshida T, Manfredini R, Eitel I, Kosuge M, Nef HM, Deshmukh A, Lerman A, Bossone E, Citro R, Ueyama T, Corrado D, Kurisu S, Ruschitzka F, Winchester D, Lyon AR, Omerovic E, Bax JJ, Meimoun P, Tarantini G, Rihal C, Y-Hassan S, Migliore F, Horowitz JD, Shimokawa H, Lüscher TF, Templin C. International Expert Consensus Document on Takotsubo Syndrome (Part II): Diagnostic Workup, Outcome, and Management. *Eur Heart J* 2018; **39**: 2047-2062 [PMID: 29850820 DOI: 10.1093/eurheartj/ehy077]

31 **Freudenberger RS**, Hellkamp AS, Halperin JL, Poole J, Anderson J, Johnson G, Mark DB, Lee KL, Bardy GH; SCD-HeFT Investigators. Risk of thromboembolism in heart failure: an analysis from the Sudden Cardiac Death in Heart Failure Trial (SCD-HeFT). *Circulation* 2007; **115**: 2637-2641 [PMID: 17485579 DOI: 10.1161/CIRCULATIONAHA.106.661397]

32 **McDonagh TA**, Metra M, Adamo M, Gardner RS, Baumbach A, Böhm M, Burri H, Butler J, Čelutkienė J, Chioncel O, Cleland JGF, Coats AJS, Crespo-Leiro MG, Farmakis D, Gilard M, Heymans S, Hoes AW, Jaarsma T, Jankowska EA, Lainscak M, Lam CSP, Lyon AR, McMurray JJV, Mebazaa A, Mindham R, Muneretto C, Francesco Piepoli M, Price S, Rosano GMC, Ruschitzka F, Kathrine Skibelund A; ESC Scientific Document Group. 2021 ESC Guidelines for the diagnosis and treatment of acute and chronic heart failure. *Eur Heart J* 2021; **42**: 3599-3726 [PMID: 34447992 DOI: 10.1093/eurheartj/ehab368]

33 **Cui L**, Tse G, Zhao Z, Bazoukis G, Letsas KP, Korantzopoulos P, Roever L, Li G, Liu T. Mid-ventricular obstructive hypertrophic cardiomyopathy with apical aneurysm: An important subtype of arrhythmogenic cardiomyopathy. *Ann Noninvasive Electrocardiol* 2019; **24**: e12638 [PMID: 30737990 DOI: 10.1111/anec.12638]

34 **Papanastasiou CA**, Zegkos T, Karamitsos TD, Rowin EJ, Maron MS, Parcharidou D, Kokkinidis DG, Karvounis H, Rimoldi O, Maron BJ, Efthimiadis GK. Prognostic role of left ventricular apical aneurysm in hypertrophic cardiomyopathy: A systematic review and meta-analysis. *Int J Cardiol* 2021; **332**: 127-132 [PMID: 33794232 DOI:

10.1016/j.ijcard.2021.03.056]
35 **Carcano C**, Kanne JP, Kirsch J. Interventricular membranous septal aneurysm: CT and MR manifestations. *Insights Imaging* 2016; **7**: 111-117 [PMID: 26687514 DOI: 10.1007/s13244-015-0456-3]
36 **Tyebally S**, Chen D, Bhattacharyya S, Mughrabi A, Hussain Z, Manisty C, Westwood M, Ghosh AK, Guha A. Cardiac Tumors: JACC CardioOncology State-of-the-Art Review. *JACC CardioOncol* 2020; **2**: 293-311 [PMID: 34396236 DOI: 10.1016/j.jaccao.2020.05.009]
37 **Pinede L**, Duhaut P, Loire R. Clinical presentation of left atrial cardiac myxoma. A series of 112 consecutive cases. *Medicine (Baltimore)* 2001; **80**: 159-172 [PMID: 11388092 DOI: 10.1097/00005792-200105000-00002]
38 **Lee VH**, Connolly HM, Brown RD Jr. Central nervous system manifestations of cardiac myxoma. *Arch Neurol* 2007; **64**: 1115-1120 [PMID: 17698701 DOI: 10.1001/archneur.64.8.1115]
39 **Nakatani S**, Ohara T, Ashihara K, Izumi C, Iwanaga S, Eishi K, Okita Y, Daimon M, Kimura T, Toyoda K, Nakase H, Nakano K, Higashi M, Mitsutake K, Murakami T, Yasukochi S, Okazaki S, Sakamoto H, Tanaka H, Nakagawa I, Nomura R, Fujiu K, Miura T, Morizane T; Japanese Circulation Society Joint Working Group. JCS 2017 Guideline on Prevention and Treatment of Infective Endocarditis. *Circ J* 2019; **83**: 1767-1809 [PMID: 31281136 DOI: 10.1253/circj.CJ-19-0549]
40 **Habets J**, Tanis W, Reitsma JB, van den Brink RB, Mali WP, Chamuleau SA, Budde RP. Are novel non-invasive imaging techniques needed in patients with suspected prosthetic heart valve endocarditis? *Eur Radiol* 2015; **25**: 2125-2133 [PMID: 25680715 DOI: 10.1007/s00330-015-3605-7]
41 **Writing Committee Members**, Otto CM, Nishimura RA, Bonow RO, Carabello BA, Erwin JP 3rd, Gentile F, Jneid H, Krieger EV, Mack M, McLeod C, O'Gara PT, Rigolin VH, Sundt TM 3rd, Thompson A, Toly C; ACC/AHA Joint Committee Members, O'Gara PT, Beckman JA, Levine GN, Al-Khatib SM, Armbruster A, Birtcher KK, Ciggaroa J, Deswal A, Dixon DL, Fleisher LA, de Las Fuentes L, Gentile F, Goldberger ZD, Gorenek B, Haynes N, Hernandez AF, Hlatky MA, Joglar JA, Jones WS, Marine JE, Mark D, Palaniappan L, Piano MR, Spatz ES, Tamis-Holland J, Wijeysundera DN, Woo YJ. 2020 ACC/AHA guideline for the management of patients with valvular heart disease: A report of the American College of Cardiology/American Heart Association Joint Committee on Clinical Practice Guidelines. *J Thorac Cardiovasc Surg* 2021; **162**: e183-e353 [PMID: 33972115 DOI: 10.1016/j.jtcvs.2021.04.002]
42 **Bazeed MF**, Moselhy MS, Rezk AI, Al-Murayeh MA. Low radiation dose non-contrast cardiac CT: is it of value in the evaluation of mechanical aortic valve. *Acta Radiol* 2012; **53**: 389-393 [PMID: 22422269 DOI: 10.1258/ar.2012.110253]
43 **Gündüz S**, Özkan M, Kalçik M, Gürsoy OM, Astarcioğlu MA, Karakoyun S, Aykan AÇ, Biteker M, Gökdeniz T, Kaya H, Yesin M, Duran NE, Sevinç D, Güneysu T. Sixty-Four-Section Cardiac Computed Tomography in Mechanical Prosthetic Heart Valve Dysfunction: Thrombus or Pannus. *Circ Cardiovasc Imaging* 2015; **8** [PMID: 26659372 DOI: 10.1161/CIRCIMAGING.115.003246]
44 **Suh YJ**, Lee S, Im DJ, Chang S, Hong YJ, Lee HJ, Hur J, Choi BW, Chang BC, Shim CY, Hong GR, Kim YJ. Added value of cardiac computed tomography for evaluation of mechanical aortic valve: Emphasis on evaluation of pannus with surgical findings as standard reference. *Int J Cardiol* 2016; **214**: 454-460 [PMID: 27096962 DOI: 10.1016/j.ijcard.2016.04.011]
45 **Coffey S**, Cox B, Williams MJ. The prevalence, incidence, progression, and risks of aortic valve sclerosis: a systematic review and meta-analysis. *J Am Coll Cardiol* 2014; **63**: 2852-2861 [PMID: 24814496 DOI: 10.1016/j.jacc.2014.04.018]
46 **Agatston AS**, Janowitz WR, Hildner FJ, Zusmer NR, Viamonte M Jr, Detrano R. Quantification of coronary artery calcium using ultrafast computed tomography. *J Am Coll Cardiol* 1990; **15**: 827-832 [PMID: 2407762 DOI: 10.1016/0735-1097(90)90282-t]
47 **Wang TKM**, Flamm SD, Schoenhagen P, Griffin BP, Rodriguez LL, Grimm RA, Xu B. Diagnostic and Prognostic Performance of Aortic Valve Calcium Score with Cardiac CT for Aortic Stenosis: A Meta-Analysis. *Radiol Cardiothorac Imaging* 2021; **3**: e210075 [PMID: 34498008 DOI: 10.1148/ryct.2021210075]
48 **Foley M**, Hall K, Howard JP, Ahmad Y, Gandhi M, Mahboobani S, Okafor J, Rahman H, Hadjiloizou N, Ruparelia N, Mikhail G, Malik I, Kanaganayagam G, Sutaria N, Rana B, Ariff B, Barden E, Anderson J, Afoke J, Petraco R, Al-Lamee R, Sen S. Aortic Valve Calcium Score Is Associated With Acute Stroke in Transcatheter Aortic Valve Replacement Patients. *J Soc Cardiovasc Angiogr Interv* 2022; **1**: 100349 [PMID: 35992189 DOI: 10.1016/j.jscai.2022.100349]
49 **Kianoush S**, Al Rifai M, Cainzos-Achirica M, Al-Mallah MH, Tison GH, Yeboah J, Miedema MD, Allison MA, Wong ND, DeFilippis AP, Longstreth W, Nasir K, Budoff MJ, Matsushita K, Blaha MJ. Thoracic extra-coronary calcification for the prediction of stroke: The Multi-Ethnic Study of Atherosclerosis. *Atherosclerosis* 2017; **267**: 61-67 [PMID: 29100062 DOI: 10.1016/j.atherosclerosis.2017.10.010]
50 **Harpaz D**, Auerbach I, Vered Z, Motro M, Tobar A, Rosenblatt S. Caseous calcification of the mitral annulus: a neglected, unrecognized diagnosis. *J Am Soc Echocardiogr* 2001; **14**: 825-831 [PMID: 11490332 DOI: 10.1067/mje.2001.111877]
51 **Dietl CA**, Hawthorn CM, Raizada V. Risk of Cerebral Embolization with Caseous Calcification of the Mitral Annulus: Review Article. *Open Cardiovasc Med J* 2016; **10**: 221-232 [PMID: 27990181 DOI: 10.2174/1874192401610010221]
52 **Hagen PT**, Scholz DG, Edwards WD. Incidence and size of patent foramen ovale during the first 10 decades of life: an autopsy study of 965 normal hearts. *Mayo Clin Proc* 1984; **59**: 17-20 [PMID: 6694427 DOI: 10.1016/s0025-6196(12)60336-x]
53 **Kim YJ**, Hur J, Shim CY, Lee HJ, Ha JW, Choe KO, Heo JH, Choi EY, Choi BW. Patent foramen ovale: diagnosis with multidetector CT--comparison with transesophageal echocardiography. *Radiology* 2009; **250**: 61-67 [PMID: 19001153 DOI: 10.1148/radiol.2501080559]
54 **Olivares-Reyes A**, Chan S, Lazar EJ, Bandlamudi K, Narla V, Ong K. Atrial septal aneurysm: a new classification in two hundred five adults. *J Am Soc Echocardiogr* 1997; **10**: 644-656 [PMID: 9282354 DOI: 10.1016/s0894-7317(97)70027-0]
55 **Kuramoto J**, Kawamura A, Dembo T, Kimura T, Fukuda K, Okada Y. Prevalence of Patent Foramen Ovale in the Japanese Population- Autopsy Study. *Circ J* 2015; **79**: 2038-2042 [PMID: 26084379 DOI: 10.1253/circj.CJ-15-0197]
56 **Mas JL**, Arquizan C, Lamy C, Zuber M, Cabanes L, Derumeaux G, Coste J; Patent Foramen Ovale and Atrial Septal Aneurysm Study Group. Recurrent cerebrovascular events associated with patent foramen ovale, atrial septal aneurysm, or both. *N Engl J Med* 2001; **345**: 1740-1746 [PMID: 11742048 DOI: 10.1056/NEJMoa011503]

57 **Amat F**, Le Bret E, Sigal-Cinqualbre A, Coblence M, Lambert V, Rohnean A, Paul JF. Diagnostic accuracy of multidetector spiral computed tomography for preoperative assessment of sinus venosus atrial septal defects in children. *Interact Cardiovasc Thorac Surg* 2011; **12**: 179-182 [PMID: 21098509 DOI: 10.1510/icvts.2010.251298]

58 **Shovlin CL**. Pulmonary arteriovenous malformations. *Am J Respir Crit Care Med* 2014; **190**: 1217-1228 [PMID: 25420112 DOI: 10.1164/rccm.201407-1254CI]

World Journal of Radiology

Submit a Manuscript: https://www.f6publishing.com

World J Radiol 2023 April 28; 15(4): 118-126

DOI: 10.4329/wjr.v15.i4.118

ISSN 1949-8470 (online)

ORIGINAL ARTICLE

Retrospective Study

Detection of tracheal branching with computerized tomography: The relationship between the angles and age-gender

Şevket Kahraman, Mesut Furkan Yazar, Hüseyin Aydemir, Mecit Kantarci, Sonay Aydin

Specialty type: Radiology, nuclear medicine and medical imaging

Provenance and peer review: Invited article; Externally peer reviewed.

Peer-review model: Single blind

Peer-review report's scientific quality classification

Grade A (Excellent): 0
Grade B (Very good): 0
Grade C (Good): C, C, C
Grade D (Fair): 0
Grade E (Poor): 0

P-Reviewer: Liu Y; Shariati MBH, Iran; Tovar JA, Spain

Received: December 26, 2022
Peer-review started: December 27, 2022
First decision: February 21, 2023
Revised: February 28, 2023
Accepted: March 24, 2023
Article in press: March 24, 2023
Published online: April 28, 2023

Şevket Kahraman, Mesut Furkan Yazar, Hüseyin Aydemir, Mecit Kantarci, Sonay Aydin, Depertmant of Radiology, Erzincan Binali Yıldırım University, Erzincan 24100, Turkey

Mecit Kantarci, Department of Radiology, Atatürk University, Erzurum 25240, Turkey

Corresponding author: Şevket Kahraman, MD, Doctor, Depertmant of Radiology, Erzincan Binali Yıldırım University, Başbağlar, 1429. Street, 24100 Erzincan Merkez/Erzincan 24100, Turkey. sevketkahraman92@gmail.com

Abstract

BACKGROUND

The data obtained on the anatomical knowledge of the tracheobronchial system can be used for diagnosis, treatment and interventional interventions in areas such as anesthesia, thoracic surgery, pulmonary physiology.

AIM

To determine the tracheobronchial branching angles in pediatric and adult populations by using the multislice computed tomography (CT) and minimum intensity projection (MinIP) technique, which is a non-invasive method.

METHODS

Our study was carried out retrospectively. Patients who underwent contrast and non-contrast CT examination, whose anatomically and pathophysiologically good tracheobronchial system and lung parenchyma images were obtained, were included in the study. Measurements were made in the coronal plane of the lung parenchyma. In the coronal plane, right main bronchus-left main bronchus angle, right upper lobe bronchus-intermedius bronchus angle, right middle lobe bronchus-right lower lobe bronchus angle, left upper lobe bronchus-left lower lobe bronchus angle were measured.

RESULTS

The study population consisted of 1511 patients, 753 pediatric (mean age: 13.4 ± 4.3; range: 1-18 years) and 758 adults (mean age: 54.3 ± 17.3; range: 19-94 years). In our study, tracheal bifurcation angle was found to be 73.3° ± 13.7° (59.6°-87°) in the whole population. In the pediatric group, the right-left main coronal level was found to be higher in boys compared to girls (74.6° ± 12.9° *vs* 71.2° ± 13.9°, P = 0.001). In the adult group, the right-left main coronal level was found to be lower in males compared to females (71.9° ± 12.9° *vs* 75.8° ± 14.7°, P < 0.001).

CONCLUSIONS

Our study, with the number of 1511 patients, is the first study in the literature with the largest number of patient populations including pediatric and adult demographic data, measuring the angle values of the tracheobronchial system using multislice CT and MinIP technique. Study data will not only be a guide during invasive procedures, but it can also guide studies to be done with imaging methods.

Key Words: Tracheobronchial branching angles; Subcarinal angle; Multislice computerized tomography; Minimum intensity projection technique

©The Author(s) 2023. Published by Baishideng Publishing Group Inc. All rights reserved.

Core Tip: This study is one of the rare studies with the highest number of patient population and measurement values in the literature measuring the branching angles of the tracheobronchial tree using the minimum intensity projection technique with multislice computed tomography in pediatric and adult populations. In this study, a wide variety of branching angles of the tracheal bronchial tree, which were not reported in the literature, were reported. Anatomical knowledge of the tracheobronchial system is essential during the use of interventional fiberoptic bronchoscopy during various airway devices, intubation, airway maneuvers. These results guide interventional procedures and offer new methods for future studies.

Citation: Kahraman Ş, Yazar MF, Aydemir H, Kantarci M, Aydin S. Detection of tracheal branching with computerized tomography: The relationship between the angles and age-gender. *World J Radiol* 2023; 15(4): 118-126

URL: https://www.wjgnet.com/1949-8470/full/v15/i4/118.htm

DOI: https://dx.doi.org/10.4329/wjr.v15.i4.118

INTRODUCTION

Trachea is a cylindrical flexible tube that provides air passage between the larynx and the lung. Trachea bifurcation angle, it is measured by the interbronchial angle, which is the angle measured at the intersection of the central axes of the right and left main bronchus, or by the subcarinal angle, which is the angle at the intersection of the lower borders of the right and left main bronchus. Many cardiac and mediastinal pathologies can cause changes in tracheal bifurcation angle[1-4].

Examination of the tracheobronchial tree can be done with invasive and noninvasive methods such as bronchoscopy, bronchograms, computed tomography (CT), magnetic resonance imaging[2,3,5]. Most previous studies measured the subcarinal angle on chest radiographs using a goniometer[6,7]. Helical CT provides volumetric imaging of chest films and accurate measurement of the subcarinal angle at a workstation using the minimum intensity projection (MinIP) technique. Because the MinIP technique uses all the data in the volume of interest to create a one/two-dimensional image, it is a technique that enables the visualization of structures of low density (*e.g.* air) at this level. This technique allows us to accurately measure the subcarinal angle compared to the coronal multiplane reconstructed image[3,8].

Anatomical knowledge of the tracheobronchial system is essential when using interventional fiberoptic bronchoscopy during various airway devices (*e.g.*, double-lumen endobronchial tube), intubation, airway maneuvers, airway reconstruction, and tracheobronchial tumor resection[9,10].

Previous studies were insufficient for the pediatric population[11-14]. In 2018, Fernandes *et al*[3] found the mean subcarinal angle of 69.75° ± 3.38° (range 66.37°-73.13°) in the measurements made with thorax CT and MinIP technique on 193 patients aged 20-60 years. Parry *et al*[5] in the measurements made with thorax CT and MinIP technique on 552 patients aged 9-85 years in 2019, they found the mean subcarinal angle to be statistically significantly larger in women than in men (78.90° ± 11.04° *vs* 67.60° ± 14.55°, $P < 0.05$). In 2018, Fernandes *et al*[3] and Parry *et al*[5] although the measurement methods are similar in his studies in 2019, the number of patients and measurement parameters are limited. In addition, the relationship between age and gender and the subcarinal angle was not clarified.

The aim of our study is to determine the tracheobronchial branching angles in pediatric and adult individuals with a high sample size population by using the multislice CT and MinIP technique, which is a non-invasive method, and to eliminate the above-mentioned literature deficiencies.

MATERIALS AND METHODS

Our institutional review board gave its approval to this retrospective study. Ethics committee did not require informed consent, as our study was retrospective.

Study population

A total of 1511 patients, including 753 pediatrics and 758 adults, were included in our study, (patients who do not obey breath commands enough to prevent image formation, tracheobronchial surgery or tracheal intubation history), patients with pneumothorax, pneumomediastinum as a result of trauma, patients with pathology that may cause mediastinal changes (mediastinal mass, mediastinal LAP, severe cardiomegaly), musculoskeletal deformity patients (scoliosis, kyphosis) and patients with diaphragmatic hernia were not included in the study. CT scanners today can scan the entire chest in a matter of seconds. Thin sections in multiple planes, including the axial, coronal and sagittal planes, can be used to quickly reconstruct images. Coronal images taken off-axis are useful for imaging the trachea in a single plane.

Patients who were unable to obtain good image quality (for example, those who were unable to hold their breath or who had motion artifacts) were excluded from the study. Thoracic CT scans were also performed in pediatric patients of all ages in order to produce the best image in the shortest amount of time. Images with poor image quality and coinciding with the expiratory phase were excluded from the study**.**

In our study, people with diseases that disrupt the anatomy and physiology of the tracheobronchial system, infective or inflammatory processes, lung cancer, significant pneumonia or collapse, and respiratory system diseases in all patient groups (adults and children) were not included in the study.

Inclusion criteria for the study; excluding the exclusion criteria, the tracheobronchial system and lung parenchyma images of the anatomically and pathophysiologically good quality were obtained in patients who underwent CT with or without contrast for any reason (Figure 1).

Imaging

This study consists of contracted and non-contrast thoracic CT examinations with a double tube 256 slice Somatom Definition Flash device (Siemens Healthcare, Forchheim, Germany). The images of the patients were evaluated using the Siemens Somatom Sensation-Syngo *via* software program from the PACS (Picture Archiving Communication System) archive on coronal planes and using the MinIP technique.

Shooting parameters and lung parenchyma images were obtained by adjusting tube voltage 120 kV, automatic tube current modulation 100-250 mAs, section thickness 1.25 mm, pitch 1.4, gantry rotation time 0.5-1 sec, FOV 455 mm. Images were acquired with adequate inspiration and in the supine position. In contrast-enhanced thorax shots, the dose was administered by administering a total of 100-120 mL of contrast material at a rate of 4 mL/sec.

Then, the images in the PACS system were measured in the coronal plane using the 25 mm MinIP technique in the Siemens (Syngo.via, Siemens Healthineers, Erlangen, Germany) software program.

Measurements were taken by 2 independent radiologists and verified by a partner radiologist. All radiologists then reviewed any discrepancies between the measurements. All investigators were blind to the age of the patients until the measurements were analysed.

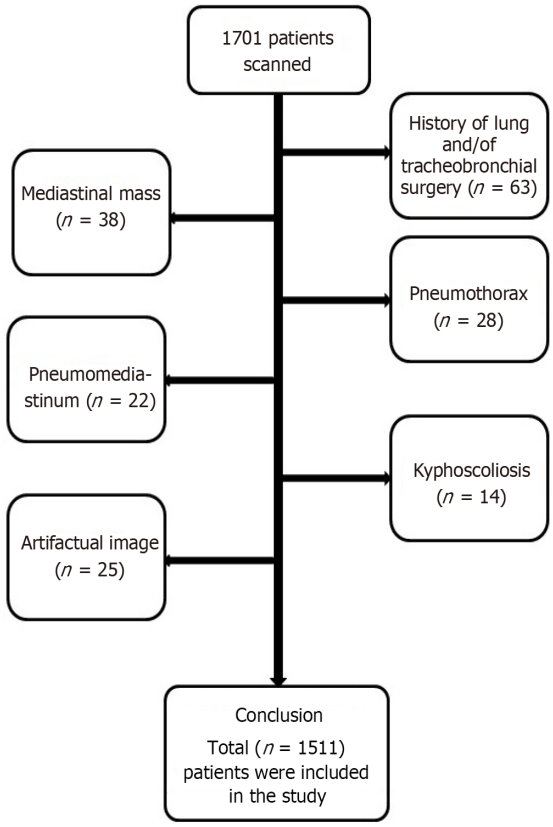
At the same time, demographic data (age, gender) of the patients were recorded. Measurements were made using the 25 mm MinIP technique obtained in the lung parenchyma window in the coronal plane *via* program. Right main bronchus-left main bronchus angle, right upper lobe bronchus-intermedius bronchus angle, right middle lobe bronchus-right lower lobe bronchus angle, left upper lobe bronchus-left lower lobe bronchus angle measurements were made in the coronal plane. It was measured as the angle at the junction of the line passing through the center of the bronchi on the long axis (Figure 2).

A data visualization technique called MinIP makes it possible to find low-density structures in a given volume. The algorithm projects the voxel with the lowest attenuation value across all views in the volume onto a 2D image, using all the data in the volume of interest to create a single bidimensional image.

Right main bronchus-left main bronchus angle (interbronchial angle) right left main coronal, right upper lobe bronchi-intermedius bronchus angle right upper-intermedius (coronal), right middle lobe bronchus-right lower lobe bronchus angle right middle-lower (coronal), left upper lobe bronchus-left lower lobe bronchial angle is abbreviated as left upper-lower (coronal).

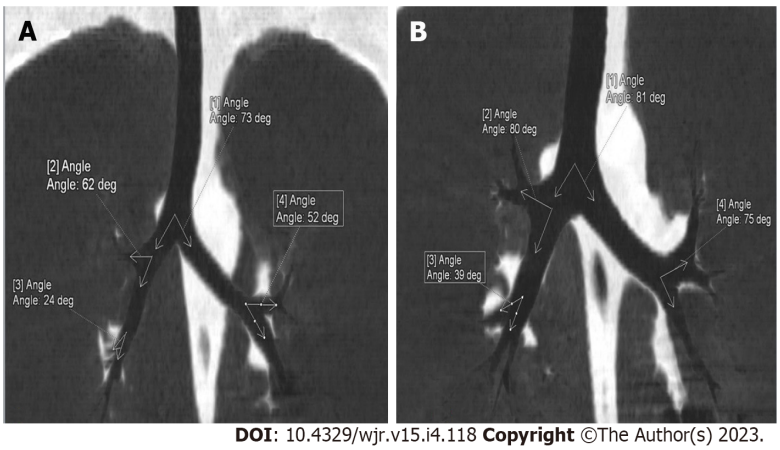
Statistical analysis

Statistical analyses of collected data were conducted using IBM SPSS Statistics for Windows 20.0 (IBM Corp., Armonk, NY, USA). Determination of the normally distributed data was conducted using the Kolmogorov-Smirnov test. Numerical variables that had normal distribution were expressed as the mean ± SD, while those with non-normal distribution were expressed as the median (min-max). The categorical variables were expressed as numbers and percentages. For comparisons between groups, the Student *T* test or Mann-Whitney *U* test were used according to normality distribution. Categorical



DOI: 10.4329/wjr.v15.i4.118 **Copyright** ©The Author(s) 2023.

Figure 1 Diagram showing the study population.



DOI: 10.4329/wjr.v15.i4.118 **Copyright** ©The Author(s) 2023.

Figure 2 Measurement of tracheobronchial angles on coronal plane thoracic images in pediatric and adult patients with MinIP technique.
A: Tracheobronchial angle measurements of a 9-year-old male pediatric patient are shown, B: Tracheobronchial angle measurements of a 25-year-old adult male patient are shown: (1) Angle of right and left main bronchus in coronal plane; (2) R upper-intermedius (coronal): The angle of the right upper lobe bronchus and the right intermedius bronchus in the coronal plane; (3) R middle-lower (coronal): The angle of the right middle lobe bronchus and the right lower lobe bronchus in the coronal plane; (4) L upper-lower (coronal): The angle of left upper lobe bronchus and left upper lobe bronchus in the coronal plane.

variables were expressed as numbers and percentages, and comparisons between groups were evaluated with Chi-square and Fisher's Exact tests. Spearman correlation analysis was used for the relationship between age and angels. $P < 0.05$ was taken as statistical significance.

RESULTS

The study population was 753 pediatrics (49.5%) (mean age: 13.4 ± 4.3 years; range: 1-18 years) and 758 adults (mean age: 54.3 ± 17.3 years; range: 19-94 years) consisted of 1511 patients. Gender distributions

were similar in pediatric and adult patient groups. Right-left main coronal, right upper-intermedius coronal and left upper-lower coronal levels did not differ in pediatric and adult patient groups, right middle-lower coronal levels were found to be lower in the pediatric group compared to the adult group (36.9 ± 12.2 *vs* 42 .4 ± 12.3, $P < 0.001$) (Table 1).

In the pediatric group, the right-left main coronal level was found to be higher in boys compared to girls (74.6 ± 12.9 *vs* 71.2 ± 13.9, $P = 0.001$), right upper-intermedius coronal, left upper-lower coronal, and right middle-lower coronal levels did not differ significantly in the pediatric group by gender (Table 2).

In the adult group, the right-left main coronal level was found to be lower in males compared to females (71.9 ± 12.9 *vs* 75.8 ± 14.7, $P < 0.001$), right upper-intermedius coronal, left upper-lower coronal and right middle-lower coronal levels did not differ significantly by gender in the adult group (Table 2).

As the age increases, the tracheal bifurcation angle passing through the central axes of the right main bronchus and the left main bronchus in the coronal plane and the angle of the right middle lobe bronchus and right lower lobe bronchus in the coronal plane increase statistically significantly (Table 3).

DISCUSSION

While there are many studies evaluating the tracheal bifurcation angle with cadaver studies and chest radiographs, there are limited studies evaluating using CT. However, it was not detected except in the study conducted by Fernandes *et al*[3], in which 193 patients reported using CT with the MinIP technique were examined. In addition, our study Mi *et al*[9] except for the measurements made with thorax CT and MPR technique on 2107 patients aged 18-89 years in 2015, it has a larger patient population than previous studies in the literature measuring the angle values of the tracheobronchial system.

Our study is a study with the largest number of patient population in our country, which measures the angle values of the tracheobronchial system using multislice CT and MinIP technique, which is a noninvasive method, and includes both pediatric and adult demographic data.

Tracheal bifurcation angle, it is measured by the interbronchial angle, which is the angle measured at the intersection of the central axes of the right and left main bronchus, or by the subcarinal angle, which is the angle at the intersection of the lower borders of the right and left main bronchus[4]. In our study, we measured the tracheal bifurcation angles by measuring the interbronchial angle. The normal values of the tracheal bifurcation angle range from 40° to 99°, with an average value of 60°–65°[11]. In our study, we found the tracheal bifurcation angle of 73.3° ± 13.7° (range 59.6°-87°).

Karabulut *et al*[11] in 2005, found the mean interbronchial angle of 77° ± 13° in a study that measured the tracheal bifurcation angle with helical CT performed on 120 patients aged 17-85 years.

The results of our study showed similar results with Karabulut *et al*[11] study and literature. The tracheal bifurcation angle may widen due to various mediastinal and cardiac pathologies, for example (subcarinal mass, lobar collapse, left atrial enlargement, generalized cardiomegaly, pericardial effusion) [4,15]. Tracheal bifurcation angle may decrease after pulmonary lobectomy[16]. Therefore, since the tracheal bifurcation angle is in a wide range and may change due to mediastinal and cardiac pathologies, diseases with mediastinal and cardiac pathologies and disrupting the anatomy and physiology of the tracheobronchial system were not included in our study. In our study, measurements were made during the inspiration phase because the tracheal bifurcation angle narrows due to the downward extension of the lungs in inspiration and expands with upward displacement of the lungs in expiration[3].

The first studies measuring the tracheal bifurcation angle (interbronchial angle) were made towards the end of the 19th century by Kamel *et al*[17] on cadavers and found the average angle of 70°[10,17]. Adriani *et al*[10] found the average tracheal bifurcation angle (interbronchial angle) of 110° in infantar. Kubota *et al*[12] found the tracheal bifurcation angle of 80° on average using chest radiography in their study on infants and children aged 0-13 years. Alavi *et al*[13] in their study of children up to 16 years of age, they found the tracheal bifurcation angle to range from 52° to 78° using chest radiography.

Ulusoy *et al*[14] in their study using multislice CT, found that the right bronchial angle was smaller than the left in their study in the 0-18 age range. Ulusoy *et al*[14] calculated the mean right subcarinal angle as 34.5° ± 8.1° degrees and the mean left subcarinal angle as 38.1° ± 8.9°. Although the mean right and left subcarinal angles were not significant in all age groups except the 0-18 age group, they were measured higher in women than in men[14]. In our study, the tracheal bifurcation angle, which is the sum of the right subcarinal angle and the left subcarinal angle, was used and our method was similar. In our study, the tracheal bifurcation angle passing through the central axes of the right main bronchus and left main bronchus in the coronal plane was found to be statistically significantly higher in boys compared to girls in our study (74.6° ± 12.9° *vs* 71.2° ± 13.9°, $P = 0.001$). The high number of cases and measurement parameters in our study suggest that our study is more reliable. The angle of the right upper lobe bronchus and the right intermedius bronchus in the coronal plane, the angle of the left upper lobe bronchus and the left lower lobe bronchus in the coronal plane, and the angle values of the right middle lobe bronchus and the right lower lobe bronchus in the coronal plane are the first measurements in the literature using the MinIP technique. However, no significant differentiation was deceted for

Table 1 Demographic and clinical characteristics

Variables (coronal)	Whole population, *n* = 1511	Pediatric group, *n* = 753	Adult group, *n* = 758	*P*
Age (year)	34.0 ± 24.0	13.4 ± 4.3	54.3 ± 17.3	< 0.001
Gender *n* (%)				
Male	755 (50.0)	371 (49.3)	384 (50.7)	0.589
Female	756 (50.0)	382 (50.7)	374 (49.3)	
Right-left main	73.3 ± 13.7	72.9 ± 13.5	73.8 ± 13.9	0.190
R upper-intermedius	69 ± 12.8	69.7 ± 12.4	68.4 ± 13.2	0.062
R middle-lower	39.7 ± 12.5	36.9 ± 12.2	42.4 ± 12.3	< 0.001
L upper-lower	58.4 ± 12.8	58.8 ± 12.8	57.9 ± 12.8	0.191

Numerical variables were expressed as mean ± SD; $P < 0.05$ shows statistical significance; R upper-intermedius: The angle of the right upper lobe bronchus and the right intermedius bronchus in the coronal plane; R middle-lower: The angle of the right middle lobe bronchus and the right lower lobe bronchus in the coronal plane; L upper-lower: The angle of the left upper lobe bronchus and the left upper lobe bronchus in the coronal plane.

Table 2 Distribution of demographic and clinical findings by gender

Variables (coronal)	Pediatric, *n* = 753		*P*	Adult, *n* = 758		*P*
	Male, *n* = 371	Female, *n* = 382		Male, *n* = 384	Female, *n* = 374	
Age (year)	13.1 ± 4.5	13.7 ± 4.1	0.055	53.4 ± 17.3	55.3 ± 17.4	0.117
Right-left main	74.6 ± 12.9	71.2 ± 13.9	0.001	71.9 ± 12.9	75.8 ± 14.7	< 0.001
R upper-intermedius	68.8 ± 11.9	70.5 ± 12.7	0.067	68.7 ± 13	68.2 ± 13.4	0.563
R middle-lower	37.2 ± 11.9	36.6 ± 12.5	0.568	42.1 ± 12.1	42.8 ± 12.4	0.435
L upper-lower	58.7 ± 13.3	58.9 ± 12.4	0.790	58.3 ± 11.9	57.5 ± 13.7	0.379

Numerical variables were expressed as mean ± SD; $P < 0.05$ shows statistical significance; R upper-intermedius: The angle of the right upper lobe bronchus and the right intermedius bronchus in the coronal plane; R middle-lower: The angle of the right middle lobe bronchus and the right lower lobe bronchus in the coronal plane; L upper-lower: The angle of the left upper lobe bronchus and the left upper lobe bronchus in the coronal plane.

Table 3 Relationship between age and angles

Variables (coronal)	r	*P*
Right-left main	0.064	0.014
R upper-intermedius	-0.098	<0.001
R middle-lower	0.167	<0.001
L upper-lower	-0.070	0.007

R upper-intermedius: The angle of the right upper lobe bronchus and the right intermedius bronchus in the coronal plane; R middle-lower: The angle of the right middle lobe bronchus and the right lower lobe bronchus in the coronal plane; L upper-lower: The angle of the left upper lobe bronchus and the left upper lobe bronchus in the coronal plane.

these measurements.

Karabulut *et al*[11] in 2005, the mean interbronchial angle was 77° ± 13° and the mean subcarinal angle was 73° ± 16° in the study of 120 patients aged 17-85 years, measuring the tracheal bifurcation angle with helical CT. They found an excellent correlation between the interbronchial angle and the subcarinal angle ($r = 0.88$, $P < 0.001$). They found that the interbronchial angle and subcarinal angle, which are tracheal bifurcation angles, were statistically significantly larger in females compared to males[11].

Murray *et al*[7] reported higher interbronchial and subcarinal angles in female patients in the measurements made using chest radiography on 122 patients with an age range of 27-85 years, but they were not statistically significant. Karabulut *et al*[11] study conducted in 2005 and our study contradicts

previous studies measuring the tracheal bifurcation angle with chest radiography, which reported that the angle of tracheal bifurcation was independent of gender[13,18,19]. Measurements with CT can be considered to be more reliable and accurate since it is possible to evaluate the anatomy of the tracheobronchial system in multiplanar (axial, sagittal and coronal) planes.

Mi *et al*[9] found the subcarinal angle, known as the sum of the right bronchial angle and the left bronchial angle, to be statistically significantly larger in women than in men, in the measurements made using thorax CT and MPR techniques on 2107 patients aged 18-89 years in 2015, similar to our study (80.1° ± 13.4° *vs* 75.1° ± 13.4°).

Khade *et al*[2] in 2016, found the mean subcarinal angle of 79.92° ± 11.6° (range 68.32°-91.52°) in 110 patients aged 10-70 years, measuring the subcarinal angle with thorax CT. Khade *et al*[2] in contrast to our study, found the subcarinal angle to be statistically insignificantly larger in men than in women (80.01° ± 12.53° *vs* 79.75° ± 9.99°, $P = 0.902$).

In 2018, Fernandes *et al*[3] found the mean subcarinal angle of 69.75° ± 3.38° (range 66.37° - 73.13°) in the measurements made with thorax CT and MinIP technique on 193 patients aged 20-60 years. Fernandes *et al*[3] found the subcarinal angle to be statistically insignificantly larger in women than in men (69.90° ± 4.07° *vs* 69.63° ± 2.75°, $P = 0.589$). Fernandes *et al*[3] found the mean subcarinal angle to be statistically significantly greater in the 20-40 age group than in the 41-60 age group (70.38° ± 3.85° *vs* 69.25° ± 2.88°, $P = 0.02$).

In a study by Kamel *et al*[17] in 2009 on tracheal morphology with CT and cadaver dissection, they found the mean subcarinal angle on thorax CT of 60 patients to be greater in women than in men (81° ± 20° *vs* 76° ± 20°).

Parry *et al*[5] in the measurements made with thorax CT and MinIP technique on 552 patients aged 9-85 years in 2019, they found the mean subcarinal angle to be statistically significantly greater in women than in men, similar to our study (78.90° ± 11.04° *vs* 67.60° ± 14.55°, $P < 0.05$).

In the current study, we measured the branching angles of the tracheobronchial tree (tracheal bifurcation angle passing through the central axes of the right main bronchus and left main bronchus in the coronal plane, the angle of the right upper lobe bronchus and the right intermedius bronchus in the coronal plane, the angle of the right middle lobe bronchus and the right lower lobe bronchus, the angle of the left upper lobe bronchus and the left lower lobe bronchus in the coronal plane) in both adult and pediatric patients. This study is one of the rare studies in the literature with the highest number of patient population and different measurement angles.

The data of other studies examining the relationship between age and tracheobronchial angle are contradictory. In 2018, Fernandes *et al*[3] found the mean subcarinal angle in the 20-40 age group statistically significantly higher than the 41-60 age group in the measurements made with thorax CT and MinIP technique on 193 patients with an age range of 20-60 years (70.38° ± 3.85° *vs* 69.25° ± 2.88°, $P = 0.02$). Khade *et al*[2] in 2016, in a study that measured the subcarinal angle with thorax CT on 110 patients with an age range of 10-70 years, they did not find any correlation with age and gender. Chunder *et al*[20] in his study conducted in 2015 on 60 cadaver specimens, the mean subcarinal angles in the 0–15 years, 16–25 years, 26–40 years, 41–55 years, and > 55 age groups were 61.4°, 52.9°, 49.2°, 48.2° and 48.2° in women, respectively; 54°, 64.3°, 56.4°, 58.4°, 57.1° and 59.5° found in males. They concluded that there was a decrease in the subcarinal angle with increasing age, except for patients aged > 55 years [20]. In our study, the trachea bifurcation angle passing through the central axes of the right main bronchus and the left main bronchus in the coronal plane, and the angle of the right middle lobe bronchus and right lower lobe bronchus in the coronal plane increase statistically with increasing age. It may have occurred due to the variability of the angle due to inspiration-expiration, various mediastinal and cardiac pathologies, measurement technique. In addition, the characteristics of the study populations such as age, gender and race may affect the results. There is a need for further studies measuring with similar methods in more standardized populations to clarify this issue.

CONCLUSION

Our study is the first study in the literature to measure the angle values of the tracheobronchial system using the multislice CT and MinIP technique with the number of 1511 patients and to have the largest patient population including both pediatric and adult demographic data. In addition, unlike previous studies, we measured all branching angles of the tracheobronchial tree and assessed their relationship with age and gender.

In our study, tracheal bifurcation angle was found to be 73.3° ± 13.7° (59.6° - 87°) in the whole population. The tracheal bifurcation angle and the angle of the right middle lobe bronchus and the right lower lobe bronchus in the coronal plane increase statistically with increasing age.

ARTICLE HIGHLIGHTS

Research background

This study is one of the few in the literature that uses the minimum intensity projection (MinIP) technique with multislice computed tomography (CT) to measure the branching angles of the tracheobronchial tree in pediatric and adult populations.

Research motivation

Our study is the first study in the literature to measure the angle values of the tracheobronchial system using the multislice CT and MinIP technique with the number of 1511 patients and to have the largest patient population including both pediatric and adult demographic data.

Research objectives

Our study's objectives are to fill the gaps in the literature by measuring the tracheobronchial branching angles in a large sample size population of pediatric and adult patients using the non-invasive multislice CT and MinIP technology.

Research methods

This study was carried out retrospectively. Patients who underwent contrast and non-contrast CT examination, whose anatomically and pathophysiologically good tracheobronchial system and lung parenchyma images were obtained, were included in the study. In the coronal plane, right main bronchus-left main bronchus angle, right upper lobe bronchus-intermedius bronchus angle, right middle lobe bronchus-right lower lobe bronchus angle, left upper lobe bronchus-left lower lobe bronchus angle were measured.

Research results

In our study, tracheal bifurcation angle was found to be 73.3° ± 13.7° (59.6°-87°) in the whole population. In the pediatric group, the right-left main coronal level was found to be higher in boys compared to girls. In the adult group, the right-left main coronal level was found to be lower in males compared to females.

Research conclusions

The tracheal bifurcation angle and the angle of the right middle lobe bronchus and the right lower lobe bronchus in the coronal plane increase statistically with increasing age.

Research perspectives

The date of this data will not only be a guide during invasive procedures, but it can also guide studies to be done with imaging methods.

FOOTNOTES

Author contributions: Aydin S drafted the manuscript; Kahraman S and Aydemir H edited and revised the manuscript; Kantarci M and Yazar MF approved the final version of the manuscript.

Institutional review board statement: The study was retrospective and could not be performed on an active concurrent human or animal subject.

Informed consent statement: Our institutional review board gave its approval to this retrospective study. Informed consent form was waiver by the institutional review board as a result of retrospective nature.

Conflict-of-interest statement: All the authors report no relevant conflicts of interest for this article.

Data sharing statement: No additional data are available.

Open-Access: This article is an open-access article that was selected by an in-house editor and fully peer-reviewed by external reviewers. It is distributed in accordance with the Creative Commons Attribution NonCommercial (CC BY-NC 4.0) license, which permits others to distribute, remix, adapt, build upon this work non-commercially, and license their derivative works on different terms, provided the original work is properly cited and the use is non-commercial. See: https://creativecommons.org/Licenses/by-nc/4.0/

Country/Territory of origin: Turkey

ORCID number: Şevket Kahraman 0000-0001-6850-3569; Mesut Furkan Yazar 0000-0002-8658-147X; Hüseyin Aydemir

0000-0002-5698-1560; Mecit Kantarci 0000-0002-1043-6719; Sonay Aydin 0000-0002-3812-6333.

S-Editor: Liu XF
L-Editor: A
P-Editor: Zhao S

REFERENCES

1 **Choorat S**, Totanarungroj K, Muangman N. Assessment of normal subcarinal angle on chest radiographs in adult Thai population. *Siriraj Med J* 2008; **60**: 264-266
2 **Khade B**, Waheed AR, Yadav N, Diwan CV. Study of sub carinal angle of human trachea by computerized tomography. *Int J Anat Res* 2016; **4**: 2828-2832 [DOI: 10.16965/ijar.2016.346]
3 **Fernandes SF**, Pradhan A. Estimation of subcarinal angle using minimum intensity projection in computed tomography. *Asian J Pharm Clin Res* 2018; **11**: 383-385 [DOI: 10.22159/ajpcr.2018.v11i4.24041]
4 **Bedair R**, Iriart X. EDUCATIONAL SERIES IN CONGENITAL HEART DISEASE: Tetralogy of Fallot: diagnosis to long-term follow-up. *Echo Res Pract* 2019; **6**: R9-R23 [PMID: 30557849 DOI: 10.1530/ERP-18-0049]
5 **Parry AH**, Wani AH, Shiekh Y, Gojwari TA. Determination of subcarinal angle of trachea using computed tomography. *Int J Res Med Sci* 2019; **7**: 1527 [DOI: 10.18203/2320-6012.ijrms20191526]
6 **Lin C**, Lee JH, Hsieh CM. The correlation between subcarinal angle and left atrial volume. *Acta Cardiol Sin* 2012; **67**: 15-96
7 **Murray JG**, Brown AL, Anagnostou EA, Senior R. Widening of the tracheal bifurcation on chest radiographs: value as a sign of left atrial enlargement. *AJR Am J Roentgenol* 1995; **164**: 1089-1092 [PMID: 7717208 DOI: 10.2214/ajr.164.5.7717208]
8 **Perandini S**, Faccioli N, Zaccarella A, Re T, Mucelli RP. The diagnostic contribution of CT volumetric rendering techniques in routine practice. *Indian J Radiol Imaging* 2010; **20**: 92-97 [PMID: 20607017 DOI: 10.4103/0971-3026.63043]
9 **Mi W**, Zhang C, Wang H, Cao J, Li C, Yang L, Guo F, Wang X, Yang T. Measurement and analysis of the tracheobronchial tree in Chinese population using computed tomography. *PLoS One* 2015; **10**: e0123177 [PMID: 25894917 DOI: 10.1371/journal.pone.0123177]
10 **Adriani J**, Griggs TS. An improved endotracheal tube for pediatric use. *Anesthesiology* 1954; **15**: 466-470 [PMID: 13189155 DOI: 10.1097/00000542-195409000-00004]
11 **Karabulut N**. CT assessment of tracheal carinal angle and its determinants. *Br J Radiol* 2005; **78**: 787-790 [PMID: 16110098 DOI: 10.1259/bjr/75107416]
12 **Kubota Y**, Toyoda Y, Nagata N, Kubota H, Sawada S, Murakawa M, Fujimori M. Tracheo-bronchial angles in infants and children. *Anesthesiology* 1986; **64**: 374-376 [PMID: 3954135 DOI: 10.1097/00000542-198603000-00015]
13 **Alavi SM**, Keats TE, O'Brien WM. The angle of tracheal bifurcation: its normal mensuration. *Am J Roentgenol Radium Ther Nucl Med* 1970; **108**: 546-549 [PMID: 5415930 DOI: 10.2214/ajr.108.3.546]
14 **Ulusoy M**, Uysal II, Kıvrak AS, Ozbek S, Karabulut AK, Paksoy Y, Dogan NU. Age and gender related changes in bronchial tree: a morphometric study with multidedector CT. *Eur Rev Med Pharmacol Sci* 2016; **20**: 3351-3357 [PMID: 27608892]
15 **Dwivedi G**, Mahadevan G, Jimenez D, Frenneaux M, Steeds RP. Reference values for mitral and tricuspid annular dimensions using two-dimensional echocardiography. *Echo Res Pract* 2014; **1**: 43-50 [PMID: 26693300 DOI: 10.1530/ERP-14-0050]
16 **Kakeda S**, Kamada K, Aoki T, Watanabe H, Nakata H. Postsurgical change in the tracheal bifurcation angle after upper lobectomy: radiographic evaluation. *Acad Radiol* 2003; **10**: 644-649 [PMID: 12809418 DOI: 10.1016/s1076-6332(03)80083-1]
17 **Kamel KS**, Lau G, Stringer MD. In vivo and in vitro morphometry of the human trachea. *Clin Anat* 2009; **22**: 571-579 [PMID: 19544298 DOI: 10.1002/ca.20815]
18 **Haskin PH**, Goodman LR. Normal tracheal bifurcation angle: a reassessment. *AJR Am J Roentgenol* 1982; **139**: 879-882 [PMID: 6981969 DOI: 10.2214/ajr.139.5.879]
19 **Coppola V**, Vallone G, Coscioni E, Coppola M, Maraziti G, Alfinito M, Di Benedetto G. [Normal value of the tracheal bifurcation angle and correlation with left atrial volume]. *Radiol Med* 1998; **95**: 461-465 [PMID: 9687921]
20 **Chunder R**, Guha R. A morphometric study of human subcarinal angle in different age groups in both sexes and its clinical implications. *Indian Journal of Basic and Applied Medical Research* 2015; **4**: 424-430

World Journal of Radiology

Submit a Manuscript: https://www.f6publishing.com

World J Radiol 2023 April 28; 15(4): 127-135

DOI: 10.4329/wjr.v15.i4.127

ISSN 1949-8470 (online)

ORIGINAL ARTICLE

Retrospective Study

Does sevoflurane sedation in pediatric patients lead to "pseudo" leptomeningeal enhancement in the brain on 3 Tesla magnetic resonance imaging?

Kiran Hilal, Kumail Khandwala, Saima Rashid, Faheemullah Khan, Shayan Sirat Maheen Anwar

Specialty type: Radiology, nuclear medicine and medical imaging

Provenance and peer review: Invited article; externally peer reviewed.

Peer-review model: Single blind

Peer-review report's scientific quality classification

Grade A (Excellent): 0
Grade B (Very good): B
Grade C (Good): C
Grade D (Fair): 0
Grade E (Poor): 0

P-Reviewer: Nagamine T, Japan; Yarmahmoodi F

Received: February 19, 2023
Peer-review started: February 19, 2023
First decision: March 15, 2023
Revised: March 28, 2023
Accepted: April 18, 2023
Article in press: April 18, 2023
Published online: April 28, 2023

Kiran Hilal, Kumail Khandwala, Faheemullah Khan, Shayan Sirat Maheen Anwar, Department of Radiology, Aga Khan University Hospital, Karachi 74800, Pakistan

Saima Rashid, Department of Anesthesiology, Aga Khan University Hospital, Karachi 74800, Pakistan

Corresponding author: Shayan Sirat Maheen Anwar, FCPS, MBBS, Assistant Professor, Department of Radiology, Aga Khan University Hospital, National Stadium Rd, Karachi 74800, Pakistan. shayan.anwar@aku.edu

Abstract

BACKGROUND

Prominent leptomeningeal contrast enhancement (LMCE) in the brain is observed in some pediatric patients during sedation for imaging. However, based on clinical history and cerebrospinal fluid analysis, the patients are not acutely ill and do not exhibit meningeal signs. Our study determined whether sevoflurane inhalation in pediatric patients led to this pattern of 'pseudo' LMCE (pLMCE) on 3 Tesla magnetic resonance imaging (MRI).

AIM

To highlight the significance of pLMCE in pediatric patients undergoing enhanced brain MRI under sedation to avoid misinterpretation in reports.

METHODS

A retrospective cross-sectional evaluation of pediatric patients between 0-8 years of age was conducted. The patients underwent enhanced brain MRI under inhaled sevoflurane. The LMCE grade was determined by two radiologists, and interobserver variability of the grade was calculated using Cohen's kappa. The LMCE grade was correlated with duration of sedation, age and weight using the Spearman rho rank correlation.

RESULTS

A total of 63 patients were included. Fourteen (22.2%) cases showed mild LMCE, 48 (76.1%) cases showed moderate LMCE, and 1 case (1.6%) showed severe LMCE. We found substantial agreement between the two radiologists in detection of pLMCE on post-contrast T1 imaging (kappa value = 0.61; $P < 0.001$). Addi-

tionally, we found statistically significant inverse and moderate correlations between patient weight and age. There was no correlation between duration of sedation and pLMCE.

CONCLUSION
pLMCE is relatively common on post-contrast spin echo T1-weighted MRI of pediatric patients sedated by sevoflurane due to their fragile and immature vasculature. It should not be misinterpreted for meningeal pathology. Knowing pertinent clinical history of the child is an essential prerequisite to avoid radiological overcalling and the subsequent burden of additional investigations.

Key Words: Brain; Pediatrics; Gadolinium contrast; Pseudo leptomeningeal enhancement; 3 Tesla magnetic resonance imaging; Sevoflurane

©The Author(s) 2023. Published by Baishideng Publishing Group Inc. All rights reserved.

Core Tip: Prominent leptomeningeal contrast enhancement (LMCE) in the brain is seen in some pediatric patients during sedation for imaging, but they do not exhibit meningeal disease. This pattern of pseudo LMCE is relatively common on post-contrast spin echo-T1-weighted magnetic resonance imaging of pediatric patients sedated by sevoflurane due to their fragile and immature vasculature. Knowing pertinent clinical history is an essential prerequisite to avoid radiological overcalling and additional investigations. Our study determined whether sevoflurane inhalation in pediatric patients led to pseudo LMCE on 3 Tesla magnetic resonance imaging.

Citation: Hilal K, Khandwala K, Rashid S, Khan F, Anwar SSM. Does sevoflurane sedation in pediatric patients lead to "pseudo" leptomeningeal enhancement in the brain on 3 Tesla magnetic resonance imaging? *World J Radiol* 2023; 15(4): 127-135
URL: https://www.wjgnet.com/1949-8470/full/v15/i4/127.htm
DOI: https://dx.doi.org/10.4329/wjr.v15.i4.127

INTRODUCTION

Contrast material for cross-sectional magnetic resonance imaging (MRI) has been used since the mid-1980s. Since then, leptomeningeal contrast enhancement (LMCE) has been detected in pathological states such as infection and carcinomatosis. Its detection is crucial for disease management, particularly in pediatric patients[1]. Because MRI acquisition is a lengthy process, general anesthesia is frequently required in pediatric patients younger than 8 years of age. Approximately 90% of the pediatric population requires deep sedation or anesthesia for reducing anxiety and movement[2]. Over 35 years, scientific societies have proposed guidelines to perform pediatric non-operating room anesthesia to minimize complications. Subsequently, each center has developed its own protocol[3]. Different pharmacological agents have specific disadvantages, such as a high failure rate, poor predictability and prolonged awakening for midazolam[4] and chloral hydrate[5], and respiratory drive depression for propofol[6].

Sevoflurane is an inhalational anesthetic and has excellent outcomes in success of sedation, safety and manageability[7]. It has a minimal potential for hepatotoxicity and nephrotoxicity and a comparatively low risk for cardiac arrhythmias. Its effects on cerebral vasodilation, increased cerebral blood flow and increased intracranial pressure are less than propofol[8-10]. In our institution we prefer to induce sedation with sevoflurane due to its rapid induction and rapid recovery. It is primarily administered in pediatric patients undergoing MRI as an outpatient procedure.

A recent study carried out in 2018 revealed that "pseudo" LMCE (pLMCE) in the brain is frequently observed on 3 Tesla (3T) post-contrast spin echo (SE) T1-weighted imaging (WI) in younger pediatric patients anesthetized with propofol and should not be misinterpreted for meningeal pathology[11]. Propofol results in reduction in the tidal volume, a mild decrease in the partial pressure of oxygen in the blood and a decrease in the fraction of inspired oxygen. These changes may lead to the pathophysiology of pLMCE secondary to cerebral vasodilation by an increase in the partial pressure of carbon dioxide as a result of smooth muscle relaxation[12,13]. The suggested mechanism of pLMCE is the retention of carbon dioxide, a potent vasodilator, resulting in increased vessel visibility, and this effect could be amplified in young pediatric patients with sensitive leptomeningeal vessels resulting in leakiness.

Based on aforementioned rationale and pathophysiology of propofol, we aimed to determine whether sevoflurane sedation leads to a similar pattern of pLMCE in the brain on 3T MRI and to determine the interobserver agreement of detecting pLMCE in patients receiving sevoflurane. We also evaluated the

degree of pLMCE and determined whether this phenomenon was correlated with sedation duration or patient age or weight.

MATERIALS AND METHODS

This was a retrospective cross-sectional study conducted in the Radiology Department of a Joint Commission International-accredited university hospital after ethical review board approval. The period of data collection was from January 2020 to June 2020.

Imaging technique

All studies were conducted on a single 3T MR unit (Canon Medical Systems Corp., Otawara, Tochigi, Japan) after administration of intravenous gadolinium. Sedation was performed by a pediatric anesthetist. The imaging parameters using 32 channel head coil for post-contrast SE T1WI were NAQ = 1, FOV = 22 cm × 22 cm, Matrix = 224 × 400, slice thickness 4.5 mm and acquisition time 1 min 30 s. The imaging parameters for post-contrast coronal fluid attenuated inversion recovery (FLAIR) were NAQ = 1, FOV = 22 cm × 22 cm, Matrix = 224 × 320, slice thickness 5 mm and acquisition time 1 min 10 s. Per our departmental protocol, FLAIR images were acquired in the coronal plane. The time interval between contrast injection and image acquisition was 10-30 s for post-contrast SE T1WI and 100-120 s for post-contrast FLAIR sequence. Axial SE T1WI, T2WI, FLAIR, susceptibility weighted imaging and diffusion weighted imaging were also performed in each patient before contrast administration. A standard weight based intravenous dose of gadolinium-based contrast was used in all patients [0.1 mL/kg of body weight of gadobutrol (Gadavist; Bayer HealthCare Pharmaceuticals, Berlin, Germany)][14].

Anesthesia technique

Standard monitoring was used with MRI compatible equipment, and general anesthesia was induced with sevoflurane 8%. Anesthesia was maintained with sevoflurane at a minimum alveolar concentration of 2%-3% along with oxygen (40%) and nitrous oxide (60%)[15,16]. This ratio of oxygen and nitrous oxide was maintained in all cases, while SpO2 was monitored for adequacy throughout the procedure. There were no complications for any case. Laryngeal masks were used to maintain the airway except for in a few patients who were already intubated or had indications for a definitive airway[3].

Inclusion criteria

The following inclusion criteria were used: (1) Pediatric patients between the ages of 0-8 years who underwent brain MRI on a 3T system; (2) Patients who received sevoflurane for sedation purposes before the procedure; and (3) Patients who had no clinical signs of meningism and/or a negative cerebrospinal fluid (CSF) analysis report, if performed.

Exclusion criteria

The following exclusion criteria were used: (1) Patients with any known or clinically suspected meningeal inflammatory or infectious condition; (2) Patients who were undergoing radiation therapy or chemotherapy; (3) Patients with known central nervous system tumors; and (4) Patients who were sedated with chloral hydrate, midazolam and propofol.

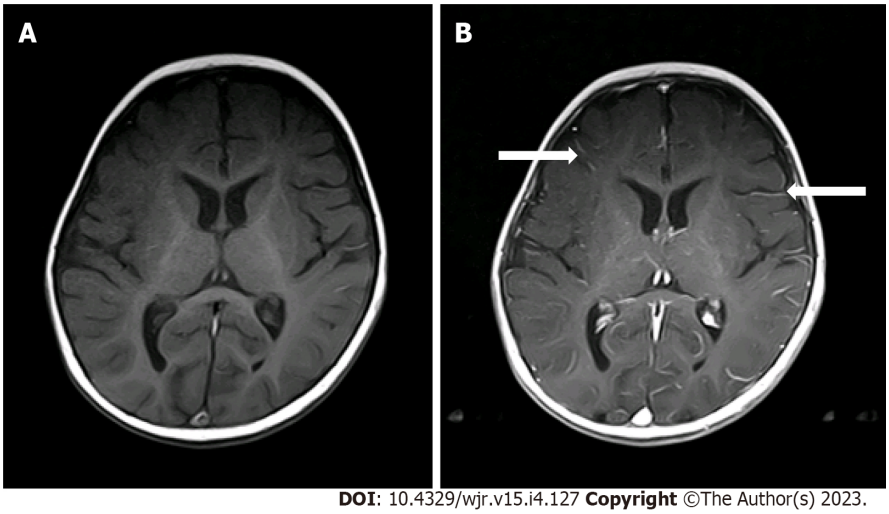
Data analysis

A total of 130 patients (0–8 years of age) underwent brain 3T MRI with contrast over a period of 6 months at our institution. Out of the 69 pediatric patients sedated by sevoflurane for 3T MRI, 2 cases were excluded due to the lack of post-contrast imaging. Four cases were excluded due to positive CSF analysis for meningitis.

Two radiologists (one pediatric radiologist and one neuroradiologist) with more than 5 years of experience reviewed the scans and independently graded the degree of pLMCE on post-contrast SE T1WI in comparison to precontrast SE T1WI. The grades were: (1) None: Minimal thin vascular structures barely visible around the sulci; (2) Mild: Linear enhancement along the depths of the sulci (Figure 1); (3) Moderate: Smooth and slightly thickened LMCE (Figure 2); and (4) Severe: Almost nodular, diffusely thickened LMCE (Figure 3). Confirmation of true meningeal enhancement or disease was also confirmed on precontrast and post-contrast FLAIR images[11,17]. The disagreements were resolved on a consensus basis.

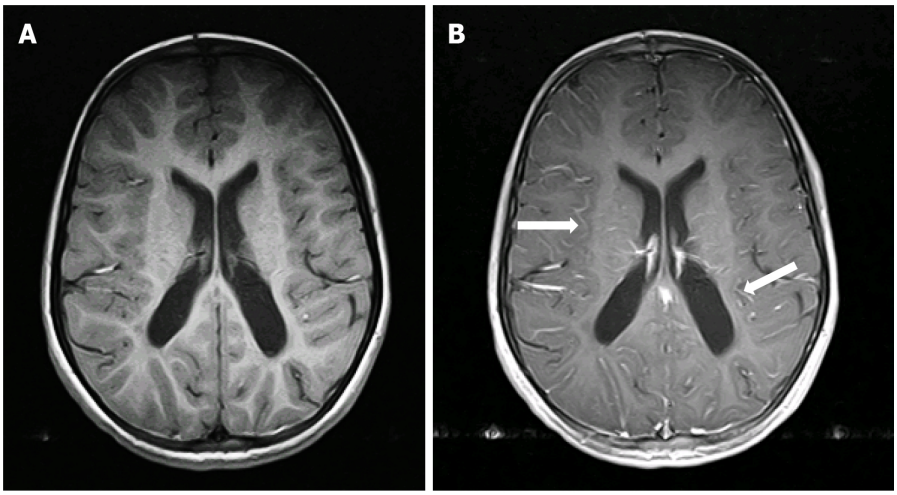
Statistical analysis

Data entry was performed in Statistical Package for Social Sciences version 20.0 software (IBM Corp., Armonk, NY, United States). Demographic data, such as age, were expressed as mean ± SD. The effect of age, weight and sex on LMCE was evaluated. The interobserver variability was calculated using Cohen's kappa statistic. The LMCE grade was correlated with the duration of sedation and patient age and weight using the Spearman rho rank correlation. Correlation coefficients $0.1 < P < 0.3$, $0.3 < P < 0.5$



DOI: 10.4329/wjr.v15.i4.127 **Copyright** ©The Author(s) 2023.

Figure 1 Mild pseudo leptomeningeal contrast enhancement in a 7-mo-old male with infantile spasms (Grade 1). A: Axial spin echo T1-weighted images; B: Axial post-contrast spin echo T1-weighted images showed pseudo leptomeningeal contrast enhancement as small vascular structures (arrows) within the depths of the sulci.



DOI: 10.4329/wjr.v15.i4.127 **Copyright** ©The Author(s) 2023.

Figure 2 Moderate pseudo leptomeningeal contrast enhancement a 7-yr-old female with developmental delays (Grade 2). A: Axial spin echo T1-weighted imaging; B: Axial post-contrast T1-weighted imaging showed pseudo leptomeningeal contrast enhancement as smooth and slightly thickened enhancements (arrows) throughout the depths of the sulci.

and > 0.5 were used as indications of weak, moderate and substantial associations, respectively. *P* values less than 0.05 were considered statistically significant.

RESULTS

A total of 63 patients were ultimately included for MRI review. All patients underwent post-contrast imaging by SE T1WI. Table 1 lists the mean patient age, weight and sedation duration. CSF studies were ordered for 7 patients (11.0%) and were negative for meningitis for all. Underlying conditions of the included patients are shown in Table 2.

The results showed that 14 cases (22.2%) had mild LMCE, 48 cases (76.1%) had moderate LMCE, and 1 case (1.6%) had severe LMCE. There were no cases that were negative for pLMCE. Overall, there was concordance with a kappa value of 0.61 ($P < 0.001$), which indicated substantial agreement between the two radiologists in detection of pLMCE on post-contrast T1 imaging. On precontrast FLAIR, no sulcul hyperintensity was noted in any patient. On post-contrast FLAIR, LMCE was absent in 63 (100%) cases, indicating the absence of true LMCE in all cases.

Table 1 Means and frequencies of patient age, sex, weight, and sedation duration

Parameter		Mean	SD	Minimum	Maximum	*n*	%
Age, mo		29.95	25.42	1.00	96.00		
Sex	Male					31	49.2
	Female					32	50.8
Weight, kg		12.03	6.25	1.30	26.50		
Duration of sedation, min		57.78	24.76	28.00	196.00		

SD: Standard deviation.

Table 2 Underlying conditions in the included pediatric patients

Diagnosis	*n*	%
Atrial septal defect	1	1.6
Autism	1	1.6
Bilateral congenital cataracts	1	1.6
Cerebral palsy	2	3.1
Congenital deafness	1	1.6
Developmental delay	7	11.1
Double aortic arch	1	1.6
Headache	1	1.6
Hypoxic ischemic encephalopathy	2	3.1
Hydrocephalus	3	4.7
Hypotonia	1	1.6
Infantile spasms	1	1.6
Metabolic disorder	2	3.1
Metachromatic leukodystrophy	2	3.1
Not available/none	14	7.9
Nystagmus	1	1.6
Retinal detachment/vitreous hemorrhage	1	1.6
Severe combined immunodeficiency	1	1.6
Seizure disorder	20	31.7

There were statistically significant, inverse, moderate correlations between patient weight and pLMCE grade and patient age and pLMCE grade (Table 3). The duration of sedation showed no significant association with pLMCE grade (P = 0.14).

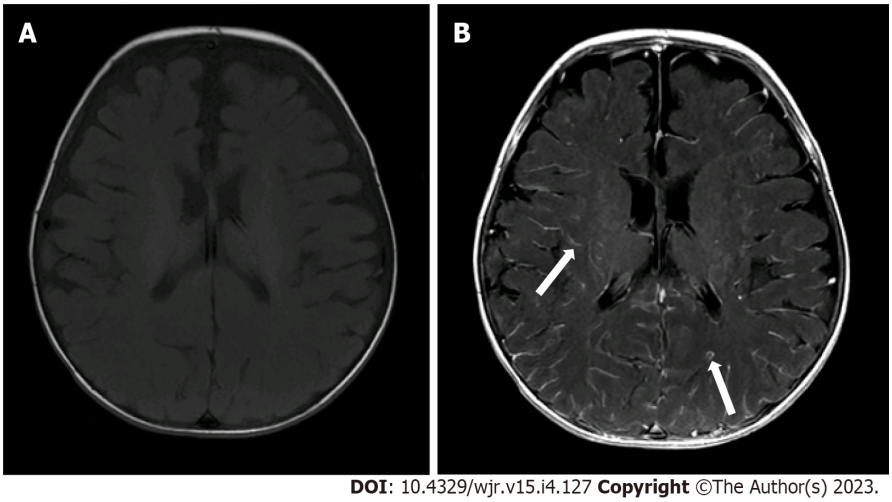
DISCUSSION

We used 3T MRI in our study because it is universally approved for imaging in pediatric patients[18]. All patients underwent SE labelling sequences, which are routinely recommended for pediatric imaging due to their quick acquisition time. MRI specifically has advantageous effects in pediatric neuroimaging due to its use of non-ionizing radiation.

The duration of sedation with sevoflurane did not appear to statistically correlate with the degree of pLMCE in our study. This is in contrast to previously published studies advocating that propofol typically results in changes in perfusion and vascular hemodynamics leading to an altered blood brain barrier and possibly pLMCE[11,13,19]. Propofol has been shown to reduce cerebral blood flow, whereas sevoflurane has been shown to reduce cerebral blood flow less than propofol. Propofol and sevoflurane

Table 3 Correlation between patient age, weight and duration of sedation with leptomeningeal contrast enhancement grade

Parameter	Spearman's rank coefficient, *P*	*P* value
Age	-0.41	0.011
Weight	-0.42	0.030
Duration of sedation	-0.18	0.142



DOI: 10.4329/wjr.v15.i4.127 **Copyright** ©The Author(s) 2023.

Figure 3 Severe pseudo leptomeningeal contrast enhancement in a 4-mo-old female with metabolic disorder (Grade 3). A: Axial spin echo T1-weighted imaging; B: Axial post-contrast spin echo T1-weighted imaging demonstrated thicker pseudo leptomeningeal contrast enhancement (arrows), appearing nearly nodular or parenchymal in some locations.

have been shown to reduce the metabolic rate of oxygen to a similar extent[20]. According to our literature search, no study has assessed the effect of sevoflurane sedation on pLMCE.

We found statistically significant, inverse, moderate correlations between the LMCE grade and patient age and weight. This indicates that the younger and smaller the child, the more immature the blood brain barrier, vasculature and dynamic perfusion changes leading to pLMCE[13,19]. We hypothesize that pLMCE represents prominent venous vasculature of the subarachnoid space in younger pediatric patients and is not true meningeal enhancement. Similar results were also obtained by McKinney *et al*[11], who also found pLMCE predominantly in SE sequences on 3T MRI using propofol. This indicates a similar mechanism of action by the two anesthetic agents. Radiologists should therefore be aware of this phenomenon and consider the patient's clinical history before labelling meningeal enhancement. This would ultimately avoid unnecessary investigations such as lumbar punctures, which are invasive and incur a financial burden on patients, especially in developing countries.

We evaluated precontrast and post-contrast FLAIR images to exclude true LMCE, which was not performed in previous studies[11,21]. No LMCE was identified on post-contrast FLAIR sequence in the 63 cases included in our study, indicating the absence of true meningeal disease and indirectly supporting pLMCE.

Our study has a few limitations of note. First, general limitations of retrospective studies apply to our study. The major limitation of the study was the use of supplemental oxygen (40%) and nitrous oxide (60%), which could not be modified due to the retrospective nature of the study. Therefore, the effect of these agents could not be separated from that of sevoflurane, making them crucial confounding factors. Sevoflurane as an anesthetic acts by vasodilation and maintains the tissue oxygen concentration in the brain. However, the tissue may suffer from hypoxia when the patient breaths room oxygen. By giving oxygen at a low concentration, such as 40%, the oxygen level is optimized and will not cause hyperoxic injury[22]. Nitrous oxide is also a vasodilator, which further helps in sustaining regional cerebral blood flow and regional cerebral blood volume when used in conjunction with sevoflurane[20]. We hypothesize that by keeping the concentrations of oxygen and nitrous oxide constant the effects of sevoflurane on vasodilation can be assessed.

Since we have included patients below 8 years of age, a control group undergoing MRI examination without anesthesia was not possible, since sedation cannot be avoided in this age group. We did not compare the sevoflurane-sedated pediatric patients with other groups of patients who underwent sedation with intravenous midazolam, chloral hydrate or propofol because of the limited number of these patients. There may be a difference in pLMCE or the degree of pLMCE between these groups;

however, this was not the objective of our study. We did not have a cohort of sedated patients that underwent MRI on a 1.5T MRI machine. Therefore the effect of magnetic strength on pLMCE could not be assessed. We also did not compare our results with juvenile or adolescent groups of pediatric patients who generally do not require anesthesia or sedation for their imaging. We could not determine the correlation of sevoflurane dose with pLMCE due to the retrospective nature of the study. These objectives can be explored in a future large scale prospective study with different cohorts of these patients.

CONCLUSION

The phenomenon of pLMCE is relatively common on post-contrast SE T1-weighted sequences of younger pediatric patients sedated by sevoflurane. However, these imaging results should not be misinterpreted for meningeal pathology. Our results showed that pLMCE may occur more frequently in younger and smaller pediatric patients due to their fragile and immature vasculature. However, further prospective studies are warranted to elucidate the exact relationship and evaluate any effect of magnetic strength and resolution on this finding.

ARTICLE HIGHLIGHTS

Research background

Prominent leptomeningeal contrast enhancement (LMCE) in the brain is seen in some pediatric patients during sedation for imaging. However, they are not acutely ill and do not exhibit meningeal signs. Our study determined whether inhaled sevoflurane anesthesia in pediatric patients led to pseudo LMCE (pLMCE) using 3 Tesla (3T) magnetic resonance imaging (MRI).

Research motivation

pLMCE on brain MRI in pediatric patients undergoing sedation with propofol has been studied. However, pLMCE due to sedation by sevoflurane (inhalation anesthetic) has not been studied so far. We therefore undertook this study in a small cohort of patients to establish our hypothesis.

Research objectives

The aim of this study was to highlight the significance of pLMCE in pediatric patients undergoing enhanced brain MRI under sedation to avoid misinterpretation in radiology reports.

Research methods

This was a retrospective cross-sectional study. Data analysis was performed by Statistical Package for Social Sciences version 20.0 software (IBM Corp.). Demographic data, such as age, were expressed as mean ± SD. The effect of age, weight and sex on LMCE was evaluated. The interobserver variability was calculated using Cohen's kappa statistic. The LMCE grade was correlated with the duration of sedation and patient age and weight using the Spearman rho rank correlation. Correlation coefficients $0.1 < P < 0.3$, $0.3 < P < 0.5$ and > 0.5 were used as indications of weak, moderate and substantial associations, respectively. $P < 0.05$ was considered statistically significant.

Research results

There was substantial agreement between the two radiologists in detection of pLMCE on post-contrast T1 imaging (kappa = 0.61; $P < 0.001$). Our results show that this pattern may occur in younger and smaller pediatric patients due to their fragile and immature vasculature. Additionally, we found statistically significant inverse and moderate correlations between patient weight and age with pLMCE grade but no correlation between pLMCE and duration of sedation.

Research conclusions

Results of our study revealed that this pattern of pLMCE is relatively common on post-contrast spin echo T1-weighted sequences of younger pediatric patients sedated by sevoflurane, on 3T MRI and should not be misinterpreted for meningeal pathology.

Research perspectives

Future prospective studies with a larger cohort and controls are warranted to elucidate the exact relationship and evaluate any effect of magnetic strength and resolution on this finding.

FOOTNOTES

Author contributions: Hilal K contributed to conceptualization, methodology, supervision, reviewing and editing; Khandwala K contributed to formal analysis and original draft preparation; Rashid S contributed to data curation, visualization and investigation; Khan F contributed to data curation and software; Anwar SSM contributed to reviewing and editing; all authors have participated in final editing of the drafts and have reviewed the final version of the paper.

Institutional review board statement: This study was approved by the Ethics Committee of Aga Khan University Hospital on April 22, 2020 (2020-3611-9104).

Informed consent statement: There was no direct patient contact and no intervention. It was just a retrospective review of files and images that is why the patient consent was waived by the ethical review committee.

Conflict-of-interest statement: All authors declare having no conflicts of interest with any related company, institution or individual.

Data sharing statement: The dataset may be provided by the corresponding author upon reasonable request.

Open-Access: This article is an open-access article that was selected by an in-house editor and fully peer-reviewed by external reviewers. It is distributed in accordance with the Creative Commons Attribution Noncommercial (CC BY-NC 4.0) license, which permits others to distribute, remix, adapt, build upon this work non-commercially, and license their derivative works on different terms, provided the original work is properly cited and the use is non-commercial. See: https://creativecommons.org/Licenses/by-nc/4.0/

Country/Territory of origin: Pakistan

ORCID number: Kiran Hilal 0000-0003-0737-3419; Kumail Khandwala 0000-0002-1730-8947; Saima Rashid 0000-0001-5630-2161; Faheemullah Khan 0000-0001-6369-743X; Shayan Sirat Maheen Anwar 0000-0003-0615-8661.

S-Editor: Ma YJ
L-Editor: A
P-Editor: Zhao S

REFERENCES

1 **Smirniotopoulos JG**, Murphy FM, Rushing EJ, Rees JH, Schroeder JW. Patterns of contrast enhancement in the brain and meninges. *Radiographics* 2007; **27**: 525-551 [PMID: 17374867 DOI: 10.1148/rg.272065155]
2 **Bhargava R**, Hahn G, Hirsch W, Kim MJ, Mentzel HJ, Olsen OE, Stokland E, Triulzi F, Vazquez E. Contrast-enhanced magnetic resonance imaging in pediatric patients: review and recommendations for current practice. *Magn Reson Insights* 2013; **6**: 95-111 [PMID: 25114547 DOI: 10.4137/MRI.S12561]
3 **Mongodi S**, Ottonello G, Viggiano R, Borrelli P, Orcesi S, Pichiecchio A, Balottin U, Mojoli F, Iotti GA. Ten-year experience with standardized non-operating room anesthesia with Sevoflurane for MRI in children affected by neuropsychiatric disorders. *BMC Anesthesiol* 2019; **19**: 235 [PMID: 31852450 DOI: 10.1186/s12871-019-0897-1]
4 **Malviya S**, Voepel-Lewis T, Eldevik OP, Rockwell DT, Wong JH, Tait AR. Sedation and general anaesthesia in children undergoing MRI and CT: adverse events and outcomes. *Br J Anaesth* 2000; **84**: 743-748 [PMID: 10895749 DOI: 10.1093/oxfordjournals.bja.a013586]
5 **Malviya S**, Voepel-Lewis T, Tait AR. Adverse events and risk factors associated with the sedation of children by nonanesthesiologists. *Anesth Analg* 1997; **85**: 1207-1213 [PMID: 9390581 DOI: 10.1097/00000539-199712000-00005]
6 **Lubisch N**, Roskos R, Berkenbosch JW. Dexmedetomidine for procedural sedation in children with autism and other behavior disorders. *Pediatr Neurol* 2009; **41**: 88-94 [PMID: 19589455 DOI: 10.1016/j.pediatrneurol.2009.02.006]
7 **Sury MR**, Harker H, Thomas ML. Sevoflurane sedation in infants undergoing MRI: a preliminary report. *Paediatr Anaesth* 2005; **15**: 16-22 [PMID: 15649158 DOI: 10.1111/j.1460-9592.2005.01456.x]
8 **Palanca BJA**, Avidan MS, Mashour GA. Human neural correlates of sevoflurane-induced unconsciousness. *Br J Anaesth* 2017; **119**: 573-582 [PMID: 29121298 DOI: 10.1093/bja/aex244]
9 **Aksenov DP**, Miller MJ, Dixon CJ, Wyrwicz AM. The effect of sevoflurane and isoflurane anesthesia on single unit and local field potentials. *Exp Brain Res* 2019; **237**: 1521-1529 [PMID: 30919011 DOI: 10.1007/s00221-019-05528-9]
10 **Stachnik J**. Inhaled anesthetic agents. *Am J Health Syst Pharm* 2006; **63**: 623-634 [PMID: 16554286 DOI: 10.2146/ajhp050460]
11 **McKinney AM**, Chacko Achanaril A, Knoll B, Nascene DR, Gawande RS. Pseudo-Leptomeningeal Contrast Enhancement at 3T in Pediatric Patients Sedated by Propofol. *AJNR Am J Neuroradiol* 2018; **39**: 1739-1744 [PMID: 30049717 DOI: 10.3174/ajnr.A5736]
12 **Machata AM**, Willschke H, Kabon B, Kettner SC, Marhofer P. Propofol-based sedation regimen for infants and children undergoing ambulatory magnetic resonance imaging. *Br J Anaesth* 2008; **101**: 239-243 [PMID: 18534971 DOI: 10.1093/bja/aen153]
13 **Szabó EZ**, Luginbuehl I, Bissonnette B. Impact of anesthetic agents on cerebrovascular physiology in children. *Paediatr*

Anaesth 2009; **19**: 108-118 [PMID: 19040505 DOI: 10.1111/j.1460-9592.2008.02826.x]

14 **Saunders DE**, Thompson C, Gunny R, Jones R, Cox T, Chong WK. Magnetic resonance imaging protocols for paediatric neuroradiology. *Pediatr Radiol* 2007; **37**: 789-797 [PMID: 17487479 DOI: 10.1007/s00247-007-0462-9]

15 **Serafini G**, Zadra N. Anaesthesia for MRI in the paediatric patient. *Curr Opin Anaesthesiol* 2008; **21**: 499-503 [PMID: 18660661 DOI: 10.1097/ACO.0b013e328304115b]

16 **Jung SM**. Drug selection for sedation and general anesthesia in children undergoing ambulatory magnetic resonance imaging. *Yeungnam Univ J Med* 2020; **37**: 159-168 [PMID: 32299181 DOI: 10.12701/yujm.2020.00171]

17 **Dietemann JL**, Correia Bernardo R, Bogorin A, Abu Eid M, Koob M, Nogueira T, Vargas MI, Fakhoury W, Zöllner G. [Normal and abnormal meningeal enhancement: MRI features]. *J Radiol* 2005; **86**: 1659-1683 [PMID: 16269979 DOI: 10.1016/s0221-0363(05)81507-0]

18 **Zimmerman RA**, Bilaniuk LT, Pollock AN, Feygin T, Zarnow D, Simon EM, Harris C. 3T Pediatric Brain Imaging. *Rivista di Neuroradiologia* 2006; **19**: 19-27 [DOI: 10.1177/197140090601900103]

19 **Harreld JH**, Helton KJ, Kaddoum RN, Reddick WE, Li Y, Glass JO, Sansgiri R, Ji Q, Feng T, Parish ME, Gajjar A, Patay Z. The effects of propofol on cerebral perfusion MRI in children. *Neuroradiology* 2013; **55**: 1049-1056 [PMID: 23673874 DOI: 10.1007/s00234-013-1187-0]

20 **Kaisti KK**, Långsjö JW, Aalto S, Oikonen V, Sipilä H, Teräs M, Hinkka S, Metsähonkala L, Scheinin H. Effects of sevoflurane, propofol, and adjunct nitrous oxide on regional cerebral blood flow, oxygen consumption, and blood volume in humans. *Anesthesiology* 2003; **99**: 603-613 [PMID: 12960544 DOI: 10.1097/00000542-200309000-00015]

21 **Ahmad A**, Azad S, Azad R. Differentiation of Leptomeningeal and Vascular Enhancement on Post-contrast FLAIR MRI Sequence: Role in Early Detection of Infectious Meningitis. *J Clin Diagn Res* 2015; **9**: TC08-TC12 [PMID: 25738054 DOI: 10.7860/JCDR/2015/11519.5387]

22 **Aksenov DP**, Dmitriev AV, Miller MJ, Wyrwicz AM, Linsenmeier RA. Brain tissue oxygen regulation in awake and anesthetized neonates. *Neuropharmacology* 2018; **135**: 368-375 [PMID: 29580952 DOI: 10.1016/j.neuropharm.2018.03.030]



Published by **Baishideng Publishing Group Inc**
7041 Koll Center Parkway, Suite 160, Pleasanton, CA 94566, USA
Telephone: +1-925-3991568
E-mail: bpgoffice@wjgnet.com
Help Desk: https://www.f6publishing.com/helpdesk
https://www.wjgnet.com



© 2023 Baishideng Publishing Group Inc. All rights reserved.

ISSN 1949-8470 (online)

World Journal of *Radiology*

World J Radiol 2023 May 28; 15(5): 136-156



Published by Baishideng Publishing Group Inc

WJR World Journal of Radiology

Contents

Monthly Volume 15 Number 5 May 28, 2023

MINIREVIEWS

136 Future of prostate imaging: Artificial intelligence in assessing prostatic magnetic resonance imaging

Chervenkov L, Sirakov N, Kostov G, Velikova T, Hadjidekov G

ORIGINAL ARTICLE

Retrospective Cohort Study

146 Chronic thromboembolic pulmonary hypertension is associated with a loss of total lung volume on computed tomography

Tsuchiya N, Xu YY, Ito J, Yamashiro T, Ikemiyagi H, Mummy D, Schiebler ML, Yonemoto K, Murayama S, Nishie A

World Journal of Radiology

Monthly Volume 15 Number 5 May 28, 2023

Contents

ABOUT COVER

Associate Editor of *World Journal of Radiology*, Mina S Makary, MD, Assistant Professor, Director, Department of Radiology, The Ohio State University Wexner Medical Center, Columbus, OH 43210, United States. mina.makary@osumc.edu

AIMS AND SCOPE

The primary aim of *World Journal of Radiology* (*WJR*, *World J Radiol*) is to provide scholars and readers from various fields of radiology with a platform to publish high-quality basic and clinical research articles and communicate their research findings online.

WJR mainly publishes articles reporting research results and findings obtained in the field of radiology and covering a wide range of topics including state of the art information on cardiopulmonary imaging, gastrointestinal imaging, genitourinary imaging, musculoskeletal imaging, neuroradiology/head and neck imaging, nuclear medicine and molecular imaging, pediatric imaging, vascular and interventional radiology, and women's imaging.

INDEXING/ABSTRACTING

The *WJR* is now abstracted and indexed in PubMed, PubMed Central, Emerging Sources Citation Index (Web of Science), Reference Citation Analysis, China National Knowledge Infrastructure, China Science and Technology Journal Database, and Superstar Journals Database. The 2022 edition of Journal Citation Reports ® cites the 2021 Journal Citation Indicator (JCI) for *WJR* as 0.48.

RESPONSIBLE EDITORS FOR THIS ISSUE

Production Editor: *Si Zhao*; **Production Department Director:** *Xu Guo*; **Editorial Office Director:** *Jia-Ping Yan*.

NAME OF JOURNAL
World Journal of Radiology

ISSN
ISSN 1949-8470 (online)

LAUNCH DATE
January 31, 2009

FREQUENCY
Monthly

EDITORS-IN-CHIEF
Thomas J Vogl

EDITORIAL BOARD MEMBERS
https://www.wjgnet.com/1949-8470/editorialboard.htm

PUBLICATION DATE
May 28, 2023

COPYRIGHT
© 2023 Baishideng Publishing Group Inc

INSTRUCTIONS TO AUTHORS
https://www.wjgnet.com/bpg/gerinfo/204

GUIDELINES FOR ETHICS DOCUMENTS
https://www.wjgnet.com/bpg/GerInfo/287

GUIDELINES FOR NON-NATIVE SPEAKERS OF ENGLISH
https://www.wjgnet.com/bpg/gerinfo/240

PUBLICATION ETHICS
https://www.wjgnet.com/bpg/GerInfo/288

PUBLICATION MISCONDUCT
https://www.wjgnet.com/bpg/gerinfo/208

ARTICLE PROCESSING CHARGE
https://www.wjgnet.com/bpg/gerinfo/242

STEPS FOR SUBMITTING MANUSCRIPTS
https://www.wjgnet.com/bpg/GerInfo/239

ONLINE SUBMISSION
https://www.f6publishing.com

© 2023 Baishideng Publishing Group Inc. All rights reserved. 7041 Koll Center Parkway, Suite 160, Pleasanton, CA 94566, USA
E-mail: bpgoffice@wjgnet.com https://www.wjgnet.com

World Journal of Radiology

Submit a Manuscript: https://www.f6publishing.com

World J Radiol 2023 May 28; 15(5): 136-145

DOI: 10.4329/wjr.v15.i5.136

ISSN 1949-8470 (online)

MINIREVIEWS

Future of prostate imaging: Artificial intelligence in assessing prostatic magnetic resonance imaging

Lyubomir Chervenkov, Nikolay Sirakov, Gancho Kostov, Tsvetelina Velikova, George Hadjidekov

Specialty type: Radiology, nuclear medicine and medical imaging

Provenance and peer review: Invited article; Externally peer reviewed.

Peer-review model: Single blind

Peer-review report's scientific quality classification

Grade A (Excellent): 0
Grade B (Very good): B, B
Grade C (Good): C, C
Grade D (Fair): D
Grade E (Poor): 0

P-Reviewer: Konovalov AB, Russia; Lei Y, China; Mijwil MM, Iraq

Received: December 19, 2022
Peer-review started: December 19, 2022
First decision: February 20, 2023
Revised: March 21, 2023
Accepted: April 10, 2023
Article in press: April 10, 2023
Published online: May 28, 2023

Lyubomir Chervenkov, Department of Diagnostic Imaging, Medical University Plovdiv, Plovdiv 4000, Bulgaria

Lyubomir Chervenkov, Nikolay Sirakov, Research Complex for Translational Neuroscience, Medical University of Plovdiv, Bul. Vasil Aprilov 15A, Plovdiv 4002, Bulgaria

Nikolay Sirakov, Department of Diagnostic Imaging, Dental Allergology and Physiotherapy, Faculty of Dental Medicine, Medical University Plovdiv, Plovdiv 4000, Bulgaria

Gancho Kostov, Department of Special Surgery, Medical University Plovdiv, Plovdiv 4000, Bulgaria

Tsvetelina Velikova, Department of Clinical Immunology, University Hospital Lozenetz, Sofia 1407, Bulgaria

Tsvetelina Velikova, Department of Medical Faculty, Sofia University St. Kliment Ohridski, Sofia 1407, Bulgaria

George Hadjidekov, Department of Radiology, University Hospital Lozenetz, Sofia 1407, Bulgaria

George Hadjidekov, Department of Physics, Biophysics and Radiology, Medical Faculty, Sofia University St. Kliment Ohridski, Sofia 1407, Bulgaria

Corresponding author: George Hadjidekov, MD, PhD, Associate Professor, Department of Radiology, University Hospital Lozenetz, 1 Kozyak Street, Sofia 1407, Bulgaria. jordiman76@yahoo.com

Abstract

Prostate cancer (Pca; adenocarcinoma) is one of the most common cancers in adult males and one of the leading causes of death in both men and women. The diagnosis of Pca requires substantial experience, and even then the lesions can be difficult to detect. Moreover, although the diagnostic approach for this disease has improved significantly with the advent of multiparametric magnetic resonance, that technology has certain unresolved limitations. In recent years artificial intelligence (AI) has been introduced to the field of radiology, providing new software solutions for prostate diagnostics. Precise mapping of the prostate has become possible through AI and this has greatly improved the accuracy of biopsy. AI has also allowed for certain suspicious lesions to be attributed to a given group according to the Prostate Imaging-Reporting & Data System classification. Finally,

AI has facilitated the combination of data obtained from clinical, laboratory (prostate-specific antigen), imaging (magnetic resonance), and biopsy examinations, and in this way new regularities can be found which at the moment remain hidden. Further evolution of AI in this field is inevitable and it is almost certain to significantly expand the efficacy, accuracy and efficiency of diagnosis and treatment of Pca.

Key Words: Artificial intelligence; Deep learning; Machine learning; Multiparametric magnetic resonance imaging; Prostate cancer; Quantitative imaging

©The Author(s) 2023. Published by Baishideng Publishing Group Inc. All rights reserved.

Core Tip: The peer reviewed literature has provided sufficient support for the continued application and development of artificial intelligence (AI) in prostate cancer clinical care. In addition, the expanding introduction of various AI-based software products created by leading companies is providing practical benefits to radiologists for improved prostate cancer diagnosis. Certainly, the known complexity of the disease and its consequential difficult diagnosis supports the continued development of new approaches for earlier and more accurate detection, such as could be provided through AI technologies.

Citation: Chervenkov L, Sirakov N, Kostov G, Velikova T, Hadjidekov G. Future of prostate imaging: Artificial intelligence in assessing prostatic magnetic resonance imaging. *World J Radiol* 2023; 15(5): 136-145
URL: https://www.wjgnet.com/1949-8470/full/v15/i5/136.htm
DOI: https://dx.doi.org/10.4329/wjr.v15.i5.136

INTRODUCTION

Prostate cancer (Pca; an adenocarcinoma) is one of the leading causes of death from oncological diseases, and it ranks second among adult males. Despite the high frequency of the disease, screening still largely relies on digital rectal examination, with low sensitivity and low specificity, and prostate-specific antigen (PSA) testing, with high sensitivity but low specificity. If the tests support a positive suspicion, a transrectal ultrasound (TRUS) biopsy is performed[1]. A Pca diagnosis is classified as either clinically significant, with the adenocarcinoma lesion requiring surgical treatment to curb the risk of metastasis, or non-significant, with follow-up recommended[2-4].

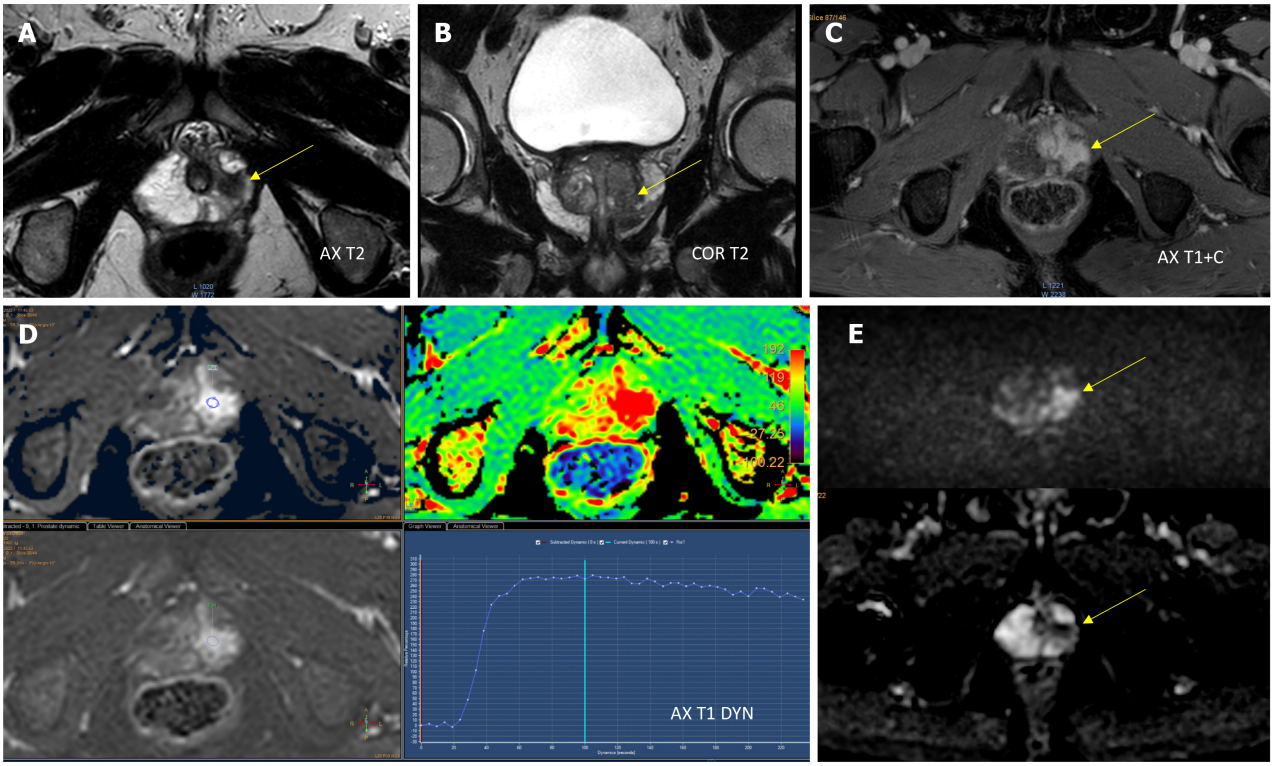
Multiparametric magnetic resonance imaging (mpMRI) is gaining ground as a primary method for Pca diagnosis. However, the diagnostic process requires a radiologist who has deep experiential knowledge with both the disease and the MRI technology[1-3,5]. The Prostate Imaging-Reporting & Data System (PI-RADS; introduced in 2012) and the 2.1 update (2019, with improved sensitivity and specificity) has begun to standardize the process by providing a classification system for findings detectable in Pca[6-8].

The mpMRI technology itself has opened up new opportunities for more accurate and earlier Pca detection (and diagnosis). It is specifically recommended for patients with elevated PSA levels but negative biopsy results and for biopsy-naïve patients who are being monitored for Pca due to risk factors (*e.g.*, age, family history, race). In addition, mpMRI is considered a safer alternative to the TRUS biopsy, as it avoids the complication risks related to the invasive biopsy procedure (*e.g.*, bleeding, infection, urinary hesitancy)[4].

Three-dimensional images of the prostate gland, including high-resolution T2-weighted image (WI), diffusion-weighted image (DWI) and dynamic contrast-enhanced (DCE) image, are obtained using mpMRI (Figure 1). The imaging findings are combined with the overall clinical profile to determine the level of risk for a clinically significant cancer, following the PI-RADS classification[4].

American and European guidelines differ from each other in their recommendations for the appropriate time of biopsy[9]. Gleason staging has proven to be an accurate approach, but it (as well as the PI-RADS) has significant limitations in diagnosis and quantification; for example, the PI-RADS system is known to risk provision of an underestimation of tumor size, especially in patients with a low PI-RADS score, while higher PI-RADS score is associated with Gleason score upgrade[10]. In addition, the inherent heterogeneity of Pca, known limitations of mpMRI, and possible biopsy inaccuracies can lead to inconsistencies in the overall assessment of the patient's condition.

Currently, the detection of a prostate carcinoma lesion depends to a large extent on the experience of the radiologist, and in some cases even experienced radiologists find it difficult to detect the lesion or to classify the detected lesion by PI-RADS. In addition, in many cases, hypertrophy of the prostate with age makes it impossible to accurately localize the lesion and consequently hinders the surgeon's ability to perform an accurate biopsy. It is also necessary to unify the description of a given lesion in relation to



DOI: 10.4329/wjr.v15.i5.136 **Copyright** ©The Author(s) 2023.

Figure 1 Apical peripheral zone with a Prostate Imaging-Reporting & Data System 5 lesion. A and B: Axial (A) and coronal (B) T2-weighted imaging (WI) revealed a homogeneous hypointense lesion in the anterior peripheral zone of the apex; C: Postcontrast axial T1WI showed pronounced enhancement of the lesion; D: Early dynamic contrast-enhanced imaging showed positive enhancement within the lesion and provided a wash-out signal intensity curve; E: Diffusion weighted imaging (DWI) and apparent diffusion coefficient (ADC) diffusion restriction [DWI (b = 1000 s/mm^2)] provided a marked hyperintense signal above the background, while the ADC map image showed a lesion with hypointense signal below the background.

generally accepted templates. Fortunately, all these limitations can be overcome by the modern software technologies based on artificial intelligence (AI)[11].

CHALLENGES IN ASSESSING PROSTATIC MRI

The Pca detection process has its weaknesses at present. Indeed, prostate carcinoma lesions are often confused with prostatitis, benign nodules, or hemorrhagic nodules, especially in the transitional zone. This often results in unnecessary biopsies[12]. Another pitfall involves the histological assessment of the biopsied lesion, with inaccuracies resulting in dangerous false-negative findings or incorrect staging[13].

AI has been applied to various diseases in the fields of imaging diagnostics and pathological profiling, most often increasing the efficiency in evaluating results. Especially as with mpMRI, different AI-based solutions have been found to allow for accurate segmentation of the prostate as well as an accurate characterization of the tumors[14]. In the field of pathology, an improvement in diagnostics has also been observed. As with any disease that is managed clinically, a radiological-pathological correlation is required, and this presents an existing lacuna that AI can fill, and certainly biomarker data will play a role as well. Increased knowledge of the pathological mechanism, as can be supported by application of AI, is a crucial component to multidisciplinary clinical care (*i.e.* collaborative care teams of radiologists, pathologists, and urologists for Pca patients). Overall, this process of incorporating AI into any disease diagnosis will also aid in the discovery of hitherto hidden relationships between different pathology-related biomarkers[15,16].

AI IN MEDICINE

AI is a computer system that performs actions similar to human intelligence. In radiology, AI has developed rapidly in recent years due to the ability of the cutting-edge technology to automatically extract information. Machine learning a subfield of AI is an algorithm that is trained for specific tasks without human intervention, which means that computers can be trained from certain examinations that have been previously described by a radiologist according to their didactic knowledge and practical

experience. As more research data, including that involving AI, accumulates, the effectiveness of software increases. Human validation is still required, after which calibration is performed, resulting in better sensitivity and specificity of the novel/improved software. A subtype of machine learning is convolutional neural networks, where different systems interact with one another[17]. Of note, this type of system is the most frequently used in the development of AI[18].

AI has already shown great benefit in improving the detection, characterization, staging and participation in adequately treating Pca. Accurate prostate segmentation is particularly important when performing mpMRI, which without AI is relatively conditional on the perceptions of individual specialists. AI can be involved in the primary detection and staging of prostate carcinoma lesions relative to the PI-RADS system. A study by Cuocolo *et al*[14] published in 2021 investigated the characterization of human *vs* AI findings and demonstrated the benefit of the latter. In addition, AI can optimize the exact site for biopsy, as well as create a three-dimensional model to accurately represent the location of the tumor and its relationship to neighboring organs, improving preoperative preparation. Still other publications from recent years have shown regularity between the findings in T2, the changes in DWI, and the density of tissue composition, allowing for the creation of radiopathological maps[19-21].

AI has already proven its utility in other fields of medicine. For example, machine learning has been used in patients with appendicitis, emerging as a tool to predict whether the disease is acute or subacute; specifically, AI showed accurately predicted result in 83.75% of the cases, precision of 84.11%, sensitivity of 81.08%, and specificity of 81.01%[22]. In general, the ever-increasing role of precision medicine, the anticipated future improvements of machine learning and deep learning, and the ongoing expansion of robotics and radiomics are likely to facilitate the robust development of reproducible MRI-based prostatic diagnostics[23].

AI CHALLENGES

The greatest challenge to establishing AI in medical practice, at the moment, is the need for large volumes of data to be integrated into the AI systems. From a practical standpoint, this necessitates a large volume of time and effort from already-taxed radiologists with expertise in prostate imaging. Another challenge is that the collected data originate from different MRI devices made by various manufacturers with varying field strengths, and from studies performed using varying protocols. Ultimately, this means that studies should be grouped according to these varying features. Considering this issue, a study by Gaur *et al*[24] has shown the AI can not only reduce the time of interpretation of MRI findings from various machines but also improve the sensitivity (from 78% to 83.8% specifically), especially when radiologists with less experience in the field were using the technologies.

CURRENT AI PRODUCTS AVAILABLE

The diagnosis of Pca involves initial detection and accurate classification of the lesion(s) finding, and it is to these processes that software companies have directed their focus. AI systems are "trained" to detect cancer by inputting voluminous data from leading experts. Several groups are reporting various AI models for prostate segmentation, intraprostatic lesion detection and classification tasks with auspicious results[25].

Improvements are being sought in the detection of prostate carcinoma lesions that are invisible to human perception, thereby increasing early diagnosis[26-29]. In Table 1, the current AI products in the prostate field are summarized[30].

"AI-Rad companion prostate MR" by Siemens Medical Solutions (Malvern, PA, United States) aids the fusion between MRI and ultrasound. Performing an ultrasound-guided biopsy alone carries risks such as hemorrhage, infection, and abscessation. Furthermore, the procedure may not provide an answer to the presence of carcinoma in a given patient if performed solely, without previous physical examination and application of other imaging modalities. At the same time, performing an mpMRI scan cannot provide a histological diagnosis. The modern model of Pca diagnosis includes an ultrasound examination in combination with a previously performed MR scan. The lesions found on the MR scan are described by a radiologist, after which the images are superimposed on the ultrasound machine and a fusion between the two methods is achieved. AI in this case assists the biopsy by applying automated segmentation of the prostate, thus saving time and increasing accuracy of the biopsy. The collaboration between the urologist and the radiologist is also improved, as it allows for additional targeting of the lesions detected by MR[31].

Another Siemens product is the “Prostate MR” tool (Siemens Healthineers, Cary, NC, United States), which is available on the syngo.via workstation and is an AI that supports the evaluation of images obtained during a mpMRI scan. Analysis time needed for the AI is extremely short – between 3 sec and 10 sec. Prostate MR supports the primary detection and classification of findings, and offers description according to pre-entered standardized report templates. The use of this type of software is extremely

Table 1 Current artificial intelligence products available in the prostate imaging field

Vendor	Product name	FDA approval class	CE approval class	Main features in prostate imaging
Siemens Healthineers	AI-Rad Companion Prostate MR	II	IIb - MDR	Segmentation, volume assessment, lesion annotation, PSA density
Quantib	Quantib® Prostate	II	IIb - MDR	Volume assessment, PSA density, segmentation, PI-RADS scoring, report structure
Quibim	QP-Prostate	II	IIb - MDR	ADC, K^{trans}, parametric maps obtainment, volume assessment, segmentation, report structure
Quibim	Perfusion pharmacokinetics modeling	N/A	IIa - MDD	K^{trans} map, volume assessment, contrast enhancement assistance
Quibim	Texture analysis	N/A	IIa - MDD	Quantification, radiomics, imaging biomarker discovery
Quibim	T2 mapping (relaxometry)	N/A	IIa - MDD	T2 values, T2 histogram
Siemens Healthineers	Prostate MR on syngo.via	N/A	IIa - MDD	Segmentation, volume assessment, lesion assessment, PI-RADS scoring
JLK Inc.	JPC-01K	N/A	I - MDD	Lesion detection
Lucida Medical	Prostate Intelligence™	N/A	I - MDD	Segmentation, lesion characterization, PI-RADS scoring, report structure
Quibim	DWI - ADC	N/A	IIa - MDD	Volume assessment, ADC support, histogram
Quibim	DWI - IVIM	N/A	IIa - MDD	ADC support, multiparametric maps, perfusion assessment

ADC: Apparent diffusion coefficient; AI: Artificial intelligence; CE: Single Market in the European economic area; DWI: Diffusion weighted imaging; FDA: Food and Drug Administration; IVIM: Intravoxel incoherent motion; JPC-01K: An artificial intelligence-based prostate cancer detection solution; K^{trans}: Volume transfer constant; MDD: Medical Devices Directive; MDR: Medical device regulation; MR: Magnetic resonance; N/A: Not applicable; PI-RADS: Prostate Imaging-Reporting & Data System; PSA: Prostate-specific antigen.

valuable for training radiologists without experience in prostate diagnostics. Indeed, it has been reported that the software application leads to a reduction of false-positive results[32].

With the advent of mpMRI, the total number of examinations performed has increased significantly worldwide[33]. Radiologists today have to interpret multiple MRI scans of the prostate, but this requires great expertise in this challenging field. New guidelines from the European Association of Urology and the American Association of Radiology suggest that an MRI be performed before any biopsy is undertaken, and currently the number of prostate biopsies in the United States and Europe alone is over 3 million[33]. Eventual involvement of AI in the interpretation algorithm may improve the detection rate, accurate localization and risk stratification of patients with suspected Pca. "Quantib® Prostate" software (Quantib, Rotterdam, Netherlands) offers fast and automated segmentation of the prostate and detection of findings on the most used mpMRI sequences [T2WI, apparent diffusion coefficient (ADC), DWI, DCE]. The software also provides assistance in the PI-RADS classification of a discovery. Finally, with the help of the software, a standardized report can be written based on pre-created templates, thereby saving time and improving the quality of the report.

DCE perfusion imaging identifies tumors according to their vessel characteristics. The Pharmacokinetic Model used in Quantib® Prostate helps detect neoplasms and quantifies tumor neoangiogenesis to stage cancer aggressiveness. This suite supports the characterization of tumoral processes in the early detection, diagnosis, treatment response evaluation and follow-up of patients with cancer. The software assesses the characteristics of the tissues, provides T2WI mapping, and depicts the changes according to segmentation. The information obtained allows for the assessment and monitoring of solid tumors, such as prostate, rectal, and liver lesions[31].

"JPC-01K" (JLK Inc., Seoul, Korea) is a neural network-based software used to characterize tumors on mpMRI. This software aims to reduce the time needed to evaluate the prostate examination findings and assist in the description of such by providing quantitative analysis. It also aims to overcome the difficulties in image analysis, which are largely dependent on the radiologist and his/her qualifications and experience. The system uses mpMR images, T2WI, DWI, and DCE as input and visualizes the location of prostate carcinoma lesions and related probabilities. According to a study carried out in one center, the accuracy of the method was 99.65%, with a time required for analysis of only 2 min. The AI at this manufacturer undergoes constant improvement through the addition of new data from leading experts.

"Prostate Intelligence™" (Lucida Medical, Cambridge, United Kingdom) is AI-based software that allows prostate tumor detection on MR images. It is intended to augment a radiologist's interpretation of prostate MRI by providing a risk score and prostate segmentation, and aiding in lesion identification and segmentation. The processing time for this software is between 1 sec and 10 sec. The DWI algorithm by Quibim (Valencia, Spain) calculates the ADC. The suite provides information on the cellular and microstructural organization of tissues and highlights the relationship between pathological changes and the diffusion of water molecules. In addition, this suite aims to characterize tumoral processes to support early detection, diagnosis, treatment response evaluation and follow-up of patients.

The DWI algorithm by Quibim is also used to analyze the microstructure changes according to intravoxel incoherent motion. The tool allows for the differentiation of pure diffusion changes due to variations in the vascular component and offers additional information complementary to conventional ADC results. This suite aims to characterize tumoral processes to support early detection, diagnosis, treatment response evaluation and follow-up of patients[31].

For timely detection, accurate diagnosis and proper treatment of the patient, we offer the algorithm presented in Figure 2.

OPPORTUNITIES

Creating teams of radiologists and pathologists to jointly decide on the most accurate diagnosis and most effective and efficient treatment methods of patients with Pca would create a more efficient approach to clinical management of the disease to achieve the most successful outcome. With the help of AI, specialists from both fields can join forces, especially when making decisions about suspicious lesions classified as PI-RADS 3. It is possible to bring together in one system all critical components disease history, PSA levels, findings from imaging studies, genetic tests, laboratory tests, physical and histological exams, and treatment(s) performed. AI can facilitate the ability to analyze all these components and compare them to databases for risk stratification and better predictability[34,35].

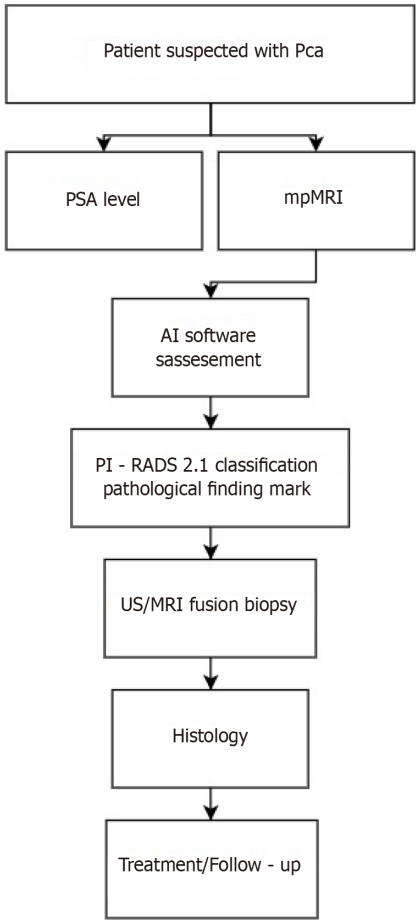
Positron emission tomography/computed tomography

Unlike most other carcinomas, the application of 18F-fludeoxyglucose (FDG) in positron emission tomography/computed tomography (PET/CT) is limited for Pca, due to the low or missing glucose consumption that is typically presented by prostate carcinoma lesions. Thus, the use of specific targeting is required. Until recently, choline was considered a promising marker (since choline uptake/concentration is high in prostatic carcinoma lesion cells). While this radioactive indicator was originally used for staging of high-risk patients as well as re-staging after biochemical relapse, its low sensitivity led to its largely being abandoned. Other markers such as 11C-acetate, 18F-oorocyclobutan-1-carboxylic acid and 18F-uciclovire have been tested but have failed to meet expectations, presenting the same characteristics as choline and low sensitivity.

The prostate-specific membrane antigen (PSMA) currently dominates all other markers in PET scans for Pca. PSMA, also known as glutamate carboxypeptidase II, is a transmembrane glycoprotein, highly expressed in prostatic carcinoma lesion cells. PSMA expression tends to increase as Gleason score increases. So far, several ^{68}gallium (^{68}GA)-labeled ligands have been designed to target PSMA; these include PSMA-11 (known as Hbed-Cc or Hbed-PSMA), PSMA-I & T, and PSMA-617. Therefore, a ^{68}germanium (GE)/^{68}GA generator with T1/2WI of 271 d is widely used (Figure 3). However, with cyclotron access, PSMA-1007 looks like a substantial breakthrough as it shows an advantage over ^{68}GA-labeled PSMA markers.

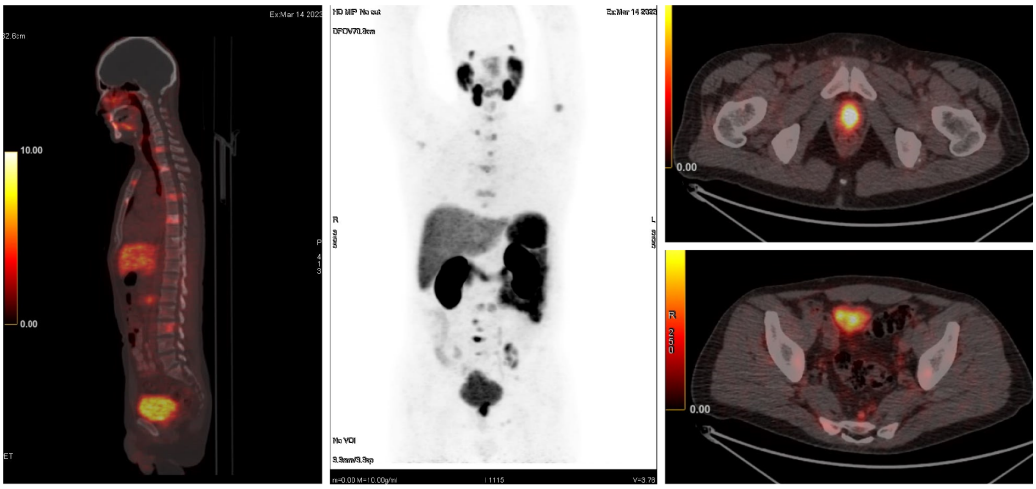
Multiple studies have shown that PET/CT with PSMA has a moderate sensitivity but a very high specificity for detecting metastases in lymph nodes and other organs. If the primary Pca shows PSMA expression, then a PSMA+ and PSMA- finding will be characterized as a secondary lesion or will be treated accordingly as a minor/benign lesion in the fragment imaging, although with the caveat of having high negative prognostic value. Due to the high monetary cost of PSMA studies, careful selection of patients suitable for examination is required. The mpMRI is superior for local assessment of the disease, and PSMA PET/MRI has an advantage in whole-body scanning. However, several restrictions are noted for patients suffering from Pca. For one, PET cameras are not always available and are missing in some of the nuclear medicine departments, especially in remote regions, for various logistical reasons. Another limitation is based in the fact that PSMA is not currently included in international guidelines. Lastly, although the utility of PSMA PET/CT in diagnosis of Pca is indisputable (outperforming diagnostics based solely on PSA, CT, and TRUS biopsy[36-40]) its role in monitoring of the disease remains unresolved.

Currently, only the "Pylarify AI™" software (Lantheus, Billerica, MA, United States) is legalized for support in PSMA PET/CT examinations, according to its demonstrated quantitative and accurate reporting. The AI software allows automated analysis of the CT examination's findings and allowing for targeting of the hotspots[41,42].



DOI: 10.4329/wjr.v15.i5.136 **Copyright** ©The Author(s) 2023.

Figure 2 Prostate cancer diagnosis algorithm. AI: Artificial intelligence; mpMRI: Multiparametric magnetic resonance imaging; MRI: Magnetic resonance imaging; Pca: Prostate cancer; PI-RADS: Prostate Imaging-Reporting & Data System; PSA: Prostate-specific antigen; US: Ultrasound.



DOI: 10.4329/wjr.v15.i5.136 **Copyright** ©The Author(s) 2023.

Figure 3 ^{68}GA prostate-specific membrane antigen positron emission tomography-computed tomographic images for a patient with prostate cancer (adenocarcinoma). The imaging revealed a primary tumor and diffuse lymph node metastatic spread as well as multiple spinal metastases.

CONCLUSION

The increased incidence of Pca in recent years and the improvement of MRI technologies have led to an increase in the number of the examinations performed on patients for diagnosis of the disease. The larger volume of data that has resulted, combined with the insufficient number and/or insufficiently trained personnel, has unfortunately complicated the clinical process and management of these patients.

AI is a powerful modern tool that offers benefits of time reduction and improved quality and accuracy of interpretation of prostatic carcinoma lesion findings according to the unified PI-RADS system. AI application to the field of radiological imaging may revolutionize the approach to Pca patients. However, there is still a long way to go until we are able to fully calibrate the individual components of the new AI-based software solutions and carry out accurate and thorough studies in this arena to gain a comprehensive understanding of the pathology of the disease and clinical care benefits of this powerful tool.

ACKNOWLEDGEMENTS

The authors are grateful for the support provided by NextGenerationEU.

FOOTNOTES

Author contributions: Chervenkov L, Velikova T and Hadjidekov G conceptualized the study; Chervenkov L, Sirakov N and Kostov G designed the methodology; Chervenkov L performed the data curation; Chervenkov L prepared the original draft of the manuscript; Velikova T and Hadjidekov G reviewed and edited the manuscript for intellectual content; All authors contributed to manuscript revision and provided approval of the final version of the manuscript to be published.

Supported by the European Union's NextGenerationEU, through the National Recovery and Resilience Plan of the Republic of Bulgaria, Project No. BG-RRP-2.004-0008-C01.

Conflict-of-interest statement: All the authors report having no relevant conflicts of interest for this article.

Open-Access: This article is an open-access article that was selected by an in-house editor and fully peer-reviewed by external reviewers. It is distributed in accordance with the Creative Commons Attribution NonCommercial (CC BY-NC 4.0) license, which permits others to distribute, remix, adapt, build upon this work non-commercially, and license their derivative works on different terms, provided the original work is properly cited and the use is non-commercial. See: https://creativecommons.org/Licenses/by-nc/4.0/

Country/Territory of origin: Bulgaria

ORCID number: Lyubomir Chervenkov 0000-0002-8380-5992; Nikolay Sirakov 0000-0002-2791-959X; Gancho Kostov 0000-0001-5137-6903; Tsvetelina Velikova 0000-0002-0593-1272; George Hadjidekov 0000-0001-6917-9887.

Corresponding Author's Membership in Professional Societies: European Society of Radiology (ESR); Bulgarian Association of Radiology (BAR); European Society of Uroradiology (ESUR); European Society of Gastroabdominal Radiology (ESGAR).

S-Editor: Liu XF
L-Editor: Filipodia
P-Editor: Zhao S

REFERENCES

1 **Ferlay J**, Colombet M, Soerjomataram I, Mathers C, Parkin DM, Piñeros M, Znaor A, Bray F. Estimating the global cancer incidence and mortality in 2018: GLOBOCAN sources and methods. *Int J Cancer* 2019; **144**: 1941-1953 [PMID: 30350310 DOI: 10.1002/ijc.31937]
2 **Fenton JJ**, Weyrich MS, Durbin S, Liu Y, Bang H, Melnikow J. Prostate-Specific Antigen-Based Screening for Prostate Cancer: Evidence Report and Systematic Review for the US Preventive Services Task Force. *JAMA* 2018; **319**: 1914-1931 [PMID: 29801018 DOI: 10.1001/jama.2018.3712]
3 **Hayes JH**, Barry MJ. Screening for prostate cancer with the prostate-specific antigen test: a review of current evidence. *JAMA* 2014; **311**: 1143-1149 [PMID: 24643604 DOI: 10.1001/jama.2014.2085]
4 **Doykov M**, Chervenkov, L. , Tsvetkova-Trichkova, S., Doykova, K., Georgiev, A. Assessment of the Utility of Multiparametric Magnetic Resonance Imaging for Initial Detection of Prostate Cancer. *Macedonian Journal of Medical Sciences* 2022; **10**: 1840-1845 [DOI: 10.3889/oamjms.2022.10401]
5 **Barbieri CE**, Bangma CH, Bjartell A, Catto JW, Culig Z, Grönberg H, Luo J, Visakorpi T, Rubin MA. The mutational landscape of prostate cancer. *Eur Urol* 2013; **64**: 567-576 [PMID: 23759327 DOI: 10.1016/j.eururo.2013.05.029]
6 **Rosenkrantz AB**, Ayoola A, Hoffman D, Khasgiwala A, Prabhu V, Smereka P, Somberg M, Taneja SS. The Learning Curve in Prostate MRI Interpretation: Self-Directed Learning Versus Continual Reader Feedback. *AJR Am J Roentgenol* 2017; **208**: W92-W100 [PMID: 28026201 DOI: 10.2214/AJR.16.16876]
7 **Turkbey B**, Rosenkrantz AB, Haider MA, Padhani AR, Villeirs G, Macura KJ, Tempany CM, Choyke PL, Cornud F,

Margolis DJ, Thoeny HC, Verma S, Barentsz J, Weinreb JC. Prostate Imaging Reporting and Data System Version 2.1: 2019 Update of Prostate Imaging Reporting and Data System Version 2. *Eur Urol* 2019; **76**: 340-351 [PMID: 30898406 DOI: 10.1016/j.eururo.2019.02.033]

8 **Georgiev A**, Chervenkov L, Doykov M, Doykova K, Uchikov P, Tsvetkova S. Surveillance Value of Apparent Diffusion Coefficient Maps: Multiparametric MRI in Active Surveillance of Prostate Cancer. *Cancers (Basel)* 2023; **15** [PMID: 36831471 DOI: 10.3390/cancers15041128]

9 **Schoots IG**, Padhani AR. Delivering Clinical impacts of the MRI diagnostic pathway in prostate cancer diagnosis. *Abdom Radiol (NY)* 2020; **45**: 4012-4022 [PMID: 32356003 DOI: 10.1007/s00261-020-02547-x]

10 **Pooli A**, Johnson DC, Shirk J, Markovic D, Sadun TY, Sisk AE Jr, Mohammadian Bajgiran A, Afshari Mirak S, Felker ER, Hughes AK, Raman SS, Reiter RE. Predicting Pathological Tumor Size in Prostate Cancer Based on Multiparametric Prostate Magnetic Resonance Imaging and Preoperative Findings. *J Urol* 2021; **205**: 444-451 [PMID: 33026934 DOI: 10.1097/JU.0000000000001389]

11 **Aggarwal K**. Machine Learning, and Deep Learning. *Iraqi Journal for Computer Science and Mathematics* 2022; **3**: 115-123 [DOI: 10.52866/ijcsm.2022.01.01.013]

12 **Loeb S**, Vellekoop A, Ahmed HU, Catto J, Emberton M, Nam R, Rosario DJ, Scattoni V, Lotan Y. Systematic review of complications of prostate biopsy. *Eur Urol* 2013; **64**: 876-892 [PMID: 23787356 DOI: 10.1016/j.eururo.2013.05.049]

13 **Etzioni R**, Penson DF, Legler JM, di Tommaso D, Boer R, Gann PH, Feuer EJ. Overdiagnosis due to prostate-specific antigen screening: lessons from U.S. prostate cancer incidence trends. *J Natl Cancer Inst* 2002; **94**: 981-990 [PMID: 12096083 DOI: 10.1093/jnci/94.13.981]

14 **Cuocolo R**, Cipullo MB, Stanzione A, Romeo V, Green R, Cantoni V, Ponsiglione A, Ugga L, Imbriaco M. Machine learning for the identification of clinically significant prostate cancer on MRI: a meta-analysis. *Eur Radiol* 2020; **30**: 6877-6887 [PMID: 32607629 DOI: 10.1007/s00330-020-07027-w]

15 **Goldenberg SL**, Nir G, Salcudean SE. A new era: artificial intelligence and machine learning in prostate cancer. *Nat Rev Urol* 2019; **16**: 391-403 [PMID: 31092914 DOI: 10.1038/s41585-019-0193-3]

16 **Raciti P**, Sue J, Ceballos R, Godrich R, Kunz JD, Kapur S, Reuter V, Grady L, Kanan C, Klimstra DS, Fuchs TJ. Novel artificial intelligence system increases the detection of prostate cancer in whole slide images of core needle biopsies. *Mod Pathol* 2020; **33**: 2058-2066 [PMID: 32393768 DOI: 10.1038/s41379-020-0551-y]

17 **Park SH**, Han K. Methodologic Guide for Evaluating Clinical Performance and Effect of Artificial Intelligence Technology for Medical Diagnosis and Prediction. *Radiology* 2018; **286**: 800-809 [PMID: 29309734 DOI: 10.1148/radiol.2017171920]

18 **Yilmaz EC**, Belue MJ, Turkbey B, Reinhold C, Choyke PL. A Brief Review of Artificial Intelligence in Genitourinary Oncological Imaging. *Can Assoc Radiol J* 2022; 8465371221135782 [PMID: 36515576 DOI: 10.1177/08465371221135782]

19 **McGarry SD**, Hurrell SL, Iczkowski KA, Hall W, Kaczmarowski AL, Banerjee A, Keuter T, Jacobsohn K, Bukowy JD, Nevalainen MT, Hohenwalter MD, See WA, LaViolette PS. Radio-pathomic Maps of Epithelium and Lumen Density Predict the Location of High-Grade Prostate Cancer. *Int J Radiat Oncol Biol Phys* 2018; **101**: 1179-1187 [PMID: 29908785 DOI: 10.1016/j.ijrobp.2018.04.044]

20 **Chatterjee A**, Bourne RM, Wang S, Devaraj A, Gallan AJ, Antic T, Karczmar GS, Oto A. Diagnosis of Prostate Cancer with Noninvasive Estimation of Prostate Tissue Composition by Using Hybrid Multidimensional MR Imaging: A Feasibility Study. *Radiology* 2018; **287**: 864-873 [PMID: 29393821 DOI: 10.1148/radiol.2018171130]

21 **Chatterjee A**, Watson G, Myint E, Sved P, McEntee M, Bourne R. Changes in Epithelium, Stroma, and Lumen Space Correlate More Strongly with Gleason Pattern and Are Stronger Predictors of Prostate ADC Changes than Cellularity Metrics. *Radiology* 2015; **277**: 751-762 [PMID: 26110669 DOI: 10.1148/radiol.2015142414]

22 **Mijwil MM**, Aggarwal K. A diagnostic testing for people with appendicitis using machine learning techniques. *Multimed Tools Appl* 2022; **81**: 7011-7023 [PMID: 35095329 DOI: 10.1007/s11042-022-11939-8]

23 **Hamm CA**, Beetz NL, Savic LJ, Penzkofer T. [Artificial intelligence and radiomics in MRI-based prostate diagnostics]. *Radiologe* 2020; **60**: 48-55 [PMID: 31802148 DOI: 10.1007/s00117-019-00613-0]

24 **Gaur S**, Lay N, Harmon SA, Doddakashi S, Mehralivand S, Argun B, Barrett T, Bednarova S, Girometti R, Karaarslan E, Kural AR, Oto A, Purysko AS, Antic T, Magi-Galluzzi C, Saglican Y, Sioletic S, Warren AY, Bittencourt L, Fütterer JJ, Gupta RT, Kabakus I, Law YM, Margolis DJ, Shebel H, Westphalen AC, Wood BJ, Pinto PA, Shih JH, Choyke PL, Summers RM, Turkbey B. Can computer-aided diagnosis assist in the identification of prostate cancer on prostate MRI? a multi-center, multi-reader investigation. *Oncotarget* 2018; **9**: 33804-33817 [PMID: 30333911 DOI: 10.18632/oncotarget.26100]

25 **Belue MJ**, Turkbey B. Tasks for artificial intelligence in prostate MRI. *Eur Radiol Exp* 2022; **6**: 33 [PMID: 35908102 DOI: 10.1186/s41747-022-00287-9]

26 **Winkel DJ**, Wetterauer C, Matthias MO, Lou B, Shi B, Kamen A, Comaniciu D, Seifert HH, Rentsch CA, Boll DT. Autonomous Detection and Classification of PI-RADS Lesions in an MRI Screening Population Incorporating Multicenter-Labeled Deep Learning and Biparametric Imaging: Proof of Concept. *Diagnostics (Basel)* 2020; **10** [PMID: 33202680 DOI: 10.3390/diagnostics10110951]

27 **Aldoj N**, Lukas S, Dewey M, Penzkofer T. Semi-automatic classification of prostate cancer on multi-parametric MR imaging using a multi-channel 3D convolutional neural network. *Eur Radiol* 2020; **30**: 1243-1253 [PMID: 31468158 DOI: 10.1007/s00330-019-06417-z]

28 **Mehralivand S**, Yang D, Harmon SA, Xu D, Xu Z, Roth H, Masoudi S, Sanford TH, Kesani D, Lay NS, Merino MJ, Wood BJ, Pinto PA, Choyke PL, Turkbey B. A Cascaded Deep Learning-Based Artificial Intelligence Algorithm for Automated Lesion Detection and Classification on Biparametric Prostate Magnetic Resonance Imaging. *Acad Radiol* 2022; **29**: 1159-1168 [PMID: 34598869 DOI: 10.1016/j.acra.2021.08.019]

29 **Winkel DJ**, Tong A, Lou B, Kamen A, Comaniciu D, Disselhorst JA, Rodríguez-Ruiz A, Huisman H, Szolar D, Shabunin I, Choi MH, Xing P, Penzkofer T, Grimm R, von Busch H, Boll DT. A Novel Deep Learning Based Computer-Aided Diagnosis System Improves the Accuracy and Efficiency of Radiologists in Reading Biparametric Magnetic Resonance

Images of the Prostate: Results of a Multireader, Multicase Study. *Invest Radiol* 2021; **56**: 605-613 [PMID: 33787537 DOI: 10.1097/RLI.0000000000000780]

30 **Greer MD**, Shih JH, Lay N, Barrett T, Bittencourt L, Borofsky S, Kabakus I, Law YM, Marko J, Shebel H, Merino MJ, Wood BJ, Pinto PA, Summers RM, Choyke PL, Turkbey B. Interreader Variability of Prostate Imaging Reporting and Data System Version 2 in Detecting and Assessing Prostate Cancer Lesions at Prostate MRI. *AJR Am J Roentgenol* 2019; **212**: 1197-1205 [PMID: 30917023 DOI: 10.2214/AJR.18.20536]

31 **Strohm L**, Hehakaya C, Ranschaert ER, Boon WPC, Moors EHM. Implementation of artificial intelligence (AI) applications in radiology: hindering and facilitating factors. *Eur Radiol* 2020; **30**: 5525-5532 [PMID: 32458173 DOI: 10.1007/s00330-020-06946-y]

32 **Yu X**. False Positive Reduction Using Multiscale Contextual Features for Prostate Cancer Detection in Multi-Parametric MRI Scans. *IEEE 17th International Symposium on Biomedical Imaging (ISBI)* 2020; 1355-1359 [DOI: 10.1109/ISBI45749.2020.9098338]

33 **Mottet N**, van den Bergh RCN, Briers E, Van den Broeck T, Cumberbatch MG, De Santis M, Fanti S, Fossati N, Gandaglia G, Gillessen S, Grivas N, Grummet J, Henry AM, van der Kwast TH, Lam TB, Lardas M, Liew M, Mason MD, Moris L, Oprea-Lager DE, van der Poel HG, Rouvière O, Schoots IG, Tilki D, Wiegel T, Willemse PM, Cornford P. EAU-EANM-ESTRO-ESUR-SIOG Guidelines on Prostate Cancer-2020 Update. Part 1: Screening, Diagnosis, and Local Treatment with Curative Intent. *Eur Urol* 2021; **79**: 243-262 [PMID: 33172724 DOI: 10.1016/j.eururo.2020.09.042]

34 **van Wijk Y**, Halilaj I, van Limbergen E, Walsh S, Lutgens L, Lambin P, Vanneste BGL. Decision Support Systems in Prostate Cancer Treatment: An Overview. *Biomed Res Int* 2019; **2019**: 4961768 [PMID: 31281840 DOI: 10.1155/2019/4961768]

35 **Lee G**, Singanamalli A, Wang H, Feldman MD, Master SR, Shih NN, Spangler E, Rebbeck T, Tomaszewski JE, Madabhushi A. Supervised multi-view canonical correlation analysis (sMVCCA): integrating histologic and proteomic features for predicting recurrent prostate cancer. *IEEE Trans Med Imaging* 2015; **34**: 284-297 [PMID: 25203987 DOI: 10.1109/TMI.2014.2355175]

36 **Hahn P**, Smith IC, Leboldus L, Littman C, Somorjai RL, Bezabeh T. The classification of benign and malignant human prostate tissue by multivariate analysis of 1H magnetic resonance spectra. *Cancer Res* 1997; **57**: 3398-3401 [PMID: 9270004]

37 **Tsechelidis I**, Vrachimis A. PSMA PET in Imaging Prostate Cancer. *Front Oncol* 2022; **12**: 831429 [PMID: 35155262 DOI: 10.3389/fonc.2022.831429]

38 **Siva S**, Udovicich C, Tran B, Zargar H, Murphy DG, Hofman MS. Expanding the role of small-molecule PSMA ligands beyond PET staging of prostate cancer. *Nat Rev Urol* 2020; **17**: 107-118 [PMID: 31937920 DOI: 10.1038/s41585-019-0272-5]

39 **Zamboglou C**, Carles M, Fechter T, Kiefer S, Reichel K, Fassbender TF, Bronsert P, Koeber G, Schilling O, Ruf J, Werner M, Jilg CA, Baltas D, Mix M, Grosu AL. Radiomic features from PSMA PET for non-invasive intraprostatic tumor discrimination and characterization in patients with intermediate- and high-risk prostate cancer - a comparison study with histology reference. *Theranostics* 2019; **9**: 2595-2605 [PMID: 31131055 DOI: 10.7150/thno.32376]

40 **Nishino M**, Hayakawa K, Minami M, Yamamoto A, Ueda H, Takasu K. Primary retroperitoneal neoplasms: CT and MR imaging findings with anatomic and pathologic diagnostic clues. *Radiographics* 2003; **23**: 45-57 [PMID: 12533639 DOI: 10.1148/rg.231025037]

41 **Nickols N**, Anand A, Johnsson K, Brynolfsson J, Borreli P, Parikh N, Juarez J, Jafari L, Eiber M, Rettig M. aPROMISE: A Novel Automated PROMISE Platform to Standardize Evaluation of Tumor Burden in (18)F-DCFPyL Images of Veterans with Prostate Cancer. *J Nucl Med* 2022; **63**: 233-239 [PMID: 34049980 DOI: 10.2967/jnumed.120.261863]

42 **Johnsson K**, Brynolfsson J, Sahlstedt H, Nickols NG, Rettig M, Probst S, Morris MJ, Bjartell A, Eiber M, Anand A. Analytical performance of aPROMISE: automated anatomic contextualization, detection, and quantification of [(18)F]DCFPyL (PSMA) imaging for standardized reporting. *Eur J Nucl Med Mol Imaging* 2022; **49**: 1041-1051 [PMID: 34463809 DOI: 10.1007/s00259-021-05497-8]

World Journal of Radiology

Submit a Manuscript: https://www.f6publishing.com

World J Radiol 2023 May 28; 15(5): 146-156

DOI: 10.4329/wjr.v15.i5.146

ISSN 1949-8470 (online)

ORIGINAL ARTICLE

Retrospective Cohort Study

Chronic thromboembolic pulmonary hypertension is associated with a loss of total lung volume on computed tomography

Nanae Tsuchiya, Yan-Yan Xu, Junji Ito, Tsuneo Yamashiro, Hidekazu Ikemiyagi, David Mummy, Mark L Schiebler, Koji Yonemoto, Sadayuki Murayama, Akihiro Nishie

Specialty type: Radiology, nuclear medicine and medical imaging

Provenance and peer review: Invited article; Externally peer reviewed.

Peer-review model: Single blind

Peer-review report's scientific quality classification

Grade A (Excellent): 0
Grade B (Very good): B, B
Grade C (Good): 0
Grade D (Fair): 0
Grade E (Poor): 0

P-Reviewer: Chen Q, China; Sharma D, India

Received: November 26, 2022
Peer-review started: November 26, 2022
First decision: March 15, 2023
Revised: April 4, 2023
Accepted: April 24, 2023
Article in press: April 24, 2023
Published online: May 28, 2023

Nanae Tsuchiya, Junji Ito, Sadayuki Murayama, Akihiro Nishie, Department of Radiology, Graduate School of Medical Science, University of the Ryukyus, Nishihara 903-0125, Okinawa, Japan

Yan-Yan Xu, Department of Radiology, China-Japan Friendship Hospital, Beijing 100029, China

Tsuneo Yamashiro, Department of Radiology, Yokohama City University, Yokohama 2360027, Japan

Hidekazu Ikemiyagi, Department of Cardiovascular Medicine, Nephrology and Neurology, Graduate School of Medicine, University of the Ryukyus, Nishihara 9030125, Okinawa, Japan

David Mummy, Center for In Vivo Microscopy and Department of Radiology, Duke University, Durham, NC 27710, United States

Mark L Schiebler, Department of Radiology, University of Wisconsin-Madison, Madison, WI 53792, United States

Koji Yonemoto, Department of Biostatistics, School of Health Sciences, Faculty of Medicine, University of the Ryukyus, Nishihara 903-0215, Okinawa, Japan

Corresponding author: Nanae Tsuchiya, MD, PhD, Lecturer, Department of Radiology, Graduate School of Medical Science, Tsuchiya, N (reprint author), Graduate School of Medical Science, University of the Ryukyus, 207 Uehara, Nishihara-Cho, Nakagami-Gun, Okinawa 903-0215, Japan. nanae7a50@hotmail.com

Abstract

BACKGROUND

Although lung volumes are usually normal in individuals with chronic thromboembolic pulmonary hypertension (CTEPH), approximately 20%-29% of patients exhibit a restrictive pattern on pulmonary function testing.

AIM

To quantify longitudinal changes in lung volume and cardiac cross-sectional area (CSA) in patients with CTEPH.

METHODS

In a retrospective cohort study of patients seen in our hospital between January

2012 and December 2019, we evaluated 15 patients with CTEPH who had chest computed tomography (CT) performed at baseline and after at least 6 mo of therapy. We matched the CTEPH cohort with 45 control patients by age, sex, and observation period. CT-based lung volumes and maximum cardiac CSAs were measured and compared using the Wilcoxon signed-rank test and the Mann-Whitney *u* test.

RESULTS

Total, right lung, and right lower lobe volumes were significantly reduced in the CTEPH cohort at follow-up *vs* baseline (total, $P = 0.004$; right lung, $P = 0.003$; right lower lobe; $P = 0.01$). In the CTEPH group, the reduction in lung volume and cardiac CSA was significantly greater than the corresponding changes in the control group (total, $P = 0.01$; right lung, $P = 0.007$; right lower lobe, $P = 0.01$; CSA, $P = 0.0002$). There was a negative correlation between lung volume change and cardiac CSA change in the control group but not in the CTEPH cohort.

CONCLUSION

After at least 6 mo of treatment, CT showed an unexpected loss of total lung volume in patients with CTEPH that may reflect continued parenchymal remodeling.

Key Words: Pulmonary hypertension; Lung; Computed tomography; Retrospective study; Lung volume measurements; Follow-up studies

©The Author(s) 2023. Published by Baishideng Publishing Group Inc. All rights reserved.

Core Tip: The total lung volume, right lower lobe volume, and cardiac cross-sectional area were reduced after at least 6 mo of follow-up after treatment in patients with chronic thromboembolic pulmonary hypertension (CTEPH). This finding suggests that structural lung changes have occurred in CTEPH, possibly from continued infarction with secondary volume loss from fibrosis or bronchoconstriction. The loss of lung volume may prove to be an important clinical consideration in CTEPH treatment because pulmonary function may continue to deteriorate despite improved right heart function in patients with CTEPH.

Citation: Tsuchiya N, Xu YY, Ito J, Yamashiro T, Ikemiyagi H, Mummy D, Schiebler ML, Yonemoto K, Murayama S, Nishie A. Chronic thromboembolic pulmonary hypertension is associated with a loss of total lung volume on computed tomography. *World J Radiol* 2023; 15(5): 146-156
URL: https://www.wjgnet.com/1949-8470/full/v15/i5/146.htm
DOI: https://dx.doi.org/10.4329/wjr.v15.i5.146

INTRODUCTION

Chronic thromboembolic pulmonary hypertension (CTEPH) is characterized by the presence of residual organized thrombi and vascular remodeling, leading to progressive pulmonary hypertension and right ventricular failure[1]. Surgical pulmonary endarterectomy (PEA) is a treatment for surgically accessible CTEPH. However, it has been reported that 17%-25% of patients undergoing PEA have residual or recurrent pulmonary hypertension[2]. In addition, approximately 30% of patients are not eligible for PEA because of the distal location of their pulmonary thromboemboli[3]; balloon pulmonary angioplasty (BPA) or medical therapy are the preferred treatment strategies for such patients[1,4,5].

Spirometry results and lung volumes are usually normal in patients with CTEPH, but approximately 20%-29% of patients exhibit a restrictive pattern on pulmonary function testing[6-8]. This reduction in lung volume is thought to be caused by parenchymal scarring from pulmonary infarction and not by displacement from proximal vessel hypertrophy and dilatation[7].

The nature of the progression of this observed reduction in lung volume in patients with CTEPH has not previously been described[3,9]. In our practice, we sometimes encounter patients who are receiving BPA or medical treatment for CTEPH but are gradually losing lung volume on chest computed tomography (CT); these patients require long-term follow-up. Based on this experience, we hypothesized that lung volume decreases over time in patients with CTEPH who have not undergone PEA. Furthermore, since heart size can be increased in patients with CTEPH and right heart failure, we suspected that this cardiomegaly might be another potential and as yet unreported contributor to the lung volume reduction seen in CTEPH.

The purpose of this study was to investigate longitudinal changes in CT lung volume and to evaluate the relationship between lung volume and heart size in patients with CTEPH.

MATERIALS AND METHODS

Our institutional review board approved this retrospective cohort study and waived the requirement for patient informed consent.

Patients

We conducted a retrospective review of patients seen at our institution between January 2012 and December 2019. Patients were initially identified using a picture archiving and communications system database, and patient selection was further refined by reviewing the electronic medical records. The inclusion criteria were a clinical diagnosis of CTEPH, age between 20 years and 90 years, chest CT performed at initial diagnosis and at the time of follow-up, and a minimum 6-mo interval between CT imaging sessions (Figure 1). We excluded patients who underwent PEA, patients for whom there was a lack of thin-slice CT images (< 2 mm) or poor image quality (*e.g.*, motion artifact from a missed breath hold), and patients with other conditions that might affect lung volume (*e.g.*, pleural effusion, underlying chronic pulmonary disease such as emphysema, interstitial lung disease, or old tuberculosis, and a history of thoracic surgery). The inclusion criterion for individuals in the control group, which was matched by age, sex, and observation period, was the presence of two chest CTs performed to observe cancer status (renal or prostate cancer for men; uterine cancer for women). Individuals were excluded from the control group if there was a lack of thin-slice CT images, poor image quality, or any abnormal findings on chest CT.

The diagnosis of CTEPH was determined by cardiologists based on a detailed medical history, physical examination, chest radiography, chest CT, echocardiography, lung ventilation–perfusion scintigraphy, right heart catheterization (RHC), and angiographic demonstration of multiple stenoses and obstruction of bilateral pulmonary arteries[10]. Radiologist reports were reviewed to determine which pulmonary arteries were affected by chronic thrombosis. Clinical data, including age, height, weight, and treatment details (*e.g.*, anticoagulant therapy, BPA), were extracted from the medical records. We also noted the results of RHC (mean pulmonary arterial pressure, cardiac output, cardiac index) and echocardiography (tricuspid regurgitation pressure gradient, left ventricular end-diastolic diameter, left ventricular end-systolic diameter) at the examination closest in time to the chest CT.

Computed tomography

Chest CT, with or without contrast, was performed as part of routine clinical practice. Two scanners were used: The Light Speed VCT 64-row CT (GE HealthCare, Milwaukee, WI, United States) and the Aquilion ONE 320-row CT (Canon Medical Systems, Odawara, Japan). Imaging was performed during a supine breath-hold at full inspiration. Instructions for full inspiration were given using an automatic voice system to keep the degree of inspiration constant. The imaging parameters were: Voltage, 120 kVp; current, automatic exposure control; collimation, 0.5 (Canon) or 0.625 mm (GE); rotation time, 0.5 sec; matrix, 512 × 512; and slice thicknesses, 1 mm (Canon) or 1.25 mm (GE).

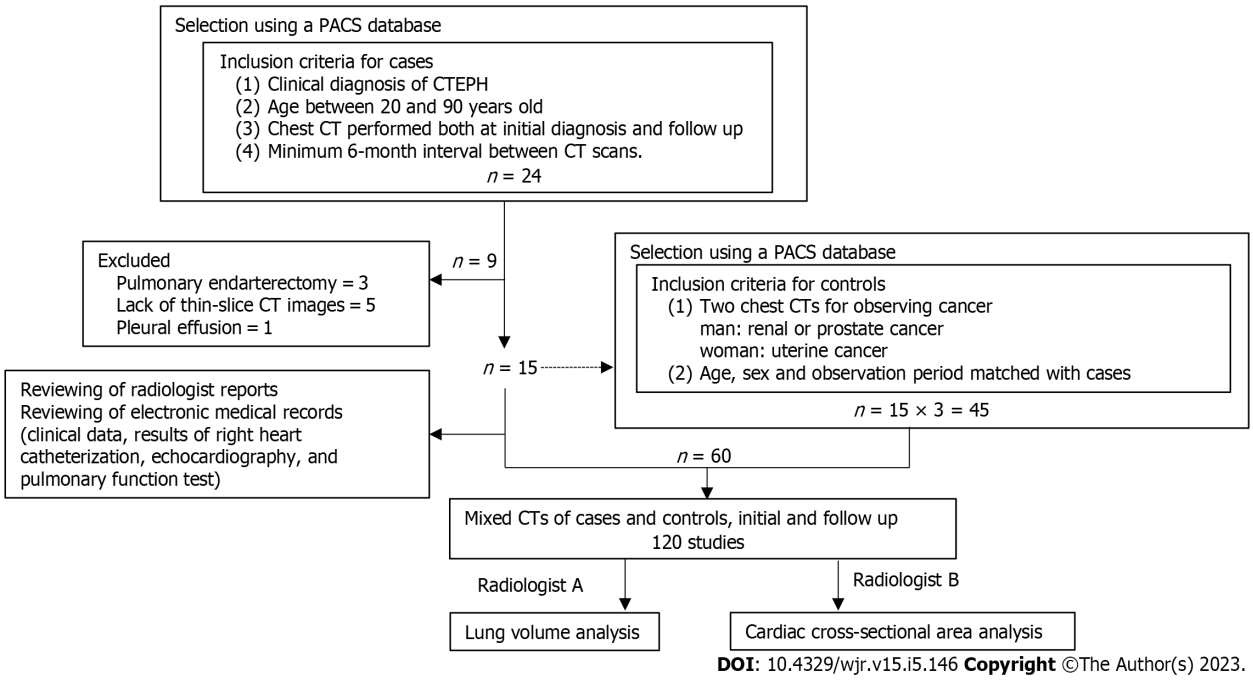
Image analysis

Lung volumes were automatically segmented and calculated using a commercially available workstation (SYNAPSE VINCENT, version 4.1; Fujifilm Healthcare Corporation, Tokyo, Japan). We used images with a soft tissue reconstruction algorithm [Standard (GE) or FC14 (Cannon)] for analysis. Lung volumes were assessed based on lobe anatomy: Right upper and middle lobe; right lower lobe; left upper lobe; and left lower lobe. The right upper and middle lobes were assessed together because of the frequent presence of incomplete lobulation.

We calculated the amount of change in lung volume between the initial CT and follow-up CT. The slice with the maximal cardiac cross-sectional area (CSA) in cm^2 was measured semiautomatically using a commercially available workstation (SYNAPSE VINCENT, version 4.1). Based on a previously published method[11], the following process was used for each patient. A hounsfield unit threshold was set to exclude the pericardial fat pad (0-300 hounsfield unit). All images that contained the heart were then identified, and the maximum cardiac CSA was determined. Finally, the boundary of the heart was traced, and the maximum cardiac CSA recorded. In addition, we calculated the size change (difference in area) in cardiac CSA between the initial and follow-up CT images. Lung volume and cardiac CSA were analyzed separately by different radiologists (NT and YX) who were blinded to the patients' clinical information (Figure 1).

Statistical analysis

The sample size for this study was determined by the following method[12]: Average lung volume, 2000 mL; standard deviation, 400 mL; effect size, 400 mL (20% of average); patient to control ratio, 1:3; α, 0.05; and power, 0.8.



DOI: 10.4329/wjr.v15.i5.146 **Copyright** ©The Author(s) 2023.

Figure 1 Study flow chart. CT: Computed tomography; CTEPH: Chronic thromboembolic pulmonary hypertension; PACS: Picture archiving and communications system.

Statistical analyses were performed using JMP 11 (SAS Institute Japan, Tokyo, Japan). Continuous variables were calculated as the mean and 95% confidence interval. The Wilcoxon signed-rank test was used to compare parameters between the initial and follow-up CT for both groups. The Mann-Whitney *U* test was used to compare parameters between patients with CTEPH and those in the control group. The Spearman correlation coefficient was used to determine the correlation between lung volume and cardiac CSA. A *P* value of less than 0.05 was considered statistically significant.

RESULTS

We identified 27 individuals with CTEPH who were seen during the study period. Of these, 24 had two chest CTs with an interval greater than 6 mo. We excluded 3 patients who underwent PEA, 5 patients who lacked thin-slice CT images, and 1 patient with a pleural effusion. The size of the CTEPH population was thus fixed at 15 (4 males and 11 females) due to the retrospective nature of the study. The mean patient age was 48 years (range: 40-83 years). The size of the control group was set at 45 individuals (3 times the size of the CTEPH group). All individuals with CTEPH received anticoagulant therapy, and 14 patients underwent BPA. Patient characteristics are summarized in Table 1. The results of echocardiography and RHC performed before and after therapy are shown in Table 2.

Comparison between initial and follow-up measurements of lung volume and cardiac CSA

The initial and follow-up measurements for lung volume are shown in Table 2. The total lung volume (P = 0.004), right lung volume (P = 0.003), and the right lower lobe volume (P = 0.01) at total lung capacity (TLC) were significantly reduced in patients with CTEPH at follow-up (Figures 2 and 3), but there were no significant longitudinal changes in lung volumes in the control group. The cardiac CSA was significantly reduced in the CTEPH cohort at follow-up (P = 0.001), but this change was not observed in the control group.

Comparison between measures of lung volume and cardiac CSA in patients with CTEPH vs controls

The lung volumes and cardiac CSA measurements for the CTEPH cohort and the control group are shown in Table 3. There was no significant difference in lung volumes between groups, but the cardiac CSA was larger in the CTEPH group than in the control group at both initial and follow-up assessments (P < 0.0001). In the CTEPH cohort, the reduction in total lung volume (P = 0.01) and in right lung volume (P = 0.007) and right lower lobe volume (P = 0.01) was significantly larger than that seen in the control group (Figure 4). The reduction in cardiac CSA in the CTEPH cohort was significantly greater than in the control group (P = 0.0002).

Table 1 Population characteristics

Characteristic	CTEPH, *n* = 15		Control, *n* = 45	*P* value
Age in yr, mean (95%CI)	48 (40, 83)		48 (40, 83)	-
Height in cm, mean (95%CI)	159 (151, 162)		159 (154, 163)	0.5
Weight in kg, mean (95%CI)	58 (49, 75)		61 (54, 72)	0.9
Interval between initial and follow-up CT in d, mean (95%CI)	547 (273, 846)		531 (294, 815)	0.9
Results of RHC and echocardiography	**Initial, *n* = 15**	**Follow-up, *n* = 15**		***P* value**
Pulmonary arterial pressure in mmHg, mean (95%CI)	47 (38, 59)	34 (23, 44)	-	0.001[b]
Cardiac output in L/min, mean (95%CI)	3.4 (2.8, 4.3)	4.6 (3.6, 6.1)	-	0.01[a]
Cardiac index in L/min/m^2, mean (95%CI)	2.2 (1.6, 2.7)	2.7 (2.4, 3.6)	-	0.01[a]
Tricuspid regurgitation pressure gradient in mmHg, mean (95%CI)	66 (51, 77)	42 (23, 61)	-	0.01[a]
Left ventricular end-diastolic diameter in mm, mean (95%CI)	38 (37, 42)	44 (41, 47)	-	0.02[a]
Left ventricular end-systolic diameter in mm, mean (95%CI)	25 (22, 28)	27 (24, 31)	-	0.5
Results of spirometry	**Initial, *n* = 10**	**Follow-up, *n* = 10**		
Vital capacity % predicted	83 (70, 102)	87 (76, 99)	-	0.2
Forced vital capacity % predicted	76 (71, 97)	83 (74, 97)	-	0.3
Forced expiratory volume-one second % predicted	74 (63, 959	83 (69, 96)	-	0.5

[a]$P < 0.05$.
[b]$P < 0.01$. CI: Confidence interval; CT: Computed tomography; CTEPH: Chronic thromboembolic pulmonary hypertension; RHC: Right heart catheterization.

Table 2 Comparison between measurements on initial and follow-up computed tomography

CT measurement	CTEPH, *n* = 15			Control, *n* = 45		
	Initial	Follow-up	*P* value	Initial	Follow-up	*P* value
Total lung volume in mL, mean (95%CI)	3238 (3016, 4494)	3360 (2687, 4043)	0.004[b]	3669 (3063, 4167)	3657 (2993, 4385)	0.9
Right lung volume in mL, mean (95%CI)	1879 (1700, 2619)	1817 (1522, 2299)	0.003[b]	1939 (1635, 2268)	1990 (1614, 2347)	0.9
Right upper + middle lobe volume in mL, mean (95%CI)	977 (913, 1103)	973 (900, 1148)	0.2	1028 (868, 1169)	1010 (865, 1212)	1.0
Right lower lobe lung volume in mL, mean (95%CI)	978 (737, 1123)	815 (611, 1111)	0.01[a]	931 (707, 1112)	911 (733, 1148)	0.8
Left lung volume in mL, mean (95%CI)	1396 (1316, 1875)	1455 (1216, 1744)	0.1	1692 (1376, 1940)	1659 (1403, 2023)	0.7
Left upper lobe lung volume in mL, mean (95%CI)	836 (752, 925)	802 (689, 1000)	0.4	867 (747, 1042)	869 (741, 1089)	0.9
Left lower lobe lung volume in mL, mean (95%CI)	636 (555, 902)	652 (476, 806)	0.05	826 (628, 939)	749 (622, 999)	0.6
Heart cross-sectional area in cm^2, mean (95%CI)	97 (86, 112)	83 (69, 100)	0.001[b]	75 (65, 85)	74 (64, 85)	0.7

[a]$P < 0.05$.
[b]$P < 0.01$. CI: Confidence interval; CT: Computed tomography; CTEPH: Chronic thromboembolic pulmonary hypertension.

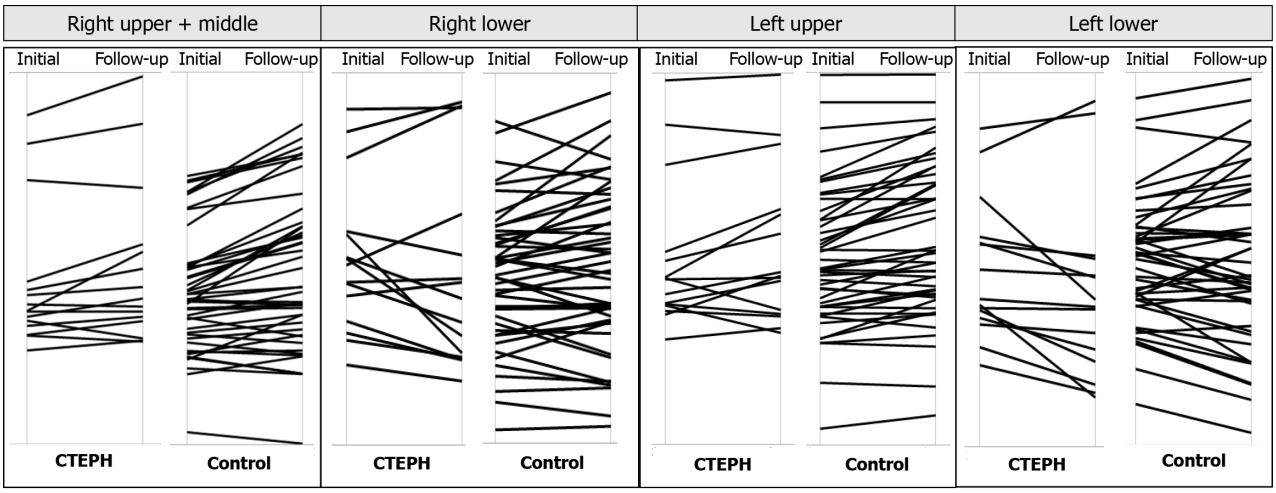
Correlation between lung volume and cardiac CSA

There were no significant correlations between lung volume and cardiac CSA in the CTEPH cohort or the control group at either initial or follow-up CT. In the CTEPH group, there were no significant correlations between lung volume change and the change in cardiac CSA. In the control group, the change in cardiac CSA was negatively correlated with total lung volume change (ρ = -0.44; $P = 0.002$), right lung volume change (ρ = -0.34; $P = 0.01$), right upper and middle lobe volume change (ρ = -0.27; $P = 0.06$), right lower lobe volume change (ρ = -0.34; $P = 0.02$), left lung volume change (ρ = -0.50; $P = 0.0004$), left upper lobe volume change (ρ = -0.40; $P = 0.0005$), and left lower lobe volume change (ρ = -0.52; $P = 0.0002$) (Figure 5).

Table 3 Lung volume and heart-size change in patients with chronic thromboembolic pulmonary hypertension and in the control group

Parameter	CTEPH, *n* = 15	Control, *n* = 45	*P* value
Total lung volume change in mL, mean (95%CI)	176 (13, 468)	39 (-228, 252)	0.01[a]
Right lung volume change in mL, mean (95%CI)	120 (47, 292)	4 (-121, 126)	0.007[b]
Right upper + middle lobe lung volume change in mL, mean (95%CI)	35 (-26, 91)	-7 (-46, 46)	0.9
Right lower lobe lung volume change in mL, mean (95%CI)	85 (19, 167)	-9 (-66, 83)	0.01[a]
Left lung volume change in mL, mean (95%CI)	23 (-37, 214)	33 (-109, 99)	0.1
Left upper lobe lung volume change in mL, mean (95%CI)	13 (-31, 81)	1 (-44, 53)	0.4
Left lower lobe lung volume change in mL, mean (95%CI)	40 (-23, 112)	9 (-59, 63)	0.1
Cardiac cross-sectional area change in cm^2, mean (95%CI)	19 (4, 25)	-0.3 (-2, 3)	0.0002[c]

[a]$P < 0.05$.
[b]$P < 0.01$.
[c]$P < 0.001$. CI: Confidence interval; CTEPH: Chronic thromboembolic pulmonary hypertension.



DOI: 10.4329/wjr.v15.i5.146 **Copyright** ©The Author(s) 2023.

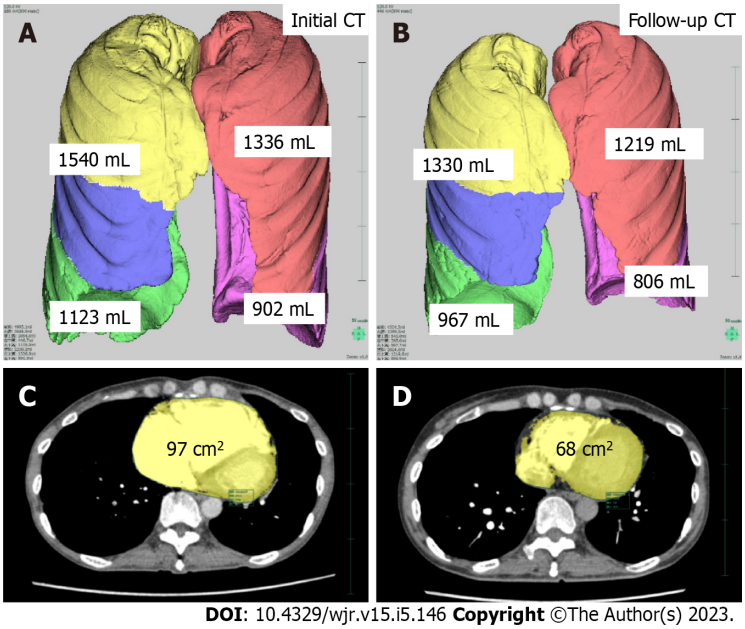
Figure 2 Parallel plots between initial computed tomography and follow-up computed tomography. The right lower lung volume decreased significantly over time in the chronic thromboembolic pulmonary hypertension (CTEPH) group. There were no significant changes in lung volume in the control group.

DISCUSSION

This pilot study showed that the lung volume in patients with CTEPH who are treated medically decreases over 6 mo of follow-up, despite a reduction in heart size during that same period. These results suggest that a reduction in lung volume may continue in patients with CTEPH who have not undergone PEA, and that this reduction may occur independently of right heart enlargement quantified using cardiac CSA.

Although decreased TLC has been previously observed in patients with CTEPH[7], this report analyzed regional contributions to reduction in lung volume using CT measurements, showing that the right lung and right lower lung have significantly reduced volumes. The reason for this may be related to continued lung remodeling and loss of parenchyma from continuing pulmonary infarction. Reports of pulmonary embolism show a striking lower lobe predominance, with an embolus rate in the right lower lobe twice that of the left lower lobe[13]. Thus, it is plausible that the right lower lung is a major contributor to lung volume reduction because of its status as a predominant region of pulmonary infarction.

A retrospective study by Morris *et al*[7] found that 22% of the 51 patients with CTEPH who were candidates for PEA had restrictive lung disease on pulmonary function testing, defined as a TLC less than 80% of predicted. They also demonstrated that the reduction in lung volume was correlated to the degree of parenchymal scarring occurring after pulmonary infarction. Pulmonary infarction is more common with peripheral pulmonary emboli than with central pulmonary emboli due to the relatively lower contribution of bronchial arterial supply to the peripheral lung[13,14].



DOI: 10.4329/wjr.v15.i5.146 **Copyright** ©The Author(s) 2023.

Figure 3 A 55-year-old female with chronic thromboembolic pulmonary hypertension was observed for 15 mo. A: The lung lobar volumes before treatment; B: The lung lobar volumes after treatment showed a loss of volume from both lung bases; C: The cardiac cross-sectional area was improved after balloon pulmonary angioplasty; D: The right ventricle returned to a normal size. CT: Computed tomography.

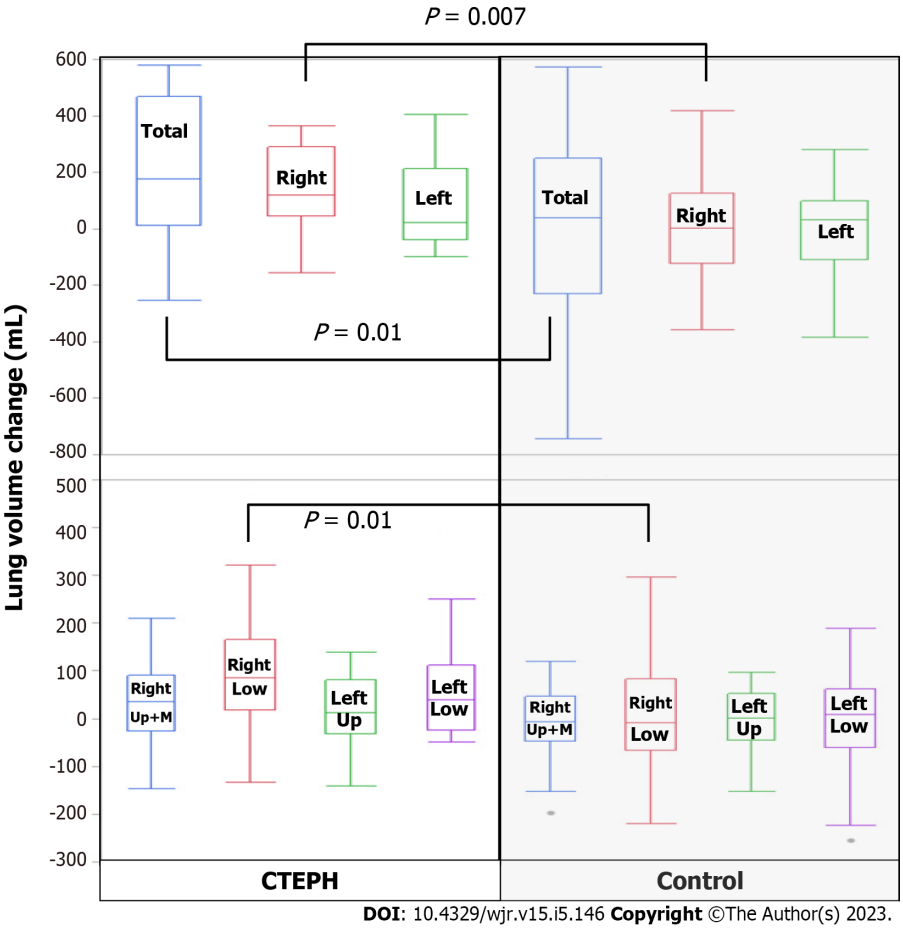
The decline in heart size seen with CTEPH is most likely related to the improvement in right ventricular function and decreased right ventricular end-diastolic and end-systolic volumes with medical therapy or BPA. Echocardiography and RHC show these improvements at follow-up. Cardiac CSA, measured in the transverse plane, is affected by the phase of ventilation. Inhalation stretches the heart in the vertical plane and reduces cardiac CSA, whereas expiration lifts the diaphragm and pushes the heart upward, increasing cardiac CSA[11]. The control group in this study had a significant negative correlation between heart size change, as measured by CSA, and lung volume change. However, the correlation between these changes disappeared in the CTEPH cohort. We initially speculated that cardiomegaly was a factor in lung volume decline in the CTEPH group. In addition to the physiologic increase in cardiac CSA caused by poor inspiration, the increase in the right ventricle and right atrium volume caused by exacerbation of right heart failure would compress the lung parenchyma, leading to a decrease in lung volume. However, we found the opposite to be true: lung volumes decreased in the CTEPH group despite a reduction in heart size. In other words, a reduction in heart size that is associated with improved heart function can occur simultaneously with a loss of lung volume in CTEPH. An additional explanation of this negative correlation between heart size and lung volume is that in normal individuals more vigorous inspiration when measuring TLC reduces venous filling of the right atrium. In patients with CTEPH, there should be less of an effect because these individuals already have volume overload in the right heart.

There have been remarkable recent advances in treatment for inoperable CTEPH, and survival has significantly improved in the population treated with medication or BPA[2]. However, whether quality of life improves after medical therapy has been controversial, and there have been no reports of changes in quality of life following BPA[15-19]. While TLC reportedly increases following BPA for CTEPH[20], this is only a short-term outcome. Further study is needed to clarify whether this temporary increase in lung volume and subsequent regression may influence quality of life in patients with CTEPH.

There are several limitations to this study. First, this is a retrospective single-center study with a small number of patients, and spirometry data are lacking. Second, height is an important factor influencing lung volume, but this was not matched between patients in the CTEPH and control groups; however, mean height was not significantly different between the groups. Therefore, this effect is likely to be negligible. Third, there were multiple hardware vendors for the CT scanners used in this project. Finally, the absolute inspiration volume for CT was not measured with spirometry.

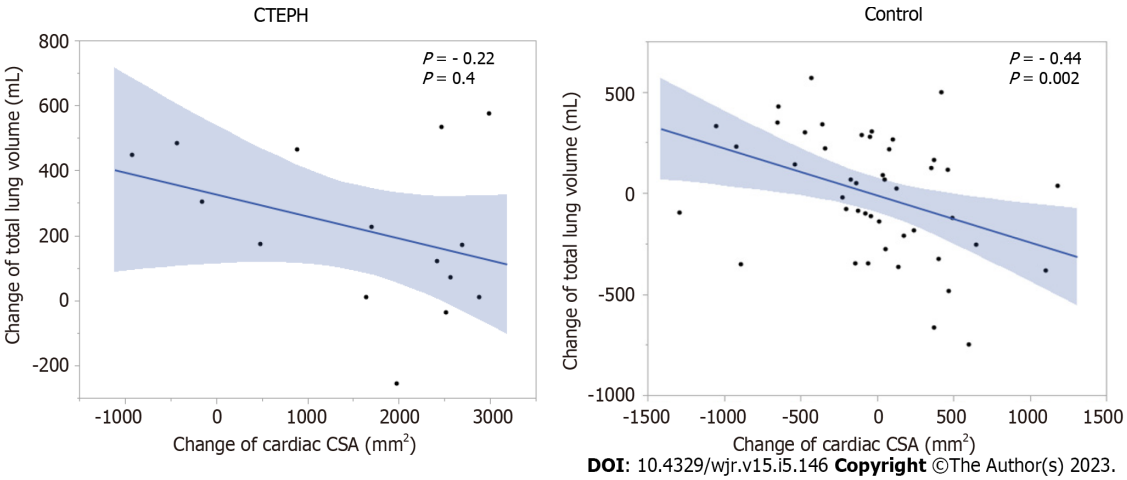
CONCLUSION

The total lung volume, right lower lobe volume, and the cardiac CSA were reduced after at least 6 mo of follow-up after treatment in patients with CTEPH. This finding suggests that structural changes in the lung have occurred, possibly from continued infarction with secondary volume loss from fibrosis or bronchoconstriction. The results of this study suggest that pulmonary function may continue to



DOI: 10.4329/wjr.v15.i5.146 **Copyright** ©The Author(s) 2023.

Figure 4 Box and whisker plots of individuals with chronic thromboembolic pulmonary hypertension and individuals in the control group. There were significant changes over time in the total lung, right lung, and right lower lobe but not the right upper and middle lobes. There was no significant change in volume in the left lung, left upper lobe, or left lower lobe. CTEPH: Chronic thromboembolic pulmonary hypertension; Up: Upper lobe; M: Middle lobe; Low: Lower lobe.



DOI: 10.4329/wjr.v15.i5.146 **Copyright** ©The Author(s) 2023.

Figure 5 Relationship between lung volume change and cardiac cross-sectional area in patients with chronic thromboembolic pulmonary hypertension group and in the control group. There was a negative correlation between total lung volume and cardiac cross-sectional area (CSA) in the control group but not in the chronic thromboembolic pulmonary hypertension (CTEPH) group.

deteriorate in patients with CTEPH despite improvements in right heart function and decreased right ventricular volumes from lowered pulmonary arterial pressure after treatment. This loss of lung volume may prove to be an important clinical consideration in CTEPH treatment.

ARTICLE HIGHLIGHTS

Research background

In chronic thromboembolic pulmonary hypertension (CTEPH), about 20% of patients have lung restriction due to parenchymal scarring. We sometimes follow CTEPH patients who gradually lose lung volume. There is no report describing the temporal change in lung volume of CTEPH patients.

Research motivation

The loss of lung volume may be an important clinical consideration in CTEPH treatment.

Research objectives

The purpose of this study was to assess the temporal lung volume changes in CTEPH.

Research methods

Included in the study were patients with CTEPH who underwent two thoracic computed tomography (CT) examinations with a between-test interval that was greater than 6 mo. We also assessed controls matched by age, sex, and observation period. The lung volume was measured on the left and right sides by thin-slice CT scanning. Lung volume was automatically measured by lung analysis software. We analyzed the lung volume changes between the initial CT and follow-up CT in patients and controls by the Wilcoxon signed-rank test.

Research results

The total and right lung volumes were significantly reduced from the initial CT to the follow-up CT in the patients with CTEPH. In CTEPH patients, there was no significant change in the left lung volume. In controls, there were no significant changes in lung volume.

Research conclusions

In patients with CTEPH, the lung volume was reduced temporally. The right lung was more affected than the left lung by the lung volume reduction.

Research perspectives

Further study is needed to clarify whether this temporary increase in lung volume and subsequent regression may influence quality of life in patients with CTEPH.

ACKNOWLEDGEMENTS

The authors are grateful to Ms. Chihiro Siroma for contribution to collection of the data.

FOOTNOTES

Author contributions: All authors contributed to the study conception and design; Tsuchiya N, Xu YY, and Ito J performed the data collection and image interpretation; Tsuchiya N and Yonemoto K performed the statistical analysis; Tsuchiya N wrote the first draft of the manuscript; and all authors commented on previous versions of the manuscript and read and approved the final manuscript.

Supported by The Japan Society for the Promotion of Science, No. 24591782.

Institutional review board statement: This study was approved by the Ethics Committee for Clinical Research of University of the Ryukyus with waiver of informed consent (Approval No., 1039).

Informed consent statement: Our institutional review board approved this retrospective cohort study and waived the requirement for patient informed consent.

Conflict-of-interest statement: All authors report having no relevant conflicts of interest for this article.

Data sharing statement: The original anonymous dataset is available upon request from the corresponding author at nanae7a50@hotmail.com.

Open-Access: This article is an open-access article that was selected by an in-house editor and fully peer-reviewed by external reviewers. It is distributed in accordance with the Creative Commons Attribution NonCommercial (CC BY-NC 4.0) license, which permits others to distribute, remix, adapt, build upon this work non-commercially, and license their derivative works on different terms, provided the original work is properly cited and the use is non-

commercial. See: https://creativecommons.org/Licenses/by-nc/4.0/

Country/Territory of origin: Japan

ORCID number: Nanae Tsuchiya 0000-0003-2556-8287; Mark L Schiebler 0000-0002-9120-5428; Akihiro Nishie 0000-0001-7103-7757.

S-Editor: Liu XF
L-Editor: Filipodia
P-Editor: Zhao S

REFERENCES

1 **Robbins IM**, Pugh ME, Hemnes AR. Update on chronic thromboembolic pulmonary hypertension. *Trends Cardiovasc Med* 2017; **27**: 29-37 [PMID: 27345156 DOI: 10.1016/j.tcm.2016.05.010]
2 **Miwa H**, Tanabe N, Jujo T, Kato F, Anazawa R, Yamamoto K, Naito A, Kasai H, Nishimura R, Suda R, Sugiura T, Sakao S, Ishida K, Masuda M, Tatsumi K. Long-Term Outcome of Chronic Thromboembolic Pulmonary Hypertension at a Single Japanese Pulmonary Endarterectomy Center. *Circ J* 2018; **82**: 1428-1436 [PMID: 29540628 DOI: 10.1253/circj.CJ-17-1242]
3 **Low AT**, Medford AR, Millar AB, Tulloh RM. Lung function in pulmonary hypertension. *Respir Med* 2015; **109**: 1244-1249 [PMID: 26033642 DOI: 10.1016/j.rmed.2015.05.022]
4 **Moriarty JM**, Khan SN, Kao SD, Saggar R. Balloon Pulmonary Angioplasty for Chronic Thromboembolic Pulmonary Hypertension. *Cardiovasc Intervent Radiol* 2018; **41**: 1826-1839 [PMID: 30039506 DOI: 10.1007/s00270-018-2012-2]
5 **Aoki T**, Sugimura K, Tatebe S, Miura M, Yamamoto S, Yaoita N, Suzuki H, Sato H, Kozu K, Konno R, Miyata S, Nochioka K, Satoh K, Shimokawa H. Comprehensive evaluation of the effectiveness and safety of balloon pulmonary angioplasty for inoperable chronic thrombo-embolic pulmonary hypertension: long-term effects and procedure-related complications. *Eur Heart J* 2017; **38**: 3152-3159 [PMID: 29029023 DOI: 10.1093/eurheartj/ehx530]
6 **Horn M**, Ries A, Neveu C, Moser K. Restrictive ventilatory pattern in precapillary pulmonary hypertension. *Am Rev Respir Dis* 1983; **128**: 163-165 [PMID: 6870057 DOI: 10.1164/arrd.1983.128.1.163]
7 **Morris TA**, Auger WR, Ysrael MZ, Olson LK, Channick RN, Fedullo PF, Moser KM. Parenchymal scarring is associated with restrictive spirometric defects in patients with chronic thromboembolic pulmonary hypertension. *Chest* 1996; **110**: 399-403 [PMID: 8697841 DOI: 10.1378/chest.110.2.399]
8 **Fukushi K**, Kataoka M, Shimura N, Inami T, Fukuda K, Yoshino H, Satoh T. Impaired Respiratory Function in Chronic Thromboembolic Pulmonary Hypertension: A Comparative Study with Healthy Control Subjects. *Ann Am Thorac Soc* 2016; **13**: 1183-1184 [PMID: 27388407 DOI: 10.1513/AnnalsATS.201601-048LE]
9 **Kahn SR**, Houweling AH, Granton J, Rudski L, Dennie C, Hirsch A. Long-term outcomes after pulmonary embolism: current knowledge and future research. *Blood Coagul Fibrinolysis* 2014; **25**: 407-415 [PMID: 24469387 DOI: 10.1097/MBC.0000000000000070]
10 **Kim NH**, Delcroix M, Jenkins DP, Channick R, Dartevelle P, Jansa P, Lang I, Madani MM, Ogino H, Pengo V, Mayer E. Chronic thromboembolic pulmonary hypertension. *J Am Coll Cardiol* 2013; **62**: D92-D99 [PMID: 24355646 DOI: 10.1016/j.jacc.2013.10.024]
11 **Tomita H**, Yamashiro T, Matsuoka S, Matsushita S, Kurihara Y, Nakajima Y. Changes in Cross-Sectional Area and Transverse Diameter of the Heart on Inspiratory and Expiratory Chest CT: Correlation with Changes in Lung Size and Influence on Cardiothoracic Ratio Measurement. *PLoS One* 2015; **10**: e0131902 [PMID: 26151361 DOI: 10.1371/journal.pone.0131902]
12 **Kohn MA**, Senyak J. Sample Size Calculators. 2021 December 20 [cited 24 January 2020]. San Francisco: UCSF CTSI [DOI: 10.3840/002042]
13 **He H**, Stein MW, Zalta B, Haramati LB. Pulmonary infarction: spectrum of findings on multidetector helical CT. *J Thorac Imaging* 2006; **21**: 1-7 [PMID: 16538148 DOI: 10.1097/01.rti.0000187433.06762.fb]
14 **Tsao MS**, Schraufnagel D, Wang NS. Pathogenesis of pulmonary infarction. *Am J Med* 1982; **72**: 599-606 [PMID: 6462058 DOI: 10.1016/0002-9343(82)90458-2]
15 **Mathai SC**, Ghofrani HA, Mayer E, Pepke-Zaba J, Nikkho S, Simonneau G. Quality of life in patients with chronic thromboembolic pulmonary hypertension. *Eur Respir J* 2016; **48**: 526-537 [PMID: 27076580 DOI: 10.1183/13993003.01626-2015]
16 **Scholzel BE**, Post MC, Thijs Plokker HW, Snijder RJ. Clinical worsening during long-term follow-up in inoperable chronic thromboembolic pulmonary hypertension. *Lung* 2012; **190**: 161-167 [PMID: 22160210 DOI: 10.1007/s00408-011-9350-z]
17 **Suntharalingam J**, Treacy CM, Doughty NJ, Goldsmith K, Soon E, Toshner MR, Sheares KK, Hughes R, Morrell NW, Pepke-Zaba J. Long-term use of sildenafil in inoperable chronic thromboembolic pulmonary hypertension. *Chest* 2008; **134**: 229-236 [PMID: 18263674 DOI: 10.1378/chest.07-2681]
18 **Jaïs X**, D'Armini AM, Jansa P, Torbicki A, Delcroix M, Ghofrani HA, Hoeper MM, Lang IM, Mayer E, Pepke-Zaba J, Perchenet L, Morganti A, Simonneau G, Rubin LJ; Bosentan Effects in iNopErable Forms of chronIc Thromboembolic pulmonary hypertension Study Group. Bosentan for treatment of inoperable chronic thromboembolic pulmonary hypertension: BENEFiT (Bosentan Effects in iNopErable Forms of chronIc Thromboembolic pulmonary hypertension), a randomized, placebo-controlled trial. *J Am Coll Cardiol* 2008; **52**: 2127-2134 [PMID: 19095129 DOI: 10.1016/j.jacc.2008.08.059]

19 **Halank M**, Hoeper MM, Ghofrani HA, Meyer FJ, Stähler G, Behr J, Ewert R, Fletcher M, Colorado P, Nikkho S, Grimminger F. Riociguat for pulmonary arterial hypertension and chronic thromboembolic pulmonary hypertension: Results from a phase II long-term extension study. *Respir Med* 2017; **128**: 50-56 [PMID: 28610669 DOI: 10.1016/j.rmed.2017.05.008]

20 **Takei M**, Kataoka M, Kawakami T, Kuwahira I, Fukuda K. Respiratory function and oxygenation after balloon pulmonary angioplasty. *Int J Cardiol* 2016; **212**: 190-191 [PMID: 27038731 DOI: 10.1016/j.ijcard.2016.03.061]



Published by **Baishideng Publishing Group Inc**
7041 Koll Center Parkway, Suite 160, Pleasanton, CA 94566, USA
Telephone: +1-925-3991568
E-mail: bpgoffice@wjgnet.com
Help Desk: https://www.f6publishing.com/helpdesk
https://www.wjgnet.com



© 2023 Baishideng Publishing Group Inc. All rights reserved.

ISSN 1949-8470 (online)

World Journal of *Radiology*

World J Radiol 2023 June 28; 15(6): 157-215



Published by Baishideng Publishing Group Inc

WJR World Journal of Radiology

Contents

Monthly Volume 15 Number 6 June 28, 2023

MINIREVIEWS

157 Acute pancreatitis: Structured report template of magnetic resonance imaging

Song LJ, Xiao B

170 Radiological parameters to predict pancreatic texture: Current evidence and future perspectives

Kalayarasan R, Himaja M, Ramesh A, Kokila K

ORIGINAL ARTICLE

Retrospective Study

182 Computed tomography angiographic study of surgical anatomy of thyroid arteries: Clinical implications in neck dissection

Bhardwaj Y, Singh B, Bhadoria P, Malhotra R, Tarafdar S, Bisht K

Observational Study

191 Role of contrast-enhanced serial/spot abdominal X-rays in perioperative follow-up of patients undergoing abdominal surgery: An observational clinical study

Dilek ON, Atay A, Gunes O, Karahan F, Karasu Ş

Prospective Study

201 Interobserver reliability of computed tomography angiography in the assessment of ruptured intracranial aneurysm and impact on patient management

Elmokadem AH, Elged BA, Abdel Razek A, El-Serougy LG, Kasem MA, EL-Adalany MA

World Journal of Radiology

Monthly Volume 15 Number 6 June 28, 2023

Contents

ABOUT COVER

Editorial Board Member of *World Journal of Radiology*, Linda Agolli, MD, Doctor, Research Scientist, Department of Radiation Oncology, Faculty of Medicine, University Hospital Carl Gustav Carus, Dresden 01307, Germany. linda.agolli@gmail.com

AIMS AND SCOPE

The primary aim of *World Journal of Radiology* (*WJR*, *World J Radiol*) is to provide scholars and readers from various fields of radiology with a platform to publish high-quality basic and clinical research articles and communicate their research findings online.

WJR mainly publishes articles reporting research results and findings obtained in the field of radiology and covering a wide range of topics including state of the art information on cardiopulmonary imaging, gastrointestinal imaging, genitourinary imaging, musculoskeletal imaging, neuroradiology/head and neck imaging, nuclear medicine and molecular imaging, pediatric imaging, vascular and interventional radiology, and women's imaging.

INDEXING/ABSTRACTING

The *WJR* is now abstracted and indexed in PubMed, PubMed Central, Emerging Sources Citation Index (Web of Science), Reference Citation Analysis, China National Knowledge Infrastructure, China Science and Technology Journal Database, and Superstar Journals Database. The 2022 edition of Journal Citation Reports ® cites the 2021 Journal Citation Indicator (JCI) for *WJR* as 0.48.

RESPONSIBLE EDITORS FOR THIS ISSUE

Production Editor: *Si Zhao*; **Production Department Director:** *Xu Guo*; **Editorial Office Director:** *Jia-Ping Yan*.

NAME OF JOURNAL
World Journal of Radiology

ISSN
ISSN 1949-8470 (online)

LAUNCH DATE
January 31, 2009

FREQUENCY
Monthly

EDITORS-IN-CHIEF
Thomas J Vogl

EDITORIAL BOARD MEMBERS
https://www.wjgnet.com/1949-8470/editorialboard.htm

PUBLICATION DATE
June 28, 2023

COPYRIGHT
© 2023 Baishideng Publishing Group Inc

INSTRUCTIONS TO AUTHORS
https://www.wjgnet.com/bpg/gerinfo/204

GUIDELINES FOR ETHICS DOCUMENTS
https://www.wjgnet.com/bpg/GerInfo/287

GUIDELINES FOR NON-NATIVE SPEAKERS OF ENGLISH
https://www.wjgnet.com/bpg/gerinfo/240

PUBLICATION ETHICS
https://www.wjgnet.com/bpg/GerInfo/288

PUBLICATION MISCONDUCT
https://www.wjgnet.com/bpg/gerinfo/208

ARTICLE PROCESSING CHARGE
https://www.wjgnet.com/bpg/gerinfo/242

STEPS FOR SUBMITTING MANUSCRIPTS
https://www.wjgnet.com/bpg/GerInfo/239

ONLINE SUBMISSION
https://www.f6publishing.com

© 2023 Baishideng Publishing Group Inc. All rights reserved. 7041 Koll Center Parkway, Suite 160, Pleasanton, CA 94566, USA
E-mail: bpgoffice@wjgnet.com https://www.wjgnet.com

World Journal of Radiology

Submit a Manuscript: https://www.f6publishing.com

World J Radiol 2023 June 28; 15(6): 157-169

DOI: 10.4329/wjr.v15.i6.157

ISSN 1949-8470 (online)

MINIREVIEWS

Acute pancreatitis: Structured report template of magnetic resonance imaging

Ling-Ji Song, Bo Xiao

Specialty type: Radiology, nuclear medicine and medical imaging

Provenance and peer review: Invited article; Externally peer reviewed.

Peer-review model: Single blind

Peer-review report's scientific quality classification

Grade A (Excellent): 0
Grade B (Very good): 0
Grade C (Good): B
Grade D (Fair): D
Grade E (Poor): 0

P-Reviewer: Mohey NM, Egypt; Nakano H, Japan

Received: March 27, 2023
Peer-review started: March 27, 2023
First decision: May 13, 2023
Revised: May 25, 2023
Accepted: June 16, 2023
Article in press: June 16, 2023
Published online: June 28, 2023

Ling-Ji Song, Bo Xiao, Department of Radiology, Sichuan Key Laboratory of Medical Imaging, The Affiliated Hospital of North Sichuan Medical College, Nanchong 637000, Sichuan Province, China

Corresponding author: Bo Xiao, Doctor, MD, PhD, Associate Professor, Department of Radiology, Sichuan Key Laboratory of Medical Imaging, The Affiliated Hospital of North Sichuan Medical College, No. 1 Maoyuan South Street, Nanchong 637000, Sichuan Province, China. xiaoboimaging@163.com

Abstract

Acute pancreatitis (AP) is a common acute abdomen disease of the digestive system. It has a potentially fatal risk because of its variable severity and various complications. With the widespread application of the Revised Atlanta Classification, new requirements for AP imaging reports are introduced. Experts in abdominal radiology and pancreatology in the United States published the first structured computed tomography reporting template for AP in 2020. However, there is no corresponding structured magnetic resonance imaging (MRI) reporting template globally. Therefore, this article focuses on the structured MRI report of AP images from our pancreatitis imaging center, which is intended to improve the systematic understanding of this disease and standardize the writing of MRI structured reports. In the meantime, we aim to promote the clinical diagnosis and assessment of MRI efficacy for AP and its multiple complications. It is further intended to facilitate academic exchanges and scientific research between different medical centers.

Key Words: Magnetic resonance imaging; Acute pancreatitis; Structured reporting; Computed tomography

©The Author(s) 2023. Published by Baishideng Publishing Group Inc. All rights reserved.

Core Tip: Acute pancreatitis (AP) is a common digestive disease. Experts in abdominal radiology and pancreatology in the United States published the first structured computed tomography reporting template for AP in 2020, but there is no corresponding structured magnetic resonance imaging (MRI) reporting template internationally. For this reason, this article focuses on the structured MRI report of AP and its standardization, which is beneficial for clinicians to diagnose and evaluate the MRI efficacy of AP and its multiple complications. At the same time, it will promote academic exchanges between different medical centers as well as scientific research and teaching.

Citation: Song LJ, Xiao B. Acute pancreatitis: Structured report template of magnetic resonance imaging. *World J Radiol* 2023; 15(6): 157-169
URL: https://www.wjgnet.com/1949-8470/full/v15/i6/157.htm
DOI: https://dx.doi.org/10.4329/wjr.v15.i6.157

INTRODUCTION

Acute pancreatitis (AP) is one of the most common causes of hospitalization due to gastrointestinal disorders and it requires multidisciplinary treatment[1,2]. AP inflammation can be confined to the pancreas itself, and can further involve other tissues and remote organs[3]. Approximately 15%-20% of AP patients will progress to severe acute pancreatitis (SAP)[4], which is potentially lethal and remains one of the most challenging diseases to date. In China, the majority of AP patients are caused by cholelithiasis, alcoholism, and hyperlipidemia[5]. With the in-depth study of pathophysiological mechanisms of AP, traditional terminologies of imaging reports related to AP have been updated in the Revised Atlanta Consensus[6]. In fact, it is both an opportunity and a challenge for radiologists. In 2020, American experts in the field of abdominal radiology and pancreatology first released AP's computed tomography (CT) structured report template[7]. It is designed based on contrast-enhanced CT. But to the best of our knowledge, magnetic resonance imaging (MRI) has additionally important values in the AP severity assessment at early-phase and differential diagnosis of AP-related collection complications [3,8,9]. However, there is a lack of corresponding MRI structured report template in this field. In this article, therefore, we have combined our clinical practice and previous research data to introduce the structured MRI report template for AP. Our aim is to facilitate the standardization of MRI report writing and clinical multidisciplinary team communication for AP patients.

IMAGING INDICATIONS OF ACUTE PANCREATITIS

AP is a dynamically changing disease. In the clinical settings, most AP patients have a typical clinical course, symptoms and signs, and serum enzyme characteristics[10]. Under normal circumstances, imaging examination is not the first or mandatory choice. However, AP patients with the following aspects need to be examined in time: (1) Difficulty in differential diagnosis of other acute abdomen disorders; (2) serum enzymatic levels do not reach the relevant threshold; (3) confirm the clinical prediction of SAP; and (4) suspected cholelithiasis and other neoplastic complications[11]. In addition, the detection of various local complications in the late stage of AP and the evaluation of curative effect after treatment are also indications for AP repeated imaging examination[6,12].

For radiologists, the first step should be to identify the patient's general information (gender, age, inducement, previous history, concomitant diseases, *etc*). It is essential for the diagnosis and treatment of pancreatic diseases. For instance, men are prone to alcoholic AP due to alcohol abuse, while women are prone to gallstone AP[13]. The occurrence of AP in adolescents may be related to genetic factors and biliopancreatic duct anatomical variants. In contrast, AP in the elderly may be severe and complicated by advanced age factors and the coexistence of multiple underlying diseases. The medical history of pregnancy, trauma, and endoscopic retrograde cholangiopancreatography (ERCP) is also important in determining the etiology of AP. Additionally, Sadr-Azodi *et al*[14] suggest that smoking may be an independent risk factor for AP. Another study further confirmed that smoking was positively associated with the development of pancreatitis[15]. Last but most importantly, patients with underlying renal disease or renal insufficiency need to avoid CT-enhanced examinations[6,16]. Accordingly, the emergence MRI can make up for the deficiency of CT.

IMAGING TECHNIQUES OF ACUTE PANCREATITIS

Early imaging of AP (within 72 h of onset) is frequently deceptive due to underestimate the true extent

of parenchymal involvement and the inability to reliably assess early complications[17,18]. However, revised Atlanta International Consensus still suggests enhanced CT is the primary imaging method for the initial diagnosis of AP patients. It can clearly diagnose AP and provide a better evaluation of pancreatic necrosis, local complications, and the severity of AP. Occasionally, the application of contrast agents has been reported to aggravate the condition of AP[19]. Also, CT examinations have radiation. So accordingly, many studies at domestic and abroad have used conventional MRI sequences combined with diffusion-weighted imaging (DWI) to detect AP. Some scholars have confirmed that the diagnostic value of the DWI technique in AP is equivalent to that of enhanced CT and exceeds the capability of plain CT[20]. They believe that DWI can be used as a powerful tool for evaluating and following up AP [20]. In addition, MRI is feasible for patients with a medical history of iodine allergy or acute renal insufficiency. Moreover, for pregnant women, children, and patients requiring multiple reviews, MRI can be utilized to evaluate the pancreas and peripancreatic conditions.

Taking our unit as an example, we use the following MRI sequences and parameters for comprehensive evaluation of AP (Tables 1 and 2), covering T1-weighted imaging (T1WI) (anatomy, hemorrhage), T2-weighted imaging (T2WI) (effusion, necrosis), DWI (early diffusion restriction), magnetic resonance cholangiopancreatography (MRCP) (observation of the pancreaticobiliary system, effusion), and contrast-enhancement scans (blood supply). Since each medical center has different MRI manufacturers and different imaging protocols, we recommend the mentioned-above sequences for reference. On the basis of our clinical practice, most AP patients are able to complete MRI examinations. Compared to enhanced CT, MRI has the following advantages for AP: (1) MRI is a non-ionizing radiation-free diagnostic imaging that can be used for patients who require multiple follow-up scans; (2) The diagnostic ability of MRI plain scan for pancreatic necrosis is comparable to that of contrast-enhanced CT[20]; (3) Fat-suppressed T1WI is more sensitive than CT for the diagnosis of pancreatic/peripancreatic hemorrhage[21]; (4) Fat-suppressed T2WI is appropriate for the detection of peripancreatic fat necrosis; (5) Fat-suppressed T2WI is significantly better than CT in showing small amounts of "non-liquid" substances within acute necrotic collection (ANC) and walled-off necrosis (WON); (6) MRCP is superior to CT in demonstrating morphological changes of main pancreatic duct (MPD) and the connectivity between the MPD and pseudocyst/WON; and (7) MRI is a reliable modality for staging the severity of AP and has predictive value for disease prognosis. Indeed, MRI has some shortcomings. For example, it is not as good as CT for peripancreatic infection gas findings. MRI needs a long scanning time, and presents difficulty in completing the examination in some SAP patients, as well as a relatively high cost. It is worth mentioning that clinicians need to clarify the advantages and disadvantages of various imaging techniques in order to select the proper examination method for each individual with AP.

STRUCTURED REPORT TEMPLATE OF MRI FOR ACUTE PANCREATITIS

As for the initial CT examination of AP, the Revised Atlanta Consensus recommends that it is better to perform CT 3 d after AP onset[6,22]. At this time, the evaluation of the degree of inflammation and the confirmation of pancreatic necrosis are more reliable, and they may help facilitate the differentiation between acute peripancreatic fluid collection (APFC) and ANC[17]. Furthermore, some scholars have found that MRI performed within 3 d is also helpful in determining the severity of AP and evaluating the prognosis[21].

The MRI structured report for AP should include the description of the pancreas itself, peripancreatic conditions, related complications, and the severity score. Moreover, changes of the lesions before and after treatment need to be described, as shown in Table 3[21,23].

INTERPRETATION AND CLINICAL VALUE OF EVALUATION INDEXES OF STRUCTURED IMAGING REPORT

Pancreatic necrosis

Pancreatic necrosis refers to the pathological accumulation of inactivated pancreatic tissue, which is a relatively common local complication of AP[24]. The extent of pancreatic necrosis can be subdivided according to the anatomical region of the organ and the percentage of unenhanced pancreatic parenchyma, such as < 30%, 31%-50%, and > 50% subcategories[25]. These subcategories are clinically significant because the volume of glandular necrosis can predict serious complications such as infection and organ failure. When talking about necrotizing pancreatitis, we previously always thought of the severity of "pancreas itself" necrosis. This is because of the influence of the scoring system based on the degree of pancreatic parenchymal necrosis proposed by Balthazar. However, the Revised Atlanta Consensus reclassified pancreatic necrosis into three subtypes: (1) Pancreatic and peripancreatic necrosis (mixed type) (Figure 1A and B); (2) peripancreatic necrosis only (Figure 1C and D); and (3) pancreatic necrosis only (Figure 2). Although the mixed type is the most prevalent in clinical practice, the latter two

Table 1 Magnetic resonance imaging sequences and parameters (1.5 Tesla) for acute pancreatitis

Sequence	Repetition time (ms)	Echo time (ms)	Slice thickness (mm)	Slice space (mm)	Matrix	Field of view (mm)	Flip angle
T1WI	6.19	2.86	2.4	0	143 × 272	300 × 400	15°
IP/OP	6.19	4.47	2.4	0	143 × 272	300 × 400	15°
T2WI	2000	78.26	5	1	256 × 152	300 × 380	150°
DWI	3611	64	6	1.2	114 × 144	300 × 380	90°
MRCP	6500	1004	60	60	336 × 336	340 × 340	160°
DCE MRI	6.19	2.86	2.4	0	143 × 272	300 × 400	15°

IP/OP: In-phase/Out-of-phase; DWI: Diffusion-weighted imaging; MRCP: Magnetic resonance cholangiopancreatography; DCE: Dynamic contrast-enhancement.

Table 2 Magnetic resonance imaging sequences and parameters (3.0 Tesla) for acute pancreatitis

Sequence	Repetition time (ms)	Echo time (ms)	Slice thickness (mm)	Slice space (mm)	Matrix	Field of view (mm)	Flip angle
T1WI	3.91	1.42	4.5	0	304 × 274	400 × 300	12°
T2WI	8963	116.16	6	20	256 × 218	380 × 300	90°
DWI	3555	63.8	6.0	20	128 × 101	380 × 300	90°
MRCP	6000	753.6	60	0	368 × 276	300 × 300	180°
DCE MRI	3.91	1.42	4.5	0	304 × 274	400 × 300	12°

DWI: Diffusion-weighted imaging; MRCP: Magnetic resonance cholangiopancreatography; DCE: Dynamic contrast-enhancement.

subtypes also require attention. As proposed by Meyrignac *et al*[26] and Çakar *et al*[27] in recent years, the amount of peripancreatic necrosis was more suitable for AP severity determination and prognostic analysis than the pancreatic necrosis score proposed by Balthazar. And meanwhile, it could better predict organ failure and secondary infection. Cucuteanu *et al*[28] found that extra-pancreatic necrotic volume was the best predictor for evaluating severe pancreatitis with an area under the curve of 0.993. MRI has good soft tissue resolution, so it is accurate to determine the nature of pancreatic necrosis and the measurement of extra-pancreatic necrotic volume.

Pancreatic divisum

Pancreatic divisum is an anatomical variation of the pancreatic duct system, with an incidence of approximately 10% in the general population. About 5% of these patients will present with symptoms [29]. MRI combined with MRCP is the first choice for the diagnosis of pancreatic divisum. It has been estimated that approximately 20% of AP patients with unknown etiology suffer from pancreatic divisum[29]. Therefore, MRI structured report template for AP should include the description of pancreatic divisum.

Peripancreatic changes

As we all known, the term "AP-related hemorrhage" is not mentioned in the Revised Atlanta Classification. Pathologically, AP is still divided into interstitial edematous pancreatitis and hemorrhagic necrotizing pancreatitis (necrotic lesions often accompanied by hemorrhagic foci)[30]. Peripancreatic fatty tissue necrosis is a form of inflammatory extension involving the peripancreatic intra-abdominal fatty tissue and adipose tissue in the retroperitoneal spaces[31]. MRI might show the intra-abdominal inflammatory involvement located in the omental or mesenteric fatty tissue regions. In our clinical practice, we found that peripancreatic fat necrosis combined with hemorrhage could be detected by MRI (patchy T1-hyperintense on fat suppression T1WI). Although early detection of this pathology condition may have no effect on patient management, necrosis combined with hemorrhage may be associated with the prognosis of AP patients. Scholars show that pancreatic/peripancreatic hemorrhage demonstrated on MR imaging (Figure 3A) has a good correlation with the severity of AP[21], which can be useful in prognostic determination.

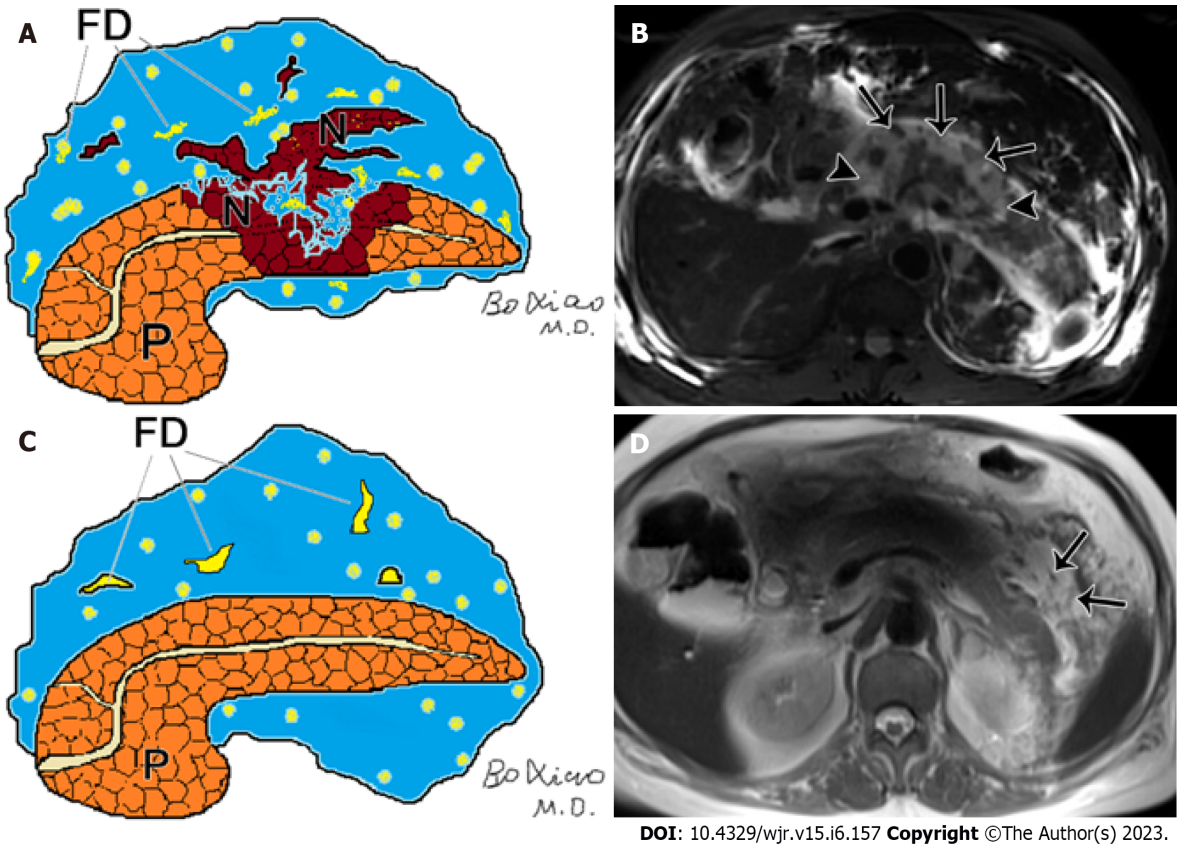
In addition to the corresponding changes in retroperitoneal spaces in AP, changes in subperitoneal spaces should also be observed. Some scholars have conducted clinical studies on this issue. AP is prone to involve the transverse colonic mesentery (incidence of 61.9%)[32] (Figure 3B). Moreover, AP also easily involved the small intestine mesentery (incidence of 67.9%)[33]. Both the transverse-mesocolon

Table 3 Structured report template of magnetic resonance imaging for acute pancreatitis

Contents	Descriptions
Pancreas itself	
Enlargement	Diffuse; Focal (head/neck/body/tail)
Edge	Clear; blur
Signal intensity	Variable owing to internal necrosis and/or hemorrhage
Enhancement	Homogeneous; Heterogeneous
Pancreatic duct	Normal; dilated (mm); stricture (mm); calculi (mm)
Pancreatic necrosis	
Position	Head; neck; body; tail
Range[1]	< 30%; 30%-50%; > 50%
Peripancreatic changes	
Renal fascia and peritoneum	Thickening (anterior renal fascia/posterior renal fascia/lateral cone fascia/lateral abdominal wall peritoneum); Enhanced or not?
Peripancreatic fat space	Clear; Blur
Peripancreatic fat necrosis	Site (retroperitoneal space/transverse colonic mesentery/small intestinal mesentery); amount (patchy/large flake); whether combined with hemorrhage (fat-suppressed T1-hyperintense)[21]
Peripancreatic collection	Position[2]; volume (linear/patchy/large); encapsulated round/oval; contents (homogeneous fluid signal/heterogeneous mixed signal)
Local complication	
I Pancreatic/peripancreatic collection (type)	Some of the features can be seen in the above peripancreatic collection
APFC	Yes or no?
ANC	Yes or no?
Pseudocyst	Yes or no? If yes, thickness of the cyst wall (mm, uniform?); Is adjacent to and pushing out adjacent organs (stomach/duodenum, *etc.*)?
WON	Yes or no? If yes, thickness of the lesion wall (mm); Whether the wall is enhanced and the pattern of enhancement? "Non-liquid substances" within WON (< 10%, 10%-40%, > 40%)[23]; Is WON close to adjacent organs (stomach/duodenum/AC/DC)?
II Infection of collection	Suggestive signs [bubble sign, air-fluid level sign]
Complicated intestinal fistula	Relationship between collection and the intestinal fistula canal, and the intestinal segment of intestinal fistula (duodenum/AC/DC)
III Pancreatic duct disruption syndrome	Site (head/neck/body); Is MPD dilated on the upstream/caudal side of the interruption (mm)? Relationship with adjacent pseudocyst/WON?
IV Vascular complications	
Venous thrombosis	SV; SMV; PV, *etc.*
Sinistral portal hypertension	Establishment of collateral vascular network[3]
Pseudoaneurysm	Size (mm) and involvement artery[4]
Organ complications	
Liver	Fatty liver (Signal difference of liver in the in-phase and out-of-phase)
Gallbladder and bile duct	Gallbladder stones (sandy/granular/filled); Common bile duct stones (site, number, size) and maximum duct diameter (mm)
Lung	Extent of pneumonia, pleural effusion
Subcutaneous and intermuscular space	Edema/effusion
Severity image score (MRSI)	(0-10) score
Comparison with previous imaging findings	For AP review, describe the pancreatic/peripancreatic changes after treatment; for surgical treatment, describe the site of the external drainage tube and internal covered metal stent

[1]The ratio of the area of pancreatic necrosis in the largest slice to the whole pancreatic area.

[2]Sites of effusion include: left/right pararenal anterior spaces, perirenal spaces, posterior pararenal spaces, omental sac, bilateral paracolic sulcus, transverse colonic mesentery, small intestinal mesentery, greater omentum, other abdominal spaces, pelvic extraperitoneal spaces, pelvis cavity, thoracic cavity, and mediastinum.
[3]Such as left/right gastric omental vein, gastrocolic trunk, short gastric vein, submucosal vein of gastric fundus and gastric coronary vein).
[4]Such as splenic artery, pancreaticoduodenal artery, gastroduodenal artery, superior mesenteric artery, and celiac trunk. APFC: Acute peripancreatic fluid collection; ANC: Acute necrotic collection; WON: Walled-off necrosis; AC: Ascending colon; DC: Descending colon; MPD: Main pancreatic duct; SV: Splenic vein; SMV: Superior mesenteric vein; PV: Portal vein; IEP: Interstitial edematous pancreatitis; ANP: Acute necrotizing pancreatitis.



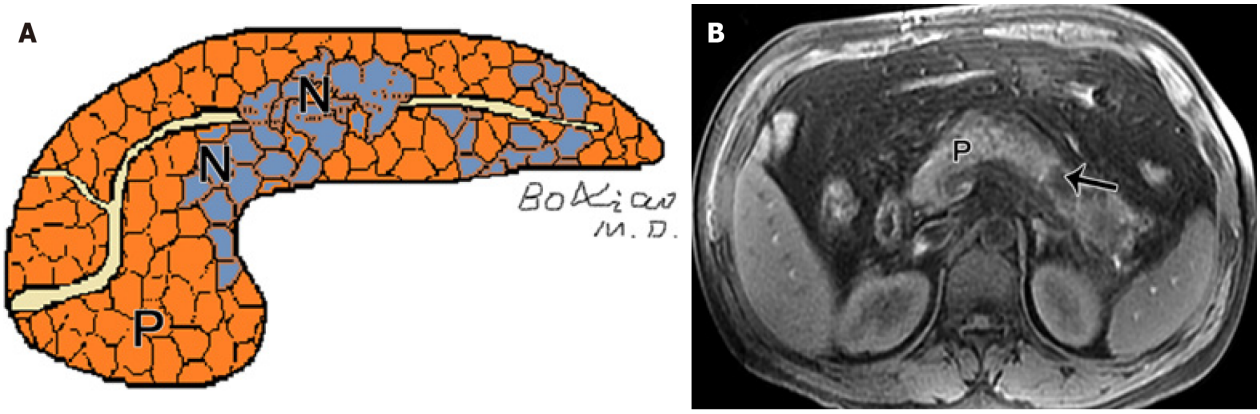
DOI: 10.4329/wjr.v15.i6.157 **Copyright** ©The Author(s) 2023.

Figure 1 Pancreatic and peripancreatic necrosis. A: Schematic diagram of pancreatic and peripancreatic necrosis (mixed type): pancreatic body necrosis (N) accompanied by peripancreatic fatty tissue debris (FD); B: A 61-year-old male with acute necrotizing pancreatitis (both pancreatic and peripancreatic necrosis). Fat-suppressed axial T1-weighted imaging shows a wide range of necrosis of the head and body of the pancreas (arrowheads), as well as peripancreatic collections containing large amounts of fat necrotic debris (arrows); C: Schematic diagram of necrotizing pancreatitis (peripancreatic necrosis alone): FD and absence of necrosis of pancreatic parenchyma; D: A 65-year-old woman with acute necrotizing pancreatitis (peripancreatic necrosis alone). Magnetic resonance imaging T2WI shows multiple patchy fatty fragments (hypointensity areas) (arrows) surrounding the pancreas.

involvement score and the mesenteric involvement score correlated well with the MRSI score[32,33]. These signs of subperitoneal space invasion can contribute to the prognostic assessment of the disease.

Local complications

The Revised Atlanta Consensus renamed four local fluid collections following AP. Of note, the exact time from the onset of the patient's initial symptoms to the imaging examination needs to be clarified. For radiologists, it is important for the correct nomenclature of peripancreatic fluid collections[2]. Typically, an imaging diagnosis of a pseudocyst or WON is reported equivalent to 4 wk after the onset of APFC (Figure 3C) or ANC (Figure 1). In particular, while characterizing the contents of a WON (Figure 3D), the percentage of solid debris within the overall fluid collection needs to be identified. That can be valuable in the choice of patient treatment decision-making. Rana *et al*[23] performed endoscopic ultrasound-guided treatment in 43 patients with symptomatic WON. When the solid necrotic debris in WON is less than 10%, only one endoscopic drainage is required. Then, at least two endoscopic drainages are required to cure patients if the necrotic debris is between 10% and 40%. If the solid necrotic debris is more than 40%, either endoscopic removal of necrotic tissue under ultrasound or surgical removal of necrotic tissue is additionally required[23]. In other words, with the increase of the amount of solid fragments, the number of transendoscopic operations will increase significantly[23].



DOI: 10.4329/wjr.v15.i6.157 **Copyright** ©The Author(s) 2023.

Figure 2 Peripancreatic necrosis only. A: Schematic diagram of necrotizing pancreatitis (pancreatic necrosis alone): Scattered necrotic lesions (N) within the pancreatic parenchyma; B: A 40-year-old man with necrotizing pancreatitis (pancreatic necrosis alone). Magnetic resonance imaging fat-suppressed T1-weighted imaging shows hypointensity area (arrow) in the pancreatic body, as well as absence of peripancreatic fat involvement.

DWI technology has a good ability to distinguish between aseptic, infected or necrotic components in WON[3,9,34]. Therefore, MRI is also a powerful tool for the qualitative and quantitative analysis of solid necrotic debris in WON.

Complications of infection

If peripancreatic fluid collection is complicated with infection, the mortality of AP patients will be significantly increased[6,35]. When gas-bubble or gas-fluid level signs appear in the APFC/ANC or pseudocyst/WON, radiologists need to describe in the MRI report and suggest infectious collections (Figure 3E). Besides, long-term fluid collections in the peripancreatic areas may erode the adjacent digestive tract and cause a secondary intestinal fistula[35]. Therefore, we need to report the segment of the intestinal canal that may be complicated by intestinal fistula. Patients with combined intestinal fistulas are indications for surgical procedures[36].

Disconnected pancreatic duct syndrome

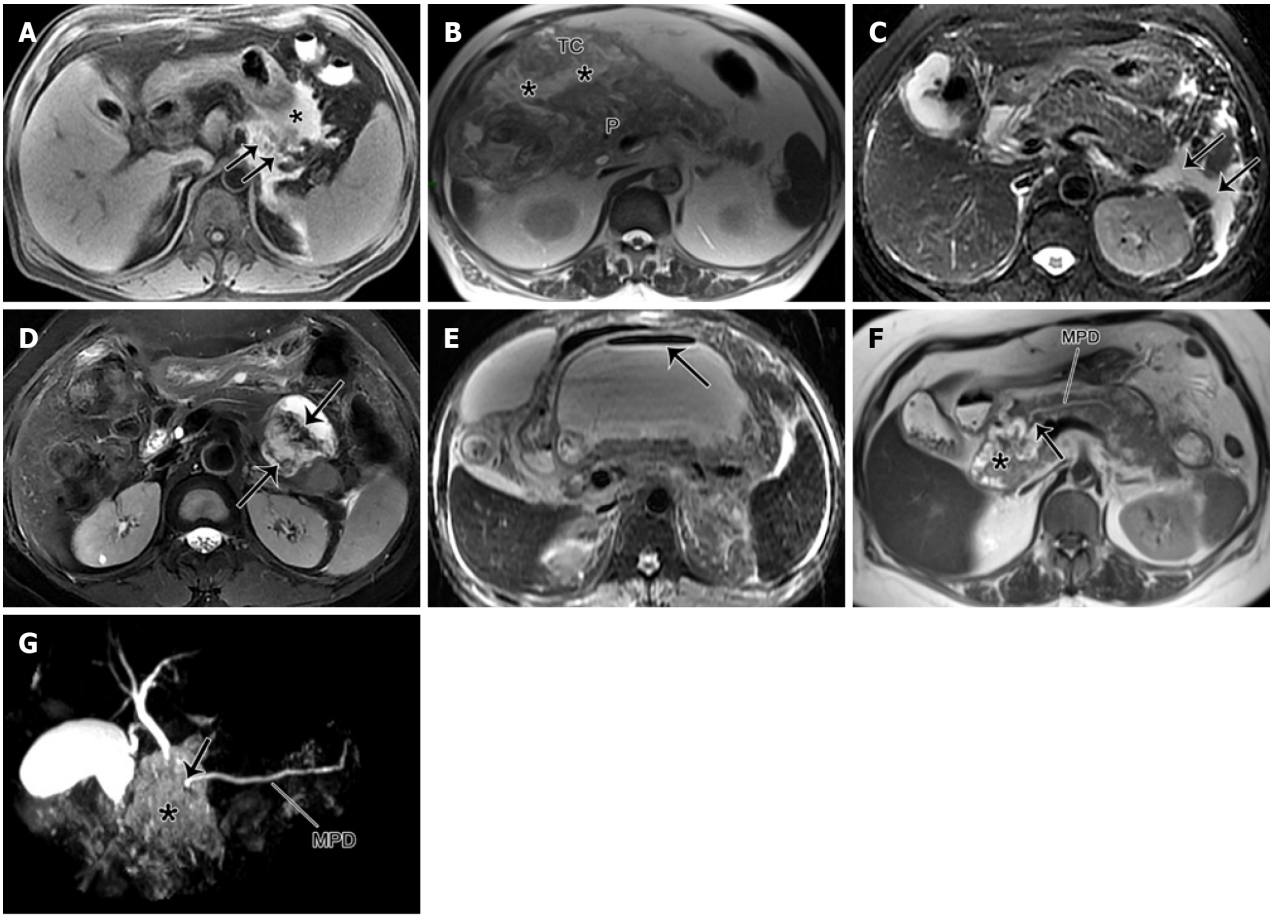
If an encapsulated fluid collection of the pancreas/peripancreatic zones involves the entire length of a pancreas (transmural necrosis), the collection lesion can often disrupt the MPD (Figure 3F and G). That is to say, it can lead to "disconnected pancreatic duct syndrome (DPDS)"[37], which is commonly seen in acute necrotizing pancreatitis. A recent prospective study shows that about 46.2% of patients with necrotizing pancreatitis will develop DPDS[38]. In addition, Maatman *et al*[39] have confirmed that an increased degree of pancreatic glandular necrosis is associated with the development of DPDS. Most importantly, the presence of such complications often requires surgical management. ERCP is the gold standard for diagnosing DPDS with 100% sensitivity, but it is invasive[40]. Magnetic resonance cholangiopancreatography (MRCP) is a non-invasive magnetic resonance technique. A recent study reported 92% sensitivity of combined MRCP and secretin MRCP in diagnosing DPDS[40]. That it can be seen that MRCP technology in MRI plays an irreplaceable role in the diagnosis of DPDS.

Vascular complications

Sinistral portal hypertension: Although chronic pancreatitis and pancreatic cancer are the main causes of sinistral portal hypertension (SPH), AP-related SPH also requires attention[41]. One study[42] found a 3.3% prevalence of SPH in 633 AP patients who underwent MRI. According to MRSI scores, the prevalence of SPH in mild, moderate, and severe AP increased progressively with 0.6%, 2.9%, and 47.8%, respectively[42]. This complication may be associated with late-phase gastrointestinal bleeding in AP patients and is therefore described in the MR structured report.

Pseudoaneurysm: Pseudoaneurysm is a rare but potentially fatal complication of AP, which is caused by reactive local arteritis following pancreatic proteolytic enzyme erosion[43]. The lesion most frequently involves the splenic, gastroduodenal, or pancreaticoduodenal arteries. If a pseudoaneurysm ruptures and bleeds, it may constitute a life-threatening emergency[24]. MRI can directly show the pseudoaneurysm lumen connected to the adjacent artery and the mural thrombus in the pseudoaneurysm lumen. On the enhanced MRI, the enhancement of the pseudoaneurysm lumen corresponds to that of an adjacent artery, while the non-enhanced area shows mural thrombus formation.

Venous thrombosis: Venous thrombosis is the most common vascular complication of AP[24]. The splenic vein is the most frequent vein invaded by inflammatory extension of the pancreas because of its proximity to the pancreas. Furthermore, the portal and superior mesenteric veins may also be involved.



DOI: 10.4329/wjr.v15.i6.157 **Copyright** ©The Author(s) 2023.

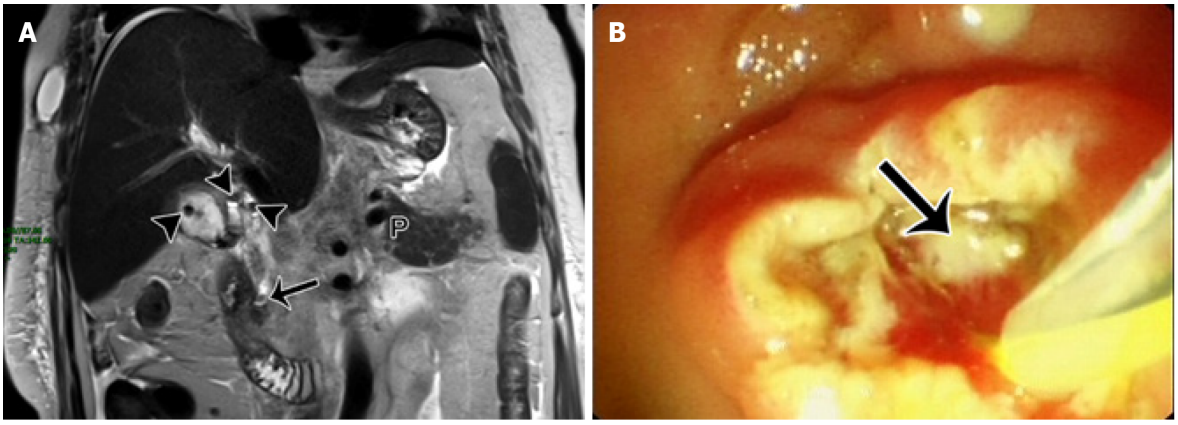
Figure 3 Pancreatic necrosis only. A: A 47-year-old male with acute necrotizing pancreatitis complicated by hemorrhage. Magnetic resonance imaging (MRI) fat-suppressed T1WI depicts a large area of hyperintensity in the pancreatic body (arrow) and peripancreatic areas (*), indicating the presence of pancreatic and peripancreatic fat necrosis with hemorrhage; B: A 73-year-old man with acute necrotizing pancreatitis complicated with transverse mesenteric effusion. MRI T1-weighted imaging (T1WI) demonstrates peripancreatic inflammation spreading from the root of mesentery to the transverse colon along the involved transverse mesentery (*). P: pancreas; C: A 63-year-old woman with acute interstitial pancreatitis with acute peripancreatic fluid collection. MRI fat-suppressed T2WI reveals the uniformly hyperintense fluid collections (arrows) around the pancreas; D: A 53-year-old woman with walled-off necrosis secondary to acute necrotizing pancreatitis (pancreatic and peripancreatic necrosis type). MRI fat-suppressed T2WI shows an enveloped necrotic collection involving the body and tail of the pancreas, with solid necrotic debris (arrows) accounting for more than 40%; E: A 45-year-old man with acute necrotizing pancreatitis accompanied by walled-off necrosis and secondary infection. MRI fat-suppressed T2WI shows extensive walled-off necrosis in the omental sac, as well as a gas-fluid level sign (arrow). Thereafter, the open surgery and drainage for infectious collections was performed; F: A 55-year-old woman with pancreatic duct disruption syndrome secondary to acute necrotizing pancreatitis with walled-off necrosis. MRI T2WI shows an enveloped necrosis lesion (*) in the pancreatic head, and a cut-off sign (arrow) of the main pancreatic duct (MPD) traveling into this lesion (*). G: MRCP reveals that the MPD of the pancreatic body and tail directly enters into the lesion (*) in a right-angle, concomitant with the interrupted MPD.

Dörffel *et al*[44] assessed this issue by color Doppler ultrasonography and found the incidence of venous thrombosis was 30% in acute non-necrotizing pancreatitis and 57% in necrotizing pancreatitis, similar to the conclusion of Jeffrey *et al*[45]. When there is venous thrombosis, MRI shows a loss of the normal vascular flow effect in the involved venous segment. After administration of contrast agent, intravenous filling defects can be seen on the enhanced venous phase images.

Organ complications/comorbidities

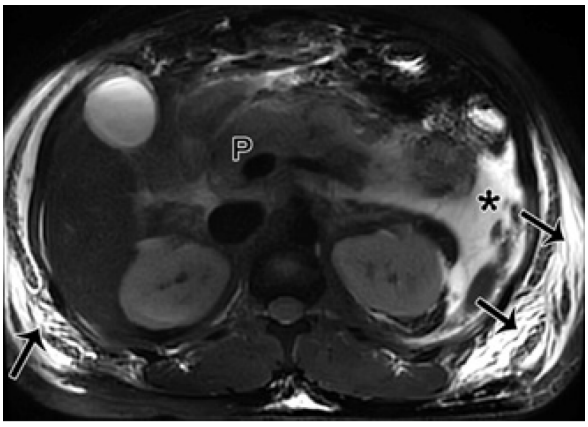
It is well known that three-quarters of the hepatic blood are supplied by the portal system. When AP occurs, many inflammatory factors and free fatty acids could be gathered in the liver during a short period of time, thereafter, MRI manifestations of fatty liver can be seen. Xiao *et al*[46] found that 66% of AP patients could be detected with signs of fatty liver on MRI. And the liver signal difference quantified by in-phase and out-of-phase images was positively correlated with MRSI. With the reduction of plasma triglyceride levels, the performance of the fatty liver on MRI can gradually return to normal[46].

The diagnosis of biliary stones, especially common bile duct stones, is suggestive for the choice of clinical treatment modality[47]. Thus, the MRI report description needs to be focused on gallstone pancreatitis (Figure 4). Furthermore, AP inflammatory exudate has a great impact on the gastrointestinal tract. It often causes damage to the intestinal barrier[48], followed by incomplete intestinal



DOI: 10.4329/wjr.v15.i6.157 **Copyright** ©The Author(s) 2023.

Figure 4 The magnetic resonance imaging report description needs to be focused on gallstone pancreatitis. A 56-year-old woman with acute gallstone pancreatitis. A: Magnetic resonance imaging T2WI coronal imaging shows multiple hypointensity stones (arrowheads) in the gallbladder and gallbladder duct, and another hypointensity stone (arrow) in the lower level of the common bile duct. The patient was underwent an endoscopic retrograde cholangiopancreatography (ERCP) procedure; B: ERCP shows a stone in the lower part of the common bile duct with suppurative conditions (arrow). P: Pancreas.



DOI: 10.4329/wjr.v15.i6.157 **Copyright** ©The Author(s) 2023.

Figure 5 Acute pancreatitis can also cause subcutaneous edema and fluid collection changes in the abdominal walls. A 25-year-old man with acute necrotizing pancreatitis and acute necrotic collection accompanied by conspicuous subcutaneous edema. Magnetic resonance imaging fat-suppressed T1-weighted imaging shows a majority of hyperintense fluid collections (*) in the left pararenal anterior space, and large flaps of hyperintense changes (arrows) in subcutaneous tissues of bilateral flanks and abdominal walls. P: Pancreas.

obstruction. This is associated with abdominal distention and increased intra-abdominal pressure in AP patients.

As far as chest CT is concerned, AP is mostly combined with pleural effusion and signs of compressive atelectasis[49]. Some scholars have suggested that this may be related to the presence of respiratory insufficiency (such as acute respiratory distress syndrome) in AP patients[50].

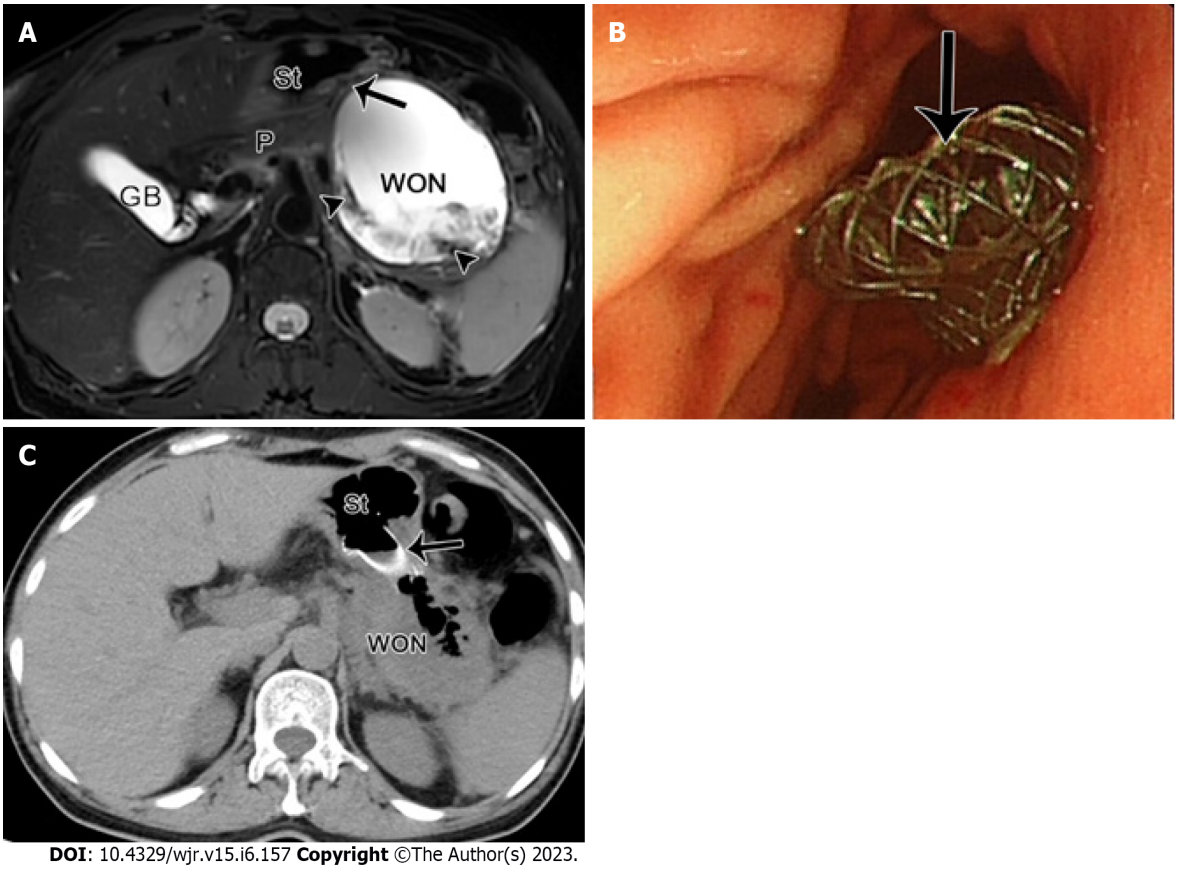
AP can also cause subcutaneous edema and fluid collection changes in the abdominal walls (Figure 5). Yang *et al*[51] found that 53.8% of AP patients showed abdominal wall edema on MRI. The abdominal wall edema score was positively correlated with the MRSI score[51]. Also, the degree of abdominal wall edema could indirectly reflect the severity of AP.

Comparison before and after treatment

The radiological changes in pancreatic/peripancreatic fluid collections before and after treatment should be described emphatically (Figure 6) in order to guide the adjustment of clinical treatment. In the cases of surgical drainage or built-in metal stents[52], the relationship between the site of the placement and the surrounding tissues and organs should be observed.

CONCLUSION

In summary, AP is a systemic and complex disease. The radiologists need to assist the clinicians in



DOI: 10.4329/wjr.v15.i6.157 **Copyright** ©The Author(s) 2023.

Figure 6 The radiological changes in pancreatic/peripancreatic fluid. A 49-year-old woman with acute necrotizing pancreatitis and pancreatic walled-off necrosis, performed by endoscopic ultrasound drainage. A: Magnetic resonance imaging fat-suppressed T1-weighted imaging shows a walled-off necrosis (WON) with a diameter of 10 cm × 9 cm in the omental sac and pancreatic body and tail, as well as numerous necrotic fragments (arrowheads) within the WON. The WON is adjacent to the gastric body; B: Thereafter, under the guidance of endoscopic ultrasonography, a fully coated mushroom metal stent (arrow) was placed through the stomach for internal drainage; C: Postoperative computed tomography image shows that the WON was apparently decreased, with a large amount of gas and a high-density stent (arrow) in place. St: Stomach, P: Pancreas, GB: Gallbladder.

selecting a reasonable imaging modality. Although enhanced CT is considered to be the main imaging method for the first diagnosis of AP patients, MRI has good soft tissue resolution and various sequence techniques. Thus, it can be better evaluated and follow up the condition of AP patients. In the writing of MR structured imaging report, we need to take into account the systematic description of the pancreas itself, peripancreatic changes, local complications, organ complications, and the dynamic changes after treatment. If the patient's condition is tolerated and the hospital equipment permits, we recommend that the patient be examined by MRI. The MRI structured report template of AP recommended in this paper could be used as a reference for different centers. Indeed, multi-center validation of MR structured report template at domestic and abroad is needed in order to constantly improve and update in the future clinical practice.

FOOTNOTES

Author contributions: Song LJ and Xiao B contributed equally to this work; Xiao B designed the research study; Song LJ performed the research; Song LJ and Xiao B analyzed the data and wrote the manuscript; All authors have read and approve the final manuscript.

Conflict-of-interest statement: All the authors declare that they have no conflict of interest.

Open-Access: This article is an open-access article that was selected by an in-house editor and fully peer-reviewed by external reviewers. It is distributed in accordance with the Creative Commons Attribution NonCommercial (CC BY-NC 4.0) license, which permits others to distribute, remix, adapt, build upon this work non-commercially, and license their derivative works on different terms, provided the original work is properly cited and the use is non-commercial. See: https://creativecommons.org/Licenses/by-nc/4.0/

Country/Territory of origin: China

ORCID number: Ling-Ji Song 0000-0003-4508-9654; Bo Xiao 0000-0001-5862-974X.

S-Editor: Liu JH
L-Editor: A
P-Editor: Zhao S

REFERENCES

1 **Li F**, Zhang F, Wan X, Wu K, Liu Q, Qiu C, Yin H, Lyu J. Infections in Acute Pancreatitis: Organisms, Resistance-Patterns and Effect on Mortality. *Dig Dis Sci* 2023; **68**: 630-643 [PMID: 36562889 DOI: 10.1007/s10620-022-07793-1]
2 **Ortiz Morales CM**, Girela Baena EL, Olalla Muñoz JR, Parlorio de Andrés E, López Corbalán JA. Radiology of acute pancreatitis today: the Atlanta classification and the current role of imaging in its diagnosis and treatment. *Radiologia (Engl Ed)* 2019; **61**: 453-466 [PMID: 31153603 DOI: 10.1016/j.rx.2019.04.001]
3 **Sureka B**, Rai B, Varshney V, Nag VL, Garg MK, Garg PK, Yadav T, Khera PS, Goel A. Quantitative diffusion-weighted magnetic resonance imaging for prediction of early infection in pancreatic collections: Results of a pilot study. *Saudi J Gastroenterol* 2020; **26**: 20-25 [PMID: 31997778 DOI: 10.4103/sjg.SJG_411_19]
4 **Pavlidis ET**, Pavlidis TE. Management of infected acute necrotizing pancreatitis. *World J Clin Cases* 2023; **11**: 482-486 [PMID: 36686342 DOI: 10.12998/wjcc.v11.i2.482]
5 **Li YL**, Zhang DD, Xiong YY, Wang RF, Gao XM, Gong H, Zheng SC, Wu D. Development and external validation of models to predict acute respiratory distress syndrome related to severe acute pancreatitis. *World J Gastroenterol* 2022; **28**: 2123-2136 [PMID: 35664037 DOI: 10.3748/wjg.v28.i19.2123]
6 **Banks PA**, Bollen TL, Dervenis C, Gooszen HG, Johnson CD, Sarr MG, Tsiotos GG, Vege SS; Acute Pancreatitis Classification Working Group. Classification of acute pancreatitis--2012: revision of the Atlanta classification and definitions by international consensus. *Gut* 2013; **62**: 102-111 [PMID: 23100216 DOI: 10.1136/gutjnl-2012-302779]
7 **Khurana A**, Nelson LW, Myers CB, Akisik F, Jeffrey BR, Miller FH, Mittal P, Morgan D, Mortele K, Poullos P, Sahani D, Sandrasegaran K, Tirkes T, Zaheer A, Patel BN. Reporting of acute pancreatitis by radiologists-time for a systematic change with structured reporting template. *Abdom Radiol (NY)* 2020; **45**: 1277-1289 [PMID: 32189022 DOI: 10.1007/s00261-020-02468-9]
8 **Türkvatan A**, Erden A, Türkoğlu MA, Seçil M, Yener Ö. Imaging of acute pancreatitis and its complications. Part 1: acute pancreatitis. *Diagn Interv Imaging* 2015; **96**: 151-160 [PMID: 24512896 DOI: 10.1016/j.diii.2013.12.017]
9 **de Freitas Tertulino F**, Schraibman V, Ardengh JC, do Espírito-Santo DC, Ajzen SA, Torrez FR, Lobo EJ, Szejnfeld J, Goldman SM. Diffusion-weighted magnetic resonance imaging indicates the severity of acute pancreatitis. *Abdom Imaging* 2015; **40**: 265-271 [PMID: 25070771 DOI: 10.1007/s00261-014-0205-y]
10 **Szatmary P**, Grammatikopoulos T, Cai W, Huang W, Mukherjee R, Halloran C, Beyer G, Sutton R. Acute Pancreatitis: Diagnosis and Treatment. *Drugs* 2022; **82**: 1251-1276 [PMID: 36074322 DOI: 10.1007/s40265-022-01766-4]
11 **Aghdassi AA**, Seidensticker M. [Imaging diagnostics in acute pancreatitis]. *Internist (Berl)* 2021; **62**: 1044-1054 [PMID: 34524469 DOI: 10.1007/s00108-021-01153-3]
12 **Brizi MG**, Perillo F, Cannone F, Tuzza L, Manfredi R. The role of imaging in acute pancreatitis. *Radiol Med* 2021; **126**: 1017-1029 [PMID: 33982269 DOI: 10.1007/s11547-021-01359-3]
13 **Yadav D**, Lowenfels AB. The epidemiology of pancreatitis and pancreatic cancer. *Gastroenterology* 2013; **144**: 1252-1261 [PMID: 23622135 DOI: 10.1053/j.gastro.2013.01.068]
14 **Sadr-Azodi O**, Andrén-Sandberg Å, Orsini N, Wolk A. Cigarette smoking, smoking cessation and acute pancreatitis: a prospective population-based study. *Gut* 2012; **61**: 262-267 [PMID: 21836026 DOI: 10.1136/gutjnl-2011-300566]
15 **Ye X**, Lu G, Huai J, Ding J. Impact of smoking on the risk of pancreatitis: a systematic review and meta-analysis. *PLoS One* 2015; **10**: e0124075 [PMID: 25879541 DOI: 10.1371/journal.pone.0124075]
16 **Obed M**, Gabriel MM, Dumann E, Vollmer Barbosa C, Weißenborn K, Schmidt BMW. Risk of acute kidney injury after contrast-enhanced computerized tomography: a systematic review and meta-analysis of 21 propensity score-matched cohort studies. *Eur Radiol* 2022; **32**: 8432-8442 [PMID: 35727320 DOI: 10.1007/s00330-022-08916-y]
17 **Rocha APC**, Schawkat K, Mortele KJ. Imaging guidelines for acute pancreatitis: when and when not to image. *Abdom Radiol (NY)* 2020; **45**: 1338-1349 [PMID: 31712865 DOI: 10.1007/s00261-019-02319-2]
18 **James TW**, Crockett SD. Management of acute pancreatitis in the first 72 hours. *Curr Opin Gastroenterol* 2018; **34**: 330-335 [PMID: 29957661 DOI: 10.1097/MOG.0000000000000456]
19 **Shinya S**, Sasaki T, Nakagawa Y, Guiquing Z, Yamamoto F, Yamashita Y. Acute pancreatitis successfully diagnosed by diffusion-weighted imaging: a case report. *World J Gastroenterol* 2008; **14**: 5478-5480 [PMID: 18803364 DOI: 10.3748/wjg.14.5478]
20 **Shinya S**, Sasaki T, Nakagawa Y, Guiquing Z, Yamamoto F, Yamashita Y. The efficacy of diffusion-weighted imaging for the detection and evaluation of acute pancreatitis. *Hepatogastroenterology* 2009; **56**: 1407-1410 [PMID: 19950800]
21 **Tang MY**, Chen TW, Bollen TL, Wang YX, Xue HD, Jin ZY, Huang XH, Xiao B, Li XH, Ji YF, Zhang XM. MR imaging of hemorrhage associated with acute pancreatitis. *Pancreatology* 2018; **18**: 363-369 [PMID: 29615311 DOI: 10.1016/j.pan.2018.03.004]
22 **Foster BR**, Jensen KK, Bakis G, Shaaban AM, Coakley FV. Revised Atlanta Classification for Acute Pancreatitis: A Pictorial Essay. *Radiographics* 2016; **36**: 675-687 [PMID: 27163588 DOI: 10.1148/rg.2016150097]
23 **Rana SS**, Bhasin DK, Sharma RK, Kathiresan J, Gupta R. Do the morphological features of walled off pancreatic necrosis on endoscopic ultrasound determine the outcome of endoscopic transmural drainage? *Endosc Ultrasound* 2014; **3**: 118-122 [PMID: 24955341 DOI: 10.4103/2303-9027.131039]

24 **Miller FH**, Keppke AL, Dalal K, Ly JN, Kamler VA, Sica GT. MRI of pancreatitis and its complications: part 1, acute pancreatitis. *AJR Am J Roentgenol* 2004; **183**: 1637-1644 [PMID: 15547203 DOI: 10.2214/ajr.183.6.01831637]

25 **Liao Q**, Ding L, Xu X, Yu C, Deng F, Xiong H, He W, Xia L, Zeng X, Lu N, Zhu Y. Pancreatic necrosis volume for predicting readmission and reintervention in acute necrotizing pancreatitis. *Eur J Radiol* 2022; **154**: 110419 [PMID: 35878514 DOI: 10.1016/j.ejrad.2022.110419]

26 **Meyrignac O**, Lagarde S, Bournet B, Mokrane FZ, Buscail L, Rousseau H, Otal P. Acute Pancreatitis: Extrapancreatic Necrosis Volume as Early Predictor of Severity. *Radiology* 2015; **276**: 119-128 [PMID: 25642743 DOI: 10.1148/radiol.15141494]

27 **Çakar İ**, Keven A, Eseroğlu E, Çubuk SM. Role of extrapancreatic necrosis volume in determining early prognosis in patients with acute pancreatitis. *Abdom Radiol (NY)* 2020; **45**: 1507-1516 [PMID: 31428812 DOI: 10.1007/s00261-019-02188-9]

28 **Cucuteanu B**, Negru D, Gavrilescu O, Popa IV, Floria M, Mihai C, Cijevschi Prelipcean C, Dranga M. Extrapancreatic necrosis volume: A new tool in acute pancreatitis severity assessment? *World J Clin Cases* 2021; **9**: 9395-9405 [PMID: 34877275 DOI: 10.12998/wjcc.v9.i31.9395]

29 **Khristenko E**, Tjaden C, Klauß M. [Pancreas divisum and pancreatitis]. *Radiologe* 2021; **61**: 541-547 [PMID: 33942124 DOI: 10.1007/s00117-021-00848-w]

30 **Wessling J**, Peitz U, Hoffmann M, Schreyer AG, Grenacher L. [Acute pancreatitis : Typical findings in computed tomography and magnetic resonance imaging]. *Radiologe* 2021; **61**: 532-540 [PMID: 34061214 DOI: 10.1007/s00117-021-00854-y]

31 **Lenhart DK**, Balthazar EJ. MDCT of acute mild (nonnecrotizing) pancreatitis: abdominal complications and fate of fluid collections. *AJR Am J Roentgenol* 2008; **190**: 643-649 [PMID: 18287434 DOI: 10.2214/AJR.07.2761]

32 **Chi XX**, Zhang XM, Chen TW, Huang XH, Yang L, Tang W, Xiao B. The normal transverse mesocolon and involvement of the mesocolon in acute pancreatitis: an MRI study. *PLoS One* 2014; **9**: e93687 [PMID: 24705446 DOI: 10.1371/journal.pone.0093687]

33 **Chi XX**, Zhang XM, Chen TW, Tang W, Xiao B, Ji YF, Huang XH. Magnetic resonance imaging for the normal mesostenium and involvement of the mesostenium in acute pancreatitis. *Biomed Res Int* 2014; **2014**: 924845 [PMID: 25136639 DOI: 10.1155/2014/924845]

34 **Islim F**, Salik AE, Bayramoglu S, Guven K, Alis H, Turhan AN. Non-invasive detection of infection in acute pancreatic and acute necrotic collections with diffusion-weighted magnetic resonance imaging: preliminary findings. *Abdom Imaging* 2014; **39**: 472-481 [PMID: 24441591 DOI: 10.1007/s00261-014-0076-2]

35 **Umapathy C**, Gajendran M, Mann R, Boregowda U, Theethira T, Elhanafi S, Perisetti A, Goyal H, Saligram S. Pancreatic fluid collections: Clinical manifestations, diagnostic evaluation and management. *Dis Mon* 2020; **66**: 100986 [PMID: 32312558 DOI: 10.1016/j.disamonth.2020.100986]

36 **Banter LR**, Maatman TK, McGuire SP, Ceppa EP, House MG, Nakeeb A, Nguyen TK, Schmidt CM, Zyromski NJ. Duodenal complications in necrotizing pancreatitis: Challenges of an overlooked complication. *Am J Surg* 2021; **221**: 589-593 [PMID: 33218676 DOI: 10.1016/j.amjsurg.2020.11.022]

37 **Vanek P**, Urban O, Trikudanathan G, Freeman ML. Disconnected pancreatic duct syndrome in patients with necrotizing pancreatitis. *Surg Open Sci* 2023; **11**: 19-25 [PMID: 36438587 DOI: 10.1016/j.sopen.2022.10.009]

38 **Maatman TK**, Roch AM, Lewellen KA, Heimberger MA, Ceppa EP, House MG, Nakeeb A, Schmidt CM, Zyromski NJ. Disconnected Pancreatic Duct Syndrome: Spectrum of Operative Management. *J Surg Res* 2020; **247**: 297-303 [PMID: 31685250 DOI: 10.1016/j.jss.2019.09.068]

39 **Maatman TK**, Roch AM, Ceppa EP, Easler JJ, Gromski MA, House MG, Nakeeb A, Schmidt CM, Sherman S, Zyromski NJ. The continuum of complications in survivors of necrotizing pancreatitis. *Surgery* 2020; **168**: 1032-1040 [PMID: 32843212 DOI: 10.1016/j.surg.2020.07.004]

40 **Timmerhuis HC**, van Dijk SM, Verdonk RC, Bollen TL, Bruno MJ, Fockens P, van Hooft JE, Voermans RP, Besselink MG, van Santvoort HC; Dutch Pancreatitis Study Group. Various Modalities Accurate in Diagnosing a Disrupted or Disconnected Pancreatic Duct in Acute Pancreatitis: A Systematic Review. *Dig Dis Sci* 2021; **66**: 1415-1424 [PMID: 32594462 DOI: 10.1007/s10620-020-06413-0]

41 **Li H**, Yang Z, Tian F. Clinical Characteristics and Risk Factors for Sinistral Portal Hypertension Associated with Moderate and Severe Acute Pancreatitis: A Seven-Year Single-Center Retrospective Study. *Med Sci Monit* 2019; **25**: 5969-5976 [PMID: 31400275 DOI: 10.12659/MSM.916192]

42 **Xie CL**, Wu CQ, Chen Y, Chen TW, Xue HD, Jin ZY, Zhang XM. Sinistral Portal Hypertension in Acute Pancreatitis: A Magnetic Resonance Imaging Study. *Pancreas* 2019; **48**: 187-192 [PMID: 30629031 DOI: 10.1097/MPA.0000000000001242]

43 **Kalas MA**, Leon M, Chavez LO, Canalizo E, Surani S. Vascular complications of pancreatitis. *World J Clin Cases* 2022; **10**: 7665-7673 [PMID: 36158481 DOI: 10.12998/wjcc.v10.i22.7665]

44 **Dörffel T**, Wruck T, Rückert RI, Romaniuk P, Dörffel Q, Wermke W. Vascular complications in acute pancreatitis assessed by color duplex ultrasonography. *Pancreas* 2000; **21**: 126-133 [PMID: 10975705 DOI: 10.1097/00006676-200008000-00004]

45 **Easler J**, Muddana V, Furlan A, Dasyam A, Vipperla K, Slivka A, Whitcomb DC, Papachristou GI, Yadav D. Portosplenomesenteric venous thrombosis in patients with acute pancreatitis is associated with pancreatic necrosis and usually has a benign course. *Clin Gastroenterol Hepatol* 2014; **12**: 854-862 [PMID: 24161350 DOI: 10.1016/j.cgh.2013.09.068]

46 **Xiao B**, Zhang XM, Jiang ZQ, Tang W, Huang XH, Yang L, Feng ZS. Fatty liver in acute pancreatitis: characteristics in magnetic resonance imaging. *J Comput Assist Tomogr* 2012; **36**: 400-405 [PMID: 22805667 DOI: 10.1097/RCT.0b013e31825977c2]

47 **Ji YF**, Zhang XM, Li XH, Jing ZL, Huang XH, Yang L, Zhai ZH. Gallbladder patterns in acute pancreatitis: an MRI study. *Acad Radiol* 2012; **19**: 571-578 [PMID: 22366559 DOI: 10.1016/j.acra.2012.01.004]

48 **Koh YY**, Jeon WK, Cho YK, Kim HJ, Chung WG, Chon CU, Oh TY, Shin JH. The effect of intestinal permeability and

endotoxemia on the prognosis of acute pancreatitis. *Gut Liver* 2012; **6**: 505-511 [PMID: 23170158 DOI: 10.5009/gnl.2012.6.4.505]

49 **Kumar P**, Gupta P, Rana S. Thoracic complications of pancreatitis. *JGH Open* 2019; **3**: 71-79 [PMID: 30834344 DOI: 10.1002/jgh3.12099]

50 **Song LJ**, Xiao B. Medical imaging for pancreatic diseases: Prediction of severe acute pancreatitis complicated with acute respiratory distress syndrome. *World J Gastroenterol* 2022; **28**: 6206-6212 [PMID: 36504558 DOI: 10.3748/wjg.v28.i44.6206]

51 **Yang R**, Jing ZL, Zhang XM, Tang W, Xiao B, Huang XH, Yang L, Feng ZS. MR imaging of acute pancreatitis: correlation of abdominal wall edema with severity scores. *Eur J Radiol* 2012; **81**: 3041-3047 [PMID: 22571930 DOI: 10.1016/j.ejrad.2012.04.005]

52 **Heckler M**, Hackert T, Hu K, Halloran CM, Büchler MW, Neoptolemos JP. Severe acute pancreatitis: surgical indications and treatment. *Langenbecks Arch Surg* 2021; **406**: 521-535 [PMID: 32910276 DOI: 10.1007/s00423-020-01944-6]

World Journal of Radiology

Submit a Manuscript: https://www.f6publishing.com

World J Radiol 2023 June 28; 15(6): 170-181

DOI: 10.4329/wjr.v15.i6.170

ISSN 1949-8470 (online)

MINIREVIEWS

Radiological parameters to predict pancreatic texture: Current evidence and future perspectives

Raja Kalayarasan, Mandalapu Himaja, Ananthakrishnan Ramesh, Kathirvel Kokila

Specialty type: Radiology, nuclear medicine and medical imaging

Provenance and peer review: Invited article; Externally peer reviewed.

Peer-review model: Single blind

Peer-review report's scientific quality classification

Grade A (Excellent): 0
Grade B (Very good): 0
Grade C (Good): C
Grade D (Fair): D
Grade E (Poor): 0

P-Reviewer: Kikuyama M, Japan; Yang F, China

Received: April 26, 2023
Peer-review started: April 26, 2023
First decision: May 19, 2023
Revised: June 3, 2023
Accepted: June 14, 2023
Article in press: June 14, 2023
Published online: June 28, 2023

Raja Kalayarasan, Mandalapu Himaja, Department of Surgical Gastroenterology, Jawaharlal Institute of Postgraduate Medical Education and Research, Puducherry 605006, India

Ananthakrishnan Ramesh, Kathirvel Kokila, Department of Radiodiagnosis, Jawaharlal Institute of Postgraduate Medical Education and Research, Puducherry 605006, India

Corresponding author: Raja Kalayarasan, MBBS, MS, MCh, FRCS (Ed), Additional Professor, Department of Surgical Gastroenterology, Jawaharlal Institute of Postgraduate Medical Education and Research, Room No. 5442, 4th floor, Super Specialty Block, Puducherry 605006, India. kalayarasanraja@yahoo.com

Abstract

Preoperative prediction of the postoperative pancreatic fistula risk is critical in the current era of minimally invasive pancreatic surgeries to tailor perioperative management, thereby minimizing postoperative morbidity. Pancreatic duct diameter can be readily measured by any routine imaging used to diagnose pancreatic disease. However, radiological evaluation of pancreatic texture, an important determinant of pancreatic fistula, has not been widely used to predict the risk of postoperative pancreatic fistula. Qualitative and quantitative assessment of pancreatic fibrosis and fat fraction provides the basis for predicting pancreatic texture. Traditionally computed tomography has been utilized in identifying and characterizing pancreatic lesions and background parenchymal pathologies. With the increasing utilisation of endoscopic ultrasound and magnetic resonance imaging for evaluating pancreatic pathologies, elastography is emerging as a promising tool for predicting pancreatic texture. Also, recent studies have shown that early surgery for chronic pancreatitis is associated with better pain relief and preservation of pancreatic function. Pancreatic texture assessment can allow early diagnosis of chronic pancreatitis, facilitating early intervention. The present review outlines the current evidence in utilizing various imaging modalities for determining the pancreatic texture based on different parameters and image sequences. However, multidisciplinary investigations using strong radiologic-pathologic correlation are needed to standardize and establish the role of these non-invasive diagnostic tools in predicting pancreatic texture.

Key Words: Pancreatic fistula; Minimally invasive; Pancreaticoduodenectomy; Pancreatic cancer; Neoplasms; Computed tomography; Endoscopic ultrasound; Ultrasonography;

Magnetic resonance imaging

©The Author(s) 2023. Published by Baishideng Publishing Group Inc. All rights reserved.

Core Tip: Preoperative prediction of pancreatic texture and pancreatic fistula risk can guide selecting patients who could derive maximum benefit from minimally invasive pancreatoduodenectomy. Also, pancreatic texture evaluation could facilitate early diagnosis of chronic pancreatitis. Endoscopic ultrasound and magnetic resonance imaging-based elastography has improved the diagnostic accuracy of pancreatic fibrosis. Future studies should focus on combining different radiological modalities and correlating with histological parameters to standardize the radiological evaluation of pancreatic texture.

Citation: Kalayarasan R, Himaja M, Ramesh A, Kokila K. Radiological parameters to predict pancreatic texture: Current evidence and future perspectives. *World J Radiol* 2023; 15(6): 170-181
URL: https://www.wjgnet.com/1949-8470/full/v15/i6/170.htm
DOI: https://dx.doi.org/10.4329/wjr.v15.i6.170

INTRODUCTION

Pancreatoduodenectomy (PD) is the primary treatment for periampullary and pancreatic malignancies. Advancements in surgical techniques and perioperative management reduced the mortality after PD to less than 5% in high-volume centers[1]. However, PD-related morbidity remains high at 30%-50%[2,3]. Postoperative pancreatic fistula (POPF) is the primary determinant of morbidity and mortality after PD. Hence it is crucial to identify patients at high risk of POPF. Previous studies have identified pancreatic texture, pancreatic duct diameter, pancreatic stump ischemia, and operative blood loss as significant risk factors for POPF[4-8].

Pancreatic texture has been reported as an important predictor of POPF[6,7]. Soft pancreas is associated with increased risk of POPF and a firm pancreas is protective against POPF. The higher the fat fraction in the pancreas, the softer the pancreas is, however it becomes harder with the increasing grade of fibrosis. Traditionally assessment of the pancreatic texture is done by intraoperative palpation or histological evaluation of the operative specimen[7]. However, these assessment techniques cannot be used for the preoperative prediction of POPF. Also, intraoperative assessment of pancreatic texture during minimally invasive surgeries, especially the robotic approach, is challenging. With advancements in surgical techniques and instrumentation, a minimally invasive approach has been increasingly used to perform PD. However, multicenter randomized controlled trials (RCTs), including the recent Chinese trial, have failed to show short-term clinical benefits with minimally invasive PD compared to the open approach[9,10]. The results of these RCTs underscore that in PD, morbidity related to the procedure rather than access determines the short-term outcomes. As most of the morbidity in PD is related to POPF, preoperative prediction of patients with high risk of POPF can guide in adopting the intraoperative and postoperative management to reduce the POPF-related morbidity and thereby reducing the overall morbidity of PD. It also helps select patients at low risk of POPF who will benefit from minimally invasive PD. Hence, attempts have been made to correlate preoperative radiological parameters with pancreatic texture[11-16].

Another application of pancreatic texture evaluation is in patients with chronic pancreatitis. Recent studies have shown that early intervention for patients with chronic pancreatitis is associated with better outcomes than delayed intervention[17,18]. Pancreatic texture evaluation could facilitate the early identification of pancreatic fibrosis. The commonly employed diagnostic modalities for the assessment of pancreatic lesions are ultrasonography (USG), computed tomography (CT), magnetic resonance imaging (MRI), and endoscopic US (EUS). The present review aims to provide an overview of various parameters that can be assessed with each radiological investigation to detect the presence of fatty or fibrotic pancreas and predict the pancreatic texture.

PANCREATIC TEXTURE AND POSTOPERATIVE PANCREATIC FISTULA

The association between pancreatic texture and POPF risk has been documented in multiple retrospective and prospective studies. Kawai *et al*[4] in a multicenter study analyzed the risk factors for POPF in 1239 patients who underwent pancreatoduodenectomy. The authors concluded that soft pancreas was one of the significant risk factors for clinical pancreatic fistula. Patients with soft pancreatic texture are at 2.7 times more risk of developing POPF. Ansorge *et al*[5], in a single-center

prospective study of 164 patients reported that softer pancreatic texture is associated with a significantly higher incidence of POPF ($P < 0.001$) and a higher incidence of symptomatic postoperative peripancreatic collections ($P = 0.071$) compared to those with firm pancreatic texture. Ridolfi *et al*[6] evaluated the morpho histological features of pancreatic stump after pancreatoduodenectomy in 143 patients and found them to be the primary determinant of pancreatic fistula after pancreatoduodenectomy. A soft pancreas was strongly associated with POPF development and with high-grade POPF. In their study 42% of patients with soft pancreas developed a high-grade fistula, compared to 4% of patients with firm pancreatic texture ($P < 0.001$). In their study pancreatic texture was confirmed with histological correlation using fibrosis and inflammation scores. Hu *et al*[7] retrospectively analysed 539 patients who underwent pancreatoduodenectomy and found a significant correlation between pancreatic texture and POPF by univariate and multivariate analysis.

However similar correlation could not be established between pancreatic texture and POPF after distal pancreatectomy. This could be because of a different mechanism for leak and fistula formation from the pancreatic remnant after distal pancreatectomy compared to pancreaticoduodenectomy, which includes pancreatoenteric anastomosis. Chong *et al*[8], in a meta-analysis that included 43 studies with 8864 patients, found no difference in clinically relevant POPF rate between soft pancreas (25.3%, 373/1477) and hard pancreas (13.5%, 72/535) ($P = 0.46$). Pancreatic gland texture and duct size are not associated with the development of pancreatic fistula following distal pancreatectomy, unlike that of pancreatoduodenectomy. Hence, assessment of pancreatic texture is more useful in patients undergoing pancreatoduodenenctomy compared to those undergoing distal pancreatectomy.

ULTRASONOGRAPHY ABDOMEN

Transabdominal USG is the commonly used initial investigation to evaluate pancreatic pathology. The grayscale B- mode USG can evaluate the echotexture of the pancreas. The echotexture of the normal pancreas is isoechoic or slightly hyperechoic compared to the normal liver and shows a granular appearance with a smooth or minimally lobulated outline (Figure 1). With age, the echogenicity of the pancreas increases due to atrophy with fatty replacement. A fatty pancreas often occurs at the same time as fatty liver, which makes diagnosis more challenging. The most common limitations in scanning the pancreas by transabdominal approach are abdominal fat in obese patients and bowel air. As predicting pancreatic texture by routine B-mode USG is challenging, USG elastography has recently been used to measure the elasticity of different tissues[19,20].

Elastography

Elastography measures the stiffness of various organs and has been used to evaluate liver fibrosis and breast lesions[19,20]. Elastography of the pancreas can be performed using transabdominal USG, EUS, or MRI[21]. The techniques of USG elastography include strain elastography and shear wave elastography (SWE)[21]. The stiffness of tissue in the strain elastography is estimated by measuring the grade of strain generated by external pressure: the greater the strain, the softer the stiffness of the target tissue. The SWE relies on the principle of acoustic radiation force impulse (ARFI) using a USG probe which propagates through the tissue, and stiffness is estimated by measuring the propagation speed of the shear wave (Figure 1). The shear wave velocity (SWV) depends on the stiffness of the tissue: the higher the SWV, the harder the target tissue[22,23]. As SWE is less operator-dependent, it is preferred over strain elastography. Strain elastography is challenging to measure when the ultrasound probe, the pancreas, and the aorta are not in line. Hence it is easy to get a fine elastogram in the pancreatic body but not in the pancreatic head and tail regions. However, SWE can be easily performed anywhere in the pancreas because ARFI can be emitted wherever desired. Over the last few years, there has been increasing interest in assessing the role of elastography in evaluating pancreatic texture, differentiating benign and malignant pancreatic lesions, and diagnosing chronic pancreatitis[24-28].

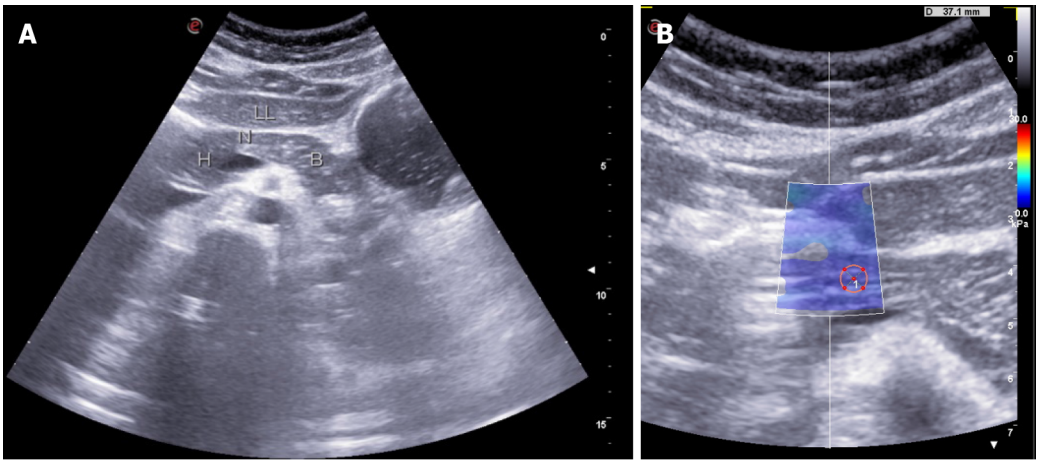
Yashima *et al*[27] used ARFI elastography of the pancreas and reported high elasticity in patients with chronic pancreatitis compared to normal patients. SWV in patients with chronic pancreatitis was significantly higher than that in healthy volunteers in each part of the pancreas (Figure 2). However, the measurement was difficult in the tail of the pancreas (Table 1). Harada *et al*[29] reported a good correlation between SWV and the histological grade of fibrosis. Pancreatic SWV, measured by preoperative ARFI imaging, was shown to have significant correlations with the grade of pathologic fibrosis, influencing the risk of POPF.

Llamoza-Torres *et al*[30], in their study of 33 patients, established the diagnostic accuracy of trans-abdominal USG-guided elastography in evaluating patients with suspected chronic pancreatitis. Patients included in the study were initially evaluated by EUS and/or MRI to establish their chronic pancreatitis status. Also, none of the included patients were found to have advanced-stage pancreatitis. The study results underscore the role of trans-abdominal USG elastography in assessing patients with early-stage chronic pancreatitis. However, the correlation with histological fibrosis was not evaluated. Further multicenter trials would be crucial to establish the role of transabdominal USG elastography in evaluating pancreatic texture and diagnosing early-stage chronic pancreatitis.

Table 1 Summary of studies evaluating the role of transabdominal ultrasonography in assessing pancreatic texture

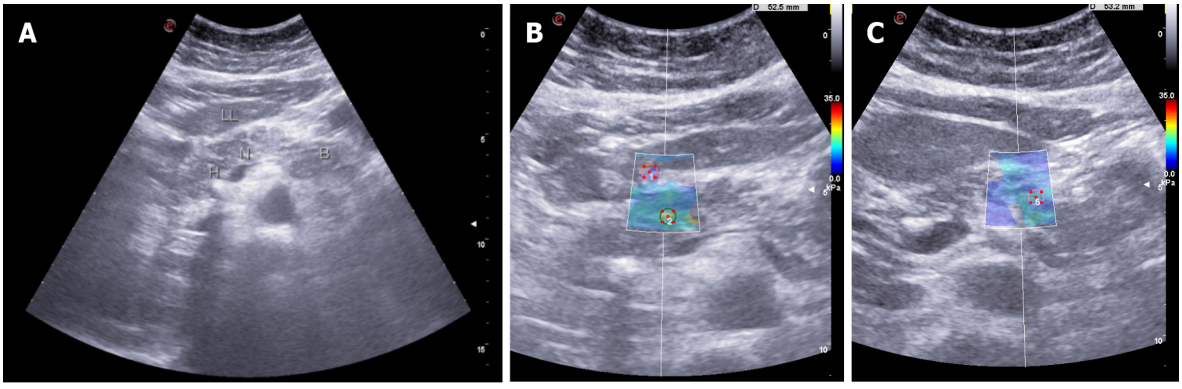
Ref.	Number of patients	Aim	Results	Conclusion	Histological correlation
Yashima *et al* [27], 2012	98	Efficacy of elastography to diagnose chronic pancreatitis	SWV cut off – 1.40 m/s; Sensitivity 75%; Specificity 72%; PPV 69%; NPV 78%	SWV in chronic pancreatitis patients higher than healthy volunteers	Not evaluated
Harada *et al* [29], 2016	68	Correlation of SWV with pathological degree of fibrosis	SWV cut off – 1.54 m/s; Sensitivity 91%; Specificity 75%; PPV 67%; NPV 93%	SWV significantly correlated with grade of fibrosis and postoperative pancreatic fistula	Good
Llamoza-Torres *et al*[30], 2016	33	Accuracy of elastography to diagnose chronic pancreatitis	SWV cut off - 1.4 m/s; Sensitivity 58%; Specificity 81%; PPV 76%; NPV 65%	SWV significantly correlated with EUS findings	Not evaluated

SWV: Shear wave velocity; PPV: Positive predictive value; NPV: Negative predictive value; EUS: Endoscopic ultrasonography.



DOI: 10.4329/wjr.v15.i6.170 **Copyright** ©The Author(s) 2023.

Figure 1 Transabdominal ultrasonography. A: Grayscale appearance of the normal pancreas (LL- Left lobe of liver, H- Head of pancreas, N- neck of pancreas, B-Body of pancreas). The pancreas is isoechoic compared to normal liver and shows a granular appearance and smooth outline; B: 2D Shear wave elastography measurement from the normal pancreas-neck region (3.84 ± 0.45 kPa).



DOI: 10.4329/wjr.v15.i6.170 **Copyright** ©The Author(s) 2023.

Figure 2 Shear wave velocity in patients with chronic pancreatitis was significantly higher than that in healthy volunteers in each part of the pancreas. A: Grayscale appearance of the pancreas in chronic calcific pancreatitis. (LL- Left lobe of liver, H- Head of pancreas, N- neck of pancreas, B-Body of pancreas). It shows a focal hyperechoic signal compared to normal liver and a mildly lobulated outline, a focus of calcification in the head region with posterior acoustic shadowing; B: 2D Shear wave elastography measurement of the pancreas in chronic calcific pancreatitis - head region (15.55 ± 2.64 kPa); C: 2D Shear wave elastography measurement of the pancreas in chronic calcific pancreatitis - region (11 ± 2.07 kPa).

COMPUTED TOMOGRAPHY ABDOMEN

Pancreatic texture on CT abdomen can be predicted based on the patterns of attenuation and enhancement of its parenchyma on various phases. They were evaluated as preoperative predictors of POPF in several studies[11-15]. While pancreatic attenuation index (PAI) like Liver Attenuation Index can measure pancreatic fat, pancreatic enhancement ratio (PER) can be measured to grade the pancreatic fibrosis (Figure 3). The higher the PER, the firmer the gland is. The presence of a higher PER and lower PAI can be considered to be associated with the low risk of development of POPF after PD.

Pancreatic attenuation index

PAI has been proposed as a simple tool by Yardimci *et al*[31] to assess pancreatic fat fraction by evaluating 76 patients who underwent PD. PAI was calculated with non-enhanced computed tomography by dividing the pancreas density measured in Household Units by the spleen density. They reported that higher PAI was associated with a high POPF rate and determined the value of 0.67 as an optimum cut-off value for predicting POPF. PAI has been reported to be useful in assessing pancreatic fat fraction by few other studies as well[11,12]. However, Gnanasekaran *et al*[32] reported that PAI was not helpful in predicting CR-POPF. Also, in their study, PAI did not correlate with histological estimation of pancreatic fat fraction. It might be due to the use of a region of interest-based assessment. In future studies, area-based assessment for the pancreatic fat fraction should be correlated with histopathological fat fraction.

Pancreatic enhancement ratio

An increase in the fibrosis of the pancreas makes the pancreatic texture hard. A fibrotic pancreas shows delayed enhancement in the pancreatic phase and nearly normal enhancement in the hepatic phase on dual-phase CT[33]. In contrast, the normal pancreas shows maximum enhancement in the pancreatic phase and washout in the hepatic phase[33]. Thus, predicting the degree of pancreatic fibrosis may be possible on analysis of enhancement patterns on pancreatic protocol CT done routinely to evaluate pancreatic tumors.

Kang *et al*[15] determined a PER cut-off of 1.10 as a useful predictor for POPF based on their retrospective analysis of 146 patients. PER on the equilibrium phase was significantly higher in the patients without POPF compared to patients with POPF (2.26 ± 3.63 *vs* 1.04 ± 0.51, $P = 0.001$). In the logistic regression analyses, PER was an independent predictor for the development of POPF (odds ratio = 0.243, $P = 0.002$). Maehira *et al*[13] retrospectively analysed 115 patients and concluded the pancreatic enhancement pattern as a reliable predictor for the development of POPF. Gnanasekaran *et al*[32] showed a positive correlation of PER with pancreatic fibrosis. Their study utilised a PER cut-off value of 0.661 which was 78% sensitive and 55 % specific in predicting POPF (Table 2). In the same study, PAI is reported to have negative correlation with PER, indicating that the pancreatic fat content and fibrosis are inversely related. However, the estimation of PER depends on the perfusion of organs with injected contrast which relies upon the hemodynamic status of the subjects. In comparison, PAI is independent of contrast injection.

MAGNETIC RESONANCE IMAGING

MRI allows the detection of fibrotic change of pancreatic parenchyma and hence can predict the risk of POPF. A normal pancreas shows hyperintensity on T1-weighted images irrespective of fat saturation. The fibrosis makes the pancreatic parenchyma to lose its high signal intensity (SI) owing to the replacement of the high protein content of the pancreas by fibrosis.

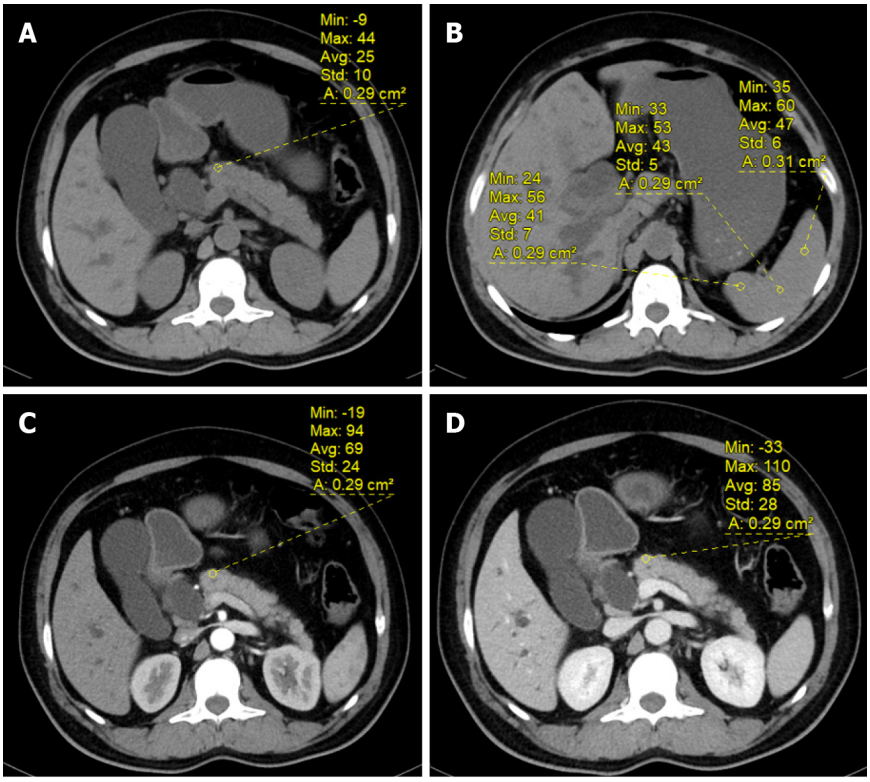
Winston *et al*[34] reported that the SI of pancreatic parenchyma, compared to that of the liver, decreases on fat-saturated T1-weighted images in patients with type 2 diabetes. Noda *et al*[35] found that the pancreatic fibrosis grade was negatively correlated with the SI ratio on in-phase T1-weighted images ($r = –0.67$, $P = -0.0002$). Another retrospective study by Watanabe *et al*[36] on 29 patients demonstrated that the SI ratio on T1-weighted images constantly decreased as the pancreatic fibrosis progressed. The higher risk of POPF is associated with a high SI ratio. Multiple regression analysis showed that pancreas-to-muscle SI ratios on T1-weighted images and apparent diffusion coefficient (ADC) values were independently associated with pancreatic fibrosis ($r(2) = 0.66$, $P < 0.001$) and with activated pancreatic stellate cell expression ($r(2) = 0.67$, $P < 0.001$). The mean pancreas-to-muscle SI ratio (± standard deviation) on T1-weighted images was higher ($P = 0.0029$) for patients with POPF (1.6 ± 0.2) than for those without (1.2 ± 0.2), and the odds ratio for POPF was 21.3 in patients with an SI ratio of 1.41 and higher[36].

Kim *et al*[16], in their pilot study, studied the correlation of pancreatic fibrosis with POPF after PD with the use of breath-hold unenhanced fat-suppressed T1 weighted images. The pancreas-to–liver SI ratio between the fistula and no fistula groups was -0.0009 ± 0.2 and -0.1297 ± 0.2, respectively ($P = 0.0004$). Each group's pancreas-to–spleen SI ratio was 0.423 ± 0.25 and 0.288 ± 0.32, respectively ($P = 0.014$). Using qualitative analysis where the pancreas SI was qualitatively assessed relative to liver and

Table 2 Summary of studies evaluating the role of computed tomography abdomen in assessing pancreatic texture

Ref.	Number of patients	PER calculation	Results	Histological correlation
Kang *et al*[15], 2017	146	1 Equilibrium phase -Pre contrast/ Pre contrast (EP- Pre/Pre); 2 Equilibrium phase -Pre contrast/ Arterial phase - Pre contrast (EP-Pre/AP-Pre)	Mean PER was significantly higher in patients without POPF than in patients with POPF. PER cut off: EP- Pre/Pre -1.10; Pre/AP-Pre - 0.60	Not evaluated
Maehira *et al*[13], 2019	115	1 Arterial phase/Portal phase (A/P); 2 Portal phase/Late phase (P/L)	Enhancement ratio is significantly higher in POPF group. PER cut off: A/P – 1.19; P/L – 1.17	Not evaluated
Gnanasekaran S *et al*[32], 2022	61	Equilibrium phase -Pre contrast/ Arterial phase - Pre contrast (EP-Pre/AP-Pre)	PER was significantly higher in patients without POPF than in patients with POPF, PER cut off – 0.673	PER correlated well with fibrosis

PER: Pancreatic enhancement ratio; POPF: Postoperative pancreatic fistula.



DOI: 10.4329/wjr.v15.i6.170 **Copyright** ©The Author(s) 2023.

Figure 3 Calculation of pancreatic attenuation index and pancreatic enhancement ratio. A: Hounsfield unit (HU) of the pancreatic neck in the plain phase; B: HU of the spleen in plain phase; C: HU of the pancreatic neck in the arterial phase; D: HU of the pancreatic neck in the equilibrium phase. ROI: Region of interest.

spleen SI using a five-point scale (-2, -1, 0, 1, 2), the SI ratios were 1.27 and 0.66 in each group (P = 0.013). The diagnostic performance for preoperative predictions of POPF was better with the qualitative analysis (Az = 0.653) than with the pancreas-to–liver SI ratio (Az = 0.640) and pancreas–spleen SI ratio (Az = 0.613); although, statistically significant difference was not found in each MRI parameter.

Yoon *et al*[37] reported that multiparametric MR imaging of the pancreas, including imaging with the T2*-corrected Dixon technique and intravoxel incoherent motion diffusion-weighted imaging (DWI), may yield quantitative information regarding pancreatic steatosis and fibrosis. The mean pancreas-to-muscle SI ratio on T1-weighted MRI values for F0, F1, and the cut-off value for predicting POPF was 1.51, 1.48, and 1.40, respectively (Table 3). Fukada *et al*[38], in their single-center retrospective study comprising 117 patients, reported 1.37 as the cut-off value for the pancreas-to-muscle SI ratio for predicting POPF.

Table 3 Summary of studies evaluating the role of magnetic resonance imaging abdomen signal intensity in assessing pancreatic texture

Ref.	Number of patients	Aim	Parameter studied	Results	Conclusion	Histological correlation
Winston *et al*[34], 1995	89	Correlation of pancreatic SI to predict the presence of pancreatic disease	PLSI	Accuracy -86%; PPV- 88	Pancreatic SI less than that of liver correlates highly with pancreatic disease, especially in younger patients	Not evaluated
Kim *et al* [16], 2009	43	Accuracy of non-enhanced fat-suppressed T1W MRI in predicting POPF	PLSI, PSSI	PLSI cut off −0.12097 (sensitivity -36%, specificity - 89%); PSSI cut off -0.29979 (sensitivity-79%, specificity-45%)	PLSI, PSSI significantly differed between POPF group and non POPF group, hence, can be useful in predicting POPF	Good
Watanabe *et al*[36], 2014	29	Efficacy of MRI in assessing degrees of pancreatic fibrosis and predicting POPF	PMSI in unenhanced T1W and T2 W images	Odds ratio of PMSI in T1 W for POPF was 21.3 in patients with an SI ratio of 1.41 and higher	T1W SI ratio and ADC measurements useful to detect advanced pancreatic fibrosis and occurrence of POPF	Good
Noda *et al* [35], 2016	29	Evaluate the noncontrast-enhanced MRI to grade pancreatic fibrosis and correlate with HbA1c values	PMSI on in- and opposed-phase T1W images	The pancreatic fibrosis grade and HbA1c value were negatively correlated with the SI ratio on opposed-phase T1W images	PMSI could be a potential biomarker for pancreatic fibrosis and elevated HbA1c values	Good
Yoon *et al* [37], 2016	165	Evaluate the multipara-metric pancreatic MRI in the quantification of pancreatic fibrosis and determine relation with POPF	PMSI on in- and opposed-phase T1, IVIM DW imaging; Perfusion fraction (*f*)	Mean SI ratio for fibrosis; F0 – 1.51; F1 – 1.48; SI ratio cutoff for POPF - 1.40; Odds of developing POPF for a 1% increase in *f* were 1.17	Multiparametric MR imaging of the pancreas may quantify pancreatic steatosis and fibrosis, and *f* was significantly associated with POPF	Good
Fukada *et al*[38], 2022	117	Predictive ability of SI ratio on T1W MRI for POPF after distal pancreatectomy	PMSI on T1W	SI ratio cutoff for POPF - 1.37; Sensitivity- 96.3% Specificity- 52.0%	PMSI is a quantitative biomarker for pancreatic characteristics	Good

T1W: T1 weighted; T2W: T2 Weighted; MRI: Magnetic resonance imaging; POPF: Postoperative pancreatic fistula; PLSI: Pancreas-to-liver signal intensity ratio; PSSI: Pancreas-to-spleen signal intensity ratio; PMSI: Pancreas-to-muscle signal intensity ratio; SI: Signal intensity; IVIM: Intravoxel incoherent motion.

Diffusion-weighted imaging

DWI is used to evaluate fibrosis using ADC values. In the fibrotic pancreas, diffusion is restricted because of the replacement of normal pancreatic parenchyma with fibrous tissue. ADC values can be used to identify the presence of fibrosis and to grade its extent. Studies have reported lower ADC values in chronic pancreatitis patients[39]. Bieliuniene *et al*[40] identified a significant negative correlation between ADC value and histologically determined pancreatic fibrosis (PF) ($r = -0.752$, $P < 0.001$). In addition, a significant negative correlation was observed between T1SI and histologically determined pancreatic fibrosis ($r = -0.631$, $P < 0.001$). Also, by combining the ADC and T1SI measurements, PF can be detected with greater sensitivity and specificity during the early stages of the disease when other clinical signs are absent.

Tirkes *et al*[41] conducted a multi institutional, prospective study to evaluate the diagnostic value of four quantitative MRI parameters in chronic pancreatitis: T1 relaxation time, extracellular fraction, fat signal fraction and ADC. Except ADC, all the parameters were reported to be significantly higher in the patients with chronic pancreatitis and also were showed to have moderately high diagnostic value after adjustment for covariates. A Q-MRI score has been proposed by combining these three MR parameters which was shown to have improved diagnostic performance. However, ADC values were reported to be not helpful for diagnosing chronic pancreatitis.

Magnetic resonance elastography

Magnetic resonance elastography (MRE) can also be used to estimate pancreatic stiffness. The technique of MRE involves three steps similar to transabdominal and EUS elastography: Generation of shear waves in the tissue, acquisition of MR images depicting the propagation of the induced shear waves, and generation of elastograms, the quantitative maps of tissue stiffness by processing the acquired images of the shear waves.

Patients with chronic pancreatitis were reported to have significantly higher stiffness values than normal people (1.53 *vs* 1.11 kPa)[42]. Wang *et al*[43] reported the usefulness of MRE for the assessment

of the severity of chronic pancreatitis and showed that the pancreatic stiffness was significantly low in healthy controls (mean -1.21 kPa), when compared to patients with a mild degree of chronic pancreatitis (mean - 1.50 kPa), and also those with a moderate/severe degree of chronic pancreatitis (mean - 1.90 kPa).

ENDOSCOPIC ULTRASONOGRAPHY ELASTOGRAPHY

EUS elastography is a novel diagnostic tool to assess pancreatic fibrosis. Like transabdominal ultrasound, EUS elastography can be strain elastography or SWE.

Strain elastography

In strain elastography, the target tissue is compressed with a EUS probe to create a stain, which is reflected on ultrasound images. Softer tissue has a larger strain when compared to harder tissues. However, this gives only qualitative estimation of tissue elasticity. Second-generation EUS elastography has been developed, giving two semi-quantitative tissue stiffness measures[28]. The strain ratio (SR), one of two semi quantitative measure is based on comparing stiffness between specific regions of interest in two tissue areas and is expressed as a relative ratio. The strain histogram (SH) is another semi-quantitative parameter representing the selected area's mean strain value.

Six articles reported the diagnostic performance of EUS strain elastography for chronic pancreatitis; three reported SR, and three used SH (Table 4)[28,44-48]. Of them two SR articles reported that EUS elastography is helpful for differentiating the normal pancreas from chronic pancreatitis[28,47]. Two of the SH articles also reported the usefulness of EUS elastography in differentiating between normal pancreas and chronic pancreatitis[44,48]. One report showed that the SH elastography values significantly correlated with the degree of fibrosis assessed on histology of the surgical specimens[45].

Shear wave elastography

Acoustic radiation force is sent to the region of interest, and this push pulse generates a shear wave at the edge. The shear wave propagates faster in harder tissues. EUS-SWE is has better diagnostic value in chronic pancreatitis than strain elastography by providing the absolute values of pancreatic hardness.

Since it is a novel investigation, only two articles report the utility of EUS-SWE[49,50]. For diagnosis of chronic pancreatitis, a SWV cut-off value of 2.19 (Rosemont criteria) and 1.96 (Japan Pancreatic Society criteria) had a sensitivity of 100% and 83%, respectively, and specificity of 94% and 100%. EUS-SWE values correlate well with the stage of chronic pancreatitis and predicted exocrine dysfunction compared to transabdominal ultrasound. EUS-SWE data are better than those published using transabdominal ultrasound[30]. However, EUS is an invasive technique compared to trans-abdominal ultrasound.

FUTURE PERSPECTIVES

Identifying potential preoperative predictors for POPF is a critical step in our journey to improve perioperative outcomes after PD. Also, early diagnosis of chronic pancreatitis is essential to improve long-term outcomes of patients undergoing surgery for chronic pancreatitis. Recent studies have shown that pancreatic texture parameters like mean positive pixel before initiating neoadjuvant therapy, kurtosis and changes in kurtosis during neoadjuvant therapy can be used in predicting response to neoadjuvant therapy[51,52]. While the current evidence suggests the promising role of radiological parameters in predicting pancreatic texture, it is essential to understand the limitations of available evidence. Most of the studies had a smaller sample size. Hence, studies with larger sample sizes and multicentric studies are required for all the radiological modalities to determine the reference values for the normal and diseased pancreas. Also, socio-demographic variables need to be correlated with the pancreatic texture in all age groups to determine appropriate reference standards for all the available radiological modalities.

Most studies have assessed individual radiological parameter's role in predicting pancreatic texture. However, studies comparing different radiological parameters are not available. Hence future studies are required to study the efficacy of one imaging modality over the other and the effectiveness of combining several radiological modalities to devise a quantitative variable such as fistula risk score based on texture.

The accepted gold standard to find the pancreatic texture is histology. Since there can be an uneven distribution of pancreatic fatty infiltration or fibrosis, using the same focal area of the pancreas in imaging modalities and histology in future studies will provide a better correlation of pancreatic texture. Also, it is essential to understand that multiple factors influence POPF. Hence, a homogenous patient population and standardized surgical techniques are prerequisites for future studies. However, it isn't easy to achieve and reproduce that in complex procedures like PD. Nevertheless, identifying

Table 4 Summary of studies evaluating the role of endoscopic ultrasonography strain elastography in assessing pancreatic texture

Ref.	Parameter used	Inference
Machado *et al*[44], 2012	SH	EUS is useful in differentiating normal pancreas and chronic pancreatitis
Iglesias-Garcia *et al*[28], 2013	SR	EUS is useful in differentiating normal pancreas and chronic pancreatitis; SR EUS elastography correlated with number of Rosemont criteria ratio
Itoh *et al*[45], 2014	SH	SH EUS elastography values significantly correlated with fibrosis on histology
Dominguez-Muñoz *et al*[46], 2015	SR	SR EUS elastography values significantly correlated with exocrine dysfunction
Kim *et al*[47], 2017	SR	EUS is useful in differentiating normal pancreas and chronic pancreatitis
Kuwahara *et al*[48], 2017	SH	EUS is useful in differentiating normal pancreas and chronic pancreatitis; SH EUS elastography correlated with number of Rosemont criteria ratio

SR: Strain ratio; SH: Strain histogram; EUS: Endoscopic ultrasonography.

potential preoperative predictors for POPF is vital in decreasing the morbidity associated with PD.

CONCLUSION

Pancreatic texture can be assessed using radiological parameters derived from preoperative imaging modalities. With advancements in imaging techniques, the accuracy of preoperative prediction of the fatty or fibrotic pancreas has improved. However, more studies are required comparing different imaging modalities to standardize their measurement. Also, the correlation of radiological parameters with histological findings is required to improve predictive accuracy.

FOOTNOTES

Author contributions: Himaja M and Kokila K did the literature search and wrote the first draft of the review; Kalayarasan R and Ramesh A conceptualized the work, supervised the writing, gave intellectual inputs, and critically revised the manuscript.

Conflict-of-interest statement: All authors have no conflicts of interest to report.

Open-Access: This article is an open-access article that was selected by an in-house editor and fully peer-reviewed by external reviewers. It is distributed in accordance with the Creative Commons Attribution NonCommercial (CC BY-NC 4.0) license, which permits others to distribute, remix, adapt, build upon this work non-commercially, and license their derivative works on different terms, provided the original work is properly cited and the use is non-commercial. See: https://creativecommons.org/Licenses/by-nc/4.0/

Country/Territory of origin: India

ORCID number: Raja Kalayarasan 0000-0003-4056-8672; Mandalapu Himaja 0009-0004-8267-2018; Ananthakrishnan Ramesh 0000-0002-1404-6400; Kathirvel Kokila 0000-0002-9157-9067.

S-Editor: Liu JH
L-Editor: A
P-Editor: Liu JH

REFERENCES

1 **Poon RT**, Fan ST, Lo CM, Ng KK, Yuen WK, Yeung C, Wong J. External drainage of pancreatic duct with a stent to reduce leakage rate of pancreaticojejunostomy after pancreaticoduodenectomy: a prospective randomized trial. *Ann Surg* 2007; **246**: 425-33; discussion 433 [PMID: 17717446 DOI: 10.1097/sla.0b013e3181492c28]
2 **Greenblatt DY**, Kelly KJ, Rajamanickam V, Wan Y, Hanson T, Rettammel R, Winslow ER, Cho CS, Weber SM. Preoperative factors predict perioperative morbidity and mortality after pancreaticoduodenectomy. *Ann Surg Oncol* 2011; **18**: 2126-2135 [PMID: 21336514 DOI: 10.1245/s10434-011-1594-6]
3 **Tzeng CW**, Katz MH, Fleming JB, Lee JE, Pisters PW, Holmes HM, Varadhachary GR, Wolff RA, Abbruzzese JL,

Vauthey JN, Aloia TA. Morbidity and mortality after pancreaticoduodenectomy in patients with borderline resectable type C clinical classification. *J Gastrointest Surg* 2014; **18**: 146-55; discussion 155 [PMID: 24129825 DOI: 10.1007/s11605-013-2371-6]

4 **Kawai M**, Kondo S, Yamaue H, Wada K, Sano K, Motoi F, Unno M, Satoi S, Kwon AH, Hatori T, Yamamoto M, Matsumoto J, Murakami Y, Doi R, Ito M, Miyakawa S, Shinchi H, Natsugoe S, Nakagawara H, Ohta T, Takada T. Predictive risk factors for clinically relevant pancreatic fistula analyzed in 1,239 patients with pancreaticoduodenectomy: multicenter data collection as a project study of pancreatic surgery by the Japanese Society of Hepato-Biliary-Pancreatic Surgery. *J Hepatobiliary Pancreat Sci* 2011; **18**: 601-608 [PMID: 21491103 DOI: 10.1007/s00534-011-0373-x]

5 **Ansorge C**, Strömmer L, Andrén-Sandberg Å, Lundell L, Herrington MK, Segersvärd R. Structured intraoperative assessment of pancreatic gland characteristics in predicting complications after pancreaticoduodenectomy. *Br J Surg* 2012; **99**: 1076-1082 [PMID: 22556164 DOI: 10.1002/bjs.8784]

6 **Ridolfi C**, Angiolini MR, Gavazzi F, Spaggiari P, Tinti MC, Uccelli F, Madonini M, Montorsi M, Zerbi A. Morphohistological features of pancreatic stump are the main determinant of pancreatic fistula after pancreatoduodenectomy. *Biomed Res Int* 2014; **2014**: 641239 [PMID: 24900974 DOI: 10.1155/2014/641239]

7 **Hu BY**, Wan T, Zhang WZ, Dong JH. Risk factors for postoperative pancreatic fistula: Analysis of 539 successive cases of pancreaticoduodenectomy. *World J Gastroenterol* 2016; **22**: 7797-7805 [PMID: 27678363 DOI: 10.3748/wjg.v22.i34.7797]

8 **Chong E**, Ratnayake B, Lee S, French JJ, Wilson C, Roberts KJ, Loveday BPT, Manas D, Windsor J, White S, Pandanaboyana S. Systematic review and meta-analysis of risk factors of postoperative pancreatic fistula after distal pancreatectomy in the era of 2016 International Study Group pancreatic fistula definition. *HPB (Oxford)* 2021; **23**: 1139-1151 [PMID: 33820687 DOI: 10.1016/j.hpb.2021.02.015]

9 **Wang M**, Li D, Chen R, Huang X, Li J, Liu Y, Liu J, Cheng W, Chen X, Zhao W, Tan Z, Huang H, Zhu F, Qin T, Ma J, Yu G, Zhou B, Zheng S, Tang Y, Han W, Meng L, Ke J, Feng F, Chen B, Yin X, Chen W, Ma H, Xu J, Lin R, Dong Y, Yu Y, Zhang H, Qin R; Minimally Invasive Treatment Group in the Pancreatic Disease Branch of China's International Exchange and Promotion Association for Medicine and Healthcare (MITG-P-CPAM). Laparoscopic versus open pancreatoduodenectomy for pancreatic or periampullary tumours: a multicentre, open-label, randomised controlled trial. *Lancet Gastroenterol Hepatol* 2021; **6**: 438-447 [PMID: 33915091 DOI: 10.1016/S2468-1253(21)00054-6]

10 **van Hilst J**, de Rooij T, Bosscha K, Brinkman DJ, van Dieren S, Dijkgraaf MG, Gerhards MF, de Hingh IH, Karsten TM, Lips DJ, Luyer MD, Busch OR, Festen S, Besselink MG; Dutch Pancreatic Cancer Group. Laparoscopic versus open pancreatoduodenectomy for pancreatic or periampullary tumours (LEOPARD-2): a multicentre, patient-blinded, randomised controlled phase 2/3 trial. *Lancet Gastroenterol Hepatol* 2019; **4**: 199-207 [PMID: 30685489 DOI: 10.1016/S2468-1253(19)30004-4]

11 **Tranchart H**, Gaujoux S, Rebours V, Vullierme MP, Dokmak S, Levy P, Couvelard A, Belghiti J, Sauvanet A. Preoperative CT scan helps to predict the occurrence of severe pancreatic fistula after pancreaticoduodenectomy. *Ann Surg* 2012; **256**: 139-145 [PMID: 22609844 DOI: 10.1097/SLA.0b013e318256c32c]

12 **Lim S**, Bae JH, Chun EJ, Kim H, Kim SY, Kim KM, Choi SH, Park KS, Florez JC, Jang HC. Differences in pancreatic volume, fat content, and fat density measured by multidetector-row computed tomography according to the duration of diabetes. *Acta Diabetol* 2014; **51**: 739-748 [PMID: 24671510 DOI: 10.1007/s00592-014-0581-3]

13 **Maehira H**, Iida H, Mori H, Kitamura N, Miyake T, Shimizu T, Tani M. Computed Tomography Enhancement Pattern of the Pancreatic Parenchyma Predicts Postoperative Pancreatic Fistula After Pancreaticoduodenectomy. *Pancreas* 2019; **48**: 209-215 [PMID: 30589830 DOI: 10.1097/MPA.0000000000001229]

14 **Hashimoto Y**, Sclabas GM, Takahashi N, Kirihara Y, Smyrk TC, Huebner M, Farnell MB. Dual-phase computed tomography for assessment of pancreatic fibrosis and anastomotic failure risk following pancreatoduodenectomy. *J Gastrointest Surg* 2011; **15**: 2193-2204 [PMID: 21948179 DOI: 10.1007/s11605-011-1687-3]

15 **Kang JH**, Park JS, Yu JS, Chung JJ, Kim JH, Cho ES, Yoon DS. Prediction of pancreatic fistula after pancreatoduodenectomy by preoperative dynamic CT and fecal elastase-1 levels. *PLoS One* 2017; **12**: e0177052 [PMID: 28493949 DOI: 10.1371/journal.pone.0177052]

16 **Kim Z**, Kim MJ, Kim JH, Jin SY, Kim YB, Seo D, Choi D, Hur KY, Kim JJ, Lee MH, Moon C. Prediction of post-operative pancreatic fistula in pancreaticoduodenectomy patients using pre-operative MRI: a pilot study. *HPB (Oxford)* 2009; **11**: 215-221 [PMID: 19590650 DOI: 10.1111/j.1477-2574.2009.00011.x]

17 **Willner A**, Bogner A, Müssle B, Teske C, Hempel S, Kahlert C, Distler M, Weitz J, Welsch T. Disease duration before surgical resection for chronic pancreatitis impacts long-term outcome. *Medicine (Baltimore)* 2020; **99**: e22896 [PMID: 33126342 DOI: 10.1097/MD.0000000000022896]

18 **Issa Y**, Kempeneers MA, Bruno MJ, Fockens P, Poley JW, Ahmed Ali U, Bollen TL, Busch OR, Dejong CH, van Duijvendijk P, van Dullemen HM, van Eijck CH, van Goor H, Hadithi M, Haveman JW, Keulemans Y, Nieuwenhuijs VB, Poen AC, Rauws EA, Tan AC, Thijs W, Timmer R, Witteman BJ, Besselink MG, van Hooft JE, van Santvoort HC, Dijkgraaf MG, Boermeester MA; Dutch Pancreatitis Study Group. Effect of Early Surgery vs Endoscopy-First Approach on Pain in Patients With Chronic Pancreatitis: The ESCAPE Randomized Clinical Trial. *JAMA* 2020; **323**: 237-247 [PMID: 31961419 DOI: 10.1001/jama.2019.20967]

19 **Forestier N**, Gaus A, Herrmann E, Sarrazin C, Bojunga J, Poynard T, Albert J, Gerber L, Schneider MD, Dultz G, Zeuzem S, Friedrich-Rust M. Acoustic radiation force impulse imaging for evaluation of antiviral treatment response in chronic hepatitis C. *J Gastrointestin Liver Dis* 2012; **21**: 367-373 [PMID: 23256119]

20 **Itoh A**, Ueno E, Tohno E, Kamma H, Takahashi H, Shiina T, Yamakawa M, Matsumura T. Breast disease: clinical application of US elastography for diagnosis. *Radiology* 2006; **239**: 341-350 [PMID: 16484352 DOI: 10.1148/radiol.2391041676]

21 **Kawada N**, Tanaka S. Elastography for the pancreas: Current status and future perspective. *World J Gastroenterol* 2016; **22**: 3712-3724 [PMID: 27076756 DOI: 10.3748/wjg.v22.i14.3712]

22 **Yin M**, Venkatesh SK, Grimm RC, Rossman PJ, Manduca A, Ehman RL. Assessment of the pancreas with MR elastography. Proceedings of the International Society for Magnetic Resonance in Medicine; Toronto, Canada' 2008: 2627

[DOI: 10.1109/iembs.1996.651961]

23 **Kawada N**, Tanaka S, Uehara H, Ohkawa K, Yamai T, Takada R, Shiroeda H, Arisawa T, Tomita Y. Potential use of point shear wave elastography for the pancreas: a single center prospective study. *Eur J Radiol* 2014; **83**: 620-624 [PMID: 24445135 DOI: 10.1016/j.ejrad.2013.11.029]

24 **Iglesias-Garcia J**, Larino-Noia J, Abdulkader I, Forteza J, Dominguez-Munoz JE. Quantitative endoscopic ultrasound elastography: an accurate method for the differentiation of solid pancreatic masses. *Gastroenterology* 2010; **139**: 1172-1180 [PMID: 20600020 DOI: 10.1053/j.gastro.2010.06.059]

25 **Ris MM**, Deitrich RA, Von Wartburg JP. Inhibition of aldehyde reductase isoenzymes in human and rat brain. *Biochem Pharmacol* 1975; **24**: 1865-1869 [PMID: 18 DOI: 10.1016/0006-2952(75)90405-0]

26 **Halaris AE**, Belendiuk KT, Freedman DX. Antidepressant drugs affect dopamine uptake. *Biochem Pharmacol* 1975; **24**: 1896-1897 [PMID: 19 DOI: 10.1016/0006-2952(75)90412-8]

27 **Yashima Y**, Sasahira N, Isayama H, Kogure H, Ikeda H, Hirano K, Mizuno S, Yagioka H, Kawakubo K, Sasaki T, Nakai Y, Tada M, Yoshida H, Omata M, Koike K. Acoustic radiation force impulse elastography for noninvasive assessment of chronic pancreatitis. *J Gastroenterol* 2012; **47**: 427-432 [PMID: 22065162 DOI: 10.1007/s00535-011-0491-x]

28 **Iglesias-Garcia J**, Domínguez-Muñoz JE, Castiñeira-Alvariño M, Luaces-Regueira M, Lariño-Noia J. Quantitative elastography associated with endoscopic ultrasound for the diagnosis of chronic pancreatitis. *Endoscopy* 2013; **45**: 781-788 [PMID: 24019131 DOI: 10.1055/s-0033-1344614]

29 **Harada N**, Ishizawa T, Inoue Y, Aoki T, Sakamoto Y, Hasegawa K, Sugawara Y, Tanaka M, Fukayama M, Kokudo N. Acoustic radiation force impulse imaging of the pancreas for estimation of pathologic fibrosis and risk of postoperative pancreatic fistula. *J Am Coll Surg* 2014; **219**: 887-94.e5 [PMID: 25262282 DOI: 10.1016/j.jamcollsurg.2014.07.940]

30 **Llamoza-Torres CJ**, Fuentes-Pardo M, Álvarez-Higueras FJ, Alberca-de-Las-Parras F, Carballo-Álvarez F. Usefulness of percutaneous elastography by acoustic radiation force impulse for the non-invasive diagnosis of chronic pancreatitis. *Rev Esp Enferm Dig* 2016; **108**: 450-456 [PMID: 27459032 DOI: 10.17235/reed.2016.4103/2015]

31 **Yardimci S**, Kara YB, Tuney D, Attaallah W, Ugurlu MU, Dulundu E, Yegen ŞC. A Simple Method to Evaluate Whether Pancreas Texture Can Be Used to Predict Pancreatic Fistula Risk After Pancreatoduodenectomy. *J Gastrointest Surg* 2015; **19**: 1625-1631 [PMID: 25982120 DOI: 10.1007/s11605-015-2855-7]

32 **Gnanasekaran S**, Durgesh S, Gurram R, Kalayarasan R, Pottakkat B, Rajeswari M, Srinivas BH, Ramesh A, Sahoo J. Do preoperative pancreatic computed tomography attenuation index and enhancement ratio predict pancreatic fistula after pancreaticoduodenectomy? *World J Radiol* 2022; **14**: 165-176 [PMID: 35978980 DOI: 10.4329/wjr.v14.i6.165]

33 **Takahashi N**, Fletcher JG, Hough DM, Fidler JL, Kawashima A, Mandrekar JN, Chari ST. Autoimmune pancreatitis: differentiation from pancreatic carcinoma and normal pancreas on the basis of enhancement characteristics at dual-phase CT. *AJR Am J Roentgenol* 2009; **193**: 479-484 [PMID: 19620446 DOI: 10.2214/AJR.08.1883]

34 **Winston CB**, Mitchell DG, Outwater EK, Ehrlich SM. Pancreatic signal intensity on T1-weighted fat saturation MR images: clinical correlation. *J Magn Reson Imaging* 1995; **5**: 267-271 [PMID: 7633102 DOI: 10.1002/jmri.1880050307]

35 **Noda Y**, Goshima S, Tanaka K, Osada S, Tomita H, Hara A, Horikawa Y, Takeda J, Kajita K, Watanabe H, Kawada H, Kawai N, Kanematsu M, Bae KT. Findings in pancreatic MRI associated with pancreatic fibrosis and HbA1c values. *J Magn Reson Imaging* 2016; **43**: 680-687 [PMID: 26201823 DOI: 10.1002/jmri.25019]

36 **Watanabe H**, Kanematsu M, Tanaka K, Osada S, Tomita H, Hara A, Goshima S, Kondo H, Kawada H, Noda Y, Tanahashi Y, Kawai N, Yoshida K, Moriyama N. Fibrosis and postoperative fistula of the pancreas: correlation with MR imaging findings--preliminary results. *Radiology* 2014; **270**: 791-799 [PMID: 24475834 DOI: 10.1148/radiol.13131194]

37 **Yoon JH**, Lee JM, Lee KB, Kim SW, Kang MJ, Jang JY, Kannengiesser S, Han JK, Choi BI. Pancreatic Steatosis and Fibrosis: Quantitative Assessment with Preoperative Multiparametric MR Imaging. *Radiology* 2016; **279**: 140-150 [PMID: 26566228 DOI: 10.1148/radiol.2015142254]

38 **Fukada M**, Murase K, Higashi T, Fujibayashi S, Kuno M, Yasufuku I, Sato Y, Kiyama S, Tanaka Y, Okumura N, Matsuhashi N, Takahashi T. The pancreas-to-muscle signal intensity ratio on T(1)-weighted MRI as a predictive biomarker for postoperative pancreatic fistula after distal pancreatectomy: a single-center retrospective study. *World J Surg Oncol* 2022; **20**: 250 [PMID: 35932021 DOI: 10.1186/s12957-022-02718-8]

39 **Nissan N**. Modifications of pancreatic diffusion MRI by tissue characteristics: what are we weighting for? *NMR Biomed* 2017; **30** [PMID: 28470823 DOI: 10.1002/nbm.3728]

40 **Bieliuniene E**, Frøkjær JB, Pockevicius A, Kemesiene J, Lukosevicius S, Basevicius A, Barauskas G, Dambrauskas Z, Gulbinas A. Magnetic Resonance Imaging as a Valid Noninvasive Tool for the Assessment of Pancreatic Fibrosis. *Pancreas* 2019; **48**: 85-93 [PMID: 30451794 DOI: 10.1097/MPA.0000000000001206]

41 **Tirkes T**, Yadav D, Conwell DL, Territo PR, Zhao X, Persohn SA, Dasyam AK, Shah ZK, Venkatesh SK, Takahashi N, Wachsman A, Li L, Li Y, Pandol SJ, Park WG, Vege SS, Hart PA, Topazian M, Andersen DK, Fogel EL; Consortium for the Study of Chronic Pancreatitis, Diabetes, Pancreatic Cancer (CPDPC). Quantitative MRI of chronic pancreatitis: results from a multi-institutional prospective study, magnetic resonance imaging as a non-invasive method for assessment of pancreatic fibrosis (MINIMAP). *Abdom Radiol (NY)* 2022; **47**: 3792-3805 [PMID: 36038644 DOI: 10.1007/s00261-022-03654-7]

42 **An H**, Shi Y, Guo Q, Liu Y. Test-retest reliability of 3D EPI MR elastography of the pancreas. *Clin Radiol* 2016; **71**: 1068.e7-1068.e12 [PMID: 27132114 DOI: 10.1016/j.crad.2016.03.014]

43 **Wang M**, Gao F, Wang X, Liu Y, Ji R, Cang L, Shi Y. Magnetic resonance elastography and T(1) mapping for early diagnosis and classification of chronic pancreatitis. *J Magn Reson Imaging* 2018 [PMID: 29537715 DOI: 10.1002/jmri.26008]

44 **Machado MC**, Coelho AM, Carneiro D'Albuquerque LA, Jancar S. Effect of ageing on systemic inflammatory response in acute pancreatitis. *Int J Inflam* 2012; **2012**: 270319 [PMID: 22292125 DOI: 10.1155/2012/270319]

45 **Itoh Y**, Itoh A, Kawashima H, Ohno E, Nakamura Y, Hiramatsu T, Sugimoto H, Sumi H, Hayashi D, Kuwahara T, Morishima T, Funasaka K, Nakamura M, Miyahara R, Ohmiya N, Katano Y, Ishigami M, Goto H, Hirooka Y. Quantitative analysis of diagnosing pancreatic fibrosis using EUS-elastography (comparison with surgical specimens). *J*

Gastroenterol 2014; **49**: 1183-1192 [PMID: 24026103 DOI: 10.1007/s00535-013-0880-4]

46 **Dominguez-Muñoz JE**, Iglesias-Garcia J, Castiñeira Alvariño M, Luaces Regueira M, Lariño-Noia J. EUS elastography to predict pancreatic exocrine insufficiency in patients with chronic pancreatitis. *Gastrointest Endosc* 2015; **81**: 136-142 [PMID: 25088920 DOI: 10.1016/j.gie.2014.06.040]

47 **Kim SY**, Cho JH, Kim YJ, Kim EJ, Park JY, Jeon TJ, Kim YS. Diagnostic efficacy of quantitative endoscopic ultrasound elastography for differentiating pancreatic disease. *J Gastroenterol Hepatol* 2017; **32**: 1115-1122 [PMID: 27862278 DOI: 10.1111/jgh.13649]

48 **Kuwahara T**, Hirooka Y, Kawashima H, Ohno E, Ishikawa T, Kawai M, Suhara H, Takeyama T, Hashizume K, Koya T, Tanaka H, Sakai D, Yamamura T, Furukawa K, Funasaka K, Nakamura M, Miyahara R, Watanabe O, Ishigami M, Hashimoto S, Goto H. Quantitative diagnosis of chronic pancreatitis using EUS elastography. *J Gastroenterol* 2017; **52**: 868-874 [PMID: 27995327 DOI: 10.1007/s00535-016-1296-8]

49 **Yamashita Y**, Tanioka K, Kawaji Y, Tamura T, Nuta J, Hatamaru K, Itonaga M, Yoshida T, Ida Y, Maekita T, Iguchi M, Kitano M. Utility of Elastography with Endoscopic Ultrasonography Shear-Wave Measurement for Diagnosing Chronic Pancreatitis. *Gut Liver* 2020; **14**: 659-664 [PMID: 31722469 DOI: 10.5009/gnl19170]

50 **Yamashita Y**, Tanioka K, Kawaji Y, Tamura T, Nuta J, Hatamaru K, Itonaga M, Ida Y, Maekita T, Iguchi M, Kitano M. Endoscopic ultrasonography shear wave as a predictive factor of endocrine/exocrine dysfunction in chronic pancreatitis. *J Gastroenterol Hepatol* 2021; **36**: 391-396 [PMID: 32511808 DOI: 10.1111/jgh.15137]

51 **Kim BR**, Kim JH, Ahn SJ, Joo I, Choi SY, Park SJ, Han JK. CT prediction of resectability and prognosis in patients with pancreatic ductal adenocarcinoma after neoadjuvant treatment using image findings and texture analysis. *Eur Radiol* 2019; **29**: 362-372 [PMID: 29931561 DOI: 10.1007/s00330-018-5574-0]

52 **Borhani AA**, Dewan R, Furlan A, Seiser N, Zureikat AH, Singhi AD, Boone B, Bahary N, Hogg ME, Lotze M, Zeh HJ III, Tublin ME. Assessment of Response to Neoadjuvant Therapy Using CT Texture Analysis in Patients With Resectable and Borderline Resectable Pancreatic Ductal Adenocarcinoma. *AJR Am J Roentgenol* 2020; **214**: 362-369 [PMID: 31799875 DOI: 10.2214/AJR.19.21152]

World Journal of Radiology

Submit a Manuscript: https://www.f6publishing.com

World J Radiol 2023 June 28; 15(6): 182-190

DOI: 10.4329/wjr.v15.i6.182

ISSN 1949-8470 (online)

ORIGINAL ARTICLE

Retrospective Study

Computed tomography angiographic study of surgical anatomy of thyroid arteries: Clinical implications in neck dissection

Yashu Bhardwaj, Brijendra Singh, Pooja Bhadoria, Rashmi Malhotra, Swarnava Tarafdar, Kanchan Bisht

Specialty type: Anatomy and morphology

Provenance and peer review: Unsolicited article; Externally peer reviewed.

Peer-review model: Single blind

Peer-review report's scientific quality classification

Grade A (Excellent): 0
Grade B (Very good): 0
Grade C (Good): C, C
Grade D (Fair): D
Grade E (Poor): 0

P-Reviewer: Taydas O, Turkey; Yang L, China

Received: March 1, 2023
Peer-review started: March 1, 2023
First decision: April 13, 2023
Revised: April 27, 2023
Accepted: May 30, 2023
Article in press: May 30, 2023
Published online: June 28, 2023

Yashu Bhardwaj, Brijendra Singh, Pooja Bhadoria, Rashmi Malhotra, Kanchan Bisht, Department of Anatomy, All India Institute of Medical Sciences, Rishikesh 249203, Uttarakhand, India

Swarnava Tarafdar, Department of Radiodiagnosis, All India Institute of Medical Sciences, Rishikesh 249203, Uttarakhand, India

Corresponding author: Rashmi Malhotra, MS, Additional Professor, Department of Anatomy, All India Institute of Medical Sciences, Rishikesh, Veerbhadra Road, Rishikesh 249201, Uttarakhand, India. rashmi.ana@aiimsrishikesh.edu.in

Abstract

BACKGROUND

The course and variations of thyroid arteries must be understood by surgeons to prevent bleeding during operative procedures of the thyroid gland. There is limited scientific literature regarding the radiological anatomy of thyroid arteries in this geographical area, the Garhwal region of Sub-Himalayan belt, which is considered to be the endemic belt of goiter. Computed tomography angiography provides a three-dimensional orientation of the vascular and surgical anatomy of the entire cervical region.

AIM

To estimate the proportion of variation in origin of thyroid arteries using Computed Tomography Angiography.

METHODS

Using Computed Tomography Angiography, the presence and origin of the superior thyroid artery, inferior thyroid artery, and thyroid ima artery were observed and assessed.

RESULTS

Out of total 210 subjects, superior thyroid artery was seen to be emerging from external carotid artery in 77.1% cases. The artery was found to be originating at the level of bifurcation of common carotid artery in 14.3% cases, whereas in 8.6% cases, it emerged as a direct branch of the common carotid artery. Similarly, the inferior thyroid artery was observed to be emerging from thyrocervical trunk, subclavian artery and vertebral artery in 95.7% cases, 3.3% and 1% cases, respectively. Thyroid ima artery was also reported in a subject, arising from the brachiocephalic trunk.

CONCLUSION
To avoid vascular injuries, excessive and uncontrollable bleeding, intra-operative difficulties, and post-operative issues, it is imperative for surgeons to be aware of the course and variations of thyroid arteries

Key Words: Thyroid arteries; Computed tomography angiography; Origin; Variation

©The Author(s) 2023. Published by Baishideng Publishing Group Inc. All rights reserved.

Core Tip: To avoid vascular injuries, excessive and uncontrollable bleeding, intra-operative difficulties, and post-operative issues, it is imperative for surgeons to be aware of the course and variations of thyroid arteries. The current study will assist the surgeons in understanding the variation in thyroid arteries among people of Garhwal and west Uttar Pradesh region in a non-invasive manner using computed tomography angiography.

Citation: Bhardwaj Y, Singh B, Bhadoria P, Malhotra R, Tarafdar S, Bisht K. Computed tomography angiographic study of surgical anatomy of thyroid arteries: Clinical implications in neck dissection. *World J Radiol* 2023; 15(6): 182-190
URL: https://www.wjgnet.com/1949-8470/full/v15/i6/182.htm
DOI: https://dx.doi.org/10.4329/wjr.v15.i6.182

INTRODUCTION

The thyroid gland is an endocrine gland, which is essential for the normal metabolism and growth of an individual. Conditions affecting the thyroid gland range from simple goiter to malignant thyroid nodule and thyroid carcinoma. Thyroidectomy or hemithyroidectomy is occasionally indicated to remove a malignant thyroid tumor. The neck is also explored for surgical procedures, such as lobectomy, selective embolization of the thyroid, emergency cricothyroidotomy, radical neck dissection, diagnostic and therapeutic catheterization, reconstruction of the aneurysm, and carotid endarterectomy[1]. Bleeding during the operative procedure of the thyroid gland may compress the trachea causing difficulty in breathing[2].

Thyroid is a richly vascularized gland, which is supplied by superior thyroid artery (STA), inferior thyroid artery (ITA) and thyroid ima artery (TIA). The superior thyroid artery usually arises from external carotid artery and runs in close proximity to external branch of superior laryngeal nerve, before entering the fascia of thyroid and giving anterior and posterior branch.

Inferior thyroid artery usually commences from thyrocervical trunk[3]. Occasionally there is presence of a single minor artery, thyroid ima artery in 10% of the individuals[4].

The course and variations of the thyroid arteries must be understood by surgeons to prevent bleeding during the operative procedure of the thyroid gland.

There is limited scientific literature regarding the radiological anatomy of thyroid arteries in this geographical area, the Garhwal region of Sub-Himalayan belt, which is considered to be the endemic belt of goiter[5]. Computed tomography (CT) angiography provides a three-dimensional orientation of the vascular and surgical anatomy of the entire cervical region. For vascular mapping, radiography is a non-invasive multiplanar imaging method[6]. The present study investigated the origin and variation of thyroid arteries with the help of CT angiography.

MATERIALS AND METHODS

The proposed study was done in the Department of Anatomy in collaboration with the Department of Radiodiagnosis over a period of 18 months. A total of 210 samples were included as per inclusion and exclusion criteria. Patients above 18 years who underwent CT angiography were included. Patients who had undergone previous common carotid occlusions or known vascular abnormalities (carotid hypoplasia, plaque in the carotid bifurcation, aneurysms) were excluded. Following the approval of Institutional Ethics Committee, with ethical clearance number AIIMS/IEC/21/323, CT angiographic data from 64-slice CT scanner and 128-slice CT scanner were collected from the Department of Radiodiagnosis. Reconstruction of the three-dimensional views of the images were done using RadiAnt DICOM Viewer (RadiAnt ©), a software installed in the MSI laptop PC. The images, thus obtained, were observed and evaluated for variations. The images were analyzed as per the general anatomical course

and branches of vessels and variations, if present, were noted. The statistical analysis was done using the chi square test and the Stuart–Maxwell test.

Study sample size

The sample size for the proposed study was 208, considering our primary objective, which was to study variation in origin of superior thyroid artery. Previous studies have shown that the percentage of variation in the superior thyroid artery ranged from 6.5%–18.5%. We selected 6.5% to calculate our sample size with 10% (65) of relative procedure and finite population correction factor as 216 with 95% of confidence level and alpha error as 5%. The calculated sample size was 208. We used Open Epi, Version 3, open source calculator for the calculation of same.

RESULTS

We collected 210 samples; however, the calculated sample size for the present study was 208. Out of total 210 participants, 162 (77.1%) participants had the superior thyroid artery originating from the external carotid artery. Participants with superior thyroid artery originating from level of bifurcation of common carotid artery were 30 (14.3%), whereas participants who had origin of superior thyroid artery from common carotid artery were 18 (8.6%). Figure 1 represents the CT angiographic image of various origin of superior thyroid artery in the axial plane.

Participants who had origin of inferior thyroid artery from thyrocervical trunk, subclavian artery, and vertebral artery were 201 (95.7%), 7 (3.3%), and 2 (1.0%), respectively. Figure 2 represent the origin of inferior thyroid artery from left & right subclavian arteries and thyrocervical trunk respectively.

Out of total 210 cases, we observed one case that had origin of thyroid ima artery from brachio-cephalic trunk (Figure 3).

The overall difference in the origin of superior thyroid artery was statistically significant (Stuart–Maxwell test: $\chi^2 = 11.632$, $P = 0.003$) (Table 1).

The overall difference in the origin of inferior thyroid artery was not statistically significant (Stuart–Maxwell test: $\chi^2 = 5.000$, $P = 0.082$) (Table 2).

The following variables were significantly associated ($P < 0.05$) with the variable 'Gender':

The association between "gender" and the "origin of STA" was investigated using the χ^2 test (Table 3).

Regarding the distribution of the origin of the STA, there was no discernible difference between the various groups ($\chi^2 = 1.409$, $P = 0.494$).

Cramer's V value for the strength of association between the two variables is 0.08, which is considered to have little or no association in this study.

The distribution of the origin of ITA did not significantly differ across the different groups ($\chi^2 = 2.059$, $P = 0.545$) (Table 4).

The connection of the two variables for Cramer's V strength was 0.1, which is considered to be little or no association in this study.

DISCUSSION

The STA is considered to be a branch of external carotid artery (ECA) in normal anatomy. The STA can also originate from common carotid artery or bifurcation of common carotid artery, according to studies that have investigated the variability in the origin site of the superior thyroid artery from the carotid arteries. The inferior thyroid artery is generally considered a branch of the thyrocervical trunk, while it can also originate from subclavian artery, vertebral artery and common carotid artery according to previous research[7]. Although thyroid ima artery is considered to originate from brachiocephalic trunk, in some cases it originates directly from arch of aorta[8].

In the present study, we have observed that the STA originated from ECA, common carotid artery (CCA) and bifurcation of common carotid artery (CCB) in 77%, 14.3% and 8.6% of the cases, respectively. However, in the case of ITA the variation in origin was seen only in 3.3% of cases from subclavian artery (SA) and in 1% case from vertebral artery (VA) with varying level of origin of thyrocervical trunk (TCT).

Sreedharan *et al*[7] in 2018 did a cadaveric study depending on the frequency of origin of STA coming from ECA, CCB, or CCA. With an incidence of 88.33%, the STA originated from ECA in 53 of the 60 hemi-neck specimens. A total of 5 out of 60 hemi-necks showed that STA appeared at the CCB in 8.33% of cases. The STA developed from the CCA in 2 of the 60 patients, with an incidence of 3.33%. In the present study the overall difference in the origin of STA was statistically significant (Stuart–Maxwell test: $\chi^2 = 11.632$, $P = 0.003$) on right and left sides, which is shown in Table 1.

Anagnostopoulou *et al*[9] in 2014 conducted a study on 68 formalin-embalmed adult cadavers regarding superior thyroid artery only and categorized their result in three major groups. Type A consisted of cases in which the STA originates from ECA, Type B includes cases in which STA originates

Table 1 Comparison between the origin of superior thyroid arteries on right and left side (*n* = 105), *n* (%)

Origin of superior thyroid artery	Category			Chi-squared test	
	Right	Left	Total	χ^2	*P* value
Bifurcation of common carotid artery	7 (6.7)	23 (21.9)	30 (14.3)	10.756	0.005
Common carotid artery	8 (7.6)	10 (9.5)	18 (8.6)		
External carotid artery	90 (85.7)	72 (68.6)	162 (77.1)		
Total	105 (100.0)	105 (100.0)	210 (100.0)		

Table 2 Comparison between the origin of inferior thyroid arteries on right and left side (*n* = 105), *n* (%)

Origin of inferior thyroid artery	Category			Fisher's exact test	
	Right	Left	Total	χ^2	*P* value
Subclavian artery	1 (1.0)	6 (5.7)	7 (3.3)	3.696	0.119
Thyrocervical trunk	103 (98.1)	98 (93.3)	201 (95.7)		
Vertebral artery	1 (1.0)	1 (1.0)	2 (1.0)		
Total	105 (100.0)	105 (100.0)	210 (100.0)		

Table 3 Association between gender and the origin of superior thyroid artery (*n* = 210), *n* (%)

Origin of STA	Gender			Chi-squared test	
	Male	Female	Total	χ^2	*P* value
External carotid Artery	89 (79.5)	73 (74.5)	162 (77.1)	1.409	0.494
Bifurcation of CCA	13 (11.6)	17 (17.3)	30 (14.3)		
CCA	10 (8.9)	8 (8.2)	18 (8.6)		
Total	112 (100.0)	98 (100.0)	210 (100.0)		

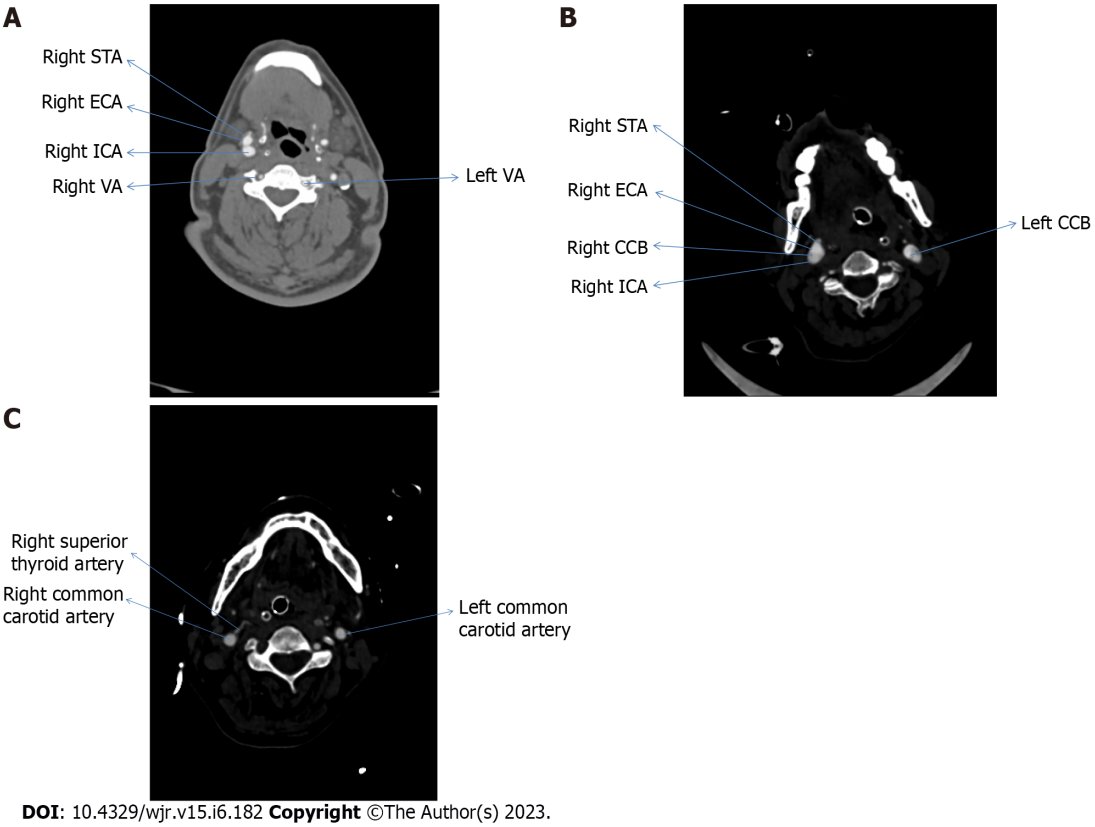
CCA: Common carotid artery; STA: Superior thyroid artery.

Table 4 Association between gender and the origin of inferior thyroid artery (*n* = 210), *n* (%)

Origin of ITA	Gender			Fisher's exact test	
	Male	Female	Total	χ^2	*P* value
Thyrocervical Trunk	107 (95.5)	94 (95.9)	201 (95.7)	2.059	0.545
SA	3 (2.7)	4 (4.1)	7 (3.3)		
VA	2 (1.8)	0 (0.0)	2 (1.0)		
Total	112 (100.0)	98 (100.0)	210 (100.0)		

ITA: Inferior thyroid artery; SA: Subclavian artery; VA: Vertebral artery.

from CCA and Type C constitutes cases in which STA originates from the level of CCB. In 36.8% (25/68) of the patients, Type A was found on the right side, and in 42.6% (29/68) of the cases, on the left. In 32.4% (22/68) and 38.2% (26/68) of the individuals, type B was seen on the right and left side, respectively. In 19.1% (13/68) and 30.9% (21/68) of cases, Type C variation was noted on the right and left sides. In our study, superior thyroid artery originated from ECA in majority of cases followed by level of CCB and then CCA, on left side with 72 (68.6%), 23 (21.9%) and 10 (9.5%) cases, respectively and on the right side the order of frequency of origin of superior thyroid artery is from ECA, CCA and then CCB contrary to study done by Anagnostopoulou *et al*[9].



DOI: 10.4329/wjr.v15.i6.182 **Copyright** ©The Author(s) 2023.

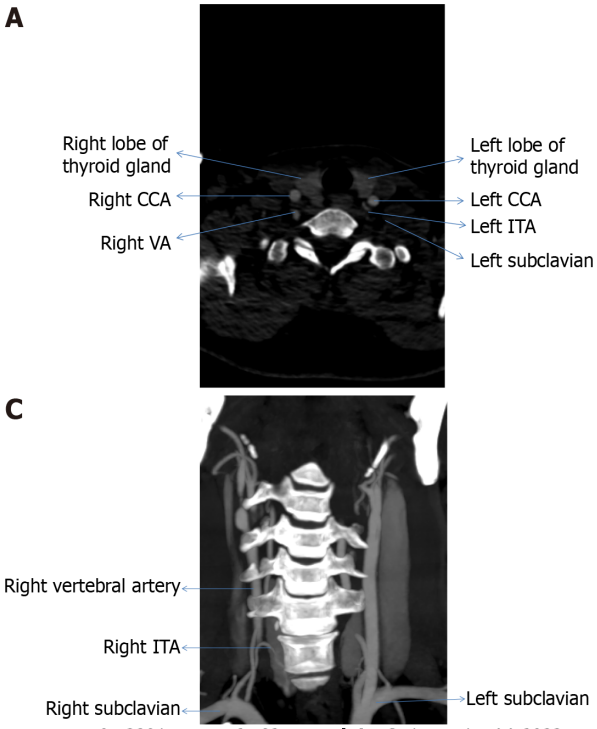
Figure 1 Computed tomography angiographic image (axial section). A: Showing the origin of the right superior thyroid artery from the external carotid artery; B: Bifurcation of the common carotid artery; C: Common carotid artery. STA: Superior thyroid artery; ECA: External carotid artery; ICA: Internal carotid artery; VA: Vertebral artery; CCB: Bifurcation of common carotid artery.

Shankar *et al*[10] in 2017 did a cadaveric study on 80 superior thyroid arteries with 40 right and 40 Left arteries, and found that it originated from the external carotid artery in 43 (53.75%), from CCB in 12 (15%), and the CCA in 25 (31.265%) cases[6]. The results of this study are similar to that of the present study as in the present study STA arose from ECA in 90 (85.7%) and 72 (68.6%) cases, on the right and left sides respectively, as the most common site of origin on both sides.

Esen *et al*[11] in 2017 did an angiographic study on 640 patients in which on the right (64.5%) and left (39.7%) sides, the STA was frequently originated from the ECA. In their study, there were 608 (95%) and 578 (90.3%) right and left ITAs emerging from the thyrocervical trunk, respectively. A single root from the SA gave rise to 18 (2.8%) right and 13 (2.0%) left ITAs. The VA was the origin of four left ITAs. In 15 patients (2.3%), the TIA was identified. A total of 12 of these were brachiocephalic arteries, 2 were right CCAs, and 1 was an aortic arch[7]. In present study the right and left STA arises from ECA in 90 (85.7%) and 72 (68.6%) cases respectively, whereas in the remaining 30 (14.3%) and 18 (8.6%) cases the STA originates from the level of CCB and main trunk of CCA respectively. However, ITA arise from TCT in 103 (98.1%) cases on right and 98 (93.3%) cases on left and among remaining cases 7 (3.3%) arise from SA and 2 (1.0%) arise from VA. We found TIA in 1 case originating from BT.

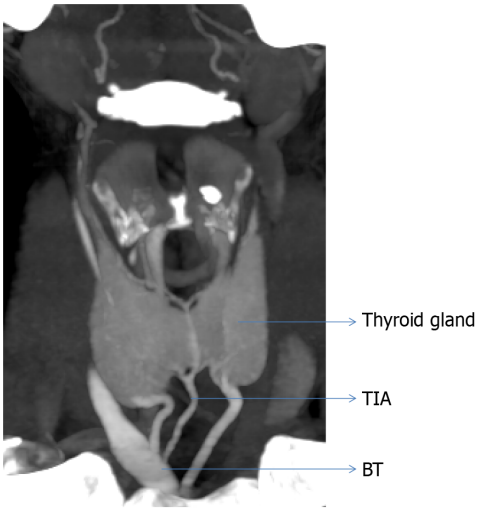
Tsegay *et al*[12] performed a cadaveric study in 2019 and observed that, the ECA was identified as the most frequent location of STA origin. The TCT gave rise to the ITA in each case, while in the present study the result for STA corresponds with the given study as in majority of cases the STA arises from ECA on both the sides, whereas in the case of ITA present study does not correspond with given study as in present study the ITA takes origin from thyrocervical trunk, SA, and VA in 201 (95.7%), 7 (3.3%) and 2 (1.0%) cases, respectively.

Gupta *et al*[13] performed an angiographic study in 2020, on 15 Indian patients indigenously from New Delhi region who were examined with a total of 25 selective STA angiograms. ECA was the primary source of STA on both sides. Ten patients (71.5%) had right STAs with ECA origins, while eight (72.5%) had left STAs with ECA origins. The bifurcation of the CCA accounted for 3 (21%) right STA and 2 (18.5%) left STA, making it the second most frequent site of STA genesis. CCA (right STA) and internal carotid artery (left STA) were the least frequent sites of origin, each accounting for one instance. In the present study, we considered a sample size of 210 patients from population of Uttarakhand, India. Gupta *el al*[13] in their study used DSA technique and also noted the branching patterns of STA only but in our study we observed the CT angiographic data and evaluated STA, ITA as well as TIA.



DOI: 10.4329/wjr.v15.i6.182 **Copyright** ©The Author(s) 2023.

Figure 2 Computed tomography. A: Origin of inferior thyroid artery from left subclavian artery; B: Right subclavian artery; C: Right thyrocervical trunk. ITA: Inferior thyroid artery; VA: Vertebral artery; CCA: Common carotid artery.



DOI: 10.4329/wjr.v15.i6.182 **Copyright** ©The Author(s) 2023.

Figure 3 Showing origin of thyroid ima artery from the brachiocephalic trunk. TIA: Thyroid ima artery; BT: Brachiocephalic trunk.

Dhindsa *et al*[14] in 2014 found during a routine cadaveric dissection on male cadaver that STA on left side was arising from CCA, while on right it was originating from ECA only[10]. In the present study, we evaluated the data of 112 male patients and found that in 89 (79.5%) cases the STA arose from ECA, in 13 (11.6%) cases STA originated from level of CCB and in 10 (8.9%) cases the STA originated from CCA main trunk.

Vázquez *et al*[15] performed a cadaveric study and indicated that there are four different types of origin of STA. In type 1 STA originated from the level of CCB in 102 (49%) of cases. Type 2 was when STA originated from CCA in 55 (27%) of cases. There is a statistically significant difference between the frequency of type 2 origins on the left and right. On the other hand, there was no statistically significant distinction between male and female Type 2 origins. In Type 3, the STA arose from ECA in 48 (23%) cases. In our study we did not categorize the types, but we found that STA arose 120 from CCA, level of CCB and ECA in 18 (8.6%), 30 (14.3%), and 162 (77.1%) cases, respectively and in our study the overall difference in the origin of STA was statistically significant (Stuart–Maxwell test: $\chi^2 = 11.632$, $P = 0.003$)

on right and left sides which is shown in Table 1.

In the present study the measurement of the thyroid arteries was not done.

CONCLUSION

In our study, 77% of the cases had ECA as the source of STA and in more than 22% of cases variation were seen in the origin of STA, from CCA and CCB. Variation in the level of bifurcation of CCA was also seen, which greatly changes the course of STA. The present study reveals the variation in origin of ITA is 4%, while its course varied with varying level of origin of TCT. We found that thyroid ima artery is not frequently present, but was present in only one case and can lead to severe hemorrhagic condition if remains unnoticed.

ARTICLE HIGHLIGHTS

Research background

An individual's normal growth and metabolism depend on the thyroid gland, an endocrine organ. Simple goiter, thyroid cancer, and malignant thyroid nodules are just a few of the conditions that can affect the thyroid gland. Sometimes it is necessary to perform a thyroidectomy or hemithyroidectomy in order to remove a malignant thyroid tumor. Additionally, the neck is examined for surgical treatments such as lobectomy, carotid endarterectomy, emergency cricothyroidotomy, radical neck dissection, diagnostic and therapeutic catheterization, and selective thyroid embolization. Breathing difficulties may result from tracheal compression brought on by bleeding during the thyroid gland surgery.

Research motivation

To avoid complications during thyroid surgeries, surgeons must be aware of the path and variations of the thyroid arteries. The Garhwal region of the Sub-Himalayan belt, which is thought to be the endemic zone of goitre, has little scientific literature on the radiological anatomy of thyroid arteries. A three-dimensional orientation of the vascular and surgical anatomy of the entire cervical region is provided by computed tomography angiography.

Research objectives

Radiography is a non-invasive multiplanar imaging technique for vascular mapping. The objective of the current research was to examine the origin and variation of thyroid arteries, with the aid of Computed Tomography angiography, Surgeons must be familiar with the course and variations of the thyroid arteries to prevent difficulties during thyroid operations.

Research methods

Patients with known vascular anomalies (carotid hypoplasia, plaque in the carotid bifurcation, aneurysms) or past common carotid occlusions were excluded. Following the Institutional Ethics Committee's consent, the Department of Radiodiagnosis obtained computed tomography (CT) angiographic data from 64-slice and 128-slice CT scanners. RadiAnt DICOM Viewer (RadiAnt), a programme installed on the MSI laptop PC, was used to reconstruct the three-dimensional views of the photos. The Stuart-Maxwell test and the chi square test were employed in the statistical study.

Research results

Out of 210 individuals, 77.1% of the time the superior thyroid artery was observed to be arising from the external carotid artery. In 14.3% of cases, the artery was shown to originate at the point where the common carotid artery splits, whereas in 8.6% of cases, it was discovered to be a direct branch of the common carotid artery. Similar to this, in 95.7%, 3.3%, and 1% of cases, respectively, the inferior thyroid artery was seen to be arising from the thyrocervical trunk, subclavian artery, and vertebral artery. Another person was found to have a thyroid ima artery that emerged from the brachiocephalic trunk.

Research conclusions

In our study, superior thyroid artery (STA) originated from external carotid artery in 77% of instances, and the common carotid artery (CCA) and common carotid bifurcation were the sources of STA in more than 22% of cases. Variation in the degree of CCA bifurcation was also observed, which significantly alters the path of STA. The current study shows that there is a 4% variance in inferior thyroid artery origin, whereas its course varies depending on the level of thyrocervical trunk origin. We discovered that the thyroid ima artery is only occasionally present in a small number of cases—it was only present in one case—and that if it goes unnoticed, it can cause serious hemorrhagic disease.

Research perspectives

The Garhwal region of the Sub-Himalayan belt, which is thought to be the endemic zone of goitre, has little scientific literature on the radiological anatomy of thyroid arteries. A three-dimensional orientation of the vascular and surgical anatomy of the entire cervical region is provided by computed tomography angiography. The objective of the current research was to examine the origin and variation of thyroid arteries, with the aid of Computed Tomography angiography, Surgeons must be familiar with the course and variations of the thyroid arteries to prevent difficulties during thyroid operations. Additional research in this area using even better methods can further add to the existing knowledge on thyroid arteries.

ACKNOWLEDGEMENTS

We would like to thank the attendants and fellows from the Radiology department of AIIMS Rishikesh as well as the laboratory staff, Mr. Devender, for their continued support and assistance during data collection.

FOOTNOTES

Author contributions: All the authors have contributed significantly to this work; Singh B, Bhadoria P and Malhotra R designed the research study; Bhardwaj Y and Tarafdar S performed the research; Bhardwaj Y, Malhotra R and Bisht K analyzed the data and wrote the manuscript; All authors have read and approved the final manuscript.

Institutional review board statement: Following the approval of Institutional Ethics Committee, with ethical clearance number AIIMS/IEC/21/323, CT angiographic data from 64-slice CT scanner and 128-slice CT scanner were collected from the Department of Radiodiagnosis.

Informed consent statement: A waiver was granted by our Institutional Ethics committee as this is a retrospective study.

Conflict-of-interest statement: The authors declare no conflict of interest.

Data sharing statement: Anonymization of data will be maintained.

Open-Access: This article is an open-access article that was selected by an in-house editor and fully peer-reviewed by external reviewers. It is distributed in accordance with the Creative Commons Attribution NonCommercial (CC BY-NC 4.0) license, which permits others to distribute, remix, adapt, build upon this work non-commercially, and license their derivative works on different terms, provided the original work is properly cited and the use is non-commercial. See: https://creativecommons.org/Licenses/by-nc/4.0/

Country/Territory of origin: India

ORCID number: Yashu Bhardwaj 0009-0008-0506-2899; Brijendra Singh 0000-0002-3501-0896; Pooja Bhadoria 0000-0001-9617-6526; Rashmi Malhotra 0000-0002-5633-5446; Swarnava Tarafdar 0000-0003-3582-8871; Kanchan Bisht 0000-0002-4615-1352.

S-Editor: Liu JH
L-Editor: A
P-Editor: Zhao S

REFERENCES

1 **Kaplan E**, Angelos P, Applewhite M, Mercier F, Grogan RH. Chapter 21. Surgery of the Thyroid. In: Feingold KR, Anawalt B, Blackman MR, Boyce A, Chrousos G, Corpas E, *et al*, editors. South. Dartmouth (MA). 2000 [DOI: 10.1016/s1530-891x(20)44840-2]
2 **Lemke J**, Schreiber MN, Henne-Bruns D, Cammerer G, Hillenbrand A. Thyroid gland hemorrhage after blunt neck trauma: case report and review of the literature. *BMC Surg* 2017; **17**: 115 [PMID: 29183351 DOI: 10.1186/s12893-017-0322-y]
3 **Allen E**, Fingeret A. Anatomy, head and neck, thyroid. InStatPearls [DOI: 10.1201/b19589-27]
4 **Gray's Anatomy**, 39th Edition: The Anatomical Basis of Clinical Practice. Vol. *American Journal of Neuroradiology* 2005; 2703-2704 [DOI: 10.1177/0310057x0503300431]
5 **Sareen N**, Kapil U, Nambiar V, Pandey RM, Khenduja P. Iodine nutritional status in Uttarakhand State, India. *Indian J Endocrinol Metab* 2016; **20**: 171-176 [PMID: 27042411 DOI: 10.4103/2230-8210.176363]

6 **Kumamaru KK**, Hoppel BE, Mather RT, Rybicki FJ. CT angiography: current technology and clinical use. *Radiol Clin North Am* 2010; **48**: 213-235, vii [PMID: 20609871 DOI: 10.1016/j.rcl.2010.02.006]

7 **Sreedharan R**, Krishna L, Shetty A. Origin of superior thyroid artery: under the surgeon's knife. *J Vasc Bras* 2018; **17**: 290-295 [PMID: 30787946 DOI: 10.1590/1677-5449.004218]

8 **Jayaraju RM**, Mohiyuddin A, Merchant S, Raj S, Sasidharan B. Thyroidea ima artery: a report of two cases. *Int J Head Neck Surg* 2015; **5**: 89-90 [DOI: 10.5005/jp-journals-10001-1188]

9 **Anagnostopoulou S**, Mavridis I. Emerging patterns of the human superior thyroid artery and review of its clinical anatomy. *Surg Radiol Anat* 2014; **36**: 33-38 [PMID: 23783368 DOI: 10.1007/s00276-013-1149-6]

10 **Shankar VV**, N K, Shetty S. A cross-sectional study of superior thyroid artery in human cadavers. *Int J Anat Res* 2017; **5**: 4751-4755 [DOI: 10.16965/ijar.2017.463]

11 **Esen K**, Ozgur A, Balci Y, Tok S, Kara E. Variations in the origins of the thyroid arteries on CT angiography. *Jpn J Radiol* 2018; **36**: 96-102 [PMID: 29204764 DOI: 10.1007/s11604-017-0710-3]

12 **Tsegay AT**, Berhe T, Amdeslase F, Hayelom H. Variations on arterial supply of thyroid gland and its clinical significance in selected universities of North Ethiopia. *Int J Anat Res* 2019; **7**: 6830-6834 [DOI: 10.16965/ijar.2019.237]

13 **Gupta P**, Bhalla AS, Thulkar S, Kumar A, Mohanti BK, Thakar A, Sharma A. Variations in superior thyroid artery: A selective angiographic study. *Indian J Radiol Imaging* 2014; **24**: 66-71 [PMID: 24851008 DOI: 10.4103/0971-3026.130701]

14 **Dhindsa GS**, Sodhi S. Variation in the origin of superior thyroid artery. *J Evol Med Dent Sci* 2014; **3**: 5969-5972 [DOI: 10.14260/jemds/2014/2691]

15 **Vázquez T**, Cobiella R, Maranillo E, Valderrama FJ, McHanwell S, Parkin I, Sañudo JR. Anatomical variations of the superior thyroid and superior laryngeal arteries. *Head Neck* 2009; **31**: 1078-1085 [PMID: 19340860 DOI: 10.1002/hed.21077]

World Journal of Radiology

Submit a Manuscript: https://www.f6publishing.com

World J Radiol 2023 June 28; 15(6): 191-200

DOI: 10.4329/wjr.v15.i6.191

ISSN 1949-8470 (online)

ORIGINAL ARTICLE

Observational Study

Role of contrast-enhanced serial/spot abdominal X-rays in perioperative follow-up of patients undergoing abdominal surgery: An observational clinical study

Osman Nuri Dilek, Arif Atay, Orgun Gunes, Furkan Karahan, Şebnem Karasu

Specialty type: Surgery

Provenance and peer review: Invited article; Externally peer reviewed.

Peer-review model: Single blind

Peer-review report's scientific quality classification

Grade A (Excellent): 0
Grade B (Very good): B
Grade C (Good): C, C
Grade D (Fair): D, D
Grade E (Poor): 0

P-Reviewer: Amagai T, Japan; Ghimire R, Nepal; Giacomelli L, Italy

Received: March 13, 2023
Peer-review started: March 13, 2023
First decision: May 9, 2023
Revised: May 17, 2023
Accepted: June 16, 2023
Article in press: June 16, 2023
Published online: June 28, 2023

Osman Nuri Dilek, Arif Atay, Furkan Karahan, Department of Surgery, İzmir Katip Celebi University, School of Medicine, İzmir 35150, Turkey

Orgun Gunes, Department of Surgery, İzmir Atatürk Education and Research Hospital, İzmir 35150, Turkey

Şebnem Karasu, Department of Radiology, İzmir Katip Celebi University, School of Medicine, İzmir 35150, Turkey

Corresponding author: Osman Nuri Dilek, FACS, Professor, Surgeon, Department of Surgery, İzmir Katip Celebi University, School of Medicine, Basın Sitesi, İzmir 35150, Turkey.
osmannuridilek@gmail.com

Abstract

BACKGROUND

Many imaging methods such as ultrasonography, computed tomography (CT), magnetic resonance imaging, and endoscopy are used to identify the problems or complications that occur in the perioperative period and to determine the appropriate therapeutic approach. Specialists at surgical clinics and intensive care units sometimes need diagnostic procedures that can give quick results or reveal unexpected results. In particular, rapid on-site evaluation of patients followed under intensive care conditions has several advantages.

AIM

To determine the problems developing in patients in the perioperative period by contrast-enhanced abdominal X-ray (CE-AXR), revealing their current status or defining the effectiveness of CE-AXR.

METHODS

The files of the patients who underwent hepatopancreatobiliary or upper gastrointestinal surgery, whose CE-AXR film was taken, were reviewed retrospectively. Abdominal X-ray radiographs taken after ingestion of a water-soluble contrast agent (iohexol, 300 mg, 50 cc vial) and its application in a drain, nasogastric tube, or stent were evaluated. The contribution of the data obtained in patients who underwent CE-AXR to the diagnosis, follow-up, and treatment processes and the effectiveness of the application were investigated.

RESULTS
CE-AXR was applied to 131 patients in our clinic, most of whom underwent hepatopancreatobiliary or upper gastrointestinal surgery. It was determined that the data obtained from CE-AXR films taken in 98 (74.8%) of the patients contributed to the diagnosis, treatment, and follow-up expectations and positively affected the clinical processes.

CONCLUSION
CE-AXR is a simple procedure that can be applied anywhere, especially in intensive care patients and at bedside, with a portable X-ray device. The simplicity of the procedure, less radiation exposure for the patients, less time wastage, reduction in the CT and endoscopy procedure burden and costs, quick results, rapid assessment of the situation, and enabling the monitoring of processes with repetitive procedures are important advantages. X-rays taken will be useful in terms of being a reference value during the follow-up period of the patient and determining the situation in medicolegal processes.

Key Words: Abdominal X-rays; Contrast medium; Diagnosis; Complication; Leakage; Radiation exposure

©The Author(s) 2023. Published by Baishideng Publishing Group Inc. All rights reserved.

Core Tip: Specialists at surgical clinics and and intensive care units sometimes need diagnostic procedures that can give quick results or reveal unexpected results. In this study, contrast-enhanced abdominal X-ray (CE-AXR) was used to evaluate diagnosis and treatment efficacy in 131 patients. We sought to determine the problems developing in patients in the perioperative period, revealing their current condition or defining the effectiveness of CE-AXR. It was found that CE-AXR accelerated and facilitated decision-making processes in selected patient groups and did not require further investigation. It was determined that the data obtained from CE-AXR contributed to the diagnosis, treatment, and follow-up expectations in 98 patients (74.8%) and also had a positive impact on clinical processes. CE-AXR is a procedure that can be performed almost anywhere with a portable X-ray machine, particularly at bedside, and in intensive care units and clinics.

Citation: Dilek ON, Atay A, Gunes O, Karahan F, Karasu Ş. Role of contrast-enhanced serial/spot abdominal X-rays in perioperative follow-up of patients undergoing abdominal surgery: An observational clinical study. *World J Radiol* 2023; 15(6): 191-200
URL: https://www.wjgnet.com/1949-8470/full/v15/i6/191.htm
DOI: https://dx.doi.org/10.4329/wjr.v15.i6.191

INTRODUCTION

A wide variety of imaging methods is used to identify the problems encountered during the follow-up of patients in surgery. Ultrasonography (USG), magnetic resonance imaging (MRI), computed tomography (CT), and endoscopic interventions are the most commonly used methods. It has been reported that interpretations in diagnostic procedures can be very variable and erroneous reporting (diagnosis) is made in 2%-20% of cases in the literature[1]. On the other hand, most diagnostic devices, except USG and mobile X-ray devices, can be used with limitations of place, time, device, and technical staff.

Direct abdominal X-ray (AXR) radiographs are one of the diagnostic devices that can be used almost everywhere in hospitals with the use of mobile X-ray devices, especially in emergency services[2]. It has also been frequently used to control subclavian, jugular, percutaneous endoscopic gastrostomy, nasogastric tube, or peritoneal dialysis catheter positions. It has been reported that while AXR detects foreign bodies with a sensitivity of 90%, it shows intestinal obstructions with a sensitivity of 49%[3]. It has been reported that the data obtained from approximately half of the patients who underwent AXR in the emergency department have no relation with the definitive diagnosis[4]. The use of mobile X-ray devices can play a vital role in the identification and decision-making of developing pathologies, especially in patients followed in intensive care units.

There are no enough studies in the literature on the use of direct/spot contrast-enhanced AXR (CE-AXR) following contrast agent administration. In this observational clinical study, we aimed to examine our CE-AXR application results in the definition and follow-up of clinical manifestations in patients hospitalized in intensive care units and clinics, mostly with hepatopancreatobiliary and upper abdominal surgery, in the light of the literature.

MATERIALS AND METHODS

Study population and data collection

The data was obtained by retrospectively examining the files of the patients who had CE-AXR films in the surgical clinic (125 beds) of our university hospital (1100 beds) between 2017 and 2021. Since hepato-pancreatobiliary (HPB) and upper gastrointestinal surgeries are mainly performed in our clinic, the patients participating in the study manily underwent pancreatic, liver, biliary tract, esophagus, and stomach surgeries. Most of the patients who underwent major surgery were followed in the intensive care unit in the early postoperative period (1-5 d). Those who were followed in the clinic or the outpatient clinic or who applied to the emergency department with serious complications were also followed in the intensive care unit. Along with conventional diagnostic tools in our hospital, mobile ultrasound and mobile X-ray devices are constantly used.

Study assessment and criteria

CE-AXR scans were performed on selected patients to control and confirm the efficacy of surgeries or to evaluate unexpected results. Outpatient X-ray devices were used in stable patients and mobile X-ray devices were used in patients hospitalized in the clinic. CE-AXR images were taken with mobile X-ray machines at bedside for patients who were thought to be evaluated in the intensive care unit. More complicated patients were transported to the radiology service with their beds and mobile life support units for conventional CT or MRI examination. In case of insufficient data obtained with CE-AXR or in patients with an unexpected pathological condition (anastomotic leakage, stricture, *etc*.), it was decided to perform MRI, magnetic resonance cholangiopancreatography (MRCP), or CT first. Data on conventional cholangiography and other conventional contrast-enhanced imaging methods were not included in the study.

Techniques

AXR radiographs taken following the ingestion of a water-soluble contrast agent (iohexol, 300 mg, 50 cc vial) in the preoperative or postoperative period and its application in a drain or stent were evaluated. CE-AXRs were taken in the early or late periods following the application according to the characteristics of the case and expectations. In patients with percutaneous transhepatic biliary drainage (PTBD), AXR imaging was performed by administering the contrast material through the catheter on postoperative 5th-10th days. While a single spot AXR radiography may be sufficient in most cases, in some of the cases, 2-3 spot AXRs were taken intermittently to monitor the intestinal passage.

In the evaluation of the results, statistical analysis methods were not used, except for numerical and proportional data for the evaluation of whether the procedure contributed to the diagnosis and treatment process.

The study was carried out in accordance with the principles of the Helsinki Declaration. As a routine procedure, written informed consent was obtained from each patient for all procedures and publications. Ethics committee approval was received for this study (2022/GOKAE/0542) from the Clinical Trials Ethics Committee.

RESULTS

CE-AXR images of 131 cases included in the study were evaluated retrospectively (Table 1). CE-AXR images taken to evaluate the patency of anastomoses, which were initially performed in our clinic only in selected patients with PTBD and have started to be applied in more patients in the last two years. CE-AXR was taken at bedside in 67 patients in the intensive care unit during their follow-up. Patients who could not be evaluated with the obtained CE-AXR images were sent to the relevant units for endoscopy, CT, or other diagnostic examinations.

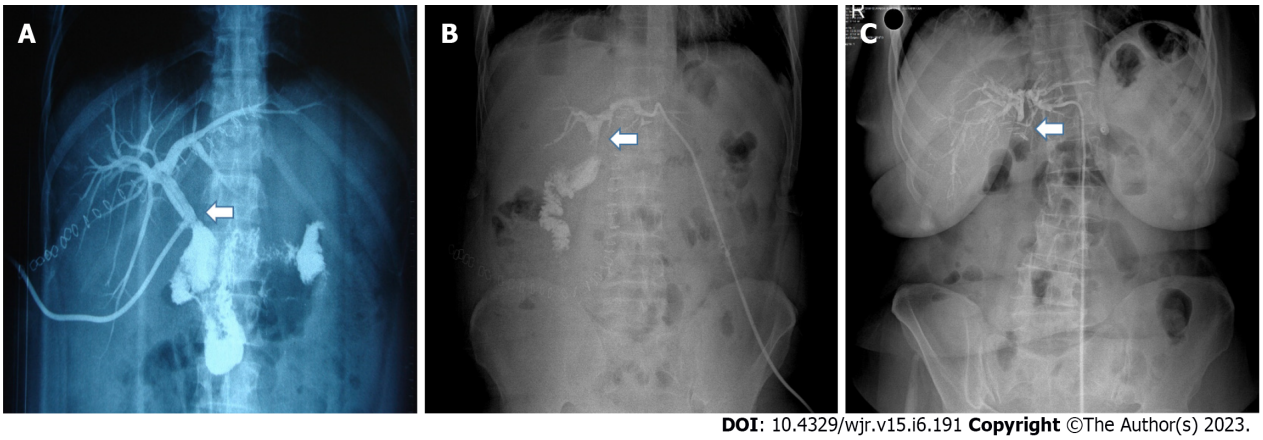
Anastomosis could be evaluated in 29 (80%) patients in CE-AXR radiographs taken with the contrast medium given through the PTBD catheter among 36 patients who underwent hepaticojejunostomy or portoenterostomy (Figure 1). Anastomotic leakage was detected in two patients, while stricture developed in two patients. It was decided to perform MRCP in seven patients who developed complications and could not be evaluated due to insufficient images.

Oral fluid-food intake is started after the routine evaluation of CE-AXR radiographs taken on the 3rd or 4th postoperative days of our patients who underwent esophagectomy (+ gastric pull-up) or total gastrectomy (+ Roux-n-Y reconstruction) (Figure 2). A descriptive image was obtained in 27 of 34 patients (79%) who underwent CE-AXR, and anastomotic leakage was detected in two of the cases (Table 1) (Figure 3). Adequate radiological imaging (Figure 4) was obtained in 15 of 18 patients (78%) with sleeve gastrectomy in our series, no complications were detected in any of them, and the patients were discharged with full recovery.

CE-AXR examinations were performed (Figure 5) to describe the continuity of the gastrointestinal transition in patients (n = 43) receiving chemotherapy or developing acute abdomen (intestinal obstruction), or postoperative patients. Definitive diagnosis was made in 27 cases (62%), and additional

Table 1 Characteristics of patients with contrast-enhanced abdominal X-ray (*n* = 131)

Procedure	*n*	Positive results (Success) *n*, %
Patency of hepaticojejunostomy (stricture? leakage?)	21	17
Patency of portoenterostomy (stricture? leakage?)	15	12
Esophagiectomy + Gastric pull-up	9	7
Total proximal gastrectomies	14	11
Bariatric surgery	18	15
Gastrointestinal anastomosis	11	9
Intestinal obstruction (etiology? levels?)	9	7
Acute abdomen? Etiology? (Perforation? leakage?)	8	4
Dysfunctional ostomies	2	-
Postoperative vomiting	13	7
Persistent vomiting (chemotherapy/follow-up period)	11	9
Total	131	98 (74.8)



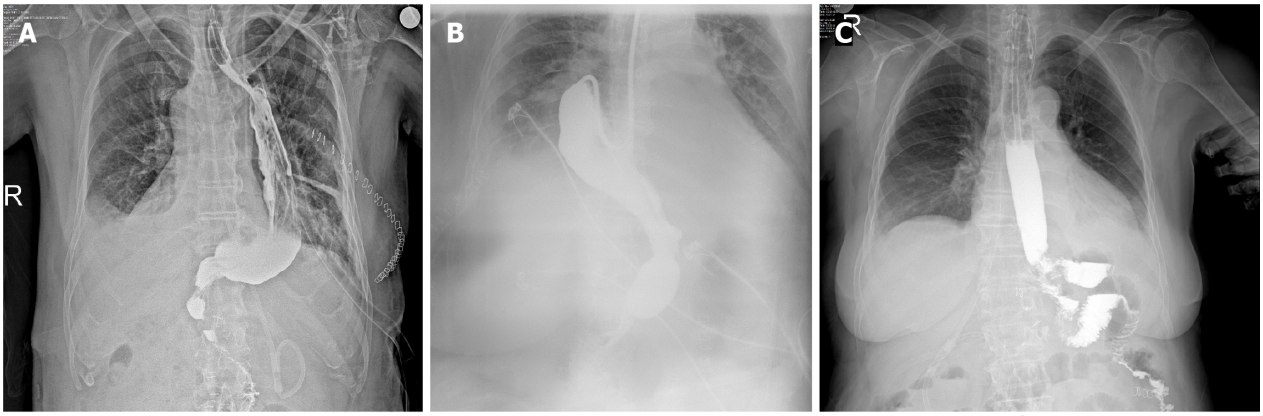
DOI: 10.4329/wjr.v15.i6.191 **Copyright** ©The Author(s) 2023.

Figure 1 Postoperative contrast-enhanced abdominal X-ray images following hepaticojejunostomy for the reconstruction of the biliary tract. A: Postoperative 14th day contrast-enhanced abdominal X-ray in a 42-year-old man with major bile duct trauma (Strasberg Bismuth E1) who underwent T-tube reconstruction; the biliary tract and anastomosis was normal; B: The anastomosis and bile flow patency was normal in a 47-year-old woman who underwent hepaticojejunostomy for major bile duct trauma (Strasberg Bismuth E2); C: The stricture (arrow) in the common hepatic duct was detected in a 38-year-old woman who developed jaundice after biliary tract trauma (Strasberg Bismuth E2) and underwent percutaneous transhepatic biliary drainage.

radiological imaging was required for a definitive diagnosis in 16 cases (Table 1). For patients who were consulted to our clinic with the suspicion of intestinal obstruction, in addition to the routine procedures applied, the passage was evaluated objectively by taking 2-3 spot images with CE-AXR. Medical treatment protocols were applied to cases with the open passage with CE-AXR, and surgical treatment for patients with CE-AXR obstruction (Figure 6). Twenty-two patients were followed with suspected nausea and vomiting (*n* = 13) or intestinal obstruction (*n* = 9); 12 of them were radiologically normal, and intestinal obstruction was found in two patients (Figure 7). Additional examinations (CT, gastroscopy, and colonoscopy) were performed on other patients for whom sufficient information could not be obtained with CE-AXR.

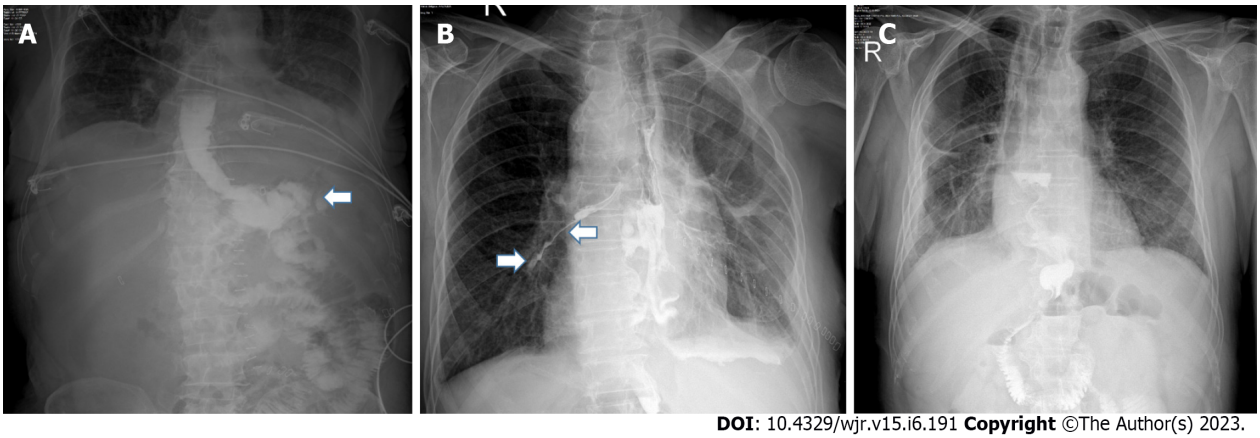
The most common causes of failure in imaging on X-rays taken to detect the presence of anastomotic stenosis or leakage were found to be lack of contrast material (amount or concentration) and timing problems (early-late). It was calculated that imaging data contributed positively to the diagnosis, follow-up, and treatment processes in 98 (74.8%) of the patients with CE-AXR.

Allergic or renal problems or technical problems related to the administration of contrast material were not encountered.



DOI: 10.4329/wjr.v15.i6.191 **Copyright** ©The Author(s) 2023.

Figure 2 Contrast-enhanced abdominal X-ray images following gastrointestinal reconstruction for stomach/esophagus tumors. A: A 67-year-old man and a 78-year-old woman who underwent esophagectomy + gastric pull-up for distal esophageal tumor. The esophagogastric passage was normal without any findings of fistula or leakage at the sites of anastomoses on the postoperative 4th day; C: The position of the jejunal loop/stump and the passage was normal in a 72-year-old woman who underwent total gastrectomy and Roux-n-Y anastomosis for cardia tumor.



DOI: 10.4329/wjr.v15.i6.191 **Copyright** ©The Author(s) 2023.

Figure 3 Contrast-enhanced abdominal X-ray images showing anastomotic leakage. A: Anastomotic leakage in a 77-year-old man with total gastric resection and Roux-n-Y anastomosis (arrows) for gastric cancer on the 6th postoperative day; B: Anastomotic leakage detected in a 63-year-old man on the postoperative 4th day who underwent esophagectomy + gastric pull-up for distal esophagus tumor; C: Repeated control contrast-enhanced abdominal X-ray showed healing in the same patient on postoperative 30th day.

DISCUSSION

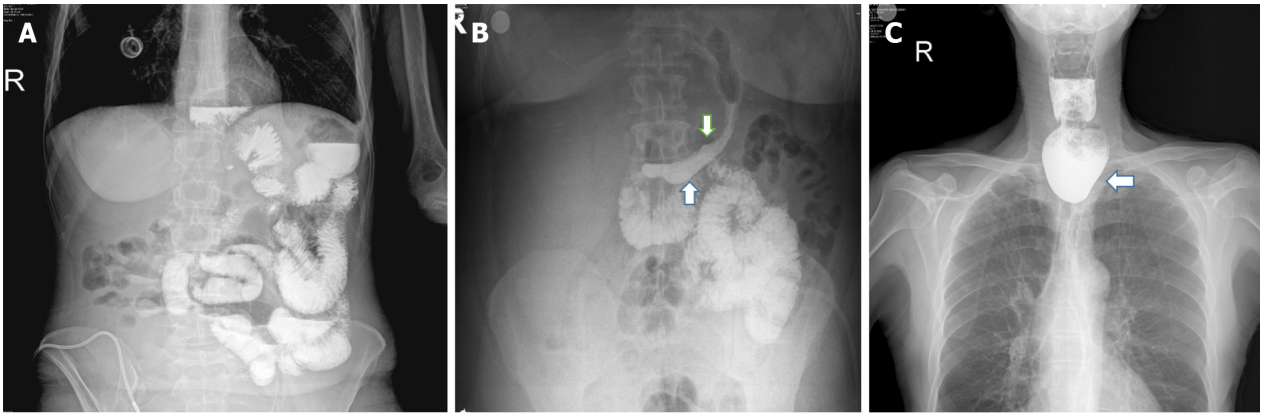
Specialists at surgical clinics and intensive care units sometimes need diagnostic procedures that can give quick results or reveal unexpected results. Radiological examinations are the most widely used and accessible diagnostic tools today[5]. Endoscopists and surgeons often make use of scope imaging during their procedures.

Direct/spot AXRs are mostly used in emergency departments to elucidate the etiology of pain[1,2,6].

AXRs are typically taken in about half of patients suffering from abdominal pain[4,5]. It has also been reported that most AXRs in emergency departments are unnecessary. It has been reported in the literature that positive X-ray results are detectable in 15.8% to 25% of patients undergoing AXRs[2-4]. Today, a wide variety of contrast agents is also used to eliminate the disadvantages of direct imaging, to obtain better images with modern imaging devices, and to make more accurate interpretations. The use of contrast media has become a common procedure in CT, MR, and USG examinations to better define organ and tissue limits. Positive results were obtained in most of the cases (n = 98, 74.8%) with CE-AXR in our series (Table 1).

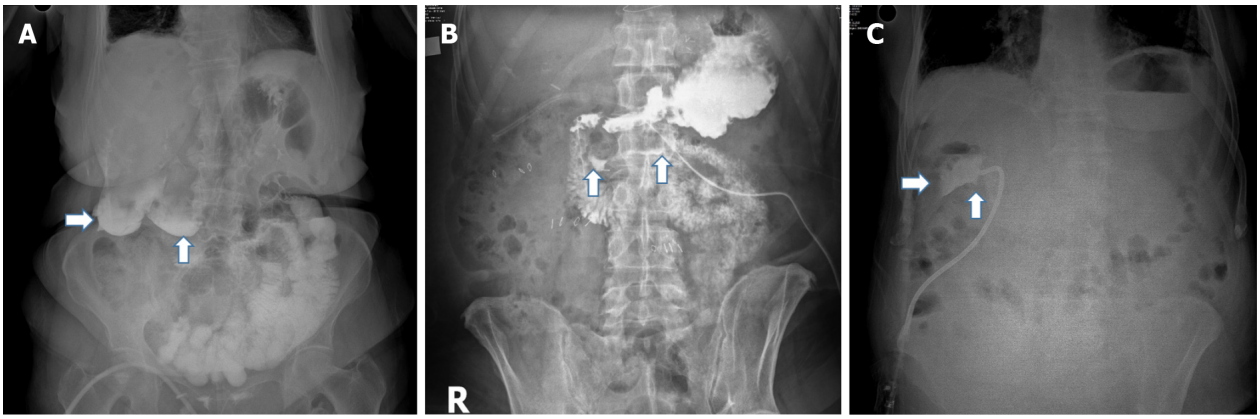
CE-AXRs were originally made to understand the status (patency, stenosis, or leak) of hepaticojejunostomy or portoenterostomies performed only in selected patients undergoing HPB surgery (Figure 1). It has also been used later to describe the current state of patients and when quick decision-making is required.

The major cause of morbidity and mortality after esophagectomy or total gastric resection is asymptomatic anastomotic leakage. Although routine radiological follow-up is not performed in the early postoperative period, it has been reported that anastomotic leakage can be overlooked even in



DOI: 10.4329/wjr.v15.i6.191 **Copyright** ©The Author(s) 2023.

Figure 4 Functionality of the gastrointestinal passage and patency of anastomosis on contrast-enhanced abdominal X-rays. A: A 57-year-old woman whose esophagojejunal anastomosis functionality and passage continuity were investigated and evaluated as normal on the 4th postoperative day; B: The gastric remnant, position, and functionality were normal in a 37-year-old woman (BMI-47.2) on the 3rd postoperative day after sleeve gastrectomy; C: Zenker's diverticulum that was unexpectedly detected in a 44-year-old man with gastric resection for gastric cancer, who presented with dysphagia in the postoperative follow-up period.



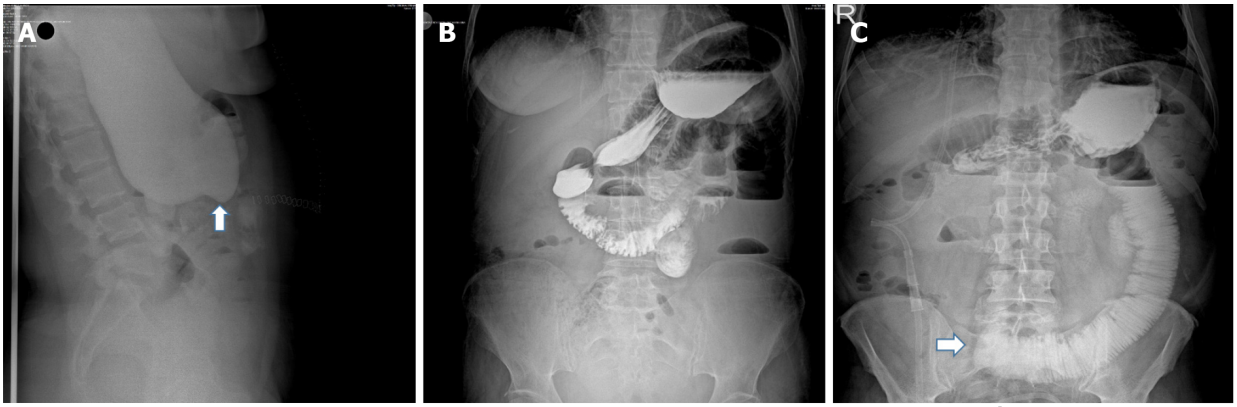
DOI: 10.4329/wjr.v15.i6.191 **Copyright** ©The Author(s) 2023.

Figure 5 Leakage and perforation on contrast-enhanced abdominal X-rays. A: Contrast material leakage into the abdominal cavity (arrows) due to the peptic ulcer perforation seen on contrast-enhanced abdominal X-ray (CE-AXR) in a 76-year-old woman who cannot be diagnosed by clinical findings; B: CE-AXR in a 57-year-old woman who underwent laparoscopic stromal tumor resection and developed unexpected abdominal pain on the 5th postoperative day showed an opening at the suture line and contrast material leakage (arrows); C: In a 68-year-old woman who underwent hilar resection and portoenterostomy for Klatskin tumor, CE-AXR obtained by administering contrast material through the drain showed the biliary fistula tract and subhepatic pouch (arrows).

routine detailed scans[7]. CE-AXR examinations, which we previously performed in selected patients, have recently begun to be routinely performed (Figures 2-4). In patients with fistula, CE-AXR can guide the location, depth, dimensions, and treatment planning of the fistula.

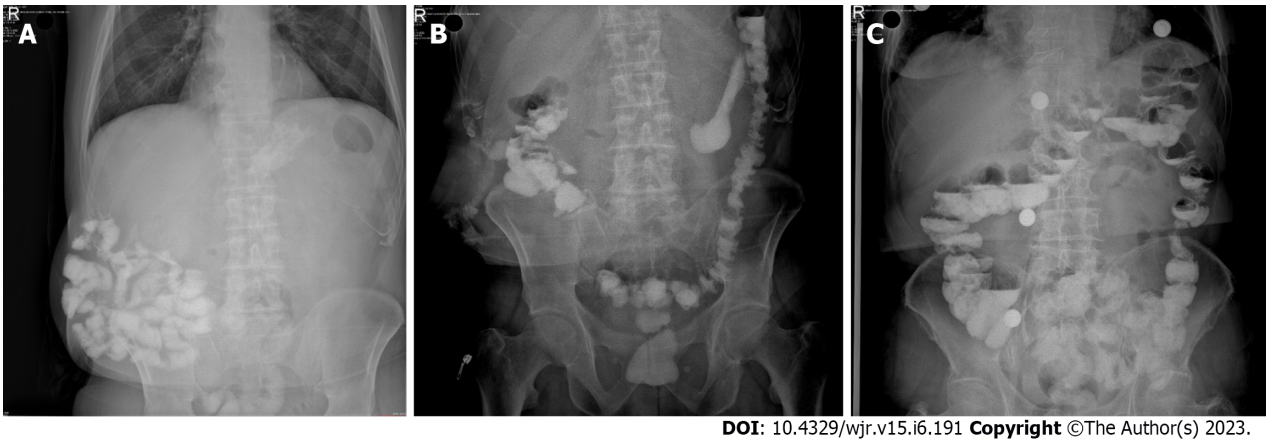
Intraoperative methylene blue injection through the nasogastric tube is a widely used method[8,9] for checking the tightness of the staple line (leakage) in bariatric and gastrointestinal surgery. Recently, intraoperative indocyanine green has been used for the same purpose[9]. Studies also report a high rate of false negativity in postoperative routine endoscopy or anastomotic leakage screening with methylene blue[10]. In our clinic, methylene blue is routinely used in surgery for the control of tightness in patients undergoing bariatric surgery. While patients were previously given methylene blue on the 3rd or 4th postoperative day, they have recently been evaluated with CE-AXR taken with oral contrast (Figure 4). We believe that it is a more objective method than evaluation with methylene blue. CE-AXR taken on the 3rd or 4th postoperative day also gives information about the resection margins (leakage), stomach balance, and passage status at the patient's discharge time. It also has advantages such as documenting the final status of the patient with the CE-AXR taken and having reference data in the controls to be made.

The continuity of the passage and the presence of perforation can be questioned with a water-soluble radiopaque contrast material to be drunk or administered through a nasogastric tube in patients who are elderly, have cooperation problems, have faint physical examination findings, and whose etiology of the acute abdomen cannot be adequately evaluated. We had cases diagnosed with peptic ulcer



DOI: 10.4329/wjr.v15.i6.191 **Copyright** ©The Author(s) 2023.

Figure 6 Contrast-enhanced abdominal X-rays showing intestinal obstruction. A: Lateral contrast-enhanced abdominal X-ray (CE-AXR) showed gastric dilation due to gastric outlet obstruction (Arrow) in a 48-year-old woman with persistent nausea and vomiting after pylorus-preserving pancreatoduodenectomy; B: Abdominal cocoon was detected on CE-AXR in a 67-year-old woman who suffered from acute abdomen; C: CE-AXR showed a 74-year-old man who was thought to develop intestinal obstruction due to adhesions (arrow).



DOI: 10.4329/wjr.v15.i6.191 **Copyright** ©The Author(s) 2023.

Figure 7 Non-surgical patients' contrast-enhanced abdominal X-rays for evaluations of intestinal passage continuity. A: A 69-year-old man underwent pancreatoduodenectomy for a pancreas tumor in the 6th postoperative year and presented with persistent nausea and vomiting due to incarcerated intestinal loops collected in a giant incisional hernia; B: It was seen in the right lower quadrant of the abdomen and the intestinal passage was evaluated as normal; C: Normal passage of the contrast material was seen on contrast-enhanced abdominal X-ray in a 59-year-old woman who was treated with chemotherapy and presented with persistent nausea and vomiting.

perforation by administering an oral contrast agent in drinking water in patients followed up with the diagnosis of acute abdomen and the cause of which could not be identified. Unexpected fistula cases were also detected (Figure 5). CE-AXR may contribute to the reduction of unnecessary laparotomy. On the other hand, it can prevent complications due to delays in diagnosis and treatment.

Gastric emptying difficulty is a serious problem in patients who have undergone major surgery, especially after pancreatoduodenectomy[11-13]. Patients receiving adjuvant chemotherapy may also experience severe nausea and vomiting from time to time. The underlying cause should be studied in certain patients receiving chemotherapy at the oncology clinic who have treatment-resistant nausea and vomiting. Delayed healing of wounds may occur because of wide incisions, high risk of infection, and chemotherapy, and patients with pancreatoduodenectomy may have more incisional hernias that can reach large sizes. Continuity of transition may be assessed with CE-AXR in patients with giant incisional hernias (Figure 7) and complaints of nausea and vomiting. CE-AXR can also prevent unnecessary surveys, procedures, and laparotomies. There may be evidence to show that the patient has recovered or improved after surgery.

Nowadays, the largest source of radiation exposure is X-ray imaging equipment used in diagnostic and therapeutic procedures. According to the global calculations, the average amount of natural radiation or exposure to Radon per person is calculated as 2.4 mSv/year (Table 2)[14-19]. More than 500 million radiological imaging examinations are performed annually in the United States. It is calculated that radiation exposure will increase progressively[14,20]. According to BEIR reports, it has been calculated that abdominal sarcoma/carcinoma may develop in one of 550-600 patients who received 20 mSv of radiation in conventional computed tomography scans[15,21]. The amount of radiation exposure

Table 2 Effective doses of radiation for various radiological procedures and activities

Form of exposure to radiation	Effective dose (mSv)
Natural background radiation for 1 yr	1.3-4.1 (mean 2.4)
Airline passenger with Subsonic flight at 36.000 feet from New York to Istanbul	0.04
Abdominal/pelvic X-ray	0.7
Barium meal/enema	3-10
Hiroshima (measured from the jawbone, 1997)	9460
Average personal dose received by Turkish people due to the Chernobyl accident	0.5
Mammogram	0.4
Chest X-ray	0.02
Intravenous pyelography-IVP	6
Abdominal CT (± contrast)	10-30
Chest/cardiac CT	7.8/16
Pelvic CT	10
Angiography/venography	11-33
CT-guided intervention	11-17
Nuclear stress test with Tc-99m/thallium	11-22
Ultrasonography	0
Abdominal MRI	0

Figures are average data compiled from different reports and may vary according to country, age, gender, devices, and other variables. 1 Gy = 1 Sv = 1000 mSv = 100 Rem. CT: Computed tomography; MRI: Magnetic resonance imaging.

caused by AXR (0.7 mSv) is higher than that by chest X-ray (0.02 mSv)[5,21,22]. The amount of radiation exposure with CE-AXR is significantly lower than that with fluoroscopy and CT (Table 2). It has been determined that CE-AXR can be taken with mobile X-ray devices at bedside and in intensive care units. It also accelerates and facilitates decision-making processes and requires no further review.

CONCLUSION

Simple and mobile devices can also play a significant role in managing medical and surgical processes. Important data can be obtained using CE-AXR to confirm clinical results, determine status, or rule out a diagnosis or event. In selected cases and series, CE-AXR has many clinical benefits and contributions. These are: (1) Very handy and quick results are available; (2) It is possible to determine whether the entities in question are present or not; (3) It is more appropriate in intensive care units and at bedside; (4) The workload in radiology (CT/MRI) and endoscopy units is reduced; (5) Exposure to irradiation is reduced; (6) The use of radiopaque substances, which have toxic effects on the kidneys and have allergic properties, will decrease; and (7) It may be a benchmark for future medical follow-ups and medicolegal proceedings.

ARTICLE HIGHLIGHTS

Research background

Although abdominal X-rays are one of the most frequently used imaging methods in emergencies, they are not as reliable as expected.

Research motivation

The desire to quickly evaluate and know the developments in patients being followed in the surgery clinic and intensive care units prompted us to conduct this study.

Research objectives
It has been designed especially for imaging at bedside in order to learn the result of the procedure or the existence and dimensions of undesirable situations in a short time.

Research methods
Initially, contrast-enhanced abdominal X ray (CE-AXR) was performed to evaluate only biliary tract anastomoses (cholangiography). Evaluation of images (CE-AXR) obtained by the application of catheters, drains, nasogastric tube, or oral contrast agent (iohexol, 300 mg, 50 cc vial) mixed with saline or water in very different clinical situations with satisfactory results (stenosis, patency, functionality, fistula, obstruction, *etc.*) was performed. File data of patients who underwent CE-AXR in the retrospective observational study were evaluated.

Research results
As a result of examining the data of a total of 131 patients, it was determined that CE-AXR, which was performed after liver, biliary tract, pancreas, esophagus, and stomach operations, provided adequate imaging in 74.8% of the cases and contributed to the diagnosis and treatment process. No complications related to the procedure were observed.

Research conclusions
CE-AXR is a very simple imaging method that has no side effects. It can be very useful in clinics and intensive care units because it can be done with mobile X-ray devices at bedside and give fast results. It also has advantages such as reducing the burden of the radiology unit and exposure to radiation.

Research perspectives
CE-AXR can contribute to the diagnosis and treatment process in patients with upper gastrointestinal (esophagus and stomach) and hepatopancratobiliary surgeries, chemotherapy patients, and cases with persistent nausea-vomiting complaints and suspected intestinal obstruction. Prospective clinical studies are needed to better understand the effectiveness of CE-AXR.

FOOTNOTES

Author contributions: Dilek ON was the designer of the study and revised the article critically for scientific content and collected the images; Güneş Ö and Atay A participated in the acquisition, analysis, and interpretation of the data, and drafted the initial manuscript; Karahan F and Karasu Ş collected and reported the patients' data and images.

Institutional review board statement: The study was carried out in accordance with the principles of the Helsinki Declaration. As a routine procedure, written informed consent was obtained from each patient for all procedures and publications. Ethics committee approval was received for this study (2022/GOKAE/0542) from the Clinical Trials Ethics Committee.

Informed consent statement: All study participants, or their legal guardians, provided informed written consent before study enrollment. The data used in this study did not involve the patients' privacy information, so the informed consent was waived by the Ethics Committee of University Hospital. All patient data obtained, recorded, and managed were only used for this study, and all patient information is strictly confidential, without any harm to the patient.

Conflict-of-interest statement: All of the authors declare that there are no conflicts of interest in connection with this paper, and the material described is not under publication or consideration for publication elsewhere.

Data sharing statement: All of the authors declare that there are no shared data in this paper, and the material described is not under publication or consideration for publication elsewhere.

STROBE statement: The authors have read the STROBE Statement—checklist of items, and the manuscript was prepared and revised according to the STROBE Statement—checklist of items.

Open-Access: This article is an open-access article that was selected by an in-house editor and fully peer-reviewed by external reviewers. It is distributed in accordance with the Creative Commons Attribution NonCommercial (CC BY-NC 4.0) license, which permits others to distribute, remix, adapt, build upon this work non-commercially, and license their derivative works on different terms, provided the original work is properly cited and the use is non-commercial. See: https://creativecommons.org/Licenses/by-nc/4.0/

Country/Territory of origin: Turkey

ORCID number: Osman Nuri Dilek 0000-0002-6313-3818; Arif Atay 0000-0001-8163-2357; Orgun Gunes 0000-0002-0576-

6086; Furkan Karahan 0000-0003-0384-8181; Şebnem Karasu 0000-0002-0106-5901.

S-Editor: Liu JH
L-Editor: Wang TQ
P-Editor: Zhao S

REFERENCES

1 **Egri C**, Darras KE, Scali EP, Harris AC. Classification of Error in Abdominal Imaging: Pearls and Pitfalls for Radiologists. *Can Assoc Radiol J* 2018; **69**: 409-416 [PMID: 30318459 DOI: 10.1016/j.carj.2018.06.006]
2 **Smith JE**, Hall EJ. The use of plain abdominal x rays in the emergency department. *Emerg Med J* 2009; **26**: 160-163 [PMID: 19234001 DOI: 10.1136/emj.2008.059113]
3 **Hassan T**, Kumwenda M, Qutab S, Naqvi SZ, Rashid H, Johnson S. Are we following iRefer guidelines from the royal college of radiology when requesting abdominal x-rays? *Cureus* 2022; **14**: e31050. [PMID: 36349071 DOI: 10.7759/cureus.31050]
4 **Campbell JP**, Gunn AA. Plain abdominal radiographs and acute abdominal pain. *Br J Surg* 1988; **75**: 554-556 [PMID: 3395821 DOI: 10.1002/bjs.1800750616]
5 **Fernandez M**, Craig S. Appropriateness of adult plain abdominal radiograph requesting in a regional Emergency Department. *J Med Imaging Radiat Oncol* 2019; **63**: 175-182 [PMID: 30628194 DOI: 10.1111/1754-9485.12847]
6 **Rosenbaum HD**, Lieber A, Hanson DJ, Pellegrino ED. A routine survey roentgenogram of the abdomen on 500 consecutive patients over 40 years of age. *Am J Roentgenol Radium Ther Nucl Med* 1964; **91**: 903-909 [PMID: 14139923]
7 **Kang H**, Ben-David K, Sarosi GA, Thomas RM. Routine Radiologic Assessment for Anastomotic Leak Is Not Necessary in Asymptomatic Patients After Esophagectomy for Esophageal Cancer. *J Gastrointest Surg* 2022; **26**: 279-285 [PMID: 35037179 DOI: 10.1007/s11605-021-05219-3]
8 **Kirby GC**, Macano CAW, Nyasavajjala SM, Sahloul M, Nijjar R, Daskalakis M, Richardson M, Singhal R. The Birmingham experience of high-pressure methylene blue dye test during primary and revisional bariatric surgery: A retrospective cohort study. *Ann Med Surg (Lond)* 2017; **23**: 32-34 [PMID: 29071067 DOI: 10.1016/j.amsu.2017.09.015]
9 **Hagen ME**, Diaper J, Douissard J, Jung MK, Buehler L, Aldenkortt F, Barcelos GK, Morel P. Early Experience with Intraoperative Leak Test Using a Blend of Methylene Blue and Indocyanine Green During Robotic Gastric Bypass Surgery. *Obes Surg* 2019; **29**: 949-952 [PMID: 30607685 DOI: 10.1007/s11695-018-03625-2]
10 **Nelson L**, Moon RC, Teixeira AF, Jawad MA. Methylene Blue or Upper GI, Which is More Effective for Detecting Leaks in Gastric Bypass Patients? *Surg Laparosc Endosc Percutan Tech* 2015; **25**: 451-454 [PMID: 26271023 DOI: 10.1097/SLE.0000000000000191]
11 **Panwar R**, Pal S. The International Study Group of Pancreatic Surgery definition of delayed gastric emptying and the effects of various surgical modifications on the occurrence of delayed gastric emptying after pancreatoduodenectomy. *Hepatobiliary Pancreat Dis Int* 2017; **16**: 353-363 [PMID: 28823364 DOI: 10.1016/S1499-3872(17)60037-7]
12 **Nojiri M**, Yokoyama Y, Maeda T, Ebata T, Igami T, Sugawara G, Yamaguchi J, Nagino M. Impact of the gastrojejunal anatomic position as the mechanism of delayed gastric emptying after pancreatoduodenectomy. *Surgery* 2018; **163**: 1063-1070 [PMID: 29325788 DOI: 10.1016/j.surg.2017.11.016]
13 **Tani M**, Terasawa H, Kawai M, Ina S, Hirono S, Uchiyama K, Yamaue H. Improvement of delayed gastric emptying in pylorus-preserving pancreaticoduodenectomy: results of a prospective, randomized, controlled trial. *Ann Surg* 2006; **243**: 316-320 [PMID: 16495694 DOI: 10.1097/01.sla.0000201479.84934.ca]
14 **Lim H**, Choi J, Kim JH, Cheong HK, Ha M. Estimation of Cancer Incidence and Mortality Risks Attributed to Diagnostic Medical Radiation Exposure in Korea, 2013. *J Korean Med Sci* 2018; **33**: e211 [PMID: 30008633 DOI: 10.3346/jkms.2018.33.e211]
15 **National Cancer Institute**, National Institute of Health. Radiation Risk Assessment Tool-lifetime cancer risk from ionizing radiation. (Accessed Dec 24, 2022). Available from: https://radiationcalculators.cancer.gov/radrat/about/
16 **Canadian Nuclear Safety Commission**. Radiation doses. (Accessed Dec 24, 2022). Available from: https://nuclearsafety.gc.ca/eng/resources/radiation/introduction-to-radiation/radiation-doses.cfm
17 **United Nations Scientific Committee on the Effects of Atomic Radiation**. UNSCEAR 2008 report to the general assembly, with scientific annexes. (Accessed Dec 24, 2022). Available from: http://www.unscear.org/unscear/en/publications/2008_1.html
18 **Nesterenko AV**, Nesterenko VB, Yablokov AV. 12. Chernobyl's radioactive contamination of food and people. *Ann N Y Acad Sci* 2009; **1181**: 289-302 [PMID: 20002056 DOI: 10.1111/j.1749-6632.2009.04837.x]
19 **Brooks AL**, Hoel DG, Preston RJ. The role of dose rate in radiation cancer risk: evaluating the effect of dose rate at the molecular, cellular and tissue levels using key events in critical pathways following exposure to low LET radiation. *Int J Radiat Biol* 2016; **92**: 405-426 [PMID: 27266588 DOI: 10.1080/09553002.2016.1186301]
20 **Huda W**, Nickoloff EL, Boone JM. Overview of patient dosimetry in diagnostic radiology in the USA for the past 50 years. *Med Phys* 2008; **35**: 5713-5728 [PMID: 19175129 DOI: 10.1118/1.3013604]
21 **Berrington de Gonzalez A**, Iulian Apostoaei A, Veiga LH, Rajaraman P, Thomas BA, Owen Hoffman F, Gilbert E, Land C. RadRAT: a radiation risk assessment tool for lifetime cancer risk projection. *J Radiol Prot* 2012; **32**: 205-222 [PMID: 22810503 DOI: 10.1088/0952-4746/32/3/205]
22 **Omori Y**, Hosoda M, Takahashi F, Sanada T, Hirao S, Ono K, Furukawa M. Japanese population dose from natural radiation. *J Radiol Prot* 2020; **40**: R99-R140 [PMID: 32031989 DOI: 10.1088/1361-6498/ab73b1]

World Journal of Radiology

Submit a Manuscript: https://www.f6publishing.com

World J Radiol 2023 June 28; 15(6): 201-215

DOI: 10.4329/wjr.v15.i6.201

ISSN 1949-8470 (online)

ORIGINAL ARTICLE

Prospective Study

Interobserver reliability of computed tomography angiography in the assessment of ruptured intracranial aneurysm and impact on patient management

Ali H Elmokadem, Basma Abdelmonaem Elged, Ahmed Abdel Razek, Lamiaa Galal El-Serougy, Mohamed Ali Kasem, Mohamed Ali EL-Adalany

Specialty type: Radiology, nuclear medicine and medical imaging

Provenance and peer review: Invited article; Externally peer reviewed.

Peer-review model: Single blind

Peer-review report's scientific quality classification

Grade A (Excellent): 0
Grade B (Very good): 0
Grade C (Good): C, C
Grade D (Fair): 0
Grade E (Poor): 0

P-Reviewer: Taheri M, Iran; uz Zaman M, Pakistan

Received: December 23, 2022
Peer-review started: December 23, 2022
First decision: March 28, 2023
Revised: April 17, 2023
Accepted: May 31, 2023
Article in press: May 31, 2023
Published online: June 28, 2023

Ali H Elmokadem, Basma Abdelmonaem Elged, Ahmed Abdel Razek, Lamiaa Galal El-Serougy, Mohamed Ali EL-Adalany, Department of Radiology, Mansoura University, Mansoura 35516, Egypt

Mohamed Ali Kasem, Department of Neurosurgery, Mansoura University, Mansoura 35516, Egypt

Corresponding author: Ali H Elmokadem, MD, PhD, Associate Professor, Department of Radiology, Mansoura University, Elgomhoria St, Mansoura 35516, Egypt.
mokademr83@gmail.com

Abstract

BACKGROUND

Aneurysmal subarachnoid hemorrhage is an emergency that can lead to a high mortality rate and many severe complications. It is critical to make a rapid radiological evaluation of ruptured intracranial aneurysms (RIAs) to determine the appropriate surgical treatment.

AIM

To assess the reliability of computed tomography angiography (CTA) in assessing different features of ruptured intracranial aneurysm and its impact on patient management.

METHODS

The final cohort of this study consisted of 146 patients with RIAs (75 male and 71 female) who underwent cerebral CTA. Their age ranged from 25 to 80, and the mean age ± SD was 57 ± 8.95 years. Two readers were asked to assess different features related to the aneurysm and perianeurysmal environment. Inter-observer agreement was measured using kappa statistics. Imaging data extracted from non-contrast computed tomography and CTA were considered to categorize the study population into two groups according to the recommended therapeutic approach.

RESULTS

The inter-observer agreement of both reviewers was excellent for the detection of

aneurysms (K = 0.95, *P* = 0.001), aneurysm location (K = 0.98, *P* = 0.001), and (K = 0.98, *P* = 0.001), morphology (K = 0.92, *P* = 0.001) and margins (K = 0.95, *P* = 0.001). There was an excellent interobserver agreement for the measurement of aneurysm size (K = 0.89, *P* = 0.001), neck (K = 0.85, *P* = 0.001), and dome-to-neck ratio (K = 0.98, *P* = 0.001). There was an excellent inter-observer agreement for the detection of other aneurysm-related features such as thrombosis (K = 0.82, *P* = 0.001), calcification (K = 1.0, *P* = 0.001), bony landmark (K = 0.89, *P* = 0.001) and branch incorporation (K = 0.91, *P* = 0.001) as well as perianeurysmal findings including vasospasm (K = 0.91, *P* = 0.001), perianeurysmal cyst (K = 1.0, *P* = 0.001) and associated vascular lesions (K = 0.83, *P* = 0.001). Based on imaging features, 87 patients were recommended to have endovascular treatment, while surgery was recommended in 59 patients. 71.2% of the study population underwent the recommended therapy.

CONCLUSION

CTA is a reproducible promising diagnostic imaging modality for detecting and characterizing cerebral aneurysms.

Key Words: Computed tomography angiography; Intracranial aneurysm; Subarachnoid hemorrhage; Intracranial hemorrhage; Observer variation

©The Author(s) 2023. Published by Baishideng Publishing Group Inc. All rights reserved.

Core Tip: This study evaluated the interobserver reliability of computed tomography angiography (CTA) in the assessment of ruptured intracranial aneurysm features among 146 patients. Our results showed good to an excellent inter-observer agreement in imaging features related to the aneurysm, aneurysm characters, measurements, and perianeurysmal information. Imaging data extracted from non-contrast computed tomography and CTA guided the multidisciplinary neurovascular team to better treatment approach selection.

Citation: Elmokadem AH, Elged BA, Abdel Razek A, El-Serougy LG, Kasem MA, EL-Adalany MA. Interobserver reliability of computed tomography angiography in the assessment of ruptured intracranial aneurysm and impact on patient management. *World J Radiol* 2023; 15(6): 201-215
URL: https://www.wjgnet.com/1949-8470/full/v15/i6/201.htm
DOI: https://dx.doi.org/10.4329/wjr.v15.i6.201

INTRODUCTION

Acute subarachnoid hemorrhage (SAH) is a medical emergency that can lead to a high mortality rate and many severe complications. The most frequent cause of non-traumatic SAH is a ruptured aneurysm. Ruptured aneurysms not only cause subarachnoid bleeding but can also cause subdural or intracerebral hematomas. It is critical to make a rapid radiological evaluation of ruptured intracranial aneurysms (RIAs) to determine the appropriate surgical treatment of SAH[1]. Different imaging modalities are used or have been used to assess intracranial vascular lesions. Digital subtraction angiography (DSA) has been considered the "gold standard" for detecting intracranial aneurysms and therapeutic decision-making. Additionally, intra-arterial cone beam computed tomography angiography (CTA) using a flat panel detector incorporates the high spatial vascular resolution of three-dimensional (3D) rotational angiography with computed tomography (CT) postprocessing techniques to increase the contrast resolution[2]. Nevertheless, it is an invasive and time-consuming technique with a reported 0.5% risk of neurological complications[3]. Magnetic resonance (MR) angiography enables visualization of intra-cranial arteries without ionizing radiation or intravenous contrast material. The performance of MR angiography in evaluating acute SAH also has been compared favorably with that of DSA. However, MR angiography can be technically challenging for acutely ill patients. Additionally, aneurysms less than 5 mm in diameter might be missed in MR angiography studies[4].

Compared to DSA, CTA is a safe, relatively inexpensive, and noninvasive imaging. CT angiography is not associated with significant patient risks other than those related to administering iodinated contrast media. Images can be relatively safely obtained without the need for arterial puncture or catheter manipulation that carries the possibility of acquiring a permanent neurologic deficit[5]. For these reasons, helical cerebral CT angiography has been widely used in detecting intracranial aneurysms, with a reported sensitivity of 70%–96%[6]. Currently, multidetector CT angiography has the ability to detect most intracranial aneurysms of 5 mm or larger. Multidetector row CT scanners provide

increased spatial resolution and decreased scanning time, which should increase the sensitivity of the technique in depicting aneurysms of less than 5 mm in diameter. Currently, CT angiography is accepted as a first-line diagnostic imaging modality for evaluating intracranial aneurysms. Nevertheless, using CT angiography to depict intracranial aneurysms showed variable sensitivity. The reported sensitivity of CTA in detections of small intracranial aneurysms (< 3 mm) varied from 28%–43% in a study that included 99 small aneurysms[7] to 83%-92% in another study had 579 small aneurysms[8].

Deciding whether to perform surgical clipping or endovascular therapy for an intracranial aneurysm is vital. Treatment of intracranial aneurysms depends on clinical features, including age, Hunt and Hess grade, neurological or medical comorbidity, and characters of the aneurysm itself. Advances in imaging technologies have improved our comprehension of the 3D geometry of cerebral aneurysms, which has further affected treatment procedures, and helps neurosurgeons in the diagnosis, planning, and assessment of the therapeutic modalities. Exact information must be obtained preoperatively regarding the location, size, and morphology of the aneurysm and the property of the aneurysmal wall, its relationship with the parent vessel and adjacent branches, vessel incorporation, presence of calcification or thrombus[9]. Perianeurysmal information such as associated vasospasm, vascular variants, presence of vascular malformations, and the relationship of the aneurysm to the bony skull base is also crucial for proper treatment method selection.

This work aims to assess the inter-observer reliability of CTA in assessing different features of RIAs and their impact on patient management.

MATERIALS AND METHODS

Study population

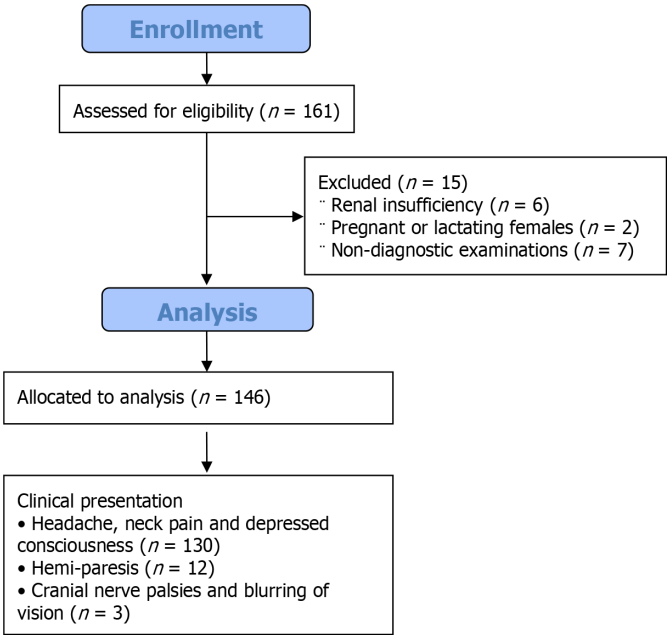
The Institutional review board approved this single-center prospective study. One hundred sixty-one consecutive patients with clinically suspected intracranial aneurysms were recruited. Inclusion criteria were adult patients with imaging signs of SAH by non-enhanced CT. The exclusion criteria were patients with renal insufficiency (n = 6), pregnant or lactating females (n = 2), and non-diagnostic examinations (n = 7). The final cohort of our study included 146 patients (75 male and 71 female). Their age ranged from 25 to 80 years, with a mean age was 57 ± 8.9 years. Once enrolled, all patients were submitted to a contrast-enhanced CTA scan for diagnosis of intracranial aneurysm. The commonest clinical presentation was a headache, neck pain, and depressed consciousness in 130 patients, hemiparesis in 12 patients, cranial nerve palsies, and blurring of vision being less common presenting symptoms in 3 patients. One patient presented in an accident. The flow chart of our study is illustrated in (Figure 1).

CTA Technique

All examinations were carried out with 160-slice computed tomography (Toshiba Aquilion Prime 160, Tochigi, Japan). Examinations were performed in a supine position with the arms of the patients beside the body. We first performed a non-contrast CT (NCCT) scan of the whole brain in an axial plane tilted along the orbitomeatal line using the following parameters: tube voltage 100 kVp, field of view (FOV) 220 mm, collimation 0.75 mm, matrix size 512 × 512, slice thickness 3.0 mm, and rotation time 1.0 s. CTA examinations were achieved using the bolus triggering technique for the timing of contrast medium injection. A region of interest (ROI) was centered at the upper end of the common carotid artery and sized to include only the lumen of the artery. The bolus triggering technique started automatically after contrast-medium injection when an attenuation value of 100 HU was reached in ROI. Non-ionic contrast medium Ultravist 370 (370 mgI/mL, Bayer Healthcare Ltd, Guangzhou, China) at a dose of 1 mL/Kg and rate of 4mL/s followed by a 50 mL saline flush administered *via* automatic injector (Medrad Stellent, Warrendale, PA) through a 20 G intravenous cannula in the antecubital fossa of either upper extremity. The following parameters were used: Tube voltage 120 kVp, automatic tube current modulation, FOV 250 mm, collimation 0.75 mm, matrix size 512 × 512, slice thickness 1.5 mm, rotation time 0.3 s. Scanning was performed in the caudocranial direction and started at the level of the aortic arch up to the vertex. Axial images were stored and transferred into the workstation as source images after reconstruction at 0.625-mm intervals. Multiplanar reformats (MPR), maximum intensity projection (MIP), and 3D volume-rendered images were used for further analysis.

Image analysis

Image analysis was conducted on the PACS system (GE Healthcare, Waukesha, WI). All CTA examinations were revised and interpreted by two experienced neuroradiologists with 14 and 8 years of experience in neurovascular imaging (AHE, BE). They independently reviewed the images blinded to patient data and final diagnosis. The following features obtained at NCCT were individually evaluated for each patient: The degree of SAH using the Fisher scale, associated parenchymal hemorrhage, hydrocephalus, and ischemic changes. Both readers were asked to predict the location of the aneurysm based on the distribution of SAH and Intraparenchymal hematoma (IPH). At CTA, both readers were asked to evaluate the following aneurysm features': (1) Number; (2) Size; (3) Location (anterior *vs*



DOI: 10.4329/wjr.v15.i6.201 **Copyright** ©The Author(s) 2023.

Figure 1 Flow chart of the study.

posterior circulation, parent artery, and affected segment); (4) Shape (saccular, fusiform, serpentine or blister); (5) Margin (sharp, irregular/daughter sacs); (6) Presence of calcification and/or thrombus; (7) The presence of branch incorporation; and (8) The orientation of the aneurysm in relation to the parent vessel (*e.g.*, pointing superior/inferior, medial/Lateral, anterior/posterior). Aneurysm size was defined by the maximum measurement of aneurysm width, neck width (the largest cross-sectional diameter of the aneurysm neck), depth (the longest diameter between the neck and dome), and aneurysm neck-to-dome length. According to size, aneurysms were classified into: (1) Small aneurysms are less than 5 mm; (2) Medium-sized aneurysms are 6–15 mm; (3) Large aneurysms are 16–25 mm; and (4) Giant aneurysms are > 25 mm. The following features related to the perianeurysmal environment were evaluated by both readers: (1) Associated vasospasm; (2) Perianeurysmal cysts; (3) Associated vascular malformations (type and classification based on relation to aneurysm); (4) Vascular variants; and (5) The relationship of the aneurysm to the bony landmarks or related osseous changes (remodeling or fractures).

Management selection

Imaging data extracted from NCCT and CTA were considered to categorize the study population into two groups according to the recommended therapeutic approach. The first group was recommended to proceed to endovascular therapy, and the second group was advised to undergo surgical management (clipping).

Features in favor of endovascular therapy (coiling) were: (1) Absence of parenchymal hematoma; (2) Posterior circulation aneurysm; (3) Small aneurysm neck < 4 mm; (4) Aneurysm diameter < 15 mm; (5) Unilobar shape; (6) Multiple aneurysms; (7) Calcification located at the aneurysm neck that might interfere with clipping; and (8) Presence of vasospasm. Coiling using balloon remolding technique or stent-assisted coiling was recommended with wide-neck aneurysms.

Features favored surgical management (clipping) Were (1) Presence of intra-parenchymal hematoma; (2) Middle cerebral and pericallosal arteries aneurysm; (3) Wide neck of the aneurysm > 4 mm; (4) Aneurysm diameter > 15 mm; (5) Abnormal configuration unsuitable for endovascular therapy; (6) Aneurysmal sac incorporating arterial branches; (7) Presence of intraluminal thrombus; and (8) Vascular variant interferes with endovascular management. Features considered in managing RIAs are listed in Table 1.

Statistical analysis:

All statistical analyses were performed with software (SPSS, version 16.0; SPSS, Chicago, Ill). The Kolmogorov-Smirnov Z-test was used to test the normality of the continuous variable groups. The CTA image quality scores were ranked and listed as a mean and standard deviation. The kappa statistic (K), including a 95%CI with an intra-class correlation (r), was used to estimate the proportion of interob-server agreement beyond that expected by chance for the image quality grading and depiction of the aneurysm, its neck, parent artery, and associated anomalies. A *P* value less than 0.05 was considered to

Table 1 Imaging features considered in the management of ruptured intracranial aneurysms

	Endovascular therapy	Surgical management
Non-contrast computed tomography	Absence of parenchymal hematoma	Presence of intra-parenchymal hematoma
Aneurysm characters	Posterior circulation aneurysms	Middle cerebral and pericallosal arteries aneurysm
	Small aneurysm neck < 4 mm	Aneurysm diameter > 15 mm Wide neck aneurysm > 4 mm
	Aneurysm diameter < 15 mm	Abnormal configuration
	Unilobar configuration	Aneurysmal sac incorporating arterial branches
	Multiple aneurysms	Presence of intraluminal thrombus
	Calcification located at the aneurysm neck	
Perianeurysmal findings	Presence of vasospasm	Vascular variants interfere with endovascular management

indicate a statistically significant difference. The K values were interpreted as follows: K values between 0.61 and 0.80 represented good; K values between 0.81 and 1.00 represented excellent agreement.

RESULTS

NCCT findings

Both readers used the Fisher scale to assess SAH. The means scores were (3.47 ± 0.6 and 3.33 ± 0.4) with a good interobserver agreement (K = 0.79, *P* = 0.001). Excellent interobserver agreement between both readers in the detection of IPH (K = 0.1, *P* = 0.001) as well as in the detection of hydrocephalus (K = 0.92, *P* = 0.001). A statistically significant strong positive correlation was found between the location of SAH and IPH on NCCT scan and the eventual location of a ruptured cerebral aneurysm in single ones and as a differentiating point of culprit aneurysm in multiple aneurysms confirmed by CTA and surgical or endovascular intervention. The sensitivity of NCCT predicting aneurysms depends on blood distribution of more than 85% in our study. Table 2 shows the inter-observer results of CT and CTA findings.

Aneurysm characters:

Detection: The first reader detected 166 aneurysms [126 single aneurysms (75.9%) and 40 multiple aneurysms (24.1%)], while 2nd reader detected 169 aneurysms [127 single aneurysms (75.1%) and 42 multiple aneurysms (24.9%)]. An excellent interobserver agreement was found between both readers in detecting an aneurysm [98.8% (K = 0.95, *P* = 0.001)]. Among multiple aneurysms, 14 were mirror image aneurysms (MA), and the remaining were non-mirror image (NMA). The commonest location of MA in our series was the M1 segment or at the middle cerebral artery (MCA) bifurcation (*n* = 3), followed by the cavernous portion of internal carotid artery (ICA) (*n* = 2) (Figure 2), the posterior communicating artery (PCOM) (*n* = 1), and ICA terminus (*n* = 1). The sensitivity of CTA compared to DSA in the detection of intracranial aneurysms was 98.8%. DSA identified 89 aneurysms in 80 patients. Among these aneurysms, CTA failed to detect one in a patient with three other aneurysms. The missed aneurysm was located in posterior cerebral artery (PCA) with diameters of 3 mm. In two cases, CTA depicted aneurysms, which DSA missed. An ICA blister and a distal MCA mycotic aneurysm were the two missed aneurysms.

Location: For most of the study, the population was harboring anterior circulation aneurysms (94%). Excellent interobserver agreement was found between both readers in the detection of aneurysms in the anterior and posterior circulation (K = 0.95, *P* = 0.001) as well as its site in parent artery and segment (K = 0.98, *P* = 0.001), and (K = 0.98, *P* = 0.001). In this study, Acom was the most affected artery, and Acom-left anterior cerebral artery (ACA) complex was the most affected segment. Both readers successfully detected intracranial aneurysms in relatively rare locations such as basilar perforators (2/L46), distal ACA (4/L46), pericallosal artery (2/L46), and azygous ACA (2/L46). Inter-observer results of the CTA location of the aneurysm are summarized in Table 3.

Morphology: Among the assessed aneurysms, (96.4%) were saccular, (2.4%) were fusiform, and (1.1%) were serpentine (Figure 3). Excellent interobserver agreement was found between both readers in the detection of aneurysm shape (K = 0.92, *P* = 0.001) and for margins (K = 0.95, *P* = 0.001). Other features such as calcification or thrombus, branch incorporation, and aneurysm orientation also show excellent inter-observer agreement. Calcification and thrombosis were detected in large and giant aneurysms (Figure 4). Branch incorporation was found in association with 55 aneurysms, one of them showed 3rd A2 segment incorporated Acom aneurysm dome (ACA trifurcation), to the best of the author's knowledge this association is not reported before in the literature (Figure 5).

Table 2 Inter-observer agreement of computed tomography and computed tomography angiography features of aneurysm

Signs		Reader 1	Reader 2	K	95% CI	*P* value	Agreement, %
NCCT findings							
SAH Fisher scale		3.47 ± 0.6	3.33 ± 0.4	0.84	0.78-0.85	< 0.001	89.50
Hydrocephalus (HCP)	Negative (N)	93	95	0.91	0.85-0.97	< 0.001	95.90
	Positive (p)	53	51				
Intraparenchymal hematoma (IPH)	Negative (N)	105	105	1	1.0-1.0	< 0.001	100.00
	Positive (p)	41	41				
Aneurysm features							
Number	Total	166	169	0.95	0.89-1.0	< 0.001	98.80
	Single	126	127				
	Multiple	40	42				
Size	Small	55	57	0.89	0.83-0.96	< 0.001	94.70
	Medium	101	102				
	Large	5	5				
	Giant	5	5				
Site	Anterior	156	157	0.94	0.83-1.0	< 0.001	99.40
	Posterior	10	12				
Shape	Saccular	160	162	0.92	0.76-1.0	< 0.001	99.40
	Fusiform	4	4				
	Serpentine	2	2				
	Blister	0	1				
Margin	Sharp	71	75	0.95	0.90-0.99	< 0.001	97.60
	Lobulated	95	94				
Thrombus		6	9	0.82	0.65-0.99	< 0.001	97.60
Calcification		9	9	1	1.0-1.0	< 0.001	100.00
Branch incorporation		50	55	0.9	0.83-0.97	< 0.001	95.90
Orientation				0.95	0.91-0.97	< 0.001	96.50
Perianeurysmal findings							
Vasospasm		21	25	0.9	0.81-0.99	< 0.001	97.60
Perianeurysmal cyst		1	1	1	1.0-1.0	< 0.001	100.0
Other vascular lesions		2	4	0.82	0.59-1.0	< 0.001	98.80
Bony relations		23	26	0.88	0.78-0.98	< 0.001	97.00
Bone fracture		1	1				
Vascular variant		84	88	0.89	0.83-0.96	< 0.001	94.90
Overall agreement				0.95	0.94-0.96	< 0.001	97.80

NCCT: Non-contrast computed tomography; SAH: Subarachnoid hemorrhage; IPH: Intraparenchymal hematoma.

Measurements: Most cases were medium-sized aneurysms (60.8%), followed by small-sized (30.1%). Both readers measured aneurysm size, neck, and dome-to-neck ratio with an excellent interobserver agreement (K = 0.89, *P* = 0.001), (K = 0.85, *P* = 0.001), and (K = 0.98, *P* = 0.001). Inter-observer results of CTA measurements of an aneurysm are summarized in Table 4.

Peri-aneurysm findings: Excellent interobserver agreement was found between both readers in detecting vasospasm in the nearby arterial segment (K = 0.91, *P* = 0.001) and detection of the perian-

Table 3 Inter-observer agreement of computed tomography angiography locations of aneurysm

Parent artery	Reader 1	Reader 2
ACOM	73	73
ACA	5	6
RT ICA	20	20
LT ICA	16	16
RT MCA	21	22
LT MCA	20	20
Basilar	8	9
LT PCA	1	1
RT Vertebral	1	1
LT SCA	0	1
K	**95%CI**	***P* value**
0.97	0.87-1.0	< 0.001
Arterial segment	**Reader 1**	**Reader 2**
ACOM- Lt ACA complex	36	36
ACOM- Rt ACA complex	34	34
ACOM proper	3	3
A1	1	1
RT A2	1	1
LT A2	0	1
Azygous A2	2	2
A3	1	1
RT MCA bifurcation	14	14
LT MCA bifurcation	15	15
RT M1	4	4
LT M1	3	3
RT M2	3	3
LT M2	2	2
M4	0	1
RT PCOM	12	12
LT PCOM	9	9
RT ICA Terminus	4	4
LT ICA Terminus	2	2
RT Cavernous ICA	4	4
LT Cavernous ICA	5	5
Basilar tip	4	4
Mid Basilar	2	3
Basilar Perforators	2	2
Rt V4	1	1
LT SCA	0	1
Lt P1	1	1
K	**95%CI**	***P* value**

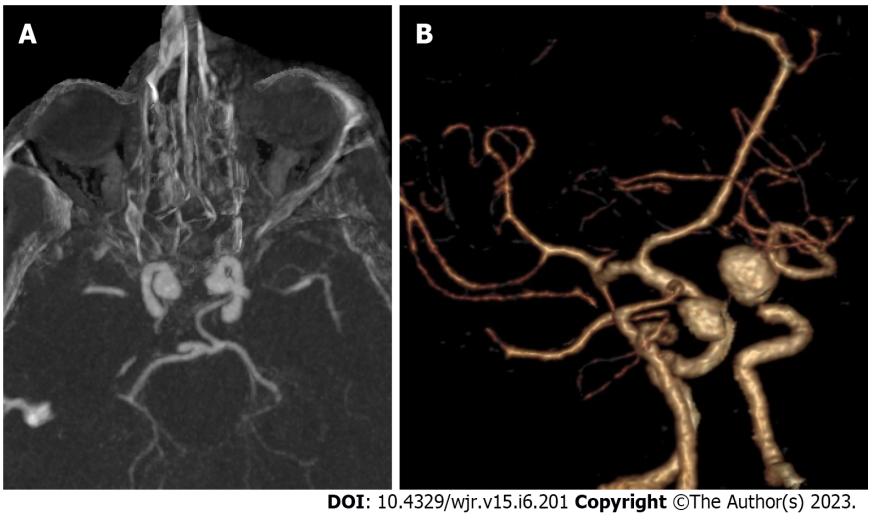
0.97	0.87-1.0	< 0.001

ACA: Anterior cerebral artery; RT: Right; ICA: Internal carotid artery; LT: Left; MCA: Middle cerebral artery; PCA: Posterior cerebral artery; SCA: Superior cerebellar artery; PCOM: Posterior communicating artery.

Table 4 Inter-observer agreement of computed tomography angiography measurements of aneurysm

	Size		Dome		Neck		Dome/neck ratio	
	Reader 1	Reader 2	Reader 1	Reader 2	Reader 1	Reader 2	Reader 1	Reader 2
Mean	7.4	7.4	3.7	3.6	2.7	2.7	1.3	1.3
Median	6	6	3	3	2.3	2.3	1.2	1.2
SD	5.44	5.47	3.2	3.1	2.1	2.1	0.8	0.8
Minimum	1.8	1.8	1	1	1	1	0.2	0.2
Maximum	40	42	22	22	20	20	4.7	5.6
ICC	0.97		0.97		0.96		0.98	
95%CI	(0.96-0.98)		(0.96-0.97)		(0.95-0.97)		(0.97-0.98)	

ICC: Interclass correlation.



DOI: 10.4329/wjr.v15.i6.201 **Copyright** ©The Author(s) 2023.

Figure 2 Mirror image intracranial aneurysms. A: Axial computed tomography angiography (CTA) in maximum intensity projection; B: Three-dimensional CTA for mirror image internal carotid artery aneurysm.

eurysmal cyst (K = 1.0, *P* = 0.001). Associated vascular lesions, including arterio-venous malformation (AVM) and developmental venous anomalies (DVA) (Figure 6), were detected by both readers with an excellent interobserver agreement (K = 0.83, *P* = 0.001). Vascular variations commonly affected the A1 segment, followed by PCA and MCA. Both readers detected an important bony variant in a case presented with a PCOM aneurysm in the form of a bridging sella turcica which was managed surgically by clitoridectomy (Figure 7).

Management: Based on imaging features, 87 patients were recommended to have endovascular treatment, while surgery was recommended in 59 patients. 71.2% of the study population underwent the recommended therapy, as 19 patients did not receive any therapy for the culprit, 66 underwent endovascular treatment, and 61 underwent surgical clipping. Only 15% of the study population needed external ventricular drain (EVD) to manage associated hydrocephalus.

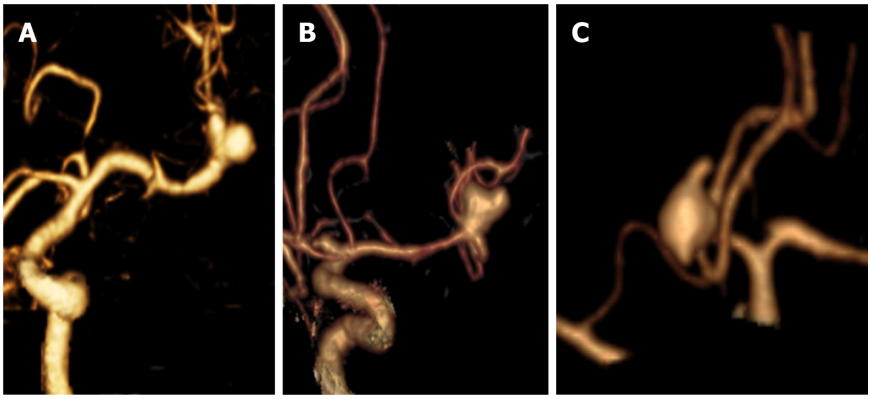
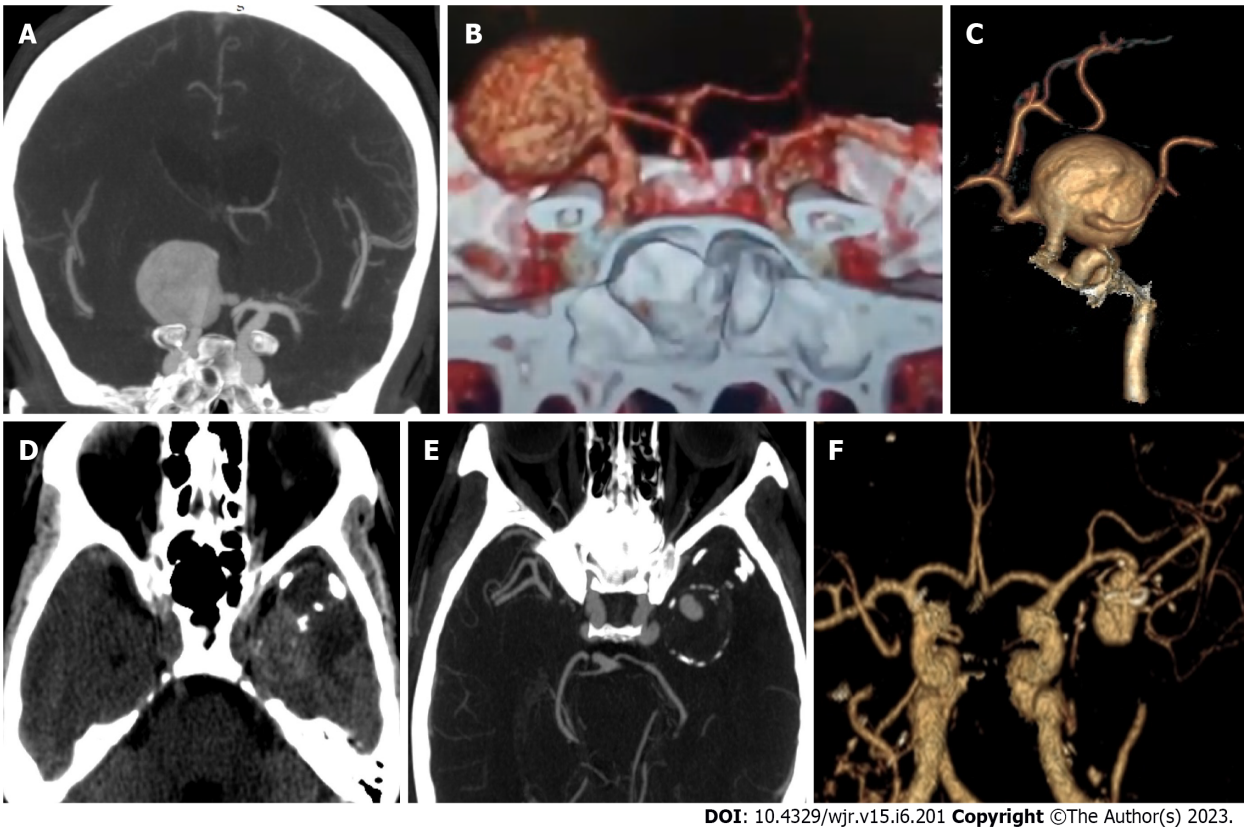


Figure 3 Morphology of intracranial aneurysms. A: Three-dimensional (3D)-computed tomography angiography (3D-CTA) for saccular aneurysm at middle cerebral artery (MCA) bifurcation with smooth margins; B: 3D-CTA for saccular aneurysm at MCA bifurcation with daughter sac; C: 3D-CTA for Acom saccular aneurysm with multiple blebs.



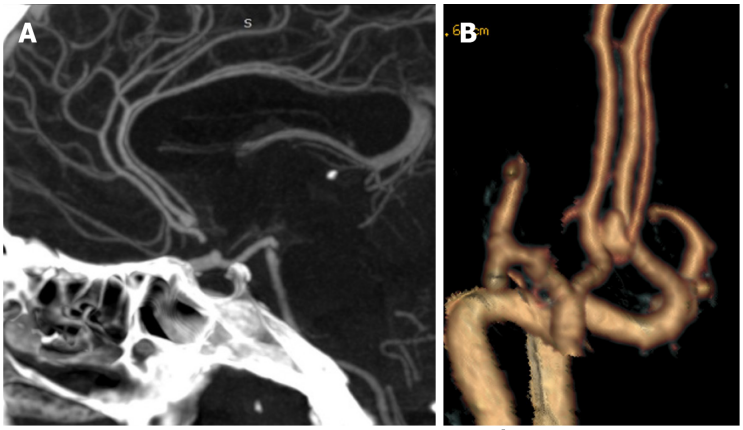
DOI: 10.4329/wjr.v15.i6.201 **Copyright** ©The Author(s) 2023.

Figure 4 Giant intracranial aneurysms. A: Axial computed tomography angiography (CTA) in maximum intensity projection (MIP); B and C: Three-dimensional (3D)-CTA for giant saccular aneurysm arising from right internal carotid artery and incorporating the origin of anterior cerebral artery and middle cerebral artery (MCA); D: non-contrast computed tomography for another patient shows a well defined lobulated lesion of mixed density in the left temporal lobe with foci of peripheral calcification; E: MIP-CTA axial image shows giant partially thrombosed saccular aneurysm of left MCA; F: 3D–CTA image shows a patent portion of left MCA aneurysm.

DISCUSSION

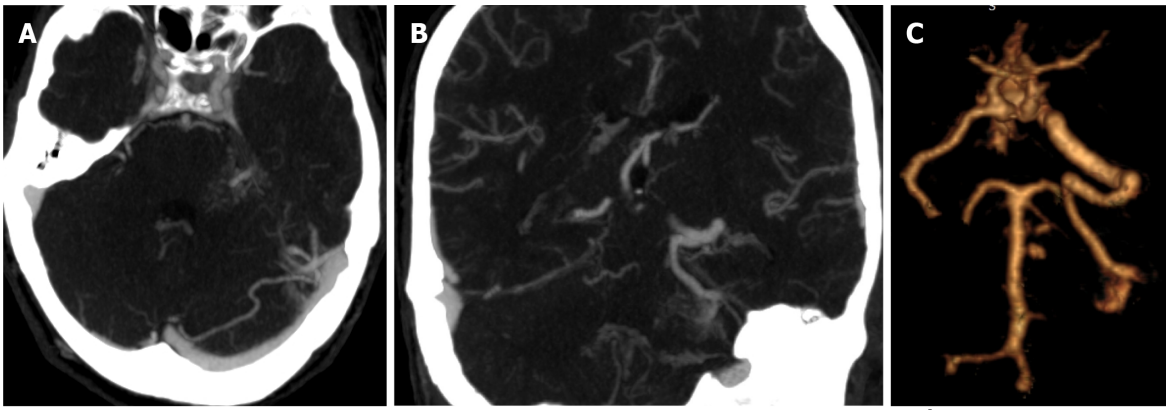
This study evaluated the interobserver reliability of CTA in the assessment of ruptured intracranial aneurysm features among 146 patients. Our results showed good to an excellent inter-observer agreement in imaging features related to the aneurysm, aneurysm characters, measurements, and perianeurysmal information. Imaging data extracted from NCCT and CTA guided the multidisciplinary neurovascular team to better treatment approach selection.

Our results showed high sensitivity of NCCT (85%) in predicting aneurysms' location depending on blood distribution with a good inter-observer agreement regarding the Fischer scale scores for SAH. The



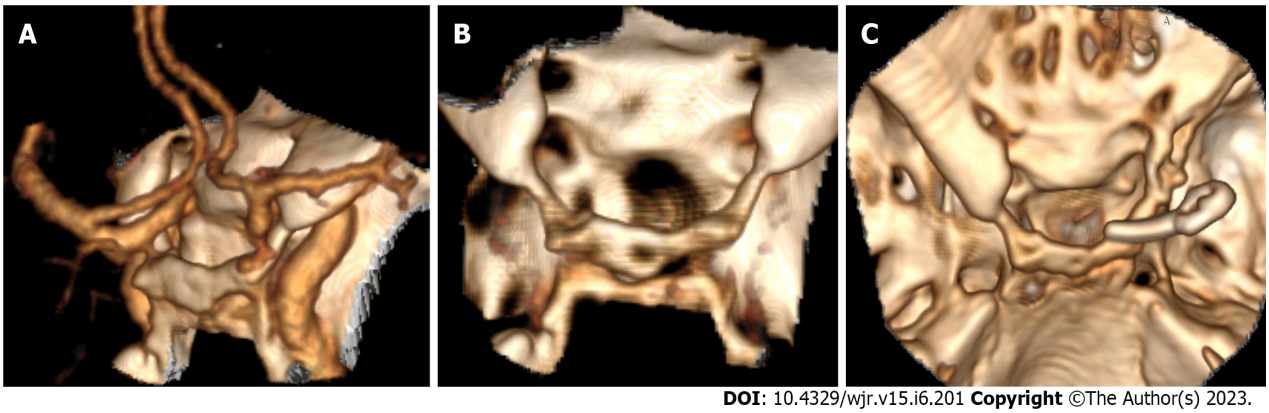
DOI: 10.4329/wjr.v15.i6.201 **Copyright** ©The Author(s) 2023.

Figure 5 Anatomical variants with intracranial aneurysms. A: Sagittal reformatted maximum intensity projection-computed tomography angiography (CTA); B: Three-dimensional-CTA for a saccular aneurysm at anterior cerebral artery trifurcation.



DOI: 10.4329/wjr.v15.i6.201 **Copyright** ©The Author(s) 2023.

Figure 6 Vascular malformation with intracranial aneurysms. A: Axial maximum intensity projection (MIP)-computed tomography angiography (CTA) shows a small saccular aneurysm that arises from the left basilar artery perforators; B: Coronal reformatted MIP-CTA shows left cerebellar developmental venous anomalies (DVA) drains into the left sigmoid sinus; C: Three-dimensional-CTA shows the basilar perforator aneurysms and the left cerebellar DVA.



DOI: 10.4329/wjr.v15.i6.201 **Copyright** ©The Author(s) 2023.

Figure 7 Bony landmarks related to the aneurysm. A: Three-dimensional (3D)-computed tomography angiography shows a posterior communicating artery aneurysm close to the anterior clinoid process; B: 3D-computed tomography (CT) for the skull base shows bridging sella and bony fusion; C: Post-operative 3D-CT shows partial clionoidectomy and metallic clip.

combination of NCCT images and CTA is a valuable tool for detecting intracranial aneurysms and predicting outcomes. Aneurysm detection could be expected by assessing the distribution of SAH, the site of the largest clot, the difference in attenuation, and the presence of mural calcification. A recent study performed on patients with SAH and multiple cerebral aneurysms found that NCCT can identify

the source of bleeding with high accuracy for ACA, ACom, and MCA aneurysms, especially with the presence of intracranial hemorrhage (ICH)[10]. Our results showed excellent inter-observer agreement for detecting acute hydrocephalus with a variable degree of acute ventricular dilation, yet only 15% of our cases need management by EVD. Our results were close to those of the study performed on 389 patients with aneurysm-associated SAH[11].

We found that CTA has a high sensitivity for detecting intracranial aneurysms and avoids false-negative results. In a meta-analysis of extracted data from 8 studies, CTA had a pooled sensitivity of 99% and specificity of 94% for detecting and ruling out cerebral aneurysms[12]. Our study had an excellent interobserver agreement for detecting the aneurysms; the first reader detected 166 aneurysms, while the second reader detected 169 aneurysms. Yang *et al*[8] revealed a similar discrepancy in number detection by two observers, as one reviewer missed three aneurysms[8]. The inter-observer discrepancy usually occurs in a set of multiple small aneurysms in uncommon locations, such as the distal MCA. In this study, we detected mirror MA in 7 patients. Our results concord with the data obtained by a recent study by Rajagopal *et al*[13].

In our study, the anterior cerebral circulation aneurysms remained the predominant location of all aneurysms detected by CTA, constituting about 94% of the anterior and 6% of the posterior circulation. Acom aneurysm is the most common location of aneurysm in our results followed by ICA and MCA aneurysms, respectively. A similar distribution was reported by previous studies that assessed CTA *vs* DSA in the detection of intracranial aneurysms[14,15]. Imaging is vitally important to determine the location of the aneurysm and its relationship to the surrounding anatomy. Data from many studies suggest that surgical clipping may be superior in managing anterior circulation aneurysms with low recurrent rates. In contrast, posterior circulation aneurysms may be better treated through an endovascular approach[16]. Both readers successfully detected intracranial aneurysms in relatively rare locations, such as basilar perforators and azygous ACA. These findings aligned with prior studiesstating that basilar perforator aneurysms are sporadic lesions often not recognized on initial imaging[17,18]. Similarly, azygos ACA aneurysm has a low incidence among intracranial aneurysms in literature ranging from 0.38 to 3.7%[19].

In this study, non-saccular intracranial aneurysms were less frequent. The margins were sharp (42.7%), and the rest were lobulated. These results partially agree with Rai *et al*[15], who reported 91% of saccular aneurysms, with only 22% having lobulated margins[15]. An irregular margin or lobulation along the margin of an aneurysm suggests rupture. It is an important observation in the setting of diffuse SAH and multiple intracranial aneurysms when treatment is directed at the culprit aneurysm [20]. Excellent inter-observer agreement was found in the assessment of branch incorporation and aneurysm orientation. The location of a branch to the aneurysm is a critical finding, as inadvertent occlusion of this branch during aneurysm treatment could have devastating consequences[21]. Therefore, it is essential to have a basic understanding of cerebral circulation and anatomical variants when interpreting CTA studies. Aneurysm orientation, especially Acom aneurysm, is a crucial element in selecting surgical *vs* endovascular management. Aneurysms with a more complex surgical approach are often assessed for endovascular therapy rather than surgical management[22].

Excellent agreement was found in this study between both readers regarding aneurysm measurements, including size, neck diameter, and dome-to-neck ratio. As the size of the aneurysm is the most significant predictor of SAH risk, accurate measurement of the aneurysm (s) is imperative for proper management. Aneurysms larger than 12 mm had a 2.6 relative risk of poor outcomes[23]. Kim *et al*[24] stated that intra-observer and interobserver variability in CTA were considerable in aneurysmal size measurements ranging from 12 to 18%. Therefore, follow-up size changes exceeding 20% in the aneurysm dimension should be considered a true change rather than a measurement error[24]. In contrast to these results, another study reported a poor ability of CTA to identify aneurysm enlargement accurately in assessing an in-vitro model. However, they recommended further human studies to confirm their findings[25]. CTA in this study detected the neck of all saccular aneurysms by both readers. Neck dimension and neck-to-dome ratio are crucial to deciding between surgical or endovascular treatment and simple coiling or adjunctive techniques to facilitate coil embolization through wide neck, such as neck remodeling using balloons or stent-assisted embolization[26].

The majority of our cases were medium-sized aneurysms (60.8%). This finding was in line with results reported by previous studies, which noted that medium-sized aneurysms were the majority of intracranial aneurysms[14,15]. We also observed that the presence of thrombosis and calcification was strongly tied to aneurysm size in large-sized and giant aneurysms compared to the corresponding intra-operative details of each case. Spontaneous thrombosis of intracranial aneurysms may occur in up to 40% of giant aneurysms, eventually becoming symptomatic due to mass effect or stroke. On the contrary, spontaneous thrombosis of a non-giant aneurysm (< 25 mm) is rarer[27]. Calcification appears to be an important pre-operative indicator of poor outcomes[28] and should be considered when deciding treatment options for a patient with a calcified aneurysm.

Perianeurysmal findings such as vasospasm, perianeurysmal cyst, associated vascular lesions or variants, and bony landmarks or pathologic changes are essential factors that might change the treatment decision. Cerebral vasospasm and resultant delayed cerebral ischemia consider a significant etiology of morbidity and mortality in patients with aneurysmal SAH (DCI)[29]. CTA is a fast and reliable tool for detecting decreases in vessel caliber, as demonstrated by excellent interobserver

agreement in this study.

The rarity of a perianeurysmal cyst may lead to a false diagnosis of cystic neoplasm and missing the possibility of a ruptured cerebral aneurysm. Interestingly, a perianeurysmal cyst was described in one out of 146 patients in our study. Pedro and Sih[30] reported a case of a sizeable pontine cyst associated with an enhancing mural nodule that was misdiagnosed as a cystic neoplasm. During surgery, an aneurysm of the left PCA was identified and clipped successfully[30].

Our work included four patients with associated vascular anomalies, including AVMs and DVA. The risk of intracranial hemorrhage in patients with coexisted AVM and aneurysm has been reported to be 7% annually, compared with 2%–4% annually for those with AVM alone or isolated intracranial aneurysm[31,32]. To our knowledge, the association between intracranial aneurysms and DVA is infrequent, and few case reports have been published[33].

In our study, both observers noted a sphenoid bone fracture and a nearby aneurysm of paraclinoid ICA secondary to head trauma. It is in agreement with results done on 5532 patients with cerebral aneurysms over 30 years by Jung *et al*[34], who state that traumatic intracranial aneurysm (TIA) after blunt brain trauma is rare and represents (0.23%)[34]. Osseous landmarks such as the optic strut and the tuberculum sellae are considered the anatomical boundary between the intradural and extradural segments of the ICA in the paraclinoid region, which is an important factor in determining treatment strategy[35].

We recommended surgical clipping or endovascular management for the culprit aneurysms based on data extracted from NCCT and CTA. 71.2% of the study population underwent the recommended therapy. The ideal therapeutic approach for RIAs is still controversial. In general, the decision on whether to clip or coil depends on several factors related to the patient, such as age and comorbidities, burden, and location of hemorrhage, aneurysm characteristics such as size, number, location, and morphology, or related procedure such as competence, technical skills and availability[36]. Endovascular treatment has been associated with shorter recovery but with higher retreatment rates and slightly higher rebleeding events[16]. An endovascular approach is indicated in a ruptured intracranial aneurysm with comorbidity, old age, narrow neck, and a posterior circulation aneurysm. Surgery is warranted if the patient is young with an MCA aneurysm and interested in durability.

There are a few limitations to this study. First, there is no correlation with conventional angiography in all cases. Second, the general drawbacks of CT include patient exposure to ionizing radiation and the risks of iodinated contrast medium. Further studies with applications of low-dose CTA, such as the use of automatic tube current modulation and a small amount of contrast medium, are recommended. Additionally, future studies using advanced CT techniques such as higher 320 slices CT scan[37], dual-energy[38] or source CTA, and time-resolved 4D CTA will improve temporal and spatial resolution and the image quality CTA. Also, applications of advanced vascular post-processing packages for analyzing CTA images will give comprehensive image interpretation in different planes and angles. We recommend further studies assessing the inter-observer agreement between neuroradiologists, neurologists, neurosurgeons, and neuro-interventionist.

CONCLUSION

We concluded that CTA is a promising diagnostic imaging modality for assessing intracranial aneurysm features that impact management and patient outcomes.

ARTICLE HIGHLIGHTS

Research background

Aneurysmal subarachnoid hemorrhage (SAH) is an emergency that can lead to a high mortality rate and many severe complications. It is critical to make a rapid radiological evaluation of ruptured intracranial aneurysms (RIAs) to determine the appropriate surgical treatment.

Research motivation

The high morbidity and mortality of RIAs nicissitate rapid diagnosis and management decision. Compared to Digital subtraction angiography, computed tomography angiography (CTA) is a safe, relatively inexpensive, and noninvasive imaging. Computed tomography (CT) angiography is not associated with significant patient risks other than those related to administering iodinated contrast media. Images can be relatively safely obtained without the need for arterial puncture or catheter manipulation that carries the possibility of acquiring a permanent neurologic deficit. Our motivation is to assess the reliability of CTA in assessing different features of ruptured intracranial aneurysm and its impact on patient management.

Research objectives

To assess the reliability of CTA in assessing different features of ruptured intracranial aneurysm and its impact on patient management. We found out that CTA is a promising diagnostic imaging modality for assessing intracranial aneurysm features and help in management decision and patient outcomes. We recommend further studies assessing the inter-observer agreement between neuroradiologists, neurologists, neurosurgeons, and neuro-interventionist.

Research methods

Helical cerebral CT angiography has been widely used in detecting intracranial aneurysms, with a reported sensitivity of 70%–96%. Currently, multidetector CT angiography has the ability to detect most intracranial aneurysms of 5 mm or larger. Multidetector row CT scanners provide increased spatial resolution and decreased scanning time, which should increase the sensitivity of the technique in depicting aneurysms of less than 5 mm in diameter. Currently, CT angiography is accepted as a first-line diagnostic imaging modality for evaluating intracranial aneurysms. Nevertheless, using CT angiography to depict intracranial aneurysms showed variable sensitivity. The reported sensitivity of CTA in detections of small intracranial aneurysms (< 3 mm) varied from 28%–43% in a study that included 99 small aneurysms to 83%-92% in another study had 579 small aneurysms. CTA examinations for 146 patients in the current study were revised and interpreted by two experienced neuroradiologists to assess the inter-observer agreement of CTA findings related to intracranial aneurysms. Data extracted from CT was considered in patient management decision.

Research results

This study evaluated the interobserver reliability of CTA in the assessment of ruptured intracranial aneurysm features among 146 patients. Our results showed good to an excellent inter-observer agreement in imaging features related to the aneurysm, aneurysm characters, measurements, and perianeurysmal information. Imaging data extracted from NCCT and CTA guided the multidisciplinary neurovascular team to better treatment approach selection. There are a few limitations to this study. First, there is no correlation with conventional angiography in all cases. Second, the general drawbacks of CT include patient exposure to ionizing radiation and the risks of iodinated contrast medium.

Research conclusions

We concluded that CTA is a promising diagnostic imaging modality for assessing intracranial aneurysm features that impact management and patient outcomes. We recommend endovascular approach in a ruptured intracranial aneurysm with comorbidity, old age, narrow neck, and a posterior circulation aneurysm, and surgical clipping is warranted if the patient is young with an MCA aneurysm and interested in durability.

Research perspectives

Further studies with applications of low-dose CTA, such as the use of automatic tube current modulation and a small amount of contrast medium, are recommended. Additionally, future studies using advanced CT techniques such as higher 320 slices CT scan, dual-energy or source CTA, and time-resolved 4D CTA will improve temporal and spatial resolution and the image quality CTA. Also, applications of advanced vascular post-processing packages for analyzing CTA images will give comprehensive image interpretation in different planes and angles.

FOOTNOTES

Author contributions: Abdel Razek A and El-Serougy LG proposed the study concept and design; Elged BA searched Database; Kasem MA performed surgical procedures; Elmokadem AH performed DSA; Elged BA, EL-Adalany MA, and El-Serougy LG contributed to analysis and interpretation of data; Elged BA and Elmokadem AH contributed to drafting of the manuscript; Elmokadem AH and Abdel Razek A contributed to Revision of the manuscript; EL-Adalany MA and El-Serougy LG supported technical, or material.

Institutional review board statement: The study was approved by Mansoura university institutional review board (IRB).

Informed consent statement: Patients were not required to give a written consent for the study as the analysis used anonymous data.

Conflict-of-interest statement: All the authors report no relevant conflicts of interest for this article.

Data sharing statement: All data generated or analyzed during this study are included in this published article.

Open-Access: This article is an open-access article that was selected by an in-house editor and fully peer-reviewed by

external reviewers. It is distributed in accordance with the Creative Commons Attribution NonCommercial (CC BY-NC 4.0) license, which permits others to distribute, remix, adapt, build upon this work non-commercially, and license their derivative works on different terms, provided the original work is properly cited and the use is non-commercial. See: https://creativecommons.org/Licenses/by-nc/4.0/

Country/Territory of origin: Egypt

ORCID number: Ali H Elmokadem 0000-0001-5119-9548; Basma Abdelmonaem Elged 0000-0002-7442-9673; Ahmed Abdel Razek 0000-0002-9613-5932; Mohamed Ali Kasem 0000-0002-2633-6472; Mohamed Ali EL-Adalany 0000-0001-8226-7814.

S-Editor: Li L
L-Editor: A
P-Editor: Zhao S

REFERENCES

1 **Turan N**, Heider RA, Roy AK, Miller BA, Mullins ME, Barrow DL, Grossberg J, Pradilla G. Current Perspectives in Imaging Modalities for the Assessment of Unruptured Intracranial Aneurysms: A Comparative Analysis and Review. *World Neurosurg* 2018; **113**: 280-292 [PMID: 29360591 DOI: 10.1016/j.wneu.2018.01.054]

2 **Al-Smadi AS**, Elmokadem A, Shaibani A, Hurley MC, Potts MB, Jahromi BS, Ansari SA. Adjunctive Efficacy of Intra-Arterial Conebeam CT Angiography Relative to DSA in the Diagnosis and Surgical Planning of Micro-Arteriovenous Malformations. *AJNR Am J Neuroradiol* 2018; **39**: 1689-1695 [PMID: 30093482 DOI: 10.3174/ajnr.A5745]

3 **Howard BM**, Hu R, Barrow JW, Barrow DL. Comprehensive review of imaging of intracranial aneurysms and angiographically negative subarachnoid hemorrhage. *Neurosurg Focus* 2019; **47**: E20 [PMID: 31786554 DOI: 10.3171/2019.9.FOCUS19653]

4 **Elsherbini MM**, Elmokadem AH, El-Morsy A, Sherif FM, Khalil1 AF. Inter-Observer Reliability of Fused Time-of-Flight MR Angiography and 3D Steady State Sequence *vs* 3D Contrast Enhanced Images in Evaluation of Neurovascular Compression. *Open Journal of Modern Neurosurgery* 2022; **12** [DOI: 10.4236/ojmn.2022.122009]

5 **Ares WJ**, Jankowitz BT, Tonetti DA, Gross BA, Grandhi R. A comparison of digital subtraction angiography and computed tomography angiography for the diagnosis of penetrating cerebrovascular injury. *Neurosurg Focus* 2019; **47**: E16 [PMID: 31675711 DOI: 10.3171/2019.8.FOCUS19495]

6 **Yoon NK**, McNally S, Taussky P, Park MS. Imaging of cerebral aneurysms: a clinical perspective. *Neurovascular Imaging* 2016; **2**: 1-7 [DOI: 10.1186/s40809-016-0016-3]

7 **Bechan RS**, van Rooij SB, Sprengers ME, Peluso JP, Sluzewski M, Majoie CB, van Rooij WJ. CT angiography versus 3D rotational angiography in patients with subarachnoid hemorrhage. *Neuroradiology* 2015; **57**: 1239-1246 [PMID: 26341107 DOI: 10.1007/s00234-015-1590-9]

8 **Yang ZL**, Ni QQ, Schoepf UJ, De Cecco CN, Lin H, Duguay TM, Zhou CS, Zhao YE, Lu GM, Zhang LJ. Small Intracranial Aneurysms: Diagnostic Accuracy of CT Angiography. *Radiology* 2017; **285**: 941-952 [PMID: 28654338 DOI: 10.1148/radiol.2017162290]

9 **Kizilkilic O**, Huseynov E, Kandemirli SG, Kocer N, Islak C. Detection of wall and neck calcification of unruptured intracranial aneurysms with flat-detector computed tomography. *Interv Neuroradiol* 2016; **22**: 293-298 [PMID: 26842608 DOI: 10.1177/1591019915626591]

10 **Sawicki M**, Kościukiewicz K, Jeżewski D, Chełstowski K, Gołofit P, Skoczylas MM, Gębka M, Grabizna K, Kołaczyk K, Zwarzany Ł, Sagan L, Poncyljusz W. Diagnostic value of non-enhanced computed tomography in identifying location of ruptured cerebral aneurysm in patients with aneurysmal subarachnoid haemorrhage. *Neurol Neurochir Pol* 2020; **54**: 47-53 [PMID: 31967317 DOI: 10.5603/PJNNS.a2020.0007]

11 **Woernle CM**, Winkler KM, Burkhardt JK, Haile SR, Bellut D, Neidert MC, Bozinov O, Krayenbühl N, Bernays RL. Hydrocephalus in 389 patients with aneurysm-associated subarachnoid hemorrhage. *J Clin Neurosci* 2013; **20**: 824-826 [PMID: 23562295 DOI: 10.1016/j.jocn.2012.07.015]

12 **Feng TY**, Han XF, Lang R, Wang F, Wu Q. Subtraction CT angiography for the detection of intracranial aneurysms: A meta-analysis. *Exp Ther Med* 2016; **11**: 1930-1936 [PMID: 27168830 DOI: 10.3892/etm.2016.3166]

13 **Rajagopal N**, Balaji A, Yamada Y, Kawase T, Kato Y. Etiopathogenesis, clinical presentation and management options of mirror aneurysms: A comparative analysis with non-mirror multiple aneurysms. *Interdisciplinary Neurosurgery* 2019; **18**: 100535 [DOI: 10.1016/j.inat.2019.100535]

14 **Maniharan S**, Athukorala ADP, Pullaperuma DLN, Pirasath S, Lekamge IN. Role of digital subtraction angiography in detection of intracranial aneurysms compared with computed tomographic angiography. *Sri Lanka Journal of Radiology* 2019; **5** [DOI: 10.4038/sljr.v5i1.76]

15 **Rai SP**, ChandRan P, Pai M, Kamath M, Bele K, Kumar A, Chakraborti S. Comparison of Morphology of Intracranial Aneurysms on Computed Tomography Angiography with Digital Subtraction Angiography and Intraoperative Findings-A Single Centre Experience. *J Clin Diagn Res* 2019; **13** [DOI: 10.7860/JCDR/2019/37967.12420]

16 **Abecassis IJ**, Zeeshan Q, Ghodke BV, Levitt MR, Ellenbogen RG, Sekhar LN. Surgical Versus Endovascular Management of Ruptured and Unruptured Intracranial Aneurysms: Emergent Issues and Future Directions. *World Neurosurg* 2020; **136**: 17-27 [PMID: 31899398 DOI: 10.1016/j.wneu.2019.12.127]

17 **Daruwalla VJ**, Syed FH, Elmokadem AH, Hurley MC, Shaibani A, Ansari SA. Large basilar perforator pseudoaneurysm: A case report. *Interv Neuroradiol* 2016; **22**: 662-665 [PMID: 27485048 DOI: 10.1177/1591019916659261]

18 **Enomoto N**, Shinno K, Tamura T, Shikata E, Shono K, Takase K. Ruptured Basilar Artery Perforator Aneurysm: A Case Report and Review of the Literature. *NMC Case Rep J* 2020; **7**: 93-100 [PMID: 32695555 DOI: 10.2176/nmccrj.cr.2019-0143]

19 **Meguins LC**, Hidalgo RC, Spotti AR, de Morais DF. Aneurysm of azygos anterior cerebral artery associated with falcine meningioma: Case Report and review of the literature. *Surg Neurol Int* 2017; **8**: 25 [PMID: 28303205 DOI: 10.4103/2152-7806.200577]

20 **Wang GX**, Gong MF, Wen L, Liu LL, Yin JB, Duan CM, Zhang D. Computed Tomography Angiography Evaluation of Risk Factors for Unstable Intracranial Aneurysms. *World Neurosurg* 2018; **115**: e27-e32 [PMID: 29567291 DOI: 10.1016/j.wneu.2018.03.083]

21 **Kawabata Y**, Nakazawa T, Fukuda S, Kawarazaki S, Aoki T, Morita T, Tsukahara T. Endovascular embolization of branch-incorporated cerebral aneurysms. *Neuroradiol J* 2017; **30**: 600-606 [PMID: 29171364 DOI: 10.1177/1971400917698002]

22 **Chen J**, Li M, Zhu X, Chen Y, Zhang C, Shi W, Chen Q, Wang Y. Anterior Communicating Artery Aneurysms: Anatomical Considerations and Microsurgical Strategies. *Front Neurol* 2020; **11**: 1020 [PMID: 33013671 DOI: 10.3389/fneur.2020.01020]

23 **Ajiboye N**, Chalouhi N, Starke RM, Zanaty M, Bell R. Unruptured Cerebral Aneurysms: Evaluation and Management. *ScientificWorldJournal* 2015; **2015**: 954954 [PMID: 26146657 DOI: 10.1155/2015/954954]

24 **Kim HJ**, Yoon DY, Kim ES, Lee HJ, Jeon HJ, Lee JY, Cho BM. Intraobserver and interobserver variability in CT angiography and MR angiography measurements of the size of cerebral aneurysms. *Neuroradiology* 2017; **59**: 491-497 [PMID: 28343249 DOI: 10.1007/s00234-017-1826-y]

25 **Al Kasab S**, Nakagawa D, Zanaty M, Bathla G, Policeni B, Soni N, Allan L, Hudson J, Limaye K, Ortega-Gutierrez S, Samaniego EA, Hasan D. In vitro accuracy and inter-observer reliability of CT angiography in detecting intracranial aneurysm enlargement. *J Neurointerv Surg* 2019; **11**: 1015-1018 [PMID: 30842308 DOI: 10.1136/neurintsurg-2019-014737]

26 **Waqas M**, Chin F, Rajabzadeh-Oghaz H, Gong AD, Rai HH, Mokin M, Vakharia K, Dossani RH, Meng H, Snyder KV, Davies JM, Levy EI, Siddiqui AH. Size of ruptured intracranial aneurysms: a systematic review and meta-analysis. *Acta Neurochir (Wien)* 2020; **162**: 1353-1362 [PMID: 32215742 DOI: 10.1007/s00701-020-04291-z]

27 **Vandenbulcke A**, Messerer M, Starnoni D, Puccinelli F, Daniel RT, Cossu G. Complete spontaneous thrombosis in unruptured non-giant intracranial aneurysms: A case report and systematic review. *Clin Neurol Neurosurg* 2021; **200**: 106319 [PMID: 33268195 DOI: 10.1016/j.clineuro.2020.106319]

28 **Bhatia S**, Sekula RF, Quigley MR, Williams R, Ku A. Role of calcification in the outcomes of treated, unruptured, intracerebral aneurysms. *Acta Neurochir (Wien)* 2011; **153**: 905-911 [PMID: 21286763 DOI: 10.1007/s00701-010-0846-8]

29 **Kolias AG**, Sen J, Belli A. Pathogenesis of cerebral vasospasm following aneurysmal subarachnoid hemorrhage: putative mechanisms and novel approaches. *J Neurosci Res* 2009; **87**: 1-11 [PMID: 18709660 DOI: 10.1002/jnr.21823]

30 **Pedro KM**, Sih IM. Perianeurysmal Parenchymal Cyst of the Pons: A Case Report and Review of Literature. *Interdisciplinary Neurosurgery* 2020; **100731** [DOI: 10.1016/j.inat.2020.100731]

31 **Chen J**, Wang Y, Li P, Chen W, Zhou J, Hu X, Zhu J, Jiang B. Treatment of a giant arteriovenous malformation associated with intracranial aneurysm rupture during pregnancy: A case report. *Exp Ther Med* 2016; **12**: 1337-1340 [PMID: 27588055 DOI: 10.3892/etm.2016.3505]

32 **Flores BC**, Klinger DR, Rickert KL, Barnett SL, Welch BG, White JA, Batjer HH, Samson DS. Management of intracranial aneurysms associated with arteriovenous malformations. *Neurosurg Focus* 2014; **37**: E11 [PMID: 25175430 DOI: 10.3171/2014.6.FOCUS14165]

33 **Li J**, Du S, Sun L, Shang F, Zhang H, Li G. Hybrid Operation of a Ruptured Aneurysm Associated with a Developmental Venous Anomaly. *World Neurosurg* 2018; **120**: 63-65 [PMID: 30099185 DOI: 10.1016/j.wneu.2018.07.292]

34 **Jung SH**, Kim SH, Kim TS, Joo SP. Surgical Treatment of Traumatic Intracranial Aneurysms: Experiences at a Single Center over 30 Years. *World Neurosurg* 2017; **98**: 243-250 [PMID: 27836703 DOI: 10.1016/j.wneu.2016.11.005]

35 **Lefevre E**, Apra C, Chodraui-Filho SF, Chauvet D, Smajda S, Piotin M, Fahed R. Reliability of Bony Landmarks to Predict Intradural Location of Paraclinoid Aneurysms. *Clin Neuroradiol* 2020; **30**: 843-848 [PMID: 32170338 DOI: 10.1007/s00062-020-00896-0]

36 **Steiner T**, Juvela S, Unterberg A, Jung C, Forsting M, Rinkel G; European Stroke Organization. European Stroke Organization guidelines for the management of intracranial aneurysms and subarachnoid haemorrhage. *Cerebrovasc Dis* 2013; **35**: 93-112 [PMID: 23406828 DOI: 10.1159/000346087]

37 **Kim HJ**, Yoon DY, Kim ES, Yun EJ, Jeon HJ, Lee JY, Cho BM. 256-row multislice CT angiography in the postoperative evaluation of cerebral aneurysms treated with titanium clips: using three-dimensional rotational angiography as the standard of reference. *Eur Radiol* 2020; **30**: 2152-2160 [PMID: 31844961 DOI: 10.1007/s00330-019-06560-7]

38 **Yun SY**, Heo YJ, Jeong HW, Baek JW, Choo HJ, Shin GW, Kim ST, Jeong YG, Lee JY, Jung HS. Dual-energy CT angiography-derived virtual non-contrast images for follow-up of patients with surgically clipped aneurysms: a retrospective study. *Neuroradiology* 2019; **61**: 747-755 [PMID: 30684114 DOI: 10.1007/s00234-019-02170-8]



Published by **Baishideng Publishing Group Inc**
7041 Koll Center Parkway, Suite 160, Pleasanton, CA 94566, USA
Telephone: +1-925-3991568
E-mail: bpgoffice@wjgnet.com
Help Desk: https://www.f6publishing.com/helpdesk
https://www.wjgnet.com



© 2023 Baishideng Publishing Group Inc. All rights reserved.

ISSN 1949-8470 (online)

World Journal of *Radiology*

World J Radiol 2023 July 28; 15(7): 216-240



Published by Baishideng Publishing Group Inc

World Journal of Radiology

Contents

Monthly Volume 15 Number 7 July 28, 2023

MINIREVIEWS

216 Progress of magnetic resonance imaging radiomics in preoperative lymph node diagnosis of esophageal cancer

Xu YH, Lu P, Gao MC, Wang R, Li YY, Song JX

ORIGINAL ARTICLE

Basic Study

226 Can the change of vasomotor activity in irritable bowel syndrome patients be detected *via* color Doppler ultrasound?

Kazci O, Ege F, Aydemir H, Kazci S, Aydin S

CASE REPORT

234 Invasive rhinocerebral mucormycosis: Imaging the temporal evolution of disease in post COVID-19 case with diabetes: A case report

Narra R, Rayapati S

World Journal of Radiology

Monthly Volume 15 Number 7 July 28, 2023

Contents

ABOUT COVER

Editorial Board Member of *World Journal of Radiology*, Kıvanç Kamburoğlu, DDS, MSc, PhD, Professor, Department of Dentomaxillofacial Radiology, Ankara University, Ankara 06500, Turkey. dtkivo@yahoo.com

AIMS AND SCOPE

The primary aim of *World Journal of Radiology* (*WJR*, *World J Radiol*) is to provide scholars and readers from various fields of radiology with a platform to publish high-quality basic and clinical research articles and communicate their research findings online.

WJR mainly publishes articles reporting research results and findings obtained in the field of radiology and covering a wide range of topics including state of the art information on cardiopulmonary imaging, gastrointestinal imaging, genitourinary imaging, musculoskeletal imaging, neuroradiology/head and neck imaging, nuclear medicine and molecular imaging, pediatric imaging, vascular and interventional radiology, and women's imaging.

INDEXING/ABSTRACTING

The *WJR* is now abstracted and indexed in PubMed, PubMed Central, Emerging Sources Citation Index (Web of Science), Reference Citation Analysis, China National Knowledge Infrastructure, China Science and Technology Journal Database, and Superstar Journals Database. The 2023 Edition of Journal Citation Reports® cites the 2022 impact factor (IF) for *WJR* as 2.5; IF without journal self cites: 2.3; 5-year IF: 2.5; Journal Citation Indicator: 0.54.

RESPONSIBLE EDITORS FOR THIS ISSUE

Production Editor: *Si Zhao*; **Production Department Director:** *Xu Guo*; **Editorial Office Director:** *Jia-Ping Yan*.

NAME OF JOURNAL
World Journal of Radiology

ISSN
ISSN 1949-8470 (online)

LAUNCH DATE
January 31, 2009

FREQUENCY
Monthly

EDITORS-IN-CHIEF
Thomas J Vogl

EDITORIAL BOARD MEMBERS
https://www.wjgnet.com/1949-8470/editorialboard.htm

PUBLICATION DATE
July 28, 2023

COPYRIGHT
© 2023 Baishideng Publishing Group Inc

INSTRUCTIONS TO AUTHORS
https://www.wjgnet.com/bpg/gerinfo/204

GUIDELINES FOR ETHICS DOCUMENTS
https://www.wjgnet.com/bpg/GerInfo/287

GUIDELINES FOR NON-NATIVE SPEAKERS OF ENGLISH
https://www.wjgnet.com/bpg/gerinfo/240

PUBLICATION ETHICS
https://www.wjgnet.com/bpg/GerInfo/288

PUBLICATION MISCONDUCT
https://www.wjgnet.com/bpg/gerinfo/208

ARTICLE PROCESSING CHARGE
https://www.wjgnet.com/bpg/gerinfo/242

STEPS FOR SUBMITTING MANUSCRIPTS
https://www.wjgnet.com/bpg/GerInfo/239

ONLINE SUBMISSION
https://www.f6publishing.com

© 2023 Baishideng Publishing Group Inc. All rights reserved. 7041 Koll Center Parkway, Suite 160, Pleasanton, CA 94566, USA
E-mail: bpgoffice@wjgnet.com https://www.wjgnet.com

World Journal of Radiology

Submit a Manuscript: https://www.f6publishing.com

World J Radiol 2023 July 28; 15(7): 216-225

DOI: 10.4329/wjr.v15.i7.216

ISSN 1949-8470 (online)

MINIREVIEWS

Progress of magnetic resonance imaging radiomics in preoperative lymph node diagnosis of esophageal cancer

Yan-Han Xu, Peng Lu, Ming-Cheng Gao, Rui Wang, Yang-Yang Li, Jian-Xiang Song

Specialty type: Radiology, nuclear medicine and medical imaging

Provenance and peer review: Unsolicited article; Externally peer reviewed.

Peer-review model: Single blind

Peer-review report's scientific quality classification

Grade A (Excellent): 0
Grade B (Very good): 0
Grade C (Good): C, C
Grade D (Fair): 0
Grade E (Poor): 0

P-Reviewer: Jeong KY, South Korea; Singh G

Received: April 18, 2023
Peer-review started: April 18, 2023
First decision: June 1, 2023
Revised: June 11, 2023
Accepted: June 30, 2023
Article in press: June 30, 2023
Published online: July 28, 2023

Yan-Han Xu, Ming-Cheng Gao, Rui Wang, Yang-Yang Li, Jian-Xiang Song, Department of Thoracic Surgery, Yancheng Third People's Hospital, Affiliated Hospital 6 of Nantong University, Yancheng 224000, Jiangsu Province, China

Peng Lu, Department of Imaging, Yancheng Third People's Hospital, Affiliated Hospital 6 of Nantong University, Yancheng 224000, Jiangsu Province, China

Corresponding author: Jian-Xiang Song, PhD, Chief Doctor, Department of Thoracic Surgery, Yancheng Third People's Hospital, Affiliated Hospital 6 of Nantong University, No. 500 Yonghe Road, Gangzha District, Yancheng 224000, Jiangsu Province, China.
jxsongycsy@163.com

Abstract

Esophageal cancer, also referred to as esophagus cancer, is a prevalent disease in the cardiothoracic field and is a leading cause of cancer-related mortality in China. Accurately determining the status of lymph nodes is crucial for developing treatment plans, defining the scope of intraoperative lymph node dissection, and ascertaining the prognosis of patients with esophageal cancer. Recent advances in diffusion-weighted imaging and dynamic contrast-enhanced magnetic resonance imaging (MRI) have improved the effectiveness of MRI for assessing lymph node involvement, making it a beneficial tool for guiding personalized treatment plans for patients with esophageal cancer in a clinical setting. Radiomics is a recently developed imaging technique that transforms radiological image data from regions of interest into high-dimensional feature data that can be analyzed. The features, such as shape, texture, and waveform, are associated with the cancer phenotype and tumor microenvironment. When these features correlate with the clinical disease outcomes, they form the basis for specific and reliable clinical evidence. This study aimed to review the potential clinical applications of MRI-based radiomics in studying the lymph nodes affected by esophageal cancer. The combination of MRI and radiomics is a powerful tool for diagnosing and treating esophageal cancer, enabling a more personalized and effectual approach.

Key Words: Esophageal cancer; Diffusion-weighted imaging; Dynamic contrast-enhanced imaging; Radiomics; Lymph nodes

©The Author(s) 2023. Published by Baishideng Publishing Group Inc. All rights reserved.

Core Tip: Precise TNM staging is crucial for developing effective treatment plans for esophageal cancer. Establishing whether esophageal cancer has lymph node metastasis before surgery remains a significant clinical challenge. However, with the continuous advancement of radiomics, high-quality clinical decision support systems have emerged, enabling more accurate determination of preoperative lymph node status in esophageal cancer. This breakthrough may lead to formulating treatment plans that adhere to individualized medical guidelines.

Citation: Xu YH, Lu P, Gao MC, Wang R, Li YY, Song JX. Progress of magnetic resonance imaging radiomics in preoperative lymph node diagnosis of esophageal cancer. *World J Radiol* 2023; 15(7): 216-225
URL: https://www.wjgnet.com/1949-8470/full/v15/i7/216.htm
DOI: https://dx.doi.org/10.4329/wjr.v15.i7.216

INTRODUCTION

According to statistical studies, esophageal cancer is a prevalent malignant tumor of the digestive system, ranking seventh in incidence and sixth in mortality worldwide[1,2]. Endoscopic therapy, chemotherapy, and surgical resection are the primary treatments for esophageal cancer, with surgery being the leading treatment method for early-stage esophageal cancer[3]. Lymph node metastasis is an important prognostic factor in surgically treatable esophageal cancer[4-6]. While lymphatic spread in esophageal cancer is highly variable, positive lymph nodes should be resected along with the tumor to improve long-term survival[7,8]. However, extended lymph node resection may increase postoperative complications and worsen the prognosis of patients with esophageal cancer. Therefore, accurate lymph node evaluation is essential for developing an appropriate treatment strategy.

Magnetic resonance imaging (MRI) is more definitive than other imaging modalities in detecting positive lymph nodes in cancer and has been increasingly used in studying esophageal squamous cell carcinoma at the T and N stages[9-13]. Additionally, radiomics has gained momentum in cancer research over recent years[14]. Radiomics can quantify inter- and intratumor heterogeneity, accurately determine the status of preoperative lymph nodes in esophageal cancer and provide a better basis for clinical decisions regarding treatment options for esophageal cancer[15]. This paper reviews the research and applications of MRI, radiomics, and combined imaging techniques to determine the status of lymph nodes in esophageal cancer.

METASTATIC FEATURES OF ESOPHAGEAL CANCER LYMPH NODES AND THEIR IMPACT ON TREATMENT

Esophageal cancer commonly metastasizes to the lower neck, upper mediastinum, and perigastric area[16,17]. The lymph node metastasis rate (LNMR) primarily depends on the location and depth of tumor infiltration[18]. Therefore, certain lymph node regions, such as the cervical segmental paraoesophageal LN, the laryngeal recurrent nerve LN, and the LN along the left gastric artery, have a high LNMR[16].

Since the prognosis of patients with esophageal cancer mainly depends on the extent of the primary tumor and the lymphatic spread of the disease, lymph node status is a crucial prognostic factor[19,20]. Thus, clarifying the extent of lymph node dissection during surgical treatment is important for the prognosis of esophageal cancer. Tong and Kim *et al*. have demonstrated that patients with esophageal cancer with lymph node metastasis have a lower 5-year survival rate [19,21-23]. The lymph node ratio (absolute number of lymph nodes removed compared to the number of lymph nodes involved) in postoperative patients was an independent predictor of overall survival. Similar studies have indicated that residual lymph node metastasis after treatment is a critical indicator for assessing survival[24]. Therefore, an accurate assessment of the extent of lymph node metastasis in esophageal cancer provides an objective basis for clinical treatment planning and a reference value for patient regression after treatment.

The treatment options for esophageal cancer primarily depend on the TNM stage of the patient. According to Mönig *et al*[17] endoscopic resection is the recommended treatment for early superficial submucosal invasive carcinoma without histologic risk factors such as lymphatic or vascular infiltration. However, the rate of lymph node metastasis in submucosal carcinoma increases with the depth of infiltration. Therefore, the current gold standard of treatment for esophageal cancer is transthoracic subtotal esophagectomy and double field lymph node dissection[25].

The extent of lymph node dissection in esophageal cancer remains controversial[26]. A randomized study found no significant improvement in long-term survival with expanded transthoracic surgery in esophageal adenocarcinoma[27, 28]. Meanwhile, Lordick *et al*[29] concluded in their discussion of early management of esophageal cancer that surgery is considered standard of care for disease without suspected lymph node involvement (T1-2 N0 M0), and if lymph node involvement of disease is suspected (T1-2 N1-3 M0), patients are recommended to undergo preoperative treatment. Only after evaluation without involvement of lymph nodes should surgery be considered. Therefore, accurately diagnosing preoperative lymph nodes remains a challenge to be addressed.

RESEARCH PROGRESS OF MRI IN LYMPH NODES OF ESOPHAGEAL CANCER

After the diagnosis of esophageal cancer is confirmed by endoscopy and biopsy, staging is crucial for treatment and prognosis. Traditional examination methods, including endoscopic ultrasound (EUS) and computed tomography (CT), play an important role in determining T stage, invasiveness of surrounding structures, and detecting distant metastases [30,31]. Recent studies have shown that 18F-fluoro-2-deoxyglucose positron emission tomography (FDG-PET/CT) examination is also valuable in detecting distant metastases[32]. However, EUS, CT, and FDG-PET(/CT) have limitations in detecting lymph node involvement, which is an important independent predictor of long-term survival in patients[33].

CT scans are commonly used as a non-invasive method to assess metastatic infiltration of esophageal cancer lymph nodes. In CT diagnosis, intra-thoracic lymph nodes with a short diameter greater than 10 mm are considered metastatic lymph nodes. However, some studies have shown that only a small percentage of metastatic lymph nodes in esophageal cancer have a short diameter greater than 10 mm[33,34].

Furthermore, a related study found that although the sensitivity of CT was 59% in detecting lymph nodes larger than 10 mm in the conventional lymph node region of esophageal cancer, the diagnostic value of lymph nodes with metastasis was still insufficient[35]. Measuring the long and short axis diameters of lymph nodes in each region of esophageal cancer in CT images and calculating the axis ratio could improve the sensitivity of CT detection of lymph node metastasis in esophageal cancer. However, the sensitivity, specificity, and accuracy of this approach are still insufficient to provide high-quality clinical decision support systems[36].

MRI is superior to CT in terms of soft tissue resolution and can accurately detect differences in water content in tissues. Its images are unique in their ability to discriminate between masses, lymph nodes, and vascular structures from each other. MRI has multi-sequence imaging and multiple image types, and can generate images from multiple levels (cross-sectional, sagittal, coronal, and various oblique views) at will, reducing the artifacts of soft tissue boundaries in the images and providing richer imaging information to clarify the nature of the lesion. Although MR imaging modalities primarily focus on morphologic changes and provide less functional information about the tumor and are not the preferred method for staging, recent studies have shown that with the technical development of diffusion-weighted imaging (DWI), dynamic contrast-enhanced (DCE)-MRI, and IVIM, MR is progressively more accurate than CT in determining resectability, mediastinal invasion, and especially lymph node involvement[37].

DWI can provide information on tissue structure and cell density by reflecting the measured apparent diffusion coefficient (ADC) of water molecule mobility, and this quantitative metric is considered a meaningful imaging biomarker in esophageal studies[38]. Since its introduction into clinical practice, DWI has been widely used to detect lymph node metastasis in various primary malignancies and is a successful method[39]. In a prognostic study of esophageal cancer treatment, Giganti *et al*[38] found that pathological ADC could be considered a prognostic factor in esophageal cancer, and DWI may become a promising and reliable diagnostic technique for esophageal cancer. Sakurada *et al*. also found that the DWI-MRI imaging technique is important in determining the lymph node status of patients with esophageal cancer by visualizing lymph nodes and performing ADC value measurement[40]. In a quantitative analysis study by Alper *et al*[34] it was found that the STIR sequence improved the detection of metastatic lymph nodes with a sensitivity of 81.3% and a specificity of 98.3%, which is consistent with the findings of the group. While the diagnostic performance of DWI and PET for lymph nodes is controversial, the study by Shuto *et al*[39] concluded that DWI showed a higher sensitivity than PET in terms of diagnostic performance of lymph nodes. Given the association between lymph node status and prognosis in esophageal cancer, we believe that DWI is a predictive modality for survival after surgery in patients with esophageal cancer.

DCE-MRI has proven useful as a functional MRI modality in assessing vascular perfusion for monitoring and predicting response to radiotherapy. The histogram analysis established in DCE-MRI is a means of extracting heterogeneous parameters from significant regions (ROI) and whole-tumor analysis of samples from the entire tumor parenchyma and interstitium that can provide a more accurate quantitative assessment of tumor biology[41]. This technique has improved the diagnostic capability of MRI. In the study by Sun *et al*[42] on radiotherapy for esophageal cancer, the results of different histogram parameters (median, mean, standard deviation, mode, skewness, kurtosis, minimum, maximum, percentile, and entropy) derived from DCE-MRI were compared and found to be useful for the assessment of tumor heterogeneity and monitoring the response to radiotherapy for esophageal cancer. Regarding lymph node status analysis, the findings of Chen *et al*[41] suggest that whole-tumor cumulative histogram analysis obtained from DCE-MRI with pharmacokinetics as a parameter may be useful for T-staging and regional lymph node status determination in esophageal squamous cell carcinoma. Although the study of lymph node status in esophageal cancer by DCE-MRI is still in its infancy, the available data and results show that DCE-MRI has a high accuracy in determining lymph node status, which is important for developing individualized treatment plans for esophageal cancer.

Recently, the StarVIBE sequence on MRI has been utilized in cases where patients are unable to hold their breath and has gradually been incorporated into studies on esophageal cancer[12,43]. Qu *et al*[44] conducted a study where MRI was shown to better predict lymph node status in patients with preoperative esophageal cancer by extracting the ROI of esophageal cancer lesions. This method demonstrated significantly improved diagnostic accuracy over CT and could facilitate better treatment planning for esophageal cancer. Therefore, MRI shows promise in aiding lymph node assessment in esophageal cancer patients, particularly when CT scans yield inconclusive results. Nevertheless, further research is required to confirm its effectiveness in clinical practice.

While the clinical value of MRI in lymph node diagnosis, treatment evaluation, and prognosis prediction has been gradually recognized, false-positive lymph nodes can also occur on MRI due to interference from cardiac motion and gastric peristaltic artifacts. Moreover, false-negative lymph nodes can also be observed in smokers and patients with pneumoconiosis or silicosis with esophageal cancer[45]. Despite advancements in radiological examination methods, further improvement in the sensitivity of lymph node metastasis determination may still be possible. For instance, the

development of new imaging techniques or the integration of multiple imaging modalities could potentially improve the accuracy of lymph node metastasis detection in esophageal cancer patients. Additionally, further studies focusing on the optimization of imaging protocols and the standardization of image interpretation criteria may lead to more accurate and reliable diagnosis of lymph node metastasis.

Process steps of radiomics

Radiomics is the application of computerized mathematical tools to image processing, transforming image data from ROI in radiological images into mineable high-dimensional feature data. The radiological features (*e.g.*, shape, texture, or waveform) extracted from them can provide information about the cancer phenotype as well as the tumor microenvironment[14]. This information is distinct and complementary to other disease-related information, including clinical features, treatment-related decision information, or genomic data[46]. When radiomics-derived data are combined with other relevant data and correlated or extrapolated to clinical disease outcomes, they can produce accurate and reliable clinical decision support systems (CDSS). These CDSS can assist clinicians in making more informed decisions regarding diagnosis, treatment planning, and prognosis prediction for patients with esophageal cancer (Figure 1).

Radiomics refers to the quantitative mapping of medical images, involving the extraction and analysis of numerous image features that are relevant to the study objectives, including clinical treatment decisions and genomic features. Radiomics studies typically encompass five phases, namely data selection, medical imaging, feature extraction, exploratory analysis, and modeling. The analysis of radiomics can be localized in the primary tumor foci, metastatic lesions, or normal tissues or can be applied to any image generated in the clinical setting. Radiomics analysis can provide valuable insights into tumor heterogeneity and microenvironment, which can aid in identifying potential biomarkers for prognosis and treatment response prediction in patients with esophageal cancer. However, further research is necessary to validate the clinical utility of radiomics in esophageal cancer and to establish standardized protocols for radiomics analysis.

Regarding image feature extraction in radiomics, it involves extracting quantitative features from images that represent the volume of interest (VOI), which are eigenvalues of an image that depend on factors such as image preprocessing (*e.g.*, filtering or intensity discretization) and reconstruction (*e.g.*, filtered backprojection or iterative reconstruction)[14]. Delineating the ROI or VOI is a critical first step in any radiomics method. However, manual, and semi-automatic segmentation methods often introduce observer bias and can be time-consuming. Additionally, inter-, and intra-observer variation in ROI/VOI delineation can affect the reproducibility and stability of radiomics features. Therefore, studies using manual or semi-automatic segmentation with manual correction should evaluate the internal and external reproducibility of derived radiomics features. To ensure result reproducibility, it is advisable to exclude irreproducible features from further analysis. Automating the segmentation process using deep learning techniques has also shown promise in improving the reproducibility and efficiency of ROI/VOI delineation in radiomics studies.

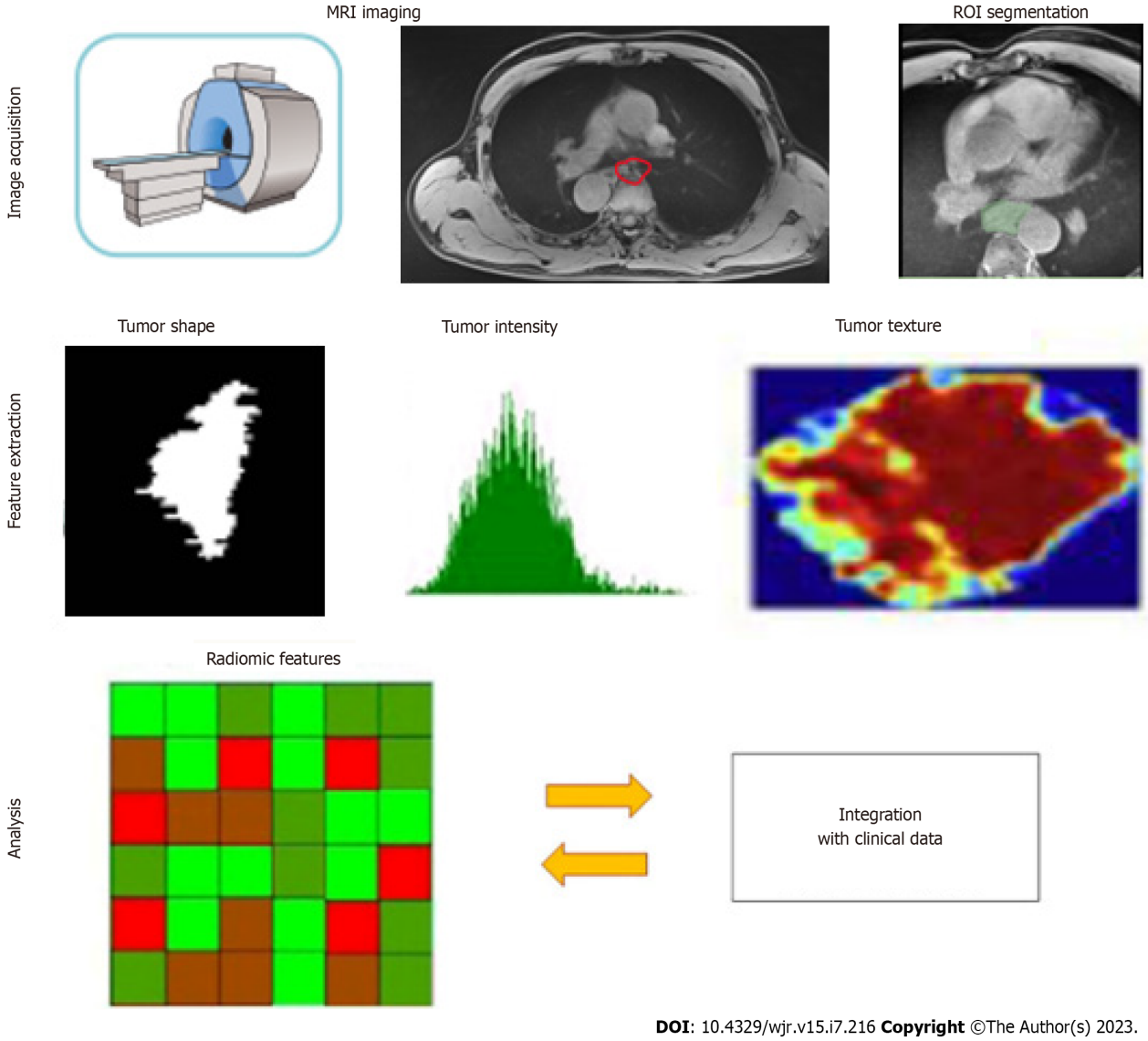
The second step in image processing is a crucial intermediary between image segmentation and feature extraction. Its objective is to standardize the images for radiomics feature extraction, including pixel spacing, grayscale intensities, and gray histogram binning, among other factors. The reliability of test-retest of extracted radiomics features depends on the image processing settings used in this step. Therefore, it is critical to carefully select and optimize the image processing settings to ensure the robustness and reproducibility of radiomics features. The pyRadiomics package, which is one of the most widely used packages for radiomics analysis, allows various image processing steps to be defined through a parameter file in YAML or JSON structured text format. This file can then be loaded into 3D Slicer or integrated into a Python framework to facilitate feature calculation.

After image segmentation and processing, the third step of radiomics feature extraction can be performed. Feature extraction involves calculating feature descriptors to quantify the gray-level features within the ROI/VOI. As there are many ways and formulas to calculate these features, it is recommended to follow the Image Biomarker Standardization Initiative (IBSI) guidelines[47].

The IBSI guidelines provide a consensus for standardized feature calculations from a matrix of all radiomics features. Different types of radiomics features exist, including intensity-based (histogram) features, shape features, texture features, transform-based features, and radial features, with different types of filters (*e.g.*, wavelet or Gaussian filters) usually applied in the feature extraction step. After feature selection/deviation is performed, subsequent statistical analysis and machine learning will be used to identify the important features that support image analysis. Dimensionality reduction is a multi-step process to exclude irreducible, redundant, and irrelevant features from the dataset.

The first step involves excluding non-replicated features, as a feature that has high intra- or inter-observer variability may be less likely to be useful. The second step is to select the most relevant variables for the corresponding task. Various methods that often rely on machine learning techniques can be used for this initial feature selection step, such as elimination filters, recursive feature elimination methods, or random forest algorithms. As these algorithms often cannot account for covariance and correlation in the data, constructing correlation clusters is the logical next step in the dimensionality reduction workflow. In some cases, this step may be combined with the previous (second) step, as few machine learning techniques can handle correlations in the data. Correlation clustering allows the visualization of highly correlated features in the data and the selection of only one representative feature per correlation cluster.

Selecting the variable with the highest bio-clinical variability in the dataset is crucial as it is likely to be the most representative of the variation within a given patient population. Once the dimensionality of the data has been reduced, the importance of the data visualization step increases. Therefore, reducing the number of features used to build statistical and machine learning models through a step called feature selection or dimensionality reduction is critical to generating valid and generalizable results. The remaining uncorrelated and highly correlated features can be used to train models for the corresponding classification tasks, and the constructed radiomics models are evaluated according to the radiomics quality score. These key steps form the basis for ensuring that the imaging histology produces high-quality CDSS.



DOI: 10.4329/wjr.v15.i7.216 **Copyright** ©The Author(s) 2023.

Figure 1 Research flow chart of radiomics based on magnetic resonance imaging in esophageal cancer. MRI: magnetic resonance imaging; ROI: Regions of interest.

Progress of CT radiomics in esophageal cancer lymph nodes

When radiomics is involved in tumor exploration, it provides a new approach in the study of cancer patients by developing and validating an imaging-based radiomic columnar map that combines radiomic features and clinical factors in the development of cancer patients. In the esophageal cancer study discussed in this article, there have been many researchers, in recent years, who have applied radiomics to the study of esophageal cancer, thus showing that radiomics is not a novel technique.

Li *et al*[48] extracted radiomic features from FDG-PET images of 152 patients with esophageal cancer and successfully predicted those patients who would not benefit from preoperative radiotherapy. Qiu *et al*[49] developed and validated a CT-based radiomic columnar map that combined radiomic features and clinical factors to predict the risk of recurrence in patients who underwent surgery after neoadjuvant chemotherapy and achieved a pathologic complete response in patients with esophageal cancer at risk of recurrence. Meanwhile, in terms of lymph nodes, which are the focus of this article, Gu *et al*[50] studied 129 sets of lymph nodes from 77 patients in the cohort (trial cohort: 102 lymph nodes from 59 patients; validation cohort: 27 lymph nodes from 18 patients) based on the radiomic features of CT to predict the treatment response and the ability of local control of locally recurrent lymph nodes after radiotherapy esophagectomy. A scoring model based on the location and length of the cancer focus and the size and status of the corresponding lymph node region as revealed by CT allowed for accurate assessment of the status of the lymph nodes, which helped in the development of the surgical approach and accurate intraoperative clearance of the corresponding lymph nodes. Meanwhile, in a case-control study of esophageal cancer, Qu *et al*[44] extracted radiomic features from CT data of 152 patients with esophageal cancer without lymph node metastases and 182 patients with lymph node metastases and found that CT radiologic features could help predict the lymph node status of patients with advanced esophageal cancer and effectively distinguish whether there were regional lymph node metastases in esophageal cancer. Moreover, Tan *et al*[51] retrospectively analyzed 230 patients with esophageal cancer who had CT examinations and found that radiomics could

help reveal intra-tumor heterogeneity and could be used as a new biomarker to determine LN status in patients with resectable esophageal cancer by using a radiomic column line graph containing 5 features in combination with CT-reported LN status (*i.e.*, size criteria). This shows that the CT radiomics model can be applied clinically to assess the lymph node status in patients with esophageal cancer prior to treatment.

Although most current radiomic studies of ESCC are based on CT and PET, preoperative MRI radiologic features are more valuable because MRI is noninvasive and has higher tissue resolution. Qu *et al*[44] 50 of 181 patients with pathologically confirmed esophageal cancer with lymph node metastases, based on T2-TSE-BLADE and StarVIBE enhancement sequences in MRI images. Nine radiographic features were selected to create radiographic features significantly associated with LN metastasis, and the model was found to distinguish well between metastatic and non-metastatic lymph nodes.

Development of MRI radiomics in tumor research

Although most of the current radiomic studies of ESCC are based on CT and PET, with the advancement of MRI techniques such as DWI, DCE-MRI, and IVIM, and the availability of high-quality imaging sequences such as the related StarVIBE and T2_BLADE, MRI has excellent soft-tissue resolution and is more conducive to the mutual discrimination between lesions, lymph nodes, and vascular structures. MRI findings such as the size, morphology, and shape of cancer foci are important for their identification in the study of tumor subtypes[52,53]. In some studies, it has been found that some specific MRI sequences can better detect lesions and aid in treatment selection[53]. The ROI generated from MRI images can be analyzed by imaging histology to extract superior imaging features. These features can be combined with clinically relevant patient information to generate high-quality CDSS to guide treatment planning.

ROI analysis of the primary tumor lesion not only yields key information about the relevant pathology but also has value for the prognostic analysis of patient survival. Shin *et al*[54] applied an MRI radiomic model to assess the pathological remission response in rectal cancer patients receiving neoadjuvant radiotherapy and found that the diagnostic value was superior to visual assessment by an experienced radiologist. Meanwhile, Li *et al*[48] extracted radiomic features from T2-weighted MRI images and combined them with clinical data for deep machine learning, which stably predicted the survival of glioma patients and helped to preoperatively assess the extent of macrophage infiltration in glioma tumors[55].

Although there is increasing interest in MRI radiomics in various areas of oncology across studies, most of the studies have focused almost exclusively on the histological and radiomic features associated with the primary tumor. It is well-known that histopathological data of the primary tumor, such as lymph-vascular invasion, histological grading, and tumor markers, are important factors used to guide or determine clinical treatment decisions. Meanwhile, when MRI radiomics is focused on the diagnosis of preoperative lymph node status, its high-quality diagnostic results can further guide treatment decisions in the clinical setting. In a study by Santucci *et al*[56], they found 3T MRI radiomics combined with histological data could predict preoperative lymph node metastasis in breast cancer patients and guide treatment planning. The results suggest that accurate prediction of lymph node status can avoid invasive surgery, such as lymph node dissection or biopsy[56]. Similar conclusions were reached in studies on the prediction of preoperative lymph node status in breast cancer, suggesting that the influential features of MRI radiomics are important for the determination of lymph node status[57-59].

It is worth noting that while the image features derived solely from the ROI of cancer foci can be used to analyze the status of lymph nodes, the CDSS obtained from both the ROI of lymph nodes and cancer foci is more clinically valuable when combined for imaging histological analysis. In Li *et al*.'s study, they combined the ROIs of both primary colon cancer lesions and lymph node lesions for imaging histological analysis, and their findings were even more convincing because they required the analysis of both cancer lesion features and lymph node features in their derived nomogram features[60].

While various high-quality MRI sequences have been studied, the analysis of optimal imaging sequences is still rare. Qu *et al*[44] selected 9 radiographic features based on the T2-TSE-BLADE and Star-VIBE enhancement sequences in MRI images to create radiographic features that are significantly associated with LN metastasis in 181 patients with pathologically confirmed lymph node metastasis. They found that the model based on this sequence effectively distinguished between metastatic and non-metastatic lymph nodes[44].

It is important to note that MRI examinations typically have a long examination time, and tumors that originate in the chest may be affected by the patient's respiratory movements, making artifacts unavoidable. While imaging histology can help reduce the impact of artifacts, it may also be beneficial to minimize examination time and extract established imaging histological features from optimal sequences to improve CDSS quality.

In oncology patients, accurately diagnosing lymph node status is critical for determining appropriate treatment options. While existing MRI radiomics studies have demonstrated its effectiveness in determining lymph node status, studies targeting focal radiomic features that link tumor features with lymph node status remain relatively uncommon. Analyzing various MRI sequences to identify sequences that yield high-quality imaging histological features may be an important area for future research.

Radiomics has garnered significant attention from researchers worldwide for its non-invasive, quantitative, and low-cost approach in diagnosing tissue characteristics, tumor staging, and treatment response. The current focus of radiomics research for esophageal cancer is on evaluating patient response and survival prognosis after different treatments. While predicting preoperative lymph node status using radiomics remains relatively rare, the numerous studies exploring various aspects of radiomics in esophageal cancer offer optimism for future research into using radiomics more widely to evaluate lymph nodes.

CONCLUSION

Although MRI has shown a trend toward superiority over other imaging methods for determining the lymph node status of esophageal cancer, the interference of respiratory motion and heartbeat specific to the chest and the presence of artifacts in imaging can affect the diagnosis of the lymph node status of esophageal cancer. Radiomics techniques use a combined medical-mathematical tool approach to convert conventional images into digital quantitative features, which have the potential to tap into the underlying biological features and heterogeneity of tumor images and have been widely used for diagnosis, differential diagnosis, and disease assessment. Radiomics can significantly improve the diagnostic specificity of lymph nodes.

However, MRI-based radiomics has not been extensively studied in esophageal cancer lymph nodes. Although some studies have found that MRI-based radiomic features are associated with lymph node metastasis, most were relatively small-sample and single-center studies, and the applicability and generalizability of the findings require further validation. The specificity of various MRI sequences and techniques for diagnosing lymph node status in esophageal cancer needs to be compared, and the quality of the images formed by the selected MRI sequences needs to be validated against histological data. Furthermore, a multicenter study should be conducted to increase the sample size and validate our findings. Successful completion of these essential steps can lead to the development of a valuable clinical decision support systems (CDSS) for esophageal cancer.

It is important to note that while radiomics analysis can be performed on medical images from different modalities, integrating cross-modality approaches using the potential information extracted from MRI, computed tomography, and PET can provide added value compared to evaluating each modality separately. However, the level of research sophistication still has low stability and generalizability, and specific study conditions and author selection can strongly influence the results.

In addition, most radiomic studies are based on retrospective data, resulting in a low evidence level. Therefore, prospective studies for validation in external cohorts or confirmatory studies, besides larger patient cohorts, are necessary to provide more reliable and generalizable results. Future studies should focus on developing standardized radiomics protocols and establishing open-access radiomics databases to promote the reproducibility and transparency of radiomics research. Radiomics has great overall potential for aiding clinical decision-making and improving patient outcomes; however, further validation and standardization are needed to ensure clinical utility.

It is essential to ensure that the imaging histology study is of high quality, addresses actual clinical needs, and can be implemented clinically to increase the likelihood of clinically relevant and valuable radiomics studies. Obtaining all relevant non-imaging data, such as demographics and bioinformatics, is critical. Standardizing the acquired images before performing radiomics analysis is essential to minimize the impact of different settings on the modeling. Implementing these key steps can lead to the formation of a valuable CDSS.

Furthermore, we believe that combining various MRI techniques and radiomics studies on esophageal cancer lymph nodes can introduce new quantitative imaging markers for medical imaging. With the precise determination of lymph node status using different MRI techniques and high-quality CDSS provided by radiomics findings, this approach may lead to significant breakthroughs in clinical studies. Preoperative personalized clinical characterization and precise treatment planning for esophageal cancer are possible with the introduction of new quantitative imaging markers.

FOOTNOTES

Author contributions: Xu YH contributed mainly to this work; Xu YH, Lu P, Gao MC, Wang R, Li YY, Song JX designed research; Xu YH, Lu P and Gao MC performed research; and Xu YH wrote the paper.

Conflict-of-interest statement: The author(s) declared no potential conflicts of interest with respect to the research, authorship, and/or publication of this article.

Open-Access: This article is an open-access article that was selected by an in-house editor and fully peer-reviewed by external reviewers. It is distributed in accordance with the Creative Commons Attribution NonCommercial (CC BY-NC 4.0) license, which permits others to distribute, remix, adapt, build upon this work non-commercially, and license their derivative works on different terms, provided the original work is properly cited and the use is non-commercial. See: https://creativecommons.org/Licenses/by-nc/4.0/

Country/Territory of origin: China

ORCID number: Yan-Han Xu 0000-0001-6230-4729; Jian-Xiang Song 0000-0003-4503-6464.

S-Editor: Ma YJ
L-Editor: A
P-Editor: Zhao S

REFERENCES

1 **Bray F**, Ferlay J, Soerjomataram I, Siegel RL, Torre LA, Jemal A. Global cancer statistics 2018: GLOBOCAN estimates of incidence and

mortality worldwide for 36 cancers in 185 countries. *CA Cancer J Clin* 2018; **68**: 394-424 [PMID: 30207593 DOI: 10.3322/caac.21492]

2 **Chen W**, Zheng R, Baade PD, Zhang S, Zeng H, Bray F, Jemal A, Yu XQ, He J. Cancer statistics in China, 2015. *CA Cancer J Clin* 2016; **66**: 115-132 [PMID: 26808342 DOI: 10.3322/caac.21338]

3 **Ishihara R**. Endoscopic Diagnosis and Treatment of Superficial Esophageal Squamous Cell Cancer: Present Status and Future Perspectives. *Curr Oncol* 2022; **29**: 534-543 [PMID: 35200548 DOI: 10.3390/curroncol29020048]

4 **Hofstetter W**, Correa AM, Bekele N, Ajani JA, Phan A, Komaki RR, Liao Z, Maru D, Wu TT, Mehran RJ, Rice DC, Roth JA, Vaporciyan AA, Walsh GL, Francis A, Blackmon S, Swisher SG. Proposed modification of nodal status in AJCC esophageal cancer staging system. *Ann Thorac Surg* 2007; **84**: 365-73; discussion 374 [PMID: 17643602 DOI: 10.1016/j.athoracsur.2007.01.067]

5 **Mariette C**, Piessen G, Briez N, Triboulet JP. The number of metastatic lymph nodes and the ratio between metastatic and examined lymph nodes are independent prognostic factors in esophageal cancer regardless of neoadjuvant chemoradiation or lymphadenectomy extent. *Ann Surg* 2008; **247**: 365-371 [PMID: 18216546 DOI: 10.1097/SLA.0b013e31815aaadf]

6 **Rice TW**, Lerut TE, Orringer MB, Chen LQ, Hofstetter WL, Smithers BM, Rusch VW, van Lanschot J, Chen KN, Davies AR, D'Journo XB, Kesler KA, Luketich JD, Ferguson MK, Räsänen JV, van Hillegersberg R, Fang W, Durand L, Allum WH, Cecconello I, Cerfolio RJ, Pera M, Griffin SM, Burger R, Liu JF, Allen MS, Law S, Watson TJ, Darling GE, Scott WJ, Duranceau A, Denlinger CE, Schipper PH, Ishwaran H, Apperson-Hansen C, DiPaola LM, Semple ME, Blackstone EH. Worldwide Esophageal Cancer Collaboration: neoadjuvant pathologic staging data. *Dis Esophagus* 2016; **29**: 715-723 [PMID: 27731548 DOI: 10.1111/dote.12513]

7 **Hosch SB**, Stoecklein NH, Pichlmeier U, Rehders A, Scheunemann P, Niendorf A, Knoefel WT, Izbicki JR. Esophageal cancer: the mode of lymphatic tumor cell spread and its prognostic significance. *J Clin Oncol* 2001; **19**: 1970-1975 [PMID: 11283129 DOI: 10.1200/JCO.2001.19.7.1970]

8 **Visser E**, van Rossum PSN, Ruurda JP, van Hillegersberg R. Impact of Lymph Node Yield on Overall Survival in Patients Treated With Neoadjuvant Chemoradiotherapy Followed by Esophagectomy for Cancer: A Population-based Cohort Study in the Netherlands. *Ann Surg* 2017; **266**: 863-869 [PMID: 28742691 DOI: 10.1097/SLA.0000000000002389]

9 **Dappa E**, Elger T, Hasenburg A, Düber C, Battista MJ, Hötker AM. The value of advanced MRI techniques in the assessment of cervical cancer: a review. *Insights Imaging* 2017; **8**: 471-481 [PMID: 28828723 DOI: 10.1007/s13244-017-0567-0]

10 **Moreno CC**, Sullivan PS, Mittal PK. MRI Evaluation of Rectal Cancer: Staging and Restaging. *Curr Probl Diagn Radiol* 2017; **46**: 234-241 [PMID: 28089690 DOI: 10.1067/j.cpradiol.2016.11.011]

11 **Qiu Y**, Zhang X, Wu Z, Wu S, Yang Z, Wang D, Le H, Mao J, Dai G, Tian X, Zhou R, Huang J, Hu L, Shen J. MRI-Based Radiomics Nomogram: Prediction of Axillary Non-Sentinel Lymph Node Metastasis in Patients With Sentinel Lymph Node-Positive Breast Cancer. *Front Oncol* 2022; **12**: 811347 [PMID: 35296027 DOI: 10.3389/fonc.2022.811347]

12 **Qu J**, Zhang H, Wang Z, Zhang F, Liu H, Ding Z, Li Y, Ma J, Zhang Z, Zhang S, Dong Y, Jiang L, Zhang W, Grimm R, Kiefer B, Kamel IR, Qin J, Li H. Comparison between free-breathing radial VIBE on 3-T MRI and endoscopic ultrasound for preoperative T staging of resectable oesophageal cancer, with histopathological correlation. *Eur Radiol* 2018; **28**: 780-787 [PMID: 28799124 DOI: 10.1007/s00330-017-4963-0]

13 **Giganti F**, Ambrosi A, Petrone MC, Canevari C, Chiari D, Salerno A, Arcidiacono PG, Nicoletti R, Albarello L, Mazza E, Gallivanone F, Gianolli L, Orsenigo E, Esposito A, Staudacher C, Del Maschio A, De Cobelli F. Prospective comparison of MR with diffusion-weighted imaging, endoscopic ultrasound, MDCT and positron emission tomography-CT in the pre-operative staging of oesophageal cancer: results from a pilot study. *Br J Radiol* 2016; **89**: 20160087 [PMID: 27767330 DOI: 10.1259/bjr.20160087]

14 **Lambin P**, Leijenaar RTH, Deist TM, Peerlings J, de Jong EEC, van Timmeren J, Sanduleanu S, Larue RTHM, Even AJG, Jochems A, van Wijk Y, Woodruff H, van Soest J, Lustberg T, Roelofs E, van Elmpt W, Dekker A, Mottaghy FM, Wildberger JE, Walsh S. Radiomics: the bridge between medical imaging and personalized medicine. *Nat Rev Clin Oncol* 2017; **14**: 749-762 [PMID: 28975929 DOI: 10.1038/nrclinonc.2017.141]

15 **Gillies RJ**, Kinahan PE, Hricak H. Radiomics: Images Are More than Pictures, They Are Data. *Radiology* 2016; **278**: 563-577 [PMID: 26579733 DOI: 10.1148/radiol.2015151169]

16 **Wang Y**, Zhu L, Xia W, Wang F. Anatomy of lymphatic drainage of the esophagus and lymph node metastasis of thoracic esophageal cancer. *Cancer Manag Res* 2018; **10**: 6295-6303 [PMID: 30568491 DOI: 10.2147/CMAR.S182436]

17 **Mönig S**, Chevallay M, Niclauss N, Zilli T, Fang W, Bansal A, Hoeppner J. Early esophageal cancer: the significance of surgery, endoscopy, and chemoradiation. *Ann N Y Acad Sci* 2018; **1434**: 115-123 [PMID: 30138532 DOI: 10.1111/nyas.13955]

18 **Nishimori H**, Hayashi S, Naito M, Murakami G, Fujita M, Hosokawa M. Mucosal lymphatic vessels of the esophagus distant from the cancer margin: morphometrical analysis using 27 surgically removed specimens of squamous cell carcinoma located in the upper or middle thoracic esophagus. *Okajimas Folia Anat Jpn* 2011; **88**: 43-47 [PMID: 22184865 DOI: 10.2535/ofaj.88.43]

19 **Markar S**, Gronnier C, Duhamel A, Pasquer A, Théreaux J, du Rieu MC, Lefevre JH, Turner K, Luc G, Mariette C. Salvage Surgery After Chemoradiotherapy in the Management of Esophageal Cancer: Is It a Viable Therapeutic Option? *J Clin Oncol* 2015; **33**: 3866-3873 [PMID: 26195702 DOI: 10.1200/JCO.2014.59.9092]

20 **Merkow RP**, Bilimoria KY, Keswani RN, Chung J, Sherman KL, Knab LM, Posner MC, Bentrem DJ. Treatment trends, risk of lymph node metastasis, and outcomes for localized esophageal cancer. *J Natl Cancer Inst* 2014; **106** [PMID: 25031273 DOI: 10.1093/jnci/dju133]

21 **Tong DK**, Law S, Kwong DL, Chan KW, Lam AK, Wong KH. Histological regression of squamous esophageal carcinoma assessed by percentage of residual viable cells after neoadjuvant chemoradiation is an important prognostic factor. *Ann Surg Oncol* 2010; **17**: 2184-2192 [PMID: 20217248 DOI: 10.1245/s10434-010-0995-2]

22 **Kim MP**, Correa AM, Lee J, Rice DC, Roth JA, Mehran RJ, Walsh GL, Ajani JA, Maru DM, Chang JY, Marom EM, Macapinlac HA, Lee JH, Vaporciyan AA, Rice T, Swisher SG, Hofstetter WL. Pathologic T0N1 esophageal cancer after neoadjuvant therapy and surgery: an orphan status. *Ann Thorac Surg* 2010; **90**: 884-90; discussion 890 [PMID: 20732513 DOI: 10.1016/j.athoracsur.2010.03.116]

23 **Sisic L**, Blank S, Weichert W, Jäger D, Springfeld C, Hochreiter M, Büchler M, Ott K. Prognostic impact of lymph node involvement and the extent of lymphadenectomy (LAD) in adenocarcinoma of the esophagogastric junction (AEG). *Langenbecks Arch Surg* 2013; **398**: 973-981 [PMID: 23887283 DOI: 10.1007/s00423-013-1101-6]

24 **Wang Q**, Yu S, Xiao Z, Liu X, Zhang W, Zhang X, He J, Sun K, Xu T, Feng Q, Zhou Z, Wang L, Yin W. Residual lymph node status is an independent prognostic factor in esophageal squamous cell Carcinoma with pathologic T0 after preoperative radiotherapy. *Radiat Oncol* 2015; **10**: 142 [PMID: 26159510 DOI: 10.1186/s13014-015-0450-4]

25 **Hölscher AH**, Bollschweiler E, Schröder W, Metzger R, Gutschow C, Drebber U. Prognostic impact of upper, middle, and lower third mucosal or submucosal infiltration in early esophageal cancer. *Ann Surg* 2011; **254**: 802-7; discussion 807 [PMID: 22042472 DOI: 10.1097/SLA.0b013e3182369128]

26 **van der Sluis PC**, Ruurda JP, Verhage RJ, van der Horst S, Haverkamp L, Siersema PD, Borel Rinkes IH, Ten Kate FJ, van Hillegersberg R. Oncologic Long-Term Results of Robot-Assisted Minimally Invasive Thoraco-Laparoscopic Esophagectomy with Two-Field Lymphadenectomy for Esophageal Cancer. *Ann Surg Oncol* 2015; **22** Suppl 3: S1350-S1356 [PMID: 26023036 DOI: 10.1245/s10434-015-4544-x]

27 **Omloo JM**, Lagarde SM, Hulscher JB, Reitsma JB, Fockens P, van Dekken H, Ten Kate FJ, Obertop H, Tilanus HW, van Lanschot JJ. Extended transthoracic resection compared with limited transhiatal resection for adenocarcinoma of the mid/distal esophagus: five-year survival of a randomized clinical trial. *Ann Surg* 2007; **246**: 992-1000; discussion 1000 [PMID: 18043101 DOI: 10.1097/sla.0b013e31815c4037]

28 **Hulscher JB**, van Sandick JW, de Boer AG, Wijnhoven BP, Tijssen JG, Fockens P, Stalmeier PF, ten Kate FJ, van Dekken H, Obertop H, Tilanus HW, van Lanschot JJ. Extended transthoracic resection compared with limited transhiatal resection for adenocarcinoma of the esophagus. *N Engl J Med* 2002; **347**: 1662-1669 [PMID: 12444180 DOI: 10.1056/nejmoa022343]

29 **Lordick F**, Mariette C, Haustermans K, Obermannová R, Arnold D; ESMO Guidelines Committee. Oesophageal cancer: ESMO Clinical Practice Guidelines for diagnosis, treatment and follow-up. *Ann Oncol* 2016; **27**: v50-v57 [PMID: 27664261 DOI: 10.1093/annonc/mdw329]

30 **DeMeester SR**. Adenocarcinoma of the esophagus and cardia: a review of the disease and its treatment. *Ann Surg Oncol* 2006; **13**: 12-30 [PMID: 16378161 DOI: 10.1245/aso.2005.12.025]

31 **Kelly S**, Harris KM, Berry E, Hutton J, Roderick P, Cullingworth J, Gathercole L, Smith MA. A systematic review of the staging performance of endoscopic ultrasound in gastro-oesophageal carcinoma. *Gut* 2001; **49**: 534-539 [PMID: 11559651 DOI: 10.1136/gut.49.4.534]

32 **Bruzzi JF**, Munden RF, Truong MT, Marom EM, Sabloff BS, Gladish GW, Iyer RB, Pan TS, Macapinlac HA, Erasmus JJ. PET/CT of esophageal cancer: its role in clinical management. *Radiographics* 2007; **27**: 1635-1652 [PMID: 18025508 DOI: 10.1148/rg.276065742]

33 **Schröder W**, Baldus SE, Mönig SP, Beckurts TK, Dienes HP, Hölscher AH. Lymph node staging of esophageal squamous cell carcinoma in patients with and without neoadjuvant radiochemotherapy: histomorphologic analysis. *World J Surg* 2002; **26**: 584-587 [PMID: 12098049 DOI: 10.1007/s00268-001-0271-5]

34 **Alper F**, Turkyilmaz A, Kurtcan S, Aydin Y, Onbas O, Acemoglu H, Eroglu A. Effectiveness of the STIR turbo spin-echo sequence MR imaging in evaluation of lymphadenopathy in esophageal cancer. *Eur J Radiol* 2011; **80**: 625-628 [PMID: 20800403 DOI: 10.1016/j.ejrad.2010.08.003]

35 **Sgourakis G**, Gockel I, Lyros O, Hansen T, Mildenberger P, Lang H. Detection of lymph node metastases in esophageal cancer. *Expert Rev Anticancer Ther* 2011; **11**: 601-612 [PMID: 21504265 DOI: 10.1586/era.10.150]

36 **Liu J**, Wang Z, Shao H, Qu D, Liu J, Yao L. Improving CT detection sensitivity for nodal metastases in oesophageal cancer with combination of smaller size and lymph node axial ratio. *Eur Radiol* 2018; **28**: 188-195 [PMID: 28677059 DOI: 10.1007/s00330-017-4935-4]

37 **Xu XQ**, Hu H, Su GY, Liu H, Hong XN, Shi HB, Wu FY. Utility of histogram analysis of ADC maps for differentiating orbital tumors. *Diagn Interv Radiol* 2016; **22**: 161-167 [PMID: 26829400 DOI: 10.5152/dir.2015.15202]

38 **Giganti F**, Salerno A, Ambrosi A, Chiari D, Orsenigo E, Esposito A, Albarello L, Mazza E, Staudacher C, Del Maschio A, De Cobelli F. Prognostic utility of diffusion-weighted MRI in oesophageal cancer: is apparent diffusion coefficient a potential marker of tumour aggressiveness? *Radiol Med* 2016; **121**: 173-180 [PMID: 26392393 DOI: 10.1007/s11547-015-0585-2]

39 **Shuto K**, Kono T, Shiratori T, Akutsu Y, Uesato M, Mori M, Narushima K, Imanishi S, Nabeya Y, Yanagawa N, Okazumi S, Koda K, Matsubara H. Diagnostic performance of diffusion-weighted magnetic resonance imaging in assessing lymph node metastasis of esophageal cancer compared with PET. *Esophagus* 2020; **17**: 239-249 [PMID: 31820208 DOI: 10.1007/s10388-019-00704-w]

40 **Sakurada A**, Takahara T, Kwee TC, Yamashita T, Nasu S, Horie T, Van Cauteren M, Imai Y. Diagnostic performance of diffusion-weighted magnetic resonance imaging in esophageal cancer. *Eur Radiol* 2009; **19**: 1461-1469 [PMID: 19172278 DOI: 10.1007/s00330-008-1291-4]

41 **Chen YL**, Li R, Chen TW, Ou J, Zhang XM, Chen F, Wu L, Jiang Y, Laws M, Shah K, Joseph B, Hu J. Whole-tumour histogram analysis of pharmacokinetic parameters from dynamic contrast-enhanced MRI in resectable oesophageal squamous cell carcinoma can predict T-stage and regional lymph node metastasis. *Eur J Radiol* 2019; **112**: 112-120 [PMID: 30777199 DOI: 10.1016/j.ejrad.2019.01.012]

42 **Sun NN**, Ge XL, Liu XS, Xu LL. Histogram analysis of DCE-MRI for chemoradiotherapy response evaluation in locally advanced esophageal squamous cell carcinoma. *Radiol Med* 2020; **125**: 165-176 [PMID: 31605354 DOI: 10.1007/s11547-019-01081-1]

43 **Azevedo RM**, de Campos RO, Ramalho M, Herédia V, Dale BM, Semelka RC. Free-breathing 3D T1-weighted gradient-echo sequence with radial data sampling in abdominal MRI: preliminary observations. *AJR Am J Roentgenol* 2011; **197**: 650-657 [PMID: 21862807 DOI: 10.2214/AJR.10.5881]

44 **Qu J**, Shen C, Qin J, Wang Z, Liu Z, Guo J, Zhang H, Gao P, Bei T, Wang Y, Liu H, Kamel IR, Tian J, Li H. The MR radiomic signature can predict preoperative lymph node metastasis in patients with esophageal cancer. *Eur Radiol* 2019; **29**: 906-914 [PMID: 30039220 DOI: 10.1007/s00330-018-5583-z]

45 **Tatsumi Y**, Tanigawa N, Nishimura H, Nomura E, Mabuchi H, Matsuki M, Narabayashi I. Preoperative diagnosis of lymph node metastases in gastric cancer by magnetic resonance imaging with ferumoxtran-10. *Gastric Cancer* 2006; **9**: 120-128 [PMID: 16767368 DOI: 10.1007/s10120-006-0365-8]

46 **Gatenby RA**, Grove O, Gillies RJ. Quantitative imaging in cancer evolution and ecology. *Radiology* 2013; **269**: 8-15 [PMID: 24062559 DOI: 10.1148/radiol.13122697]

47 **Zwanenburg A**, Vallières M, Abdalah MA, Aerts HJWL, Andrearczyk V, Apte A, Ashrafinia S, Bakas S, Beukinga RJ, Boellaard R, Bogowicz M, Boldrini L, Buvat I, Cook GJR, Davatzikos C, Depeursinge A, Desseroit MC, Dinapoli N, Dinh CV, Echegaray S, El Naqa I, Fedorov AY, Gatta R, Gillies RJ, Goh V, Götz M, Guckenberger M, Ha SM, Hatt M, Isensee F, Lambin P, Leger S, Leijenaar RTH, Lenkowicz J, Lippert F, Losnegård A, Maier-Hein KH, Morin O, Müller H, Napel S, Nioche C, Orlhac F, Pati S, Pfaehler EAG, Rahmim A, Rao AUK, Scherer J, Siddique MM, Sijtsema NM, Socarras Fernandez J, Spezi E, Steenbakkers RJHM, Tanadini-Lang S, Thorwarth D, Troost EGC, Upadhaya T, Valentini V, van Dijk LV, van Griethuysen J, van Velden FHP, Whybra P, Richter C, Löck S. The Image Biomarker Standardization Initiative: Standardized Quantitative Radiomics for High-Throughput Image-based Phenotyping. *Radiology* 2020; **295**: 328-338 [PMID: 32154773 DOI: 10.1148/radiol.2020191145]

48 **Li Y**, Beck M, Päßler T, Lili C, Hua W, Mai HD, Amthauer H, Biebl M, Thuss-Patience PC, Berger J, Stromberger C, Tinhofer I, Kruppa J, Budach V, Hofheinz F, Lin Q, Zschaeck S. A FDG-PET radiomics signature detects esophageal squamous cell carcinoma patients who do not benefit from chemoradiation. *Sci Rep* 2020; **10**: 17671 [PMID: 33077841 DOI: 10.1038/s41598-020-74701-w]

49 **Qiu Q**, Duan J, Deng H, Han Z, Gu J, Yue NJ, Yin Y. Development and Validation of a Radiomics Nomogram Model for Predicting Postoperative Recurrence in Patients With Esophageal Squamous Cell Cancer Who Achieved pCR After Neoadjuvant Chemoradiotherapy Followed by Surgery. *Front Oncol* 2020; **10**: 1398 [PMID: 32850451 DOI: 10.3389/fonc.2020.01398]

50 **Gu L**, Liu Y, Guo X, Tian Y, Ye H, Zhou S, Gao F. Computed tomography-based radiomic analysis for prediction of treatment response to salvage chemoradiotherapy for locoregional lymph node recurrence after curative esophagectomy. *J Appl Clin Med Phys* 2021; **22**: 71-79 [PMID: 34614265 DOI: 10.1002/acm2.13434]

51 **Tan X**, Ma Z, Yan L, Ye W, Liu Z, Liang C. Radiomics nomogram outperforms size criteria in discriminating lymph node metastasis in resectable esophageal squamous cell carcinoma. *Eur Radiol* 2019; **29**: 392-400 [PMID: 29922924 DOI: 10.1007/s00330-018-5581-1]

52 **Kim JY**, Seo HB, Park S, Moon JI, Lee JW, Lee NK, Lee SW, Bae YT. Early-stage invasive ductal carcinoma: Association of tumor apparent diffusion coefficient values with axillary lymph node metastasis. *Eur J Radiol* 2015; **84**: 2137-2143 [PMID: 26318821 DOI: 10.1016/j.ejrad.2015.08.009]

53 **Liu C**, Ding J, Spuhler K, Gao Y, Serrano Sosa M, Moriarty M, Hussain S, He X, Liang C, Huang C. Preoperative prediction of sentinel lymph node metastasis in breast cancer by radiomic signatures from dynamic contrast-enhanced MRI. *J Magn Reson Imaging* 2019; **49**: 131-140 [PMID: 30171822 DOI: 10.1002/jmri.26224]

54 **Shin J**, Seo N, Baek SE, Son NH, Lim JS, Kim NK, Koom WS, Kim S. MRI Radiomics Model Predicts Pathologic Complete Response of Rectal Cancer Following Chemoradiotherapy. *Radiology* 2022; **303**: 351-358 [PMID: 35133200 DOI: 10.1148/radiol.211986]

55 **Wang Q**, Xiang L, Liu J. Re: Feng G, Hong Y, Li L, *et al*. Anterior decompression and nonstructural bone grafting and posterior fixation for cervical facet dislocation with traumatic disc herniation. Spine (Phila Pa 1976). 2012;37:2082–8. *Spine (Phila Pa 1976)* 2013; **38**: 967 [PMID: 23660805 DOI: 10.1097/BRS.0b013e31828fc937]

56 **Santucci D**, Faiella E, Cordelli E, Sicilia R, de Felice C, Zobel BB, Iannello G, Soda P. 3T MRI-Radiomic Approach to Predict for Lymph Node Status in Breast Cancer Patients. *Cancers (Basel)* 2021; **13** [PMID: 34066451 DOI: 10.3390/cancers13092228]

57 **Han L**, Zhu Y, Liu Z, Yu T, He C, Jiang W, Kan Y, Dong D, Tian J, Luo Y. Radiomic nomogram for prediction of axillary lymph node metastasis in breast cancer. *Eur Radiol* 2019; **29**: 3820-3829 [PMID: 30701328 DOI: 10.1007/s00330-018-5981-2]

58 **Dong Y**, Feng Q, Yang W, Lu Z, Deng C, Zhang L, Lian Z, Liu J, Luo X, Pei S, Mo X, Huang W, Liang C, Zhang B, Zhang S. Preoperative prediction of sentinel lymph node metastasis in breast cancer based on radiomics of T2-weighted fat-suppression and diffusion-weighted MRI. *Eur Radiol* 2018; **28**: 582-591 [PMID: 28828635 DOI: 10.1007/s00330-017-5005-7]

59 **Liu J**, Sun D, Chen L, Fang Z, Song W, Guo D, Ni T, Liu C, Feng L, Xia Y, Zhang X, Li C. Radiomics Analysis of Dynamic Contrast-Enhanced Magnetic Resonance Imaging for the Prediction of Sentinel Lymph Node Metastasis in Breast Cancer. *Front Oncol* 2019; **9**: 980 [PMID: 31632912 DOI: 10.3389/fonc.2019.00980]

60 **Li M**, Zhang J, Dan Y, Yao Y, Dai W, Cai G, Yang G, Tong T. A clinical-radiomics nomogram for the preoperative prediction of lymph node metastasis in colorectal cancer. *J Transl Med* 2020; **18**: 46 [PMID: 32000813 DOI: 10.1186/s12967-020-02215-0]

World Journal of Radiology

Submit a Manuscript: https://www.f6publishing.com

World J Radiol 2023 July 28; 15(7): 226-233

DOI: 10.4329/wjr.v15.i7.226

ISSN 1949-8470 (online)

ORIGINAL ARTICLE

Basic Study

Can the change of vasomotor activity in irritable bowel syndrome patients be detected *via* color Doppler ultrasound?

Omer Kazci, Fahrettin Ege, Huseyin Aydemir, Saliha Kazci, Sonay Aydin

Specialty type: Radiology, nuclear medicine and medical imaging

Provenance and peer review: Invited article; Externally peer reviewed.

Peer-review model: Single blind

Peer-review report's scientific quality classification

Grade A (Excellent): 0
Grade B (Very good): B
Grade C (Good): C
Grade D (Fair): 0
Grade E (Poor): 0

P-Reviewer: Baeg MK, South Korea; Lv L, China

Received: April 25, 2023
Peer-review started: April 25, 2023
First decision: June 19, 2023
Revised: June 20, 2023
Accepted: July 7, 2023
Article in press: July 7, 2023
Published online: July 28, 2023

Omer Kazci, Department of Radiology, Ankara Training and Research Hospital, Ankara 06600, Turkey

Fahrettin Ege, Department of Neurology, VM Medicalpark Hospital, Ankara 06600, Turkey

Huseyin Aydemir, Sonay Aydin, Department of Radiology, Erzincan Binali Yildirim University Mengucek Gazi Training and Research Hospital, Erzincan 24400, Turkey

Saliha Kazci, Department of Epidemiology, Ankara University Faculty of Medicine, Ankara 06600, Turkey

Corresponding author: Sonay Aydin, MD, PhD, Academic Editor, Associate Professor, Department of Radiology, Erzincan Binali Yildirim University Mengucek Gazi Training and Research Hospital, Başbağlar, Hacı Ali Akın Cd. No. 32, 24100 Erzincan Merkez/Erzincan, Erzincan 24400, Turkey. sonay.aydin@erzincan.edu.tr

Abstract

BACKGROUND

Irritable bowel syndrome (IBS) is one of the most frequently referred conditions to the gastrointestinal outpatient clinic. The pathophysiology of IBS has not been determined with certainty. Visceral hypersensitivity is indicated as one of the pathophysiologies. The sympathetic nervous system is primarily in charge of controlling the arteries, and its effect is vasospasm in the medium and large arteries, resulting in decreased blood flow.

AIM

To demonstrate, using Doppler evaluation of the brachial artery, that sympathetic activity impairs vasomotor performance due to autonomic neuropathy, which we believe is associated with IBS.

METHODS

There were 58 participants in the study. The control group consisted of 29 healthy patients, while the remaining 29 patients had been diagnosed with IBS. Patients who met the Rome IV criteria and had IBS were included in the study. People with known polyneuropathy or non-IBS chronic conditions that can progress were excluded from the trial, as were those with essential hypertension, diabetes mellitus, cardiovascular disease, or peripheral arterial disease, and patients diagnosed with anxiety or depression. Those with moderate to severe carpal

tunnel syndrome or a median nerve lesion due to trauma were also excluded from the trial. A Doppler probe was used to measure the baseline diameter and flow rates of the brachial artery from 2 cm superior to the antecubital fossa. The Doppler probe remained stationary throughout the experiment, allowing for continuous measurements. Then, to activate the sympathetic fibers, an electrical stimulus for 5 s with an intensity of 10 mA and a frequency of 1 Hz was applied to the median nerve at the wrist level *via* the bipolar stimulus electrode. The artery diameter and flow rates were measured again immediately following the fifth stimulus.

RESULTS

In healthy persons with no history of chronic illness, there was a statistically significant decrease in flow rate after stimulation ($P < 0.001$). In addition, stimulation resulted in a statistically significant reduction in the diameter of the brachial artery ($P < 0.001$). Patients diagnosed with IBS had statistically significant vasodilation and an increase in flow rate.

CONCLUSION

Sympathetic stimulation causes a reduction in vascular diameter and blood flow, whereas it has the reverse effect on IBS patients. In investigating the involvement of autonomic neuropathy in the development of IBS, significant changes in brachial artery Doppler parameters were observed before and after stimulation of the median nerve with low-current sensory stimulation. This method is thought to be more user-friendly and comfortable than other methods described in the literature.

Key Words: Irritable bowel syndrome; Doppler ultrasonography; Brachial artery; Median nerve; Peripheral neuropathy; Autonomic neuropathy

©The Author(s) 2023. Published by Baishideng Publishing Group Inc. All rights reserved.

Core Tip: It has been noted that the autonomic activity of individuals who suffer from irritable bowel syndrome (IBS) differs from that of healthy people. Colored Doppler ultrasonography can be utilized as a noninvasive diagnostic tool that can be performed at any age and at any age, is comfortable for the patient, and does not require further patient compliance to show autonomic dysfunction in patients with IBS.

Citation: Kazci O, Ege F, Aydemir H, Kazci S, Aydin S. Can the change of vasomotor activity in irritable bowel syndrome patients be detected *via* color Doppler ultrasound? *World J Radiol* 2023; 15(7): 226-233
URL: https://www.wjgnet.com/1949-8470/full/v15/i7/226.htm
DOI: https://dx.doi.org/10.4329/wjr.v15.i7.226

INTRODUCTION

Irritable bowel syndrome (IBS) is a common chronic disease that causes constipation, diarrhea, or both, as well as abdominal pain or cramps, and can significantly reduce quality of life and work productivity. The diagnosis can be made with confidence if organic diseases are ruled out and characteristic symptoms are present. Environmental factors such as stress, food intolerance, enteric infections, and antibiotics, as well as patient-related factors such as variability in pain perception, variability in brain-gut interaction, dysbiosis, increased intestinal permeability, increased intestinal mucosal immune activation, and visceral hypersensitivity, are considered potential etiologies[1,2]. The autonomic nervous system modulates visceral sensitivity, and the central nervous system influences gastrointestinal secretion and activity *via* the enteric nervous system and autonomic pathways[3,4].

Some studies have found differences in autonomic activity between IBS subgroups. In studies with IBS and control groups, in patients with IBS, in the study of Karling *et al*[5], the heart rate variability was evaluated in the supine position with the head 70° upwards; an increase in sympathetic nervous system activation was observed, but no significant change in parasympathetic nervous system activation was found[5]. Adeyemi *et al*[6] investigated heart rate variability under orthostatic stress, deep inspiration, and resting states and discovered an increase in sympathetic nervous system activation and a decrease in parasympathetic nervous system activation[6]. Van Orshoven *et al*[7] measured blood pressure, heart rate, heart rate variability, and muscle sympathetic nerve activity before, during, and after a standard meal. As a result, parasympathetic nervous system activation decreased while sympathetic nervous system activation increased. There was no discernible difference[7]. Tanaka *et al*[8] investigated fingertip blood flow during, before, and after cold stress and discovered an increase in sympathetic nervous system activation[8]. Spaziani *et al*[9] used baroreceptor sensitivity to assess heart rate and blood pressure variability before, during, and after rectal distension and found a decrease in baroreceptor sensitivity and an increase in blood pressure[9]. In a study by Yildirim *et al*[10], neuropathy tests (standing, Valsalva, deep inspiration, isometric exercise, and cold application) were evaluated, and it was discovered that sympathetic activity increased while parasympathetic activity decreased[10].

Doppler ultrasonography is a type of ultrasonographic imaging that is used to determine the morphology of vascular structures as well as the direction, amount, and shape of blood flow in them. The laser Doppler method is widely used to assess sympathetic vasoconstrictor function. In the literature, it is emphasized that continuous wave Doppler ultrasound is a valid alternative approach to laser Doppler flowmetry in healthy volunteers[11], as well as that it can be used to detect the normal and abnormal functioning of the peripheral sympathetic nervous system[12]. The benefits of using color Doppler ultrasonography include the fact that it has no known side effects, does not contain radiation, can be used at any time and age including pregnancy, is easy to apply, does not require additional patient compliance, and is a noninvasive diagnostic method.

Almost all research into autonomic dysfunction in IBS is out of date. The goal of this study was to determine if autonomic dysfunction can be demonstrated in IBS patients using this new color Doppler ultrasonography (CDUS)-based method, as well as to reevaluate the presence of autonomic dysfunction in IBS, which has been described in previous studies.

MATERIALS AND METHODS

The participants signed a declaration form declaring that all participants and/or their legal guardians granted informed permission. The studies adhered to the most recent edition of the Declaration of Helsinki, and the Ankara City Hospital No. 2 Clinical Research Ethics Committee authorized the procedures.

Patients who met the Rome IV criteria and had IBS were included in the study. People with known polyneuropathy or non-IBS chronic conditions that can progress were excluded from the trial, as were those with essential hypertension, diabetes mellitus, cardiovascular disease, peripheral arterial disease, and patients diagnosed with anxiety or depression. Those with moderate to severe carpal tunnel syndrome or a median nerve lesion due to trauma were also excluded from the trial.

The technical models are associated with "studies on sensory nerve conduction." These non-invasive approaches are utilized in routine clinical electrophysiological examinations to detect peripheral neuropathies. Four hours before the experiment, nicotine, caffeine, alcohol, and exercise were restricted. Before measuring the subjects' blood pressure, heart rate, and body temperature, they rested for 10 min in a seated position with their forearms supinated. The study was carried out at temperatures between 22 C and 24 C. Individuals were encouraged to remain as motionless as possible and were verbally informed at each test stage following a 10-min rest period (for example, before the Doppler measurement was performed and before the electrical stimulation began). The diameter and flow rates of the right brachial artery were measured from 2 cm above the antecubital fossa using a 9 Hz linear probe of the LOQIC P9 USG Doppler device (GE Healthcare, Chicago, IL, United States) (Figure 1A). A radiologist with 8 years of experience in Doppler took these readings. The Doppler sensor remained stationary during the experiment, allowing for continuous readings. Then an electrical stimulation of 10 mA intensity and 1 Hz frequency was applied to the median nerve at the level of the wrist for 5 s using the bipolar stimulus electrode of the Neuropack S1 MEB-9400A EMG/EP system (Nihon Kohden Co., Tokyo, Japan), in the direction of the sensory fibers (orthodromically) (Figure 1B). Immediately after the sixth stimulation, artery diameter and flow rates were measured again. Some demonstrative examinations can be seen in Figures 2 and 3.

In addition to sociodemographic data such as age and sex, the diameters and flow rates of the brachial arteries were recorded as final data before and after electrical stimulation in the healthy control group and IBS patients.

Statistical analyses

The variables were investigated using analytical methods (Kolmogorov-Smirnov/Shapiro-Wilk's test) to determine whether they were normally distributed. Descriptive analyses were presented using frequencies and percentages for the categorical variables, mean ± SD for normally distributed variables, and median (25P-75P) for the non-normally distributed variables. The Student's *t*-test or Mann–Whitney U test was used for the comparison of continuous variables in independent groups, and the paired samples *t*-test was used in dependent groups. $P < 0.05$ was considered statistically significant. Statistical analyses were performed using SPSS (20.0; Armonk, NY, United States).

RESULTS

The study included 58 people, 29 of whom were diagnosed with IBS and 29 of whom were in the control group. Thirty (51.7%) of the 58 participants in the study were women, with a median age of 36 (min-max: 18-64). The female/male ratios (51.7%/48.3%) were the same in both groups ($P = 1.000$), and the median age of the IBS group [36 (min-max: 31-48)] was comparable to that of the control group [36 (min-max: 30-49)] ($P = 0.864$).

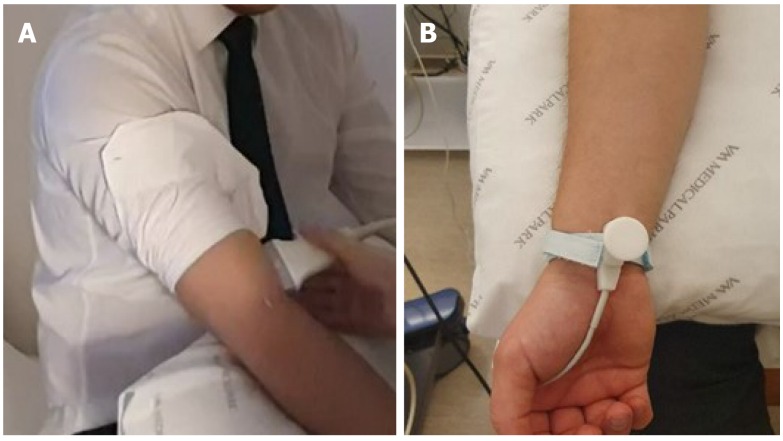
Table 1 shows brachial artery flow measurements before and after median nerve stimulation in IBS and control groups. While the median pre-stimulation flow rate in the IBS group was 60.2 mL/min, the post-stimulation flow rate was 78.1 mL/min. Mean flow rates before and after stimulation in the control group were 77.5 and 39.7 mL/min, respectively. The decrease in flow seen in the control group with median nerve stimulation could not be replicated in the IBS group.

Before median nerve stimulation, the mean brachial artery diameter in the IBS group was 3.44 mm, while it was 3.43 mm in the control group. While the diameters measured before median stimulation in the IBS and control groups were not statistically different ($P = 0.092$), the diameters measured after stimulation were statistically significant ($P < 0.001$). While median nerve stimulation caused a decrease in diameter in the control group, it caused an increase in the IBS group

Table 1 Brachial artery flow measurements before and after stimulation according to ırritable bowel syndrome and control groups

	Pre-stimulation flow rate (mL/min), mean ± SD	Post-stimulation flow rate (mL/min), mean ± SD	*P* value
IBS (n = 29)	60.2 ± 28.8	78.1 ± 42.5	0.002
Control (n = 29)	77.5 ± 36.5	39.7 ± 19.1	< 0.001
P value	0.05	< 0.001	

IBS: Irritable bowel syndrome.



DOI: 10.4329/wjr.v15.i7.226 **Copyright** ©The Author(s) 2023.

Figure 1 Positioning of the Doppler ultrasound probe and bipolar stimulus electrode. A: Positioning of the Doppler ultrasound probe, 2 cm above the antecubital fossa using a 9 Hz linear probe; B: Positioning of the bipolar stimulus electrode.

(Table 2).

Before the stimulus, there was no significant difference in the flow rate and artery diameters between the control and study groups (Tables 1 and 2).

Table 3 shows the changes in brachial artery flow and diameter measurements after median nerve stimulation. While there was a median increase in brachial artery output of 9.10 (min-max: 0.00-33.70) mL/min and a median increase in brachial artery diameter of 0.20 (min-max: 0.00-0.40) mm in the IBS group, the changes in flow and diameter were decreased in the control group. Median brachial artery output was 33.00 (min-max: 24.20-42.50) mL/min, and median brachial artery diameter was 0.50 (min-max: 0.40-0.90) mm in the control group. The participants in the IBS and control groups had a significant difference in brachial artery flow rates (P < 0.001) and diameters (P < 0.001) before and after median nerve stimulation. The change in flow and diameter after stimulation was statistically significant in both the IBS and control groups (P < 0.001 for both sexes).

By evaluating the changes in brachial artery flow (Table 4) and diameter (Table 5) according to the presence of chronic disease in the male and female groups, statistical significance was maintained for both sexes. In other words, the change in flow and diameter following stimulation was statistically significant (P < 0.001 for both sexes) in both the IBS and control groups.

DISCUSSION

The primary goal of our research was to use CDUS to detect autonomic dysfunction in IBS patients. In our study, there was an increase in brachial artery diameter and flow rate in IBS patients measured with Doppler ultrasonography before and after median nerve stimulation, whereas there was a decrease in the control group.

Changes in flow and diameter after median nerve stimulation were found to be statistically significant in both IBS patients and the control group, regardless of sex. This is the first study to compare autonomic dysfunction in IBS patients based on age and sex, and to use CDUS to assess sympathetic autonomic functions in IBS patients.

Previously, Eicke *et al*[11] used continuous-wave Doppler ultrasound and laser Doppler flowmetry to detect blood flow changes in the radial artery during sympathetic stimulation (deep breathing and coughing) and compared the two methods. They discovered a decrease in flow in the radial artery after sympathetic stimulation using both continuous-wave Doppler ultrasound and laser Doppler flowmetry. As a result, they determined that continuous-wave Doppler ultrasound can be used in blood flow measurements after sympathetic stimulation as laser Doppler flowmetry[11].

Several studies have reported differences in sympathetic and parasympathetic autonomic activity in IBS patients. The majority of these studies looked at both sympathetic and parasympathetic activity.

Table 2 Brachial artery diameter measurements before and after stimulation according to IBS and control groups

	Diameter before stimulus (mm), mean ± SD	Diameter after stimulus (mm), mean ± SD	*P* value
IBS	3.4 ± 0.5	3.7 ± 0.5	0.01
Control	3.4 ± 0.5	2.8 ± 0.6	< 0.001
P value	0.92	< 0.001	

IBS: Irritable bowel syndrome.

Table 3 Changes in brachial artery flow and diameter with stimulation

	Flow difference before and after stimulus (mL/min), median (25P-75P)	Diameter difference before and after stimulus (mm), median (25P-75P)
IBS	9.10 (0.00-33.70)	0.20 (0.00-0.40)
Control	-33.00 (-42.50 to -24.20)	-0.50 (-0.90 to -0.40)
P value	< 0.001	< 0.001

IBS: Irritable bowel syndrome; P: Percentile.

Table 4 The difference in flow rate between ırritable bowel syndrome and the control group before and after stimulation, according to gender

		The difference in flow rate between before and after a stimülation (mL/min), median (25P-75P)	*P* value
Female	IBS (*n* = 15)	11.90 (0.00-35.70)	< 0.001
	Control (*n* = 15)	-25.50 (-39.40 to -21.60)	
Male	IBS (*n* = 14)	6.55 (-0.60-25.50)	< 0.001
	Control (*n* = 14)	-39.75 (-58.90 to -32.00)	

IBS: Irritable bowel syndrome; P: Percentile.

Table 5 Diameter difference before and after stimulation between ırritable bowel syndrome and control groups according to sex

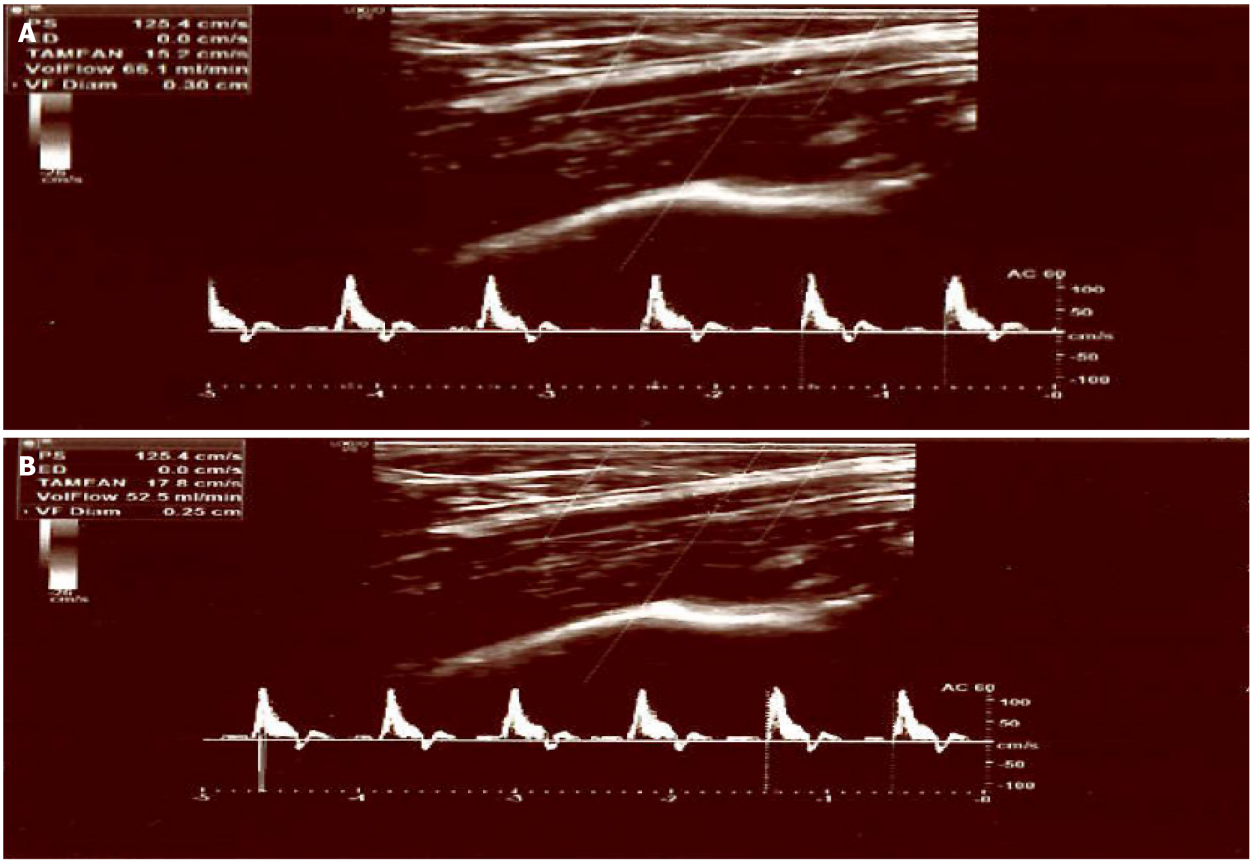
		The difference in diameter between before and after a stimulation (mm), median (25P-75P)	*P* value
Female	IBS (*n* = 15)	0.20 (0.00-0.40)	< 0.001
	Control (*n* = 15)	-0.50 (-1.00 to -0.30)	
Male	IBS (*n* = 14)	0.30 (0.00-0.50)	< 0.001
	Control (*n* = 14)	-0.60 (-0.90 to -0.40)	

IBS: Irritable bowel syndrome; P: Percentile.

Karling *et al*[5] investigated autonomic activity differences in their study, which included 18 patients with IBS and 36 control groups, by evaluating heart rate variability in the supine position with the head 70° upwards. When compared to healthy people, IBS patients showed an increase in sympathetic nervous system activation but no significant change in parasympathetic nervous system activation[5].

Adeyemi *et al*[6] investigated autonomic activity differences in 35 patients with IBS and 18 control groups in a study that included orthostatic stress, deep inspiration, and resting-state heart rate variability. In the study, IBS patients had an increase in sympathetic nervous system activation at rest and a decrease in parasympathetic nervous system activation under orthostatic stress and deep inspiration compared to healthy individuals[6].

Van Orshoven *et al*[7] investigated autonomic activity differences and muscle sympathetic nerve activity in 18 patients with IBS and 19 control groups by evaluating blood pressure, heart rate, and heart rate variability during, before, and



DOI: 10.4329/wjr.v15.i7.226 **Copyright** ©The Author(s) 2023.

Figure 2 Before and after electrical stimulation, the brachial artery flow/diameter parameters at control participant. A: Before electrical stimulation, the brachial artery volume flow rates/diameter values of a 45-year-old healthy control participant were measured to be 66.1 mL/min, 3 mm; B: The post-stimulation values of the same patient were 52.5 mL/min, 2.5 mm.

after consumption of a standard meal. When IBS patients were compared to healthy people, there was no decrease in parasympathetic nervous system activation, an increase in sympathetic nervous system activation, or a significant change in muscle sympathetic nerve activity[7].

The study group and control group were monitored, and autonomic neuropathy tests (standing posture, Valsalva, deep inspiration, isometric exercise, and cold application) were used in the study conducted by Yildirim *et al*[10], which included 50 patients with IBS and 49 control groups. The study discovered that when IBS patients were compared to healthy people, sympathetic activity increased while parasympathetic activity decreased[10].

There are also studies that only assessed sympathetic system dysfunction.

Tanaka *et al*[8] investigated autonomic activity differences in 59 patients with IBS and 40 control groups by measuring fingertip blood flow during, before, and after cold stress. In the study, IBS patients had higher levels of sympathetic nervous system activation than healthy people[8].

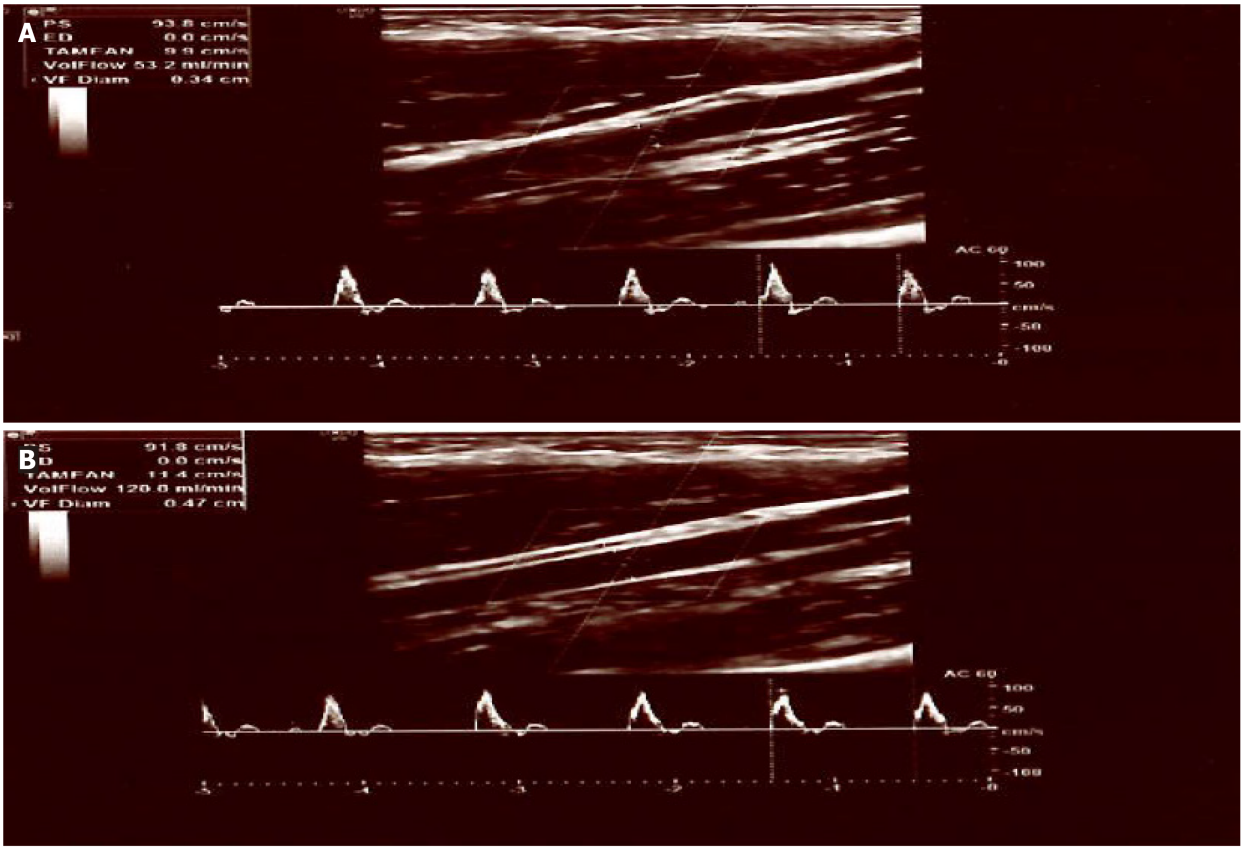
Spaziani *et al*[9] used baroreceptor sensitivity to assess heart rate and blood pressure variability before, during, and after rectal distension in 39 patients with IBS and 98 control groups. In the study, IBS patients were found to have lower baroreceptor sensitivity and a higher increase in blood pressure after rectal distension when compared to healthy individuals[9].

We have demonstrated, as in previous studies, that autonomic dysfunction exists in IBS patients. The method we used in our study is low-cost, simple, and comfortable for the patient, and it does not necessitate additional patient compliance. We described a novel method for demonstrating sympathetic autonomic dysfunction in IBS patients.

Our research had some limitations. The fact that CDUS measurements of brachial artery diameter and flow are user-dependent adds to the measurement's subjectivity. A single researcher measured everything in a single session. As a result, interobserver and intraobserver variability cannot be shown. Furthermore, the study's limitations include the relatively small study population and the fact that IBS subtypes were not evaluated separately. Another limitation of the current study was the lack of investigation into parasympathetic autonomic functions.

CONCLUSION

Our findings show that a new CDUS-based method can successfully detect sympathetic autonomic dysfunction in IBS patients. This method is thought to be more user-friendly and comfortable than other methods described in the literature.



DOI: 10.4329/wjr.v15.i7.226 **Copyright** ©The Author(s) 2023.

Figure 3 Before and after electrical stimulation, the brachial artery flow/diameter parameters in a patient diagnosed with irritable bowel syndrome. A: Before electrical stimulation, the brachial artery flow/diameter parameters of a 38-year-old female patient diagnosed with irritable bowel syndrome were assessed to be 53.2 mL/min, 3.2 mm; B: The post-stimulation values of the same patient were 120 mL/min, 4.7 mm.

ARTICLE HIGHLIGHTS

Research background

Irritable bowel syndrome (IBS) is one of the most common illnesses referred to the gastrointestinal outpatient clinic. The pathophysiology of IBS is not completely understood. One of the pathophysiologies is visceral hypersensitivity. The sympathetic nervous system is primarily responsible for managing the arteries, and its consequence is vasospasm in the medium and large arteries, which results in decreased blood flow.

Research motivation

Our impetus came from our study's adoption of a novel approach to assess changes in vasomotor activity in IBS patients.

Research objectives

We wanted to employ a different way to determine the change in vasomotor activity in persons with IBS in our study.

Research methods

The diameter and flow velocities of the brachial artery were determined using a probe with Doppler examination at the diameter of the antecubital fossa. To activate the sympathetic fibers, bipolar stimulation was applied to the median nerve at the wrist. Brachial artery diameter and flow velocities were assessed again immediately after the fifth stimulation.

Research results

In our study, a statistically significant decrease was found in brachial artery flow velocity and diameter after sympathetic stimulation in healthy individuals without a history of chronic disease. In patients with IBS, a statistically significant increase was found in brachial artery flow velocity and diameter after sympathetic stimulation.

Research conclusions

As a result, sympathetic activation reduces artery width and blood flow in healthy people. In people with IBS, it has the opposite effect. Detection of changes in brachial artery diameter and flow velocity by Doppler examination is thought to be more useful and comfortable than other methods described in the literature.

Research perspectives

It has been discovered that the autonomic activity of persons suffering from IBS differs from that of healthy people. Colored Doppler ultrasonography can be used as a noninvasive diagnostic method that can be conducted at any age, is comfortable for the patient, and does not require additional patient compliance in patients with IBS.

FOOTNOTES

Author contributions: Kazci O, Ege F, and Kazci S contributed equally to this work; Aydemir H wrote the manuscript; Aydin S, Kazci S, and Kazci O performed the experiments; Aydemir H and Ege F provided technical support and suggestions; Aydin S participated in writing and modifying the manuscript; Kazci O designed the study; All authors approved the final manuscript.

Institutional review board statement: The studies adhered to the most recent edition of the Declaration of Helsinki, and the Ankara City Hospital No. 2 Clinical Research Ethics Committee authorized the procedures, No. E2-22-1307.

Informed consent statement: The participants signed a declaration form declaring that all participants and/or their legal guardians granted informed permission.

Conflict-of-interest statement: All the authors report no relevant conflicts of interest for this article.

Data sharing statement: No additional data are available.

Open-Access: This article is an open-access article that was selected by an in-house editor and fully peer-reviewed by external reviewers. It is distributed in accordance with the Creative Commons Attribution NonCommercial (CC BY-NC 4.0) license, which permits others to distribute, remix, adapt, build upon this work non-commercially, and license their derivative works on different terms, provided the original work is properly cited and the use is non-commercial. See: https://creativecommons.org/Licenses/by-nc/4.0/

Country/Territory of origin: Turkey

ORCID number: Omer Kazci 0000-0003-0846-1074; Fahrettin Ege 0000-0001-9502-7510; Huseyin Aydemir 0000-0002-5698-1560; Saliha Kazci 0000-0002-8937-9939; Sonay Aydin 0000-0002-3812-6333.

S-Editor: Li L
L-Editor: Filipodia
P-Editor: Zhao S

REFERENCES

1 **Chey WD**, Kurlander J, Eswaran S. Irritable bowel syndrome: a clinical review. *JAMA* 2015; **313**: 949-958 [PMID: 25734736 DOI: 10.1001/jama.2015.0954]
2 **Camilleri M**. Diagnosis and Treatment of Irritable Bowel Syndrome: A Review. *JAMA* 2021; **325**: 865-877 [PMID: 33651094 DOI: 10.1001/jama.2020.22532]
3 **Iovino P**, Azpiroz F, Domingo E, Malagelada JR. The sympathetic nervous system modulates perception and reflex responses to gut distention in humans. *Gastroenterology* 1995; **108**: 680-686 [PMID: 7875470 DOI: 10.1016/0016-5085(95)90439-5]
4 **Gibbons CH**. Basics of autonomic nervous system function. *Handb Clin Neurol* 2019; **160**: 407-418 [PMID: 31277865 DOI: 10.1016/B978-0-444-64032-1.00027-8]
5 **Karling P**, Nyhlin H, Wiklund U, Sjöberg M, Olofsson BO, Bjerle P. Spectral analysis of heart rate variability in patients with irritable bowel syndrome. *Scand J Gastroenterol* 1998; **33**: 572-576 [PMID: 9669625 DOI: 10.1080/00365529850171800]
6 **Adeyemi EO**, Desai KD, Towsey M, Ghista D. Characterization of autonomic dysfunction in patients with irritable bowel syndrome by means of heart rate variability studies. *Am J Gastroenterol* 1999; **94**: 816-823 [PMID: 10086672 DOI: 10.1111/j.1572-0241.1999.00861.x]
7 **van Orshoven NP**, Andriesse GI, van Schelven LJ, Smout AJ, Akkermans LM, Oey PL. Subtle involvement of the parasympathetic nervous system in patients with irritable bowel syndrome. *Clin Auton Res* 2006; **16**: 33-39 [PMID: 16477493 DOI: 10.1007/s10286-006-0307-x]
8 **Tanaka T**, Manabe N, Hata J, Kusunoki H, Ishii M, Sato M, Kamada T, Shiotani A, Haruma K. Characterization of autonomic dysfunction in patients with irritable bowel syndrome using fingertip blood flow. *Neurogastroenterol Motil* 2008; **20**: 498-504 [PMID: 18248583 DOI: 10.1111/j.1365-2982.2007.01039.x]
9 **Spaziani R**, Bayati A, Redmond K, Bajaj H, Mazzadi S, Bienenstock J, Collins SM, Kamath MV. Vagal dysfunction in irritable bowel syndrome assessed by rectal distension and baroreceptor sensitivity. *Neurogastroenterol Motil* 2008; **20**: 336-342 [PMID: 18179607 DOI: 10.1111/j.1365-2982.2007.01042.x]
10 **Yildirim AE**, Korkmaz M, Altun R, Sandikçi SC, Ocal S, Selçuk H. Is there any association between irritable bowel syndrome subgroups and autonomous dysfunction. *Eur Rev Med Pharmacol Sci* 2016; **20**: 1315-1322 [PMID: 27097952]
11 **Eicke BM**, Milke K, Schlereth T, Birklein F. Comparison of continuous wave Doppler ultrasound of the radial artery and laser Doppler flowmetry of the fingertips with sympathetic stimulation. *J Neurol* 2004; **251**: 958-962 [PMID: 15316800 DOI: 10.1007/s00415-004-0471-7]
12 **Kazci O**, Ege F. Evaluation of Sympathetic Vasomotor Activity of the Brachial Arteries Using Doppler Ultrasound. *Med Sci Monit* 2023; **29**: e939352 [PMID: 36908037 DOI: 10.12659/MSM.939352]

World Journal of Radiology

Submit a Manuscript: https://www.f6publishing.com

World J Radiol 2023 July 28; 15(7): 234-240

DOI: 10.4329/wjr.v15.i7.234

ISSN 1949-8470 (online)

CASE REPORT

Invasive rhinocerebral mucormycosis: Imaging the temporal evolution of disease in post COVID-19 case with diabetes: A case report

Ramakrishna Narra, Shravya Rayapati

Specialty type: Radiology, nuclear medicine and medical imaging

Provenance and peer review: Unsolicited article; Externally peer reviewed.

Peer-review model: Single blind

Peer-review report's scientific quality classification

Grade A (Excellent): 0
Grade B (Very good): 0
Grade C (Good): C, C
Grade D (Fair): 0
Grade E (Poor): 0

P-Reviewer: Jain M, India; Yu YB, China

Received: April 3, 2023
Peer-review started: April 3, 2023
First decision: May 19, 2023
Revised: June 2, 2023
Accepted: June 26, 2023
Article in press: June 26, 2023
Published online: July 28, 2023

Ramakrishna Narra, Shravya Rayapati, Department of Radiodiagnosis, Katuri Medical College, Guntur, Andhra Pradesh 522018, India

Corresponding author: Ramakrishna Narra, DNB, MD, MNAMS, Academic Editor, Professor, Department of Radiodiagnosis, Katuri Medical College, Flat No. 30, 1/2 Chandramoulinagar, Guntur, Andhra Pradesh 522018, India. narra.ramki29@gmail.com

Abstract

BACKGROUND

Rhinocerebral mucormycosis (RCM) is a rare, fatal, invasive fungal infection infecting mainly patients with immunocompromised conditions, such as diabetes mellitus, hematologic malignancies, and organ transplantations. Coronavirus disease 2019 (COVID-19) disease in these patients further weakens the immune system due to several factors, including hypoxia, corticosteroid usage (further increasing hyperglycemic status), mechanical ventilation, increased serum ferritin levels, endothelitis due to free radicals, and glucose receptor protein upregulation. Timely diagnosis, judicious treatment decisions, and diabetes control with proper treatment guidelines in patients with coexisting COVID-19 disease can reduce complication rates and improve survival.

CASE SUMMARY

A 75-year-old male patient with diabetes and hypertension diagnosed with COVID-19 presented to the emergency department. Laboratory examinations revealed elevated blood glucose levels, as well as ketone bodies in the urine. He was treated with oxygen and steroids, as well as insulin to correct blood glucose levels. He complained of a headache 10 d later, and imaging demonstrated mucosal thickening in bilateral sphenoidal, ethmoidal, and maxillary sinuses with hyperdense foci in the right maxillary sinus but without central nervous system involvement. Surgical debridement was performed, and a histopathological study revealed fungi hyphae. Systemic antifungals (amphotericin b and posaconazole) were administered. Subsequently, on 15th day he developed right lower limb weakness and left lateral rectus palsy. There was slow but steady progress, and he was discharged. However, he presented to emergency department 1mo later with altered sensorium and poor control of diabetes resulted in an intracranial spread of mucormycosis, which ultimately led to the patient's poor prognosis and slow recovery.

CONCLUSION
Prompt early diagnosis, judicious treatment decisions, and diabetes control with proper treatment guidelines are necessary in patients with COVID-19 associated invasive RCM to reduce complication rates and improve patient survival.

Key Words: Rhinocerebral mucormycosis; COVID-19 disease; Corticosteroids; Diabetes mellitus; Diabetic ketoacidosis; Case report

©The Author(s) 2023. Published by Baishideng Publishing Group Inc. All rights reserved.

Core Tip: Coronavirus disease 2019 associated invasive rhinocerebral mucormycosis is potentially life threatening in patients with uncontrolled diabetes mellitus and diabetic ketoacidosis. Early diagnosis and imaging the disease progression with proper treatment guidelines are essential for reducing the morbidity and mortality in these patients.

Citation: Narra R, Rayapati S. Invasive rhinocerebral mucormycosis: Imaging the temporal evolution of disease in post COVID-19 case with diabetes: A case report. *World J Radiol* 2023; 15(7): 234-240
URL: https://www.wjgnet.com/1949-8470/full/v15/i7/234.htm
DOI: https://dx.doi.org/10.4329/wjr.v15.i7.234

INTRODUCTION

Mucormycosis is a rare opportunistic and potentially lethal infection caused by members of the family mucoraceae, order mucorales, and class zygomycetes[1]. It is caused by fungi, which may be found in decaying food, soil, or other organic matter, such as animal excreta.

Rhinocerebral mucormycosis (RCM) is the most common type, accounting for 30%-50% of cases. Its extension to the orbit and brain is usual, making it a potentially life-threatening disease. Immunocompromised patients are especially susceptible, and timely diagnosis and judicious intervention are of utmost importance for the successful management and prevention of intracranial extension. Patients with coronavirus disease 2019 (COVID-19) with uncontrolled diabetes and diabetic ketoacidosis on corticosteroid treatment are potentially susceptible to invasive RCM and need aggressive treatment to prevent further morbidity and mortality. Other reported immunocompromised conditions include blood dyscrasias, malnutrition, neutropenia, iron overload, organ transplantation, and immunosuppressive therapy[2]. Microscopic demonstration of fungal hyphae-mucormycosis with high blood glucose levels and serum ferritin and ketone levels should alert the clinician for appropriate care and aggressive treatment[3].

CASE PRESENTATION

Chief complaints

A 75-year-old male patient diagnosed with positive reverse transcription polymerase chain reaction for COVID-19 infection was admitted to the emergency department.

History of present illness

A 75-year-old male patient diagnosed with positive reverse transcription polymerase chain reaction for COVID-19 infection was admitted to the emergency department with fever, sore throat and generalized weakness for 3 d.

On 10th day he complained of frontal headache. On 15th day he complained of persistent frontal headache and left orbital pain, and a dragging sensation in the right foot. After 1 mo he progressed into altered sensorium and seizures and was admitted to emergency department.

History of past illness

He is known diabetic and hypertensive for 10 years.

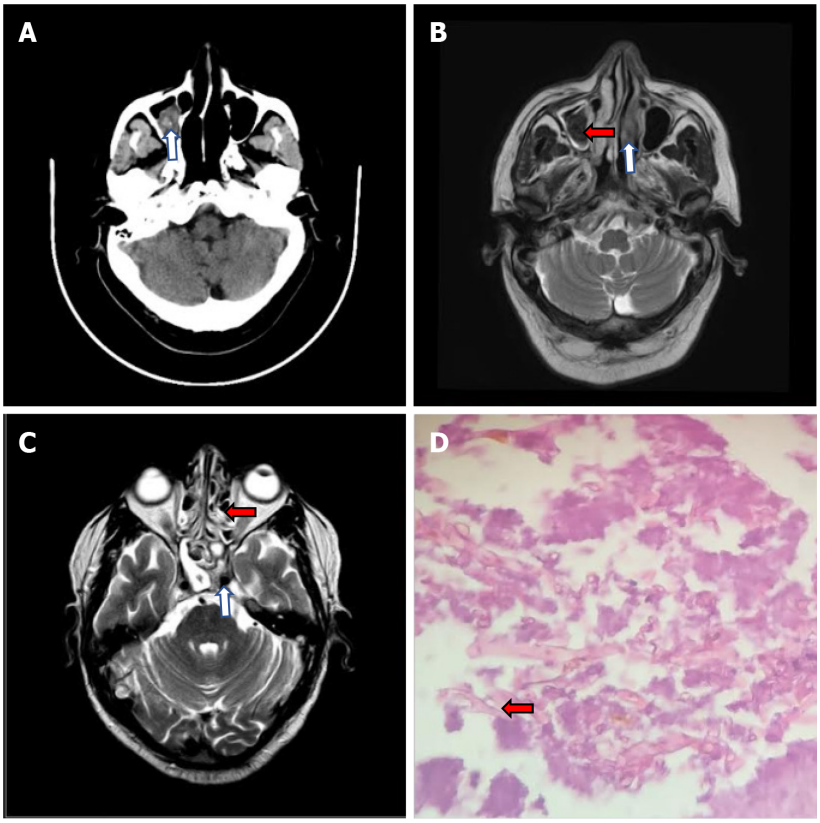
Personal and family history

No significant personal and family history.

Physical examination

On examination at admission temperature was 102.5 ^{0}F, pulse rate: 124/min, blood pressure (BP): 150/100 mmHg.

On 10th day temperature was 101.5 ^{0}F, pulse rate: 88/min, BP: 150/90 mmHg. On 15th day temperature was 99 ^{0}F, pulse rate: 108/min, BP: 130/90 mmHg, neurological examination revealed reduced power in the right lower limb (2/5) and



DOI: 10.4329/wjr.v15.i7.234 **Copyright** ©The Author(s) 2023.

Figure 1 Images of patient with post COVID-19 mucormycosis. A: Axial computed tomography image of brain, 10 d post admission demonstrating hyperdensity in right maxillary sinus (white arrow); B: Axial T2 weighted (T2W) and magnetic resonance imaging (MRI) image of brain demonstrating mucosal thickening with hypointensity within right maxillary sinus (red arrow) and hypointense left inferior turbinate (white arrow); C: Axial T2W and MRI image of brain demonstrating bilateral sphenoid and ethmoidal sinusitis (red arrow) with normal flow void within left internal carotid artery (white arrow); D: Histopathology slide demonstrating broad, aseptate ,branched hyphae of mucormycosis (red arrow).

left lateral rectus palsy. On 30th day temperature was 102 ^{0}F, pulse rate: 115/min, BP: 160/100 mmHg, glasgow coma scale was poor (8/15).

Laboratory examinations

On admission: Elevated C-reactive protein (188 mg/dL), serum ferritin (513 ng/mL), blood glucose (400 mg/dL), and glycosylated hemoglobin (16%) levels and the presence of ketone bodies (+++) in the urine. Other parameters were within the normal limits: Hemoglobin of 11 gm%; red blood cells of 5.2 × 10^{6}/μL; total leukocyte count of 9000/cumm; differential leukocyte count, including neutrophils of 75%, lymphocytes of 22%, eosinophils of 02%, and macrophages of 01%; platelets of 2.4 Lakhs/cumm; serum potassium of 3.8 mmol/L; serum sodium of 138 mmol/L; blood urea of 12 mg/dL; and serum creatinine of 0.8 mg/dL.

On 10th day C-reactive protein (106 mg/dL), serum ferritin (498 ng/mL), blood glucose (260 mg/dL), and the presence of ketone bodies (+) in the urine.

On 15th day C-reactive protein (108 mg/dL), serum ferritin (450 ng/mL), blood glucose (250 mg/dL), and the presence of ketone bodies (+) in the urine.

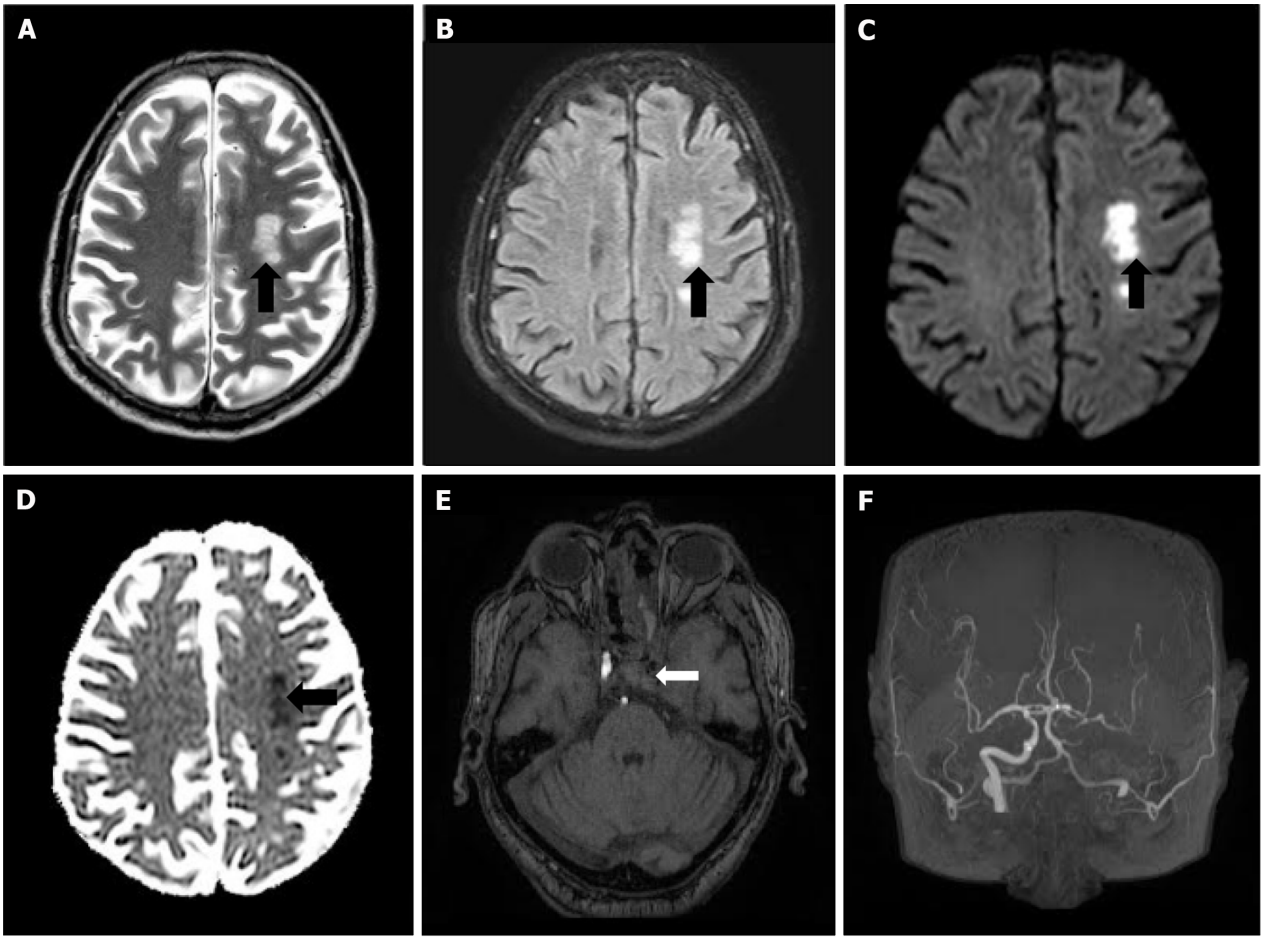
After 1 mo C-reactive protein (198 mg/dL), serum ferritin (415 ng/mL), blood glucose (450 mg/dL), and the presence of ketone bodies (+++) in the urine.

Rest of the routine laboratory investigations were within normal limits.

Imaging examinations

On 10th day post admission computed tomography (CT) and magnetic resonance imaging (MRI) demonstrated mucosal thickening in the bilateral ethmoidal, sphenoidal and maxillary sinuses with hyperdensity (CT) and hypointensity (MRI) in the right maxillary sinus suggestive of fungal sinusitis (Figure 1A-C). The patient underwent functional endoscopic sinus surgery under general anesthesia, and a biopsy was performed for histopathological examination which revealed fungus of mucorales species (Figure 1D).

On 15th day post admission MRI scan of the brain, paranasal sinuses and the orbits with IV contrast was advised which demonstrated acute infarcts in the watershed territories of left anterior cerebral artery, middle cerebral artery and posterior cerebral arteries (Figure 2A-D) with filling defects in the left cavernous sinus suggestive of cavernous sinus thrombosis. In addition magnetic resonance angiogram demonstrated complete occlusion of left internal carotid artery (ICA) (Figure 2E and F).



DOI: 10.4329/wjr.v15.i7.234 **Copyright** ©The Author(s) 2023.

Figure 2 Images of patient with post COVID-19 mucormycosis. A and B: Axial T2-weighted and axial fluid attenuated inversion recovery images of brain 15 d post admission demonstrating acute infarcts (black arrows); C and D: In left centrum semiovale with diffusion restriction on diffusion-weighted imaging and reversal on apparent diffusion coefficient represented by black arrows; E and F: Magnetic resonance angiography (MRA) images of Brain demonstrating loss of flow signal is noted in left internal carotid artery (white arrow) on source images and absent left internal carotid artery on maximum intensity projection MRA.

After 1 mo MRI of brain with IV contrast demonstrated an hyperintense lesion on T2 Weighted and fluid attenuated inversion recovery sequence with surrounding edema and peripheral rim enhancement of approximately 21 mm × 12 mm in the right basi-frontal lobe with restriction on diffusion weighted imaging and reduced apparent diffusion coefficient suggestive of fungal abscess (Figure 3). CT and MRI of brain demonstrated destruction of cribriform plate, clivus, sphenoid sinus and magnetic resonance spectroscopy demonstrated elevated lactate peak within the lesion (Figure 4).

FINAL DIAGNOSIS

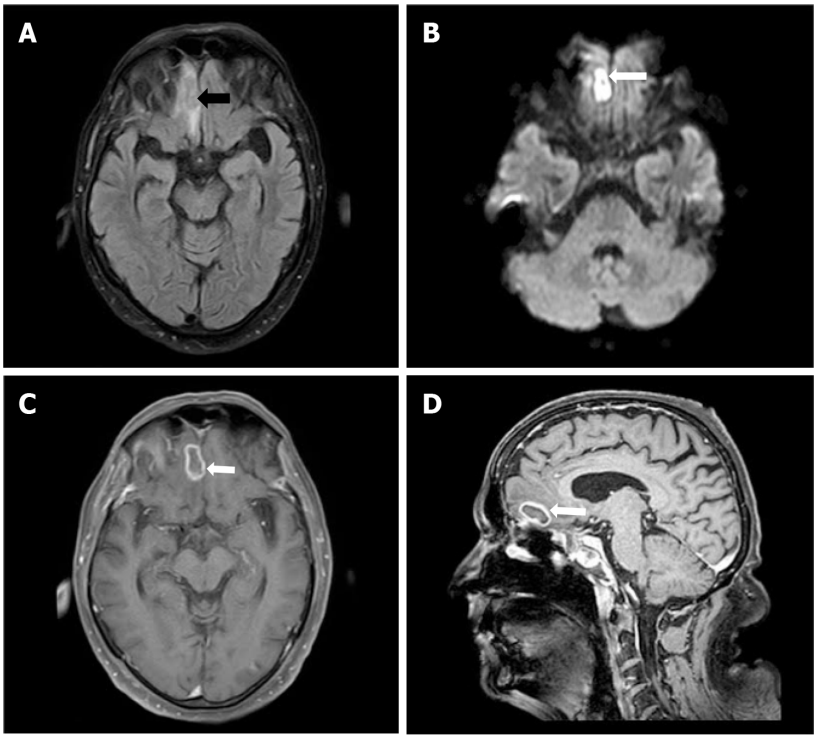
Post COVID-19 associated invasive RCM.

TREATMENT

On admission: Patient was given mechanical ventilation and oxygen support, anti-pyretics, azithromycin, remedesivir (200 mg loading dose) followed by 100 mg daily for 5 d, and intravenous dexamethasone 10 mg intravenous for 10 d. The patient was administered insulin 0.1 U/kg as an intravenous bolus dose followed by infusion of 0.1 U/kg/h for a targeted glucose level of 200 mg/dL.

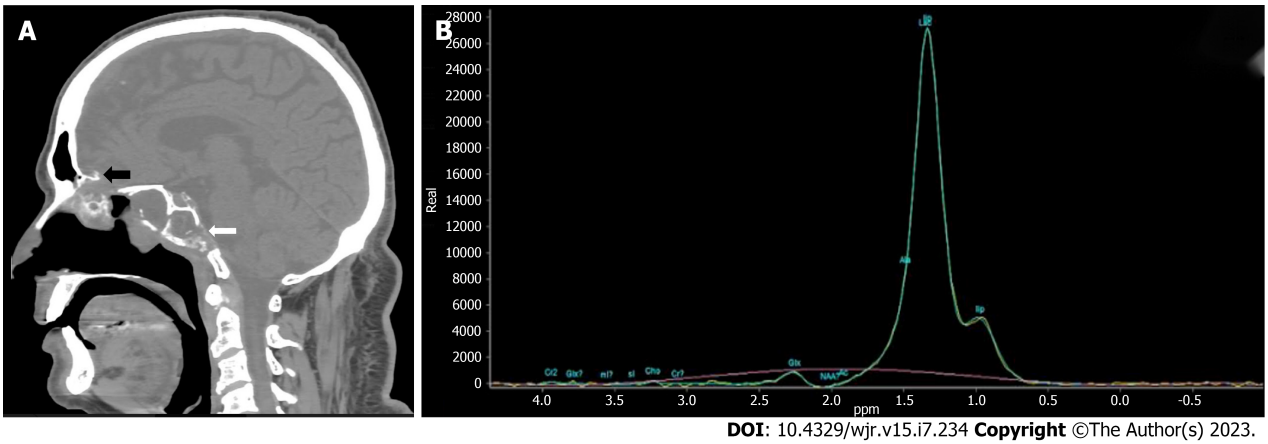
On 10th day: The patient was advised and started with amphotericin b injection at 3 mg/kg/day for 14 d and oral posaconazole at 300 mg twice daily for 6 wk. The renal profile was checked every 3 d for nephrotoxicity from amphotericin b. Poor patient tolerance was noted and steroids discontinued.

On 15th day: The patient was administered aspirin 150 mg, clopitab 75 mg, and atorvastatin 40 mg. After stabilization and rehabilitation patient was counselled for diabetes control and discharged. He was maintained on human mixtard insulin thrice daily.



DOI: 10.4329/wjr.v15.i7.234 **Copyright** ©The Author(s) 2023.

Figure 3 Images of patient with post COVID-19 mucormycosis. A and B: Magnetic resonance imaging of brain after one month demonstrating isointense area with surrounding edema (black arrow) on axial fluid attenuated inversion recovery with restriction on diffusion-weighted imaging (white arrow); C and D: Post-contrast axial and sagittal T1 weighted images demonstrating rim enhancement of the lesion-s/ofungal abscess (white arrow).



DOI: 10.4329/wjr.v15.i7.234 **Copyright** ©The Author(s) 2023.

Figure 4 Images of patient with post COVID-19 mucormycosis. A: Computerized tomography of brain after one month mid sagittal reformatted section in bone window demonstrating destruction of cribriform plate (black arrow), sphenoid sinus and clivus (white arrow); B: Magnetic resonance spectroscopy with a voxel placed in right frontal lobe fungal abscess demonstrating lactate peak at 1.33 ppm.

After 1mo: The patient was treated with antiepileptics, and insulin and anti-fungal treatment was continued with supportive treatment.

OUTCOME AND FOLLOW-UP

After stabilization there was very slow recovery of the patient with residual neurological deficits and increased morbidity.

DISCUSSION

RCM is a rare invasive infection caused by fungi of the class phycomycetes commonly involving the nasal and sinus mucosae of immunocompromised patients and spreads rapidly to the orbit and brain. Diabetes mellitus (especially with ketoacidosis) and hematologic malignancies with neutropenia are the principal predisposing factors. High blood glucose levels and ketoacidosis in diabetes enhance fungal growth. The altered number or function of neutrophils increases the risk of infection because they are responsible for defense against fungi[3]. COVID-19 disease in these patients further weakens the immune system due to several factors, including hypoxia, corticosteroid usage (further increasing hyperglycemic status), mechanical ventilation, increased serum ferritin levels, endothelitis due to free radicals, and glucose receptor protein upregulation, increased iron reduces the function of gamma interferon which prevents phagocytic function on fungus[4]. Other identified risk factors are steroid therapy, organ transplantation, chemotherapy, and chronic kidney disease[5-7]. Extensive angioinvasion is considered the main cause of vascular thrombosis and tissue necrosis. Vascular involvement is a more common cause of increased morbidity and mortality, resulting in ICA thrombosis causing brain ischemic infarcts and infiltrating the cavernous sinus and orbital apex, causing facial cellulitis and vision loss. Histopathological examination of the thrombus demonstrated the fungus in some cases of ICA thrombosis following thrombectomy[8]. Mucormycosis may spread intracranially from the paranasal sinuses along the cribriform plate into the anterior cranial fossa, leading to a cerebral abscess.

Brain and paranasal sinus MRI provides a better evaluation of intracranial and soft tissue involvement, skull base invasion, perineural spread, and vascular obstruction. MRI contrast study demonstrates orbital soft tissue invasion, skull base infiltration, perineural spread, intracranial complications, and vascular obstruction, involving the ICA[9,10].

At present, antifungal therapy and aggressive surgical debridement are used in active mucormycosis treatment. The overall mortality of patients with mucormycosis remains high and approaches 40% in patients with diabetes with invasive mucormycosis despite antifungal therapy and surgical debridement. Prophylactic treatment with antiplatelet drugs, including aspirin, clopitab, and statins, should also be initiated in aggressive cases where complications, such as ICA occlusion, thrombosis, and angioinvasion may develop.

Our case report explains the disease progression from infection initially involving the paranasal sinuses to subsequent brain involvement. Mucosal thickening of the bilateral sphenoidal, ethmoidal, and maxillary sinuses was initially noted on imaging in the present report, with no central nervous system involvement with a normal ICA and without any bony involvement. However, ICA thrombosis causing ischemic infarcts was noted on subsequent imaging, probably due to poor patient compliance to antifungal drugs causing increased fungal growth. The patient was stabilized and treated with aspirin 150 mg, clopitab 75 mg, and atorvastatin 40 mg and rehabilitation. However, the patient was readmitted to the hospital with seizures and altered consciousness after a few days, and subsequent imaging revealed the spread of infection through the destruction of the cribriform plate and clivus to the brain causing a cerebral abscess. This was due to poor diabetes control and diabetic ketoacidosis after patient discharge, which caused the intracranial spread of the disease.

CONCLUSION

Invasive RCM is a rare but fatal fungal infection that primarily affects immunocompromised patients. Early diagnosis and prompt management with aggressive surgical intervention and antifungal therapy are crucial for improving patient outcomes. This case report highlights the importance of close monitoring and imaging in patients with post-COVID-19 treated with oxygen therapy and corticosteroids, as well as diabetes, and ensuring optimal glycemic control to prevent rapid disease progression and intracranial spread. Regular monitoring of serum ferritin levels, lymphocyte count and further strengthening the immune system with regular follow-up imaging is essential to monitor disease progression and identify potential complications.

ACKNOWLEDGEMENTS

Dr Rama Krishna Gorantla for his expert advice and guidance.

FOOTNOTES

Author contributions: Narra R reviewed the manuscript and designed the study; Rayapati S prepared the manuscript, and collected materials for the study.

Informed consent statement: Informed written consent was obtained from the patient and his relatives for the publication of this report and any accompanying images.

Conflict-of-interest statement: All the authors report no relevant conflicts of interest for this article.

CARE Checklist (2016) statement: The authors have read the CARE Checklist (2016) and the manuscript was prepared and revised according to the CARE Checklist (2016).

Open-Access: This article is an open-access article that was selected by an in-house editor and fully peer-reviewed by external reviewers. It is distributed in accordance with the Creative Commons Attribution NonCommercial (CC BY-NC 4.0) license, which permits others to distribute, remix, adapt, build upon this work non-commercially, and license their derivative works on different terms, provided the original work is properly cited and the use is non-commercial. See: https://creativecommons.org/Licenses/by-nc/4.0/

Country/Territory of origin: Mayotte

ORCID number: Ramakrishna Narra 0000-0002-1850-6136.

S-Editor: Qu XL
L-Editor: A
P-Editor: Zhao S

REFERENCES

1 **Kim JG**, Park HJ, Park JH, Baek J, Kim HJ, Cha IH, Nam W. Importance of immediate surgical intervention and antifungal treatment for rhinocerebral mucormycosis: a case report. *J Korean Assoc Oral Maxillofac Surg* 2013; **39**: 246-250 [PMID: 24471053 DOI: 10.5125/jkaoms.2013.39.5.246]
2 **Mallis A**, Mastronikolis SN, Naxakis SS, Papadas AT. Rhinocerebral mucormycosis: an update. *Eur Rev Med Pharmacol Sci* 2010; **14**: 987-992 [PMID: 21284348]
3 **Dilek A**, Ozaras R, Ozkaya S, Sunbul M, Sen EI, Leblebicioglu H. COVID-19-associated mucormycosis: Case report and systematic review. *Travel Med Infect Dis* 2021; **44**: 102148 [PMID: 34454090 DOI: 10.1016/j.tmaid.2021.102148]
4 **Aggarwal SK**, Kaur U, Talda D, Pandey A, Jaiswal S, Kanakan A, Singh A, Chakrabarti SS. Case Report: Rhino-orbital Mucormycosis Related to COVID-19: A Case Series Exploring Risk Factors. *Am J Trop Med Hyg* 2021; **106**: 566-570 [PMID: 34902834 DOI: 10.4269/ajtmh.21-0777]
5 **Spellberg B**, Edwards J Jr, Ibrahim A. Novel perspectives on mucormycosis: pathophysiology, presentation, and management. *Clin Microbiol Rev* 2005; **18**: 556-569 [PMID: 16020690 DOI: 10.1128/CMR.18.3.556-569.2005]
6 **Bhansali A**, Bhadada S, Sharma A, Suresh V, Gupta A, Singh P, Chakarbarti A, Dash RJ. Presentation and outcome of rhino-orbital-cerebral mucormycosis in patients with diabetes. *Postgrad Med J* 2004; **80**: 670-674 [PMID: 15537854 DOI: 10.1136/pgmj.2003.016030]
7 **Onyango JF**, Kayima JK, Owen WO. Rhinocerebral mucormycosis: case report. *East Afr Med J* 2002; **79**: 390-393 [PMID: 12638836 DOI: 10.4314/eamj.v79i7.8845]
8 **Kashyap S**, Bernstein J, Ghanchi H, Bowen I, Cortez V. Diagnosis of Rhinocerebral Mucormycosis by Treatment of Cavernous Right Internal Carotid Artery Occlusion With Mechanical Thrombectomy: Special Case Presentation and Literature Review. *Front Neurol* 2019; **10**: 264 [PMID: 30972005 DOI: 10.3389/fneur.2019.00264]
9 **McDevitt GR Jr**, Brantley MJ, Cawthon MA. Rhinocerebral mucormycosis: a case report with magnetic resonance imaging findings. *Clin Imaging* 1989; **13**: 317-320 [PMID: 2598114 DOI: 10.1016/0899-7071(89)90065-x]
10 **Parsi K**, Itgampalli RK, Vittal R, Kumar A. Perineural spread of rhino-orbitocerebral mucormycosis caused by Apophysomyces elegans. *Ann Indian Acad Neurol* 2013; **16**: 414-417 [PMID: 24101833 DOI: 10.4103/0972-2327.116921]



Published by **Baishideng Publishing Group Inc**
7041 Koll Center Parkway, Suite 160, Pleasanton, CA 94566, USA
Telephone: +1-925-3991568
E-mail: bpgoffice@wjgnet.com
Help Desk: https://www.f6publishing.com/helpdesk
https://www.wjgnet.com



© 2023 Baishideng Publishing Group Inc. All rights reserved.

ISSN 1949-8470 (online)

World Journal of *Radiology*

World J Radiol 2023 August 28; 15(8): 241-255



Published by Baishideng Publishing Group Inc

WJR

World Journal of Radiology

Contents

Monthly Volume 15 Number 8 August 28, 2023

ORIGINAL ARTICLE

Retrospective Study

241 Appearance of aseptic vascular grafts after endovascular aortic repair on [(18)F]fluorodeoxyglucose positron emission tomography/computed tomography

Bennett P, Tomas MB, Koch CF, Nichols KJ, Palestro CJ

CASE REPORT

250 Rare portal hypertension caused by Abernethy malformation (Type IIC): A case report

Yao X, Liu Y, Yu LD, Qin JP

World Journal of Radiology

Monthly Volume 15 Number 8 August 28, 2023

Contents

ABOUT COVER

Editorial Board Member of *World Journal of Radiology*, Francesco Lassandro, MD, Doctor, Medical Assistant, Radiology Section, Department of Services, Azienda Ospedali dei Colli, Monaldi Hospital, Naples 80131, Italy. f.lassandro@gmail.com

AIMS AND SCOPE

The primary aim of *World Journal of Radiology* (*WJR*, *World J Radiol*) is to provide scholars and readers from various fields of radiology with a platform to publish high-quality basic and clinical research articles and communicate their research findings online.

WJR mainly publishes articles reporting research results and findings obtained in the field of radiology and covering a wide range of topics including state of the art information on cardiopulmonary imaging, gastrointestinal imaging, genitourinary imaging, musculoskeletal imaging, neuroradiology/head and neck imaging, nuclear medicine and molecular imaging, pediatric imaging, vascular and interventional radiology, and women's imaging.

INDEXING/ABSTRACTING

The *WJR* is now abstracted and indexed in PubMed, PubMed Central, Emerging Sources Citation Index (Web of Science), Reference Citation Analysis, China National Knowledge Infrastructure, China Science and Technology Journal Database, and Superstar Journals Database. The 2023 Edition of Journal Citation Reports® cites the 2022 impact factor (IF) for *WJR* as 2.5; IF without journal self cites: 2.3; 5-year IF: 2.5; Journal Citation Indicator: 0.54.

RESPONSIBLE EDITORS FOR THIS ISSUE

Production Editor: *Si Zhao*; **Production Department Director:** *Xu Guo*; **Editorial Office Director:** *Jia-Ping Yan*.

NAME OF JOURNAL
World Journal of Radiology

ISSN
ISSN 1949-8470 (online)

LAUNCH DATE
January 31, 2009

FREQUENCY
Monthly

EDITORS-IN-CHIEF
Thomas J Vogl

EDITORIAL BOARD MEMBERS
https://www.wjgnet.com/1949-8470/editorialboard.htm

PUBLICATION DATE
August 28, 2023

COPYRIGHT
© 2023 Baishideng Publishing Group Inc

INSTRUCTIONS TO AUTHORS
https://www.wjgnet.com/bpg/gerinfo/204

GUIDELINES FOR ETHICS DOCUMENTS
https://www.wjgnet.com/bpg/GerInfo/287

GUIDELINES FOR NON-NATIVE SPEAKERS OF ENGLISH
https://www.wjgnet.com/bpg/gerinfo/240

PUBLICATION ETHICS
https://www.wjgnet.com/bpg/GerInfo/288

PUBLICATION MISCONDUCT
https://www.wjgnet.com/bpg/gerinfo/208

ARTICLE PROCESSING CHARGE
https://www.wjgnet.com/bpg/gerinfo/242

STEPS FOR SUBMITTING MANUSCRIPTS
https://www.wjgnet.com/bpg/GerInfo/239

ONLINE SUBMISSION
https://www.f6publishing.com

© 2023 Baishideng Publishing Group Inc. All rights reserved. 7041 Koll Center Parkway, Suite 160, Pleasanton, CA 94566, USA
E-mail: bpgoffice@wjgnet.com https://www.wjgnet.com

World Journal of Radiology

Submit a Manuscript: https://www.f6publishing.com

World J Radiol 2023 August 28; 15(8): 241-249

DOI: 10.4329/wjr.v15.i8.241

ISSN 1949-8470 (online)

ORIGINAL ARTICLE

Retrospective Study

Appearance of aseptic vascular grafts after endovascular aortic repair on [(18)F]fluorodeoxyglucose positron emission tomography/computed tomography

Paige Bennett, Maria Bernadette Tomas, Christopher F Koch, Kenneth J Nichols, Christopher J Palestro

Specialty type: Radiology, nuclear medicine and medical imaging

Provenance and peer review: Invited article; Externally peer reviewed.

Peer-review model: Single blind

Peer-review report's scientific quality classification

Grade A (Excellent): 0
Grade B (Very good): B, B
Grade C (Good): 0
Grade D (Fair): 0
Grade E (Poor): 0

P-Reviewer: Covantsev S, Russia; Long X, China

Received: March 28, 2023
Peer-review started: March 28, 2023
First decision: June 1, 2023
Revised: June 15, 2023
Accepted: July 27, 2023
Article in press: July 27, 2023
Published online: August 28, 2023

Paige Bennett, Department of Radiology, LIJMC Northwell Health, New Hyde Park, NY 11040, United States

Paige Bennett, Maria Bernadette Tomas, Kenneth J Nichols, Christopher J Palestro, Department of Radiology, Zucker School of Medicine at Hofstra/Northwell, Hempstead, NY 11549, United States

Christopher F Koch, Division of Nuclear Medicine and Molecular Imaging, Department of Radiology, Northwell Health, New Hyde Park, NY 11040, United States

Corresponding author: Paige Bennett, MD, Professor, Department of Radiology, LIJMC Northwell Health, Rm C204, 27005 76th Avenue, New Hyde Park, NY 11040, United States.
pbennett1@northwell.edu

Abstract

BACKGROUND

Diagnosis of prosthetic vascular graft infection with [(18)F]fluorodeoxyglucose positron emission tomography/computed tomography (18F-FDG PET/CT) allows for early detection of functional changes associated with infection, based on increased glucose utilization by activated macrophages and granulocytes. Aseptic vascular grafts, like all foreign bodies, can stimulate an inflammatory response, which can present as increased activity on 18F-FDG PET/CT. Consequently, distinguishing aseptic inflammation from graft infection, though important, can be difficult. In the case of endovascular aneurysm repair (EVAR), a minimally invasive procedure involving the transfemoral insertion of an endoprosthetic stent graft, the normal postoperative appearance of these grafts on 18F-FDG PET/CT can vary over time, potentially confounding study interpretation.

AIM

To investigate the visual, semiquantitative, and temporal characteristics of aseptic vascular grafts in patients status post EVAR.

METHODS

In this observational retrospective cohort study, patients with history of EVAR who underwent 18F-FDG PET/CT for indications other than infection were

identified retrospectively. All patients were asymptomatic for graft infection - no abdominal pain, fever of unknown origin, sepsis, or leukocytosis - at the time of imaging and for ≥ 2 mo after each PET/CT. Imaging studies such as CT for each patient were also reviewed, and any patients with suspected or confirmed vascular graft infection were excluded. One hundred two scans performed on 43 patients (34 males; 9 females; age = 77 ± 8 years at the time of the final PET/CT) were retrospectively reviewed. All 43 patients had an abdominal aortic (AA) vascular graft, 40 patients had a right iliac (RI) limb graft, and 41 patients had a left iliac (LI) limb graft. Twenty-two patients had 1 PET/CT and 21 patients had from 2 to 9 PET/CTs. Grafts were imaged between 2 mo to 168 mo (about 14 years) post placement. Eight grafts were imaged within 6 mo of placement, including three that were imaged within three months of placement. The mean interval between graft placement and PET/CT for all 102 scans was 51 ± 39 mo. PET/CT data was reconstructed with region-of-interest analysis of proximal, mid and distal portions of the grafts and background ascending aorta. Maximum standardized uptake value (SUV_{max}) was recorded for each region. SUV_{max}-to-background uptake ratios (URs) were calculated. Visual assessment was performed using a 2-pattern grading scale: Diffuse (homogeneous uptake less than liver uptake) and focal (one or more areas of focal uptake in any part of the graft). Statistical analysis was performed.

RESULTS

In total, there were 306 AA grafts, 285 LI grafts, 282 RI grafts, and 306 ascending aorta background SUV_{max} measurements. For all 102 scans, mean SUV_{max} values for AA grafts were 2.8-3.0 along proximal, mid, and distal segments. Mean SUV_{max} values for LI grafts and RI grafts were 2.7-2.8. Mean SUV_{max} values for background were 2.5 ± 0.5. Mean URs were 1.1-1.2. Visual analysis of the scans reflected results of quantitative analysis. On visual inspection, 98% revealed diffuse, homogeneous 18F-FDG uptake less than liver. Graft URs and visual pattern categories were significantly associated for AA graft URs (F-ratio = 21.5, $P < 0.001$), LI graft URs (F-ratio = 20.4, $P < 0.001$), and RI graft URs (F-ratio = 30.4, $P < 0.001$). Thus, visual patterns of 18F-FDG uptake corresponded statistically significantly to semiquantitative URs. The age of grafts showing focal patterns was greater than grafts showing diffuse patterns, 87 ± 89 *vs* 50 ± 37 mo, respectively ($P = 0.02$). URs were significantly associated with graft age for AA grafts ($r = 0.19$, $P = 0.001$). URs were also significantly associated with graft age for LI grafts ($r = 0.25$, $P < 0.0001$), and RI grafts ($r = 0.31$, $P < 0.001$). Quartiles of similar numbers of graft (n = 25-27) grouped by graft age indicated that URs were significantly higher for 4th quartile *vs* 2nd quartile URs (F-ratio = 19.5, $P < 0.001$). When evaluating URs, graft SUVmax values within 10%-20% of the ascending aorta SUV_{max} is evident in aseptic grafts, except for grafts in the oldest quartiles. In this study, grafts in the oldest quartiles (> 7 years post EVAR) showed SUV_{max} up to 30% higher than the ascending aorta SUV_{max}.

CONCLUSION

Characteristics of an aseptic vascular stent graft in the aorta and iliac vessels on 18F-FDG PET/CT include graft SUV_{max} values within 10%-20% of the ascending aorta background SUV_{max}. The SUV_{max} of older aseptic grafts can be as much as 30% above background. The visual uptake pattern of diffuse, homogeneous uptake less than liver was seen in 98% of aseptic vascular grafts, making this pattern particularly reassuring for clinicians.

Key Words: Aseptic vascular grafts; Endovascular aortic repair; [(18)F]fluorodeoxyglucose positron emission tomography/computed tomography

©The Author(s) 2023. Published by Baishideng Publishing Group Inc. All rights reserved.

Core Tip: In patients post endovascular aortic repair who undergo [(18)F]fluorodeoxyglucose positron emission tomography/computed tomography, aseptic vascular grafts show maximum standardized uptake value (SUV_{max}) within 10%-20% of background ascending aorta SUV_{max} values. Older aseptic vascular grafts can show up to 30% higher uptake *vs* background compared with younger aseptic vascular grafts. The visual uptake pattern of diffuse, homogeneous uptake less than liver was seen in 98% of aseptic vascular grafts, making this pattern particularly reassuring for clinicians.

Citation: Bennett P, Tomas MB, Koch CF, Nichols KJ, Palestro CJ. Appearance of aseptic vascular grafts after endovascular aortic repair on [(18)F]fluorodeoxyglucose positron emission tomography/computed tomography. *World J Radiol* 2023; 15(8): 241-249
URL: https://www.wjgnet.com/1949-8470/full/v15/i8/241.htm
DOI: https://dx.doi.org/10.4329/wjr.v15.i8.241

INTRODUCTION

Diagnosis of prosthetic vascular graft infection with [(18)F]fluorodeoxyglucose positron emission tomography/computed tomography (18F-FDG PET/CT) allows for detection of early functional changes associated with infection, based on

increased glucose utilization by activated macrophages and granulocytes. 18F-FDG PET/CT can be an important diagnostic adjunct to CT, which depends on anatomic changes, such as perigraft air, fluid, soft tissue, fistula, and abscess for diagnosis of infection. However, sterile vascular grafts, like all foreign bodies, can stimulate an aseptic inflammatory response that presents as increased activity on 18F-FDG PET/CT. Consequently, distinguishing aseptic inflammation from vascular graft infection can be difficult, and standardized interpretation criteria for differentiating between these two conditions have not been universally adopted[1].

Currently, medical literature supports diagnostic sensitivity and specificity of 18F-FDG PET/CT in diagnosing vascular graft infection of 89%-98% and 59%-81%, respectively[2,3]. Note that the lower specificity raises the possibility of false-positive interpretations of 18F-FDG uptake on PET/CT. This has important clinical consequences, including unnecessary long-term antibiotic therapy, invasive procedures, and potential for graft explantation which carries an 18%-30% mortality rate due to complications[1,4,5]. As the negative predictive value of 18F-FDG PET/CT for excluding vascular graft infection is high (about 93%), the expected physiological patterns of 18F-FDG uptake in uninfected vascular grafts should be identified to avoid false-positive interpretation[4,6].

However, evidence on the appearance of aseptic vascular grafts over time on 18F-FDG PET/CT is sparse, maximum standardized uptake value (SUV_{max}) cutoff values for aseptic grafts have not been clearly defined, and visual pattern analysis is often suggested to distinguish aseptic from infected vascular grafts[2,7-10]. In the case of endovascular aneurysm repair (EVAR), a minimally invasive procedure involving the transfemoral insertion of an endoprosthetic stent graft, the normal postoperative appearance of these grafts on 18F-FDG PET/CT can vary over time, potentially confounding study interpretation[11,12]. Thus, this study was performed to evaluate visual, semiquantitative, and temporal characteristics of aseptic endovascular aneurysm grafts on 18F-FDG PET/CT.

MATERIALS AND METHODS

Patients

In this observational retrospective cohort study, patients with history of EVAR who underwent 18F-FDG PET/CT for indications other than infection were identified retrospectively. All patients were asymptomatic for graft infection - no abdominal pain, fever of unknown origin, sepsis, or leukocytosis - at the time of imaging and for ≥ 2 mo after each PET/CT. Imaging studies such as CT for each patient were also reviewed, and any patients with suspected or confirmed vascular graft infection were excluded. One hundred two scans performed on 43 patients (34 males; 9 females; age = 77 ± 8 years at the time of the final PET/CT) were retrospectively reviewed. All 43 patients had an abdominal aortic (AA) vascular graft, 40 patients had a right iliac (RI) limb graft, and 41 patients had a left iliac (LI) limb graft. Twenty-two patients had 1 PET/CT and 21 patients had from 2 to 9 PET/CTs. Grafts were imaged between 2 mo to 168 mo (about 14 years) post placement. Eight grafts were imaged within 6 mo of placement, including three that were imaged within three months of placement. The mean interval between graft placement and PET/CT for all 102 scans was 51 ± 39 mo. Types of graft material were obtained from the patients' medical records, when available (n = 19). The Institutional Review Board approved this retrospective study and the requirement to obtain informed consent was waived. All data were handled in compliance with the Health Insurance Portability and Accountability Act of 1996.

Data acquisition

Data were acquired on 4 PET/CT systems: 2 Siemens Biograph mCT 64 (Munich, Germany) and 2 GE D710 (GE Healthcare, Chicago, IL, United States) systems. Data were reconstructed using manufacturer recommended 18F-FDG PET/CT reconstruction parameters on associated workstations at which data were acquired.

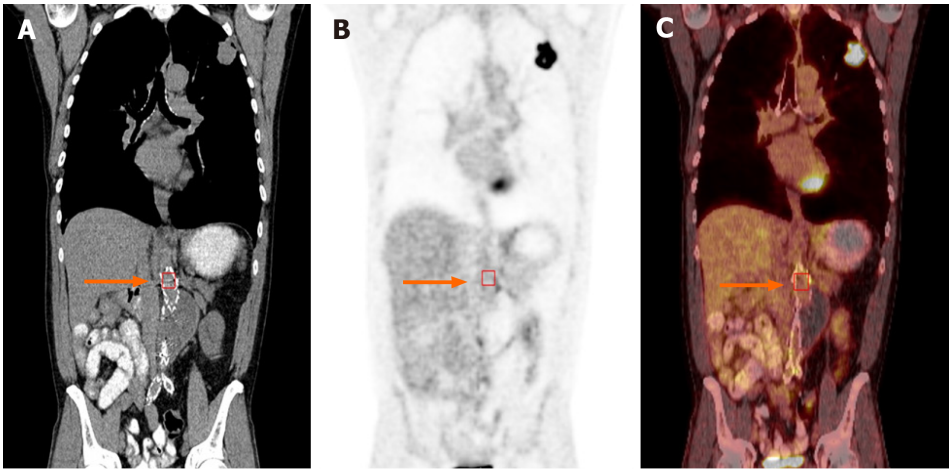
Image analysis

All reconstructed data were reviewed on a single GE AW workstation (GE Healthcare, Chicago, IL, United States). One nuclear medicine physician (MBT) analyzed all PET/CT images and obtained semiquantitative SUV_{max} using manually drawn region of interest (ROI) analysis. For each graft, a square ROI was drawn encompassing the width of the graft, cross-referenced on CT and confirmed on fused PET/CT images (Figure 1). ROIs were drawn around the proximal, mid, and distal portions of the AA graft, and SUV_{max} was recorded for each region. A similar ROI was used to measure SUV_{max} in the ascending aorta as the background (BKG) reference. SUV_{max} was also measured at proximal, mid, and distal portions of the RI and LI grafts when present. ROIs for each of the 3 locations along the grafts were placed equidistant.

Analyses were performed for SUV_{max} values to avoid underrepresentation of 18F-FDG uptake that could result from sampling tissue outside of graft tissues. To avoid the possibility of different PET/CT systems or software generating SUV_{max} values that were different from one another, the uptake ratio (UR) of SUV_{max} was calculated for each graft location using the formula: UR = SUV_{max} graft/SUV_{max} BKG. The URs were analyzed to minimize effects of using different PET/CT systems and image reconstruction algorithms.

Visual assessment

The same nuclear medicine physician who placed ROIs for semiquantitative analysis also classified uptake according to two visual patterns for aseptic grafts: Diffuse and focal. Diffuse was defined as mild, homogeneous uptake less than liver. Focal was defined as one or more areas of focal uptake in any part of the graft. Reference for visual analysis was 18F-FDG uptake in the liver.



DOI: 10.4329/wjr.v15.i8.241 **Copyright** ©The Author(s) 2023.

Figure 1 Coronal [(18)F]fluorodeoxyglucose positron emission tomography/computed tomography showing example of region of interest analysis on an abdominal aortic graft (arrow). A: Non-contrast computed tomography (CT); B: Positron emission tomography (PET); C: Fused PET/CT images.

Statistical analysis

Analyses were performed using commercially available software ("MedCalc" Statistical Software version 20.110; MedCalc Software Ltd, Ostend, Belgium; https://www.medcalc.org; 2022). Values were reported as mean ± SD. The Kolmogorov-Smirnov method assessed whether continuous variables were normally distributed and provided means and distribution percentiles. ANOVA with Bonferroni correction compared SUV_{max} and URs grouped by age of grafts, ROI locations, and graft material. Significance of differences between mean values were assessed by the unpaired student's *t*-test for normally distributed variables and by the Mann-Whitney test for non-normally distributed variables. Significance of changes over time was determined by linear regression of URs *vs* graft age. Linear regression of URs *vs* the time difference from the first through the last scan was performed for each patient with more than 1 PET/CT. Also, a separate subgroup analysis of patients with 3 or more scans was performed similarly with URs compared with the time difference from the first through the last scan of each patient. The Tukey test was applied to URs to detect outliers. For all tests, $P < 0.05$ was defined as statistically significant, or as adjusted by Bonferroni corrections for comparisons among multiple categories.

RESULTS

In total, there were 306 AA grafts, 285 LI grafts, 282 RI grafts, and 306 BKG SUV_{max} measurements. For all 102 scans, mean SUV_{max} values for AA grafts were 2.8-3.0 along proximal, mid, and distal segments (Table 1). Mean SUV_{max} values for LI grafts and RI grafts were 2.7-2.8. Mean SUV_{max} values for BKG were 2.5 ± 0.5 (Table 2). Mean URs were 1.1-1.2 (Tables 1 and 2).

Of the 43 patients, graft material was identifiable for 10 patients who had polyethylene terephthalate (PT) grafts and 9 patients who had polytetrafluoroethylene (PTFE) grafts. There were 87 SUV_{max} measurements of PT grafts and 78 SUV_{max} measurements of PTFE grafts. ANOVA indicated a modest difference (F-ratio = 5.1, $P = 0.03$) of AA graft URs between PT and PTFE graft materials (1.2 ± 0.3 *vs* 1.1 ± 0.2, $P = 0.03$).

URs were significantly associated with graft age for AA grafts ($r = 0.19$, $P = 0.001$) (Figure 2). URs were also significantly associated with graft age for LI grafts ($r = 0.25$, $P < 0.0001$), and RI grafts ($r = 0.31$, $P < 0.001$). Quartiles of similar numbers of graft (n = 25-27) grouped by graft age indicated that URs were significantly higher for 4th quartile *vs* 2 nd quartile URs (F-ratio = 19.5, $P < 0.001$) (Table 3). URs were similar for patients for whom graft placement was < 3 mo *vs* those with older grafts and were likewise similar for patients for whom graft placement was < 6 mo *vs* those with older grafts (F-ratio < 2.0, $P > 0.05$). While correlation of URs versus graft age was significant for all AA grafts (Figure 2), when analyzed separately by location, strongest correlation *vs* AA graft age was for proximal ROIs, less strong for mid ROIs, and not significant for distal ROIs (Figure 3). The highest UR value (2.89) corresponded to the patch region of the graft in one patient.

Patients with multiple PET/CT studies

A total of 80 18F-FDG PET/CTs were performed on the 21 patients with repeat scans: 5 patients had 2; 8 patients had 3; 3 patients had 4; 3 patients had 6; 1 patient had 7; and 1 patient had 9 scans. Correlations of URs over time from the first through the last scan were not significant ($r = 0.10$, $P = 0.09$) (Figure 4). There were 210 URs evaluated for the subgroup of patients with 3 or more scans. For this subgroup, URs were not correlated with time from the first through the last scan ($r = 0.12$, $P = 0.07$).

Table 1 Maximum standardized uptake value and uptake ratios for aortic graft locations

Location	SUV_{max}	Uptake ratio
Proximal aortic graft	2.8 ± 0.8	1.1 ± 0.3
Mid aortic graft	2.9 ± 0.8	1.2 ± 0.3
Distal aortic graft	3.0 ± 0.9	1.2 ± 0.3
Background	2.5 ± 0.5	-

SUV_{max}: Maximum standardized uptake value.

Table 2 Maximum standardized uptake value for grafts and background (ascending aorta), uptake ratios are listed for grafts

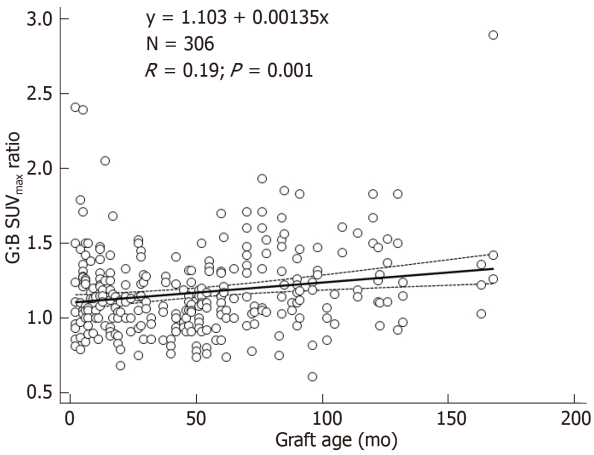
Location	SUV_{max}	Uptake ratio
Aortic graft	2.9 ± 0.8	1.2 ± 0.3
Left Iliac graft	2.7 ± 0.8	1.1 ± 0.3
Right Iliac graft	2.8 ± 0.8	1.2 ± 0.4
Background	2.5 ± 0.5	-

SUV_{max}: Maximum standardized uptake value.

Table 3 Graft age and uptake ratios segregated into quartiles by graft age

Graft, age, quartile	Graft age (mo)	Uptake ratio		
		Aortic graft	L-Iliac graft	R-Iliac graft
1	9 ± 4	1.2 ± 0.2	1.1 ± 0.2[a]	1.1 ± 0.2[a]
2	31 ± 10	1.1 ± 0.2[a]	1.1 ± 0.2[a]	1.1 ± 0.2[a]
3	60 ± 9	1.1 ± 0.3[a]	1.1 ± 0.3[a]	1.1 ± 0.4[a]
4	107 ± 24	1.3 ± 0.3	1.3 ± 0.4	1.4 ± 0.4

[a]$P < 0.05$ *versus* graft age quartile #4.



DOI: 10.4329/wjr.v15.i8.241 **Copyright** ©The Author(s) 2023.

Figure 2 Graft uptake ratios *vs* graft age in months for abdominal aortic grafts. SUV_{max}: Maximum standardized uptake value.

Visual analyses

Visual analysis of the scans reflected results of quantitative analysis (Table 4). On visual inspection, 98% revealed diffuse, homogeneous 18F-FDG uptake less than liver. Graft URs and visual pattern categories were significantly associated for AA graft URs (F-ratio = 21.5, $P < 0.001$), LI graft URs (F-ratio = 20.4, $P < 0.001$), and RI graft URs (F-ratio = 30.4, $P < 0.001$). Thus, visual patterns of 18F-FDG uptake corresponded statistically significantly to semiquantitative URs. The age of grafts showing focal patterns was greater than grafts showing diffuse patterns, 87 ± 89 *vs* 50 ± 37 mo, res-pectively ($P = 0.02$).

Visual uptake patterns were similar for different graft materials, when known, in that similar percentages of PT grafts and PTFE grafts were scored with focal visual patterns (2% *vs* 1%, $P = 0.63$) (Table 5), and similar to the 2% (6/306) of focal visual patterns for all grafts (Table 4).

Tests for outliers

The Tukey test showed there were 3 outlier cases for 3 different patients among the 306 graft URs. Even after excluding these 3 cases, there was significant association with URs and graft age for AA graft URs ($r = 0.19$, $P = 0.001$) (Figure 2). Similarly, there was significant association with URs and graft age for LI graft URs ($r = 0.25$, $P < 0.001$) and RI graft URs ($r = 0.31$, $P < 0.001$). Thus, no results were altered by excluding the 3 outliers.

DISCUSSION

In this study, the 18F-FDG PET/CT appearance of aseptic vascular grafts was delineated on 43 patients post EVAR without clinical signs and symptoms of vascular graft infection who underwent 18F-FDG PET/CT for oncologic indications. Visual, semiquantitative SUV_{max} and graft-to-background UR analysis was performed for 306 AA grafts, 285 LI grafts and 282 RI grafts. To our knowledge, this is the largest analysis of aseptic vascular graft appearance on 18F-FDG PET/CT to date.

All patients with aseptic aortic and iliac grafts showed graft SUV_{max} values of 3 or below. This is supported by a study by Tsuda *et al*[13] showing SUV_{max} below 4.5 in uninfected grafts, which was not dependent on time after surgery or whether the graft was placed in an open or endovascular fashion. Other studies have reported SUV_{max} values greater than 3.8-4.5 as significant for infection, which is supported by this study showing lower SUV_{max} values in aseptic grafts[14,15].

As SUV_{max} values can vary based on differences in PET/CT scanners, reconstruction algorithms and quality control efforts, we chose to include graft-to-background URs in our analyses. When evaluating URs, graft SUV_{max} values within 10%-20% of the ascending aorta SUV_{max} is evident in aseptic grafts, except for grafts in the oldest quartiles. In this study, grafts in the oldest quartile (> 7 years post EVAR) showed SUV_{max} up to 30% higher than the ascending aorta SUV_{max}.

The highest difference in URs was evident in PT grafts compared to PTFE grafts, although this modest difference is likely not clinically significant (1.2 ± 0.3 *vs* 1.1 ± 0.2, $P = 0.03$). When vascular grafts are encountered in the PET/CT clinic, two measurements of the ascending aorta and the graft can help to confirm a clinically noninfected appearance.

Visual analysis of vascular grafts in these patients was useful to detect a diffuse, homogeneous pattern of 18F-FDG uptake less than liver uptake, with results comparable to semiquantitative SUV_{max} and UR analysis. This suggests that visual comparison to the liver during image evaluation can be used to confirm a noninfected graft. The uptake pattern of 18F-FDG in aseptic vascular grafts was usually diffuse (300/306 = 98%), making this pattern particularly reassuring for clinicians.

When considering graft age, our data show a tendency for older grafts to exhibit higher 18F-FDG uptake. Those in the oldest quartile of the study (mean age 107 ± 24 mo) had mean URs of 1.3-1.4. Grafts in the lower 3 graft-age quartiles had mean URs closer to 1.1. Therefore, clinicians should consider the possibility of graft SUV_{max} being as much as 30% above ascending aorta background for old vascular grafts, particularly in proximal graft regions.

Limitations of this study include its retrospective nature, with chart review analysis the only means available to confirm absence of vascular graft infection in these patients. In addition, not all patients had contrast-enhanced CT for correlation with presence or absence of findings of vascular graft infection on anatomic imaging. Information regarding graft material composition was not available on all patients, potentially limiting analysis based on graft material. Another limitation is that a sole reader evaluated all data points on the PET/CT scans, including SUV_{max} and visual analysis. Therefore, interobserver variability in interpretation was not analyzed. Finally, our study did not include analysis of 18F-FDG PET/CT in patients with suspected or confirmed vascular graft infections, to compare with findings in aseptic vascular grafts in a similar patient population.

CONCLUSION

For 18F-FDG PET/CT interpreters, the visual, semiquantitative, and temporal characteristics of aseptic vascular stent grafts in patients' status post EVAR can be useful in interpreting PET/CT, whether stent grafts are encountered as incidental findings on oncologic scans or on scans performed for suspected vascular graft infection. Our findings reinforce prior research in determining the characteristics of aseptic vascular grafts in a large cohort of grafts analyzed over time.

Table 4 Frequency of visual uptake patterns for all grafts and uptake ratios

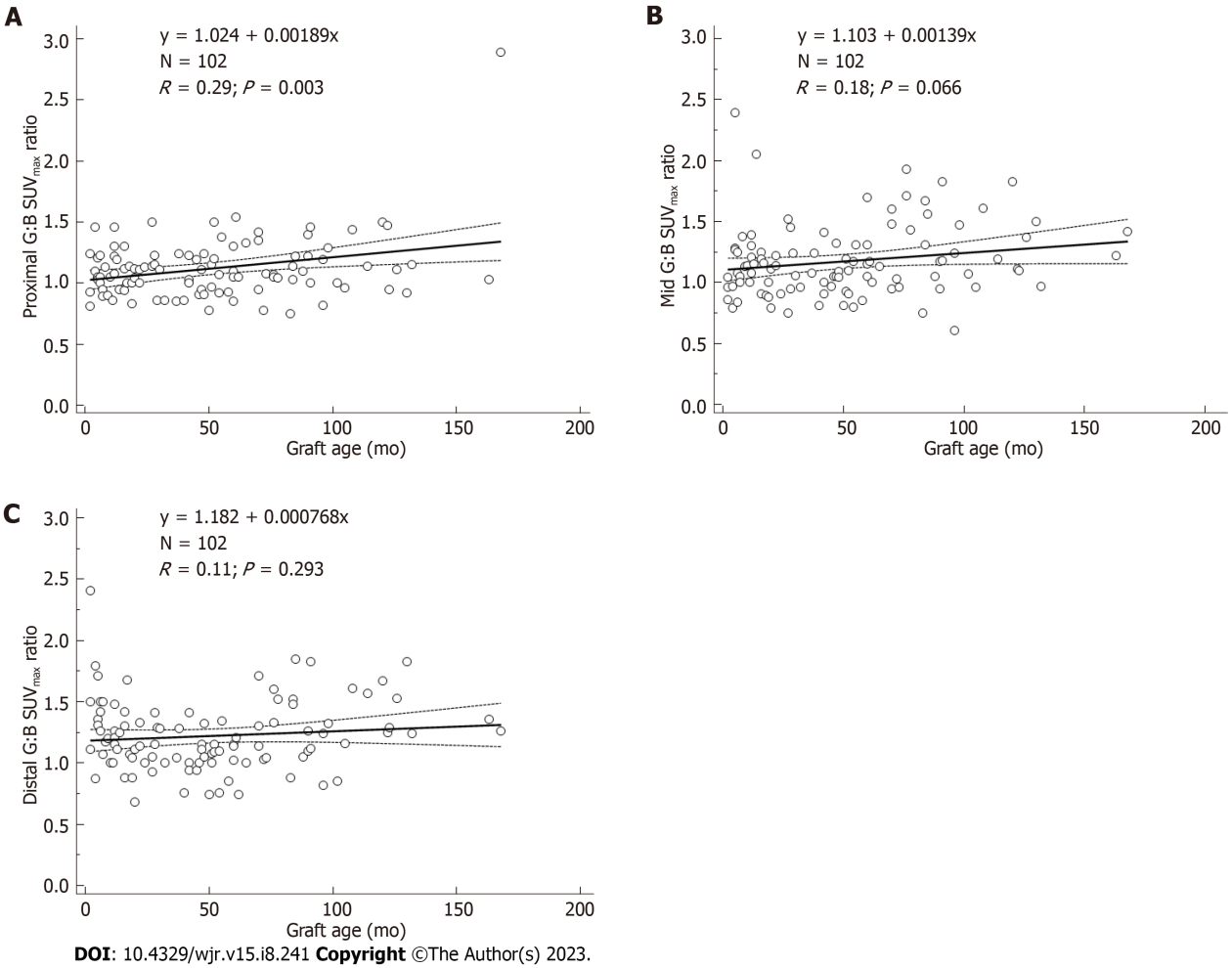
Visual uptake pattern	*n*	Uptake ratio
Diffuse	300	1.1 ± 0.3
Focal	6	1.8 ± 0.7[a]

[a]*P* < 0.05 *versus* "Diffuse".

Table 5 Frequency of visual uptake patterns and uptake ratios analyzed by graft type

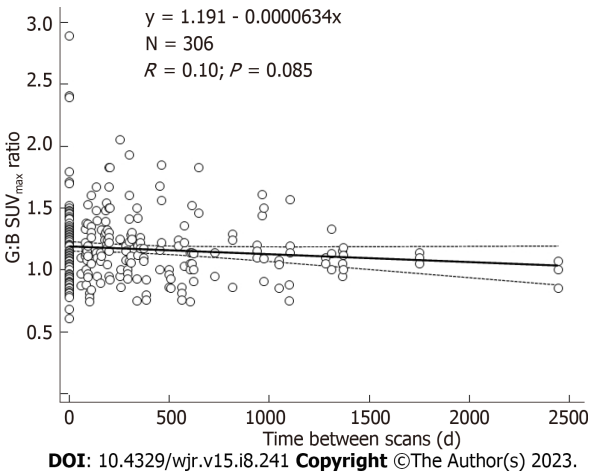
Visual uptake pattern	PT grafts		PTFE grafts	
	n	Uptake ratio	*n*	Uptake ratio
Diffuse	85	1.2 ± 0.3	77	1.1 ± 0.2
Focal	2	1.9 ± 0.7[a]	1	1.5

[a]*P* < 0.05 *versus* "Diffuse".
PT: Polyethylene terephthalate; PTFE: Polytetrafluoroethylene.



DOI: 10.4329/wjr.v15.i8.241 **Copyright** ©The Author(s) 2023.

Figure 3 Uptake ratios *vs* graft age in months. A: Proximal regions; B: Mid regions; C: Distal regions of abdominal aortic grafts.



DOI: 10.4329/wjr.v15.i8.241 **Copyright** ©The Author(s) 2023.

Figure 4 Uptake ratios of abdominal aortic grafts for all patients at all scan times. SUV_{max}: Maximum standardized uptake value.

ARTICLE HIGHLIGHTS

Research background

On [(18)F]fluorodeoxyglucose positron emission tomography/computed tomography (18F-FDG PET/CT), the inflammatory response caused by endoprosthetic stent grafts after endovascular aneurysm repair (EVAR) can show increased 18F-FDG uptake. However, the visual, semiquantitative, and temporal characteristics of uninfected, or aseptic, endovascular aneurysm grafts has not been fully elucidated.

Research motivation

Characterization of aseptic vascular stent grafts on 18F-FDG PET/CT is important to distinguish the normal inflammatory response to graft material *vs* vascular graft infection.

Research objectives

The purpose of this study was to characterize aseptic vascular stent grafts over time.

Research methods

In this observational retrospective cohort study, patients with EVAR who underwent 18F-FDG PET/CT for routine oncologic indications were included. Any patients with suspected or confirmed vascular stent graft infection were excluded. Visual and semiquantitative region of interest (ROI) analysis with maximum standardized uptake value (SUV_{max}) and graft-to-background ascending aorta uptake ratios (URs) of the grafts were obtained. We compared visual analysis and semiquantitative values, grouped by age of grafts, ROI locations, and graft materials.

Research results

Characteristics of an aseptic vascular stent graft on 18F-FDG PET/CT include graft SUV_{max} values within 10%-20% of the ascending aorta background SUV_{max}. The SUV_{max} of older aseptic grafts can be as much as 30% above background. The visual uptake pattern of diffuse, homogeneous uptake less than liver was seen in 98% of aseptic vascular stent grafts.

Research conclusions

Aseptic vascular stent grafts post endovascular repair show mildly increased 18F-FDG uptake, with mean graft-to-background URs of 1.1-1.2. Diffuse homogeneous 18F-FDG uptake less than liver in vascular stent grafts is particularly reassuring as a sign of an uninfected graft.

Research perspectives

This study reinforces prior research in characterizing aseptic vascular grafts on 18F-FDG PET/CT.

FOOTNOTES

Author contributions: Bennett P and Nichols KJ wrote the manuscript; Palestro C, Nichols KJ, and Tomas MB designed the research study; Tomas MB performed image analysis and chart review; Koch CF performed chart review; Nichols KJ, Tomas MB and Palestro C analyzed the data; and all authors have read and approved the final manuscript.

Institutional review board statement: Our Institutional Review Board approved this retrospective study. All data were handled in compliance with the Health Insurance Portability and Accountability Act of 1996.

Informed consent statement: The requirement to obtain informed consent was waived.

Conflict-of-interest statement: All the authors report no relevant conflicts of interest for this article.

Data sharing statement: The original anonymous dataset is available upon reasonable request from the corresponding author at pbennett1@northwell.edu.

Open-Access: This article is an open-access article that was selected by an in-house editor and fully peer-reviewed by external reviewers. It is distributed in accordance with the Creative Commons Attribution NonCommercial (CC BY-NC 4.0) license, which permits others to distribute, remix, adapt, build upon this work non-commercially, and license their derivative works on different terms, provided the original work is properly cited and the use is non-commercial. See: https://creativecommons.org/Licenses/by-nc/4.0/

Country/Territory of origin: United States

ORCID number: Paige Bennett 0009-0002-4639-0481; Maria Bernadette Tomas 0000-0002-3858-2347; Christopher F Koch 0000-0002-8339-8362; Kenneth J Nichols 0000-0003-2010-7078; Christopher J Palestro 0000-0002-5998-832X.

S-Editor: Wang JJ
L-Editor: A
P-Editor: Wang JJ

REFERENCES

1 **Casali M**, Lauri C, Altini C, Bertagna F, Cassarino G, Cistaro A, Erba AP, Ferrari C, Mainolfi CG, Palucci A, Prandini N, Baldari S, Bartoli F, Bartolomei M, D'Antonio A, Dondi F, Gandolfo P, Giordano A, Laudicella R, Massollo M, Nieri A, Piccardo A, Vendramin L, Muratore F, Lavelli V, Albano D, Burroni L, Cuocolo A, Evangelista L, Lazzeri E, Quartuccio N, Rossi B, Rubini G, Sollini M, Versari A, Signore A. State of the art of (18)F-FDG PET/CT application in inflammation and infection: a guide for image acquisition and interpretation. *Clin Transl Imaging* 2021; **9**: 299-339 [PMID: 34277510 DOI: 10.1007/s40336-021-00445-w]

2 **Arnon-Sheleg E**, Keidar Z. Vascular Graft Infection Imaging. *Semin Nucl Med* 2023; **53**: 70-77 [PMID: 36104271 DOI: 10.1053/j.semnuclmed.2022.08.006]

3 **Bowles H**, Ambrosioni J, Mestres G, Hernández-Meneses M, Sánchez N, Llopis J, Yugueros X, Almela M, Moreno A, Riambau V, Fuster D, Miró JM; Hospital Clinic Endocarditis Study Group. Diagnostic yield of (18)F-FDG PET/CT in suspected diagnosis of vascular graft infection: A prospective cohort study. *J Nucl Cardiol* 2020; **27**: 294-302 [PMID: 29907934 DOI: 10.1007/s12350-018-1337-1]

4 **Chrapko BE**, Chrapko M, Nocuń A, Zubilewicz T, Stefaniak B, Mitura J, Wolski A, Terelecki P. Patterns of vascular graft infection in 18F-FDG PET/CT. *Nucl Med Rev Cent East Eur* 2020; **23**: 63-70 [PMID: 33007092 DOI: 10.5603/NMR.a2020.0015]

5 **Schaefers JF**, Donas KP, Panuccio G, Kasprzak B, Heine B, Torsello GB, Osada N, Usai MV. Outcomes of Surgical Explantation of Infected Aortic Grafts After Endovascular and Open Abdominal Aneurysm Repair. *Eur J Vasc Endovasc Surg* 2019; **57**: 130-136 [PMID: 30146325 DOI: 10.1016/j.ejvs.2018.07.021]

6 **Sarrazin JF**, Trottier M, Tessier M. How useful is 18F-FDG PET/CT in patients with suspected vascular graft infection? *J Nucl Cardiol* 2020; **27**: 303-304 [PMID: 30046981 DOI: 10.1007/s12350-018-1377-6]

7 **Jamar F**, Buscombe J, Chiti A, Christian PE, Delbeke D, Donohoe KJ, Israel O, Martin-Comin J, Signore A. EANM/SNMMI guideline for 18F-FDG use in inflammation and infection. *J Nucl Med* 2013; **54**: 647-658 [PMID: 23359660 DOI: 10.2967/jnumed.112.112524]

8 **Reinders Folmer EI**, Von Meijenfeldt GCI, Van der Laan MJ, Glaudemans AWJM, Slart RHJA, Saleem BR, Zeebregts CJ. Diagnostic Imaging in Vascular Graft Infection: A Systematic Review and Meta-Analysis. *Eur J Vasc Endovasc Surg* 2018; **56**: 719-729 [PMID: 30122333 DOI: 10.1016/j.ejvs.2018.07.010]

9 **Mahmoodi Z**, Salarzaei M, Sheikh M. Prosthetic vascular graft infection: A systematic review and meta-analysis on diagnostic accuracy of 18FDG PET/CT. *Gen Thorac Cardiovasc Surg* 2022; **70**: 219-229 [PMID: 34309812 DOI: 10.1007/s11748-021-01682-6]

10 **Rojoa D**, Kontopodis N, Antoniou SA, Ioannou CV, Antoniou GA. 18F-FDG PET in the Diagnosis of Vascular Prosthetic Graft Infection: A Diagnostic Test Accuracy Meta-Analysis. *Eur J Vasc Endovasc Surg* 2019; **57**: 292-301 [PMID: 30241981 DOI: 10.1016/j.ejvs.2018.08.040]

11 **Keidar Z**, Pirmisashvili N, Leiderman M, Nitecki S, Israel O. 18F-FDG uptake in noninfected prosthetic vascular grafts: incidence, patterns, and changes over time. *J Nucl Med* 2014; **55**: 392-395 [PMID: 24516259 DOI: 10.2967/jnumed.113.128173]

12 **Liddy S**, Mallia A, Collins CD, Killeen RP, Skehan S, Dodd JD, Subesinghe M, Murphy DJ. Vascular findings on FDG PET/CT. *Br J Radiol* 2020; **93**: 20200103 [PMID: 32356457 DOI: 10.1259/bjr.20200103]

13 **Tsuda K**, Washiyama N, Takahashi D, Natsume K, Ohashi Y, Hirano M, Takeuchi Y, Shiiya N. 18-Fluorodeoxyglucose positron emission tomography in the diagnosis of prosthetic aortic graft infection: the difference between open and endovascular repair. *Eur J Cardiothorac Surg* 2022; **63** [PMID: 36394268 DOI: 10.1093/ejcts/ezac542]

14 **Kim A**, Koshevarova V, Shure A, Joseph S, Villanueva-Meyer J, Bhargava P. FDG PET/CT in abdominal aortic graft infection: A case report and literature review. *Radiol Case Rep* 2023; **18**: 27-30 [PMID: 36324849 DOI: 10.1016/j.radcr.2022.09.106]

15 **Rahimi M**, Adlouni M, Ahmed AI, Alnabelsi T, Chinnadurai P, Al-Mallah MH. Diagnostic Accuracy of FDG PET for the Identification of Vascular Graft Infection. *Ann Vasc Surg* 2022; **87**: 422-429 [PMID: 35760267 DOI: 10.1016/j.avsg.2022.05.029]

World Journal of Radiology

Submit a Manuscript: https://www.f6publishing.com

World J Radiol 2023 August 28; 15(8): 250-255

DOI: 10.4329/wjr.v15.i8.250

ISSN 1949-8470 (online)

CASE REPORT

Rare portal hypertension caused by Abernethy malformation (Type IIC): A case report

Xin Yao, Yang Liu, Li-Dan Yu, Jian-Ping Qin

Specialty type: Gastroenterology and hepatology

Provenance and peer review: Unsolicited article; Externally peer reviewed.

Peer-review model: Single blind

Peer-review report's scientific quality classification

Grade A (Excellent): 0
Grade B (Very good): 0
Grade C (Good): C
Grade D (Fair): D
Grade E (Poor): 0

P-Reviewer: Ghazanfar A, United Kingdom; Pizanias M, United Kingdom

Received: June 16, 2023
Peer-review started: June 16, 2023
First decision: July 19, 2023
Revised: July 23, 2023
Accepted: July 31, 2023
Article in press: July 31, 2023
Published online: August 28, 2023

Xin Yao, Yang Liu, Li-Dan Yu, Jian-Ping Qin, Department of Gastroenterology, General Hospital of Western Theater Command, Chengdu 610083, Sichuan Province, China

Corresponding author: Jian-Ping Qin, MD, Chief Physician, Department of Gastroenterology, General Hospital of Western Theater Command, No. 270 Rongdu Road, Chengdu 610083, Sichuan Province, China. jpqqing@163.com

Abstract

BACKGROUND

Abernethy malformation is a rare congenital vascular malformation with a portosystemic shunt that may clinically manifest as cholestasis, dyspnea, or hepatic encephalopathy, among other conditions. Early diagnosis and classification are very important to further guide treatment. Typically, patients with congenital portosystemic shunts have no characteristics of portal hypertension. Herein, we report an 18-year-old female with prominent portal hypertension that manifested mainly as rupture and bleeding of esophageal varices. Imaging showed a thin main portal vein, no portal vein branches in the liver, and bleeding of the esophageal and gastric varices caused by the collateral circulation upwards from the proximal main portal vein. Patients with Abernethy malformation type I are usually treated with liver transplantation, and patients with type II are treated with shunt occlusion, surgery, or transcatheter coiling. Our patient was treated with endoscopic surgery combined with drug therapy and had no portal hypertension and good hepatic function for 24 mo of follow-up.

CASE SUMMARY

This case report describes our experience in the diagnosis and treatment of an 18-year-old female with Abernethy malformation type IIC and portal hypertension. This condition was initially diagnosed as cirrhosis combined with portal hypertension. The patient was ultimately diagnosed using liver histology and subsequent imaging, and the treatment was highly effective. To publish this case report, written informed consent was obtained from the patient, including the attached imaging data.

CONCLUSION

Abernethy malformation type IIC may develop portal hypertension, and traditional nonselective beta-blockers combined with endoscopic treatment can achieve high efficacy.

Key Words: Abernethy malformation; congenital absence of portal vein; portal hypertension

©The Author(s) 2023. Published by Baishideng Publishing Group Inc. All rights reserved.

Core Tip: Abernethy malformation is a rare congenital vascular malformation with portosystemic shunts that may clinically manifest as cholestasis, dyspnea, or hepatic encephalopathy, among other conditions. Typically, patients with congenital portosystemic shunts have no characteristics of portal hypertension. We reported an 18-year-old woman with Abernethy malformation type II and portal hypertension. This condition was initially diagnosed as cirrhosis combined with portal hypertension. The patient was ultimately diagnosed by liver puncture and biopsy with subsequent imaging.

Citation: Yao X, Liu Y, Yu LD, Qin JP. Rare portal hypertension caused by Abernethy malformation (Type IIC): A case report. *World J Radiol* 2023; 15(8): 250-255
URL: https://www.wjgnet.com/1949-8470/full/v15/i8/250.htm
DOI: https://dx.doi.org/10.4329/wjr.v15.i8.250

INTRODUCTION

Among patients accompanied by portal hypertension, Esophageal variceal bleeding is a frequent complication. However, although the prevalence of Abernethy malformation is approximately 1 in 30000–50000 people[1], and it typically presents no characteristics of portal hypertension, this congenital occult disease should not be ignored in clinical practice. As imaging studies have progressed, the diagnosis of Abernethy malformation has increased. The shunts of Abernethy malformation type II most often occur in the main portal vein (MPV) and in the mesenteric, gastric, and splenic veins[2]. To date, no reports have described the shunt entering the splenic hilum through the splenic vein and establishing collateral circulation, which then enters the inferior vena cava (IVC) through the splenorenal shunt. In addition, this patient developed portal hypertension, which was treated effectively.

CASE PRESENTATION

Chief complaints

An 18-year-old woman was admitted to our hospital with a 10-d history of left upper abdominal distension, pain, and discomfort, accompanied by hematemesis.

History of present illness

The patient had no history of present illness.

History of past illness

The patient had no history of past illness.

Personal and family history

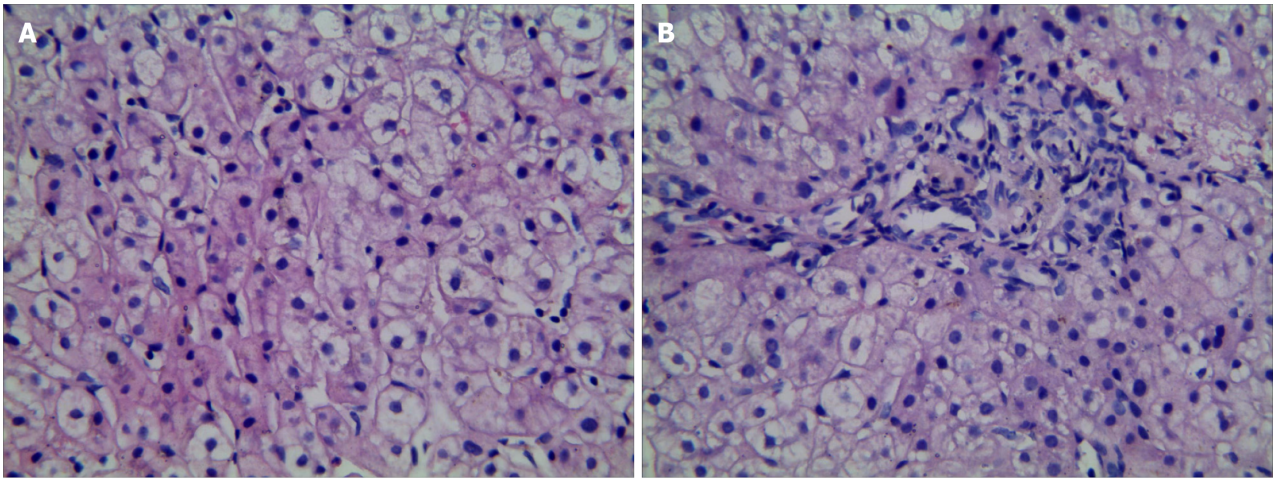
The patient had no special personal history or family history.

Physical examination

Physical examination showed no abnormalities, except for the spleen palpable 2 cm below the left costal margin.

Laboratory examinations

On routine blood tests, the hematocrit was 25.6%, the hemoglobin concentration was 73 g/L, the red blood cell count was 3.71 × 10^{12}/L, the platelet count was 152 × 10^{9}/L, and the white blood cell count was 1.31 × 10^{9}/L. The results of laboratory examinations were Child–Pugh grade A liver function. Test results for hepatitis and autoimmune antibodies were negative. Ceruloplasmin was normal. Bone marrow (BM) smear displayed active proliferation of karyocytes, with 59% granulocytes and 22% erythroid cells (granulocytes/erythroid cell ratio of 2.68); most of the mature red blood cells were expanded in the central light-stained area. Active proliferation of BM tissue was shown on BM puncture and biopsy without other special changes. Punctured hepatic tissue. The structure of hepatic lobules was normal, the hepatic sinusoids were not dilated, the diameter of the central vein was generally normal, and the hepatic parenchyma had no obvious inflammatory changes. No portal vein branch entering the hepatic lobule was detected. The number and shape of small bile ducts in the portal area were normal, and the stroma was infiltrated by a small number of chronic inflammatory cells (Figure 1).



DOI: 10.4329/wjr.v15.i8.250 **Copyright** ©The Author(s) 2023.

Figure 1 The number and shape of small bile ducts in the portal area were normal, and the stroma was infiltrated by a small number of chronic inflammatory cells. A and B: Punctured hepatic tissue with hematoxylin and eosin staining (× 400).

Imaging examinations

Colonoscopy suggested no abnormalities. Gastroscopy revealed severe esophageal varices (type G1OV1). Further imaging with 320-detector row computed tomography (CT) angiography and three-dimensional (3D) reconstruction of the portal vein showed a thin MPV, no portal vein branch in the liver, disordered vessels at the proximal MPV, and esophageal varices caused by collateral circulation upwards at the origin of the portal vein. The superior mesenteric vein and the splenic vein formed a common trunk. After entering the splenic hilum, the splenic vein formed collateral circulation along the lower left side of the vertebral body, resulting in a venous tumor thrombus, and then flowed into the renal vein and returned to the IVC (Figure 2). Ultrasound of the portal vein showed no portal vein branch in the liver, a thin MPV with blood flow, no thrombosis or cavernous transformation, reversed blood flow in the splenic vein, and thickened hepatic arteries suspected to be compensation. Cardiac ultrasound showed no abnormalities.

FINAL DIAGNOSIS

Abernethy malformation type IIC: Portal hypertension.

TREATMENT

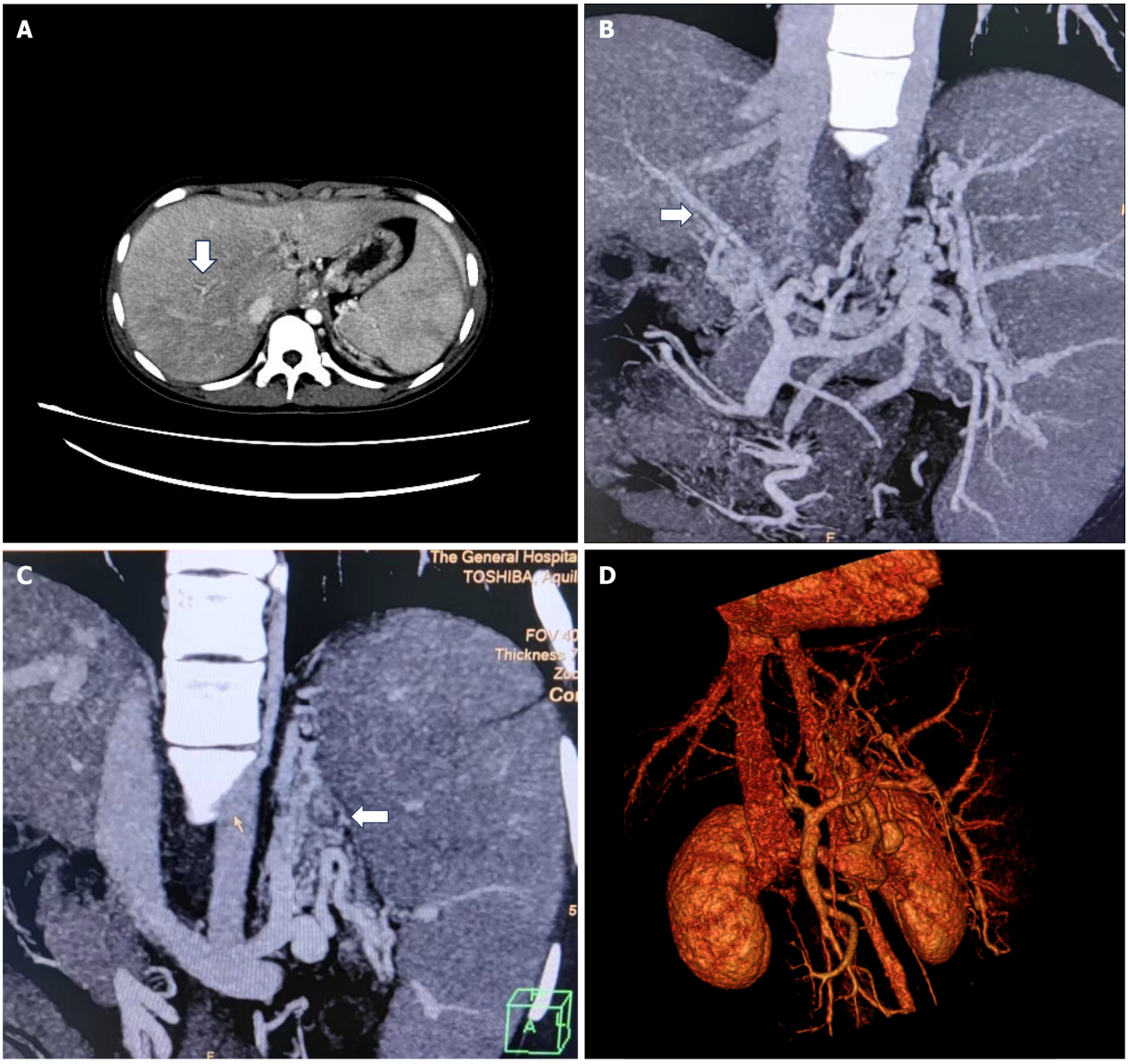
Patients with Abernethy malformation type II can be treated with shunt occlusion and liver transplantation, and the patient selected conservative treatment. After the first endoscopic ligation of esophageal varices, endoscopic treatment was carried out 3 consecutive times at an interval of 1 mo. Simultaneously, 10 mg of oral propranolol hydrochloride was given 3 times/d. The heart rate was controlled at approximately 55 times/min.

OUTCOME AND FOLLOW-UP

Three months later, gastroscopy indicated esophageal varices (mild, RC-) and a local scar after ligation. Thus, 2.5 mg of warfarin per day was administered. The patient was followed up for 24 consecutive months and showed no portal hypertension and Child–Pugh grade A.

DISCUSSION

John Abernethy first reported Abernethy malformation, also known as a congenital extrahepatic portosystemic shunt, in 1793. Abernethy malformation is a rare clinical disease with a prevalence of one case out of 30000–50000[1]. It is characterized by the absence or dysplasia of the portal vein caused by abnormal development of fetal umbilical veins and vitelline veins, with abnormal shunts between the portal vein system and the vena cava system[3]. In 1994, Morgan *et al* [2] defined Abernethy malformation type I as the absence of portal vein flow in the liver caused by the congenital absence of the portal vein. Abernethy malformation type II was defined as a significant reduction in intrahepatic blood flow



DOI: 10.4329/wjr.v15.i8.250 **Copyright** ©The Author(s) 2023.

Figure 2 After entering the splenic hilum, the splenic vein formed collateral circulation along the lower left side of the vertebral body, resulting in a venous tumor thrombus, and then flowed into the renal vein and returned to the inferior vena cava. A: The main portal vein was thin, and no portal vein branch was found in the liver (arrow); B: The vessels were disordered at the proximal main portal vein, and esophageal varices were caused by collateral circulation upward at the portal vein origin. The superior mesenteric vein and the splenic vein formed a common trunk (arrow); C and D: After entering the splenic hilum, the splenic vein established collateral circulation (forming a venous tumour), flowed into the renal vein and returned to the inferior vena cava (arrow).

caused by a thin MPV. In type I Abernethy malformation patients, the superior mesenteric vein does not merge with the splenic vein, and merging of the superior mesenteric vein with the splenic vein is classified as type Ib. In 2011, Lautz *et al* [4] classified patients with congenital portal vein dysplasia into type IIa (shunt occurring in the left or right portal vein of the liver, including patent ductus venosus), type IIb (shunt occurring in the MPV), and type IIc (shunt occurring in the mesenteric veins, gastric veins, or splenic veins) based on the different anatomical positions of the portosystemic shunts. However, this classification method includes patients with congenital intrahepatic portosystemic shunts and is not widely used.

The clinical manifestations of Abernethy malformation vary greatly, from incidental detection to hepatoencephalopathy and hepatic failure, and depend on the type of abnormality. Patients may be asymptomatic or present with nonspecific symptoms, such as hypergalactosemia, hyperbilirubinemia, and hyperammonemia, due to delayed metabolism of these metabolites in the liver or their metabolism outside of the liver[5,6]. Abernethy malformation may also cause pulmonary venous congestion, leading to hepatopulmonary syndrome, which manifests as dyspnea caused by pulmonary hypertension and even syncope[7]. In addition, Abernethy malformation can be complicated by multiple malformations[2], such as congenital heart disease, skeletal muscle system malformations, and polysplenia. When patients visit with symptoms, including dyspnea and varicose veins of the lower limbs[8], misdiagnosis or missed diagnosis is likely. This patient was admitted due to rupture and bleeding of esophageal varices, which is easily misdia-

gnosed as cirrhotic portal hypertension accompanied by cavernous transformation of the portal vein. Hepatobiliary abnormalities, such as cirrhosis, veno-occlusive disease, noncirrhotic portal fibrosis, and biliary atresia, were excluded based on the percutaneous liver biopsy. A BM smear and biopsy excluded hematological system-related diseases. The thin portal vein and no portal vein branches in the liver indicated Abernethy malformation. However, CT showed a similar cavernous transformation at the proximal portal vein, so Abernethy malformation needed to be differentiated from extrahepatic portal vein obstruction-related diseases.

Imaging is the preferred diagnostic method for Abernethy malformations. Abdominal ultrasound can be used as a preliminary screening tool. Portal vein CT angiography and 3D reconstruction can help identify abnormal development of the portal vein and the anatomy of extrahepatic shunts in Abernethy malformations. Webb *et al*[9] described the ultrasound display of the portal vein in Abernethy malformations as an intact empty hepatic hilum with portal vein block appearing as a wide, rhombic high-level echo band. Patients with congenital portosystemic shunts do not have characteristics of portal hypertension, such as splenomegaly, varicosity, and collateral branches[10]. A recent study[11] suggested that acquired extrahepatic portosystemic shunts are usually detected in patients with cirrhosis. In addition, noncirrhotic portal vein thrombosis may also present manifestations similar to Abernethy malformation. In this patient, an ultrasound of the portal vein showed no portal vein branches in the liver, thrombosis, or cavernous transformation but showed thin MPV with visible blood flow signals and reversed blood flow in the splenic vein. Although the CT of this patient showed a similar cavernous transformation in the MPV, the author's team believes that extrahepatic portal vein obstruction caused by chronic thrombosis and cavernous transformation of the portal vein was excluded by ultrasound. No shunt between the portal vein and the splenic vein was detected, but after entering the splenic hilum, the blood flowed back to the IVC in the form of a thick "spleen kidney" shunt through the collateral circulation, which is different from the usual form of Abernethy syndrome and may be another manifestation of Abernethy malformation type IIC. Several studies[12, 13] showed that various congenital malformations are related to Abernethy malformation, and cardiac abnormalities are the most common. This patient presented with no abnormalities on cardiac ultrasound, so cardiac malformations could be excluded. We speculate that this patient may have a congenital hypoplastic portal vein system. Because of the thin MPV and no portal vein branch, the "splenorenal communicating branch" that should degenerate during development continued to exist chronically. The blood flow returning to the liver was blocked at the portal vein origin, forming regional portal hypertension (consistent with the appearance of abundant capillary collateral circulation around the MPV origin on CT, which is similar to cavernous transformation). In addition, the blood flow of the splenic vein was reversed, causing splenic congestion and swelling, and then returned to the IVC through the splenic-renal communicating branch.

Hepatic damage in patients with Abernethy malformations is milder than the damage in patients with cirrhosis, and the increases in bilirubin and aminopherase are often not obvious[14]. This patient's hepatic function was normal, with no hepatic encephalopathy, which is in line with previous research results[5,15]. Most patients with Abernethy malformations have elevated blood ammonia, but fewer patients present with hepatic encephalopathy. Although the thin portal vein may lead to insufficient blood flow to the liver, the hepatic artery may play a compensatory role in the long-term course of the disease, which is consistent with hepatic artery thickening on portal ultrasound and compensatory performance.

Liver transplantation is the main treatment method for Abernethy malformation type I. Patients with Abernethy malformation type II are treated with shunt occlusion and liver transplantation[6,16]. The choice of an interventional or surgical method is based on the degree of extrahepatic portosystemic shunts, the anatomical position of shunts, and the diameter of the shunts. The liver tumors, hepatopulmonary syndrome, and hyperammonemia disappear after the occlusion of the abnormal shunts[4,15]. Portal hypertension caused by Abernethy malformation has not been reported; thus, we first recommended liver transplantation for this patient, and the patient finally chose conservative treatment. Endoscopic ligation may aggravate portal hypertension, slow portal vein blood flow, and form thrombi[17]. Therefore, nonselective beta-blockers and anticoagulant drugs were added. After 24 mo of follow-up, the patient presented with no complications of portal hypertension or portal thrombosis and good hepatic function. We will continue to monitor this patient.

CONCLUSION

Abernethy malformation type IIC may cause portal hypertension, and combining traditional nonselective beta-blockers with endoscopic therapy is an effective treatment.

FOOTNOTES

Author contributions: Yao X wrote the paper; Liu Y collected the data; Yu LD collected the data; Qin JP participated in and guided the operation, conceptualized the idea, and finalized the manuscript.

Informed consent statement: Informed written consent was obtained from the patient for publication of this report and any accompanying images.

Conflict-of-interest statement: All the authors declare that they have no conflict of interests to report.

CARE Checklist (2016) statement: The authors have read the CARE Checklist (2016), and the manuscript was prepared and revised

according to the CARE Checklist (2016).

Open-Access: This article is an open-access article that was selected by an in-house editor and fully peer-reviewed by external reviewers. It is distributed in accordance with the Creative Commons Attribution NonCommercial (CC BY-NC 4.0) license, which permits others to distribute, remix, adapt, build upon this work non-commercially, and license their derivative works on different terms, provided the original work is properly cited and the use is non-commercial. See: https://creativecommons.org/Licenses/by-nc/4.0/

Country/Territory of origin: China

ORCID number: Xin Yao 0000-0002-9977-6153; Yang Liu 0000-0003-1700-3890; Li-Dan Yu 0000-0001-5261-2496; Jian-Ping Qin 0000-0001-7834-8830.

S-Editor: Liu JH
L-Editor: A
P-Editor: Zhao S

REFERENCES

1 **Abernethy J**. Account of Two Instances of Uncommon Formation in the Viscera of the Human Body: From the Philosophical Transactions of the Royal Society of London. *Med Facts Obs* 1797; **7**: 100-108 [PMID: 29106224]
2 **Morgan G**, Superina R. Congenital absence of the portal vein: two cases and a proposed classification system for portasystemic vascular anomalies. *J Pediatr Surg* 1994; **29**: 1239-1241 [PMID: 7807356 DOI: 10.1016/0022-3468(94)90812-5]
3 **Peček J**, Fister P, Homan M. Abernethy syndrome in Slovenian children: Five case reports and review of literature. *World J Gastroenterol* 2020; **26**: 5731-5744 [PMID: 33088165 DOI: 10.3748/wjg.v26.i37.5731]
4 **Lautz TB**, Tantemsapya N, Rowell E, Superina RA. Management and classification of type II congenital portosystemic shunts. *J Pediatr Surg* 2011; **46**: 308-314 [PMID: 21292079 DOI: 10.1016/j.jpedsurg.2010.11.009]
5 **Ponziani FR**, Faccia M, Zocco MA, Giannelli V, Pellicelli A, Ettorre GM, De Matthaeis N, Pizzolante F, De Gaetano AM, Riccardi L, Pompili M, Rapaccini GL. Congenital extrahepatic portosystemic shunt: description of four cases and review of the literature. *J Ultrasound* 2019; **22**: 349-358 [PMID: 30357760 DOI: 10.1007/s40477-018-0329-y]
6 **Uchida H**, Sakamoto S, Kasahara M, Kudo H, Okajima H, Nio M, Umeshita K, Ohdan H, Egawa H, Uemoto S; Japanese Liver Transplantation Society. Longterm Outcome of Liver Transplantation for Congenital Extrahepatic Portosystemic Shunt. *Liver Transpl* 2021; **27**: 236-247 [PMID: 32463947 DOI: 10.1002/lt.25805]
7 **Lin XQ**, Rao JY, Xiang YF, Zhang LW, Cai XL, Guo YS, Lin KY. Case Report: A Rare Syncope Case Caused by Abernethy II and a Review of the Literature. *Front Cardiovasc Med* 2021; **8**: 784739 [PMID: 35059447 DOI: 10.3389/fcvm.2021.784739]
8 **Wang W**, Li Q, Wen L. An Unusual Cause of Left Lower Extremity Varicose Veins. *Gastroenterology* 2022; **162**: e9-e11 [PMID: 34390728 DOI: 10.1053/j.gastro.2021.08.010]
9 **Webb LJ**, Berger LA, Sherlock S. Grey-scale ultrasonography of portal vein. *Lancet* 1977; **2**: 675-677 [PMID: 71493 DOI: 10.1016/s0140-6736(77)90492-5]
10 **Ghuman SS**, Gupta S, Buxi TB, Rawat KS, Yadav A, Mehta N, Sud S. The Abernethy malformation-myriad imaging manifestations of a single entity. *Indian J Radiol Imaging* 2016; **26**: 364-372 [PMID: 27857464 DOI: 10.4103/0971-3026.190420]
11 **Kumar P**, Bhatia M, Garg A, Jain S, Kumar K. Abernethy malformation: A comprehensive review. *Diagn Interv Radiol* 2022; **28**: 21-28 [PMID: 34914605 DOI: 10.5152/dir.2021.20474]
12 **Kim ES**, Lee KW, Choe YH. The Characteristics and Outcomes of Abernethy Syndrome in Korean Children: A Single Center Study. *Pediatr Gastroenterol Hepatol Nutr* 2019; **22**: 80-85 [PMID: 30671377 DOI: 10.5223/pghn.2019.22.1.80]
13 **Ponziani FR**, Faccia M, Zocco MA, Giannelli V, Pellicelli A, Ettorre GM, De Matthaeis N, Pizzolante F, De Gaetano AM, Riccardi L, Pompili M, Rapaccini GL. Congenital extrahepatic portosystemic shunt: description of four cases and review of the literature. *J Ultrasound* 2019; **22**: 349-358 [PMID: 30357760 DOI: 10.1007/s40477-018-0329-y]
14 **Alonso-Gamarra E**, Parrón M, Pérez A, Prieto C, Hierro L, López-Santamaría M. Clinical and radiologic manifestations of congenital extrahepatic portosystemic shunts: a comprehensive review. *Radiographics* 2011; **31**: 707-722 [PMID: 21571652 DOI: 10.1148/rg.313105070]
15 **Zhou M**, Zhang J, Luo L, Wang B, Zheng R, Li L, Jing H, Zhang S. Surgical Ligation for the Treatment of an Unusual Presentation of Type II Abernethy Malformation. *Ann Vasc Surg* 2020; **65**: 285.e1-285.e5 [PMID: 31705994 DOI: 10.1016/j.avsg.2019.10.094]
16 **Tanaka H**, Saijo Y, Tomonari T, Tanaka T, Taniguchi T, Yagi S, Okamoto K, Miyamoto H, Sogabe M, Sato Y, Muguruma N, Tsuneyama K, Sata M, Takayama T. An Adult Case of Congenital Extrahepatic Portosystemic Shunt Successfully Treated with Balloon-occluded Retrograde Transvenous Obliteration. *Intern Med* 2021; **60**: 1839-1845 [PMID: 33456037 DOI: 10.2169/internalmedicine.5914-20]
17 **Wang L**, Guo X, Shao X, Xu X, Zheng K, Wang R, Chawla S, Basaranoglu M, Qi X. Association of endoscopic variceal treatment with portal venous system thrombosis in liver cirrhosis: a case-control study. *Therap Adv Gastroenterol* 2022; **15**: 17562848221087536 [PMID: 35574427 DOI: 10.1177/17562848221087536]



Published by **Baishideng Publishing Group Inc**
7041 Koll Center Parkway, Suite 160, Pleasanton, CA 94566, USA
Telephone: +1-925-3991568
E-mail: bpgoffice@wjgnet.com
Help Desk: https://www.f6publishing.com/helpdesk
https://www.wjgnet.com



© 2023 Baishideng Publishing Group Inc. All rights reserved.

ISSN 1949-8470 (online)

World Journal of *Radiology*

World J Radiol 2023 September 28; 15(9): 256-280



Published by Baishideng Publishing Group Inc

World Journal of Radiology

Contents

Monthly Volume 15 Number 9 September 28, 2023

REVIEW

256 Role of pulmonary perfusion magnetic resonance imaging for the diagnosis of pulmonary hypertension: A review

Lacharie M, Villa A, Milidonis X, Hasaneen H, Chiribiri A, Benedetti G

CASE REPORT

274 Distinctive magnetic resonance imaging features in primary central nervous system lymphoma: A case report

Liu LH, Zhang HW, Zhang HB, Liu XL, Deng HZ, Lin F, Huang B

World Journal of Radiology

Monthly Volume 15 Number 9 September 28, 2023

Contents

ABOUT COVER

Editorial Board Member of *World Journal of Radiology*, Alberto Tagliafico, MD, Assistant Professor, Department of Health Sciences (DISSAL), University of Genova, Genova 16138, Italy. alberto.tagliafico@unige.it

AIMS AND SCOPE

The primary aim of *World Journal of Radiology* (*WJR*, *World J Radiol*) is to provide scholars and readers from various fields of radiology with a platform to publish high-quality basic and clinical research articles and communicate their research findings online.

WJR mainly publishes articles reporting research results and findings obtained in the field of radiology and covering a wide range of topics including state of the art information on cardiopulmonary imaging, gastrointestinal imaging, genitourinary imaging, musculoskeletal imaging, neuroradiology/head and neck imaging, nuclear medicine and molecular imaging, pediatric imaging, vascular and interventional radiology, and women's imaging.

INDEXING/ABSTRACTING

The *WJR* is now abstracted and indexed in PubMed, PubMed Central, Emerging Sources Citation Index (Web of Science), Reference Citation Analysis, China National Knowledge Infrastructure, China Science and Technology Journal Database, and Superstar Journals Database. The 2023 Edition of Journal Citation Reports® cites the 2022 impact factor (IF) for *WJR* as 2.5; IF without journal self cites: 2.3; 5-year IF: 2.5; Journal Citation Indicator: 0.54.

RESPONSIBLE EDITORS FOR THIS ISSUE

Production Editor: *Si Zhao*; **Production Department Director:** *Xu Guo*; **Editorial Office Director:** *Jia-Ping Yan*.

NAME OF JOURNAL
World Journal of Radiology

ISSN
ISSN 1949-8470 (online)

LAUNCH DATE
January 31, 2009

FREQUENCY
Monthly

EDITORS-IN-CHIEF
Thomas J Vogl

EDITORIAL BOARD MEMBERS
https://www.wjgnet.com/1949-8470/editorialboard.htm

PUBLICATION DATE
September 28, 2023

COPYRIGHT
© 2023 Baishideng Publishing Group Inc

INSTRUCTIONS TO AUTHORS
https://www.wjgnet.com/bpg/gerinfo/204

GUIDELINES FOR ETHICS DOCUMENTS
https://www.wjgnet.com/bpg/GerInfo/287

GUIDELINES FOR NON-NATIVE SPEAKERS OF ENGLISH
https://www.wjgnet.com/bpg/gerinfo/240

PUBLICATION ETHICS
https://www.wjgnet.com/bpg/GerInfo/288

PUBLICATION MISCONDUCT
https://www.wjgnet.com/bpg/gerinfo/208

ARTICLE PROCESSING CHARGE
https://www.wjgnet.com/bpg/gerinfo/242

STEPS FOR SUBMITTING MANUSCRIPTS
https://www.wjgnet.com/bpg/GerInfo/239

ONLINE SUBMISSION
https://www.f6publishing.com

© 2023 Baishideng Publishing Group Inc. All rights reserved. 7041 Koll Center Parkway, Suite 160, Pleasanton, CA 94566, USA
E-mail: bpgoffice@wjgnet.com https://www.wjgnet.com

World Journal of Radiology

Submit a Manuscript: https://www.f6publishing.com

World J Radiol 2023 September 28; 15(9): 256-273

DOI: 10.4329/wjr.v15.i9.256

ISSN 1949-8470 (online)

REVIEW

Role of pulmonary perfusion magnetic resonance imaging for the diagnosis of pulmonary hypertension: A review

Miriam Lacharie, Adriana Villa, Xenios Milidonis, Hadeer Hasaneen, Amedeo Chiribiri, Giulia Benedetti

Specialty type: Radiology, nuclear medicine and medical imaging

Provenance and peer review: Unsolicited article; Externally peer reviewed.

Peer-review model: Single blind

Peer-review report's scientific quality classification

Grade A (Excellent): 0
Grade B (Very good): 0
Grade C (Good): C, C
Grade D (Fair): 0
Grade E (Poor): 0

P-Reviewer: Liu YJ, Taiwan; Xu L, China

Received: July 27, 2023
Peer-review started: July 27, 2023
First decision: September 4, 2023
Revised: September 16, 2023
Accepted: September 22, 2023
Article in press: September 22, 2023
Published online: September 28, 2023

Miriam Lacharie, Oxford Centre of Magnetic Resonance Imaging, University of Oxford, Oxford OX3 9DU, United Kingdom

Adriana Villa, Department of Diagnostic and Interventional Radiology, German Oncology Centre, Limassol 4108, Cyprus

Xenios Milidonis, Deep Camera MRG, CYENS Centre of Excellence, Nicosia, Cyprus, Nicosia 1016, Cyprus

Hadeer Hasaneen, School of Biomedical Engineering & Imaging Sciences, King's College London, London WC2R 2LS, United Kingdom

Amedeo Chiribiri, School of Biomedical Engineering and Imaging Sciences, Kings Coll London, Div Imaging Sci, St Thomas Hospital, London WC2R 2LS, United Kingdom

Giulia Benedetti, Department of Cardiovascular Imaging and Biomedical Engineering, King's College London, London WC2R 2LS, United Kingdom

Corresponding author: Miriam Lacharie, MSc, Researcher, Oxford Centre of Magnetic Resonance Imaging, University of Oxford, John Radcliffe Hospital, Headington, Oxford OX3 9DU, Oxford OX3 9DU, United Kingdom. miriam.lacharie@cardiov.ox.ac.uk

Abstract

Among five types of pulmonary hypertension, chronic thromboembolic pulmonary hypertension (CTEPH) is the only curable form, but prompt and accurate diagnosis can be challenging. Computed tomography and nuclear medicine-based techniques are standard imaging modalities to non-invasively diagnose CTEPH, however these are limited by radiation exposure, subjective qualitative bias, and lack of cardiac functional assessment. This review aims to assess the methodology, diagnostic accuracy of pulmonary perfusion imaging in the current literature and discuss its advantages, limitations and future research scope.

Key Words: Pulmonary perfusion MRI; Pulmonary hypertension; Dynamic contrast enhanced magnetic resonance imaging; Chronic thromboembolic pulmonary hypertension; Computed tomography pulmonary angiography; Chronic thromboembolic disease

©The Author(s) 2023. Published by Baishideng Publishing Group Inc. All rights reserved.

Core Tip: Chronic thromboembolic pulmonary hypertension is an under-diagnosed disorder with high mortality if not diagnosed on time, however it can be fully cured with efficient diagnostic tools. Pulmonary perfusion magnetic resonance imaging (MRI) provides a non-invasive, reliable, radiation free and safer diagnostic test potentially replacing the standard techniques. Cardiopulmonary MRI also provides a comprehensive cardiopulmonary assessment in one single visit resulting in patients' convenience and better utilization of healthcare resources and time.

Citation: Lacharie M, Villa A, Milidonis X, Hasaneen H, Chiribiri A, Benedetti G. Role of pulmonary perfusion magnetic resonance imaging for the diagnosis of pulmonary hypertension: A review. *World J Radiol* 2023; 15(9): 256-273
URL: https://www.wjgnet.com/1949-8470/full/v15/i9/256.htm
DOI: https://dx.doi.org/10.4329/wjr.v15.i9.256

INTRODUCTION

Pulmonary perfusion is crucial for the assessment of lung function, since proper pulmonary blood flow (PBF) and pulmonary ventilation are prerequisites for effective gas exchange. Pulmonary perfusion can be assessed by measuring mean pulmonary artery pressure (mPAP), pulmonary venous resistance (PVR), and pulmonary artery wedge pressure (PAWP) during right heart catheterization (RHC).

This normal pulmonary perfusion and ventilation pattern can be altered by several physiological and pathological conditions, including vascular (as in cases of chronic pulmonary thromboembolic disease - CTED) and parenchymal alterations (as in cases of lung fibrosis)[1]. These situations can lead to pulmonary hypertension (PH), PH is defined as mPAP of > 20 mmHg and PVR > 2.0 Woods Units[2].

PH is not a single entity, but rather a spectrum of disorders and can be due to multifactorial underlying pathophysiological mechanisms. Current guidelines classify PH in five types based on clinical presentation and aetiology: pulmonary arterial hypertension (PAH), PH due to left heart disease, PH due to lung disease, PH due to CTED (CTEPH) and PH due to unknown mechanisms (*e.g.*, associations include sarcoidosis, sickle cell anaemia, metabolic disorders, and others). Among all PH subtypes, CTEPH is the only treatable form; therefore, early, and accurate differential diagnosis is critical for therapy and prognosis[3,4].

CTEPH is caused by the chronic occlusion of pulmonary arteries due to thromboembolic material with subsequent increased mPAP and PVR, potentially leading to right heart failure and death if left untreated[5,6]. Risk factors for pulmonary thromboembolic vessel occlusion are age over 70, female gender, pulmonary embolism at first venous thromboembolic event, deep vein thrombosis, chronic obstructive pulmonary disease, heart failure and atrial fibrillation [7]. This article will discuss contemporary diagnostic methods to diagnose PH, what methods have been researched so far in medical literature and their diagnostic accuracy. It further explores advantages and limitations of current methods routinely used in clinical practice. It also discusses newly emerging techniques and future horizons of research in PH diagnosis.

Current imaging modalities used for PH diagnosis

Currently, the differential diagnosis of PH involves a multimodality approach including RHC, echocardiography, nuclear medicine based planer ventilation/perfusion scintigraphy scan (V/Q), single photon emission computed tomography (SPECT) scintigraphy and more recently a hybrid approach of combining SPECT and conventional computed tomography (SPECT-CT) scan[8]. All nuclear medicine techniques involve intravenous injection of radionuclide which emits gamma rays after reaching the region of interest in the body. These gamma rays are detected by gamma cameras providing functional assessment of lungs.

Planer scintigraphy has been largely replaced by SPECT because in SPECT gamma cameras rotate over a 360-degree arc around the patient providing three dimensional images which are crucial to detect small segmental perfusion defects.

Recently, hybrid SPECT-CT has also been used for clinical practice. It involves two different types of scans at the same time, a nuclear medicine scan involving radionuclide aerosol of technetium-99m diethylenetriaminepentaacetic acid delivered through a non-breathing mask which reaches to the distal tracheobronchial tree to reflect regional ventilation. Second part of study is an intravenous injection of TC-99m macro aggregates which gets lodged in pulmonary precapillary arterioles to provide pulmonary perfusion assessment *via* gamma camera[9,10]. At the same time, conventional CT scanner built in with the SPECT scintigraphy machine provides the anatomical details. Consequently, hybrid SPECT-CT can be considered superior to planar scintigraphy and SPECT alone.

Additionally, computed tomography pulmonary angiography (CTPA) has also been demonstrated to accurately detect pulmonary embolism, however it lacks the ability of dynamic pulmonary perfusion to detect perfusion defects at segmental and sub segmental pulmonary level. CTPA involves intravenous injection of iodine-based contrast injection and imaging of pulmonary arteries for the detection of contrast filling defect denoting pulmonary embolism.

Sensitivity and specificity of CTPA for pulmonary embolism varies from 83% to 100% and with recent advancements in SPECT the potential for routinely used modalities for CTEPH detection has been validated for pulmonary perfusion defect detection[11,12]. This is made possible by the high image resolution offered by multi slice CT scanning, allowing an accurate assessment of the location and severity of thromboembolic material up to the sub-segmental level, providing crucial information for the assessment of patients with CTEPH considered suitable for pulmonary endarterectomy (PEA)

[13]. Recently, dual energy computed tomography (CT) has further improved the assessment of patients with PH, thanks to the assessment of regional pulmonary perfusion with iodine perfusion maps[14].

Visual assessment of SPECT scintigraphy, SPECT-CT scintigraphy and CTPA images by expert radiologists is the routine clinical practice to identify partially or completely occluded pulmonary vessels and to assess lung perfusion.

Limitations of CTPA, V/Q scan and SPECT scintigraphy

Routine clinical tests for PH diagnosis are limited by radiation exposure causing carcinogenic stochastic effects (long-term cancer-causing effects after radiation exposure) and rarely deterministic effects (acute high dose exposure if radiation dose exceeds 100 mGy leading to skin erythema, organ damage/failure)[15]. However, these effects are extremely rare due to sophisticated equipment and specialised radiation dose lowering parameters.

The concern is exacerbated for women of child-bearing age, particularly considering the high female-to-male ratio (4.8:1) of incidence and prevalence of PH worldwide and harmful effects on foetal organogenesis[16,17]. Moreover, periodical follow-up to assess the disease progression is vital for PH management, imposing further radiation exposure.

The average effective radiation dose of V/Q scan has been estimated as 1.29 mSv, breast absorbed dose 0.37 mGy, uterus-absorbed dose 0.46 mGy and foetal absorbed doses of 0.40 mGy[18]. SPECT scintigraphy uses radionuclide doses of 25 to 30 MBq for ventilation and 100-120 MBq is usually required for a successful perfusion study[9,19].

Another limitation of current techniques like CTPA is ionising radiation exposure. The effective radiation dose of CTPA has been estimated to be 21 mSv and breast absorbed dose from 44 mGy to as high as 70 mGy to radiosensitive breast tissue[18,20]. Potential carcinogenic ionising radiation exposure and the need for frequent follow-up assessments by conventional tests for PH patients are a few limitations of current imaging tests for pulmonary embolism-based PH diagnosis[21].

Furthermore, as PH can inevitably affect cardiac functions, a single test including the assessment of left and right ventricular function and myocardial tissue characterisation would be desirable for a comprehensive assessment.

In a relevant study, researchers validated that cardiac magnetic resonance imaging (MRI) derived pulmonary artery pressure ejection fraction, RV stroke volume, cardiac output, ventricular mass index and pulmonary blood flow in non-treated lobes correlated with pulmonary blood flow changes in treated lobes post balloon pulmonary angioplasty $P < 0.05$. Furthermore, utility of pulmonary artery pulsatility and pulmonary artery flow measurement by cardiac MRI as an early marker of pulmonary hypertension has also been verified in another prospective study[22]. Therefore, these studies emphasize the significance of a comprehensive, non-invasive and ionising radiation free cardiopulmonary assessment using cardiac magnetic resonance and pulmonary MRI in a single setting.

Finally, in clinical practice these imaging tests are assessed visually only, which is prone to an observer-dependent evaluation, and the availability of quantitative analysis techniques could provide additional value.

Need of improved imaging assessment of CTEPH

Unfortunately, CTEPH retains high mortality, and the mean life expectancy has been reported as less than three years if left untreated[3,23]. Currently, CTEPH can be treated with PEA, which consists of the surgical resection of the thromboembolic material. Before PEA, the three-year mortality of CTEPH was over 50%[24]. It has been demonstrated that PEA can lead to significant improvements in hemodynamic and exercise capacity[23]. Delayed treatment however is still associated with poor prognosis, therefore early detection of CTEPH is critical[25].

A prospective European study of 679 patients with CTEPH, of which 386 underwent PEA, reported an in-hospital mortality rate as low as 4.7% and 1-year mortality of 7%, while the exercise capacity and pulmonary vascular resistance were significantly improved[26]. In another study, the mortality rate in 1500 consecutive CTEPH patients post PEA was investigated between 1999 and 2010. Outcomes were compared between historical cohorts and more recent patients, who received surgical treatment for distal disease affecting smaller pulmonary vessels. A significant reduction of mortality rate from 5.2% to 2.2% was observed, despite the more distal disease, reflecting a continuous improvement in surgical techniques and highlighting the need for more sensitive tests capable of identifying distal disease[27].

Most of CTEPH patients in these studies stated remarkable relief from symptoms after PEA and a return to near normal hemodynamic values[26-28]. These promising results of surgical treatment support the quest for new diagnostic methods capable of early differential diagnosis and further developments of surgical techniques for targeted intervention. Moreover, improved diagnostic tools are necessary for differentiating CTEPH from the other four types of PH because treatment pathways vary accordingly. Currently, this differentiation is based only on imaging tests that employ ionising radiations.

Recently, pulmonary perfusion MRI has been emerged as a powerful tool for the assessment of pulmonary hypertension, and particularly for the differential diagnosis of CTEPH[29]. Perfusion MRI can be performed using dynamic contrast imaging or without contrast using arterial spin labelling[30].

The aim of this review article is to provide an overview of the published studies on lung perfusion MRI, highlighting the limitations of standard tests and the role of perfusion MRI as a diagnostic tool for PH. Moreover, the review focuses on the methodology, advantages, challenges, and future directions for pulmonary perfusion MRI and its potential contribution to overall healthcare policies.

LITERATURE SEARCH

A comprehensive literature search was performed using, PubMed, EMBASE and Medline databases. To develop the literature search question, a PICO framework was adopted: Population; PH patients, Intervention; MRI, Comparison;

SPECT/CTPA, Outcome; diagnostic accuracy. Original prospective and retrospective studies were included in the literature search with or without direct comparison of pulmonary perfusion MRI to gold standard tests for the diagnosis of PH[31-55] in Table 1. Tables 2-4 provide the PICO framework, eligibility criteria for included studies and facet analysis with search strategy respectively. Figure 1 demonstrates the PRSMA flow chart for literature search.

Note that the acronym "Dynamic contract enhanced MRI (DCE-MRI)" was frequently used in the selected studies instead of pulmonary perfusion MRI.

Pulmonary perfusion MRI - methodology

MRI uses the interaction between a magnetic field, hydrogen ions in the body and radiofrequency pulses to generate diagnostic images in multiple planes with high spatial resolution and without the need for ionising radiation. An MRI sequence involves repeated application of radiofrequency pulses to the magnetized hydrogen ions in the body and measuring the MRI signals while the hydrogen ions are demagnetized over time (echo time, TE)[56]. Because of the inherent difference in magnetic susceptibility between lung parenchyma and air, MRI of lungs is prone to wider frequency distribution and phase dispersion, leading to suboptimal noisy images[57]. To mitigate this susceptibility effect, recent advancements in lung MRI are ultra-short echo and zero echo time acquisitions, allowing accelerated scan time whilst preserving optimal image quality[58,59].

For fast pulmonary vasculature imaging, gradient pulse sequences with short radiofrequency repetition time and short time to receive the signal are typically employed, which allows acquisition of dynamic images of the lungs in real time as contrast agent flows through the pulmonary vasculature[60] (Figure 2[34]).

A commonly used gradient echo pulse sequence for perfusion MRI is 3-dimensional fast low angle shot (FLASH) MRI acquiring dynamic perfusion images of lungs[61]. The dynamic visualisation of the first pass of the contrast agent across the pulmonary circulation is a crucial requirement for the assessment of lung perfusion[61,62].

Several studies have used 3D FLASH perfusion MRI for the detection of chronic thromboembolic disease[33,34,37,63]. However, 3D FLASH perfusion MRI is limited by reduced image resolution and anatomical coverage[64,65]. This is due to the under sampling of the MRI k-space in FLASH MRI imaging. This under sampling of data leads to fast imaging at the expense of image resolution and anatomical coverage.

Ideally, a combination of high temporal resolution (fast imaging) – capable to resolve the dynamic first-pass of the contrast agent, full coverage of the lung fields, and high spatial resolution to capture small pulmonary defects would be required for the optimal differential diagnosis of CTED.

Recently, simultaneous multi-slice (SMS) balanced steady state free precession (b-SSFP) imaging has emerged to solve this problem, allowing better anatomical coverage, increased image resolution and accelerated scan time enabling acquisition of multiple slices simultaneously[65,66]. Therefore, it potentially leads to better visualisation of small pulmonary perfusion defects which can be easily missed in case of sub optimal image quality.

SMS b-SSFP has been recently validated for cardiac perfusion imaging where it doubled spatial coverage by acquiring 6 slices at the same time it takes for conventional sequences to acquire 3 slices, while preserving in-plane resolution[65]. The use of SMS b-SSFP for pulmonary perfusion imaging has not been extensively researched, yet further research is warranted considering its promising results for increased anatomical coverage with high image resolution and shorter scan time for cardiac perfusion.

Additionally, pulmonary perfusion MRI involves antero-posterior coronal images covering both lungs and image acquisition on inspiration to minimize respiratory artefacts. To assess perfusion defects, a gadolinium-based MRI contrast injection is used, which offers hyper-intense or hypo-intense signals depending on the amount of blood perfusion in the region of interest over time (dynamic imaging). Recently, free breathing lung MRI was also validated for image quality and reproducibility, showing promise for increased patient comfort during scanning of PH and patients with other lung diseases causing poor breath holding[67,68].

Pulmonary perfusion MRI images can be assessed qualitatively and quantitatively.

Qualitative (visual) assessment of pulmonary perfusion MRI

Current clinical practice is to visually assess the lung perfusion MRI images during the passage of contrast agent through the pulmonary circulation. Dynamic pulmonary perfusion MRI leads to the visualisation of pulmonary arteries' contrast distribution: a pulmonary segment with normal perfusion shows a good and homogeneous perfusion, while the lung territory supplied by a pulmonary artery with partial or complete occlusion due to thromboembolic material will show reduced and delayed perfusion. Impaired lung perfusion can be visually assessed as a wedge-shaped perfusion defect on the pulmonary perfusion images.

However, this observer based qualitative assessment is prone to inter- and intra-observer variations leading to subjective interpretations[69,70].

Quantitative assessment of pulmonary perfusion MRI

To mitigate subjective bias, pulmonary perfusion MRI also allows quantification of perfusion parameters: Pulmonary blood flow, pulmonary blood volume and mean transient time of blood flow (Figures 3 and 4[33,50]) which requires tracing of the contrast agent passing through the tissue of interest and an arterial input function (AIF) curve corresponding to the signal intensity in the blood pool over time[66].

Perfusion quantification is based on the principles of the indicator dilution theory, relating the AIF and tissue enhancement curves *via* the process of deconvolution[71-73], and is often used for the measurement of myocardial blood flow[74]. Pulmonary blood volume (PBV) and mean transit time (MTT) can be subsequently estimated according to the central volume theorem[33,73]. Quantification is, however, significantly impacted by the nonlinear relationship of the

Table 1 Characteristics of included studies

Ref.	Study design	Patients (*n*)	Demographics	Aims	Methodology	Analysis	Results (95%CI)
Amundsen *et al*[31], 1997	Prospective, qualitative	7	7 patients with suspected PE	To evaluate the feasibility of perfusion MRI for detection of perfusion defects distal to suspected pulmonary embolism compared to V/Q	Rapid acquisition of two sets of dynamic images in coronal and trans axial plane	Qualitative analysis (MRI Vs V/Q)	Perfusion MRI correctly identified 16/18 lung segments with perfusion defects
Amundsen *et al*[32], 2002	Prospective, qualitative	42	20 suspected PE, 11 Pneumonias, 11 COPD	To compare perfusion MRI and V/Q for the perfusion defects detection	Rapid acquisition of two sets of dynamic images in coronal and trans axial plane with an inversion recovery gradient MRI sequence	Qualitative analysis (MRI Vs V/Q)	For PE: Intra-modality kappa = 0.77, Inter-observer kappa = 0.92
Ohno *et al*[33], 2004	Prospective, qualitative	40	Controls=15, (Mean age 42 yr), PH patients=25, (Mean age 61 yr)	To assess regional differences in quantitative pulmonary perfusion parameters using MRI	Three dimensional ultrafast DCE-MRI was performed and PBF, PBV & MTT measured by signal intensity time course curve	MATLAB, For PBF, MTT, PBV, Mean, SD, ANOVA, Fisher's PLSD test	PBF, PBV & MTT showed significant differences between normal volunteers and patients with PH ($P < 0.05$)
Nikolaou *et al* [34], 2005	Prospective, qualitative	29	16 females (mean age 54 ± 17 yr), 13 males (Mean age 57 ± 15 yr)	Pulmonary hypertension & CTEPH differen-tiation by perfusion MRI and pulmonary angiography	Turbo fast low angle shot gradient echo MRI sequence was performed by using generalized auto calibrating partially parallel technique or GRAPPA	Student t test for significance, ROC using SPSS software	**ROC:** MRA = 0.85, MRI = 0.82, MRA, MRI combined0.90
Kluge *et al* [35], 2005	Prospective, qualitative	31	15 females, 18 males, (Mean age 59.4 yr) with acute PE	To compare the feasibility of perfusion MRI with CT for follow up examination in acute PE	Contrast enhanced 3-dimensional fast low angle shot or FLASH sequence was used for perfusion MRI and time to peak and peak enhancement was measured	T test for paired samples using SPSS	Follow up examination using MRI were feasible compared to CT for all patients
Kluge *et al* [36], 2006	Prospective, qualitative	41	41 patients with suspected PE	To assess the agreement of perfusion MRI with SPECT for identifying perfusion defects	Contrast enhanced 3-dimensional fast low angle shot or FLASH sequence was used for perfusion MRI	Not given	MRI and SPECT agreement kappa Lobar = 0.98, Segmental = 0.98, Subsegmental = 0.69
Ohno *et al*[37], 2007	Prospective, qualitative	28	Controls=14, (Mean age 34 yr), PH patients=14, (Mean age 41 yr)	To measure diagnostic potential of DCE-MRI for pulmonary hypertension	Three dimensional ultrafast DCE-MRI was performed and PBF, PBV & MTT measured by signal intensity time course curve	MATLAB, For PBF, MTT, PBV, MathWorks, Mean, SD, T test	Difference for study groups: PBF: $P < 0.0001$, PBV: $P < 0.0001$, MTT: $P < 0.0001$
Ley *et al*[38], 2007	Prospective, qualitative	25	Controls=5, PH patients=20	To measure diagnostic potential of DCE-MRI for pulmonary hypertension	Contrast enhanced 3-dimensional fast low angle shot or FLASH sequence was used for perfusion MRI	Quantitative analysis of PBF, PBV and MTT, Mann-Whitney U-test	PBF, PBV & MTT showed significant differences between normal volunteers and patients with PH ($P < 0.05$)
Ohno *et al*[39], 2008	Prospective, qualitative	27	Controls = 9, 18 gender and age matched CTD patients	To measure diagnostic potential of DCE-MRI for PAH	PBF, MTT and PBV measured by DCE-MRI and correlated by %DL(CO) measured by pulmonary function test and mPAP, sPAP measured by doppler echo	MATLAB, MathWorks, Mean, SD, T test, Correlation test	PBF, MTT, PBV correlated positively with %DL(CO) & sPAP ($P < 0.05$), PBF& PBV correlated positively with mPAP& moderately with PVR ($P < 0.05$)
Ohno *et al*[40], 2010	Prospective, qualitative	50	50 PE patients with acute pulmonary thromboembolism (APTE)	To measure diagnostic potential of DCE-MRI for acute pulmonary	PBF, PBV, MTT & APTE index measured by DCE-MRI using 3-dimensional spoiled	ROC curve, Logistic regression	PBF and MTT significantly lower for APTE segments to non-APTE segments (

				thromboembolism (APTE)	gradient sequence, MPAP, PVR measured by RHC. RV/LV diameter ratio, APTE index measured by CT & MRA		$P < 0.05$), APTE indexes from all modalities proved significant predictors for differentiating APTE patients
Stein *et al*[41], 2010	Prospective, qualitative	371	371 adults with diagnosed or excluded pulmonary embolism- (PIOPED III)	To assess performance of MRA and venography for pulmonary embolism detection	MRA was compared with CTPA, V/Q scan, venous ultrasonography, D-dimer assay, and clinical assessment, Qualitative assessment by expert reader only	Chi-square test ANOVA	Technically adequate images for MRA: SE: 78%, SP: 99%
Kang *et al*[42], 2011	Prospective, qualitative	35	35 PAH patients (Mean age 44 yr)	To assess if Cardiac MRI based pulmonary artery distensibility index correlates with RHC estimates for PAH	Pulmonary artery distensibility indices were derived from transverse view MRI and compared with PVR using RHC	Correlation	Non-invasive MRI based pulmonary artery distensibility index correlates with RHC based estimates $P < 0.001$
Ohno *et al*[43], 2012	Prospective, qualitative	24	Response group=13, Non-response group=11, 12 females & 12 males mean age 68 yr ± 8.6	CTPA, MRA & DCE-MRI comparison for treatment response in inoperable CTEPH patients	PBF, PBV, MTT measured by DCE-MRI using 3-dimensional spoiled gradient sequence, RV/LV diameter ratio and embolic burden measured by CTPA & MRA	Mean of student T test, Correlation, ROC curve analysis, McNemar's test	DCE-MRI SP = 90%, AC = 95%, CTPA SP = 36%, AC = 70%, MRA SP = 54%, AC = 79%
Ley *et al*[44], 2013	Prospective, qualitative	20 PAH or CTEPH patients	Controls 10, Training group 10	To evaluate if training improves pulmonary perfusion in PH as assessed by MR perfusion imaging	Training group received in hospital exercise training while control group received conventional rehabilitation. 6 min walk test, PBF, PBV, MTT & peak flow velocity measured by MR perfusion were assessed for both groups from baseline to 3 wk	Mann-Whitney-Wilcoxon test, Spearman correlation coefficient	Training group had significantly improved 6-min walk test, MR flow and MR perfusion
Rajaram *et al* [45], 2013	Prospective, qualitative	132	78 CTEPH patients	To compare the diagnostic accuracy of perfusion MRI for CTEPH Vs. CTPA and V/Q	Pulmonary perfusion MRI using time resolved 3-Dimensional spoiled gradient and pulmonary MRA were compared with CTPA and V/Q	Not given	SE, SP in %, MRI: 97, 92, V/Q: 96, 90, CTPA: 94, 98
Revel *et al*[46], 2013	Prospective, qualitative	274	274 suspected PE patients	To evaluate unenhanced, enhanced perfusion and MR angiography for PE detection	Unenhanced steady state free precession or SSFP, fast spoiled gradient echo for perfusion MRI and MR angiography were compared with CTPA	Chi-squared Kappa statistics	Kappa agreement MRA = 0.77, Perfusion MRI = 0.51, Unenhanced MRI = 0.62
Sugimoto *et al* [47], 2013	Prospective, qualitative	34	34 congenital heart disease patients	To assess if velocity encoded cine imaging can measure pulmonary artery pressure in children with congenital heart disease	Pulmonary blood flow (QP), systemic blood flow (QS), acceleration time, ejection time, peak velocity, and maximal change in flow rate during ejection (MCFR) were measured by velocity encoded MRI and RHC		Velocity encoded MRI correlated strongly with RHC for QS, right to left QP ratio and QP/QS. Suggesting usefulness of MRI for pulmonary artery pressure measurement
Schoenfeld *et al*[48], 2015	Prospective, qualitative	64	64 ruled out or confirmed PE patients	To compare perfusion weighted Fourier decomposition or PW-FD to DCE-MRI for PE detection	Time resolved angiography with stochastic trajectories or TWIST for DCE-MRI was used and compared with PW-FD	Qualitative only, Kappa statistics	For PW-FD per patient basis, SE = 100%, SP = 95%, PPV = 98%, NPV = 98%, Intraobserver k = 0.96, Interobserver k = 0.96
Ingrisch *et al* [49], 2016	Prospective, qualitative	18	8 acute PE, 10 controls	DCE-MRI evaluation for acute PE	Qualitative assessment of presence and	Cohen's kappa, Fisher's	SE: 87-93%, SP: 90-95%, PPV: 87-93%,

				detection compared with CTPA	absence of perfusion defects using DCE-MRI using TWIST sequence	exact test	NPV: 90-95%, Inter-reader agreement: k = 0.77, Intra-modality agreement: $P < 0.001$
Johns *et al*[50], 2017	Prospective, qualitative	74	20 male, 26 female, Mean age 62 ± 14 yr	DCE-MRI, SPECT & CTPA comparison for CTEPH diagnosis	Qualitative comparison of presence/absence of perfusion defects on DCE-MRI using fast spoiled gradient echo, perfusion, SPECT and CTPA	2*2 predictive table, Kappa (k) for inter-observer agreement	SE: 100%, SP: 81%, PPV: 90%, NPV: 100%, Inter-observer agreement for DCE-MRI: k = 0.88, SPECT: (k = 0.80)
Voskrebenzev *et al*[51], 2018	Prospective, qualitative	5	2 controls, 1 CTEPH patient 1 CF patient, 1 obstructive pulmonary disease patient	To assess the feasibility of phase resolved functional lung MRI (PREFUL) for quantitative reginal ventilation and perfusion	Time to peak, V/Q maps and fractional ventilation flow volume were calculated using PREFUL MRI	Full Cardiac and respiratory cycle were sorted using PREFUL	Post endarterectomy, CTEPH patient showed increased perfusion time to peak in visual agreement with DCE-MRI
Agoston-Coldea *et al* [52], 2018	Prospective, qualitative	30	30 consecutive patients with COPD and suspected secondary pulmonary hypertension	To evaluate ability of CMR right ventricular parameters and pulmonary artery stiffness to identify pulmonary hypertension	Clinical examination. 6-min walk test, echocardiography, RHC and cardiac functions and late gadolinium CMR imaging with phase contrast flow imaging of pulmonary artery. Followed up for a mean period of 16 mo	ROC curve analysis, Kolmogorov-Smirnov test, ANOVA test. Fischer's exact test	Pulse wave velocity: SE = 93.5%, SP = 92.8%
Schoenfeld *et al*[53], 2019	Prospective, qualitative	29	20 CTEPH patients	Cardiopulmonary evaluation of treatment response after BPA in CTEPH patients	PBF and first pass bolus kinetic parameters and biventricular mass and functions were evaluated using MRI	Paired two sides Wilcoxon rank sum test, Spearman p correlation, Multiple linear regression	Post BPA, PBF changes in treated lobes were significantly higher than non-treated lobes $P < 0.05$, MRI derived pulmonary artery pressure ejection fraction, RV stroke volume, CO, ventricular mass index & PBF in non-treated lobes correlated with PBF changes in treated lobes $P < 0.05$
Ray *et al*[54], 2019	Prospective, qualitative	51	20 mild PH, 31 moderate to severe PAH	Utility of pulmonary artery pulsatility by cardiac MRI as an early marker of pulmonary hypertension	Standards steady state free precession or cine SSFP for pulmonary artery pulsatility and phased contrast MRI imaging for pulmonary flow assessment	Wilcoxon rank sum test, Roc analysis	Pulmonary artery pulsatility declined from normal (53%), mild (22%) and moderate to severe PAH (17%)
Alsady *et al* [55], 2021	Prospective, qualitative	20	20 CTEPH patients	To compare DCE-MRI and computed tomography for lung perfusion defects before and after pulmonary endarterectomy	Lobe based analysis of perfusion defects using DCE-MRI and PBF and PBV measurement, comparison with dual energy computed tomography	Pearson product-moment correlation, Paired t test using MATLAB	Correlation between CT and MRI based perfusion defects ($r > 0.78$; $P < 0.001$)
Torres *et al* [56], 2022	Prospective, qualitative	41	20 IPF patients	DCE-MRI for the evaluation of lung perfusion in IPF	PBF CV, FVC% predicted %DL(CO) and LCI% were evaluated using DCE-MRI	Regression analysis, Spearman rank correlation	DCE-MRI identified regional perfusion defects between controls and IPF ($P < 0.05$). Correlation observed between PBF CV and %DL(CO) ($r = 0.48$, $P < 0.001$)

AC: Diagnostic accuracy; APTE: Acute pulmonary thromboembolism; BPA: Balloon pulmonary angioplasty; CI: Confidence interval; COPD: Chronic obstructive pulmonary disease; CTEPH: Chronic thromboembolic pulmonary hypertension; CTPA: computed tomography pulmonary angiography; CO: Cardiac output; CV: Coefficient of variation; DCE-MRI: Dynamic contrast enhanced magnetic resonance imaging; %DL(CO): Diffusing capacity of carbon monoxide; LV: Left ventricle; LCI: %(lung clearance index), MRA: Magnetic resonance angiography; MTT: Mean transit time; NPV: Negative predictive value; PAP: pulmonary artery pressure; PBF: Pulmonary blood flow; PBV: Pulmonary blood volume; PE: Pulmonary embolism; FVC: % Percent predicted

forced vital capacity; PPV: positive predictive value; PVR: Pulmonary venous resistance; ROC: Receiver operating curve; SE: Sensitivity; SP: Specificity; sPAP: Systolic pulmonary artery pressure; SPECT: Single photon emission Computed tomography; SPSS: Statistical package for social sciences; RV: Right ventricle; V/Q: Ventilation perfusion scan.

measured signal with contrast agent concentration leading to errors in quantitative metrics.

Non-linearity is caused by spatial signal variations due to variations in sensitivity profiles of MRI surface coils, contrast bolus related T2* decay and subsequent signal loss[66]. To mitigate this effect, a dual-contrast bolus approach can be used, where a dilute (low concentration) bolus is injected for AIF measurement and a neat (high concentration) bolus is subsequently injected for signal intensity measurement in the lung tissue[75]. Researchers reported that the dual-bolus approach is feasible for pulmonary perfusion MRI, reducing the inherent nonlinearity between contrast concentration and signal intensity[76].

Recently, the dual-sequence approach was introduced to avoid the complexity of injector set up and issues of non-linearity for cardiac perfusion MRI[77]. The dual-sequence approach is more practical in busy clinical settings, as it involves injection of a single contrast bolus. The sequence acquires a low resolution slice by FLASH readout for sampling the AIF, followed by acquisition of high resolution short-axis slices using SSFP or FLASH readout[78]. This dual-sequence technique has been validated for cardiac perfusion imaging for its linearity for signal conversion to contrast bolus concentration[66].

Clinically, MRI perfusion quantification permits user-independence quantification of PBF, PBV and MTT at the global, lobar, and segmental pulmonary levels, minimising inter- and intra-observer qualitative bias[69]. Quantification of perfusion parameters allow narrowing down the differential diagnosis of lesions associated with increased or decreased PBF or PBV, (as in the case of chronic thromboembolic partial or complete obstruction of pulmonary vasculature[79].

Diagnostic accuracy of pulmonary perfusion in the literature

Evaluation of pulmonary thromboembolic disease by lung perfusion MRI is a relatively new imaging technique, and its diagnostic potential has been reported comparable with the routinely performed tests of CTPA and SPECT scintigraphy [43,50,63]. The diagnostic accuracy of pulmonary perfusion has been tested qualitatively and quantitatively.

Qualitative assessment: An early feasibility study looking at the diagnostic accuracy of perfusion MRI for detecting lung perfusion defects in patients with pulmonary embolism revealed a good inter-modality agreement with V/Q scan by correctly identifying 16 out of 18 perfusion defects[31].

The diagnostic accuracy of pulmonary perfusion MRI has been demonstrated comparable to V/Q scan measured by the Kappa statistic (k) for inter-observer and inter-modality agreement (inter-observer agreement: k = 0.63 and inter-modality agreement: k = 0.79) in another prospective qualitative study assessing the treatment response of inoperable CTEPH patients[34].

A prospective qualitative study on 78 CTEPH patients assessing the diagnostic accuracy of pulmonary perfusion MRI concluded a sensitivity of 97% and specificity of 92% compared to V/Q and CTPA[45]. Another qualitative comparison for evaluating the diagnostic potential of pulmonary perfusion MRI for the detection of pulmonary embolism reported a sensitivity of 87%-93% and a specificity of 90%-95% with an inter-observer agreement of k = 0.77[49]. Similarly, another study prospectively comparing the diagnostic potential of perfusion MRI, perfusion SPECT and CTPA revealed sensitivity 100% and specificity 81% with inter-observer agreement of k=0.88 for perfusion MRI compared to inter-observer agreement of k = 0.80 ($P < 0.0001$) for SPECT scintigraphy[50].

Quantitative assessment: Prospective quantitative studies affirm the diagnostic potential of pulmonary perfusion MRI by measuring the perfusion parameters of PBF, PBV and MTT for normal, CTEPH and PH of other aetiologies leading to early differential diagnosis and better disease management[37,39,40,43].

Pulmonary perfusion parameters of PBF, PBV and MTT for healthy volunteers and PH patients were quantitatively assessed in a prospective study. Pulmonary perfusion parameters were significantly lower for PH patients accurately differentiating the two study groups[33]. Furthermore, pulmonary perfusion MRI diagnostic accuracy was confirmed in another relevant study where significant results were reported for all three pulmonary perfusion MRI parameters correctly differentiating the two study groups and aiding the differential diagnosis of primary pulmonary hypertension [37].

Additionally, the capability of pulmonary perfusion MRI for the evaluation of disease severity and progression of PAH was compared with pulmonary function test and Doppler echocardiography. Pulmonary perfusion MRI was positively correlated with diffusing capacity of carbon monoxide %DL(CO) measured by pulmonary function test. In the same study, pulmonary perfusion MRI parameters of PBF, PBV and MTT were also positively correlated with mean pulmonary artery pressure and systolic pulmonary artery pressure measured by Doppler echocardiography[39]. This significant correlation implies promising diagnostic potential of pulmonary perfusion MRI for detecting PAH when compared to routine tests.

In another quantitative prospective study, specificity and accuracy of pulmonary perfusion MRI were compared with MDCT and magnetic resonance angiography (MRA) for PH diagnosis. Specificity and accuracy were significantly higher for pulmonary perfusion MRI when right ventricle/Left ventricle diameter ratio and acute pulmonary thromboembolic indices were compared for perfusion MRI, MDCT and MRA ($P < 0.05$). This implies comparable diagnostic capability for pulmonary perfusion MRI to routine tests for PH diagnosis. In this study, PBF was reported as a more accurate perfusion MRI parameter than PBV and MTT[40].

Table 2 Population (P), Intervention (I), Comparison (C), and Outcomes (O) model

PICO	
Population	Pulmonary hypertension patients
Intervention	Cardio-pulmonary MRI, DCE-MRI and/or MRA and/or PREFUL Imaging
Comparator	Computed tomography pulmonary angiography (CTPA) and/or ventilation perfusion (V/Q) scan
Outcome	Diagnostic accuracy
Time frame	1997-2022
Study type	Original retrospective or prospective studies and randomised controlled trials only

MRI: Magnetic resonance imaging; DCE-MRI: Dynamic-contrast enhanced MRI; MRA: Magnetic resonance angiography; PREFUL: Phase resolved functional lung imaging.

Table 3 Inclusion and exclusion criteria for study selection

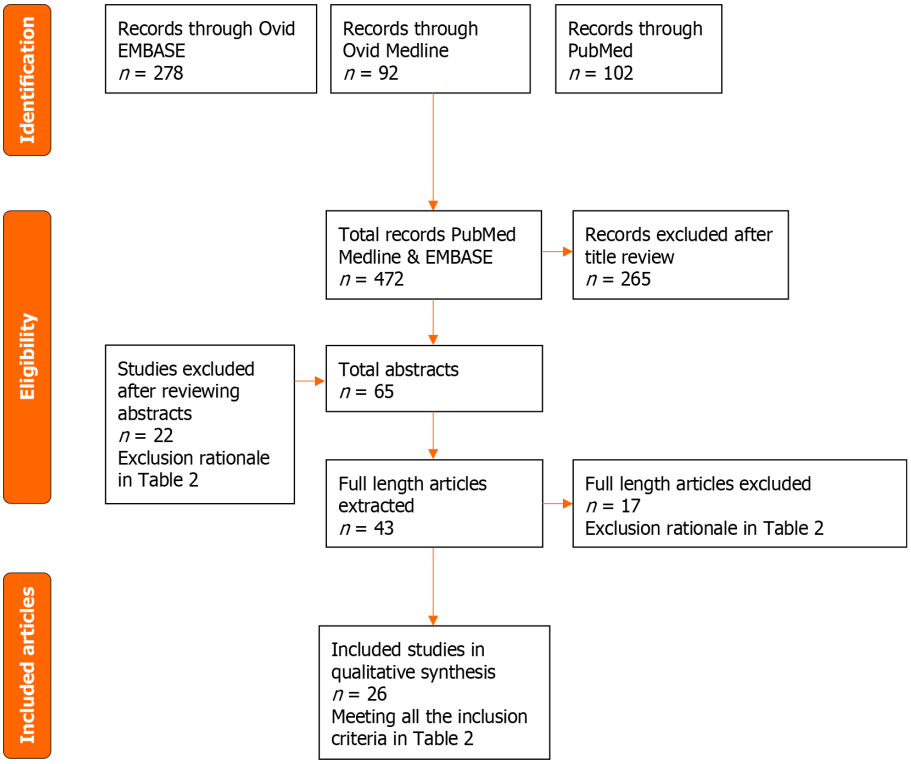
Inclusion criteria	Exclusion criteria	Rationale
All publication to date	N/A	To avoid missing any relevant studies
English articles	Articles not translated into English	Difficult comprehension
Known or suspected PH patients	Other pulmonary conditions	Pulmonary hypertension is the focus of the study
Original research Prospective/Retrospective only	Reviews, meta-analyses, and case reports	Complicates the results Irrelevant study designs
Papers discussing diagnostic accuracy of MRI, CTPA and V/Q scan	Papers discussing diagnostic accuracy of gas exchange and other techniques	Irrelevant for current study focus

CTPA: Computed tomography pulmonary angiography; MRI: Magnetic resonance imaging; N/A: Not applicable; PH: Pulmonary hypertension.

Table 4 Facet analysis and search strategy

Electronic database	Search string
PubMed	("Pulmonary hypertension" OR "Pulmonary arterial hypertension" OR "Chronic Thromboembolic Pulmonary Hypertension" OR "Left heart pulmonary hypertension" OR "Lung disease pulmonary hypertension" OR "Pulmonary veno-occulusive disease") AND ("Magnetic Resonance Imaging" OR "Pulmonary perfusion Magnetic Resonance Imaging" OR "Cardiac Magnetic Resonance Imaging" OR "Magnetic resonance angiography" OR "Phase resolved functional " OR "Dynamic Contrast Enhanced-Magnetic Resonance Imaging" OR "3Dimensional Dynamic Contrast Enhanced-Magnetic Resonance Imaging" AND ("Computed Tomography pulmonary angiography" OR Ventilation/perfusion scan") AND ("Specificity" OR "Sensitivity" OR "Diagnostic accuracy" OR "Positive predictive value" OR "Area under the curve" OR "screening accuracy")
EMBASE	("Pulmonary hypertension" OR "Pulmonary arterial hypertension" OR "Chronic Thromboembolic Pulmonary Hypertension" OR "Left heart pulmonary hypertension" OR "Lung disease pulmonary hypertension" OR "Pulmonary veno-occulusive disease") AND ("Magnetic Resonance Imaging" OR "Pulmonary perfusion Magnetic Resonance Imaging" OR "Cardiac Magnetic Resonance Imaging" OR "Magnetic resonance angiography" OR "Phase resolved functional " OR "Dynamic Contrast Enhanced-Magnetic Resonance Imaging" OR "3Dimensional Dynamic Contrast Enhanced-Magnetic Resonance Imaging" AND ("Computed Tomography pulmonary angiography" OR Ventilation/perfusion scan") AND ("Specificity" OR "Sensitivity" OR "Diagnostic accuracy" OR "Positive predictive value" OR "Area under the curve" OR "screening accuracy")
Medline	("Pulmonary hypertension" OR "Pulmonary arterial hypertension" OR "Chronic Thromboembolic Pulmonary Hypertension" OR "Left heart pulmonary hypertension" OR "Lung disease pulmonary hypertension" OR "Pulmonary veno-occulusive disease") AND ("Magnetic Resonance Imaging" OR "Pulmonary perfusion Magnetic Resonance Imaging" OR "Cardiac Magnetic Resonance Imaging" OR "Magnetic resonance angiography" OR "Phase resolved functional " OR "Dynamic Contrast Enhanced-Magnetic Resonance Imaging" OR "3Dimensional Dynamic Contrast Enhanced-Magnetic Resonance Imaging" AND ("Computed Tomography pulmonary angiography" OR Ventilation/perfusion scan") AND ("Specificity" OR "Sensitivity" OR "Diagnostic accuracy" OR "Positive predictive value" OR "Area under the curve" OR "screening accuracy")

Moreover, researchers compared the accuracy of treatment response in inoperable CTEPH patients using pulmonary perfusion MRI, CTPA and MRA. This comparative prospective study found higher diagnostic accuracy (95%) and specificity (90%) for pulmonary perfusion MRI compared to CTPA to differentiate treatment responders and non-responders[43]. A recent quantitative study assessed the regional PBF pre and post PEA using pulmonary perfusion MRI and compared it with exercise capacity post PEA for CTEPH patient. They concluded a positive correlation between perfusion MRI for identifying improvement in PBF in the lower lungs and exercise capacity after successful surgery[80].



DOI: 10.4329/wjr.v15.i9.256 **Copyright** ©The Author(s) 2023.

Figure 1 PRISMA flow chart for literature search.

This literature search concludes the approving potential of pulmonary perfusion MRI for the differential diagnosis of PH. However, most of these comparative studies were single centre with small sample size, therefore further large-scale multicentre research is recommended.

Hyperpolarised inhaled contrast agent pulmonary MRI

Hyperpolarised gases like ^{3}He, ^{129}Xe and Oxygen-enhanced ^{1}H have also gained popularity for assessing pulmonary ventilation and perfusion in lung diseases. A retrospective study on 15 patients was conducted to assess regional lung ventilation as part of pre-operative planning of lobectomy, pneumonectomy or lung volume reduction surgery. This study reported good agreement between ^{3}He MRI and scintigraphy ventilation imaging to diagnose ventilation defects [81]. Another case study of CTEPH patient demonstrated the use of ^{3}He ventilation scan combined with dynamic contrast enhanced perfusion MRI to assess the treatment response of pre and post PEA[82].

^{129}Xe is of particular interest for CTEPH diagnosis because ^{129}Xe has an ability to dissolve in pulmonary tissues. After inhalation, ^{129}Xe is easily soluble in lung tissues and blood leading to frequency shift which can be quantitatively measured by MR spectroscopy[83]. ^{129}Xe has been tested to demonstrate a reduced uptake of red blood cells in CTEPH and pulmonary vascular disease patients indicating perfusion defects[84,85]. Another study on 10 PAH patients, ^{129}Xe MRI showed reduced RBC amplitude oscillations on MRI spectroscopy implying its potential to diagnose pulmonary vascular diseases from other lung disorders[86]. These initial results reflect the potential of combining hyperpolarised gas MRI imaging with cardiopulmonary MRI to comprehensively assess the structural and functional ventilation and perfusion pulmonary disorders.

However, hyperpolarised inhaled contrast agent pulmonary MRI is still an emerging modality and further large-scale research is needed to strengthen its diagnostic potential to conventional perfusion scintigraphy.

Advantages of pulmonary perfusion MRI

Ionising radiation free diagnostic test: Screening and follow-up scans to monitor the disease progression is a crucial part of management strategy for patients with PH. In a prospective longitudinal study in a cohort of 675 emergency department patients researchers concluded that at least one third of patients undergoing CTPA were called for a follow up scan within 5 years, with one fifth of patients being women younger than 40 years old[21]. In addition, it is estimated that 5% to 11% of CTPA scans for the diagnosis of CTEPH are repeated due to artefacts and technical reasons, which further exacerbate the risk of excessive radiation dose in another study[87]. This unnecessary ionising radiation exposure can be reduced by using pulmonary perfusion MRI at screening and diagnostic stages of CTEPH leading to better patient healthcare strategy.

An all-inclusive test: Besides lung perfusion imaging, the cardiac assessment is also important in patients with PH. Cardiac involvement in PH is an inevitable step in the disease progression and PH due to left heart disease is the most common type[88,89]. It is reported that more than half of heart failure patients suffer from PH[90]. The pressure increase

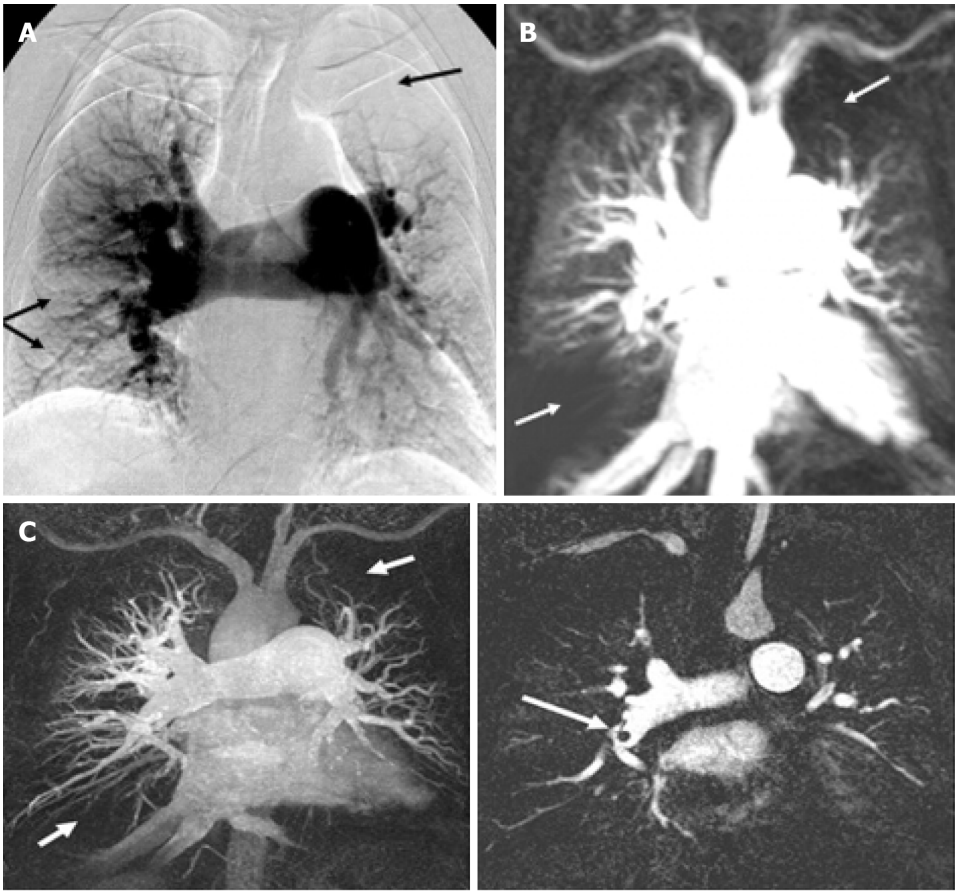


Figure 2 Comparing digital subtraction angiography, pulmonary perfusion magnetic resonance imaging and magnetic resonance angiography for identifying perfusion defects in chronic thromboembolic pulmonary hypertension patient. A: Digital subtraction angiography showing perfusion defects (arrows) in left upper lobe and right lower lobe due to thromboembolic occlusion; B: Magnetic resonance imaging perfusion image at peak enhancement showing hypo-intense perfusion defects at same locations; C: Magnetic resonance angiogram of the same patient demonstrating dark thromboembolic material in the right pulmonary artery corresponding to perfusion defects at the same location. Citation: Nikolaou K, Schoenberg SO, Attenberger U, Scheidler J, Dietrich O, Kuehn B, Rosa F, Huber A, Leuchte H, Baumgartner R, Behr J, Reiser MF. Pulmonary arterial hypertension: diagnosis with fast perfusion MR imaging and high-spatial-resolution MR angiography--preliminary experience. *Radiology 2005*; 236: 694-703 [PMID: 15994997 DOI: 10.1148/radiol.2361040502].

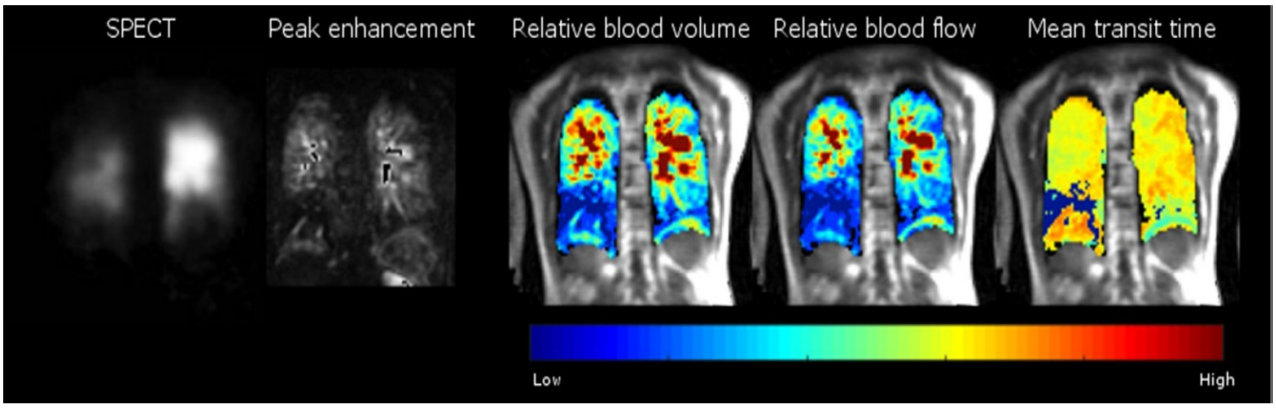


Figure 3 Comparing single photon emission computed tomography and dynamic contract enhanced perfusion magnetic resonance imaging for identifying perfusion defects in chronic thromboembolic pulmonary hypertension patient. Left to right, single photon emission computed tomography and Perfusion magnetic resonance imaging (MRI) at peak enhancement of a chronic thromboembolic pulmonary hypertension patient showing perfusion defects in right and left lower lobes. On the right, semi-quantitative pulmonary blood flow, pulmonary blood volume & mean transit time maps acquired from perfusion MRI demonstrating reduced flow at the same locations. Note left to right scale depicting lower to higher pulmonary blood flow values. Citation: Johns CS, Swift AJ, Rajaram S, Hughes PJC, Capener DJ, Kiely DG, Wild JM. Lung perfusion: MRI vs. SPECT for screening in suspected chronic thromboembolic pulmonary hypertension. *J Magn Reson Imaging* 2017; 46: 1693-1697 [PMID: 28376242 DOI: 10.1002/jmri.25714].

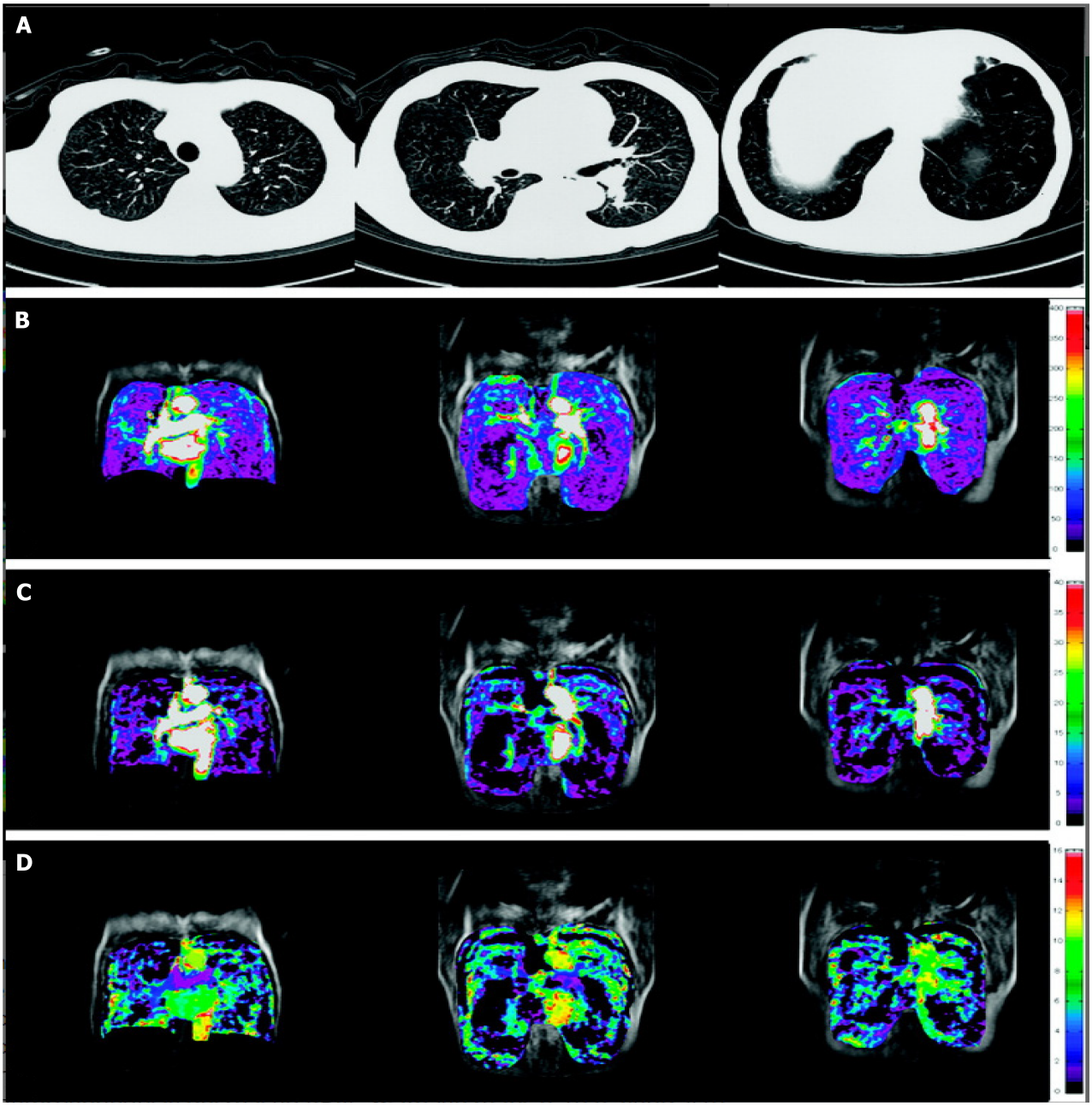


Figure 4 Comparing computed tomography chest and dynamic contract enhanced perfusion magnetic resonance imaging for identifying perfusion defects in pulmonary hypertension patient with COPD. A: Chest computed tomography showing lobular emphysema in the lungs; B-D: Quantitative perfusion maps (anterior to posterior) showing heterogeneously reduced pulmonary blood flow, pulmonary blood volume and mean transit time respectively representing thromboembolic occlusion in respective pulmonary segments. Note on the right-hand side, quantitative scale from top to bottom showing higher to lower quantitative values. Citation: Ohno Y, Hatabu H, Murase K, Higashino T, Kawamitsu H, Watanabe H, Takenaka D, Fujii M, Sugimura K. Quantitative assessment of regional pulmonary perfusion in the entire lung using three-dimensional ultrafast dynamic contrast-enhanced magnetic resonance imaging: Preliminary experience in 40 subjects. *J Magn Reson Imaging* 2004; 20: 353-365 [PMID: 15332240 DOI: 10.1002/jmri.20137].

in the pulmonary arteries leads to an increase in the RV pressure and cardiac remodelling, correlated with increased mortality. RV end-systolic volume index has been reported as an independent predictor of PAH prognosis in a study using 288 derivation cohort and 288 validation PAH cohort[91].

Moreover, another relevant study validated that cardiac MRI based pulmonary artery distensibility index correlates positively with the right heart catheterization estimates for PAH, suggesting non-invasive cardiac MRI a valuable tool for PAH diagnosis[42].

Additionally, cardiac magnetic resonance imaging has also been used to assess pulmonary artery pressure measurements in children with congenital heart disease. Researchers found velocity encoded flow cardiac MRI images strongly correlated with right heart catheterization for systemic blood flow (QS), right to left pulmonary blood flow (QP) ratio and QP/QS ratio[47]. This suggests usefulness of cardiac MRI for pulmonary artery pressure measurement by using the standard SSFP cine imaging and phase contrast flow imaging.

Pulmonary perfusion can be combined with cardiac MRI, including cardiac cine images for structural and functional assessment of heart chambers, blood flow assessment by phase contrast imaging, MRA, post contrast late gadolinium enhancement imaging for myocardial fibrosis/scarring and four-dimensional phase contrast pulmonary artery flow scan. A comprehensive cardio-pulmonary assessment can be achieved in a single examination during the same visit, leading to better use of health resources and limiting the patients' stress[83].

Quantification mitigates observer bias: MRI pulmonary perfusion offers quantification of PBF, PBV and MTT with improved diagnostic accuracy. In a study assessing the diagnostic accuracy of qualitative and quantitative cardiac MR perfusion in coronary artery disease, the level of training was reported as a major determinant for the accuracy of qualitative assessment (the diagnostic accuracy of level-3 operators was 83.6%, level-2 operators 65.7% and level-1 operators 55.7%, $P < 0.001$), while the diagnostic accuracy of quantitative assessment was 86.3% (significantly higher than level-2 and level-1 operators), highlighting the usefulness of operator-independent quantification techniques[70].

Moreover, higher consistency and reproducibility results were achieved using quantification techniques, and an increased sensitivity (from 77% to 83%) was reported when using quantitative measures for the evaluation of myocardial perfusion[92]. Researchers also studied MRI signal abnormalities in the brain and reported higher reproducibility and accuracy of quantification techniques compared to qualitative analysis by expert radiologists[93]. The quantification of MRI perfusion parameters mitigates this observer bias, which is not achievable with current tests to diagnose PH.

Contrast nephrotoxicity comparison

CT scan uses iodine-containing contrast media which can unfortunately cause serious complications, such as contrast induced nephropathy. Gadolinium-based contrast agents are considered safer than iodinated contrast media, thus they can be safely used also in patients with impaired kidney function[94]. CT contrast also involves a huge dose and contrast related discomfort has also been reported. Additionally, the iodine-based contrast can potentially worsen the thyroid function, on the other hand gadolinium based MRI contrast agents have been reported safer for pregnant patients and patients with compromised renal functions[95]. Some other contraindications for CT contrast injection include multiple myeloma and metformin.

CONSIDERATIONS REGARDING PULMONARY PERFUSION MRI

Claustrophobia and magnet safety related issues

An MRI scanner is a long, tunnel-like enclosed chamber where patients need to lie down still for a long time (minimum 40 min). Patients are further fastened by the radiofrequency coil placed on the chest. The MRI scanner also produces loud banging noise (110 decibels at its loudest)[96]. Lying down still for a long time in such an enclosed chamber and tolerating the loud noise can be challenging for claustrophobic patients or patients with hearing problems. Magnet related safety for medical devices' including cardiac pacemakers, aneurysmal clips, intra orbital metallic injury and some other incompatible metallic implants are some other limitations of MRI scanning.

Consideration about image resolution, scan time and respiratory artefacts

In comparison to computed tomography, MRI is prone to breathing artefacts and it inherently retains low image resolution for moving organs like heart and lungs. Scan time is another limitation for MRI, longer scan time leads to patient discomfort. To mitigate, advanced motion correction techniques of parallel imaging, patient training for breath hold, respiratory/ electrocardiogram gating for cardiac MRI and saturation band to supress signal from moving chest wall and heart motion have been adapted[97].

Moreover, recently researchers have successfully validated free breathing, real time MRI imaging with short scan time and high image resolution for cardiac perfusion imaging[98,99]. More research is warranted to apply this technique for pulmonary perfusion

Technical challenges of pulmonary perfusion quantification

Pulmonary perfusion quantification is technically challenging. It needs a skilled operator and availability of a specific software package for quantification. Furthermore, it is prone to errors when images have respiratory and motion artefacts. Lack of integration with other clinical findings while quantification is another limitation.

Future directions

The Fleischner Society's position paper recommends MRI for clinical use for cystic fibrosis, lung cancer staging, lung nodule characterisation and pulmonary hypertension. The position paper endorses further investigating the role of perfusion MRI for the diagnosis of chronic obstructive pulmonary disease and pulmonary parenchymal abnormalities in future[57]. However, MRI imaging for lungs is still limited in clinical and research fields implying the need for further clinically implementable research in this field[57,100]. An ongoing prospective, multicentre, comparative phase III clinical trial (Change-MRI) is currently being carried out to compare the diagnostic accuracy of perfusion MRI and SPECT scintigraphy for CTEPH diagnosis[101]. Pulmonary perfusion MRI has clinical and technical aspects to be considered for future research on this topic.

Clinically, combining cardiac magnetic resonance with pulmonary perfusion imaging can help differentiate lung disorders of multiple aetiologies. 4-dimentional flow MRI imaging to assess pulmonary artery pressure has been demonstrated to aid CTEPH diagnosis[53,102,103]. Moreover, as SMS b-SSFP MRI sequence has been validated for better

anatomical coverage and improved resolution for cardiac imaging, its use can be expanded for pulmonary perfusion imaging and specifically thromboembolic vascular lung disorders. Additionally, sophisticated software to quantitatively analyse perfusion parameters can further improve diagnostic accuracy in future[57].

Quantitative analysis of perfusion MRI parameters of PBF, PBV and MTT can be performed manually or automatically. Manual quantification can be time consuming and laborious. To improve efficiency, researchers established the validity of automated quantitative analysis for myocardial perfusion MRI and found it more efficient and reproducible than manual analysis[104-106].

Similarly, the automatic analysis of lung MRI has also been researched using artificial intelligence (AI) and deep learning algorithms for automatic lung segmentation of 20 cystic fibrosis patients. This study found automatic lung segmentation comparable with manual segmentation and capable of accurate estimation of lung volume[107]. Researchers also used AI techniques to automatically quantify the neonatal lung structure and compared it with manual segmentation by expert operators. This study found that AI-supported automatic segmentation of lung MRI was accurate and comparable to expert-level accuracy[108]. Therefore, for efficiency of time and consistency of diagnostic parameters, further research on the accuracy of automatic lung segmentation and quantification of perfusion parameters is recommended.

Currently, the dual-bolus approach is preferred in routine clinical practice for perfusion MRI imaging, but the dual-sequence approach to account for signal intensity nonlinearity and operator-friendly set up of injector pump in busy clinical settings is also recommended for future research on this topic[66].

CONCLUSION

PH is multifactorial and requires timely multimodality differential diagnosis for better disease prognosis. Pulmonary perfusion MRI can be considered a reliable and safe diagnostic imaging tool with comparable diagnostic accuracy to reference gold standards of SPECT, CTPA and V/Q imaging. It offers cardiopulmonary assessment when combined with CMR at the same visit without any radiation exposure making it a comprehensive test for screening, differential diagnosis and follow up scans for PH management. Furthermore, quantification of pulmonary perfusion parameters could improve the reliability and accuracy of diagnostic testing and help mitigate subjective interpretation of imaging findings which is not possible by qualitative assessment alone offered by standard tests.

FOOTNOTES

Author contributions: Villa ADM was responsible for the review concept; Lacharie M drafted the manuscript; Lacharie M provided critical revision of the manuscript for important intellectual content; and all authors critically reviewed the content.

Conflict-of-interest statement: Authors declare no conflict of interest for this article.

Open-Access: This article is an open-access article that was selected by an in-house editor and fully peer-reviewed by external reviewers. It is distributed in accordance with the Creative Commons Attribution NonCommercial (CC BY-NC 4.0) license, which permits others to distribute, remix, adapt, build upon this work non-commercially, and license their derivative works on different terms, provided the original work is properly cited and the use is non-commercial. See: https://creativecommons.org/Licenses/by-nc/4.0/

Country/Territory of origin: United Kingdom

ORCID number: Miriam Lacharie 0000-0002-7282-6894; Adriana Villa 0000-0002-9355-0372; Xenios Milidonis 0000-0002-5446-9459; Amedeo Chiribiri 0000-0003-3394-4289.

Corresponding Author's Membership in Professional Societies: Health and Care Professionalcouncil, RA75559.

S-Editor: Liu JH
L-Editor: A
P-Editor: Zhao S

REFERENCES

1 **Verhoeff K**, Mitchell JR. Cardiopulmonary physiology: why the heart and lungs are inextricably linked. *Adv Physiol Educ* 2017; **41**: 348-353 [PMID: 28679570 DOI: 10.1152/advan.00190.2016]

2 **Maron BA**. Revised Definition of Pulmonary Hypertension and Approach to Management: A Clinical Primer. *J Am Heart Assoc* 2023; **12**: e029024 [PMID: 37026538 DOI: 10.1161/JAHA.122.029024]

3 **Galiè N**, Humbert M, Vachiery JL, Gibbs S, Lang I, Torbicki A, Simonneau G, Peacock A, Vonk Noordegraaf A, Beghetti M, Ghofrani A, Gomez Sanchez MA, Hansmann G, Klepetko W, Lancellotti P, Matucci M, McDonagh T, Pierard LA, Trindade PT, Zompatori M, Hoeper M; ESC Scientific Document Group. 2015 ESC/ERS Guidelines for the diagnosis and treatment of pulmonary hypertension: The Joint Task Force for the Diagnosis and Treatment of Pulmonary Hypertension of the European Society of Cardiology (ESC) and the European Respiratory

Society (ERS): Endorsed by: Association for European Paediatric and Congenital Cardiology (AEPC), International Society for Heart and Lung Transplantation (ISHLT). *Eur Heart J* 2016; **37**: 67-119 [PMID: 26320113 DOI: 10.1093/eurheartj/ehv317]

4 **Kiely DG**, Levin D, Hassoun P, Ivy DD, Jone PN, Bwika J, Kawut SM, Lordan J, Lungu A, Mazurek J, Moledina S, Olschewski H, Peacock A, Puri GD, Rahaghi F, Schafer M, Schiebler M, Screaton N, Tawhai M, Van Beek EJ, Vonk-Noordegraaf A, Vanderpool RR, Wort J, Zhao L, Wild J, Vogel-Claussen J, Swift AJ. EXPRESS: Statement on imaging and pulmonary hypertension from the Pulmonary Vascular Research Institute (PVRI). *Pulm Circ* 2019; **9**: 2045894019841990 [PMID: 30880632 DOI: 10.1177/2045894019841990]

5 **Lan NSH**, Massam BD, Kulkarni SS, Lang CC. Pulmonary Arterial Hypertension: Pathophysiology and Treatment. *Diseases* 2018; **6** [PMID: 29772649 DOI: 10.3390/diseases6020038]

6 **Yaghi S**, Novikov A, Trandafirescu T. Clinical update on pulmonary hypertension. *J Investig Med* 2020; **68**: 821-827 [PMID: 32241822 DOI: 10.1136/jim-2020-001291]

7 **Martinez C**, Wallenhorst C, Teal S, Cohen AT, Peacock AJ. Incidence and risk factors of chronic thromboembolic pulmonary hypertension following venous thromboembolism, a population-based cohort study in England. *Pulm Circ* 2018; **8**: 2045894018791358 [PMID: 29985100 DOI: 10.1177/2045894018791358]

8 **Ohno Y**, Koyama H, Lee HY, Miura S, Yoshikawa T, Sugimura K. Contrast-enhanced CT- and MRI-based perfusion assessment for pulmonary diseases: basics and clinical applications. *Diagn Interv Radiol* 2016; **22**: 407-421 [PMID: 27523813 DOI: 10.5152/dir.2016.16123]

9 **Mortensen J**, Gutte H. SPECT/CT and pulmonary embolism. *Eur J Nucl Med Mol Imaging* 2014; **41** Suppl 1: S81-S90 [PMID: 24213621 DOI: 10.1007/s00259-013-2614-5]

10 **Musch G**, Layfield JD, Harris RS, Melo MF, Winkler T, Callahan RJ, Fischman AJ, Venegas JG. Topographical distribution of pulmonary perfusion and ventilation, assessed by PET in supine and prone humans. *J Appl Physiol (1985)* 2002; **93**: 1841-1851 [PMID: 12381773 DOI: 10.1152/japplphysiol.00223.2002]

11 **Doğan H**, de Roos A, Geleijins J, Huisman MV, Kroft LJ. The role of computed tomography in the diagnosis of acute and chronic pulmonary embolism. *Diagn Interv Radiol* 2015; **21**: 307-316 [PMID: 26133321 DOI: 10.5152/dir.2015.14403]

12 **Soler X**, Hoh CK, Test VJ, Kerr KM, Marsh JJ, Morris TA. Single photon emission computed tomography in chronic thromboembolic pulmonary hypertension. *Respirology* 2011; **16**: 131-137 [PMID: 20920137 DOI: 10.1111/j.1440-1843.2010.01867.x]

13 **Grosse A**, Grosse C, Lang I. Evaluation of the CT imaging findings in patients newly diagnosed with chronic thromboembolic pulmonary hypertension. *PLoS One* 2018; **13**: e0201468 [PMID: 30059549 DOI: 10.1371/journal.pone.0201468]

14 **Remy-Jardin M**, Faivre JB, Pontana F, Molinari F, Tacelli N, Remy J. Thoracic applications of dual energy. *Semin Respir Crit Care Med* 2014; **35**: 64-73 [PMID: 24481760 DOI: 10.1055/s-0033-1363452]

15 **Havránková R**. Biological effects of ionizing radiation. *Cas Lek Cesk* 2020; **159**: 258-260 [PMID: 33445930]

16 **Levine DJ**. Pulmonary arterial hypertension: updates in epidemiology and evaluation of patients. *Am J Manag Care* 2021; **27**: S35-S41 [PMID: 33710842 DOI: 10.37765/ajmc.2021.88609]

17 **Lin EC**. Radiation risk from medical imaging. *Mayo Clin Proc* 2010; **85**: 1142-1146 [PMID: 21123642 DOI: 10.4065/mcp.2010.0260]

18 **Astani SA**, Davis LC, Harkness BA, Supanich MP, Dalal I. Detection of pulmonary embolism during pregnancy: comparing radiation doses of CTPA and pulmonary scintigraphy. *Nucl Med Commun* 2014; **35**: 704-711 [PMID: 24743314 DOI: 10.1097/MNM.0000000000000114]

19 **Bajc M**, Neilly B, Miniati M, Mortensen J, Jonson B. Methodology for ventilation/perfusion SPECT. *Semin Nucl Med* 2010; **40**: 415-425 [PMID: 20920632 DOI: 10.1053/j.semnuclmed.2010.07.002]

20 **Schembri GP**, Miller AE, Smart R. Radiation dosimetry and safety issues in the investigation of pulmonary embolism. *Semin Nucl Med* 2010; **40**: 442-454 [PMID: 20920634 DOI: 10.1053/j.semnuclmed.2010.07.007]

21 **Kline JA**, Courtney DM, Beam DM, King MC, Steuerwald M. Incidence and predictors of repeated computed tomographic pulmonary angiography in emergency department patients. *Ann Emerg Med* 2009; **54**: 41-48 [PMID: 18838194 DOI: 10.1016/j.annemergmed.2008.08.015]

22 **Ray JC**, Burger C, Mergo P, Safford R, Blackshear J, Austin C, Fairweather D, Heckman MG, Zeiger T, Dubin M, Shapiro B. Pulmonary arterial stiffness assessed by cardiovascular magnetic resonance imaging is a predictor of mild pulmonary arterial hypertension. *Int J Cardiovasc Imaging* 2019; **35**: 1881-1892 [PMID: 29934885 DOI: 10.1007/s10554-018-1397-y]

23 **Olsson KM**, Meyer B, Hinrichs J, Vogel-Claussen J, Hoeper MM, Cebotari S. Chronic thromboembolic pulmonary hypertension. *Dtsch Arztebl Int* 2014; **111**: 856-862 [PMID: 25585582 DOI: 10.3238/arztebl.2014.0856]

24 **Riedel M**, Stanek V, Widimsky J, Prerovsky I. Longterm follow-up of patients with pulmonary thromboembolism. Late prognosis and evolution of hemodynamic and respiratory data. *Chest* 1982; **81**: 151-158 [PMID: 7056079 DOI: 10.1378/chest.81.2.151]

25 **Gopalan D**, Delcroix M, Held M. Diagnosis of chronic thromboembolic pulmonary hypertension. *Eur Respir Rev* 2017; **26** [PMID: 28298387 DOI: 10.1183/16000617.0108-2016]

26 **Mayer E**, Jenkins D, Lindner J, D'Armini A, Kloek J, Meyns B, Ilkjaer LB, Klepetko W, Delcroix M, Lang I, Pepke-Zaba J, Simonneau G, Dartevelle P. Surgical management and outcome of patients with chronic thromboembolic pulmonary hypertension: results from an international prospective registry. *J Thorac Cardiovasc Surg* 2011; **141**: 702-710 [PMID: 21335128 DOI: 10.1016/j.jtcvs.2010.11.024]

27 **Madani MM**, Auger WR, Pretorius V, Sakakibara N, Kerr KM, Kim NH, Fedullo PF, Jamieson SW. Pulmonary endarterectomy: recent changes in a single institution's experience of more than 2,700 patients. *Ann Thorac Surg* 2012; **94**: 97-103 [PMID: 22626752 DOI: 10.1016/j.athoracsur.2012.04.004]

28 **Jenkins D**, Mayer E, Screaton N, Madani M. State-of-the-art chronic thromboembolic pulmonary hypertension diagnosis and management. *Eur Respir Rev* 2012; **21**: 32-39 [PMID: 22379172 DOI: 10.1183/09059180.00009211]

29 **Hopkins SR**, Wielpütz MO, Kauczor HU. Imaging lung perfusion. *J Appl Physiol (1985)* 2012; **113**: 328-339 [PMID: 22604884 DOI: 10.1152/japplphysiol.00320.2012]

30 **Aziz M**, Krishnam M, Madhuranthakam AJ, Rajiah P. Update on MR imaging of the pulmonary vasculature. *Int J Cardiovasc Imaging* 2019; **35**: 1483-1497 [PMID: 31030315 DOI: 10.1007/s10554-019-01603-y]

31 **Amundsen T**, Kvaerness J, Jones RA, Waage A, Bjermer L, Nilsen G, Haraldseth O. Pulmonary embolism: detection with MR perfusion imaging of lung--a feasibility study. *Radiology* 1997; **203**: 181-185 [PMID: 9122390 DOI: 10.1148/radiology.203.1.9122390]

32 **Amundsen T**, Torheim G, Kvistad KA, Waage A, Bjermer L, Nordlid KK, Johnsen H, Asberg A, Haraldseth O. Perfusion abnormalities in pulmonary embolism studied with perfusion MRI and ventilation-perfusion scintigraphy: an intra-modality and inter-modality agreement study. *J Magn Reson Imaging* 2002; **15**: 386-394 [PMID: 11948827 DOI: 10.1002/jmri.10092]

33 **Ohno Y**, Hatabu H, Murase K, Higashino T, Kawamitsu H, Watanabe H, Takenaka D, Fujii M, Sugimura K. Quantitative assessment of

regional pulmonary perfusion in the entire lung using three-dimensional ultrafast dynamic contrast-enhanced magnetic resonance imaging: Preliminary experience in 40 subjects. *J Magn Reson Imaging* 2004; **20**: 353-365 [PMID: 15332240 DOI: 10.1002/jmri.20137]

34 **Nikolaou K**, Schoenberg SO, Attenberger U, Scheidler J, Dietrich O, Kuehn B, Rosa F, Huber A, Leuchte H, Baumgartner R, Behr J, Reiser MF. Pulmonary arterial hypertension: diagnosis with fast perfusion MR imaging and high-spatial-resolution MR angiography--preliminary experience. *Radiology* 2005; **236**: 694-703 [PMID: 15994997 DOI: 10.1148/radiol.2361040502]

35 **Kluge A**, Gerriets T, Lange U, Bachman G. MRI for short-term follow-up of acute pulmonary embolism. Assessment of thrombus appearance and pulmonary perfusion: a feasibility study. *Eur Radiol* 2005; **15**: 1969-1977 [PMID: 15891888 DOI: 10.1007/s00330-005-2760-7]

36 **Kluge A**, Gerriets T, Stolz E, Dill T, Mueller KD, Mueller C, Bachmann G. Pulmonary perfusion in acute pulmonary embolism: agreement of MRI and SPECT for lobar, segmental and subsegmental perfusion defects. *Acta Radiol* 2006; **47**: 933-940 [PMID: 17077044 DOI: 10.1080/02841850600885377]

37 **Ohno Y**, Hatabu H, Murase K, Higashino T, Nogami M, Yoshikawa T, Sugimura K. Primary pulmonary hypertension: 3D dynamic perfusion MRI for quantitative analysis of regional pulmonary perfusion. *AJR Am J Roentgenol* 2007; **188**: 48-56 [PMID: 17179345 DOI: 10.2214/AJR.05.0135]

38 **Ley S**, Mereles D, Risse F, Grünig E, Ley-Zaporozhan J, Tecer Z, Puderbach M, Fink C, Kauczor HU. Quantitative 3D pulmonary MR-perfusion in patients with pulmonary arterial hypertension: correlation with invasive pressure measurements. *Eur J Radiol* 2007; **61**: 251-255 [PMID: 17045440 DOI: 10.1016/j.ejrad.2006.08.028]

39 **Ohno Y**, Koyama H, Nogami M, Takenaka D, Matsumoto S, Onishi Y, Matsumoto K, Murase K, Sugimura K. Dynamic perfusion MRI: capability for evaluation of disease severity and progression of pulmonary arterial hypertension in patients with connective tissue disease. *J Magn Reson Imaging* 2008; **28**: 887-899 [PMID: 18821609 DOI: 10.1002/jmri.21550]

40 **Ohno Y**, Koyama H, Matsumoto K, Onishi Y, Nogami M, Takenaka D, Yoshikawa T, Matsumoto S, Sugimura K. Dynamic MR perfusion imaging: capability for quantitative assessment of disease extent and prediction of outcome for patients with acute pulmonary thromboembolism. *J Magn Reson Imaging* 2010; **31**: 1081-1090 [PMID: 20432342 DOI: 10.1002/jmri.22146]

41 **Stein PD**, Chenevert TL, Fowler SE, Goodman LR, Gottschalk A, Hales CA, Hull RD, Jablonski KA, Leeper KV Jr, Naidich DP, Sak DJ, Sostman HD, Tapson VF, Weg JG, Woodard PK; PIOPED III (Prospective Investigation of Pulmonary Embolism Diagnosis III) Investigators. Gadolinium-enhanced magnetic resonance angiography for pulmonary embolism: a multicenter prospective study (PIOPED III). *Ann Intern Med* 2010; **152**: 434-443 [PMID: 20368649 DOI: 10.7326/0003-4819-152-7-201004060-00008]

42 **Kang KW**, Chang HJ, Kim YJ, Choi BW, Lee HS, Yang WI, Shim CY, Ha J, Chung N. Cardiac magnetic resonance imaging-derived pulmonary artery distensibility index correlates with pulmonary artery stiffness and predicts functional capacity in patients with pulmonary arterial hypertension. *Circ J* 2011; **75**: 2244-2251 [PMID: 21757816 DOI: 10.1253/circj.cj-10-1310]

43 **Ohno Y**, Koyama H, Yoshikawa T, Nishio M, Matsumoto S, Matsumoto K, Aoyama N, Nogami M, Murase K, Sugimura K. Contrast-enhanced multidetector-row computed tomography vs. Time-resolved magnetic resonance angiography vs. contrast-enhanced perfusion MRI: assessment of treatment response by patients with inoperable chronic thromboembolic pulmonary hypertension. *J Magn Reson Imaging* 2012; **36**: 612-623 [PMID: 22566188 DOI: 10.1002/jmri.23680]

44 **Ley S**, Fink C, Risse F, Ehlken N, Fischer C, Ley-Zaporozhan J, Kauczor HU, Klose H, Gruenig E. Magnetic resonance imaging to assess the effect of exercise training on pulmonary perfusion and blood flow in patients with pulmonary hypertension. *Eur Radiol* 2013; **23**: 324-331 [PMID: 22886553 DOI: 10.1007/s00330-012-2606-z]

45 **Rajaram S**, Swift AJ, Telfer A, Hurdman J, Marshall H, Lorenz E, Capener D, Davies C, Hill C, Elliot C, Condliffe R, Wild JM, Kiely DG. 3D contrast-enhanced lung perfusion MRI is an effective screening tool for chronic thromboembolic pulmonary hypertension: results from the ASPIRE Registry. *Thorax* 2013; **68**: 677-678 [PMID: 23349220 DOI: 10.1136/thoraxjnl-2012-203020]

46 **Revel MP**, Sanchez O, Lefort C, Meyer G, Couchon S, Hernigou A, Niarra R, Chatellier G, Frija G. Diagnostic accuracy of unenhanced, contrast-enhanced perfusion and angiographic MRI sequences for pulmonary embolism diagnosis: results of independent sequence readings. *Eur Radiol* 2013; **23**: 2374-2382 [PMID: 23652845 DOI: 10.1007/s00330-013-2852-8]

47 **Sugimoto M**, Kajino H, Kajihama A, Nakau K, Murakami N, Azuma H. Assessment of pulmonary arterial pressure by velocity-encoded cine magnetic resonance imaging in children with congenital heart disease. *Circ J* 2013; **77**: 3015-3022 [PMID: 24088305 DOI: 10.1253/circj.cj-13-0626]

48 **Schönfeld C**, Cebotari S, Voskrebenzev A, Gutberlet M, Hinrichs J, Renne J, Hoeper MM, Olsson KM, Welte T, Wacker F, Vogel-Claussen J. Performance of perfusion-weighted Fourier decomposition MRI for detection of chronic pulmonary emboli. *J Magn Reson Imaging* 2015; **42**: 72-79 [PMID: 25227559 DOI: 10.1002/jmri.24764]

49 **Ingrisch M**, Maxien D, Meinel FG, Reiser MF, Nikolaou K, Dietrich O. Detection of pulmonary embolism with free-breathing dynamic contrast-enhanced MRI. *J Magn Reson Imaging* 2016; **43**: 887-893 [PMID: 26391931 DOI: 10.1002/jmri.25050]

50 **Johns CS**, Swift AJ, Rajaram S, Hughes PJC, Capener DJ, Kiely DG, Wild JM. Lung perfusion: MRI vs. SPECT for screening in suspected chronic thromboembolic pulmonary hypertension. *J Magn Reson Imaging* 2017; **46**: 1693-1697 [PMID: 28376242 DOI: 10.1002/jmri.25714]

51 **Voskrebenzev A**, Gutberlet M, Klimeš F, Kaireit TF, Schönfeld C, Rotärmel A, Wacker F, Vogel-Claussen J. Feasibility of quantitative regional ventilation and perfusion mapping with phase-resolved functional lung (PREFUL) MRI in healthy volunteers and COPD, CTEPH, and CF patients. *Magn Reson Med* 2018; **79**: 2306-2314 [PMID: 28856715 DOI: 10.1002/mrm.26893]

52 **Agoston-Coldea L**, Lupu S, Mocan T. Pulmonary Artery Stiffness by Cardiac Magnetic Resonance Imaging Predicts Major Adverse Cardiovascular Events in patients with Chronic Obstructive Pulmonary Disease. *Sci Rep* 2018; **8**: 14447 [PMID: 30262820 DOI: 10.1038/s41598-018-32784-6]

53 **Schoenfeld C**, Hinrichs JB, Olsson KM, Kuettner MA, Renne J, Kaireit T, Czerner C, Wacker F, Hoeper MM, Meyer BC, Vogel-Claussen J. Cardio-pulmonary MRI for detection of treatment response after a single BPA treatment session in CTEPH patients. *Eur Radiol* 2019; **29**: 1693-1702 [PMID: 30311032 DOI: 10.1007/s00330-018-5696-4]

54 **Moher Alsady T**, Kaireit TF, Behrendt L, Winther HB, Olsson KM, Wacker F, Hoeper MM, Cebotari S, Vogel-Claussen J. Comparison of dual-energy computer tomography and dynamic contrast-enhanced MRI for evaluating lung perfusion defects in chronic thromboembolic pulmonary hypertension. *PLoS One* 2021; **16**: e0251740 [PMID: 34138864 DOI: 10.1371/journal.pone.0251740]

55 **Torres LA**, Lee KE, Barton GP, Hahn AD, Sandbo N, Schiebler ML, Fain SB. Dynamic contrast enhanced MRI for the evaluation of lung perfusion in idiopathic pulmonary fibrosis. *Eur Respir J* 2022; **60** [PMID: 35273033 DOI: 10.1183/13993003.02058-2021]

56 **Yousaf T**, Dervenoulas G, Politis M. Advances in MRI Methodology. *Int Rev Neurobiol* 2018; **141**: 31-76 [PMID: 30314602 DOI: 10.1016/bs.irn.2018.08.008]

57 **Hatabu H**, Ohno Y, Gefter WB, Parraga G, Madore B, Lee KS, Altes TA, Lynch DA, Mayo JR, Seo JB, Wild JM, van Beek EJR, Schiebler

ML, Kauczor HU; Fleischner Society. Expanding Applications of Pulmonary MRI in the Clinical Evaluation of Lung Disorders: Fleischner Society Position Paper. *Radiology* 2020; **297**: 286-301 [PMID: 32870136 DOI: 10.1148/radiol.2020201138]

58 **Alsop DC**, Hatabu H, Bonnet M, Listerud J, Gefter W. Multi-slice, breathhold imaging of the lung with submillisecond echo times. *Magn Reson Med* 1995; **33**: 678-682 [PMID: 7596272 DOI: 10.1002/mrm.1910330513]

59 **Mayo JR**, MacKay A, Müller NL. MR imaging of the lungs: value of short TE spin-echo pulse sequences. *AJR Am J Roentgenol* 1992; **159**: 951-956 [PMID: 1414805 DOI: 10.2214/ajr.159.5.1414805]

60 **Gordon Y**, Partovi S, Müller-Eschner M, Amarteifio E, Bäuerle T, Weber MA, Kauczor HU, Rengier F. Dynamic contrast-enhanced magnetic resonance imaging: fundamentals and application to the evaluation of the peripheral perfusion. *Cardiovasc Diagn Ther* 2014; **4**: 147-164 [PMID: 24834412 DOI: 10.3978/j.issn.2223-3652.2014.03.01]

61 **Patel SH**, Batchala PP, Schallert K, Patrie JT, Abbas SO, Ornan DA, Mukherjee S, Huerta T, Mugler JP 3rd. 3D fast low-angle shot (FLASH) technique for 3T contrast-enhanced brain MRI in the inpatient and emergency setting: comparison with 3D magnetization-prepared rapid gradient echo (MPRAGE) technique. *Neuroradiology* 2021; **63**: 897-904 [PMID: 33118042 DOI: 10.1007/s00234-020-02590-x]

62 **Cuenod CA**, Balvay D. Perfusion and vascular permeability: basic concepts and measurement in DCE-CT and DCE-MRI. *Diagn Interv Imaging* 2013; **94**: 1187-1204 [PMID: 24211260 DOI: 10.1016/j.diii.2013.10.010]

63 **Rajaram S**, Swift AJ, Capener D, Telfer A, Davies C, Hill C, Condliffe R, Elliot C, Hurdman J, Kiely DG, Wild JM. Diagnostic accuracy of contrast-enhanced MR angiography and unenhanced proton MR imaging compared with CT pulmonary angiography in chronic thromboembolic pulmonary hypertension. *Eur Radiol* 2012; **22**: 310-317 [PMID: 21887483 DOI: 10.1007/s00330-011-2252-x]

64 **Deshmane A**, Gulani V, Griswold MA, Seiberlich N. Parallel MR imaging. *J Magn Reson Imaging* 2012; **36**: 55-72 [PMID: 22696125 DOI: 10.1002/jmri.23639]

65 **Nazir MS**, Neji R, Speier P, Reid F, Stäb D, Schmidt M, Forman C, Razavi R, Plein S, Ismail TF, Chiribiri A, Roujol S. Simultaneous multi slice (SMS) balanced steady state free precession first-pass myocardial perfusion cardiovascular magnetic resonance with iterative reconstruction at 1.5 T. *J Cardiovasc Magn Reson* 2018; **20**: 84 [PMID: 30526627 DOI: 10.1186/s12968-018-0502-7]

66 **Kellman P**, Hansen MS, Nielles-Vallespin S, Nickander J, Themudo R, Ugander M, Xue H. Myocardial perfusion cardiovascular magnetic resonance: optimized dual sequence and reconstruction for quantification. *J Cardiovasc Magn Reson* 2017; **19**: 43 [PMID: 28385161 DOI: 10.1186/s12968-017-0355-5]

67 **Ingrisch M**, Maxien D, Schwab F, Reiser MF, Nikolaou K, Dietrich O. Assessment of pulmonary perfusion with breath-hold and free-breathing dynamic contrast-enhanced magnetic resonance imaging: quantification and reproducibility. *Invest Radiol* 2014; **49**: 382-389 [PMID: 24473368 DOI: 10.1097/RLI.0000000000000020]

68 **Maxien D**, Ingrisch M, Meinel FG, Reiser M, Dietrich O, Nikolaou K. Quantification of pulmonary perfusion with free-breathing dynamic contrast-enhanced MRI--a pilot study in healthy volunteers. *Rofo* 2013; **185**: 1175-1181 [PMID: 23884909 DOI: 10.1055/s-0033-1350128]

69 **Borhani AA**, Hosseinzadeh K. Quantitative Versus Qualitative Methods in Evaluation of T2 Signal Intensity to Improve Accuracy in Diagnosis of Pheochromocytoma. *AJR Am J Roentgenol* 2015; **205**: 302-310 [PMID: 26204279 DOI: 10.2214/AJR.14.13273]

70 **Villa ADM**, Corsinovi L, Ntalas I, Milidonis X, Scannell C, Di Giovine G, Child N, Ferreira C, Nazir MS, Karady J, Eshja E, De Francesco V, Bettencourt N, Schuster A, Ismail TF, Razavi R, Chiribiri A. Importance of operator training and rest perfusion on the diagnostic accuracy of stress perfusion cardiovascular magnetic resonance. *J Cardiovasc Magn Reson* 2018; **20**: 74 [PMID: 30454074 DOI: 10.1186/s12968-018-0493-4]

71 **Jerosch-Herold M**. Quantification of myocardial perfusion by cardiovascular magnetic resonance. *J Cardiovasc Magn Reson* 2010; **12**: 57 [PMID: 20932314 DOI: 10.1186/1532-429X-12-57]

72 **Jerosch-Herold M**, Wilke N, Stillman AE. Magnetic resonance quantification of the myocardial perfusion reserve with a Fermi function model for constrained deconvolution. *Med Phys* 1998; **25**: 73-84 [PMID: 9472829 DOI: 10.1118/1.598163]

73 **Zierler K**. Indicator dilution methods for measuring blood flow, volume, and other properties of biological systems: a brief history and memoir. *Ann Biomed Eng* 2000; **28**: 836-848 [PMID: 11144667 DOI: 10.1114/1.1308496]

74 **Calamante F**. Arterial input function in perfusion MRI: a comprehensive review. *Prog Nucl Magn Reson Spectrosc* 2013; **74**: 1-32 [PMID: 24083460 DOI: 10.1016/j.pnmrs.2013.04.002]

75 **Ishida M**, Schuster A, Morton G, Chiribiri A, Hussain S, Paul M, Merkle N, Steen H, Lossnitzer D, Schnackenburg B, Alfakih K, Plein S, Nagel E. Development of a universal dual-bolus injection scheme for the quantitative assessment of myocardial perfusion cardiovascular magnetic resonance. *J Cardiovasc Magn Reson* 2011; **13**: 28 [PMID: 21609423 DOI: 10.1186/1532-429X-13-28]

76 **Risse F**, Semmler W, Kauczor HU, Fink C. Dual-bolus approach to quantitative measurement of pulmonary perfusion by contrast-enhanced MRI. *J Magn Reson Imaging* 2006; **24**: 1284-1290 [PMID: 17051533 DOI: 10.1002/jmri.20747]

77 **Broadbent DA**, Biglands JD, Ripley DP, Higgins DM, Greenwood JP, Plein S, Buckley DL. Sensitivity of quantitative myocardial dynamic contrast-enhanced MRI to saturation pulse efficiency, noise and t1 measurement error: Comparison of nonlinearity correction methods. *Magn Reson Med* 2016; **75**: 1290-1300 [PMID: 25946025 DOI: 10.1002/mrm.25726]

78 **Gatehouse PD**, Elkington AG, Ablitt NA, Yang GZ, Pennell DJ, Firmin DN. Accurate assessment of the arterial input function during high-dose myocardial perfusion cardiovascular magnetic resonance. *J Magn Reson Imaging* 2004; **20**: 39-45 [PMID: 15221807 DOI: 10.1002/jmri.20054]

79 **Jahng GH**, Li KL, Ostergaard L, Calamante F. Perfusion magnetic resonance imaging: a comprehensive update on principles and techniques. *Korean J Radiol* 2014; **15**: 554-577 [PMID: 25246817 DOI: 10.3348/kjr.2014.15.5.554]

80 **Schoenfeld C**, Cebotari S, Hinrichs J, Renne J, Kaireit T, Olsson KM, Voskrebenzev A, Gutberlet M, Hoeper MM, Welte T, Haverich A, Wacker F, Vogel-Claussen J. MR Imaging-derived Regional Pulmonary Parenchymal Perfusion and Cardiac Function for Monitoring Patients with Chronic Thromboembolic Pulmonary Hypertension before and after Pulmonary Endarterectomy. *Radiology* 2016; **279**: 925-934 [PMID: 26727392 DOI: 10.1148/radiol.2015150765]

81 **Altes TA**, Rehm PK, Harrell F, Salerno M, Daniel TM, De Lange EE. Ventilation imaging of the lung: comparison of hyperpolarized helium-3 MR imaging with Xe-133 scintigraphy. *Acad Radiol* 2004; **11**: 729-734 [PMID: 15217589 DOI: 10.1016/j.acra.2004.04.001]

82 **Marshall H**, Kiely DG, Parra-Robles J, Capener D, Deppe MH, van Beek EJ, Swift AJ, Rajaram S, Hurdman J, Condliffe R, Elliot CA, Wild JM. Magnetic resonance imaging of ventilation and perfusion changes in response to pulmonary endarterectomy in chronic thromboembolic pulmonary hypertension. *Am J Respir Crit Care Med* 2014; **190**: e18-e19 [PMID: 25171318 DOI: 10.1164/rccm.201310-1842IM]

83 **Saunders LC**, Hughes PJC, Alabed S, Capener DJ, Marshall H, Vogel-Claussen J, van Beek EJR, Kiely DG, Swift AJ, Wild JM. Integrated Cardiopulmonary MRI Assessment of Pulmonary Hypertension. *J Magn Reson Imaging* 2022; **55**: 633-652 [PMID: 34350655 DOI: 10.1002/jmri.27849]

84 **Wang Z**, He M, Bier E, Rankine L, Schrank G, Rajagopal S, Huang YC, Kelsey C, Womack S, Mammarappallil J, Driehuys B. Hyperpolarized (129) Xe gas transfer MRI: the transition from 1.5T to 3T. *Magn Reson Med* 2018; **80**: 2374-2383 [PMID: 30024058 DOI: 10.1002/mrm.27377]

85 **Dahhan T**, Kaushik SS, He M, Mammarappallil JG, Tapson VF, McAdams HP, Sporn TA, Driehuys B, Rajagopal S. Abnormalities in hyperpolarized (129)Xe magnetic resonance imaging and spectroscopy in two patients with pulmonary vascular disease. *Pulm Circ* 2016; **6**: 126-131 [PMID: 27162620 DOI: 10.1086/685110]

86 **Wang Z**, Bier EA, Swaminathan A, Parikh K, Nouls J, He M, Mammarappallil JG, Luo S, Driehuys B, Rajagopal S. Diverse cardiopulmonary diseases are associated with distinct xenon magnetic resonance imaging signatures. *Eur Respir J* 2019; **54** [PMID: 31619473 DOI: 10.1183/13993003.00831-2019]

87 **U-King-Im JM**, Freeman SJ, Boylan T, Cheow HK. Quality of CT pulmonary angiography for suspected pulmonary embolus in pregnancy. *Eur Radiol* 2008; **18**: 2709-2715 [PMID: 18651151 DOI: 10.1007/s00330-008-1100-0]

88 **Mehra P**, Mehta V, Sukhija R, Sinha AK, Gupta M, Girish MP, Aronow WS. Pulmonary hypertension in left heart disease. *Arch Med Sci* 2019; **15**: 262-273 [PMID: 30697278 DOI: 10.5114/aoms.2017.68938]

89 **Rosenkranz S**, Howard LS, Gomberg-Maitland M, Hoeper MM. Systemic Consequences of Pulmonary Hypertension and Right-Sided Heart Failure. *Circulation* 2020; **141**: 678-693 [PMID: 32091921 DOI: 10.1161/CIRCULATIONAHA.116.022362]

90 **Calderaro D**, Alves Junior JL, Fernandes CJCDS, Souza R. Pulmonary Hypertension in General Cardiology Practice. *Arq Bras Cardiol* 2019; **113**: 419-428 [PMID: 31621783 DOI: 10.5935/abc.20190188]

91 **Swift AJ**, Capener D, Johns C, Hamilton N, Rothman A, Elliot C, Condliffe R, Charalampopoulos A, Rajaram S, Lawrie A, Campbell MJ, Wild JM, Kiely DG. Magnetic Resonance Imaging in the Prognostic Evaluation of Patients with Pulmonary Arterial Hypertension. *Am J Respir Crit Care Med* 2017; **196**: 228-239 [PMID: 28328237 DOI: 10.1164/rccm.201611-2365OC]

92 **Yun CH**, Tsai JP, Tsai CT, Mok GS, Sun JY, Hung CL, Wu TH, Huang WT, Yang FS, Lee JJ, Cury RC, Fares A, Nshisso LD, Bezerra HG. Qualitative and semi-quantitative evaluation of myocardium perfusion with 3 T stress cardiac MRI. *BMC Cardiovasc Disord* 2015; **15**: 164 [PMID: 26642757 DOI: 10.1186/s12872-015-0159-1]

93 **Wei X**, Warfield SK, Zou KH, Wu Y, Li X, Guimond A, Mugler JP 3rd, Benson RR, Wolfson L, Weiner HL, Guttmann CR. Quantitative analysis of MRI signal abnormalities of brain white matter with high reproducibility and accuracy. *J Magn Reson Imaging* 2002; **15**: 203-209 [PMID: 11836778 DOI: 10.1002/jmri.10053]

94 **Hasebroock KM**, Serkova NJ. Toxicity of MRI and CT contrast agents. *Expert Opin Drug Metab Toxicol* 2009; **5**: 403-416 [PMID: 19368492 DOI: 10.1517/17425250902873796]

95 **Webb JA**, Thomsen HS, Morcos SK; Members of Contrast Media Safety Committee of European Society of Urogenital Radiology (ESUR). The use of iodinated and gadolinium contrast media during pregnancy and lactation. *Eur Radiol* 2005; **15**: 1234-1240 [PMID: 15609057 DOI: 10.1007/s00330-004-2583-y]

96 **Salvi R**, Sheppard A. Is Noise in the MR Imager a Significant Risk Factor for Hearing Loss? *Radiology* 2018; **286**: 609-610 [PMID: 29356640 DOI: 10.1148/radiol.2017172221]

97 **Serai SD**, Hu HH, Ahmad R, White S, Pednekar A, Anupindi SA, Lee EY. Newly Developed Methods for Reducing Motion Artifacts in Pediatric Abdominal MRI: Tips and Pearls. *AJR Am J Roentgenol* 2020; **214**: 1042-1053 [PMID: 32023117 DOI: 10.2214/AJR.19.21987]

98 **Scannell CM**, Correia T, Villa ADM, Schneider T, Lee J, Breeuwer M, Chiribiri A, Henningsson M. Feasibility of free-breathing quantitative myocardial perfusion using multi-echo Dixon magnetic resonance imaging. *Sci Rep* 2020; **10**: 12684 [PMID: 32728198 DOI: 10.1038/s41598-020-69747-9]

99 **McElroy S**, Ferrazzi G, Nazir MS, Evans C, Ferreira J, Bosio F, Mughal N, Kunze KP, Neji R, Speier P, Stäb D, Ismail TF, Masci PG, Villa ADM, Razavi R, Chiribiri A, Roujol S. Simultaneous multislice steady-state free precession myocardial perfusion with full left ventricular coverage and high resolution at 1.5 T. *Magn Reson Med* 2022; **88**: 663-675 [PMID: 35344593 DOI: 10.1002/mrm.29229]

100 **Ley S**, Ley-Zaporozhan J. Pulmonary perfusion imaging using MRI: clinical application. *Insights Imaging* 2012; **3**: 61-71 [PMID: 22695999 DOI: 10.1007/s13244-011-0140-1]

101 **Lasch F**, Karch A, Koch A, Derlin T, Voskrebenzev A, Alsady TM, Hoeper MM, Gall H, Roller F, Harth S, Steiner D, Krombach G, Ghofrani HA, Rengier F, Heußel CP, Grünig E, Beitzke D, Hacker M, Lang IM, Behr J, Bartenstein P, Dinkel J, Schmidt KH, Kreitner KF, Frauenfelder T, Ulrich S, Hamer OW, Pfeifer M, Johns CS, Kiely DG, Swift AJ, Wild J, Vogel-Claussen J. Comparison of MRI and VQ-SPECT as a Screening Test for Patients With Suspected CTEPH: CHANGE-MRI Study Design and Rationale. *Front Cardiovasc Med* 2020; **7**: 51 [PMID: 32328500 DOI: 10.3389/fcvm.2020.00051]

102 **Lechartier B**, Chaouat A, Aubert JD, Schwitter J; Swiss Society for Pulmonary Hypertension (SSPH). Magnetic resonance imaging in pulmonary hypertension: an overview of current applications and future perspectives. *Swiss Med Wkly* 2022; **152**: w30055 [PMID: 35262319 DOI: 10.4414/smw.2022.w30055]

103 **Ota H**, Sugimura K, Miura M, Shimokawa H. Four-dimensional flow magnetic resonance imaging visualizes drastic change in vortex flow in the main pulmonary artery after percutaneous transluminal pulmonary angioplasty in a patient with chronic thromboembolic pulmonary hypertension. *Eur Heart J* 2015; **36**: 1630 [PMID: 25736251 DOI: 10.1093/eurheartj/ehv054]

104 **Jacobs M**, Benovoy M, Chang LC, Corcoran D, Berry C, Arai AE, Hsu LY. Automated Segmental Analysis of Fully Quantitative Myocardial Blood Flow Maps by First-Pass Perfusion Cardiovascular Magnetic Resonance. *IEEE Access* 2021; **9**: 52796-52811 [PMID: 33996344 DOI: 10.1109/access.2021.3070320]

105 **Scannell CM**, Veta M, Villa ADM, Sammut EC, Lee J, Breeuwer M, Chiribiri A. Deep-Learning-Based Preprocessing for Quantitative Myocardial Perfusion MRI. *J Magn Reson Imaging* 2020; **51**: 1689-1696 [PMID: 31710769 DOI: 10.1002/jmri.26983]

106 **Xue H**, Davies RH, Brown LAE, Knott KD, Kotecha T, Fontana M, Plein S, Moon JC, Kellman P. Automated Inline Analysis of Myocardial Perfusion MRI with Deep Learning. *Radiol Artif Intell* 2020; **2**: e200009 [PMID: 33330849 DOI: 10.1148/ryai.2020200009]

107 **Weng AM**, Heidenreich JF, Metz C, Veldhoen S, Bley TA, Wech T. Deep learning-based segmentation of the lung in MR-images acquired by a stack-of-spirals trajectory at ultra-short echo-times. *BMC Med Imaging* 2021; **21**: 79 [PMID: 33964892 DOI: 10.1186/s12880-021-00608-1]

108 **Mairhörmann B**, Castelblanco A, Häfner F, Pfahler V, Haist L, Waibel D, Flemmer A, Ehrhardt H, Stoecklein S, Dietrich O, Foerster K, Hilgendorff A, Schubert B. Deep Learning-Based Magnetic Resonance Imaging Lung Segmentation and Volumetric Marker Extraction in Preterm Infants. 2021 Preprint. Available from: medRxiv 2021.08.06.21261648 [DOI: 10.1101/2021.08.06.21261648]

World Journal of Radiology

Submit a Manuscript: https://www.f6publishing.com

World J Radiol 2023 September 28; 15(9): 274-280

DOI: 10.4329/wjr.v15.i9.274

ISSN 1949-8470 (online)

CASE REPORT

Distinctive magnetic resonance imaging features in primary central nervous system lymphoma: A case report

Li-Hong Liu, Han-Wen Zhang, Hong-Bo Zhang, Xiao-Lei Liu, Hua-Zhen Deng, Fan Lin, Biao Huang

Specialty type: Radiology, nuclear medicine and medical imaging

Provenance and peer review: Unsolicited article; Externally peer reviewed.

Peer-review model: Single blind

Peer-review report's scientific quality classification

Grade A (Excellent): 0
Grade B (Very good): B
Grade C (Good): 0
Grade D (Fair): D
Grade E (Poor): 0

P-Reviewer: Mahmoud MZ, Saudi Arabia

Received: June 30, 2023
Peer-review started: June 30, 2023
First decision: August 24, 2023
Revised: September 4, 2023
Accepted: September 22, 2023
Article in press: September 22, 2023
Published online: September 28, 2023

Li-Hong Liu, Han-Wen Zhang, Xiao-Lei Liu, Hua-Zhen Deng, Fan Lin, Department of Radiology, The First Affiliated Hospital of Shenzhen University, Health Science Center, Shenzhen Second People's Hospital, Shenzhen 518036, Guangdong Province, China

Han-Wen Zhang, Hong-Bo Zhang, Biao Huang, The Second School of Clinical Medicine, Southern Medical University, Guangzhou 510282, Guangdong Province, China

Hong-Bo Zhang, Department of Radiology, Sun Yat-Sen University, Shenzhen 518000, Guangdong Province, China

Biao Huang, Department of Radiology, Guangdong Provincial People's Hospital, Guangdong Academy of Medical Sciences, Guangzhou 510000, Guangdong Province, China

Corresponding author: Han-Wen Zhang, MD, Doctor, Department of Radiology, The First Affiliated Hospital of Shenzhen University, Health Science Center, Shenzhen Second People's Hospital, No. 3002 Sungangxi Road, Shenzhen 518036, Guangdong Province, China.
zhwstarcraft@outlook.com

Abstract

BACKGROUND

Primary central nervous system lymphoma (PCNSL) is a rare malignant tumor originating from the lymphatic hematopoietic system. It exhibits unique imaging manifestations due to its biological characteristics.

CASE SUMMARY

Magnetic resonance imaging (MRI) with diffusion-weighted imaging (DWI), perfusion-weighted imaging (PWI), and magnetic resonance spectroscopy was performed. The imaging findings showed multiple space-occupying lesions with low signal on T1-weighted imaging, uniform high signal on T2-weighted imaging, and obvious enhancement on contrast-enhanced scans. DWI revealed diffusion restriction, PWI demonstrated hypoperfusion, and spectroscopy showed elevated choline peak and decreased N-acetylaspartic acid. The patient's condition significantly improved after hormone shock therapy.

CONCLUSION

This case highlights the distinctive imaging features of PCNSL and their importance in accurate diagnosis and management.

Key Words: Primary central nervous system lymphoma; Primary central nervous system

lymphoma; Diffusion-weighted imaging; Perfusion-weighted imaging; Magnetic resonance imaging; Case report

©The Author(s) 2023. Published by Baishideng Publishing Group Inc. All rights reserved.

Core Tip: Primary central nervous system lymphoma (PCNSL) is a rare tumor of the central nervous system with distinctive imaging features. This case report highlights the imaging manifestations of multiple PCNSL lesions using diffusion-weighted imaging, perfusion-weighted imaging, and magnetic resonance imaging. Accurate diagnosis is crucial for appropriate management. Further research and larger studies are needed to enhance the understanding and diagnostic accuracy of PCNSL.

Citation: Liu LH, Zhang HW, Zhang HB, Liu XL, Deng HZ, Lin F, Huang B. Distinctive magnetic resonance imaging features in primary central nervous system lymphoma: A case report. *World J Radiol* 2023; 15(9): 274-280
URL: https://www.wjgnet.com/1949-8470/full/v15/i9/274.htm
DOI: https://dx.doi.org/10.4329/wjr.v15.i9.274

INTRODUCTION

Primary central nervous system lymphoma (PCNSL) is an exceptionally rare and aggressive malignancy originating within the central nervous system. Despite its infrequency, PCNSL presents unique diagnostic and therapeutic challenges, rendering it a subject of profound clinical importance[1]. In recent years, advanced imaging techniques, including diffusion-weighted imaging (DWI), perfusion-weighted imaging (PWI), and magnetic resonance (MR) spectroscopy, have greatly enhanced our ability to comprehend the disease and its distinctive manifestations[2].

While previous studies have provided valuable insights into the broader understanding of PCNSL, there is a critical gap in characterizing the imaging features on an individual case level[3]. This study endeavors to bridge this gap by conducting an in-depth examination of DWI, PWI, and MR spectroscopy findings in a single PCNSL case. By scrutinizing these imaging modalities within the unique context of this individual case, we aim to contribute to the comprehensive understanding of PCNSL's imaging features and their potential clinical implications[4].

The primary research problem addressed in this study is to delineate the specific magnetic resonance imaging (MRI) imaging manifestations of PCNSL within the scope of a single case analysis and to comprehend their diagnostic and clinical significance. To accomplish this, we have conducted a detailed analysis of DWI, PWI, and MR spectroscopy findings in the context of this singular PCNSL case.

CASE PRESENTATION

Chief complaints

A 79-year-old female patient with a previously unremarkable medical history presented with a sudden onset of unexplained dizziness accompanied by projectile vomiting, characterized by the ejection of gastric contents. She also reported a sense of heaviness and weakness in her limbs.

History of present illness

Initial evaluation at another medical facility revealed the presence of multiple intracranial space-occupying lesions. These lesions were detected through a computed tomography scan, which indicated the involvement of the cerebellar hemisphere, corpus callosum's splenium, and the left parietal lobe.

History of past illness

No special notes.

Personal and family history

No special notes.

Physical examination

Physical examination revealed no abnormalities.

Laboratory examinations

The platelet specific volume was slightly elevated. The monocyte count was mildly elevated. The bacterial content in the urine test increased [4225.40, reference value: 0-4000 (/μL)].

Imaging examinations

Upon admission, the patient underwent a comprehensive evaluation, including MRI with DWI, PWI, and MR spectroscopy (MRS). The MRI results confirmed the presence of multiple space-occupying lesions, characterized by low signal intensity on T1-weighted imaging, uniform high signal intensity on T2-weighted imaging, and prominent enhancement on contrast-enhanced scans (Figure 1). DWI further revealed diffusion restriction, while PWI demonstrated hypoperfusion in all the identified lesions. Additionally, spectroscopy (MRS) depicted an elevated choline peak and decreased N-acetylaspartic acid. Notably, MRS also revealed the presence of a Lip peak within the lesion (Figure 2). These combined imaging features strongly suggested the possibility of PCNSL.

FINAL DIAGNOSIS

Pathological examination of the intracranial lesion confirmed the presence of an aggressive B-cell lymphoma. Immunohistochemical analysis demonstrated the following profile: CD21 (-), CD10 (-), CD20 (+), CD3 (background T-cells +), CD30 (-), PAX-5 (+), Bcl-6 (+), MUM-1 (+), Ki-67 (approximately 80%), CD5 (-), CD23 (-), Bcl-2 (-), CyclinD1 (-), CD79A (+), C-MYC (approximately 30%+), P53 (10%+ with varying intensity), GFAP (glial cells +). Importantly, Epstein-Barr virus-encoded small RNA (EBER) was not detected. These findings confirmed the diagnosis of diffuse large B-cell lymphoma of the non-germinal center B-cell (non-GCB) subtype, supporting the diagnosis of PCNSL.

TREATMENT

Treatment and response

In response to the initial presentation and MRI findings, the patient underwent a diagnostic trial of steroid therapy. This treatment led to a significant improvement in the patient's neurological condition, although it was accompanied by the emergence of certain neuropsychiatric symptoms. Subsequent administration of medications, including lorazepam and olanzapine, resulted in a notable improvement in the patient's neuropsychiatric symptoms. Follow-up MRI examinations indicated a reduction in enhancement in the lesions located in the hippocampus and left parietal lobe, with the other lesions remaining stable or showing slight reductions (Figure 3).

OUTCOME AND FOLLOW-UP

The patient subsequently received standardized lymphoma immunotherapy and chemotherapy regimens, and her prognosis remains favorable.

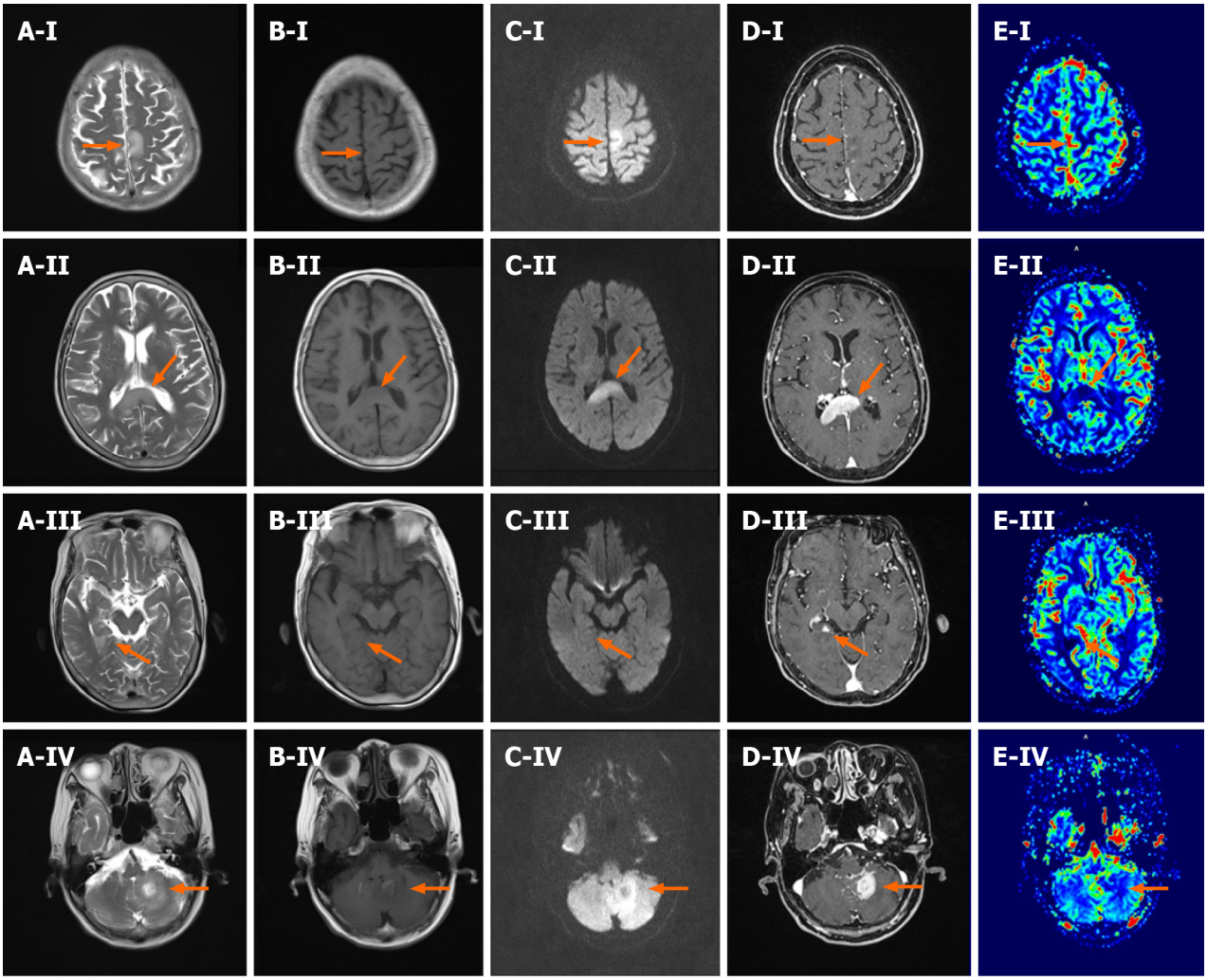
DISCUSSION

There is no lymphoid tissue present within the central nervous system, making brain lymphomas relatively rare. Currently, the origin of intracerebral lymphoma can be attributed to the following factors: Firstly, reactive lymphocytes enter the brain tissue during intracerebral infection and undergo malignant transformation through various mechanisms. Secondly, activated peripheral lymphocytes transform into tumor cells and migrate to the brain through the bloodstream, resulting in tumors primarily located around the ventricles, basal ganglia, and frontoparietal lobes. Thirdly, undifferentiated pluripotent stem cells surrounding blood vessels in the brain may serve as the source of intracerebral lymphoma. Histologically, intracerebral lymphomas exhibit predominant sleeve-shaped growth, infiltrating the surrounding brain parenchyma, and demonstrating multicentric growth within the tumor[5].

PCNSL typically presents as supratentorial lesions, with predilection sites in the cerebral hemisphere, corpus callosum, basal ganglia, and thalamus[6]. The imaging findings of PCNSL are closely related to its pathological features. In this case, the lesions were confined to the brain tissue, involving both supratentorial and infratentorial areas, which is relatively rare[7].

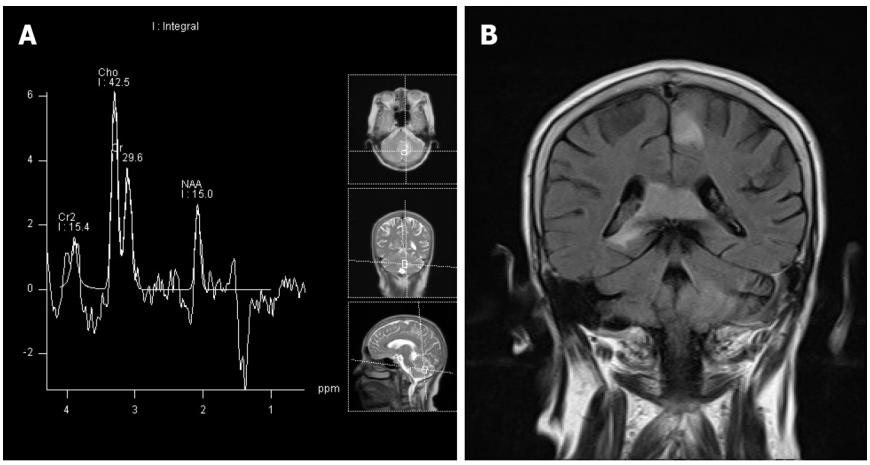
On conventional MRI, PCNSL shows iso-hypointensity on T1-weighted imaging and iso-hypointensity on T2-weighted imaging[8]. DWI demonstrates diffusion restriction due to densely arranged tumor cells. According to Lin *et al*[9], their study suggests that combining DWI ADC value with T1WI enhanced scan can aid in the differentiation of glioblastoma from PCNSL. PWI reveals hypoperfusion, reflecting the hypo-vascular nature of PCNSL[10]. Contrast-enhanced scans show uniform enhancement when the tumor invades adjacent brain parenchyma and disrupts the blood-brain barrier (BBB). In our previous study, we compared high-grade glioma (HGG) with lymphoma using dynamic contrast-enhanced (DCE) imaging, and found that lymphoma has more obvious damage to the BBB, resulting in transfer constant(K^{trans}) values even higher than HGG[11]. The characteristic imaging features, such as the "fist sign," "sharp horn sign," and "butterfly wing sign,"(usually occurs in the corpus callosum) are associated with the tumor's angiophilic growth.

MRS plays a crucial role in the evaluation of PCNSL. Elevated choline peak, decreased N-acetylaspartic acid, and a towering lipid peak are commonly observed[12]. The towering lipid peak is highly specific for the diagnosis of PCNSL, attributed to the accelerated turnover of lymphocytes and macrophages. PCNSL should be differentiated from



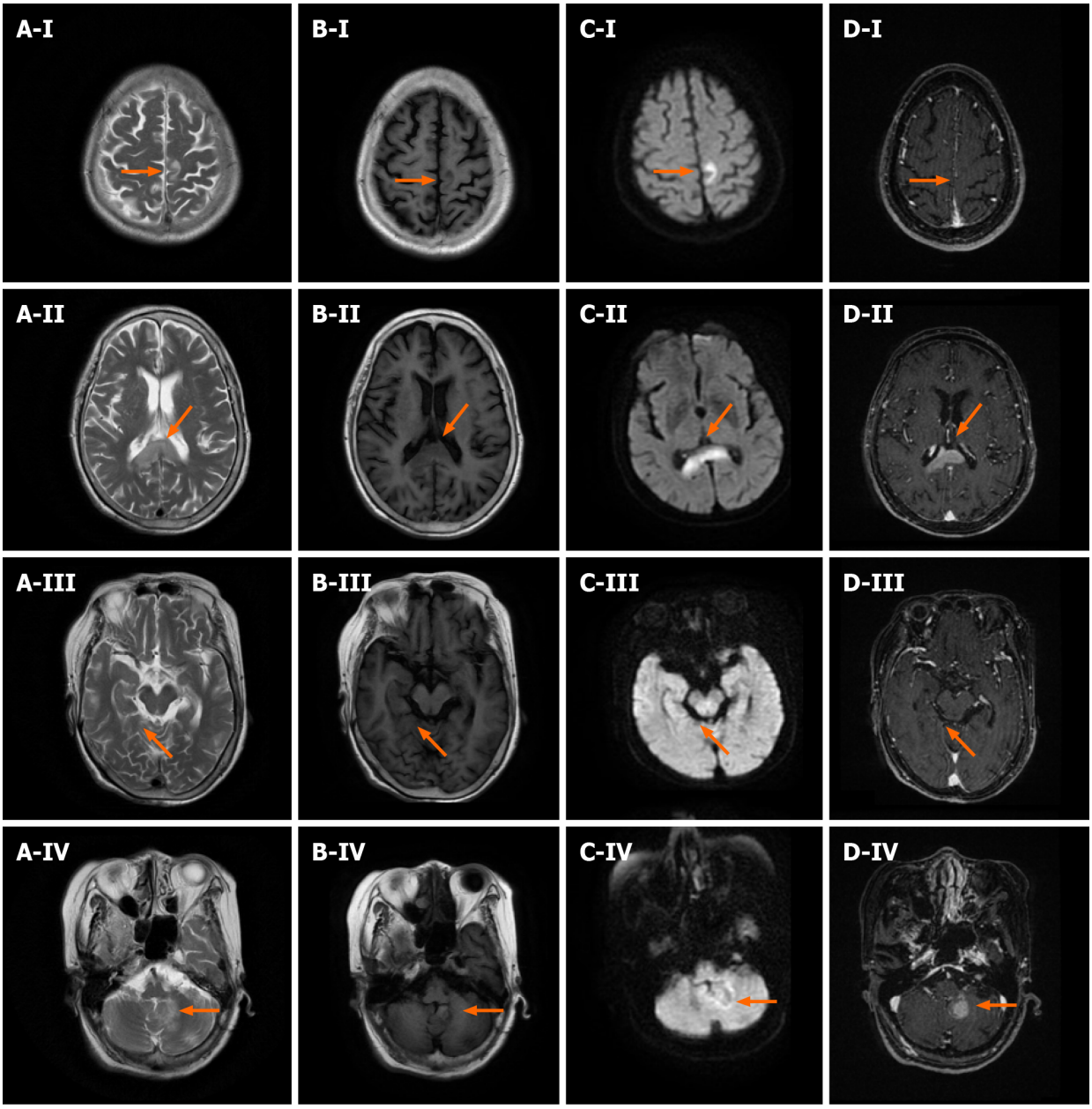
DOI: 10.4329/wjr.v15.i9.274 **Copyright** ©The Author(s) 2023.

Figure 1 Images of the patient prior to corticosteroid pulse therapy. A: T2WI; B: T1WI; C: Diffusion-weighted imaging; D: T1-weighted enhanced scan; E: Dynamic susceptibility contrast perfusion-weighted imaging cerebral blood volume; I: parietal lobe lesions; II: corpus callosum lesions; III: hippocampal lesions; IV: Left cerebellar hemisphere lesions.



DOI: 10.4329/wjr.v15.i9.274 **Copyright** ©The Author(s) 2023.

Figure 2 Notably, magnetic resonance spectroscopy also revealed the presence of a lip peak within the lesion. A: Magnetic resonance spectroscopy; B: Butterfly sign when primary central nervous system lymphoma is located in the corpus callosum.



DOI: 10.4329/wjr.v15.i9.274 **Copyright** ©The Author(s) 2023.

Figure 3 Images of the patient following corticosteroid pulse therapy. A: T2WI; B: T1WI; C: Diffusion-weighted imaging; D: T1-weighted enhanced scan; I: Parietal lobe lesions; II: Corpus callosum lesions; III: Hippocampal lesions; IV: Left cerebellar hemisphere lesions.

demyelinating diseases, as their imaging findings may resemble each other[13]. Hormone shock therapy can provide symptomatic relief in both PCNSL and demyelinating diseases, but recovery of symptoms after hormone therapy withdrawal is indicative of PCNSL.

In addition to our contributions to the understanding of PCNSL, it is essential to recognize the limitations of our study. The utilization of a single-case design inherently limits the generalizability of our findings to a broader population of PCNSL patients. Future research should strive to replicate these findings in larger cohorts to establish their broader applicability. Furthermore, our study primarily focuses on the imaging aspects of PCNSL, and future investigations could explore the correlation between imaging features and specific clinical outcomes. These considerations highlight both the strengths and the areas for improvement in our research.

CONCLUSION

This single-case analysis of PCNSL has shed light on the distinctive MRI imaging features of this rare malignancy. By employing advanced techniques such as DWI, PWI, and MR spectroscopy, we have provided a comprehensive characterization of PCNSL's imaging manifestations. However, it is important to acknowledge the limitations of this study. The use of a single-case design restricts the generalizability of our findings to a broader population. Future research should

aim to replicate these findings in larger cohorts of PCNSL patients to establish their broader applicability. Additionally, our study focused on the imaging aspects, and future investigations could explore the correlation between imaging features and specific clinical outcomes. Despite these limitations, our study contributes valuable insights into the unique imaging features of PCNSL and serves as a foundation for further research in this area.

FOOTNOTES

Author contributions: Case studies were provided by Liu LH; Zhang HW wrote the article; Deng HZ searched the literature; Zhang HB analyzed the case; Huang B and Lin F revised and reviewed the manuscript; Huang B (huangbiao@gdph.org.cn), Lin F (foxetfoxet@gmail.com), and Zhang HW contributed equally to this research.

Supported by National Natural Science Foundation of China, No. 82071871; Guangdong Basic and Applied Basic Research Foundation, No. 2021A1515220131; Guangdong Medical Science and Technology Research Fund Project, No. 2022111520491834; and Clinical Research Project of Shenzhen Second People's Hospital, China, No. 20223357022.

Informed consent statement: The patient signed an informed consent to the publication of this case.

Conflict-of-interest statement: The author(s) declared no potential conflicts of interest with respect to the research, authorship, and/or publication of this article.

CARE Checklist (2016) statement: The authors have read the CARE Checklist (2016), and the manuscript was prepared and revised according to the CARE Checklist (2016).

Open-Access: This article is an open-access article that was selected by an in-house editor and fully peer-reviewed by external reviewers. It is distributed in accordance with the Creative Commons Attribution NonCommercial (CC BY-NC 4.0) license, which permits others to distribute, remix, adapt, build upon this work non-commercially, and license their derivative works on different terms, provided the original work is properly cited and the use is non-commercial. See: https://creativecommons.org/Licenses/by-nc/4.0/

Country/Territory of origin: China

ORCID number: Han-Wen Zhang 0000-0001-5731-7429; Fan Lin 0000-0003-1595-2736.

S-Editor: Liu JH
L-Editor: A
P-Editor: Liu JH

REFERENCES

1 **Krebs S**, Barasch JG, Young RJ, Grommes C, Schöder H. Positron emission tomography and magnetic resonance imaging in primary central nervous system lymphoma-a narrative review. *Ann Lymphoma* 2021; **5** [PMID: 34223561 DOI: 10.21037/aol-20-52]
2 **Schaff LR**, Grommes C. Primary central nervous system lymphoma. *Blood* 2022; **140**: 971-979 [PMID: 34699590 DOI: 10.1182/blood.2020008377]
3 **Deng B**, Dai Y, Wang Q, Yang J, Chen X, Liu TT, Liu J. The clinical analysis of new-onset status epilepticus. *Epilepsia Open* 2022; **7**: 771-780 [PMID: 36214088 DOI: 10.1002/epi4.12657]
4 **Han Y**, Wang ZJ, Li WH, Yang Y, Zhang J, Yang XB, Zuo L, Xiao G, Wang SZ, Yan LF, Cui GB. Differentiation Between Primary Central Nervous System Lymphoma and Atypical Glioblastoma Based on MRI Morphological Feature and Signal Intensity Ratio: A Retrospective Multicenter Study. *Front Oncol* 2022; **12**: 811197 [PMID: 35174088 DOI: 10.3389/fonc.2022.811197]
5 **Barajas RF**, Politi LS, Anzalone N, Schöder H, Fox CP, Boxerman JL, Kaufmann TJ, Quarles CC, Ellingson BM, Auer D, Andronesi OC, Ferreri AJM, Mrugala MM, Grommes C, Neuwelt EA, Ambady P, Rubenstein JL, Illerhaus G, Nagane M, Batchelor TT, Hu LS. Consensus recommendations for MRI and PET imaging of primary central nervous system lymphoma: guideline statement from the International Primary CNS Lymphoma Collaborative Group (IPCG). *Neuro Oncol* 2021; **23**: 1056-1071 [PMID: 33560416 DOI: 10.1093/neuonc/noab020]
6 **Weller M**. The vanishing role of whole brain radiotherapy for primary central nervous system lymphoma. *Neuro Oncol* 2014; **16**: 1035-1036 [PMID: 24958097 DOI: 10.1093/neuonc/nou120]
7 **Bhattacharjee R**, Gupta M, Singh T, Sharma S, Khanna G, Parvaze SP, Patir R, Vaishya S, Ahlawat S, Singh A, Gupta RK. Role of intra-tumoral vasculature imaging features on susceptibility weighted imaging in differentiating primary central nervous system lymphoma from glioblastoma: a multiparametric comparison with pathological validation. *Neuroradiology* 2022; **64**: 1801-1818 [PMID: 35435463 DOI: 10.1007/s00234-022-02946-5]
8 **Toh CH**, Wei KC, Chang CN, Ng SH, Wong HF. Differentiation of primary central nervous system lymphomas and glioblastomas: comparisons of diagnostic performance of dynamic susceptibility contrast-enhanced perfusion MR imaging without and with contrast-leakage correction. *AJNR Am J Neuroradiol* 2013; **34**: 1145-1149 [PMID: 23348763 DOI: 10.3174/ajnr.A3383]
9 **Lin X**, Lee M, Buck O, Woo KM, Zhang Z, Hatzoglou V, Omuro A, Arevalo-Perez J, Thomas AA, Huse J, Peck K, Holodny AI, Young RJ. Diagnostic Accuracy of T1-Weighted Dynamic Contrast-Enhanced-MRI and DWI-ADC for Differentiation of Glioblastoma and Primary CNS Lymphoma. *AJNR Am J Neuroradiol* 2017; **38**: 485-491 [PMID: 27932505 DOI: 10.3174/ajnr.A5023]
10 **Kang KM**, Choi SH, Chul-Kee P, Kim TM, Park SH, Lee JH, Lee ST, Hwang I, Yoo RE, Yun TJ, Kim JH, Sohn CH. Differentiation between glioblastoma and primary CNS lymphoma: application of DCE-MRI parameters based on arterial input function obtained from DSC-MRI. *Eur*

Radiol 2021; **31**: 9098-9109 [PMID: 34003350 DOI: 10.1007/s00330-021-08044-z]

11 **Zhang HW**, Lyu GW, He WJ, Lei Y, Lin F, Feng YN, Wang MZ. Differential diagnosis of central lymphoma and high-grade glioma: dynamic contrast-enhanced histogram. *Acta Radiol* 2020; **61**: 1221-1227 [PMID: 31902220 DOI: 10.1177/0284185119896519]

12 **Du X**, He Y, Lin W. Diagnostic Accuracy of the Diffusion-Weighted Imaging Method Used in Association With the Apparent Diffusion Coefficient for Differentiating Between Primary Central Nervous System Lymphoma and High-Grade Glioma: Systematic Review and Meta-Analysis. *Front Neurol* 2022; **13**: 882334 [PMID: 35812103 DOI: 10.3389/fneur.2022.882334]

13 **Miyajima T**, Ohigashi H, Yaguchi H, Teshima T. Neurolymphomatosis in Intravascular Large B-cell Lymphoma. *Intern Med* 2023; **62**: 1381-1382 [PMID: 36198588 DOI: 10.2169/internalmedicine.0021-22]



Published by **Baishideng Publishing Group Inc**
7041 Koll Center Parkway, Suite 160, Pleasanton, CA 94566, USA
Telephone: +1-925-3991568
E-mail: bpgoffice@wjgnet.com
Help Desk: https://www.f6publishing.com/helpdesk
https://www.wjgnet.com



© 2023 Baishideng Publishing Group Inc. All rights reserved.

ISSN 1949-8470 (online)

World Journal of *Radiology*

World J Radiol 2023 October 28; 15(10): 281-303



Published by Baishideng Publishing Group Inc

WJR

World Journal of Radiology

Contents

Monthly Volume 15 Number 10 October 28, 2023

ORIGINAL ARTICLE

Retrospective Study

281 Does the use of computed tomography scenogram alone enable diagnosis in cases of bowel obstruction?

Kadirhan O, Kızılgoz V, Aydin S, Bilici E, Bayat E, Kantarci M

293 Two-point Dixon and six-point Dixon magnetic resonance techniques in the detection, quantification and grading of hepatic steatosis

Elfaal M, Supersad A, Ferguson C, Locas S, Manolea F, Wilson MP, Sam M, Tu W, Low G

World Journal of Radiology

Monthly Volume 15 Number 10 October 28, 2023

Contents

ABOUT COVER

Editorial Board Member of *World Journal of Radiology*, Ozum Tuncyurek, Doctor, MD, Associate Professor, Radiology, Near East University Faculty of Medicine, Nicosia 99100, Cyprus. ozum.tuncyurek@gmail.com

AIMS AND SCOPE

The primary aim of *World Journal of Radiology* (*WJR*, *World J Radiol*) is to provide scholars and readers from various fields of radiology with a platform to publish high-quality basic and clinical research articles and communicate their research findings online.

WJR mainly publishes articles reporting research results and findings obtained in the field of radiology and covering a wide range of topics including state of the art information on cardiopulmonary imaging, gastrointestinal imaging, genitourinary imaging, musculoskeletal imaging, neuroradiology/head and neck imaging, nuclear medicine and molecular imaging, pediatric imaging, vascular and interventional radiology, and women's imaging.

INDEXING/ABSTRACTING

The *WJR* is now abstracted and indexed in PubMed, PubMed Central, Emerging Sources Citation Index (Web of Science), Reference Citation Analysis, China National Knowledge Infrastructure, China Science and Technology Journal Database, and Superstar Journals Database. The 2023 Edition of Journal Citation Reports® cites the 2022 impact factor (IF) for *WJR* as 2.5; IF without journal self cites: 2.3; 5-year IF: 2.5; Journal Citation Indicator: 0.54.

RESPONSIBLE EDITORS FOR THIS ISSUE

Production Editor: *Si Zhao*; **Production Department Director:** *Xu Guo*; **Editorial Office Director:** *Jia-Ping Yan*.

NAME OF JOURNAL
World Journal of Radiology

ISSN
ISSN 1949-8470 (online)

LAUNCH DATE
January 31, 2009

FREQUENCY
Monthly

EDITORS-IN-CHIEF
Thomas J Vogl

EDITORIAL BOARD MEMBERS
https://www.wjgnet.com/1949-8470/editorialboard.htm

PUBLICATION DATE
October 28, 2023

COPYRIGHT
© 2023 Baishideng Publishing Group Inc

INSTRUCTIONS TO AUTHORS
https://www.wjgnet.com/bpg/gerinfo/204

GUIDELINES FOR ETHICS DOCUMENTS
https://www.wjgnet.com/bpg/GerInfo/287

GUIDELINES FOR NON-NATIVE SPEAKERS OF ENGLISH
https://www.wjgnet.com/bpg/gerinfo/240

PUBLICATION ETHICS
https://www.wjgnet.com/bpg/GerInfo/288

PUBLICATION MISCONDUCT
https://www.wjgnet.com/bpg/gerinfo/208

ARTICLE PROCESSING CHARGE
https://www.wjgnet.com/bpg/gerinfo/242

STEPS FOR SUBMITTING MANUSCRIPTS
https://www.wjgnet.com/bpg/GerInfo/239

ONLINE SUBMISSION
https://www.f6publishing.com

© 2023 Baishideng Publishing Group Inc. All rights reserved. 7041 Koll Center Parkway, Suite 160, Pleasanton, CA 94566, USA
E-mail: bpgoffice@wjgnet.com https://www.wjgnet.com

World Journal of Radiology

Submit a Manuscript: https://www.f6publishing.com

World J Radiol 2023 October 28; 15(10): 281-292

DOI: 10.4329/wjr.v15.i10.281

ISSN 1949-8470 (online)

ORIGINAL ARTICLE

Retrospective Study

Does the use of computed tomography scenogram alone enable diagnosis in cases of bowel obstruction?

Ozlem Kadirhan, Volkan Kızılgoz, Sonay Aydin, Esra Bilici, Ekrem Bayat, Mecit Kantarci

Specialty type: Radiology, nuclear medicine & medical imaging

Provenance and peer review: Invited article; Externally peer reviewed.

Peer-review model: Single blind

Peer-review report's scientific quality classification

Grade A (Excellent): 0
Grade B (Very good): 0
Grade C (Good): 0
Grade D (Fair): D
Grade E (Poor): 0

P-Reviewer: Ciarambino T, Italy

Received: July 28, 2023
Peer-review started: July 28, 2023
First decision: September 14, 2023
Revised: September 26, 2023
Accepted: October 11, 2023
Article in press: October 11, 2023
Published online: October 28, 2023

Ozlem Kadirhan, Volkan Kızılgoz, Sonay Aydin, Esra Bilici, Ekrem Bayat, Mecit Kantarci, Department of Radiology, Erzincan Binali Yıldırım University, Faculty of Medicine, Erzincan 24000, Turkey

Mecit Kantarci, Department of Radiology, Ataturk University, Faculty of Medicine, Erzurum 25000, Turkey

Corresponding author: Sonay Aydin, MD, Associate Professor, Department of Radiology, Erzincan Binali Yıldırım University, Faculty of Medicine, Haci Ali Akin cd., Erzincan 24000, Turkey. sonay.aydin@erzincan.edu.tr

Abstract

BACKGROUND

Ileus is a pathological condition of the abdomen that presents as a medical emergency. It is characterized by potential complications such as perforation and ischemia, which can lead to significant morbidity and mortality if not promptly addressed. The successful management of ileus relies heavily on the timely and precise identification of the condition. While conventional radiography (CR) is commonly used as the primary diagnostic tool, its accuracy in identifying obstructions ranges from 46% to 80%. Furthermore, the diagnostic accuracy of identifying the location and etiology of intestinal obstruction by CR is limited, therefore making computed tomography (CT) the ideal imaging modality in this regard.

AIM

To determine the presence of acute bowel obstruction (BO) on abdominal CT scenogram images and the accuracy of determining its possible location, taking into account the experience of the observers.

METHODS

A retrospective screening was conducted on an ensemble of 46 individuals who presented to the emergency department between January 2021 and January 2022 with severe abdominal pain and were subsequently monitored for suspected ileus. The abdominal CT scans of these patients were assessed by three radiologists with varying levels of experience (1, 3, and 10 years) at different intervals (1 mo apart). The evaluation focused on determining the presence or absence of BO, as well as identifying the potential location of the obstruction (small bowel or large bowel). The study employed Kappa statistics to assess inter-

observer variances, while the McNamer test was used to evaluate obstruction and segmentation discrepancies between observations. A significance level of $P < 0.05$ was determined to indicate statistical significance.

RESULTS

Out of the total sample size of 46 patients, 15 individuals (32.6%) were identified as female, while the remaining 31 individuals (67.4%) were identified as male. The ultimate diagnosis of 42 instances (91.3%) indicated ileus resulting from mechanical obstruction (MO). Among these patients, 14 (33%) experienced obstruction in the large bowel (LB), while 28 (66%) experienced obstruction in the small bowel (SB). The initial evaluation yielded sensitivity rates of 76.19%, 83.31%, and 83.33%, and diagnostic accuracy rates of 69.56%, 76.08%, and 80.43% for the detection of BO among the three observers. The initial study revealed that the average sensitivity of three observers in detecting the presence of ileus caused by MO was 80.94%, while the diagnostic accuracy was 75.35%. Based on the first evaluation, the senior observer demonstrated the highest sensitivity (85.71%), negative predictive value (92.60%), and diagnostic accuracy (80.43%) when accurately estimating the thick and thin segmentation, as per the final diagnosis. There was no statistically significant disparity observed in the sensitivities pertaining to the identification of ileus during the second assessment, as well as the precise determination of the segment level inside the LB or SB, when comparing the second and third observers. Nevertheless, although there was no statistically significant alteration in the detection rate of ileus by the first observer, there was a notable rise in the accuracy rate of segment estimating (73.91%). The senior assessor had a higher level of accuracy in assessing the existence of ileus and segmentation compared to the other evaluators in both evaluations.

CONCLUSION

The findings of our study indicate that the sensitivity and accuracy rates of abdominal CT scenogram scans in diagnosing acute MOs are similar to or greater than those of CR. Additionally, the study revealed that radiologists with more experience demonstrated a higher likelihood of accurately predicting the existence and potential localization of MO compared to their less experienced counterparts.

Key Words: Ileus; Computed tomography; Scenogram scan; Radiography

©The Author(s) 2023. Published by Baishideng Publishing Group Inc. All rights reserved.

Core Tip: This retrospective study aims to determine the accuracy of detecting the presence and possible location of obstruction on computed tomography (CT) scenogram images of the abdomen, which can be used as the primary imaging method in the diagnosis of acute bowel obstruction, taking observer experience into account. The experienced observer had the highest sensitivity (83.33%), positive predictive value (94.59%), and diagnostic accuracy (80.43%) for detecting mechanical obstruction (MO). The diagnostic accuracy of the same observer in estimating the segmentation of a MO was 80.43%. These findings show that CT scenogram images alone can demonstrate high diagnostic accuracy and sensitivity in relation to years of experience in diagnosing ileus.

Citation: Kadirhan O, Kızılgoz V, Aydin S, Bilici E, Bayat E, Kantarci M. Does the use of computed tomography scenogram alone enable diagnosis in cases of bowel obstruction? *World J Radiol* 2023; 15(10): 281-292
URL: https://www.wjgnet.com/1949-8470/full/v15/i10/281.htm
DOI: https://dx.doi.org/10.4329/wjr.v15.i10.281

INTRODUCTION

Diagnostic imaging is necessary to determine the existence, location, severity, and potential cause of bowel obstruction (BO) when it is suspected based on clinical indicators and physical examination results[1]. BO is a medical disorder that can arise from either mechanical or functional causes, impeding the regular flow of intestinal contents. The choice of therapy, whether surgical or non-surgical, and subsequent follow-up treatments, will depend on the underlying cause of the obstruction. According to existing literature, it has been reported that around 20% of surgical admissions related to acute abdominal discomfort can be attributed to BO[2]. Timely identification of this condition has significance in terms of averting potential consequences such as perforation and ischemia.

Conventional radiography (CR) is the primary imaging modality utilized for determining the existence of ileus, owing to its widespread availability and cost-effectiveness[3]. Nevertheless, CR is not typically capable of accurately displaying the precise position, extent, and etiology of BO, nor can it effectively identify secondary indications such as aberrant wall thickening, pneumatous acid, and intestinal viability. In contrast, computed tomography (CT) is widely regarded as the preferred modality for addressing these diagnostic needs[4]. The literature has demonstrated a range of 90-95% accuracy for CT in the diagnosis of high-grade intestinal obstructions[5-8]. CT scenogram images are acquired with the patient lying in the supine posture, and they offer a comprehensive overview of the region of interest. These images are obtained

with minimal radiation exposure. The utilization of X-rays in both CT and CR imaging techniques results in the generation of ionizing radiation. Ionizing radiation induces heritable alterations in the genetic code *via* deoxyribonucleic acid damage. It has been reported that ionizing radiation can cause cataracts, skin burns, temporary or permanent infertility in the case of exposure to high doses, and various cancers in the case of intermittent exposure to low doses[9]. In a published study, 1012 patients who presented to the emergency department and simultaneously underwent chest X-ray and CT scan were included. This study demonstrated that a single imaging method was able to accurately diagnose the patients in 77.1% of the cases involving trauma and 80.4% of the cases without trauma. Consequently, the prompt referral of patients to appropriate treatment was facilitated, as there was no requirement for a second imaging method. This demonstrates the importance of minimizing the utilization of imaging techniques that include ionizing radiation, in light of the potential adverse consequences[10]. A study revealed that the utilization of CT scenogram images as a standalone diagnostic tool for BO exhibited an interobserver sensitivity ranging from 93% to 86% and a specificity ranging from 85% to 87%. These findings were similar to the outcomes reported for axial CT and the combination of axial and coronal CT[11].

The purpose of this study was to determine the presence and potential location of obstruction on CT scenogram images of the abdomen, which can be used as a primary imaging method in the diagnosis of acute BO, taking observer experience into consideration.

MATERIALS AND METHODS

The research undertaken in this study received approval from the Erzincan University Ethics Committee (Decision no: E-21142744 804.01-128338 Date: December 7, 2021) and was carried out in compliance with the principles outlined in the Declaration of Helsinki.

The retrospective design of the study necessitated the exemption of informed consent. A retrospective investigation was conducted on a cohort of 46 patients who were brought to the emergency department between January 2021 and January 2022. These patients presented with acute abdomen and were subsequently followed up due to suspicion of BO. As part of the evaluation, multi-detector abdominal CT scans were performed. The CT scans underwent anonymization processes and were thereafter uploaded to designated workstations.

The coronal abdominal CT scenogram images of the patients enrolled in the study were assessed by three radiologists who had varying levels of experience, with one having 1 year, another having 3 years, and the third having 10 years of experience. These radiologists were blinded to the final diagnosis of the patients. The abdominal CT scenogram images were assessed at two separate time points, with a one-month interval, to determine the presence of BO (coded as 1 for presence and 0 for absence). Additionally, the localization of the potential obstruction (either in the small bowel or the large bowel) was evaluated in cases where obstruction was suspected.

The ultimate diagnosis was determined by reviewing medical records, surgical reports, and pathology results. The exclusion of BO can be achieved through the identification and treatment of an alternative illness, or by confirming that the patient has not undergone exploratory laparotomy and does not exhibit any indications of prolonged discomfort, abscess, or unexplained fever throughout their hospitalization.

The investigation of inter-observer differences was conducted using Kappa statistics. The percentages of inter-observer and intra-observer agreement were determined by dividing the total number of instances with complete agreement by the overall number of instances. Cohen's Kappa statistics were employed to assess the level of agreement, accounting for the agreement that could occur by chance. Interpretation of the Kappa statistic is as follows: When the value is less than 0.00, the level of agreement is considered poor; when the value falls between 0.00 and 0.20, the agreement is categorized as mild; when the value ranges from 0.21 to 0.40, the agreement is considered fair; when the value falls between 0.41 and 0.60, the agreement is categorized as moderate; when the value ranges from 0.61 to 0.80, the agreement is categorized as considerable; and when the value falls between 0.81 and 1.00, the agreement is virtually perfect. The present study examined the inter-observer appraisal of obstruction and segmentation differences using the McNamer test. The statistical analyses were conducted using the SPSS (Statistical Package for the Social Sciences, SPSS Inc., Chicago, IL, United States) 21.0 software package. Statistical significance was determined by a P value threshold of less than 0.05.

RESULTS

Demographic findings: Out of the total sample size of 46 patients, 15 individuals (32.6%) were identified as female, while the remaining 31 participants (67.4%) were classified as male. The ultimate diagnosis of 42 instances, accounting for 91.3% of the total, indicated ileus resulting from MO. Out of the total number of patients, 14 individuals (33%) exhibited obstruction in the large bowel (LB), whereas 28 individuals (66%) experienced obstruction in the small bowel (SB). A comprehensive breakdown of the factors contributing to obstruction is presented in Table 1. Several case studies are illustrated in Figures 1-4.

The initial assessment scenario for identifying the existence of obstruction: The initial sensitivity findings of the three observers analyzing the abdominal CT scenogram images were 76.19%, 83.31%, and 83.33%, while their diagnostic accuracy results in recognizing the existence of BO were 69.56%, 76.08%, and 80.43%, respectively. The average sensitivity estimate for all three observers in detecting ileus caused by MO during the initial examination was determined to be 80.94%, with a corresponding diagnostic accuracy of 75.35%. The third observer demonstrated the greatest sensitivity (83.33%), positive predictive value (94.59%), and diagnostic accuracy (80.43%) among all observers, as shown in Table 2.

Table 1 Etiologies of cases with mechanical obstruction in this study

Causes of mechanical obstruction	Case count
Postoperative adhesion	**21**
Hernia	**10**
Epigastric	2
Femoral	2
Incisional	1
Indirect inguinal	2
Umbilical	2
Obturator	1
Colon cancer	**6**
Ascending	1
Descending	2
Transverse	1
Sigmoid	2
Volvulus	**3**
Sigmoid	3
Ileitis due to Crohn's disease	**1**
Closed loop obstruction	**1**

Table 2 Observer's concordance with the final diagnosis of obstruction in the scenogram, *n* (%)

	Mechanical obstruction by final diagnosis			Specificity, %	Sensitivity, %	PPV, %	NPV, %	Accuracy, %
	Yes	None	Total					
I Observer								
Yes	32 (76.2)	4 (100)	36 (78.3)	76.19	0	88.88	0	69.56
None	10 (23.8)	0 (0)	10 (21.7)					
II Observer								
Yes	35 (83.3)	4 (100)	39 (84.8)	83.31	0	89.74	0	76.08
None	7 (16.7)	0 (0)	7 (15.2)					
III Observer								
Yes	35 (83.3)	2 (50)	37 (80.4)	83.33	50	94.59	22.23	80.43
None	7 (16.7)	2 (50)	9 (19.6)					
Total	42 (91.3)	4 (8.7)	46 (100)					

Initial examination of obstruction segmentation assessment: Based on the initial evaluation's segmentation according to the final diagnosis, the three observers demonstrated accuracy rates of 54.33%, 65.22%, and 80.43% in estimating the segmentation level of the large and small bowel. Notably, these rates were observed to increase proportionally with the observers' years of experience. In addition, when comparing the results of the 3rd observer with 10 years of experience in accurately evaluating the MO segmentation level to those of the other observers (Table 3), it was seen that this observer had the highest diagnostic sensitivity (85.71%) and negative predictive value (92.60%).

Second assessments: There was no statistically significant distinction observed between the second and third observers in their ability to detect the existence of BO during the second repeated evaluation. Additionally, there was no significant difference in their accuracy in predicting the level of the large or small bowel segment in the presence of obstruction, as well as their sensitivity. The P value obtained was greater than 0.05. Nevertheless, although there was no statistically significant difference in the rate of detecting obstruction by the initial evaluator ($P > 0.05$), there was a noteworthy rise in the rate of accurately estimating segmentation ($P = 0.022$) (Table 4). The diagnostic accuracy for estimating the localization of obstruction segmentation by the first observer increased from 54.33% (Table 3) to 73.91% (Table 6),

Table 3 Concordance of the segmentation diagnoses of the observers with the final diagnosis in the scenogram, *n* (%)

	Mechanical obstruction segment by final diagnosis			Specificity, %	Sensitivity, %	PPV, %	NPV, %	Accuracy, %
	Large	Small	Total					
I Observer								
Large	12 (85.7)	19 (59.4)	31 (67.4)	85.70	40.62	38.67	86.69	54.33
Small	2 (14.3)	13 (40.6)	15 (32.6)					
II Observer								
Large	8 (57.1)	10 (31.3)	18 (39.1)	57.14	68.75	44.40	78.60	65.22
Small	6 (42.9)	22 (68.8)	28 (60.9)					
III Observer								
Large	12 (85.7)	7 (21.9)	19 (41.3)	85.71	78.12	63.12	92.60	80.43
Small	2 (14.3)	25 (78.1)	27 (58.7)					
Total	14 (30.4)	32 (69.6)	46 (100)					

Table 4 Inter-observation agreement of obstruction and segmentation diagnoses in the scenogram in repeat measurements by the observers, *n* (%)

	Observer	Positive predict rate (large)	Negative predict rate (small)	*P* value[a]
Obstruction	I	36 (100)	8 (80)	0.500
	II	35 (89.7)	6 (85.7)	0.375
	III	36 (97.3)	8 (88.9)	0.999
Segmentation	I	20 (64.5)	13 (86.7)	**0.022**
	II	16 (88.9)	23 (82.1)	0.453
	III	18 (94.7)	26 (96.3)	0.999

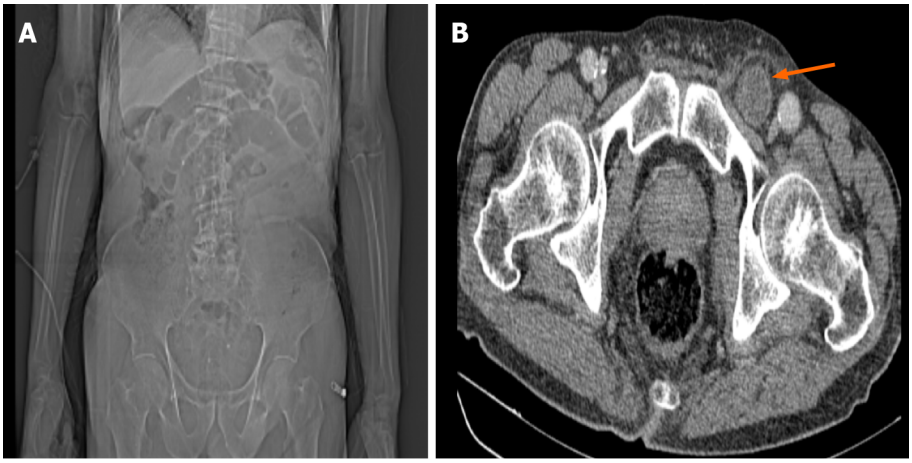
[a]McNamer test.

Table 5 Concordance of observers' second scenogram obstruction diagnoses with the final diagnosis, *n* (%)

	Mechanical obstruction by final diagnosis			Specificity, %	Sensitivity, %	PPV, %	NPV, %	Accuracy, %
	Yes	None	Total					
I Observer								
Yes	34 (81)	4 (100)	38 (82.6)	81	0	88.47	0	73.91
None	8 (19)	0 (0)	8 (17.4)					
II Observer								
Yes	32 (76.2)	4 (100)	36 (78.3)	76.19	0	88.88	0	69.56
None	10 (23.8)	0 (0)	10 (21.7)					
III Observer								
Yes	35 (83.3)	2 (50)	37 (80.4)	83.33	50	94.59	22.23	80.43
None	7 (16.7)	2 (50)	9 (19.6)					
Total	42 (91.3)	4 (8.7)	46 (100)					

Table 6 Concordance of the segmentation diagnoses of the observers with the final diagnosis in the second scenogram, *n* (%)

	Mechanical obstruction segment by final diagnosis			Specificity, %	Sensitivity, %	PPV, %	NPV, %	Accuracy, %
	Large	Small	Total					
I Observer								
Large	12 (85.7)	10 (31.3)	22 (47.8)	85.71	68.75	54.50	91.68	73.91
Small	2 (14.3)	22 (68.8)	24 (52.2)					
II Observer								
Large	9 (64.3)	12 (37.5)	21 (45.7)	64.29	62.50	42.82	80.03	63.04
Small	5 (35.7)	20 (62.5)	25 (54.3)					
III Observer								
Large	13 (92.9)	6 (18.8)	19 (41.3)	92.86	81.25	68.39	96.30	84.78
Small	1 (7.1)	26 (81.3)	27 (58.7)					
Total	14 (30.4)	32 (69.6)	46 (100)					



DOI: 10.4329/wjr.v15.i10.281 **Copyright** ©The Author(s) 2023.

Figure 1 A 79-year-old male patient admitted to the emergency department with a complaint of abdominal pain that was more pronounced in the left groin. A: Computed tomography (CT) scenogram image shows distension in the small intestine segments; B: Axial CT image shows an incarcerated femoral hernia in the left femoral region (arrow). The first observer, who looked at the scenogram images, reported that there was a possible obstruction at the large intestine level, and the 2nd and 3rd observers reported that there was a possible obstruction at the level of the small intestine.

indicating a noticeable improvement. The accuracy of the 3rd observer in correctly predicting the presence of MO (Table 5) and identifying the potential location of segmentation (Table 6) during the second evaluation was higher compared to the other evaluators.

Intra-rater compliance: Upon evaluation of the Cohen Kappa coefficients pertaining to intra-observer agreement in the diagnosis of MO, it was shown that a moderate level of agreement existed between the first and second observers. Similarly, there was moderate agreement in the diagnosis of obstruction between observers I-III and II-III. The study analyzed Cohen Kappa coefficients to assess the level of agreement among evaluators in diagnosing the potential segmentation location of MO. The results indicated a moderate level of agreement between evaluators I-III and evaluators II-III ($P < 0.05$). Nevertheless, it was noted that there existed a limited level of concordance between I and II (indicating poor agreement), and it was found that there was no statistically significant evidence of agreement ($P = 0.228$) (Table 7).

DISCUSSION

BO is a frequently observed clinical condition within the field of general surgery. Failure to urgently diagnose this condition can lead to serious complications, including perforation and ischemia. Therefore, it is of utmost importance to promptly identify and refer patients with suspected small or large BO to the appropriate medical specialty. According to available reports, it has been shown that roughly 75% of mechanical obstructions affecting the gastrointestinal tract are

Table 7 Inter-rater (intra-observation) agreement of the evaluators' diagnoses of obstruction and segmentation on the scenogram, *n* (%)

	Observer	Positive predict rate	Negative predict rate	κ (95%CI)	*P* value
Obstruction	I *vs* II	34 (94.4)	5 (50)	0.498 (0.336-0.660)	0.001
	I *vs* III	33 (91.7)	6 (60)	0.536 (0.382-0.690)	< 0.001
	II *vs* III	35 (95.5)	5 (55.6)	0.548 (0.386-0.710)	< 0.001
Segmentation	I *vs* II	14 (45.2)	11 (73.3)	0.151 (0.03-0.272)	0.228
	I *vs* III	18 (58.1)	14 (93.3)	0.426 (0.314-0.538)	0.001
	II *vs* III	13 (68.4)	22 (81.5)	0.503 (0.373-0.633)	0.001

CI: Confidence interval; κ: Cohen Kappa.



DOI: 10.4329/wjr.v15.i10.281 **Copyright** ©The Author(s) 2023.

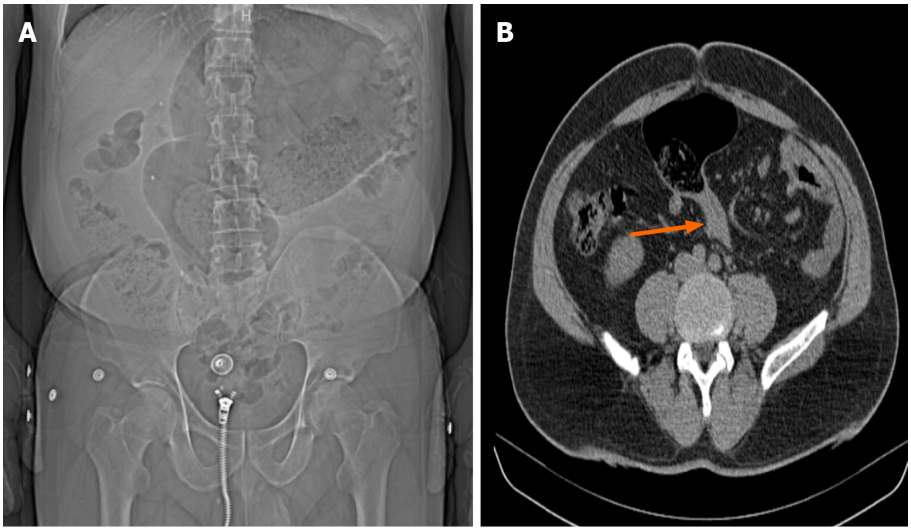
Figure 2 A 49-year-old male patient admitted to the emergency room with complaints of abdominal pain and vomiting. A: In the computed tomography (CT) scenogram, sudden narrowing at the level of the splenic flexure and distension in the proximal and distal colon loops are seen; B: In the coronal CT image, a mass lesion causing a circular increase in wall thickness is seen at the level of the splenic flexure. All three observers reported a possible obstruction at the level of the large intestine.

specifically localized within the SB[12,13]. In our study, consistent with the literature, there was a predominance of small bowel obstruction (SBO), with a prevalence rate of 66%.

The causes of a MO at the level of the SB can be adhesions, internal and external hernias, primary or extraintestinal neoplasia, stricture due to Crohn's disease, malrotation, duplication cysts, hematoma, ischemic stricture, invagination, endometriosis, and foreign body[14]. Adhesions are commonly identified as the primary cause of MO in western countries, whereas hernias and malignancies are also recognized as significant contributors to this condition[3,15-17]. The total frequency of the aforementioned three etiologies exceeds 80%[18]. In our research, the underlying causes of obstruction occurring in the SB were primarily attributed to surgical adhesions, with external hernias being the second most prevalent factor.

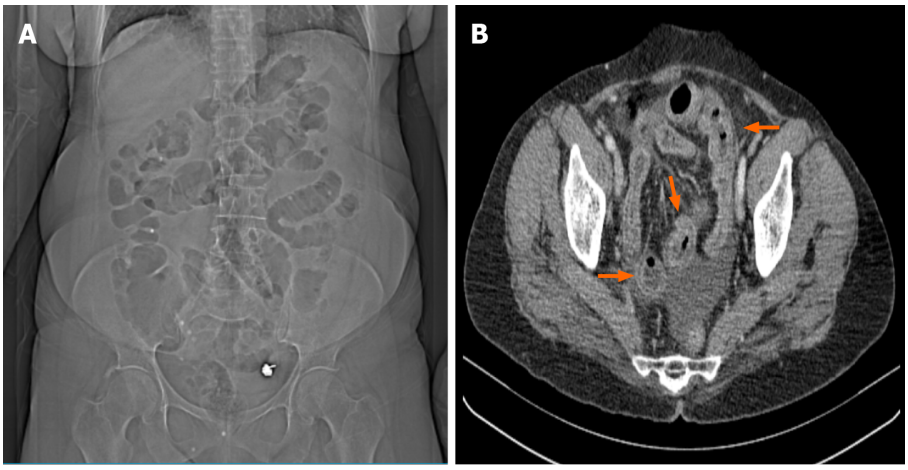
The causes of MO at the level of the LB include colorectal cancer, diverticulitis, volvulus, stricture owing to Crohn's disease, non-colorectal malignancy, endometriosis, ischemic stenosis, hernia, adhesions, fecal impaction, and foreign body[13,19]. Over 60% of cases of colonic obstruction are caused by colon malignancies[2,20], with the sigmoid colon and splenic flexure being the most prevalent locations[21]. In our study, the most common cause among the etiologies of colon involvement was colon cancer, and the most common location was the sigmoid colon. Volvulus is the second most common (10%-15%) cause of LBO. The second most frequent (10%–15%) cause of obstruction of the LB is volvulus. Volvulus is observed at low frequencies (< 1%) at the transverse colon and splenic flexure levels, but at high rates in the colon at the sigmoid (60%-75%) and cecum (25%-33%) levels[2,5]. According to our study, volvulus, which is localized at the sigmoid colon level, is the second most frequent cause of MO in the LB.

Anamnesis and physical exam results by themselves are insufficient for diagnosis and appropriate guidance; in cases of suspected BO, evaluation in conjunction with imaging techniques is crucial. However, depending on the extent of BO, diagnosis might be challenging even with advancements in abdominal imaging[22]. BO can be diagnosed using a variety of radiological modalities, including barium exams, enteroclysis, CT, ultrasound, and CR.



DOI: 10.4329/wjr.v15.i10.281 **Copyright** ©The Author(s) 2023.

Figure 3 A 56-year-old male patient admitted to the emergency department with complaints of abdominal pain, gas and inability to pass stool. A: In the computed tomography (CT) scanogram, swelling in the midline of the abdomen and folds in the colon loops are seen; B: In the coronal CT image, narrowing in the lower transition zones secondary to sigmoid volvulus is observed (arrow). All three observers reported a possible obstruction at the level of the large intestine.



DOI: 10.4329/wjr.v15.i10.281 **Copyright** ©The Author(s) 2023.

Figure 4 A 61-year-old female patient admitted to the emergency department complaining of abdominal pain. A: Radiolucent air values in the large and small intestine segments are seen in the computed tomography (CT) scenogram image; B: Axial CT image shows trilaminar thickness increase (red arrows) in the small intestine wall compatible with ileitis, dilated appearance in the mesenteric vascular structures and free fluid in the pelvic area. Following observation of the scenogram images, the first observer reported a possible obstruction at the small intestine level, the second observer reported a possible obstruction at the large intestine level, and the third observer reported that no mechanical obstruction was detected.

In patients presenting with abdominal pain and suspected BO, the primary objective of imaging is to detect possible obstruction, and CR is the first preferred imaging modality due to its low cost and low radiation exposure. The literature reports the diagnostic accuracy of CR for detecting BO to range from 46%-80%[3] and its sensitivity has been shown to range from 19%-86%[3,16,23]. The observed proportional difference may be attributed to variations in the severity of obstruction among the patients included in the studies.

CT is indicated for patients presenting with suspected BO in cases where the patient's clinical symptoms and initial CR findings are inconclusive. In order to effectively manage early treatment in cases of ileus, it is crucial to accurately determine the localization, etiology, severity of obstruction, transition point, and the presence of additional findings such as abnormal wall thickening, pneumatosis, strangulation, and pneumoperitoneum within the affected intestinal segment. Therefore, the utilization of a CT scan is imperative in order to validate the diagnosis and ascertain supplementary observations in contrast to CR[4]. CT has been documented to have a high diagnostic sensitivity (94%-100%) and diagnostic accuracy (90%-95%) for determining the presence and severity of complete or high-grade BO[24]. The diagnostic precision of CT is diminished when there is incomplete low-grade or intermittent obstruction. In such instances, enteroclysis and CT enteroclysis are the preferred approaches for assessing the existence and severity of BO[7].

In addition to established imaging techniques employed in CT, localizer radiographs, also referred to as scout, topogram, or scenogram images, and are acquired to facilitate identification of the initial and final positions of the scanning range. These radiographs rely on the anatomical landmarks of the patients to accurately determine the desired scan area[25]. CT scenogram images are a valuable contemporary implementation of conventional abdominal radiography. They serve the purpose of identifying supplementary information that aids in making a direct diagnosis of specific pathologies or narrowing down the differential diagnosis. This is achieved by examining findings both within and outside the scanned field of view. CT scenogram images can be utilized to assess many entities, including foreign substances (such as those that are undesirable, characterized by devices, or localized within the body), air-related findings (such as bowel gas pattern, pneumoperitoneum, and pneumatosis), calcifications, trauma/bone-related concerns, as well as soft tissues[26,27]. However, there have been reports indicating that scenogram images are eliminated from CT scanning examinations at a frequency of up to 75%, or alternatively, they are disregarded by a majority of radiologists when interpreting CT examinations[28-30]. In this study, the presence and possible location of the obstruction on abdominal CT scenograms, which can be used as the primary imaging modality in the diagnosis of acute BO, were contrasted with the final diagnosis, taking the observer's experience into account. There is only one study in the literature that examines the diagnostic accuracy of CT scenogram images in BO by different observers, taking into account the periods of experience. The diagnostic sensitivity reported in this study varies from 93% to 86%, with an average of 88%. These findings demonstrate a similarity to the results obtained for axial and axial plus coronal CT within the same investigation[11]. In our study, the evaluators' ability to accurately detect the existence of MO through the assessment of CT scenogram images exhibited a range of sensitivity values, spanning from 76.19% to 83.33%. The average sensitivity for diagnostic purposes was determined to be 80.94%.

The CT scenogram images can be classified into two categories based on the patterns of intestinal gas: Obstructive patterns and non-obstructive patterns. Imaging modalities of mechanical BO typically indicate decompressed loops in the distal region of the obstruction, as well as abnormally expanded bowel loops in the proximal region of the obstruction. Similar, imaging findings are present at levels showing distension on CT scenogram images. Supine CR images have characteristic findings expected in BO. The expected findings in an obstruction at the level of SB segments are enlarged air- or liquid-filled intestine with a diameter greater than 2.5-3 cm, colorectal gas deficiency, enlarged stomach, gasless abdomen, stretch sign, SB enlargement disproportionate to the colon, pseudotumor sign, *etc.* LBO is characterized by enlarged air- or liquid-filled bowel segments greater than 9 cm in the cecum and 6 cm in other levels of the colon, rectal gas deficiency, and SB dilatation, which may sometimes be accompanied by check valve system disorder[18]. These characteristic findings can also be identified in CT scenogram images.

Closed loop obstructions arise as a result of many factors such as adhesions, internal hernias, congenital malformations, or iatrogenic mesenteric deformities. These obstructions specifically affect a distinct segment and involve nearby sites of obstruction. In these instances, there exists a potential hazard of ischemia and necrosis resulting from total occlusion. While CT scenogram images may exhibit distinctive indicators of SBOs, similar to CRs, the proximal segment typically displays less tension and the closed loop segment tends to contain fluid, resulting in a normal or "non-specific" appearance on imaging[31].

Sigmoid volvulus refers to an abnormal bending of the sigmoid colon along its mesenteric axis, being the predominant type of colonic volvulus with a prevalence ranging from 60%-75% of cases[32]. In CT scenogram images, the characteristic inverted U-shaped swollen sigmoid colon pointing to the right upper quadrant seen on CRs, disproportionate sigmoid distension, proximal colon dilatation, absence of rectal gas or dilated sigmoid colon cephalo extension above the transverse colon (northern exposure), and sigmoid findings such as the 'coffee bean' sign describing the distandual segment with central coated walls can be identified[33,34]. It has been reported that an inverted U-shape can be seen in 86%-94% of cases[33,35] and the "coffee bean" sign can be seen in 76% of cases[33] in CT scenogram images.

Abdominal CT scans are frequently employed in the evaluation of patients who present with abdominal pain and are thought to have BO. These scans are commonly used to identify specific abnormalities, such as pneumoperitoneum and pneumatosis, which serve as indicators of the existence of severe or extensive obstruction. The evaluation of pneumoperitoneum presents challenges when using supine radiographs. In cases where there is suspicion, chest radiographs are primarily employed as they have the capability to detect even small amounts of intraperitoneal gas, as little as 1 mL[36]. The assessment of pneumoperitoneum is more challenging when using supine radiographs. However, several subtle features have been documented that could potentially indicate the existence of pneumoperitoneum. These findings are typically observed on CT scenogram images. These findings are: Rigler sign, right upper quadrant gas sign, falciform ligament sign, football sign, and inverted V sign[37,38]. Pneumatosis intestinalis is the presence of gas in the intestinal wall, and it is a warning sign for ischemia and impending perforation in the event of BO[32]. Pneumatosis typically appears as gas accumulation in the lower part of the intestine, whereas pseudopneumatosis refers to the entrapment of gas inside the stool's wall. This condition can provide a resemblance to genuine pneumatosis when observed using abdominal radiography or CT scenogram images. However, distinguishing between pseudopneumatosis and actual pneumatosis is more effectively achieved through the use of CT scans[39]. Portal venous gas is an additional indication of possible ischemia resulting from BO, which can be shown on CRs in situations of significant severity[40]. In our study, there were no cases with perforation-pneumoperiteneum, ischemia-pneumatosis findings secondary to severe MO.

The scarcity of research in the existing body of literature regarding the diagnosis of BO and the determination of the potential obstructed segment using CT scenogram images is evident. The insufficient attention provided by radiologists to these factors, together with their correlation to seniority level, underscores the significance of this research.

The retrospective nature of this study, the small number of patients, and the fact that, despite the high diagnostic accuracy of the results reported by the observers, they failed to provide clear indications of the criteria upon which they based their estimates constituted limitations. Other limitations of CT scenogram images include limited resolution, supine positioning, and two-dimensional planar presentation of complex three-dimensional anatomy. In addition, the fact that

the female/male ratio is not suitable statistically for the comparison of parameters between genders is another limitation of this study. As the symptom and anamnesis information of most of the cases included in the study was not accessible, the evaluation was carried out mainly and only on radiological images. Incorporating clinical information into the evaluation process may alter study data.

CONCLUSION

This study revealed that the sensitivity and accuracy rates for detecting the presence and segmentation of MO on abdominal CT scenogram images were comparable to or greater than those observed in CR, particularly in relation to the radiologist's level of experience. While scenogram images are typically not given much attention during CT scans and are often disregarded by radiologists during interpretation, it is crucial to examine and incorporate any relevant data from CT scenogram images into the diagnostic report.

ARTICLE HIGHLIGHTS

Research background

The effective management of ileus is heavily reliant on prompt and precise diagnosis, as a failure to achieve this may lead to adverse health outcomes and potential loss of life. While conventional radiography (CR) is commonly used as the primary imaging modality for patients with a preliminary diagnosis of ileus, its diagnostic accuracy in identifying the specific site and underlying cause of bowel obstruction (BO) is limited. Due to this constraint, computed tomography (CT) has emerged as the most suitable imaging modality in this particular situation.

Research motivation

CT scenogram images have the potential to assess several entities, encompassing air-related observations such as intestinal gas pattern, pneumoperitoneum, and pneumatosis. However, there are reports showing that scenogram images are omitted from CT scan examinations up to 75% of the time, or alternatively, ignored by the majority of radiologists when interpreting CT examinations. There exists a singular study within the literature that investigates the diagnostic sensitivity of CT scans in detecting BO, specifically considering the varying levels of expertise among different observers. Our intention was to make a scholarly contribution within this particular field of study.

Research objectives

This study aims to determine the presence of acute BO on abdominal CT scenogram images and the accuracy with which its possible location can be determined, taking into account the experience of the observers.

Research methods

A retrospective screening was performed on a group of 46 people who arrived at the emergency room with acute abdominal pain between January 2021 and January 2022 and were subsequently evaluated for suspected ileus. The patients' abdominal CT images were evaluated at different intervals (1 mo apart) by three radiologists with varying degrees of expertise (1, 3, and 10 years). The assessment focused on establishing the presence or absence of BO as well as the likely location of the obstruction (small bowel or large bowel).

Research results

In the first evaluation by 3 radiologists to detect the presence of BO, the rate of detecting the presence of ileus due to mechanical obstruction (MO) was 80.94% and the diagnostic accuracy was 75.35%. Among all observers, the third observer had the highest sensitivity (83.33%), positive predictive value (94.59%), and diagnostic accuracy (80.43%). Considering the segmentation according to the final diagnosis at the first evaluation, the sensitivity (85.71%) and diagnostic accuracy (80.43%) values were highest in the senior observer's correct estimation of the large and small bowel segmentation. In the second evaluation, the senior observer's prediction of the presence of ileus and segmentation was more accurate than the other observers. Compared to the second evaluation, while there was no significant change in the rate of the first observer detecting the presence of ileus, there was an increase in the rate of correctly predicting the segmentation (73.91%). No significant change was detected in the other observers' estimates of the presence of MO and possible localization at different periods.

Research conclusions

Our results show that the sensitivity and accuracy of abdominal CT scenogram images in detecting the presence and segmentation of acute MO in relation to seniority is similar to or higher than CR.

Research perspectives

Considering the possible contribution of CT scenogram images to the diagnosis of some pathologies such as ileus, more studies are needed to diagnose these and similar pathologies and to narrow down the differential diagnosis.

FOOTNOTES

Author contributions: Kadirhan O, Kızılgoz V, Aydin S, Bilici E, Bayat E, Kantarci M contributed to conceptualization, validation, formal analysis, resources, data curation; Kadirhan O, Kızılgoz V, and Aydin S contributed to methodology, investigation, writing – original draft preparation, writing – review & editing, visualization, supervision; Kadirhan O and Aydin S contributed to project administration.

Institutional review board statement: The research undertaken in this study received approval from the Erzincan University Ethics Committee (Decision no: E-21142744 804.01-128338 Date: 07/12/ 2021) and was carried out in compliance with the principles outlined in the Declaration of Helsinki.

Informed consent statement: As the study was designed retrospectively, no written informed consent form was obtained from patients.

Conflict-of-interest statement: All the authors have no conflicts of interest to declare.

Data sharing statement: Participants approved publication of their data after anonymization.

Open-Access: This article is an open-access article that was selected by an in-house editor and fully peer-reviewed by external reviewers. It is distributed in accordance with the Creative Commons Attribution NonCommercial (CC BY-NC 4.0) license, which permits others to distribute, remix, adapt, build upon this work non-commercially, and license their derivative works on different terms, provided the original work is properly cited and the use is non-commercial. See: https://creativecommons.org/Licenses/by-nc/4.0/

Country/Territory of origin: Turkey

ORCID number: Ozlem Kadirhan 0000-0003-2175-084X; Volkan Kızılgoz 0000-0003-3450-711X; Sonay Aydin 0000-0002-3812-6333; Esra Bilici 0009-0007-9983-8901; Ekrem Bayat 0000-0003-1335-4839; Mecit Kantarci 0000-0002-1043-6719.

S-Editor: Liu JH
L-Editor: Webster JR
P-Editor: Liu JH

REFERENCES

1 **Herlinger H**, Rubesin SE, Morris JB. Small bowel obstruction. In: Gore RM, Levine MS, editors. Textbook of gastrointestinal radiology. 2nd ed. Philadelphia, Pa: Saunders; 2000; 815–837 [DOI: 10.1016/b978-1-4160-2332-6.50055-5]
2 **Welch JP**. Bowel obstruction: differential diagnosis and clinical management. 1987 [DOI: 10.1001/jama.1990.03450030118046]
3 **Maglinte DD**, Reyes BL, Harmon BH, Kelvin FM, Turner WW Jr, Hage JE, Ng AC, Chua GT, Gage SN. Reliability and role of plain film radiography and CT in the diagnosis of small-bowel obstruction. *AJR Am J Roentgenol* 1996; **167**: 1451-1455 [PMID: 8956576 DOI: 10.2214/ajr.167.6.8956576]
4 **Liu P**, Zhu H, Zhang X, Feng A, Zhu X, Sun Y. Predicting Survival for Hepatic Arterial Infusion Chemotherapy of Unresectable Colorectal Liver Metastases: Radiomics Analysis of Pretreatment Computed Tomography. *J Transl Int Med* 2022; **10**: 56-64 [PMID: 35702189 DOI: 10.2478/jtim-2022-0004]
5 **Gore RM**, Miller FH, Pereles FS, Yaghmai V, Berlin JW. Helical CT in the evaluation of the acute abdomen. *AJR Am J Roentgenol* 2000; **174**: 901-913 [PMID: 10749221 DOI: 10.2214/ajr.174.4.1740901]
6 **Maglinte DD**, Heitkamp DE, Howard TJ, Kelvin FM, Lappas JC. Current concepts in imaging of small bowel obstruction. *Radiol Clin North Am* 2003; **41**: 263-283, vi [PMID: 12659338 DOI: 10.1016/s0033-8389(02)00114-8]
7 **Suri S**, Gupta S, Sudhakar PJ, Venkataramu NK, Sood B, Wig JD. Comparative evaluation of plain films, ultrasound and CT in the diagnosis of intestinal obstruction. *Acta Radiol* 1999; **40**: 422-428 [PMID: 10394872 DOI: 10.3109/02841859909177758]
8 **Balthazar EJ**. George W. Holmes Lecture. CT of small-bowel obstruction. *AJR Am J Roentgenol* 1994; **162**: 255-261 [PMID: 8310906 DOI: 10.2214/ajr.162.2.8310906]
9 **Karavas E**, Ece B, Aydın S, Kocak M, Cosgun Z, Bostanci IE, Kantarci M. Are we aware of radiation: A study about necessity of diagnostic X-ray exposure. *World J Methodol* 2022; **12**: 264-273 [PMID: 36159099 DOI: 10.5662/wjm.v12.i4.264]
10 **Fatihoglu E**, Aydin S, Gokharman FD, Ece B, Kosar PN. X-ray Use in Chest Imaging in Emergency Department on the Basis of Cost and Effectiveness. *Acad Radiol* 2016; **23**: 1239-1245 [PMID: 27426978 DOI: 10.1016/j.acra.2016.05.008]
11 **Jaffe TA**, Martin LC, Thomas J, Adamson AR, DeLong DM, Paulson EK. Small-bowel obstruction: coronal reformations from isotropic voxels at 16-section multi-detector row CT. *Radiology* 2006; **238**: 135-142 [PMID: 16293807 DOI: 10.1148/radiol.2381050489]
12 **Markogiannakis H**, Messaris E, Dardamanis D, Pararas N, Tzertzemelis D, Giannopoulos P, Larentzakis A, Lagoudianakis E, Manouras A, Bramis I. Acute mechanical bowel obstruction: clinical presentation, etiology, management and outcome. *World J Gastroenterol* 2007; **13**: 432-437 [PMID: 17230614 DOI: 10.3748/wjg.v13.i3.432]
13 **Drożdż W**, Budzyński P. Change in mechanical bowel obstruction demographic and etiological patterns during the past century: observations from one health care institution. *Arch Surg* 2012; **147**: 175-180 [PMID: 22351915 DOI: 10.1001/archsurg.2011.970]
14 **Sabiston DC**, Townsend CM, Beauchamp R, Evers BM, Mattox KL. Sabiston textbook of surgery: the biological basis of modern surgical practice: Wb Saunders Philadelphia; 2001 [DOI: 10.1007/s10350-008-9293-5]
15 **Jeffrey RB**. Small bowel obstruction. In: Federle MP, Jeffrey RB, Woodward PJ, Borhani AA, eds. Diagnostic imaging: abdomen, 2nd ed. Salt Lake City, Utah: Amirsys, 2010; 44–47 [DOI: 10.2214/ajr.142.1.91]
16 **Frager DH**, Baer JW. Role of CT in evaluating patients with small-bowel obstruction. *Semin Ultrasound CT MR* 1995; **16**: 127-140 [PMID: 7794603 DOI: 10.1016/0887-2171(95)90005-5]

17 **Miller G**, Boman J, Shrier I, Gordon PH. Etiology of small bowel obstruction. *Am J Surg* 2000; **180**: 33-36 [PMID: 11036136 DOI: 10.1016/s0002-9610(00)00407-4]

18 **Paulson EK**, Thompson WM. Review of small-bowel obstruction: the diagnosis and when to worry. *Radiology* 2015; **275**: 332-342 [PMID: 25906301 DOI: 10.1148/radiol.15131519]

19 **Cappell MS**, Batke M. Mechanical obstruction of the small bowel and colon. *Med Clin North Am* 2008; **92**: 575-597, viii [PMID: 18387377 DOI: 10.1016/j.mcna.2008.01.003]

20 **Biondo S**, Parés D, Frago R, Martí-Ragué J, Kreisler E, De Oca J, Jaurrieta E. Large bowel obstruction: predictive factors for postoperative mortality. *Dis Colon Rectum* 2004; **47**: 1889-1897 [PMID: 15622582 DOI: 10.1007/s10350-004-0688-7]

21 **Garcia-Valdecasas JC**, Llovera JM, deLacy AM, Reverter JC, Grande L, Fuster J, Cugat E, Visa J, Pera C. Obstructing colorectal carcinomas. Prospective study. *Dis Colon Rectum* 1991; **34**: 759-762 [PMID: 1914740 DOI: 10.1007/bf02051066]

22 **Matrawy KA**, El-Shazly MJAJom. Intestinal obstruction: role of multi-slice CT in emergency department. 2014; 50: 171-178 [DOI: 10.1016/j.ajme.2014.01.005]

23 **Shrake PD**, Rex DK, Lappas JC, Maglinte DD. Radiographic evaluation of suspected small bowel obstruction. 1991; 86 [DOI: 10.53347/rid-149375]

24 **Boudiaf M**, Soyer P, Terem C, Pelage JP, Maissiat E, Rymer R. Ct evaluation of small bowel obstruction. *Radiographics* 2001; **21**: 613-624 [PMID: 11353110 DOI: 10.1148/radiographics.21.3.g01ma03613]

25 American Association of Physicists in Medicine. AAPM CT Lexicon version 1.3. 2012

26 **Lee MH**, Lubner MG, Mellnick VM, Menias CO, Bhalla S, Pickhardt PJ. The CT scout view: complementary value added to abdominal CT interpretation. *Abdom Radiol (NY)* 2021; **46**: 5021-5036 [PMID: 34075469 DOI: 10.1007/s00261-021-03135-3]

27 **Bian Y**, Jiang H, Zheng J, Shao C, Lu J. Basic Pancreatic Lesions: Radiologic-pathologic Correlation. *J Transl Int Med* 2022; **10**: 18-27 [PMID: 35702187 DOI: 10.2478/jtim-2022-0003]

28 **Daffner RH**. Reviewing CT Scout Images: Observations of an Expert Witness. *AJR Am J Roentgenol* 2015; **205**: 589-591 [PMID: 26295646 DOI: 10.2214/AJR.15.14405]

29 **Berlin L**. Reviewing the CT scout view: medicolegal and ethical considerations. *AJR Am J Roentgenol* 2014; **202**: 1264-1266 [PMID: 24848823 DOI: 10.2214/AJR.12.10444]

30 **Berlin L**. Medicolegal--malpractice and ethical issues in radiology. CT scout views and standard of care. *AJR Am J Roentgenol* 2014; **203**: W741 [PMID: 25415741 DOI: 10.2214/AJR.14.13442]

31 **Balthazar EJ**, Birnbaum BA, Megibow AJ, Gordon RB, Whelan CA, Hulnick DH. Closed-loop and strangulating intestinal obstruction: CT signs. *Radiology* 1992; **185**: 769-775 [PMID: 1438761 DOI: 10.1148/radiology.185.3.1438761]

32 **Jaffe T**, Thompson WM. Large-Bowel Obstruction in the Adult: Classic Radiographic and CT Findings, Etiology, and Mimics. *Radiology* 2015; **275**: 651-663 [PMID: 25997131 DOI: 10.1148/radiol.2015140916]

33 **Levsky JM**, Den EI, DuBrow RA, Wolf EL, Rozenblit AM. CT findings of sigmoid volvulus. *AJR Am J Roentgenol* 2010; **194**: 136-143 [PMID: 20028915 DOI: 10.2214/AJR.09.2580]

34 **Javors BR**, Baker SR, Miller JA. The northern exposure sign: a newly described finding in sigmoid volvulus. *AJR Am J Roentgenol* 1999; **173**: 571-574 [PMID: 10470881 DOI: 10.2214/ajr.173.3.10470881]

35 **Burrell HC**, Baker DM, Wardrop P, Evans AJ. Significant plain film findings in sigmoid volvulus. *Clin Radiol* 1994; **49**: 317-319 [PMID: 8013194 DOI: 10.1016/s0009-9260(05)81795-7]

36 **James B**, Kelly B. The abdominal radiograph. *Ulster Med J* 2013; **82**: 179-187 [PMID: 24505155]

37 **Menuck L**, Siemers PT. Pneumoperitoneum: importance of right upper quadrant features. *AJR Am J Roentgenol* 1976; **127**: 753-756 [PMID: 973660 DOI: 10.2214/ajr.127.5.753]

38 **Levine MS**, Scheiner JD, Rubesin SE, Laufer I, Herlinger H. Diagnosis of pneumoperitoneum on supine abdominal radiographs. *AJR Am J Roentgenol* 1991; **156**: 731-735 [PMID: 2003436 DOI: 10.2214/ajr.156.4.2003436]

39 **Wang JH**, Furlan A, Kaya D, Goshima S, Tublin M, Bae KT. Pneumatosis intestinalis versus pseudo-pneumatosis: review of CT findings and differentiation. *Insights Imaging* 2011; **2**: 85-92 [PMID: 22347936 DOI: 10.1007/s13244-010-0055-2]

40 **Liebman PR**, Patten MT, Manny J, Benfield JR, Hechtman HB. Hepatic--portal venous gas in adults: etiology, pathophysiology and clinical significance. *Ann Surg* 1978; **187**: 281-287 [PMID: 637584 DOI: 10.1097/00000658-197803000-00012]

World Journal of Radiology

Submit a Manuscript: https://www.f6publishing.com

World J Radiol 2023 October 28; 15(10): 293-303

DOI: 10.4329/wjr.v15.i10.293

ISSN 1949-8470 (online)

ORIGINAL ARTICLE

Retrospective Study

Two-point Dixon and six-point Dixon magnetic resonance techniques in the detection, quantification and grading of hepatic steatosis

Mohamed Elfaal, Alanna Supersad, Craig Ferguson, Stephanie Locas, Florin Manolea, Mitchell P Wilson, Medica Sam, Wendy Tu, Gavin Low

Specialty type: Radiology, nuclear medicine and medical imaging

Provenance and peer review: Unsolicited article; Externally peer reviewed.

Peer-review model: Single blind

Peer-review report's scientific quality classification

Grade A (Excellent): A
Grade B (Very good): 0
Grade C (Good): 0
Grade D (Fair): 0
Grade E (Poor): 0

P-Reviewer: Ji G, China

Received: September 6, 2023
Peer-review started: September 6, 2023
First decision: September 19, 2023
Revised: September 20, 2023
Accepted: September 28, 2023
Article in press: September 28, 2023
Published online: October 28, 2023

Mohamed Elfaal, Alanna Supersad, Craig Ferguson, Stephanie Locas, Florin Manolea, Mitchell P Wilson, Medica Sam, Wendy Tu, Gavin Low, Department of Radiology & Diagnostic Imaging, University of Alberta, Edmonton T6G2B7, Alberta, Canada

Corresponding author: Gavin Low, MBChB, MPhil, MRCS, FRCR, Professor, Department of Radiology & Diagnostic Imaging, University of Alberta, WMC 2B2.41 8440-112 ST, Edmonton T6G2B7, Alberta, Canada. gavinlow@mic.ca

Abstract

BACKGROUND

Hepatic steatosis is a very common problem worldwide.

AIM

To assess the performance of two- and six-point Dixon magnetic resonance (MR) techniques in the detection, quantification and grading of hepatic steatosis.

METHODS

A single-center retrospective study was performed in 62 patients with suspected parenchymal liver disease. MR sequences included two-point Dixon, six-point Dixon, MR spectroscopy (MRS) and MR elastography. Fat fraction (FF) estimates on the Dixon techniques were compared to the MRS-proton density FF (PDFF). Statistical tests used included Pearson's correlation and receiver operating characteristic.

RESULTS

FF estimates on the Dixon techniques showed excellent correlation (≥ 0.95) with MRS-PDFF, and excellent accuracy [area under the receiver operating characteristic (AUROC) ≥ 0.95] in: (1) Detecting steatosis; and (2) Grading severe steatosis, ($P < 0.001$). In iron overload, two-point Dixon was not evaluable due to confounding T2* effects. FF estimates on six-point Dixon *vs* MRS-PDFF showed a moderate correlation (0.82) in iron overload *vs* an excellent correlation (0.97) without iron overload, ($P < 0.03$). The accuracy of six-point Dixon in grading mild steatosis improved (AUROC: 0.59 to 0.99) when iron overload cases were excluded. The excellent correlation (> 0.9) between the Dixon techniques *vs* MRS-PDFF did not change in the presence of liver fibrosis ($P < 0.01$).

CONCLUSION

Dixon techniques performed satisfactorily for the evaluation of hepatic steatosis but with exceptions.

Key Words: Chemical shift encoded Dixon magnetic resonance techniques; Hepatic steatosis; Liver fat quantification; Magnetic resonance spectroscopy; Proton density fat fraction; Ultrasound

©The Author(s) 2023. Published by Baishideng Publishing Group Inc. All rights reserved.

Core Tip: Fat fraction (FF) estimates on the Dixon techniques (two-point Dixon and six-point Dixon) have excellent correlation with magnetic resonance spectroscopy-proton density FF (MRS-PDFF), and excellent accuracy in detecting steatosis, and grading severe steatosis. However, in iron overload, two-point Dixon was not evaluable due to confounding effect on liver signal from T2* decay. The excellent correlation between the Dixon techniques *vs* MRS-PDFF was not affected by co-existing liver fibrosis.

Citation: Elfaal M, Supersad A, Ferguson C, Locas S, Manolea F, Wilson MP, Sam M, Tu W, Low G. Two-point Dixon and six-point Dixon magnetic resonance techniques in the detection, quantification and grading of hepatic steatosis. *World J Radiol* 2023; 15(10): 293-303
URL: https://www.wjgnet.com/1949-8470/full/v15/i10/293.htm
DOI: https://dx.doi.org/10.4329/wjr.v15.i10.293

INTRODUCTION

Non-alcoholic fatty liver disease (NAFLD) is the most common chronic liver disease worldwide with a global prevalence of 25% (estimated at 1 billion people)[1-5]. Roughly 20% have non-alcoholic steatohepatitis (NASH), characterized by hepatocyte injury and inflammation. These patients are at risk for progression to liver fibrosis and cirrhosis[6]. Consequently, steatosis and fibrosis may frequently co-exist in the liver. NAFLD is also associated with metabolic syndrome, type 2 diabetes and cardiovascular disease[6]. Accurate detection, quantification and grading of steatosis are necessary for risk stratification, to monitor disease progression and to assess the treatment response.

Liver biopsy is the reference standard for liver fat evaluation but is invasive and can be associated with pain, bleeding and death (1 in 10000)[7]. It has poor patient acceptability and is not suitable as a screening tool or for longitudinal patient monitoring. Biopsy is associated with high sampling variability as it only evaluates 1:50000th of the liver[8]. As steatosis often affects the liver non-uniformly, biopsy may be poorly representative. Finally, the histopathology assessment is a qualitative process prone to intra- and inter-reader variability[7].

B-mode ultrasound (US) is the first-line imaging test for investigating patients with suspected parenchymal liver disease. It is non-invasive, easy to perform, inexpensive and widely available. However, it has questionable utility as a screening tool due to poor sensitivity in mild steatosis[1,6,9]. Magnetic resonance spectroscopy (MRS) is widely regarded as the non-invasive reference standard for liver fat quantification. It is strongly correlated with histopathology and has been touted as a replacement for biopsy[10-12]. It can directly measure the chemical composition of liver fat and produces a proton density fat fraction (PDFF) according to the formula: PDFF = F/(F + W), where F and W are the unconfounded signals of protons within mobile fat and mobile water molecules, respectively. MRS has drawbacks including a limited spatial coverage and is technically demanding requiring specialized software and expertise so is generally only available in large academic centers.

Chemical shift encoded fat and water separation MR techniques are based on the principle that fat and water protons oscillate at different resonant frequencies. The fat-water resonance frequency differences (225 Hz at 1.5 T and 450 Hz at 3 T) create phase shifts that can be used to separate fat and water signals. The first chemical shift fat and water separation method, termed 'two-point Dixon', was described in 1984[13]. This technique involves the dual-echo acquisition of T1 weighted in-phase (IP) and opposed-phased (OP) images that can be used to generate separated fat-only and water-only images. This allows the hepatic FF to be calculated as follows[6]: FF% = (IP - OP)/(2 × IP). Two-point Dixon sequences are part of the routine toolkit of MR liver imaging worldwide, and have been performed in many clinical applications over the years. These are familiar sequences to practicing body MR radiologists, easy to perform, can sample large areas of the liver, and do not require sophisticated software. However, 1st generation fat quantification on two-point Dixon is prone to underestimation due to confounders such as B_0 inhomogeneity, T1 bias, T2* effects, noise bias, spectral complexity of fat, eddy currents and J-coupling[6]. Fat quantification is also adversely affected by liver iron overload due to T2* decay which has opposing effects to fat on liver signal leading to inaccuracies. Additionally, the two-point Dixon technique has a narrower dynamic range of 0%-50% liver FF although this approximates the normal biologic range in humans so is not generally a practical limitation[1,14]. Recent advances have led to the development of modern Dixon sequences that are corrected for confounders leading to more accurate liver fat quantification[1,14,15]. These complex multi-echo chemical shift encoded techniques utilize both the phase and magnitude of the MR signal and can provide fat quantification [MR imaging (MRI)-PDFF] over the entire physical range (0%-100%). The most common method involves the acquisition of 6 echos and is termed 'six-point Dixon'. By performing automatic segmentectomy, multi-echo Dixon techniques can generate whole liver fat quantification. Confounder corrected R2* maps, acquired simultaneously, provide fat-corrected

liver iron quantification. Unlike two-point Dixon which is performed ubiquitously in clinical liver imaging worldwide, six-point Dixon requires dedicated software that has to be purchased separately, so access to this technique is limited clinically.

On this background, the primary aim of this study was to assess the diagnostic performance of 1st generation two-point Dixon (widely available clinically) and modern six-point Dixon MR techniques (limited access clinically) in the detection, quantification and grading of hepatic steatosis, using MRS as the reference standard. The secondary aims were: (1) To assess the confounding effects of iron overload on the Dixon techniques, a subgroup analysis was performed in patients with and without iron overload; (2) As steatosis and fibrosis are often found together in NAFLD patients, a subgroup analysis was performed to determine if liver fibrosis had an influence on FF estimates; and (3) To assess the accuracy of US for detecting and grading hepatic steatosis, a subgroup analysis was performed in patients with an US examination within 6 mo of the MR.

MATERIALS AND METHODS

This was a retrospective single-center cross-sectional study. Institutional ethics and review board approval was granted and the requirement for informed patient consent was waived. From July 2021 to February 2022 (8 mo), all consecutive adult patients (≥ 18 years old) that underwent a per-protocol clinical MR examination for the combined assessment of liver fat, iron and fibrosis for suspected diffuse parenchymal liver disease and without known focal liver lesions, were entered into the study. Three patients were excluded from the study due to technically poor-quality MR examinations.

MR protocol

All examinations were performed on a 1.5-T MR system (Magnetom Aera, Siemens Healthcare, Erlangen, Germany) using an 18-channel body matrix array coil. The technical MR parameters are included in Table 1. Additionally, an MR elastography (MRE) examination was also performed using a commercially available clinical system (Resoundant, MN, United States).

Data processing and analysis

For the MR examination, the proprietary liver fat and iron quantification software (LiverLab, Siemen Healthcare) automatically generates the following information on picture archiving and communication system (PACS): (1) A report of the mean MRI-PDFF (%) and mean R2* (s^{-1}) of the entire liver (segmentectomy) and of a selected region of interest (ROI); and (2) A spectroscopy report of the mean MRS-PDFF (%) of a 27 cm^3 voxel. The MRI-PDFF (segmentectomy) and MRS-PDFF data as well as liver stiffness data acquired on MRE were imported into an Excel spreadsheet. Only the primary investigative team (Mohamed Elfaal and Alanna Supersad) had access to this data.

After removing patient identifying information, the following anonymized datasets were entered into 1 of 2 research folders on PACS. Cases were randomized within each folder and allocated unique research identification numbers. Folder 1 contained the T1 IP and OP MR images (two-point Dixon) of all patients. Folder 2 contained the static and cine US images of patients with an US within 6 mo of the MR. Three fellowship trained board-certified radiologists (with 2 years, 2 years, and 5 years of clinical experience, respectively) independently analyzed cases in folder 1. The readers were blinded to the clinical data. Using a well-established and validated technique, each reader manually placed 4 circular ROIs over the liver (2 in each hepatic lobe) on both the T1 IP and OP MR images[16]. The ROI size was set to a minimum threshold of 4 cm in diameter/12.6 cm^2 area and ROIs were placed taking care to avoid large vessels, bile ducts and the liver margin. The hepatic FF on two-point Dixon was calculated using the formula[6], FF = (IP - OP)/(2 × IP).

Three other fellowship trained board-certified radiologists (with 3 years, 4 years, and 2 years of clinical experience, respectively) independently analyzed cases in folders 2. The readers were blinded to the background clinical data. For folder 2, the readers were required to assess if hepatic steatosis was present or absent on the US images, and determine the grade of steatosis. The following US criteria were used[17,18]: (1) Mild steatosis: Liver echogenicity exceeds that of the renal cortex; (2) Moderate steatosis: Poor delineation of the echogenic walls of the intrahepatic portal vein branches; and (3) Severe steatosis: Loss of definition of the posterior hepatic margin or diaphragm outline.

Reader data on folders 1 and 2 were submitted to the primary investigative team for export into the excel spreadsheet. For folder 1, a group averaged FF on two-point Dixon was calculated for each case. For folder 2, the group decision on whether steatosis was present or absent on each case was determined by the majority rule. Cases that did not meet agreement by at least 2 of the 3 readers were not included in the final analysis.

Sample size calculation

An a-prior power analysis was performed on G* Power. Assuming a mild effect size of 0.4, alpha of 0.05 and beta of 0.2, a minimum sample size of 52 was needed to achieve a power of 0.8.

Statistical analysis

The following statistical tests were used: (1) Intraclass correlation coefficient (ICC) to calculate the inter-reader agreement for FF estimates on two-point Dixon; (2) Pearson's correlation and Bland Altman to assess the inter-test correlation and variability, respectively, for FF estimates on two-point Dixon *vs* MRS, and six-point Dixon *vs* MRS; (3) Linear regression to model the relationship between two-point Dixon *vs* MRS, and six-point Dixon *vs* MRS for fat quantification; (4) Receiver operating characteristic (ROC) analysis to determine the accuracy of two-point Dixon, six-point Dixon and US

Table 1 Acquisition parameters for the magnetic resonance sequences

	Two-point Dixon	Six-point Dixon	MRS
TR (ms)	6.68	15.6	3000
TE (ms)	2.39, 4.77	2.38, 4.76, 7.14, 9.52, 11.90, 14.28	12, 24, 36, 48, 72
Flip angle	10°	4°	90°
Matrix size	288 mm × 176 mm	160 mm × 97 mm	N/A[1]
FOV (mm)	400	450	N/A[1]
Bandwidth (kHz/pixel)	470	1080	1200
Slice thickness (mm)	3	3.5	N/A[1]
NSA	1	1	1
Parallel imaging, acceleration factor	CAIPIRINHA 2	CAIPIRINHA 4	-

[1]Magnetic resonance spectroscopy was performed on a 30 mm × 30 mm × 30 mm voxel.
FOV: Field of view; NSA: Number of signal averages; MRS: Magnetic resonance spectroscopy; TR: Time to repetition; TE: Time to echo; N/A: Not applicable.

for the detection and grading of steatosis; and (5) Fleiss kappa to calculate the inter-reader agreement for detecting steatosis on US. The kappa (*k*) value interpretation as suggested by Cohen was used: $k < 0.20$ (poor agreement), 0.21-0.40 (fair agreement), 0.41-0.60 (moderate agreement), 0.61-0.80 (good agreement), and 0.81-1.00 (excellent agreement)[19].

Statistical analysis was performed on IBM SPSS (version 26) and MedCalc (version 19.6.1). A *P* value of < 0.05 was considered statistically significant. Statistical review was performed by a study author with training in medical statistics.

RESULTS

There were 62 patients including 33 males (53.2%) and 29 females (46.8%). The mean age was 54.4 ± 13.2 years and ranged from 18 to 80 years. Past medical history included obesity in 23 (37.1%), diabetes in 16 (25.8%), dyslipidemia in 15 (24.2%), hypertension in 14 (22.6%), NASH in 3 (4.8%), NAFLD in 2 (3.2%), hepatitis B in 1 (1.6%), hepatitis C in 1 (1.6%) and hypothyroidism in 1 (1.6%). The body mass index (BMI) was available in 33 patients (53.2%) with a mean BMI of 34.7 ± 7.8 kg/m^2 (range 19.8-60.4 kg/m^2). Accordingly, 25 (40.3%) were obese (BMI ≥ 30 kg/m^2) and 6 (9.7%) were overweight (BMI 25-29.9 kg/m^2).

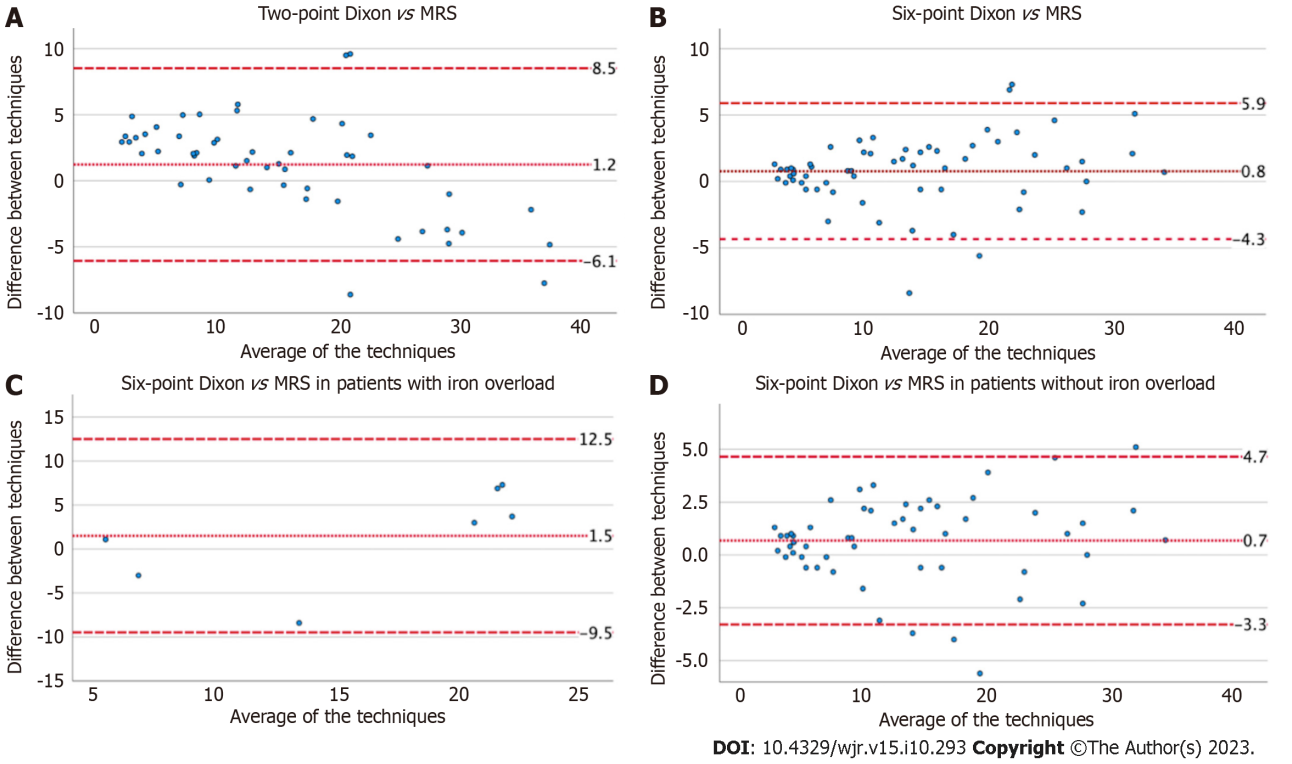
The mean MRS-PDFF was 13.6% ± 8.9% (range 2.6%-34.3%). As proposed by Starekova *et al*[6], PDFF thresholds for mild, moderate and severe hepatic steatosis were set as 5%, 15% and 25%, respectively. Using MRS-PDFF as the reference standard, mild steatosis was found in 23 (37.1%), moderate steatosis in 15 (24.2%), severe steatosis in 9 (14.5%), and a non-steatotic liver in 15 (24.2%).

Seven patients (11.3%) had hepatic iron overload - all were of mild grade. This was associated with a mean R2* of 88.2 ± 21.7 s^{-1} (range 70.4-133.3 s^{-1}) and a mean liver iron concentration of 2.8 ± 2.8 mg/g Fe_{dw} (range 2.2-4.4 mg/g Fe_{dw}). The FF was not evaluable on two-point Dixon in any of these patients as T2* effects from iron led to net signal loss on the IP images relative to the OP images resulting in erroneously negative calculations using the FF formula. The 7 cases were removed from the two-point Dixon dataset so the resulting dataset ($n = 55$) consisted of only cases with a normal liver iron concentration (< 2 mg/g Fe_{dw}). In contrast, six-point Dixon was not failed by iron overload and this dataset ($n = 62$) included a mixed cohort of cases with and without iron overload.

The liver stiffness was acquired in 60 patients and not evaluable in two others due to technical failure of MRE. A liver stiffness cut-off of ≥ 2.9 Ka was used to indicate the presence of liver fibrosis (F1 or higher)[20]. Accordingly, there were 24 patients (36.9%) with liver fibrosis and 36 patients (55.4%) without liver fibrosis.

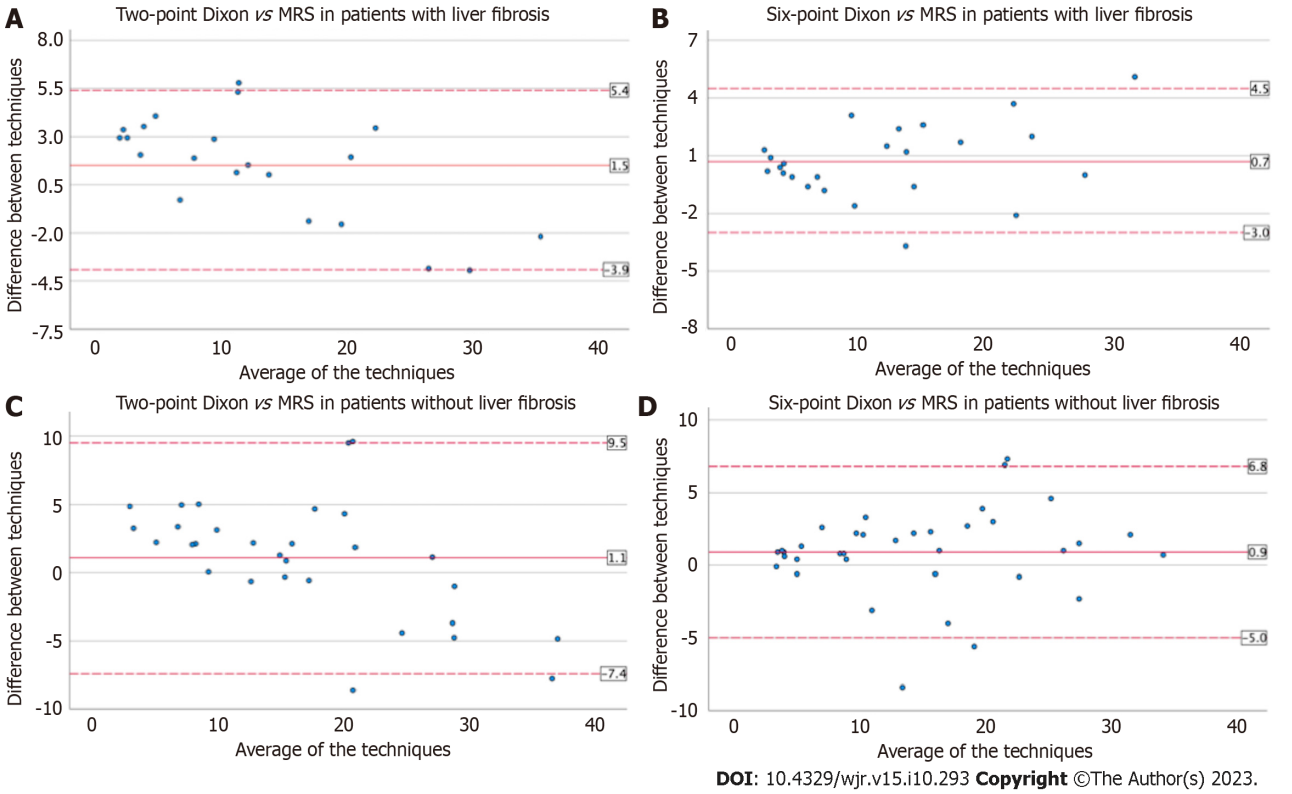
ICC showed an excellent inter-reader agreement of 0.99 [95% confidence interval (CI): 0.99-1, $P < 0.001$] for calculating the FF estimates on two-point Dixon. Pearson showed an excellent inter-test correlation of 0.95 and 0.96, respectively, for FF estimates on two-point Dixon *vs* MRS-PDFF and six-point Dixon *vs* MRS-PDFF, $P < 0.001$. On six-point Dixon *vs* MRS-PDFF, a moderate correlation (0.82) was noted in iron overload *vs* an excellent correlation (0.97) without iron overload, $P < 0.03$. In comparison, liver fibrosis did not affect the correlation between FF estimates and the MRS-PDFF. Excellent correlations of 0.98 (fibrosis) *vs* 0.98 (no fibrosis) on two-point Dixon and 0.92 (fibrosis) *vs* 0.94 (no fibrosis) on six-point Dixon were noted, $P < 0.01$.

Bland Altman was used to assess the inter-test variability of FF estimates on the Dixon techniques *vs* MRS-PDFF (Figures 1 and 2). The mean difference between tests and 95% lower and upper limits of agreement (LOA) were: (1) 1.2% and -6.1%, 8.5% on two-point Dixon *vs* 0.8% and -4.3%, 5.9% on six-point Dixon; (2) 1.5% and -9.5%, 12.5% (iron overload) *vs* 0.7% and -3.3%, 4.7% (no iron overload), on six-point Dixon; (3) 1.5% and -3.9%, 5.4% (liver fibrosis) *vs* 1.1% and -7.4%, 9.5% (no liver fibrosis), on two-point Dixon; and (4) 0.7% and -3%, 4.5% (liver fibrosis) *vs* 0.9% and -5%, 6.8% (no liver fibrosis), on six-point Dixon.



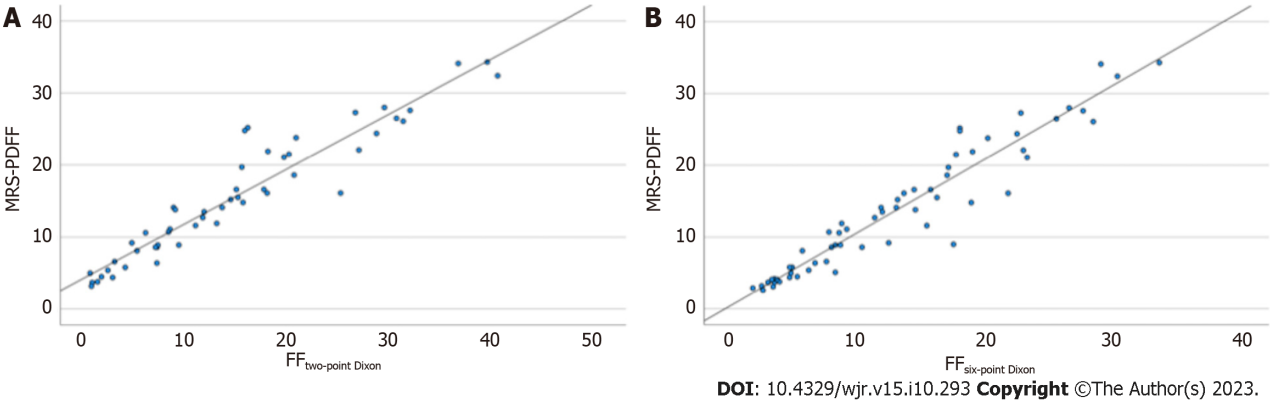
DOI: 10.4329/wjr.v15.i10.293 **Copyright** ©The Author(s) 2023.

Figure 1 Bland Altman plots demonstrate the inter-test variability for fat fraction estimates. A: Two-point Dixon *vs* magnetic resonance spectroscopy (MRS); B: Six-point Dixon *vs* MRS; C and D: Patients with and without liver iron overload on six-point Dixon *vs* MRS. MRS: Magnetic resonance spectroscopy.



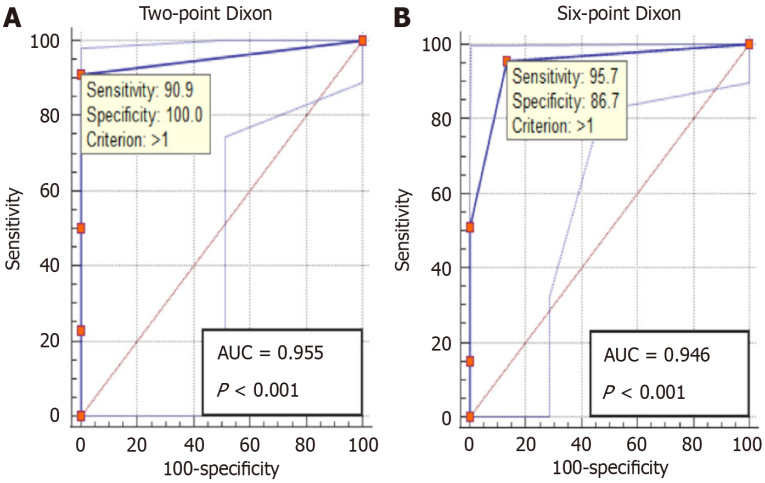
DOI: 10.4329/wjr.v15.i10.293 **Copyright** ©The Author(s) 2023.

Figure 2 Bland Altman plots demonstrate the inter-test variability for fat fraction estimates *vs* magnetic resonance spectroscopy for patients with and without liver fibrosis on two-point Dixon and six-point Dixon. A: Two-point Dixon *vs* magnetic resonance spectroscopy (MRS) in patients with liver fibrosis; B: Six-point Dixon *vs* MRS in patients with liver fibrosis; C: Two-point Dixon *vs* MRS in patients without liver fibrosis; D: Six-point Dixon *vs* MRS in patients without liver fibrosis. MRS: Magnetic resonance spectroscopy.



DOI: 10.4329/wjr.v15.i10.293 **Copyright** ©The Author(s) 2023.

Figure 3 Scatterplots demonstrate a strong linear relationship. A: Scatterplots demonstrate a strong linear relationship between two-point Dixon *vs* magnetic resonance spectroscopy (MRS); B: Scatterplots demonstrate a strong linear relationship between six-point Dixon *vs* MRS for liver fat quantification. MRS: Magnetic resonance spectroscopy; PDFF: Proton density fat fraction.



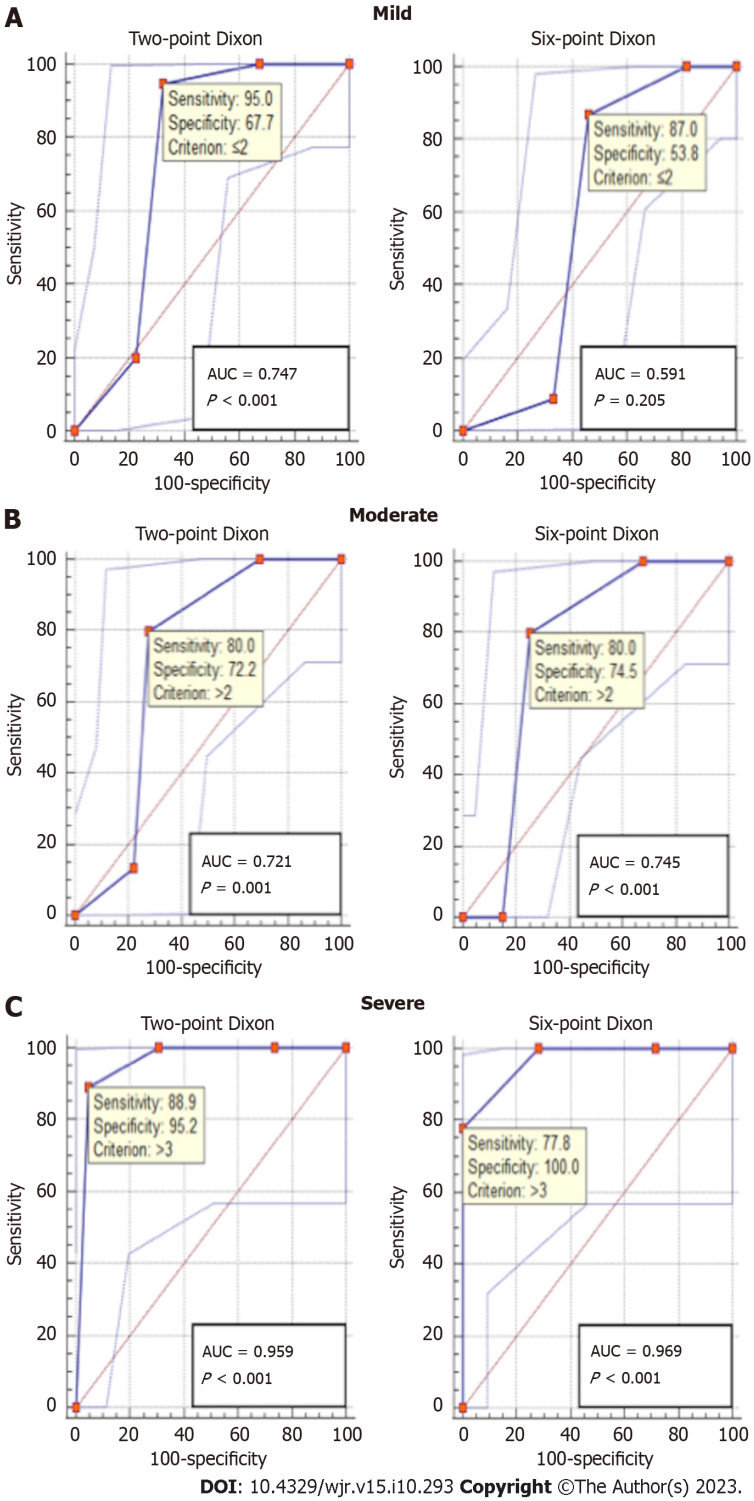
DOI: 10.4329/wjr.v15.i10.293 **Copyright** ©The Author(s) 2023.

Figure 4 Receiver operating characteristic analysis demonstrates excellent accuracy for detecting hepatic steatosis on two-point Dixon and six-point Dixon. A: Two-point Dixon; B: Six-point Dixon. AUC: Area under the curve.

Linear regression showed a highly significant linear relationship between the Dixon techniques and MRS for liver fat quantification ($P < 0.001$) (Figure 3). For two-point Dixon, the regression equation was: MRS-PDFF (%) = 4.67 + 0.76 ($FF_{\text{two-point Dixon}}$). The R^2 was 0.90 signifying that 90% of the variance in MRS-PDFF was predictable from the FF estimates on two-point Dixon. For six-point Dixon, the regression equation was: MRS-PDFF (%) = 0.59 + 1.02 ($FF_{\text{six-point Dixon}}$). The R^2 was 0.92 signifying that 92% of the variance in MRS-PDFF was predictable from the FF estimates on six-point Dixon.

ROC analysis showed an excellent accuracy for detecting steatosis on both two-point Dixon [area under the ROC (AUROC) = 0.96, 95%CI: 0.86-0.99, $P < 0.001$] and six-point Dixon (AUROC = 0.95, 95%CI: 0.86-0.99, $P < 0.001$) (Figure 4). Similarly, an excellent accuracy was found for grading severe steatosis on both two-point Dixon (AUROC = 0.96, 95%CI: 0.87-1, $P < 0.001$) and six-point Dixon (AUROC = 0.97, 95%CI: 0.89-1, $P < 0.001$) (Figure 5). For grading moderate steatosis, there was fair accuracy on both two-point Dixon (AUROC = 0.72, 95%CI: 0.58-0.84, $P = 0.001$) and six-point Dixon (AUROC = 0.75, 95%CI: 0.62-0.85, $P < 0.001$). For grading mild steatosis, the accuracy was fair on two-point Dixon (AUROC = 0.75, 95%CI: 0.61-0.86, $P < 0.01$) but poor on six-point Dixon (AUROC = 0.59, 95%CI: 0.46-0.71, $P = 0.21$). When patients with iron overload were removed from the analysis, the accuracy for grading mild steatosis increased to excellent on six-point Dixon (AUROC = 0.99, 95%CI: 0.91-1.00, $P < 0.001$) (Figure 6A).

There were 29 patients that had an US examination within 6 mo of the MR. Fleiss kappa found a moderate inter-reader agreement ($k = 0.45$, 95%CI: 0.33-0.58, $P < 0.001$) for detecting steatosis on US. For grading steatosis, the inter-reader agreement was moderate for both mild steatosis ($k = 0.44$, 95%CI: 0.23-0.65, $P < 0.001$) and severe steatosis ($k = 0.42$, 95%CI: 0.21-0.63, $P < 0.001$), and fair for moderate steatosis ($k = 0.28$, 95%CI: 0.10-0.49, $P = 0.01$). Conversely, the inter-reader agreement for detecting a non-steatotic liver on US was excellent ($k = 0.82$, 95%CI: 0.61-1, $P < 0.001$). ROC analysis demonstrated that US had a good accuracy for detecting steatosis (AUROC = 0.86, 95%CI: 0.67-0.96, $P < 0.001$) but was inferior in grading steatosis. US showed poor accuracy in grading mild steatosis (AUROC = 0.62, 95%CI: 0.41-0.80, $P = 0.27$) and only fair accuracy in grading both moderate steatosis (AUROC = 0.79, 95%CI: 0.59-0.93, $P < 0.001$) and severe steatosis (AUROC = 0.78, 95%CI: 0.58-0.92, $P < 0.01$) (Figures 6B and 7).

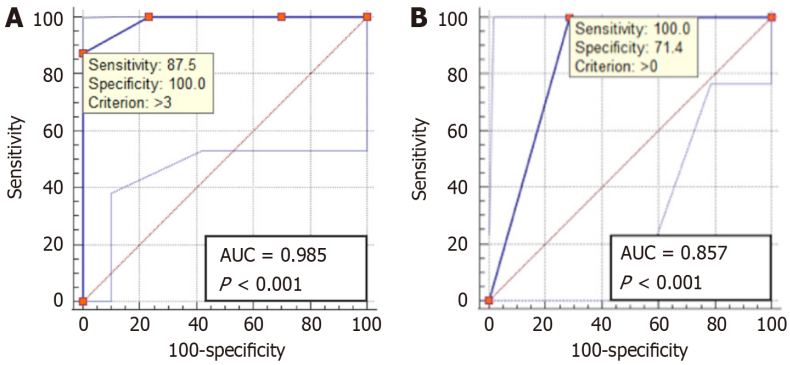


DOI: 10.4329/wjr.v15.i10.293 **Copyright** ©The Author(s) 2023.

Figure 5 Receiver operating characteristic analysis. A: The accuracy for grading mild hepatic steatosis on two-point Dixon and six-point Dixon; B: The accuracy for grading moderate hepatic steatosis on two-point Dixon and six-point Dixon; C: The accuracy for grading severe hepatic steatosis on two-point Dixon and six-point Dixon. Two-point Dixon was performed in patients with no iron overload while six-point Dixon was performed in a mixed cohort of patients with and without iron overload. AUC: Area under the curve.

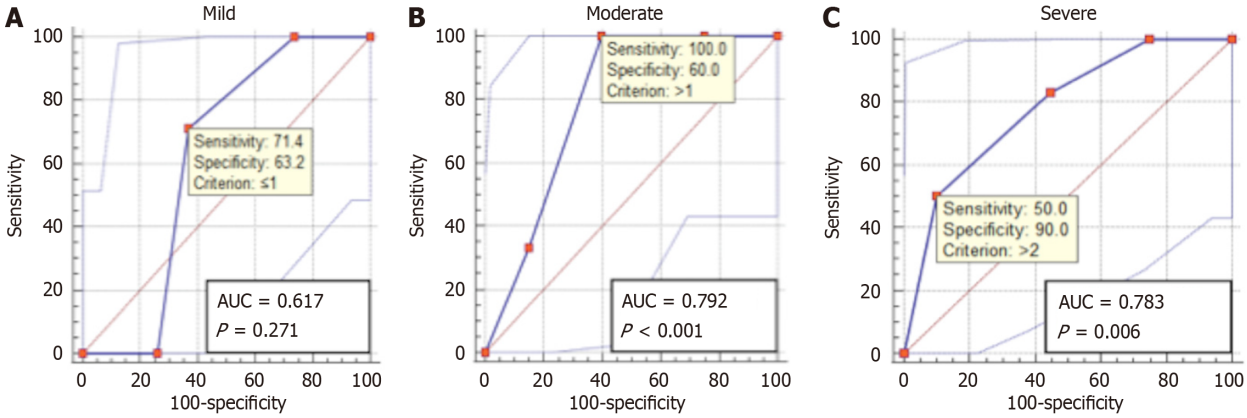
DISCUSSION

MRS-PDFF is widely recognized as the most accurate non-invasive biomarker of hepatic steatosis[10-12,21-24]. In our study, we found an excellent correlation (≥ 0.95) between FF estimates on two- and six-point Dixon *vs* MRS-PDFF (P < 0.001). The findings are concordant with the correlations (0.8-0.99) reported in other studies[25-28]. We also demonstrated a strong linear relationship between the Dixon techniques and MRS for liver fat quantification as defined by the equations MRS-PDFF (%) = 4.67 + 0.76 ($FF_{\text{two-point Dixon}}$) and MRS-PDFF (%) = 0.59 + 1.02 ($FF_{\text{six-point Dixon}}$). Findings on ROC analysis demonstrate that the Dixon techniques have excellent accuracy for detecting hepatic steatosis (AUROC ≥ 0.95, P < 0.001)



DOI: 10.4329/wjr.v15.i10.293 **Copyright** ©The Author(s) 2023.

Figure 6 Receiver operating characteristic analysis. A: Receiver operating characteristic (ROC) analysis demonstrates excellent accuracy for grading mild hepatic steatosis on six-point Dixon in patients with no iron overload; B: ROC analysis demonstrates good accuracy for detecting hepatic steatosis on ultrasound. AUC: Area under the curve.



DOI: 10.4329/wjr.v15.i10.293 **Copyright** ©The Author(s) 2023.

Figure 7 Receiver operating characteristic analysis shows the accuracy for grading mild, moderate and severe hepatic steatosis on ultrasound. A: The accuracy for grading mild hepatic steatosis on ultrasound; B: The accuracy for grading moderate hepatic steatosis on ultrasound; C: The accuracy for grading severe hepatic steatosis on ultrasound. AUC: Area under the curve.

and in grading severe steatosis (AUROC ≥ 0.96, $P < 0.001$) as well as fair accuracy in grading moderate steatosis (AUROC ≥ 0.72, $P = 0.001$). Two-point Dixon also showed fair accuracy for grading mild steatosis (AUROC = 0.75, $P < 0.01$). However, the main limitation of two-point Dixon is that it cannot be used to estimate the FF in iron overload. Despite this, two-point Dixon, a ubiquitous abdominal MR sequence, has the notable practical advantage of being widely available clinically worldwide unlike six-point Dixon or MRS, where clinical access is limited to a number of large specialized centres. In many centers that do not have access to the latter, two-point Dixon may be used as a pragmatic option (''a poor man's fat quantification'') in the absence of iron overload. Moreover, FF estimates on two-point Dixon are technically simple to perform manually and have excellent inter-reader agreement (0.99, $P < 0.001$). In comparison, six-point Dixon can be used in iron overload although subgroup analysis suggests that this test performs better in patients without iron overload. Comparing FF estimates *vs* MRS-PDFF, inter-test correlation was moderate (0.82) in patients with iron overload *vs* excellent (0.97) in patients without iron overload, $P < 0.001$. Bland Altman showed a slightly wider inter-test disparity between FF estimates *vs* MRS-PDFF in patients with iron overload (mean difference = 1.5%, LOA of -9.5%, 12.5%) compared to patients without iron overload (mean difference = 0.7%, LOA of -3.3%, 4.7%). Iron overload also negatively affected the accuracy of six-point Dixon in grading mild steatosis. When patients with iron overload were removed from the analysis, the AUROC increased from 0.59 to 0.99 ($P < 0.001$). Unlike iron overload, liver fibrosis did not affect the correlation between FF estimates on the Dixon techniques and MRS-PDFF. Correlation remained excellent (> 0.9) whether fibrosis was present or absent, $P < 0.01$. Inter-test variability on Bland Altman was similar in patients with or without fibrosis.

US had a poorer diagnostic performance in evaluating hepatic steatosis compared to MRI. The inter-reader agreement was moderate on US *vs* excellent on the Dixon techniques. The accuracy for detecting steatosis was also lower on US (AUROC = 0.86, $P < 0.001$) compared to the Dixon techniques (AUROC ≥ 0.95, $P < 0.001$). Similarly, US had a lower accuracy (AUROC = 0.78, $P < 0.01$) than the Dixon techniques (AUROC ≥ 0.96, $P < 0.001$) in grading severe steatosis.

The study had several limitations. This was a single-center retrospective analysis performed on a relatively modest number of patients. Notwithstanding, the study was adequately powered to detect statistically significant differences. Future multi-institution studies are necessary to determine the generalizability of our findings. Our study cohort was

drawn from patients with suspected diffuse parenchymal liver disease, of which 75.8% had hepatic steatosis on MRS-PDFF. While the high prevalence of steatosis in the study provided a valuable source of data for analysis, we acknowledge that our study is skewed by selection bias and does not reflect the true prevalence of steatosis in the general population. Finally, our study was performed exclusively on a single vendor 1.5-T MR platform using clinically available proprietary software. We did not evaluate the confounding effects of higher magnet strengths (*e.g.*, 3-T), different manufacturer platforms, software or protocols as it was not within the scope of our study. An *ex-vivo* phantom study reported that multi-echo Dixon techniques were accurate and reliable across 1.5-T and 3-T, different clinical platforms and multiple institutions[29]. However, a similar study in a large patient population with various grades of hepatic steatosis would be helpful to establish the clinical translatability of the findings.

CONCLUSION

In conclusion, our study findings suggest that in general the Dixon techniques perform satisfactorily for the detection, quantification and grading of hepatic steatosis but with exceptions. Two-point Dixon is a clinically widely available 1st generation technique while six-point Dixon is a modern technique that is not routinely available clinically in many centers. The main weakness of two-point Dixon is that it cannot be used in iron overload due to unmitigated signal decay from T2* effects[30]. In comparison, six-point Dixon can be used in iron overload, although its ability to grade mild steatosis may be compromised suggesting imperfect confounder correction. Additionally, liver fibrosis did not appear to have an impact on FF estimates on the Dixon techniques - a finding that to our knowledge has not been previously reported. Lastly, both Dixon techniques showed superior inter-reader agreement and accuracy for detecting steatosis compared to US. Ability to grade severe steatosis was also better on MR.

ARTICLE HIGHLIGHTS

Research background

Hepatic steatosis is a global healthcare concern.

Research motivation

There is a clinical need to determine how good existing magnetic resonance (MR) techniques are in evaluating hepatic steatosis.

Research objectives

The primary objective was to test the diagnostic performance of two- and six-point Dixon MR techniques in evaluating hepatic steatosis.

Research methods

A retrospective single center study was performed in patients with suspected diffuse parenchymal liver disease. All patients underwent MR imaging assessment with two-point Dixon, six-point Dixon and MR spectroscopy. Findings on two-point Dixon and six-point Dixon were compared against the reference standard, MR spectroscopy.

Research results

We found an excellent correlation (≥ 0.95) between fat fraction estimates on two- and six-point Dixon when compared against magnetic resonance spectroscopy ($P < 0.001$).

Research conclusions

Two- and six-point Dixon are useful MR techniques for evaluating patients with hepatic steatosis.

Research perspectives

MR techniques can provide accurate non-invasive assessment of hepatic steatosis.

FOOTNOTES

Author contributions: Elfaal M, Supersad A, Ferguson C, Locas S, Manolea F, Wilson MP, Sam M, Tu W, and Low G contributed to data collection, data analysis, editing the manuscript; and all authors approved the final manuscript.

Institutional review board statement: The study was reviewed and approved by the Ethics Committee of the University of Alberta, Canada and the Institutional Review Board of Alberta Health Services and Northern Alberta Clinical Trials and Research Centre.

Informed consent statement: The Ethics Committee of the University of Alberta, Canada, waived the requirement for signed informed consent for this retrospective study for which anonymous clinical data was used.

Conflict-of-interest statement: All the authors report no relevant conflicts of interest for this article.

Data sharing statement: No additional data is available.

Open-Access: This article is an open-access article that was selected by an in-house editor and fully peer-reviewed by external reviewers. It is distributed in accordance with the Creative Commons Attribution NonCommercial (CC BY-NC 4.0) license, which permits others to distribute, remix, adapt, build upon this work non-commercially, and license their derivative works on different terms, provided the original work is properly cited and the use is non-commercial. See: https://creativecommons.org/Licenses/by-nc/4.0/

Country/Territory of origin: Canada

ORCID number: Mitchell P Wilson 0000-0002-1630-5138; Medica Sam 0000-0002-3962-633X; Gavin Low 0000-0002-4959-8934.

S-Editor: Wang JJ
L-Editor: A
P-Editor: Zhao S

REFERENCES

1 **Starekova J**, Reeder SB. Liver fat quantification: where do we stand? *Abdom Radiol (NY)* 2020; **45**: 3386-3399 [PMID: 33025153 DOI: 10.1007/s00261-020-02783-1]
2 **Byrne CD**, Targher G. NAFLD: a multisystem disease. *J Hepatol* 2015; **62**: S47-S64 [PMID: 25920090 DOI: 10.1016/j.jhep.2014.12.012]
3 **Estes C**, Razavi H, Loomba R, Younossi Z, Sanyal AJ. Modeling the epidemic of nonalcoholic fatty liver disease demonstrates an exponential increase in burden of disease. *Hepatology* 2018; **67**: 123-133 [PMID: 28802062 DOI: 10.1002/hep.29466]
4 **Perumpail BJ**, Khan MA, Yoo ER, Cholankeril G, Kim D, Ahmed A. Clinical epidemiology and disease burden of nonalcoholic fatty liver disease. *World J Gastroenterol* 2017; **23**: 8263-8276 [PMID: 29307986 DOI: 10.3748/wjg.v23.i47.8263]
5 **Younossi ZM**, Koenig AB, Abdelatif D, Fazel Y, Henry L, Wymer M. Global epidemiology of nonalcoholic fatty liver disease-Meta-analytic assessment of prevalence, incidence, and outcomes. *Hepatology* 2016; **64**: 73-84 [PMID: 26707365 DOI: 10.1002/hep.28431]
6 **Starekova J**, Hernando D, Pickhardt PJ, Reeder SB. Quantification of Liver Fat Content with CT and MRI: State of the Art. *Radiology* 2021; **301**: 250-262 [PMID: 34546125 DOI: 10.1148/radiol.2021204288]
7 **Bravo AA**, Sheth SG, Chopra S. Liver biopsy. *N Engl J Med* 2001; **344**: 495-500 [PMID: 11172192 DOI: 10.1056/NEJM200102153440706]
8 **Ratziu V**, Charlotte F, Heurtier A, Gombert S, Giral P, Bruckert E, Grimaldi A, Capron F, Poynard T; LIDO Study Group. Sampling variability of liver biopsy in nonalcoholic fatty liver disease. *Gastroenterology* 2005; **128**: 1898-1906 [PMID: 15940625 DOI: 10.1053/j.gastro.2005.03.084]
9 **Cleveland E**, Bandy A, VanWagner LB. Diagnostic challenges of nonalcoholic fatty liver disease/nonalcoholic steatohepatitis. *Clin Liver Dis (Hoboken)* 2018; **11**: 98-104 [PMID: 30147867 DOI: 10.1002/cld.716]
10 **Roldan-Valadez E**, Favila R, Martínez-López M, Uribe M, Ríos C, Méndez-Sánchez N. In vivo 3T spectroscopic quantification of liver fat content in nonalcoholic fatty liver disease: Correlation with biochemical method and morphometry. *J Hepatol* 2010; **53**: 732-737 [PMID: 20594607 DOI: 10.1016/j.jhep.2010.04.018]
11 **van Werven JR**, Schreuder TC, Aarts EO, Nederveen AJ, Meijer JW, Berends FJ, Janssen IM, Mulder CJ, Jansen PL, Stoker J. Hepatic steatosis in morbidly obese patients undergoing gastric bypass surgery: assessment with open-system 1H-MR spectroscopy. *AJR Am J Roentgenol* 2011; **196**: W736-W742 [PMID: 21606262 DOI: 10.2214/AJR.10.5215]
12 **McPherson S**, Jonsson JR, Cowin GJ, O'Rourke P, Clouston AD, Volp A, Horsfall L, Jothimani D, Fawcett J, Galloway GJ, Benson M, Powell EE. Magnetic resonance imaging and spectroscopy accurately estimate the severity of steatosis provided the stage of fibrosis is considered. *J Hepatol* 2009; **51**: 389-397 [PMID: 19505740 DOI: 10.1016/j.jhep.2009.04.012]
13 **Dixon WT**. Simple proton spectroscopic imaging. *Radiology* 1984; **153**: 189-194 [PMID: 6089263 DOI: 10.1148/radiology.153.1.6089263]
14 **Dyke JP**. Quantitative MRI Proton Density Fat Fraction: A Coming of Age. *Radiology* 2021; **298**: 652-653 [PMID: 33475469 DOI: 10.1148/radiol.2020204356]
15 **Reeder SB**, Sirlin CB. Quantification of liver fat with magnetic resonance imaging. *Magn Reson Imaging Clin N Am* 2010; **18**: 337-357, ix [PMID: 21094444 DOI: 10.1016/j.mric.2010.08.013]
16 **Hong CW**, Cui JY, Batakis D, Xu Y, Wolfson T, Gamst AC, Schlein AN, Negrete LM, Middleton MS, Hamilton G, Loomba R, Schwimmer JB, Fowler KJ, Sirlin CB. Repeatability and accuracy of various region-of-interest sampling strategies for hepatic MRI proton density fat fraction quantification. *Abdom Radiol (NY)* 2021; **46**: 3105-3116 [PMID: 33609166 DOI: 10.1007/s00261-021-02965-5]
17 **Saadeh S**, Younossi ZM, Remer EM, Gramlich T, Ong JP, Hurley M, Mullen KD, Cooper JN, Sheridan MJ. The utility of radiological imaging in nonalcoholic fatty liver disease. *Gastroenterology* 2002; **123**: 745-750 [PMID: 12198701 DOI: 10.1053/gast.2002.35354]
18 **Rodge GA**, Goenka MK, Goenka U, Afzalpurkar S, Shah BB. Quantification of Liver Fat by MRI-PDFF Imaging in Patients with Suspected Non-alcoholic Fatty Liver Disease and Its Correlation with Metabolic Syndrome, Liver Function Test and Ultrasonography. *J Clin Exp Hepatol* 2021; **11**: 586-591 [PMID: 34511820 DOI: 10.1016/j.jceh.2020.11.004]
19 **Landis JR**, Koch GG. The measurement of observer agreement for categorical data. *Biometrics* 1977; **33**: 159-174 [PMID: 843571]
20 **Guglielmo FF**, Venkatesh SK, Mitchell DG. Liver MR Elastography Technique and Image Interpretation: Pearls and Pitfalls. *Radiographics* 2019; **39**: 1983-2002 [PMID: 31626569 DOI: 10.1148/rg.2019190034]
21 **Gu J**, Liu S, Du S, Zhang Q, Xiao J, Dong Q, Xin Y. Diagnostic value of MRI-PDFF for hepatic steatosis in patients with non-alcoholic fatty liver disease: a meta-analysis. *Eur Radiol* 2019; **29**: 3564-3573 [PMID: 30899974 DOI: 10.1007/s00330-019-06072-4]
22 **Reeder SB**, Cruite I, Hamilton G, Sirlin CB. Quantitative Assessment of Liver Fat with Magnetic Resonance Imaging and Spectroscopy. *J Magn Reson Imaging* 2011; **34**: 729-749 [PMID: 22025886 DOI: 10.1002/jmri.22775]

23 **Szczepaniak LS**, Nurenberg P, Leonard D, Browning JD, Reingold JS, Grundy S, Hobbs HH, Dobbins RL. Magnetic resonance spectroscopy to measure hepatic triglyceride content: prevalence of hepatic steatosis in the general population. *Am J Physiol Endocrinol Metab* 2005; **288**: E462-E468 [PMID: 15339742 DOI: 10.1152/ajpendo.00064.2004]

24 **Ajmera V**, Loomba R. Imaging biomarkers of NAFLD, NASH, and fibrosis. *Mol Metab* 2021; **50**: 101167 [PMID: 33460786 DOI: 10.1016/j.molmet.2021.101167]

25 **Kramer H**, Pickhardt PJ, Kliewer MA, Hernando D, Chen GH, Zagzebski JA, Reeder SB. Accuracy of Liver Fat Quantification With Advanced CT, MRI, and Ultrasound Techniques: Prospective Comparison With MR Spectroscopy. *AJR Am J Roentgenol* 2017; **208**: 92-100 [PMID: 27726414 DOI: 10.2214/AJR.16.16565]

26 **Yurdaisik I**, Nurili F. Accuracy of Multi-echo Dixon Sequence in Quantification of Hepatic Steatosis. *Cureus* 2020; **12**: e7103 [PMID: 32231898 DOI: 10.7759/cureus.7103]

27 **Hayashi T**, Saitoh S, Takahashi J, Tsuji Y, Ikeda K, Kobayashi M, Kawamura Y, Fujii T, Inoue M, Miyati T, Kumada H. Hepatic fat quantification using the two-point Dixon method and fat color maps based on non-alcoholic fatty liver disease activity score. *Hepatol Res* 2017; **47**: 455-464 [PMID: 27351583 DOI: 10.1111/hepr.12767]

28 **Idilman IS**, Keskin O, Celik A, Savas B, Elhan AH, Idilman R, Karcaaltincaba M. A comparison of liver fat content as determined by magnetic resonance imaging-proton density fat fraction and MRS versus liver histology in non-alcoholic fatty liver disease. *Acta Radiol* 2016; **57**: 271-278 [PMID: 25855666 DOI: 10.1177/0284185115580488]

29 **Hu HH**, Yokoo T, Bashir MR, Sirlin CB, Hernando D, Malyarenko D, Chenevert TL, Smith MA, Serai SD, Middleton MS, Henderson WC, Hamilton G, Shaffer J, Shu Y, Tkach JA, Trout AT, Obuchowski N, Brittain JH, Jackson EF, Reeder SB; RSNA Quantitative Imaging Biomarkers Alliance PDFF Biomarker Committee. Linearity and Bias of Proton Density Fat Fraction as a Quantitative Imaging Biomarker: A Multicenter, Multiplatform, Multivendor Phantom Study. *Radiology* 2021; **298**: 640-651 [PMID: 33464181 DOI: 10.1148/radiol.2021202912]

30 **Colgan TJ**, Zhao R, Roberts NT, Hernando D, Reeder SB. Limits of Fat Quantification in the Presence of Iron Overload. *J Magn Reson Imaging* 2021; **54**: 1166-1174 [PMID: 33783066 DOI: 10.1002/jmri.27611]



Published by **Baishideng Publishing Group Inc**
7041 Koll Center Parkway, Suite 160, Pleasanton, CA 94566, USA
Telephone: +1-925-3991568
E-mail: bpgoffice@wjgnet.com
Help Desk: https://www.f6publishing.com/helpdesk
https://www.wjgnet.com



© 2023 Baishideng Publishing Group Inc. All rights reserved.

ISSN 1949-8470 (online)

World Journal of *Radiology*

World J Radiol 2023 November 28; 15(11): 304-337



Published by Baishideng Publishing Group Inc

World Journal of Radiology

Contents

Monthly Volume 15 Number 11 November 28, 2023

ORIGINAL ARTICLE

Retrospective Study

304 Radiomics analysis with three-dimensional and two-dimensional segmentation to predict survival outcomes in pancreatic cancer

Saleh M, Virarkar M, Mahmoud HS, Wong VK, Gonzalez Baerga CI, Parikh M, Elsherif SB, Bhosale PR

Basic Study

315 Imaging assessment of photosensitizer emission induced by radionuclide-derived Cherenkov radiation using charge-coupled device optical imaging and long-pass filters

Aung W, Tsuji AB, Rikiyama K, Nishikido F, Obara S, Higashi T

META-ANALYSIS

324 Association between late gadolinium enhancement and outcome in dilated cardiomyopathy: A meta-analysis

Feng XY, He WF, Zhang TY, Wang LL, Yang F, Feng YL, Li CP, Li R

World Journal of Radiology

Monthly Volume 15 Number 11 November 28, 2023

Contents

ABOUT COVER

Peer Reviewer of *World Journal of Radiology*, Melissa Bersanelli, MD, Adjunct Professor, Chief Doctor, Medical Oncology Unit, University Hospital of Parma, Parma 43126, Italy. bersamel@libero.it

AIMS AND SCOPE

The primary aim of *World Journal of Radiology* (*WJR*, *World J Radiol*) is to provide scholars and readers from various fields of radiology with a platform to publish high-quality basic and clinical research articles and communicate their research findings online.

WJR mainly publishes articles reporting research results and findings obtained in the field of radiology and covering a wide range of topics including state of the art information on cardiopulmonary imaging, gastrointestinal imaging, genitourinary imaging, musculoskeletal imaging, neuroradiology/head and neck imaging, nuclear medicine and molecular imaging, pediatric imaging, vascular and interventional radiology, and women's imaging.

INDEXING/ABSTRACTING

The *WJR* is now abstracted and indexed in PubMed, PubMed Central, Emerging Sources Citation Index (Web of Science), Reference Citation Analysis, China National Knowledge Infrastructure, China Science and Technology Journal Database, and Superstar Journals Database. The 2023 Edition of Journal Citation Reports® cites the 2022 impact factor (IF) for *WJR* as 2.5; IF without journal self cites: 2.3; 5-year IF: 2.5; Journal Citation Indicator: 0.54.

RESPONSIBLE EDITORS FOR THIS ISSUE

Production Editor: *Si Zhao*; **Production Department Director:** *Xu Guo*; **Editorial Office Director:** *Jia-Ping Yan*.

NAME OF JOURNAL
World Journal of Radiology

ISSN
ISSN 1949-8470 (online)

LAUNCH DATE
January 31, 2009

FREQUENCY
Monthly

EDITORS-IN-CHIEF
Thomas J Vogl

EDITORIAL BOARD MEMBERS
https://www.wjgnet.com/1949-8470/editorialboard.htm

PUBLICATION DATE
November 28, 2023

COPYRIGHT
© 2023 Baishideng Publishing Group Inc

INSTRUCTIONS TO AUTHORS
https://www.wjgnet.com/bpg/gerinfo/204

GUIDELINES FOR ETHICS DOCUMENTS
https://www.wjgnet.com/bpg/GerInfo/287

GUIDELINES FOR NON-NATIVE SPEAKERS OF ENGLISH
https://www.wjgnet.com/bpg/gerinfo/240

PUBLICATION ETHICS
https://www.wjgnet.com/bpg/GerInfo/288

PUBLICATION MISCONDUCT
https://www.wjgnet.com/bpg/gerinfo/208

ARTICLE PROCESSING CHARGE
https://www.wjgnet.com/bpg/gerinfo/242

STEPS FOR SUBMITTING MANUSCRIPTS
https://www.wjgnet.com/bpg/GerInfo/239

ONLINE SUBMISSION
https://www.f6publishing.com

© 2023 Baishideng Publishing Group Inc. All rights reserved. 7041 Koll Center Parkway, Suite 160, Pleasanton, CA 94566, USA
E-mail: bpgoffice@wjgnet.com https://www.wjgnet.com

World Journal of Radiology

Submit a Manuscript: https://www.f6publishing.com

World J Radiol 2023 November 28; 15(11): 304-314

DOI: 10.4329/wjr.v15.i11.304

ISSN 1949-8470 (online)

ORIGINAL ARTICLE

Retrospective Study

Radiomics analysis with three-dimensional and two-dimensional segmentation to predict survival outcomes in pancreatic cancer

Mohammed Saleh, Mayur Virarkar, Hagar S Mahmoud, Vincenzo K Wong, Carlos Ignacio Gonzalez Baerga, Miti Parikh, Sherif B Elsherif, Priya R Bhosale

Specialty type: Radiology, nuclear medicine and medical imaging

Provenance and peer review: Invited article; Externally peer reviewed.

Peer-review model: Single blind

Peer-review report's scientific quality classification

Grade A (Excellent): 0
Grade B (Very good): B
Grade C (Good): C
Grade D (Fair): 0
Grade E (Poor): 0

P-Reviewer: Lin W, China

Received: August 28, 2023
Peer-review started: August 28, 2023
First decision: September 19, 2023
Revised: September 20, 2023
Accepted: October 23, 2023
Article in press: October 23, 2023
Published online: November 28, 2023

Mohammed Saleh, Hagar S Mahmoud, Vincenzo K Wong, Priya R Bhosale, Department of Diagnostic Radiology, The University of Texas MD Anderson Cancer Center, Houston, TX 77030, United States

Mayur Virarkar, Carlos Ignacio Gonzalez Baerga, Sherif B Elsherif, Department of Diagnostic Radiology, The University of Florida College of Medicine, Jacksonville, FL 32209, United States

Miti Parikh, Keck School of Medicine, University of South California, Los Angeles, CA 90033, United States

Corresponding author: Carlos Ignacio Gonzalez Baerga, MD, Research Assistant, Department of Diagnostic Radiology, The University of Florida College of Medicine, 655 8th Street West, Jacksonville, FL 32209, United States. carlos.gonzalezbaerga@jax.ufl.edu

Abstract

BACKGROUND

Radiomics can assess prognostic factors in several types of tumors, but considering its prognostic ability in pancreatic cancer has been lacking.

AIM

To evaluate the performance of two different radiomics software in assessing survival outcomes in pancreatic cancer patients.

METHODS

We retrospectively reviewed pretreatment contrast-enhanced dual-energy computed tomography images from 48 patients with biopsy-confirmed pancreatic ductal adenocarcinoma who later underwent neoadjuvant chemoradiation and surgery. Tumors were segmented using TexRad software for 2-dimensional (2D) analysis and MIM software for 3D analysis, followed by radiomic feature extraction. Cox proportional hazard modeling correlated texture features with overall survival (OS) and progression-free survival (PFS). Cox regression was used to detect differences in OS related to pretreatment tumor size and residual tumor following treatment. The Wilcoxon test was used to show the relationship between tumor volume and the percent of residual tumor. Kaplan-Meier analysis was used to compare survival in patients with different tumor densities in Hounsfield units for both 2D and 3D analysis.

RESULTS
3D analysis showed that higher mean tumor density [hazard ratio (HR) = 0.971, P = 0.041)] and higher median tumor density (HR = 0.970, P = 0.037) correlated with better OS. 2D analysis showed that higher mean tumor density (HR = 0.963, P = 0.014) and higher mean positive pixels (HR = 0.962, P = 0.014) correlated with better OS; higher skewness (HR = 3.067, P = 0.008) and higher kurtosis (HR = 1.176, P = 0.029) correlated with worse OS. Higher entropy correlated with better PFS (HR = 0.056, P = 0.036). Models determined that patients with increased tumor size greater than 1.35 cm were likely to have a higher percentage of residual tumors of over 10%.

CONCLUSION
Several radiomics features can be used as prognostic tools for pancreatic cancer. However, results vary between 2D and 3D analyses. Mean tumor density was the only variable that could reliably predict OS, irrespective of the analysis used.

Key Words: Radiomics; Pancreas; Cancer; Segmentation

©The Author(s) 2023. Published by Baishideng Publishing Group Inc. All rights reserved.

Core Tip: The use of radiomics to assess pancreatic cancer has been limited. This retrospective study evaluated the performance of 2-dimensional (2D) and 3D radiomic software in determining survival outcomes of pancreatic cancer patients. The mean tumor density was the only variable to reliably predict overall survival (OS) irrespective of the type of analysis. Mean tumor density may be able to differentiate survival and potentially may be help in treatment planning irrespective of the texture analysis software used. Higher skewness [hazard ratio (HR) = 3.067, P = 0.008] and higher kurtosis (HR = 1.176, P = 0.029) correlated with worse OS based on 2D analysis.

Citation: Saleh M, Virarkar M, Mahmoud HS, Wong VK, Gonzalez Baerga CI, Parikh M, Elsherif SB, Bhosale PR. Radiomics analysis with three-dimensional and two-dimensional segmentation to predict survival outcomes in pancreatic cancer. *World J Radiol* 2023; 15(11): 304-314
URL: https://www.wjgnet.com/1949-8470/full/v15/i11/304.htm
DOI: https://dx.doi.org/10.4329/wjr.v15.i11.304

INTRODUCTION

Pancreatic cancer is an aggressive malignancy causing 7%-8% of cancer-related deaths in the United States[1]. The 5-year overall survival (OS) rate is currently less than 5% despite aggressive multimodality treatment approaches, which mainly include neoadjuvant chemoradiation followed by surgery[2,3]. Up to 60% of patients experience recurrence following definitive therapy[3-5]. Pretreatment stratification of patients based on risk of recurrence and mortality may help determine the aggressiveness of the treatment plan and guide optimal management.

Several risk factors may affect pancreatic cancer prognosis and OS, such as vascular invasion, lymph node metastasis, tumor stage, and tumor differentiation[6]. Although some prognostic factors may be evaluated by conventional imaging, several others require invasive histologic assessment, which is expensive, carries the risk of complications such as infections or bleeding, and may not provide a complete evaluation of the tumor owing to sampling variability.

There is increasing interest in radiomics because it converts qualitative and subjective imaging data into quantitative and objective data through complex algorithms to provide information that a radiologist cannot extract with the naked eye. Several studies have demonstrated that radiomics can noninvasively assess tumor grade, lymph node metastasis, and other prognostic factors for multiple types of tumors[7-9]. However, only a few studies have evaluated the use of radiomics for assessing prognosis for pancreatic tumors[10-13]. Additionally, texture analysis values extracted *via* artificial intelligence programs are software-dependent and may vary among software programs due to differing algorithms and processing. For example, MIM performs a 3-dimensional (3D) volumetric analysis, whereas TexRad performs a cross-sectional 2D analysis of only a single slice.

Given this discrepancy, the primary objective of the current study was to determine whether pancreatic tumor texture features can reliably be used as prognostic indicators to provide reproducible results independent of the artificial intelligence software or type of analysis used.

MATERIALS AND METHODS

Patients

This retrospective single-center study was reviewed and approved by the Institutional Review Board in compliance with HIPAA guidelines. Institutional records between January 2012 and November 2020 were accessed. Our inclusion criteria

included patients undergoing a baseline (pretreatment) contrast-enhanced dual-energy computed tomography (CT) study of the primary pancreatic tumor before chemoradiation and subsequent surgery. Patients who did not have: (1) Baseline pretreatment CT study data; (2) Histologic confirmation of a primary tumor of the pancreas; and/or (3) Visible tumors on the CT study were excluded from the analysis. Forty-eight patients met the inclusion criteria. An undergraduate research student searched the patients' medical records for date of birth, date of first CT study, date of diagnosis, date of last follow-up, date of surgery, histological tumor size, tumor histologic characteristics, and histologic differentiation, presence of adenopathy, both before and after treatment, type of neoadjuvant therapy received, recurrence state, date of recurrence, vital status, and date of death, if applicable. Tumor responses were based on a comparative evaluation of pre- and post-treatment scans and were evaluated by the Response Evaluation Criteria in Solid Tumors criteria.

CT protocol and image acquisition

All patients underwent the pretreatment abdominal contrast-enhanced dual-energy CT study *via* a 64-detector row Discovery CT750 HD CT scanner (Gemstone Spectral Imaging, GE Healthcare, Milwaukee, WI) with a multiphasic pancreatic protocol with rapid switching. Images were acquired intravenously after injecting 125-150 mL of Omnipaque 350 (Mallinckrodt, St Louis, MO) at a rate of 4-5 mL/s. Bolus tracking was used. When a 100-Hounsfield unit (HU) increase was detected at the origin of the celiac axis, images were obtained with a diagnostic scan delay of 20 s, from the level of the hemidiaphragm to the iliac crest, using a rapid switching dual-energy technique (80 kVp and 140 kVp). The scan duration was 5 s for the abdomen. The late arterial/pancreatic parenchymal phase was obtained approximately 40-45 s after the start of contrast injection, and an additional 20-s delay scan using a 120-kVp conventional non-dual-energy imaging technique, resulting in a portal venous phase, was obtained approximately 65-70 s after the start of contrast injection. Images in the pancreatic parenchymal and portal venous phases were reconstructed at 2.5-mm slice thickness. The scan parameters were as follows: Tube current 125-600 ms, tube voltage 120 kVp, pitch 0.98:1, slice thickness 0.6-5 mm, revolution time 0.8 s, table feed speed 39.375 mm/rotation, and field of view 440 mm.

Radiomics workflow

Our study included two separate segmentation programs: MIM software version 6.9.4 (MIM Software Inc) and TexRad Research version 3.9 (Cambridge Computed Imaging LTD). Both radiomics workflows started with tumor segmentation on the treatment-naïve imaging studies, followed by feature extraction. The tumors were segmented by a research fellow in the abdominal radiology department under the supervision of an oncologic radiologist with ten years of experience.

3D segmentation: The portal venous phase was used for segmentation. The tumors were contoured on MIM software using the 3D brush on the axial, coronal, and sagittal planes (Figure 1) by an abdominal radiologist with ten years of clinical experience. A research fellow assisted in extracting the texture features on MIM and saved them on an encrypted server. Seventeen texture features [integral total value (HU × Ml), kurtosis, maximum HU, mean HU, maximum mean HU ratio, median HU, median minimum HU ratio, minimum HU, minimum mean HU ratio, skewness, sphere value (cm), standard deviation, standard deviation mean HU ratio, total HU, volume, voxel count, and entropy], all belonging to first-order statistics, were extracted *via* an algorithm developed by MIM Software Inc for the texture analysis of CT scans (Table 1).

2D segmentation: The images evaluated in 2D segmentation were also derived from the portal venous phase uploaded to the commercially available TexRad research software. 2D segmentation was performed using the polygon region of interest tool. The slice with the greatest tumor diameter was used, and textural radiomic features were extracted automatically from the images within the region of interest. A total of 6 texture features (entropy, kurtosis, mean HU, mean positive pixels, skewness, and standard deviation) were extracted. Because TexRad software applies spatial scale filters and MIM's algorithm does not, only values without using a spatial scale filter were considered to compare the two software programs.

Statistical analyses

For 2D and 3D analysis, the correlation between tumor size and percentage of residual tumor based on histological evaluation was assessed using simple linear regression. The Wilcoxon test was used to show the relationship between tumor volume and the percent of residual tumor. The Youden index was used to determine the optimal cutoff for predicting residual tumors based on tumor size. Also, a receiver operating characteristic curve was generated to predict the performance of tumor size in estimating residual tumors.

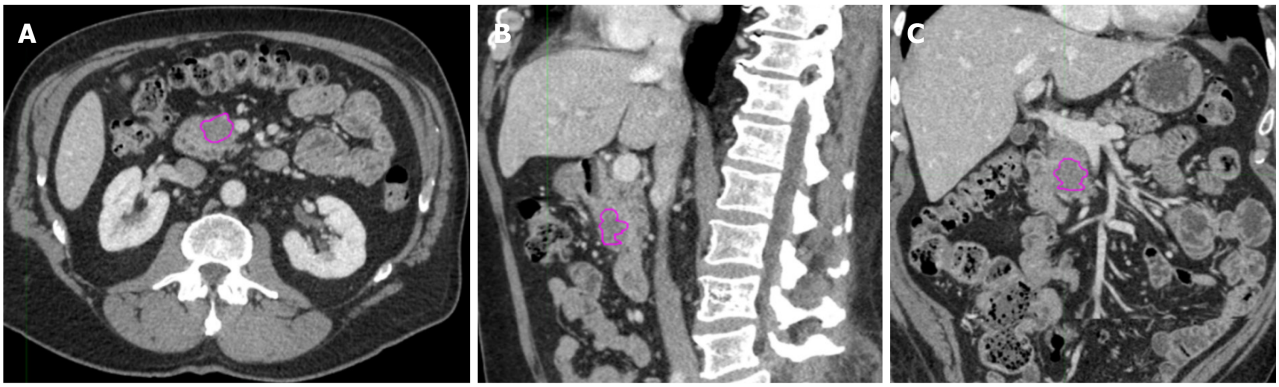
Simple logistic regression was used to correlate the texture features with post-treatment adenopathy. A Cox proportional hazards model was used to fit univariate models identifying associations between texture features and OS and progression-free survival (PFS). Cox regression was used to detect any significant association between OS and the percentage of residual tumor following treatment or tumor size.

For 2D and 3D analysis, recursive partitioning analysis was carried out using the R package "rpart" to identify a cutoff that can predict OS by mean HU value. All tests were two-sided, and $P < 0.05$ was considered statistically significant. Statistical analysis was done using SAS version 9.4 (SAS Institute, Cary, NC). The Kaplan-Meier analysis was used to compare survival in patients with different tumor densities in HU for both 2D and 3D analysis.

Table 1 Radiomic features extracted from segmentation programs

MIM Software Inc (3D segmentation)	Cambridge Computed Imaging LTD (2D segmentation)
Integral total value	Entropy
Kurtosis	Kurtosis
Maximum HU	Mean HU
Mean HU	Mean positive pixels
Maximum mean HU ratio	Skewness
Median HU	Standard deviation
Median minimum HU ratio	
Minimum HU	
Minimum mean HU ratio	
Skewness	
Sphere value	
Standard deviation	
Standard deviation mean HU ratio	
Total HU	
Volume	
Voxel count	
Entropy	

HU: Hounsfield units; 2D: Two-dimensional; 3D: Three-dimensional.



DOI: 10.4329/wjr.v15.i11.304 **Copyright** ©The Author(s) 2023.

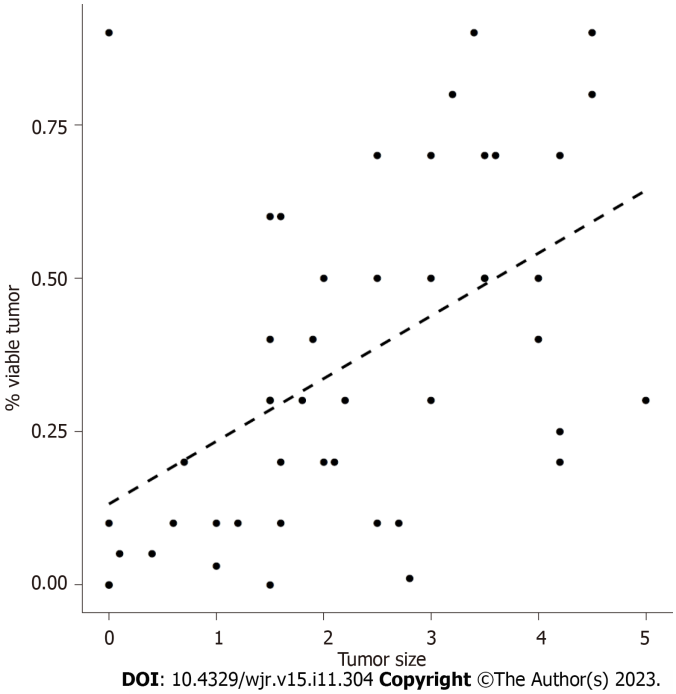
Figure 1 Example of contouring using the 3-dimensional brush on MIM software in the different planes. A: Axial; B: Sagittal; C: Coronal.

RESULTS

The patients' mean ± SD age was 61.2 ± 12.8 years, with a median age of 61.9. Patient ages ranged from 18.6 years to 88.9 years. Linear regression showed that histologic tumor size was correlated with residual tumor [correlation coefficient = 0.51, 95% confidence interval (CI): 0.26-0.70, Figure 2]. Using a cutoff of 1.35 cm, based on histologic tumor size, our models showed that patients with a tumor size greater than 1.35 cm are at risk of having more than 10% residual tumor (sensitivity = 0.64, specificity = 0.94, accuracy = 0.85, P = 0.015; Figures 3 and 4).

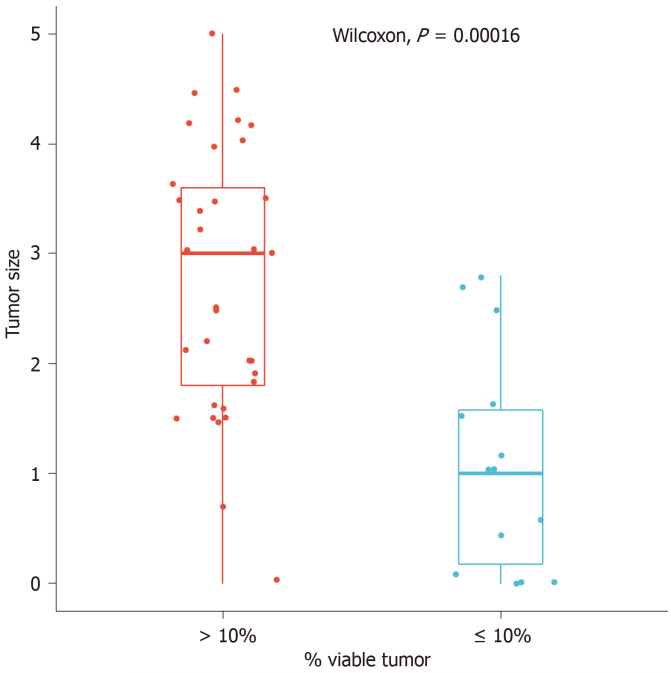
3D analysis

Linear regression showed that histologic tumor size was correlated with residual tumor (correlation coefficient = 0.51, 95%CI: 0.26-0.70, Figure 2). Using a cutoff of 1.35 cm, based on histologic tumor size, our models showed that patients with a tumor size greater than 1.35 cm are at risk of having more than 10% residual tumor (sensitivity = 0.64, specificity = 0.94, accuracy = 0.85, P = 0.015; Figures 3 and 4).



DOI: 10.4329/wjr.v15.i11.304 **Copyright** ©The Author(s) 2023.

Figure 2 Linear regression showing that residual tumor was significantly linearly correlated with tumor size (*P* = 0.0002). Using tumor size as the predictor (x-axis), the slope is 0.1023, meaning that for every single unit increase in tumor size, there is a 10.23% increase in the percentage of residual tumors.

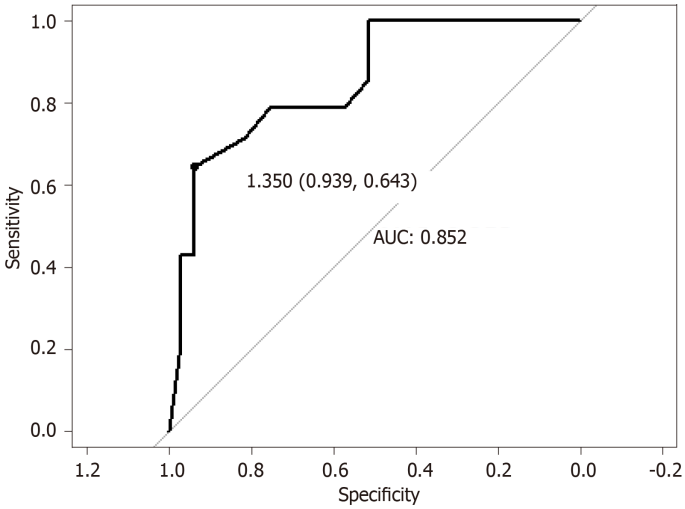


DOI: 10.4329/wjr.v15.i11.304 **Copyright** ©The Author(s) 2023.

Figure 3 Box plot showing the relationship between tumor size and residual tumor in our cohort.

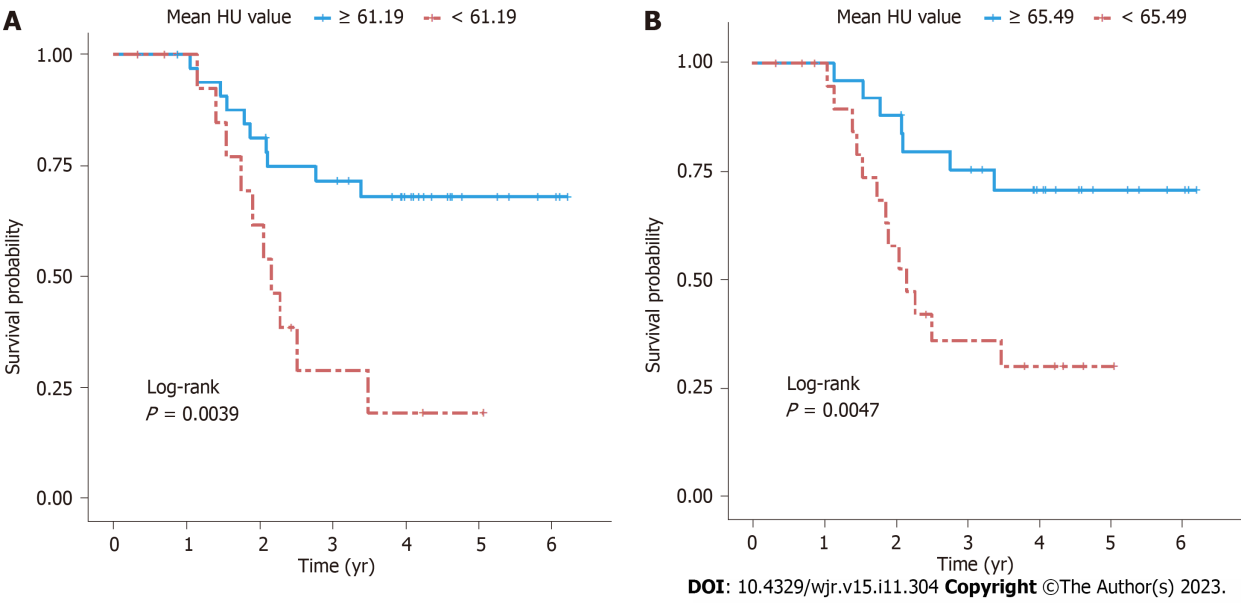
Linear regression analysis showed that mean HU [correlation coefficient = -0.0040, standard error (SE) = 0.0018, *P* = 0.0326], median HU (correlation coefficient = -0.0039, SE = 0.0019, *P* = 0.0373), and minimum mean HU ratio (correlation coefficient = -0.1038, SE = 0.0499, *P* = 0.0406) were inversely correlated with the percentage of residual tumor following treatment.

The univariate Cox proportional hazards model showed that mean HU and median HU were significantly correlated with OS [mean HU: hazard ratio (HR) = 0.971, 95%CI: 0.945-0.999, *P* = 0.041; median HU: HR = 0.970, 95%CI: 0.942-0.998, *P* = 0.037]. A cutoff value of mean HU ≥ 61.185 significantly predicted better OS (*P* = 0.0039; Figure 5A). None of the texture features significantly correlated with post-treatment adenopathy or PFS risk.



DOI: 10.4329/wjr.v15.i11.304 **Copyright** ©The Author(s) 2023.

Figure 4 Receiver operating characteristic curve showing that 1.35-cm tumor size is the optimal cutoff point for predicting ≤ 10% residual tumor, determined by the Youden index. This model predicts ≤ 10% residual tumor with an area under the curve of 0.852, sensitivity of 0.643, and specificity of 0.939. AUC: Area under the curve.



DOI: 10.4329/wjr.v15.i11.304 **Copyright** ©The Author(s) 2023.

Figure 5 Kaplan-Meier curves. A: Kaplan-Meier curves comparing patients with mean Hounsfield units (HU) value greater or less than 61.185, based on 3-dimensional analysis. Log-rank *P* = 0.0039 indicates that patients with mean HU ≥ 61.185 had significantly better overall survival than those with mean HU < 61.185; B: Kaplan-Meier curves comparing patients with mean HU value greater or less than 65.485, based on 2-dimensional analysis. Log-rank *P* = 0.0047 indicates that patients with mean HU ≥ 65.485 had significantly better overall survival than those with mean HU < 65.485. HU: Hounsfield units.

2D analysis

Without a spatial scale filter, high tumor entropy (correlation coefficient = -0.641, SE = 0.301, *P* = 0.039), increased mean HU (correlation coefficient = -0.004, SE = 0.002, *P* = 0.032), and high mean positive pixels (correlation coefficient = -0.005, SE = 0.002, *P* = 0.032) correlated with less than 10% residual tumor following treatment. Entropy is also positively associated with PFS (HR = 0.056, 95%CI: 0.004-0.831, *P* = 0.036).

For 2D values, a cutoff of 65.485 for mean HU was appropriate for differentiating mortality risk; patients with equal or higher values than the threshold had significantly better OS (*P* = 0.0047; Figure 5B). High mean positive pixels were associated with better OS (*P* = 0.014), whereas high kurtosis (*P* = 0.029) and skewness (*P* = 0.007) were associated with worse OS (Table 2). No significant correlations existed between texture features at 0 spatial scale filter and post-treatment adenopathy.

Table 2 Univariate Cox proportional hazards model for overall survival (hazard ratio < 1 indicates better prognosis)

SSF	Variable	Hazard ratio	95% CI	*P* value
0	Kurtosis	1.176	1.017-1.361	0.029
0	Mean HU	0.963	0.935-0.993	0.014
0	MPP	0.962	0.933-0.992	0.014
0	Skewness	3.067	1.345-6.993	0.008
2	Entropy	0.042	0.003-0.636	0.022
2	Mean HU	0.975	0.961-0.989	0.001
3	Mean HU	0.980	0.968-0.991	< 0.001
4	Kurtosis	1.071	1.000-1.146	0.048
4	Mean HU	0.985	0.974-0.995	0.003
4	MPP	1.012	1.000-1.023	0.046
4	SD	1.006	1.001-1.011	0.016
5	MPP	1.009	1.002-1.017	0.012
5	SD	1.006	1.001-1.011	0.010
6	MPP	1.007	1.002-1.013	0.008
6	SD	1.006	1.001-1.011	0.011

Without a spatial scale filter (SSF), patients with high kurtosis and skewness had worse overall survival. Patients with elevated mean Hounsfield units and mean positive pixels had better overall survival. Several other significant findings were found when an SSF was applied (2 through 6). HU: Hounsfield units; SSF: Spatial scale filter; MPP: Mean positive pixels; 95%CI: 95% confidence interval.

DISCUSSION

Our study suggests that baseline CT-based texture features are noninvasive prognostic indicators that can help predict residual tumors, response to therapy, and prognosis in patients with pancreatic cancer. We also found that some of these textural features are reproducible irrespective of the software or analysis used. 3D and 2D analyses showed that higher tumor density correlated with better OS and lower residual tumors. However, unlike 3D analysis, the 2D analysis also showed that higher skewness and higher kurtosis were correlated with worse OS and higher entropy was correlated with better PFS.

Our study showed that tumor density was a predictor of OS, irrespective of the texture analysis software used. The findings of Cassinotto *et al*[14] corroborate our findings. In that study, hypoattenuating pancreatic adenocarcinomas on preoperative scans were associated with worse disease-free survival. In addition, hypoattenuating tumors were associated with an increased risk of lymph node metastasis and high tumor grade, which explained the poor survival outcomes compared with patients with hyperattenuating tumors. Fukukura *et al*[15] also demonstrated that hypoattenuating pancreatic tumors on pretreatment scans may independently predict worse OS in patients undergoing surgery or receiving adjuvant treatments. Another study by Zhu *et al*[16] showed that hypoattenuating pancreatic tumors treated with surgical resection were associated with poorer disease-free survival compared with hyperattenuating pancreatic tumors. Hypoattenuating tumors have been shown to have a greater degree of necrosis, an indicator of tumor hypoxia, and, therefore, accelerated malignant potential. This radiologic-pathologic association helps explain the association of hypoattenuation with poor prognosis[17,18].

Higher tumor density (mean HU) and smaller tumor size correlated with a lower percentage of residual tumors following treatment. Our findings suggest that smaller and/or hyperattenuating tumors on the portal venous phase of contrast-enhanced CT will likely respond to chemotherapy because they showed a lower percentage of residual tumors following treatment. To our knowledge, no previous studies have evaluated this correlation. Several studies have shown that patients with pancreatic cancer showing greater than 10% residual tumor following treatment have a worse prognosis[19,20]. Okubo *et al*[21] showed that patients with residual tumors greater than 220 mm^2 had a higher risk of lymphatic, perineural, and vascular invasion. This variable was an independent predictor of a worse recurrence-free survival. In our study, hyperattenuating tumors correlated with lower residual tumors after therapy, which likely explains the correlation between higher tumor density and better survival outcomes. Therefore, using tumor density on baseline scans as a prognostic predictor could help clinicians plan management, with the higher-risk group potentially receiving more aggressive therapies or undergoing more aggressive monitoring.

2D analysis showed that skewness and kurtosis were inversely correlated with OS. Attiyeh *et al*[22] developed two separate models with 255 radiomics features that measure pixel spatial variation, including kurtosis and skewness; their models demonstrated that tumors with greater heterogeneity were associated with poor OS. Their datasets predicted OS with a concordance index of 0.69 to 0.74. Data from Cozzi *et al*[23] corroborated the finding that higher heterogeneity

correlates with worse prognosis; they found that tumors with lower homogeneity and higher dissimilarity textural features were associated with worse OS. However, skewness and kurtosis were not associated with survival outcomes in their study.

Increasing heterogeneity has also been associated with poor prognosis, irrespective of the imaging modality. For example, Hyun *et al*[24] reported that intratumoral heterogeneity measured by positron emission tomography textural features in pancreatic cancer patients predicted 2-year OS with an area under the curve of up to 0.72 using entropy features. Although studies evaluating the relationship between tumor heterogeneity and prognosis in pancreatic cancer are limited, tumor heterogeneity in other types of cancer has been shown to increase the risk of tumor recurrence, metastasis, resistance to treatment, and death[25,26]. Our 3D texture analysis extracted values of kurtosis and entropy. However, these values did not correlate with OS, and this might be because of the differences in features extracted between 3D and 2D analyses.

Although our study and other studies assessing pancreatic and colorectal cancers[27-29] have shown that higher entropy correlates with better prognosis, several others have shown that higher entropy correlates with worse prognosis in various cancers. This variability in the current literature suggests that entropy should not be used to predict prognosis in pancreatic cancer without further exploration. In our study, 2D analysis showed that higher entropy correlated with better PFS and less residual tumor following treatment. Sandrasegaran *et al*[29] reported similar findings; they observed better median OS times in patients with tumors with high entropy. However, this did not reach statistical significance. Cassinotto *et al*[14] showed that higher entropy correlated with less perineural invasion in pancreatic cancer, with an odds ratio of 0.018, which can help explain the positive prognostic implications of high entropy.

Although entropy reflects tumor heterogeneity similarly to skewness and kurtosis, entropy correlated differently with OS and PFS in our study; higher entropy was correlated with better prognosis. Other studies have shown that high entropy is associated with prognosis, poor treatment response, and aggressiveness in colorectal, pulmonary, and central nervous system tumors[27,30-32]. Several factors might explain these results. Unlike skewness and kurtosis, entropy analyzes randomness in the gray levels rather than in the distribution of gray levels in a region of interest[33]. Furthermore, tumor biology differs substantially among different organs, so what holds true in other organs may not be the same for the pancreas.

Additionally, entropy is prone to alterations in processing and image acquisition because entropy is area-dependent, whereby any region of interest covering less than 200 pixels can lead to the inaccurate estimation of entropy's relationship with any variable[34,35]. TexRad estimates entropy based on Shannon's model, the most straightforward and earliest model for estimating entropy. Still, TexRad might overestimate entropy by assuming that the pixels within a region of interest have an identical distribution and are entirely independent of neighboring pixels[34,36]. Given the insufficient data about the prognostic implications of entropy for pancreatic cancers, further studies are required to accurately assess the prognostic impact of entropy.

Our study has several strengths. Because all images were obtained on the same scanner, any heterogeneity in the results that may arise from using different scanners has been ruled out. Additionally, most studies using radiomics to evaluate response to treatment usually use delta radiomics to compare pretreatment and post-treatment scans. For example, Nasief *et al*[37] demonstrated that delta-radiomic features obtained during treatment periods could distinguish poor responders from good responders with an area under the curve of 0.94. Our pretreatment findings allow identifying patients who are more likely to respond before any treatment using baseline imaging, allowing for treatment selection that minimizes morbidity and thus limits expenses. This contrasts delta radiomics, which evaluates response after treatment has begun. Another strength of our study is comparing 2D and 3D analysis using TexRad and MIM software, respectively. It is well known that radiomics depend on how they are processed, and the software used[38,39]. However, our comparison showed that tumor density (mean HU) is a consistent and valid predictor of OS and PFS, irrespective of the type of analysis used.

Our study has some limitations. Our sample size was small, and it was a retrospective study. Therefore, more extensive prospective studies are needed to validate our findings. Additionally, CT acquisition factors might affect texture analysis variables; however, the effect is minimal. Lastly, our results were not externally validated and can only be directly applied to clinical practice with further validation.

CONCLUSION

In conclusion, tumor density (mean HU) was the only variable in our study that could reliably predict OS and PFS, irrespective of the type of analysis used. This variable may be used as a prognostic indicator to differentiate high-risk patients from low-risk patients and could be used for treatment planning. However, prospective studies will be beneficial to validate our findings externally.

ARTICLE HIGHLIGHTS

Research background

Radiomics can determine prognostic factors of several types of tumors.

Research motivation
Lack of evidence supporting radiomic studies on pancreatic cancer.

Research objectives
Compare two different radiomic softwares in assessing survival outcomes in pancreatic cancer patients.

Research methods
Retrospective review of pretreatment dual energy computed tomography (CT) images of 48 patients with biopsy confirmed lesions. Tumors were segmented using TexRad [2-dimensional (2D)] analysis software and MIM (3D) analysis software and radiomic features were extracted to compare with overall surgical (OS) and progression free survival (PFS).

Research results
3D analysis demonstrates that higher mean tumor density and median tumor density correlated with better OS, while 2D analysis showed that higher mean tumor density and mean positive pixels correlated with better OS. 2D analysis also showed higher skewness and kurtosis correlated with worse OS. Higher entropy correlated with better PFS. Patients with increased tumor size greater than 1.35 cm were likely to have a higher percentage of residual tumor above 10%.

Research conclusions
Radiomic features can serve as prognosis tools for pancreatic cancer and determine OS.

Research perspectives
This study serves as a guide for future research that can be verified through a prospective approach, while also contributing to possible alternatives to determine prognosis in patients using radiomic features.

ACKNOWLEDGEMENTS

We thank Erica Goodoff, Senior Scientific Editor in the Research Medical Library at The University of Texas MD Anderson Cancer Center, for editing this article.

FOOTNOTES

Author contributions: Saleh M, Virarkar M, Mahmoud HS, Wong VK, Gonzalez Baerga CI, Parikh M, Elsherif SB, and Bhosale PR have equally contributed to this paper with conception and design of the study, literature review and analysis, drafting and critical revision and editing, and final approval of the final version.

Institutional review board statement: The study was reviewed and approved by the University of Texas MD Anderson Cancer Center Institutional Review Board (approval No. 4 IRB00005015).

Informed consent statement: The informed consent was waived by the University of Texas MD Anderson Cancer Center Institutional Review Board.

Conflict-of-interest statement: All the authors report no relevant conflicts of interest for this article.

Data sharing statement: No additional data are available.

Open-Access: This article is an open-access article that was selected by an in-house editor and fully peer-reviewed by external reviewers. It is distributed in accordance with the Creative Commons Attribution NonCommercial (CC BY-NC 4.0) license, which permits others to distribute, remix, adapt, build upon this work non-commercially, and license their derivative works on different terms, provided the original work is properly cited and the use is non-commercial. See: https://creativecommons.org/Licenses/by-nc/4.0/

Country/Territory of origin: United States

ORCID number: Mayur Virarkar 0000-0002-5825-3102; Carlos Ignacio Gonzalez Baerga 0009-0008-9487-8303; Priya R Bhosale 0000-0003-4014-4941.

S-Editor: Wang JJ
L-Editor: A
P-Editor: Wang JJ

REFERENCES

1 **Siegel RL**, Miller KD, Jemal A. Cancer statistics, 2019. *CA Cancer J Clin* 2019; **69**: 7-34 [PMID: 30620402 DOI: 10.3322/caac.21551]

2 **Malla M**, Fekrmandi F, Malik N, Hatoum H, George S, Goldberg RM, Mukherjee S. The evolving role of radiation in pancreatic cancer. *Front Oncol* 2022; **12**: 1060885 [PMID: 36713520 DOI: 10.3389/fonc.2022.1060885]

3 **Krishnan S**, Chadha AS, Suh Y, Chen HC, Rao A, Das P, Minsky BD, Mahmood U, Delclos ME, Sawakuchi GO, Beddar S, Katz MH, Fleming JB, Javle MM, Varadhachary GR, Wolff RA, Crane CH. Focal Radiation Therapy Dose Escalation Improves Overall Survival in Locally Advanced Pancreatic Cancer Patients Receiving Induction Chemotherapy and Consolidative Chemoradiation. *Int J Radiat Oncol Biol Phys* 2016; **94**: 755-765 [PMID: 26972648 DOI: 10.1016/j.ijrobp.2015.12.003]

4 **Griffin JF**, Smalley SR, Jewell W, Paradelo JC, Reymond RD, Hassanein RE, Evans RG. Patterns of failure after curative resection of pancreatic carcinoma. *Cancer* 1990; **66**: 56-61 [PMID: 2354408 DOI: 10.1002/1097-0142(19900701)66:1<56::aid-cncr2820660112>3.0.co;2-6]

5 **Brody JR**, Costantino CL, Potoczek M, Cozzitorto J, McCue P, Yeo CJ, Hruban RH, Witkiewicz AK. Adenosquamous carcinoma of the pancreas harbors KRAS2, DPC4 and TP53 molecular alterations similar to pancreatic ductal adenocarcinoma. *Mod Pathol* 2009; **22**: 651-659 [PMID: 19270646 DOI: 10.1038/modpathol.2009.15]

6 **Dell'Aquila E**, Fulgenzi CAM, Minelli A, Citarella F, Stellato M, Pantano F, Russano M, Cursano MC, Napolitano A, Zeppola T, Vincenzi B, Tonini G, Santini D. Prognostic and predictive factors in pancreatic cancer. *Oncotarget* 2020; **11**: 924-941 [PMID: 32206189 DOI: 10.18632/oncotarget.27518]

7 **Hosny A**, Parmar C, Coroller TP, Grossmann P, Zeleznik R, Kumar A, Bussink J, Gillies RJ, Mak RH, Aerts HJWL. Deep learning for lung cancer prognostication: A retrospective multi-cohort radiomics study. *PLoS Med* 2018; **15**: e1002711 [PMID: 30500819 DOI: 10.1371/journal.pmed.1002711]

8 **Wu S**, Zheng J, Li Y, Yu H, Shi S, Xie W, Liu H, Su Y, Huang J, Lin T. A Radiomics Nomogram for the Preoperative Prediction of Lymph Node Metastasis in Bladder Cancer. *Clin Cancer Res* 2017; **23**: 6904-6911 [PMID: 28874414 DOI: 10.1158/1078-0432.CCR-17-1510]

9 **Horvat N**, Veeraraghavan H, Khan M, Blazic I, Zheng J, Capanu M, Sala E, Garcia-Aguilar J, Gollub MJ, Petkovska I. MR Imaging of Rectal Cancer: Radiomics Analysis to Assess Treatment Response after Neoadjuvant Therapy. *Radiology* 2018; **287**: 833-843 [PMID: 29514017 DOI: 10.1148/radiol.2018172300]

10 **Tang TY**, Li X, Zhang Q, Guo CX, Zhang XZ, Lao MY, Shen YN, Xiao WB, Ying SH, Sun K, Yu RS, Gao SL, Que RS, Chen W, Huang DB, Pang PP, Bai XL, Liang TB. Development of a Novel Multiparametric MRI Radiomic Nomogram for Preoperative Evaluation of Early Recurrence in Resectable Pancreatic Cancer. *J Magn Reson Imaging* 2020; **52**: 231-245 [PMID: 31867839 DOI: 10.1002/jmri.27024]

11 **Nasief H**, Zheng C, Schott D, Hall W, Tsai S, Erickson B, Allen Li X. A machine learning based delta-radiomics process for early prediction of treatment response of pancreatic cancer. *NPJ Precis Oncol* 2019; **3**: 25 [PMID: 31602401 DOI: 10.1038/s41698-019-0096-z]

12 **Zhang Y**, Lobo-Mueller EM, Karanicolas P, Gallinger S, Haider MA, Khalvati F. Prognostic Value of Transfer Learning Based Features in Resectable Pancreatic Ductal Adenocarcinoma. *Front Artif Intell* 2020; **3**: 550890 [PMID: 33733206 DOI: 10.3389/frai.2020.550890]

13 **Chakraborty J**, Midya A, Gazit L, Attiyeh M, Langdon-Embry L, Allen PJ, Do RKG, Simpson AL. CT radiomics to predict high-risk intraductal papillary mucinous neoplasms of the pancreas. *Med Phys* 2018; **45**: 5019-5029 [PMID: 30176047 DOI: 10.1002/mp.13159]

14 **Cassinotto C**, Chong J, Zogopoulos G, Reinhold C, Chiche L, Lafourcade JP, Cuggia A, Terrebonne E, Dohan A, Gallix B. Resectable pancreatic adenocarcinoma: Role of CT quantitative imaging biomarkers for predicting pathology and patient outcomes. *Eur J Radiol* 2017; **90**: 152-158 [PMID: 28583627 DOI: 10.1016/j.ejrad.2017.02.033]

15 **Fukukura Y**, Takumi K, Higashi M, Shinchi H, Kamimura K, Yoneyama T, Tateyama A. Contrast-enhanced CT and diffusion-weighted MR imaging: performance as a prognostic factor in patients with pancreatic ductal adenocarcinoma. *Eur J Radiol* 2014; **83**: 612-619 [PMID: 24418286 DOI: 10.1016/j.ejrad.2013.12.016]

16 **Zhu L**, Shi X, Xue H, Wu H, Chen G, Sun H, He Y, Jin Z, Liang Z, Zhang Z. CT Imaging Biomarkers Predict Clinical Outcomes After Pancreatic Cancer Surgery. *Medicine (Baltimore)* 2016; **95**: e2664 [PMID: 26844495 DOI: 10.1097/MD.0000000000002664]

17 **Kong B**, Cheng T, Wu W, Regel I, Raulefs S, Friess H, Erkan M, Esposito I, Kleeff J, Michalski CW. Hypoxia-induced endoplasmic reticulum stress characterizes a necrotic phenotype of pancreatic cancer. *Oncotarget* 2015; **6**: 32154-32160 [PMID: 26452217 DOI: 10.18632/oncotarget.5168]

18 **Hattori Y**, Gabata T, Zen Y, Mochizuki K, Kitagawa H, Matsui O. Poorly enhanced areas of pancreatic adenocarcinomas on late-phase dynamic computed tomography: comparison with pathological findings. *Pancreas* 2010; **39**: 1263-1270 [PMID: 20467344 DOI: 10.1097/MPA.0b013e3181dbc583]

19 **White RR**, Xie HB, Gottfried MR, Czito BG, Hurwitz HI, Morse MA, Blobe GC, Paulson EK, Baillie J, Branch MS, Jowell PS, Clary BM, Pappas TN, Tyler DS. Significance of histological response to preoperative chemoradiotherapy for pancreatic cancer. *Ann Surg Oncol* 2005; **12**: 214-221 [PMID: 15827813 DOI: 10.1245/ASO.2005.03.105]

20 **Chatterjee D**, Katz MH, Rashid A, Varadhachary GR, Wolff RA, Wang H, Lee JE, Pisters PW, Vauthey JN, Crane C, Gomez HF, Abbruzzese JL, Fleming JB. Histologic grading of the extent of residual carcinoma following neoadjuvant chemoradiation in pancreatic ductal adenocarcinoma: a predictor for patient outcome. *Cancer* 2012; **118**: 3182-3190 [PMID: 22028089 DOI: 10.1002/cncr.26651]

21 **Okubo S**, Kojima M, Matsuda Y, Hioki M, Shimizu Y, Toyama H, Morinaga S, Gotohda N, Uesaka K, Ishii G, Mino-Kenudson M, Takahashi S. Area of residual tumor (ART) can predict prognosis after post neoadjuvant therapy resection for pancreatic ductal adenocarcinoma. *Sci Rep* 2019; **9**: 17145 [PMID: 31748528 DOI: 10.1038/s41598-019-53801-2]

22 **Attiyeh MA**, Chakraborty J, Doussot A, Langdon-Embry L, Mainarich S, Gönen M, Balachandran VP, D'Angelica MI, DeMatteo RP, Jarnagin WR, Kingham TP, Allen PJ, Simpson AL, Do RK. Survival Prediction in Pancreatic Ductal Adenocarcinoma by Quantitative Computed Tomography Image Analysis. *Ann Surg Oncol* 2018; **25**: 1034-1042 [PMID: 29380093 DOI: 10.1245/s10434-017-6323-3]

23 **Cozzi L**, Comito T, Fogliata A, Franzese C, Franceschini D, Bonifacio C, Tozzi A, Di Brina L, Clerici E, Tomatis S, Reggiori G, Lobefalo F, Stravato A, Mancosu P, Zerbi A, Sollini M, Kirienko M, Chiti A, Scorsetti M. Computed tomography based radiomic signature as predictive of survival and local control after stereotactic body radiation therapy in pancreatic carcinoma. *PLoS One* 2019; **14**: e0210758 [PMID: 30657785 DOI: 10.1371/journal.pone.0210758]

24 **Hyun SH**, Kim HS, Choi SH, Choi DW, Lee JK, Lee KH, Park JO, Kim BT, Choi JY. Intratumoral heterogeneity of (18)F-FDG uptake predicts survival in patients with pancreatic ductal adenocarcinoma. *Eur J Nucl Med Mol Imaging* 2016; **43**: 1461-1468 [PMID: 26872788 DOI: 10.1007/s00259-016-3316-6]

25 **Verbeke C**. Morphological heterogeneity in ductal adenocarcinoma of the pancreas - Does it matter? *Pancreatology* 2016; **16**: 295-301 [PMID:

26924665 DOI: 10.1016/j.pan.2016.02.004]

26 **Bandyopadhyay S**, Basturk O, Coban I, Thirabanjasak D, Liang H, Altinel D, Adsay NV. Isolated solitary ducts (naked ducts) in adipose tissue: a specific but underappreciated finding of pancreatic adenocarcinoma and one of the potential reasons of understaging and high recurrence rate. *Am J Surg Pathol* 2009; **33**: 425-429 [PMID: 19092633 DOI: 10.1097/PAS.0b013e3181908e42]

27 **Ng F**, Ganeshan B, Kozarski R, Miles KA, Goh V. Assessment of primary colorectal cancer heterogeneity by using whole-tumor texture analysis: contrast-enhanced CT texture as a biomarker of 5-year survival. *Radiology* 2013; **266**: 177-184 [PMID: 23151829 DOI: 10.1148/radiol.12120254]

28 **Lubner MG**, Stabo N, Lubner SJ, del Rio AM, Song C, Halberg RB, Pickhardt PJ. CT textural analysis of hepatic metastatic colorectal cancer: pre-treatment tumor heterogeneity correlates with pathology and clinical outcomes. *Abdom Imaging* 2015; **40**: 2331-2337 [PMID: 25968046 DOI: 10.1007/s00261-015-0438-4]

29 **Sandrasegaran K**, Lin Y, Asare-Sawiri M, Taiyini T, Tann M. CT texture analysis of pancreatic cancer. *Eur Radiol* 2019; **29**: 1067-1073 [PMID: 30116961 DOI: 10.1007/s00330-018-5662-1]

30 **Chee CG**, Kim YH, Lee KH, Lee YJ, Park JH, Lee HS, Ahn S, Kim B. CT texture analysis in patients with locally advanced rectal cancer treated with neoadjuvant chemoradiotherapy: A potential imaging biomarker for treatment response and prognosis. *PLoS One* 2017; **12**: e0182883 [PMID: 28797063 DOI: 10.1371/journal.pone.0182883]

31 **Zhao Q**, Shi CZ, Luo LP. Role of the texture features of images in the diagnosis of solitary pulmonary nodules in different sizes. *Chin J Cancer Res* 2014; **26**: 451-458 [PMID: 25232219 DOI: 10.3978/j.issn.1000-9604.2014.08.07]

32 **Ryu YJ**, Choi SH, Park SJ, Yun TJ, Kim JH, Sohn CH. Glioma: application of whole-tumor texture analysis of diffusion-weighted imaging for the evaluation of tumor heterogeneity. *PLoS One* 2014; **9**: e108335 [PMID: 25268588 DOI: 10.1371/journal.pone.0108335]

33 **Guan Y**, Li W, Jiang Z, Chen Y, Liu S, He J, Zhou Z, Ge Y. Whole-Lesion Apparent Diffusion Coefficient-Based Entropy-Related Parameters for Characterizing Cervical Cancers: Initial Findings. *Acad Radiol* 2016; **23**: 1559-1567 [PMID: 27665235 DOI: 10.1016/j.acra.2016.08.010]

34 **Dercle L**, Ammari S, Bateson M, Durand PB, Haspinger E, Massard C, Jaudet C, Varga A, Deutsch E, Soria JC, Ferté C. Limits of radiomic-based entropy as a surrogate of tumor heterogeneity: ROI-area, acquisition protocol and tissue site exert substantial influence. *Sci Rep* 2017; **7**: 7952 [PMID: 28801575 DOI: 10.1038/s41598-017-08310-5]

35 **Shannon CE**. A Mathematical Theory of Communication. New York: Nokia Bell Labs, 1948; 27: 379-423

36 **Razlighi QR**, Kehtarnavaz N, Nosratinia A. Computation of image spatial entropy using quadrilateral Markov random field. *IEEE Trans Image Process* 2009; **18**: 2629-2639 [PMID: 19674952 DOI: 10.1109/TIP.2009.2029988]

37 **Nasief H**, Hall W, Zheng C, Tsai S, Wang L, Erickson B, Li XA. Improving Treatment Response Prediction for Chemoradiation Therapy of Pancreatic Cancer Using a Combination of Delta-Radiomics and the Clinical Biomarker CA19-9. *Front Oncol* 2019; **9**: 1464 [PMID: 31970088 DOI: 10.3389/fonc.2019.01464]

38 **Defeudis A**, De Mattia C, Rizzetto F, Calderoni F, Mazzetti S, Torresin A, Vanzulli A, Regge D, Giannini V. Standardization of CT radiomics features for multi-center analysis: impact of software settings and parameters. *Phys Med Biol* 2020; **65**: 195012 [PMID: 32575082 DOI: 10.1088/1361-6560/ab9f61]

39 **Foy JJ**, Robinson KR, Li H, Giger ML, Al-Hallaq H, Armato SG 3rd. Variation in algorithm implementation across radiomics software. *J Med Imaging (Bellingham)* 2018; **5**: 044505 [PMID: 30840747 DOI: 10.1117/1.JMI.5.4.044505]

World Journal of Radiology

Submit a Manuscript: https://www.f6publishing.com

World J Radiol 2023 November 28; 15(11): 315-323

DOI: 10.4329/wjr.v15.i11.315

ISSN 1949-8470 (online)

ORIGINAL ARTICLE

Basic Study

Imaging assessment of photosensitizer emission induced by radionuclide-derived Cherenkov radiation using charge-coupled device optical imaging and long-pass filters

Winn Aung, Atsushi B Tsuji, Kazuaki Rikiyama, Fumihiko Nishikido, Satoshi Obara, Tatsuya Higashi

Specialty type: Radiology, nuclear medicine and medical imaging

Provenance and peer review: Unsolicited article; Externally peer reviewed.

Peer-review model: Single blind

Peer-review report's scientific quality classification

Grade A (Excellent): 0
Grade B (Very good): B
Grade C (Good): 0
Grade D (Fair): 0
Grade E (Poor): 0

P-Reviewer: Zhou J, China

Received: October 3, 2023
Peer-review started: October 3, 2023
First decision: October 17, 2023
Revised: October 26, 2023
Accepted: November 17, 2023
Article in press: November 17, 2023
Published online: November 28, 2023

Winn Aung, Atsushi B Tsuji, Kazuaki Rikiyama, Satoshi Obara, Tatsuya Higashi, Department of Molecular Imaging and Theranostics, Institute for Quantum Medical Science, National Institutes for Quantum Science and Technology, Chiba 263-8555, Japan

Fumihiko Nishikido, Department of Advanced Nuclear Medicine Sciences, Institute for Quantum Medical Science, National Institutes for Quantum Science and Technology, Chiba 263-8555, Japan

Corresponding author: Winn Aung, MBBS, PhD, Senior Researcher, Department of Molecular Imaging and Theranostics, Institute for Quantum Medical Science, National Institutes for Quantum Science and Technology, 4-9-1 Anagawa, Inage-ku, Chiba 263-8555, Japan.
winn.aung@qst.go.jp

Abstract

BACKGROUND

Radionuclides produce Cherenkov radiation (CR), which can potentially activate photosensitizers (PSs) in phototherapy. Several groups have studied Cherenkov energy transfer to PSs using optical imaging; however, cost-effectively identifying whether PSs are excited by radionuclide-derived CR and detecting fluorescence emission from excited PSs remain a challenge. Many laboratories face the need for expensive dedicated equipment.

AIM

To cost-effectively confirm whether PSs are excited by radionuclide-derived CR and distinguish fluorescence emission from excited PSs.

METHODS

The absorbance and fluorescence spectra of PSs were measured using a micro-plate reader and fluorescence spectrometer to examine the photo-physical properties of PSs. To mitigate the need for expensive dedicated equipment and achieve the aim of the study, we developed a method that utilizes a charge-coupled device optical imaging system and appropriate long-pass filters of different wavelengths (manual sequential application of long-pass filters of 515, 580, 645, 700, 750, and 800 nm). Tetrakis (4-carboxyphenyl) porphyrin (TCPP) was utilized as a model PS. Different doses of copper-64 ($^{64}CuCl_2$) (4, 2, and 1 mCi) were used as CR-producing radionuclides. Imaging and data acquisition were

performed 0.5 h after sample preparation. Differential image analysis was conducted by using ImageJ software (National Institutes of Health) to visually evaluate TCPP fluorescence.

RESULTS

The maximum absorbance of TCPP was at 390–430 nm, and the emission peak was at 670 nm. The CR and CR-induced TCPP emissions were observed using the optical imaging system and the high-transmittance long-pass filters described above. The emission spectra of TCPP with a peak in the 645–700 nm window were obtained by calculation and subtraction based on the serial signal intensity (total flux) difference between $^{64}CuCl_2$ + TCPP and $^{64}CuCl_2$. Moreover, the differential fluorescence images of TCPP were obtained by subtracting the $^{64}CuCl_2$ image from the $^{64}CuCl_2$ + TCPP image. The experimental results considering different $^{64}CuCl_2$ doses showed a dose-dependent trend. These results demonstrate that a bioluminescence imaging device coupled with different long-pass filters and subtraction image processing can confirm the emission spectra and differential fluorescence images of CR-induced TCPP.

CONCLUSION

This simple method identifies the PS fluorescence emission generated by radionuclide-derived CR and can contribute to accelerating the development of Cherenkov energy transfer imaging and the discovery of new PSs.

Key Words: Tetrakis (4-carboxyphenyl) porphyrin; Photosensitizer emission; Radionuclide; Cherenkov radiation; Optical imaging; Long-pass filters

©The Author(s) 2023. Published by Baishideng Publishing Group Inc. All rights reserved.

Core Tip: Radionuclides produce Cherenkov radiation (CR), which can potentially activate photosensitizers (PSs) in phototherapy. However, a cost-effective method to determine whether radionuclide-derived CR excites PSs and the measurement of fluorescence emitted by excited PS remain elusive. We propose a cost-effective method using a charge-coupled device optical imaging system combined with long-pass filters and subtraction image processing to distinguish CR and PS fluorescence emission. As a proof-of-concept, $^{64}CuCl_2$ and the PS tetrakis (4-carboxyphenyl) porphyrin were used in the experiments. This method can contribute to accelerating the development of Cherenkov energy transfer imaging and the discovery of new PSs.

Citation: Aung W, Tsuji AB, Rikiyama K, Nishikido F, Obara S, Higashi T. Imaging assessment of photosensitizer emission induced by radionuclide-derived Cherenkov radiation using charge-coupled device optical imaging and long-pass filters. *World J Radiol* 2023; 15(11): 315-323

URL: https://www.wjgnet.com/1949-8470/full/v15/i11/315.htm

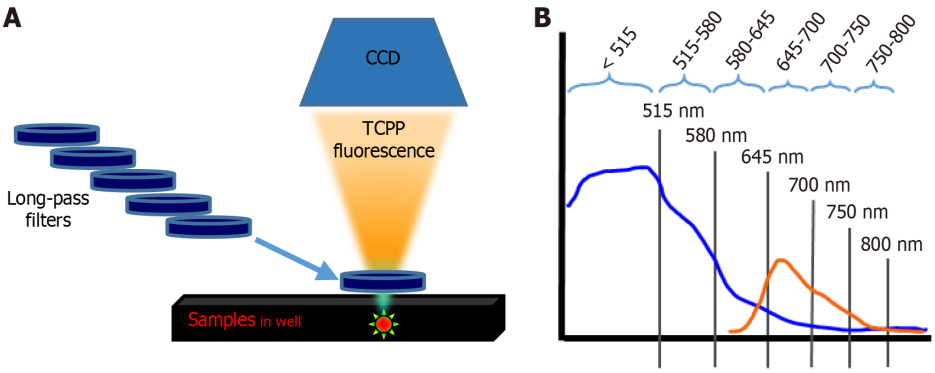
DOI: https://dx.doi.org/10.4329/wjr.v15.i11.315

INTRODUCTION

Cherenkov radiation (CR) is the emission of photons when a charged particle moves faster than the speed of light in a medium[1]. Various radionuclides produce Cherenkov optical emission[2], which can potentially activate photosensitizers (PSs). This comprehensive phenomenon is interesting for various applications, including phototherapy, because it overcomes the limitations of light penetration[3,4]. Various researchers have been investigating CR-induced photodynamic therapy using certain radioisotopes[5-8]. Unfortunately, the availability of suitable PSs is currently limited and more effective PSs are needed.

Recently, photons from CR emitted from common radioisotopes have been detected using a highly sensitive charge-coupled device (CCD) optical imaging system[9,10]. However, when the radionuclide and PS coexist, the broad and continuous spectrum of the Cherenkov optical emission overlaps with the PS emission spectrum, obscuring the latter. Confirming whether the CR excites the PS is challenging because the required dedicated optical imaging devices (with built-in filters) are expensive. A method for distinguishing the Cherenkov optical emission from the PS fluorescence without expensive, dedicated instruments would benefit laboratories.

We evaluate whether an optical imaging system based on a CCD camera and different long-pass filters (Figure 1) can effectively detect and separate the radionuclide-derived CR emission from the CR-induced PS fluorescence spectrum. We used commercially available tetrakis (4-carboxyphenyl) porphyrin (TCPP) as a model PS, which can be conjugated to nanomaterials and applied to antimicrobial and anticancer phototherapies[11,12]. Among the various types of PSs, porphyrin-based PSs are commonly used for phototherapy[13]. The beta-emitting isotope Copper-64 ($^{64}CuCl_2$; $T_{1/2}$ = 12.7 h; β^+, 0.653 MeV; β^-, 0.579 MeV) was employed as a CR-producing radionuclide. This is a simple and cost-effective method to determine whether the fluorescence emitted from the PS is effectively the result of excitation by CR from a radionuclide.



DOI: 10.4329/wjr.v15.i11.315 **Copyright** ©The Author(s) 2023.

Figure 1 Schematic diagram of the optical imaging approach used to detect Cherenkov optical emission and to separate the fluorescence emission of tetrakis (4-carboxyphenyl) porphyrin induced by Cherenkov optical emission. A: Long-pass filters step-cut the Cherenkov light, allowing the separation of tetrakis (4-carboxyphenyl) porphyrin (TCPP) emission; B: The Cherenkov light emitted from the radionuclide was gradually cut off with the appropriate long-pass filters of different wavelengths. The blue and orange curves are schematic representations of the Cherenkov optical emission and TCPP fluorescence spectra, respectively. CCD: Charge-coupled device optical imaging system.

MATERIALS AND METHODS

Materials

TCPP (molecular weight: 790.79) was purchased from Tokyo Chemical Industry Co., Ltd. (TCI, Tokyo, Japan). The chemical structure of TCPP is shown in Figure 2A. Phosphate Buffer (PB) was purchased from Wako Pure Chemical Co. (WAKO, Osaka, Japan). The beta-emitting isotope $^{64}CuCl_2$ was synthesized and provided by the Institute's Department of Advanced Nuclear Medicine Sciences (Chiba, Japan).

Examination of photo-physical properties of TCPP

Aqueous solutions of 0.1 mol/L TCPP were prepared by dissolving TCPP powder in PB (pH 7.4). The TCPP sample (100 μmol/L) was transferred to a 96-well plate. A SpectraMax M5 microplate reader (Molecular Devices, LLC, San Jose, CA, United States) with an operating range of 300–850 nm in 10 nm increments was used to record the absorbance spectrum of the sample. The three-dimensional fluorescence spectrum of TCPP was acquired using a JASCO FP-6600 fluorescence spectrometer (JASCO, Tokyo, Japan) equipped with a xenon lamp. The fluorescence emission intensity (FI) was measured at excitation wavelengths ranging from 350 nm to 600 nm in 5 nm increments. The emission wavelengths were measured in the 350–850 nm range in 2 nm increments. These measurements enabled the maximum excitation and emission wavelengths of TCPP to be determined.

Measurement of the concentration-dependent TCPP fluorescence intensity

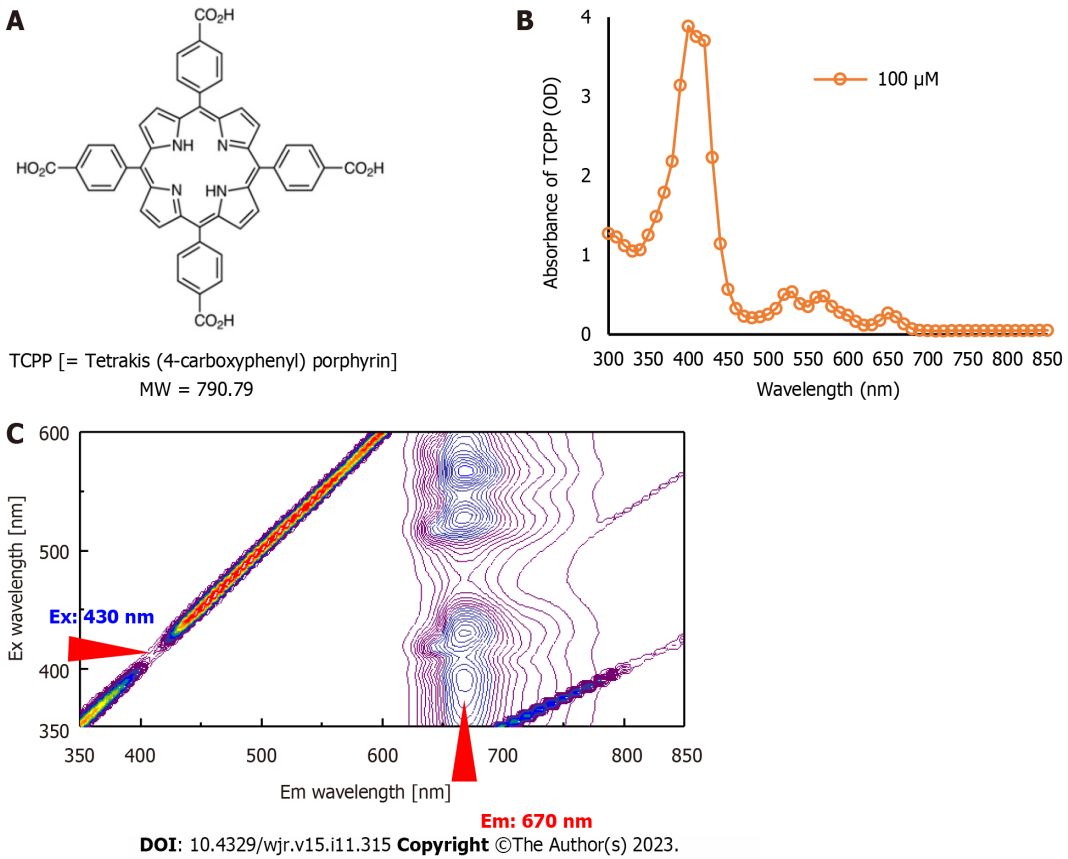
The concentration-dependent FI of TCPP was measured using an Infinite 200 PRO multimode microplate reader (Tecan Japan Co., Ltd., Kawasaki, Japan) by setting the excitation wavelength to 430 nm, emission wavelength to 670 nm, gain to 79, and by integrating for 20 μs. A series of different TCPP concentrations (5, 10, 15, 20, 25, 30, 35, 40, 45, 50, 55, 60, 65, 70, 75, and 80 μmol/L) in PB were used for FI measurements. For spectral analysis, low TCPP concentrations (5, 10, 15, 20, 25, and 30 μmol/L) were measured using a multimode microplate reader (Tecan) operating in the emission wavelength range of 500–850 nm in 2 nm increments. The acquired FI was plotted against the wavelength.

Imaging with the VISQUE fluorescence imaging device

To visualize the LED-induced fluorescence emission from TCPP, TCPP solutions (1 mmol/L and 100 μmol/L) were added to a Nunc™ Flat-Bottom Microplate (96-well, Black) (Thermo Fisher Scientific, Roskilde, Denmark) and imaged with the VISQUE InVivo Smart fluorescence imaging and analysis system (Vieworks Co., Ltd, Gyeonggi, Korea) using the following specific excitation and emission filter combinations: Blue light (390–490 nm) excitation and red light (690–740 nm) emission. Constant parameters (exposure time: 500 ms; binning: 1 × 1; light intensity: Middle; mode: Low gain) were set and used for imaging.

Detection of radionuclide-derived CR and TCPP emission induced by CR with IVIS optical imaging system

The TCPP (30 μmol/L) and radionuclide $^{64}CuCl_2$ (4 mCi) were prepared in a 96-well black microplate (Thermo Fisher Scientific). At 0.5 h after preparing the samples, the CR emitted from the radionuclide was visualized using a sensitive CCD camera equipped with an IVIS Lumina optical imaging system (PerkinElmer, Waltham, MA, United States). The luminescent imaging mode with fixed acquisition parameters [emission filter: Open; excitation filter: Block; exposure time: 2 min; binning: 4 × 4; F/Stop (f): 1; field of view (FOV): 5 cm] was used in all experiments. Images of the wells containing the samples were acquired first. The optical signal intensity [total flux (photon/s)] was measured in the regions of interests (ROIs) corresponding to the sample-containing wells, and one empty well was used for background subtraction. Moreover, several high-transmittance long-pass filters of different wavelengths (515, 580, 645, 700, 750, and



DOI: 10.4329/wjr.v15.i11.315 **Copyright** ©The Author(s) 2023.

Figure 2 Chemical structure and photo-physical properties of tetrakis (4-carboxyphenyl) porphyrin. A: Chemical structure of tetrakis (4-carboxyphenyl) porphyrin (TCPP); B: Absorption spectrum of TCPP (100 μmol/L) at 25°C in phosphate buffer; C: Three-dimensional fluorescence spectral analysis of TCPP. Fluorescence emission was observed around 670 nm with an excitation wavelength of 430 nm. Em: Emission wavelength; Ex: Excitation wavelength; MW: Molecular weight; μM: μmol/L.

800 nm) were used to separate the emission spectrum of TCPP and the Cherenkov light emitted by the radionuclide. A schematic of the experimental setup is shown in Figure 1. Each filter was manually placed on the wells, and images were acquired sequentially (Figure 1A). Image analysis was performed using Living Image 2.6 (PerkinElmer). First, the total flux of the wells containing samples was obtained by subtracting the total flux of the empty background. Subsequently, for each well, the total flux emitted within the window of the adjacent wavelengths of the two filters was calculated from the difference in the total flux measured with each respective filter (Figure 1B). For all pairs of wavelength windows, the total flux of $^{64}CuCl_2$ + TCPP and $^{64}CuCl_2$ was obtained by subtracting the total flux of the PB-filled wells. Second, the emission spectrum of TCPP was acquired by plotting the total flux difference between $^{64}CuCl_2$ + TCPP and $^{64}CuCl_2$ in the respective wavelength ranges. In addition, differential image analysis was performed to visually assess TCPP fluorescence by subtracting the $^{64}CuCl_2$ image from the $^{64}CuCl_2$ + TCPP image using ImageJ [https://imagej.nih.gov/ij/; National Institutes of Health (NIH), Bethesda, Maryland, United States][14]. The same experiment was also performed with 2 mCi and 1 mCi $^{64}CuCl_2$.

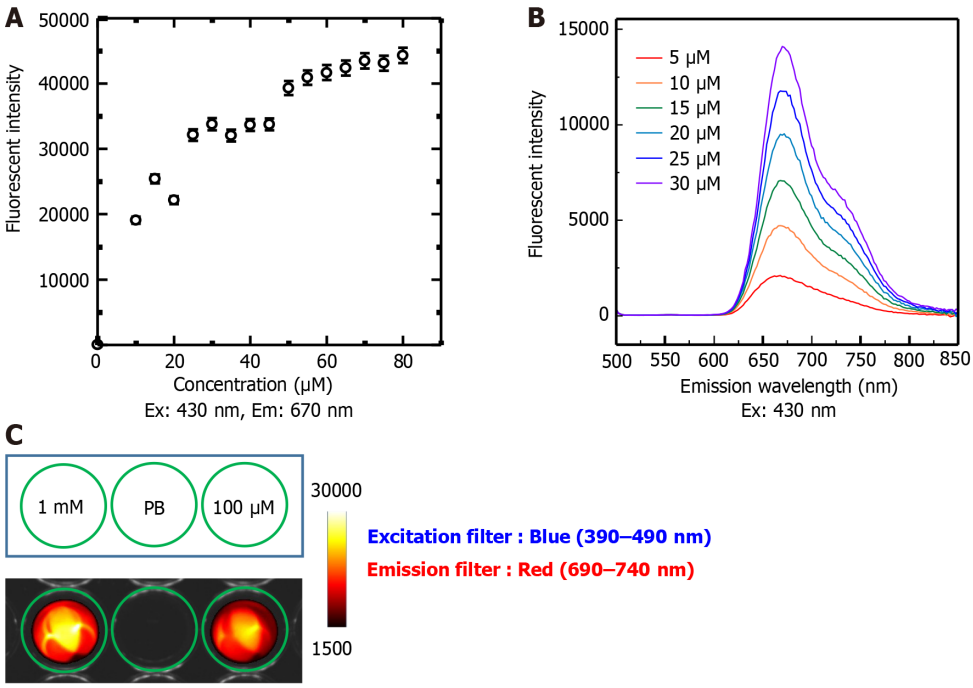
RESULTS

Absorbance and fluorescence spectra of TCPP

The peak of the TCPP absorbance spectrum was in the 390–430 nm range (Figure 2B). In the three-dimensional fluorescence spectral analysis, the peak emission of TCPP was approximately 670 nm with excitation wavelengths of 350–600 nm (Figure 2C). Among the excitation wavelengths, 430 nm was considered the peak excitation wavelength for TCPP because it induced the highest fluorescence emission from TCPP and approximately corresponded with the wavelength of the most intense CR peak.

Concentration-dependent TCPP fluorescence

The FI of TCPP (5–80 μmol/L) linearly correlated with concentrations up to approximately 30 μmol/L. Above 30 μmol/L, the FI slope decreased (Figure 3A). This is likely due to TCPP stacking in the samples. Therefore, only low TCPP concentrations (5–30 μmol/L) were used for fluorescence spectral analysis. We found that the 430 nm wavelength excited TCPP to fluoresce over a range of wavelengths (625–775 nm) with a peak at 670 nm (Figure 3B).



DOI: 10.4329/wjr.v15.i11.315 **Copyright** ©The Author(s) 2023.

Figure 3 Tetrakis (4-carboxyphenyl) porphyrin fluorescence emission. A: Fluorescence emission intensity of tetrakis (4-carboxyphenyl) porphyrin (TCPP) prepared at different concentrations (5, 10, 15, 20, 25, 30, 35, 40, 45, 50, 55, 60, 65, 70, 75, and 80 μmol/L in PB) measured by setting the excitation wavelength to 430 nm and emission wavelength to 670 nm. The relationship is linear up to approximately 30 μmol/L; B: The fluorescence spectra of low TCPP concentrations (5, 10, 15, 20, 25, and 30 μmol/L) were measured with the excitation wavelength set to 430 nm; C: Visualization of TCPP fluorescence emission using a light-emitting diode light source, blue light excitation filter (390–490 nm), and red light emission filter (690–740 nm). Em: Emission wavelength; Ex: Excitation wavelength; mM: mmol/L; PB: Phosphate buffer; μM: μmol/L.

Imaging of TCPP with VISQUE imaging device

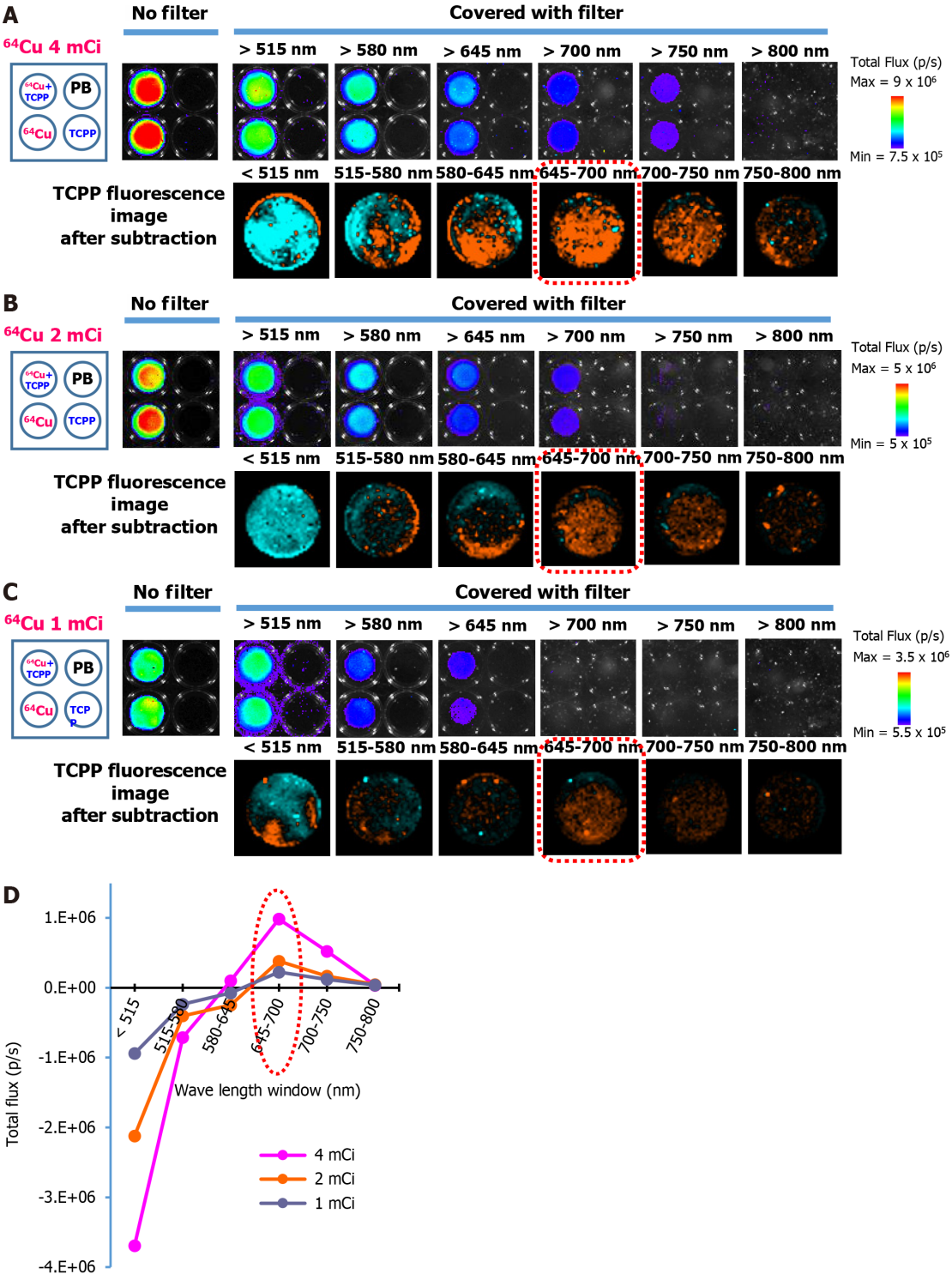
The inherent fluorescence characteristics of TCPP emission could be visualized and confirmed using a fluorescence imaging system with a light-emitting diode light source and a set of filters for blue light (390–490 nm) excitation and red light (690–740 nm) emission (Figure 3C). Both filters were compatible with the excitation/emission wavelengths of TCPP (430/670 nm).

Detection of CR and separation of CR-induced emission spectrum of TCPP

At 0.5 h after preparing the samples in the wells, images were acquired without a filter. Cherenkov luminescence from the radionuclide was detected in the two wells on the left containing $^{64}CuCl_2$ + TCPP and $^{64}CuCl_2$, respectively. In contrast, luminescence was not visualized in the two wells on the right containing either PB or TCPP (Figure 4A, upper row). The total flux produced from the light emission of the radionuclides decreased when the wells were covered with long-pass filters of different wavelengths. Serial application of long-pass filters of 515, 580, 645, 700, 750, and 800 nm resulted in a sequential decrease in total flux measured from the ROIs of wells with $^{64}CuCl_2$ only (Figure 4A, upper row, lower left well) and $^{64}CuCl_2$ + TCPP (Figure 4A, upper row, upper left well). The TCPP emission spectral band was separated using the following calculation. First, the total flux emitted from $^{64}CuCl_2$ + TCPP and $^{64}CuCl_2$ at two adjacent wavelengths was measured. Second, the optical signals for the serial pairs of the wavelength window were calculated based on the difference in the signals measured with each filter. Subsequently, the emission spectrum of TCPP was calculated by subtracting the total flux of $^{64}CuCl_2$ from that of $^{64}CuCl_2$ + TCPP. The resulting spectrum is shown in Figure 4. Using ImageJ software (NIH), differential image analysis was conducted by subtracting the $^{64}CuCl_2$ image from the $^{64}CuCl_2$ + TCPP image to visually evaluate TCPP fluorescence (Figure 4A, lower row). The spectral peaks with the maximum intensity were in the 645–700 nm window, marked by the red dotted rim in the lower row of Figure 4A and the line graph in Figure 4D. Similar results were obtained for the other two doses, 2 mCi (Figure 4B and D) and 1 mCi (Figure 4C and D). The total flux exhibited a dose-dependent tendency.

DISCUSSION

This study demonstrates that imaging with an optical imaging device coupled with different long-pass filters and subtraction image processing separates the spectra of CR and PS emissions, providing optical images of the emission from a PS at different wavelengths. Although distinguishing the Cherenkov light from the PS emission was difficult, the subtraction image processing effectively separated them. Thus, the combined use of a device set and image processing



DOI: 10.4329/wjr.v15.i11.315 **Copyright** ©The Author(s) 2023.

Figure 4 Detection of Cherenkov radiation and emission spectrum of tetrakis (4-carboxyphenyl) porphyrin induced by Cherenkov radiation. A: Bioluminescence imaging of prepared samples $^{64}CuCl_2$ (4 mCi) and $^{64}CuCl_2$ (4 mCi) + tetrakis (4-carboxyphenyl) porphyrin (TCPP) (30 μmol/L) with or without covering by long-pass filters (upper row), and TCPP fluorescence image after subtraction in differential image analysis (lower row); B: Similar images acquired from the experiment using $^{64}CuCl_2$ (2 mCi); C: Similar images acquired from the experiment using $^{64}CuCl_2$ (1 mCi); D: TCPP fluorescence spectrum calculated by subtracting the total flux of $^{64}CuCl_2$ from that of $^{64}CuCl_2$ + TCPP. The spectral peak was found in the 645–700 nm window. The peak is indicated by the red dotted circle. ^{64}Cu: $^{64}CuCl_2$; PB: Phosphate buffer; μM: μmol/L.

could be utilized in laboratories with optical imaging devices.

The three-dimensional fluorescence spectral analysis showed that TCPP was excited by light wavelengths from 350 nm to 600 nm, producing a large Stokes shift and an emission peak at approximately 670 nm. The CR spectrum was continuous, peaking at high frequencies (ultraviolet/blue)[15,16]. Therefore, the absorption profile of TCPP (390–430 nm) matched the Cherenkov emission profile.

A bioluminescence imaging device, an IVIS optical imaging system with six different long-pass filters, can provide various optical images of CR plus PS emission. Our lab has an IVIS imaging system and six long-pass filters that are not built into the device but used for other purposes. We manually placed each filter on the wells containing ^{64}Cu and PS and captured optical images (Figure 4A-C, upper rows). When the wells were covered with long-pass filters, the total flux derived from ^{64}Cu-containing wells decreased when the wavelength of the applied filters increased. This could occur because the wavelength of the filters exceeded the maximum emission peak of CR (350–500 nm) and cut off the Cherenkov light. Visually distinguishing the emission from $^{64}CuCl_2$ and $^{64}CuCl_2$ + TCPP is challenging, even though the TCPP emission spectrum can be calculated (Figure 4D). Thus, an additional process is required to visualize only the light emitted from the PS.

The PS emissions were distinguished from the CR emissions using image processing. The image data acquired by the IVIS system were processed using ImageJ, a simple and free software package provided by NIH, to obtain the differential image. The TCPP fluorescence image was easily generated by subtracting the $^{64}CuCl_2$ image from the $^{64}CuCl_2$ + TCPP image (Figure 4A-C, lower rows). These results displayed a dose-dependent trend. Moreover, both the TCPP fluorescence images (Figure 4A-C, lower rows) and spectra (Figure 4D) were consistent with the results obtained from the fluorescence spectral analysis of the TCPP (Figure 3B), showing a fluorescence peak at 645–700 nm.

Overall, the developed method could be used to compare different PSs and provide information to select the optimal PS. In addition, various laboratories with conventional optical imaging devices could easily apply this method when conducting studies. Some laboratories have appropriate long-pass filters, whereas others could obtain them inexpensively. The ImageJ software is available to all laboratories; however, only a few laboratories can currently screen for appropriate PSs for Cherenkov energy transfer imaging. The proposed method could enable more laboratories to perform these procedures, contributing to the accelerated development of Cherenkov energy transfer imaging for multiple applications. The main objective of this study was to demonstrate the feasibility of the proposed method as a proof of concept; however, the method would need to be more comprehensively tested to address possible limitations. First, the reproducibility would have to be determined and statistically assessed. Second, we evaluated only one PS, namely TCPP. Further studies would have to compare the results for different PSs. Third, we used only one radionuclide, $^{64}CuCl_2$. Other beta-emitting radioactive sources producing decay products with energies above the Cerenkov threshold (approximately 220 keV) could be employed in future studies[17]. The next step would therefore entail more detailed examinations.

CONCLUSION

A simple method using a CCD optical imaging system in combination with different high-transmission long-pass filters and subtraction image processing was capable of potentially evaluating whether PS candidates are reliably excited by radionuclide-derived CR to produce fluorescence emission. The widespread adoption of this method could be expected to contribute to the discovery of a range of new effective PSs.

ARTICLE HIGHLIGHTS

Research background

Cherenkov radiation (CR) is the emission of photons when a charged particle moves faster than the speed of light in a medium. Various radionuclides produce Cherenkov optical emission, which can potentially activate photosensitizers (PSs) in phototherapy.

Research motivation

Several researchers are investigating CR-induced photodynamic therapy using radioisotopes and Cherenkov energy transfer to PSs using optical imaging. However, the effective management of the process, particularly the cost-effective confirmation that a PS is excited by CR and identifying appropriate PSs, remains a challenge.

Research objectives

The purpose of this study is to propose a cost-effective method to determine whether the PS is excited by radionuclide-derived CR and to distinguish the fluorescence emission from PS excitation.

Research methods

Tetrakis (4-carboxyphenyl) porphyrin (TCPP) and Copper-64 ($^{64}CuCl_2$) were utilized as a model PS and a CR-producing radionuclide, respectively. The photo-physical properties (absorbance and fluorescence spectra) of TCPP were measured using a microplate reader and fluorescence spectrometer. Imaging and data acquisition were performed with a charge-coupled device optical imaging system and appropriate long-pass filters of different wavelengths. To visually evaluate the TCPP fluorescence, differential image analysis was conducted using ImageJ software (National Institutes of Health).

Research results

Optical imaging coupled with high-transmittance long-pass filters and subtraction image processing separated the

emission spectra of the radionuclide-derived CR and TCPP. The emission spectra of TCPP were obtained by calculation and subtraction based on the serial signal intensity (total flux) difference between $^{64}CuCl_2$ + TCPP and $^{64}CuCl_2$. In addition, the differential fluorescence images of TCPP were acquired by subtracting the $^{64}CuCl_2$ image from the $^{64}CuCl_2$ + TCPP image.

Research conclusions

This simple and cost-effective method could confirm the PS fluorescence emission generated by radionuclide-derived CR. Moreover, the method can contribute to accelerating the development of Cherenkov energy transfer imaging and the discovery of new effective PSs.

Research perspectives

Several laboratories with conventional optical imaging devices would be able to acquire suitable long-pass filters at low cost and easily apply this method to compare different PSs to identify the optimal PS. A potential limitation of this study, namely the use of limited experiments with only one PS and one radionuclide, could be addressed by conducting much more detailed examinations as the next step.

ACKNOWLEDGEMENTS

The authors thank the members of the Cyclotron Operation Section for providing ^{64}Cu. We are grateful to Osada Kensuke and Yamaya Taiga for their helpful discussions and suggestions.

FOOTNOTES

Author contributions: Aung W conceptualized and designed the study; Aung W, Rikiyama K and Nishikido F conducted the experiments and analyzed the data; Obara S performed the subtraction image processing; Aung W and Tsuji AB wrote the manuscript; Tsuji AB and Higashi T coordinated the research and contributed to manuscript preparation; all authors contributed to manuscript revision; All authors read and approved the final manuscript.

Supported by Grant-in-Aid for Scientific Research (C) from the Japan Society for the Promotion of Science, No. 21K07740.

Institutional review board statement: This study was reviewed and approved by the Institutional Review Board of National Institutes for Quantum Science and Technology, No. 07-1064-28. No animals or animal-derived samples or patients or patient-derived samples were included in this study.

Conflict-of-interest statement: The authors declare no potential conflicts of interest for this article.

Data sharing statement: All relevant data were presented in the manuscript. Further information is available from the corresponding author at winn.aung@qst.go.jp.

ARRIVE guidelines statement: The authors have read the ARRIVE guidelines, and the manuscript was prepared and revised according to the ARRIVE guidelines.

Open-Access: This article is an open-access article that was selected by an in-house editor and fully peer-reviewed by external reviewers. It is distributed in accordance with the Creative Commons Attribution NonCommercial (CC BY-NC 4.0) license, which permits others to distribute, remix, adapt, build upon this work non-commercially, and license their derivative works on different terms, provided the original work is properly cited and the use is non-commercial. See: https://creativecommons.org/Licenses/by-nc/4.0/

Country/Territory of origin: Japan

ORCID number: Winn Aung 0000-0002-0896-7158; Atsushi B Tsuji 0000-0003-2726-288X; Kazuaki Rikiyama 0000-0001-6474-535X; Fumihiko Nishikido 0000-0002-2952-281X; Satoshi Obara 0000-0002-2577-4243; Tatsuya Higashi 0000-0002-8338-4737.

Corresponding Author's Membership in Professional Societies: Japanese Society of Nuclear Medicine, No. 11047.

S-Editor: Lin C
L-Editor: Filipodia
P-Editor: Zhao S

REFERENCES

1 **Cherenkov PA**. Visible Light from Clear Liquids Under the Action of Gamma Radiation. *CR (Dokl) Acad Sci URSS* 1934; **2**: 451-454 [DOI: 10.3103/s1062873812120271]

2 **Ruggiero A**, Holland JP, Lewis JS, Grimm J. Cerenkov luminescence imaging of medical isotopes. *J Nucl Med* 2010; **51**: 1123-1130 [PMID: 20554722 DOI: 10.2967/jnumed.110.076521]

3 **Klein JS**, Sun C, Pratx G. Radioluminescence in biomedicine: physics, applications, and models. *Phys Med Biol* 2019; **64**: 04TR01 [PMID: 30524090 DOI: 10.1088/1361-6560/aaf4de]

4 **Ran C**, Zhang Z, Hooker J, Moore A. In vivo photoactivation without "light": use of Cherenkov radiation to overcome the penetration limit of light. *Mol Imaging Biol* 2012; **14**: 156-162 [PMID: 21538154 DOI: 10.1007/s11307-011-0489-z]

5 **Kotagiri N**, Sudlow GP, Akers WJ, Achilefu S. Breaking the depth dependency of phototherapy with Cerenkov radiation and low-radiance-responsive nanophotosensitizers. *Nat Nanotechnol* 2015; **10**: 370-379 [PMID: 25751304 DOI: 10.1038/nnano.2015.17]

6 **Hartl BA**, Hirschberg H, Marcu L, Cherry SR. Activating Photodynamic Therapy *in vitro* with Cerenkov Radiation Generated from Yttrium-90. *J Environ Pathol Toxicol Oncol* 2016; **35**: 185-192 [PMID: 27481495 DOI: 10.1615/JEnvironPatholToxicolOncol.2016016903]

7 **Kamkaew A**, Cheng L, Goel S, Valdovinos HF, Barnhart TE, Liu Z, Cai W. Cerenkov Radiation Induced Photodynamic Therapy Using Chlorin e6-Loaded Hollow Mesoporous Silica Nanoparticles. *ACS Appl Mater Interfaces* 2016; **8**: 26630-26637 [PMID: 27657487 DOI: 10.1021/acsami.6b10255]

8 **Guo R**, Jiang D, Gai Y, Qian R, Zhu Z, Gao Y, Jing B, Yang B, Lan X, An R. Chlorin e6-loaded goat milk-derived extracellular vesicles for Cerenkov luminescence-induced photodynamic therapy. *Eur J Nucl Med Mol Imaging* 2023; **50**: 508-524 [PMID: 36222853 DOI: 10.1007/s00259-022-05978-4]

9 **Robertson R**, Germanos MS, Li C, Mitchell GS, Cherry SR, Silva MD. Optical imaging of Cerenkov light generation from positron-emitting radiotracers. *Phys Med Biol* 2009; **54**: N355-N365 [PMID: 19636082 DOI: 10.1088/0031-9155/54/16/N01]

10 **Spinelli AE**, D'Ambrosio D, Calderan L, Marengo M, Sbarbati A, Boschi F. Cerenkov radiation allows *in vivo* optical imaging of positron emitting radiotracers. *Phys Med Biol* 2010; **55**: 483-495 [PMID: 20023328 DOI: 10.1088/0031-9155/55/2/010]

11 **Zhang Y**, Ma J, Wang D, Xu C, Sheng S, Cheng J, Bao C, Li Y, Tian H. Fe-TCPP@CS nanoparticles as photodynamic and photothermal agents for efficient antimicrobial therapy. *Biomater Sci* 2020; **8**: 6526-6532 [PMID: 33103167 DOI: 10.1039/d0bm01427c]

12 **Li B**, Wang X, Chen L, Zhou Y, Dang W, Chang J, Wu C. Ultrathin Cu-TCPP MOF nanosheets: a new theragnostic nanoplatform with magnetic resonance/near-infrared thermal imaging for synergistic phototherapy of cancers. *Theranostics* 2018; **8**: 4086-4096 [PMID: 30128038 DOI: 10.7150/thno.25433]

13 **Malatesti N**, Munitic I, Jurak I. Porphyrin-based cationic amphiphilic photosensitisers as potential anticancer, antimicrobial and immunosuppressive agents. *Biophys Rev* 2017; **9**: 149-168 [PMID: 28510089 DOI: 10.1007/s12551-017-0257-7]

14 **U. S. National Institutes of Health**. ImageJ. [cited 12 February 2023]. Available from: https://imagej.nih.gov/ij/

15 **Spinelli AE**, Boschi F. Novel biomedical applications of Cerenkov radiation and radioluminescence imaging. *Phys Med* 2015; **31**: 120-129 [PMID: 25555905 DOI: 10.1016/j.ejmp.2014.12.003]

16 **Dothager RS**, Goiffon RJ, Jackson E, Harpstrite S, Piwnica-Worms D. Cerenkov radiation energy transfer (CRET) imaging: a novel method for optical imaging of PET isotopes in biological systems. *PLoS One* 2010; **5**: e13300 [PMID: 20949021 DOI: 10.1371/journal.pone.0013300]

17 **Ciarrocchi E**, Belcari N. Cerenkov luminescence imaging: physics principles and potential applications in biomedical sciences. *EJNMMI Phys* 2017; **4**: 14 [PMID: 28283990 DOI: 10.1186/s40658-017-0181-8]

World Journal of Radiology

Submit a Manuscript: https://www.f6publishing.com

World J Radiol 2023 November 28; 15(11): 324-337

DOI: 10.4329/wjr.v15.i11.324

ISSN 1949-8470 (online)

META-ANALYSIS

Association between late gadolinium enhancement and outcome in dilated cardiomyopathy: A meta-analysis

Xin-Yi Feng, Wen-Feng He, Tian-Yue Zhang, Ling-Li Wang, Fan Yang, Yu-Ling Feng, Chun-Ping Li, Rui Li

Specialty type: Radiology, nuclear medicine and medical imaging

Provenance and peer review: Unsolicited article; Externally peer reviewed.

Peer-review model: Single blind

Peer-review report's scientific quality classification

Grade A (Excellent): 0
Grade B (Very good): 0
Grade C (Good): C
Grade D (Fair): 0
Grade E (Poor): 0

P-Reviewer: Barison A, Italy

Received: August 17, 2023
Peer-review started: August 17, 2023
First decision: September 14, 2023
Revised: September 29, 2023
Accepted: October 23, 2023
Article in press: October 23, 2023
Published online: November 28, 2023

Xin-Yi Feng, Tian-Yue Zhang, Ling-Li Wang, Fan Yang, Yu-Ling Feng, Chun-Ping Li, Rui Li, Department of Radiology, The Affiliated Hospital of North Sichuan Medical College, Nanchong 637000, Sichuan Province, China

Wen-Feng He, Department of Cardiology, The Affiliated Hospital of North Sichuan Medical College, Nanchong 637000, Sichuan Province, China

Corresponding author: Rui Li, PhD, Doctor, Department of Radiology, The Affiliated Hospital of North Sichuan Medical College, Maoyuan South Road, Shunqing District, Nanchong 637000, Sichuan Province, China. ddtwg_nsmc@163.com

Abstract

BACKGROUND

The prognostic value of late gadolinium enhancement (LGE) derived from cardiovascular magnetic resonance (CMR) is well studied, and several new metrics of LGE have emerged. However, some controversies remain; therefore, further discussion is needed, and more precise risk stratification should be explored.

AIM

To investigate the associations between the positivity, extent, location, and pattern of LGE and multiple outcomes in dilated cardiomyopathy (DCM).

METHODS

PubMed, Ovid MEDLINE, and Cochrane Library were searched for studies that investigated the prognostic value of LGE in patients with DCM. Pooled hazard ratios (HRs) and 95% confidence intervals were calculated to assess the role of LGE in the risk stratification of DCM.

RESULTS

Nineteen studies involving 7330 patients with DCM were included in this meta-analysis and covered a wide spectrum of DCM, with a mean left ventricular ejection fraction between 21% and 50%. The meta-analysis revealed that the presence of LGE was associated with an increased risk of multiple adverse outcomes (all-cause mortality, HR: 2.14; arrhythmic events, HR: 5.12; and composite endpoints, HR: 2.38; all $P < 0.001$). Furthermore, every 1% increment in the extent of LGE was associated with an increased risk of all-cause mortality. Analysis of a subgroup revealed that the prognostic value varied based on different location and pattern of LGE. Additionally, we found that LGE was a

stronger predictor of arrhythmic events in patients with greater left ventricular ejection fraction.

CONCLUSION
LGE by CMR in patients with DCM exhibited a substantial value in predicting adverse outcomes, and the extent, location, and pattern of LGE could provide additional information for risk stratification.

Key Words: Cardiac magnetic resonance; Dilated cardiomyopathy; Late gadolinium enhancement; Meta-analysis; Myocardial fibrosis; Prognosis

©The Author(s) 2023. Published by Baishideng Publishing Group Inc. All rights reserved.

Core Tip: The prognostic value of late gadolinium enhancement (LGE) is well studied, and several new metrics of LGE have emerged. However, some controversies remain; therefore, further discussion is needed, and a more precise risk stratification should be explored.

Citation: Feng XY, He WF, Zhang TY, Wang LL, Yang F, Feng YL, Li CP, Li R. Association between late gadolinium enhancement and outcome in dilated cardiomyopathy: A meta-analysis. *World J Radiol* 2023; 15(11): 324-337
URL: https://www.wjgnet.com/1949-8470/full/v15/i11/324.htm
DOI: https://dx.doi.org/10.4329/wjr.v15.i11.324

INTRODUCTION

Dilated cardiomyopathy (DCM) is a heterogeneous heart muscle disease with a prevalence of 1 in 2500 adults. Even with advances in therapy, the prognosis of patients with DCM remains poor (the 5-year mortality rate was as high as 20%) and varies considerably among individuals[1]. Therefore, prognostic stratification in DCM has become a demanding issue in clinical practice.

Currently, the left ventricular ejection fraction (LVEF) is a common applicable indicator for risk stratification in patients with DCM. However, the strategy of using the LVEF alone as a prognostic factor is inadequate in predicting adverse outcomes[2]. Occurring in approximately 30% of patients with DCM, myocardial scar is the most important underlying pathology of sudden cardiac death (SCD) events and the major substrate for ventricular arrhythmia. Late gadolinium enhancement (LGE) based on cardiovascular magnetic resonance (CMR) is currently the gold standard for evaluating localized myocardial fibrosis. Studies have confirmed that LGE is an independent and powerful predictor of adverse outcomes in DCM and could increase the prognostic value of LVEF[2-4].

However, most studies have focused on the presence of LGE and adverse outcomes. With the continuously developing research on LGE in patients with DCM, more studies have incorporated new indicators (the extent, location, and pattern of LGE) to assess the outcomes in patients with DCM, other than just the presence of LGE. Therefore, this meta-analysis was designed to evaluate the role of those novel indicators of LGE in the risk stratification of DCM.

MATERIALS AND METHODS

The network meta-analysis extension of the Preferred Reporting Items for Systematic Reviews and Meta-Analyses (PRISMA-NMA) guidelines provided support in guiding this review[5].

Data sources and search strategy

The following databases were searched according to the methods recommended by the Cochrane Handbook: PubMed, Ovid MEDLINE, and Cochrane Library. Studies were searched using relevant controlled vocabulary thesauruses (Medical Subject Headings terms for PubMed) and synonyms for these terms: "dilated cardiomyopathy," "cardiac magnetic resonance," "late gadolinium enhancement," and "prognosis." The details of the search strategy adopted for PubMed, Ovid MEDLINE, and the Cochrane Library are shown in the Appendix. These searches were limited to cohort studies and were finalized in December 2021.

Eligibility criteria and outcomes

Observational cohort studies, both prospective and retrospective, were included in the meta-analysis if they reported the prognostic value of LGE in DCM and specified the exclusion of ischemic heart disease (*i.e.*, any medical documentation (coronary angiography, myocardial perfusion imaging, or medical records) that indicated the presence of ischemic heart disease and significant coronary artery disease); moreover, studies with transmural LGE without any history of coronary artery disease or myocardial infarction were included if the imaging phenotype including LGE distribution was not coherent with an ischemic insult in a specific coronary artery territory. When the population of a study also included

patients with cardiomyopathies other than DCM, only those with DCM were considered for the meta-analysis. Furthermore, only studies that quantified the extent of LGE as a percentage of left ventricular mass were included in the meta-analysis. The endpoints were classified into three subgroups: (1) All-cause mortality; (2) arrhythmic events, including SCD, cardiac arrest due to ventricular fibrillation (VF), sustained ventricular tachycardia (VT), or appropriate implantable cardioverter–defibrillator (ICD) intervention; and (3) composite endpoints, including all-cause mortality and cardiac events. Cardiac events, included cardiac death[2] (death after a period of clinical deterioration in the signs and symptoms of heart failure despite medical treatment), arrhythmic events, and heart failure. SCD was defined as an unexpected death either within 1 h of the onset of cardiac symptoms in the absence of progressive cardiac deterioration; during sleep; or within 24 h of last being seen alive[6]. VF was defined as irregular or regular tachycardia with regards to polarity, amplitude, morphology, and sequence of intracardiac electrograms, with a mean cycle length of £240 ms (*i.e.*, ^{3}250 beats/min). Sustained VT was defined as tachycardia originating in the ventricle with a rate >100 beats/min and lasting > 30 s or requiring an intervention for termination. Appropriate ICD intervention was defined as a device shock or antitachycardia overdrive pacing delivered in response to a ventricular tachyarrhythmia and documented by stored intracardiac electrocardiogram data[7].

Data extraction and quality assessment

Data were extracted and analyzed by two independent investigators and were reported on standardized forms; consensus was reached through a discussion in case of disagreements. Moreover, data on hazard ratios (HRs) and 95% confidence intervals (CIs), adjusted and unadjusted variables in the regression model, author names, year of publication, sample size, age, percentage of male patients, LGE status (its presence, extent, location, and pattern), follow-up duration, LVEF, and left ventricular end-diastolic volume index (LVEDVi) were recorded if available.

The Newcastle–Ottawa Quality Assessment Scale (NOS) was used for quality assessment, as shown in Table 1, and the quality of the selected studies was evaluated and determined based on the selection of the study groups and the outcomes of interest. The NOS scoring system is as follows. A study scored 1 star for each item within the selection and outcome categories, and a maximum of 2 stars was given for comparability. Nine NOS stars were used to assess the risk of bias. A study with nine stars (four for selection, two for comparability, and three for outcome) was considered to have a low risk of bias, and a study with ≥ 5 stars (two for selection, one for comparability, and two for outcome) was considered to have a medium risk of bias. A study with < 5 stars (0 stars for either of the three fields or 1 star for comparability or outcome) was considered to have a high risk of bias.

Data analysis

Pooled HR and 95%CIs were calculated using a fixed-effects model. The heterogeneity between studies was assessed using Q and I^2 tests; heterogeneity was considered significant if I^2 ≥ 50%, and the studies will be recalculated using a random-effects model. Furthermore, the meta-analysis was performed using the D–L method if heterogeneity existed, and sensitivity analysis was used to assess the stability of the results.

Publication bias was evaluated using Egger's and Begg's tests; trim and fill analysis was used if there was publication bias. Sensitivity analysis using the leave-one-out method was performed, which allowed the calculation of estimates by omitting one study at a time. All analyses were performed using STATA, version 16. *P* values of < 0.05 were used to denote statistical significance.

The study has been registered with PROSPERO (number: CRD42023382021).

RESULTS

Search results

Figure 1 shows a flow chart for the search process and study selection. Overall, 147 citations were identified using PubMed (117 citations), Ovid MEDLINE (12 citations), and the Cochrane Library (18 citations). After screening the article titles and abstracts, 26 full-text articles of possible relevance were recruited, and 121 duplicate or irrelevant articles were excluded. Finally, 19 of the 26 relevant articles were included based on the inclusion criteria.

Quality assessment of the included studies

The quality of the included studies was assessed using the NOS, as shown in Table 1. None of the included studies had a high risk of bias; however, two studies had a low risk of bias[7,8]. For the study selection, 14 studies had a low risk of bias [6-19], and 5 had a medium risk of bias[3,5,20-22]. In terms of comparability, 8 studies had a low risk of bias[7-9,12,13,15,16,19], 7 studies had a medium risk of bias [3,11,14,17,18,21], and 5 studies had a high risk of bias[5,6,10,20,22]. Regarding outcomes, 8 studies had a low risk of bias [3,5,6,7,8,10,14,18] and 11 studies had a medium risk of bias[9,11-13,15-17,19-21,22].

Study characteristics

This study analyzed data from 7330 individuals (age ranging from 33 to 76 years; 68% were men) from 19 full-text studies from Asia, Europe, and North America. Of the 7330 patients, 2856 (39.0%) had myocardial LGE, and the follow-up duration ranged from 1 to 132 mo.

Among the 19 selected studies, 4 studies were multicenter[12,16,21,22] and 3 studies were retrospective studies[9,21,22]. 14 studies reported the relationship between the presence of LGE and adverse outcomes[3,5,7,6-14,17,18,21,22], 4

Table 1 Risk of bias assessment in the meta-analysis

Ref.	Selection				Comparability	Outcome			Total score
	Exposed cohort	Nonexposed cohort	Ascertainment of exposure	Outcome of interest		Assessment of outcome	Length of follow-up	Adequacy of follow-up	
Halliday *et al* [6], 2019	1	1	1	1	0	1	1	1	7
Gulati *et al* [2], 2013	0	1	1	1	1	1	1	1	7
Behera *et al* [9], 2020	1	1	1	1	2	0	1	1	8
Tateishi *et al* [10], 2015	1	1	1	1	0	1	1	1	7
Lehrke *et al* [11], 2011	1	1	1	1	1	1	0	1	7
Perazzolo *et al*[7], 2014	1	1	1	1	2	1	1	1	9
Neilan *et al* [12], 2013	1	1	1	1	2	1	0	1	8
Yamada *et al* [13], 2014	1	1	1	1	2	0	1	1	8
Buss *et al* [14], 2015	1	1	1	1	1	1	1	1	8
Mikami *et al* [15], 2016	1	1	1	1	2	1	0	1	8
Puntmann *et al*[16], 2016	1	1	1	1	2	1	0	1	8
Masci *et al* [17], 2012	1	1	1	1	1	1	0	1	7
Šramko *et al* [8], 2013	1	1	1	1	2	1	1	1	9
Amzulescu *et al*[20], 2015	0	1	1	1	0	0	1	1	5
Alba *et al* [21], 2020	1	1	1	0	1	0	1	1	6
Xu *et al*[18], 2021	1	1	1	1	1	1	1	1	8
Barison *et al* [19], 2020	1	1	1	1	2	0	1	1	8
Halliday *et al* [4], 2017	0	1	1	1	0	1	1	1	6
Di Marco *et al* [22], 2021	1	1	1	0	0	0	1	1	5

The total score was 9, and the higher the score, the lower the bias, besides, scores ≤ 5 means a relative high risk of bias.

studies that reported on the extent of LGE[3,12,16,20], 2 studies[6,15] that reported on the location of LGE and 1 study[6] that reported on the pattern of LGE were adjusted for age, sex, and LVEF, and a portion of those studies were modified for the New York Heart Association Functional Classification[5,6,10,11,21].

The detailed data on the author, year of publication, sample size, age, percentage of male patients, LGE status, follow-up duration, LVEF, and LVEDVi are shown in Table 2.

Data synthesis

Positivity for LGE and adverse outcomes: Overall, 18 studies, involving 7168 patients (2793 had LGE), reported the association between the positivity of LGE and adverse outcomes. The included outcomes of the subgroup analysis were all-cause mortality (4 articles), arrhythmic events (9 articles), and composite endpoints (12 articles). All-cause mortality

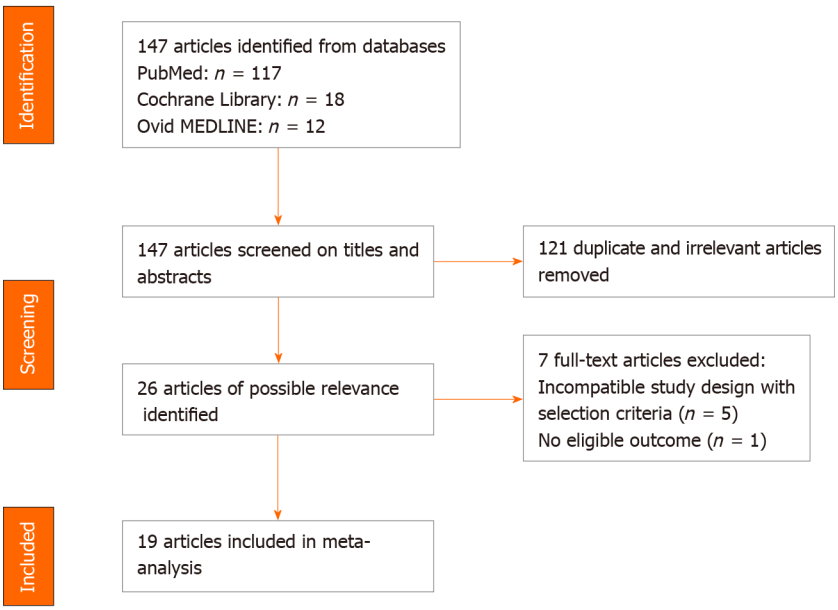
Table 2 Description of the studies included in the meta-analysis

Ref.	Type of study	Patients enrolled	Mean/median age (yr)	Male (%)	LGE present, *n* (%)	Mean/Median Follow-Up Time	Endpoint included in analysis	Mean/median LVEF (%)	Mean/median LVEDVi (mL/m²)
Halliday *et al*[6], 2019	Prospective	874	LGE negative: 51.0 ± 15.1; LGE extent (0.00%-2.55%): 52.8 ± 14.4; LGE extent (2.55%-5.10%): 53.7 ± 14.6; LGE extent (> 5.10%): 56.2 ± 14.6	588 (67.3)	300 (34.3)	4.9 yr (range, 3.5-7.0 yr)	All cause mortality; arrhythmic events: SCD and aborted SCD.	39 (range, 29-50)	LGE negative: 126.3 ± 36.6; the extent of LGE (0.00-2.55%): 147.9 ± 46.1; the extent of LGE (2.55%-5.10%): 142.8 ± 49.8; the extent of LGE (> 5.10%): 135.5 ± 37.3
Gulati *et al* [2], 2013	Prospective	472	51.1 ± 14.7	324 (68.6)	142 (30.1)	5.3 yr (range, 31 d-11.0 yr)	Arrhythmic events: SCD and aborted SCD; all cause mortality	37±13	135.1 ± 44.3
Behera *et al* [9], 2020	Retrospective	112	LGE negative: 45.5 (range, 33.0-58.7); LGE positive: 40.0 (range, 24.5-54.5)	LGE negative: 42 (61.8); LGE positive: 30 (68.2)	44 (39.3)	745 ± 320 d	Composite endpoint: All-cause mortality, resuscitated cardiac arrest, sustained VT/appropriate ICD shock, HF hospitalization	LGE negative: 31.5 (range, 28.0-36.2); LGE positive: 32.5 (range, 27.0-41.0)	LGE negative: 104.0 (range, 77.0-125.0); LGE positive: 137.0 (range, 87.5-225.2)
Tateishi *et al*[10], 2015	Prospective	207	50 ± 16	165 (80)	105 (50.7)	44 mo (range, 23-62 mo)	Composite endpoint: Cardiac death, cardiac transplantation, LV assist device implantation, appropriate ICD discharge for VT or VF, and rehospitalisation for HF	27 ± 11	143 ± 57
Lehrke *et al* [11], 2011	Prospective	184	51.55 ± 1.1	138 (75)	72 (39.1)	685 ± 30 d	Composite endpoint: Cardiac death, hospitalisation for decompensated HF, or appropriate ICD discharge	LGE negative: 44 (range, 33.1-50.9); LGE positive: 31 (range, 20.9-42.2)	LGE negative: 109 (range, 92.7-137.6); LGE positive: 133 (range, 116-161)
Perazzolo *et al*[7], 2014	Prospective	137	No arrhythmic events: 47 (range, 37-60); arrhythmic events: 59 (range, 43-70)	108 (78.8)	76 (55.5)	3 yr (range, 31 d-9.6 yr)	Arrhythmic events: SCD, cardiac arrest due to VF, sustained VT, or appropriate ICD intervention.	No arrhythmic events:33 (range, 28-40); arrhythmic events: 30 (range, 29-40)	No arrhythmic events: 109 (range, 87-140); arrhythmic events: 123 (range, 105-143)
Neilan *et al* [12], 2013	Prospective	162	55 ± 14	106 (65)	81 (50)	29 ± 18 mo	Composite endpoint: Cardiovascular death and appropriate ICD therapy; arrhythmic events: ATP, ICD discharge, and non-heart failure cardiovascular death	28 ± 9	140 ± 50
Yamada *et al*[13], 2014	Prospective	57	55 ± 13	40 (70.2)	25 (44)	71 ± 32 mo	Composite endpoint: Cardiac death, hospitalization for decompensated HF, or documented	LGE negative: 36 ± 13; LGE positive: 30 ± 11	LGE negative: 120 ± 39; LGE positive: 141 ± 47

							lethal arrhythmia, including VT and VF		
Buss *et al* [14], 2015	Prospective	210	52 ± 15	159 (76)	79 (38)	5.3 yr	Composite endpoint: Cardiac events together with the occurrence of hospitalization due to congestive HF	36.1 ± 13.8	132 ± 48
Mikami *et al*[15], 2016	Prospective	118	57 ± 14	68 (58)	66 (56)	2.1 ± 1.3 yr	Composite endpoint: Cardiac mortality or appropriate ICD therapy; arrhythmic events: Appropriate ICD therapy or SCD	32 ± 12	119 ± 42
Puntmann *et al*[16], 2016	Prospective	637	50 (range, 37-76 yr)	395 (62)	171 (27)	22 mo (range, 19-25 mo)	All cause mortality	47 (range, 29-50)	109 (range, 89-132)
Masci *et al* [17], 2012	Prospective	125	59 ± 14	82 (65.6)	50 (40)	14.2 mo (range, 6.5–28.8 mo)	Composite endpoint: Cardiac death and HF hospitalization	33 ± 10	LGE negative: 124 ± 35; LGE positive: 140 ± 39
Šramko *et al*[8], 2013	Prospective	42	Idiopathic: 45 ± 12; inflammatory: 42 ± 8	30 (71.4)	28 (66.7)	25 ± 9 mo	Composite endpoint: Cardiac death, urgent heart transplantation, and hospitalization for worsening HF	Idiopathic DC: 22 ± 11; Inflammatory DC: 21 ± 9	Idiopathic: 137 ± 39; Inflammatory: 148 ± 46
Amzulescu *et al*[20], 2015	Prospective	162	55 ± 15	102 (63.0)	63 (39)	3.4 yr (range, 1.5-6.3 yr)	Composite endpoint: Cardiovascular death, heart transplantation, LV assist device implantation, resuscitated cardiac arrest, and appropriate device shocks	24.6 ± 8.4	161.6 ± 52
Alba *et al* [21], 2020	Retrospective	1672	56 ± 14	1185 (70.9)	650 (39)	2.3 yr (range, 1.0-4.3 yr)	Composite endpoint: All-cause mortality, heart transplantation, or left ventricular assist device implant; arrhythmic events: SCD or appropriate ICD shock	33 ± 11	118 ± 27
Xu *et al* [18], 2021	Prospective	412	48.0 ± 14.4	300 (72.8)	201 (48.8)	28.1 mo (range, 19.3-43.0 mo)	Composite endpoint: All-cause mortality and HF readmission; all-cause mortality	23.7 ± 9.8	185.6 ± 58.9
Barison *et al*[19], 2020	Prospective	183	66 (range, 56-73 yr)	134 (73)	116 (63)	30 mo (range, 10-65 mo)	Composite endpoint: Appropriate ICD shock and cardiac death; arrhythmic events: appropriate ICD shock	24 (range, 21-31)	143 (range, 120-168)

Halliday *et al*[4], 2017	Prospective	399	49.9 ± 15.3	254 (63.7)	101 (25.3)	4.6 yr (range, 3.5-7.0 yr)	Arrhythmic events: SCD or Aborted SCD	49.6 ± 4.9	111.1 ± 19.4
Di Marco *et al*[22], 2021	Retrospective	1165	58 (range, 48-68)	768 (65.9)	486 (41.7)	36 mo (range, 20-58 mo)	Arrhythmic events: Appropriate ICD therapies, sustained VT, resuscitated cardiac arrest, and sudden death	39 (range, 30-46)	118 (range, 99-142)

Values are *n*, mean ± SD, or *n* (%) unless otherwise indicated; LGE: Late gadolinium enhancement; VT: Ventricular tachycardia; VF: Ventricular fibrillation; HF: Heart failure; ICD: Implantable cardioverter-defibrillator; SCD: Sudden cardiac death; LV: Left ventricular; ATP: Anti-tachycardia pacing.



DOI: 10.4329/wjr.v15.i11.324 **Copyright** ©The Author(s) 2023.

Figure 1 Flow diagram of the selection of articles.

occurred in 313 patients (4.4% of patients of the 18 included studies), of who 172 had LGE (6.2% of LGE-positive patients) and 141 had no LGE (3.2% of LGE-negative patients), with a risk difference between LGE-positive and LGE-negative patients of 12.2% (95%CI: 9.1%–15.3%; $P < 0.001$). Besides, arrhythmic events and composite endpoints occurred in 256 (3.6%) and 603 (8.4%) patients, respectively.

In the pooled analysis, positivity for LGE was associated with an increased risk of all-cause mortality (HR: 2.14; 95%CI: 1.68–2.72; $P < 0.001$), arrhythmic events (HR: 5.12, 95%CI: 3.24–8.07, $P < 0.001$), and composite endpoints (HR: 2.38, 95%CI: 1.83–3.11, $P < 0.001$), as shown in Figure 2. A random-effects model was used for studies on arrhythmic events with significant heterogeneity ($I^2 = 67.9\%$; $P = 0.002$), and sensitivity analysis using the leave-one-out method showed that the study by Alba *et al*[21] may be the source of heterogeneity. However, Egger's and Begg's tests showed that there was publication bias in the presence of LGE and composite endpoints; after conducting a trim and fill analysis and adjusting for the effect size for funnel plot asymmetry, the *P* values before and after the trim and fill analysis were less than 0.001, indicating that no significant changes occurred and the results were reliable.

The extent of LGE and adverse outcomes: Two studies were included in the subgroup analysis of all-cause mortality, including 313 participants with LGE and 796 without LGE, with 101 all-cause mortality occurred during the follow-up period, and the pooled HR of all-cause mortality for every 1% increment in the extent of LGE was 1.10 (95%CI: 1.06–1.14; $P < 0.001$) (Figure 3A). In the analysis of the outcome of composite endpoints, two studies recruited 179 patients with LGE and 166 without LGE, with 79 composite endpoints occurred during the follow-up period, however, even random-effects model was used for studies on composite endpoints with significant heterogeneity ($I^2 = 64.0\%$; $P = 0.096$); the result showed that every 1% increment in the extent of LGE only has numerically increased the risk of composite endpoints without reaching statistical significance 1.22 (95%CI: 0.91–1.63; $P < 0.001$).

The LGE locations and adverse outcomes: Recently, several LGE metrics, including location and pattern, have emerged as new indicators for risk prediction. Subgroup analysis, which included two studies (LGE was present in 501 patients and absent in 785 patients; all-cause mortality occurred in 212 patients), showed that LGE located in the septum (pooled

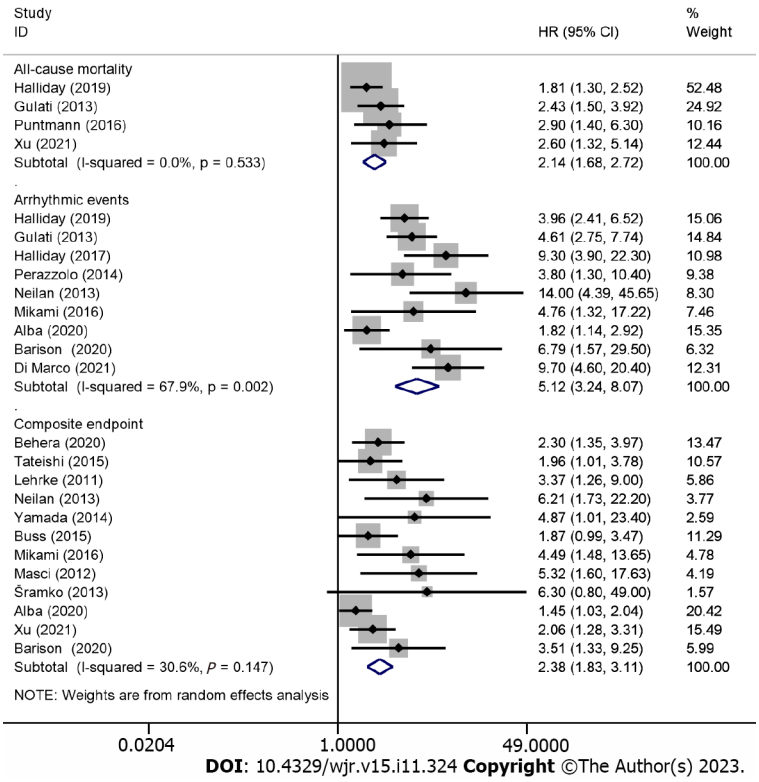


Figure 2 The forest plot of risk of adverse outcomes in dilated cardiomyopathy patients with the presence of late gadolinium enhancement.

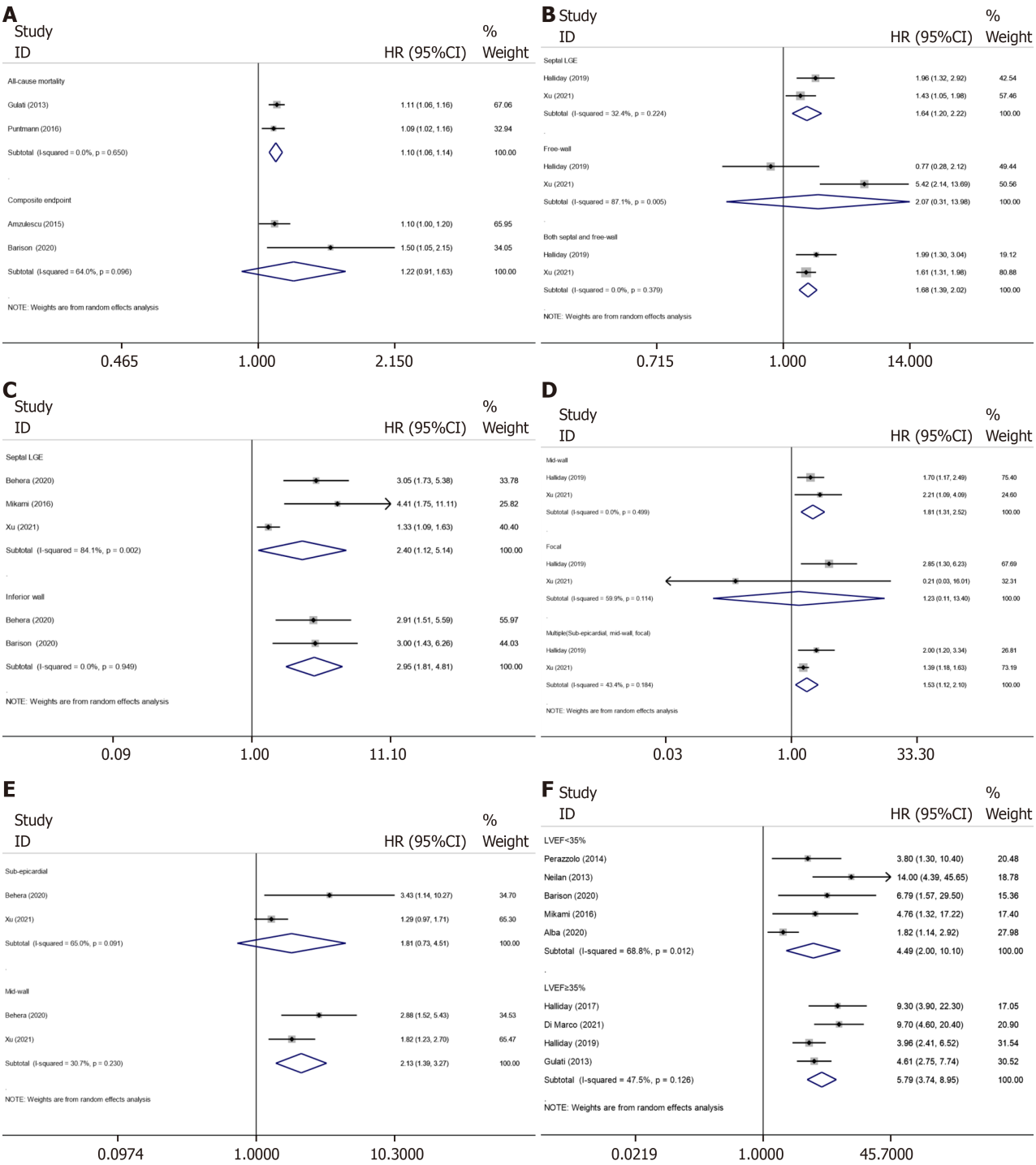
HR: 1.64; 95%CI: 1.20–2.22; $P < 0.001$) and in both the septum and free wall (pooled HR: 1.68; 95%CI: 1.39–2.02; $P < 0.001$) can predict all-cause mortality. However, LGE located in the free wall only has numerically increased the risk of all-cause mortality without reaching statistical significance (pooled HR: 2.07; 95%CI: 0.31–13.98; $P = 0.457$) (Figure 3B). A random-effects model was used for studies on free-wall LGE with significant heterogeneity ($I^2 = 87.1\%$; $P = 0.005$).

The subgroup analysis for predicting composite endpoints included five studies (Figure 3C), including 471 LGE-positive participants and 466 LGE-negative participants, and the number of composite endpoints was 297. The pooled HRs for septal and inferior LGE of composite endpoints were 2.40 (95%CI: 1.12–5.14, $P = 0.025$) and 2.95 (95%CI: 1.81–4.81, $P < 0.001$), respectively; a random-effects model was used to analyze the heterogeneity in the septal LGE group ($I^2 = 84.1\%$; $P = 0.002$), sensitivity analysis using the leave-one-out method showed that the study by Xu *et al*[18]. may be the source of heterogeneity, and the heterogeneity may result from the unadjusted HR.

The LGE patterns and adverse outcomes: In addition to the mid-wall pattern of LGE, recent studies have found that LGE has many other patterns, such as focal and sub-epicardial patterns, which can also provide stratification information for adverse outcomes. Subgroup analysis for all-cause mortality, which included 501 patients with myocardial LGE and 785 without LGE from two studies, was performed for the mid-wall, focal, and multiple (mid-wall, sub-epicardial, and focal) patterns of LGE; death occurred in 212 patients, and the pooled HRs were 1.81 (95%CI: 1.31–2.52; $P < 0.001$), 1.23 (95%CI: 0.11–13.40; $P = 0.867$; not statistical significance), and 1.53 (95%CI: 1.12–2.10; $P < 0.001$), respectively (Figure 3D).

The relationship between the patterns of LGE and composite endpoints was also analyzed; subgroup analysis was performed and included two studies involving 245 LGE-positive patients and 279 LGE-negative patients, with 195 composite endpoints during the follow-up period. Our analysis showed that mid-wall (pooled HR: 2.13; 95%CI: 1.39–3.27; $P = 0.001$) patterns of LGE can predict composite endpoints (Figure 3E), even random-effects model was used for studies on sub-epicardial LGE with significant heterogeneity ($I^2 = 65.0\%$; $P = 0.091$), these results showed that sub-epicardial LGE has numerically increased the risk of composite endpoints without reaching statistical significance (pooled HR: 1.81; 95%CI: 0.73–4.51; $P = 0.202$).

Positive effect of LGE and arrhythmic events on different ranges of LVEF: As the studies included in our meta-analysis all demonstrated indications of LVEF, we also performed a subgroup analysis to assess the impact of LGE on DCM for different ranges of LVEF by dividing those studies into two groups (LVEF < 35% and LVEF ≥ 35%). The analysis, which included nine studies (LGE was present in 2018 patients and absent in 3164 patients; arrhythmic events occurred in 256 patients), showed that LGE is a stronger predictor of arrhythmic events in patients with a greater LVEF, and the pooled HRs for positive LGE with LVEF < 35% and LVEF ≥ 35% were 4.49 (95%CI: 2.00–10.10; $P < 0.001$) and 5.79 (95%CI: 3.74–8.95; $P < 0.001$), respectively (Figure 3F). A random-effects model was used for studies on LVEF < 35% with significant heterogeneity ($I^2 = 68.8\%$; $P = 0.012$).



DOI: 10.4329/wjr.v15.i11.324 **Copyright** ©The Author(s) 2023.

Figure 3 The forest plot of association between extent, location, and pattern of late gadolinium enhancement and adverse outcomes. A: Association between extent of late gadolinium enhancement (LGE) and adverse outcomes; B: Association between locations of LGE and all-cause mortality; C: Association between locations of LGE and composite endpoint; D: Association between patterns of LGE and all-cause mortality; E: Association between patterns of LGE and composite endpoint; F: Association between the positive of LGE and arrhythmic events in different ranges of left ventricular ejection fraction.

DISCUSSION

LGE detected by CMR represents a myocardial scar, which could provide a foundation for ventricular re-entrant arrhythmia and is the main cause of SCD in multiple myocardiopathies[23]. Although LGE is observed in approximately 30% of patients with DCM, several studies support the prognostic power of LGE[3,4]. This meta-analysis included 7330 patients with DCM, confirmed the prognostic value of LGE for multiple adverse endpoints, and investigated the association between the extent, location, and pattern of LGE and outcomes.

Prior meta-analyses have evaluated the prognostic value of LGE in DCM[24-26]. However, the sample size of our meta-analysis was larger, and given the increasing numbers of studies published in the past few years about the characteristics

of LGE (extent, location, and pattern), we considered that focusing on novel indicators was appropriate. The relevant number of studies included allowed subgroup analyses between the extent, location, and pattern of LGE and outcomes.

The presence of LGE and adverse outcomes

Myocardial fibrosis is strongly associated with ventricular remodeling[11,27]. The prognostic value of LGE is independent of left ventricular parameters and can provide additional information on LVEF[28]. Additionally, the predictive ability of LGE was found to be better in patients with higher LVEF[22].

In our meta-analysis, LGE was present in approximately 40% of the patients with DCM under study and was strongly and significantly associated with multiple adverse outcomes. The relationship between LGE and the endpoints was particularly obvious for arrhythmic events (pooled HR: 5.12, 95%CI: 3.24–8.07, $P < 0.001$). This will be extremely meaningful for risk stratification mainly based on LVEF, as most SCD cases did not have severely reduced LVEF[23]. Moreover, the finding that the predictive power of LGE was better in patients with greater LVEF regarding the endpoint of arrhythmic events in our subgroup analysis confirmed the results of a previous study[22]. The severely reduced LVEF detected in patients with DCM represents an adversely remodeled left ventricle, which can lead to self-organized criticality and cascading mechanical collapse, and ultimately result in SCD[29]. However, in the absence of a severely remodeled left ventricle, LGE provides the foundation for ventricular re-entrant arrhythmia, which can be the major cause of adverse outcomes.

The extent of LGE and adverse outcomes

A study suggests that the susceptibility to re-entrant arrhythmias may be increased with the extent of LGE[19], indicating that the evaluation of the extent of LGE plays an important role in determining the prognosis of patients with DCM.

As a continuous variable, every 1% increment in LGE extent can predict all-cause mortality in our meta-analysis. However, even though only studies that quantified the extent of LGE as a percentage of the left ventricular mass were included in our meta-analysis, heterogeneity among studies was inevitable because of the differences in the measurement methods and parameters of LGE quantification used among the included studies. However, Halliday *et al*[6] and Behera *et al*[9] demonstrated that the correlation between the extent of LGE and outcomes seems to be nonlinear, as a small increase in the extent of LGE could significantly increase the risk of adverse outcomes.

One potential mechanism is that the induction of arrhythmia can be influenced by the texture and spatial distribution of fibrosis, the formation and dynamics of which are mostly determined by the maximal local fibrosis level; thus, the composition of myocardial fibrosis, rather than volume, may be the main determinant of arrhythmia[30]. Another mechanism that may explain these results is that ventricular arrhythmia most likely originates from the regions between myocardial fibrosis and healthy tissue with slow conduction[31,32]. Therefore, more precise identification of heterogeneous zones between healthy myocardium and myocardial fibrosis and the accurate discrimination of the texture and type of myocardial fibrosis may help better predict the prognosis of patients with DCM.

The LGE locations and adverse outcomes

Studies mainly focused on septal LGE, which is the most common location of LGE. However, recent studies have shown that LGE can also occur in the free wall with a high incidence[6,18], suggesting that LGE located in this location is worth further exploration.

Our meta-analysis found that septal LGE is associated with all-cause mortality and composite endpoints, which is consistent with the findings of previous studies. Furthermore, combined septal and free-wall LGE was more closely associated with all-cause mortality, as multi-location LGE may result in a larger extent of myocardial fibrosis.

The location of LGE may be related to its underlying etiology. LGE of idiopathic DCM is frequently located in the septum for unclear reasons, whereas LGE of DCM caused by viral myocarditis is usually located in the free wall. This is because cardiotropic viruses that originate from the bloodstream can cause pericarditis; the free wall in direct contact with the pericardium is the prime location for migration of inflammatory cells. The scar microstructure may be varied for the underlying etiology and cause a different risk[33].

However, because the number of studies included in this study was small and whether free-wall LGE is a protective or adverse factor remains controversial[6,18], further investigation regarding the prognosis of the distribution of LGE is still required.

The LGE patterns and adverse outcomes

As the most typical LGE pattern, mid-wall LGE was associated with an increased risk of all-cause mortality and composite endpoints in this study. However, our subgroup analyses showed that sub-epicardial and focal pattern of LGE were not statistically significant in predicting adverse outcome; in this case, more studies are required to confirm their prognostic value.

The sub-endocardial and transmural patterns of LGE have been considered to be indicators of previous myocardial infarction[34,35]. However, several studies have investigated the role of transmural LGE, which is not coherent with coronary artery territory (indicating that this pattern is not of an ischemic origin), and sub-endocardial LGE in determining the prognosis of patients with DCM[21,22]. Di Marco *et al*[22] have found that transmural LGE was associated with a heightened risk of adverse outcomes. Through the aforementioned studies, it is suggested that more attention should be paid to those "ischemia LGE patterns" rather than simply seeing it as myocardial infarct in patients with DCM.

In addition to focusing on the pattern of LGE itself, the number of coexisting LGE patterns must also be considered. In our meta-analysis, patients with multiple patterns of LGE (sub-epicardial, mid-wall, and focal) were at a greater risk of

all-cause mortality than those without LGE. One possibility is that more LGE patterns may represent a higher heterogeneity of fibrosis. However, the prognostic ability of multiple LGE patterns is not as good as that of one single pattern in some other studies[6,18]. The limited number of patients with multiple LGE patterns may be responsible for the controversial results. Therefore, more trials are needed to draw a more certain conclusion.

Furthermore, Di Marco *et al*[22] have found that the combination of LVEF strata and LGE status may help improve risk stratification in patients with DCM. Based on the results of this study, the next subdivision of various indicators (extent, location, and pattern) of LGE, particularly the free-wall LGE, and the integration of those indicators with varying clinical parameters may be more helpful in predicting the prognosis of patients with DCM.

Study limitations

The limitations of this study are that most included studies were observational; selection bias should be anticipated; and this meta-analysis can only detect associations but not causality. Additionally, the exclusion and inclusion criteria were different among the included studies, and there was a wide variety on the definitions of the endpoints. Finally, the data on the location and pattern of LGE were limited, which can explain the significant heterogeneity in some subgroup analyses; further studies enrolling more eligible patients are required.

CONCLUSION

CMR-LGE exhibited a substantial prognostic value in predicting all-cause mortality, arrhythmic events and composite endpoints in patients with DCM. The extent, location, and pattern of LGE could provide additional information for risk stratification.

ARTICLE HIGHLIGHTS

Research background

LGE as a prognostic indicator of dilated cardiomyopathy (DCM) has been extensively studied, and several new metrics of late gadolinium enhancement (LGE), such as its extent, location, and pattern, have emerged. However, whether some indicators are protective or risk factors and whether the combination of left ventricular ejection fraction (LVEF) strata and LGE has a better predictive value remains controversial; therefore, further discussion is required, and more precise risk stratification should be explored.

Research motivation

This meta-analysis aimed to detect the predictive performance of the extent, location, and pattern of LGE, to compare and screen these new indicators of LGE, and provide novel concepts for improving the risk stratification algorithm for adverse outcomes of DCM.

Research objectives

The research objectives of this meta-analysis were to investigate the associations between the positivity and extent, location, and pattern of LGE derived from CMR and multiple outcomes. We found that the presence of LGE was associated with an increased risk of multiple adverse outcomes (all-cause mortality, arrhythmic events, and composite endpoints). Furthermore, an increase in the extent of LGE and a different location and pattern of LGE may impact the prognosis. Although the current studies and meta-analyses mainly focus on the relationship between the presence of LGE and prognosis, our study found that LGE is a stronger predictor of arrhythmic events in patients with greater LVEF, and that the different types of LGE were equally predictive, which suggested that these new indicators and their combinations may help improve the risk stratification.

Research methods

We followed the guidelines of PRISMA-NMA, registered with PROSPERO, and extracted data from databases recommended by the Cochrane Handbook. After discussion, we reached a consensus and classified the endpoints into three; the pooled HRs and 95%CIs obtained by using STATA were applied to evaluate the effectiveness of the new metrics of LGE. The Newcastle–Ottawa Quality Assessment Scale was used for quality assessment. Publication bias was assessed using Egger's and Begg's tests, and a sensitivity analysis was performed using the leave-one-out method, to assess the stability of the results.

Research results

CMR-LGE is a strong prognostic marker for patients with DCM. The extent, location, and pattern of LGE provided additional information for risk stratification. Further studies are needed to determine whether free-wall LGE is a protective or risk factor, and whether the focal or sub-epicardial pattern of LGE has predictive value.

Research conclusions

CMR-LGE is a strong prognostic marker for patients with DCM. The extent, location, and pattern of LGE provided

additional information for risk stratification. Further studies are needed to determine whether free-wall LGE is a protective or risk factor, and whether the focal or sub-epicardial pattern of LGE has predictive value.

Research perspectives

The prognostic value of different locations and patterns of LGE needs to be confirmed in future studies, and the combined predictive value of these predictors warrants further exploration.

FOOTNOTES

Co-first authors: Xin-Yi Feng and Wen-Feng He.

Author contributions: Feng XY participated in the study design, contributed to data analysis and interpretation, and drafted the manuscript; He WF contributed to the preparation, editing and review of the manuscript; Zhang TY carried out data acquisition, performed data analysis and interpretation and edited the manuscript; Wang LL, Feng YL, and Li CP carried out data acquisition and performed data analysis and interpretation; Li R contributed to quality control of data and algorithm, and editing and review of the manuscript; All authors read and approved the final manuscript.

Supported by the Research Grant of the National Natural Science Foundation of China, No. 81801674; Sichuan Province Science and Technology Support Program, No. 2021YJ0242.

Conflict-of-interest statement: All the authors declare that they have no competing interests.

PRISMA 2009 Checklist statement: The authors have read the PRISMA 2009 Checklist, and the manuscript was prepared and revised according to the PRISMA 2009 Checklist.

Open-Access: This article is an open-access article that was selected by an in-house editor and fully peer-reviewed by external reviewers. It is distributed in accordance with the Creative Commons Attribution NonCommercial (CC BY-NC 4.0) license, which permits others to distribute, remix, adapt, build upon this work non-commercially, and license their derivative works on different terms, provided the original work is properly cited and the use is non-commercial. See: https://creativecommons.org/Licenses/by-nc/4.0/

Country/Territory of origin: China

ORCID number: Rui Li 0000-0002-5716-9259.

S-Editor: Liu JH
L-Editor: A
P-Editor: Liu JH

REFERENCES

1 **Jefferies JL**, Towbin JA. Dilated cardiomyopathy. *Lancet* 2010; **375**: 752-762 [PMID: 20189027 DOI: 10.1016/S0140-6736(09)62023-7]

2 **Gulati A**, Jabbour A, Ismail TF, Guha K, Khwaja J, Raza S, Morarji K, Brown TD, Ismail NA, Dweck MR, Di Pietro E, Roughton M, Wage R, Daryani Y, O'Hanlon R, Sheppard MN, Alpendurada F, Lyon AR, Cook SA, Cowie MR, Assomull RG, Pennell DJ, Prasad SK. Association of fibrosis with mortality and sudden cardiac death in patients with nonischemic dilated cardiomyopathy. *JAMA* 2013; **309**: 896-908 [PMID: 23462786 DOI: 10.1001/jama.2013.1363]

3 **Leyva F**, Taylor RJ, Foley PW, Umar F, Mulligan LJ, Patel K, Stegemann B, Haddad T, Smith RE, Prasad SK. Left ventricular midwall fibrosis as a predictor of mortality and morbidity after cardiac resynchronization therapy in patients with nonischemic cardiomyopathy. *J Am Coll Cardiol* 2012; **60**: 1659-1667 [PMID: 23021326 DOI: 10.1016/j.jacc.2012.05.054]

4 **Halliday BP**, Gulati A, Ali A, Guha K, Newsome S, Arzanauskaite M, Vassiliou VS, Lota A, Izgi C, Tayal U, Khalique Z, Stirrat C, Auger D, Pareek N, Ismail TF, Rosen SD, Vazir A, Alpendurada F, Gregson J, Frenneaux MP, Cowie MR, Cleland JGF, Cook SA, Pennell DJ, Prasad SK. Association Between Midwall Late Gadolinium Enhancement and Sudden Cardiac Death in Patients With Dilated Cardiomyopathy and Mild and Moderate Left Ventricular Systolic Dysfunction. *Circulation* 2017; **135**: 2106-2115 [PMID: 28351901 DOI: 10.1161/CIRCULATIONAHA.116.026910]

5 **Hutton B**, Salanti G, Caldwell DM, Chaimani A, Schmid CH, Cameron C, Ioannidis JP, Straus S, Thorlund K, Jansen JP, Mulrow C, Catalá-López F, Gøtzsche PC, Dickersin K, Boutron I, Altman DG, Moher D. The PRISMA extension statement for reporting of systematic reviews incorporating network meta-analyses of health care interventions: checklist and explanations. *Ann Intern Med* 2015; **162**: 777-784 [PMID: 26030634 DOI: 10.7326/M14-2385]

6 **Halliday BP**, Baksi AJ, Gulati A, Ali A, Newsome S, Izgi C, Arzanauskaite M, Lota A, Tayal U, Vassiliou VS, Gregson J, Alpendurada F, Frenneaux MP, Cook SA, Cleland JGF, Pennell DJ, Prasad SK. Outcome in Dilated Cardiomyopathy Related to the Extent, Location, and Pattern of Late Gadolinium Enhancement. *JACC Cardiovasc Imaging* 2019; **12**: 1645-1655 [PMID: 30219397 DOI: 10.1016/j.jcmg.2018.07.015]

7 **Perazzolo Marra M**, De Lazzari M, Zorzi A, Migliore F, Zilio F, Calore C, Vettor G, Tona F, Tarantini G, Cacciavillani L, Corbetti F, Giorgi B, Miotto D, Thiene G, Basso C, Iliceto S, Corrado D. Impact of the presence and amount of myocardial fibrosis by cardiac magnetic resonance on arrhythmic outcome and sudden cardiac death in nonischemic dilated cardiomyopathy. *Heart Rhythm* 2014; **11**: 856-863 [PMID: 24440822 DOI: 10.1016/j.hrthm.2014.01.014]

8 **Šramko M**, Kubánek M, Tintěra J, Kautznerová D, Weichet J, Malušková J, Franeková J, Kautzner J. Utility of combination of cardiac magnetic resonance imaging and high-sensitivity cardiac troponin T assay in diagnosis of inflammatory cardiomyopathy. *Am J Cardiol* 2013; **111**: 258-264 [PMID: 23102878 DOI: 10.1016/j.amjcard.2012.09.024]

9 **Behera DR**, V K AK, K K NN, S S, Nair KKM, G S, T R K, Gopalakrishnan A, S H. Prognostic value of late gadolinium enhancement in cardiac MRI of non-ischemic dilated cardiomyopathy patients. *Indian Heart J* 2020; **72**: 362-368 [PMID: 33189195 DOI: 10.1016/j.ihj.2020.06.011]

10 **Tateishi E**, Noguchi T, Goto Y, Morita Y, Ishibashi-Ueda H, Yamada N, Kanzaki H, Nishimura K, Miyamoto Y, Anzai T, Ogawa H, Yasuda S. Prognostic impact of blood pressure response plus gadolinium enhancement in dilated cardiomyopathy. *Heart* 2015; **101**: 774-780 [PMID: 25761994 DOI: 10.1136/heartjnl-2014-307007]

11 **Lehrke S**, Lossnitzer D, Schöb M, Steen H, Merten C, Kemmling H, Pribe R, Ehlermann P, Zugck C, Korosoglou G, Giannitsis E, Katus HA. Use of cardiovascular magnetic resonance for risk stratification in chronic heart failure: prognostic value of late gadolinium enhancement in patients with non-ischaemic dilated cardiomyopathy. *Heart* 2011; **97**: 727-732 [PMID: 21097819 DOI: 10.1136/hrt.2010.205542]

12 **Neilan TG**, Coelho-Filho OR, Danik SB, Shah RV, Dodson JA, Verdini DJ, Tokuda M, Daly CA, Tedrow UB, Stevenson WG, Jerosch-Herold M, Ghoshhajra BB, Kwong RY. CMR quantification of myocardial scar provides additive prognostic information in nonischemic cardiomyopathy. *JACC Cardiovasc Imaging* 2013; **6**: 944-954 [PMID: 23932642 DOI: 10.1016/j.jcmg.2013.05.013]

13 **Yamada T**, Hirashiki A, Okumura T, Adachi S, Shimazu S, Shimizu S, Morimoto R, Takeshita K, Naganawa S, Kondo T, Murohara T. Prognostic impact of combined late gadolinium enhancement on cardiovascular magnetic resonance and peak oxygen consumption in ambulatory patients with nonischemic dilated cardiomyopathy. *J Card Fail* 2014; **20**: 825-832 [PMID: 25151210 DOI: 10.1016/j.cardfail.2014.08.005]

14 **Buss SJ**, Breuninger K, Lehrke S, Voss A, Galuschky C, Lossnitzer D, Andre F, Ehlermann P, Franke J, Taeger T, Frankenstein L, Steen H, Meder B, Giannitsis E, Katus HA, Korosoglou G. Assessment of myocardial deformation with cardiac magnetic resonance strain imaging improves risk stratification in patients with dilated cardiomyopathy. *Eur Heart J Cardiovasc Imaging* 2015; **16**: 307-315 [PMID: 25246506 DOI: 10.1093/ehjci/jeu181]

15 **Mikami Y**, Cornhill A, Heydari B, Joncas SX, Almehmadi F, Zahrani M, Bokhari M, Stirrat J, Yee R, Merchant N, Lydell CP, Howarth AG, White JA. Objective criteria for septal fibrosis in non-ischemic dilated cardiomyopathy: validation for the prediction of future cardiovascular events. *J Cardiovasc Magn Reson* 2016; **18**: 82 [PMID: 27839514 DOI: 10.1186/s12968-016-0300-z]

16 **Puntmann VO**, Carr-White G, Jabbour A, Yu CY, Gebker R, Kelle S, Hinojar R, Doltra A, Varma N, Child N, Rogers T, Suna G, Arroyo Ucar E, Goodman B, Khan S, Dabir D, Herrmann E, Zeiher AM, Nagel E; International T1 Multicentre CMR Outcome Study. T1-Mapping and Outcome in Nonischemic Cardiomyopathy: All-Cause Mortality and Heart Failure. *JACC Cardiovasc Imaging* 2016; **9**: 40-50 [PMID: 26762873 DOI: 10.1016/j.jcmg.2015.12.001]

17 **Masci PG**, Barison A, Aquaro GD, Pingitore A, Mariotti R, Balbarini A, Passino C, Lombardi M, Emdin M. Myocardial delayed enhancement in paucisymptomatic nonischemic dilated cardiomyopathy. *Int J Cardiol* 2012; **157**: 43-47 [PMID: 21176853 DOI: 10.1016/j.ijcard.2010.11.005]

18 **Xu Y**, Lin J, Liang Y, Wan K, Li W, Wang J, Zhu Y, Mui D, Wang L, Li Y, Cheng W, Sun J, Zhang Q, Han Y, Chen Y. Prognostic value of left ventricular remodelling index in idiopathic dilated cardiomyopathy. *Eur Heart J Cardiovasc Imaging* 2021; **22**: 1197-1207 [PMID: 32658979 DOI: 10.1093/ehjci/jeaa144]

19 **Barison A**, Aimo A, Mirizzi G, Castiglione V, Ripoli A, Panchetti L, Rossi A, Giannoni A, Startari U, Aquaro GD, Emdin M, Piacenti M. The extent and location of late gadolinium enhancement predict defibrillator shock and cardiac mortality in patients with non-ischaemic dilated cardiomyopathy. *Int J Cardiol* 2020; **307**: 180-186 [PMID: 32067833 DOI: 10.1016/j.ijcard.2020.02.028]

20 **Amzulescu MS**, Rousseau MF, Ahn SA, Boileau L, de Meester de Ravenstein C, Vancraeynest D, Pasquet A, Vanoverschelde JL, Pouleur AC, Gerber BL. Prognostic Impact of Hypertrabeculation and Noncompaction Phenotype in Dilated Cardiomyopathy: A CMR Study. *JACC Cardiovasc Imaging* 2015; **8**: 934-946 [PMID: 26189121 DOI: 10.1016/j.jcmg.2015.04.015]

21 **Alba AC**, Gaztañaga J, Foroutan F, Thavendiranathan P, Merlo M, Alonso-Rodriguez D, Vallejo-García V, Vidal-Perez R, Corros-Vicente C, Barreiro-Pérez M, Pazos-López P, Perez-David E, Dykstra S, Flewitt J, Pérez-Rivera JÁ, Vazquez-Caamaño M, Katz SD, Sinagra G, Køber L, Poole J, Ross H, Farkouh ME, White JA. Prognostic Value of Late Gadolinium Enhancement for the Prediction of Cardiovascular Outcomes in Dilated Cardiomyopathy: An International, Multi-Institutional Study of the MINICOR Group. *Circ Cardiovasc Imaging* 2020; **13**: e010105 [PMID: 32312112 DOI: 10.1161/CIRCIMAGING.119.010105]

22 **Di Marco A**, Brown PF, Bradley J, Nucifora G, Claver E, de Frutos F, Dallaglio PD, Comin-Colet J, Anguera I, Miller CA, Schmitt M. Improved Risk Stratification for Ventricular Arrhythmias and Sudden Death in Patients With Nonischemic Dilated Cardiomyopathy. *J Am Coll Cardiol* 2021; **77**: 2890-2905 [PMID: 34112317 DOI: 10.1016/j.jacc.2021.04.030]

23 **Stecker EC**, Vickers C, Waltz J, Socoteanu C, John BT, Mariani R, McAnulty JH, Gunson K, Jui J, Chugh SS. Population-based analysis of sudden cardiac death with and without left ventricular systolic dysfunction: two-year findings from the Oregon Sudden Unexpected Death Study. *J Am Coll Cardiol* 2006; **47**: 1161-1166 [PMID: 16545646 DOI: 10.1016/j.jacc.2005.11.045]

24 **Becker MAJ**, Cornel JH, van de Ven PM, van Rossum AC, Allaart CP, Germans T. The Prognostic Value of Late Gadolinium-Enhanced Cardiac Magnetic Resonance Imaging in Nonischemic Dilated Cardiomyopathy: A Review and Meta-Analysis. *JACC Cardiovasc Imaging* 2018; **11**: 1274-1284 [PMID: 29680351 DOI: 10.1016/j.jcmg.2018.03.006]

25 **Di Marco A**, Anguera I, Schmitt M, Klem I, Neilan TG, White JA, Sramko M, Masci PG, Barison A, Mckenna P, Mordi I, Haugaa KH, Leyva F, Rodriguez Capitán J, Satoh H, Nabeta T, Dallaglio PD, Campbell NG, Sabaté X, Cequier Á. Late Gadolinium Enhancement and the Risk for Ventricular Arrhythmias or Sudden Death in Dilated Cardiomyopathy: Systematic Review and Meta-Analysis. *JACC Heart Fail* 2017; **5**: 28-38 [PMID: 28017348 DOI: 10.1016/j.jchf.2016.09.017]

26 **Duan X**, Li J, Zhang Q, Zeng Z, Luo Y, Jiang J, Chen Y. Prognostic value of late gadolinium enhancement in dilated cardiomyopathy patients: a meta-analysis. *Clin Radiol* 2015; **70**: 999-1008 [PMID: 26116301 DOI: 10.1016/j.crad.2015.05.007]

27 **Wu KC**, Weiss RG, Thiemann DR, Kitagawa K, Schmidt A, Dalal D, Lai S, Bluemke DA, Gerstenblith G, Marbán E, Tomaselli GF, Lima JA. Late gadolinium enhancement by cardiovascular magnetic resonance heralds an adverse prognosis in nonischemic cardiomyopathy. *J Am Coll Cardiol* 2008; **51**: 2414-2421 [PMID: 18565399 DOI: 10.1016/j.jacc.2008.03.018]

28 **Assomull RG**, Prasad SK, Lyne J, Smith G, Burman ED, Khan M, Sheppard MN, Poole-Wilson PA, Pennell DJ. Cardiovascular magnetic resonance, fibrosis, and prognosis in dilated cardiomyopathy. *J Am Coll Cardiol* 2006; **48**: 1977-1985 [PMID: 17112987 DOI: 10.1016/j.jacc.2006.07.049]

29 **Packer M**. What causes sudden death in patients with chronic heart failure and a reduced ejection fraction? *Eur Heart J* 2020; **41**: 1757-1763

[PMID: 31390006 DOI: 10.1093/eurheartj/ehz553]

30 **Kazbanov IV**, ten Tusscher KH, Panfilov AV. Effects of Heterogeneous Diffuse Fibrosis on Arrhythmia Dynamics and Mechanism. *Sci Rep* 2016; **6**: 20835 [PMID: 26861111 DOI: 10.1038/srep20835]

31 **Hsia HH**, Marchlinski FE. Electrophysiology studies in patients with dilated cardiomyopathies. *Card Electrophysiol Rev* 2002; **6**: 472-481 [PMID: 12438831 DOI: 10.1023/a:1021109130276]

32 **Estner HL**, Zviman MM, Herzka D, Miller F, Castro V, Nazarian S, Ashikaga H, Dori Y, Berger RD, Calkins H, Lardo AC, Halperin HR. The critical isthmus sites of ischemic ventricular tachycardia are in zones of tissue heterogeneity, visualized by magnetic resonance imaging. *Heart Rhythm* 2011; **8**: 1942-1949 [PMID: 21798226 DOI: 10.1016/j.hrthm.2011.07.027]

33 **Mahrholdt H**, Wagner A, Deluigi CC, Kispert E, Hager S, Meinhardt G, Vogelsberg H, Fritz P, Dippon J, Bock CT, Klingel K, Kandolf R, Sechtem U. Presentation, patterns of myocardial damage, and clinical course of viral myocarditis. *Circulation* 2006; **114**: 1581-1590 [PMID: 17015795 DOI: 10.1161/CIRCULATIONAHA.105.606509]

34 **McCrohon JA**, Moon JC, Prasad SK, McKenna WJ, Lorenz CH, Coats AJ, Pennell DJ. Differentiation of heart failure related to dilated cardiomyopathy and coronary artery disease using gadolinium-enhanced cardiovascular magnetic resonance. *Circulation* 2003; **108**: 54-59 [PMID: 12821550 DOI: 10.1161/01.CIR.0000078641.19365.4C]

35 **Zhao S**. Letter to the editor: is it time for imaging to level with pathology? *Int J Cardiovasc Imaging* 2020; **36**: 2249-2250 [PMID: 32677022 DOI: 10.1007/s10554-020-01936-z]



Published by **Baishideng Publishing Group Inc**
7041 Koll Center Parkway, Suite 160, Pleasanton, CA 94566, USA
Telephone: +1-925-3991568
E-mail: bpgoffice@wjgnet.com
Help Desk: https://www.f6publishing.com/helpdesk
https://www.wjgnet.com



© 2023 Baishideng Publishing Group Inc. All rights reserved.

ISSN 1949-8470 (online)

World Journal of *Radiology*

World J Radiol 2023 December 28; 15(12): 338-369



Published by Baishideng Publishing Group Inc

WJR

World Journal of Radiology

Contents

Monthly Volume 15 Number 12 December 28, 2023

ORIGINAL ARTICLE

Retrospective Study

338 Deep learning-based magnetic resonance imaging reconstruction for improving the image quality of reduced-field-of-view diffusion-weighted imaging of the pancreas

Takayama Y, Sato K, Tanaka S, Murayama R, Goto N, Yoshimitsu K

Observational Study

350 Factors associated with gastrointestinal stromal tumor rupture and pathological risk: A single-center retrospective study

Liu JZ, Jia ZW, Sun LL

359 Methods for improving colorectal cancer annotation efficiency for artificial intelligence-observer training

Grudza M, Salinel B, Zeien S, Murphy M, Adkins J, Jensen CT, Bay C, Kodibagkar V, Koo P, Dragovich T, Choti MA, Kundranda M, Syeda-Mahmood T, Wang HZ, Chang J

World Journal of Radiology

Monthly Volume 15 Number 12 December 28, 2023

Contents

ABOUT COVER

Peer Reviewer of *World Journal of Radiology*, Lee K Rousslang, MD, Resident Physician, Department of Radiology, Tripler Army Medical Center, Honolulu, HI 96859, United States. lee.k.rousslang.civ@mail.mil

AIMS AND SCOPE

The primary aim of *World Journal of Radiology* (*WJR*, *World J Radiol*) is to provide scholars and readers from various fields of radiology with a platform to publish high-quality basic and clinical research articles and communicate their research findings online.

WJR mainly publishes articles reporting research results and findings obtained in the field of radiology and covering a wide range of topics including state of the art information on cardiopulmonary imaging, gastrointestinal imaging, genitourinary imaging, musculoskeletal imaging, neuroradiology/head and neck imaging, nuclear medicine and molecular imaging, pediatric imaging, vascular and interventional radiology, and women's imaging.

INDEXING/ABSTRACTING

The *WJR* is now abstracted and indexed in PubMed, PubMed Central, Emerging Sources Citation Index (Web of Science), Reference Citation Analysis, China Science and Technology Journal Database, and Superstar Journals Database. The 2023 Edition of Journal Citation Reports® cites the 2022 impact factor (IF) for *WJR* as 2.5; IF without journal self cites: 2.3; 5-year IF: 2.5; Journal Citation Indicator: 0.54.

RESPONSIBLE EDITORS FOR THIS ISSUE

Production Editor: *Si Zhao*; **Production Department Director:** *Xu Guo*; **Editorial Office Director:** *Jia-Ping Yan*.

NAME OF JOURNAL
World Journal of Radiology

ISSN
ISSN 1949-8470 (online)

LAUNCH DATE
January 31, 2009

FREQUENCY
Monthly

EDITORS-IN-CHIEF
Thomas J Vogl

EDITORIAL BOARD MEMBERS
https://www.wjgnet.com/1949-8470/editorialboard.htm

PUBLICATION DATE
December 28, 2023

COPYRIGHT
© 2023 Baishideng Publishing Group Inc

INSTRUCTIONS TO AUTHORS
https://www.wjgnet.com/bpg/gerinfo/204

GUIDELINES FOR ETHICS DOCUMENTS
https://www.wjgnet.com/bpg/GerInfo/287

GUIDELINES FOR NON-NATIVE SPEAKERS OF ENGLISH
https://www.wjgnet.com/bpg/gerinfo/240

PUBLICATION ETHICS
https://www.wjgnet.com/bpg/GerInfo/288

PUBLICATION MISCONDUCT
https://www.wjgnet.com/bpg/gerinfo/208

ARTICLE PROCESSING CHARGE
https://www.wjgnet.com/bpg/gerinfo/242

STEPS FOR SUBMITTING MANUSCRIPTS
https://www.wjgnet.com/bpg/GerInfo/239

ONLINE SUBMISSION
https://www.f6publishing.com

© 2023 Baishideng Publishing Group Inc. All rights reserved. 7041 Koll Center Parkway, Suite 160, Pleasanton, CA 94566, USA
E-mail: bpgoffice@wjgnet.com https://www.wjgnet.com

World Journal of Radiology

Submit a Manuscript: https://www.f6publishing.com

World J Radiol 2023 December 28; 15(12): 338-349

DOI: 10.4329/wjr.v15.i12.338

ISSN 1949-8470 (online)

ORIGINAL ARTICLE

Retrospective Study

Deep learning-based magnetic resonance imaging reconstruction for improving the image quality of reduced-field-of-view diffusion-weighted imaging of the pancreas

Yukihisa Takayama, Keisuke Sato, Shinji Tanaka, Ryo Murayama, Nahoko Goto, Kengo Yoshimitsu

Specialty type: Radiology, nuclear medicine and medical imaging

Provenance and peer review: Unsolicited article; Externally peer reviewed.

Peer-review model: Single blind

Peer-review report's scientific quality classification

Grade A (Excellent): 0
Grade B (Very good): B, B
Grade C (Good): C
Grade D (Fair): 0
Grade E (Poor): 0

P-Reviewer: Zhao CF, China; Xiang-Ke Niu, China

Received: October 22, 2023
Peer-review started: October 22, 2023
First decision: November 2, 2023
Revised: November 12, 2023
Accepted: December 4, 2023
Article in press: December 4, 2023
Published online: December 28, 2023

Yukihisa Takayama, Keisuke Sato, Shinji Tanaka, Ryo Murayama, Nahoko Goto, Kengo Yoshimitsu, Department of Radiology, Faculty of Medicine, Fukuoka University, Fukuoka 8140180, Japan

Corresponding author: Yukihisa Takayama, MD, PhD, Associate Professor, Department of Radiology, Faculty of Medicine, Fukuoka University, 7-45-1 Nanakuma, Jonan-ku, Fukuoka 8140180, Japan. ytakayama@fukuoka-u.ac.jp

Abstract

BACKGROUND

It has been reported that deep learning-based reconstruction (DLR) can reduce image noise and artifacts, thereby improving the signal-to-noise ratio and image sharpness. However, no previous studies have evaluated the efficacy of DLR in improving image quality in reduced-field-of-view (reduced-FOV) diffusion-weighted imaging (DWI) [field-of-view optimized and constrained undistorted single-shot (FOCUS)] of the pancreas. We hypothesized that a combination of these techniques would improve DWI image quality without prolonging the scan time but would influence the apparent diffusion coefficient calculation.

AIM

To evaluate the efficacy of DLR for image quality improvement of FOCUS of the pancreas.

METHODS

This was a retrospective study evaluated 37 patients with pancreatic cystic lesions who underwent magnetic resonance imaging between August 2021 and October 2021. We evaluated three types of FOCUS examinations: FOCUS with DLR (FOCUS-DLR+), FOCUS without DLR (FOCUS-DLR−), and conventional FOCUS (FOCUS-conv). The three types of FOCUS and their apparent diffusion coefficient (ADC) maps were compared qualitatively and quantitatively.

RESULTS

FOCUS-DLR+ (3.62, average score of two radiologists) showed significantly better qualitative scores for image noise than FOCUS-DLR− (2.62) and FOCUS-conv (2.88) ($P < 0.05$). Furthermore, FOCUS-DLR+ showed the highest contrast ratio (CR) between the pancreatic parenchyma and adjacent fat tissue for b-values of 0

and 600 s/mm² (0.72 ± 0.08 and 0.68 ± 0.08) and FOCUS-DLR− showed the highest CR between cystic lesions and the pancreatic parenchyma for the b-values of 0 and 600 s/mm² (0.62 ± 0.21 and 0.62 ± 0.21) ($P < 0.05$), respectively. FOCUS-DLR+ provided significantly higher ADCs of the pancreas and lesion (1.44 ± 0.24 and 3.00 ± 0.66) compared to FOCUS-DLR− (1.39 ± 0.22 and 2.86 ± 0.61) and significantly lower ADCs compared to FOCUS-conv (1.84 ± 0.45 and 3.32 ± 0.70) ($P < 0.05$), respectively.

CONCLUSION

This study evaluated the efficacy of DLR for image quality improvement in reduced-FOV DWI of the pancreas. DLR can significantly denoise images without prolonging the scan time or decreasing the spatial resolution. The denoising level of DWI can be controlled to make the images appear more natural to the human eye. However, this study revealed that DLR did not ameliorate pancreatic distortion. Additionally, physicians should pay attention to the interpretation of ADCs after DLR application because ADCs are significantly changed by DLR.

Key Words: Deep learning-based reconstruction; Magnetic resonance imaging; Reduced field-of-view; Diffusion-weighted imaging; Pancreas

©The Author(s) 2023. Published by Baishideng Publishing Group Inc. All rights reserved.

Core Tip: This study evaluated the efficacy of deep learning-based reconstruction (DLR) for image quality improvement in reduced-field-of-view diffusion-weighted imaging (DWI) of the pancreas. DLR can significantly denoise images without prolonging the scan time or decreasing the spatial resolution. The denoising level of DWI can be controlled to make the images appear more natural to the human eye. However, this study revealed that DLR did not ameliorate pancreatic distortion. Additionally, physicians should pay attention to the interpretation of apparent diffusion coefficients (ADCs) after DLR application because ADCs are significantly changed by DLR.

Citation: Takayama Y, Sato K, Tanaka S, Murayama R, Goto N, Yoshimitsu K. Deep learning-based magnetic resonance imaging reconstruction for improving the image quality of reduced-field-of-view diffusion-weighted imaging of the pancreas. *World J Radiol* 2023; 15(12): 338-349

URL: https://www.wjgnet.com/1949-8470/full/v15/i12/338.htm

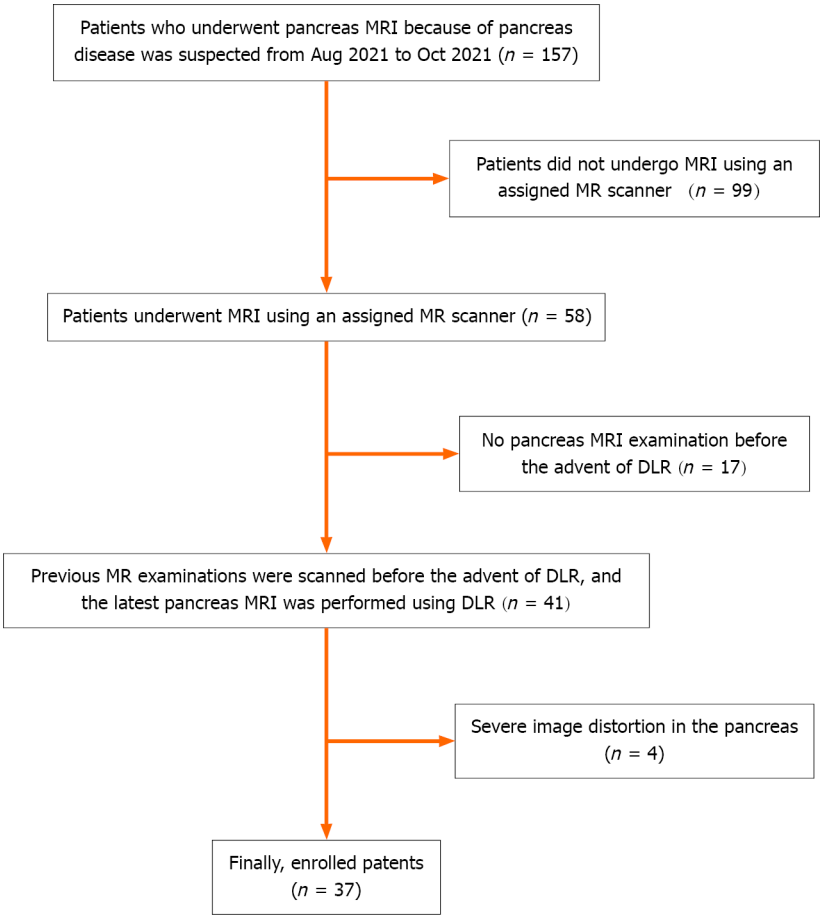
DOI: https://dx.doi.org/10.4329/wjr.v15.i12.338

INTRODUCTION

Diffusion-weighted imaging (DWI) is a widely adopted magnetic resonance imaging (MRI) technique in clinical practice [1-3]. DWI is useful for detecting and characterizing malignant and non-malignant tumors[2,4]. The detection of pancreatic cancer using DWI has been reported to be equivalent to that using dynamic contrast-enhanced computed tomography when DWI is added to magnetic resonance cholangiopancreatography (MRCP)[5,6]. DWI can be used to predict the histological grade of pancreatic neuroendocrine tumors and differentiate malignant from benign intraductal papillary neoplasms (IPMNs)[7-9].

The diagnosis of abdominal lesions based on DWI can be difficult due to artifacts such as motion, ghosting, and distortion; the pancreas is especially susceptible to these artifacts because it exists deep in the abdomen. Reduced-field-of-view (reduced-FOV) DWI is one solution to reduce artifacts in DWI[8,10-13]. In particular, imaging of the pancreas has been shown to improve image quality, such as visualization of anatomical structures, contrast-to-noise ratio (CNR), and lesion conspicuity, and reduce artifacts, such as ghosting, susceptibility, motion, and aliasing artifacts, compared to full-FOV DWI[8,10,14]. Further improvements in the image quality of pancreatic DWI would allow radiologists to detect pancreatic tumors earlier, especially small pancreatic lesions, and help predict tumor malignancy or aggressiveness.

Recently, deep learning (DL) has been applied to radiology for the detection of lesions, evaluation, and image segmentation[9,15,16]. DL is a subcategory of machine learning; therefore, a subset of artificial intelligence[17,18]. DL-based reconstruction (DLR) can reduce image noise and truncation artifacts, improving the signal-to-noise ratio (SNR) and the sharpness of anatomical structures and lesions[9,15,16]. We hypothesized that a combination of reduced-FOV DWI and DLR would improve the DWI image quality of the pancreas without prolonging scan time. To the best of our knowledge, no previous studies have evaluated this hypothesis. This study aimed to evaluate the efficacy of DLR in improving the image quality in reduced-FOV DWI of the pancreas.



DOI: 10.4329/wjr.v15.i12.338 **Copyright** ©The Author(s) 2023.

Figure 1 A summary flowchart of the patient selection. MRI: Magnetic resonance imaging; MR: Magnetic resonance; DLR: Deep learning-based reconstruction.

MATERIALS AND METHODS

Patients

This study was approved by the Institutional Review Board of our hospital. The requirement of written informed consent was waived because this was a retrospective analysis of image post-processing of clinical magnetic resonance (MR) data. Between August 2021 and October 2021, 157 consecutive patients who underwent pancreatic MRI at our institute were investigated. The inclusion criteria were as follows: (1) Patients undergoing annual MRI studies for follow-up of pancreatic cystic lesions; (2) whose MR examinations were performed using an assigned MR scanner; and (3) previous pancreatic MR images were scanned before the advent of DLR, but the latest pancreatic MR images were performed using DLR. Patients were excluded if the pancreas could not be evaluated due to severe distortion. Ultimately, 37 patients [15 females, 22 males; median age (range), 66 years (41–85 years)] were enrolled. Figure 1 shows a flow chart of the patient selection process. Among the 37 patients, 21 were suspected to have IPMN on endoscopic retrograde cholangiopancreatography and/or MRI. The other 16 patients were diagnosed with unspecified pancreatic cystic lesions, such as IPMN and lymphoepithelial cysts, but their diagnosis was not confirmed.

MRI

All examinations were performed using a clinical 3.0-Tesla MR system (Discovery MR750w 3.0T; GE Healthcare, Waukesha, WI, United States). In addition to routine MRI, such as T1-weighted imaging, T2-weighted imaging, full-FOV DWI, and MRCP, each patient underwent reduced-FOV DWI with field-of-view optimized and constrained undistorted single-shot (FOCUS).

The DLR, *i.e.*, AIR™ Recon DL (GE Healthcare), is a vendor-supplied MRI reconstruction algorithm based on a deep convolutional network trained on a database of more than 10000 pairs of artifact-free, high-SNR, high-spatial-resolution image, plus the corresponding low SNR, low-spatial-resolution images[19]. It converts truncation artifacts into improved image sharpness while simultaneously denoising the images[19]. The AIR™ Recon DL was already trained before being installed on the assigned MRI machine, so it was ready to integrate into our MRI reconstruction pipeline. Our motivation for introducing DLR was to improve the image quality of FOCUS of the pancreas, because it suffers from a low SNR and the limitation of not providing good results at higher b-value settings.

Table 1 Details of imaging parameters

Parameters	FOCUS-DLR+/–	FOCUS-conv
Repetition time, ms	3000–10000	3500–15000
Echo time, ms	60	60
Flip angle, degree	90	90
FOV, mm^2	220 × 110	220 × 110
Matrix	120 × 64	130 × 40
FOV reduction	Anterior-posterior	Anterior-posterior
Slice thickness, mm	3	4
Slice gap, mm	3	5
Number of slices	20–30	15–20
Number of excitations	4	8
b-values, s/mm^2	0 and 600	0 and 600
Band width, Hz/pixel	1950	1300
Respiratory compensation	Respiratory-triggered with navigator echo	Respiratory-triggered with or without navigator echo
Deep learning reconstruction factor	Moderate	N/A
Scan time, min	2–5	3–10

The repetition time, number of slices and scan time varied depending on the patients' condition. DLR: Deep learning-based reconstruction; FOCUS: Field-of-view optimized and constrained undistorted single-shot; FOCUS-conv: Conventional field-of-view optimized and constrained undistorted single-shot; FOV: Field of view; N/A: Not applicable.

In this study, three types of FOCUS were evaluated. First, two types of FOCUS images are generated from a single set of raw FOCUS scanning data. One type of FOCUS was reconstructed with the use of DLR; it is referred to hereafter as "FOCUS-DLR+." The other type of FOCUS was reconstructed without DLR ("FOCUS-DLR−"). Furthermore, all enrolled patients had undergone a previous MR examination that included a conventional FOCUS ("FOCUS-conv"), which was widely used in clinical practice before the advent of DLR, and before other improvements that are currently standard on the MR scanner. The average difference (range) in the length of time between FOCUS-DLR+/− and FOCUS-conv was 842.8 (181–2007) d.

The details of the imaging parameters of FOCUS-DLR+/− and FOCUS-conv are shown in Table 1. A two-dimensional (2D) spatially selective echoplanar radiofrequency (RF) excitation pulse was used for FOCUS. This reduces the excitation volume in the phase-encoding and slice-selective directions[11]. In a 2D RF pulse, the displacement between fat and water is designed such that the excited fat profile is completely outside the excited water profile; therefore, a fat-suppression technique is unnecessary[11]. A b-value of 600 s/mm^2 was used as the maximum b-value in this study, because FOCUS-conv with a b-value of 600 s/mm^2 provided acceptable image quality to visualize the pancreatic parenchyma. We also obtained an apparent diffusion coefficient (ADC) map for each type of FOCUS based on the signal intensity (SI) decay of each pixel on DWI with b-values of 0 and 600 s/mm^2.

Image assessment

We conducted qualitative and quantitative comparisons among the three FOCUS types and their ADC maps. The comparison between FOCUS-DLR+ and FOCUS-DLR− was aimed at evaluating DLR by comparing the efficacy of DLR to improve DWI image quality and assessing ADC maps. We also conducted a comparison between FOCUS-DLR+ and FOCUS-conv and between FOCUS-DLR− and FOCUS-conv. This was because the differences between FOCUS-DLR+/− and FOCUS-conv included not only the use of DLR but also updates to the MR scanner, including the update of the MR console to include the AIR™ Recon software.

A study coordinator (Takayama Y, with 23 years of experience in interpreting abdominal MRI) searched and displayed the patients' MRI datasets using a picture archiving and communication system (PACS) (Rapideye, Canon Medical Systems, Tokyo). For qualitative comparison: (1) Sharpness of the pancreatic contour; (2) image noise; (3) distortion of the pancreas; (4) visualization of pancreatic cystic lesions; and (5) visualization of the main pancreatic duct (MPD) were independently evaluated by two radiologists (R1: Tanaka S and R2: Sato K, with 7 and 6 years of experience in interpreting abdominal MRI, respectively), who were blinded to imaging information and the patient's clinical data. (1), (2), (3), and (4) were evaluated using each type of FOCUS with a b-value of 600 s/mm^2, and (5) was evaluated using ADC maps. Qualitative assessments were performed using a 4-point scoring system. The image-quality scores are listed in Table 2.

Table 2 Image-quality scores in the qualitative assessment

Qualitative assessment	1	2	3	4
Sharpness of the pancreas contour	Entire pancreas contour is unclear	< 50% of the pancreas contour is clear	≥ 50% of the pancreas contour is clear	Entire pancreas contour is clear
Image noise	Severe noise; no visualization of any organs	Moderate noise; compromised diagnostic capability of FOCUS is more than ≥ 50% of the image	Mild noise; compromised the diagnostic capability of FOCUS is < 50% of the image	No or slight noise on the image
Distortion of the pancreas	Severe distortion; no visualization of the whole pancreas	Moderate distortion; no visualization is ≥ 50% of the pancreas	Mild distortion; no visualization is < 50% of the pancreas	No distortion of the pancreas
Visualization of pancreas cystic lesion	No visualization of pancreas cystic lesion	Pancreas cystic lesion is visible, but its SI is low	Pancreas cystic lesion is visible with high SI, but its contour is unclear	Pancreas cystic lesion is clearly visible with high SI and clear contour
Visualization of MPD on ADC map	No visualization of MPD	Visible MPD is < 50% of the pancreas	Visible MPD is ≥ 50% of the pancreas	Whole MPD is visible

MPD: Main pancreatic duct; ADC: Apparent diffusion coefficient; SI: Signal intensity; FOCUS: Field-of-view optimized and constrained undistorted single-shot.

For quantitative comparison, we calculated the following: (1) Contrast ratios (CRs) between the pancreatic parenchyma and adjacent fat tissue, hereafter referred to as "$CR_{pancreas\text{-}fat}$"; (2) CRs between pancreatic cystic lesion and pancreatic parenchyma ("$CR_{lesion\text{-}pancreas}$"); (3) the ADC of pancreatic parenchyma ("$ADC_{pancreas}$"); and (4) the ADC of pancreatic cystic lesions ("ADC_{lesion}") for the three types of FOCUS and their ADC maps after drawing polygonal regions of interest (ROIs) on the pancreatic parenchyma, adjacent fat tissue and pancreatic cystic lesion. CRs were calculated for each type of FOCUS, with b-values of 0 and 600 s/mm^2. CRs and ADCs were evaluated by the same two radiologists (R1 and R2) using the same PACS after completion of the qualitative assessments. $CR_{pancreas\text{-}fat}$ and $CR_{lesion\text{-}pancreas}$ were calculated instead of SNR or CNR because: (1) FOCUS does not include background air within the imaging area; and (2) a parallel imaging technique was used for the scan; thus, it was impossible to measure background air noise. CRs were calculated using the following formula:

$CR_{pancreas\text{-}fat} = (SI_{pancreas} - SI_{fat})/ (SI_{panceras} + SI_{fat})$

$CR_{lesion\text{-}pancreas} = (SI_{lesion} - SI_{pancreas})/ (SI_{lesion} + SI_{pancreas})$

$SI_{pancreas}$ is the SI of the pancreatic parenchyma, SI_{fat} is the SI of adjacent fat tissue, and SI_{lesion} is the SI of the pancreatic cystic lesion. In this study, all CRs are presented as absolute values.

Regarding the calculation of CRs and ADCs, the routine MRI findings of the patients were used for the localization of MPD and pancreatic cystic lesions. To calculate $CR_{pancreas\text{-}fat}$ and $ADC_{pancreas}$, three as-large-as-possible polygonal ROIs were drawn for each patient on the head, body, and tail of the pancreas to avoid MPD, lesions, and artifacts on the FOCUS images using b-values of 0 and 600 s/mm^2. Three additional large-as-possible polygonal ROIs were drawn near the head, body, and tail of the pancreas to avoid vessels, lesions, air, and artifacts for each patient. For $CR_{lesion\text{-}pancreas}$ and ADC_{lesion}, as-large-as-possible polygonal ROIs were drawn within the pancreatic cystic lesion and the adjacent pancreatic parenchyma on the same axial slice where the lesions showed the maximum diameter. If there were several lesions in the pancreas, the largest lesion was selected for the calculation.

The same ROIs were duplicated for the FOCUS-DLR+, FOCUS-DLR−, and ADC maps. ROIs of similar size for FOCUS-conv and its ADC map were drawn as those of FOCUS-DLR+/−. In addition to qualitative and quantitative comparisons, we compared the scan time between FOCUS-DLR+/− and FOCUS-conv.

Statistical analysis

To compare image-quality scores, CRs, and ADCs among the three types of FOCUS, the Friedman test was performed. When the Friedman test showed a significant result, the Bonferroni post-hoc test was performed for pairwise comparisons among the three types of FOCUS.

The inter-reader agreement between the image-quality scores of the two radiologists was analyzed using weighted kappa statistics. The kappa values are interpreted as follows: < 0: No agreement; 0–0.20: Slight agreement; 0.21–0.40: Fair agreement; 0.41–0.60: Moderate agreement; 0.61–0.80: Substantial agreement; and 0.81–1.00: Almost perfect agreement.

Comparisons of CRs and ADCs among the three types of FOCUS were analyzed after the measurement results of the two radiologists were combined because it was difficult for them to draw the same ROIs at the same locations of the pancreatic parenchyma, adjacent fat tissue, and pancreatic cystic lesions. Finally, the paired t-test was performed for the comparison of scan time between FOCUS-DLR+/− and FOCUS-conv. All statistical analyses were performed with IBM SPSS Statistics 25.0 (IBM Japan, Tokyo). For the Friedman test and paired t-test, P values <0.05 were considered significant and $P < 0.0167$ (0.05/3) for the Bonferroni post-hoc test was considered significant.

Table 3 The results of the two radiologists' qualitative assessments

Qualitative assessment	Reader	Mean image-quality score			*P* value			
					Friedman test	Bonferroni post-hoc test		
		FOCUS-DLR+	FOCUS-DLR-	FOCUS-conv		FOCUS-DLR+ *vs* FOCUS-DLR-	FOCUS-DLR+ *vs* FOCUS-conv	FOCUS-DLR- *vs* FOCUS-conv
Sharpness of pancreas contour	R1	3.32	3	2.24	< 0.001[1]	0.31	< 0.001[1]	0.0011
	R2	3.32	3.03	2.05	< 0.001[1]	0.49	< 0.001[1]	< 0.001[1]
Image noise	R1	3.65	2.7	2.86	< 0.00 1[1]	< 0.001[1]	< 0.001[1]	1
	R2	3.59	2.54	2.7	< 0.001[1]	< 0.001[1]	< 0.001[1]	0.97
Distortion of pancreas	R1	3.16	3.11	3.05	0.05	N/A	N/A	N/A
	R2	3.11	3.18	3.05	0.73	N/A	N/A	N/A
Visualization of pancreas cystic lesion	R1	3.7	3.49	2.89	< 0.001[1]	0.67	0.0161	0.35
	R2	3.62	3.32	2.7	< 0.001[1]	0.24	0.0011	0.17
Visualization of MPD on ADC map	R1	2.97	2.54	2.19	< 0.001[1]	0.17	0.0031	0.49
	R2	2.73	2.24	1.99	< 0.001[1]	0.11	0.0011	0.35

[1]A significant difference.

DLR: Deep learning-based reconstruction; FOCUS: Field-of-view optimized and constrained undistorted single-shot; FOCUS-conv: Conventional field-of-view optimized and constrained undistorted single-shot; ADC: Apparent diffusion coefficient; MPD: Main pancreatic duct; N/A: Not available.

RESULTS

Qualitative image assessments

The detailed results of the qualitative assessments by the two radiologists are shown in Table 3. Radiologists obtained similar results. The Friedman test showed significant differences between the three types of FOCUS in image-quality scores for pancreatic contour sharpness, image noise, visualization of pancreatic cystic lesions, and visualization of MPD on the ADC map ($P < 0.05$). There were no significant differences in the image-quality scores for pancreatic distortion among the three types of FOCUS ($P > 0.05$).

The Bonferroni post-hoc test revealed that FOCUS-DLR+ and FOCUS-DLR− showed significantly higher image-quality scores for the sharpness of the pancreas contour than FOCUS-conv ($P < 0.0167$), but there were no significant differences between FOCUS-DLR+ and FOCUS-DLR− ($P > 0.0167$). Regarding image-quality scores of the image noise, FOCUS-DLR+ showed significantly higher scores than FOCUS-DLR− and FOCUS-conv ($P < 0.0167$), but there were no significant differences in scores between FOCUS-DLR− and FOCUS-conv ($P > 0.0167$). FOCUS-DLR+ showed significantly higher image-quality scores for visualization of the pancreatic cystic lesion and visualization of MPD on the ADC map compared to FOCUS-conv ($P < 0.0167$), but there were no significant differences between FOCUS-DLR+ and FOCUS-DLR− or between FOCUS-DLR+ and FOCUS-conv ($P > 0.0167$).

Inter-reader agreements

Table 4 provides the results of the inter-reader agreement between the two radiologists. All qualitative assessments showed significant agreement ($P < 0.001$).

Quantitative image assessments

The average (range) of the ROIs of the pancreatic parenchyma, the adjacent fat tissue, and the cystic lesion of the pancreas drawn by the two radiologists were the following: R1, 170.9 mm² (57.3–325.0 mm²), 235.3 mm² (50.2–791.75 mm²) and 92.7 mm² (22.2–457.6 mm²); R2, 236.3 mm² (72.4–676.53 mm²), 151.5 ± 38.2 mm² (70.9–253.66 mm²) and 104.6 mm² (22.2–551.0 mm²), respectively.

The detailed results of the quantitative assessment are presented in Table 5. The Friedman test showed significant differences between the three types of FOCUS regarding $CR_{pancreas\text{-}fat}$ using b-values of 0 and 600 s/mm², $CR_{lesion\text{-}pancreas}$ using b-values of 0 and 600 s/mm², $ADC_{pancreas}$ and ADC_{lesion} ($P < 0.05$).

The Bonferroni post-hoc test revealed that FOCUS-DLR+ showed significantly higher $CR_{pancreas\text{-}fat}$ using b-values of 0 and 600 s/mm² compared to FOCUS-DLR− and FOCUS-conv, and FOCUS-DLR− showed significantly higher $CR_{pancreas\text{-}fat}$ than FOCUS-conv ($P < 0.0167$).

FOCUS- DLR− showed a significantly higher $CR_{lesion\text{-}pancreas}$ using b-values of 0 and 600 s/mm² compared to FOCUS-DLR+ and FOCUS-conv, and FOCUS-DLR+ showed significantly higher $CR_{lesion\text{-}pancreas}$ than FOCUS-conv ($P < 0.0167$).

Table 4 Inter-reader agreement between the two radiologists

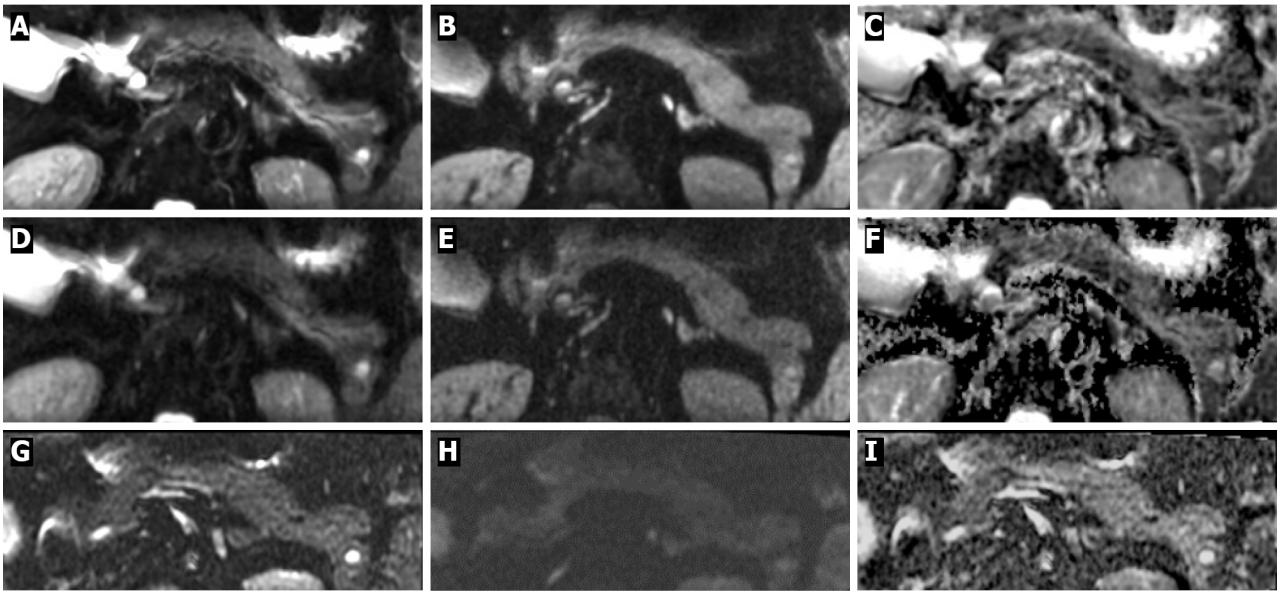
Qualitative assessment	Imaging	κ value (95%CI)	*P* value
Sharpness of pancreas contour	FOCUS-DLR+	0.73 (0.52–0.95)	< 0.001[1]
	FOCUS-DLR-	0.69 (0.45–0.93)	< 0.001[1]
	FOCUS-conv	0.66 (0.43–0.89)	< 0.001[1]
Image noise	FOCUS-DLR+	0.69 (0.46–0.92)	< 0.001[1]
	FOCUS-DLR-	0.70 (0.50–0.90)	< 0.001[1]
	FOCUS-conv	0.64 (0.42–0.87)	< 0.001[1]
Distortion of pancreas	FOCUS-DLR+	0.61 (0.40–0.82)	< 0.001[1]
	FOCUS-DLR-	0.71 (0.53–0.89)	< 0.001[1]
	FOCUS-conv	0.61 (0.41–0.82)	< 0.001[1]
Visualization of pancreas cystic lesion	FOCUS-DLR+	0.80 (0.56–1.03)	< 0.001[1]
	FOCUS-DLR-	0.76 (0.60–0.93)	< 0.001[1]
	FOCUS-conv	0.71 (0.51–0.91)	< 0.001[1]
Visualization of MPD on ADC map	FOCUS-DLR+	0.67 (0.51–0.83)	< 0.001[1]
	FOCUS-DLR-	0.75 (0.60–0.90)	< 0.001[1]
	FOCUS-conv	0.74 (0.54–0.94)	< 0.001[1]

[1]A significant difference. *P* values were obtained by the weighted κ statistic.
κ values: < 0, no agreement; 0–0.20, slight agreement; 0.21–0.40, fair agreement; 0.41–0.60, moderate agreement; 0.61–0.80, substantial agreement; and 0.81–1.00, almost perfect agreement. 95%CI: 95% confidence intervals; DLR: Deep learning-based reconstruction; FOCUS: Field-of-view optimized and constrained undistorted single-shot; FOCUS-conv: Conventional field-of-view optimized and constrained undistorted single-shot; ADC: Apparent diffusion coefficient; MPD: Main pancreatic duct.

Table 5 The results of quantitative assessments

Quantitative assessments	mean ± SD			*P* values			
				Friedman test	Bonferroni post-hoc test		
	FOCUS-DLR+	FOCUS-DLR-	FOCUS-conv		FOCUS-DLR+ *vs* FOCUS-DLR-	FOCUS-DLR+ *vs* FOCUS-conv	FOCUS-DLR- *vs* FOCUS-conv
$CR_{pancreas\text{-}fat}$ on FOCUS with b value of 600 s/mm^2	0.68 ± 0.08	0.49 ± 0.10	0.27 ± 0.11	< 0.001[1]	< 0.001[1]	< 0.001[1]	< 0.001[1]
$CR_{pancreas\text{-}fat}$ on FOCUS with b value of 0 s/mm^2	0.72 ± 0.08	0.65 ± 0.08	0.40 ± 0.11	< 0.001[1]	< 0.001[1]	< 0.001[1]	< 0.001[1]
$CR_{lesion\text{-}pancreas}$ on FOCUS with b value of 600 s/mm^2	0.51 ± 0.26	0.62 ± 0.21	0.01 ± 0.26	< 0.001[1]	< 0.001[1]	< 0.001[1]	< 0.001[1]
$CR_{lesion\text{-}pancreas}$ on FOCUS with b value of 0 s/mm^2	0.53 ± 0.21	0.62 ± 0.21	0.17 ± 0.19	< 0.001[1]	< 0.001[1]	< 0.001[1]	< 0.001[1]
$ADC_{pancreas+}$ (× 10^{-3} mm^2/s)	1.44 ± 0.24	1.39 ± 0.22	1.84 ± 0.45	< 0.001[1]	< 0.001[1]	< 0.001[1]	< 0.001[1]
ADC_{lesion} (× 10^{-3} mm^2/s)	3.00 ± 0.66	2.86 ± 0.61	3.32 ± 0.70	< 0.001[1]	< 0.001[1]	< 0.001[1]	< 0.001[1]

[1]A significant difference.
mean ± SD were calculated from the combined data of two radiologists' measurements. All CRs are presented in absolute values. 95%CI: 95% confidence intervals; DLR: Deep learning-based reconstruction; FOCUS: Field-of-view optimized and constrained undistorted single-shot; FOCUS-conv: Conventional field-of-view optimized and constrained undistorted single-shot; ADC: Apparent diffusion coefficient; MPD: Main pancreatic duct; CR: Contrast ratio.



DOI: 10.4329/wjr.v15.i12.338 **Copyright** ©The Author(s) 2023.

Figure 2 A 45-year-old male with an unspecified pancreas cyst. Reduced-field-of-view diffusion-weighted image [field-of-view optimized and constrained undistorted single-shot (FOCUS)] with b-values of 0 and 600 s/mm^2, and apparent diffusion coefficient (ADC) maps of FOCUS-deep learning-based reconstruction (DLR)+ (A-C), FOCUS-DLR− (D-F), and conventional FOCUS (FOCUS-conv) (G-I). FOCUS-DLR+ provides reduced image noise and better contrast ratio between the pancreas parenchyma and adjacent fat tissue [contrast ratios (CR)$_{pancreas-fat}$] compared to FOCUS-DLR- and FOCUS-conv. Both FOCUS-DLR+ and FOCUS-DLR- show better image-quality scores for sharpness of pancreas contour, CR$_{pancreas-fat}$, and contrast ratio between the pancreas cystic lesion and pancreas parenchyma (CR$_{lesion-pancreas}$) compared to FOCUS-conv. FOCUS-DLR- provides a better CR$_{lesion-pancreas}$ than FOCUS-DLR+, but there is no difference in the image-quality score for visualization of the cystic lesion of the pancreas between FOCUS-DLR+ and FOCUS-DLR-. The average image-quality scores from two radiologists for FOCUS-DLR+, FOCUS-DLR- and FOCUS-conv are as follows: Sharpness of the pancreas contour, 3.5, 3.0, and 2.0; image noise, 3.5, 2.5, and 2.0; and visualization of pancreatic cystic lesion, 3.0, 2.5, 1.0, respectively. The average CR$_{pancreas-fat}$ and CR$_{lesion-pancreas}$ on FOCUS with a b-value of 600 s/mm^2 from two radiologists for FOCUS-DLR+, FOCUS-DLR- and FOCUS-conv are 0.54 and 0.75, 0.38 and 0.81, and 0.23 and 0.10, respectively. The average ADCs of the pancreatic parenchyma and pancreatic cystic lesion of two radiologists for FOCUS-DLR+, FOCUS-DLR- and FOCUS-conv are 1.59 and 2.28, 1.49 and 2.26, and 1.93 and 4.01 (× 10^{-3} mm^2/s), respectively.

FOCUS-conv showed significantly higher ADC$_{pancreas}$ and ADC$_{lesion}$ compared to FOCUS-DLR+ and FOCUS-DLR−, and FOCUS-DLR+ showed significantly higher ADC$_{pancreas}$ and ADC$_{lesion}$ compared to FOCUS-DLR− ($P < 0.0167$).

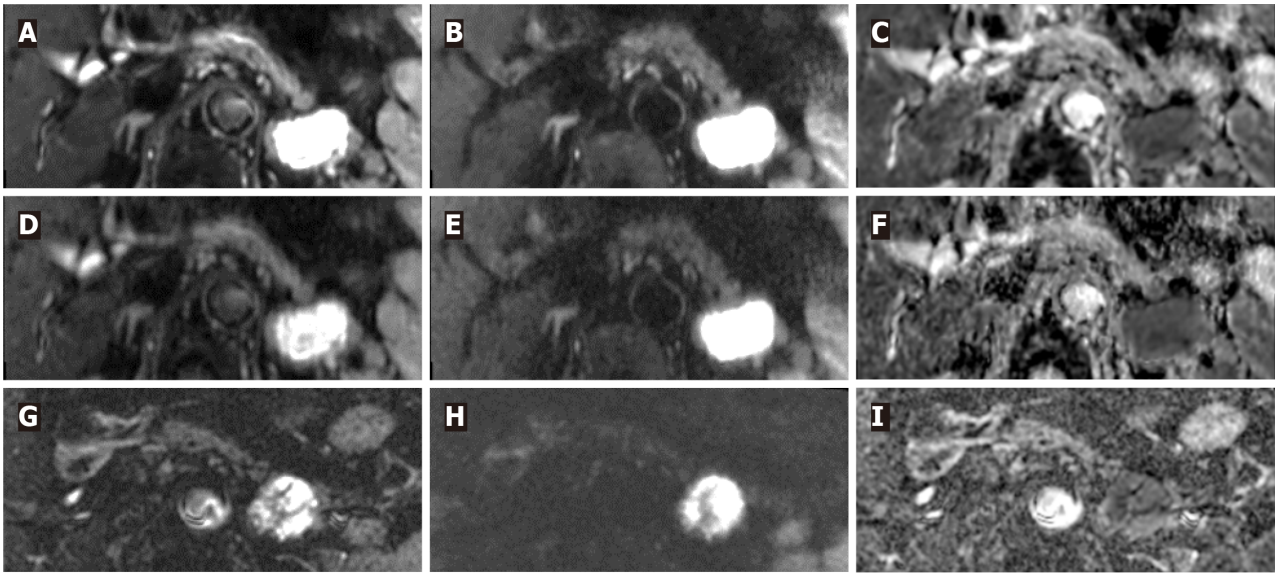
The average scan time of FOCUS-DLR+/− (3 min 27 s) was significantly shorter than that of FOCUS-conv (6 min 28 S) ($P < 0.001$). Figures 2 and 3 show representative images of FOCUS-DLR+, FOCUS-DLR−, and FOCUS-conv.

DISCUSSION

Our findings showed that FOCUS-DLR+ can significantly denoise images without prolonging the scan time or decreasing the spatial resolution compared to FOCUS-DLR− and FOCUS-conv. This result is consistent with studies that analyzed the effectiveness of DLR in brain, musculoskeletal, and prostate MRI examinations[8,16,20]. DLR has demonstrated superiority over other denoising methods. Filter-based noise reduction is commonly applied to data reconstruction pipelines to mitigate image noise[21]. However, this method removes image noise and degrades SIs of structural details, resulting in blurred images[9]. On average, an increased number of signals is also effective in obtaining higher-SNR images; however, this method requires longer scan times[4]. A decrease in spatial resolution can reduce image noise because the image SNR is proportional to the voxel size[11]. However, the decrease in spatial resolution is a disadvantage for diagnosis, especially for the depiction of small lesions.

Another benefit of DLR for denoising is that it can control the level of denoising of DWI to make the images appear more natural to the human eye. DLR can improve CR$_{pancreas-fat}$ on FOCUS using a b-value of 600 s/mm^2, and CR$_{pancreas-fat}$ and CR$_{lesion-pancreas}$ on FOCUS using a b-value of 0 s/mm^2. We speculated that a higher CR would clarify the pancreatic parenchyma and lesions. In fact, FOCUS-DLR− showed higher CR$_{lesion-pancreas}$ than FOCUS-DLR+ with a b-value of 600 s/mm^2. This result could be related to an increased in SIs of the pancreatic parenchyma on FOCUS-DLR+ compared to that on FOCUS-DLR−. However, the results of CR$_{lesion-pancreas}$ on FOCUS with a b-value of 600 s/mm^2 did not indicate that the detection of pancreatic cystic lesions would be affected by the use of DLR. Instead, DLR is helpful to determine whether there is a lesion inside or outside the tissue.

FOCUS-DLR+ showed a higher image-quality score for the sharpness of the pancreas contour compared to FOCUS-conv, but no significant differences were observed between FOCUS-DLR+ and FOCUS-DLR−. We suggest that FOCUS-DLR+ may be effective in visualizing anatomical structures and lesions in the pancreas. DLR has been reported to be useful in improving image sharpness because it can effectively eliminate truncation artifacts, while denoising is



DOI: 10.4329/wjr.v15.i12.338 **Copyright** ©The Author(s) 2023.

Figure 3 A 70-year-old male with an unspecified pancreas cyst. Reduced-field-of-view diffusion-weighted image [field-of-view optimized and constrained undistorted single-shot (FOCUS)] with b-values of 0 and 600 s/mm^2, and apparent diffusion coefficient (ADC) maps of FOCUS-deep learning-based reconstruction (DLR)+ (A-C), FOCUS-DLR- (D-F), and conventional FOCUS (FOCUS-conv) (G-I). FOCUS-DLR+ provides reduced image noise and better contrast ratio between the pancreas parenchyma and adjacent fat tissue [contrast ratios (CR)$_{pancreas-fat}$] compared to FOCUS-DLR- and FOCUS-conv. Both FOCUS-DLR+ and FOCUS-DLR- show better image-quality scores for sharpness of pancreas contour, CR$_{pancreas-fat}$, and contrast ratio between the pancreas cystic lesion and pancreas parenchyma (CR$_{lesion-pancreas}$) compared to FOCUS-conv. FOCUS-DLR- provides a better CR$_{lesion-pancreas}$ than FOCUS-DLR+, but there is no difference in the image-quality score for visualization of the cystic lesion of the pancreas between FOCUS-DLR+ and FOCUS-DLR-. The average image-quality scores from two radiologists for FOCUS-DLR+, FOCUS-DLR- and FOCUS-conv are as follows: Sharpness of the pancreas contour, 4.0, 3.0, and 2.0; image noise, 4.0, 3.0, and 3.0; and visualization of pancreatic cystic lesion, 4.0, 4.0, 3.0, respectively. The average CR$_{pancreas-fat}$ and CR$_{lesion-pancreas}$ on FOCUS with a b-value of 600 s/mm^2 from two radiologists for FOCUS-DLR+, FOCUS-DLR- and FOCUS-conv are 0.54 and 0.75, 0.38 and 0.81, and 0.23 and 0.10, respectively. The average ADCs of the pancreatic parenchyma and pancreatic cystic lesion of two radiologists for FOCUS-DLR+, FOCUS-DLR- and FOCUS-conv are 1.24 and 1.15, 1.20 and 1.15, and 1.98 and 1.60 (× 10^{-3} mm^2/s), respectively.

controlled independently[9,16]. Truncation artifacts are caused by incomplete sampling of high spatial frequencies in the Fourier domain (k-space), creating edge ringing in the final reconstructed image, which can be mitigated by increasing the spatial resolution[11,16]. Reduced-FOV DWI can provide a higher spatial resolution than full-FOV DWI[11]. Thus, reduced-FOV DWI may decrease truncation artifacts, regardless of the application of DLR. We speculated that the improvement in the sharpness of the pancreatic contour could be so subtle that it could be difficult for the human eye to recognize.

Our results also revealed that DLR did not ameliorate pancreatic distortion. No previous study has concluded that DLR could be effective in improving image distortion; therefore, our current findings seem reasonable. We used the single-shot echoplanar imaging sequence, which is occasionally disturbed by distortion artifacts in the phase-encoding direction[8,10,14]. In the present study, the pancreas of some patients was distorted due to adjacent air in the gastrointestinal tract. We concluded that DLR could not modify the severe distortions of pancreatic images in the post-processing pipeline after the scan. To reduce image distortion, air must be removed within the scan area or the parameter settings must be modified.

Regarding the comparison of ADCs, FOCUS-DLR+ showed higher image-quality scores for the visualization of MPD on an ADC map compared to FOCUS-conv, but no significant differences were observed between FOCUS-DLR+ and FOCUS-DLR− or between FOCUS- DLR− and FOCUS-conv. This result may be related to the differences in image noise and CRs among the three types of FOCUS. Generally, MPD shows a higher ADC than the pancreatic parenchyma. The high ADC of the MPD is easy for the human eye to recognize on the ADC map; therefore, the DLR might not influence the qualitative assessment of the visualization of MPD on ADC maps.

ADC$_{pancreas}$ and ADC$_{lesion}$ acquired from FOCUS-DLR+ were significantly higher than those of FOCUS-DLR− and significantly lower than those of FOCUS-conv. ADCs can vary depending on the MRI apparatus, selection of b-values, and the existence of artifacts[13,22]. Image noise on DWI may also affect the calculation of ADC[23]. The ADC metrics derived from reduced-FOV DWI are controversial; both increased and decreased ADCs of reduced-FOV DWI have been reported compared to full-FOV DWI[13]. Our results indicated that ADCs could vary with the use of DLR due to differences in the SIs of the pancreatic parenchyma and pancreatic cystic lesions and in the level of image noise between the three types of FOCUS. Although ADC measurements may be helpful in differentiating malignancy from non-malignancy as a supplement to other imaging modalities, the interpretation of ADCs after DLR requires further study. One limitation of this study is that we were unable to evaluate ADC$_{pancreas}$ or ADC$_{lesion}$ by referring to standard references of pathological findings or larger patient populations. In summary, we could not estimate how DLR affected the calculation results of ADCs and lesion characterization.

There are some limitations to this study. First, we analyzed a small number of patients from a single center. It may be difficult to avoid bias in our results and speculations. A large-scale, multicenter study would be necessary to validate our results. The retrospective design of this study is also a potential source of bias. Second, none of the patients enrolled had solid pancreatic tumors, such as pancreatic carcinoma or neuroendocrine tumors. The diagnosis of such lesions on the FOCUS and ADC maps is of great interest to radiologists. Unfortunately, it was impossible to evaluate these lesions by comparing FOCUS-DLR+/− with FOCUS-conv simply because no patients with such lesions presented for annual follow-up MR examinations. The mechanism by which DLR affects lesion detectability, especially in small pancreatic carcinomas, remains unknown. Third, we used the vendor-supplied DLR that was already trained before being installed on MRI machine. On the other hand, the machine learning model is widely regarded as a black box. It meant that we could not know detailed processes of DLR to improve the image quality of FOCUS-DLR+. Although we evaluated our data using common analysis methods, it might be necessary to prove whether or not our methodology was appropriate to evaluate the effectiveness of DLR. Finally, the b-values used in the analyses of the reduced-FOV were 0 and 600 s/mm^2 for the aforementioned reasons. These b-values make it impossible to compare our findings with those of previous studies.

CONCLUSION

The use of DLR improved the image noise and CRs on FOCUS without prolonging the scan time. However, the interpretation of ADCs on FOCUS, with or without DLR, requires further study.

ARTICLE HIGHLIGHTS

Research background

A combination of these techniques would improve diffusion-weighted imaging (DWI) image quality without prolonging the scan time but would influence the apparent diffusion coefficient calculation.

Research motivation

The image quality of reduced-field-of-view DWI [field-of-view optimized and constrained undistorted single-shot (FOCUS)] of the pancreas suffers from a low signal-to-noise ratio and the limitation of not providing good results at higher b-value settings.

Research objectives

This study aimed to evaluate the efficacy of deep learning-based reconstruction (DLR) for image quality improvement of FOCUS of the pancreas.

Research methods

This was a retrospective study evaluated 37 patients with pancreatic cystic lesions who underwent magnetic resonance imaging between August 2021 and October 2021. We evaluated three types of FOCUS examinations: FOCUS with DLR (FOCUS-DLR+), FOCUS without DLR (FOCUS-DLR−), and conventional FOCUS (FOCUS-conv). The three types of FOCUS and their apparent diffusion coefficient (ADC) maps were compared qualitatively and quantitatively.

Research results

FOCUS-DLR+ (3.62, average score of two radiologists) showed significantly better qualitative scores for image noise than FOCUS-DLR− (2.62) and FOCUS-conv (2.88) ($P < 0.05$). Furthermore, FOCUS-DLR+ showed the highest contrast ratios (CRs) between the pancreatic parenchyma and adjacent fat tissue for b-values of 0 and 600 s/mm^2 (0.72 ± 0.08 and 0.68 ± 0.08) and FOCUS-DLR− showed the highest CR between cystic lesions and the pancreatic parenchyma for the b-values of 0 and 600 s/mm^2 (0.62 ± 0.21, and 0.62 ± 0.21) ($P < 0.05$), respectively. FOCUS-DLR+ provided significantly higher ADCs of the pancreas and lesion (1.44 ± 0.24 and 3.00 ± 0.66) compared to FOCUS-DLR− (1.39 ± 0.22 and 2.86 ± 0.61) and significantly lower ADCs compared to FOCUS-conv (1.84 ± 0.45 and 3.32 ± 0.70) ($P < 0.05$), respectively.

Research conclusions

DLR improved image noise and CRs on FOCUS without prolonging the scan time. However, caution should be exercised when interpreting the ADCs after DLR.

Research perspectives

This study revealed that DLR can significantly denoise images without prolonging the scan time or decreasing the spatial resolution. However, DLR did not ameliorate pancreatic distortion and physicians should pay attention to the interpretation of ADCs after DLR application.

FOOTNOTES

Author contributions: Takayama Y and Yoshimitsu K designed the research and wrote the paper; Sato K, Tanaka S, Murayama R, and Goto N contributed to data collection, data analysis, and all authors approved the final manuscript.

Institutional review board statement: This study was reviewed and approved by the Ethics Committee of Fukuoka University [Approval No. U21-966].

Informed consent statement: The requirement for written informed consent was waived because this was a retrospective analysis of image post-processing of clinical MR data.

Conflict-of-interest statement: The authors declare that they have no conflict of interest.

Data sharing statement: No additional data is available.

Open-Access: This article is an open-access article that was selected by an in-house editor and fully peer-reviewed by external reviewers. It is distributed in accordance with the Creative Commons Attribution NonCommercial (CC BY-NC 4.0) license, which permits others to distribute, remix, adapt, build upon this work non-commercially, and license their derivative works on different terms, provided the original work is properly cited and the use is non-commercial. See: https://creativecommons.org/Licenses/by-nc/4.0/

Country/Territory of origin: Japan

ORCID number: Yukihisa Takayama 0000-0002-2029-9316.

S-Editor: Lin C
L-Editor: A
P-Editor: Lin C

REFERENCES

1 **Kwee TC**, Takahara T, Ochiai R, Nievelstein RA, Luijten PR. Diffusion-weighted whole-body imaging with background body signal suppression (DWIBS): features and potential applications in oncology. *Eur Radiol* 2008; **18**: 1937-1952 [PMID: 18446344 DOI: 10.1007/s00330-008-0968-z]

2 **Qayyum A**. Diffusion-weighted imaging in the abdomen and pelvis: concepts and applications. *Radiographics* 2009; **29**: 1797-1810 [PMID: 19959522 DOI: 10.1148/rg.296095521]

3 **Takahara T**, Imai Y, Yamashita T, Yasuda S, Nasu S, Van Cauteren M. Diffusion weighted whole body imaging with background body signal suppression (DWIBS): technical improvement using free breathing, STIR and high resolution 3D display. *Radiat Med* 2004; **22**: 275-282 [PMID: 15468951]

4 **Takayama Y**, Nishie A, Asayama Y, Ishigami K, Kakihara D, Ushijima Y, Fujita N, Shirabe K, Takemura A, Honda H. Image quality and diagnostic performance of free-breathing diffusion-weighted imaging for hepatocellular carcinoma. *World J Hepatol* 2017; **9**: 657-666 [PMID: 28588750 DOI: 10.4254/wjh.v9.i14.657]

5 **Park MJ**, Kim YK, Choi SY, Rhim H, Lee WJ, Choi D. Preoperative detection of small pancreatic carcinoma: value of adding diffusion-weighted imaging to conventional MR imaging for improving confidence level. *Radiology* 2014; **273**: 433-443 [PMID: 24991989 DOI: 10.1148/radiol.14132563]

6 **Takakura K**, Sumiyama K, Munakata K, Ashida H, Arihiro S, Kakutani H, Tajiri H. Clinical usefulness of diffusion-weighted MR imaging for detection of pancreatic cancer: comparison with enhanced multidetector-row CT. *Abdom Imaging* 2011; **36**: 457-462 [PMID: 21643939 DOI: 10.1007/s00261-011-9728-7]

7 **Jiang D**, Dou W, Vosters L, Xu X, Sun Y, Tan T. Denoising of 3D magnetic resonance images with multi-channel residual learning of convolutional neural network. *Jpn J Radiol* 2018; **36**: 566-574 [PMID: 29982919 DOI: 10.1007/s11604-018-0758-8]

8 **Kim H**, Lee JM, Yoon JH, Jang JY, Kim SW, Ryu JK, Kannengiesser S, Han JK, Choi BI. Reduced Field-of-View Diffusion-Weighted Magnetic Resonance Imaging of the Pancreas: Comparison with Conventional Single-Shot Echo-Planar Imaging. *Korean J Radiol* 2015; **16**: 1216-1225 [PMID: 26576110 DOI: 10.3348/kjr.2015.16.6.1216]

9 **Ogawa R**, Kido T, Nakamura M, Nozaki A, Lebel RM, Mochizuki T. Reconstruction of cardiovascular black-blood T2-weighted image by deep learning algorithm: A comparison with intensity filter. *Acta Radiol Open* 2021; **10**: 20584601211044779 [PMID: 34594576 DOI: 10.1177/20584601211044779]

10 **Tanabe M**, Higashi M, Benkert T, Imai H, Miyoshi K, Kameda F, Ariyoshi S, Ihara K, Ito K. Reduced Field-of-View Diffusion-Weighted Magnetic Resonance Imaging of the Pancreas With Tilted Excitation Plane: A Preliminary Study. *J Magn Reson Imaging* 2021; **54**: 715-720 [PMID: 33704860 DOI: 10.1002/jmri.27590]

11 **Saritas EU**, Cunningham CH, Lee JH, Han ET, Nishimura DG. DWI of the spinal cord with reduced FOV single-shot EPI. *Magn Reson Med* 2008; **60**: 468-473 [PMID: 18666126 DOI: 10.1002/mrm.21640]

12 **Mannelli L**, Monti S, Corrias G, Fung MM, Nyman C, Golia Pernicka JS, Do RKG. Comparison of Navigator Triggering Reduced Field of View and Large Field of View Diffusion-Weighted Imaging of the Pancreas. *J Comput Assist Tomogr* 2019; **43**: 143-148 [PMID: 30119065 DOI: 10.1097/RCT.0000000000000778]

13 **Warndahl BA**, Borisch EA, Kawashima A, Riederer SJ, Froemming AT. Conventional vs. reduced field of view diffusion weighted imaging of the prostate: Comparison of image quality, correlation with histology, and inter-reader agreement. *Magn Reson Imaging* 2018; **47**: 67-76 [PMID: 29103977 DOI: 10.1016/j.mri.2017.10.011]

14 **Donati F**, Casini C, Cervelli R, Morganti R, Boraschi P. Diffusion-weighted MRI of solid pancreatic lesions: Comparison between reduced field-of-view and large field-of-view sequences. *Eur J Radiol* 2021; **143**: 109936 [PMID: 34464906 DOI: 10.1016/j.ejrad.2021.109936]

15 **Yasaka K**, Akai H, Kunimatsu A, Kiryu S, Abe O. Deep learning with convolutional neural network in radiology. *Jpn J Radiol* 2018; **36**: 257-272 [PMID: 29498017 DOI: 10.1007/s11604-018-0726-3]

16 **Wang X**, Ma J, Bhosale P, Ibarra Rovira JJ, Qayyum A, Sun J, Bayram E, Szklaruk J. Novel deep learning-based noise reduction technique for prostate magnetic resonance imaging. *Abdom Radiol (NY)* 2021; **46**: 3378-3386 [PMID: 33580348 DOI: 10.1007/s00261-021-02964-6]

17 **Baştanlar Y**, Ozuysal M. Introduction to machine learning. *Methods Mol Biol* 2014; **1107**: 105-128 [PMID: 24272434 DOI: 10.1007/978-1-62703-748-8_7]

18 **Nilsson TH**, Nelson TM. Delayed monochromatic hue matches indicate characteristics of visual memory. *J Exp Psychol Hum Percept Perform* 1981; **7**: 141-150 [PMID: 6452491 DOI: 10.1037//0096-1523.7.1.141]

19 **Kim M**, Kim HS, Kim HJ, Park JE, Park SY, Kim YH, Kim SJ, Lee J, Lebel MR. Thin-Slice Pituitary MRI with Deep Learning-based Reconstruction: Diagnostic Performance in a Postoperative Setting. *Radiology* 2021; **298**: 114-122 [PMID: 33141001 DOI: 10.1148/radiol.2020200723]

20 **Kidoh M**, Shinoda K, Kitajima M, Isogawa K, Nambu M, Uetani H, Morita K, Nakaura T, Tateishi M, Yamashita Y. Deep Learning Based Noise Reduction for Brain MR Imaging: Tests on Phantoms and Healthy Volunteers. *Magn Reson Med Sci* 2020; **19**: 195-206 [PMID: 31484849 DOI: 10.2463/mrms.mp.2019-0018]

21 **Bouhrara M**, Maring MC, Spencer RG. A simple and fast adaptive nonlocal multispectral filtering algorithm for efficient noise reduction in magnetic resonance imaging. *Magn Reson Imaging* 2019; **55**: 133-139 [PMID: 30149058 DOI: 10.1016/j.mri.2018.08.011]

22 **Zhu J**, Zhang J, Gao JY, Li JN, Yang DW, Chen M, Zhou C, Yang ZH. Apparent diffusion coefficient normalization of normal liver: Will it improve the reproducibility of diffusion-weighted imaging at different MR scanners as a new biomarker? *Medicine (Baltimore)* 2017; **96**: e5910 [PMID: 28099354 DOI: 10.1097/MD.0000000000005910]

23 **Jones DK**, Basser PJ. "Squashing peanuts and smashing pumpkins": how noise distorts diffusion-weighted MR data. *Magn Reson Med* 2004; **52**: 979-993 [PMID: 15508154 DOI: 10.1002/mrm.20283]

World Journal of Radiology

Submit a Manuscript: https://www.f6publishing.com

World J Radiol 2023 December 28; 15(12): 350-358

DOI: 10.4329/wjr.v15.i12.350

ISSN 1949-8470 (online)

ORIGINAL ARTICLE

Observational Study

Factors associated with gastrointestinal stromal tumor rupture and pathological risk: A single-center retrospective study

Jia-Zheng Liu, Zhong-Wen Jia, Ling-Ling Sun

Specialty type: Radiology, nuclear medicine and medical imaging

Provenance and peer review: Unsolicited article; Externally peer reviewed.

Peer-review model: Single blind

Peer-review report's scientific quality classification

Grade A (Excellent): 0
Grade B (Very good): B
Grade C (Good): C
Grade D (Fair): D
Grade E (Poor): E

P-Reviewer: Dimofte GM, Romania; Nishida T, Japan

Received: August 26, 2023
Peer-review started: August 26, 2023
First decision: October 9, 2023
Revised: October 26, 2023
Accepted: December 12, 2023
Article in press: December 12, 2023
Published online: December 28, 2023

Jia-Zheng Liu, Zhong-Wen Jia, Ling-Ling Sun, Department of Radiology, The Fourth Affiliated Hospital of China Medical University, Shenyang 110033, Liaoning Province, China

Corresponding author: Zhong-Wen Jia, PhD, Chief Physician, Department of Radiology, The Fourth Affiliated Hospital of China Medical University, No. 4 Chongshan East Road, Huanggu District, Shenyang 110033, Liaoning Province, China. jiazhongwen@126.com

Abstract

BACKGROUND

Gastrointestinal stromal tumor (GIST) is a rare gastrointestinal mesenchymal tumor with potential malignancy. Once the tumor ruptures, regardless of tumor size and mitotic number, it can be identified into a high-risk group. It is of great significance for the diagnosis, treatment, and prognosis of GIST if non-invasive examination can be performed before surgery to accurately assess the risk of tumor.

AIM

To identify the factors associated with GIST rupture and pathological risk.

METHODS

A cohort of 50 patients with GISTs, as confirmed by postoperative pathology, was selected from our hospital. Clinicopathological and computed tomography data of the patients were collected. Logistic regression analysis was used to evaluate factors associated with GIST rupture and pathological risk grade.

RESULTS

Pathological risk grade, tumor diameter, tumor morphology, internal necrosis, gas-liquid interface, and Ki-67 index exhibited significant associations with GIST rupture ($P < 0.05$). Gender, tumor diameter, tumor rupture, and Ki-67 index were found to be correlated with pathological risk grade of GIST ($P < 0.05$). Multifactorial logistic regression analysis revealed that male gender and tumor diameter ≥ 10 cm were independent predictors of a high pathological risk grade of GIST [odds ratio (OR) = 11.12, 95% confidence interval (95%CI): 1.81-68.52, $P = 0.01$; OR = 22.96, 95%CI: 2.19-240.93, $P = 0.01$]. Tumor diameter ≥ 10 cm, irregular shape, internal necrosis, gas-liquid interface, and Ki-67 index ≥ 10 were identified as independent predictors of a high risk of GIST rupture (OR = 9.67, 95%CI: 2.15-43.56, $P = 0.01$; OR = 35.44, 95%CI: 4.01-313.38, $P < 0.01$; OR = 18.75, 95%CI: 3.40-103.34, $P < 0.01$; OR = 27.00, 95%CI: 3.10-235.02, $P < 0.01$; OR = 4.43, 95%CI: 1.10-

17.92, $P = 0.04$).

CONCLUSION

Tumor diameter, tumor morphology, internal necrosis, gas-liquid, and Ki-67 index are associated with GIST rupture, while gender and tumor diameter are linked to the pathological risk of GIST. These findings contribute to our understanding of GIST and may inform non-invasive examination strategies and risk assessment for this condition.

Key Words: Gastrointestinal stromal tumors; Imaging findings; Tumor rupture; Pathological risk grades

©The Author(s) 2023. Published by Baishideng Publishing Group Inc. All rights reserved.

Core Tip: Gastrointestinal stromal tumor (GIST) biopsy is inconvenient, has a low yield, and easily leads to tumor metastasis. It is of great significance for the diagnosis, treatment, and prognosis of GIST if non-invasive examination can be performed before surgery to accurately assess the risk of tumor. The results of our study found that tumor diameter, tumor morphology, internal necrosis, and gas-liquid interface are related to the rupture of GIST, and sex and tumor diameter are related to the pathological risk of GIST. The results of this study provides ideas for non-invasive examination and risk assessment of GIST.

Citation: Liu JZ, Jia ZW, Sun LL. Factors associated with gastrointestinal stromal tumor rupture and pathological risk: A single-center retrospective study. *World J Radiol* 2023; 15(12): 350-358
URL: https://www.wjgnet.com/1949-8470/full/v15/i12/350.htm
DOI: https://dx.doi.org/10.4329/wjr.v15.i12.350

INTRODUCTION

Gastrointestinal stromal tumor (GIST), a rare mesenchymal tumor of the gastrointestinal tract, presents a potential for malignancy and constitutes 1%-3% of gastrointestinal malignancies[1,2]. Immunohistochemical analysis of GIST typically reveals positive expression of CD117, CD34, or DOG-1[3,4]. Due to its invasive nature and propensity for recurrence and metastasis, the clinical assessment of prognosis following GIST surgery heavily relies on pathological evaluation. However, preoperative selection of appropriate treatment methods lacks a foundation based on pathological assessment. Notably, imaging characteristics of GIST have been observed, and significant disparities in postoperative pathological risk grades have been identified between GISTs exhibiting distinct computed tomography (CT) features prior to surgery, thereby highlighting the crucial role of CT in GIST diagnosis[5,6].

GISTs display unpredictable and variable biological behavior, rendering the distinction between benign and malignant tumors challenging[2,7]. In the early stages, GISTs were classified as either benign or malignant; however, clinical experience has revealed that tumors initially determined as "benign" by histopathology may later metastasize. Consequently, many pathologists advocate for grouping based on pathological risk grades[8,9]. Once the tumor ruptures, irrespective of size and mitotic count, it can be classified into a high-risk group.

GIST biopsy is inconvenient and has a limited yield, and open biopsies can potentially induce tumor metastasis, precluding risk assessment in such cases. Risk assessment cannot be performed for biopsied cases. Therefore, needle biopsy is not recommended prior to surgery for GISTs that can be completely resected[10]. Given the divergent treatment and prognosis of GISTs compared to non-epithelial tumors like lymphoma and schwannoma, preoperative imaging diagnosis and evaluation assume paramount importance. The ability to perform non-invasive examinations before surgery to accurately assess tumor risk would hold significant implications for GIST diagnosis, treatment, and prognosis. In light of this, we postulated that imaging findings possess clinical utility in predicting GIST rupture and pathological risk. Consequently, this study aimed to offer insights into non-invasive examination strategies and risk assessment for GISTs by examining the correlation between imaging findings and GIST rupture and pathological risk.

MATERIALS AND METHODS

Patients

Fifty patients diagnosed with GISTs were included in this retrospective study, following confirmation of the diagnosis through postoperative pathology at our institution. The patients' clinicopathological and CT data were systematically collected. The study cohort consisted of individuals aged between 18 and 84 years, comprising 28 males and 22 females. In order to ensure the reliability and relevance of the data, specific inclusion and exclusion criteria were applied. The inclusion criteria encompassed patients who had undergone biopsy or surgery at our hospital, with complete and well-documented pathological data, clear risk grading, and comprehensive clinical and CT data available. Furthermore, only

primary tumors were considered. Patients who had not undergone CT examination prior to surgery or whose CT image quality was deemed inadequate were excluded. Additionally, cases with uncertain tumor pathological risk grading or those involving tumor relapse were also excluded from the study cohort.

Data collected

In this investigation, we meticulously gathered a comprehensive set of clinical and pathological data from a cohort of 50 patients diagnosed with GISTs. The dataset encompassed crucial patient demographics such as age and gender, as well as pivotal pathological indicators including risk grade, tumor diameter, morphology, necrosis, rupture status, gas-liquid interface, tumor location, mitotic figures, and Ki-67 index. The assessment of pathological risk was meticulously categorized into four distinct levels, namely, very low, low, moderate, and high, enabling a comprehensive evaluation of the disease severity[8,11,12] (Supplementary Table 1).

CT scanning and indicators

Contrast-enhanced CT scanning was performed using a 256-slice computed tomography scanner (Brilliance iCT, Philips) with the following scanning conditions: Peak kilovoltage of 120 and tube current (mA) ranging from 138 to 458. The following parameters were assessed: (1) Tumor diameter: The maximum diameter of the tumor was measured on the coronal image; (2) Tumor morphology: The shape of the tumor was evaluated to determine if it exhibited a regular shape. A tumor with an elliptical or round shape was considered regular; (3) Boundary: The boundary of the tumor was assessed based on the presence of a clear boundary or an unclear boundary. An unclear boundary indicated a potential for invasion; (4) Primary tumor site: The primary tumor site was determined based on the location of the initial lesion; (5) Necrosis: The presence of a necrotic area was determined based on the CT results; and (6) Gas-liquid interface: The presence of a gas-liquid interface was assessed based on the imaging results. These parameters were evaluated to assess the risk factors associated with GIST rupture and pathological risk.

Criteria for tumor rupture

The criteria for tumor rupture included: (1) Tumor rupture or overflow; (2) Presence of bloody ascites; (3) Gastrointestinal perforation at the tumor site; (4) Microscopic infiltration of adjacent organs; (5) Intra-lesional dissection or segmental resection; and (6) Incisional biopsy[12,13].

Statistical analysis

SPSS 26.0 (IBM Corp, Armonk, NY) software was used for statistical analyses. Enumeration data are expressed as frequencies, and statistical analysis was performed by the χ^2 test. Pearson correlation was used to analyze the correlation between age, gender, pathological risk grade, tumor diameter, tumor morphology, internal necrosis, tumor rupture, gas-liquid interface, tumor site, mitotic figures, and Ki-67 index. $P < 0.05$ was considered statistically significant.

RESULTS

Analysis of related factors of GIST rupture

The results of the comparison of clinical data between the unruptured and ruptured GISTs are shown in Table 1. Statistical analysis showed that pathological risk, tumor diameter, tumor morphology, internal necrosis, and gas-liquid interface were associated with GIST rupture ($P < 0.05$). The differences in age, gender, primary site, mitotic count, and Ki-67 index of the ruptured group and the unruptured group were not statistically significant ($P > 0.05$). GISTs with a high pathological risk grade, large tumor diameter, irregular shape, internal tumor necrosis, and gas-fluid interface were prone to rupture.

Analysis of risk factors in GIST patients

The pathological risk grade assessment of GISTs was carried out through various observation indicators of CT images. The results showed that there were 24 cases of low risk, 6 cases of intermediate risk, and 20 cases of high risk. The analysis results showed that gender, tumor diameter, tumor rupture, and Ki-67 index were associated with the pathological risk grade of GISTs ($P < 0.05$) (Table 2). We found that male GIST patients had a higher pathological risk grade, and the longer the tumor diameter, the higher the pathological risk of GISTs. GIST patients whose tumors were prone to rupture had a higher pathological risk grade, multiple gas shadows were common in the central necrotic area of ruptured tumors (Figure 1A), gas-liquid interface (Figure 1B) was visible in the tumor, and pus coating was formed next to the tumor (Figure 1C).

Logistic regression analysis of factors associated with pathologic risk grade of GISTs

The results of the logistic regression analysis of the factors associated with the pathological risk grade of GISTs are shown in Table 3. Multifactorial logistic regression analysis showed that male gender and tumor diameter ≥ 10 cm were independently correlated with a high pathological risk grade of GISTs [odds ratio (OR) = 11.12, 95% confidence interval (95%CI): 1.81-68.52, $P = 0.01$; OR = 22.96, 95%CI: 2.19-240.93, $P = 0.01$].

Table 1 Comparison of clinical data between unruptured and ruptured gastrointestinal stromal tumors

	Unruptured group (*n* = 38)	Rupture group (*n* = 12)	Statistical value	*P* value
Age (yr)	64.79 ± 9.75	57.17 ± 20.61	1.24	0.24
Gender			2.31	0.13
Male	19	9		
Female	19	3		
Pathological risk grade			8.47	0.02
Low risk	21	3		
Intermediate risk	6	0		
High risk	11	9		
Tumor diameter (cm)	3.25 (2, 5.25)	9.0 (4.5, 13.63)	2.60	0.01
Tumor shape			17.56	< 0.01
Irregular	9	11		
Regular	29	1		
Internal necrosis			15.35	< 0.01
No	30	2		
Yes	8	10		
Gas-liquid interface			23.68	< 0.01
Absence	27	1		
Presence	11	11		
Primary site			0.23	0.63
Gastric	22	6		
Small bowel	16	6		
Mitotic count (50/HPF)	6.11 ± 2.60	6.17 ± 1.64	0.08	0.94
Ki-67 index (%)	5.50 (4.75, 8.00)	7.50 (5.00, 14.25)	1.15	0.25

HPF: High-power field.

Logistic regression analysis of factors associated with GIST rupture

The results of the logistic regression analysis of the factors associated with the tumor rupture of GIST are shown in Table 4. Multifactorial logistic regression analysis showed that tumor diameter ≥ 10 cm, irregular shape, internal necrosis, gas-liquid interface, and Ki-67 index ≥ 10 were independently correlated with a high risk of tumor rupture of GISTs (OR = 9.67, 95%CI: 2.15-43.56, $P = 0.01$; OR = 35.44, 95%CI: 4.01-313.38, $P < 0.01$; OR = 18.75, 95%CI: 3.40-103.34, $P < 0.01$; OR = 27.00, 95%CI: 3.10-235.02, $P < 0.01$; OR = 4.43, 95%CI: 1.10-17.92, $P = 0.04$).

DISCUSSION

In this study, our findings indicated that certain factors are associated with the rupture of GISTs in the patients that we screened. These factors include tumor diameter, tumor shape, internal necrosis, and gas-liquid interface. Additionally, we found that being male and having a tumor diameter ≥ 10 cm are independent correlates of a high pathological risk grade of GISTs.

GIST is a gastrointestinal tumor that has seen a significant increase in the incidence and diagnosis rate in recent years. Rupture and bleeding of GISTs are considered to be serious and dangerous complications that require urgent attention[2,14]. The clinical manifestations of spontaneous tumor rupture and hemorrhage are atypical, characterized by a rapid onset. Many patients are admitted to the hospital with acute abdomen, resulting in delayed surgery. Therefore, timely diagnosis and treatment are crucial for improving patient prognosis[15,16].

Tumor rupture is an important risk factor for recurrence after GIST resection and is also an indicator for adjuvant imatinib therapy[13]. Numerous studies have confirmed that tumor rupture is associated with an increased risk of recurrence. For example, Yanagimoto *et al*[17] identified that tumor size, mitotic count, tumor location, and tumor rupture were important prognostic factors for GIST. Hølmebakk *et al*[18] and Nishida *et al*[19] found that tumor rupture was an

Table 2 Analysis of related factors of pathological risk grade of gastrointestinal stromal tumors

	Low risk (*n* = 24)	Intermediate risk (*n* = 6)	High risk (*n* = 20)	χ^2 value	*P* value
Age (yr)				1.94	0.38
< 60	5	2	8		
≥ 60	19	4	12		
Gender				8.10	0.02
Male	9	3	16		
Female	15	3	4		
Tumor diameter (cm)				10.47	0.01
< 10	22	6	11		
≥ 10	2	0	9		
Tumor shape				2.26	0.32
Irregular	9	1	10		
Regular	15	5	10		
Internal necrosis				5.37	0.07
No	18	5	9		
Yes	6	1	11		
Tumor rupture				8.47	0.02
No	21	6	11		
Yes	3	0	9		
Gas-liquid interface				0.79	0.67
Absence	15	3	10		
Presence	9	3	10		
Primary site				3.46	0.18
Gastric	16	4	8		
Small bowel	8	2	12		
Mitotic count (50/HPF)				4.49	0.11
< 5	8	3	3		
≥ 5	16	2	17		
Ki-67 index (%)				6.30	0.04
< 10	21	5	11		
≥ 10	3	1	9		

HPF: High-power field.

independent prognostic factor for recurrence-free survival. These findings highlight the significance of tumor rupture in evaluating the prognosis of GIST patients and its association with the poor outcomes.

Furthermore, approximately half of GIST ruptures are spontaneous and cannot be prevented. Therefore, there is growing interest in studying factors related to tumor rupture[19-22]. Our study identified tumor diameter, tumor shape, internal necrosis, and the presence of gas-liquid interface as factors associated with GIST rupture. Previous research has also reported that larger tumor diameters are associated with a higher risk of rupture[19], and that larger tumors are more likely to experience necrosis in the central region[23]. Positive resection margins have also been strongly linked to tumor rupture[24]. Moreover, the clinical presentation of GISTs, such as an unclear tumor boundary, irregular tumor shape, and the presence of a gas-liquid interface in imaging scans, can indicate aggressive behavior and malignancy. Gas-liquid interface detection in GISTs is currently uncommon, but researchers believe that it predicts severe disease in GIST patients[25-27]. Our study found that necrosis and rupture were more likely to occur when an air-liquid interface was present, and these factors were important indicators of poor prognosis in GIST patients. However, it is important to note that the definition of tumor rupture remains controversial, and consistent standards have yet to be established[18]. Some

Table 3 Logistic regression analysis of factors associated with the pathological risk grade of gastrointestinal stromal tumors

	B	S.E.	Wald	Sig.	Exp (B)	95%CI for Exp (B)	
						Lower	Upper
Age ≥ 60 yr	0.44	0.90	0.24	0.63	1.55	0.27	9.07
Male gender	2.41	0.93	6.75	0.01	11.12	1.81	68.52
Tumor diameter ≥ 10 cm	3.13	1.20	6.83	0.01	22.96	2.19	240.93
Irregular shape	0.50	1.12	0.20	0.65	1.65	0.18	14.92
Internal necrosis	-1.40	1.21	1.35	0.25	0.25	0.02	2.62
Gas-liquid interface	0.50	1.26	0.16	0.69	1.64	0.14	19.48
Small bowel tumor	-0.15	0.87	0.03	0.87	0.87	0.16	4.76
50/HPF ≥ 5	-0.33	0.87	0.14	0.71	0.72	0.13	3.96
Ki-67 index ≥ 10	2.18	1.15	3.56	0.06	8.82	0.92	84.49

95%CI: 95% confidence interval; HPF: High-power field.

Table 4 Logistic regression analysis of factors associated with rupture of gastrointestinal stromal tumors

	B	S.E.	Wald	Sig.	Exp (B)	95%CI for Exp (B)	
						Lower	Upper
Age ≥ 60 yr	0.21	0.71	0.08	0.77	1.23	0.31	4.93
Male gender	-1.10	0.74	2.20	0.14	0.33	0.08	1.43
Tumor diameter ≥ 10 cm	2.27	0.77	8.72	< 0.01	9.67	2.15	43.56
Irregular shape	3.57	1.11	10.30	< 0.01	35.44	4.01	313.38
Internal necrosis	2.93	0.87	11.33	< 0.01	18.75	3.40	103.34
Gas-liquid interface	3.30	1.10	8.91	< 0.01	27.00	3.10	235.02
Small bowel tumor	-0.32	0.66	0.23	0.63	0.73	0.20	2.67
50/HPF ≥ 5	-0.84	0.85	0.97	0.33	0.43	0.08	2.29
Ki-67 index ≥ 10	1.49	0.71	4.36	0.04	4.43	1.10	17.92
High pathological risk grade	-1.31	0.74	3.12	0.08	0.27	0.06	1.16

95%CI: 95% confidence interval; HPF: High-power field.

researchers consider macroscopic damage of tumor pseudocapsule as tumor rupture[19].

In cases of GISTs with high pathological risk grades, CT signs of malignancy include invasive tumor growth, large size with uneven density and unclear boundaries, hemorrhage, liquefaction, necrosis or cystic degeneration, inhomogeneous enhancement on CT enhancement, and the presence of thick tumor blood vessels around the tumor in the arterial phase. Additionally, GISTs metastasizing to other organs and extra-GISTs located outside the gastrointestinal tract are prone to malignancy. Our study found that gender, tumor diameter, rupture, and Ki-67 index were closely associated with pathological risk grades. Lower pathological risk grades of GIST are characterized by slow tumor growth, smaller tumor diameters (usually less than 5.0 cm), round or oval shapes, uniform enhancement on scans, no invasion of surrounding tissues, and no distant organ metastasis. Conversely, higher pathological risk grades indicate worse growth and larger tumor diameters. These tumors are more likely to experience liquefaction and necrosis due to a relative lack of blood supply. Our study suggests that combining CT examination with tumor diameter, morphology, internal necrosis, gas-liquid interface, and Ki-67 index can facilitate early non-invasive assessment of GIST tumor rupture risk, providing valuable information for clinical decision-making. Additionally, clinical diagnostic information can be used to predict the pathological risk grades of GISTs, aiding in further clinical diagnosis and treatment.

There are some limitations to this study that should be acknowledged. First, the small number of GIST samples included warrants further studies with larger sample sizes. Second, the study primarily focused on GIST cases occurring in the gastric and small bowel, which may not fully reflect the relationship between tumor location and tumor rupture and pathological risk grade. Therefore, it is necessary to include more GIST cases in uncommon sites. Lastly, the study lacks information on treatment modalities and the presence of metastases.



DOI: 10.4329/wjr.v15.i12.350 **Copyright** ©The Author(s) 2023.

Figure 1 Computed tomography images of ruptured gastrointestinal stromal tumors. A: Rupture of a giant gastrointestinal stromal tumor at the colosplenic flexure, with multiple gas shadows (arrow) seen in the central necrotic zone; B: Rupture of a small intestinal stromal tumor. The arrow points to the ruptured opening of the tumor, and the gas-liquid interface was seen in the abdominal cavity; C: A ruptured small intestinal stromal tumor. Gas can be seen in the tumor, and the arrow points to the formation of pus coating around the tumor.

CONCLUSION

In summary, our study has substantiated the association between tumor diameter, tumor shape, internal necrosis, and gas-liquid interface with the occurrence of GIST rupture. Furthermore, we have identified gender and tumor diameter as independent factors influencing the pathological risk grade of GISTs. By leveraging the power of CT detection and integrating the aforementioned factors, we have successfully demonstrated the potential of non-invasive early assessment for GIST rupture and pathological risk grade. These findings hold significant promise in enhancing the clinical decision-making process by providing valuable insights.

ARTICLE HIGHLIGHTS

Research background

Gastrointestinal stromal tumor (GIST) is a rare gastrointestinal mesenchymal tumor. It is of great significance for the diagnosis, treatment, and prognosis of GIST if non-invasive examination can be performed before surgery to accurately assess the risk of tumor.

Research motivation

If accurate assessment of GIST tumor risk through non-invasive examination is the focus of this study, it can provide valuable insights into non-invasive examination strategies and risk assessment of GISTs.

Research objectives

To investigate the factors associated with GIST rupture and pathological risk, and provide insights into non-invasive examination techniques and risk assessment for GISTs.

Research methods

A cohort of 50 GIST patients was selected from our hospital. Clinicopathological and CT data of the patients were collected. Logistic regression analysis was used to evaluate factors associated with GIST rupture and pathological risk grade.

Research results

Male gender and tumor diameter ≥ 10 cm were independent predictors of a high pathological risk grade of GISTs [odds ratio (OR) = 11.12, 95% confidence interval (95%CI): 1.81-68.52, P = 0.01; OR = 22.96, 95%CI: 2.19-240.93, P = 0.01]. Tumor diameter ≥ 10 cm, irregular shape, internal necrosis, gas-liquid interface, and Ki-67 index ≥ 10 were identified as independent predictors of a high risk of GIST rupture (OR = 9.67, 95%CI: 2.15-43.56, P = 0.01; OR = 35.44, 95%CI: 4.01-313.38, P < 0.01; OR = 18.75, 95%CI: 3.40-103.34, P < 0.01; OR = 27.00, 95%CI: 3.10-235.02, P < 0.01; OR = 4.43, 95%CI: 1.10-17.92, P = 0.04).

Research conclusions

Tumor diameter, tumor morphology, internal necrosis, gas-liquid interface, and Ki-67 index are associated with GIST rupture, while gender and tumor diameter are linked to the pathological risk of GISTs. These findings contribute to our understanding of GISTs and may inform non-invasive examination strategies and risk assessment for this condition.

Research perspectives

In later studies, we can further verify our conclusions in large-sample clinical studies to better guide clinical non-invasive examination and risk assessment of GISTs.

FOOTNOTES

Author contributions: Jia ZW conceived the idea; Liu JZ and Sun LL collected and analyzed the data; Liu JZ wrote the paper; all the authors discussed the results and contributed to the final manuscript.

Institutional review board statement: The study was reviewed and approved by The Fourth Affiliated Hospital of China Medical University Institutional Review Board.

Informed consent statement: Patients were not required to give informed consent to the study because the analysis used anonymous clinical data that were obtained after each patient agreed to treatment by written consent.

Conflict-of-interest statement: All the authors have no conflicts of interest to disclose.

Data sharing statement: The data used to support the findings of this study are available from the corresponding author upon request.

STROBE statement: The authors have read the STROBE Statement—checklist of items, and the manuscript was prepared and revised according to the STROBE Statement—checklist of items.

Open-Access: This article is an open-access article that was selected by an in-house editor and fully peer-reviewed by external reviewers. It is distributed in accordance with the Creative Commons Attribution NonCommercial (CC BY-NC 4.0) license, which permits others to distribute, remix, adapt, build upon this work non-commercially, and license their derivative works on different terms, provided the original work is properly cited and the use is non-commercial. See: https://creativecommons.org/Licenses/by-nc/4.0/

Country/Territory of origin: China

ORCID number: Zhong-Wen Jia 0009-0003-3835-1666.

S-Editor: Lin C
L-Editor: Wang TQ
P-Editor: Lin C

REFERENCES

1 Gastrointestinal stromal tumours. *Nat Rev Dis Primers* 2021; **7**: 21 [PMID: 33737509 DOI: 10.1038/s41572-021-00262-5]
2 **Ho MY**, Blanke CD. Gastrointestinal stromal tumors: disease and treatment update. *Gastroenterology* 2011; **140**: 1372-6.e2 [PMID: 21420965 DOI: 10.1053/j.gastro.2011.03.017]
3 **Koo DH**, Ryu MH, Kim KM, Yang HK, Sawaki A, Hirota S, Zheng J, Zhang B, Tzen CY, Yeh CN, Nishida T, Shen L, Chen LT, Kang YK. Asian Consensus Guidelines for the Diagnosis and Management of Gastrointestinal Stromal Tumor. *Cancer Res Treat* 2016; **48**: 1155-1166 [PMID: 27384163 DOI: 10.4143/crt.2016.187]
4 **Qi ZP**, Shi Q, Liu JZ, Yao LQ, Xu MD, Cai SL, Li B, Take I, Zhang YQ, Chen WF, Zhong YS, Zhou PH. Efficacy and safety of endoscopic submucosal dissection for submucosal tumors of the colon and rectum. *Gastrointest Endosc* 2018; **87**: 540-548.e1 [PMID: 28987548 DOI: 10.1016/j.gie.2017.09.027]
5 **Choi YR**, Kim SH, Kim SA, Shin CI, Kim HJ, Han JK, Choi BI. Differentiation of large (≥ 5 cm) gastrointestinal stromal tumors from benign subepithelial tumors in the stomach: radiologists' performance using CT. *Eur J Radiol* 2014; **83**: 250-260 [PMID: 24325848 DOI: 10.1016/j.ejrad.2013.10.028]
6 **Teoh WC**, Teo SY, Ong CL. Gastrointestinal stromal tumors presenting as gynecological masses: usefulness of multidetector computed tomography. *Ultrasound Obstet Gynecol* 2011; **37**: 107-109 [PMID: 20737452 DOI: 10.1002/uog.8801]
7 **Ibrahim A**, Chopra S. Succinate Dehydrogenase-Deficient Gastrointestinal Stromal Tumors. *Arch Pathol Lab Med* 2020; **144**: 655-660 [PMID: 31169996 DOI: 10.5858/arpa.2018-0370-RS]
8 **Raut CP**, Espat NJ, Maki RG, Araujo DM, Trent J, Williams TF, Purkayastha DD, DeMatteo RP. Efficacy and Tolerability of 5-Year Adjuvant Imatinib Treatment for Patients With Resected Intermediate- or High-Risk Primary Gastrointestinal Stromal Tumor: The PERSIST-5 Clinical Trial. *JAMA Oncol* 2018; **4**: e184060 [PMID: 30383140 DOI: 10.1001/jamaoncol.2018.4060]
9 **Chu H**, Pang P, He J, Zhang D, Zhang M, Qiu Y, Li X, Lei P, Fan B, Xu R. Value of radiomics model based on enhanced computed tomography in risk grade prediction of gastrointestinal stromal tumors. *Sci Rep* 2021; **11**: 12009 [PMID: 34103619 DOI: 10.1038/s41598-021-91508-5]
10 **Wei ZG**, Han C, Li JD. Treatment Experts Group for Gastrointestinal Stromal. *Shijie Huaren Xiaohua Zazhi* 2010; **18**: 65-69 [DOI: 10.11569/wcjd.v18.i1.65]
11 **Wei SC**, Xu L, Li WH, Li Y, Guo SF, Sun XR, Li WW. Risk stratification in GIST: shape quantification with CT is a predictive factor. *Eur Radiol* 2020; **30**: 1856-1865 [PMID: 31900704 DOI: 10.1007/s00330-019-06561-6]
12 **Fletcher CD**, Berman JJ, Corless C, Gorstein F, Lasota J, Longley BJ, Miettinen M, O'Leary TJ, Remotti H, Rubin BP, Shmookler B, Sobin

LH, Weiss SW. Diagnosis of gastrointestinal stromal tumors: A consensus approach. *Hum Pathol* 2002; **33**: 459-465 [PMID: 12094370 DOI: 10.1053/hupa.2002.123545]

13 **Nishida T**, Hølmebakk T, Raut CP, Rutkowski P. Defining Tumor Rupture in Gastrointestinal Stromal Tumor. *Ann Surg Oncol* 2019; **26**: 1669-1675 [PMID: 30868512 DOI: 10.1245/s10434-019-07297-9]

14 **Faigel DO**, Abulhawa S. Gastrointestinal stromal tumors: the role of the gastroenterologist in diagnosis and risk stratification. *J Clin Gastroenterol* 2012; **46**: 629-636 [PMID: 22858511 DOI: 10.1097/MCG.0b013e3182548f6c]

15 **Blay JY**, Kang YK, Nishida T, von Mehren M. Gastrointestinal stromal tumours. *Nat Rev Dis Primers* 2021; **7**: 22 [PMID: 33737510 DOI: 10.1038/s41572-021-00254-5]

16 **Fan X**, Han H, Sun Z, Zhang L, Chen G, Mzee SAS, Yang H, Chen J. Prognostic Value of Bleeding in Gastrointestinal Stromal Tumors: A Meta-Analysis. *Technol Cancer Res Treat* 2021; **20**: 15330338211034259 [PMID: 34323156 DOI: 10.1177/15330338211034259]

17 **Yanagimoto Y**, Takahashi T, Muguruma K, Toyokawa T, Kusanagi H, Omori T, Masuzawa T, Tanaka K, Hirota S, Nishida T. Re-appraisal of risk classifications for primary gastrointestinal stromal tumors (GISTs) after complete resection: indications for adjuvant therapy. *Gastric Cancer* 2015; **18**: 426-433 [PMID: 24853473 DOI: 10.1007/s10120-014-0386-7]

18 **Hølmebakk T**, Hompland I, Bjerkehagen B, Stoldt S, Bruland ØS, Hall KS, Boye K. Recurrence-Free Survival After Resection of Gastric Gastrointestinal Stromal Tumors Classified According to a Strict Definition of Tumor Rupture: A Population-Based Study. *Ann Surg Oncol* 2018; **25**: 1133-1139 [PMID: 29435684 DOI: 10.1245/s10434-018-6353-5]

19 **Nishida T**, Cho H, Hirota S, Masuzawa T, Chiguchi G, Tsujinaka T; Kinki GIST Study Group. Clinicopathological Features and Prognosis of Primary GISTs with Tumor Rupture in the Real World. *Ann Surg Oncol* 2018; **25**: 1961-1969 [PMID: 29752602 DOI: 10.1245/s10434-018-6505-7]

20 **Hacking S**, Jackson K, Johnston R, Grogan E, Walmsley R, Armstrong L, Coleman J, Grieve J, Robinson S, Frew K, Aujayeb A. GIST-related malignant ascites with large-volume paracentesis complicated by myocardial infarction and tumour rupture. *BMJ Support Palliat Care* 2023; **13**: e93-e95 [PMID: 32792419 DOI: 10.1136/bmjspcare-2020-002506]

21 **Misawa S**, Takeda M, Sakamoto H, Kirii Y, Ota H, Takagi H. Spontaneous rupture of a giant gastrointestinal stromal tumor of the jejunum: a case report and literature review. *World J Surg Oncol* 2014; **12**: 153 [PMID: 24885725 DOI: 10.1186/1477-7819-12-153]

22 **Santoyo-Villalba J**, Triguero-Cabrera J, García-Jiménez A. Acute abdomen secondary to massive bleeding due to rupture of liver metastases of a gastrointestinal stroma tumor. *Cir Cir* 2021; **89**: 93-96 [PMID: 34762635 DOI: 10.24875/CIRU.20001313]

23 **Miettinen M**, Lasota J. Gastrointestinal stromal tumors: pathology and prognosis at different sites. *Semin Diagn Pathol* 2006; **23**: 70-83 [PMID: 17193820 DOI: 10.1053/j.semdp.2006.09.001]

24 **Hølmebakk T**, Bjerkehagen B, Hompland I, Stoldt S, Boye K. Relationship between R1 resection, tumour rupture and recurrence in resected gastrointestinal stromal tumour. *Br J Surg* 2019; **106**: 419-426 [PMID: 30507040 DOI: 10.1002/bjs.11027]

25 **Sureka B**, Bansal K, Arora A. Torricelli-Bernoulli Sign in Gastrointestinal Stromal Tumor. *AJR Am J Roentgenol* 2015; **205**: W468 [PMID: 26397359 DOI: 10.2214/AJR.15.14926]

26 **Fortman BJ**. Torricelli-Bernoulli sign in an ulcerating gastric leiomyosarcoma. *AJR Am J Roentgenol* 1999; **173**: 199-200 [PMID: 10397126 DOI: 10.2214/ajr.173.1.10397126]

27 **Liu T**, Lin G, Peng H, Huang L, Jiang X, Li H, Cai K, Jiang J, Guo L, Du X, Tang J, Zhang W, Chen J, Ye Y. Clinicopathological characteristics and prognosis of gastrointestinal stromal tumors containing air-fluid levels. *PLoS One* 2021; **16**: e0261566 [PMID: 34919581 DOI: 10.1371/journal.pone.0261566]

World Journal of Radiology

Submit a Manuscript: https://www.f6publishing.com

World J Radiol 2023 December 28; 15(12): 359-369

DOI: 10.4329/wjr.v15.i12.359

ISSN 1949-8470 (online)

ORIGINAL ARTICLE

Observational Study

Methods for improving colorectal cancer annotation efficiency for artificial intelligence-observer training

Matthew Grudza, Brandon Salinel, Sarah Zeien, Matthew Murphy, Jake Adkins, Corey T Jensen, Curtis Bay, Vikram Kodibagkar, Phillip Koo, Tomislav Dragovich, Michael A Choti, Madappa Kundranda, Tanveer Syeda-Mahmood, Hong-Zhi Wang, John Chang

Specialty type: Radiology, nuclear medicine and medical imaging

Provenance and peer review: Unsolicited article; Externally peer reviewed.

Peer-review model: Single blind

Peer-review report's scientific quality classification

Grade A (Excellent): 0
Grade B (Very good): B
Grade C (Good): C
Grade D (Fair): 0
Grade E (Poor): 0

P-Reviewer: Fu L, China; Zhu L, China

Received: October 3, 2023
Peer-review started: October 3, 2023
First decision: October 9, 2023
Revised: November 13, 2023
Accepted: December 5, 2023
Article in press: December 5, 2023
Published online: December 28, 2023

Matthew Grudza, School of Biological Health and Systems Engineering, Arizona State University, Tempe, AZ 85287, United States

Brandon Salinel, Phillip Koo, John Chang, Department of Radiology, Banner MD Anderson Cancer Center, Gilbert, AZ 85234, United States

Sarah Zeien, Matthew Murphy, School of Osteopathic Medicine, A.T. Still University, Mesa, AZ 85206, United States

Jake Adkins, Department of Abdominal Imaging, MD Anderson Cancer Center, Houston, TX 77030, United States

Corey T Jensen, Department of Abdominal Imaging, University Texas MD Anderson Cancer Center, Houston, TX 77030, United States

Curtis Bay, Department of Interdisciplinary Sciences, A.T. Still University, Mesa, AZ 85206, United States

Vikram Kodibagkar, School of Biological and Health Systems Engineering, Arizona State University, Tempe, AZ 85287, United States

Tomislav Dragovich, Madappa Kundranda, Division of Cancer Medicine, Banner MD Anderson Cancer Center, Gilbert, AZ 85234, United States

Michael A Choti, Department of Surgical Oncology, Banner MD Anderson Cancer Center, Gilbert, AZ 85234, United States

Tanveer Syeda-Mahmood, Hong-Zhi Wang, IBM Almaden Research Center, IBM, San Jose, CA 95120, United States

Corresponding author: John Chang, MD, PhD, Doctor, Department of Radiology, Banner MD Anderson Cancer Center, 2940 E. Banner Gateway Drive, Suite 315, Gilbert, AZ 85234, United States. changresearch1@gmail.com

Abstract

BACKGROUND

Missing occult cancer lesions accounts for the most diagnostic errors in retro-

spective radiology reviews as early cancer can be small or subtle, making the lesions difficult to detect. Second-observer is the most effective technique for reducing these events and can be economically implemented with the advent of artificial intelligence (AI).

AIM

To achieve appropriate AI model training, a large annotated dataset is necessary to train the AI models. Our goal in this research is to compare two methods for decreasing the annotation time to establish ground truth: Skip-slice annotation and AI-initiated annotation.

METHODS

We developed a 2D U-Net as an AI second observer for detecting colorectal cancer (CRC) and an ensemble of 5 differently initiated 2D U-Net for ensemble technique. Each model was trained with 51 cases of annotated CRC computed tomography of the abdomen and pelvis, tested with 7 cases, and validated with 20 cases from The Cancer Imaging Archive cases. The sensitivity, false positives per case, and estimated Dice coefficient were obtained for each method of training. We compared the two methods of annotations and the time reduction associated with the technique. The time differences were tested using Friedman's two-way analysis of variance.

RESULTS

Sparse annotation significantly reduces the time for annotation particularly skipping 2 slices at a time ($P < 0.001$). Reduction of up to 2/3 of the annotation does not reduce AI model sensitivity or false positives per case. Although initializing human annotation with AI reduces the annotation time, the reduction is minimal, even when using an ensemble AI to decrease false positives.

CONCLUSION

Our data support the sparse annotation technique as an efficient technique for reducing the time needed to establish the ground truth.

Key Words: Artificial intelligence; Colorectal cancer; Detection

©The Author(s) 2023. Published by Baishideng Publishing Group Inc. All rights reserved.

Core Tip: Minimizing diagnostic errors for colorectal cancer may be most effectively performed with artificial intelligence (AI) second observer. Supervised training of AI-observer will require high volume of annotated training cases. Comparing skip-slice annotation and AI-initiated annotation shows that skipping slices does not affect the training outcome while AI-initiated annotation does not significantly improve annotation time.

Citation: Grudza M, Salinel B, Zeien S, Murphy M, Adkins J, Jensen CT, Bay C, Kodibagkar V, Koo P, Dragovich T, Choti MA, Kundranda M, Syeda-Mahmood T, Wang HZ, Chang J. Methods for improving colorectal cancer annotation efficiency for artificial intelligence-observer training. *World J Radiol* 2023; 15(12): 359-369
URL: https://www.wjgnet.com/1949-8470/full/v15/i12/359.htm
DOI: https://dx.doi.org/10.4329/wjr.v15.i12.359

INTRODUCTION

Colorectal cancer (CRC) is the third most common cancer in the United States, developing in about 4.3% of men and 4.0% of women. It is the second highest cause of cancer-related deaths in the United States, responsible for about 53200 deaths per year[1]. Likewise, CRC has also become the third most common cancer in China and is increasing in incidence in major countries such as Brazil and Russia[2]. Although early detection of CRC through established screening can greatly increase survival probability, resistance to the various invasive and noninvasive forms of screening persists[3-5]. This is reflected in the fact that up to 40% of CRC is diagnosed in the emergency department[6]. The rise in CRC incidence in adults younger than 55 also indicates a need for improved detection through non-screening methods[7-9]. Therefore, cross-sectional imaging remains important in early incidental diagnosis of CRC. However, up to 40% of the features of early CRC can be missed by radiologists when analyzing these scans[10-13]. This indicates a need for a "second-observer" to assist the busy radiologist in order to minimize false negatives which can result in reduced survival due to a delay in diagnosis[10].

Artificial intelligence (AI) has the potential to improve early disease detection, as shown by the recently approved algorithm for detecting intracranial hemorrhage on computed tomography (CT) and has been proposed for similar application in gastric cancer[14,15]. This model can be trained with the relatively low 39000 cases because of the low variation in brain anatomy and the simpler disease pattern on CT. CRC varies significantly in location and appearance because of the heterogeneity in anatomy and disease. The model training could be accomplished by using supervised

training (requires ground truth with potentially fewer training cases) rather than unsupervised training (uses more training cases without ground truth).

In supervised training, inputs with established ground-truth is important for training model. Although supervised training requires lower volume of data, the necessary volume of training data is quite large and would require significant amount of time to label the ground-truth by trained personnel[16-18]. Several potential methods for decreasing the time to establish the ground truth for supervised training have been evaluated. These methods include image level labeling, bounding boxes to localize the site of cancer, sparse labeling, and deploying an incompletely trained AI-model for first pass segmentation followed by human adjustment (AI-Init)[19,20]. Image level labeling and bounding box techniques consider different level of image information for localizing cancer and are expected to require significantly less human intervention. However, these may require more cases for training. For true supervised training, the level of annotation contains significantly more detail, which requires human interaction. This human interaction can be minimized with sparse annotation that skips slices during segmentation or having the rudimentarily trained AI algorithm perform the initial segmentation, which is subsequently modified by humans. In this report, we compared the improvement in amount of time spent on annotating the CRC between the last two techniques (sparse annotation by skip-slicing and AI-Init).

MATERIALS AND METHODS

CRC cases

The CRC cases were obtained from our respective cancer centers, which are tertiary and quaternary referral centers, between the years of 2012 through 2018 as well as cases from The Cancer Imaging Archive (TCGA-COAD) public domain images which were used to compare the outcomes of the techniques[21]. Our training and validating cases included 58 CRC cancer cases (27 males and 31 females) and 59 normal cases and consisted of CT scans of the abdomen and pelvis cases with a mixture of intravenous (IV) contrast enhanced and unenhanced studies. 51 of the cancer cases were used for training while 7 were retained for validation. The cases were retrieved from the picture archiving and communications system of the respective institutions and de-identified. The de-identified cases and their annotations were transferred between the research sites and the medical centers through the HIPPA compliant cloud server from Box.com. 20 of the 25 cases (8 males and 12 female) from TCGA-COAD were used to test the outcome of the training using the two different training techniques. The 5 excluded cases did not have clearly identifiable CRC on CT scans. The imaging stage of the 58 CRC cases and the 20 The Cancer Imaging Archive (TCIA) cases are listed in Table 1.

Cancer annotation

The location and slices of the cancer were identified on the CT images using ITK-SNAP (versions 3.6.0 and 3.8.0; www.itksnap.org)[22]. For annotation, the CT axial slices containing the CRC from our cancer center and from TCGA-COAD were identified and a contour outlining the edges of the cancer was drawn using the drawing tool. All the CT slices containing the tumor were segmented. At the time of training, to simulate sparse annotation, the skip-slice training would evenly skip one or two annotated slices among those containing the tumor from being used in training AI methods for every annotated tumor slice used for training. For AI-Init technique, the TCGA-COAD cases were initially segmented by the trained AI-model after training with the 51 CRC and 59 normal cases described in the previous section. This segmented model was then viewed with ITK-SNAP and adjusted to the ground truth established by human segmentation. The time required to fully adjust the contour and to eliminate false positives and to correct the false negatives was recorded for each TCGA-COAD case.

AI algorithm

The AI algorithm used in the project is a 2D U-Net, which is a convolutional neural network (CNN). The U-Net is a popular image segmentation algorithm for medical image segmentation tasks because it requires less training inputs than other techniques and is more robust with small training dataset[23]. In addition, recent research findings show that 2D U-Net has equivalent performance as that of 3D U-Net, but with lower computational requirement[24,25]. Inputs to the CNN consisted of 2D images with 512 × 512 pixels. The training dataset was augmented using the standard affine transformation with up to 30° rotation and up to 30% scale variation applied to the training patches. The CNN uses a 3 × 3 kernel and has 5 encoding layers containing 32, 64, 128, 256, and 512 filters and 5 decoding layers with each layer containing 512, 256, 128, 64, and 32 filters, respectively. Adam optimizer was used for training the model, and the model with the best validation accuracy was chosen. The network was trained using all the training cases, treating each image of a subject's study as a case, with 1 case per batch and trained with 200 epochs. The 7 validation cases were used to choose the optimal model parameters while the 20 TCGA-COAD cases were used to validate the final accuracy of the different techniques. For evaluating the effects of sparse-annotation, the AI model was trained with either all of the slices of annotation or evenly skipping either 1 or 2 slices of annotation for every slice used for training.

In order to determine how to improve the AI-Init technique in establishing the ground-truth, we also developed a simple ensemble model with each individual component of the ensemble being an independently trained 2D U-Net model with a random initiation. This was obtained to improve the specificity of the AI segmentation. To this end, we trained five randomly initialized U-Net models for voting-based model ensemble. Each of these five model is trained as described in the previous paragraph. The difference is that the final decision is based on the voter ensemble inference technique. For voting-based model ensemble, a voxel is labeled as tumor by the algorithm if and only if at least certain number of automatic segmentation models label the voxel as tumor. The U-Net models were also trained with the skip

Table 1 Clinical and protocol details of training and test cases

	Training cases (*n* = 58)	Test cases (*n* = 20)
AJCC stage		
Stage 1	0	5
Stage 2	15	5
Stage 3	14	7
Stage 4	29	3
T stage		
T1	0	2
T2	0	4
T3	21	13
T4	37	1
Location		
Right	39	17
Transverse	3	2
Left	16	1
CT slice thickness (mm)		
7	0	1
5	29	17
3-4	25	0
2 or less	4	2
Contrast		
IV+PO	27	18
IV	22	1
PO	4	1
None	5	0

AJCC: American Joint Commission on Cancer; CT: Computed tomography; IV: Intravenous; PO: Positive oral.

annotation technique (with skip 0, 1, and 2 slices). We then compared the accuracy and number of false positives per case to see how the ensemble method would influence the time required to adjust the segmentation results. For this approach, the model ensemble approach generated 3 unique segmentation algorithms (for each annotation technique) based on whether at least one, two, or three member(s) of the ensemble identified the same lesion. The segmentation was reviewed using ITK-SNAP.

Accuracy and sensitivity analysis

To analyze the algorithm's accuracy, the AI-generated segmentations were compared to ground-truth annotations, which were established as described previously. The AI model generated a DICOM image series for each case with the number of slices for each case ranging from 60-400. The cancer segmented by the AI model was compared to the annotated ground truth in 3D to determine the false positives, false negatives, and the Dice coefficient (DSC). A false positive was considered any segmentation created by the algorithm that did not overlap any part of the ground-truth segmentation. A false negative was considered as any image series with human annotated tumor that was not identified by the algorithm's segmentations. For true positive segmentation, DSC was visually estimated and categorized to be 0%-25%, 26%-50%, and > 50%. We obtained visual estimate as we do not have readily available software for full DSC calculation.

Time analysis for AI-Init and skip-slice annotation methods

In order to measure the amount of time saved by initiating annotation by the rudimentarily-trained AI model (as described earlier), we recorded the time required for annotating the CRC. The time required for initial, full annotation of CRC as well as the time required to adjust the AI produced model were acquired. For adjusting the AI-model, the obtained time included the time to adjust the boundary of the CRC and for erasing the false positives. We randomly selected 3 large, 3 medium, and 3 small CRC from the TCIA dataset and analyzed these times. The sizes of the CRC were

considered small, medium, or large if the lesion spanned ≤ 5 CT slices, 5-15 CT slices, and ≥ 15 CT slices, respectively. The median and average times were calculated. These same 9 cases were used for measuring the time needed to complete skip-slice annotation by annotating every other or every third slices of the tumor mass.

RESULTS

Comparison of training and TCIA datasets

The details of the location of the tumor and the scanning protocols from the training and TCIA testing datasets are listed in Table 1. The training dataset contains more higher stage cancers with 74 % of cases at stage 3 or 4 while the TCIA dataset has 50% of the cases at stage 3 or 4. All of the training cases is T3 or T4 in T-stage, while the TCIA dataset has 70% of the cases being T3 or T4. 67% of the training dataset has right-sided tumor (being defined as ascending colon) while the TCIA test dataset has 85% of the cases being right-sided. In terms of scanning protocol, 50% of the training dataset has 5 mm slice thickness while 90% of the TCIA testing dataset has slice thickness being 5 mm or more. In terms of contrast administration, the training dataset has 47% of the cases with IV and positive oral (PO) contrast while the TCIA dataset has 90% of the cases with both IV and PO contrast. 38% of the training dataset has just IV contrast whereas TCIA data has 5% of cases with IV contrast only.

Segmentations from skip-slice annotation trained AI-model

The AI-models generated by skip-slice annotation did not significantly alter the segmentation outcome of the AI-model. Figure 1 shows two separate cases segmented by the AI-models; although there is very subtle difference in the segmentations, the difference could not be detected by the measure that we chose (false positives per case, sensitivity, and DSC). For all three models, the sensitivity was 80% and the false positive lesions identified per case was 22. The DSC category distribution was 25% for 0-0.25, 60% for 0.26-0.5, and 15% for > 0.5.

Ensemble voting for decreasing false positives per case

Prior to obtaining the AI-initiated annotation, we aimed to minimize the number of false positives per case as the false positives could decrease the efficiency of this technique in establishing the ground-truth. To do this, we chose a simple voting-based ensemble method to reduce the number of false positives per case. When the number of votes required by the ensemble technique for determining tumor segmentation is increased, there is a corresponding drop in false positives per case while there is also a decrease in sensitivity, although the drop in false positives was much greater than the drop in sensitivity. The DSC distribution also shifts toward more cases being in 0 to 0.25 category. These data are shown in Tables 2 and 3. Figures 2 and 3 show an example of both agreement and disagreement between 1- and 2-voter models.

Time needed to adjust AI-Init segmentation and to complete skip-slide annotation

The models from the section above were used to generate the initial annotation of CRC which was then adjusted manually to fit the established ground truth. The amount of time required to modify these annotations to the ground truth was then recorded for 3 randomly selected cases from each of the large, medium, and small tumors. The complexity of these cases was determined as described in the methods section. The amount of time required to adjust these cases is listed in Table 4, along with the median and average. The measured time includes the time needed to remove the false positives as well as contouring the false negative lesions. The data show that AI-Init does decrease the time required to annotate the cases, although a statistical test of the distributions among the measured annotation time from the original, 1-voter, and 2-voter model using the Friedman's two-way analysis of variance by ranks did not yield statistical significance ($P = 0.121$). Some improvement is seen, primarily, with medium sized tumors.

For skip-slice annotation, the actual timed annotation revealed significant reduction in time needed to complete the annotation (Table 4). Although the reduction is not proportional, the differences are significant between full annotation and either skip-1 or skip-2 slice methods, using the Friedman's two-way analysis of variance by ranks. The *P*-values for univariate analysis between fully-annotated and skip-1, fully-annotated and skip 2, and skip-1 and skip-2 annotation style are 0.034, < 0.001, and 0.034. When using multivariate analysis, the same *P*-values are 0.102, < 0.001, and 0.102. This suggests that skipping slices can reduce the labor necessary for establishing the ground-truth for supervised or semi-supervised training of AI models, and in multivariate analysis, the time different is statistically significant when higher number of slices are skipped.

DISCUSSION

Our results provide a direct comparison of annotation techniques for supervised training of AI models as second observer for detecting CRC. Supervised AI-model training by skipping-slices of CRC did not appreciably influence the outcome of segmentation. There were very subtle visual differences, but these were not detectable with the measures used. No significant segmentation difference could be detected when skipping up to 2 slices. For AI-initiated annotation, the model does not improve the time spent annotating large and small cancers, but does show some improvement for medium sized tumors. These methods allow for time-reduction in annotating the ground truth so supervised training of AI-models could be more efficient and allow greater participation by busy radiologists.

Table 2 Sensitivity and false positives/case for ensemble technique

	Single voter	2 voter	3 voter
Sensitivity	0.8	0.6	0.3
False positives/case	21.95	7.55	3.7

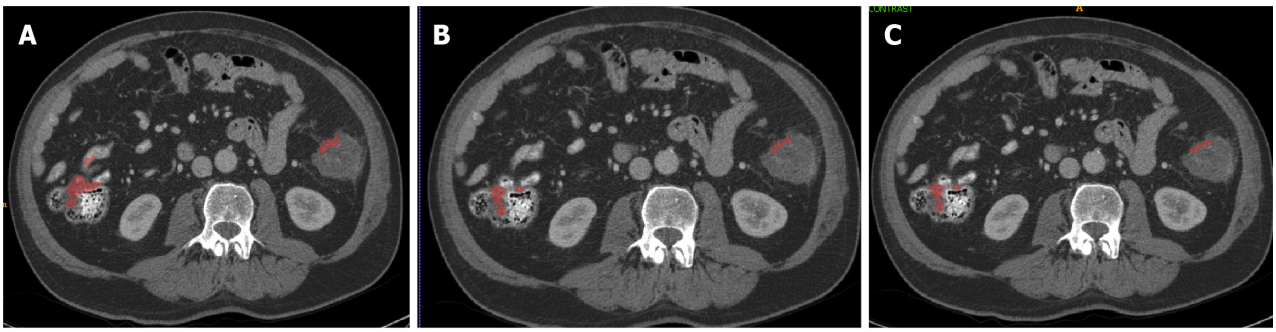
Table 3 Dice coefficient distribution for ensemble technique

Percentage of cases	Estimated dice coefficient			
	0	0-0.25	0.25-0.5	> 0.5
Single voter	20	5	60	15
2 voter	40	35	20	5
3 voter	70	15	10	5

Table 4 Amount of time needed to annotate the tumor

Lesion size	Annotation time based on technique (Min:Sec ± min)				
	Manual (*n* = 3 each)	AI-single voter (*n* = 3 each)	AI-2-voter (*n* = 3 each)	Skip-1 (*n* = 3 each)	Skip-2 (*n* = 3 each)
Large	22:09 ± 0.18	21:00 ± 0.23	20:29 ± 0.22	8:58 ± 1.22	5:34 ± 1.19
Medium	15:06 ± 0.4	10:37 ± 0.25	9:13 ± 0.15	4:58 ± 2.57	1:14 ± 1.38
Small	5:54 ± 0.07	6:26 ± 0.03	5:44 ± 0.02	2:23 ± 0.14	1:24 ± 0.28

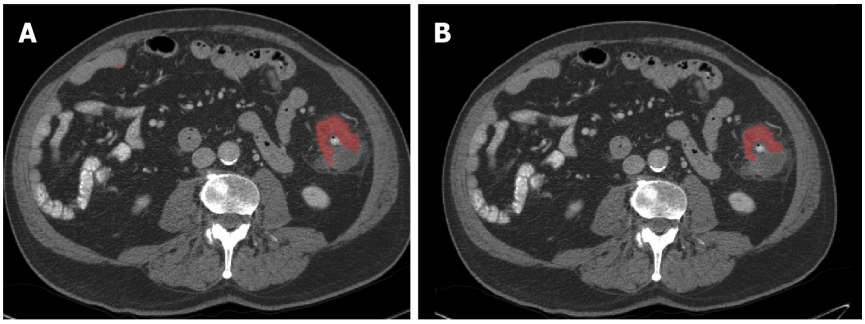
AI: Artificial intelligence.



DOI: 10.4329/wjr.v15.i12.359 **Copyright** ©The Author(s) 2023.

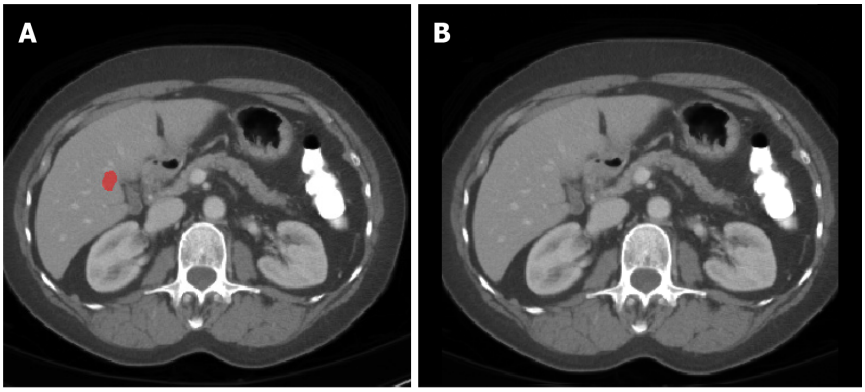
Figure 1 Artificial intelligence segmentation by models with skipped slice training. A-C: Artificial intelligence (AI) segmented lesion by model trained without skipping slices (A), with skipping 1 slice (B), and with skipping 2 slices (C). There is slight difference in the segmentation, but insufficient to modify the Dice coefficient. The cancer is in the descending colon, only a small portion of which was segmented by AI model. The slightly larger false positive lesion may be due to slightly different slice level.

Skip-slice annotation is similar to a sparse-annotation technique, which has been explored in the literature. This technique was tested in confocal images of Xenopus kidney segmentation[19]. Cicek *et al*[19] showed that the DSC equivalent (intersection of union) improved with increasing slices in each axis, starting with one slice in each direction. Increasing the annotated slices was equivalent to increasing the number of ground-truth pixels based on their study. The authors achieved their annotation goal using up to 9% of all the available pixels as ground truth for training. With this training, the network achieved segmentation with 85% overlap with the ground truth. Our data also support this finding that not all ground truth needs to be presented to an AI-algorithm to train the algorithm properly. The difference between Cicek *et al*[19] and our study is that they began with the minimal number of slices while we evaluated from the maximum number of slices. Increasing from the minimum showed that minimalist approach may underfit the algorithm, while maximal approach may over-fit the network. The minimum necessary amount of established ground truth pixel for optimal network training is yet to be identified so that the amount of human effort in establishing ground truth can be minimized while maintaining optimal AI model training.



DOI: 10.4329/wjr.v15.i12.359 **Copyright** ©The Author(s) 2023.

Figure 2 Examples of lesion agreement by 1- and 2-voter ensemble technique. A and B: 1- (A) and 2- (B) voter(s) model agreeing on the same tumor mass, although 2-voters mark less of the mass.



DOI: 10.4329/wjr.v15.i12.359 **Copyright** ©The Author(s) 2023.

Figure 3 Example of lesion disagreement by 1- and 2-voter ensemble technique. A and B: 1- (A) voter model marks a false positive in the liver which is rejected by 2- (B) voter model.

The literature reports multiple techniques for minimizing false positives, particularly regarding pulmonary nodule reduction which can be categorized into ones that use single modes of information (imaging only) or multimodal technique (combines imaging with clinical information). Jin *et al*[26] constructed a false-positive reduction algorithm for pulmonary nodule detection. This is constructed as a separate algorithm that could serve as add on to a nodule detector. They combined several methods to avoid the traps that cause false-positives. First, they deployed a 3D residual CNN which minimizes the effect of diminishing gradient in the stochastic gradient descent algorithm during training, so as to avoid local minima that may trap the algorithm. They also combined spatial pooling and cropping which provides multi-scale contextual information to improve the learning process. A similar technique uses multiscale contextual information where variable amount of the pulmonary nodule and surrounding normal lung is included for training[27,28]. The multiple levels of information are integrated and significantly lower the false positives[27,28]. Lastly, online hard sample selection training was chosen to maximize training of hard-to-discern examples so that the network can learn from its own failures. This technique replaces a portion of correctly detected training cases with ones that were previously missed so that the network can learn the features of the missed cases to improve its outcome[29].

The multimodal technique is a broad category of AI technique where different aspects of a patient's clinical information are integrated to improve the classification and prediction algorithm. The additional information restricts the bias and variance of the model to improve the accuracy of the outcome[30]. For our algorithm, we employed the simulated multimodal technique with ensemble voting by integrating information from different instances of the AI model. This is similar to selecting 5 different models from the same model space to restrict bias and variance[30]. By generating 5 models from the base CNN technique, we chose a lesion to be cancer only if 2 or 3 of the 5 models agreed on a pixel being cancerous. This allowed us to dramatically decrease the number of false positives per case. This, however, also decreased sensitivity of the model. This trade-off is also seen with ensemble techniques trained with clinical data in predicting diabetic retinopathy[31]. Other studies have shown that the information contains different degree of relevance [32,33]. In the study by Boehm *et al*[32], applying all available information regarding a patient (clinical, genetic, histological, and radiological) resulted in less accurate outcome than one that deployed a limited dataset (genetic, histological, and radiological). Likewise the study by Iseke *et al*[33] which used both clinical and imaging information to predict hepatocellular carcinoma recurrence after treatment did not achieve a better prediction than using imaging alone. Multimodal AI can provide better outcomes, but only with the appropriate dataset; overloading the AI system with lower relevance data may over-fit the system to a less than optimal parameter space.

The findings that skip-slice annotation may reduce the time required for establishing the ground-truth for AI model training can significantly impact the development of AI models in imaging research. Annotating the ground truth requires trained personnel capable of identifying normal and abnormal structures on CT images, who are typically physicians or physicians in training. As we have shown in Table 4, full annotation of a case will require anywhere from 5-20 min, which can be reduced significantly with skip-slice annotation. This will significantly reduce the time of the highly trained personnel, who are involved in busy clinical work. Minimizing the time spent in establishing the ground-truth should theoretically improve participation of these highly trained personnel in assisting AI research in medical imaging.

There are several limitations to the present study. The first is the small size of the training and testing dataset. These training and testing dataset is also unbalanced and unmatched in both stage of the disease and the scanning protocol. Table 1 showed that the training dataset consists of higher stage disease than the testing dataset which may limit detection of the earlier stage disease in the testing dataset. In addition, the training dataset also has lower proportion of the cases containing both IV and PO contrast and has thinner slice images. It is uncertain if the blur from the thicker slices may influence the decision of the model, but the trained model have been exposed to thicker slices with IV and PO contrast. It will be interesting to evaluate the dilutive effect on model performance when the model is trained with a broader range of protocols and stages of the disease. The current model with limited training dataset is not generalizable, but it does show the potential of the second observer with better trained model[34]. Another limitation of the study is the lack of full software for calculating the precision, F1 score, and DSC of the model outcome. The sensitivity provided in the present study is equivalent to the recall measure of the model.

CONCLUSION

In comparing the different techniques for reducing annotation time to establish the ground truth, we developed a U-NET model in detecting CRC. This pilot model has the potential to serve as a second observer with further research. In order to accelerate AI second observer training, we compared different techniques of annotation in minimizing this data preparation work. Our results showed that skip slice annotation may lead to the most time reduction as there was minimal effect on model outcome when slices are skipped, leading to proportional decrease in time needed to annotate. Although AI-initiated segmentation may lead to reduced annotation time, it tends to reduce time for medium sized lesion while large complex and small lesions do not benefit. At this time, skipping slices may result in the most time efficient method for annotating cancer on training images.

ARTICLE HIGHLIGHTS

Research background

Up to 40% of colorectal cancer (CRC) goes undetected on initial computed tomography (CT) scan performed in either the emergency department or outpatient imaging setting. This delay in diagnosis significantly impacts the overall survival of the patients. The ultimate goal is to develop an artificial intelligence (AI)-based second observer for clinical integration so as to improve the clinical diagnosis of CRC on CT studies.

Research motivation

The development of deep learning has shown that AI can potentially serve as a second observer to assist busy radiologist at a reasonable cost, as second reader has been shown in past research to improve imaging diagnosis. However, to develop an AI second observer, large number of training cases with annotated ground truth is required necessitating significant time commitment on the part of the research radiologists.

Research objectives

Our main objective in this research is to compare skip-slice annotation with AI-initiated annotation in time savings for annotating the ground truth for training dataset preparation. Saving annotation time will help improve the efficiency in dataset preparation. Our secondary objective was to evaluate whether ensemble technique could help improve false positive rate for AI-initiated annotation technique. Decreasing false positives per case will make the model more acceptable by clinical radiologist.

Research methods

The dataset was manually annotated for the entire tumor as well as skipping annotation by one or two slices was measured; 9 total cases were randomly selected to measure the time required to annotate these tumors. These datasets were used to train 2D U-Net model with 5 encoding and 5 decoding layers, using the Adam optimizer. The model accuracy consisting of sensitivity, Dice coefficient estimate, and false positive per case were used to evaluate the model accuracy. The rudimentary AI model was also used to annotate the ground truth; the times required to adjust the annotation for the 9 cases from manually annotation were also measured.

Research results

We found that the model trained on skip-slice annotation did not have significant difference in tumor segmentation as a

fully annotated dataset and which is statistically significant, thus showing that skip slice annotation can reduce the data preparation time. Although AI-initiated annotation also reduces time, the difference was not statistically significant. Ensemble technique is shown to reduce false positive per case, but at decreased sensitivity.

Research conclusions

This study proposes that skip-slice annotation can improve the efficiency in data preparation for AI model training. The significance is that it will reduce the time commitment of highly trained medical personnel in participating in AI medical imaging research.

Research perspectives

The future direction of the present research is that this should improve the efficiency in training dataset development given the decreased annotation time.

ACKNOWLEDGEMENTS

The authors would like to thank Gene A Hoyer and Judith C Hoyer for their generous support in funding the publication of this manuscript.

FOOTNOTES

Author contributions: Grudza M and Kodibagkar V contributed to the data analysis and initial write up of the manuscript; Salinel B, Zeien S, and Murphy M contributed to the ground truth of the training and testing dataset; Adkins J and Jensen CT contributed to the data curating from MD Anderson; Syeda-Mahmood T and Wang HZ contributed to the AI Model development and training; Bay C contributed to the statistical analysis of the data; Koo P, Dragovich T, Choti MA, and Kundranda M contributed to the Banner MD Anderson data collection and manuscript revision; Chang J conceived and oversaw the entire project and the manuscript writeup.

Institutional review board statement: The study was reviewed and approved by the Banner MD Anderson Cancer Center IRB.

Informed consent statement: The study was approved by Banner MD Anderson Cancer Center IRB with exemption for individual consent due to retrospective nature of the data collection.

Conflict-of-interest statement: All the authors report no relevant conflicts of interest for this article.

Data sharing statement: Dataset can be available by contacting the corresponding author at john.chang@bannerhealth.com.

STROBE statement: The authors have read the STROBE Statement-checklist of items, and the manuscript was prepared and revised according to the STROBE Statement-checklist of items.

Open-Access: This article is an open-access article that was selected by an in-house editor and fully peer-reviewed by external reviewers. It is distributed in accordance with the Creative Commons Attribution NonCommercial (CC BY-NC 4.0) license, which permits others to distribute, remix, adapt, build upon this work non-commercially, and license their derivative works on different terms, provided the original work is properly cited and the use is non-commercial. See: https://creativecommons.org/Licenses/by-nc/4.0/

Country/Territory of origin: United States

ORCID number: Tomislav Dragovich 0000-0002-1569-2172; Madappa Kundranda 0000-0002-9237-2666; John Chang 0000-0003-2896-1586.

S-Editor: Wang JJ
L-Editor: A
P-Editor: Zhao S

REFERENCES

1 **American Cancer Society**. Key Statistics for Colorectal Cancer. [cited 15 July 2023]. Available from: https://www.cancer.org/cancer/types/colon-rectal-cancer/about/key-statistics.html
2 **Xie Y**, Shi L, He X, Luo Y. Gastrointestinal cancers in China, the USA, and Europe. *Gastroenterol Rep (Oxf)* 2021; **9**: 91-104 [PMID: 34026216 DOI: 10.1093/gastro/goab010]
3 **Akram A**, Juang D, Bustamante R, Liu L, Earles A, Ho SB, Wang-Rodriguez J, Allison JE, Gupta S. Replacing the Guaiac Fecal Occult Blood Test With the Fecal Immunochemical Test Increases Proportion of Individuals Screened in a Large Healthcare Setting. *Clin Gastroenterol Hepatol* 2017; **15**: 1265-1270.e1 [PMID: 28167157 DOI: 10.1016/j.cgh.2017.01.025]
4 **Weiser E**, Parks PD, Swartz RK, Thomme JV, Lavin PT, Limburg P, Berger BM. Cross-sectional adherence with the multi-target stool DNA test for colorectal cancer screening: Real-world data from a large cohort of older adults. *J Med Screen* 2021; **28**: 18-24 [PMID: 32054393 DOI:

10.1177/0969141320903756]
5 **Gupta S**. Screening for Colorectal Cancer. *Hematol Oncol Clin North Am* 2022; **36**: 393-414 [PMID: 35501176 DOI: 10.1016/j.hoc.2022.02.001]
6 **Esteva M**, Ruidíaz M, Sánchez MA, Pértega S, Pita-Fernández S, Macià F, Posso M, González-Luján L, Boscá-Wats MM, Leiva A, Ripoll J; DECCIRE GROUP. Emergency presentation of colorectal patients in Spain. *PLoS One* 2018; **13**: e0203556 [PMID: 30273339 DOI: 10.1371/journal.pone.0203556]
7 **Dharwadkar P**, Zaki TA, Murphy CC. Colorectal Cancer in Younger Adults. *Hematol Oncol Clin North Am* 2022; **36**: 449-470 [PMID: 35577711 DOI: 10.1016/j.hoc.2022.02.005]
8 **Fisher DA**, Saoud L, Finney Rutten LJ, Ozbay AB, Brooks D, Limburg PJ. Lowering the colorectal cancer screening age improves predicted outcomes in a microsimulation model. *Curr Med Res Opin* 2021; **37**: 1005-1010 [PMID: 33769894 DOI: 10.1080/03007995.2021.1908244]
9 **Wu Y**, Jiao N, Zhu R, Zhang Y, Wu D, Wang AJ, Fang S, Tao L, Li Y, Cheng S, He X, Lan P, Tian C, Liu NN, Zhu L. Identification of microbial markers across populations in early detection of colorectal cancer. *Nat Commun* 2021; **12**: 3063 [PMID: 34031391 DOI: 10.1038/s41467-021-23265-y]
10 **Rodriguez R**, Perkins B, Park PY, Koo PJ, Kundranda M, Chang JC. Detecting early colorectal cancer on routine CT scan of the abdomen and pelvis can improve patient's 5-year survival. *Arch Biomed Clin Res* 2019; **1**: 1-6 [DOI: 10.15761/ABCR.1000102]
11 **Mangat S**, Kozoriz MG, Bicknell S, Spielmann A. The Accuracy of Colorectal Cancer Detection by Computed Tomography in the Unprepared Large Bowel in a Community-Based Hospital. *Can Assoc Radiol J* 2018; **69**: 92-96 [PMID: 29458958 DOI: 10.1016/j.carj.2017.12.005]
12 **Balthazar EJ**, Megibow AJ, Hulnick D, Naidich DP. Carcinoma of the colon: detection and preoperative staging by CT. *AJR Am J Roentgenol* 1988; **150**: 301-306 [PMID: 3257314 DOI: 10.2214/ajr.150.2.301]
13 **Johnson CD**, Flicek KT, Mead-Harvey C, Quillen JK. Strategies for improving colorectal cancer detection with routine computed tomography. *Abdom Radiol (NY)* 2023; **48**: 1891-1899 [PMID: 36961532 DOI: 10.1007/s00261-023-03884-3]
14 **Arbabshirani MR**, Fornwalt BK, Mongelluzzo GJ, Suever JD, Geise BD, Patel AA, Moore GJ. Advanced machine learning in action: identification of intracranial hemorrhage on computed tomography scans of the head with clinical workflow integration. *NPJ Digit Med* 2018; **1**: 9 [PMID: 31304294 DOI: 10.1038/s41746-017-0015-z]
15 **Cao R**, Tang L, Fang M, Zhong L, Wang S, Gong L, Li J, Dong D, Tian J. Artificial intelligence in gastric cancer: applications and challenges. *Gastroenterol Rep (Oxf)* 2022; **10**: goac064 [PMID: 36457374 DOI: 10.1093/gastro/goac064]
16 **Bangert P**, Moon H, Woo JO, Didari S, Hao H. Active Learning Performance in Labeling Radiology Images Is 90% Effective. *Front Radiol* 2021; **1**: 748968 [PMID: 37492167 DOI: 10.3389/fradi.2021.748968]
17 **Sermesant M**, Delingette H, Cochet H, Jaïs P, Ayache N. Applications of artificial intelligence in cardiovascular imaging. *Nat Rev Cardiol* 2021; **18**: 600-609 [PMID: 33712806 DOI: 10.1038/s41569-021-00527-2]
18 **Willemink MJ**, Koszek WA, Hardell C, Wu J, Fleischmann D, Harvey H, Folio LR, Summers RM, Rubin DL, Lungren MP. Preparing Medical Imaging Data for Machine Learning. *Radiology* 2020; **295**: 4-15 [PMID: 32068507 DOI: 10.1148/radiol.2020192224]
19 **Cicek O**, Abdulkadir A, Lienkamp SS, Brox T, Ronneberger O. 3D U-Net: Learning dense volumetric segmentation from sparse annotation. 2016 Preprint. Available from: arXiv:1606.06650 [DOI: 10.48550/arXiv.1606.06650]
20 **Kervadec H**, Dolz J, Wang S, Granger E, Ayed IB. Bounding boxes for weakly supervised segmentation: Global constraints get close to full supervision. 2004 Preprint. Available from: arXiv:2004.06816v1 [DOI: 10.48550/arXiv.2004.06816]
21 **The Cancer Imaging Archive**. The Cancer Genome Atlas Colon Adenocarcinoma Collection (TCGA-COAD). [cited 15 July 2023]. Available from: https://wiki.cancerimagingarchive.net/pages/viewpage.action?pageId=16712033
22 **Yushkevich PA**, Piven J, Hazlett HC, Smith RG, Ho S, Gee JC, Gerig G. User-guided 3D active contour segmentation of anatomical structures: significantly improved efficiency and reliability. *Neuroimage* 2006; **31**: 1116-1128 [PMID: 16545965 DOI: 10.1016/j.neuroimage.2006.01.015]
23 **Ronneberger O**, Fischer P, Brox T. U-Net: Convolutional networks for biomedical image segmentation. 2015 Preprint. Available from: arXiv:1505.04597v1 [DOI: 10.48550/arXiv.1505.04597]
24 **Srikrishna M**, Heckemann RA, Pereira JB, Volpe G, Zettergren A, Kern S, Westman E, Skoog I, Schöll M. Comparison of Two-Dimensional- and Three-Dimensional-Based U-Net Architectures for Brain Tissue Classification in One-Dimensional Brain CT. *Front Comput Neurosci* 2021; **15**: 785244 [PMID: 35082608 DOI: 10.3389/fncom.2021.785244]
25 **Zettler N**, Mastmeyer A. Comparison of 2D vs. 3D U-Net Organ Segmentation in abdominal 3D CT images. 2021 Preprint. Available from: arXiv:2107.04062v1 [DOI: 10.48550/arXiv.2107.04062]
26 **Jin H**, Li Z, Tong R, Lin L. A deep 3D residual CNN for false-positive reduction in pulmonary nodule detection. *Med Phys* 2018; **45**: 2097-2107 [PMID: 29500816 DOI: 10.1002/mp.12846]
27 **Dou Q**, Chen H, Yu L, Qin J, Heng PA. Multilevel Contextual 3-D CNNs for False Positive Reduction in Pulmonary Nodule Detection. *IEEE Trans Biomed Eng* 2017; **64**: 1558-1567 [PMID: 28113302 DOI: 10.1109/TBME.2016.2613502]
28 **Kim BC**, Yoon JS, Choi JS, Suk HI. Multi-scale gradual integration CNN for false positive reduction in pulmonary nodule detection. *Neural Netw* 2019; **115**: 1-10 [PMID: 30909118 DOI: 10.1016/j.neunet.2019.03.003]
29 **Shrivastava A**, Gupta A, Girschick R. Training region-based object detectors with online hard example mining. 2016 Preprint. Available from: arXiv:1604.03540v1 [DOI: 10.48550/arXiv.1604.03540]
30 **Seni G**, Elder JF. Ensemble Methods in Data Mining: Improving Accuracy Through Combining Predictions. In: Synthesis Lectures on Data Mining and Knowledge Discovery. Germany: Springer, 2010
31 **Yang T**, Zhang L, Yi L, Feng H, Li S, Chen H, Zhu J, Zhao J, Zeng Y, Liu H. Ensemble Learning Models Based on Noninvasive Features for Type 2 Diabetes Screening: Model Development and Validation. *JMIR Med Inform* 2020; **8**: e15431 [PMID: 32554386 DOI: 10.2196/15431]
32 **Boehm KM**, Aherne EA, Ellenson L, Nikolovski I, Alghamdi M, Vázquez-García I, Zamarin D, Long Roche K, Liu Y, Patel D, Aukerman A, Pasha A, Rose D, Selenica P, Causa Andrieu PI, Fong C, Capanu M, Reis-Filho JS, Vanguri R, Veeraraghavan H, Gangai N, Sosa R, Leung S, McPherson A, Gao J; MSK MIND Consortium, Lakhman Y, Shah SP. Multimodal data integration using machine learning improves risk stratification of high-grade serous ovarian cancer. *Nat Cancer* 2022; **3**: 723-733 [PMID: 35764743 DOI: 10.1038/s43018-022-00388-9]
33 **Iseke S**, Zeevi T, Kucukkaya AS, Raju R, Gross M, Haider SP, Petukhova-Greenstein A, Kuhn TN, Lin M, Nowak M, Cooper K, Thomas E, Weber MA, Madoff DC, Staib L, Batra R, Chapiro J. Machine Learning Models for Prediction of Posttreatment Recurrence in Early-Stage Hepatocellular Carcinoma Using Pretreatment Clinical and MRI Features: A Proof-of-Concept Study. *AJR Am J Roentgenol* 2023; **220**: 245-255 [PMID: 35975886 DOI: 10.2214/AJR.22.28077]

34 **Korfiatis P**, Suman G, Patnam NG, Trivedi KH, Karbhari A, Mukherjee S, Cook C, Klug JR, Patra A, Khasawneh H, Rajamohan N, Fletcher JG, Truty MJ, Majumder S, Bolan CW, Sandrasegaran K, Chari ST, Goenka AH. Automated Artificial Intelligence Model Trained on a Large Data Set Can Detect Pancreas Cancer on Diagnostic Computed Tomography Scans As Well As Visually Occult Preinvasive Cancer on Prediagnostic Computed Tomography Scans. *Gastroenterology* 2023; **165**: 1533-1546.e4 [PMID: 37657758 DOI: 10.1053/j.gastro.2023.08.034]



Published by **Baishideng Publishing Group Inc**
7041 Koll Center Parkway, Suite 160, Pleasanton, CA 94566, USA
Telephone: +1-925-3991568
E-mail: bpgoffice@wjgnet.com
Help Desk: https://www.f6publishing.com/helpdesk
https://www.wjgnet.com



© 2023 Baishideng Publishing Group Inc. All rights reserved.